

Editorial

Members and friends of the European Ceramic Society will wish to give particular thanks to Dr G. N. Babini for his many contributions during the years of his office as President. Dr Babini and colleagues from the Italian Ceramic Society have given particular emphasis to widening the set of activities within the European Ceramic Society to include educational work in ceramics (with Professor Desmaison as the Chair of the Working Group), the coordination of research and development activity in ceramics (with Professor Freer as Chair of the Working Group) and other activities including industrial, publications and communications issues. There is no doubt that the Society will take on added life as a consequence of these initiatives.

It is important also to recognise the vigour and effectiveness of Italian colleagues and notably of Dr Bellosi as the Conference Chair in organising the Fourth European Ceramic Society Conference at Riccione (Italy) in the first week of October 1995. The meeting was impressive for its programme, for its wide level of participation and, not least, for the unfailing courtesies extended to visitors by the hosts. In this regard the Conference continued the tradition so well established in Maastricht, in Augsburg and in Madrid.

In line with the constitution of the Society, the Presidency has now passed from Dr Babini to Professor J. F. Baumard (Groupe Français de la Céramique) and all members of the Society will, in thanking Dr Babini, wish to give every support to Professor Baumard for the period of his office. The 1997 meeting of the Society will be held in Versailles, France, from 22–26 June 1997.

The 1995 meeting saw a growth in the number of member countries within the European Ceramic Society and steps will be taken in the coming months to ensure full representation of these countries on the Editorial Board of the Journal. In this way, participation will be extended to Denmark, to Hungary, to Latvia, to Rumania, to the Slovak Republic and to Turkey.

Recognising the full international standing of the Society, attention has been again given to the issue of abstracts and to the language in which they appear. As indicated in an earlier Editorial, the former practice of publishing each abstract in English, French and German did incur substantial delay in the appearance of papers as a consequence of the required translation. Following responses to the earlier Editorial and in particular a suggestion made by Professor Grittner, the Council of the Society has now decided to adopt an arrangement whereby the abstract to a paper will be published in English and, optionally, in one other European language where this is the wish of the author or authors and where the two abstracts are provided with the manuscript. It is hoped that this arrangement can reflect the wishes of contributors to the Journal and that it can reinforce the value of the publication to all those in its audience.

Richard Brook
Editor

Model Experiments Concerning Abnormal Grain Growth in Silicon Nitride

Wolfgang Dressler,^{a*} Hans-Joachim Kleebe,^{b†} Michael J. Hoffmann,^a Manfred Rühle^b & Günter Petzow^a

^aMax-Planck-Institut für Metallforschung, Institut für Werkstoffwissenschaft, Pulvermetallurgisches Laboratorium, Heisenbergstr. 5, D-70569 Stuttgart 80, Germany

^bMax-Planck-Institut für Metallforschung, Institut für Werkstoffwissenschaft, Seestraße 92, D-70174 Stuttgart 1, Germany

(Received 30 December 1994; accepted 9 September 1995)

Abstract

*Model experiments were designed to study abnormal grain growth in Si_3N_4 -based ceramics. Experiments relating inhomogeneous crystalline secondary-phase distribution to exaggerated grain growth conclusively showed that abnormal grain growth is not governed by secondary-phase distribution, because a rapid homogenization of locally formed liquid occurs via capillary forces. Further investigations were focussed on intrinsic properties of the α - Si_3N_4 -starting powders. The influence of: (i) β - Si_3N_4 -grain morphology; (ii) β - Si_3N_4 -nuclei density, and (iii) β - Si_3N_4 -grain-size distribution of the powder blends on microstructural development were analyzed. The results revealed that a large basal plane of β - Si_3N_4 seeds energetically and kinetically favours grain growth. However, this effect is only partly responsible for abnormal grain growth. The formation of elongated Si_3N_4 grains, such as in *in situ* reinforced Si_3N_4 materials, strongly depends on the amount and grain-size distribution of β - Si_3N_4 nuclei present in the α - Si_3N_4 -starting powder.*

1 Introduction

Silicon nitride-based ceramics exhibit excellent mechanical and thermo-mechanical properties. However, potential engineering application is strongly limited owing to their given brittleness, i.e. their low fracture toughness.^{1,2} A number of research activities focussed on the study of possible toughening mechanisms in ceramic materials.^{3–14}

*Now at Technische Hochschule Darmstadt, Fachbereich Materialwissenschaft, Fachgebiet Disperse Feststoffe, Hilpertstraße, 31/D, D-64295 Darmstadt, Germany.

†Now at Universität Bayreuth, Lehrstuhl für Keramik und Verbundwerkstoffe, Ludwig Thoma Straße 36 B, D-95440 Bayreuth, Germany.

Investigations on the reinforcement of monolithic ceramic matrices by incorporation of discontinuous secondary phases, such as metallic particles, SiC whiskers or platelets, have provided some basic understanding of the complex crack/microstructure interaction.^{15,16} The observed increase in fracture resistance was mainly attributed to crack deflection and crack bridging mechanisms.^{1,2,17,18} In some cases crack branching was also observed.¹⁹ However, reinforcing ceramic matrices with secondary phases may also limit the applicability of such composites, in particular, because the achieved toughness improvement can be limited: (i) to relatively low service temperatures; (ii) by an anisotropic toughness within the composite or (iii) difficulties during densification. Therefore, one of the most promising toughening strategy is the reinforcement by elongated Si_3N_4 grains, grown *in situ* in a fine-grained Si_3N_4 matrix.^{20–22} This would result in a highly isotropic toughness up to high service temperatures and no restricted densification, provided that densification to closed porosity (about 94% theoretical density) can be completed before exaggerated *in situ* growth of β - Si_3N_4 grains takes place. A number of studies were reported on the observation of abnormal grain growth in Si_3N_4 ceramics prepared with various metal-oxide additions and densified by different processing techniques.^{23–25} In these investigations a correlation between resulting fracture toughness and the morphology of β - Si_3N_4 grains was found. In particular, a higher aspect ratio as well as a higher grain diameter yields an improved fracture resistance.^{26,27} It was recently reported that the same toughening effect applies for liquid-phase sintered SiC ceramics with *in situ* grown large α -SiC particles embedded in a fine grained matrix.^{28–30} It should be noted that the strength of *in situ* toughened, completely densified Si_3N_4 ceramics can be limited by the occurrence of large

β - Si_3N_4 grains, since they may act as crack initiation sites.²⁵

The observation of exaggerated grain growth and its relation to improved fracture resistance in Si_3N_4 ceramics is well established. However, only limited studies are reported on the effect of intrinsic β - Si_3N_4 -grain characteristics on microstructural variations upon densification.²²⁻²⁷ No model experiments, verifying possible parameters affecting exaggerated grain growth, have been reported to date. Therefore, this paper is based on model experiments designed to study abnormal grain growth in Si_3N_4 ceramics. Apart from a model proposed for the inhomogeneous distribution of crystalline secondary phases enhancing grain growth, the intrinsic properties of the Si_3N_4 -starting powders were investigated. In this context, the influence of the β - Si_3N_4 -grain morphology, the β - Si_3N_4 -nuclei density, and the β - Si_3N_4 grain-size distribution within the starting powder blends on exaggerated grain growth are discussed.

2 Experimental Procedures

2.1 Inhomogeneous distribution of crystalline secondary phases

Post-sintered reaction bonded Si_3N_4 material (SRBSN), containing approximately 20–25 vol% of elongated β - Si_3N_4 particles in the microstructure, was processed. The Si-powder blend, containing 5 wt% Y_2O_3 + 1 wt% Al_2O_3 (Y/Al) as sintering aids, was dry milled in a planetary mill. The Si-powder compacts were prepared by uniaxial die-pressing and subsequent cold isostatic pressing at 630 MPa. All powder compacts were nitrided subject to a heating-rate of 6°C/h, a maximum temperature of 1420°C, a nitridation atmosphere of 90 vol% N_2 and 10 vol% H_2 , a gas pressure of 950 mbars and a nitriding time of 120 h. Post-densification involved a two-step gas-pressure sintering cycle: 1875°C, 90 min at 0.5 MPa N_2 and 1920°C, 60 min at 10 MPa N_2 . The microstructure evolution and, in particular, the formation of crystalline secondary phases were studied by X-ray diffraction at early stages of nitridation. In addition, nitrided samples as well as materials processed by deliberately interrupting the sintering cycle at intermediate temperatures of 1550, 1650, 1750, and 1850°C were studied by SEM and TEM. Secondary phase identification was performed by both X-ray diffraction and electron diffraction (during TEM observations). Microstructure characterization of the materials prepared by model experiments, described below, was performed using optical microscopy.

2.1.1 Model experiment using an embedded, pre-synthesized crystalline phase

Additive doped (24.1 wt% Yb_2O_3 + 0.5 wt% Al_2O_3) silicon nitride powder compacts (UBE-SN-E10, further designated as E10; β = 4.1%) with embedded crystalline Ca-stabilized Yb-apatite- ($\text{Yb}_9\text{Ca}(\text{SiO}_4)_6\text{ON}$) as well as Yb-silicate-phases ($\text{Yb}_2\text{Si}_2\text{O}_7$) were produced by cold isostatic pressing at 630 MPa. Yb-apatite- and Yb-silicate-powders were received by precipitation of $\text{Yb}(\text{OH})_3$ onto SiO_2 (formation of Yb-silicate) or SiO_2 and Si_3N_4 (formation of Yb-apatite) from an alkaline (pH = 11) 0.5 molar $\text{Yb}(\text{NO}_3)_3$ solution and subsequent calcination at 800°C according to Gröbner.³¹ The crystallization of the cold isostatically pressed (55 MPa) powder compacts was performed at 1600°C, 1 h at 0.1 MPa N_2 (Yb-apatite) and 1400°C, 14 h in air ($\text{Yb}_2\text{Si}_2\text{O}_7$). The model specimens, consisting of a Si_3N_4 powder compact which contained a crystalline secondary-phase core, were subjected to a heat treatment at 1700°C for a period of 1 h under 0.1 MPa N_2 .

2.1.2 Model experiment preparing a sandwich specimen

A sintered (1780°C, 50 min, 0.1 MPa N_2 + 10 min, 1.6 MPa N_2) additive containing (10.7 wt% Y_2O_3 + 3.6 wt% Al_2O_3) Si_3N_4 specimen was cut into three plates (SN1, SN2, SN3). $\text{Y}_2\text{Si}_2\text{O}_7$ -powder was produced by ultrasonic mixing of Y_2O_3 and SiO_2 in n-hexan for 5 min. After cold isostatic pressing (630 MPa) the powder compacts were crystallized in air using a heating time of 14 h and a maximum temperature of 1400°C. The crystalline $\text{Y}_2\text{Si}_2\text{O}_7$ -silicate (YS) was arranged between two dense Si_3N_4 slabs (SN1, SN2) of the pre-sintered material. This sandwich specimen and, as a reference, the third Si_3N_4 -plate (SN3) were heat treated for 1 h at 1800°C under a nitrogen pressure of 0.1 MPa.

2.2 Influence of β - Si_3N_4 particle morphology

An α -rich Si_3N_4 powder (UBE-SN-ESP, further designated as ESP; α > 97%), attrition milled with 11.5 wt% Y_2O_3 + 2.9 wt% Al_2O_3 used as sintering aids, was subsequently doped with 5 vol% β - Si_3N_4 whiskers (UBE-SN-WB) and mixed in a roller mill, in order to avoid extensive whisker damage during processing. Powder compacts were prepared via cold-isostatic pressing at 630 MPa. After densification of these powder blends via gas-pressure sintering (1930°C, 1 h at 10 MPa N_2) polished and plasma-etched specimen surfaces were investigated by SEM.

2.3 Effect of initial β - Si_3N_4 nuclei density and grain-size distribution

Two α -rich Si_3N_4 powders (E10 and ESP) doped with various amounts of equiaxed β - Si_3N_4 nuclei

Table 1. Powder characteristics of the Si_3N_4 -starting powders and powder blends. The β - Si_3N_4 content and β -crystallite radius of the powder mixtures are calculated using the rule of mixture

Powder	β -content (vol %)	β -crystallite- radius (μm)	Denka powder content (vol %)	Nuclei density ($N/\mu\text{m}^3$)
UBE-SN-ESP (ESP)	3	0.10	0	6.5
UBE-SN-E10 (E10)	4.1	0.06	0	40.8
Denka	97.5	0.14	0	76.3
Denka/ESP 4/96	6.8	0.10	4	9.3
Denka/ESP 8/92	10.6	0.10	8	12.1
Denka/E10 4/96	7.8	0.06	4	42.2
Denka/E10 20/80	22.8	0.08	20	48

(see Table 1), using a Denka starting powder with a β - Si_3N_4 content of approximately 97%, were applied to study the influence of initial β - Si_3N_4 content on the final microstructure by comparing the microstructural development of the doped and undoped powders. The β - Si_3N_4 content, as well as the crystallite size of the starting powders and mixtures, were determined by means of X-ray analysis applying a Seyffert powder diffractometer and the Scherrer equation, which correlates the peak broadening (β) with the crystallite radius (r). The instrumental peak broadening ($I = 0.1429^\circ$) was determined by measuring the peak width of the 111-peak of a stress free silicon single crystal. This results in the following equation:

$$r = \frac{1}{2} \cdot \frac{0.89 \cdot \lambda}{(\beta - I) \cdot \cos \theta} \quad (1)$$

where λ is the wave length of the X-ray radiation ($\lambda = 154.056 \text{ pm}$) and θ is the peak position. The evaluation was performed by using the (210) α - Si_3N_4 reflection. Detailed sedimentation experiments of the used starting powders and X-ray analysis of the generated grain-size fractions, which were discussed in detail elsewhere,²⁵ revealed that the grain-size distributions of the α - and β -particles are similar. This enables the determination of the β - Si_3N_4 -crystallite size by measuring the average size of the α -crystals. Then the nuclei density, N , of the starting powders and mixtures can be calculated from:²⁵

$$N = \frac{3}{4 \cdot 10^4 \cdot \pi} \cdot \sum_i \frac{\beta_i \cdot A_i}{r_{\beta_i}^3} \quad (2)$$

In this equation β_i is the volume fraction of β - Si_3N_4 , A_i the Si_3N_4 -content (vol%) and r_{β_i} the β -crystallite size of the participating starting powders. The powder characteristics are summarized in Table 1. Densification was achieved by adding 10 vol% sintering aids ($\text{Y}_2\text{O}_3 + \text{Al}_2\text{O}_3$) either by gas pressure sintering (1950°C, 1 h at 10 MPa N_2) or by pressureless sintering (1780°C, 20 min at 0.1 MPa N_2) in a graphite resistance furnace.

2.4 Microstructural characterization

The overall microstructure of the materials was investigated by optical microscopy, scanning electron microscopy (SEM), and transmission electron microscopy (TEM). SEM investigations were performed using polished and subsequently plasma-etched surfaces of the consolidated materials. TEM foils were prepared following standard techniques, which involve grinding, dimpling, and ion thinning to electron transparency. The TEM foils were finally coated with a light carbon film to reduce charging under the electron beam.

Quantitative microstructural evaluation was performed using a semi-automatic image analyser of Imtronic (Computer-Vertriebs-Union, Berlin). This PC operated apparatus enables not only the automatic and interactive reconstruction of the grain boundary network but also the measurement of the minimum and maximum Ferret-diameter of each reconstructed grain. This analysis provides the 2-dimensional length/aspect-ratio distribution of the observed microstructure. In order to get sufficient statistical reliability at least 2000 grains of the quantitative analysed microstructures were measured. Owing to the fact that the known toughening models are based on the real 3-dimensional particle parameters, the 3-dimensional length/aspect-ratio distribution was calculated by means of a novel computer program (for further details see Refs 25 and 32).

3 Results

3.1 Inhomogenous distribution of crystalline secondary phases

Low magnification SEM and TEM studies of the Y/Al-doped material after nitridation, but before final densification, revealed crystalline secondary phases in the RBSN. Additional X-ray diffraction analysis parallel to electron diffraction studies on these phases indicated the formation of H-phase, $\text{Y}_5(\text{SiO}_4)_3\text{N}$, at an early stage of nitridation (see Fig. 1). After consolidation, the material exhibited

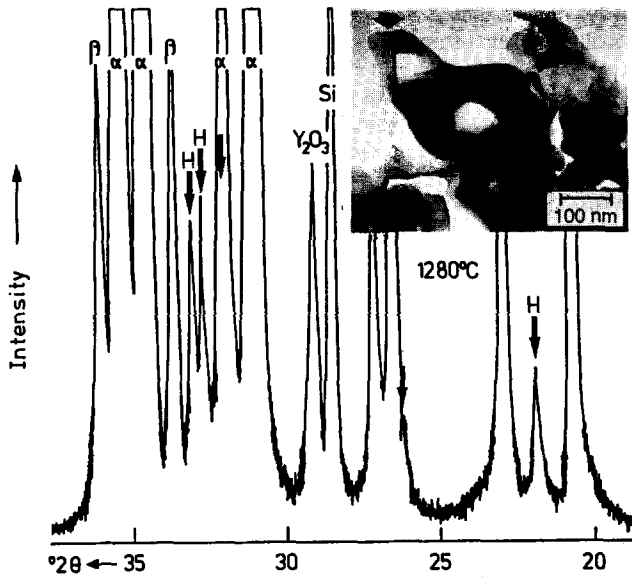


Fig. 1. X-ray diffraction pattern of the Y/Al-doped RBSN material revealing the H-phase formation at an early stage of nitridation (nitriding temperature = 1280°C). The inset shows a TEM bright-field image of the H-phase in the nitrided sample (RBSN).

an overall microstructure consisting of about 20–25% by volume of large elongated β - Si_3N_4 grains embedded in a fine-grained matrix, as depicted in Fig. 2. Crystalline secondary phases were present at triple-grain junctions. During SEM observations of Y/Al-fluxed materials, obtained by interrupting the gas-pressure sintering cycle at temperatures of 1550, 1650, and 1750°C, only homogeneous, fine-grained silicon nitride particles were evident. However, the onset of the formation of elongated silicon nitride grains was observed at higher sintering temperatures $\geq 1850^\circ\text{C}$. This result is consistent with findings from Mitomo *et al.*,²⁷ who reported the onset of abnormal grain growth at about 1850°C. The experimental results regarding the microstructural development, based on SEM and TEM observations, suggest a growth mechanism schematically depicted in Fig. 3.

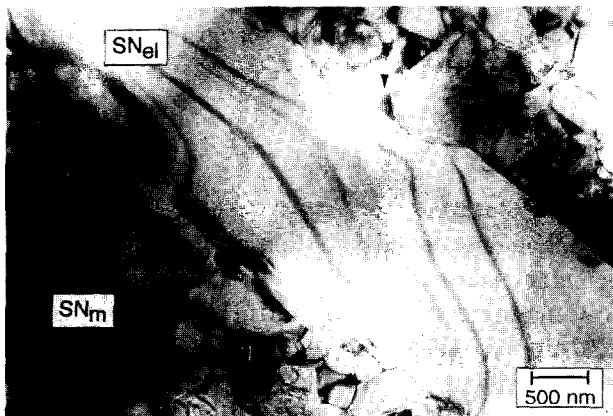


Fig. 2. Low magnification TEM bright-field image of Y/Al-containing SRBSN showing elongated β - Si_3N_4 grains (SN_{el}) in a fine-grained β - Si_3N_4 matrix (SN_m). The darker regions in the image correspond to the crystalline secondary phase located at multi-grain junctions.

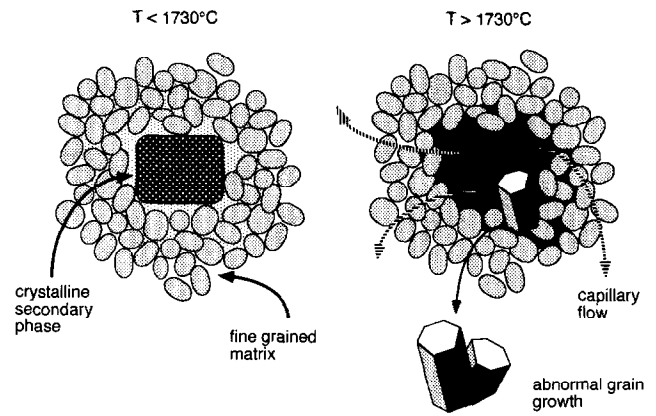


Fig. 3. Schematic illustration of the proposed mechanism of the elongated-grain formation for an inhomogeneous distribution of crystalline secondary phases.

In the proposed model it is assumed that metastable crystalline secondary phases, revealing a high thermal stability field,^{33,34} are already formed at an early stage of densification. The assumption is supported by the X-ray diffraction findings at temperatures as low as 1280°C (see also Fig. 1). During subsequent sintering, these phases remain stable up to their melting point, while the eutectic liquid has already formed at a lower temperature and facilitates initial densification. The eutectic temperature in the SiO_2 - Si_3N_4 - Y_2O_3 ternary system lies at 1550°C (filled triangle in the phase diagram shown in Fig. 4).^{35,36} The eutectic temperature, however, is lower owing to the Al_2O_3 -content of the Si-starting powder blend. With increasing temperature, dissolution/precipitation occurs simultaneously with the α/β - Si_3N_4 -phase transformation, which is complete at about 1650°C for these materials. At 1630°C (cross-section of the phase diagram in Fig. 4), the secondary H-phase is still crystalline. Even at 1730°C (dashed line in the diagram), this phase still lies

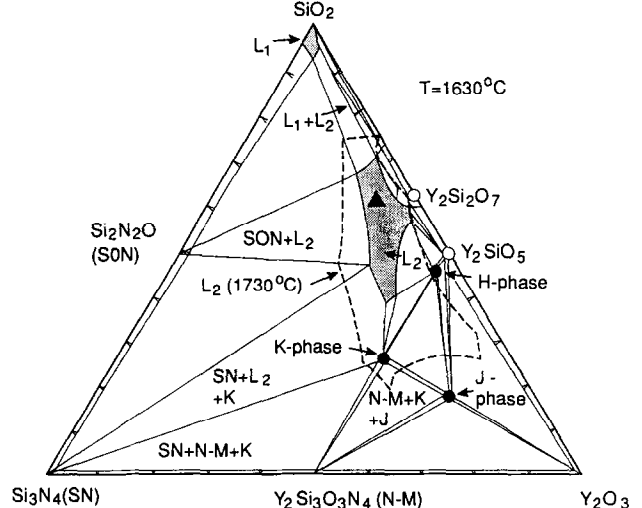


Fig. 4. Phase diagram for the Y_2O_3 - Si_3N_4 - SiO_2 system indicating the H-phase.^{35,36}

outside the liquid phase field. It is thought that the crystalline secondary phase only melts at higher sintering temperatures, forming excess liquid. This excess liquid is inhomogeneously distributed over the entire sample, owing to the inhomogeneous distribution of crystalline secondary phase at lower sintering temperatures, which is thought to initiate both increased densification and the onset of abnormal grain growth. A strong increase in densification rate at temperatures of about 1800°C was experimentally confirmed by dilatometer measurements during sintering. Moreover, the formation of large, elongated $\beta\text{-Si}_3\text{N}_4$ grains, randomly oriented in the sintered body, was also reported.³⁶ It is thought that some of the excess liquid will progress through the RBSN pore channels by capillary forces and simultaneously permit densification, but it is presumed in this model that excess liquid remains at the site containing the original metastable Y–Si–oxinitride phase. This liquid would act as a flux for the rapid growth of highly-elongated $\beta\text{-Si}_3\text{N}_4$ grains by a dissolution–reprecipitation process.

The proposed model is based on two requirements. Firstly, upon liquid formation the wetting liquid should not be drawn completely out of the central reservoir into the surrounding porous RBSN matrix. This situation could arise if the volume of liquid exceeds the porosity in the RBSN and also, if densification occurs simultaneously with capillary extrusion. Secondly, exaggerated $\beta\text{-Si}_3\text{N}_4$ grain growth and elongation is required to occur at the liquid reservoir, whereas normal coarsening should prevail in the surrounding matrix. To prove these requirements additional model experiments were designed.

3.1.1 Model experiment using an embedded pre-synthesized crystalline phase

In order to verify the model described above a large piece of pre-synthesized crystalline secondary phase (5 mm in diameter) was embedded in a Si_3N_4 -powder compact and subsequently consolidated, as schematically depicted in Fig. 5. It was

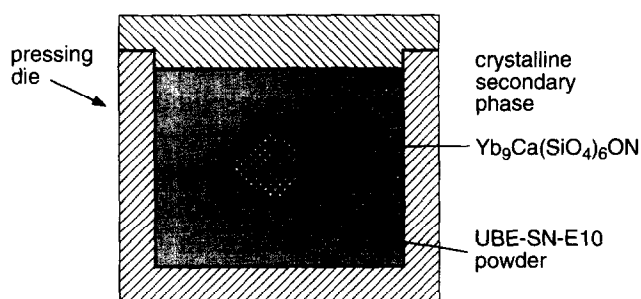
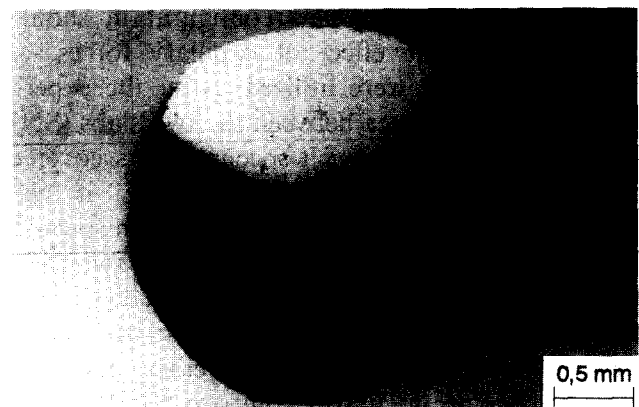
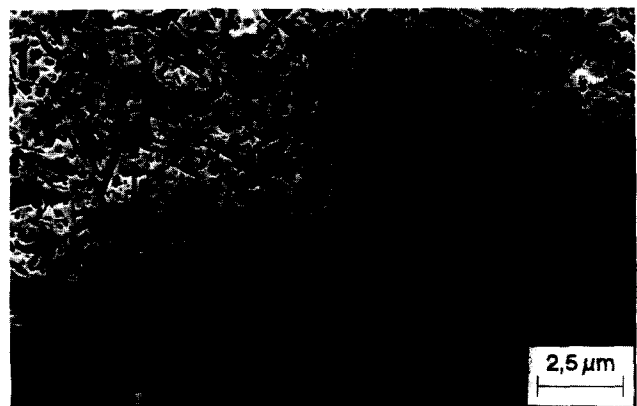


Fig. 5. Schematic illustrating the cold-isostatic pressing arrangement of silicon nitride green bodies with an embedded crystalline secondary phase.

expected that in the region around the embedded crystalline secondary phase, or at the secondary phase/matrix interface, a high amount of excess liquid was formed during sintering, which would strongly enhance abnormal grain growth. However, optical and scanning electron microscopy on cross-sections of the samples revealed an unexpected result, as shown in Fig. 6. In the case of the Yb–silicate ($\text{Yb}_2\text{Si}_2\text{O}_7$) containing material, a large pore, containing a small pocket of residue secondary phase, had formed at the site of the formerly embedded pre-synthesized crystalline secondary phase (Fig. 6 (a)). This seemingly suggests that the excess liquid was nearly completely drawn from the central reservoir into the bulk material upon sintering. A closer inspection of the boundary between the residue secondary phase and the Si_3N_4 -bulk (compare Fig. 6 (b)) gave no evidence for enhanced exaggerated grain growth in this region. The apatite ($\text{Yb}_9\text{Ca}(\text{SiO}_4)_6\text{ON}$) containing material revealed a similar behaviour. The secondary phase was completely drawn into the bulk and no abnormal grain growth was observed. Hence, it is concluded that, in the present model



(a)



(b)

Fig. 6. Secondary phase containing specimen (compare Fig. 5) after heat treatment (1700°C , 1 h, 0.1 MPa N_2). (a) Optical micrograph showing the residue secondary phase pocket (white), the Si_3N_4 bulk material (gray), the formed hole (black), and a thin film of embedding material (dark gray). (b) SEM micrograph of the boundary between the secondary phase and the bulk material showing no abnormal grain growth.

experiments, high capillary forces were responsible for an homogeneous distribution of the excess liquid phase throughout the samples, which resulted in microstructures indistinguishable from materials sintered without the incorporation of crystalline phases. The main difference between the inhomogeneities (excess liquid) formed during post-sintering of reaction-bonded Si_3N_4 (see section 3.1) and the liquid generated in the present model specimens is that at the beginning of the sintering process the deliberately created inhomogeneities are surrounded by a highly porous Si_3N_4 -powder compact. Therefore, a second model experiment was designed to minimize the porosity effect.

3.1.2 Model experiment preparing a sandwich specimen

In order to suppress the influence of high capillary forces, a sandwich specimen was prepared using a dense Si_3N_4 slab with the pre-synthesized crystalline secondary phase and another dense Si_3N_4 slab on top, as schematically shown in Fig. 7. This sandwich and the reference (SN3) were heated above the melting temperature of the crystalline secondary phase and a cross section of the joined sample was prepared. This configuration should greatly reduce the effect of capillary forces, as dense Si_3N_4 slabs were utilized. After the experiment, the contact area between the two slabs (SN1 and SN2) of the sandwich specimen was covered with a secondary phase film. Hence, it was thought that enhanced abnormal grain growth would occur at the interface between the two slabs and the interlayer. SEM microscopy studies of the cross sections, however, revealed that the microstructural development of the model specimen and the reference are identical (compare Fig. 8 (a and b)). No pronounced exaggerated grain growth was observed.

Diffusion processes along the interface led to a uniform distribution of the secondary phase between the two Si_3N_4 -slabs at the applied sintering temperatures, where all secondary phase present in the system is thought to be liquid. The reported results clearly exclude the initially proposed effect of inhomogeneously distributed crystalline secondary phases on abnormal grain growth in Si_3N_4

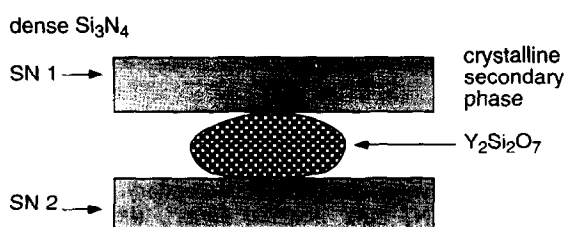


Fig. 7. Schematic showing the sandwich specimen before sintering.

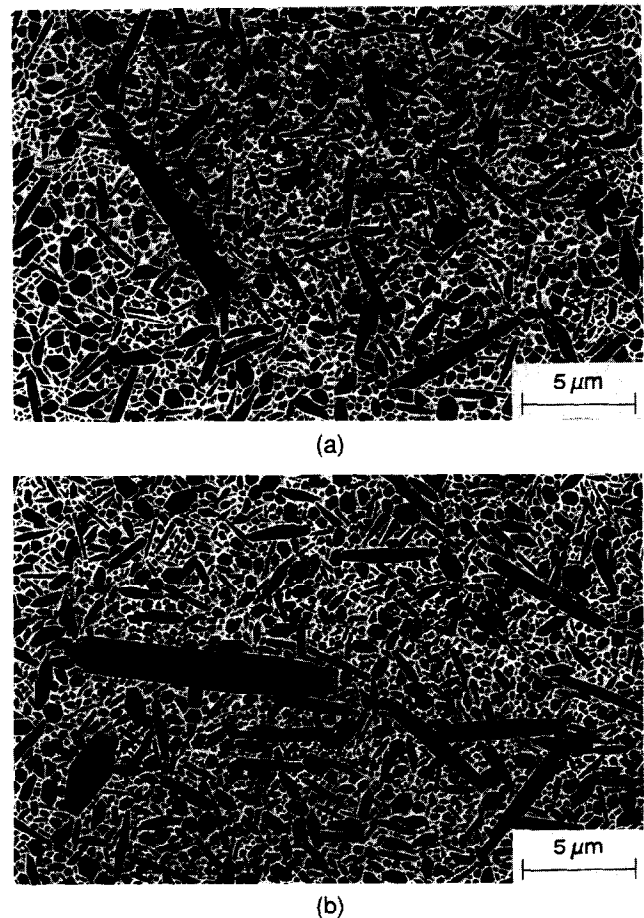


Fig. 8. Microstructures of (a) the sandwich specimen (directly at the edge where the material was in contact with the secondary phase) and (b) reference specimen after a heat treatment at 1800°C for a period of 1 h under 0.1 MPa N_2 . The SEM micrographs show no significant difference in grain-size distribution. This suggests that an inhomogeneous distributed liquid phase does not cause abnormal grain growth.

materials. Accordingly, the development of exceptionally large grains has to be due to intrinsic powder properties such as the α/β - Si_3N_4 -content and grain-size distribution as well as the β -nuclei morphology, which is discussed in the following sections.

3.2 Influence of β - Si_3N_4 particle morphology

The influence of the intrinsic morphology of β - Si_3N_4 particles present in the starting powder on the microstructural development of gas-pressure sintered materials was studied. An α -rich Si_3N_4 powder was therefore doped with 5 vol% β - Si_3N_4 whiskers. After densification of the powder blend, the microstructure of the consolidated material was investigated by optical microscopy and SEM on polished and plasma-etched specimen surfaces. Plasma etching is a very sensitive technique regarding small chemical changes in the material. The etching rate strongly depends on the Al-content of the Si_3N_4 grains; a higher Al-concentration in the solid solution results in a lower plasma-etching rate.

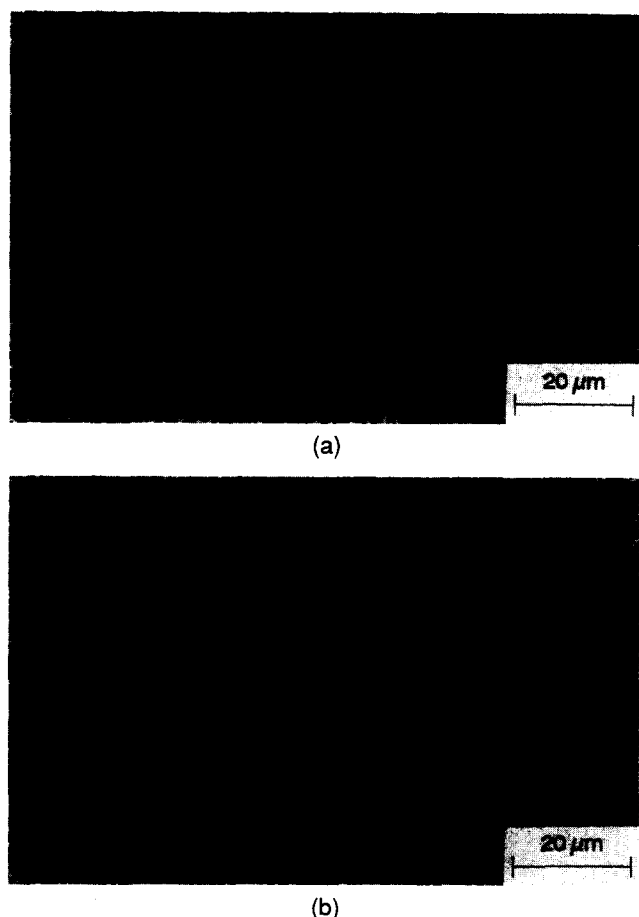


Fig. 9. Influence of powder morphology on microstructural development. Microstructures of (a) $\beta\text{-Si}_3\text{N}_4$ whisker doped and (b) undoped UBE-SN-ESP materials after gas pressure sintering (1930°C, 60 min, 10 MPa N_2).

Figure 9 shows the microstructures of the $\beta\text{-Si}_3\text{N}_4$ whisker doped (a) and the undoped (b) ceramics. The $\beta\text{-Si}_3\text{N}_4$ whisker containing material possesses a significantly greater number of large elongated grains, which have a deeper etched core surrounded by a rim structure. Analytical TEM-measurements reveal that the core is Al free while the rim structure contains, apart from Si and N, additional Al and O (Fig. 10 (a and b)). These findings and the fact that the observed cores are elongated and aligned parallel to the length direction of the abnormally grown crystals (Fig. 11) suggest that the Al-containing outer region of the large elongated $\beta\text{-Si}_3\text{N}_4$ grains grew epitaxially on the starting Al-free $\beta\text{-Si}_3\text{N}_4$ whiskers. Owing to the kinetic growth advantage of the basal plane compared to the prism planes in Si_3N_4 crystals,^{37,38} the whiskers revealed a higher growth rate in length direction rather than in width upon sintering. The aspect ratio of the epitaxially grown region (excluding the core) of the large β -crystal shown in Fig. 11 (a) amounts to about 23. In contrast to this, the aspect ratio of the initial $\beta\text{-Si}_3\text{N}_4$ nuclei runs to about 4.5. In comparison to the more globular, equiaxed $\beta\text{-Si}_3\text{N}_4$ grains present in the

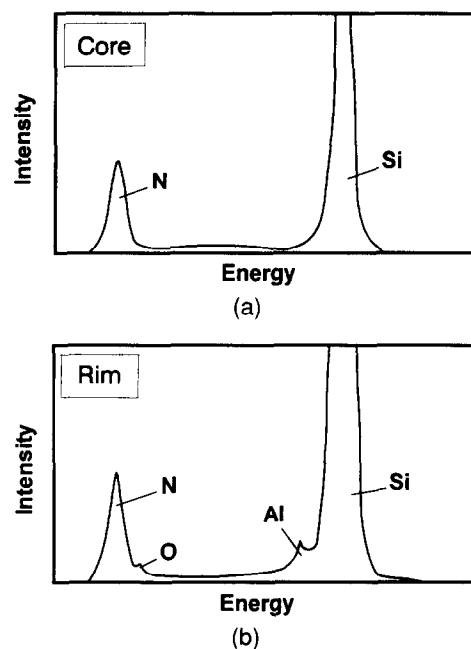


Fig. 10. EDX-analysis (TEM) of an elongated large $\beta\text{-Si}_3\text{N}_4$ -crystal in the $\beta\text{-Si}_3\text{N}_4$ whisker doped material consisting of (a) an Al-free core and (b) an Al-containing rim structure (see also Fig. 11(b)).

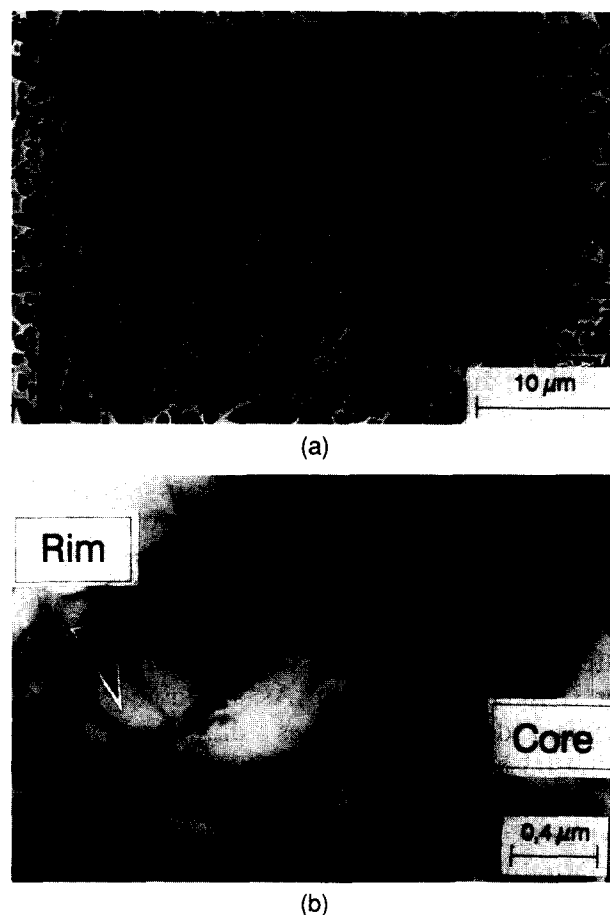


Fig. 11. (a) SEM-micrograph of a large $\beta\text{-Si}_3\text{N}_4$ -grain possessing a deeper etched core (Al-free) having an aspect ratio of 4.5 and a rim structure with an aspect ratio of 23. (b) TEM-micrograph of a $\beta\text{-Si}_3\text{N}_4$ -crystal with an elongated core-structure.

starting powder, the added whiskers showed, right from the beginning of sintering, a relatively high growth rate of the basal planes and, hence,

exhibited very large grains ($> 50 \mu\text{m}$) with high aspect ratios (up to 15). It is important to note that the initially elongated shape of the whiskers remains during the α - β -transformation and the following grain coarsening. The results seemingly suggest that it is possible to directly influence the resulting microstructure via the morphology of the pre-existing β - Si_3N_4 nuclei, as the morphology of whisker-like particles is preserved during consolidation.

3.3 Effect of initial β - Si_3N_4 nuclei density and β - Si_3N_4 grain-size distribution

Two α -rich Si_3N_4 powders (E10 and ESP), doped with various amounts of equiaxed β - Si_3N_4 nuclei, using a Denka starting powder with a β - Si_3N_4 content of approximately 97%, were utilized to study the influence of initial β - Si_3N_4 content on the final microstructure.

In the case of α -rich ESP powders the β - Si_3N_4 doping results in a grain refinement, because the number of grains per unit area raises from $0.56 \text{ N}/\mu\text{m}^2$ for the undoped specimen to $0.72 \text{ N}/\mu\text{m}^2$ and $0.86 \text{ N}/\mu\text{m}^2$ by increasing the amount of β -nuclei from $6.5 \text{ N}/\mu\text{m}^3$ (undoped) to $9.3 \text{ N}/\mu\text{m}^3$ and $12.1 \text{ N}/\mu\text{m}^3$ in the starting powder, as can be seen from Table 1 and Fig. 12. It is important to note that the average crystallite size of the α - (ESP: $r = 0.10 \mu\text{m}$) and the added β -powder (Denka: $r = 0.14 \mu\text{m}$) are in the same order of magnitude. This result is consistent with investigations reported by Iskoe *et al.*,³⁹ who assumed that the dissolution of β - Si_3N_4 during densification is negligible.

In contrast to the results of the ESP material (grain refinement), SEM analysis of polished and plasma-etched surfaces of the E10-specimens show a coarsening of the general microstructure with increasing β - Si_3N_4 -nuclei density, as can be seen from Fig. 13. Here, the added β - Si_3N_4 -nuclei (Denka) are about two times larger in size compared to the β -particles in the α -rich starting powder (E10: $r = 0.06 \mu\text{m}$). As a consequence, the particle density decreases dramatically from 30.5 to $3.5 \text{ N}/\mu\text{m}^3$ by increasing the β -nuclei density from 40.8 to $76.3 \text{ N}/\mu\text{m}^3$. The size-shape histograms (weighted by volume) derived from quantitative microstructural analysis of Denka/E10-specimens reveal a decrease of the volume fraction of grains having a length smaller than $0.5 \mu\text{m}$ from 11.5 vol% (E10) to 0.5 vol% (Denka) with increasing β - Si_3N_4 -content (see Fig. 14). Simultaneously, the mean grain length and grain diameter increases from 0.36 to $0.80 \mu\text{m}$ and from 0.12 to $0.45 \mu\text{m}$, respectively. Additionally, low β -doping leads to an enhanced grain growth in the length direction, but to a decrease in aspect ratio

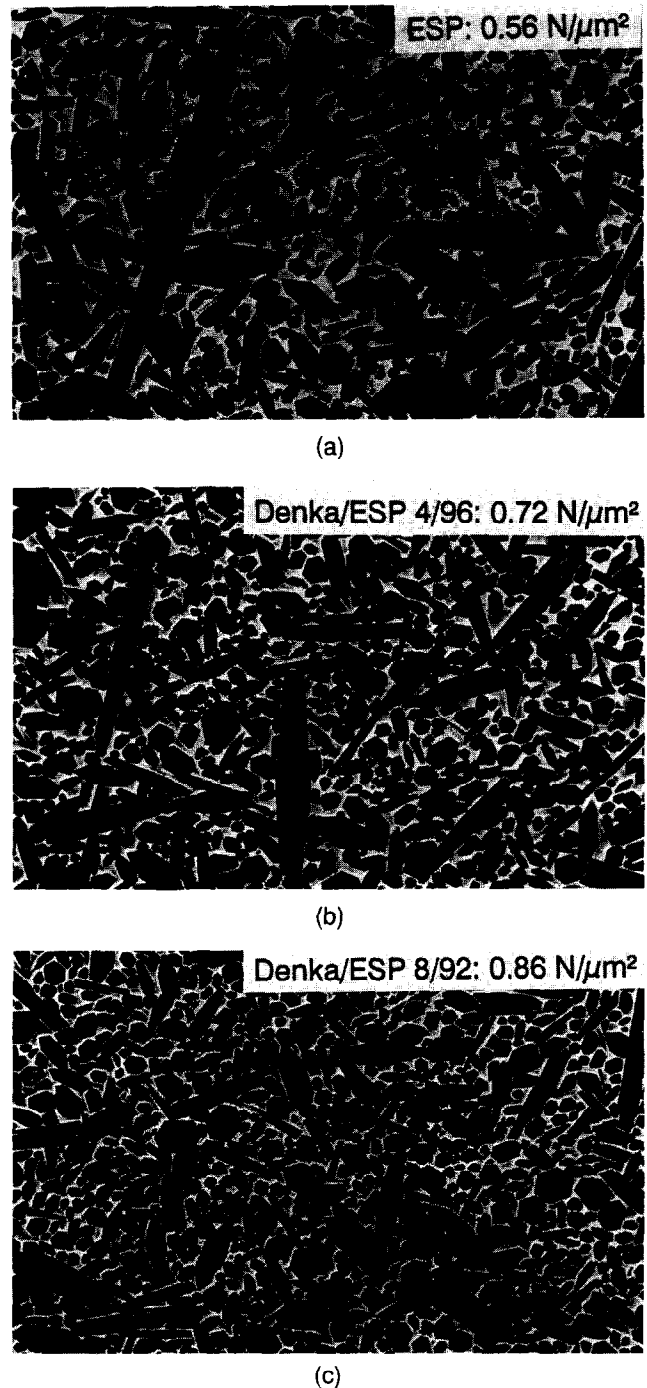


Fig. 12. Microstructure of gas pressure sintered (1950°C , 1 h, 10 MPa N_2) (a) undoped ESP; (b) Denka/ESP-mixture 4/96, and (c) Denka/ESP-mixture 8/92. The number of grains per unit area rises from (a) $0.56 \text{ N}/\mu\text{m}^2$ and (b) $0.72 \text{ N}/\mu\text{m}^2$ to (c) $0.86 \text{ N}/\mu\text{m}^2$ by increasing the amount of β -nuclei from (a) $6.5 \text{ N}/\mu\text{m}^3$ and (b) $9.3 \text{ N}/\mu\text{m}^3$ to (c) $12.1 \text{ N}/\mu\text{m}^3$ in the starting powder.

of the coarser grains (Denka/E10 4/96), owing to the initially large grain width of the added β -particles (Denka). Further addition of β -nuclei (Denka/E10 20/80) results in a reduction of the maximum grain length and aspect ratio. Utilizing pure β - Si_3N_4 (Denka) powder as starting material produces a homogeneous equiaxed microstructure possessing a low mean aspect ratio of 1.8 in comparison to specimens sintered from α -rich-powder (E10) which exhibited a mean aspect ratio of 2.7.

4 Discussion

4.1 Secondary phase inhomogeneities

The experimental results clearly showed that the formation of crystalline secondary phases at an early stage of sintering does not govern abnormal grain growth. It is concluded that high capillary forces draw the excess liquid into the bulk of the material, resulting in a higher densification rate and, as a consequence, in a uniform microstructure. No enhanced exaggerated grain growth was observed in either of the model experiments performed. Most importantly, the specimen containing a residue pocket of secondary phase after sintering (see Fig. 6) reveals no abnormal grain growth into the remaining glass pocket. The obtained microstructures after densification, utilizing pre-synthesized crystalline phases, were indistinguishable from the microstructures observed after sintering of common starting powder compacts.

4.2 Intrinsic powder properties

Since the generated secondary phase inhomogeneities do not cause the often observed abnormal grain growth, the intrinsic powder properties must be responsible for the exaggerated growth of individual crystals. The $\beta\text{-Si}_3\text{N}_4$ doping of α -rich powders on the one hand results in grain refinement if the dopant (Denka) possesses a comparable crystallite size to the α -rich matrix powder (ESP) and if the nuclei density is low (see Table 1

and Fig. 12). On the other hand, provided that the added β -nuclei (Denka) are larger than the β -particles in the α -rich powder (E10) and that the nuclei density is high, grain coarsening is observed (see Table 1 and Figs 13, 14), since the $\beta\text{-Si}_3\text{N}_4/\beta\text{-Si}_3\text{N}_4$ particle interaction is enhanced.

The results presented clearly revealed that, if the $\beta\text{-Si}_3\text{N}_4$ nuclei density reaches a certain value, depending on the grain-size distribution of the starting powder, a dissolution of the smaller $\beta\text{-Si}_3\text{N}_4$ particles is observed followed by a coarsening of the microstructure. These results can be explained using the model schematically shown in Fig. 15. In this diagram C_G^α and C_G^β represent the equilibrium concentrations of α - and β -particles in a

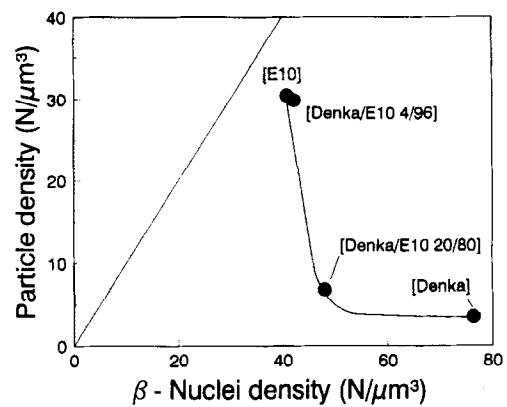


Fig. 13. Influence of β -nuclei density in the starting powder on particle density of sintered Si_3N_4 -ceramics. Within the dotted area the particle density is higher than the nuclei density. Since the investigated specimens are located outside the dotted area it is suggested that no nucleation takes place during sintering.

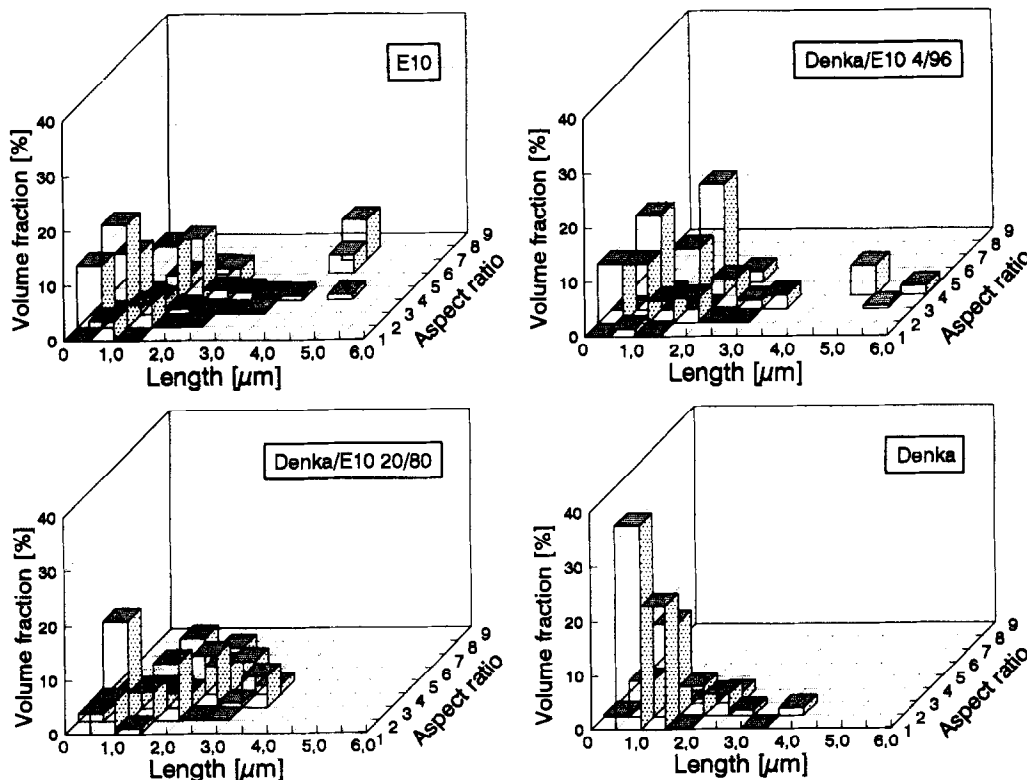


Fig. 14. Quantitative microstructural analysis of Denka/E10-composites with various ratios of mixture. (a) 0/100, (b) 4/96, (c) 20/80, and (d) 100/0.

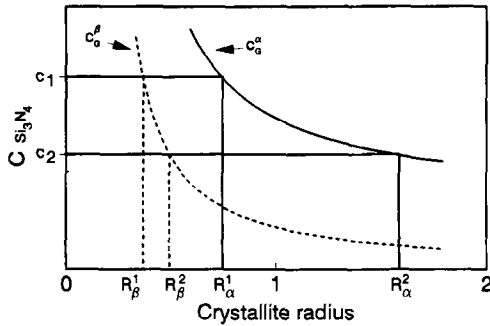


Fig. 15. Dependency of equilibrium concentrations of α - and β - Si_3N_4 modification on crystallite radius. If the Si_3N_4 -concentration in the liquid decreases from C_1 to C_2 the critical radii of dissolution increase from R_β^1 to R_β^2 and from R_α^1 to R_α^2 .

solvent. According to Wagner⁴⁰ these concentrations depend on the radius of the crystal (R), the surface energy σ , the temperature T as well as the constants C_0 and K , as summarized in the following equation:

$$C_G = C_0 \cdot \exp\left(\frac{\sigma}{R} \cdot \frac{K}{T}\right) \quad (3)$$

This relation has been derived by assuming a spherical shape of the examined particles. A deviation of the spherical morphology results in a different constant K , as calculated by Dressler.²⁵ Since the transformation enthalpy of the reaction $\alpha\text{-Si}_3\text{N}_4 \rightarrow \beta\text{-Si}_3\text{N}_4$ is negative, the equilibrium concentration of the α -phase, C_G^α , must be higher in comparison to C_G^β , as depicted in Fig. 15. C_1 and C_2 are arbitrary Si_3N_4 -concentrations in the liquid phase directly at the particle surface during the solution reprecipitation process, which causes the α/β -transformation as well as the grain coarsening. In the Ostwald Ripening model of Wagner⁴⁰ these concentrations depend on the particle dimension and the mean concentration of the solute, because the crystals in this model are isolated from each other and thus the concentration gradients do not overlap. In contrast to that, the solid phase fraction in our experiments is so high that the Si_3N_4 concentrations at the particle surfaces are controlled by the surrounding crystals and their size distribution. At a given Si_3N_4 -concentration in the liquid (C_1 or C_2) the radii $R_\beta^{1,2}$ and $R_\alpha^{1,2}$ are critical grain sizes, which means that all particles being smaller dissolve whereas larger crystals grow.

This model predicts the dissolution of small β -crystals if they are located within the diffusion gradient of a larger β -particle. For example: a small β -particle having a crystallite radius between R_β^1 and R_β^2 dissolves if the Si_3N_4 -concentration in the liquid phase directly at its surface is reduced from c_1 to c_2 due to the growth of an adjacent larger β -crystal. This condition is satisfied in the

case of the Denka/E10-specimens (see Figs 13 and 14). By adding the coarse β -rich Denka powder to the fine grained E10 the small β -nuclei of the E10-powder start to dissolve in an early stage of α/β -transformation owing to the increase of the critical radius of dissolution (R_β). In the case of the Denka/ESP-materials, the $\beta\text{-Si}_3\text{N}_4$ -nuclei density is lower and the added β -particles are of the same sizes. Thus, the probability that two β -crystals influence each other is lower and, due to the smaller size difference, the Denka β -grains cannot dissolve the ESP β -nuclei. Consequently, the particle density after sintering increases by raising the amount of β -particles in the starting powder, as depicted in Fig. 12, which leads to a grain refinement.

The increase in maximum particle length observed at low β -doping of E10-powder (see Fig. 14) as well as the globularization and the simultaneous decrease of the maximum grain length by further raising the $\beta\text{-Si}_3\text{N}_4$ -fraction can also be explained by this model. At low concentrations of coarse $\beta\text{-Si}_3\text{N}_4$ -particles (Denka/E10 4/96, see Table 1) these grains grow by dissolution of the surrounding α - and $\beta\text{-Si}_3\text{N}_4$ -crystals. If the amount of large β -grains is further increased (Denka/E10 20/80, see Table 1) growth in the length direction of the coarse particles is reduced due to steric hindrance. The effect of steric hindrance was shown by growth experiments performed by Krämer and Hoffmann.^{41,42} Moreover, large particles consume more material during grain growth in comparison to smaller crystals, which also causes a reduction in aspect ratio.

In Fig. 16 the abnormal grain growth of the whisker doped material (see also Fig. 11) is shown schematically. The exceptionally high growth rate in the c -direction is due to the large basal plane of the $\beta\text{-Si}_3\text{N}_4$ -whiskers. This large basal plane corresponds to a very low equilibrium concentration of

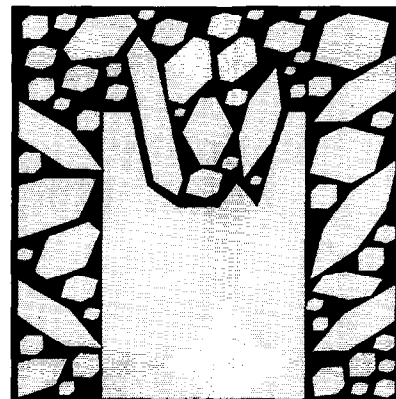


Fig. 16. Model of abnormal grain growth in Si_3N_4 -ceramics. The larger particles reduce the Si_3N_4 -concentration in front of their basal plane and thus dissolve smaller particles in growth direction. This enables abnormal grain growth of crystals possessing a large basal plane in comparison to the surrounding particles.

Si_3N_4 in the surrounding liquid phase (see Fig. 15). Therefore, close to the abnormal growing particles the critical radius of dissolution is extraordinarily high. This enables the very fast dissolution of adjacent smaller particles and the observed exceptionally high aspect ratio (23) of the rim structure grown during sintering.

The investigations unequivocally reveal that a broad β - Si_3N_4 -grain-size distribution in the starting powder causes exaggerated grain growth due to solution of α - as well as small β - Si_3N_4 -particles and reprecipitation onto larger β - Si_3N_4 -grains. Moreover, the morphology of the initially existing β -crystals also influences the resulting microstructure of the sintered ceramic. In addition, the effect of abnormal grain growth is enhanced by high sintering temperatures and long sintering times, as shown in earlier investigations.²⁵

5 Summary

Inhomogeneous distribution of crystalline secondary phases, formed at an early stage of consolidation, can lead to a local enrichment of the liquid phase during sintering at elevated temperatures. However, based on model experiments it can be concluded that crystalline secondary phases do not govern exaggerated grain growth, since a rapid homogenization of locally formed liquid occurs via capillary forces. A large basal plane of growing β -particles surrounded by smaller β -crystals or dissolving α - Si_3N_4 grains enhances grain growth due to kinetic and energetic reasons. Model experiments clearly showed that the formation of such elongated particles, grown *in situ* in the Si_3N_4 matrices, strongly depends on the amount, grain-size distribution, and morphology of β - Si_3N_4 nuclei in the starting powder.

6 Conclusions

Earlier studies confirm that an appreciable toughening effect can be monitored in Si_3N_4 -based ceramics owing to the *in situ* development of elongated β - Si_3N_4 grains. However, in order to reach high fracture toughness accompanied by high strength, the abnormal grain growth has to be controlled. By using α - Si_3N_4 -starting powders having a broad intrinsic β - Si_3N_4 grain-size distribution unfavourably large particles may grow, which can act as crack initiation sites. In order to optimize mechanical properties, Si_3N_4 -powders should possess a narrow β - Si_3N_4 -grain-size distribution and have faceted, elongated β - Si_3N_4 -crystals. Ceramics prepared from such starting

powders should exhibit microstructures containing a large amount of elongated Si_3N_4 -grains without exaggerated grain growth development, and therefore combine both high strength and high fracture toughness.

The results presented show that tailoring of the final Si_3N_4 microstructures becomes possible by controlling the β - Si_3N_4 -nuclei in the starting powder.

Acknowledgement

The authors are greatly indebted to Elmar Hampp for preparing the crystalline phases used in the model experiments and for helpful discussions.

References

1. Evans, A. G., Perspective on the development of high-toughness ceramics. *J. Am. Ceram. Soc.*, **73**(2) (1990) 187–206.
2. Becher, P. F., Microstructural design of toughened ceramics. *J. Am. Ceram. Soc.*, **74**(2) (1991) 255–69.
3. Lange, F. F., Fracture toughness of Si_3N_4 as a function of the initial α -content. *J. Am. Ceram. Soc.*, **62**(7–8) (1979) 428–30.
4. Faber, K. T. & Evans, A. G., Crack deflection processes — I. Theory. *Acta Metall.*, **31**(4) (1983) 565–76.
5. Becher, P. F. & Wei, G. C., Toughening behaviour in SiC-whisker-reinforced alumina. *J. Am. Ceram. Soc.*, **67**(12) (1984) C267–9.
6. Evans, A. G. & McMeeking, R. M., On the toughening of ceramics by strong reinforcements. *Acta Metall.*, **34**(12) (1986) 2435–41.
7. Rühle, M., Dalgleish, B. J. & Evans, A. G., On the toughening of ceramics by whiskers. *Scr. Metall.*, **21**(5) (1987) 681–6.
8. Becher, P. F., Hsueh, C.-H., Angelini, P. & Tiegs, T. N., Toughening behavior in whisker-reinforced ceramic matrix composites. *J. Am. Ceram. Soc.*, **71**(12) (1988) 1050–61.
9. Campbell, G. H., Rühle, M., Dalgleish, B. J. & Evans, A. G., Whisker toughening: a comparison between aluminium oxide and silicon nitride toughened with silicon carbide. *J. Am. Ceram. Soc.*, **73**(3) (1990) 521–30.
10. Klebe, H.-J., Corbin, N. D., Willkens, C., & Rühle, M., Transmission electron microscopy studies of silicon nitride/silicon carbide interfaces. *Mat. Res. Soc. Symp. Proc.*, **170** (1990) 79–84.
11. Bengisu, T. M., Inal, O. T. & Tosyalı, O., On whisker toughening in ceramic materials. *Acta Metall. Mater.*, **39**(11) (1991) 2509–17.
12. Mitomo, M. & Uenosono, S., Gas-pressure sintering of β -silicon nitride. *J. Mater. Sci.*, **26** (1991) 3940–4.
13. Kawashima, T., Okamoto, H., Yamamoto, H. & Kitamura, A., Grain size dependence of the fracture toughness of silicon nitride ceramics. *J. Ceram. Soc. Jpn.*, **99**(4) (1991) 320–3.
14. Hirao, K., Nagaoka, T., Brito, M. E. & Kanzaki, S., Microstructure control of silicon nitride by seeding with rodlike β -silicon nitride particles. *J. Am. Ceram. Soc.*, **77**(7) (1994) 1857–62.
15. Rödel, J., Crack closure forces in ceramics; characterization and formation. *J. Eur. Ceram. Soc.*, **9** (1992) 323–34.
16. Lawn, B., *Fracture of brittle solids*, Second Edition. Cambridge University Press, Cambridge, UK, 1993.
17. Rödel, J., Interaction between crack deflection and crack bridging. *J. Eur. Ceram. Soc.*, **10** (1992) 143–50.

18. Steinbrech, R. W., Toughening mechanisms for ceramic materials. *J. Eur. Ceram. Soc.*, **10** (1992) 131–42.
19. Kleebe, H.-J., Unger, S., Meißner, E. & Ziegler, G., Microstructure and toughness correlation in silicon nitride ceramics. In *Proc. of 8th CIMTEC*, Florenz, Italy, 28 June–4 July (1994), in press.
20. Tani, E., Umabayashi, S., Kishi, K., Kobayashi, K. & Nishijima, M., Gas-pressure sintering of Si_3N_4 with concurrent addition of Al_2O_3 and 5 wt% rare earth oxide: High fracture toughness Si_3N_4 with fiber-like structure. *Am. Ceram. Soc. Bull.*, **65**(9) (1986) 1311–15.
21. Hwang, C. J. & Tien, T.-Y., Microstructural development in silicon nitride ceramics. *Materials Science Forum*, **47** (1989) 84–109.
22. Wu, F., Zhuang, H., Ma, L. & Fu, X., Self-reinforced silicon nitride by gas-pressure sintering. *Ceram. Eng. Sci. Proc.*, **14**(1–2) (1993) 321–32.
23. Hirosaki, N., Akimune, Y. & Mitomo, M., Effect of grain growth of β -silicon nitride on strength, Weibull modulus, and fracture toughness. *J. Am. Ceram. Soc.*, **76**(7) (1993) 1892–4.
24. Hampf, F., Konstitution, Sinterverhalten und Eigenschaften von Keramiken auf der Basis des Systems Si_3N_4 - Yb_2O_3 - SiO_2 . Ph. D. Thesis, University of Stuttgart (1993).
25. Dressler, W., Gefügeentwicklung und mechanische Eigenschaften von Si_3N_4 -Keramiken. Ph.D. Thesis, University of Stuttgart (1993).
26. Mitomo, M., Tsutsumi, M., Tanaka, H., Uenosono, S. & Saito, F., Grain growth during gas-pressure sintering of β -silicon nitride. *J. Am. Ceram. Soc.*, **73**(8) (1990) 2441–5.
27. Mitomo, M. & Uenosono, S., Microstructural development during gas-pressure sintering of α -silicon nitride. *J. Am. Ceram. Soc.*, **75**(1) (1992) 103–8.
28. Padture, N. P. & Lawn, B., Short-crack properties of *in situ* silicon carbide with heterogeneous microstructure. *J. Am. Ceram. Soc.*, (1994), in press.
29. Padture, N. P., *In situ* toughened silicon carbide. *J. Am. Ceram. Soc.*, **77**(2) (1994) 519–23.
30. Lee, S. K. & Kim, C. H., Effects of α -SiC versus β -SiC starting powders on microstructure and fracture toughness of SiC sintered with Al_2O_3 - Y_2O_3 additives. *J. Am. Ceram. Soc.*, **77**(6) (1994) 1655–8.
31. Gröbner, J., Synthese und Charakterisierung von Yb-silikaten und Yb-Oxinitriden. Thesis, University of Stuttgart (1991).
32. Hartmann, S., Mücklich, F., Ohser, H. J., Dressler, W. & Petzow, G., Quantitative Charakterisierung von Si_3N_4 -Gefügen durch räumliche Parameter. *Proceedings Metallographietagung*, Dresden 1992; Sonderbände der Praktischen Metallographie, **24** Riederer Verlag, 1993.
33. Wills, R. R., Stewart, R. W., Cunningham, J. A. & Wimmer, J. M., The silicon lanthanide oxynitrides. *J. Mater. Sci.*, **11** (1976) 749–59.
34. Wills, R. R., Holmquist, S., Wimmer, J. M. & Cunningham, J. A., Phase relationships in the system silicon nitride-yttria-silica. *J. Mater. Sci.*, **11** (1976) 1305–9.
35. Braue, W., Wötting, G. & Ziegler, G., Influence of sintering conditions and mechanical properties at room and high temperatures for selected Y-Al-Si-O-N materials. *Science of Ceramics*, **13** (1986) 341–5.
36. Kleebe, H.-J. & Ziegler, G., Influence of crystalline secondary phases on the densification behavior of RBSN during post-sintering under increased nitrogen pressure. *J. Am. Ceram. Soc.*, **72**(12) (1989) 2314–17.
37. Krämer, M., Untersuchungen zur Wachstumskinetik von β - Si_3N_4 in Keramiken und Oxinitridgläsern. Ph.D. Thesis, University of Stuttgart (1991).
38. Lai, K.-R. & Tien, T.-Y., Kinetics of β - Si_3N_4 grain growth in Si_3N_4 ceramics sintered under nitrogen pressure. *J. Am. Ceram. Soc.*, **76**(1) (1993) 91–6.
39. Iskoe, J. L. & Lange, F. F., Development of microstructure and mechanical properties during hot pressing of Si_3N_4 . *Ceramic Microstructures '76, With Emphasis on Energy Related Applications*, 1976, pp. 669–78.
40. Wagner, C., Theorie der Alterung von Niederschlägen durch Umlösen. *Zeitschrift für Elektrochemie*, **65** (1961) 581–91.
41. Krämer, M., Hoffmann, M. J. & Petzow, G., Grain growth kinetics of Si_3N_4 during α/β transformation. *Acta Metall. Mater.*, **41**(10) (1993) 2939–47.
42. Hoffmann, M. J., Analysis of microstructural development and mechanical properties of Si_3N_4 ceramics. In *Tailoring Mechanical Properties of Si_3N_4 Ceramics*, eds M. J. Hoffmann & G. Petzow, Cluwer Academic Publ., Dordrecht, NATO ASI Series I: Applied Science, **246** 1994 pp. 59–72.

Chemical Vapour Deposition of Silicon Nitride Filaments from Silicon Subhydrides and Ammonia

Britta Linner,^a Michael A. Guggenberger,^a Klaus J. Hüttinger^{a*} & Hans-Joachim Kleebe^b

^aInstitut für Chemische Technik, Universität Karlsruhe, D-76128 Karlsruhe, Germany

^bLehrstuhl Keramik und Verbundwerkstoffe, Universität Bayreuth, D-95440 Bayreuth, Germany

(Received 16 September 1994; accepted 25 May 1995)

Abstract

This paper describes the synthesis of monocrystalline α -silicon nitride filaments. The synthesis is based on a catalysed chemical vapour deposition process using iron or iron alloys as catalysts and silicon subhydrides and ammonia as gaseous precursors of silicon nitride. For in situ production of silicon subhydrides by gasification of silicon powder with hydrogen superficially nitrated silicon powder was used to guarantee constant production rates up to 10 h and more. The kinetics of filament growth are shown to be determined by the solubility of nitrogen in and the diffusion of nitrogen through the catalyst particle.

1 Introduction

Advanced monolithic ceramics for application as structural materials at very high temperatures still exhibit decisive disadvantages, i.e. high-temperature creep and low damage tolerance. Reinforcement fibres for the synthesis of ceramic matrix composites, which are more promising for such applications, are of limited usefulness. (i) Carbon fibres are stable at very high temperature, but readily undergo oxidation above 500°C. Therefore, the problem is shifted to complex oxidation protection systems. (ii) Ceramic fibres based on silicon carbide, alumina or mullite have limited high-temperature stability for various reasons, i.e. recrystallization and reactions between the phases of the non-stoichiometric fibre materials. (iii) Whiskers are monocrystalline and thus stable, but problems arise from their geometry,^{1,2}

For future development, the production of high-temperature stable ceramic fibres via the polymer route seems to be the most attractive one, but much work still remains to be done. As an alternative

and less complex route, the synthesis of monocrystalline silicon nitride filaments was investigated.^{3–5} The design considerations for such a synthesis lead to a catalysed chemical vapour deposition process. Such a process is based on adsorption and dissociation of volatile compounds at the catalyst surface, dissolution of the elements forming the desired compound, and precipitation of this compound.

As nitrogen sources molecular nitrogen and ammonia were selected, but filaments were only obtained when ammonia was used.

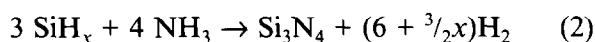
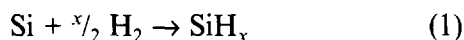
For environmental reasons, chlorosilanes were never considered as silicon source. Instead, monosilane, SiH₄, and silicon subhydrides, SiH_x (x = 1, 2), were investigated. The use of monosilane was studied intensively, but all attempts failed because monosilane was decomposed before entering the reaction zone. Therefore, a synthesis for the production of silicon subhydrides had to be developed.

In selecting the catalyst material the following criteria were assumed to be decisive: solubility of silicon and nitrogen, but no formation of a stable nitride. Iron seemed and proved to fulfil these requirements. As nitrogen solubility in iron at temperatures above 1000°C is extremely low, iron alloys of solubility enhancing elements were investigated.

A suitable substrate material for the catalyst particles should neither be attacked by the gas phase nor wetted by the catalyst particles. Alumina ceramic was tested and found to be applicable. As an insulator, it cannot form selective electron–electron interactions with a metal and then favour wetting. Non-wetting of the substrate by the catalyst is an indispensable necessity for filament growth, which only occurs if the catalyst particle is located at the tip of the growing filament.

Including the necessary *in situ* production of silicon subhydrides SiH_x by reaction of silicon powder with hydrogen the total process of filament growth can be described by eqns (1) and (2):

*To whom correspondence should be addressed.



Experimental details were described earlier.⁵ Experimental studies were performed at 1300 and 1350°C using various flow rates of N_2/NH_3 and SiH_x/H_2 mixtures. Besides iron, iron–chromium and iron–manganese alloys were studied as catalysts. The filaments were analysed using scanning electron microscopy, electron probe micro-analysis, X-ray diffraction, infra-red spectroscopy, and transmission electron microscopy. The tensile strength of the filaments was measured at a gauge length between 6 and 10 mm.

2 Thermodynamics

Figures 1(a) and (b) show the Gibbs' free reaction enthalpy of SiH_4 and SiH formation from silicon and hydrogen, and Si_3N_4 formation from SiH and nitrogen or ammonia, respectively. With increasing temperature the stability of SiH_4 decreases whereas that of SiH increases. At a desired reaction temperature of about 1300°C, the stability of both compounds is similar. According to the ΔG° values a gasification of silicon with hydrogen should lead to both SiH_4 and SiH ; thermodynamic data for further subhydrides are not available. Experimentally, only silicon subhydrides SiH_x were found; they were decomposed forming a silicon mirror at the colder end of the reactor. Surprisingly, the SiH_x partial pressure obtained by hydro-

gasification of silicon at 1300°C is up to three orders of magnitude higher than that calculated from the thermodynamic data (0.19 mbar versus 1.36×10^{-4} mbar).

Figure 1(b) shows that silicon nitride formation should be possible with both nitrogen and ammonia. Two effects can account for the negative results with nitrogen. (i) The low adsorption probability of nitrogen as compared with ammonia at an iron surface, which is some orders of magnitude lower.⁷ (ii) The high difference of bond dissociation energies of N_2 and NH_3 : N-N , 945 kJ mol^{-1} ; H-NH_2 , 431 kJ mol^{-1} ; H-N , 310 kJ mol^{-1} ; H-NH , unknown).

In the presence of a catalyst such as iron, the single steps of the catalysed reaction (eqn (2)) are as follows:

- (1) dissociative adsorption of SiH_x at the catalyst surface and formation of an iron–silicon alloy, Fe_ySi_z ;
- (2) dissociative adsorption of NH_3 or, as discussed above, fragments of NH_3 at the catalyst surface and diffusion of the nitrogen atoms through the catalyst particle;
- (3) precipitation of Si_3N_4 from the catalyst particle.

To facilitate the discussion of step (1) the iron–silicon phase diagram is presented in Fig. 2.⁸ At the reaction temperature of 1300°C, dissolution of silicon in iron yields a solid alloy up to 22 at% silicon. With still higher silicon contents, up to about 37 at%, a melt is formed. This holds for a bulk material. With very small catalyst particles the solidification line may be shifted to lower silicon concentrations. Above 37 at%, silicon dissolution by dissociation of SiH_x is only possible if free silicon is precipitated simultaneously. The driving force of silicon precipitation is given by the following reactions (eqns (3)–(5)):

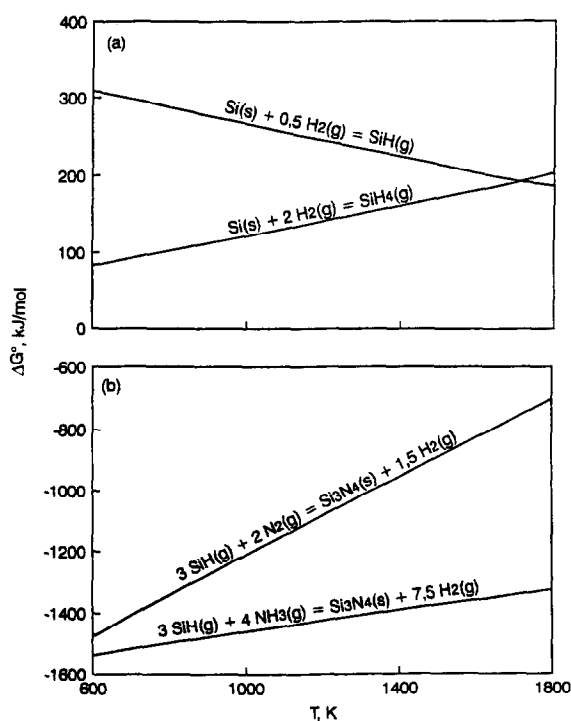


Fig. 1. Gibbs' free enthalpy of the formation of (a) silicon hydrides and (b) silicon nitride.

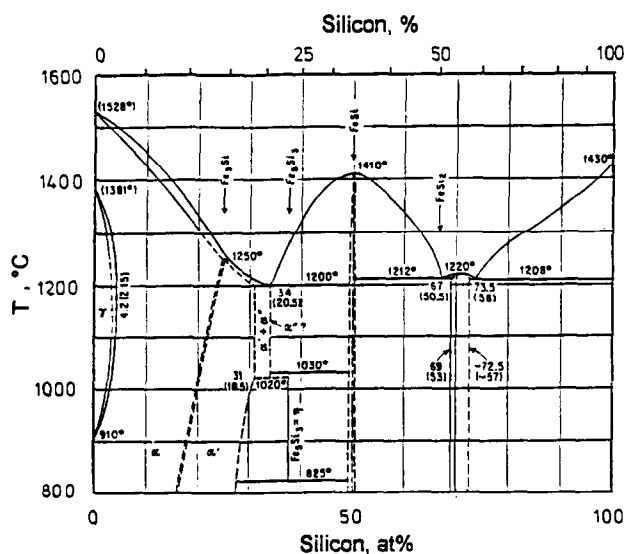


Fig. 2. The iron–silicon phase diagram.⁷

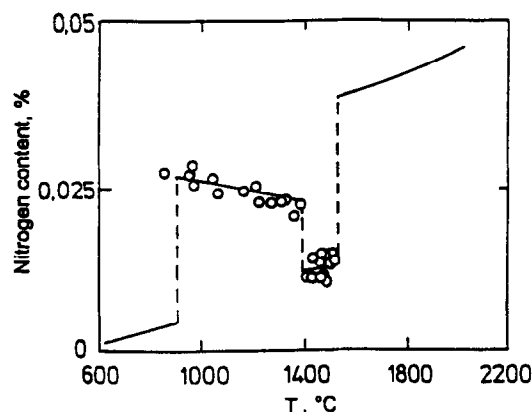
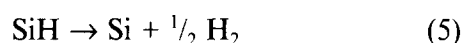
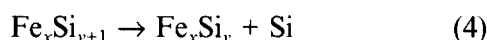
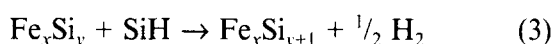


Fig. 3. Solubility of nitrogen in pure iron.⁸



The reaction according to eqn (5) is strongly exothermic. The Gibbs' free enthalpy at 1300°C amounts to -230 kJ mol^{-1} .

Experimental results on filament formation showed that the filaments are not hollow, but massive. For this reason, volume diffusion of nitrogen atoms through the catalyst particle is assumed. Solubility data of nitrogen in pure iron are shown in Fig. 3.⁹ At 1300°C the solubility of nitrogen in γ -iron is very low. In the presence of silicon the nitrogen solubility decreases even more. The thermodynamic considerations suggest that the growth rate of Si_3N_4 filaments is kinetically limited by the low nitrogen solubility in the possible ferro-silicon alloys. Several elements are known to increase nitrogen solubility:⁹ $\text{Ti} > \text{V} > \text{Cr} > \text{Mn}$.

However, an alloying element has to be selected not only from the viewpoint of nitrogen solubility, but also from the viewpoint of nitrogen diffusion. Both properties depend on the lattice being formed.

3 Synthesis of Silicon Subhydrides

As was pointed out in Section 1, all experiments of filament deposition with monosilane, SiH_4 , were unsuccessful. Hence, the synthesis of silicon subhydrides, SiH_x , is of essential importance. Initial experiments to gasify silicon with hydrogen at sufficiently high temperatures of about 1300°C did not produce acceptable results due to sintering of the silicon particles; the reaction rate approached zero after approximately 1 h reaction time. On the other hand, a constant gasification rate for at least 10 h was desired. The problem of sintering was solved by partially nitriding the silicon powder

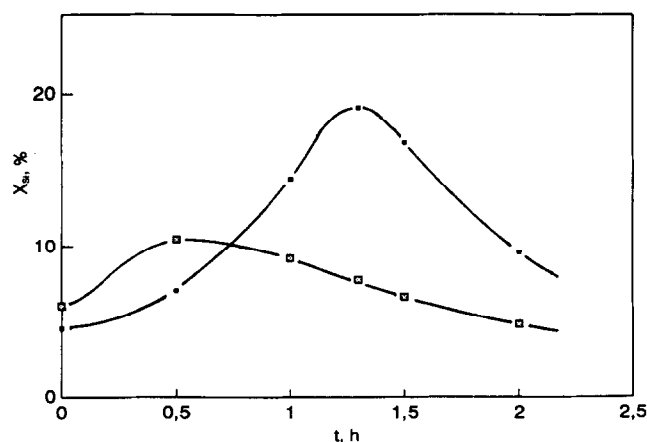


Fig. 4. Conversion of superficially nitrided silicon powder I to silicon subhydrides after 5 h reaction with hydrogen at 1300°C as a function of the nitridation time of the powder at 1150°C (■) and 1200°C (□).

before gasifying it with hydrogen. In view of the importance of this process, detailed results will be described in the following. They were found with a high-purity silicon powder I (99.9%, particle size 40–100 μm).

A fundamental result is presented in Fig. 4. It shows the conversion of superficially nitrided silicon powder after 5 h reaction time with hydrogen at 1300°C as a function of the nitridation time of the powder. At both nitridation temperatures investigated (1150 and 1200°C) silicon conversion to SiH_x increases up to a maximum and then decreases again. The maximum apparently corresponds to an optimum fit of sintering inhibition and diffusion of hydrogen and silicon subhydrides through the silicon nitride layer. The maximum conversion found after nitridation at 1150°C is higher. At 1200°C enhanced sintering of the powder during nitridation was observed.

The results shown in Fig. 4 are based on a powder which was nitrided with a nitrogen/hydrogen mixture of 90:10. As shown in Fig. 5, this gas composition used for nitridation is obviously

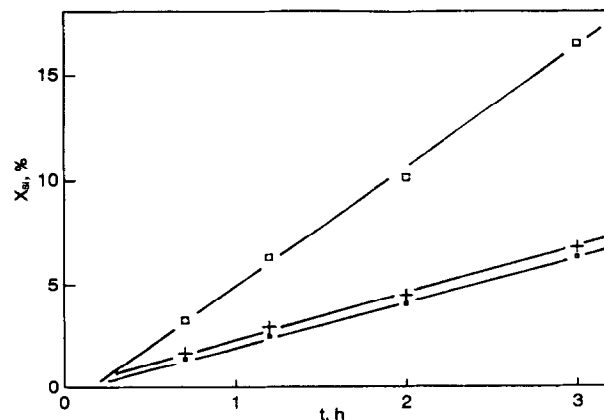


Fig. 5. Conversion of silicon powder I to silicon subhydride at 1150°C using various nitrogen/hydrogen mixtures (□, 90:10; □, 80:20; +, 95:5) as a function of the reaction time; volume flow: 3.5 l h^{-1} (ntp).

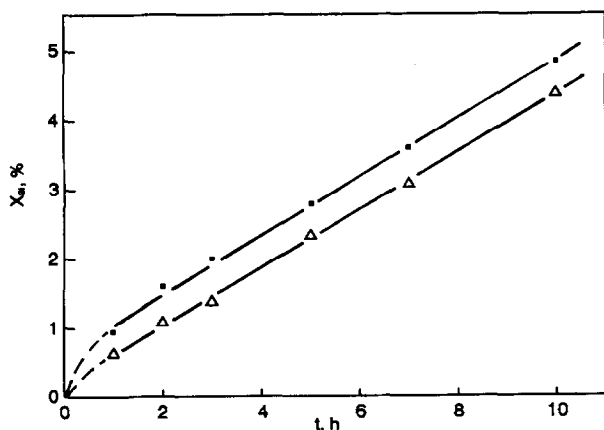


Fig. 6. Conversion of superficially nitrated silicon powder I to silicon subhydrides at 1300°C using various hydrogen flows: \square , 8.71 h^{-1} ; Δ , 5.1 h^{-1} .

optimum; with higher or lower hydrogen contents the nitridation rate is lower for various reasons. With the lower hydrogen partial pressure, reduction of the silica surface layer may not be sufficient, whereas partial gasification with hydrogen may occur when a higher hydrogen partial pressure is used.

The nitrated powders were tested for continuous SiH_x production. The results are shown in Fig. 6. After an initial stronger increase of the gasification rate it remains constant over the entire time interval studied. The results shown in Figs 4–6 are fully reproducible, but are strongly dependent on the silicon powder used.

Further studies on nitridation were performed using another high-purity silicon powder II and ammonia for nitridation. The reason was that, during nitridation with the nitrogen/hydrogen mixture, partial sintering occurred even at 1150°C. Figure 7 shows the degree of conversion of silicon to silicon nitride as a function of the reaction time at temperatures of 1000, 1100 and 1150°C. Two further curves are presented. The dotted line was found at 1150°C with the N_2/H_2 mixture (90:10).

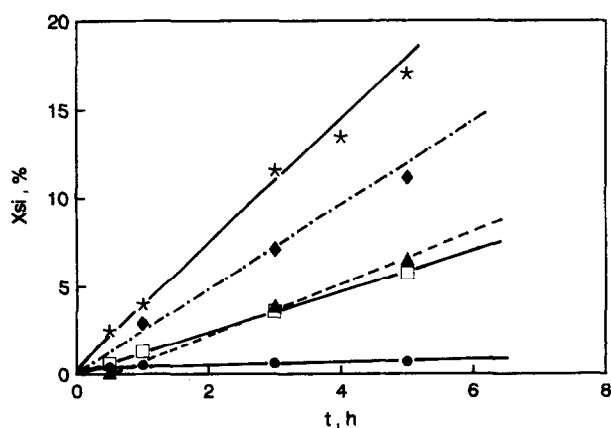


Fig. 7. Conversion of silicon powder II to silicon nitride at various temperatures and various nitriding atmospheres as a function of the reaction time: 1000°C, 1 h^{-1} NH_3 ; (\bullet); 1100°C, 1 h^{-1} NH_3 (\square); 1150°C, 1 h^{-1} NH_3 (\star); 1150°C, 6 l h^{-1} NH_3 (\blacklozenge); 1150°C, 3.5 l h^{-1} N_2/H_2 , 90:10 (\blacktriangle).

It can be seen that the same nitridation rate was obtained with ammonia already at 1100°C. Even more remarkable is the experimental observation that the silicon powder never sintered when ammonia was used for nitridation.

The above results with ammonia were obtained with an ammonia flow of 1 l h^{-1} (ntp). A further experiment using an ammonia flow of 6 l h^{-1} yielded a lower nitridation rate (Fig. 7, dashed line). This result indicates that the overall rate of silicon nitridation is limited by dissociation of the ammonia. If a lower flow is used, partial decomposition of ammonia by formation of NH_2 or NH may already occur in the gas phase. This conclusion is confirmed by the linear relationship between silicon conversion to silicon nitride and reaction time. Normally, a decrease in silicon conversion with increasing reaction time or increasing silicon nitride layer thickness would be expected. The linear relationship means that the rate of nitridation is proportional to the amount of nitrogen atoms formed per unit time.

In subsequent experiments it was investigated whether the agent used for nitridation of a silicon powder has any effect on the gasification with hydrogen. Samples of silicon powder II of nearly equal degree of nitridation (NH_3 , 1100°C, 5 h; N_2/H_2 , 1150°C, 5 h) were used for these experiments. The results at 1300°C are shown in Fig. 8. The rates are constant after 1 h reaction time and the steady-state gasification rates of both powders are also equal. The result indicates that not the nitridation agent, but the degree of nitridation is the decisive quantity for the gasification with hydrogen. At 1150°C, results on the nitridation rate of both silicon powders with the N_2/H_2 mixture (90:10) are available (Figs 5 and 7). They show that silicon powder II is less reactive. In view of this result it is remarkable that silicon

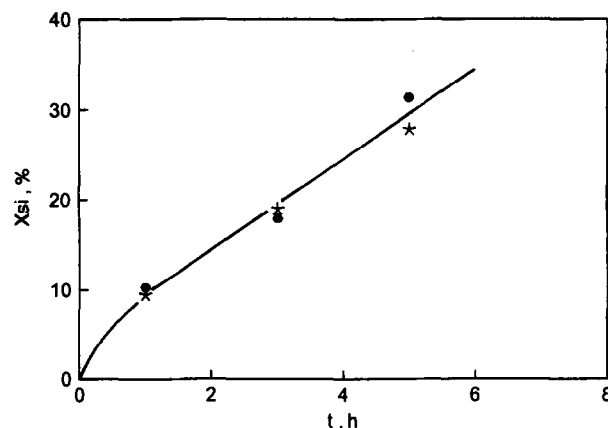


Fig. 8. Conversion of two superficially nitrated silicon powders II with an equal degree of nitridation to silicon subhydrides at 1300°C as a function of the reaction time, hydrogen flow 12 l h^{-1} (ntp): 1100°C, 5 h, 1 h^{-1} NH_3 (\bullet); 1150°C, 5 h, 3.5 l h^{-1} N_2/H_2 (\star).

powder II shows a higher gasification rate with hydrogen than powder I. The results underline that the process of SiH_x synthesis using superficially nitrided silicon powder still exhibits substantial potential for development. It may be assumed that iron should be a catalyst of both nitridation and hydrogen gasification. For this reason, further studies will focus on using ferro-silicon alloys with silicon contents of $>90\%$.

4 Synthesis of Filaments

4.1 Kinetics of filament growth

Fundamental studies of filament growth were performed at 1300°C using iron as catalyst. The diameter of the iron particles was between 3 and $5\ \mu\text{m}$. The intrinsic problem of the synthesis lies in the volume flows and partial pressure of SiH_x and NH_3 . According to the *in situ* synthesis of SiH_x , this agent is introduced into the reaction zone of the reactor as a constituent of the hydrogen flow. The partial pressure of SiH_x can be varied by using different hydrogen flows. According to thermodynamic calculations it may not exceed 1.36×10^{-4} mbar. Experimentally partial pressures of up to 0.19 mbar were found. NH_3 is introduced into the reaction zone of the reactor using N_2 as carrier and diluent gas. N_2 was found to be inactive in the formation of silicon nitride filaments.

Using optimum compositions of the gas phase, filaments with excellent crystalline perfection were obtained not only at 1300°C as used in the fundamental studies, but also at 1350°C . Results on filament deposition with iron as a catalyst are shown in Fig. 9, the effect of some alloying elements of iron is presented in Fig. 10.

In both diagrams, the weight of the filaments deposited as a function of the deposition time is plotted. The weight instead of the length of the

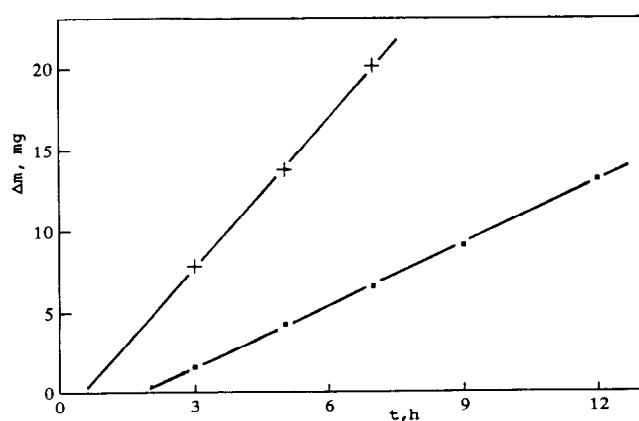


Fig. 9. Deposition kinetics of silicon nitride filaments with Fe, as catalyst. Gas composition: $12\ \text{l h}^{-1}\ \text{H}_2$, $0.3\ \text{l h}^{-1}\ \text{N}_2$, $0.3\ \text{l h}^{-1}\ \text{NH}_3$; 1350°C (+) and 1300°C (■).

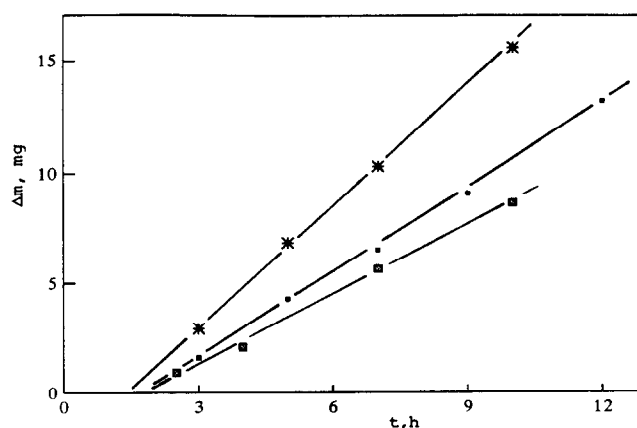


Fig. 10. Deposition kinetics of silicon nitride filaments at 1300°C with Fe (■), FeCr 70 (★) and FeMn 80 (⊞) as catalysts; gas composition: $0.3\ \text{l h}^{-1}\ \text{N}_2$, $0.3\ \text{l h}^{-1}\ \text{NH}_3$, $12\ \text{l h}^{-1}\ \text{H}_2$.

filaments is used, because the length of the filaments is not uniform and difficult to determine accurately. Under steady-state conditions, i.e. after the incubation period, the growth rate of the filaments is of the order of $1\ \text{cm h}^{-1}$.

The flow rates and partial pressures were optimised towards deposition of filaments with high crystalline perfection. The effect of temperature in filament deposition with iron is strong; the activation energy calculated from the two temperatures investigated amounts to $375\ \text{kJ mol}^{-1}$.

As follows from Fig. 10, the effect of chromium and manganese as alloying elements of iron on the growth rate of the filaments is different and quite surprising. Both transition metals are known to strongly increase the nitrogen solubility of iron.⁹ Therefore it was astonishing that the deposition rate with ferro-manganese was lower than that with pure iron. Obviously, the solubility of nitrogen is not the only parameter controlling the growth rate of the filaments. The slowed growth rate with the ferro-manganese alloy is probably caused by a reduced diffusion rate of nitrogen. Further studies and theoretical calculations are necessary to clarify this point. A discussion based on the lattice formed by the catalyst is problematic because catalyst particles are not necessarily operating in a truly solid state.

4.2 Analysis of filaments

The morphologies of the filaments and especially of the filament heads were studied by scanning electron microscopy (SEM). Typical examples are shown in Figs 11(a) and (b). Figure 11(a) depicts a perfectly spherical filament head whereas a polyhedral filament head can be seen in Fig. 11(b). The shape of the filament heads is related to the silicon content, which was analysed by electron probe micro-analysis (EPMA). A catalyst with a spherical shape is obviously operating in a highly

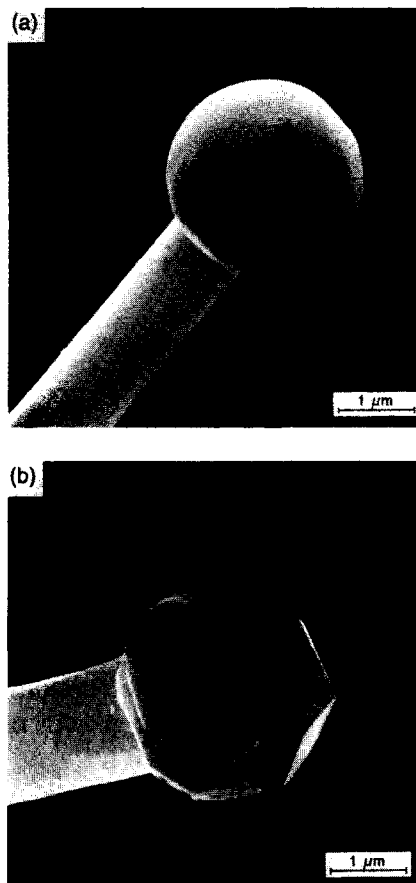


Fig. 11. Scanning electron micrographs of silicon nitride filaments obtained at 1300°C. Gas composition: 0.3 l h⁻¹ N₂, 0.3 l h⁻¹ NH₃, and 12 l h⁻¹ H₂ (a) and 8 l h⁻¹ H₂ (b).

viscous state corresponding to a low silicon content of approximately 6%. On the other hand, the polyhedrally shaped catalyst particle should be formed during resolidification from a true liquid. EPMA of this catalyst particle showed a silicon content of nearly 20%. According to the iron-silicon phase diagram, this catalyst particle was definitely operating in the liquid state.

Filaments with high crystalline perfection are only obtained if the silicon content of the catalyst particle is limited. Beyond a certain silicon content not only silicon nitride but also free silicon are precipitated simultaneously from the catalyst during growth of the filaments. Such reaction conditions are undesired.

Figures 12(a)–(e) show some Fourier transform infra-red (FT-IR) spectra. The lowest one was found with crystalline α -silicon nitride powder; it is used as a standard. From Figs 12(a)–(d) the partial pressure of silicon subhydrides in the gas phase during deposition was reduced. The FT-IR spectrum of a crystalline α -silicon nitride filament is shown in Fig. 12(d). With increasing partial pressure of the silicon subhydrides, equivalent to an increasing silicon content of the catalyst particles, the absorption bands become broader and even disappear.

It should be noted that the spectrum of the crystalline α -silicon nitride powder (Fig. 12(e)) is not completely identical to the spectrum of the filament with high crystalline perfection (Fig. 12(d)). Two absorption bands at 941 cm⁻¹ and 957 cm⁻¹ cannot be observed. Texture effects may account for this. A similar FT-IR spectrum as shown in Fig. 12(d) was published in the literature for α -silicon nitride whiskers.¹⁰

Figure 13 shows an X-ray diffraction (XRD) pattern of filaments with high crystalline perfection. All typical reflections of α -silicon nitride can be found, but not further peaks.

From the above results it cannot yet be concluded whether the filaments are polycrystalline or monocrystalline. To obtain an answer to this question the tensile strength and modulus of crystalline filaments were determined. For the strength, a mean value of 30 ± 2 GPa was found. The Young's modulus could only be determined indirectly. Therefore, the determined value of 660 GPa should be viewed only as a rough estimate. From the data, a strain-to-failure of 4.6% was calculated. For a brittle material a value of 10% is theoretically postulated. In relation to this value, a strain-to-failure of about 5% is a good indication of a very low concentration of growth defects.

For further analysis of the crystalline perfection of the filaments (compare Figs 12(d) and 13), preliminary transmission electron microscopy (TEM) investigations were performed. To (1) avoid deterioration or alteration of the filament surface structure and (2) investigate a rather large area of the fibres, the filaments were placed on a carbon grid and the typically utilized argon-ion thinning technique to achieve electron transparency was omitted. Moreover, to minimize electrostatic charging under the electron beam, another carbon grid was placed on top of the TEM sample. Hence, bright-field images in addition to electron diffraction patterns were obtained from the filaments. It should be noted that under these conditions, since the silicon nitride filaments are relatively thick (up to 1.2 μm in diameter), diffuse scattering is strongly enhanced mainly in the core region of the filaments. Therefore, the crystalline perfection of those filaments can only be analysed in the surface regions rather than in the core region, which would require TEM cross-section preparation. However, the applied technique allowed us to show unequivocally that the filaments investigated are monocrystalline (single crystals), as depicted in Fig. 14(a).

Using convergent beam electron diffraction (CBED) on one filament showed no change in the corresponding electron diffraction pattern over the

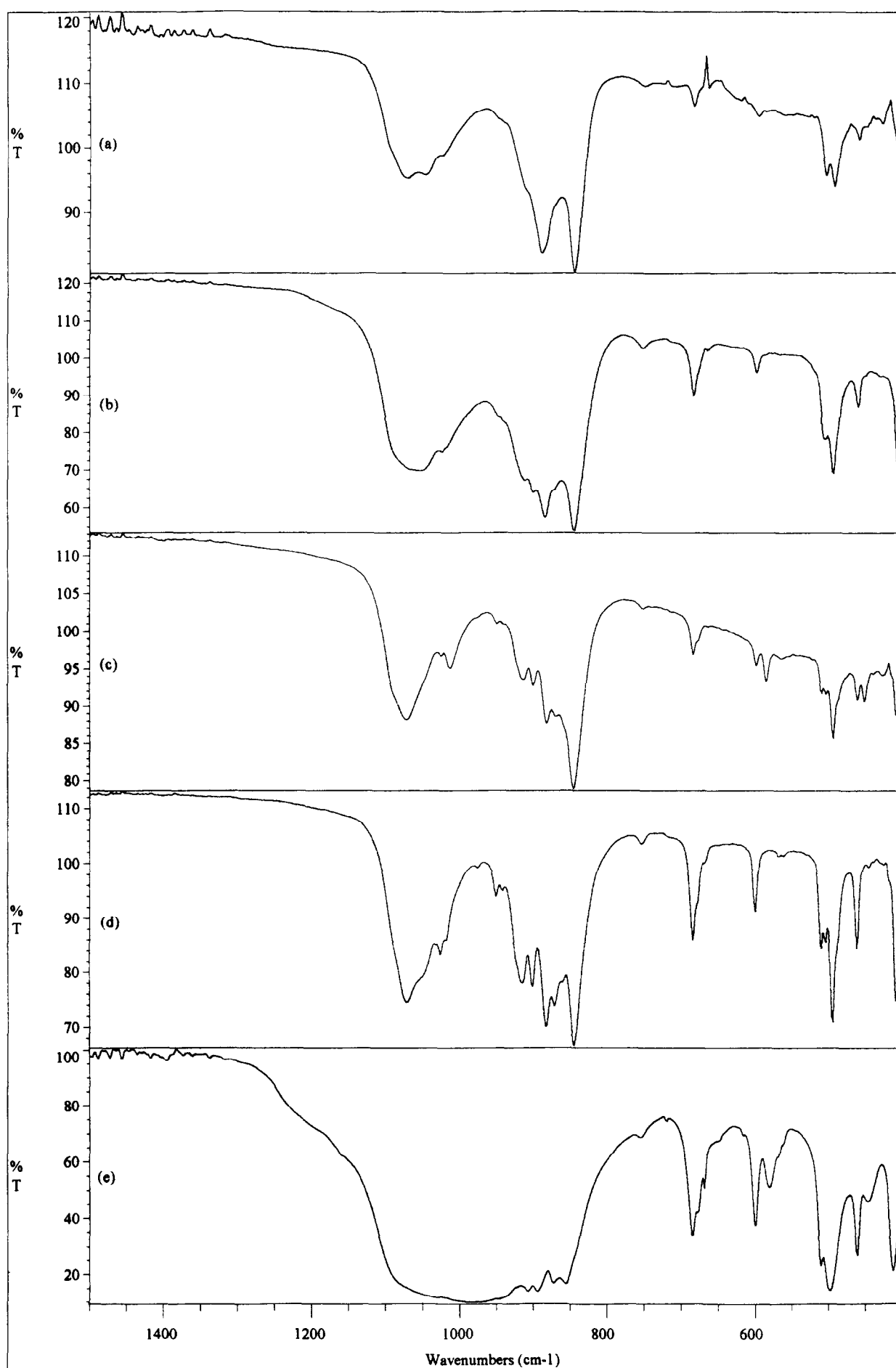


Fig. 12. FT-IR spectra of silicon nitride filaments obtained at 1300°C. Gas composition: 0.3 l h⁻¹ N₂, 0.3 l h⁻¹ NH₃, and 5 l h⁻¹ H₂ (a), 8 l h⁻¹ H₂ (b), 10 l h⁻¹ H₂ (c) and 12 l h⁻¹ H₂ (d). (e) Crystalline α -Si₃N₄ powder for reference.

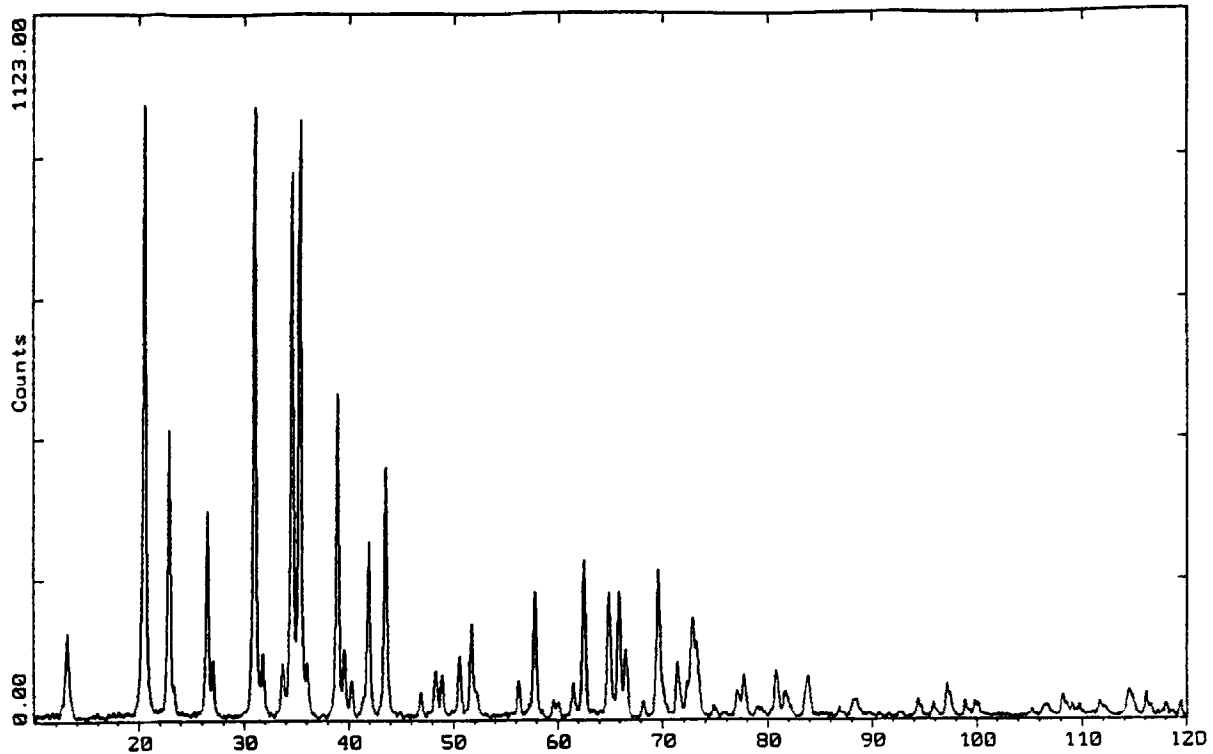


Fig. 13. X-ray diffraction pattern of silicon nitride filaments obtained at 1300°C. Gas composition: 0.3 l h⁻¹ N₂, 0.3 l h⁻¹ NH₃ and 12 l h⁻¹ H₂.

entire length of the filament, with the only exception of small tilts due to bending of the fibres during TEM-sample preparation.

Apart from being single crystals, which applies to all filaments investigated, the filament surface is very smooth. No growth defects were observed. In some rare occasions small silicon nitride particles were found attached to the surface of the filaments, but they clearly do not appear as growth defects (see Fig. 14(b)).

Analysing electron diffraction patterns, in addition to CBED, first order lower zone (FOLZ) ring analysis indicated α -Si₃N₄ as the only crystalline phase, which is consistent with the XRD results. Attempts to analyse the growth direction of the filaments failed since two low-indexed zone axes are required, which was out of the limited tilting range of the microscope (Philips CM20FEG operating at 200 kV, tilt range $\pm 15^\circ$). TEM cross-section preparation would allow determination of the growth direction of the filaments; such work is under way.

It should be noted that all filaments typically show a thin surface film, which is thought to be amorphous. The presence of such a thin surface layer could be due to surface oxidation during processing even at very low oxygen partial pressure. The FT-IR spectra shown in Figs 12(a)–(d) reveal oxygen-backbone vibrations at wavenumbers around 1050 cm⁻¹, which may be related to the presence of the observed thin surface coatings of the filaments.

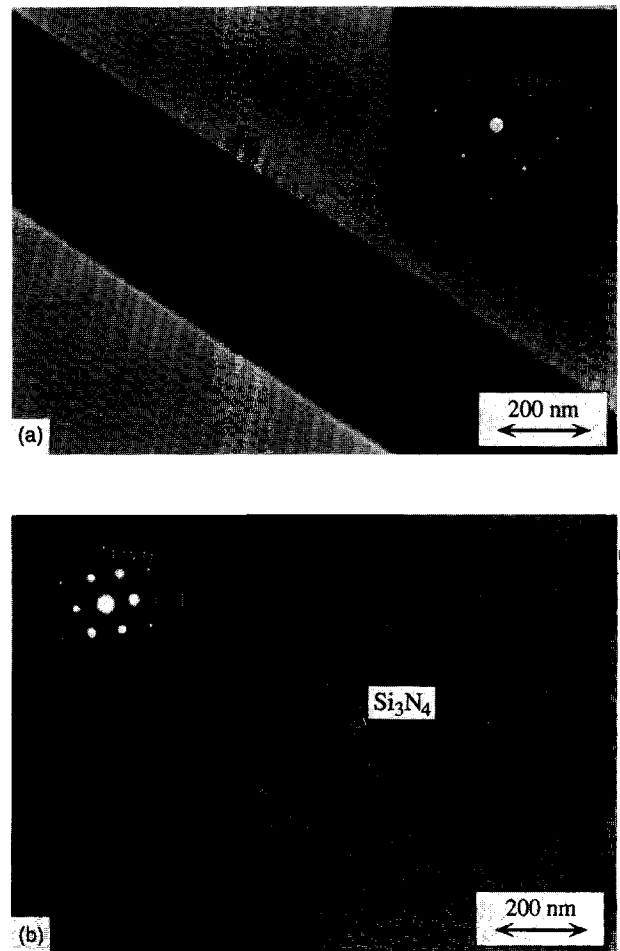


Fig. 14. Transmission electron micrographs of silicon nitride filaments obtained at 1300°C. Gas composition: 0.3 l h⁻¹ N₂, 0.3 l h⁻¹ NH₃ and 12 l h⁻¹ H₂. (a) Single filament, (b) filament with attached silicon nitride particle; with converging beam electron diffraction pattern (inset).

5 Summary

Monocrystalline α -silicon nitride filaments have been synthesized by catalysed chemical vapour deposition using iron and iron alloys as catalysts and silicon subhydrides and ammonia as precursor gases for silicon nitride. Monosilane was found to be decomposed before entering the reaction zone; therefore, a synthesis for the production of silicon subhydrides by *in situ* gasification of a superficially nitrated silicon powder was developed.

The development potential of the overall synthesis may mainly be seen in optimizing the catalyst composition. Increasing the reaction temperature from 1300°C to higher temperatures is critical because non-catalysed gas-phase reactions are difficult to control. As compared with pure iron as catalyst, an optimized catalyst should exhibit a higher nitrogen solubility and favour the diffusion of nitrogen atoms. To design such an optimized catalyst, thermodynamic calculations will be carried out.

Acknowledgement

Financial support of these studies by the German Research Foundation (DFG) is gratefully acknowledged.

References

1. Bunsell, A. R. in *Encyclopedia of Composites*, Vol. 2, ed. S. M. Lee. VCH, New York, 1990, p. 158.
2. Hüttinger, K. J. & Greil, P., *cfi/Ber. DKG*, **69** (1992) 446.
3. Hüttinger, K. J. & Pieschnick, T. W., *Adv. Mater.*, **6** (1994) 62.
4. Hüttinger, K. J. & Pieschnick, T. W., *J. Mater. Sci.*, **29** (1994) 2879.
5. Pieschnick, T. W., PhD thesis, Karlsruhe University, 1993.
6. Barin, I., *Thermochemical Data of Pure Substances*, 1. Auflage, VCH, Weinheim, 1989.
7. Schlögl, R., in *Catalytic Ammonia Synthesis*, ed. J. R. Jennings. Plenum Press, New York, 1992.
8. Hansen, M., *Constitution of Binary Alloys*. McGraw-Hill, New York, 1958.
9. Satir-Kolorz, A., Feichtinger, H. K. & Speidel, M. O., *Gießereiforschung*, **42** (1990) 36.
10. Gopalakrishnan, P. S., *et al.*, *J. Mater. Soc. Lett.*, **12** (1993) 1422.

Tribochemically Assisted Wear of Silicon Nitride Ball

E. Jisheng,^a T. A. Stolarski^{a*} & D. T. Gawne^b

^aDepartment of Mechanical Engineering and ^bDepartment of Materials Technology, Brunel University, Uxbridge, Middlesex, UB8 3PH, UK

(Received 27 January 1995; revised version received 31 May 1995; accepted 9 June 1995)

Abstract

The response of silicon nitride balls to different chemical additives contained in a diamond slurry was studied in a high speed four-ball machine. It was found that there are two effective inorganic chemical additives: acid additive (A) and alkaline additive (B). Use of A or B in the diamond slurry resulted in a high material removal rate and a rough surface. With an increase in the size of the diamond particles contained in the slurry, the material removal rate and the roughness of the surface also increased. Addition of sulfur-containing additives into the diamond slurries produced a decrease in the material removal rate but a smoother surface. The presence of water in the oil-based diamond slurry gave an increase in the material removal rate and a relatively smooth surface. In the ester-containing slurry, there was an increase in the material removal rate and the roughness of the surface.

1 Introduction

The in-service benefits of using advanced engineering ceramics (good chemical inertness, hardness, high temperature stability, low conduction of heat and high wear resistance) have led to their increasing use in industry. Unfortunately, engineering ceramics are very susceptible to surface damage during machining and surface finish operations, which affects their subsequent behaviour during service. To avoid damage during machining operations, the conventional grinding of engineering ceramics, for example, is a slow and expensive process, which often accounts for a significant portion of the total cost. Typically, surface finishing of ceramic components for high contact stress applications constitutes about 50% of the total cost of manufacturing.

With a continuous increase in the demand for

advanced engineering ceramics, interest in their surface finishing processes has been steadily growing. Many modern surface finishing processes have been developed, such as magnetic force-assisted grinding, creep-feed grinding, ultrasonic-assisted grinding and energy-beam assisted grinding.^{1,2} However, it seems that the dominant and the most effective industrial practice for the surface finishing of engineering ceramics is still a grinding process using diamond slurries. To understand the grinding process and the factors affecting high material removal rates and controlling surface damage, a comprehensive study into the optimum conditions of grinding silicon nitride balls in diamond slurries was carried out.³

Nowadays, increasing attention is being paid to the potential of using tribochemical effects during surface finishing of engineering ceramics.⁴ Based on experimental results of adding many kinds of additives into the base oil, Gates and Hsu⁵ produced a list of prowear and antiwear effects of the additives during sliding of engineering ceramics under lubricated conditions. Later, Wang and Hsu⁶ reported an increase in the material removal rate during chemically assisted machining of engineering ceramics. However, it appears that there is a need to understand the mechanism of the process taking place during grinding of engineering ceramics in the diamond slurry, so that the effectiveness of tribochemistry in the surface finishing of brittle materials can be maximized.

In this paper, the results of a study on the chemically assisted grinding of silicon nitride balls are presented. The work concentrates on understanding of tribochemical effects occurring during grinding in diamond slurries containing different chemical additives, in order to develop more effective grinding processes of engineering ceramics.

2 Experimental Procedure

2.1 Apparatus

All experiments presented in this paper were

*To whom correspondence should be addressed.

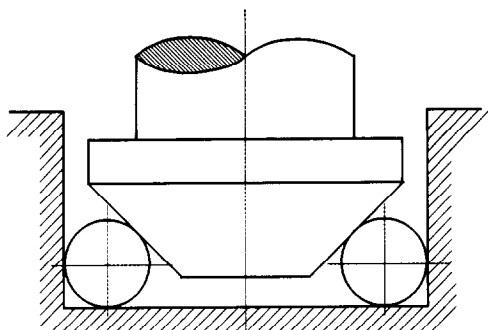


Fig. 1. Schematic diagram of the three-point configuration used for the grinding experiment.

carried out on a model contact configuration. In the normal configuration, an upper ball is located in the collet carried by the vertically mounted spindle. Three lower balls are allowed to rotate freely in a special race when brought into loaded contact with the single upper ball. In the study reported here, the configuration was modified as shown in Fig. 1. The upper ball was replaced by a metal cone with an angle of 90° and the three lower balls were replaced by nine silicon nitride balls with 6.5 mm diameter. The balls were free to rotate inside a metal cup. The cone together with the spindle was driven by an electronically controlled motor. In this case, each ball was in contact with the cup at two points and with the cone at one point. For this reason, the configuration was called 'three-point contact'.

2.2 Materials

The silicon nitride balls with 6.5 mm diameter were manufactured by the method of hot-isostatic

pressing. The cone and cup were fabricated from 304 grade stainless steel.

In this study, two types of grinding liquid were used: base diamond slurry and 'tribochemical' slurry. The base diamond slurry contained diamond particles of different size. They were 1 μm or 15 μm oil-based diamond slurries (O-type) and 1 μm or 15 μm water-based diamond slurries (W-type). The seven variations of tribochemical slurry used are characterized in Table 1.

Two types of chemical additive were used: inorganic additives and organic additives. The inorganic additives were of an acid type (additive A) and an alkaline type (additive B). The organic additives are listed in Table 2.

To prepare a grinding liquid with tribochemical action, 15 μm diamond particles were suspended in the tribochemical slurry. The concentration of diamond particles was 2 wt%. Seven organic additives were added into the O-type oil-based diamond slurries in different weight concentrations. The inorganic additives were added to the pre-mixed diamond slurry with 50% W-type (water-based) and 50% O-type (oil-based) diamond slurries (WODS).

2.3 Experiments

A typical experiment began by placing silicon nitride balls on the pre-run track in the stainless steel cup and submerging them in about 4 ml of diamond slurry (1 or 15 μm diamond particle size). The load of 400 N was carefully applied to the set of nine silicon nitride balls. The test was

Table 1. Properties of the tribochemical slurries

Slurry	Composition of additive	Pour point ($^\circ\text{C}$)	Colour	Viscosity at 40°C (cSt)	Flash point ($^\circ\text{C}$)
853	Highly refined mineral oil	< 18	amber	19.0	190
854	Highly refined mineral oil	< 9	amber	30.0	200
855	Ester basestocks	< 20	amber	27-31	180
856	Poly-alpha-olefin	—	colourless	5	135
857	Poly-alpha-olefin	< 68	colourless	31	200
858	Polyoxyalkylene glycol ether	< 25	yellow	180	180
884	Ester basestocks	< 20	amber	85	180

Table 2. Properties of the organic additives

Additive	Composition	Odour	Water solubility	Density (kg m^{-3})	Flash point ($^\circ\text{C}$)	Viscosity at 40°C (cSt)	Viscosity at 100°C (cSt)
995	Ca sulfonate	mild	insoluble	1220	160	1200	60
996	Na sulfonate	mild	partially soluble	—	160	—	200
997	Olefin sulfide	mild	insoluble	1045	> 100	45	6
998	Olefin ester sulfide	strong	insoluble	960	190	300	35
HT312	Sulfide	mild	insoluble	1160	95	—	9.5
DBDS	Dibenzylsulfide	mild	—	—	—	—	—
NSE	Natural sulfurized ester	strong	—	—	—	—	—

carried out at the 3000 rev min⁻¹ rotational speed of the spindle and lasted for 1 h.

The silicon nitride blank balls, in the as-received condition, had rough surfaces of the order of 100–200 μm R_a and contained surface imperfections. Therefore, they were subjected to a run-in process before the grinding test to remove the rough surface layer and imperfections. Running-in was carried out in the two steps. Firstly, 0.5 g of 15 μm diamond paste was smeared on the set of blank silicon nitride balls and 4 ml of a 15 μm oil-based diamond slurry was added into the stainless steel cup. The set of nine blank balls was pre-run at 100 N and 700 rev min⁻¹ speed for 1 h. Then, the load was increased to 200 N and the speed increased to 3000 rev min⁻¹. Under this condition, the silicon nitride balls were run-in for 2 h. During this process, approximately 300 μm of silicon nitride was removed from each ball, which resulted in the average reduction of their diameters from the initial 6.8 mm to 6.5 mm.

After the running-in of the silicon nitride balls, they were ready for the test (i.e. ~ 6.5 mm diameter). Before and after the tests, all silicon nitride balls and the stainless steel cup were ultrasonically cleaned thoroughly in solvents. The material removal was assessed by the decrease in diameter of the silicon nitride balls after the grinding test. The material removal rate per unit time was calculated. Scanning electron microscopy (SEM) was used to obtain micrographs of the surfaces of the silicon nitride balls at low and high magnifications before and after the grinding tests under the different conditions.

3 Results

3.1 Material removal rate in the presence of water

Grinding tests were carried out in WODS. Figure 2 shows how the water affects the material removal rate of the silicon nitride balls during grinding in the diamond slurry: an improvement ($\sim 30\%$ increase) in the material removal rate of the silicon nitride balls was achieved during grinding in the WODS comparing with grinding in the oil-based diamond slurry.

3.2 Material removal rate in the presence of inorganic additives

3.2.1 Different inorganic additives

To examine the effect of inorganic additives with different chemical characteristics, two kinds of inorganic additives, i.e. acid additive (A) and alkline additive (B), were used. They were added into the pre-mixed diamond slurry consisting of 50% water-

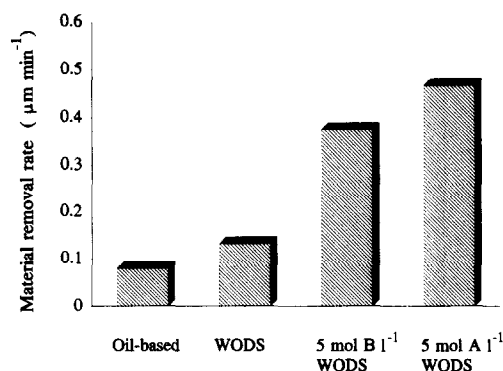


Fig. 2. Effect of water and inorganic additives on the material removal rate of silicon nitride balls during grinding at 400 N load and 3000 rev min⁻¹ speed in 1 μm WODS.

based and 50% oil-based diamond slurries (WODS). Figure 2 shows the material removal rate after grinding silicon nitride balls in the 1 μm oil-based diamond slurry, 1 μm WODS, 5 mol dm⁻³ of A in 1 μm WODS and 5 mol dm⁻³ of B in 1 μm WODS. It is seen from Fig. 2 that the lowest material removal rate took place during grinding in the oil-based diamond slurry. Adding 5 mol dm⁻³ of A or B into 1 μm WODS resulted in an increase of the material removal rate. The increase is greater than sixfold and greater than fourfold, respectively, for 5 mol dm⁻³ of A and B in 1 μm WODS.

3.2.2 Concentration of inorganic additives

The effect of different concentrations of additives A and B in 1 μm WODS on the material removal rate of silicon nitride balls was also studied. The results are given in Fig. 3. It is seen that the material removal rate increases with increasing concentration of both the additives. It appears from Fig. 3 that the initial dramatic increase in material removal rate stabilizes at a constant value even though a further increase in the concentration of additives takes place. Figure 3 also shows that the material removal rates were higher during grinding in WODS with the additive A than with the additive B throughout the whole range of concentrations.

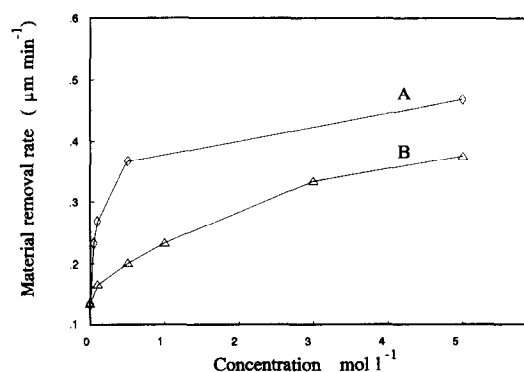


Fig. 3. Variation of the material removal rate of silicon nitride balls with the concentration of inorganic additives in 1 μm WODS during grinding at 400 N load and 3000 rev min⁻¹ speed.

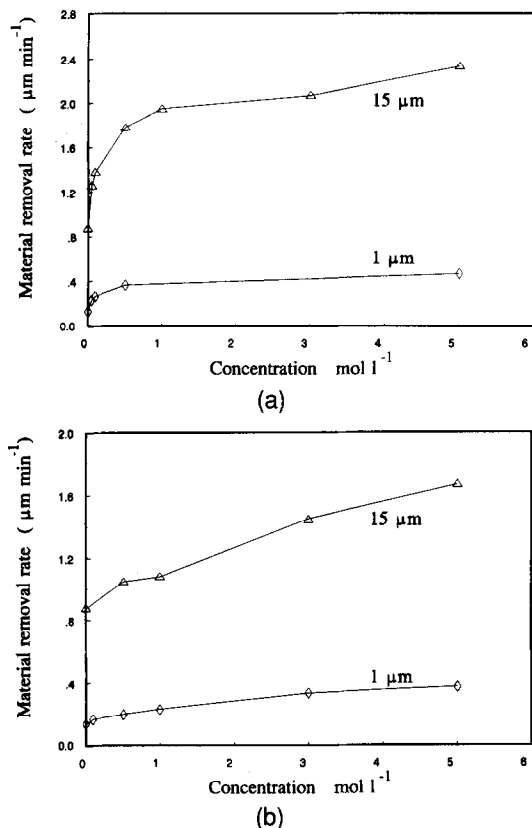


Fig. 4. Variation of the material removal rate of silicon nitride balls with the concentration of inorganic additive A (a) and inorganic additive B (b) in 1 μm and 15 μm WODS during grinding at 400 N load and 3000 rev min^{-1} speed.

3.2.3 Effect of diamond particle size

Inorganic additives were added to WODS containing diamond particles of different sizes. Figures 4(a) and (b) show the rate of material removal resulting from grinding in the 1 or 15 μm WODS with varying concentrations of additives A and B, respectively. It is seen that the material removal rate increases both with increasing size of the diamond particles and increasing concentration of inorganic additives. The material removal rate is over five times higher when grinding in the 15 μm slurry with the inorganic additive A or B than in the corresponding slurry containing 1 μm diamond particles.

As indicated earlier, there was an initial sharp increase in the material removal rate with increasing concentration of additive A. Afterwards the rate stabilized at a more or less constant value.

3.3 Material removal rate in the presence of organic additives

3.3.1 Different base tribochemical slurries

Tribochemical effects produced by organic additives during grinding of silicon nitride balls were studied by adding 15 μm diamond particles to a number of base tribochemical slurries. To compare the grinding behaviour, a reference slurry

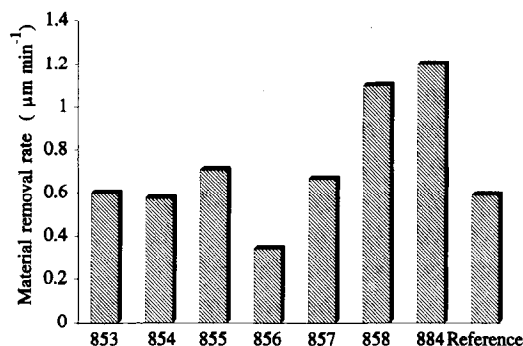


Fig. 5. Material removal rate of silicon nitride balls during grinding at 400 N load and 3000 rev min^{-1} speed in the tribochemical slurries with 15 μm diamond particles.

was produced by removing the diamond particles from the oil-based slurry and replacing them by the same 15 μm diamond particles used for base tribochemical slurries. This slurry was called the reference slurry. Figure 5 gives the material removal rates during grinding in the various tribochemical diamond slurries and reference slurry. It appears from Fig. 5 that the highest material removal rate was achieved during grinding in the 884 diamond slurry and the lowest in the 856 diamond slurry.

A high material removal rate also occurred during grinding in the 858 diamond slurry, as shown in Fig. 5. However, it was found that after grinding the silicon nitride balls were not completely spherical, the maximum difference in diameter being almost 10 μm . A difference in diameter was also found after grinding the silicon nitride balls in the 856 and 857 diamond slurries; this time the difference was 6 and 8 μm , respectively.

3.3.2 Base diamond slurry with organic additives

To study the effect of organic additives on the grinding behaviour of the silicon nitride balls, seven different additives were added into 1 μm oil-based diamond slurry at a concentration of 1 wt%. The results are shown in Fig. 6. It is seen that a decrease in the material removal rate occurred during grinding in HT312, dibenzyl disulfide (DBDS)

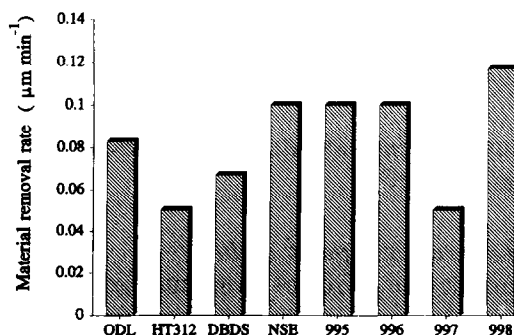


Fig. 6. Effect of organic additives on material removal rate of silicon nitride balls during the grinding at 400 N load and 3000 rev min^{-1} speed in 1 μm oil-based diamond slurry.

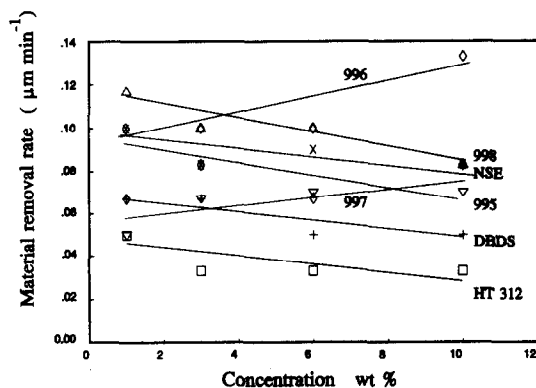


Fig. 7. Variation of the material removal rate of silicon nitride balls with concentration of organic additives in 1 μm diamond slurry during grinding at 400 N load and 3000 rev min^{-1} speed.

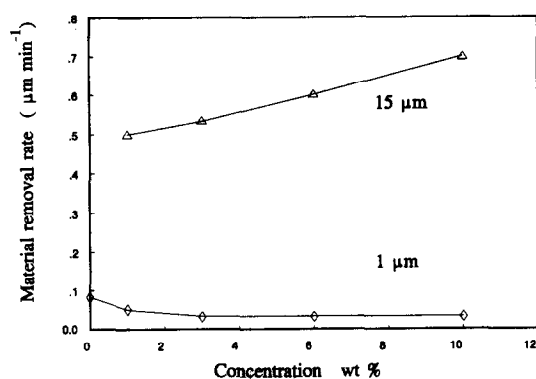


Fig. 8. Effect of the concentration of organic additives and the size of diamond particles in a diamond slurry on the material removal rate of silicon nitride balls during grinding at 400 N load and 3000 rev min^{-1} speed.

and 997 slurries. On the other hand, an increase occurred when natural sulfide ester (NSE), 995, 996 and 998 slurries were used.

The material removal rate as a function of organic additive concentration in 1 μm oil-based slurry was also examined. The results indicate that, during grinding in most of the diamond slurries, the material removal rate decreases with an increase in the concentration of organic additive (see Fig. 7). However, the reverse results were obtained using 996 and 997 organic additives, with the material removal rate increasing. Figure 8 gives the variation of the material removal rate with increasing concentration of the HT312 additive in 1 and 15 μm diamond slurries.

4 Discussion

4.1 Characteristics of ground surface in the presence of water

It was reported that, during sliding of silicon nitride in the presence of water, both friction and wear decrease.⁷ In this study, in contrast, an increase in the material removal rate occurs during grinding

of the silicon nitride in the oil-based diamond slurry containing water (see Fig. 2). Examining the surfaces after tests in both oil-based diamond slurry and WODS, it is evident from Fig. 9 that different surface appearances were produced during grinding. Both surfaces are covered with scratches on the micrometre scale, which indicates a ploughing action during grinding (see Figs 9(a) and (c)). At a high magnification, scratches on the nanometre scale can also be seen on the ground surfaces (see Figs 9(b) and (d)).

It is apparent from Fig. 9 that there are two major differences between both ground surfaces. All the scratches on the surface produced by the grinding test in 1 μm oil-based slurry have very clear edges (Fig. 9(a)). However, it seems that the scratches on the surface produced by the grinding test in WODS are shallower and smaller than those produced by the grinding test in 1 μm oil-based diamond slurry (see Fig. 9(c)). It is evident at a high magnification that the edges of the scratches are not sharp (see Fig. 9(d)). On the other hand, the number of the scratches decreased dramatically after grinding in 1 μm WODS, as shown in Figs 9(c) and (d). It can be postulated, therefore, that the surface produced by grinding in WODS is smoother than that in the oil-based diamond slurry. This is in agreement with the finding⁴ that a smooth surface resulted from the tribochemical nature of the reaction of silicon nitride with water.

4.2 Characteristics of ground surface in the presence of inorganic additives

Addition of additive A or B to WODS caused a remarkable increase in the material removal rate, as shown in Figs 2 and 3. Examination of the ground surfaces reveals an uneven topography after the tests in 1 μm WODS with 5 mol dm^{-3} of A or B. This can be seen in Figs 10(a) and (b). These figures indicate that the high rate of material removal is accompanied by the formation of a relatively rough surface.

Closer examination of Fig. 10(a) reveals the existence of black areas on a white background under a scanning electron microscope. At high magnification, the black areas look very smooth, as can be seen in Fig. 11(a). The white areas are rough with an open surface texture and are considered to be pitted regions created by tribochemical action, as can be seen in Fig. 11(b). With decreasing concentration of the additive A in WODS, the percentage of the pitted regions in the total contact surface decreased. Finally, at the lowest concentration of A in 1 μm WODS equal to 0.05 mol dm^{-3} , the pitted regions were reduced to islands as shown in Fig. 12(a). More characteristic features

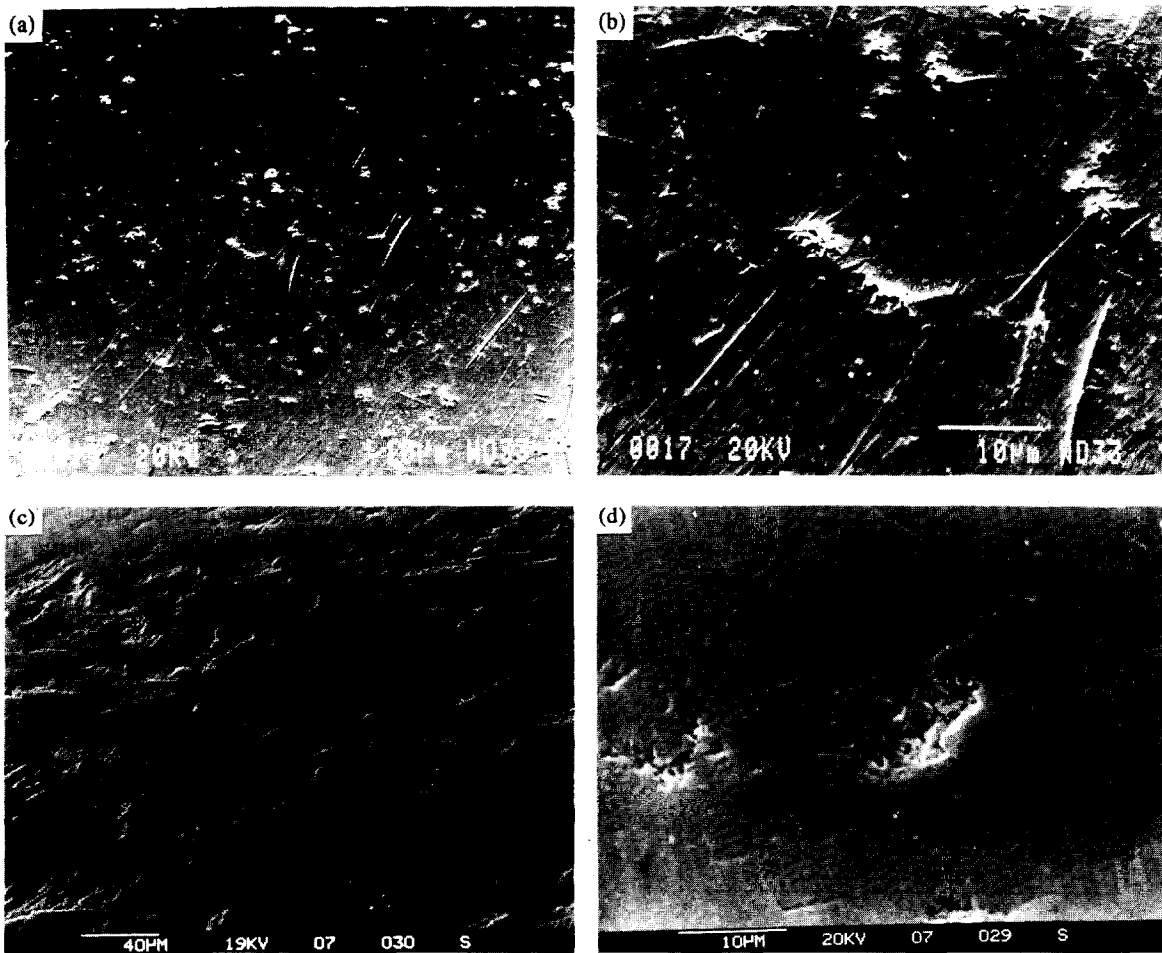


Fig. 9. SEM micrographs of ground surfaces of silicon nitride balls after grinding tests at $3000 \text{ rev min}^{-1}$ speed and 400 N load in $1 \mu\text{m}$ oil diamond slurry (a and b) and $1 \mu\text{m}$ WODS (c and d).

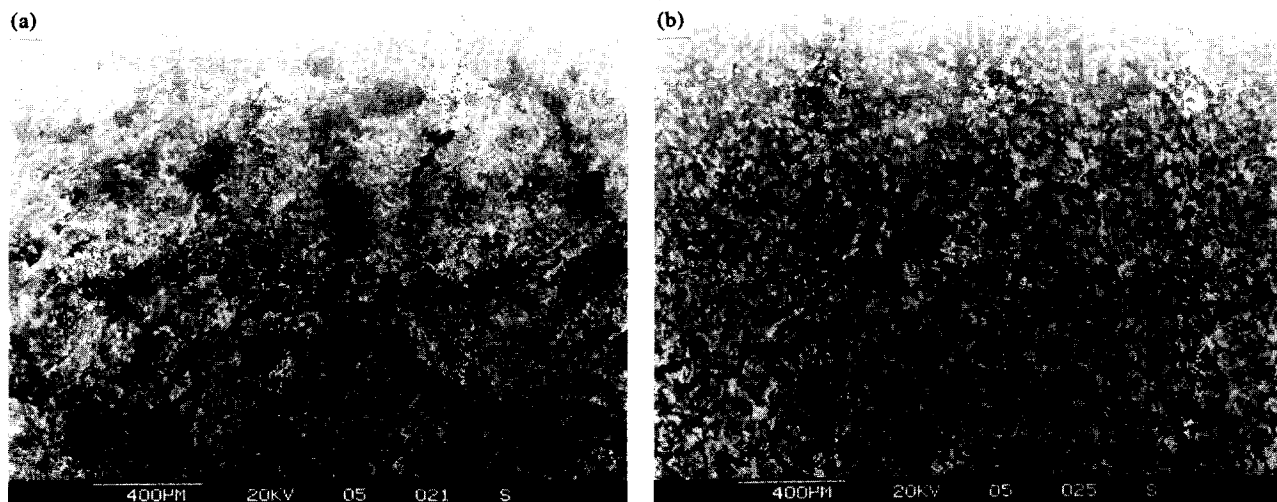


Fig. 10. SEM micrographs of ground surfaces after grinding tests of 1 h duration under 400 N load and $3000 \text{ rev min}^{-1}$ speed in (a) 5 mol dm^{-3} of A in $1 \mu\text{m}$ WODS and (b) 5 mol dm^{-3} of B in $1 \mu\text{m}$ WODS.

produced by grinding in 0.05 mol dm^{-3} of A in $1 \mu\text{m}$ WODS are shown in Figs 12(b) and (c).

Figure 10(b) reveals that there are many pitted regions produced by the grinding test in 5 mol dm^{-3} of B in $1 \mu\text{m}$ WODS. Examination of these regions at a high magnification indicates that they appear to be pits on a smooth black surface (see Fig. 13(a)). Like the pitted regions formed by the

grinding test in 5 mol dm^{-3} of A in $1 \mu\text{m}$ WODS, the pitted regions show a rough surface with an open surface texture (see Fig. 13(b)).

4.3 Characteristics of ground surface in the presence of organic additives

The diamond slurries with organic additives included the blank, the sulfur-containing and the

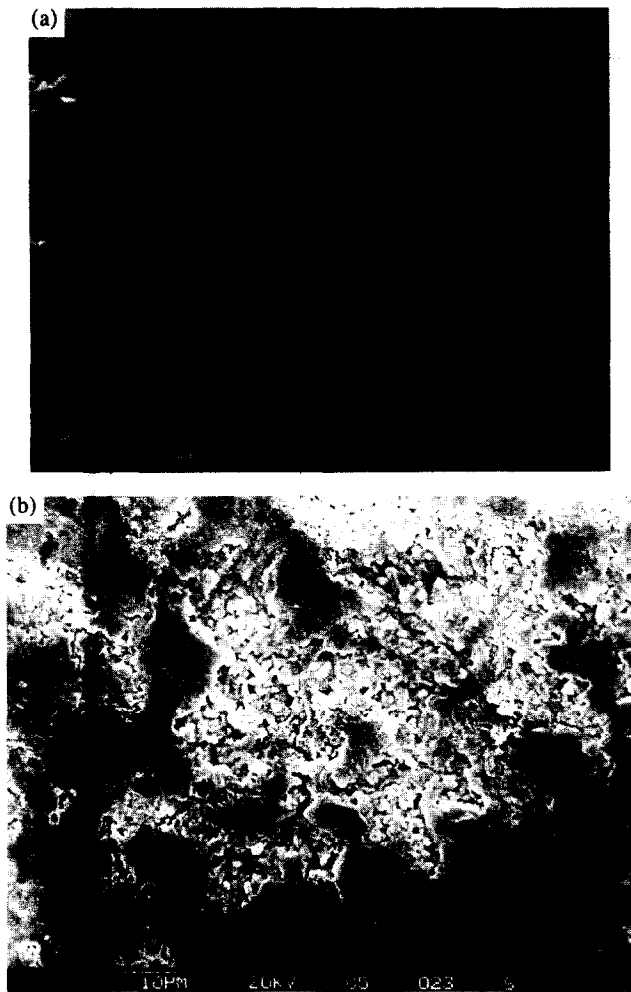


Fig. 11. SEM micrographs of ground surfaces after grinding tests of 1 h duration under 400 N load and 3000 rev min⁻¹ speed in 5 mol dm⁻³ of A in 1 μm WODS. (a) Smooth black area, (b) rough pitted region.

ester-containing diamond slurries. The blank diamond slurries were those without an organic additive, and included the oil-based, the highly refined mineral oils 853 and 854, the poly-alpha-olefins 856 and 857, and polyoxyalkylene glycol ether 858. With the exception of the 858 slurry, all blank slurries gave a similar material removal rate, as shown in Fig. 5. However, the 856, 857 and 858 slurries caused ovality of the balls which is an undesired side-effect.

The sulfur-containing slurries included the HT312, the 997 and the DBDS diamond slurries. The experimental results indicated a decrease in the material removal rate during grinding tests in the sulfur-containing slurries due to the presence of the sulfur-containing additives (see Fig. 6). However, microscopic examination of ground surfaces revealed an excellent surface finish, as can be seen in Figs 14(a) and (c). Gates and Hsu⁵ pointed out that the smooth surface of the silicon nitride results from the formation of a surface film during sliding in the sulfur-containing slurries. A study on the surface micro-topography at high magnification showed the existence of very fine scratches pro-

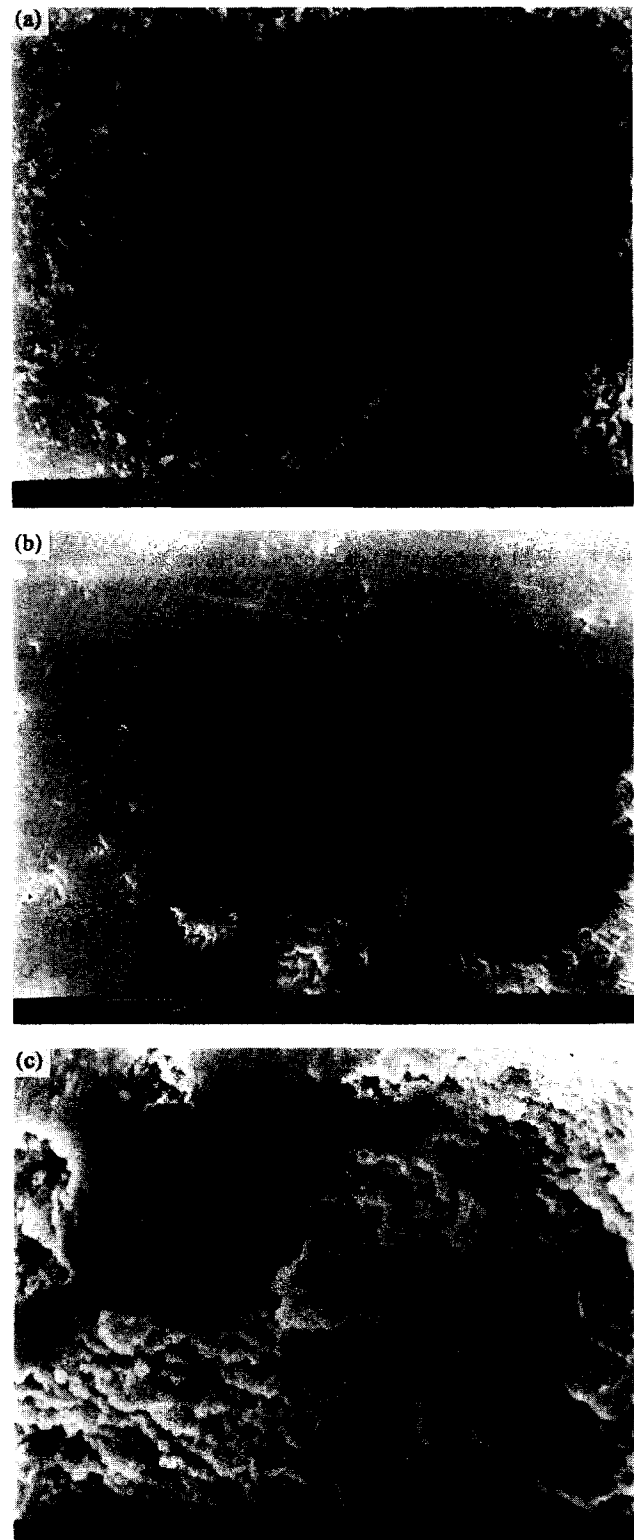


Fig. 12. SEM micrographs of ground surfaces after grinding tests of 1 h duration under 400 N load and 3000 rev min⁻¹ speed in 0.05 mol dm⁻³ of A in 1 μm WODS. (a) Islands of the pitted region, (b) smooth black area, (c) rough pitted region.

duced by micro-cutting after grinding tests in the sulfur-containing slurries, as shown in Figs 14(b) and (d). Some pitted regions a few micrometres in size were also found, as can be seen in Fig. 14(d).

The 995 and 996 additives are metal-containing sulfonates. The material removal rate was slightly higher during grinding with these additives than in the blank oil-based diamond slurry (see Fig. 6).

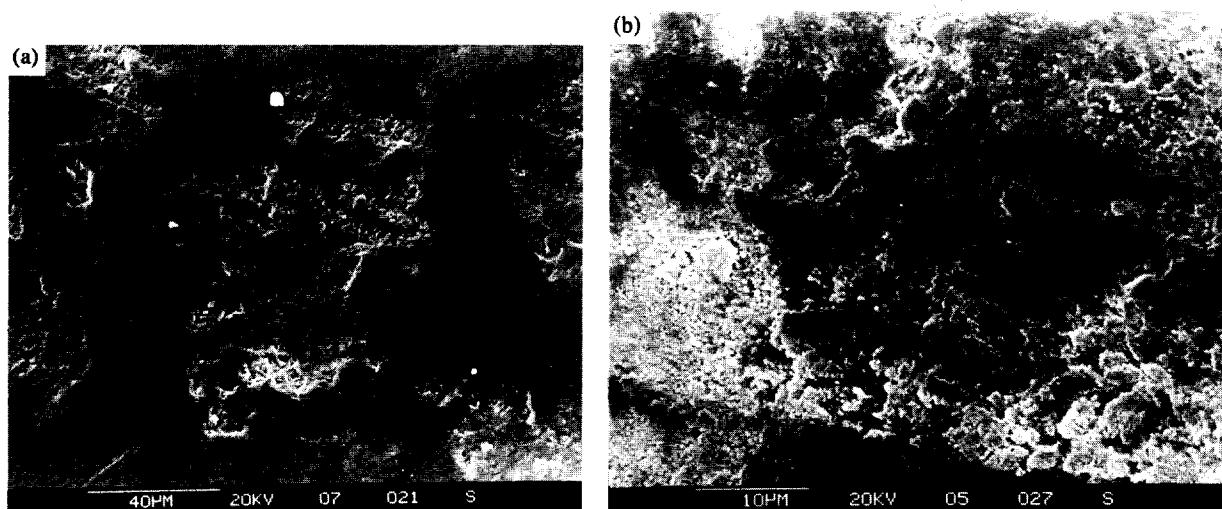


Fig. 13. SEM micrographs of ground surfaces after grinding tests of 1 h duration under 400 N load and 3000 rev min⁻¹ speed in 5 mol dm⁻³ of B in 1 μm WODS. (a) Pitted region resembling a pit on the smooth black area, (b) rough pitted region.

It was found that the slurry viscosity increased upon the addition of the 995 and 996 additives. Figure 15 shows the ground surface of silicon nitride ball after the test in the 995 and 996 slurries. It is seen from Figs 15(a) and (c) that most regions on the ground surface show an excellent surface finish. Observation of the ground surface at a high magnification indicates the presence of a few deep grinding scratches (see Figs 15(b) and (d)).

Ester-containing diamond slurries consisted of

the 855, the 884, the 998 and the NSE slurries. From Figs 5 and 6, it is apparent that grinding in the ester-containing slurries resulted in an increase in the material removal rate. Microscopic examination of the surfaces ground in the 998 and NSE slurries revealed fine scratches and pitted regions, as shown in Fig. 16. Both 998 and NSE contain sulfur, which may have contributed to the polishing process. However, the exact mechanism is not known.

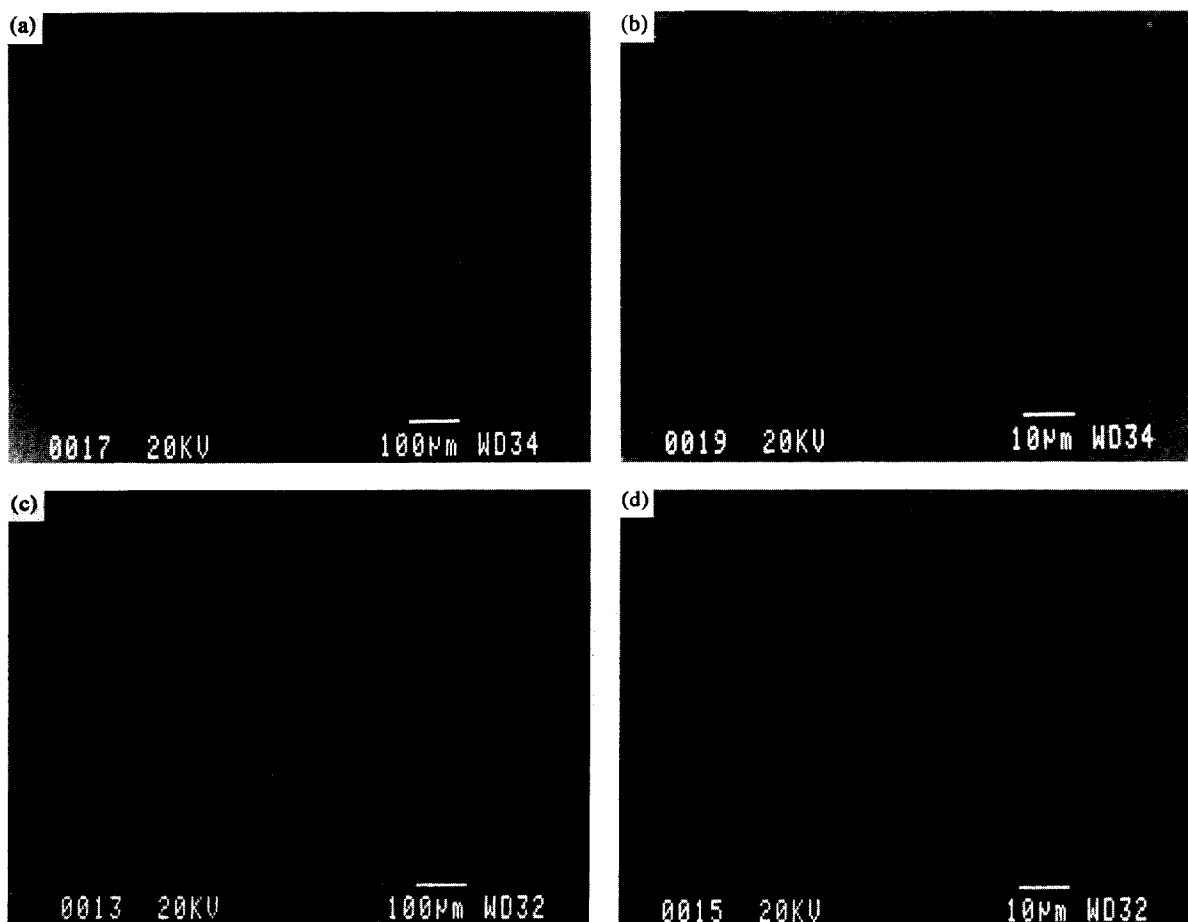


Fig. 14. SEM micrographs of ground surfaces after grinding tests of 1 h duration under 400 N load and 3000 rev min⁻¹ speed in 1 wt% of 997 in 1 μm diamond slurry (a and b) and 1 wt% of DBDS in 1 μm diamond slurry (c and d).

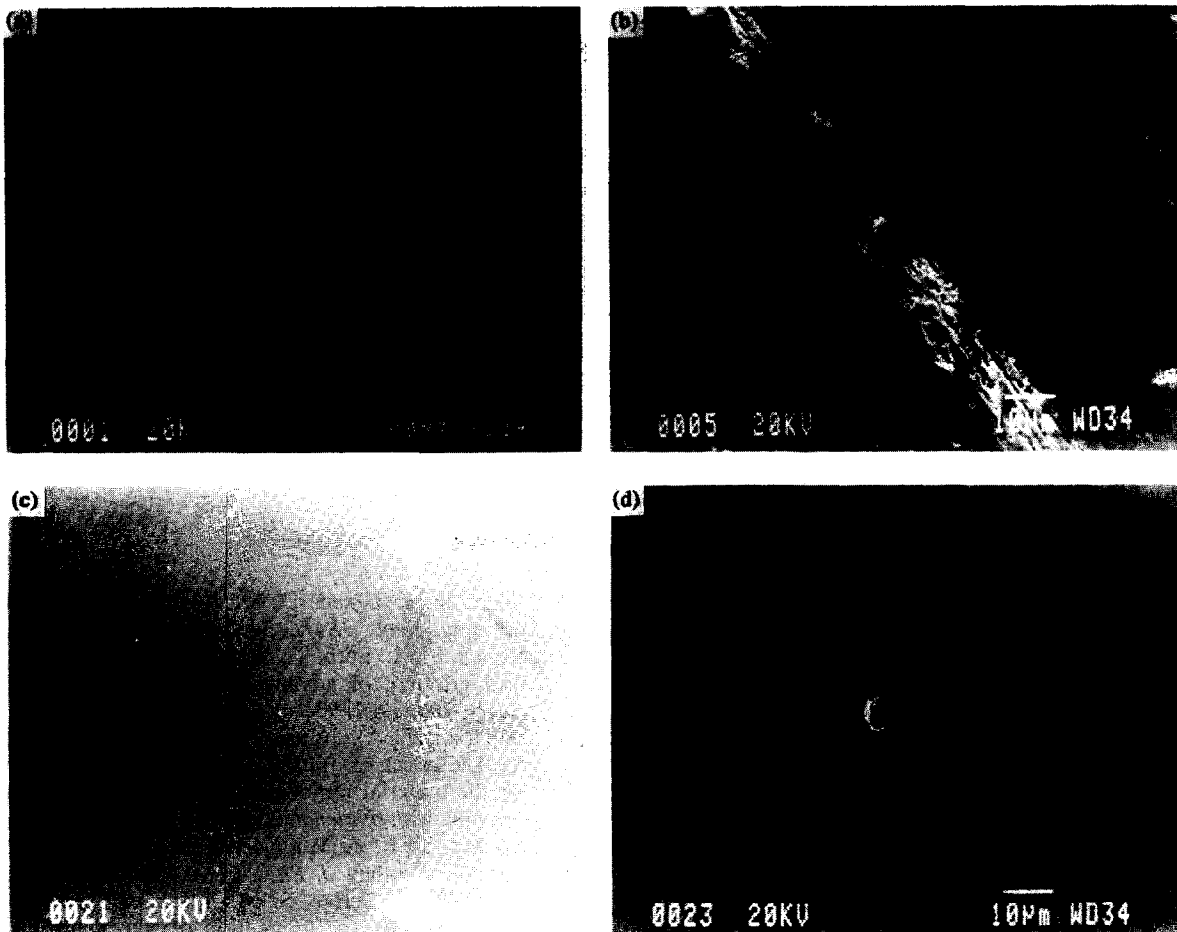


Fig. 15. SEM micrographs of ground surfaces after grinding tests of 1 h duration under 400 N load and 3000 rev min⁻¹ speed in 1 wt% of 995 in 1 μm diamond slurry (a and b) and 1 wt% of 996 in 1 μm diamond slurry (c and d).

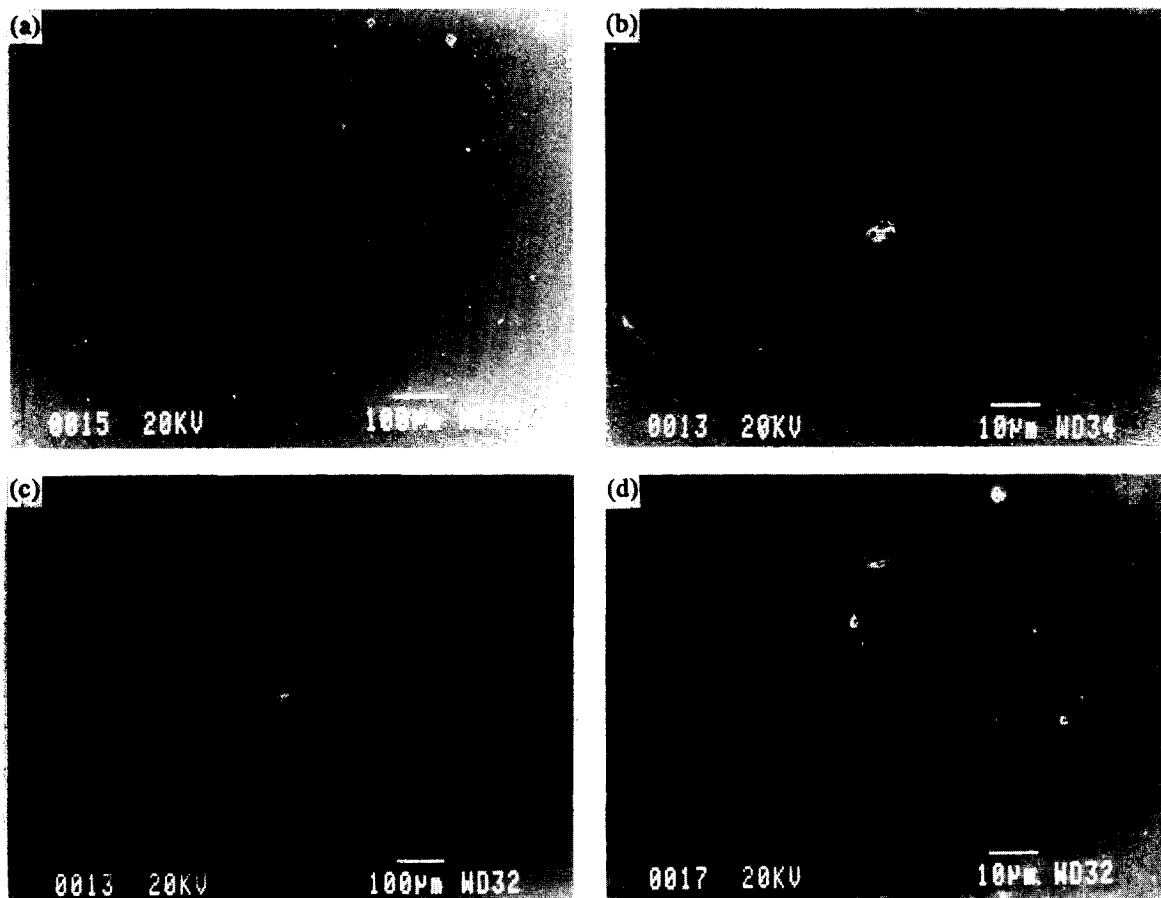


Fig. 16. SEM micrographs of ground surfaces after grinding tests of 1 h duration under 400 N load and 3000 rev min⁻¹ speed in 1 wt% of 998 in 1 μm diamond slurry (a and b) and 1 wt% of NSE in 1 μm diamond slurry (c and d).

5 Conclusions

From the results reported in this paper, the following conclusions can be drawn.

- (1) It has been found that the acid additive (A) and alkaline additive (B) are very effective additives to a diamond grinding slurry, increasing the rate of material removal from the silicon nitride balls. Inclusion of additive A or B into the mixture of 50% water-based and 50% oil-based diamond slurry increased the material removal rate six or four times, respectively.
- (2) The material removal rate of the silicon nitride balls increases both with increasing concentration of inorganic additive (A or B) and increasing size of diamond particles in the slurry.
- (3) Examination of ground surfaces revealed rough, pitted regions within a smooth surface. It was found that the surface produced by grinding in the diamond slurry with additive A or B is relatively rough.
- (4) The presence of water in a diamond slurry increases the material removal rate, and the resulting surface is very smooth.
- (5) The effect of three groups of organic additives on the rate of material removal was studied in the oil-based diamond slurry. A decrease in the material removal rate was noted in the presence of sulfur-containing additives. Addition of ester-based additives resulted in an

increase of the material removal rate. The metal-containing sulfonate additives acted primarily as a viscosity improver. The significant increase in viscosity of the diamond slurry resulted in an increased material removal rate.

Acknowledgements

The authors would like to thank the Engineering and Physical Science Research Council and the Defence Research Agency for the support of the research reported in this paper.

References

1. Kato, K. & Umehara, N., A study on magnetic fluid grinding. *Trans. JSME*, **54** (1988) 1.
2. Rezaei, S. M., Suto, T., Waida, T. & Noguchi, H., Creep feed grinding of advanced ceramics. *Proc. Inst. Mech. Engrs*, **206** (1992) 93.
3. Stolarski, T. A., Jisheng, E., Gawne, D. T. & Panesar, S., The effect of applied load and abrasive particle size on the material removal rate of silicon nitride artefacts. *Ceramics International*, **2** (1995) 355.
4. Fischer, T. E. & Mullins, W. M., Chemical aspects of ceramic tribology. *J. Phys. Chem.*, **96** (1992) 5690.
5. Gates, R. S. & Hsu, S. M., Effect of selected chemical compounds on the lubrication of silicon nitride. *STLE, Tribology Trans.*, **34** [3] (1992) 417.
6. Wang, J. C. & Hsu, S. M., Chemical assisted machining of ceramics. *J. Tribology, Trans. ASME*, **116** (1994) 423.
7. Gee, M. G. & Butterfield, D., The combined effect of speed and humidity on the wear and friction of silicon nitride. *Wear*, **162-164** (1993) 234.

Reaction-Bonded Titanium Nitride Ceramics

A. Pivkina,^{a,b} P. J. van der Put,^{a*} Yu. Frolov^b & J. Schoonman^a

^aLaboratory for Applied Inorganic Chemistry, Delft University of Technology, PO Box 5045, 2600 GA Delft, The Netherlands

^bInstitute of Chemical Physics, Kosygina Street 4, 117977 Moscow, Russia

(Received 15 August 1994; revised version received 23 May 1995; accepted 9 June 1995)

Abstract

Reaction-bonded titanium nitride (RBTN) ceramics were formed using high surface area titanium powder (surface area $20 \text{ m}^2 \text{ g}^{-1}$), and nitrogen gas as precursor reactants. The titanium precursor was made by the combustion synthesis technique.¹ Owing to their microstructure and internal porosity, the metal particles are highly reactive towards nitrogen, and can be fully converted to the mononitride at comparatively low temperatures and short reaction times. Nitridation kinetics of these powders were determined at temperatures of up to 1000°C by means of insitu gravimetry. Dry-pressed binderless porous titanium pellets were heat-treated in pure nitrogen at temperatures of up to 1000°C , and fully converted to the porous TiN compacts with dimensional changes less than 5%. A reaction mechanism is proposed. The difference between the relative density of the final product and the packing density of the green body was negligibly small, but there is a considerable increase in the gas permeability and mechanical strength during nitridation. The porous end product is a suitable matrix for further applications and for making composites by infiltration deposition.

1 Introduction

Reaction bonding is a well-established ceramic forming method.² Of the many conceivable ceramic materials that can be made by reaction bonding, so far only reaction-bonded silicon nitride (RBSN) and reaction-bonded silicon carbide (RBSC) are produced on a commercial scale. These reaction-bonded products have acceptable to good properties, yet are not fully dense as a result of the use of gaseous reactants. The main benefit of reaction-bonding is that it produces near net shape articles.

TiN has good intrinsic properties such as high hardness, high electronic conductivity and a low coefficient of friction, but is not a mainstream structural ceramic. Titanium nitride ceramics are difficult to process, except by chemical vapour deposition (CVD), due to low sinter activity and low diffusion rates.

The use of self-heating synthesis (SHS) of refractory materials has gained attention in recent years,^{1,3} but these SHS products are not reaction-bonded ceramics. This raises the question of whether reaction bonding is feasible as a near net shape processing technique for titanium nitride ceramics. Several patents exist⁴⁻⁶ on high-temperature synthesis of reaction-bonded titanium nitride (RBTN) from coarse (sponge) titanium powder using nitrogen and ammonia precursors. The low diffusion coefficients in TiN, however, slow down the reaction-bonding processes and preclude formation of RBTN other than by brute force. Surface coating of the titanium particles with TiN, which shields the interior of the particles from nitridation, prevents full conversion when reacting titanium with nitrogen to titanium mononitride. The Pilling–Bedworth rule would predict stable scale formation and self-limitation in the titanium nitridation reaction. However, by using specially tailored Ti powders made by a new technique,¹ we have observed that full conversion of the metal to porous RBTN under mild conditions is possible, as this paper will show. The nature of the solid precursor particles, in particular their surface area, is the main limiting factor for the possibility of processing reaction-bonded ceramics based on passivating scale-forming metals.

After a short description of the combustion wave method, which is a novel way for forming the high surface area titanium precursors, this paper will concentrate on nitridation kinetics of titanium powder and green pressed compacts, and also on the morphological aspects of reaction-bonded titanium nitride. Mechanical strength and argon permeability of the compacts are reported.

*To whom correspondence should be addressed.

2 Synthesis and Characterization of Titanium Powder made by the Combustion Wave Method

The metal precursor used for RBTN was a novel type of titanium powder supplied by the Institute of Chemical Physics, Moscow. The method for making the high surface area titanium powders is based on high-temperature reduction of TiO_2 using magnesium as a reductant. Commercial grade TiO_2 paint pigment powders (99.8%) were mixed with a slight excess of fine Mg powder (99.7%, 44 μm), and pressed into cylindrical tablets (diameter 5 cm, height 20 cm, porosity 10%). They were put into a reactor under argon (1 bar), and locally heated for ignition. The heat of the SHS reaction:



is sufficient to sustain the conversion reaction once ignited. In the reaction front of the combustion wave the measured maximum temperatures were $> 2000^\circ\text{C}$.

The solid product, which consists of a mixture of Ti, unreacted Mg, MgO and unreacted TiO_2 , was leached with hydrochloric acid, washed with distilled water, dried, milled and sieved in air. Analysis revealed the following impurities (weight percent): 0.8% Mg; 0.5% MgO; 2% TiO_2 ; 0.01% Cl.

Figures 1(a) and (b) show scanning electron micrographs of the titanium powder particles. Some self-similarity is observable in these powders.

The specific surface area of the titanium powders was measured by BET using krypton. It varied with particle (cluster) size as Fig. 2 shows. The particle size fractions were 1, 15 and 200 μm . Assuming self-similarity, one obtains a surface fractal dimension of 2.67,⁷ a value as high as that of porous coconut charcoal. Such a high surface dimension suggests a gas-phase mechanism rather than a liquid intermediate during reductive formation of the powder.

It is of some interest to compare the morphologies of the titanium powders obtained by different methods. The industrial Kroll method of producing sponge titanium by reducing TiCl_4 in molten magnesium yields metal powders having a specific surface area of the order of $0.1 \text{ m}^2 \text{ g}^{-1}$ after milling. For contrast to the morphology of the combustion wave generated titanium powder, the morphology of a commercial sample of sponge titanium powder is given in Fig. 1(c).

Since the adiabatic reaction temperature is well above the melting points of magnesium and titanium dioxide, and the reaction times are short, the SHS process for the novel titanium powders consists of a complicated set of local reactions between solid, liquid and vapour phases, leading to coral-like morphologies and high specific

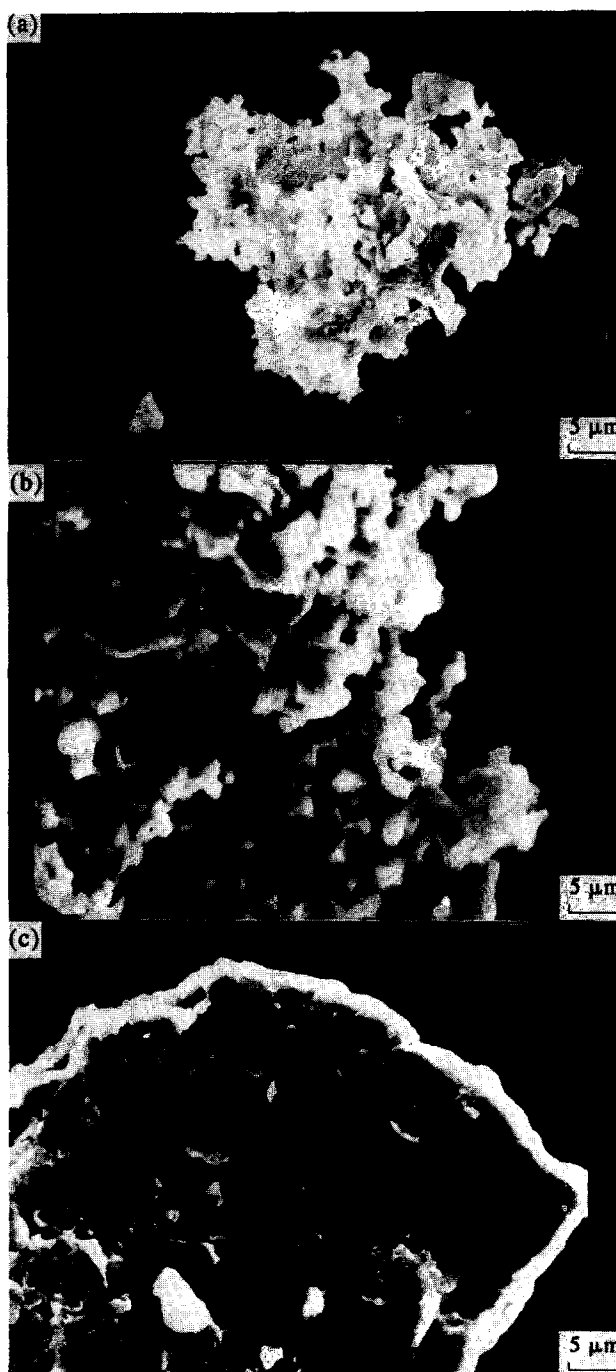


Fig. 1. SEM micrographs of combustion wave generated titanium particles: (a) $d = 15 \mu\text{m}$, (b) $d = 200 \mu\text{m}$, (c) industrial Kroll Ti particle, $d = 63 \mu\text{m}$.

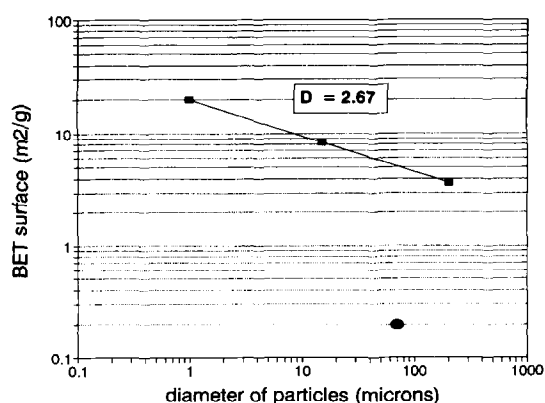


Fig. 2. Measured specific area of Ti powders as a function of particle size; ■, combustion wave generated Ti; ●, industrial Kroll Ti.

surface areas (up to $20 \text{ m}^2 \text{ g}^{-1}$). The combustion wave method for making high surface area metal powders, which are stable enough for use as precursors of reaction-bonded nitride ceramics, is a convenient process which can be scaled up for bulk production.

3 Nitridation of Titanium Powder and Dry-pressed Powder Compacts to RBTN

Direct conversion of the combustion wave generated titanium precursor to TiN by reaction with pure nitrogen was studied with two groups of samples: free uncompact loose powder, and compacted green pellets, dry-pressed from the metal powder. The nitridation rates were determined by *in situ* thermogravimetry, and the product characteristics were studied using X-ray diffraction (XRD), metallography and porosimetry.

3.1 Materials, samples and methods; experimental aspects

The nitrogen and argon gases used were supplied by Air Products and had a purity of $>99.9999\%$ and $>99.9995\%$, respectively. The gases were further purified to a level of 5×10^{-8} of oxygen-containing species by a packed bed of titanium granules kept at a temperature of 660°C .

The particle size, surface area and morphology of the unreacted and reacted powders and compacts were characterized using scanning electron microscopy (SEM; Jeol, JSM-35), BET measurements (Micrometric Instrument Corporation), an XRD system (Philips PW 1840/01/11), and Mercury intrusion porosimetry (Porosimeter 2000).

The preparation process for the Ti pellets was as follows: precursor powder was hydraulically pressed under vacuum ($P_{\text{max}} = 3.8 \text{ kbar}$). Pellets were 1 cm in diameter and about 0.05 cm thick. The porosity as measured from the external size of a weighed pellet varied between 0.20 and 0.45. The degree of homogeneity of the Ti tablets was established by optical micrographs and scanning electron microscopy. The C-ring diametral compression test was performed as previously described,⁸ with Ti and TiN rings for the mechanical strength evaluation. The nitridation kinetics of titanium powders and green powder compacts were determined by *in situ* measurement of the sample weight increase in a vertical tube CVD reactor equipped with a thermobalance (C.I. Electronics Microforce Balance) with vacuum head and computer control unit. Its capacity was 5 g, the sensitivity $0.1 \mu\text{g}$.

For the free powder nitridation experiments the platinum cup of the thermobalance was equipped

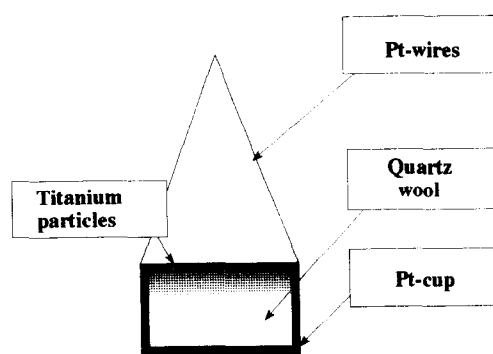


Fig. 3. Schematic presentation of the quartz wool bed used for free powder nitridation experiments.

with a quartz wool bed on which titanium powder (up to 40 mg) was placed as shown in Fig. 3. This arrangement provided uninhibited access of nitrogen to all particles. In all cases, powder having a narrow particle-size distribution was used in order to minimize the effect of packing variations.

The nitridation procedure was as follows. Initially, the samples were heated in an argon atmosphere at a rate of $100^\circ\text{C min}^{-1}$ up to the reaction temperature, which varied between 600 and 1000°C . Then the reactor was evacuated to 0.1 mbar using a single-stage mechanical rotary vacuum pump, the reactor was filled to 1 bar with nitrogen, and the weight increase recorded at constant temperature. All experiments were carried out at atmospheric pressure.

The progressive changes in the porous structure of Ti compacts before and after nitridation were evaluated using SEM observations, porosimetry and forced argon flow permeability measurements as described in Ref. 8.

3.2 Kinetics of titanium powder nitridation

As mentioned above, a thin layer of Ti particles was placed on the quartz wool bed in the platinum cup. No changes in the conversion rate were observed for samples of initial weight varying

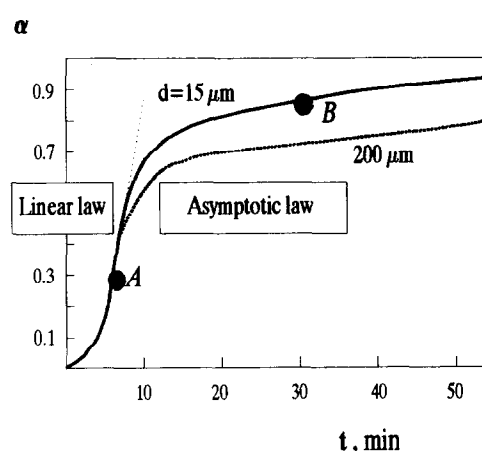


Fig. 4. Experimental nitridation kinetics of Ti particles at $T = 1000^\circ\text{C}$. Points A and B correspond to quenched samples.

from 9 to 20 mg, which indicates that there were no packing effects, and particle nitridation rates are not affected by the presence of the other particles in this weight range. Figure 4 shows the intrinsic kinetics of Ti powder nitridation as derived from the relative weight increase α measured with the thermobalance. The degree of conversion $\alpha(t)$ is defined as the instantaneous weight increase of the titanium sample during nitridation divided by the expected final weight increase on full nitridation of the titanium sample to stoichiometric TiN. After an initial transient slow rate corresponding to an incubation period due to breakdown of the passivating surface oxide film, a behaviour linear with time was observed for α at the first stage of nitridation. The relative conversion rate did not appear to depend on particle size or on the reaction temperature between 820 and 1000°C, suggesting that in the first reaction stage there is uninhibited diffusion of nitrogen into all particles, and the measured nitrogen dissolution rate is of the order of $8.3 \times 10^{-4} \text{ mol}\cdot\text{s}^{-1}$.

After attaining a degree of conversion α of approximately 0.5, the linear kinetic law changed to an asymptotic one. At this stage the conversion rate depends more strongly on temperature and particle size. As expected, higher conversion rates are observed with increasing temperature, and decreasing particle size. At comparatively modest reaction temperatures, complete conversion of titanium to titanium nitride is possible within reaction times of about 3 h. These results show that the intrinsic kinetics can be adequately described by the combination of dissolution and diffusion rate laws.

To determine reaction intermediates, some titanium powder samples were nitrided for a short time at 1000°C and subsequently quenched. The quenching procedure was as follows: the reactor was evacuated to 0.1 mbar using a mechanical rotary vacuum pump, flushed with argon to 1 bar, and cooled under argon to room temperature by removing the furnace from the fixed reactor tube. Points A and B in Fig. 4 were analyzed *ex situ* by X-ray diffraction. The presence of hcp α -Ti(N) (nitrogen-containing titanium) structures and small amounts of δ -TiN for sample A and fcc δ' -TiN as well as tetragonal δ' -TiN in sample B was established by XRD. As these phases are known to be stable on cooling to room temperature, they can be assumed to have been formed during the nitridation reaction.

These results and the phase diagram suggest the following path during reaction of titanium with nitrogen. The phase diagram for the system Ti-N has been reported by Lengauer.⁹ According to the phase diagram the initial titanium particles have

the hcp structure (α -Ti), which converts to tetragonal β -Ti at a temperature of 882°C. Nitrogen dissolves in (β -Ti) up to saturation (3 at%)¹⁰ after which threshold concentration the β -Ti lattice re-converts to the (α -Ti) hcp structure, which is able to dissolve nitrogen up to a concentration of 23 at%. Further reaction with gaseous nitrogen yields δ -TiN. According to the phase diagram tetragonal ϵ -Ti₂N exists at a temperature of 1000°C, but it converts to substoichiometric fcc δ -TiN.

Figure 5 represents the crystal cell volume versus nitrogen content for the Ti-N system. The titanium particles swell somewhat during nitridation as observed in SEM micrographs of sample A (Fig. 6). Increase in volume results in a decrease of the permeability of micropores inside the Ti particle, as shown by Fig. 13.

The diffusion coefficient of nitrogen in titanium solutions and titanium nitrides is reported to vary within orders of magnitude with the evolution of

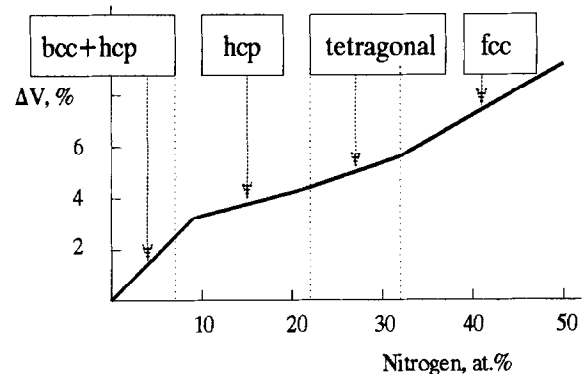


Fig. 5. Predicted evolution of the crystal cell volume during Ti nitridation at 1000°C.

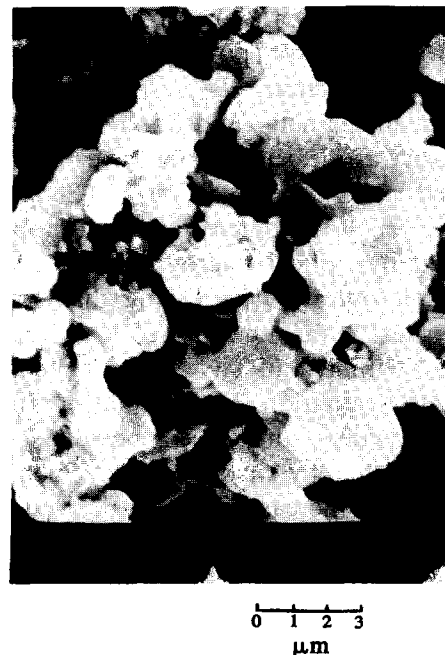


Fig. 6. SEM micrograph of a completely converted Ti particle. Swelling during nitridation is observed.

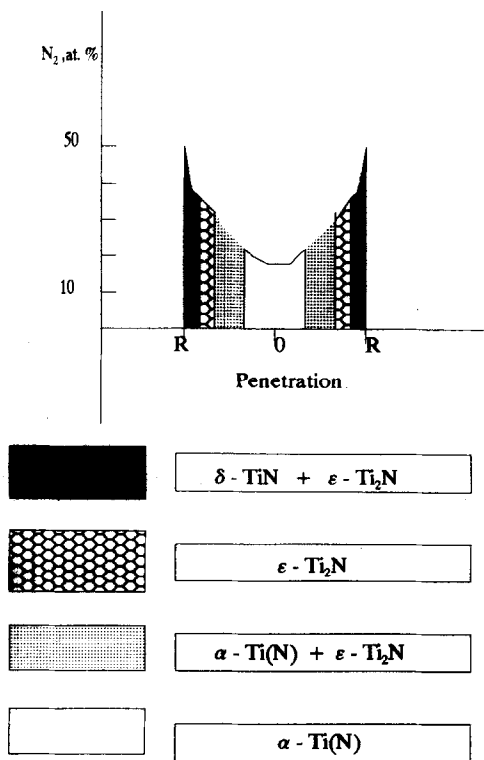


Fig. 7. Diffusion profile of nitrogen inside a Ti particle, $T = 1000^{\circ}\text{C}$ (qualitative picture).

crystal structure.^{10,11} The ratio of the nitrogen diffusion coefficients in β -Ti, α -Ti and δ -TiN is of the order of 100:10:1. This suggests that titanium is first rapidly saturated with nitrogen at a rate limited by the dissolution reaction. Subsequently, nitrides form at a much slower rate which increasingly becomes diffusion limited. The observed kinetics are consistent with this reaction path. Figure 7 shows the concentration profile of nitrogen in a titanium particle during reaction. This qualitative picture, which is based on the TiN phase diagram, diffusion rates and our experimental results, reflects the evolution of the titanium particle during conversion by nitridation.

3.3 Nitridation kinetics of pressed green titanium powder compacts

Dry-pressed titanium compacts have been nitrided, and the dependence has been established of the kinetics, morphology and local degree of conversion on particle size, reaction temperature, and compact density.

Figures 8, 9 and 10 show that the overall kinetic behaviour of compacts is similar to that of free powder particles. In the initial stages of nitridation the kinetic curves of both types of sample virtually coincide. The rate of compact nitridation starts to diverge from that of powders in the asymptotic part, which is the domain of higher conversion degrees. In this much slower nitride formation step, the differences between kinetic

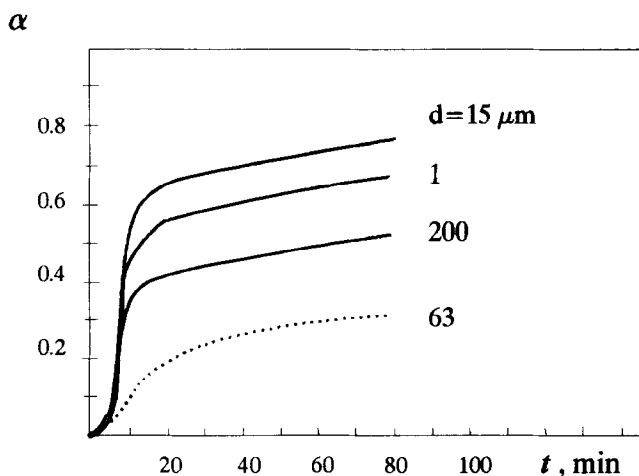


Fig. 8. Experimental nitridation kinetics of Ti pellets at 1000°C : —, combustion wave generated Ti; ---, industrial Kroll Ti. Original particle sizes are indicated in the figure.

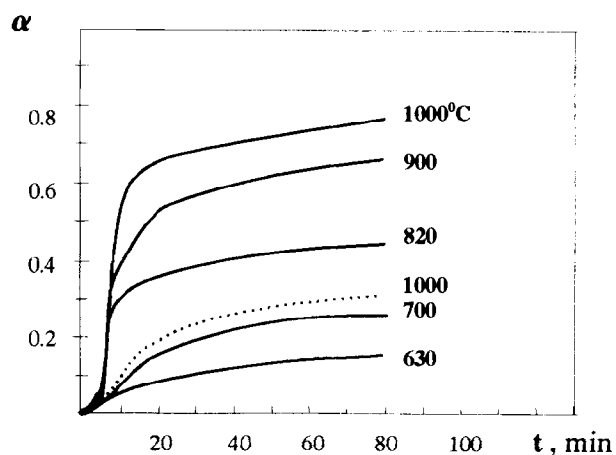


Fig. 9. Experimental nitridation kinetics of Ti pellets at different temperatures: —, combustion wave generated Ti, original particle size $15\ \mu\text{m}$; ---, industrial Kroll Ti.

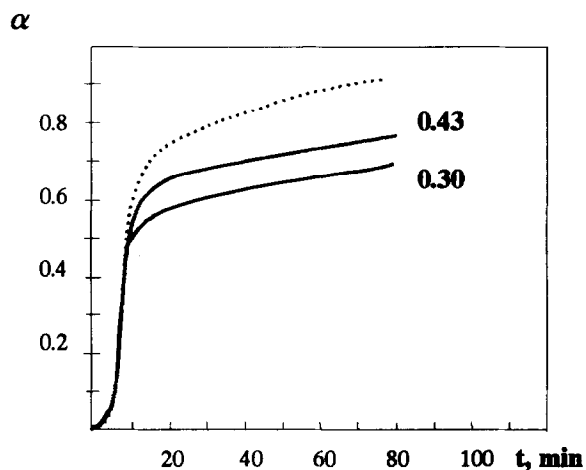


Fig. 10. Experimental nitridation kinetics of Ti pellets (—) and powder (---) at 1000°C . Values of the porosity are indicated in the figure.

behaviour of powder and compact are quite pronounced.

The titanium compacts pressed from powders having smaller primary particles reacted faster,

with the exception of powder with particle size of $1\ \mu\text{m}$. The higher surface area of the smaller particles accounts qualitatively for their enhanced reactivity in this domain. The exceptional behaviour of the $1\ \mu\text{m}$ powder is probably an effect caused by the pressing process: small particles (aggregates) pack much better than the larger agglomerates when press-forged together. Therefore in the pressed compact these small particles may possibly be less accessible for the gas. Compacts made from Kroll process titanium powders were less reactive than combustion synthesized titanium, as is to be expected considering the morphology and the surface area of powders.

The reaction temperature has two effects. Higher temperatures lead to higher rates in the asymptotic domain. Second, there is no linear first stage for the pellets reacted at temperatures below 700°C . Also, this stage seems to be absent in the nitridation reaction of the Kroll titanium tablets.

Figure 10 shows the nitridation kinetics for the pellets having different porosities in comparison with intrinsic titanium powder behaviour as discussed in Section 3.2. The initial linear part of the process coincides for both types of samples, as does the conversion degree (about 25 at% of N) which separates the linear and asymptotic domains. The higher the porosity, the faster the overall reaction rate.

The microstructure of the sample which was nitrided for 3 min is shown in Fig. 11. It clearly shows the yellow-gold coloured surfaces of the grains (white in Fig. 11), as well as those of the tubular pores inside the grains. Nitrogen flow takes place through intergrain voids and the pores of individual particles (agglomerates). Particle swelling on dissolution of nitrogen is observed in SEM micrographs of this sample (Fig. 12).

Figure 13 presents the microstructure of another partially converted sample (degree of conversion: 0.73) as observed by optical microscopy; gold-

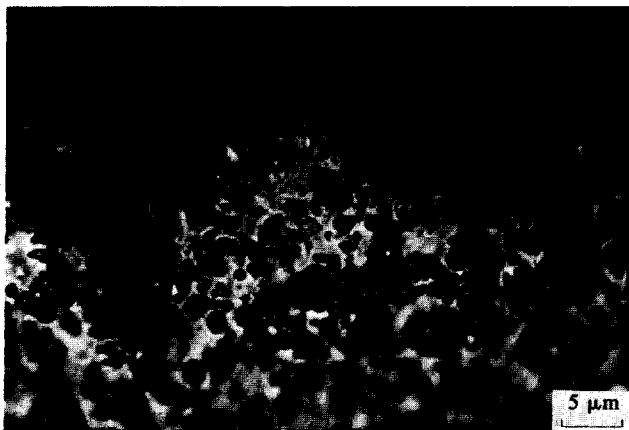


Fig. 11. Micrograph of the cross-section of a Ti pellet (nitridation time 3 min). Tubular pores in the interior of the particles and the yellow-gold surfaces of grains are observed.

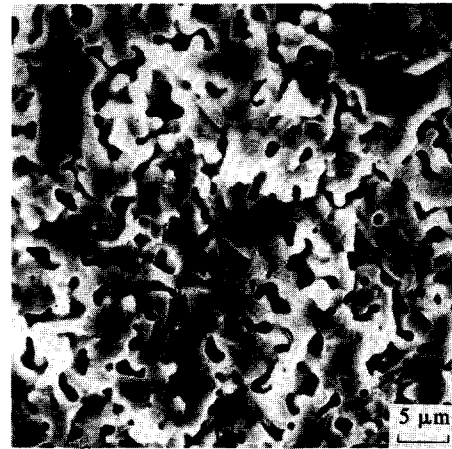


Fig. 12. SEM micrograph of the sample of Fig. 11. Particle swelling inside a porous pellet is observed.

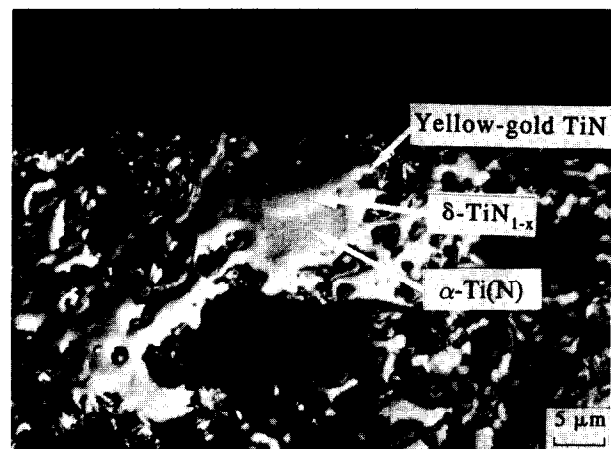


Fig. 13. Micrograph of the cross-section of a Ti particle inside a pellet (conversion 73%).

coloured TiN crystals surround large particles which are not fully converted. The crystal structure of these particles is of interest. The dark grey and light grey parts of the titanium particles (interferometric contrast enhancement) can be attributed to two kinds of crystal structure: hcp $\alpha\text{-Ti(N)}$ and fcc $\delta\text{-TiN}_{1-x}$. Externally, the metal particles are covered with a layer of yellow-gold TiN.

4 Microstructure and Properties of TiN Compacts

The measured difference in apparent porosity of compacts before and after nitridation was $< 2\%$, and is within the error of experiments.

Qualitative SEM micrographs of the porous structures of untreated and nitridated samples (Figs 14(a) and (b)) indicate the structural evolution during the conversion process: the TiN compact is expected to have a larger pore size, less porous surface area and a more interconnected solid-phase network.

Heat treatment in nitrogen results in neck formation between touching particles via reaction sintering and eliminates the void phase inside the

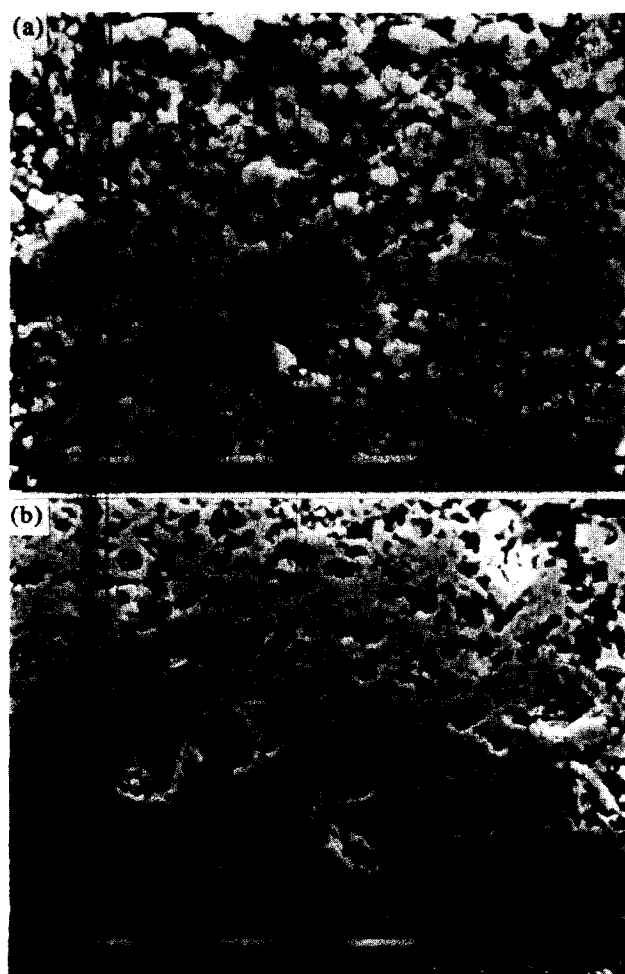


Fig. 14. SEM micrographs of the compacts before (a) and after (b) nitridation.

particles (or agglomerates). The titanium nitride layer formation prevents further metal matrix shrinkage, and there are slight dimensional changes of the Ti compact during nitridation, while without a nitrogen atmosphere (in argon) the Ti compact shrinks dramatically (the porosity falls from 45% to 10%) at the same temperature – time conditions.

Table 1 presents the results of mercury intrusion porosimetry. Evolution of the porous structure leads to an increase of the average pore size of up to 40%. The total surface area of the pores and interparticle voids decrease, and so does the interconnected porosity.

Results of the measurements of macroscopic properties which are strongly influenced by the pore structure, such as gas permeability and

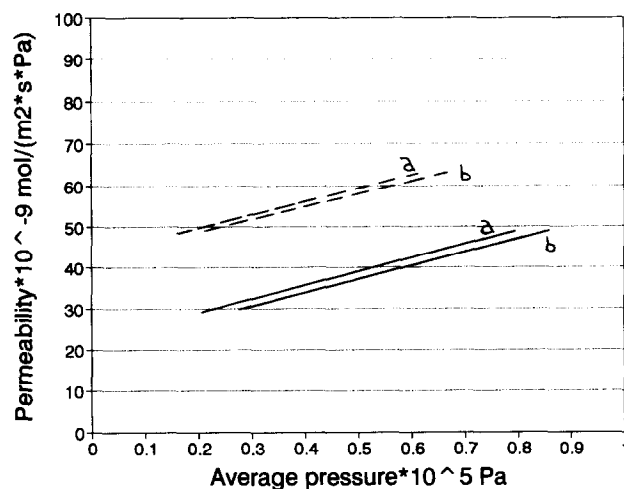


Fig. 15. Gas permeability of two compacts labelled a and b, before and after nitridation (—, Ti; ---, TiN).

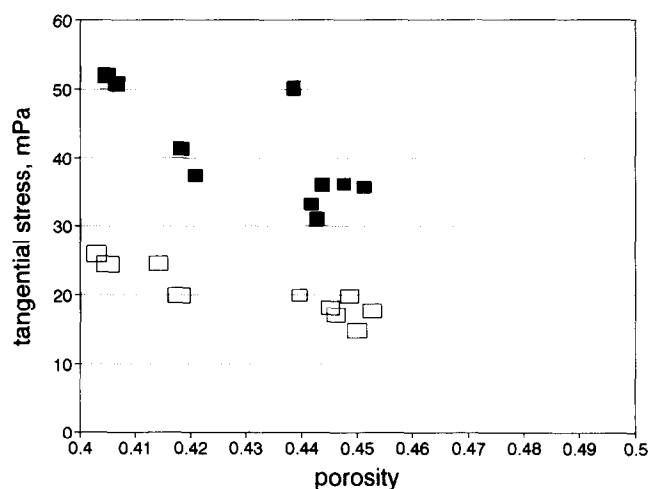


Fig. 16. Results of the C-ring diametral compression test of Ti (□) and TiN (■).

mechanical strength, are shown in Figs 15 and 16, respectively. The observed gas permeability increase up to 45% can be attributed to the growth of the pore size and the number of open pores. The strength of the compact increases considerably with nitridation, and the maximal tangential stress in Ti samples can be doubled by the present reaction-bonding process.

5 Conclusions

Porous titanium nitride ceramics can be fabricated in near net shape using combustion wave generated

Table 1. Parameters of the porous structure of compacts

	Mercury intrusion porosimetry				
	Apparent porosity	Interconnected porosity	Closed porosity (%)	Pore radius (nm)	Surface of pores (m ² g ⁻¹)
Ti	0.443	0.392	11.5	299	2.15
TiN	0.445	0.417	6.2	422	0.91

Ti powder having a high specific surface area and a high chemical activity. The observed kinetics indicate a two-step process: a rapid dissolution of nitrogen in α -Ti, and a slower heterogeneous reaction of the nitrogen-saturated α -Ti with N_2 to TiN.

Porous Ti pellets can be fully converted to the TiN compacts with small dimensional change, and practically without a change in porosity. Also, the final product shows a considerable increase in gas permeability and mechanical strength.

These ceramics can be applied in membrane technology, as porous electrodes, and are considered to be a suitable matrix for further gas-phase infiltration treatment to form composite ceramics.

References

1. Merzhanov, A. G., *Combustion and Plasma Synthesis of High-Temperature Materials*, eds Z. A. Munir and J. B. Holt. VCH, New York, 1990, pp. 1–53.
2. Riley, F.L., Silicon nitridation. In NATO ASI Ser. E, Vol. 65, *Progress in Nitrogen Ceramics*, ed. F. L. Riley. Martinus Nijhoff Publ, Boston, 1983, p. 121.
3. Wang, L. L., Munir, Z. A. & Maximov, Y. M., Thermite reactions: their utilization in the synthesis and processing of materials. *J. Mater. Sci.*, **28** (1993) 3693–708.
4. Nakamura, Y. & Uchino, K., Titanium nitride. Japanese Patent 61 97,111 [86 97,111], 15 May 1986.
5. Nakamura, Y. & Uchino, K., Metal nitrides. Japanese Patent 61 83,604 [86 83,604], 28 April 1986.
6. Ananjin, V. N. & Belyaev, V. V., Manufacture of tubular filter from sintered Ti. *Zh. Otkrytiya i Izobreteniya*, **31** (1991) 383.
7. Avnir, D., Farin, D. & Pfeifer, P., *J. Coll. Interf. Sci.*, **103** (1985) 1112.
8. Dekker, J. P., CVD techniques for the synthesis or modification of porous ceramics. PhD thesis, Delft University of Technology, Delft, 1994.
9. Lengauer, W., The titanium–nitrogen system: a study of phase reactions in the subnitride region by means of diffusion couples. *Acta Metall. Mater.*, **39** (1991) 2985–96.
10. Bars, J.-P., Etchessahar, E. & Debuigne, J., Etude cinétique, diffusionnelle et morphologique de la nitruration du titane par l'azote. *J. Less-Common Metals*, **52** (1976) 51–76.
11. Levinskii, Yu., Investigation of the diffusion of nitrogen in titanium. *Neorganicheskie Materialy*, **4** (1968) 2068–73.

Temperature Stability of Samarium-Doped α -Sialon Ceramics

Zhijian Shen,^a Thommy Ekström^b & Mats Nygren^{b*}

^aDepartment of Materials Science and Engineering, Zhejiang University, Hangzhou 310027, P. R. China

^bDepartment of Inorganic Chemistry, Arrhenius Laboratory, University of Stockholm, S-106 92 Stockholm, Sweden

(Received 31 January 1995; revised version received 2 June 1995; accepted 9 June 1995)

Abstract

Dense Sm-doped α -sialon ceramics along the tie line $\text{Sm}_x\text{Si}_{12-4.5x}\text{Al}_{4.5x}\text{O}_{1.5x}\text{N}_{16-1.5x}$ between Si_3N_4 and $\text{Sm}_2\text{O}_3\cdot 9\text{AlN}$ were prepared by hot-pressing at 1800°C. The materials were subsequently heat-treated at different temperatures in the range 1300–1750°C for different times. The samples were either cooled by turning the furnace off, yielding a cooling rate (T_{col}) $\approx 50^\circ\text{C min}^{-1}$ or quenched ($T_{\text{col}} \geq 400^\circ\text{C min}^{-1}$) by quickly moving the samples to a connected cooling chamber. It was found necessary to apply this quenching technique in order to reveal the true phase relations at high temperatures. It was found from phase analysis of quenched samples that the α -sialon phase is formed for $0.3 < x < 0.61$, in equilibrium with a liquid phase. The α -sialon was only stable at temperatures above 1650°C, while at lower temperatures it transformed to the more stable β -sialon modification together with an Al-containing Sm melilite (M') phase. The z -value of β -sialon as well as the Al content of the M' -phase were found to correlate with the degree of α -sialon decomposition. This decomposition affects also the microstructure of the ceramics, i.e. small and almost equi-axed β -sialon grains form together with the M' -phase crystals located at the grain boundaries. The mechanical properties deteriorate: both hardness and fracture toughness of the materials decrease from 21 to 20 GPa and 4.5 to 2.5 MPa $m^{1/2}$ for unaged and aged samples, respectively.

1 Introduction

Sialon-based ceramics have gained attention in recent years, because it has become obvious that these materials in general combine less expensive preparation techniques with a possibility of controlling the mechanical properties by fairly simple

means.^{1–3} By altering the overall composition slightly, or by replacing the commonly used yttria sintering aid by other rare-earth element oxides, both hardness and fracture toughness can be changed in a controlled way. Recently, it has also been shown that the phase composition and the microstructure of α - β -sialon ceramics can be greatly affected by heat-treatment procedures when rare-earth oxides are used as sintering aids.⁴ The α -sialon phase was observed to be less stable at lower temperatures and decomposed partly to rare-earth rich intergranular phases and β -sialon with a remarkably elongated crystal shape. It was pointed out by Mandal and co-workers that this might open another way of controlling the mechanical properties of the final sialon ceramics.⁴

The presence of α -sialon in the α - β -sialon ceramics contributes especially to the hardness, which is an important physical property in many applications where high abrasive wear resistance is crucial, e.g. in metal cutting tools.¹ The monophasic α -sialon ceramic is therefore an interesting material as the ultimate hardness for the sialon ceramics is achieved, but preparations must be made within restricted overall compositions.² The general formula for α -sialon can be expressed as $\text{R}_x\text{Si}_{12-(m+n)}\text{Al}_{m+n}\text{O}_n\text{N}_{16-n}$, where $m(\text{Si-N})$ are replaced by $m(\text{Al-N})$, and $n(\text{Si-N})$ by $n(\text{Al-O})$, and the valency discrepancy introduced by the former process is compensated by the R metal cation. The elements R which have been reported so far to stabilize the α -sialon modification are Li, Mg, Ca, Y, and the rare-earth metals except La, Ce, Pr, and Eu.^{5,6} Although all the mentioned cations or combinations of these can stabilize the α -sialon structure, extensive studies have mainly been carried out in the yttrium-containing system.^{7–11} In the latter system the α -sialon compositional field has a fairly small two-dimensional extension in the plane Si_3N_4 – $\text{Al}_2\text{O}_3\cdot\text{AlN}$ – $\text{YN}\cdot 3\text{AlN}$.^{2,7} Studies of the sub-solidus phase relationships in Si_3N_4 – AlN –rare-earth oxide systems at 1700°C show that the

*To whom correspondence should be addressed.

different rare-earth stabilized α -sialons have compositional fields quite similar to that of the yttrium-doped α -sialon. The only difference is that the solubility limits of the rare-earth element stabilized α -sialon widen slightly with decreasing size of the rare-earth cations.⁶

The most widely used preparation route for α -sialon ceramics is high-temperature liquid-phase sintering using α - Si_3N_4 , AlN and appropriate metal oxides powders as starting materials. Many previous studies have been devoted to the reaction sequences occurring during the heating part of the sintering cycle, i.e. in the yttrium-doped¹² or in the other rare-earth metal-doped α -sialon systems.¹³⁻¹⁵ These studies show that the formation of yttrium- and rare-earth metal-stabilized α -sialon have similar reaction sequences. At temperatures above the lowest eutectic, yttrium- or rare-earth rich intermediate oxide or oxynitride phases tend to form in small amounts, re-dissolving at higher temperatures, around 1500°C, when the formation of the α -sialon phase starts. The melilite phases, $\text{R}_2\text{O}_3 \cdot \text{Si}_3\text{N}_4$, often containing aluminium in solid solution (M' -phases), thus occur frequently together with the α -sialon but dissolve at higher temperatures. Melilite is thus transiently formed during heating to the sintering temperature, and the amount of M' -phase is usually fairly large for the rare-earth metals Nd and Sm. The amount of M' -phase obtained passes through a maximum between 1500 and 1600°C. The decomposition of the M' -phase releases a large amount of the doping element, which facilitates the precipitation of α -sialon and assists the final densification. The melting point of the melilite phase is therefore of importance, and Cheng and Thompson showed that the relatively low melting point of the Sm-doped M' -phase gave improved densification compared with Nd-doped ceramics, where the melilite phase had a considerably higher melting temperature.¹⁵

Very few studies have been concerned with changes in the phase assembly that might take place during the cooling part of the sintering cycle. After sintering the furnace is normally turned off and left to cool, and it is generally believed that only minor reactions, if any, take place during the cooling. Most post sintering studies have been directed towards the effects of prolonged heat treatments at temperatures substantially lower than the sintering temperature in order to crystallize the glassy grain-boundary phase in an attempt to obtain better high-temperature properties. However, it was surprisingly shown recently by Mandal and co-workers⁴ and by Ekström and Shen¹⁷ that the cooling rate applied from the sintering temperature to a great extent determines the microstructure of α -sialon

containing ceramics. The α -sialon thus seems to be unstable at temperatures below 1600°C and decomposes to other phases, and new β -sialon crystals are formed. Recent independent work by Cheng and Thompson^{15,16} on post heat treatment of Sm-doped α -sialon ceramics at 1500–1600°C confirmed these findings, and they observed a decrease of the α -sialon content accompanied by an increase of the M' -phase (as precipitate at the grain boundaries), and β -sialon was also formed in increasing amounts.

Our present work on silicon nitride based ceramics is devoted to studies on the relative stability of different rare-earth doped α -sialon phases in both pure α - and mixed α - and β -sialon systems. Some preliminary studies indicated that the stability of the α -sialon depends on the rare-earth element used.¹⁷ The decomposition of α -sialon was also temperature-dependent and most easily seen in systems where larger cations like Nd and Sm were used, or when a residual liquid phase was present to aid the process. In these cases some post sintering reactions can take place even with 'normal' cooling rates (~ 40 – $50^\circ\text{C min}^{-1}$). In this article we will report a more detailed study of the phase stability of the samarium-doped α -sialon system. This is partly because it has been reported that the sinterability of samarium-doped sialon ceramics is excellent,¹⁵ and additional knowledge of the thermal stability of these ceramics is therefore of importance. The effect on the mechanical properties is also of great interest. We have prepared a great number of samples along the Si_3N_4 – $\text{Sm}_2\text{O}_3 \cdot 9\text{AlN}$ join line within the α -sialon plane mentioned above, and the α -sialon forming region and the thermal stability of the formed α -sialon along this line is assessed. The relation between the thermal stability of Sm-stabilized α -sialon and the formation of other Sm-rich phases like the M' -phase will be discussed, as well as the variation of the microstructure and the mechanical properties with the degree of decomposition of the α -sialon phase.

2 Experimental Procedure

The compositions selected for the present work were located on the join between Si_3N_4 and $\text{Sm}_2\text{O}_3 \cdot 9\text{AlN}$, with the overall compositions $\text{Sm}_x \text{Si}_{12-4.5x} \text{Al}_{4.5x} \text{O}_{1.5x} \text{N}_{16-1.5x}$ where $x = 0.25, 0.35, 0.4, 0.6, 0.7, 0.8$ and 1.0 . Starting powders were Si_3N_4 (Ube, SN-E10), AlN (H.C. Starck-Berlin, grade A) and Sm_2O_3 (99.9%, Johnson Matthey Chemicals Ltd). The samarium oxide was calcined at 1000°C for 2 h before use, to remove any adsorbed water. When calculating the composi-

Table 1. Overall composition for samples of $\text{Sm}_x\text{Si}_{12-4.5x}\text{Al}_{4.5x}\text{O}_{1.5x}\text{N}_{16-1.5x}$ system

Sample no.	Overall x -value	Amounts (wt%) ^a		
		Sm_2O_3	Si_3N_4	AlN
ASM025	0.25	7.29	85.54	7.76
ASM035	0.35	9.95	80.03	10.59
ASM04	0.4	11.24	77.37	11.95
ASM06	0.6	16.10	67.32	17.11
ASM07	0.7	18.36	62.63	19.53
ASM08	0.8	20.53	58.14	21.82
ASM10	1.0	24.58	49.75	26.14

^aThe total amount of $\text{Sm}_2\text{O}_3 + \text{Si}_3\text{N}_4 + \text{AlN}$ exceeds 100% in order to compensate for the excess oxygen content of Si_3N_4 and AlN .

tions of the samples, corrections were made for the small amounts of oxygen present in the Si_3N_4 and AlN raw materials. The analysed oxygen content of the silicon nitride powder corresponded to 2.74 wt% SiO_2 and of the aluminium nitride powder to 1.9 wt% Al_2O_3 . The overall compositions (wt%) after correction are listed in Table 1.

The carefully weighed starting materials (50 g) were mixed/milled in water-free propanol for 24 h in a rotating plastic jar, using sialon media. Pellets of dried powders (about 5 g) were first compacted in a steel die, followed by hot-pressing (HP) in nitrogen for 2 h at 1800°C and 25 MPa in a graphite resistance furnace. The hot-pressed samples were then cooled at a rate (T_{col}) of $\sim 50^\circ\text{C min}^{-1}$ to 1000°C, i.e. much slower than the quenched samples prepared as described below, with $T_{\text{col}} \geq 400^\circ\text{C min}^{-1}$.

Selected specimens were subsequently heat-treated in different ways. Some samples were embedded in a mixture of Si_3N_4 , AlN and BN packing powder in a carbon crucible and re-heated in nitrogen to 1750°C in a normal graphite sintering furnace. After heat treatment for 30 min at this temperature, some samples were quenched to room temperature by quickly moving them to a separate cooling chamber attached to the furnace. Other samples were quenched from 1750 to 1650 or to 1550°C and held at this temperature for another 24 h before quenching to room temperature. Samples quenched from 1750°C to room temperature were re-heated either to 1300 or 1450°C and held (embedded in the same powder bed as above) at these temperatures in nitrogen for up to 30 days in order to allow a study of the effects of prolonged heat treatments at lower temperatures on the phase content of the samples.

The densities of the sintered specimens were measured according to Archimedes principle. Before physical characterization, the specimens were ground and polished using standard techniques.

Hardness (HV10) and indentation fracture toughness (K_{IC}) at room temperature were obtained with a Vickers diamond indenter with a 98 N (10 kg) load, and the fracture toughness was evaluated according to the method of Anstis *et al.*,¹⁸ assuming a value of 300 GPa for Young's modulus.

Crystalline phases were characterized by their X-ray diffraction (XRD) patterns obtained in a Guinier-Hägg focusing camera with Si as internal standard. The X-ray films were evaluated with a computer-linked SCANPI system,⁹ and the cell parameters were determined with use of the program PIRUM.²⁰ The z -value of the β -sialon phase, $\text{Si}_{6-z}\text{Al}_2\text{O}_z\text{N}_{8-2z}$, was obtained from the mean values of z_a and z_c given by the following equations:²¹

$$\begin{aligned} a &= 7.603 + 0.0297z \text{ \AA} \\ c &= 2.907 + 0.0255z \text{ \AA} \end{aligned} \quad (1)$$

The x -value of the melilite (M') solid solution $\text{Sm}_2\text{Si}_{3-x}\text{Al}_x\text{O}_{3+x}\text{N}_{4-x}$ was obtained using the equations given by Cheng and Thompson:¹⁶

$$\begin{aligned} a &= 7.690 + 0.049x \text{ \AA} \\ c &= 4.985 + 0.037x \text{ \AA} \end{aligned} \quad (2)$$

In the quantitative estimation of the amounts of crystalline phases, the integrated intensities of the following reflections were used: (1 0 2) and (2 1 0) of the α -sialon, (1 0 1) and (2 1 0) of the β -sialon, and (2 1 1) of the Sm-melilite phase. The corrected relative weight fraction of each phase was then calculated from the expression:

$$W_k = (I_k/K_k) / \sum_{i=1}^n (I_i/K_i) \quad 1 \leq k \leq n \quad (3)$$

where W_k is the weight fraction of phase k , n is the number of crystalline phases present, and K_i is a constant for the intensity I_i of the selected reflection (hkl) of phases i . The K_i constants were calculated theoretically according to a procedure outlined in Ref. 22, and experimentally determined using calibration curves.

After application of a carbon coating, polished surfaces of hot-pressed and heat-treated samples were examined in a scanning electron microscope (Jeol JSM 820, equipped with a Link 10000 EDX analyser). The Si, Al and Sm contents were determined by energy dispersive X-ray (EDX) analysis, and the data given below are obtained from calibration curves and represent mean values of at least five point measurements.

3 Results and Discussion

The hot-pressed (1800°C) samples were found to be fully densified, as revealed by optical and

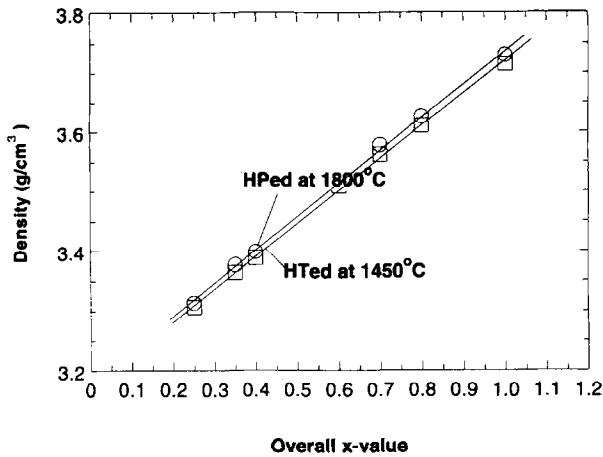


Fig. 1. Density as a function of the overall composition (x -value) in $\text{Sm}_x\text{Si}_{12-4.5x}\text{Al}_{4.5x}\text{O}_{1.5x}\text{N}_{16-1.5x}$ for samples hot-pressed at 1800°C (25 MPa, 2 h) as well as for samples subsequently heat-treated at 1450°C for 24 h.

scanning electron microscopy studies on polished cross-sections of sintered bodies. The observed density as a function of the overall x -value for α -sialon samples, both hot-pressed (HP) and post heat-treated (HT) at 1450°C for 24 h, are shown in Fig. 1. The density increases with increasing amount of Sm in both cases, as expected. The heat-treated samples have a slightly lower density than the hot-pressed samples, but no porosity was found in either type. Thus the difference in density may be assumed to reflect mainly the changes occurring when α -sialon is partly decomposed to form minor amounts of other phases, yielding a compact with a lower density, see below. It should also be mentioned that the samples re-heated at 1750°C, quenched to 1550–1650°C and heated for extended periods of time at these temperatures showed a slight weight loss which, however, never exceeded 2 wt%. This weight loss is probably due mainly to volatilization of SiO and should not significantly affect the microstructure and mechanical properties of the material (determined from the interior of the compacts).

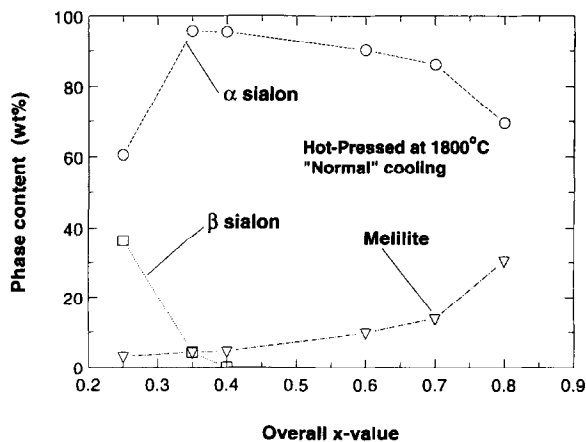


Fig. 2. Phase content as a function of the overall composition of $\text{Sm}_x\text{Si}_{12-4.5x}\text{Al}_{4.5x}\text{O}_{1.5x}\text{N}_{16-1.5x}$. The data refer to samples hot-pressed (1800°C) and normally cooled ($\sim 50^\circ\text{C min}^{-1}$).

3.1 On the α -sialon formation along the $\text{Si}_3\text{N}_4\text{-Sm}_2\text{O}_3\text{-9AlN}$ line

Figure 2 shows the relation between the observed phase contents of hot-pressed samples, cooled at a rate of $\sim 50^\circ\text{C min}^{-1}$, and the overall composition of the α -sialon. In the range $0.25 \leq x \leq 0.35$ the materials consisted mainly of two phases, namely α - and β -sialon, but a minor amount of the melilite phase is also found. In the range $0.40 \leq x \leq 0.60$ the major phase was α -sialon, but all materials also contained some melilite phase, increasing in amount with increasing x -value. For higher x -values the amount of α -sialon decreased significantly, and besides melilite small amounts of Si-Al-O-N polytypoid phases were identified.

Hot-pressed and furnace cooled samples always contained some other crystalline phase besides α -sialon. These results show similarities with previous studies on Y-doped α -sialon.^{11,12} The phase content of these samples, which were re-heated to 1750°C and held this temperature for 0.5 h before being quenched ($T_{\text{col}} \geq 400^\circ\text{C min}^{-1}$) to room temperature, exhibited a different phase composition. In the range $0.25 \leq x \leq 0.35$ a two-phase α - β sialon mixture was found, but no crystalline grain-boundary phase was detected. Monophasic α -sialon compacts were obtained in the compositional range $0.4 \leq x \leq 0.8$, as demonstrated in Fig. 3. It should be stressed, however, that the apparently monophasic α -sialon samples contained some amorphous glassy phase (as will be shown below) and that the homogeneity range indicated in this figure does not represent the true solid solution range. The difference in the phase content of these compacts (see Figs 2 and 3) demonstrates that post heat treatment and cooling rate have a significant influence on amount and type of phases formed.

To further enhance the decomposition of the α -sialon phase, the HP compositions were heat-treated at 1450°C for 24 h. In this case even more melilite was obtained in all samples, accompanied

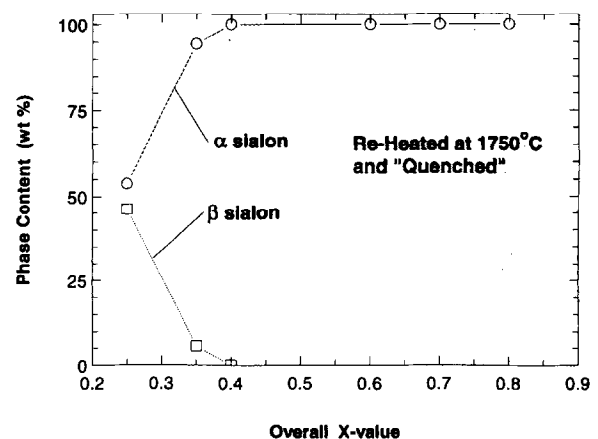


Fig. 3. Phase content as a function of the overall composition for samples quenched from 1750°C.

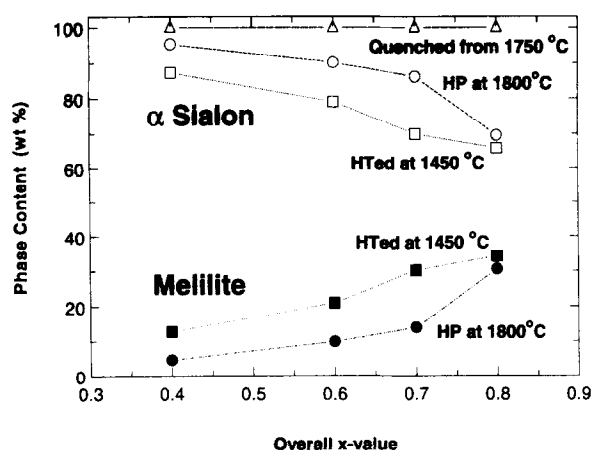


Fig. 4. Comparison of the phase composition for samples prepared in different ways, see text.

by a decrease of the α -sialon content as illustrated in Fig. 4. The formation of larger amounts of melilite at a holding time of 24 h at 1450°C should not be surprising. The very rapid initial formation of melilite in HP samples cooled at a rate of 50°C min⁻¹ is somewhat more surprising, however, as the temperature range of M'-phase stability is traversed within 8 min. It has, however, previously been observed that melilite can be formed rapidly in these types of system.¹⁷

The samples quenched from 1750°C seem to be the ones which yield the most reliable picture of the conditions at high temperature. To accurately assess the extension of the α -sialon solid solution range along the investigated compositional line, it is also important to remember that the X-ray amorphous glassy phase might hold a considerable amount of the added samarium. The variation in unit cell dimensions of α -sialon in quenched samples as a function of the amount of added samarium (overall x -value) and the x -value measured by careful EDX analysis measurements of the α -sialon grains will give different results, as illustrated in Figs 5 and 6, respectively.

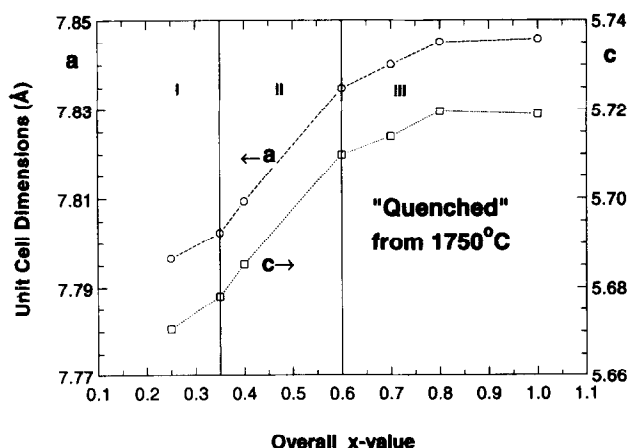


Fig. 5. Unit cell dimensions of α -sialon versus overall composition in $\text{Sm}_x\text{Si}_{12-4.5x}\text{Al}_{4.5x}\text{O}_{1.5x}\text{N}_{16-1.5x}$, for samples quenched from 1750°C.

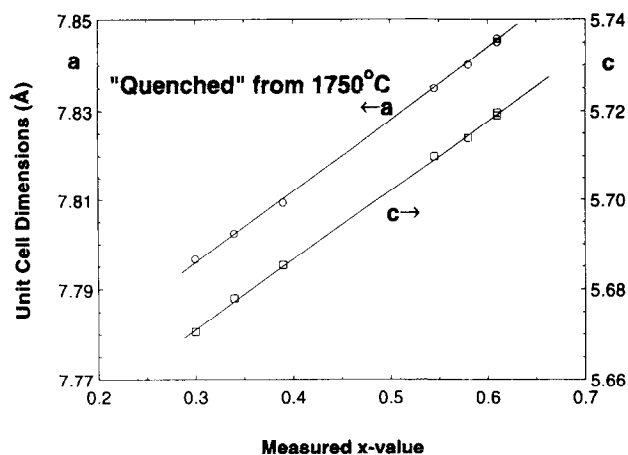


Fig. 6. Unit cell dimensions of α -sialon versus EDX-measured x -value for samples quenched from 1750°C, see text.

The results shown in Fig. 5 are difficult to interpret (see below), and yet the extent of the solution range of α -sialons has been determined from similar diagrams in the past. The α -sialon lattice expands in both the a and c dimensions with increase of overall x -value, more or less over the whole investigated compositional range, but the steepest slope is obtained in range II. In ranges I and III, the α -sialon phase co-exists with β -sialon and polytypoid phases, respectively, suggesting that area II might represent a solid solution range. However, the shifts in lattice parameters plotted in Fig. 6 against measured x -values (including also data from α -sialon grains in the multi-phase areas I and III) show that the true solid solution range is most probably $0.30 \leq x \leq 0.61$ at 1750°C. The shift in unit cell dimensions of α -sialon as a function of the measured x -value can be expressed by the following relationships:

$$\begin{aligned} a &= 7.75 + 0.158x \text{ \AA} \\ c &= 5.62 + 0.154x \text{ \AA} \end{aligned} \quad (4)$$

According to the formula $\text{Sm}_x\text{Si}_{12-4.5x}\text{Al}_{4.5x}\text{O}_{1.5x}\text{N}_{16-1.5x}$, the Si/Al atomic ratio of pure α -sialon on the $\text{Si}_3\text{N}_4\text{-Sm}_2\text{O}_3\cdot 9\text{AlN}$ line can be expressed as

$$\text{Si/Al} = 2.667x^{-1} - 1 \quad (5)$$

and is drawn as a solid line in Fig. 7, where the measured Si/Al atomic ratios of the α -sialon phase in the samples quenched from 1750°C are also plotted versus the measured x -value. It can be seen that the calculated and observed Si/Al ratios in the single-phase α -sialon range are in good agreement with each other. One sample at a low x -value has a somewhat lower observed Si/Al ratio, and one reason might be that this material is in a two-phase α - β -sialon area. The α -sialon composition in equilibrium with β -sialon might have slipped somewhat from the investigated compositional line and along the edge of the

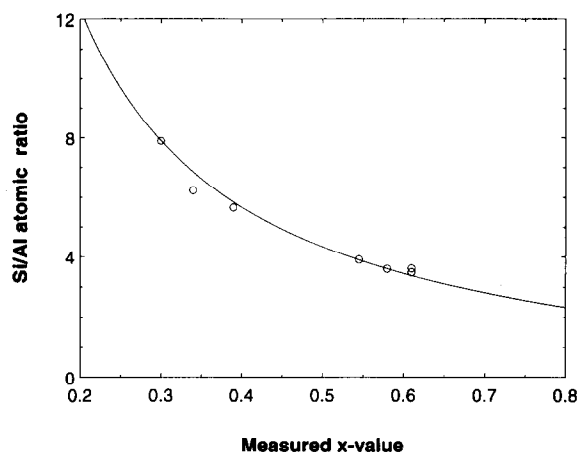


Fig. 7. Si/Al atomic ratio in α -sialon versus EDX-measured x -value for samples quenched from 1750°C, the solid line is obtained according to Eqn (5).

two-phase α -sialon region towards a lower Si/Al ratio. In any case, Fig. 7 shows that the composition of obtained α -sialon phase is close to the Si_3N_4 - Sm_2O_3 -9AlN line.

Using the relations between the lattice parameters and composition given in Eqn (4), the extension of the α -sialon forming region can be estimated for samples hot-pressed at 1800°C and for those post heat-treated at 1450°C for 24 h. The HP samples were found to have the same homogeneity range as those quenched from 1750°C, i.e. $0.30 \leq x \leq 0.61$, while the ones heat-treated at 1450°C had a slightly narrower range, $0.30 \leq x \leq 0.55$, indicating that the high x -value limit is temperature-dependent.

Scanning electron micrographs of typical samples quenched from 1750°C are shown in Fig. 8 (recorded in back-scattered electron mode). The α -sialon phase appears with grey contrast in the micrographs and the samarium-rich amorphous intergranular phase with a white contrast, while the β -sialon grains in the samples appear black and have the typical elongated shape of hexagonal rods.

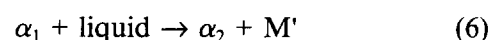
The micrograph of a sample in the mixed α - β -sialon range (with an overall composition of $x = 0.25$) revealed the presence of very elongated β -sialon grains (with a z -value 0.39) and equi-axed α -sialon grains having a grain size distribution ranging from 0.2 to 4 μm (see Fig. 8(a)). For compositions close to the α - β boundary ($x = 0.35$) some β -sialon still existed in the α -sialon structure, as seen in Fig. 8(b). The microstructure of the samples in the single-phase α -sialon range consisted predominantly of α -sialon grains, which were surrounded by some residual amorphous intergranular phase, and the content of amorphous phase increased with the increasing overall x -value. For even higher x -values ($x \geq 0.80$) the microstructure contained more glassy phase and small, dark, plate-like polytypoid crystals.

A new phase with bright SEM appearance was formed in the samples with $x \geq 0.8$. This new phase occurred as white squares (indicating it to be Sm-rich) in the SEM micrographs at low magnification, see Fig. 8(e). According to the EDX analysis these white areas had a metal composition of Si (65.4 at%), Al (22.7 at%) and Sm (12.6 at%). However, at high magnification one can easily see that some elongated grains are present in the matrix of this phase (see Fig. 8(f)), and the EDX analysis suggested them to be α -sialon grains. Some of these α -sialon crystals have aspect ratios of up to 10. Although elongated α -sialon crystals have sometimes been noted in the past, aspect ratios of this magnitude have never been seen. It thus seems likely that this Sm-rich matrix promotes growth of elongated α -sialon grains.

3.2 On the formation of melilite solid solutions during cooling part of the sintering cycle

Two HP samples, ASM04 and ASM06, were quenched (after being heat-treated for 24 h) from different temperatures in the range $1300 \leq T \leq 1650^\circ\text{C}$ in order to find the optimal precipitation temperature and determine the thermal stability range of the samarium-based M'-phase. The obtained data are summarized in Fig. 9. It should be noted that some M'-phase was present in the HP compacts used as starting material in this study (see Fig. 4) and that the same amount is found in samples heat-treated at 1300°C. This low temperature thus does not seem to cause any changes in the phase composition of the materials, which might be due to the fact that no liquid phase is present at this temperature. At higher heat-treatment temperatures, reaction took place however, and these temperatures are well above the eutectic liquid formation temperature. In the ASM04 sample, the maximum amount of M'-phase seems to have formed at 1450°C, and some M'-phase was still present in the sample heated at 1550°C but even less than in starting material. In the case of the ASM06 sample, the maximum amount of M'-phase also occurred in those heat-treated at 1450°C, and M' was still present after heat treatment at 1650°C.

The formation of the M'-phase at 1450°C was accompanied by a decrease of the α -sialon content as well as by a change of the unit cell dimensions of α -sialon, see Figs 9 and 10. Thus the M' formation is not solely the result of devitrification of the residual grain-boundary liquid phase but also due to the reaction:



where α_2 is an α -sialon with a lower x -value than α_1 . This process is similar to the one suggested by

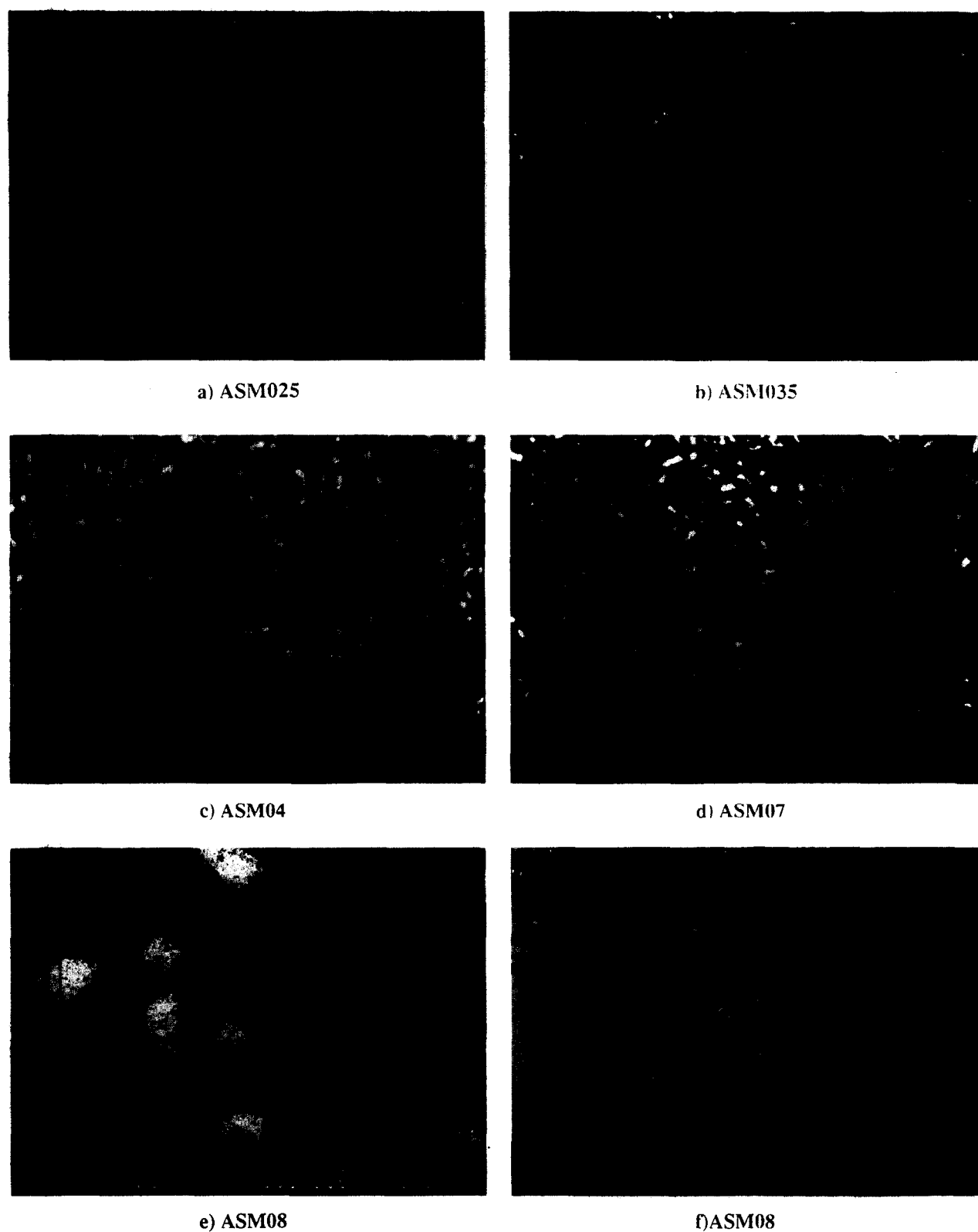
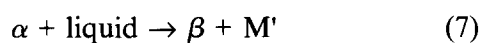


Fig. 8. Back-scattered SEM micrographs for samples quenched from 1750°C: (a) ASM025; (b) ASM035; (c) ASM04; (d) ASM07; (e) and (f) ASM08.

Cheng and Thompson¹⁶ and is said to be valid for both Sm-based α - and α - β -sialon ceramics:



In this case the M' -phase formation is thus accompanied by $\alpha \rightarrow \beta$ transformation. Both possibilities seem to be reasonable, but might occur under different conditions. The key point is, however, that in both

cases the liquid takes an active part in the reaction.

Heat treatment of the hot-pressed α -sialon compacts at 1650°C, which is close to the decomposition temperature of the M' -phase, generally leads to a grain coarsening of α -sialon (see Fig. 11). In the HP material, most of the initially present M' -phase dissolved, implying that the overall α -sialon grain composition tends to move towards

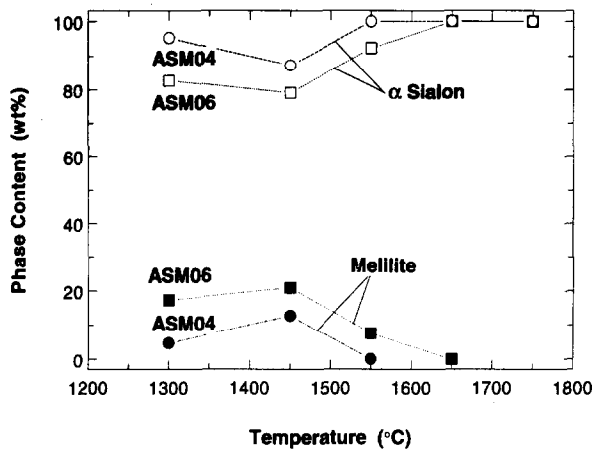


Fig. 9. Phases present in ASM04 and ASM06 samples after heat treatment at different temperatures for 24 h.

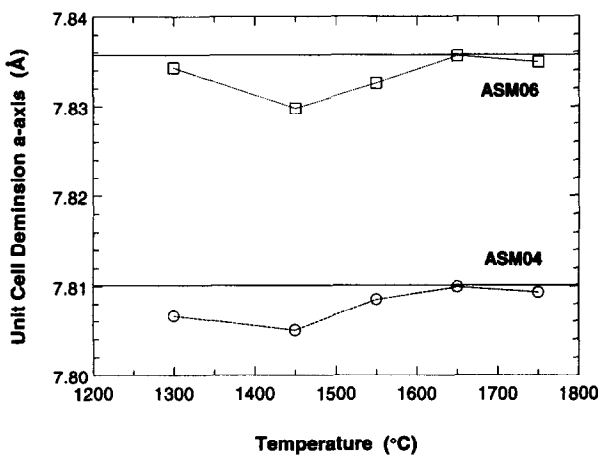


Fig. 10. Unit cell dimensions of α -sialon in ASM04 and ASM06 samples after heat treatment at different temperatures for 24 h.

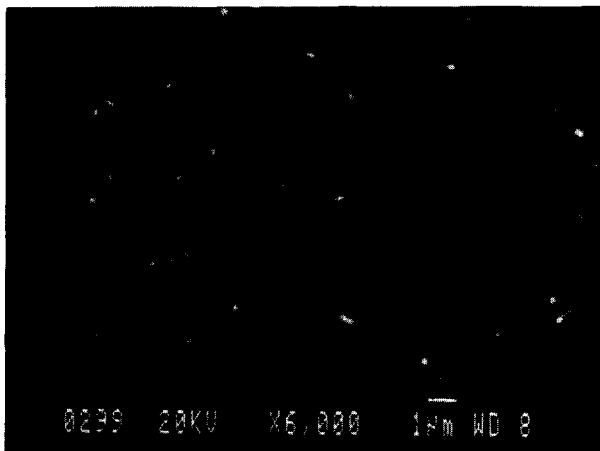


Fig. 11. Back-scattered SEM micrographs for ASM04 sample quenched from 1650°C after heat treatment for 24 h.

that found in samples quenched from 1750°C (see the unit cell dimensions in Fig. 10). The unit cell of α -sialon is, however, slightly larger at 1650°C than at 1750°C, possibly because the Sm released when the M'-phase dissolves is mainly taken up by the α -sialon and not to the same extent by the liquid. This means that true equilibrium between the liquid phase, the M'-phase and the α -sialon phase is not reached.

Previous work on the reaction sequence occurring during heating of the samarium-doped α -sialon system has shown that the M'-phase is transiently formed, melting at about 1700°C.¹³⁻¹⁵ The present results confirm that samples heat-treated at 1750°C and quenched do not contain any M'-phase. However, samples exposed to a 'normal' cooling rate of 50°C min⁻¹ do contain some M'-phase, which shows that the M'-phase forms rapidly upon cooling. This cooling rate is similar to that used by Cheng and Thompson when they prepared two Sm-doped α -sialons with $x \approx 0.4$ ^{15,16} In all essential parts their phase analysis can also be interpreted on the basis that the main part of the M'-phase is formed during the cooling process.

3.3 Decomposition of samarium-doped α -sialon

From the results presented above we know that the initial formation of melilite M'-phase is rapid, but not what is going to happen during prolonged heat treatment. A pure α -sialon (sample ASM04) was therefore heat-treated at 1450°C from 1 to 30 days in a protective nitrogen atmosphere. The result of the phase analysis is summarized in Fig. 12. This study shows that α -sialon transforms to M'-phase and β -sialon upon prolonged heat treatment but that during the first 24 h of heat treatment the amount of M'-phase is dramatically increased (accompanied by a decrease of α -sialon content) without β -sialon formation. The initial reaction can therefore be expressed by Eqn (6) given above. When the M'-phase is formed, the composition of the α -sialon grains changes as seen in Fig. 13.

Prolonged heat treatment yields more M'-phase, accompanied by formation of β -sialon grains. During this process the composition of the residual α -sialon remains constant (see Fig. 13), indicating a different reaction pathway. The mechanism suggested by Cheng and Thompson¹⁶ for Sm-doped α -sialon ceramics (Eqn(7)) might be possible, but

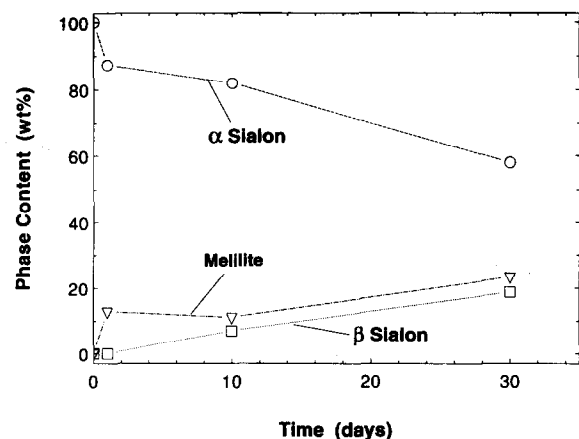


Fig. 12. Phases present in ASM04 samples after heat treatment at 1450°C for 1-30 days.

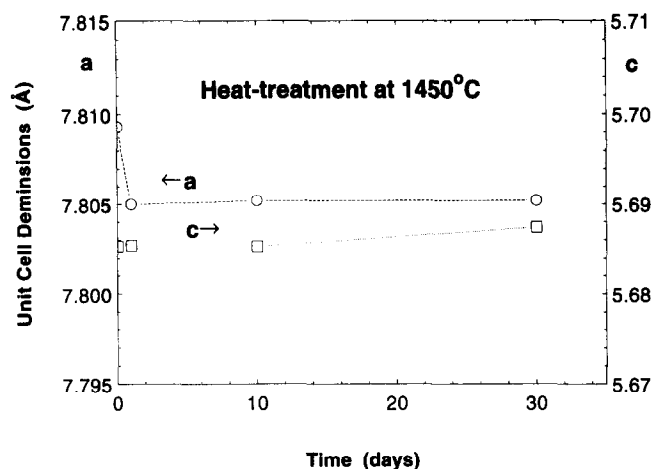


Fig. 13. Unit cell dimensions of α -sialon in ASM04 samples after heat treatment at 1450°C for 1–30 days.

our data do not exclude a reaction pathway such as:



The changes in microstructure were followed by recording back-scattered SEM micrographs of ASM04 samples after different times of heat treatment at 1450°C, and the results are illustrated in Fig. 14. Some systematic structure differences are

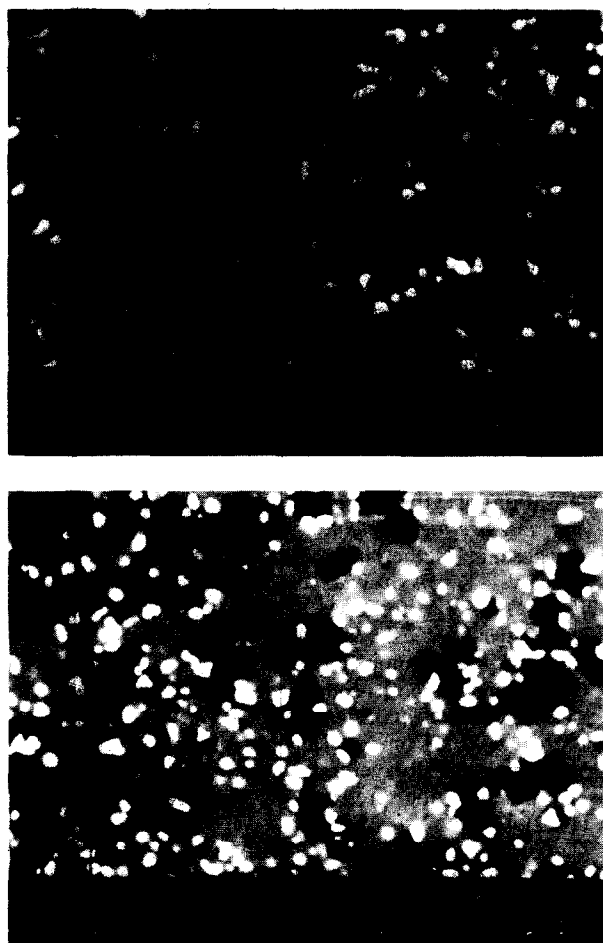


Fig. 14. Back-scattered SEM micrographs for samples heat-treated at 1450°C for (a) 10 and (b) 30 days.

noticed, firstly by comparison with the micrograph of the same sample quenched from 1750°C (Fig. 8(c)). As shown above (Fig. 8(c)), the microstructures of quenched samples (from 1750°C) predominantly consisted of α -sialon grains surrounded by some residual grain-boundary glass phase. Heat treatment at 1450°C for 1 day resulted in inhomogeneous precipitation of the M'-phase. Thus, in accordance with Cheng and Thompson,¹⁶ large areas containing no or very small amounts of residual glassy grain-boundary phase were found, see Fig. 14.

The XRD and EDX studies confirmed that the melilite formed after 1 day of heat treatment had the composition $\text{Sm}_2\text{Si}_{3-x}\text{Al}_x\text{O}_{3+x}\text{N}_{4-x}$ with $x \approx 0.7$. The compositions of the M'-phase and β -sialon phase changed with further heat treatment. Thus the z -value of the formed β -sialon decreased from $z = 0.33$ (10 days) to 0.25 (30 days), and a slight increase of the x -value of M'-phase occurred from $x = 0.28$ (10 days) to 0.66 (30 days). This indicates that the α -sialon decomposition is a diffusion-controlled process, and the α -sialon content, the amount and composition of β -sialon and of M'-phase are correlated. In summary, the results show that in the temperature region $1300 < T \leq 1650^\circ\text{C}$ the α -sialon formed at higher temperatures decomposes into the more stable M'- and β -sialon phases.

3.4 Mechanical properties

The Vickers hardness (HV10) and the indentation fracture toughness (K_{Ic}) were measured for hot-pressed and heat-treated samples at room temperature. The results for hot-pressed samples are shown in Fig. 15. The general trend is that the mixed α - β -sialon materials in range I have higher toughness but lower hardness, whereas the α -sialon in range II is very hard but brittle. Materials in the range III, which contain more glass and some sialon polytypoids, are even more brittle.

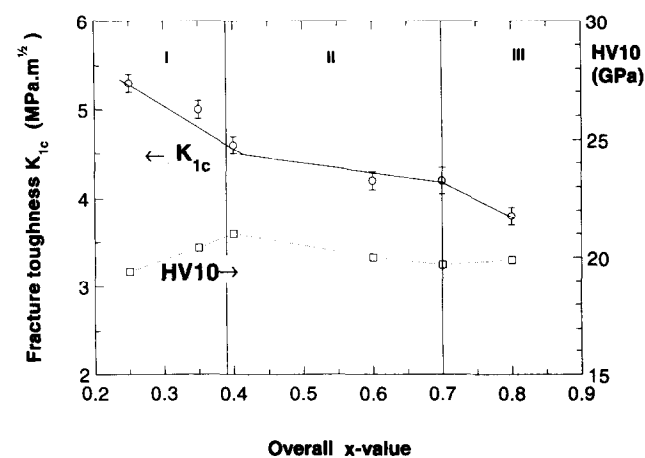


Fig. 15. Vickers hardness HV10 and indentation toughness K_{Ic} for samples hot-pressed at 1800°C.

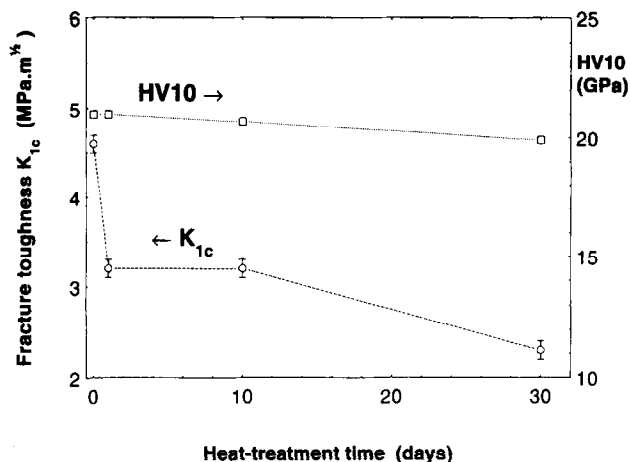


Fig. 16. Vickers hardness HV10 and indentation toughness K_{1c} for ASM04 samples heat-treated at 1450°C, as functions of the time of heat treatment.

The hardness of mixed α - β -sialons in range I increases with increasing α -sialon content; however, the toughness changed in the opposite way as previously found for α - β -sialons in other systems.^{1,3} The highest hardness values were obtained for materials in range II ($0.35 < x < 0.7$), in agreement with the fact that these materials have the highest α contents. The drop in hardness that occurs in range III can be explained by the decrease of the α -sialon content and the presence of increasing amounts of both intergranular phases and sialon polytypoids.

The Vickers hardness (HV10) and indentation fracture toughness (K_{1c}) for the samples (ASM04) heat-treated at 1450°C are given in Fig. 16. Both HV10 and K_{1c} decrease with increasing time of heat treatment. This can be understood in terms of the shifts in phase composition discussed above.

4 Conclusions

- (1) α -Sialon is a stable phase and can co-exist with a liquid phase at temperatures exceeding 1550–1650°C (depending on the α composition) in the Sm-doped α -sialon system. The homogeneity range for $\text{Sm}_x\text{Si}_{12-4.5x}\text{Al}_{4.5x}\text{O}_{1.5x}\text{N}_{16-1.5x}$ was found to be $0.30 < x < 0.61$.
- (2) α -Sialon grains formed at high temperatures decompose into β -sialon and an Al-containing Sm-melilite (M') phase when re-heated at temperatures below 1550–1650°C. This reaction is diffusion controlled. The amounts and compositions of the α -sialon, β -sialon and melilite M'-phases are strongly correlated.
- (3) The M'-phase formation temperature depends on the overall composition of the α -sialon samples, and the M'-phase tends to form at a slightly higher temperature in the samples with

higher Sm content. Most M'-phase is formed at temperatures just above the eutectic.

- (4) The formation of the M'-phase by decomposition of α -sialon can proceed by two different mechanisms. Initially, M'-phase precipitation occurs as expressed in Eqn (6), yielding an α -sialon with lower Sm content. After devitrification of the residual grain-boundary liquid phase, the decomposition of α -sialon takes place as expressed in Eqn (8).
- (5) When α -sialon decomposes, small and almost equi-axed β -sialon grains form together with a very fine-grained precipitate of the M'-phase, which leads to a decrease of both hardness and fracture toughness of the materials.

Acknowledgements

This study has been supported by the Swedish Research Council for Engineering Sciences. Zhijian Shen thanks the Swedish Institute for a scholarship during the period when the work was carried out.

References

1. Ekström, T., Effect of composition, phase content and microstructure on the performance of yttrium Si-Al-O-N ceramics. *Mater. Sci. Eng.*, **A109** (1989) 341–9.
2. Ekström, T. & Nygren, M., SiAlON ceramics. *J. Am. Ceram. Soc.*, **75** (1992) 259–76.
3. Ekström, T., Sialon ceramics sintered with yttria and rare earth oxides. *Mater. Res. Soc. Symp. Proc.*, **287** (1992) 121–32.
4. Mandal, H., Thompson, D. P. & Ekström, T., Reversible α - β -sialon transformation in heat-treated sialon ceramics. *J. Eur. Ceram. Soc.*, **12** (1993) 421–9.
5. Hampshire, S., Park, H. K., Thompson, D. P. & Jack, K. H., α -Sialon ceramics. *Nature*, London, **274** (1987) 88–82.
6. Huang, Z. K., Tien, T. Y. & Yen, T. S., Subsolidus phase relationships in Si_3N_4 -AlN-rare earth oxide systems. *J. Am. Ceram. Soc.*, **69** (1986) C-241–2.
7. Sun, W. Y., Tien, T. Y. & Yen, T. S., Solubility limits of α -sialon solid solutions in the system Si, Al, Y/N,O. *J. Am. Ceram. Soc.*, **74** (1991) 2547–50.
8. Slasor, S. & Thompson, D. P., Preparation and characterisation of yttrium α -sialons. In *Non-oxide Technical and Engineering Ceramics*, ed. S. Hampshire, Elsevier, Amsterdam, Netherlands, 1985, pp. 223–9.
9. Ishizawa, K., Ayuzawa, N., Shiranita, A., Taki, M., Ushida, N. & Mitomo, M., Properties of α -sialon ceramics. *Yogyo Kyokaishi*, **94** (1986) 183–5.
10. Mitomo, M., Izumi, F., Babdo, Y. & Sekikawa, Y., Characterisation of α -sialon ceramics. In *Proc. Int. Symp. Ceram. Components Engine*, (1983) 377–86.
11. Bartek, A., Ekström, T., Herbertsson, H., & Johnsson, T., Yttrium α - β -sialon ceramics by hot isostatic pressing and post-hot isostatic pressing. *J. Am. Ceram. Soc.*, **75**(2) (1992) 432–9.
12. Cao, G. Z., & Metselaar, R., α -SiAlON ceramics: a review. *Chem. Mater.*, **3** (1991) 242–52.
13. Hampshire, S., Reilly, K. P. J. O., Leigh, L. & Redington, M., Formation of α - β SiAlON with neodymium and samarium modifying cations. In *High Tech Ceramics*, ed. P. Vincenzini, Elsevier Publishers BV, Amsterdam, Netherlands, 1983, pp.933–40.

14. Wang, P. L., Sun, W. Y. & Yen, T. S., Sintering and formation behaviour of R- α -sialon (R=Nd, Sm, Gd, Dy, Er and Yb). *Eur. J. Solid State Inorg. Chem.*, **t.31**, (93) (1994) 104.
15. Cheng, Y. B. & Thompson, D. P., Preparation and grain boundary devitrification of samarium α -sialon ceramics. *J. Eur. Ceram. Soc.*, **14** (1994) 13–21.
16. Cheng, Y. B. & Thompson, D. P., Aluminium-containing nitrogen melilite phase. *J. Am. Ceram. Soc.*, **77** (1994) 143–8.
17. Ekström, T. & Shen, Z. J., Temperature stability of rare earth doped α -sialon Ceramics. In *5th Int. Symp. on Ceramic Materials and Components for Engines*, eds D. S. Yan, X. R. Fu & S. X. Shi, World Scientific, Singapore, 1995, pp. 206–10.
18. Anstis, G. R., Chantikul, P., Lawn, B. R. & Marshall, D. P., A critical evaluation of indentation techniques for measuring fracture toughness: I. direct crack measurements. *J. Am. Ceram. Soc.*, **64** (1981) 533.
19. Johansson, K.-E., Palm, T. & Werner, P.-E., An automatic microdensitometer for X-ray powder diffraction photographs. *J. Phys.*, **E13** (1980) 1289–91.
20. Werner, P.-E., A Fortran program for least-squares refinement of crystal structure cell dimension, *Arkiv för Kemi*, **31**(43) (1969) 513.
21. Ekström, T., Käll, P.-O., Nygren, M. & Olsson, P.-O., Dense single-phase β -sialon ceramics by glass-encapsulated hot isostatic pressing. *J. Mater. Sci.*, **24** (1989) 1853–61.
22. Käll, P.-O., Quantitative phase analysis of Si_3N_4 -based materials. *Chem. Scripta*, **28** (1988) 439–46.

Determination of the Active-to-Passive Transition in the Oxidation of Silicon Carbide in Standard and Microwave-Excited Air

Marianne J. H. Balat

Institut de Science et de Génie des Matériaux et Procédés (I.M.P. - C.N.R.S.), BP 5, 66125 Font-Romeu, Odeillo, France

(Received 27 January 1995; revised version received 31 May 1995; accepted 31 May 1995)

Abstract

The active-to-passive transition is determined on sintered silicon carbide for two atmospheres: standard air and air excited by microwaves, as a function of oxygen partial pressure and temperature. The experiments were done at low total pressure ranging from 10^3 to 25×10^3 Pa and at high temperature from 1385 to 1765°C at a constant air flow rate. The results are compared with literature data and we try to explain why they are so many differences between all the experimental and theoretical results.

1 Introduction

Silicon carbide is used as a protective material of carbon/carbon or carbon/silicon carbide composites for the nose cap and the wing leading edges of the space shuttle to prevent high temperature oxidation. During the atmospheric re-entry of hypersonic vehicles, the shock wave produces excited species (ions, atoms, molecules, electrons) and a convective thermal flux which lead to chemical and physical attacks of the protective material. So it is necessary to determine the conditions of pressure and temperature at which a non-reversible degradation of the silicon carbide occurs using an experimental device working close to realistic re-entry conditions.

The oxidation of silicon carbide is divided in two regimes separated by the transition zone: (i) the passive oxidation with the formation of a silica layer on the SiC surface, resulting in a net mass increase according to:



(ii) the active oxidation, at higher temperature with vaporization of the two oxides SiO and CO leading to a net weight loss according to:



First, we have made a theoretical thermodynamic calculation based on the models of Eriksson¹ and Wagner.² The Eriksson's model (SOLGASMIX) is based on the free-energy minimization method for a constant temperature and pressure values. The constraints of the model are: closed system, mass conservation and Duhem's phase rule. Wagner's model, modified for silicon carbide, is well suited because it takes into account the mass transfer constraints (open system) with the hypothesis of diffusion limitation type and leads to an analytical determination of the transition point in terms of oxygen partial pressure in the bulk gas for each temperature.

For each phase (solid, gaseous), the mass balance for each atomic compound is established and then the interface mass conservation (steady state). The flux density J_i of compound i at the interface is expressed by Fick's law:

$$J_i = -D_i(P_i^\infty - P_i^w)/\delta_i RT, \quad (3)$$

with D_i the mass transfer coefficient of i in the carrier gas N_2 , $D_i = D_{i,N_2}$, δ_i the thickness of the boundary concentration layer, R the ideal gas constant, T the temperature, P_i the partial pressure of the species i in the bulk gas (P_i^∞) and at the interface (P_i^w). So we obtain (superscript G is used for the gaseous phase):

$$J_{\text{O}_2}^G + J_{\text{SiO}}^G = 0 \text{ and } J_{\text{N}_2}^G = 0. \quad (4)$$

With the two hypotheses: $P_{\text{O}_2}^w = 0$ (interface consumption) and $P_{\text{SiO}}^\infty = 0$ (boundary layer concentration) and according to Wagner's approximation about the ratio of the thicknesses (for a laminar flow, here $\text{Re} < 1$), we obtain:

$$P_{\text{O}_2}^\infty = (D_{\text{SiO}}/D_{\text{O}_2})^{1/2} \cdot P_{\text{SiO}}^w. \quad (5)$$

Then the oxygen partial pressure is expressed in terms of thermodynamical parameters accounting for the equilibria (1) and (2) with the two constants K_1 and K_2 defined by:

Table 1 Oxygen partial pressure and temperature for the active to passive theoretical transition in the oxidation of silicon carbide

T(K)	1473	1573	1673	1773	1873	1973	2073
$P_{O_2}^\infty$ (Pa)	9	57	297	1242	4410	13628	37558

$$K_1 = \exp(-\Delta G_1^\circ/RT) = P_{CO}^w \cdot (P_{O_2}^w)^{-3/2} \quad (6)$$

$$K_2 = \exp(-\Delta G_2^\circ/RT) = P_{SiO}^w \cdot P_{CO}^w/P_{O_2}^w \quad (7)$$

Finally, the oxygen partial pressure of transition in the bulk is:

$$P_{O_2}^\infty = \left(\frac{D_{SiO}}{D_{O_2}}\right)^{3/8} \left(\frac{D_{CO}}{D_{O_2}}\right)^{1/8} K_2^{3/4} K_1^{-1/2} \quad (8)$$

In the case of an ideal gas at low density, the diffusion coefficient can be approximated by the Chapman-Enskog theory.³ For the equilibrium constants, the JANAF⁴ tables were used. Table 1 gives the values of temperature and pressure for the transition.

In terms of $P_{O_2}^\infty$ equivalent, the same result for the transition is obtained in the case of atomic oxygen.⁵

2 Literature Data

Many authors have worked on the determination of the transition⁶⁻¹⁹ (Table 2) but the results are very different and now we try to explain the observed differences according to:

- for theoretical calculations: the enthalpies and the diffusion coefficient values;
- for experimental results: the nature of the silicon carbide, the composition and the gas flow, the partial and total pressures, the temperature level and

measurement, the method used and the criterion taken for transition (presence of bubbles, passivation by silica or only presence of a silica layer, etc.).

2.1 Theoretical comparison

Various authors⁵⁻⁸ have worked on the theoretical determination of the transition line (Fig. 1). We have used the Wagner's model as has Singhal, but the differences observed between the two results result from:

- the values taken for the formation enthalpies of SiC (Janaf tables of 1971 and 1985) have a difference of nearly 30%: at 2100 K, $\Delta G_f^\circ(\text{SiC}) = 58.162$ kJ/mol in 1971 and 44.738 in 1985;
- the value of the diffusion coefficients D_{SiO} and D_{O_2} : the ratio D_{SiO}/D_{O_2} is equal to 0.16 for Singhal and 0.44 for us, leading to a difference of 47%.

For nickel,⁷ the explanation is very different because the role of condensed SiO(l) is taken into

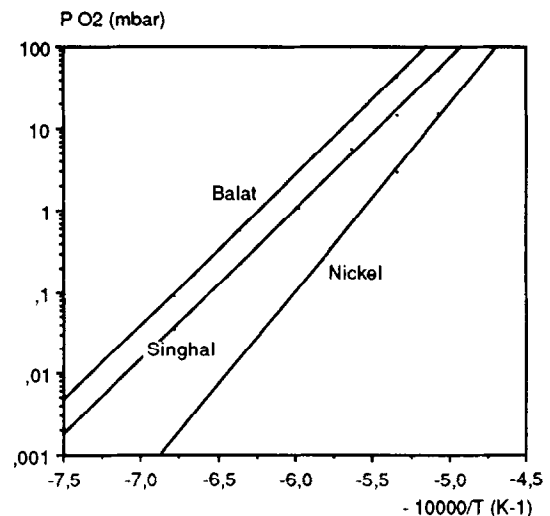


Fig. 1. Oxygen partial pressure versus temperature for the active to passive transition of SiC — theoretical determination.

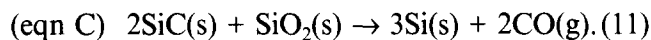
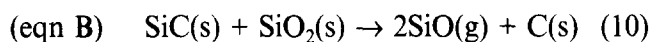
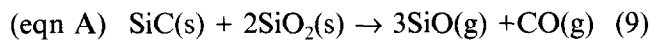
Table 2. Literature data, tests conditions and materials used for the studies on the active to passive transition in the oxidation of silicon carbide

Authors	SiC material	Gas	Flow (cm ³ /s)	P_{O_2} (Pa)	P total (Pa)	Method	Range T (°C) measure
Singhal ⁶	—	O ₂	—	—	—	theory	—
Nickel ⁷	—	O ₂	—	—	—	theory	—
Heuer ⁸	—	O ₂	—	—	—	theory	—
Balat ⁵	α and β	O ₂ + N ₂	—	—	—	theory	—
Gulbransen ⁹	monocrystal α 6H	O ₂	static	1-100	1-100	TGA	927-1520 thermocouple
Hinze ¹⁰	HP β	O ₂ + Ar	1.42	5.5-932	2×10^4	TGA	1350-1550 thermocouple
Vaughn ¹¹	sintered α + C, B, N	Dry air (without H ₂ O)	0.17-1.66	2.5-125	12.5-625	TGA	1350-1550 thermocouple
Narushima ¹²	CVD β	O ₂ + Ar	1.42-12.50	6-500	10^5	TGA	1567-1650 thermocouple
Dickinson ¹³	—	O ₂ + N ₂	—	—	10^5	—	—
Keys ¹⁴	sintered	Dry O ₂	static	$1.3-9.3 \times 10^4$	$1.3-9.3 \times 10^4$	TGA	1300-1500
Pampuch ¹⁵	CVD	O ₂	2.77	10^5	10^5	furnace	—
Rosner ¹⁶	CVD β	O ₂ + N ₂	20	0.4-133	133	TGA	1477-2127
Balat	on W filament sintered α 6H and CVD	O	20	0.01-6.65	—	—	opt. pyrometry
Balat	sintered α 6H and CVD	air	1.11	$200-5 \times 10^3$	$10^3-2.5 \times 10^4$	solar furnace	1385-1765
Balat	sintered α 6H and CVD	O ₂ , N ₂ , O, etc.	1.11	$200-10^3$	$10^3-5 \times 10^3$	solar furnace	opt. pyrometry

account and also the carbon activity. At high carbon activities, the incompatibility between silicon carbide and silica determines the transition while at lower carbon activities and at high temperatures, the incompatibility between SiC and SiO(l) marks the transition. Moreover, the chemical interaction in the layer SiO(l)–SiO₂ layer could cause bubbles formation at 1700–1800°C due to the CO pressure value. For Heuer,⁸ the theoretical calculation using the volatility diagrams for the Si–O–C system leads to a same result as us (one value given for 1427°C).

2.2 Experimental results on sintered SiC

Various authors^{9,10,11,14} have worked on the determination of the transition zone on sintered materials (Fig. 2). Gulbransen *et al.*⁹ consider three possible thermodynamical equilibria for the transition reported here:



Doing experiments, they conclude that the active/passive transition is best described by equilibrium (C) (relation 11), but in our case, we have never found solid silicon or graphite in the products, so we think that the correct transition is determined by the equilibrium (A). The experimental results we have obtained with silicon carbide are in agreement with equilibrium (A) (Fig. 2).

Moreover, the transition is introduced by the interaction of silicon carbide and silica, this is not really correct because it is preferable to study the interaction of solid silicon carbide with the gaseous phase (pure oxygen or a mixture containing oxygen). They also suggest that the transition is sensible to the total pressure, to the presence of

an inert gas and to the counterflow mass balance conditions in the boundary layer.

The results of Hinze *et al.*¹⁰ are also different. This may be due to the nature of the silicon carbide (β -SiC polycrystalline HP), and the nature of the gas (Ar + O₂) at a total pressure of 2×10^4 Pa, higher than those used by Gulbransen, Vaughn and us.

The results of Keys¹⁴ show the same behavior as Hinze's, this may be explained by the same total high pressure range.

For Vaughn and Maahs,¹¹ the position of the transition is linked to the gas flow rate, moreover the conditions given before. The transition temperature, for a given partial pressure moves towards higher temperatures as the flow rate is increased. The reported values for Vaughn in Fig. 2 are given for the higher gas flow of $1.66 \text{ cm}^3 \text{ s}^{-1}$, near the one we have used.

2.3 Experimental results on CVD SiC

We, Narushima,¹² Rosner¹⁶ have worked with CVD β -silicon carbide (Fig. 3). The results are also different essentially according to the total pressure used. Rosner worked at very low total pressure (133 Pa max) so the transition could be influenced by the pressure level (molecular gas flow regime). The pressure range of Narushima and us is closely related, so the difference between the experimental results is not so important. Narushima gives several values according to the gas flow (from 1.42 to $12.5 \text{ cm}^3 \text{ s}^{-1}$) and the results are very far from the others. This difference in the position of the transition line is attributed to a non-equilibrium state at the SiC surface when the gas flow rate increases too much.

The shift between the three curves can be explained by the total pressure level. The theoretical

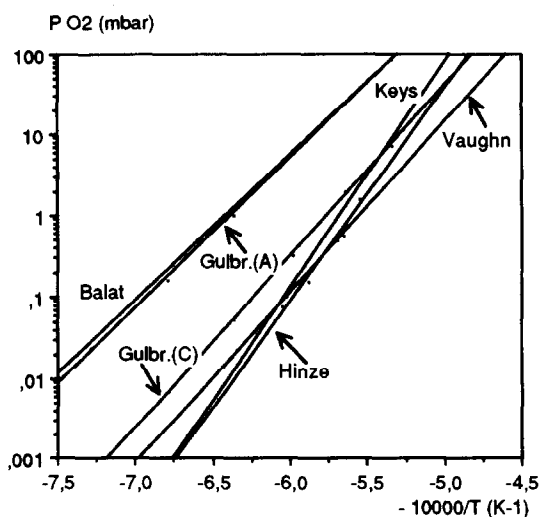


Fig. 2. Oxygen partial pressure versus temperature for the active to passive transition of SiC under standard atmosphere — experimental determination for sintered silicon carbide.

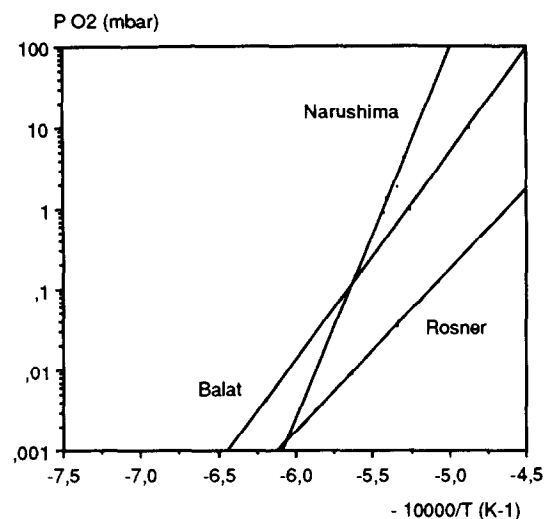


Fig. 3. Oxygen partial pressure versus temperature for the active to passive transition of SiC under standard atmosphere — experimental determination for CVD silicon carbide.

line (Wagner's model) is located at lower temperature for a fixed pressure, this model being based on the hypothesis of a diffusion limitation type. In Table 2, the total pressures are increasing from Rosner to Narushima, so probably the control of the reaction is a kinetic one for them. By increasing the total pressure, the line will be displaced towards low temperature, going to a diffusion reaction control.

2.4 Experimental results under dissociated atmosphere Only Rosner¹⁶ and us have worked under atomic oxygen to determine the transition (Fig. 4) in order to simulate atmospheric re-entry environment. The main differences are

— gas nature: in Rosner's case, the initial medium is made of 3% nitrogen and 97% argon, then a microwave discharge (at $P = 133$ Pa) is created to liberate atomic nitrogen which reacts in post-discharge with nitrogen monoxide giving atomic oxygen and molecular nitrogen;

— silicon carbide nature: sintered (so with binding material) or CVD SiC on C/SiC material in our case and CVD SiC on W filament for Rosner;

— gas flow: $1.11 \text{ cm}^3 \text{ s}^{-1}$ in our case and $20 \text{ cm}^3 \text{ s}^{-1}$ for Rosner, this acts on the oxygen dissociated concentration.

The shift between the experimental straight lines may be due to the nature of the reactive gas (pure atomic oxygen for Rosner) and also, as we have seen before, to the total pressure level.

3 Experimental Procedure

Figure 5 represents the experimental set-up called MESOX (Moyen d'Essai Solaire d'OXYdation)

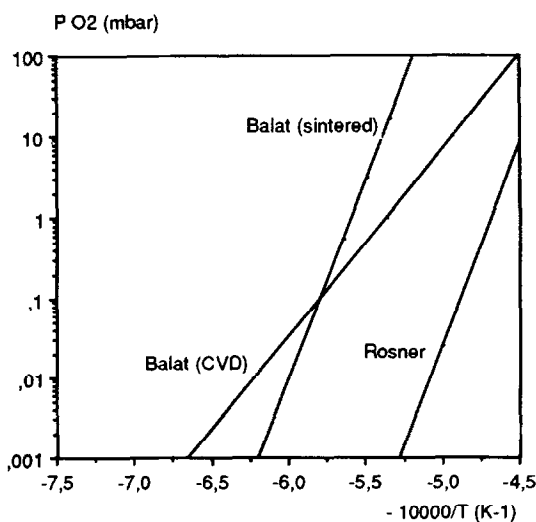


Fig. 4. Oxygen partial pressure versus temperature for the active to passive transition of SiC — experimental determination under excited air (Balat) or atomic oxygen (Rosner).

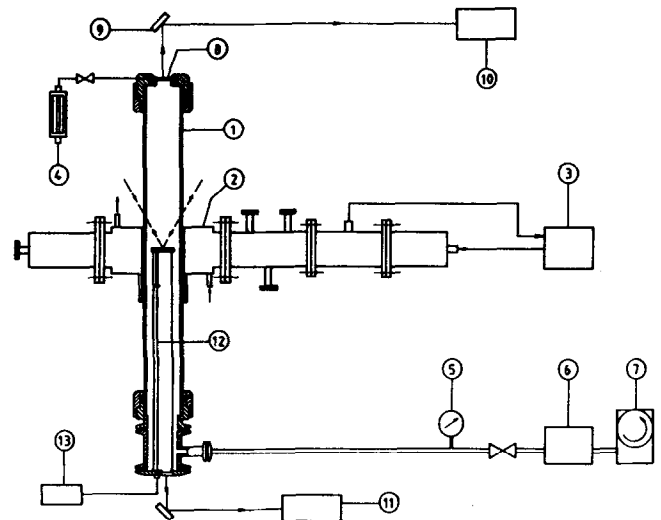


Fig. 5. Experimental set-up: (1) silica vessel, (2) wave guide, (3) microwave generator, (4) flowmeter, (5) manometer, (6) pressure regulator, (7) vacuum pump, (8) viewport, (9) mirror, (10) optical pyrometer, (11) spectroradiometer, (12) optical fiber probe, (13) bi-chromatic pyrometer.

which associates a solar radiation concentrator (to heat up samples to 2300°C for diameters of 25 mm min and 40 mm max) to a microwave generator (for the gas dissociation). The total pressures are between 10^2 and 10^5 Pa. This set-up was chosen to test samples in conditions closed to those encountered during an atmospheric reentry of space shuttles (very different from TGA measurement).

The device is composed of a silica cylindrical vessel ($\Phi_{\text{int}} = 50$ mm, 500 mm high) which crosses the refrigerated wave guide. Inside the vessel, a zirconia tube with a zirconia sample-holder supports the materials. The microwave generator (0–1200 W, 2450 MHz) works at a constant power of 300 W for the results presented. The incident and reflected powers are measured. The device is placed at the focus of a solar furnace, the heat fluxes can reach 3.5 MW/m^2 , thus elevated temperatures on materials such as SiC may be obtained. A regulator and a gauge are used in order to control precisely the pressure during the experiment. An optical pyrometer equipped with a filter centred at $5.5 \mu\text{m}$ gives the color temperature. The measure is performed with a CaF_2 viewport and a mirror. The correction of the temperature due to the emittance is done *a posteriori* with a value of 0.90 for SiC and SiO_2 at this wavelength.²⁰ The uncertainty in the temperature due to the emittance correction is $\pm 1.5\%$ at 1500°C for a variation of $\pm 5\%$ on ϵ . An original optical fiber probe with a sapphire rod is linked to a bi-chromatic pyrometer for the temperature measurement of the rear face (= without sun) of the sample.

The atomic oxygen concentration (in the ground state $2P^3P_J$ with $J = 2, 1, 0$) was estimated

by Laser Induced Fluorescence (LIF) at 5 cm from the microwave discharge with an accuracy of $\pm 20\%$. For an input power of 300 W and for a gas flow of $1.11 \text{ cm}^3 \text{ s}^{-1}$, the atomic oxygen concentration is comprised between 5×10^{11} and $8.5 \times 10^{13} \text{ at} \cdot \text{cm}^{-3}$ when the total pressure goes from 600 to 5000 Pa.

4 Results and Discussion

The cylindrical samples are sintered α -SiC (6H) (density $3.15 \times 10^3 \text{ kg/m}^3$, theoretical value: $3.21 \times 10^3 \text{ kg/m}^3$) containing as major impurities 1% B, less than 2000 ppm Si and SiO_2 , and less than 1000 ppm of Fe, C and (Na+K+Ca+Mg). The sample dimensions are 25 mm diameter and 3 mm high. The upper face (exposed to the solar radiation) is polished using a $1 \mu\text{m}$ diamond polishing compound, then cleaned ultrasonically in acetone and ethanol and dried before testing.

The CVD SiC samples are composite structures provided by a French society, S.E.P. (Société Européenne de Propulsion). They are 2D C/SiC composites with a coating of CVD β SiC and they tested as received. The sample dimensions are the same.

4.1 Experimental protocol

Before each experiment, the pressure and the air flow ($1.11 \text{ cm}^3 \text{ s}^{-1}$) are fixed. For the experiments performed under plasma, the plasma is started after the pressure stabilization and before solar heating. The gradual opening of a shutter placed between the sample and the concentrated solar radiation allows the control of the temperature level. The thermal history of each sample is represented in Fig. 6 with a temperature increase of $4^\circ/\text{s}$ then a plateau of nearly 400 s and finally a decrease at a rate of $2^\circ/\text{s}$. The duration of the plateau is large enough to indicate the active oxidation regime. In fact, during the temperature raising and decreasing at every pressure, silica formation takes place. But on the temperature plateau, when active oxidation occurs, the surface of silicon carbide is very damaged and the silica formation when decreasing

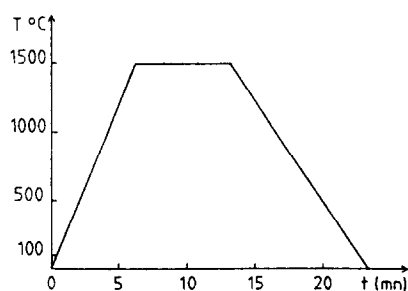


Fig. 6. Thermal history of the sample.

the temperature does not affect the phenomenon as SEM micrographs reveal.

The modification of the sample is controlled by weighing, X-ray diffraction (XRD), scanning electron microscopy (SEM) and Ayers spectroscopy.

4.2 Experiments under standard air for sintered SiC

The results are presented in Fig. 7. For samples (●), after the oxidation test run, the surface is covered with a very thin passive silica layer, the mass gain being weak. For other samples (○), the surface after oxidation is damaged with a very large specific area (Fig. 8(c)). The relative mass losses are comprised between 0.1 and 3.6%. These results under standard air are in good agreement with the thermodynamic calculation (straight line Th.).

4.3 Experiments under microwave-excited air for sintered SiC

The results are presented in Fig. 7 and are far from those predicted by thermodynamics. All (▲) samples have a passive silica layer after oxidation. For a sample located far from the transition line, the thickness of the silica layer is about 150 nm. For other samples after oxidation, the surface is very damaged and as previously the surface is very divided (Fig. 8 (e)). The relative mass losses are comprised between 1 and 4%. In the case of dissociated air, the transition zone is located at lower pressure for the same temperature. So, the dissociation significantly enlarges the p-t domain characterized by the presence of a passive silica layer. The great difference observed between the results and theory may be attributed to out-of-equilibrium phenomena and/or kinetics surface activation.

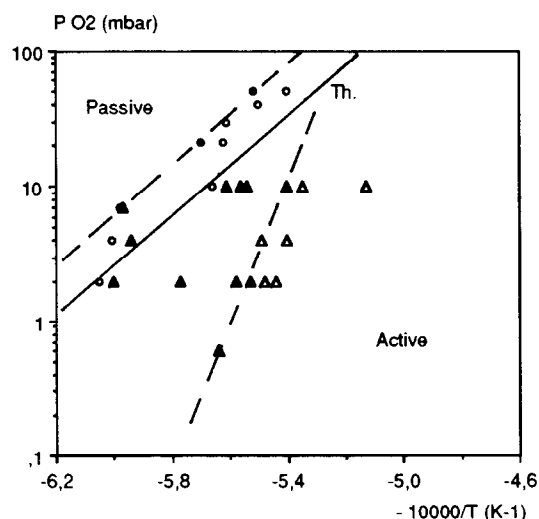


Fig. 7. Oxygen partial pressure versus temperature for the active to passive transition of SiC under molecular (o) and dissociated (Δ) air — experimental determination for sintered silicon carbide in dotted line. ● or ▲: samples with a passive silica layer; ○ or Δ : active oxidation. The theoretical continuous line is that of Balat.

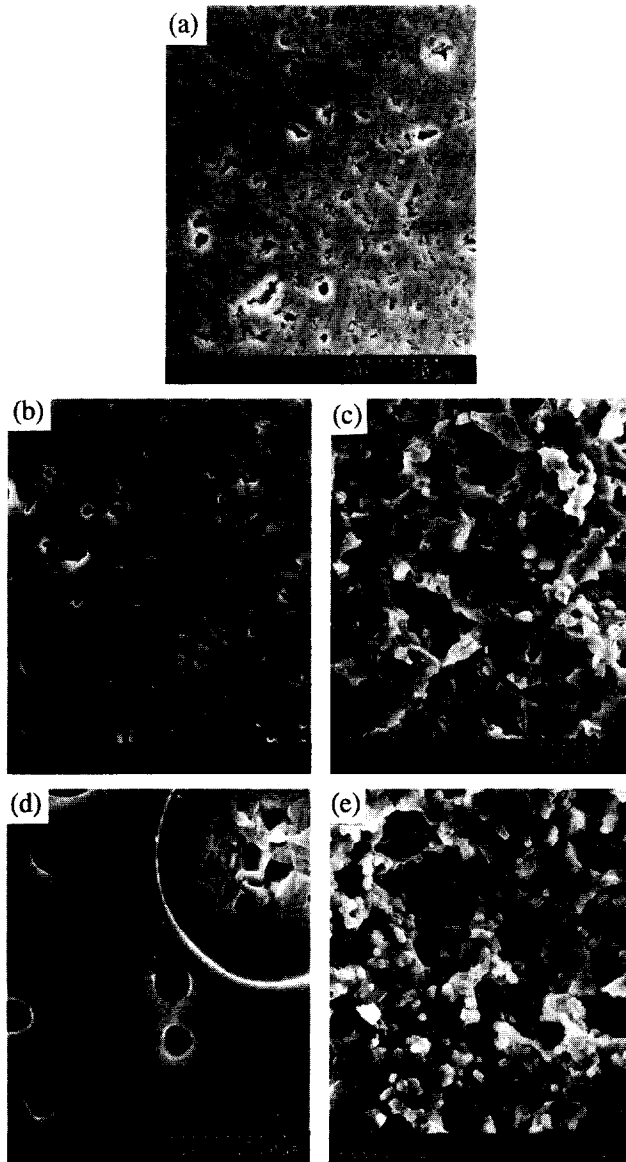


Fig. 8. SEM micrographs of sintered silicon carbide: (a) before oxidation, (b) after passive oxidation under standard air ($T = 1480^{\circ}\text{C}$, $P_{\text{O}_2} = 2.1 \times 10^3 \text{ Pa}$), (c) after active oxidation under standard air ($T = 1510^{\circ}\text{C}$, $P_{\text{O}_2} = 3 \times 10^3 \text{ Pa}$), (d) after passive oxidation under excited air ($T = 1580^{\circ}\text{C}$, $P_{\text{O}_2} = 10^3 \text{ Pa}$) and (e) after active oxidation under excited air ($T = 1595^{\circ}\text{C}$, $P_{\text{O}_2} = 10^3 \text{ Pa}$).

4.4 Experiments under standard air for CVD SiC on C/SiC composites

As previously, for samples (●), after the oxidation test run, the surface is covered with a very thin passive silica layer but there is always a weak mass loss for each sample (max 0.5% relative), this probably due to the porosity and the access of oxygen to the carbon fiber (Fig. 9). Thus the mass loss is not always representative of an active oxidation, it depends on the nature of the material (substrate + coating). The surface observation by SEM provides better information on the active to passive transition. For other samples (○), the surface after oxidation is very damaged, so the oxidation regime is active. The relative mass losses are comprised between 0.7% and 2.9%.

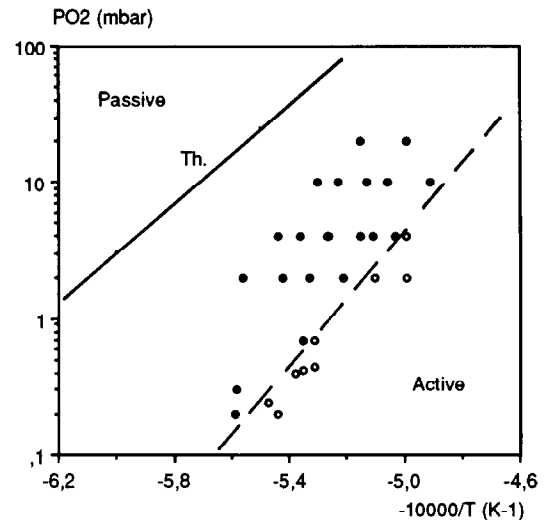


Fig. 9. Oxygen partial pressure versus temperature for the active to passive transition of SiC under standard air (○) — experimental determination for CVD silicon carbide in dotted line. ●: samples with a passive silica layer; o: active oxidation. The theoretical continuous line is that of Balat.

The results are very far from the thermodynamic calculation and this behavior is very different from the one obtained with the sintered silicon carbide.

Figure 10 presents SEM micrographs of samples before treatment (sample 3200), in the passive region (sample 3406) and in the active one (sample 3206). The silicon carbide is very damaged on the sample 3206 and the bare carbon fibers can be seen.

4.5 Experiments under microwave-excited air for CVD SiC on C/SiC composites

The results are presented in Figure 11. All (▲) samples have a passive silica layer after oxidation with very weak mass losses. For other samples (Δ), after oxidation, the surface is damaged (active regime). The relative mass losses are comprised between 0.8% and 3.1%.

The observed difference between the standard and excited atmospheres is very weak (about 20–30° in the studied pressure range). It seems that, contrary to sintered silicon carbide and the results of Rosner, the use of atomic oxygen decreases the passive zone. So this behavior shows the importance of the nature of the silicon carbide on the position of the transition line.

Figure 10 shows SEM micrographs of samples in the passive zone (sample 3390) and in the active one (sample 3203). The active oxidation takes place in the cracks of the silicon carbide layer.

5 Conclusions

The active to passive transition in the oxidation of silicon carbide is examined for two kinds of mate-

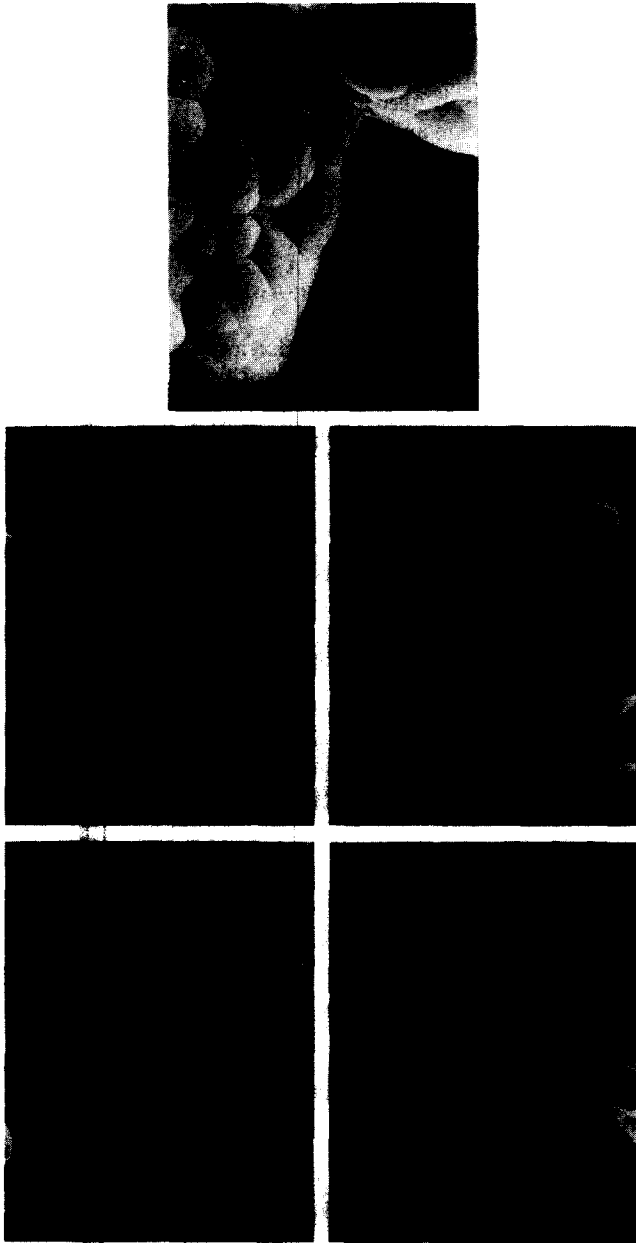


Fig. 10. SEM micrographs of CVD β silicon carbide (3200) before oxidation, (3406) after passive oxidation under standard air ($T = 1646^\circ\text{C}$, $P_{\text{O}_2} = 200$ Pa), (3206) after active oxidation under standard air ($T = 1687^\circ\text{C}$, $P_{\text{O}_2} = 200$ Pa), (3390) after passive oxidation under excited air ($T = 1740^\circ\text{C}$, $P_{\text{O}_2} = 10^3$ Pa) and (3203) after active oxidation under excited air ($T = 1758^\circ\text{C}$, $P_{\text{O}_2} = 10^3$ Pa).

rials (sintered and CVD) under standard and atmospheric re-entry conditions and compared to the literature data. Several differences in the results are observed due to the nature of the silicon carbide, the gas flow rate and its nature, and the total pressure used.

The influence of the total pressure level is very important and can explain the control of the reaction (kinetic or diffusion limitation) and so the position of the transition line. It is necessary to do more experiments at higher total pressure to find out its role, the transition line will be moved towards the theoretical calculation (under diffusion control).

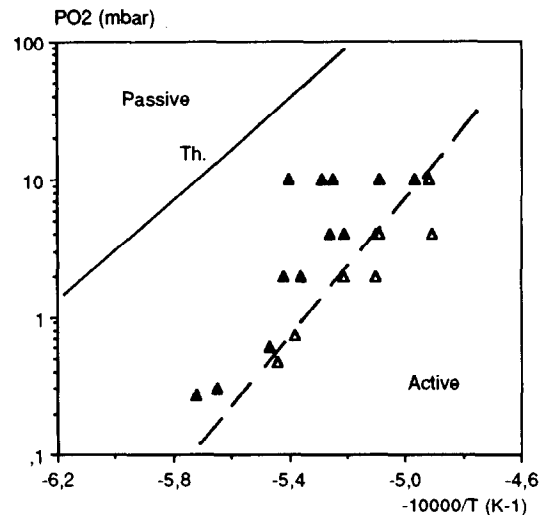


Fig. 11. Oxygen partial pressure versus temperature for the active to passive transition of SiC under excited air Δ — experimental determination for CVD silicon carbide in dotted line. \blacktriangle : samples with a passive silica layer; \triangle : active oxidation.

Moreover, to show the influence of the silicon carbide nature, several experiments will be done on CVD SiC (made in our laboratory) deposited on sintered SiC. It is also necessary to understand the differences observed between the two atmospheres (standard and excited) on the position of the transition zone.

Acknowledgement

The author wants to thank the S.E.P. society for the authorization of publication of industrial results and for its financial support of this work (Contract 487210).

References

1. Eriksson, G., Thermodynamic studies of high temperature equilibria XII Solgasmix. *Chem. Scrip.*, **8** (1973) 100–3.
2. Wagner, C., Passivity during the oxidation of silicon at elevated temperature. *J. Appl. Phys.*, **29** (1958) 1295–7.
3. Bird, R. B., Stewart, W. E. & Lightfoot, E. N., In *Transport Phenomena*. J. Wiley, New York (1960) pp. 508–13.
4. Chase, M. W., Davies J. R. *et al.*, *JANAF Thermodynamical Tables*, 3rd Ed., *J. Phys. Chem. Ref. Data*, **14** suppl. 1 (1985).
5. Balat, M., Flamant, G., Malé, G. & Pichelin G., Active to passive transition in the oxidation of silicon carbide at high temperature and low pressure in molecular and atomic oxygen. *J. Mater. Sci.*, **27** (1992) 697–703.
6. Singhal, S. C., Thermodynamic analysis of the high-temperature stability of silicon nitride and silicon carbide. *Ceramurgia*, **2** (1976) 123–30.
7. Nickel, K. G., The role of condensed silicon monoxide in the active-to-passive oxidation transition of silicon carbide. *J. Europ. Ceram. Soc.*, **9** (1992) 3–8.
8. Heuer, A. H. & Lou, V. L., Volatility diagrams for silica, silicon nitride and silicon carbide and their application to high-temperature decomposition and oxidation. *J. Am. Ceram. Soc.*, **73** (1990) 2789–803.
9. Gulbransen, E. A. & Jansson, S. A., The high-temperature

- oxidation, reduction and volatilization reactions of silicon and silicon carbide. *Oxid. Met.*, **4** (1972) 181–201.
10. Hinze, J. W. & Graham, H. C., The active oxidation of silicon and silicon carbide in the viscous gas-flow regime. *J. Electrochem. Soc.*, **123** (1976) 1066–73.
 11. Vaughn, W. L. & Maahs, H. G., Active-to-passive transition in the oxidation of silicon carbide and silicon nitride in air. *J. Am. Ceram. Soc.*, **73** (1990) 1540–3.
 12. Narushima, T., Goto, T., Iguchi, Y. & Hirai, T., High-temperature active oxidation of chemically vapor-deposited silicon carbide in Ar-O₂ atmosphere. *J. Am. Ceram. Soc.*, **74** (1991) 2583–6.
 13. Dickinson, R. C., Oxidation protection. In *Proceedings of the Oxidation-Resistant Carbon-Carbon Composites for Hypersonic Vehicle Application Workshop*, Hampton VA, Sept. 1987, NASA Conf. Public. 2501, pp. 129–41.
 14. Keys, L. H., The oxidation of silicon carbide. In *Proceedings of the Symposium on Properties of High Temperature Alloys*, **77-1**, Electrochem. Soc., Princeton NJ, (1977) 681–96.
 15. Pampuch, R. & Jonas, S., New aspects of the oxidation of silicon carbide. *Sci. Ceram.*, **9** (1977) 300–7.
 16. Rosner, D. E. & Allendorf, H. D., High temperature kinetics of the oxidation and nitridation of pyrolytic silicon carbide in dissociated gases. *J. Phys. Chem.*, **74** (1970) 1829–39.
 17. Antill, J. E. & Warburton, J. B., Active to passive transition in the oxidation of silicon carbide, *Corros. Sci.*, **11** (1971) 337–42.
 18. Kim, H. E. & Moorehead, A. J., Effect of active oxidation on the flexural strength of α -SiC, *J. Am. Ceram. Soc.*, **73** (1990) 1868–72.
 19. Schiroky, G. H., Oxidation behavior of chemically vapor-deposited silicon carbide, *Adv. Ceram. Mater.*, **2** (1987) 137–41.
 20. Touloukian, Y. S. & De Witt, D. P., *Thermal Radiative Properties — Non Metallic Solids*, Vol. 8. Plenum Press, New-York (1972).

Modification of PTCR Behavior of $(\text{Sr}_{0.2}\text{Ba}_{0.8})\text{TiO}_3$ Materials by Post-Heat Treatment after Microwave Sintering

Horng-Yi Chang,^a Kuo-Shung Liu^a & I.-Nan Lin^b

^aDepartment of Materials Science and Engineering, and ^bMaterials Science Center, National Tsing-Hua University, Hsinchu, 30043 Taiwan, Republic of China

(Received 13 February 1995; revised 18 May 1995; accepted 19 May 1995)

Abstract

$(\text{Sr}_{0.2}\text{Ba}_{0.8})\text{TiO}_3$ materials have been effectively densified by microwave sintering process. The grain size ($\sim 6 \mu\text{m}$) and PTCR characteristics ($T_c = 50^\circ\text{C}$, $\rho_{\text{max}}/\rho_{\text{min}} \approx 10^2$) of the as-sintered samples vary insignificantly with sintering temperature (1100–1180°C) and soaking time (10–40 min). However, lowering the cooling rate after sintering substantially increases the resistivity jump ($\rho_{\text{max}}/\rho_{\text{min}}$) from 10^2 to 10^{5-3} , without altering the microstructure. Subsequent annealing, on the other hand, substantially modifies the microstructure and PTCR characteristics. The resistivity jump increases monotonously with heat treatment temperature (T_{ht}) and reaches ($\rho_{\text{max}}/\rho_{\text{min}}$) $\approx 10^7$ for samples heat-treated at 1300°C for 2 h. The grain size remains nearly unchanged for $T_{\text{ht}} \leq 1200^\circ\text{C}$ and grows markedly for samples heat-treated at a higher temperature. The effective trap level is estimated to be $E_s = 1.46 \text{ eV}$. The activation energy for the densification rate is $Q_{\text{MS}} = 8.2 \text{ kcal/mol}$ for microwave sintering and $Q_{\text{cs}} = 62.5 \text{ kcal/mol}$ for conventional sintering process.

1 Introduction

Since their discovery in 1955, semiconducting BaTiO_3 materials, which possess positive temperature coefficient of resistivity (PTCR) characteristics, have found extensive application as thermistors, safety circuits, degaussers, and other devices.^{1,2} The models of Heywang and Jonker³⁻⁵ are the most popular conduction models used to account for the PTCR behavior of these materials. According to these models, the Schottky barrier induced by the surface states existing at grain boundary regions leads to high resistivity of the materials in the paraelectric phase at a tempera-

ture higher than the Curie temperature (T_c). The spontaneous polarization which occurs in the ferroelectric state, when $T < T_c$, results in compensation of surface states^{5,6} and lowers the resistivity of the materials. Therefore, the concentration of effective surface states, N_s , is one of the dominating factors which determine the resistivity jump of the materials. The PTCR characteristics of these materials are, thereby, tremendously influenced by the processing parameters which modify the surface states of the materials.⁷⁻¹⁵

The preparation of these materials by conventional sintering process normally requires a very high sintering temperature ($>1350^\circ\text{C}$), even when liquid phase sintering aids are applied¹⁶. The microwave sintering process, on the other hand, has been observed to densify the ceramic materials at a very rapid rate and at a substantially lower temperature.¹⁷⁻²¹ This technique is, therefore, adopted in this study in an attempt to rapidly sinter the donor-doped $(\text{Sr}_{0.2}\text{Ba}_{0.8})\text{TiO}_3$ materials. The effect of processing parameters, such as sintering temperature, soaking time, cooling rate and the post-heat treatment schemes, on the microstructure and PTCR properties of these materials is systematically examined. The correlation of the defect chemistry possibly occurred during processing with the electrical behavior of the samples will be discussed.

2 Experimental Procedure

The $(\text{Sr}_{0.2}\text{Ba}_{0.8})\text{TiO}_3$ powders, which contained 0.3 mol% Sb_2O_3 as semiconductive dopants and 5 mol% AST ($\text{Al}_2\text{O}_3:\text{SiO}_2:\text{TiO}_2 = 4:9:3$) as sintering aids, were prepared by the conventional mixed oxide method. In which, the mixtures containing high purity oxides of proper proportion were ball-milled in a plastic jar, using plastic-coated iron

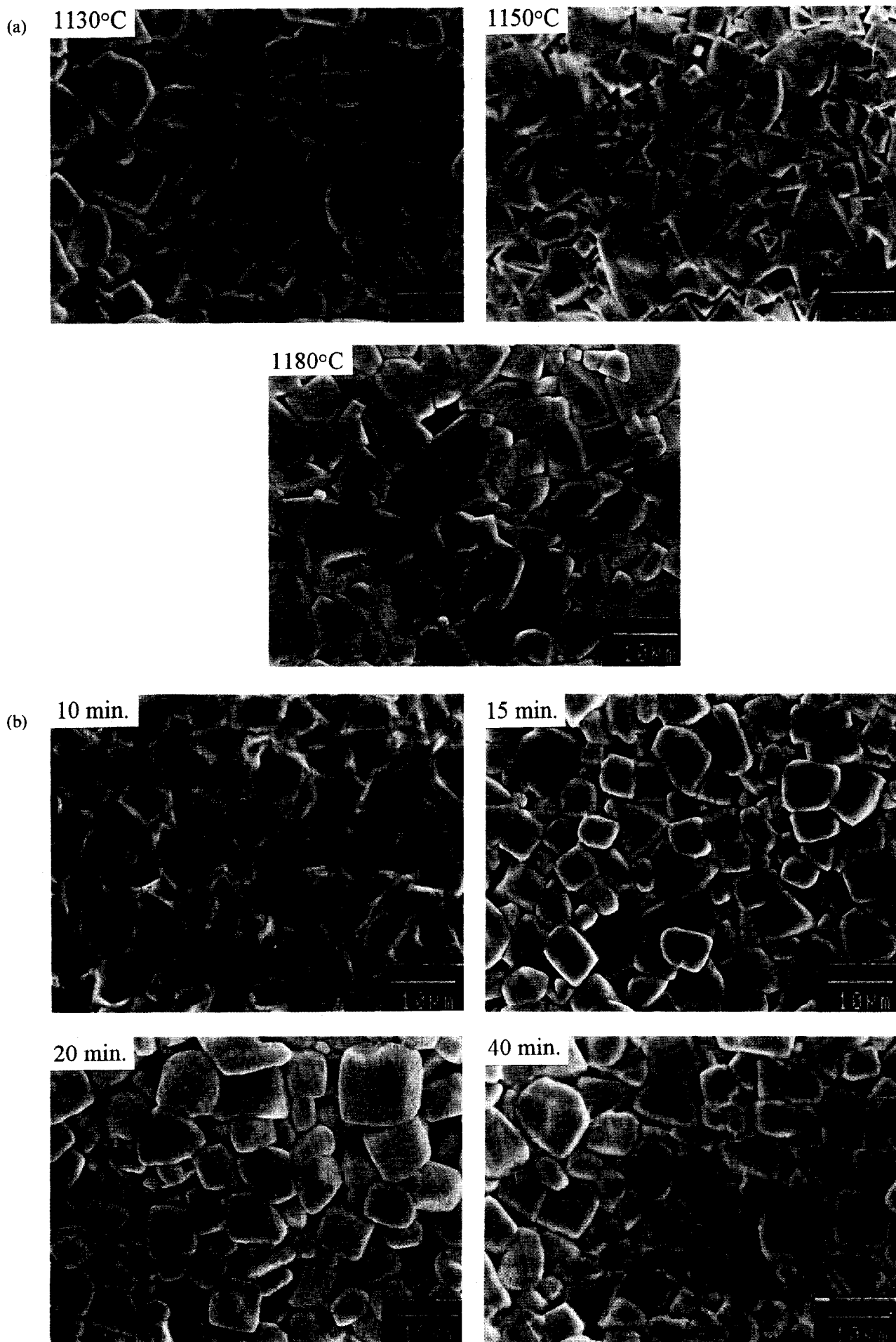


Fig. 1. Microstructure of the $(\text{Sr}_{0.2}\text{Ba}_{0.8})\text{TiO}_3$ samples microwave sintered: (a) at 1130–1180°C for 40 min and (b) at 1130°C for 10–40 min, cooled at 154°C/min.

balls, with deionized water, for 8 h. They were then calcined at 1000°C in air for 4 h, followed by pulverization in a ball-mill for 8 h to around 1 μm size. The green compacts made of these powders were heated at 600°C for 1 h to remove the binders (PVA) and then microwave sintered at 1100–1180°C for 10–40 min in an applicator made of WR284 waveguide. The 2.45 GHz microwave generated from commercial source (Gerling GL107 magnetron) was used to heat up the samples. The temperature profile was then measured using Pt–13%Rh thermocouple, placed near the sample surface. The heating rate was controlled at 50°C/min and the cooling rate was varied (4°C/min, 9°C/min, or 154°C/min). In the annealing experiments, the materials microwave sintered at 1130°C for 40 min (cooled at 154°C/min) were heat-treated at either 1000, 1130, 1200, 1250, or 1300°C for 2 h in an electrical furnace. The heating and cooling rate in the annealing process were all controlled at 5°C/min. To facilitate the comparison of the microwave sintering process with the conventional sintering process, the green compacts of the same materials were sintered in a resistive heating furnace by a two-step process. The samples were preheated at 1200°C for 2 h, followed by rapidly heating to 1225, 1250, 1275 or 1300°C and then sintered at that temperature for 2 h. The preheating and cooling rate were controlled at 5°C/min.

The density of the samples is measured by Archimedes' method and the densification rate is calculated by dividing the change in density value by the time interval at temperature. The crystal structure and microstructure of the sintered samples were examined using Rigaku D/max-IIB X-ray diffractometer and Joel JSM-840A scanning electron microscope (SEM), respectively. The average grain size of the samples is estimated from the SEM micrographs by linear interception method. The resistivity–temperature (ρ – T) properties of these samples were measured using H.P. 3457A multimeter after the In–Ga alloy was rubbed onto the sample surface to serve as electrodes.

3 Results

The beneficial effect of microwave sintering technique on enhancing densification process of the $(\text{Sr}_{0.2}\text{Ba}_{0.8})\text{TiO}_3$ material is enormous, as illustrated by the fact that the samples microwave-sintered at 1180°C for 20 min already reach the same density ($\sim 95\%$ T.D.) as those sintered by the furnace-heating process at 1300°C for 2 h. In other words, the diffusivity of the cations and anions in these materials is substantially enhanced in the microwave

sintering process. The microstructure of the samples varies insignificantly with the sintering temperature and soaking time. The grain size of the samples increases slightly with sintering temperature, from around 6 μm for 1130°C-sintered samples to around 9 μm for 1180°C-sintered samples (Fig. 1(a)) and the grain size is around 6 μm for all samples microwave sintered at 1130°C for 10–40 min (Fig. 1(b)).

To facilitate the comparison, the microstructures of the $(\text{Sr}_{0.2}\text{Ba}_{0.8})\text{TiO}_3$ materials sintered by conventional method in two-step process are shown in Figs 2(a)–(c). These figures indicate that the growth of the grains can be triggered only when the sintering temperature is higher than 1275°C, which is slightly higher than the eutectic point reported¹⁶ for $(\text{Sr}_{0.2}\text{Ba}_{0.8})\text{TiO}_3$ and AST system. Compared to the microstructure of the samples directly sintered at 1300°C for 2 h shown in Fig. 2(d), the uniformity of the grain size distribution has been substantially improved by a two-step sintering process, and that of the microwave sintered samples is even better (c.f. Fig. 1). The temperature range suitable for the microwave sintering process is, however, very narrow. The materials are hardly sintered when the sintering temperature is maintained at 1100°C or lower. The sintering process is rather unstable and the thermal runaway phenomenon frequently occurs when the sintering temperature is increased to 1190°C or higher. The crystal structure of the calcined powders and the as-microwave sintered $(\text{Sr}_{0.2}\text{Ba}_{0.8})\text{TiO}_3$ samples are shown in Figs 3(a) and (b), respectively. The (002) and (200) diffraction peaks are only barely split, indicating that the c/a ratio of the materials is very small. The tetragonality, (i.e. c/a ratio) of the samples does not vary with the temperature and soaking time in the microwave sintering process. It is also not significantly different from that of the conventionally-sintered samples (c.f. Fig. 3(d)).

To further elucidate how the microwave sintering process enhances the sintering behavior of the $(\text{Sr}, \text{Ba})\text{TiO}_3$ materials, the activation energy (Q) for the densification process is evaluated from the densification rate of the samples. For this purpose, a simplified densification theory²³ was adopted, that is,

$$\begin{aligned} dg/dt &= JAN\Omega = (96\pi\gamma\Omega/kTG^3) \cdot D_0 \exp(-Q/kT) \\ &= (K/T) \cdot D_0 \exp(-Q/kT) \end{aligned}$$

where J is the diffusive flux, A is the area over which diffusion acts, N is number density of pores and Ω is the atomic volume. Moreover, γ is surface energy, G is grain size and K is a geometric factor, D_0 is the pre-exponential term of diffusivity, k and T are the Boltzmann constant and temperature, respectively, and dg/dt is the densification

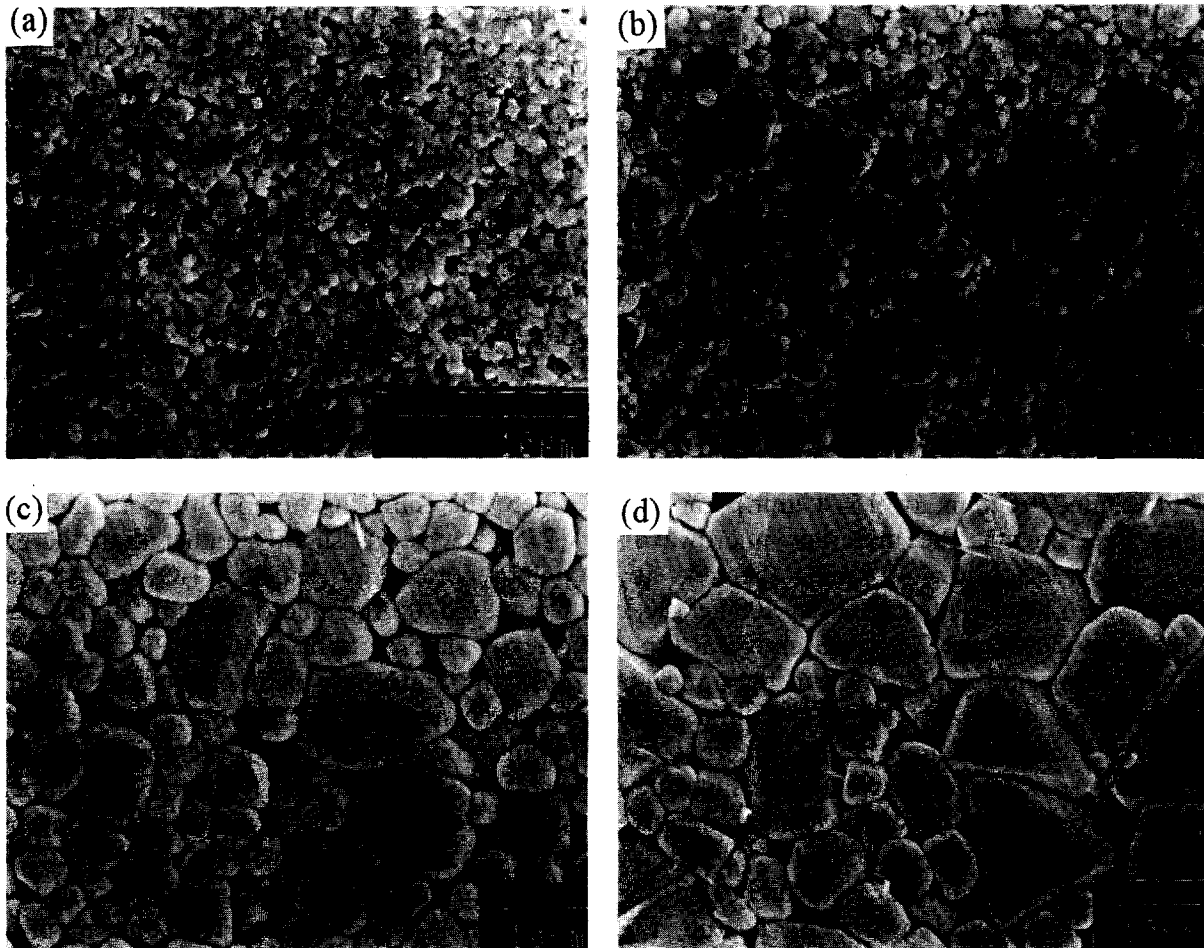


Fig. 2. The microstructure of $(\text{Sr}_{0.2}\text{Ba}_{0.8})\text{TiO}_3$ samples sintered by conventional method in two-step process: (a) 1200°C -2 h; (b) 1275°C -2 h after 1200°C -2 h; (c) 1300°C -2 h after 1200°C -2 h and (d) that directly sintered at 1300°C -2 h.

rate of the samples. The activation energy (Q) for densification can be estimated from the Arrhenius plot of the densification rate. Figure 4, in which the density of the microwave-sintered and furnace-sintered samples are listed as the inset, shows that the activation energy for densification in microwave sintering process ($Q_{\text{MS}} = 8.2 \text{ kcal/mol}$) is significantly smaller than that of the conventional sintering process ($Q_{\text{CS}} = 62.5 \text{ kcal/mol}$). The deviation of the data corresponding to the samples furnace-sintered at 1275 or 1300°C (open triangles) from the Arrhenius plot is presumably

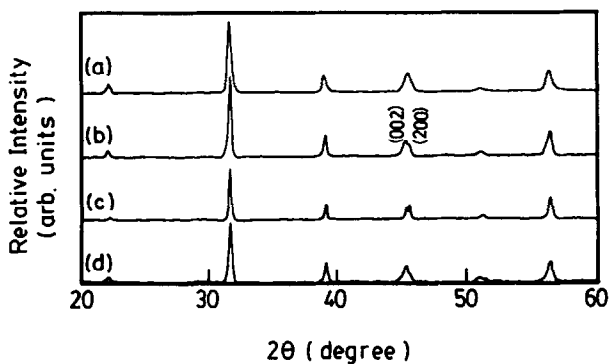


Fig. 3. The X-ray diffraction patterns of $(\text{Sr}_{0.2}\text{Ba}_{0.8})\text{TiO}_3$ samples: (a) as calcined powders; (b) as microwave sintered (at 1180°C for 40 min); (c) 1200°C -2 h annealed (after microwave sintering) and (d) the 1300°C -2 h conventionally sintered samples.

caused by the change in the densification mechanism, since the liquid phase is expected to occur for these samples at these temperatures. The samples are densified by solid state diffusion mechanism when sintering temperature is lower.

The above mentioned results indicate that the microwave sintering process can densify the $(\text{Sr}_{0.2}\text{Ba}_{0.8})\text{TiO}_3$ materials at a substantially lower temperature than the conventional sintering process.

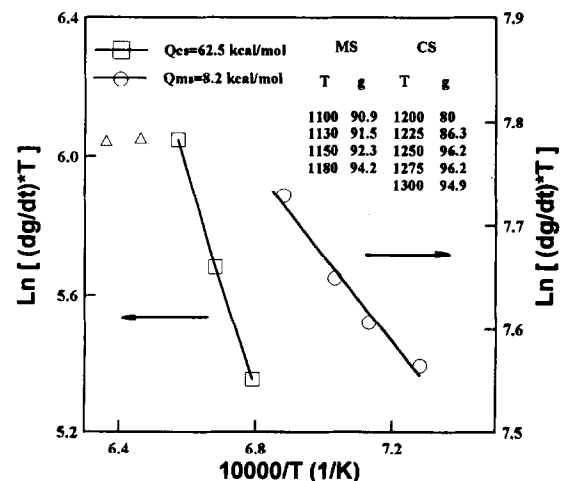


Fig. 4. The Arrhenius plots for densification rate of the samples sintered by the microwave sintering process (MS) and the conventional sintering process (CS). The inset shows the density of these samples. (T: sintering temperature in $^\circ\text{C}$; g: density in % of theoretical density).

The additional benefit of utilizing the microwave sintering technique is the capability of initiating the densification process without triggering the grain boundary migration. Consequently, the materials are densified without grain growth, leading to a microstructure with a fine and very uniform grain size distribution. The microwave sintering process is, therefore, substantially advantageous over the conventional sintering process in the preparation of the $(\text{Sr}_{0.2}\text{Ba}_{0.8})\text{TiO}_3$ PTCR materials.

The resistivity-temperature properties of the samples vary moderately with the sintering temperature and soaking time. The minimum (ρ_{\min}) and maximum (ρ_{\max}) resistivity of the samples alter only slightly with the sintering conditions. The resistivity ratio ($\alpha = \rho_{\max}/\rho_{\min}$) slightly increases with sintering temperature but varies insignificantly with soaking time (Fig. 5, curve 3). The positive temperature coefficient of resistivity (PTCR) of these samples, which is defined as

$$p = \{(\log \rho_{-T_c + \Delta T} - \log \rho_{T_c}) / \Delta T\}$$

is around $p = 0.01 \Omega\text{-cm}/^\circ\text{C}$ for $T_c = 50^\circ\text{C}$ and $\Delta T = 100^\circ\text{C}$, and the resistivity ratio is around $\alpha = 10^{1.75}$. The Curie temperature of these samples is roughly the same ($T_c \approx 50^\circ\text{C}$).

According to the Heywang and Jonker³⁻⁵ models, the PTCR behavior of these materials primarily arises from the Schottky barrier formed at grain boundary regions. Besides the common practices to modify the potential barrier by artificially doping some modifiers, (e.g. Mn),⁹⁻¹⁰ the cooling rate after sintering has been observed to effectively modify the defect chemistry near the grain boundary regions by the oxidation-reduction process so as to increase the PTCR behavior of BaTiO_3 ¹¹ and $(\text{Sr}, \text{Ba})\text{TiO}_3$ ¹² samples. The same approach is thereby adopted here to improve the PTCR properties of the microwave sintered samples. Figure 5 shows that reducing the cooling rate does lead to

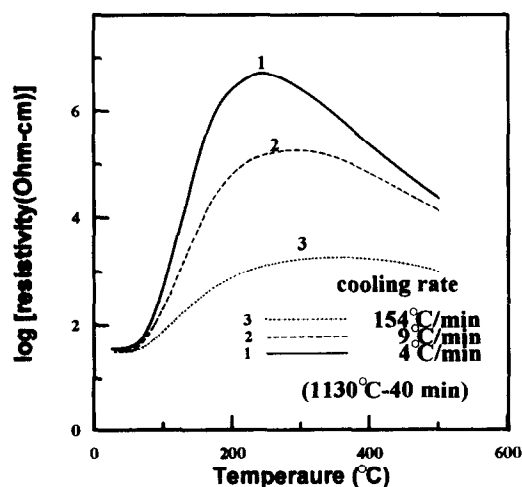


Fig. 5. The resistivity-temperature properties of the $(\text{Sr}_{0.2}\text{Ba}_{0.8})\text{TiO}_3$ samples as microwave sintered at 1130°C (40 min) and cooled at different rate (4– $154^\circ\text{C}/\text{min}$).

a tremendous change in resistivity-temperature characteristics. It does not cause any significant modification on the microstructure of the samples. As the cooling rate decreases, the maximum resistivity (ρ_{\max}) increases markedly while the minimum resistivity (ρ_{\min}) remains unchanged, such that the resistivity jump ($\alpha = \rho_{\max}/\rho_{\min}$) increases substantially from $\alpha = 10^{1.75}$ ($p = 0.01 \Omega\text{-cm}/^\circ\text{C}$) for $154^\circ\text{C}/\text{min}$ -cooled samples to $\alpha = 10^{4.85}$ ($p = 0.04 \Omega\text{-cm}/^\circ\text{C}$) for $4^\circ\text{C}/\text{min}$ -cooled samples. The temperature of maximum resistivity (T_{\max}) shifts slightly towards a lower temperature as the cooling rate after sintering is reduced. Similar behavior has also been observed in the BaTiO_3 and $(\text{Sr}_{0.2}\text{Ba}_{0.8})\text{TiO}_3$ materials sintered by conventional process^{11,12} and was accounted for by the model that the grain boundary regions are richer in cationic vacancies, due to the compensation of the oxygen vacancies by the inward diffused oxygen ions during the cooling period. These atomic vacancies act as effective electron traps and increase the Schottky barrier height of the materials. This model is adopted to quantitatively estimate the effective trap level induced in Fig. 5 and will be discussed later.

The residue stress induced by the isostatic pressure is another factor which has been reported to markedly influence the dielectric constant and, hence, the Schottky barrier height of the $(\text{Sr}, \text{Ba})\text{TiO}_3$ ²⁴ materials. The 1130°C (40 min) sintered ($154^\circ\text{C}/\text{min}$ cooled) samples were thus heat-treated at 1000 – 1200°C for 2 h and then slowly cooled ($5^\circ\text{C}/\text{min}$) to examine the influences of residual stress possibly induced by a rapid cooling process on the characteristics of these materials. Figures 6(a–c) show that the microstructure of these samples has not been modified. The contrasting increase of the grain boundaries in the micrograph of 1200°C -annealed samples (Fig. 6(c)) is due to the thermal etching effect on the polished samples. On the other hand, Fig. 7(a) indicates that the maximum resistivity (ρ_{\max}) of the samples was increased and the T_{\max} -value was also shifted towards a lower temperature for the samples heat-treated. The higher the heat treatment temperature the larger the modification is.

The other phenomenon of interest is the influence of grain size on the PTCR properties of the materials. Figures 6(c–e) illustrate that the grains start to grow when the heat treating temperature (T_{ht}) is higher than 1250°C . The variation of grain size with T_{ht} is plotted in the inset of Fig. 7. The X-ray diffraction patterns shown in Fig. 3(c) infer that the tetragonality of the materials remains the same. The ρ - T curves in Fig. 7(b) show that the ρ_{\max} value abruptly increases and the resistivity ratio markedly jumps whenever the grain growth has occurred. Excellent PTCR behavior is obtained

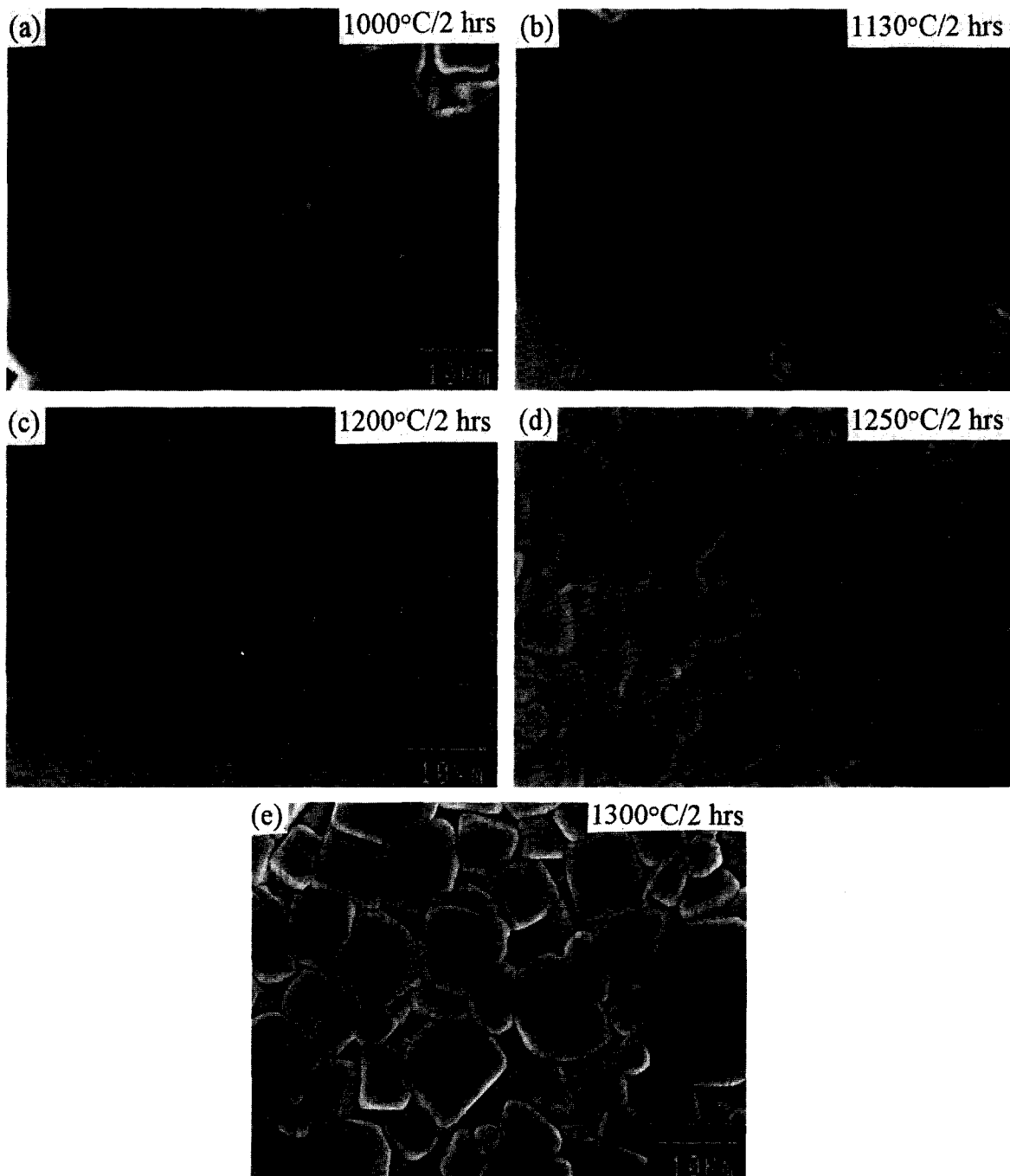


Fig. 6. The microstructure of $(\text{Sr}_{0.2}\text{Ba}_{0.8})\text{TiO}_3$ samples microwave sintered at 1130°C for 40 min and heat treated at: (a) 1000°C ; (b) 1130°C ; (c) 1200°C ; (d) 1250°C and (e) 1300°C for 2 h.

for samples heat-treated at 1300°C for 2 h ($\alpha = 10^7$, $\rho = 0.053 \Omega\text{-cm}/^\circ\text{C}$). Interestingly; the grain size of the 1300°C (2 h) heat-treated samples (microwave-sintered) is the same as that of the samples sintered by a conventional method, (two-step process) at 1300°C for 2 h (c.f. Figs 2(c) and 6(e)). The tetragonality of the two samples are almost the same (c.f. Figs 3(c) and (d)). However, the ρ - T characteristics of the microwave-sintered samples (after heat treatment), which is shown as a dash-dotted curve in Fig. 7(b), are significantly superior to that of the conventionally sintered samples (dotted curve, Fig. 7(b)). This phenomenon reveals the importance of having a uniform grain size distribution on the electrical properties of the PTCR materials.

4 Discussion

The annealing process after microwave sintering was observed to modify the PTCR behavior of the $(\text{Sr}_{0.2}\text{Ba}_{0.8})\text{TiO}_3$ material in a very similar way with the cooling rate did, *viz.*, the T_{max} -value lowered as the ρ_{max} increased (c.f. Figs. 5 and 7). The increase in resistivity, accompanied by the decrease in T_{max} -value, due to slow cooling rate has been ascribed to the increase in the concentration of the effective electron traps, *i.e.* cationic vacancies.^{11,12} The same mechanism is adopted to account for the effect of heat treatment on the ρ - T behavior shown in Fig. 7. In other words, the cationic vacancies, which act as effective electron

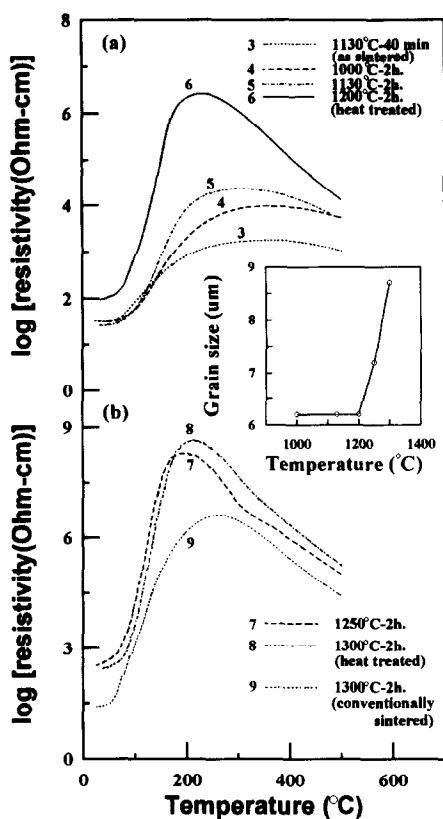


Fig. 7. The resistivity-temperature (ρ - T) properties of $(\text{Sr}_{0.2}\text{Ba}_{0.8})\text{TiO}_3$ samples microwave sintered at 1130°C and then heat treated (a) at 1000–1200°C for 2 h, including that of the as-sintered samples (dotted curve) and (b) at 1250–1300°C for 2 h, including that of the samples sintered by conventional process at 1300°C for 2 h (dotted curve). The inset shows the grain size of the annealed samples.

traps, are larger in concentration when heat-treated at higher temperature. This occurs probably due to the fact that the equilibrium concentration of cationic and anionic vacancy pairs generated at higher temperature is larger so that the residue concentration of the cationic vacancies, after re-oxidation due to inward diffusion of oxygen during cooling process, is significantly higher.

Since the samples shown in Figs 5 and 7 are of similar microstructure and the cooling rate during microwave sintering or post-annealing process only modifies the concentration of effective electron traps, i.e. cationic vacancies, the energy level of these effective traps can be evaluated from the $\log(\rho_{\max}/\rho_{\min})-T_{\max}^{-1}$ plot.¹¹ The $(\rho_{\max}/\rho_{\min})$ and T_{\max} values estimated from ρ - T curves in Figs 5 and 7 are plotted in Fig. 8, showing that the energy levels of the effective traps (E_s) induced by cooling rate process (open circles) is very close to that by the annealing process (solid circles). That is, $E_s = 1.36$ eV + E_f . This phenomenon confirms again, that the effective electron traps induced in the two processes are of the same nature. The Fermi level (E_f) of the $(\text{Sr}_{0.2}\text{Ba}_{0.8})\text{TiO}_3$ semiconducting oxide is usually close to the donor level ($E_d \approx 0.1$ eV)²⁵ in

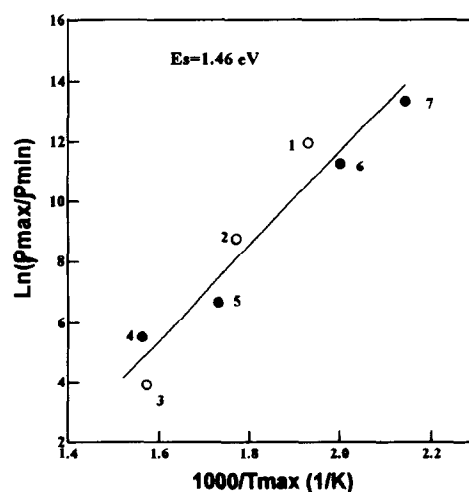


Fig. 8. The $\log(\rho_{\max}/\rho_{\min})-T_{\max}^{-1}$ plot of the resistivity-temperature curves for estimating the effective trap level; open symbols and closed symbols correspond to the ρ - T curves in Figs 5 and 7, respectively.

the donor-doped materials. The effective trap level is, therefore, concluded to be $E_s \approx 1.46$ eV.

5 Conclusions

The microwave sintering process has been observed in this study to effectively densify the $(\text{Sr}_{0.2}\text{Ba}_{0.8})\text{TiO}_3$ materials at substantially lower temperature than the conventional sintering process does. However, the sintering temperature should be controlled in a very narrow range (1130–1180°C). Neither the sintering temperature nor the soaking time in the microwave sintering process shows significant influence on the PTCR behavior and the microstructure of the as-microwave sintered samples. Contrarily, the cooling rate at the end of sintering cycle or the post-heat treatment after sintering exhibits a tremendous effect on increasing the PTCR properties of the samples. The resistivity jump (ρ_{\max}/ρ_{\min}) reaches 10^7 for samples heat-treated at 1300°C for 2 h. The effective trap level is estimated to be around $E_s \approx 1.46$ eV and is assumed to have been resulted from the excess cationic vacancies residing in the regions near grain boundaries. The activation energy for the densification in the microwave sintering process is estimated to be $Q_{\text{MS}} = 8.2$ kcal/mol, which is significantly smaller than that of the conventional sintering process ($Q_{\text{CS}} = 62.5$ kcal/mol).

Acknowledgment

The authors would like to thank the National Science Council, Republic of China, for financial support of this manuscript under Contract No. NSC83-0404-E-007-050.

References

- Wakino, K. & Fujikawa, N., BaTiO₃ and its applications. *Electron. Ceram.*, **2**(5) (1971) 73–6.
- Wakino, K. & Fujikawa, N., Semiconducting BaTiO₃ and its applications. *Electron. Ceram.*, **2**(7) (1971) 65–71.
- Heywang, W., Barium titanate as a semiconductor with blocking layers. *Solid-State Electron.*, **3** (1961) 51–8.
- Heywang, W., Resistivity anomaly in doped barium titanate. *J. Am. Ceram. Soc.*, **47**(10) (1964) 484–90.
- Jonker, G. H., Some aspects of semiconducting barium titanate. *Solid-State Electron.*, **7** (1964) 895–903.
- Huybrechts, B., Ishizaki, K. & Takata, M., Experimental evaluation of the acceptor-states compensation in positive-temperature-coefficient-type barium titanate. *J. Am. Ceram. Soc.*, **75**(3) (1992) 722–4.
- Alles, A. B., Amarakoon, V. R. W. & Burdick, V. L., Positive temperature coefficient of resistivity effect in undoped, atmospherically reduced barium titanate. *J. Am. Ceram. Soc.*, **72**(1) (1989) 148–51.
- Al-Allak, H. M., Brinkman, A. W., Russell, G. J. & Woods, J., The effect of Mn on the positive temperature coefficient of resistance characteristics of donor doped BaTiO₃ ceramics. *J. Appl. Phys.*, (1988) 4530–5.
- Illingsworth, J., Al-Allak, H. M., Brinkman, A. W. & Woods, J., The influence of Mn on the grain-boundary potential barrier characteristics of donor-doped BaTiO₃ ceramics. *J. Appl. Phys.*, **67**(4) (1990) 2088–92.
- Ihrig, H., PTC effect in BaTiO₃ as a function of doping with 3d elements. *J. Am. Ceram. Soc.*, **64**(10) (1981) 617–20.
- Lin, T. F., Hu, C. T. & Lin, I. N., Defects restoration during cooling and annealing in PTC type barium titanate ceramics. *J. Mater. Sci.*, **25** (1990) 3029–33.
- Chen, H. P. & Tseng, T. Y., The effect of cooling rate on the positive temperature coefficient resistivity characteristics of lanthanum-doped Ba_{0.8}Sr_{0.2}TiO₃ ceramics, *J. Mater. Sci. Lett.*, **8** (1989) 1483–5.
- Huybrechts, B., Ishizaki, K. & Takata, M., Influence of high oxygen partial pressure annealing on the positive temperature coefficient of Mn-doped Ba_{0.8}Sr_{0.2}TiO₃. *J. Europ. Ceram. Soc.*, **11** (1993) 395–400.
- Huybrechts, B., Ishizaki, K. & Takata, M., Proposed phenomenological PTCR model and accompanying phenomenological PTCR chart. *J. Am. Ceram. Soc.*, **77**(1) (1994) 286–8.
- Al-Allak, H. M., Russell, G. J. & Woods, J., The effect of annealing on the characteristics of semiconducting BaTiO₃ positive temperature coefficient of resistance devices. *J. Phys. D: Appl. Phys.*, **20** (1987) 1645–51.
- Cheng, H. F., Lin, T. F., Hu, C. T. & Lin, I. N., Effect of sintering aids on microstructures and PTCR characteristics of (Sr_{0.2}Ba_{0.8})TiO₃ ceramics. *J. Am. Ceram. Soc.*, **76**(4) (1993) 827–32.
- Sutton, W. H., Microwave processing of ceramic materials. *Bull. Am. Ceram. Soc.*, **68**(2) (1989) 376–86.
- Warrier, K. G. K., Varma, H. K., Mani, T. V. & Damodaran, A. D., Rapid method for the preparation of 123 superconductor using microwaves. *J. Am. Ceram. Soc.*, **75**(7) (1992) 1990–2.
- Janney, M. A., Calhoun, C. L. & Kimrey, H. D., Microwave sintering of solid oxide fuel cell materials: I. Zirconia–8 mol% Yttria. *J. Am. Ceram. Soc.*, **75**(2) (1992) 341–6.
- Aliouat, M., Mazo, L. & Desgardin, G., Microwave sintering of oxides. *Mater. Res. Soc. Symp. Proc.*, **189** (1990) 229–35.
- Selmi, F., Guerin, F., Yu, X. D., Varadan, V. K. Varadan, V. V. & Komarneni, S., Microwave calcination and sintering of barium strontium titanate. *Mater. Lett.*, **12** (1992) 424–8.
- Al-Allak, H. M., Parry, T. V., Russell, G. J. & Woods, J., Effects of aluminum on the electrical and mechanical properties of PTCR BaTiO₃ ceramics as a function of the sintering temperature. *J. Mater. Sci.*, **23** (1988) 1083–9.
- German, R. M., Sintering. In *Powder Metallurgy Science*, Metal Powder Industries Federation, Princeton, New Jersey, 1984, pp. 145–200.
- Amin, A. & Holmes, M. B., Pressure and temperature dependencies of the direct-current resistance of semiconducting (Ba, Sr)TiO₃ and (Ba, P_d)TiO₃. *J. Am. Ceram. Soc.* **71**(12) (1988) C482–3.
- Herbert, J. M., Positive temperature coefficient (PTC) resistors. In *Ferroelectric Transducers and Sensors*, Gordon and Breach Science Publishers Ltd., London, 1982, pp. 157.

Powder Preparation, Mechanical and Electrical Properties of Cubic Zirconia Ceramics

I. Ábrahám & G. Gritzner*

Institut für Chemische Technologie Anorganischer Stoffe, Johannes Kepler Universität, A-4040 Linz, Austria

(Received 2 September 1993; revised version received 9 January 1995; accepted 15 June 1995)

Abstract

Cubic zirconia ceramics, doped either with 8 mol% Y_2O_3 or with 12 mol% MgO and CaO, were prepared from precursor material obtained via co-precipitation with ammonia from aqueous metal chloride solutions. Precipitation experiments with and without the addition of surfactant were carried out. Different methods of drying were employed followed by calcination and attrition steps to obtain oxidic precursors. The powders were characterized by particle size distribution, scanning electron microscopy and specific surface areas. Following isostatic compaction the oxide powders were sintered at 1600 and 1700°C for 4 h. The effects of the powder characteristics and the drying procedures on the mechanical properties of the sintered bodies were investigated.

1 Introduction

Pure zirconia is known to have three polymorphs under atmospheric pressure, with monoclinic, tetragonal and cubic symmetry. The cubic and tetragonal forms are unstable at room temperature. The temperature range of the stability of these phases, however, can be lowered by doping zirconia with other oxides, such as Y_2O_3 , CaO or MgO.^{1–3} The content of the dopants determines whether the tetragonal or the cubic phase will be stabilized.

Cubic zirconia doped either with Y_2O_3 , MgO or CaO is found to have a rather low bend strength.^{4,6} The mechanical properties of the sintered ceramics, however, depend strongly on the powder characteristics, such as particle size and particle size distribution, and on the morphology as well as agglomeration of the starting oxides⁷ and on the thermal treatment.⁸ Different ways to

co-precipitate doped amorphous hydroxide precursors, various drying procedures as well as attrition milling of the calcined oxides have been investigated in this study to learn about the effects of the powder characteristics and sintering procedures on the mechanical properties of cubic zirconia.

Zirconia with fluorite structure exhibits considerable electrical conductivity at elevated temperatures^{9–15} due to the migration of oxygen vacancies introduced by the stabilizers. The specific conductivities and the temperature dependences of the conductivities will be reported.

2 Experimental Procedure

2.1 Sample preparation

Aqueous solutions of $ZrOCl_2 \cdot 8H_2O$ (Merck, Germany) (0.2 mol dm^{-3}) containing the appropriate amounts of $Y(NO_3)_3 \cdot 5H_2O$, $MgCl_2 \cdot 6H_2O$ and $CaCl_2 \cdot 2H_2O$ (all from Merck) were prepared. In some experiments sodium laurylsulfate (0.05 g dm^{-3}) was added to both the metal salt solutions and to the aqueous ammonia. The co-precipitation process was carried out by spraying the aqueous metal salt solutions into vigorously stirred concentrated ammonia solutions. The pH was kept above 10 during the precipitation by adding excess amounts of ammonia solution. Stirring was continued for 1 h after spraying was completed. The co-precipitated hydroxides were then filtered and washed with distilled water until no Cl^- ion was present in the filtrate. Further powder treatments were carried out as follows: (i) hydroxides prepared in the presence of sodium laurylsulfate were either spray dried or washed with ethanol and dried at 100°C in air, (ii) hydroxides made by co-precipitation without adding sodium laurylsulfate were washed with ethanol and dried at 100°C in air. All hydroxides were calcined at 750°C for 2 h. The spray-dried hydroxides were used as

*To whom correspondence should be addressed.

obtained from the calcination. The calcined oxide powders from the other preparation techniques were attrited in 1-propanol for 4 h with zirconia balls (2 mm diameter, 1000 min⁻¹).

Pellets (10 mm diameter × 4 mm height) and blocks (25 × 20 × 40 mm) were compacted isostatically at 70 MPa. The blocks for bend strength measurements were presintered at 1000°C for 1 h and cut to a geometry of 4 × 5 × 30 mm. The specimens were then sintered at 1600°C and 1700°C, respectively, for 4 h. The heating rate was 5°C min⁻¹ until 1200°C and 3°C min⁻¹ up to the final sintering temperature. The sintered bodies were then ground to the respective dimensions and diamond polished to a 3 μm finish on the tensile surface. The edges of the tensile surfaces were chamfered. Density, three-point bend strengths, Vickers hardness and fracture toughness were measured from the ceramic specimens. Etching was performed in potassium hydrogensulfate melts at 250°C for 10 min.

2.2 Characterization

The doped zirconia powders were investigated by X-ray diffraction (Rigaku D/max IIA, Japan) for the phase content. The particle sizes and particle size distributions were determined by a laser particle sizer (Coulter LS 130, USA), the specific surfaces were measured by BET on a Quantasorb system (Quantachrome, USA). The densities of the sintered specimens were measured by the means of Archimedes' principle in iso-octane (2,2,4-trimethylpentane). Theoretical densities were calculated following the theory of Ingel and Lewis¹⁶ from the lattice parameters.^{6,17,18} The Vickers hardness and fracture toughness were tested on the polished surfaces using a Vickers diamond indenter with a load (*P*) of 100 N. The K_{Ic} values were calculated as: $K_{Ic} = 0.0824 P c^{-3/2}$.¹⁹⁻²¹ Three-point bend strengths were measured on 3 × 4 × 30 mm specimens with 20 mm span width, using six to 10 bars for each composition and sintering temperature. The load was increased by 12 N s⁻¹. Scanning electron micrographs of the specimen were made on a JEOL-JSM-T300A electron microscope (Jeol, Japan). Light microscopy studies were made on a Neovar-Pol microscope (Reichert, Austria). Grain sizes of the sintered bodies were obtained from the intercept technique. The crystallite sizes were calculated from the BET specific surface areas according to the formula:

$d = 6 (\rho A_s)^{-1}$ (where *d* is crystallite size, *A_s* specific surface area and ρ theoretical density of the oxide). The electrical conductivities were measured by the d.c. four-probe technique between 380 and 1080°C. Contacts were made with platinum paint.

3 Results

3.1 X-ray diffraction

The dried hydroxide powders were amorphous according to X-ray diffraction; the calcined powders and the sintered bodies showed only the peaks of the cubic phase (Fig. 1). There was no observable phase transformation due to surface treatment (polishing) or upon fracture.

3.2 Powder characteristics

The average particle sizes, the specific surface areas and the calculated crystallite sizes are sum-

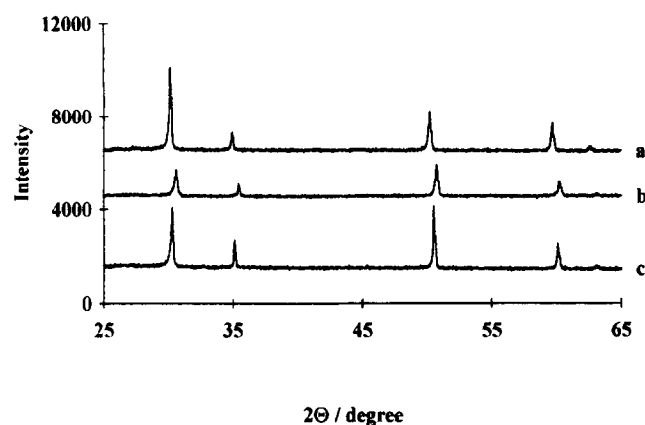


Fig. 1. X-ray diffraction of cubic zirconias sintered at 1700°C; (a) doped with 8 mol% Y₂O₃; (b) doped with 12 mol% MgO; (c) doped with 12 mol% CaO.

Table 1. Average particle sizes and specific surface areas of co-precipitated and calcined doped cubic zirconia powders^a

Sample	Average particle size (vol. stat.) (μm)	Average particle size (number. st.) (μm)	Specific surface area (m ² g ⁻¹)	Average crystallite size ^b (nm)
8Y ^c	19.5	1.85	—	—
8Y ^d	12.5	0.18	42.4	23.8
8Y ^e	2.0	0.18	49.9	20.2
8Y ^f	1.9	0.21	39.4	25.6
8Y ^g	0.7	0.17	48.2	20.9
12Mg ^c	26.6	2.83	—	—
12Mg ^d	8.9	0.19	26.8	37.4
12Mg ^e	8.6	0.18	46.5	21.6
12Mg ^f	2.8	0.24	30.8	32.6
12Mg ^g	0.6	0.16	45.5	22.0
12Ca ^c	24.1	1.95	—	—
12Ca ^d	7.5	0.18	43.7	23.2
12Ca ^e	5.1	0.18	26.9	37.6
12Ca ^f	1.9	0.24	39.0	26.0
12Ca ^g	0.7	0.17	53.8	18.8

^a8Y: doped with 8 mol% Y₂O₃, 12Mg: doped with 12 mol% MgO, 12Ca: doped with 12 mol% CaO.

^bCalculated from the specific surface area.

^cCo-precipitated without sodium laurylsulphate and calcined.

^dCo-precipitated with sodium laurylsulphate and calcined.

^eCo-precipitated with sodium laurylsulphate, spray dried and calcined.

^fCo-precipitated without sodium laurylsulphate, calcined and attrited.

^gCo-precipitated with sodium laurylsulphate, calcined and attrited.

marized in Table 1. The particle size distributions are shown in Figs 2–4. Precipitation without sodium laurylsulfate followed by calcination resulted in strongly agglomerated powders with average particle sizes of about 20–26 μm . Adding sodium laurylsulfate to the co-precipitation process yielded particle sizes around 7–13 μm . Spray drying of the co-precipitated hydroxides led to a reduction in the particle sizes, but hard agglomerates were subsequently formed during the calcination process. These hard agglomerates prevented proper densification during the sintering process. The spray-dried and calcined powders consisted of dense spheres of 2–5 μm diameter as shown in Fig. 5. All calcined powders with the exception of the spray-dried samples were attrited, leading to considerably smaller particle sizes. The attrited powders were rather homogeneous in particle size distribution as shown in Figs 6 and 7. The particles consisted of prime crystallites with diameters below 50 nm (Fig. 7) in agreement with crystallite diameters calculated from the specific surface areas (Table 1).

3.3 Density and grain size

Densities of the sintered bodies are summarized in Table 2. The relative densities of the specimens

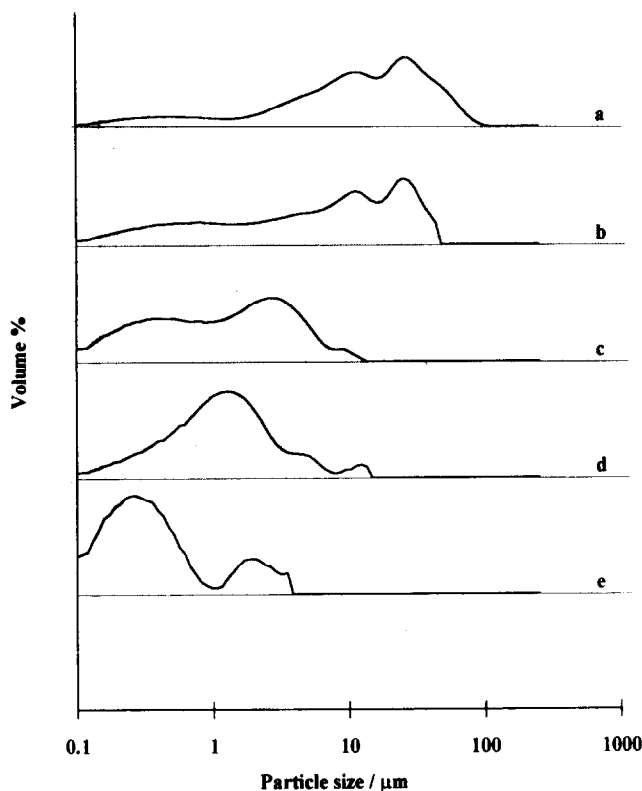


Fig. 2. Particle size distribution of zirconia powders doped with 8 mol% Y_2O_3 : (a) co-precipitated without sodium laurylsulphate and calcined; (b) co-precipitated with sodium laurylsulphate and calcined; (c) co-precipitated with sodium laurylsulphate, spray dried and calcined; (d) co-precipitated without sodium laurylsulphate, calcined and attrited; (e) co-precipitated with sodium laurylsulphate, calcined and attrited.

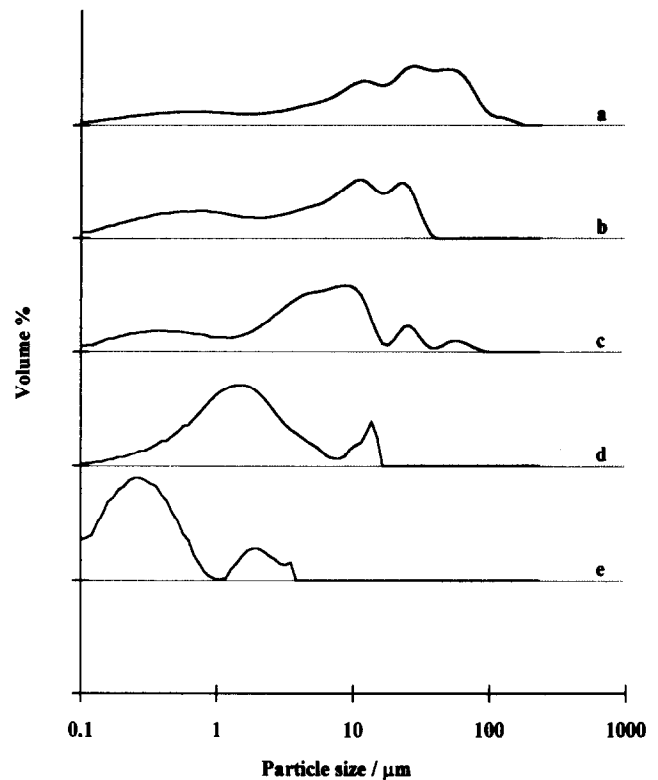


Fig. 3. Particle size distribution of zirconia powders doped with 12 mol% MgO : (a) co-precipitated without sodium laurylsulphate and calcined; (b) co-precipitated with sodium laurylsulphate and calcined; (c) co-precipitated with sodium laurylsulphate, spray dried and calcined; (d) co-precipitated without sodium laurylsulphate, calcined and attrited; (e) co-precipitated with sodium laurylsulphate, calcined and attrited.

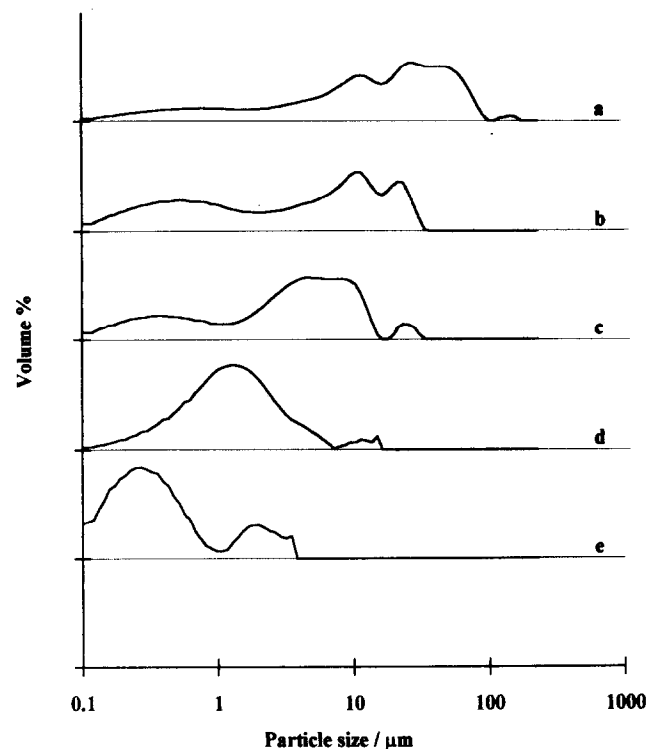


Fig. 4. Particle size distribution of zirconia powders doped with 12 mol% CaO : (a) co-precipitated without sodium laurylsulphate and calcined; (b) co-precipitated with sodium laurylsulphate and calcined; (c) co-precipitated with sodium laurylsulphate, spray dried and calcined; (d) co-precipitated without sodium laurylsulphate, calcined and attrited; (e) co-precipitated with sodium laurylsulphate, calcined and attrited.

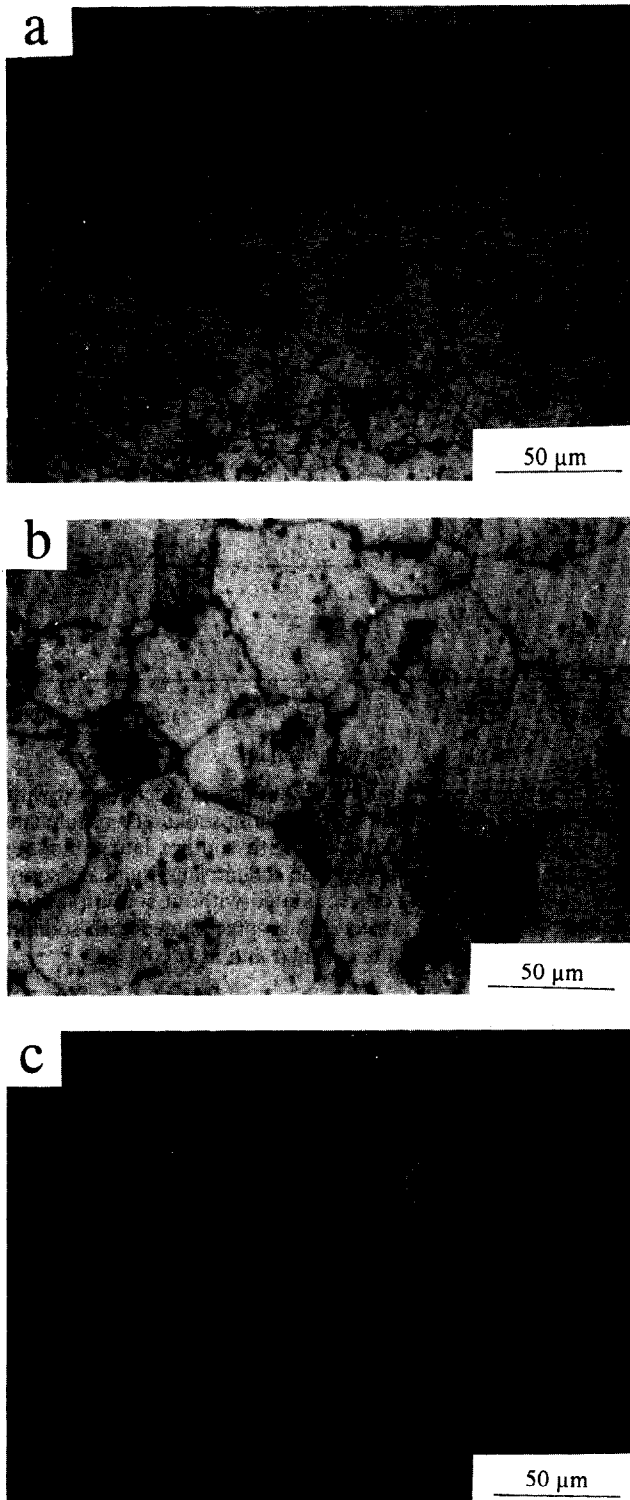


Fig. 5. Scanning electron micrographs of the calcined oxides from spray-dried hydroxides co-precipitated in the presence of sodium laurylsulphate. Magnification: 10 000 \times . (a) Doped with 8 mol% Y_2O_3 ; (b) doped with 12 mol% MgO ; (c) doped with 12 mol% CaO .

prepared from the attrited powders and sintered at 1600°C were >96% and reached 97–99% for specimens sintered at 1700°C. The densification process for bodies made from the spray-dried powders yielded relative densities <90%. These rather low values are due to the poor sinterability of the hard agglomerates formed during the calci-

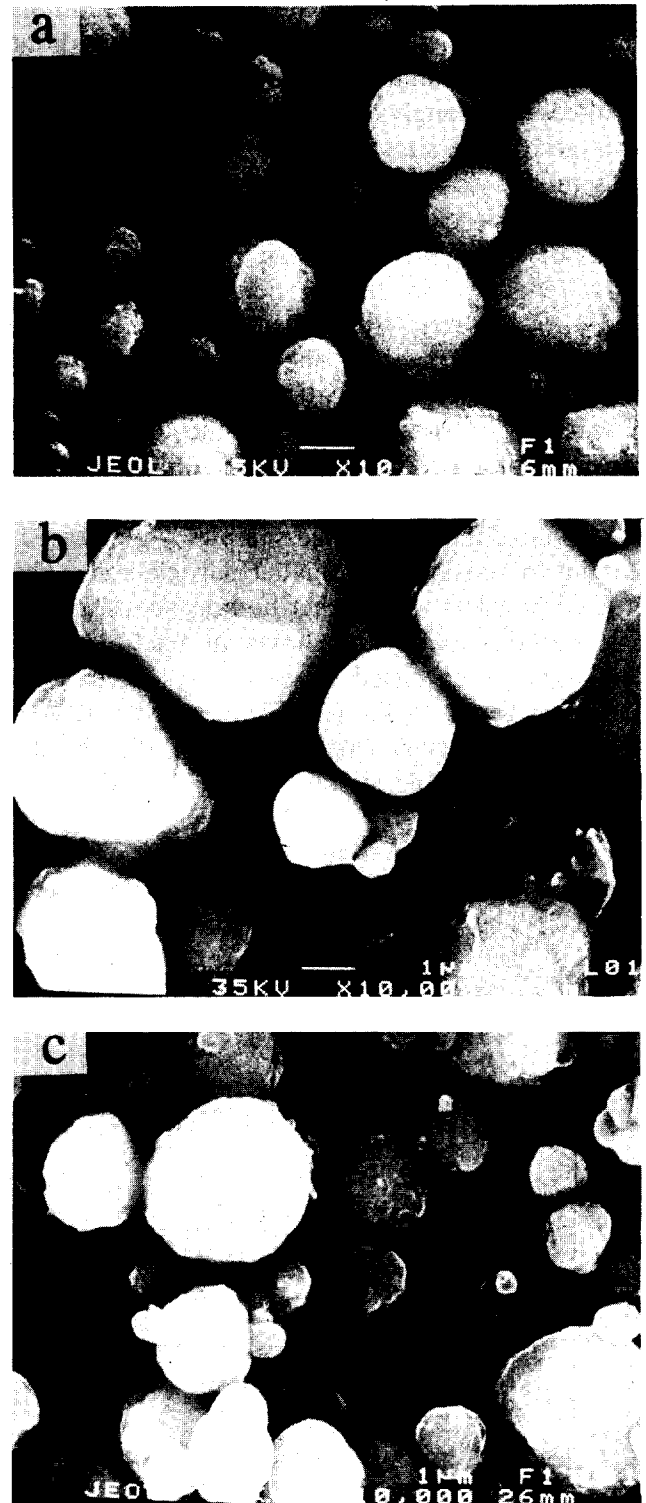


Fig. 6. Scanning electron micrographs of the calcined and attrited oxides from hydroxides co-precipitated without sodium laurylsulphate. Magnification: 20 000 \times . (a) Doped with 8 mol% Y_2O_3 ; (b) doped with 12 mol% MgO ; (c) doped with 12 mol% CaO .

nation, which were not destroyed during compaction.

Considerable grain growth was experienced during sintering. Yttria-doped zirconia sintered at 1700°C exhibited grain sizes of about 20 to 25 μm , magnesia- and calcia-doped bodies gave grain sizes of 30 to 40 μm (Fig. 8).

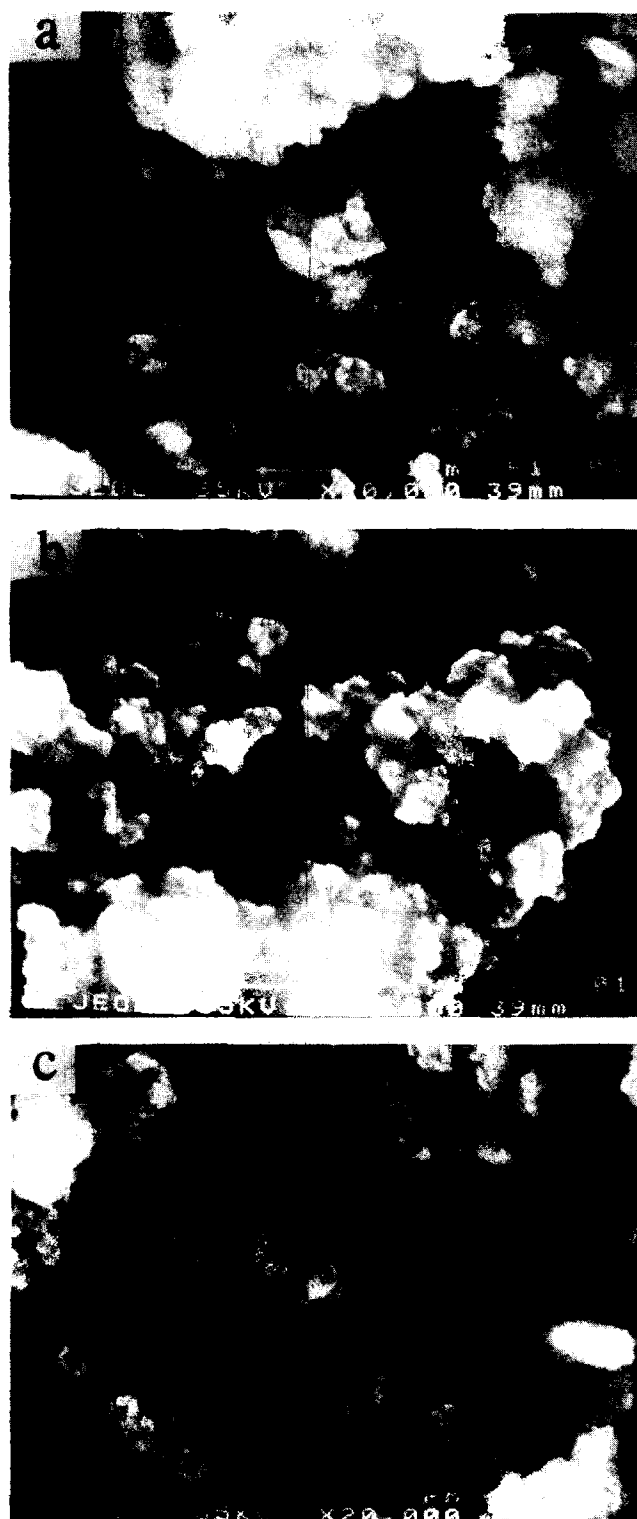


Fig. 7. Scanning electron micrographs of the calcined and attrited oxides from hydroxides co-precipitated in the presence of sodium laurylsulphate. Magnification: 30 000 \times . (a) Doped with 8 mol% Y_2O_3 ; (b) doped with 12 mol% MgO ; (c) doped with 12 mol% CaO .

3.4 Vickers hardnesses and K_{Ic} values

The application of surface-active material during co-precipitation followed by attrition of the calcined powders increased the Vickers hardnesses of the ceramics significantly (Table 2). The hardnesses reached 18.1 GPa for the yttria-, 16.2 GPa for the magnesia- and 15.8 GPa for the calcia-

Table 2. Densities, relative densities and Vickers hardnesses and K_{Ic} values of doped, cubic zirconia ceramics^a

Sample	Sintering temp. ($^{\circ}C$)	Density ($g\ cm^{-3}$)	Relative density (%) ^b	Vickers hardness (GPa)	K_{Ic} ($MPa\ m^{1/2}$)
8Y ^c	1600	5.74	96	9.4	2.4
8Y ^d	1600	5.29	89	3.3	1.8
8Y ^e	1600	5.73	96	17.6	2.6
8Y ^f	1600	5.19	87	7.8	2.3
8Y ^c	1700	5.73	96	9.2	3.1
8Y ^d	1700	5.33	90	3.8	2.1
8Y ^e	1700	5.75	97	18.1	2.9
8Y ^f	1700	5.36	90	9.8	2.4
12Mg ^c	1600	5.67	98	12.6	3.9
12Mg ^d	1600	5.18	89	5.0	2.5
12Mg ^e	1600	5.75	99	16.5	4.3
12Mg ^f	1600	5.10	88	5.6	2.5
12Mg ^c	1700	5.67	98	13.7	4.2
12Mg ^d	1700	5.27	91	8.9	2.6
12Mg ^e	1700	5.75	99	16.2	4.4
12Mg ^f	1700	5.17	89	7.1	2.4
12Ca ^c	1600	5.61	98	8.5	2.5
12Ca ^d	1600	5.51	96	11.3	2.4
12Ca ^e	1600	5.69	99	15.8	4.5
12Ca ^f	1600	5.15	90	5.2	2.2
12Ca ^c	1700	5.62	98	9.6	3.5
12Ca ^d	1700	5.56	97	12.4	3.1
12Ca ^e	1700	5.72	99	15.8	4.5
12Ca ^f	1700	5.16	90	7.0	2.3

^a8Y: doped with 8 mol% Y_2O_3 , 12Mg: doped with 12 mol% MgO , 12Ca: doped with 12 mol% CaO .

^bPercentage of the theoretical density, the latter calculated by the theory of Ingel and Lewis¹⁸ from the lattice parameters.^{5,19,20}

^cCo-precipitated without sodium laurylsulphate, calcined and attrited.

^dCo-precipitated with sodium laurylsulphate and calcined.

^eCo-precipitated with sodium laurylsulphate, calcined and attrited.

^fCo-precipitated with sodium laurylsulphate, spray dried and calcined.

stabilized specimen sintered at 1700 $^{\circ}C$. The fracture toughnesses of the ceramics also improved when attrited powders were used as precursor material.

3.5 Strength

The measured three-point bend strengths with standard deviations, the Weibull moduli and the grain sizes are given in Table 3. Samples prepared from attrited precursor material obtained from co-precipitation with addition of laurylsulfate showed an increase in bend strength from 63 to 91 MPa for yttria-stabilized, from 71 to 98 MPa for the magnesia-stabilized and from 60 to 75 MPa for the calcia stabilized cubic zirconias sintered at 1700 $^{\circ}C$ compared with samples precipitated without surface-active substances.

3.6 Conductivity

The electrical conductivities at 1000 $^{\circ}C$ of the ceramics prepared from hydroxides co-precipitated with sodium laurylsulfate were measured to be 0.12, 0.072 and 0.032 $S\ cm^{-1}$ for the yttria-,

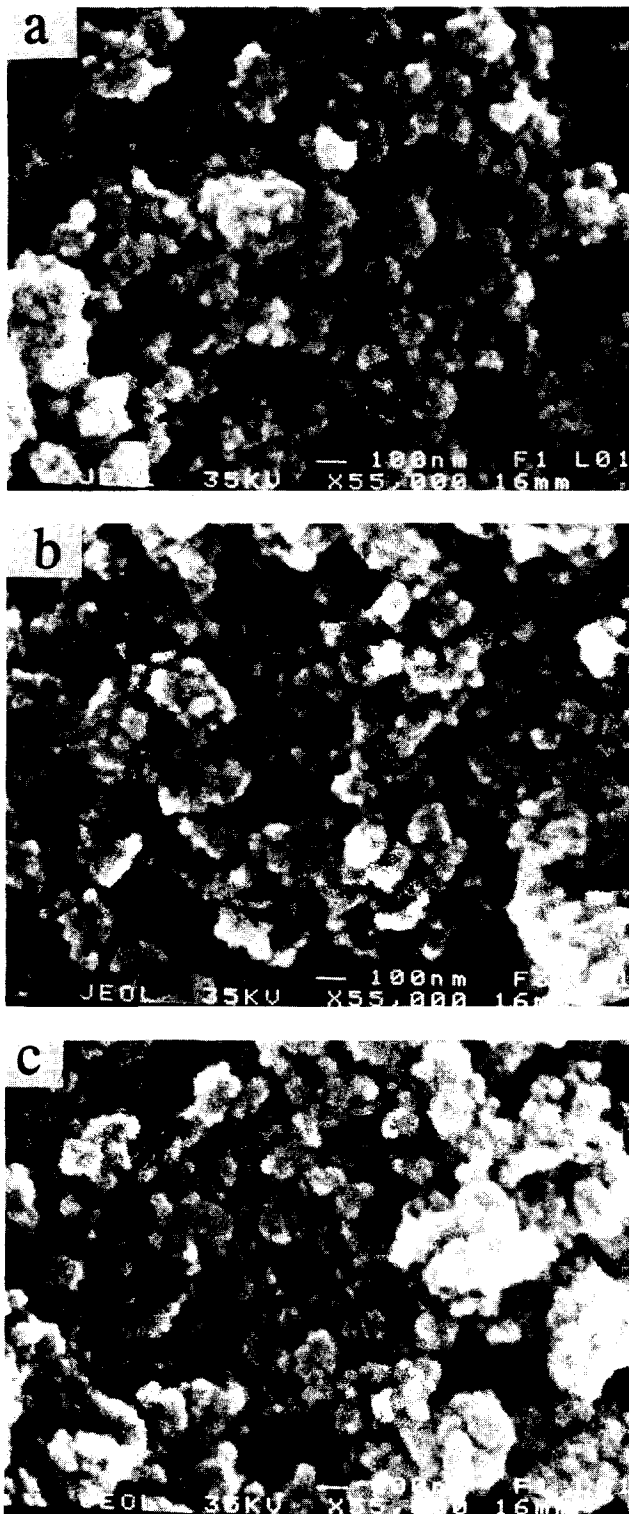


Fig. 8. Optical micrographs of the polished and etched surfaces of ceramics sintered at 1700°C. Magnification 400×. (a) Doped with 8 mol% Y_2O_3 ; (b) doped with 12 mol% MgO; (c) doped with 12 mol% CaO.

magnesia- and calcia-doped samples, respectively. The temperature dependences of the total ionic conductivities of the doped samples are shown in Fig. 9 as Arrhenius plots. Literature data for cubic zirconia doped with 8 mol% yttria at 1000°C vary between 0.036 and 0.13 $S\ cm^{-1}$ (Ref. 9) and 0.16 $S\ cm^{-1}$.^{10,11} Values between 0.16 and 0.19 $S\ cm^{-1}$ have been measured for tapes by a two-point

Table 3. Three-point bend strengths and Weibull moduli of doped cubic zirconia ceramics^a

Sample	Sintering temp. (°C)	Three-point bend strength (MPa)	Standard deviation (MPa)	Weibull modulus, m	Grain size (μm)
8Y ^b	1600	60	12	4.0	24
8Y ^b	1700	63	9	7.0	26
8Y ^c	1600	82	12	3.7	16
8Y ^c	1700	91	17	2.9	20
12Mg ^b	1600	55	8	6.5	14
12Mg ^b	1700	71	14	4.5	28
12Mg ^c	1600	89	5	11.7	28
12Mg ^c	1700	98	15	5.2	41
12Ca ^b	1600	61	15	3.7	29
12Ca ^b	1700	60	11	5.1	35
12Ca ^c	1600	74	12	5.7	33
12Ca ^c	1700	75	12	3.6	40

^a8Y: doped with 8 mol% Y_2O_3 , 12Mg: doped with 12 mol% MgO, 12Ca: doped with 12 mol% CaO.

^bCo-precipitated without sodium laurylsulphate, calcined and attrited.

^cCo-precipitated with sodium laurylsulphate, calcined and attrited.

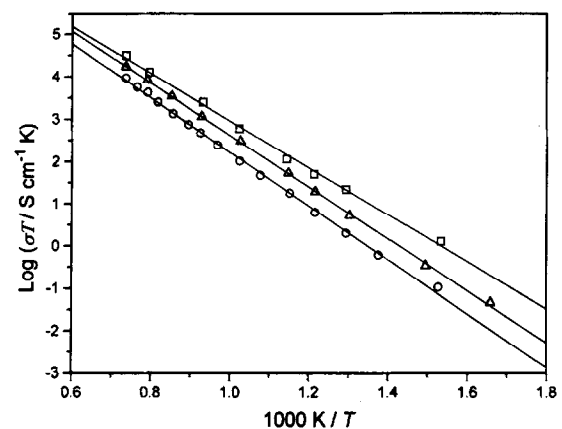


Fig. 9. $\text{Log}(\sigma T)$ versus $1/T$ plots for the conductivities (σ) of doped cubic zirconia: \square , doped with 8 mol% Y_2O_3 ; Δ , doped with 12 mol% MgO; \circ , doped with 12 mol% CaO.

a.c. technique.¹² Measurements on commercially available yttria-doped zirconias yielded specific conductivities of between 0.09 and 0.125 $S\ cm^{-1}$.¹³ The conductivities measured by us compare well with the data reported in literature. The specific conductivities of our yttria-doped samples decreased to about 0.09 $S\ cm^{-1}$ upon annealing at 1000°C for 30 days. Decreases in the conductivities of yttria-doped zirconias have been reported recently.^{11,13} The specific conductivities at 1000°C for zirconia doped with 12 mol% calcia have been reviewed.^{9,15} The published values ranged between 0.004 and 0.067 $S\ cm^{-1}$.

4 Conclusions

The mechanical properties of the sintered bodies depended strongly on the wet-chemical prepara-

tion techniques, the drying procedures and the attrition of the oxidic precursors. Spraying aqueous solutions of the respective metal chlorides into aqueous ammonia resulted in prime crystallites with diameters below 50 nm. These crystallites aggregated during the precipitation step to particles several μm in size. The particle sizes after calcination were affected by both the addition of surfactant during the co-precipitation process and the drying procedure. Addition of the surfactant during the precipitation step yielded soft agglomerates which broke during the attrition step. The best mechanical properties and the highest relative densities (96–99%) were obtained for powders co-precipitated with addition of surfactant, which were attrited after calcination; the worst properties were obtained for powders which were not subjected to attrition. Spray drying of the hydroxides yielded hard, spherical particles with poor densification behaviour, yielding sintered bodies with relative densities below <90%.

Acknowledgements

Financial support by the Jubiläumsfonds der österreichischen Nationalbank is gratefully appreciated. The authors thank Dipl. Ing. M. Ratajski for the electron micrographs and Mr K. Kellner for X-ray diffraction and electrical measurements. One of us (I.A.) thanks the State of Upper Austria for a scholarship.

References

- Subbarao, E. C., in *Advances in Ceramics, Vol. 3, Science and Technology of Zirconia*, eds A. H. Heuer & L. W. Hobbs, American Ceramic Society, Columbus, Ohio, 1981, p. 9.
- Stubican, V. S. & Hellmann, J. R., in *Advances in Ceramics, Vol. 3, Science and Technology of Zirconia*, eds A. H. Heuer and L. W. Hobbs, American Ceramic Society, Columbus, Ohio, 1981, p. 25.
- Grain, C. F., Phase relation in the $\text{ZrO}_2\text{-MgO}$ system. *J. Am. Ceram. Soc.*, **50** (1967) 288.
- Jue, J.-F. & Virkar, A. V., Fabrication microstructural characterization and mechanical properties of polycrystalline t'-zirconia. *J. Am. Ceram. Soc.*, **73** (1990) 3650.
- Swain, M. V., Garvie, R. C. & Hannink, R. H. J., Influence of thermal decomposition on the mechanical properties of magnesia stabilized cubic zirconia. *J. Am. Ceram. Soc.*, **66** (1983) 358.
- Abraham, I. & Gritzner, G., Mechanical properties of doped cubic zirconia ceramics. *J. Mater. Sci. Lett.*, **12** (1993) 995.
- Shi, J.-L., Gao, J.-H., Lin, Z.-X. & Yen, T.-S., Sintering behaviour of fully agglomerated zirconia compacts. *J. Am. Ceram. Soc.*, **74** (1991) 994.
- Kim, D.-H. & Kim, C. H., Entrapped gas effect in the fast firing of yttria-doped zirconia. *J. Am. Ceram. Soc.*, **75** (1992) 716.
- Etsell, H. & Flengas, S.N., The electrical properties of solid oxide electrolytes. *Chem. Rev.*, **70** (1970) 339.
- Yamamoto, O., Takeda, Y., Kanno, R., Kohno, K. & Kamiharai, T., Electrical conductivity of polycrystalline tetragonal zirconia $\text{ZrO}_2\text{-M}_2\text{O}_3$. *J. Mater. Sci. Lett.*, **8** (1989) 198.
- Ciacchi, F. T & Badwal, P. S., The system $\text{Y}_2\text{O}_3\text{-Sc}_2\text{O}_3\text{-ZrO}_2$: phase stability and ionic conductivity studies. *J. Eur. Ceram. Soc.*, **7** (1991) 197.
- Raeder, H., Simon, C., Charties, T. & Toftegaard, H. L., Tape casting of zirconia for ion conducting membranes: a study of dispersants. *J. Eur. Ceram. Soc.*, **13** (1994) 485.
- Raeder, H., Norby, T. & Osborg, P. E., Ageing of yttria stabilized zirconia electrolytes at 1000°C. in *Ceramic Processing Science and Technology*, eds H. Hauser, G. L. Messing & S.-I. Hirano, *Ceramic Transactions*, Vol. 51, American Ceramic Society, Westerville, Ohio, 1995, p. 719.
- Rothman, S. J., Nowicki, L. J., Aldred, A. T. & Dees, D. W., Ion conductivity and crystal structure in zirconia-thorium oxide-yttrium oxide mixtures. *Adv. Ceram. Mater.*, **3** (1988) 143.
- Tien, Y. & Subbarao, E. C., X-ray and electrical conductivity study of the fluorite phase in the system $\text{ZrO}_2\text{-CaO}$. *J. Chem. Phys.*, **39** (1963) 1041.
- Ingel, P. & Lewis, III D., Lattice parameters and density for Y_2O_3 -stabilized ZrO_2 . *J. Am. Ceram. Soc.*, **69** (1986) 325.
- Yashima, M., Ishizawa, N. & Yoshimura, M., Application of an ion-packing model based on defect clusters to zirconia solid solutions: I. Modeling and local structure of solid solutions. *J. Am. Ceram. Soc.*, **75** (1992) 1541.
- Yashima, M., Ishizawa, N. & Yoshimura, M., Application of an ion-packing model based on defect clusters to zirconia solid solutions: II. Applicability of Vegard's law. *J. Am. Ceram. Soc.*, **75** (1992) 1550.
- Ponton, C. B. & Rawlings, R. D., Vickers indentation fracture toughness test Part I. Review of literature and formulation of standardized toughness equations. *Mater. Sci. Technol.*, **5** (1989) 865.
- Evans, A. G. & Charles, E. A., Fracture toughness determination by indentation. *J. Am. Ceram. Soc.*, **59** (1976) 371.
- Niihara, K., Morena, R. & Hasselman, D. P. H., Evaluation of K_{Ic} of brittle solids by the indentation method with low crack-to-indent ratios. *J. Mater. Sci. Lett.*, **1** (1982) 13.

Preparation of Ca- β'' -Al₂O₃ from Alumina Gel

Mirosław M. Bućko & Maria Cichocińska

Faculty of Material Science and Ceramics, University of Mining and Metallurgy, Al. Mickiewicza 30, Cracow, Poland

(Received 26 July 1994; accepted 25 May 1995)

Abstract

Using aluminium nitrate solution containing calcium and magnesium cations, and saturated ammonium oxalate solution in concentrated ammonium hydroxide as precipitating agent, alumina gel was prepared. The gel was calcined at different heating rates up to 400°C and then at different temperatures and soaking times. The calcination products successively appeared as aluminium oxides, calcium aluminate and calcium-beta''-alumina. The obtained calcium-beta''-alumina crystallites were plate-shaped and the direction perpendicular to the crystallite surface was parallel to the Z-axis. It was found that the kinetics of calcium-beta''-alumina synthesis depends on the presence of a molten salt during the gel thermal treatment. The mechanism of calcium-beta''-alumina formation is proposed as a reaction between formerly produced calcium aluminate and aluminium oxide of the alpha form. Sintered bodies prepared from the calcium-beta''-alumina powder were characterized by good ionic conductivity.

1 Introduction

For many years, compositions containing β - and β'' -alumina have aroused interest as ionic conductors.^{1,2} They are potential materials for batteries,³ sensors,⁴ electrochemical probes⁵ and for investigation of thermodynamic data in oxide systems.⁶ There are several preparation routes that allow β - and β'' -alumina powders, sintered bodies and monocrystals to be obtained. In the case of β -aluminas containing monovalent cations, direct high-temperature synthesis, often followed by sintering of the resulting powder, is the simplest way leading to the polycrystalline material. The precursors usually applied in such a case are sodium and lithium carbonate, aluminium oxides of the α - or γ -form^{7,8} as well as bayerite, gibbsite or boehmite.⁹ The zeta-process is a type of direct synthesis in which compositions of formula M₂O·5Al₂O₃ (where M = Na and/or Li) are used as a precursor.

Thermal decomposition of the appropriate nitrate mixtures is also a useful process.¹¹ It has recently been found that the sol-gel technique gives good results in the preparation of β -alumina fine powders,^{12–14} thin films and coatings.¹⁵

To prepare β'' -Al₂O₃ containing ions of a higher valence state, the sodium ions in Na- β'' -Al₂O₃ can be exchanged for di- or trivalent ions.¹⁶ It is also possible to use the direct, high-temperature reaction of aluminium oxide, calcium and magnesium carbonates.^{17,18}

It has been found that β'' -aluminas containing divalent cations transform at elevated temperatures to the magnetoplumbite structure, which shows no ionic conductivity.¹⁹ This has been found from ionic conductivity measurements in relation to the thermal history of samples²⁰ and X-ray diffraction studies.²¹ The mechanism of the β'' -Al₂O₃ to magnetoplumbite structure transformation is not explained as well as the conditions under which this transformation takes place. According to Schaefer and Weppner²² it occurs at a temperature of ~1400°C during 20 h soaking, whereas Kirchnerova *et al.*²¹ state that it can be observed at temperatures >1000°C. These facts suggest that only low-temperature synthesis of the divalent β'' -aluminas can be applied. The above-mentioned ion exchange technique cannot secure the proper microstructure of the material, since changes in the microstructure and grain habit have been reported²² to occur during the ion exchange process.

The aim of the present work was to study the preparation of magnesium-stabilized calcium-beta''-alumina ceramics using aluminium hydroxide gel as a precursor.

2 Experimental

1.2 M aluminium nitrate solution was used. The proper amounts of calcium and magnesium carbonates were added to this solution. The molar ratio of the components was 6:1:0.6, as recalculated

to aluminium, calcium and magnesium oxides, respectively. Saturated ammonium oxalate solution in concentrated (~26 wt%) ammonium hydroxide was applied as the precipitating agent. It was found that the concentration of the saturated ammonium oxalate in the concentrated ammonium hydroxide is about 0.06 mol l^{-1} . Such a solution secures the quantitative precipitation of calcium oxalate. Also, the concentration of the hydroxide ions secures the quantitative precipitation of magnesium hydroxide. Chemical analysis corroborates these statements.

The Al–Ca–Mg nitrate solution was introduced slowly into the vigorously stirred precipitating solution; the amount added was a 10% excess, based on the stoichiometric proportion. The precipitated slurry was filtered off and the filtrate subjected to chemical analysis. The precipitated gel was dried at 70°C and calcined at temperatures up to 400°C . Two heating rates were applied: 1 and $10^\circ\text{C min}^{-1}$. During this operation the total decomposition of ammonium nitrate takes place. Powders prepared by the described procedure were examined by scanning electron microscopy (SEM) and by differential thermal analysis (DTA) using a heating rate of 6°C min^{-1} at temperatures $>400^\circ\text{C}$. Changes of the powder morphology and phase composition during calcination at $1000\text{--}1350^\circ\text{C}$ for a soaking time of at least 1 h were followed by transmission electron microscopy and X-ray diffraction.

On the basis of the results obtained, conditions for the preparation of a larger quantity of the pure β'' -alumina phase powder were determined. The precipitated gel was filtered, dried, heated at the rate of 1°C min^{-1} up to 400°C and then calcined at 1350°C for 3 h. The obtained powder was ground for 12 h in dry acetone using zirconia grinding media and a rotary-vibratory mill. After milling the powder was dried at 70°C and isostatically pressed under 350 MPa, and then sintered at 1550°C for 2 h. The four-probe a.c. and impedance spectroscopy methods were used to determine the electrical properties of the sintered bodies. The impedance spectra were recorded using a system based on the Tesla 508 impedance meter, with platinum electrodes sputtered on two faces of the pellets. The preparation routes of the calcium-beta"-alumina powders and sintered bodies are presented in Fig. 1.

3 Results and Discussion

The X-ray diffraction patterns of the dried gels show the peaks of ammonium nitrate and a wide increase of the background characteristic for

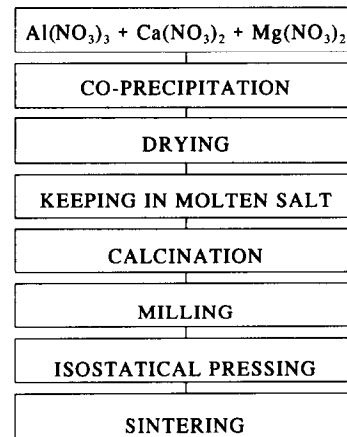


Fig. 1. Preparation routes.

amorphous material. No peaks of calcium oxalate and magnesium hydroxide were detected. It follows from the diffraction patterns (Fig. 2) that during heating the following calcination products successively appear: calcium aluminate $\text{CaO}\cdot 2\text{Al}_2\text{O}_3$, γ -, θ - and α -aluminium oxides, and calcium-beta"-alumina.²³ The DTA curves show the ammonium nitrate decomposition and an endothermic peak at $\sim 400^\circ\text{C}$ that can be attributed to the decomposition of aluminium hydroxide. There are two probable reasons why calcium oxalate and magnesium hydroxide were not detected. The first is the small percentage by weight of these substances and the second is the formation of other compounds by the calcium and magnesium, not simply oxalate and hydroxide. This later phenomenon was often found in co-precipitated materials.

The rate of temperature increase up to 400°C strongly influenced the amount of $\text{Ca}\cdot\beta''\text{-Al}_2\text{O}_3$ produced during further heating. Comparison of the diffraction patterns of powders heated at various rates up to 400°C and then calcined at 1300°C

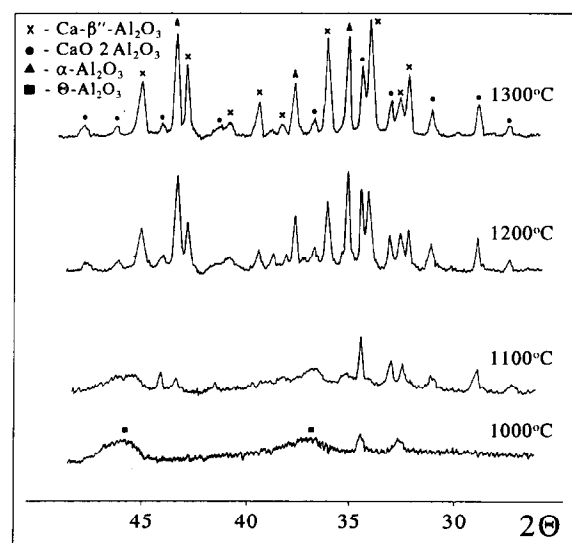


Fig. 2. Diffraction patterns of the powders calcined for 1 h at different temperatures.

for 1 h shows an increased amount of β'' -phase in the material heated at a slower rate. Rapid heating leads to the violent reaction yielding brown nitrogen oxide vapour. During the slow temperature increase, this salt melts at $\sim 180^\circ\text{C}$ and then decomposes at $\sim 230^\circ\text{C}$. It was found that the co-precipitated gel subjected to prolonged heating at 200°C under cover also results in a higher Ca- β'' -Al₂O₃ phase content in the product calcined at 1300°C than observed without this operation.

SEM studies of the powder morphology, after total removal of ammonium nitrate, revealed that both powders (i.e. heated at different rates) are composed of $\sim 0.2\ \mu\text{m}$ grains linked to each other. However, in the powder heated at $1^\circ\text{C}\ \text{min}^{-1}$ these grains are linked more closely than in the rapidly heated sample. This is illustrated by the microphotographs presented in Fig. 3. This difference in powder morphology and phase composition can most probably be attributed to the way in which the ammonium nitrate decomposition takes place. It cannot be excluded that products of the precipitation partially dissolve in the molten salt. This may lead to better homogeneity of calcium and magnesium in the alumina gel. Rapid heating does not allow the liquid phase long enough to act on the co-precipitate. It was also found that differences in the phase composition of the powders

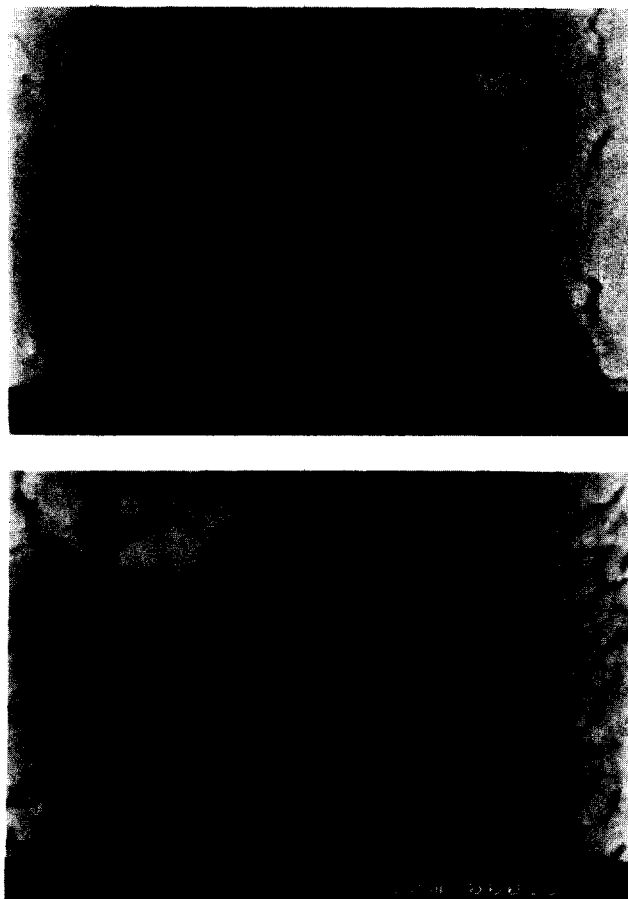


Fig. 3. SEM pictures of the powders heated to 400°C at different rates: (a) $1^\circ\text{C}\ \text{min}^{-1}$ and (b) $10^\circ\text{C}\ \text{min}^{-1}$.

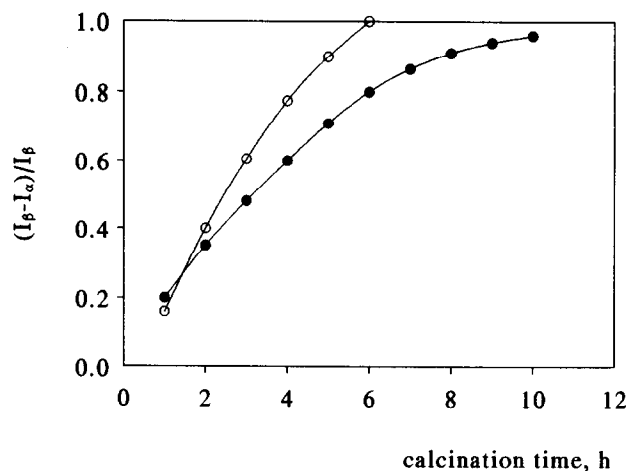


Fig. 4. Mutual intensity changes of the (1 0 4) reflection of α -Al₂O₃ and the (2 0 4) reflection of Ca- β'' -Al₂O₃ measured in the powders heated to 400°C at different rates: $1^\circ\text{C}\ \text{min}^{-1}$ (○) and $10^\circ\text{C}\ \text{min}^{-1}$ (●).

heated at different rates were only of kinetic character. This phenomenon is illustrated by the mutual intensity changes of the α - and β'' -alumina reflections (Fig. 4).

The microphotographs in Fig. 5 illustrate the changes of powder morphology. Figure 5(a) shows the powder at the initial stage of the reaction obtained by calcining the gel at 1100°C for 1 h. By electron diffraction it was found that both the smaller (30 nm diameter) isometric particles and the larger (70 nm diameter) particles are composed of a mixture of calcium aluminate, CaO·2Al₂O₃, and aluminium oxide of the θ -form. After calcination at 1200°C for 1 h plate-shaped crystallites appear, Fig. 5(b), their smaller dimensions being equal to those of the agglomerates of the isometric particles. It was established that the plate-like crystallites were calcium-beta''-alumina. In the powder calcined at 1300°C for 2 h (Fig. 5(c)) plate-like crystallites, from 0.2 to $1.4\ \mu\text{m}$ in size, were in the majority. In addition, using electron diffraction it was found that the direction perpendicular to the crystallite surface is parallel to the Z-axis of its crystallographic structure. An additional experiment showed that the α -alumina powder prepared by the same method, under the same conditions, was characterized by crystallites similar in size but isometric in shape.

In the case of the powder calcined isothermally at 1000°C , the reaction products that appear first are aluminium oxide of the γ -form and calcium aluminate, CaO·2Al₂O₃. During the process calcium aluminate remains unchanged but the γ -alumina transforms into the θ - and α -forms. Calcination prolonged to 20 h results in a powder composed of a mixture of α -alumina and calcium aluminate. Traces of β'' -alumina can be detected in samples calcined for up to 200 h. At calcination higher temperature changes of the phase contents are

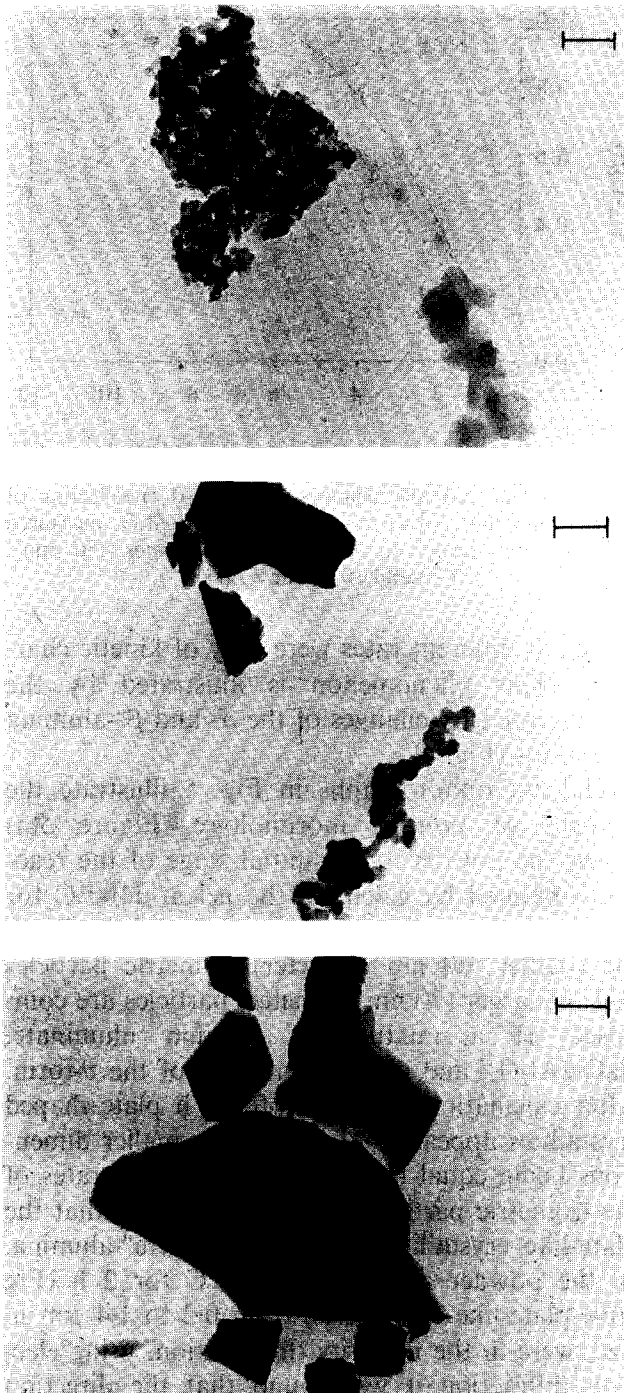


Fig. 5. Morphology of the powders calcined: (a) at 1100°C for 1 h, (b) at 1200°C for 1 h and (c) at 1300°C for 2 h. Scale bars: 150 nm (a and b) and 0.2 μm (c).

similar, although they occur much more rapidly. At 1200°C both α - and β'' -alumina appear practically simultaneously.

Based on the facts as described above, the mechanism of calcium- β'' -alumina formation can be proposed as follows. During heating the alumina hydroxide gel decomposes into a low-temperature form of aluminium oxide. A part of this oxide reacts with calcium oxalate to give calcium aluminate. Further heating transforms the aluminium oxide into its higher temperature forms. At the same time, individual crystallites of both aluminium oxide and calcium aluminate link

together to form agglomerates. Then, α -alumina reacts with calcium aluminate and forms the β'' -alumina phase. The reaction starts at the interphase boundary, the β'' -alumina nucleus is then increased by the diffusion of calcium cations from calcium aluminate to the aluminium oxide. The preferential directions of the β'' -alumina crystallite growth would be the ones along the plane perpendicular to the Z-axis. The irregular, not completely hexagonal, plate-like appearance of the Ca- β'' -Al₂O₃ particles (see Fig. 5(c)) suggests their formation through coalescence from the smaller crystallites. The occurrence of the β'' -alumina phase at 1000°C only when aluminium oxide is completely transformed into the α -form suggests that, for the synthesis of Ca- β'' -Al₂O₃, the formation of the crystalline structure of aluminium oxide with a densely hexagonally packed anion sublattice is necessary.

The sintered bodies obtained from the β'' -alumina powders were characterized by the microstructure presented in Fig. 6. It is evident that the grains of the material are not isometric, suggesting that the original crystallite shape has been preserved, at least to some extent.

The dependence of conductivity on temperature is presented in Fig. 7. The activation energy of the

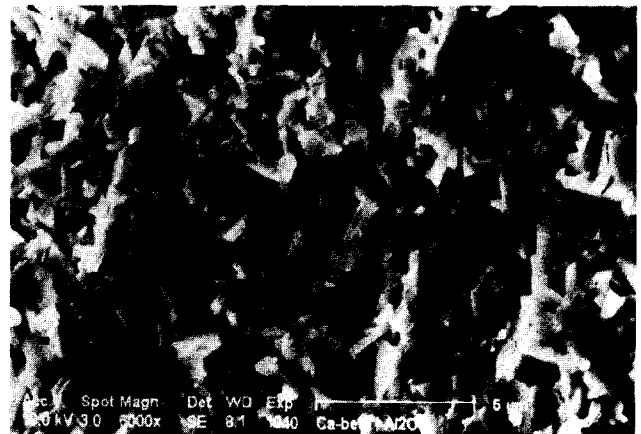


Fig. 6. Fracture surface of Ca- β'' -Al₂O₃.

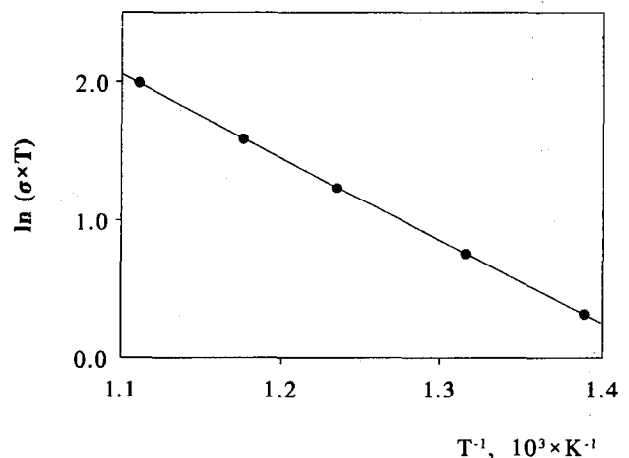


Fig. 7. Temperature dependence of Ca- β'' -Al₂O₃ conductivity.

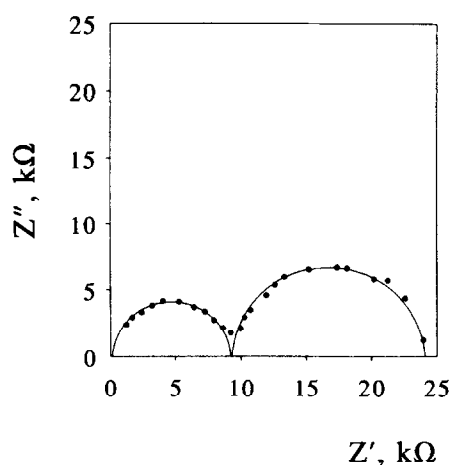


Fig. 8. Impedance spectra of Ca- β'' -Al₂O₃ measured at 300°C.

conductivity process determined on the basis of this dependence is 50.1 kJ mol⁻¹. The impedance spectra recorded at 300°C are presented in Fig. 8 and yield the following values of conductivity: bulk conductivity $\sigma_b = 2.40 \times 10^{-5} (\Omega \text{ cm})^{-1}$; grain boundary conductivity $\sigma_{gb} = 1.50 \times 10^{-5} (\Omega \text{ cm})^{-1}$. Both the diagrams and the calculated values are characteristic of β'' -alumina type conductors.^{19,24}

4 Conclusions

The observations made during this study allow the following conclusions to be drawn.

- (1) The application of alumina gel and the co-precipitation-calcination method allow a material with beta''-alumina structure to be obtained.
- (2) The kinetics of the beta''-alumina synthesis depends on the presence of a molten salt during the precursor thermal treatment.
- (3) The probable mechanism of calcium-beta''-alumina formation is the reaction between formerly produced calcium aluminate, CaO·2Al₂O₃, and aluminium oxide of the alpha-form.
- (4) Sintered bodies obtained from the powder prepared in this manner are characterized by good ionic conductivity.

The fact that material with the Ca- β'' -Al₂O₃ structure and good ionic conductivity can be prepared via direct high-temperature synthesis leads to the conclusion that more work should be done to address the problem of metastability of that phase and its high-temperature degradation. To describe these phenomena in detail the following factors should be taken into consideration: the effect of the stabilizing cation type, the effect of contamination, the stabilizing effect of microstructure, and the kinetics of the degradation process.

Acknowledgements

The present work is part of the Polish Scientific Research Committee project No. 3 3632 92 3. The authors wish to thank Professors Grzegorz Róg and Krzysztof Haberko for their helpful discussions.

References

1. Kummer, J. T., β -Alumina electrolytes. *Prog. Solid State Chem.*, **7** (1972) 141–75.
2. Farrington, G. C. & Dunn, B., Divalent beta''-aluminas: high conductivity solid electrolytes for divalent cations. *Solid State Ionics*, **7**(4) (1982) 267–81.
3. Sammels, A. F. & Schumacher, B., Secondary calcium solid electrolyte high temperature battery. *J. Electrochem. Soc.*, **133** (1986) 235–6.
4. Avniel, Y. C., Investigations into the viability of sulphur detection with beta-alumina electrolytes. In *Extended Abstracts*, 9th International Conference of Solid State Ionics, The Hague, The Netherlands, 1993, p. 274.
5. Róg, G., Kozłowska-Róg, A., Zakuła, K., Bogusz, W. & Pycior, W., Calcium-alumina and Nasicon electrolytes in galvanic cells with solid reference electrodes for detection of sulphur oxides in gases. *J. Appl. Electrochem.*, **21** (1991) 308–12.
6. Róg, G., Pycior, W., Zakuła, K., Kozłowska-Rog, A., & Bućko, M., Calcium-beta''-alumina: preparation, properties, and application to the solid oxide galvanic cells. *Electrochim. Acta*, **38**(2/3) (1993) 365–9.
7. van Zyl, A. & Schaefer, G. W., New directions in β -alumina synthesis. *ISSI Lett.*, **1**(1) (1990) 3–4.
8. Kvachkov, R., Yanakiev, A., Poulieff, C. N., Balkanov, J., Yankulov, P. D. & Budevski, E., Effect of the starting Al₂O₃ and of the method of preparation on the characteristics of Li-stabilized β'' -Al₂O₃ ceramics. *J. Mater. Sci.*, **16** (1981) 2710–16.
9. van Zyl, A., Thackeray, M. M., Duncan, G. K., Kingon, A. I. & Heckroodt, R. O., The synthesis of beta alumina from aluminium hydroxide and oxyhydroxide precursors. *Mater. Res. Bull.*, **28**(2) (1993) 145–57.
10. Youngblood, G. E., Virkar, A. V., Cannon, W. R. & Gordon, R. S., Sintering process and heat treatment schedules for conductivity, lithia-stabilized β'' -Al₂O₃. *Am. Ceram. Soc. Bull.*, **56**(2) (1977) 206–210, 212.
11. Nagai, M., Kushida, T. & Nishino, T., Fabrication and evaluation of porous β/β'' -Al₂O₃ ceramics prepared by the sol-gel process. *Solid State Ionics*, **35** (1989) 213–16.
12. Colucci, G., Negro, A., Visconte, E., Pijolat, C. & Lalauze, R., Non-conventional syntheses of beta-alumina powders. *Ceram. Int.*, **16** (1990) 225–9.
13. Yamaguchi, S., Terabe, K. & Iguchi, Z., Formation and crystallization of beta-alumina from precursor prepared by sol-gel method using metal alkoxides. *Solid State Ionics*, **25**(2-3) (1987) 171–6.
14. Terabe, K., Yamaguchi, S., Iguchi, Y. & Imai, A., Characterization of sodium β -alumina prepared by sol-gel method. *Solid State Ionics*, **40/41** (1990) 111–14.
15. Yoldas, B. E. & Partlow, D. P., Formation of continuous beta alumina films and coatings at low temperatures. *Ceram. Bull.*, **59**(6) (1980) 640–2.
16. Whiter, J. & Fray, D. J., The preparation and electrical properties of polycrystalline calcium β'' -alumina. *Solid State Ionics*, **17**(1) (1985) 1–6.
17. Kumar, R. V. & Kay, D. A. R., The utilization of galvanic cells using Ca- β'' -alumina solid electrolytes in a thermodynamic investigations of the CaO-Al₂O₃ system. *Met. Trans.*, **16B**(3) (1985) 107–12.

18. Hong, Y., Hong, D., Peng, Y., Li, L. & Wei, S., The fabrication and properties of polycrystalline $\text{Ca}\beta''\text{-Al}_2\text{O}_3$ tube. *Solid State Ionics*, **25** (1987) 301–5.
19. Schaefer, G. W., van Zyl, A. & Weppner, W., Direct synthesis of divalent beta alumina and related phases. *Solid State Ionics*, **40/41** (1990) 154–7.
20. Rohrer, G. S., Davies, P. K. & Farington, G. C., The effect of thermal history on the ionic conductivity of $\text{Pb(II)-}\beta''\text{-alumina}$. *Solid State Ionics*, **28–30** (1988) 354–7.
21. Kirchnerova, J., Petric, A., Bale, C. W. & Pelton, A. D., Dense polycrystalline calcium β' - and β -aluminas: synthesis, XRD characterization and thermal stability. *Mater. Res. Bull.*, **26(6)** (1991) 527–34.
22. Schaefer, G. W. & Weppner, W., Preparation of divalent beta-alumina ceramics via ion exchange from K- and Na- β'' -alumina ceramics. *Solid State Ionics*, **53–56** (1992) 59–563.
23. International Centre for Diffraction Data, cards: 10–173, 23–1037, 25–122, 33–252.
24. Dorner, G., Durakpasa, H., Faflek, G. & Breiter, M. W., Production and characterization of polycrystalline (Na, Ca) β'' -alumina. *Solid State Ionics*, **53–56** (1992) 553–8.

In-Plane Microstructure of Plasma-Sprayed Mg–Al Spinel and 2/1-Mullite Based Protective Coatings: An Electron Microscopy Study

W. Braue,^a G. Paul,^a R. Pleger,^a H. Schneider^a & J. Decker^b

^aGerman Aerospace Research Establishment (DLR), Materials Research Institute, D-51147 Cologne, Germany

^bGerman Institute for Refractories and Ceramics, D-53113 Bonn, Germany

(Received 30 January 1995; revised version received 12 June 1995; accepted 23 June 1995)

Abstract

Planar specimens prepared from thin plasma-sprayed Mg–Al spinel and 2/1-mullite layers are investigated via conventional and analytical transmission electron microscopy in order to evaluate the constraints of rapid solidification on the in-plane microstructure at different scales of resolution.

Despite intrinsic differences in the nature and density of structural defects between the two materials studied, their gross-scale microstructures share a characteristic sequence starting from (i) large, spherical core grains, followed by (ii) a radial chill-zone exhibiting columnar to dendritic grain morphologies, which eventually leads to (iii) an impingement zone formed by the intersection of different chill-zones.

Relief of thermomechanical strain from the core grains and chill zones gives rise to an equiaxed sub-grain architecture and intensive microcracking in the impingement zone. Moreover, the impingement zone represents the region of highest and most varied lattice defect density.

1 Introduction

Plasma-sprayed oxide coatings deposited on metallic or ceramic substrates define a unique class of materials which are well established in different fields of industrial application, such as thermal insulation (thermal barrier coatings), protection against oxidation or corrosive attack, and wear resistance.

Coating materials particularly pursued in this approach are zirconia,^{1–3} alumina,^{4–7} cordierite $\text{Mg}_2\text{Al}_3[\text{AlSi}_5\text{O}_{18}]^8$ and forsterite Mg_2SiO_4 .⁸ Because of their good thermal shock resistance, spinel (MgAl_2O_4) coatings have been exploited for various applications in chemical engineering and steel

production.^{9,10} Mullite, $\text{Al}_{4+x}\text{Si}_{2-2x}\text{O}_{10-x}$ (with $0.2 < x < 0.5$) exhibits an oxygen-deficient orthorhombic structure, where x defines the number of oxygen atoms missing per unit cell.^{11–13} This constituent is a potential candidate for thermal protection layers since it offers high thermal stability and good thermal shock resistance along with both low thermal expansion and low thermal conductivity.^{14,15} Because of the close match in thermal expansion coefficients, mullite-based protective layers also perform well as corrosion resistant coatings for SiC-based heat exchanger tubes.¹⁶ Moreover, mullite has been successfully employed as an oxidation-resistant coating for molybdenum substrates.^{17,18}

Besides their attractive thermomechanical properties, a major motivation for selection of spinel and mullite plasma-deposited layers in the present research stems from the fact that both materials are ideally suited as model components in extended alumina systems. Alumina is certainly one of the best studied ceramic plasma-sprayed systems in the literature (see Ref. 7 for review). It is a principal constituent in the $\text{SiO}_2\text{–Al}_2\text{O}_3$ ¹⁹ and $\text{MgO–Al}_2\text{O}_3$ ²⁰ phase diagrams. Alumina polymorphs were reported to occur in spinel and mullite microstructures in case of deviations from stoichiometry and/or kinetic constraints during cool-down.^{21–23}

Non-equilibrium conditions during ultrasonic transport and deposition of plasma-sprayed materials create a complex pattern of interdependent experimental parameters. Because of the extreme quenching rates during deposition, which are of the order of 10^6 K s^{-1} ,^{8,9} the microstructures and thus the physical properties of plasma-sprayed materials differ significantly from their conventionally densified counterparts.^{24–27}

The present study focuses on the lateral microstructural variation during the first stage of

coating build-up. Plane view transmission electron microscopy (TEM) specimens were prepared from thin layers of thermally sprayed Mg–Al spinel and 2/1-mullite and investigated by means of conventional and analytical TEM. The so-derived 2D microstructural features are referred to as in-plane microstructure. This approach particularly addresses the following aspects:

- (i) the gross microstructure (grain size, grain morphology, macroporosity) of as-sprayed deposits on a micron scale;
- (ii) the phase stability during plasma-spraying, focusing on the occurrence of metastable phases due to local variations in the cooling rate during deposition; and
- (iii) the nature and density of structural defects in the as-sprayed grains, which are expected due to varying high stresses during impact with the cold substrate.

The two-dimensional microstructural analysis of a thin protective coating as pursued in this study is a simplified approach which has its limitations in assessing variations of grain morphology and texture normal to the substrate surface. The interaction of newly arrived with previously deposited material during solidification depends on the heat flux gradient^{1,7} through the layer in a complex manner, thus turning the thickening process of the coating into more than just a simple 3D layer by layer repetition of the in-plane microstructure. For most applications however, the very first layers of the as-sprayed microstructure are crucial for the performance of the coating, particularly in terms for adhesion between the substrate and the protective coating. Moreover, a well-defined reference plane is mandatory for addressing the complex microstructure of layered structures such as plasma-sprayed materials. Therefore, it is anticipated that an assessment of the in-plane microstructural features including different scales of resolution (macroscopic versus microscopic) will contribute valuable information for further optimization of plasma-sprayed thermal protection layers and a better understanding of the 3D architecture within thick coatings.

2 Experimental Procedures

Mullite powder derived from melt-grown ('fused-mullite') batches exhibiting a powder particle size distribution of 10–40 μm was supplied by Huels Inc., Troisdorf, Germany. The spinel powder derived from melt-grown material (grain size between 20 and 40 μm) was obtained from the same supplier.

A Metco 4 MP plasma gun utilizing a gun

power of 375 kW was employed in this study using N_2 as primary gas (flow rate 35 l min^{-1}), H_2 as secondary gas (flow rate 7 l min^{-1}) and N_2 as carrier gas, respectively. The powders were sprayed from a distance of 70 mm on to the surface of a sillimanite (Al_2SiO_5) substrate utilizing an average feeding rate of 40 g min^{-1} . The substrate was not preheated, resulting in relatively poor adhesion of the coatings and predominantly lateral heat flow through the coating. The average thickness of the plasma-sprayed layers after several passes was of the order of 100 μm .

A Philips EM 430T TEM/STEM transmission electron microscope operating at 300 kV was employed in this study. The very first layer of the coatings adjacent to the substrate were sampled for preparation of plane view specimens. Electron-transparent thin foils were prepared by standard ceramographic techniques involving dimpling and 5 keV argon ion-beam thinning. HREM images (see Section 3.3) were processed by a digital image processing system consisting of a CCD-camera, a frame-grabber, a personal computer and an image processing program (Synoptics Ltd, UK).

3 Results and Discussion

The gross-scale microstructural patterns of as-sprayed spinel and mullite coatings are described in Section 3.1. In the two subsequent sections we first comment on intrinsic characteristics of the spinel and the mullite microstructure, such as the phase stability during transport and deposition (Section 3.2), and then discuss the defect structure of as-sprayed grains (Section 3.3).

3.1 General microstructure of as-sprayed spinel and mullite layers

Solidification of as-sprayed ceramic coatings is primarily controlled by local heat flux gradients utilizing free surfaces for heterogeneous nucleation, such as the periphery of large grains. This issue has been emphasized in previous research⁷ for both as-sprayed metallic alloys and Al_2O_3 -rich ceramics and we also found it to be an important concept for both plasma-sprayed materials investigated in this study.

The occurrence of large spherical grains embedded in a fine-grained matrix of different grain morphology defined a characteristic microstructural feature for both spinel and mullite layers. The large grains defined the nucleation 'core' (following a notation employed in Ref. 7 for as-sprayed metallic coatings) of a characteristic sequence of the in-plane microstructure. This pattern can be rationalized in terms of a three-step

development (stages I–III), which also comprises the chronology during deposition and solidification. The core grains are referred as stage I. Figure 1 gives a typical example for a core grain in the spinel layer imaged at low magnification. Because core grains generally were homogeneous single-phase with a grain size about the same as the particle size of the starting batch, they probably represent primary constituents which were only marginally melted in the plasma torch and resolidified on the substrate without being fragmented during impact. It is important to note that with the exception of occasional twinning in the mullite system (see Section 3.2), a very low-defect density was observed in all the core grains examined.

Due to the relatively poor adhesion of the as-sprayed materials to the sillimanite substrate, the preferred direction of the heat flow during cool-down is supposed to extend within the plasma layers rather than normal towards the substrate. The radial temperature gradient extending perpendicular to the surface of the core grains in the plane of the coating favoured the development of defect-free columnar grains with their growth axes parallel to the direction of the heat flux. Because this growth morphology is very similar to the chill-zone observed in solidified ingots,²⁸ this microstructure is referred as the ‘chill-zone’ or region II. This zone of columnar grain growth (labelled region 2 in Figs 1 and 2) extends radially from the large core grains until it eventually interferes with similar chill-zones from other core grains to create an ‘impingement zone’ (region 3 in Fig. 1).

During the development of the in-plane microstructure the impingement zone is considered to



Fig. 1. TEM bright-field (BF) micrograph displaying the characteristic gross microstructure of an in-plane section of as-sprayed Mg-Al spinel layer: a large spherical core grain (region 1), followed by a chill-zone with columnar grain morphology (region 2), which eventually leads to an impingement zone (region 3) with intensive microcracking. Details of regions II and III are revealed in Figs 2 and 3, respectively.



Fig. 2. Chill-zone in spinel (region 2 in Fig. 1), exhibiting a typical columnar grain morphology around the periphery of a spinel core grain (TEM BF). The beam directions are parallel to $[1\ 1\ 1]$ (core grain) and $[0\ 1\ \bar{1}]$ (chill-zone), respectively.

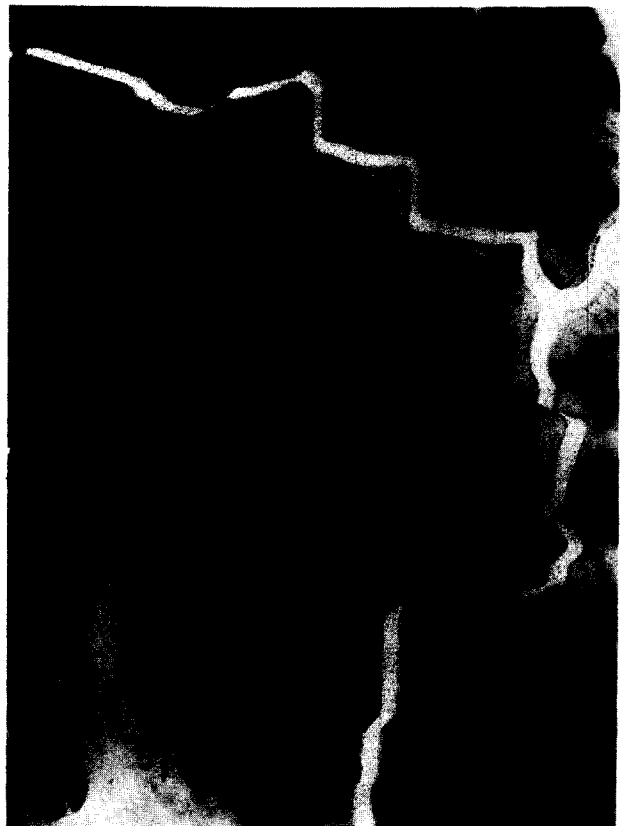


Fig. 3. Impingement zone in spinel (region 3 from Fig. 1), revealing mosaic-like microstructure (beam direction parallel $[0\ 1\ 0]$) and microcracks emerging from intersection of different chill-zones.

evolve last. In spinel (Fig. 3), it is characterized by a mosaic-like microstructure exhibiting an equiaxed subgrain morphology bounded by $\{1\ 0\ 0\}$ and $\{1\ 1\ 0\}$ planes, along with intensive microcracking and considerable intergranular porosity. As discussed in Section 3.3 in more detail, the impingement zone represents the region of highest lattice defect density. The noticeable change in grain morphology from columnar in the chill-zones to equiaxed in the impingement zone is attributed to a slowing of the cooling rate as the coating coverage of the substrate increases. This effect will favour more isotropic grain morphologies similar to observations of other plasma-sprayed materials.^{1,7} It is assumed that the core grains represent the larger particle size fraction of the starting powder batch which were only partially molten during ultrasonic transport. In contrast, the microstructures of the chill- and impingement zones are considered to result from smaller, fully molten particle deposition on the substrate. After the quench from the liquid, solidification is controlled by anisotropic thermal gradients defined by the cooling conditions in the predeposited material.

The three-stage microstructural sequence [core grain (I) \rightarrow chill-zone (II) \rightarrow impingement zone (III)] was also observed for the mullite deposit, as summarized in Figs 4–7. The occurrence of columnar grains (Fig. 4) attached to the surface of large



Fig. 5. Early stages in development of dendritic grain morphology in the mullite layer. Note the high density of intra-granular porosity.

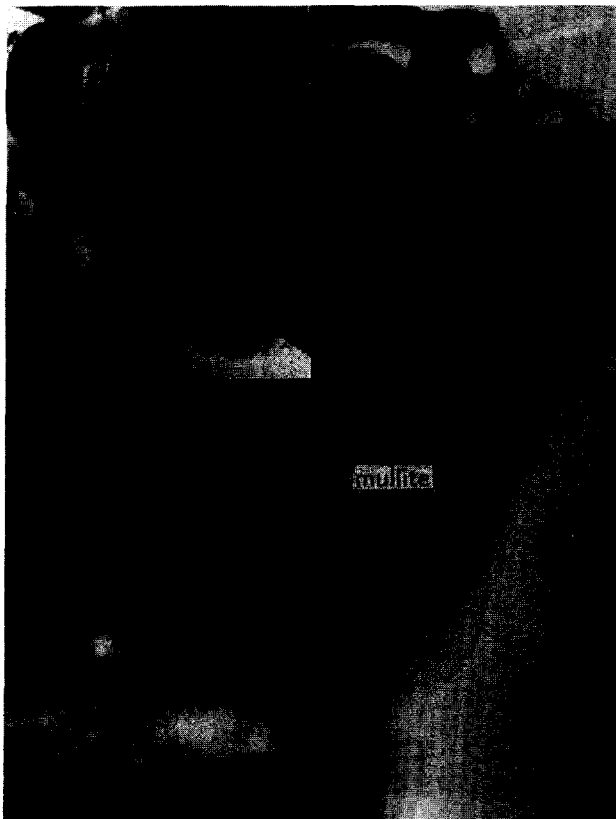


Fig. 4. Columnar grain morphology of as-sprayed mullite from chill-zone (labelled 2) close to core grain (labelled 1), as shown in the inset. Mullite orientation is parallel to $[0\ 0\ 1]$.



Fig. 6. Final stage in development of dendritic grain morphology in as-sprayed mullite, embedded in amorphous phase (labelled g).

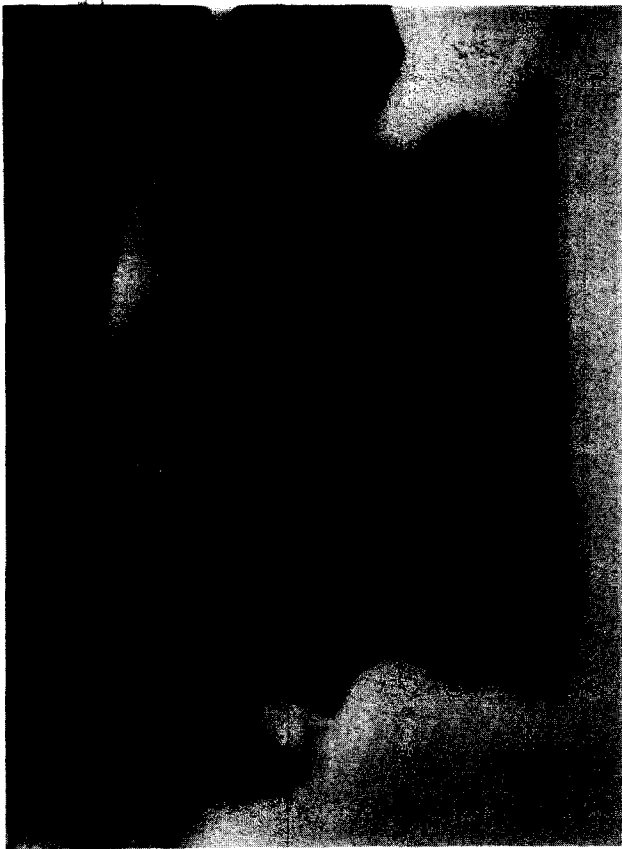


Fig. 7. Mullite aggregate attached to a continuous alumina- and silica-rich glassy phase (labelled g). Beam direction is parallel to $[0\ 1\ 0]$.

core grains in the mullite layer indicates that its microstructural development was similar to spinel. The growth axis is approximately parallel to $[1\ 1\ 0]$, deviating from the normal growth axis of mullite, which is parallel to $[0\ 0\ 1]$.²⁹

Locally the mullite grain morphology along the spreading chill-zone can change from columnar, through smooth droplet-like grains with isolated pockets of amorphous phase (Fig. 5) to, eventually, typical dendrites attached to a continuous interdendritic amorphous phase (Fig. 6), which is similar to the amorphous interlayer found in sintered bodies. The dendrite tips consist of macroscopic $\{1\ 1\ 0\}$ planes, and the growth direction in this case is approximately parallel to $[0\ 1\ 0]$. Residual pockets of SiO_2 -rich amorphous phase acting as a sink for Al and some impurities are associated with equiaxed mullite aggregates bound by $\{1\ 1\ 0\}$ planes, as shown in Fig. 7. Such areas most likely represent local compositional deviations from the bulk, pushing the composition into the mullite plus SiO_2 field of the Al_2O_3 - SiO_2 phase diagram.¹⁹ Similar microstructures have been reported from directional solidification experiments in the Al_2O_3 - SiO_2 system.³⁰ Compared to spinel, the mullite system seems to be particularly sensitive to fluctuations along the liquid/solid interface, which may be attributed to its lower

intrinsic thermal conductivity and/or local variation in temperature gradient.

Impingement zones as defined by the intersection of chill-zones from several core grains are also established in the mullite deposits (see Fig. 8; to be compared with Fig. 3). The subgrain boundary network is often parallel to $\{1\ 1\ 0\}$ planes. The dislocation density within the subgrains is low (see Section 3.3); most dislocations were single and isolated, but a few dipoles were observed.

In the spinel and mullite layers investigated, macroporosity is scattered heterogeneously throughout the in-plane microstructure (Fig. 9). Porosity is generally more pronounced in the mullite deposits. The pore size may reach a micron, with the pores bounded intragranularly in most cases. The pores are spherical, indicating entrapment of gaseous species in the molten, low-viscosity feedstock material during plasma spraying. An interlaminar type of macroporosity is also observed which gives rise to a characteristic striation pattern (Fig. 10) in the columnar grain structure of the chill-zone. On a much smaller scale compared to these macropores, the columnar mullite grains themselves exhibited numerous faceted intragranular pores (denoted by arrowheads in Fig. 10), very similar to Kirkendall voids in conventionally densified Al_2O_3 -rich materials.^{31,32}

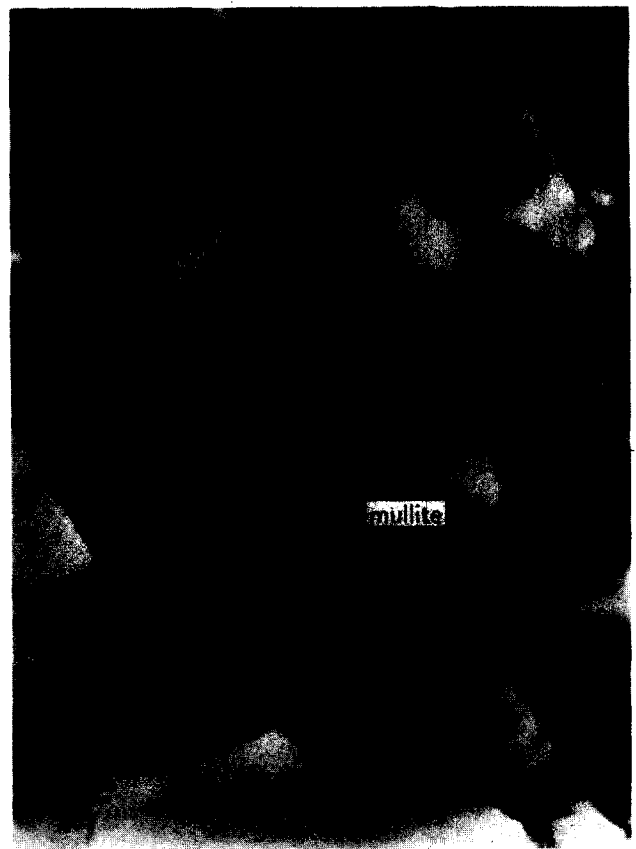


Fig. 8. Impingement zone in as-sprayed mullite (compare with Fig. 3). Small-angle grain boundaries and a rectangular $\{1\ 1\ 0\}$ grain morphology create a mosaic-like pattern. Note the lack of intergranular porosity.

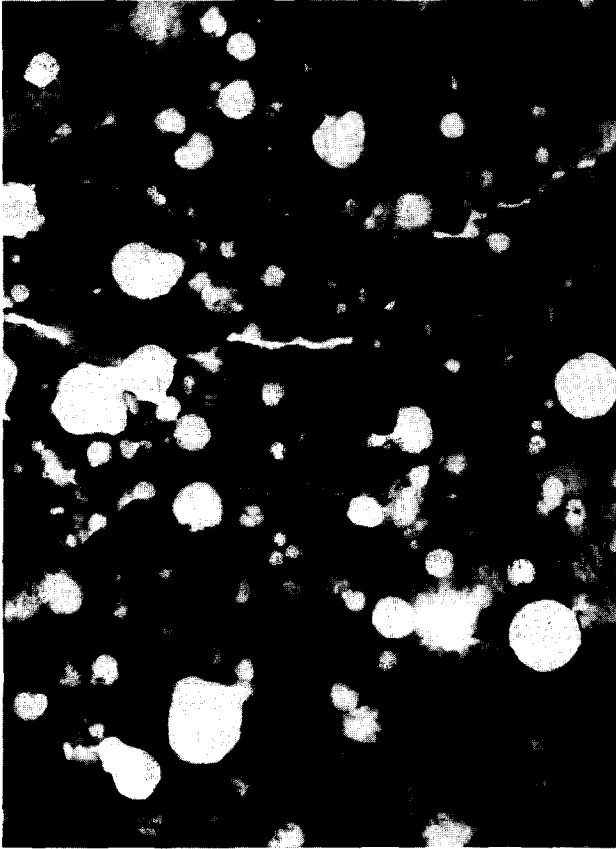


Fig. 9. Mullite layer exhibiting large-scale porosity, taken from area where the chill-zone meets the impingement zone.



Fig. 10. Columnar mullite grains exhibiting extensive interlaminar porosity (extending from top to bottom of micrograph) along with numerous faceted intragranular pores (indicated by arrows).

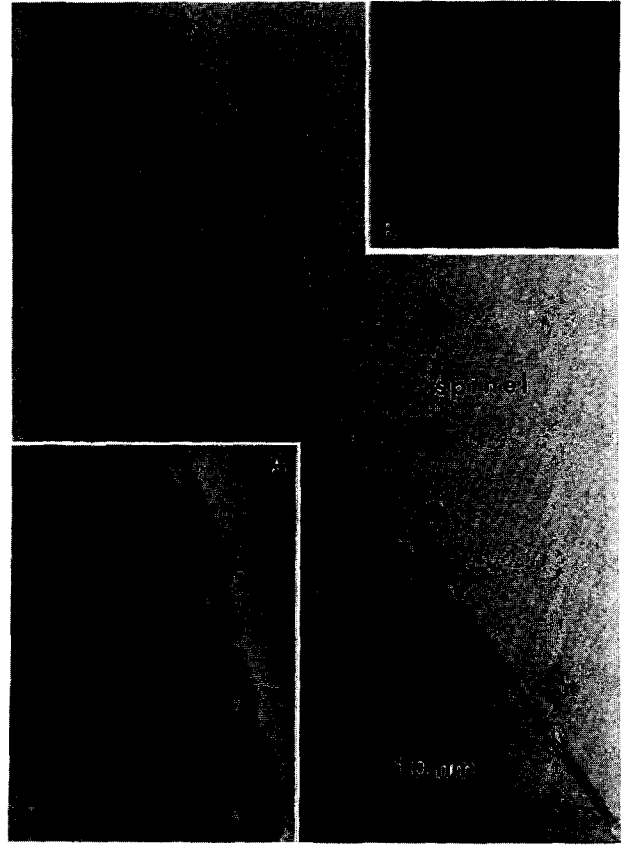


Fig. 11. Defocused BF image of edge-on grain boundary in spinel, revealing grain boundary precipitates. Inset A shows the wedge of a similar but tilted grain boundary, proving that the precipitates are strictly confined to the grain boundary. Inset B reveals a faceted amorphous precipitate bounded by low-energy spinel planes.

In contrast to the micropores concentrated in the mullite chill-zones, the spinel layers exhibited numerous submicrometre-sized features which are strictly confined to grain boundaries (Fig. 11). They are particularly abundant in the impingement zone where they coexist with the dislocations in the subgrain boundaries. In Fig. 11, a spinel grain boundary from a very thin region of the specimen is imaged edge-on under defocus conditions, revealing a sequence of tiny elongated 'precipitates' of the order of 10 nm. Inset A shows their accumulation within the wedge of a tilted grain boundary. These precipitates are (i) sometimes faceted (see inset B in Fig. 11) and (ii) consist of amorphous material, as revealed by convergent beam electron diffraction (CBED). During small-probe analysis in the microscope radiation effects occurred easily, so their composition was impossible to identify unambiguously.

The different types of macro- and microporosity affect both the elastic modulus and the thermal conductivity of the spinel and mullite layers. As an increased pore volume accounts for better relaxation of thermal stresses, as-sprayed ceramic materials exhibit superior thermal shock resis-

tance, compared to their dense counterparts.^{24–27} Studies of plasma-sprayed PSZ-based thermal barrier coatings² have demonstrated that porosity is indeed a desirable microstructural parameter for those applications where harsh thermal cycling conditions, e.g. in engine components, define the major challenge for the performance of the protective coating. In conjunction with the anisotropic grain morphology of the in-plane microstructure, porosity and microcracks contribute to the non-elastic stress/strain behaviour reported for plasma-sprayed coatings.^{26,27}

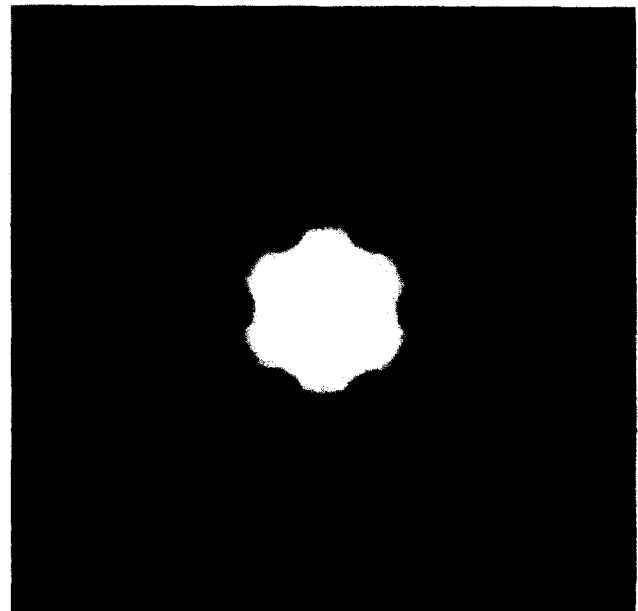
3.2 Phase stability and chemical gradients in as-sprayed spinel and mullite coatings

Phase stability in plasma-sprayed materials depends on kinetic and energetic constraints related to nucleation and growth of the constituents along the solid/liquid interface during quenching. These constraints control whether the chemical composition and constitution of the feedstock materials match that of the deposited layer. In this context plasma-sprayed alumina is a well-documented model system for the occurrence of metastable transition alumina phases due to rapid cool-down (see Ref. 7 for review).

As-sprayed spinel is a homogeneous single-phase material as demonstrated by small-probe microanalysis and electron diffraction. A large-angle CBED pattern demonstrated the characteristic three-fold symmetry along the $[1\ 1\ 1]$ axis and corresponding HOLZ-line pattern in the $(0\ 0\ 0)$ diffraction disc in agreement with the MgAl_2O_4 cell dimensions (Fig. 12). No $\gamma\text{-Al}_2\text{O}_3$ precipitates were detected in the spinel. These would be expected if substantial evaporation of MgO occurred causing formation of non-stoichiometric $(\text{Al}_2\text{O}_3)_n\text{MgO}$ ($n > 1$) spinels.¹⁵

Compared to the rather straightforward phase relationships in the binary $\text{MgO-Al}_2\text{O}_3$,^{19,20} the $\text{Al}_2\text{O}_3\text{-SiO}_2$ system is more complex; metastable phase equilibria may arise due to notably slow nucleation kinetics for formation of mullite solid solutions and/or alumina during crystallization from a melt.^{34,35} As discussed below in more detail, the basic mechanisms to accommodate chemical gradients during plasma spraying in the binary $\text{Al}_2\text{O}_3\text{-SiO}_2$ system is the formation of metastable transition alumina polymorphs, which are quite frequently observed. (The occasional formation of a mullite species which is more Al-rich and heavily twinned compared to the standard as-sprayed 2/1-mullite is most likely to be controlled by the stoichiometry of the mullite feedstock material (see Section 3.3).)

In as-sprayed mullite layers, single grains of cubic $\eta\text{-Al}_2\text{O}_3$ located at triple-grain junctions



(a)



(b)

Fig. 12. CBED patterns obtained from spinel $[1\ 1\ 1]$ core grain as displayed in Fig. 1. (a) Composite pattern consisting of zero-order Laue zone (ZOLZ) pattern plus first-order Laue zone (FOLZ) ring. (b) arrangement of the higher-order Laue zone (HOLZ) lines around the $[1\ 1\ 1]$ pole in the central $(0\ 0\ 0)$ disc clearly reveals a three-fold pattern, thus confirming the cubic symmetry of the crystal investigated.

were identified by selected area diffraction (Fig. 13). The zone axis of the selected area diffraction (SAD) pattern (see inset) is parallel to $[1\ 1\ \bar{2}]$ with continuous streaking along the $\langle 1\ 1\ 1 \rangle$ and $\langle 1\ 3\ 1 \rangle$ directions. The streaking is due to structural disorder of $\eta\text{-Al}_2\text{O}_3$ which has a spinel-type structure.^{35–37} Often types of submicrometre-size intragranular inclusions were observed in the equiaxed subgrains from mullite impingement zones. A large secondary phase grain (Fig. 14(a)) located on a small-angle grain boundary was identified as monoclinic $\theta\text{-Al}_2\text{O}_3$ by means of CBED (see insets A and B in

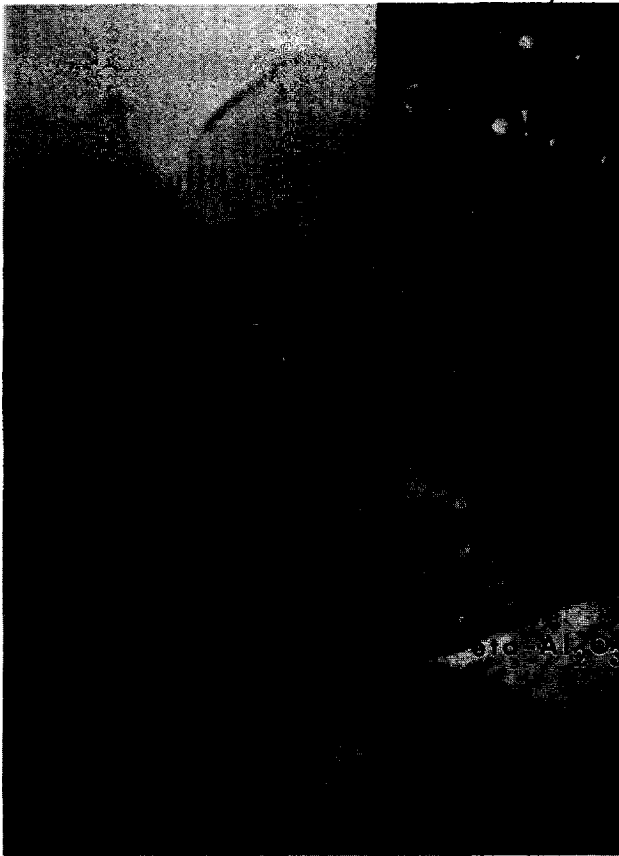


Fig. 13. $n\text{-Al}_2\text{O}_3$ at triple grain junction of as-sprayed 2/1-mullite. Orientation is parallel $[1\ 1\ \bar{2}]$. Note streaking parallel to $\{1\ 1\ 1\}$ and $\{1\ 3\ 1\}$ in the SAD pattern inserted. Centre of SAD aperture is given by circle.

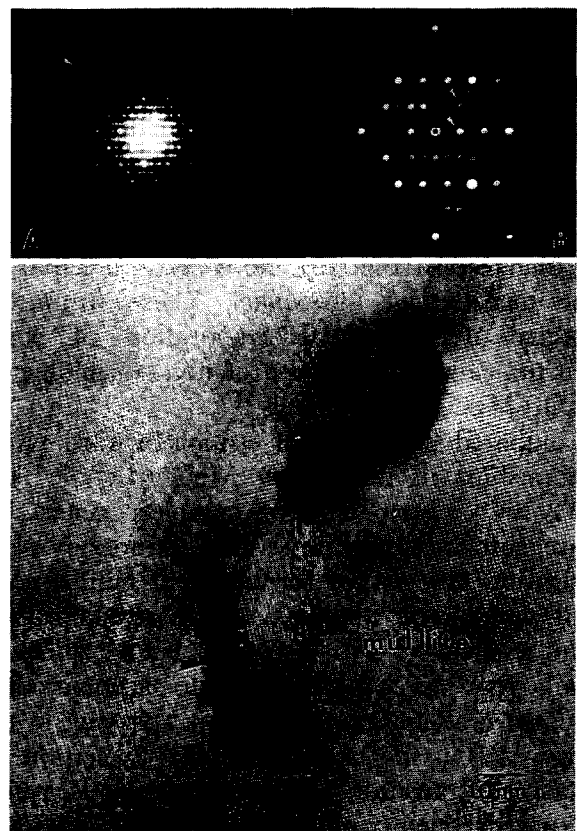
Fig. 14(b)). Tiny secondary phase inclusions with planar defects detected in the same area (Fig. 14(b)) were identified as transition alumina phases via digital image analysis.

The rationale for the formation of transition alumina polymorphs in as-sprayed layers instead of the thermodynamically stable phase corundum is based on the cooling rate and nucleation kinetics during plasma spraying:

- (1) Plasma-sprayed alumina-rich ceramic systems have shown that the formation of metastable transition aluminas is mostly controlled by the cooling rate.⁷ A slow cooling rate favours positioning of Al^{3+} in octahedral coordination, thus leading to the formation of corundum. Slow cooling is seldom achieved during plasma spraying. Instead, fast cooling rates which favour tetrahedral coordination of Al^{3+} are more common, which give rise to the formation of transition aluminas.
- (2) The interaction of phase stability and cooling rate is clearly a function of the particle size.⁷ Small particles are characterized by high quenching rates, favouring the formation of transition aluminas for reasons discussed previously.



(a)



(b)

Fig. 14. (a) HREM image of mullite subgrains in $[0\ 0\ 1]$ orientation, including an intragranular $\theta\text{-Al}_2\text{O}_3$ particle. FOLZ and ZOLZ regions of a $[\bar{1}\ 3\ 1]$ zone axis pattern are shown in insets A and B in Fig. 14(b). (b) FOLZ and ZOLZ patterns obtained from $\theta\text{-Al}_2\text{O}_3$ (top), $[0\ 0\ 1]$ HREM image of mullite, exhibiting small intragranular precipitates with planar defects, indicated by arrows (bottom).

- (3) The formation of metastable transition polymorphs may also be controlled via the critical free energy for heterogeneous nucleation of alumina polymorphs. As emphasized by Ref. 38, the critical energy threshold is by definition lower for a transition alumina polymorph than for the thermodynamically stable phase corundum.

The frequent observation of transition alumina phases in plasma-sprayed alumina reported in the literature^{7,21,22,38} and in mullite plasma layers, as observed during this research, can be rationalized in terms of Ostwald's step rule³⁹ which emphasizes the significance of the nucleation energy for crystallization of polymorphic systems. Such systems do not spontaneously form the most stable precipitation product, but rather pass sequentially through several intermediate stages with higher energies, before eventually the stable configuration with the lowest free energy is obtained.

The majority of mullite core grains investigated were homogeneous single phase 2/1-material. Reciprocal ($h\ 0\ l$) lattice sections of mullite core grains (Fig. 15) yield the typical diffuse superstructure pattern^{12,13} centred at $a^* \sim 1/3$ and $2/3$ and $c^* \sim 1/2$, indicating that the distribution of oxygen vacancies on O(C) sites in the structure of as-sprayed mullite was not affected by the constraints of rapid solidification. However, some core grains were detected that contained nanoscale twin lamellae parallel to (0 0 1) planes. The twinned structure of such a core grain is displayed at high magnification in Fig. 16, after tilting the crystal into a [0 1 0] zone axis orientation so that the twin planes are edge-on. The corresponding diffraction pattern (see inset) is basically that of Fig. 15, superimposed with the effects of twinning

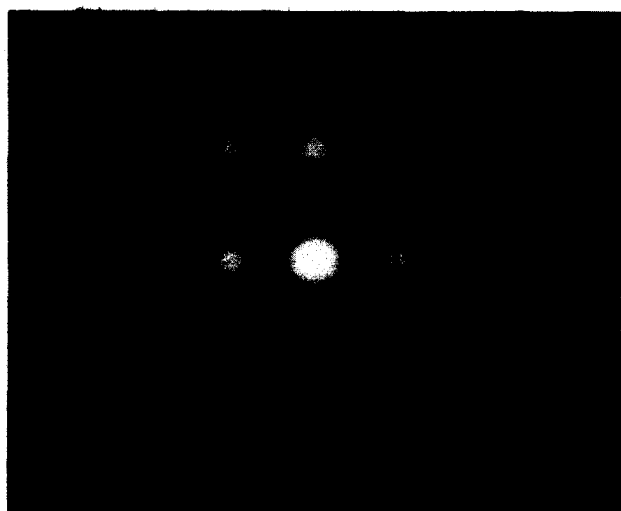


Fig. 15: ($h0l$) reciprocal lattice section of as-sprayed 2/1-mullite, displaying sharp and diffuse reflections as well as diffuse streaks in an a^*/c^* plot. The diffraction pattern was obtained from the mullite core grain shown in the inset of Fig. 4.



Fig. 16. Twin lamellae of as-sprayed mullite core grain, tilted into a [0 1 0] orientation (see corresponding SAD pattern inserted). The (0 0 1) twin boundaries are imaged edge-on.

on (0 0 1), as well as double diffraction as discussed in Ref. 33.

With ~ 79 wt% as determined via small-probe microanalysis (EDS), the Al_2O_3 content of the twinned mullite grain was considerably higher than the ~ 75 wt% Al_2O_3 for the untwinned species, determined by the same method. This finding is in fair agreement with the solid solution range-derived for melt-cooled mullites.³³ The Al_2O_3 -rich end member, exceeding ~ 80 wt% Al_2O_3 , incorporates the same twin structure as observed in the present study, while the 83 wt% Al_2O_3 batch exhibits exsolved $\alpha\text{Al}_2\text{O}_3$ precipitates in a twin mullite matrix, indicating that the 83 wt% composition is the nominal mullite solid solution end member under normal conditions. It is believed that the formation of twinned Al-rich mullite core grains is controlled by the purity of the starting material and does not represent an intrinsic effect unique to the plasma-spraying process.

3.3 Nanoscale defect structure of as-sprayed spinel and mullite subgrains from impingement zones

The high quenching rates during deposition of thermally sprayed materials can introduce a variety of structural defects to the in-plane microstructure, which have been well explored for metallic systems in the literature.⁷

With the exception of the occasional twinned Al-rich mullites, (see Section 3.2), the core grains and the peripheral chill-zones in spinel and mullite are basically defect-free. If any structural defects are accumulated in the in-plane microstructure, they are clearly related to the impingement zone (see Section 3.1). The microstructurally irregular impingement zone provides a convenient sink for the relief of thermomechanical strains generated from the core and the chill-zone grains of the deposits. The strain energy released into the impingement zone not only gives rise to the formation of the typical subgrain structure dominated by small-angle grain boundaries (Figs 3 and 8), but also introduces intergranular cracks. Given a subsequent annealing treatment at high temperatures, substantial recrystallization of the impingement zone is expected to take place.

A more detailed TEM inspection shows that the subgrains from the spinel impingement zone contain characteristic structural defects such as point defects and stacking faults. For reasons related to the intrinsic differences in crystal structure between spinel and mullite, these defects are either less pronounced or completely absent in the analogous mullite microstructure:

- (i) Spinel subgrains contained a significant level of point defects. Agglomeration of point defects resulted in formation of dislocation loops which were imaged in dark-field (Fig. 17). Smaller loops or point defect clusters appeared as white dots. No extra effort was undertaken in this study to discriminate between the different natures (vacancy versus interstitial type) of the loops. The thermal history of the spinel deposits investigated, however, strongly suggests that they resulted from agglomeration of thermal vacancies during the quench.
- (ii) The subgrain boundaries in plasma-sprayed spinel layers acted as possible sinks for agglomeration of point defects, which eventually lead to the formation of the grain boundary precipitates discussed in Section 3.1.
- (iii) The spinel subgrains contained planar faults lying on low-index planes, similar to those reported from Verneuil-grown spinel single crystals⁴⁰ and other spinel materials.⁴¹ Depending on the local specimen thickness and the extinction distances of the reflections involved, these faults show typical α -fringe contrast when being studied under different imaging conditions.⁴² In addition to straight fault segments, wavy faults associated with domain-like structures were observed in the spinel subgrains (Fig. 18). Although their characteristic appearance is similar to anti-phase

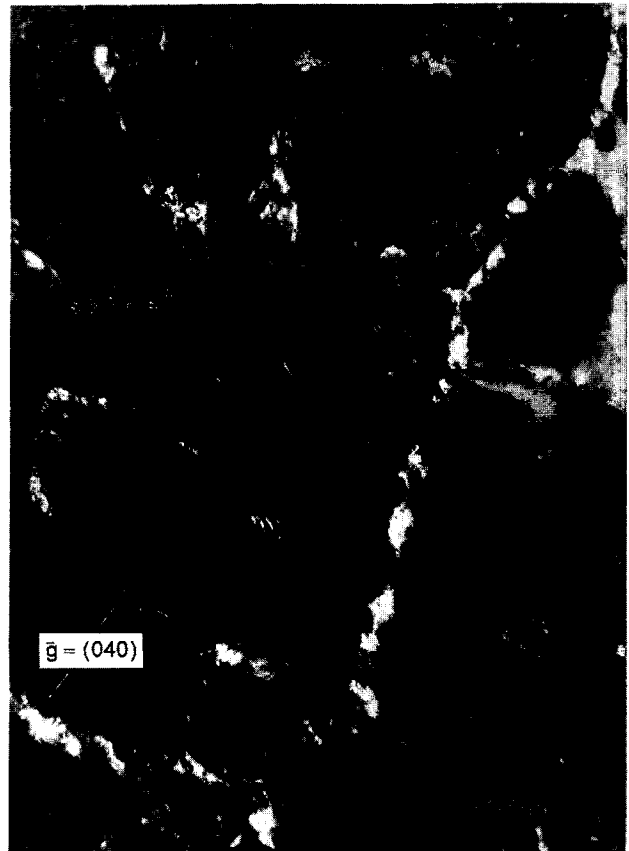


Fig. 17. Dark-field image from spinel subgrain taken with $\vec{g} = (0\ 4\ 0)$. Beam direction is parallel $[1\ 0\ \bar{3}]$. Small dislocation loops are indicated by arrows. The white band extending through the micrograph represents the trace of a subgrain boundary.

boundaries (APB) in ordered f.c.c. alloys,²⁸ they are stacking faults because the corresponding SAD pattern did not reveal sharp superlattice reflections. This is different from most ordered crystal structures,^{43,44} where strong APB fringe contrast is observed only for superlattice reflection, leaving no or only faint residual contrast for fundamental reflection images.

Moreover, the faults in plasma-sprayed spinel are arranged in an irregular, non-periodic

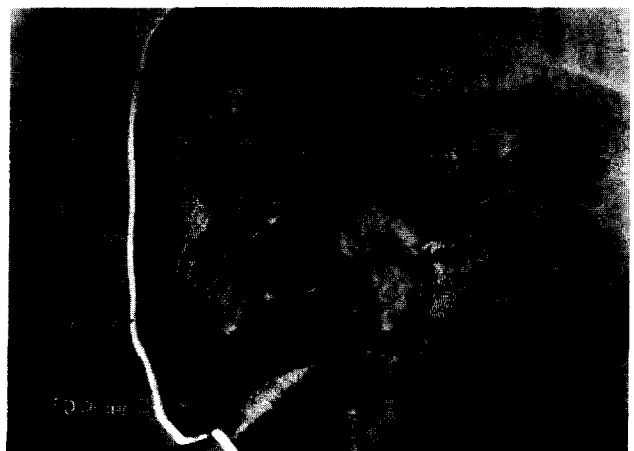


Fig. 18. Wavy faults in spinel subgrain (TEM BF). Beam direction is parallel to $[3\ 1\ \bar{1}0]$.

pattern with a rather low density. Instead of generating a sharp, well-defined super-reflection, the low fault density in combination with their non-periodic arrangement give rise to weak diffuse streaks in reciprocal space only. The size of the streaks ($\sim 0.01 \text{ nm}^{-1}$) is given by the reciprocal value of the average fault-to-fault distance (see Fig. 18) which is 100 nm at the most. This is a much larger scale compared to ordered alloys such as CuAuII, where the APBs are regularly spaced with a period of $\sim 0.2 \text{ nm}$.⁴³ The lattice spacing of the $g(hkl)$ vectors controlling contrast in Fig. 18 is $\sim 0.25 \text{ nm}$, resulting in a spot-to-spot distance of 4 nm^{-1} in the SAD pattern. Relative to this distance, the streaks resulting from the faults in spinel are less than 1% apart, leaving little margin to separate them clearly from the main Bragg spots.

Figures 19 and 20 demonstrate the effect of the faults by direct imaging of an appropriate set of spinel lattice planes. First, notice the rather limited distribution of curved faults (denoted by white arrowheads) in a spinel subgrain (Fig. 19). This micrograph also shows that the faults are pinned by the intragranular precipitates (indicated by black arrows) discussed in Section 3.1, or possibly by dislocations lying underneath the plane of the TEM foil (not shown). The precipitates act as obstacles for the mobility of fault segments during

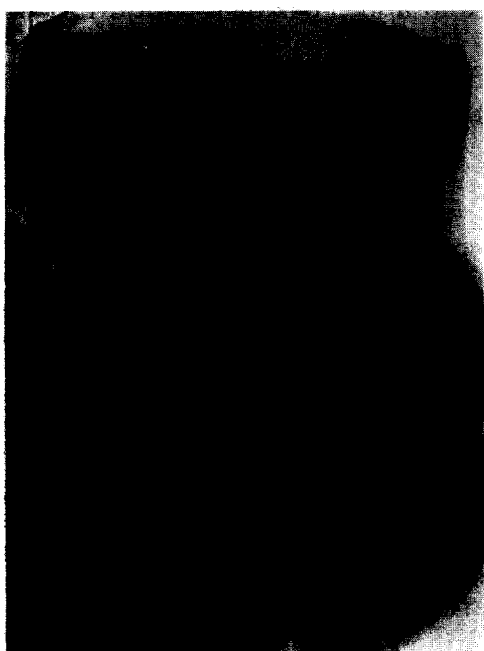


Fig. 19. Wavy stacking faults (indicated by white arrowheads) in spinel subgrain, pinned by low-angle tilt boundary (centre of micrograph) and intragranular precipitates (see black arrowheads). Beam direction is parallel $[0 \bar{5} 1]$. Thickness fringes and bend contours are also visible due to buckling of the thin foil. For higher magnification of boxed region see Fig. 20.

the coarsening process of the domain-like structure. The boxed area from a thin region of the specimen encompasses a typical fault/precipitate configuration and is shown at higher magnification in Fig. 20. The projection of the fault plane is almost edge-on in regions E and F where it appears quite narrow. In region D, it is inclined to the foil. The specimen was tilted to a $[0 k l]$ orientation thus revealing $\{2 0 0\}$ lattice fringes which extend across the whole area displayed in Fig. 20.

A close examination of the fringes in region E revealed that they are discontinuous across the trace of the fault plane: two stacks of $\{2 0 0\}$ fringes (indicated by the black boxes marked 1 and 2) were selected from both sides of the fault, processed via digital image analysis and reassembled in the inset. When looking along the boundary between stacks 1 and 2 (see inset), the displacement of the $\{2 0 0\}$ fringes by $a_0/2$ becomes obvious.

No systematic investigation of possible fault vectors in spinel has been conducted in this study. Although Fig. 19 provides the displacement of $\{2 0 0\}$ planes in projection only, the situation displayed is consistent with displacement vectors of the type $a/2 \langle h 0 0 \rangle$ or $a/2 \langle 1 1 0 \rangle$ common to

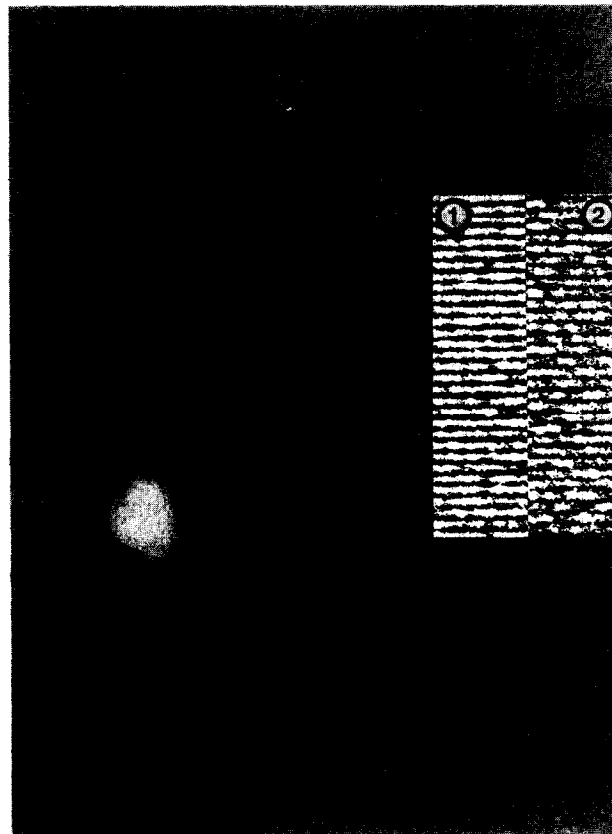


Fig. 20. Spinel $\{2 0 0\}$ lattice fringes from a $[0 \bar{5} 1]$ orientation, showing the displacement of $a_0/2$ across a wavy fault in a subgrain (detail from Fig. 19). Two sets of $\{2 0 0\}$ fringes (indicated by black boxes marked 1 and 2) were selected from both sides of the fault in region E, processed by digital image analysis and reassembled in the inset: the $a_0/2$ displacement becomes obvious along the boundary between stacks 1 and 2.

spinel,⁴⁰ depending on whether or not the displacement vector is confined to $(0 \bar{5} 1)$, the plane of presentation in Fig. 19. As discussed in Ref. 40, stacking faults in spinel have a preference for $\{1 0 0\}$ followed by $\{1 1 0\}$ and other low-index planes. It is the relatively isotropic stacking fault energy associated with low-index planes in spinel which gives rise to the formation of wavy rather than straight faults. The faults are considered as typical growth defects during lateral spread of the impingement zone.

4 Conclusions

The in-plane microstructure derived in the present TEM study illustrates the lateral growth pattern for the very first layers of plasma-sprayed Al_2O_3 -rich ceramic feedstock materials. This interpretation relies on several assumptions, such as constant conditions during ultrasonic transport and deposition and negligible heat flow from the layer to the substrate due to rather poor adhesion. From these studies, the following conclusions can be drawn:

- (1) Despite the rather chaotic impression the in-plane microstructure gives at first glance, the underlying growth pattern appears to be remarkably similar and straightforward for both spinel and mullite. It consists of a characteristic sequence starting from a large spherical defect-free core grain (region I) that acts as the nucleation site for a peripheral chill-zone (region II) exhibiting columnar to dendritic grain morphologies. During build-up of the layer, interference of different chill-zones leads to the formation of an impingement zone (region III). Due to the combined effects of the columnar grain morphology and the associated interlamellar porosity in the chill-zones as well as the microcracks in the impingement zones, the in-plane microstructure provides sufficient weak zones to accommodate residual stresses due to thermal expansion mismatch and/or thermal cycling.
- (2) The occurrence of metastable submicrometre-sized transition alumina polymorphs in the mullite layer is related to the slow nucleation kinetics of stable constituents in the Al_2O_3 - SiO_2 binary and may be rationalized in terms of Ostwald's step rule. The occasional formation of a twinned mullite species which is more Al_2O_3 -rich compared to the average 2/1-mullite is most likely to be related to the purity of the feedstock material. The diffuse super-reflection pattern as derived from a^*c^* reciprocal lattice

sections indicated that the structural short- and long-range order of as-sprayed mullite are left unaffected by the constraints of rapid solidification.

- (3) While the core grains along with the surrounding chill-zones indicate the effects of thermal gradients during the early stages of deposition, the subgrain structure and the microcracks of the impingement zone reflect the relief of thermomechanical strains which have accumulated during lateral growth of the layer. The mosaic-like subgrain structure clearly reflects the thermally induced defect arrangement on growing grain impingement which is effective during solidification. Particularly in spinel, the impingement zone acts as the major sink for structural defects. This is documented by the agglomeration of point defects to form dislocation loops in the subgrains, the formation of grain boundary precipitates and the occurrence of often wavy stacking faults. Subsequent annealing treatments may favour recrystallization in the impingement zones associated with considerable grain growth.

Acknowledgements

It is a pleasure to acknowledge the stimulating discussions with G. Welsch, Case Western Reserve University, Cleveland, OH, USA and Ray Carpenter, Arizona State University, Tempe, AZ, USA (who also provided a critical review of the draft). This research was partially funded by a grant from the Deutsche Forschungsgemeinschaft (DFG), Bonn, Germany which is gratefully appreciated.

References

1. Harmsworth, P. D. & Stevens, R., Microstructure of zirconia-yttria plasma-sprayed thermal barrier coatings. *J. Mater. Sci.*, **27** (1992) 616-24.
2. Adam, P. & Johner G., Thermal barrier coatings (TBC) in aircraft engines. Status and lines of development. In *Advanced Materials Research and Developments For Transport. Ceramic Coatings For Heat Engines*, eds I. Kvernes, W. J. G. Bunk and I. G. Wurm. Les Editions de Physique, Les Ulis, 1985, pp. 265-87.
3. LeLait, L., Alperine, S., Diot, C. & Mévrel, M., Thermal barrier coatings: microstructural investigation after annealing. *Mater. Sci. Eng.*, **A121** (1989) 475-82.
4. Kuroda, K., Hanagiri, S., Suginosita, M., Taira, H., Tamura, S., Saka, H. & Imura, T., Microstructural characterization of plasma-sprayed oxide ceramics. *ISIJ Int.*, **29** (1989) 234-9.
5. Wilms, V. & Herman, H., Plasma spraying of Al_2O_3 and Al_2O_3 - Y_2O_3 . *Thin Solid Films*, **39** (1976) 251-62.
6. Wilms, V. H. S., The microstructure of plasma sprayed ceramic coatings. PhD thesis, State University of New York, Stony Brook, NY, 1978.

7. Safai, S. & Herman, H., Plasma-sprayed materials. In *Treatise on Materials Science and Technology*, ed. H. Herman, Vol. 20. Academic Press, New York, 1981, pp 183–214.
8. Wang, H. G., Zhu, Y. M. & Herman, H., Structure of plasma-sprayed oxides in the MgO–Al₂O₃–SiO₂ system *J. Mater. Sci.*, **24** (1989) 4414–8.
9. Wang H. G. & Herman, H., Structure and properties of plasma-sprayed spinel. *Am. Ceram. Soc. Bull.*, **68** (1989) 97–102.
10. Gruetzner, H. & Weiss, H., Development of ceramic plasma-sprayed coatings against slag attack for the steel industry. In *Adv. Thermal Spraying: Proc. 11th Int. Thermal Spraying Conf.* Pergamon, New York, 1986, pp 349–57.
11. Cameron, W. E., Mullite: a substituted alumina. *Am. Mineral.*, **62** (1977) 747–55.
12. Guse, W. & Saalfeld, H., Das diffuse Beugungsbild von Mullit, 2 Al₂O₃·SiO₂. *Z. Krist.*, **143** (1976) 177–87
13. Saalfeld, H., The domain structure of 2:1 mullite (2 Al₂O₃·SiO₂). *N. Jb. Miner. Abh.*, **134** (1979) 305–16
14. Schneider, H. & Eberhard, E., Thermal expansion of mullite, *J. Am. Ceram. Soc.*, **73** (1990) 2073–6.
15. Aksay, I. A., Dabbs, D. M. & Sarikaya, M., Mullite for structural, electronic and optical applications *J. Am. Ceram. Soc.*, **74** (1991) 2358–68.
16. Butt, D. P., Mecholsky Jr, J. J., van Rodde, M. & Price, J. R., Effects of plasma sprayed ceramic coatings on the strength distribution of silicon carbide materials *J. Am. Ceram. Soc.*, **73** (1990) 2690–6.
17. Henne, R. & Weber, W., Progress in the development of high-temperature oxidation-preventing coatings for molybdenum by application of the low-pressure-plasma-spraying technique. *High Temp. High Pressures*, **18** (1986) 223–32.
18. Disam, J., Sickinger, A. & Wilms, V., The effect of the chamber and spraying parameters of the LPPS method on the structure of mullite coatings, *Conf. on Thermal Research and Applications*, Long Beach, CA, May 1990.
19. Levin, E. M., McMurdie, H. F. & Reser, M. K. (eds), *Phase Diagrams For Ceramists*, 3rd edn, The American Ceramic Society, Columbus, OH, 1974.
20. Doukhan, N., Doukhan, J. C. & Escaig, B., TEM study of high temperature precipitation in (Al₂O₃)_n MgO spinels *Mater. Res. Bull.*, **11** (1976) 125–34.
21. McPherson, R., Formation of metastable phases in flame- and plasma-prepared alumina. *J. Mater. Sci.*, **8** (1973) 851–8.
22. Dager, A., Fargeot, D. & Laval, J. P., Metastable phases of alumina. In *Mater. Res. Soc. Symp. Proc. Vol. 21*. The Materials Research Society, Pittsburgh, PA, 1984.
23. Chuanxian, D., Zatorski, R. A. & Herman, H., Oxide powders for plasma spraying — the relationship between powder characteristics and coating properties. *Thin Solid Films*, **118** (1984) 467–75.
24. McPherson, R. & Shafer, B. V., Interlamellar contact within plasma-sprayed coatings. *Thin Solid Films*, **97** (1982) 201–4.
25. Shi, K. S., Quian, Z. Y. & Zhuang, M. S., Microstructure and properties of sprayed ceramic coatings. *J. Am. Ceram. Soc.*, **71** (1988) 924–9.
26. Lutz, E. H., Microstructure and properties of plasma ceramics. *J. Am. Ceram. Soc.*, **77** (1994) 1274–80.
27. Hsueh, C. H., Some considerations of determination of residual stresses and Young's moduli in ceramic coatings. *J. Am. Ceram. Soc.*, **74** (1991) 1646–9.
28. Porter, D. A. & Easterling, K. E., *Phase Transformations in Metals and Alloys*. Van Nostrand Reinhold, New York, 1981.
29. Troeger, W. E., Optische Bestimmung der gesteinsbildenden Minerale, Teil 2. In *E. Schweizerbart'sche Verlagsbuchhandlung*. Naegle & Obermiller, Stuttgart, 1971.
30. Michel, D., Mazerolles, L. & Portier, R., Directional solidification in the alumina–silica system: microstructures and interfaces. In *Mullite and Mullite Matrix Composites*, eds S. Somiya, R. F. Davis and J. A. Pask. The American Ceramic Society, Westerville, OH, 1990.
31. Powell-Dogan, C. A. & Heuer, A. H., Microstructure of 96% alumina ceramics: I. Characterization of the as-sintered materials. *J. Am. Ceram. Soc.*, **73** (1990) 3670–6.
32. Merk, N. & Thomas, G., Structure and composition characterization of submicronic mullite whiskers. *J. Mater. Res.*, **6** (1991) 825–34.
33. Kriven, W. M. & Pask, J. A., Solid solution range and microstructures of melt-grown mullite. *J. Am. Ceram. Soc.*, **66** (1983) 649–54.
34. Pask, J. A., Critical review of phase equilibria in the Al₂O₃–SiO₂ system. In *Ceramic Transactions Vol. 6: Mullite and Mullite Matrix Composites*, eds S. Somiya, R. F. Davis and J. A. Pask. The American Ceramic Society, Westerville, OH, 1990, pp. 1–13.
35. Wefers, K. & Misra, C., Oxides and hydroxides of aluminum, Alcoa Technical Papers No. 19, Aluminum Company of America, Pittsburgh, PA, 1987.
36. Wilson, S. J., Phase transformations and development of microstructure in boehmite-derived transition aluminas. *Br. Cer. Soc. Proc.*, **28** (1979) 281–94.
37. Morrissey, K. J., Czanderna, K. K., Merrill, R. P. & Carter, C. B., Transition alumina structures studied using HREM. *Ultramicroscopy*, **18** (1985) 379–86.
38. McPherson, R., On the formation of thermally sprayed alumina coatings. *J. Mater. Sci.*, **15** (1980) 3141–9.
39. Ostwald, W., Studien ueber die Bildung und Umwandlung fester Koerper I. Abhandlung: Uebersaettigung und Ueberkaltung. *Z. Physik. Chemie*, **22** (1897) 289–330.
40. Lewis, M. H., Defects in spinel crystals grown by the Verneuil process. *Phil. Mag.*, **14** (1966) 1003–18.
41. Mitchell, T. E., Lagerloef, K. P. D. & Heuer, A. H., Dislocations in ceramics. In *Dislocations and Properties of Real Materials: Proc. 5th Anniversary of the Concept of Dislocation in Crystals*. The Institute of Metals, London, 1985.
42. Amelingckx, S. & van Landuyt, J., Contrast effects at planar interfaces. In *Electron Microscopy in Mineralogy*, ed. H. R. Wenk. Springer, Berlin, 1976, 68–112.
43. Glossop, A. B. & Pashley, D. W., The direct observation of abt-phase domain boundaries in ordered copper–gold (CuAu) alloy. *Proc. Roy. Soc.*, **A250** (1959) 132–46.
44. Hirsch, P., Howie, A., Nicholson, R. B., Pashley, D. W. & Whelan, M. J., *Electron Microscopy of Thin Crystals*. Robert E. Krieger Publishing Company, 1977.

Foreword

The name of mullite comes from the Island of Mull in Western Scotland, where it was first found in nature. It was in 1924 that Bowen and Greig published their basic work on the occurrence of mullite. Bowen and Greig stated: 'Since this paper was written we have discovered crystals of the 3:2 compound in natural rocks from the Island of Mull. We propose the name mullite to designate the compound in a forthcoming paper of the *Journal of the Washington Academy of Science* where this natural occurrence of the mineral is described.'

Because of its high temperature–low pressure formation conditions, mullite occurs only very rarely in nature. It sometimes is found in high temperature metamorphosed rocks of the sanidinite facies and at the contact of alumina-rich sedimentary rocks with basaltic melts (so-called buchites or sillimanite buchites). Mullite formation was also described in hornfelses (porcellanite) which develop on the contact of bauxite with olivine dolerite intrusions.

In spite of its rareness in natural rocks, mullite is perhaps the most important phase in the field of traditional ceramics. This can be explained by its occurrence as a main constituent in pottery, porcelains, sanitary ceramics, and structural clay products such as building bricks, pipes, tiles, and in refractories. Based on the importance of mullite for technical refractory and ceramic products, in 1956 Robert B. Sosman made a rather poetic statement about mullite in comparing a journey to

the Isle of Mull with a pilgrimage. Though our less sentimental generation may have problems seeing things in a similar way, many of us agree with Sosman that mullite is one of the most important ceramic phases.

Beside its value for conventional ceramics, mullite has become a strong candidate material for advanced structural and functional ceramics in recent years. The use of mullite has, e.g. been discussed for high temperature engineering materials, electronic packaging materials, optical materials, porous materials and as a matrix for ceramic composites. The reasons for this development are the outstanding thermo-mechanical properties of mullite:

- Low thermal expansion
- Low thermal conductivity
- Excellent creep resistance
- Good chemical stability
- Oxidation resistance

Congresses and workshops especially dedicated to crystal chemistry, processing, characterization and properties of mullite took place in Tokyo, Japan, in 1987, and in Seattle, USA, in 1990. The international conference in Irsee 1994 was the third to be held on mullite. This workshop brought together basic science researchers with material scientists, and with engineers occupied with the production of technical compounds from all over the world (Fig. 1).

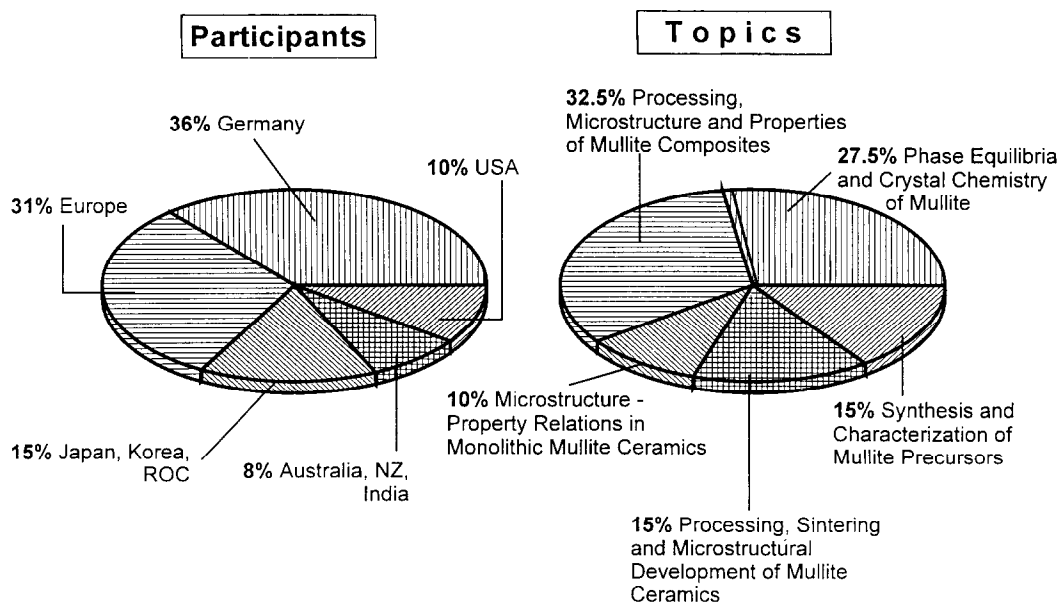


Fig. 1. International Mullite Workshop in Irsee 1994 (Mullite '94). Participants (total number: 52) and topics of scientific sessions.

Topics of the conference were:

- Phase equilibria and crystal chemistry of mullite
- Synthesis and characterization of mullite precursors
- Processing, sintering and microstructural development of mullite ceramics
- Microstructure–property relations in monolithic mullite ceramics
- Processing, microstructure and properties of mullite composites.

The Mullite '94 Workshop provided new, and some most interesting results, which often were discussed late into the night. I believe that most participants will agree that this was a very success-

ful meeting, which was also due to the beautiful environment and the relaxed atmosphere in the old Swabian 'Kloster Irsee'.

On behalf of the participants I gratefully acknowledge the indispensable financial support of the United States Air Force European Office of Aerospace Research and Development (EOARD) and the German Aerospace Research Establishment (DLR). I also thank the staff of the Institute for Materials Research of the DLR, especially Dr B. Saruhan, Mr J. Hermanns and W. Luxem for their help in organizing the meeting.

**H. Schneider, German Aerospace Research
Establishment (DLR), Institute for Materials
Research, 51147 Köln, Germany**

Importance of Starting Materials on Reactions and Phase Equilibria in the Al_2O_3 – SiO_2 System

Joseph A. Pask

Department of Materials Science & Mineral Engineering, University of California, Berkeley, CA 94720, USA

(Accepted 22 July 1995)

Abstract

Disagreements in the high Al_2O_3 side of the phase equilibrium diagram for the Al_2O_3 – SiO_2 system have been reported consistently. Some of the disagreements are significantly different and have been reported many times. It is thus necessary to eliminate experimental errors as being primarily responsible. An examination and analysis of the starting materials and the development of a fundamental understanding of the chemical reactions that take place provide an explanation for the reported differences. The objective of this report is to briefly review the disagreements and correlate them with the starting materials and the associated solid-state reactions that occur in reaching stable or metastable equilibrium.

1 Literature Review

A review of a chronological assemblage of selected papers brings out the disagreements. In 1909 Shepherd *et al.*¹ published the first phase equilibrium diagram which indicated that sillimanite ($\text{Al}_2\text{O}_3 \cdot \text{SiO}_2$, 62.92 wt% Al_2O_3) was the only binary compound in the Al_2O_3 – SiO_2 system; this compound was subsequently shown to be metastable at standard conditions of temperature and pressure and stable only at high pressures. In 1924, Bowen and Greig^{2,3} published the first phase equilibrium at standard conditions which showed that mullite ($3\text{Al}_2\text{O}_3 \cdot 2\text{SiO}_2$, 71.80 wt% Al_2O_3) was the only compound and that it melted incongruently at 1828°C with no solid solution range determined (Fig. 1). In 1950 and 1951, Bauer *et al.*^{4,5} grew a single crystal of mullite containing about 83 wt% Al_2O_3 ($3\text{Al}_2\text{O}_3$ – SiO_2) by the flame fusion process. These experiments raised doubts as to the reported incongruent melting of mullite.

In 1951, Toropov and Galakhov⁶ heated mixtures of alumina gel and quartz; the mullite that formed melted congruently at about 1900°C. In

1954, Shears and Archibald⁷ reported mullite with a solid solution range from $3\text{Al}_2\text{O}_3 \cdot 2\text{SiO}_2$ to $2\text{Al}_2\text{O}_3 \cdot \text{SiO}_2$ (77.24 wt% Al_2O_3) which melted congruently at approximately 1810°C. In 1960, Welch⁸ supported the proposed solid solution range and incongruent melting. In 1958, Trömel *et al.*⁹ showed some data mostly in support of congruent melting behaviour. However, they also showed data generally indicating that in short time runs no corundum was obtained when it should have been found with incongruent melting, but that increasing the time caused the corundum to appear.

In 1962, Aramaki and Roy¹⁰ showed mullite with a solid solution range of 71.8–74.3 wt% Al_2O_3 and a congruent melting point that was supported by the position of the α - Al_2O_3 liquidus (Fig. 1). They also determined that the solid solution range was extended to 77.3 wt% Al_2O_3 under metastable conditions which is not shown in the figure. They employed samples prepared from dry mixtures of reagent grade α - Al_2O_3 and powdered fused SiO_2 glass. The samples were held at temperature and quenched in mercury or water.

In 1972, Davis and Pask,¹¹ using semi-infinite diffusion couples of sapphire (α - Al_2O_3) and fused SiO_2 at temperatures up to 1750°C, determined the solid solution range of mullite as 71.0–74.0 wt% Al_2O_3 . In 1975, Aksay and Pask¹² extended these experiments to higher temperatures and reported an α - Al_2O_3 liquidus profile (Fig. 2) that was similar to that of Bowen and Greig^{2,3} with a peritectic at ~55 wt% Al_2O_3 which supported mullite as having an incongruent melting point. Single crystals of mullite were grown by the Czochralski technique in 1974 by Guse¹³ and Guse and Mateika¹⁴ of the 2:1 type instead of the 3:1 type obtained by the flame fusion process. In 1980, Shindo¹⁵ also grew single crystals of the 2:1 type by the 'slow cooling float zone method' but showed incongruent melting.

In 1983, Prochazka and Klug¹⁶ showed a solid solution range that shifted to higher Al_2O_3 contents with increase in temperature from 1600°C up

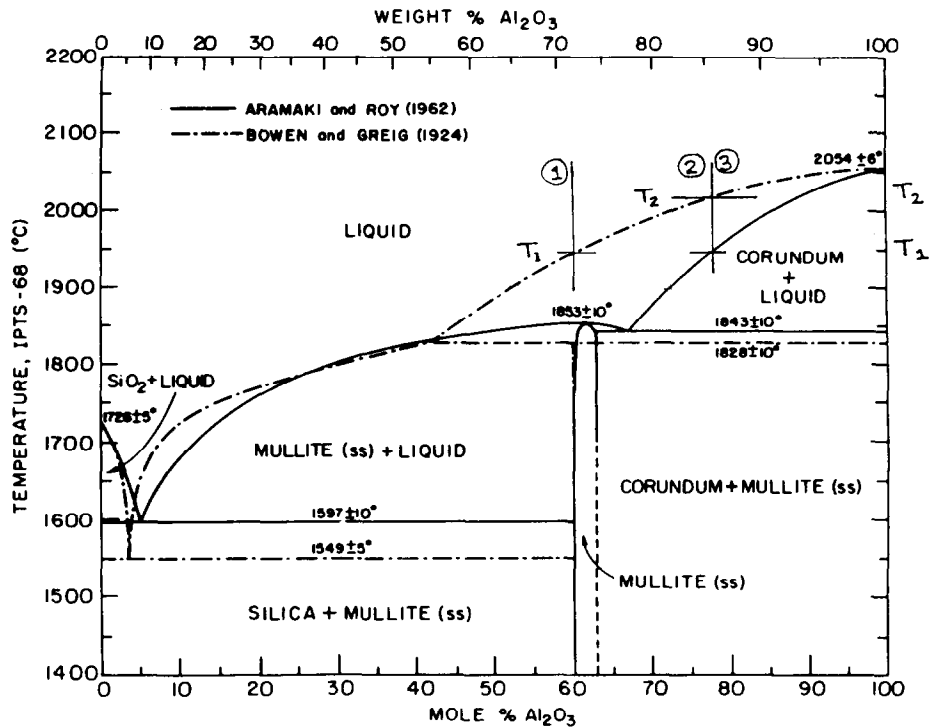


Fig. 1. Superimposed $\text{SiO}_2\text{-Al}_2\text{O}_3$ phase equilibrium diagrams as determined by Bowen and Greig^{2,3} and Aramaki and Roy.¹⁰

to about 1890°C, where the mullite reached the 2:1 composition (77.2 wt% Al_2O_3) and melted congruently since the peritectic composition had a slightly higher Al_2O_3 content. In 1987, Klug *et al.*¹⁷ modified the diagram wherein the $\alpha\text{-Al}_2\text{O}_3$ liquidus peritectic composition shifted to a slightly lower Al_2O_3 content than 77.2 wt% Al_2O_3 which technically indicated that the mullite melted incongruently. The latter diagram is included in Fig. 2. In both papers, homogeneous aluminosilicate powders produced by sol-gel processing from $\text{AlO}(\text{OH})$ and tetraethyl orthosilicate (TEOS) were used.

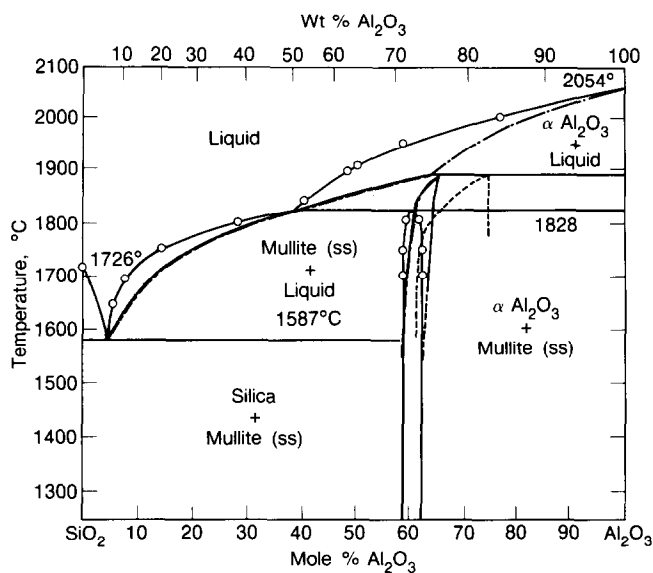


Fig. 2. Phase equilibrium diagrams by Klug *et al.*¹⁷ (dot-dash line) and Aksay and Pask¹² (light solid line) superimposed. Nature of reported solid solution regions for mullite illustrated.

Many other studies on this system have been published. Sufficient experimental support is available for either opinion. It is thus not necessary to review them in detail. More extensive discussions of the phase equilibria are presented in several other review papers.¹⁸⁻²¹ The diagrams shown in Figs 1 and 2 will suffice for further discussions.

2 Starting Materials

Various starting materials have been used to provide the Al_2O_3 and SiO_2 molecules for a desired composition. In the earlier studies Al_2O_3 was introduced primarily as $\alpha\text{-Al}_2\text{O}_3$ powders of controlled particle size. It was mixed with fine ground fused SiO_2 , quartz or cristobalite. A given mixture was normally heated above the liquidus temperature until it formed a homogeneous liquid phase, lowered to and held at the test temperature, and quenched. The homogenization step is critical since $\alpha\text{-Al}_2\text{O}_3$ does not react rapidly because of the sluggishness of the liquid due to some covalency and high bond strength of $\alpha\text{-Al}_2\text{O}_3$. On the other hand, if $\alpha\text{-Al}_2\text{O}_3$ is melted completely, then nucleation and precipitation also may not occur easily on cooling especially when the aluminosilicate liquid does not become saturated with Al_2O_3 molecules. Kinetic problems then arise.

More recent studies utilized starting materials prepared chemically from alkoxides and sol-gels so that single-phase and diphasic gels were attained, i.e. no Al_2O_3 is introduced as $\alpha\text{-Al}_2\text{O}_3$. Any segre-

gation or clustering of like atoms in single-phase gels could be critical since they can lead to nucleation and formation of colloidal particles, i.e. diphasic gel mixtures. Single-phase gels have also been called polymeric gels.^{22,23} The basic objective of this approach is to attain or approach homogeneous mixing on an atomic or molecular basis. Sacks *et al.*²⁴ have reviewed the literature on the preparation of starting materials.

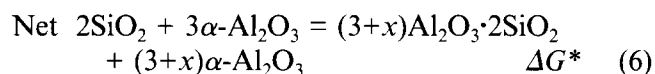
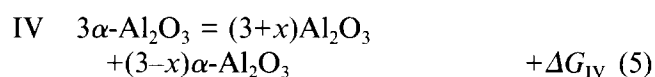
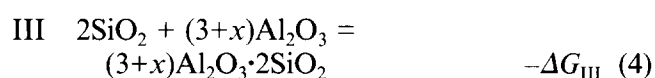
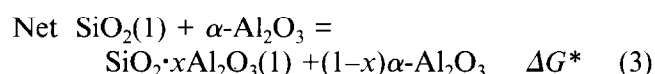
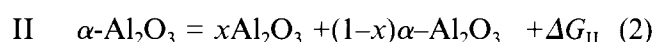
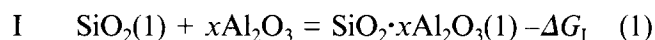
3 Mechanisms of Reactions

The critical factor in determining the nature of the solid-state reactions that occur in reaching equilibrium compositions at elevated temperatures in this system is the presence or absence of α - Al_2O_3 in the starting materials as a source of Al_2O_3 molecules. The α - Al_2O_3 particles react with SiO_2 at their interfaces to form mullite at temperatures below about 1828°C by interdiffusion of the cations through the forming mullite, which is a slow process. This kinetic effect could be counteracted in powder mixtures by reducing the particle size of α - Al_2O_3 and thereby increasing the overall rate by increasing the interfacial area. At temperatures above 1828°C mullite does not form, and α - Al_2O_3 is dissolved in the SiO_2 liquid to form aluminosilicate liquids. The most reactive precursors are those chemically prepared, wherein homogeneous atomic mixtures are formed in the absence of α - Al_2O_3 as a constituent. In this case the reaction rates are considerably faster.

Davis and Pask¹¹ developed the technique of using diffusion couples of sapphire single crystals and fused SiO_2 up to 1750°C to obtain kinetic data on mullite formation as well as equilibrium compositions. Aksay and Pask¹² extended the technique to higher temperatures. Analysis of polished cross-sections at a number of temperatures for Al and Si with an electron microprobe provided data for calculating concentration profiles for Al_2O_3 and SiO_2 and determining equilibrium compositions at the interfaces. It was determined that the reaction rates at the interfaces are faster than the diffusion rates away from them. The composition at a given temperature thus remained constant at a given interface and maintained equilibrium. Below about 1828°C and down to about 1634°C mullite grew at the α - Al_2O_3 / SiO_2 interface and the resulting compositions at the liquid/mullite and mullite/ α - Al_2O_3 interfaces were also at equilibrium. The fact that the Al_2O_3 content of about 55 wt% at the peritectic at 1828°C remains constant and is less than that of mullite theoretically indicates incongruent decomposition of mullite in the presence of α - Al_2O_3 .

It is now necessary to determine the nature of the driving forces for the solid-state reactions occurring at the interfaces of the α - Al_2O_3 / SiO_2 diffusion couples since they determine the composition of the α - Al_2O_3 liquidus. Experimental temperatures above 1828°C will be considered first. SiO_2 dissolves Al_2O_3 . The driving force is the reduction of the internal free energy of the fused SiO_2 as Al_2O_3 molecules are incorporated into the liquid's atomic structure according to step I (Eqn (1)). The Al_2O_3 molecules are obtained by surface dissociation of crystalline Al_2O_3 by breaking bonds for which energy is required according to step II (Eqn (2)). The required energy is provided by the release of internal free energy by the siliceous liquid as it incorporates Al_2O_3 molecules into its structure. Summation of these step reactions above 1828°C results in the observed net reaction (Eqn (3)).

At experimental temperatures below 1828°C mullite forms at the interface. Energetically it appears more favourable to form mullite than to continue dissolving α - Al_2O_3 , i.e. $\Delta G_{III} > \Delta G_I$ (Eqn (4) > Eqn (1)). ΔG_{III} is greater than ΔG_{IV} (Eqn (5)) which results in the net reaction (Eqn (6)) being negative and the determining occurrence of the reaction. If $\Delta G_{IV} > \Delta G_{III}$, then the net ΔG^* is positive and the reaction will not take place.



With the formation of mullite two interfaces have to be considered: liquid/mullite and mullite/ α - Al_2O_3 . In this case the α - Al_2O_3 atomic structure does not change with temperature but the SiO_2 content of the mullite decreases slightly at temperatures approaching dissociation. The bulk structures and compositions along the interfaces at a given temperature are at equilibrium as represented in Eqns (4), (5) and (6), and provide data for the phase equilibrium diagram.

The relative values for the free energies for the step reactions (1) plus (2) and (4) plus (5) determine the amount of solution and compositions. As the solution proceeds, ΔG_I and ΔG_{III} become

less negative until ΔG^* becomes zero in both cases with the establishment of equilibrium for the test temperature. With continuation of the reaction, when large quantities of the reactants are present, the equilibrium compositions are maintained at the interfaces because the reaction rates are faster than the diffusion rates. In an experimental study, the constancy of the compositions at the interface were verified.^{11,12} It is evident that these reactions do not continue when one of the reactants is consumed.

It should be further evident that at these points the chemical potentials for Al_2O_3 and SiO_2 are equal in the silicate liquid and the mullite but neither phase is necessarily saturated with Al_2O_3 molecules. The limiting factor in these cases is established by the bond strength of the $\alpha\text{-Al}_2\text{O}_3$ atomic structure, which determines the amount of energy necessary to dissociate an Al_2O_3 molecule (Eqns (2) and (5)). Thus, if another source of Al_2O_3 is used whose atomic bond strength is weaker, i.e. ΔG_{II} and ΔG_{IV} are smaller, then the aluminosilicate liquid could dissolve more Al_2O_3 molecules before equilibrium is reached or until the liquid structure itself becomes saturated with Al_2O_3 molecules. In such cases, the liquid is supersaturated relative to $\alpha\text{-Al}_2\text{O}_3$, but it tends to retain the dissolved Al_2O_3 molecules in the absence of saturation and $\alpha\text{-Al}_2\text{O}_3$ nuclei or particles.

In the reported studies, the maximum availability of Al_2O_3 molecules is provided by single-phase sol-gel mixtures wherein essentially atomic homogeneity is present in the absence of any clusters or colloidal assemblages. Compounds can form by rearrangement of atoms and molecules or by short-range diffusion. In the absence of strong $\alpha\text{-Al}_2\text{O}_3$ bonds, more Al_2O_3 molecules can become available for the mullite composition which can vary within the solid solution range with temperature.

The alumina-silica system is subject to significant indications of metastability based on equally verified equilibria experiments. At present, because of lack of adequate thermodynamic data, it is difficult to unequivocally claim that one of the experimentally determined phase equilibria diagrams is stable and others are metastable. It is thus more logical to differentiate them on the basis of the nature of the critical starting materials. In this system that material is alumina. It has been shown that the nature of the most controversial equilibria are dependent on the presence or absence of $\alpha\text{-Al}_2\text{O}_3$ as the starting material for a source of Al_2O_3 molecules. Thus, the diagrams can be differentiated on this basis. The earliest reported diagrams were derived with the use of fine-ground $\alpha\text{-Al}_2\text{O}_3$ or forms of alumina, e.g. $\gamma\text{-Al}_2\text{O}_3$, that

readily converted to $\alpha\text{-Al}_2\text{O}_3$ before they were completely reacted. Silica was added as fine-ground, fused or crystalline SiO_2 . Later diagrams were determined with sol-gel or alkoxide type of starting materials. In these cases the objective was to introduce the Al_2O_3 molecules on the basis of a homogeneous atomic mixture.

In summary, the significance of the types of starting materials used is that the bond strengths of the different types are dependent on their atomic and electronic structures. $\alpha\text{-Al}_2\text{O}_3$ has strong bonds requiring a relatively large amount of energy for release of Al_2O_3 molecules in comparison with the energy requirement for dissociation from a sol-gel type of starting material. Silica has a high degree of covalency which makes restructuring more difficult. Both states lead to difficulties affecting the kinetics of nucleation and precipitation of $\alpha\text{-Al}_2\text{O}_3$. Another factor that leads to slow kinetics is the nature of the structure and bonding of aluminosilicate liquids, which at present are not completely understood.

An illustration of the above discussions can be made by use of Fig. 1. When the $\alpha\text{-Al}_2\text{O}_3/\text{SiO}_2$ diffusion couple is held at 1950°C , the equilibrium liquid composition (about 72 wt% Al_2O_3) at the interface is indicated by pt. 1 which provides a point on the $\alpha\text{-Al}_2\text{O}_3$ liquidus of Bowen and Greig's^{2,3} diagram. Aramaki and Roy,¹⁰ on the other hand, used dried mixtures of reagent-grade activated $\alpha\text{-Al}_2\text{O}_3$ and powdered SiO_2 glass, homogenized them at temperatures above the 'high temperature liquidus' so that all of the $\alpha\text{-Al}_2\text{O}_3$ particles were dissolved to form an aluminosilicate liquid, and lowered the temperature to the test temperature. They found that a composition equivalent to pt. 2 (about 86 wt% Al_2O_3) was in equilibrium with $\alpha\text{-Al}_2\text{O}_3$ at 1950°C .

At this point it is important to consider, on the basis of basic principles, the general behaviour of aluminosilicate liquids with changes in composition and temperature at standard pressures. Mixtures of various condensed phases equivalent to aluminosilicate liquid compositions undergo complete melting on raising the temperature above the liquidus temperatures. The atomic and molecular homogeneity of the liquid, if not present, would be expected to increase with increase in temperature and/or time. With decrease in temperature some clustering would be expected. On dropping below the liquidus with saturation, nuclei formation would be started. Their type and rate of actual formation would be controlled by kinetic factors and their composition. On cooling liquids with more than 55 wt% Al_2O_3 too rapidly, $\alpha\text{-Al}_2\text{O}_3$ nuclei may not form easily because the liquid is not saturated with Al_2O_3 molecules.

Dropping below the melting temperature of mullite, the liquid structure and composition are such that it becomes saturated with mullite which precipitates.

This behaviour can be illustrated by experiments with a series of starting mixtures with an increasing amount of Al_2O_3 from about 55 wt%.²⁵ The mixtures are first homogenized above the liquidus temperature and then cooled rapidly or quenched. Mixtures with increasing amounts of Al_2O_3 up to about 84 wt% do not easily nucleate α - Al_2O_3 and mullite is precipitated whose Al_2O_3 content is higher than that of the starting mixture, with which it converges at about 83 wt%. With still higher amounts of Al_2O_3 in the starting mixture, liquid becomes saturated with Al_2O_3 and the first precipitates are spherulites of α - Al_2O_3 followed by mullite with a lower Al_2O_3 content. The coprecipitates of mullite have about 77 wt% Al_2O_3 , which corresponds to $2Al_2O_3 \cdot SiO_2$ mullite. These results indicate that at 1950°C the aluminosilicate liquids become saturated with Al_2O_3 at a total content of about 83 wt% Al_2O_3 .

X-ray diffraction analyses of mullites by Kriven and Pask²⁶ showed that mullite with increasing amounts of Al_2O_3 up to about 77 wt% Al_2O_3 saturated the Si sites with Al atoms. Further increase of Al_2O_3 up to about 83 wt% resulted in the formation of a crystallographic superstructure superimposed on the mullite structure. These Al_2O_3 values for mullite supported the Al_2O_3 content of about 83 wt% for the single crystal grown by the flame fusion process,^{4,5} and about 77 wt% for the crystal grown at a constant temperature by the Czochralski technique.^{13,14}

The experimental variations in the Al_2O_3 content of mullite indicate that structures and bond strengths of the mullite are critically dependent on the reaction environment. Competition for Al_2O_3 molecules between the aluminosilicate structures and Al_2O_3 when present as part of the reacting mixture, as pointed out above, determines the composition variabilities that have been reported in the literature. Use of chemically-prepared starting mixtures to give more homogeneous atomic structures also introduces some variability because the atomic structure of the amorphous mixtures are expected to change with increasing temperature and changing conditions. The development of better homogeneity could result in increasing availability of Al_2O_3 molecules from the liquid structure. This behaviour would account for the increasing Al_2O_3 content of the mullite with temperature as seen in the diagram of Klug *et al.*¹⁷ shown in Fig. 2. It is thus supported experimentally that the maximum content of Al_2O_3 in the mullite structure is about 77 wt%. In the presence

of α - Al_2O_3 at the time of mullite growth, however, the maximum amount is about 74 wt% because of the lesser availability of Al_2O_3 molecules. The mullites with Al_2O_3 contents above 77 wt% up to about 84 wt% appear only on quenching melts from above the liquidus temperature. The Al_2O_3 molecules in excess of the total available Si/Al atomic sites are accommodated by a crystallographic superstructure as pointed out by Kriven and Pask.²⁶ At about 84 wt% Al_2O_3 the aluminosilicate structure becomes saturated with Al_2O_3 molecules. Further additions cause the primary precipitation of Al_2O_3 spherulites on cooling.

3.1 Effect of rate of cooling

There have been several definitive experiments indicating the importance of kinetics in determining the nature of the phase equilibria with different cooling rates.¹² Three diffusion couples of sapphire/fused SiO_2 were heated together at 1900°C for 15 min. They were cooled together by turning off the furnace and directing the flow of a stream of He gas onto the assembly of sealed crucibles so that small differences existed in their rate of cooling.

Figure 3 shows polished cross-sections perpendicular to the interfaces of the three specimens, with the sapphire on the bottom of the photographs. The specimen in photo A, which was cooled the fastest, shows precipitates of mullite; the specimen in photo C, which was cooled the slowest, shows precipitates of Al_2O_3 ; and the photo B specimen, which was cooled at an intermediate rate, shows large mullite precipitates with small precipitates of Al_2O_3 in the glass phase between. Average diffusion profiles into the fused SiO_2 established at 1900°C were identical for all three specimens with an overall composition of 63 wt% Al_2O_3 in the aluminosilicate at the interfaces. This composition liquid was in equilibrium with Al_2O_3 but its structure was not saturated with Al_2O_3 molecules as previously described. In photo C, the cooling rate was slow enough so that α - Al_2O_3 nuclei formed at the interface, leading to the formation of elongated α - Al_2O_3 crystals. In photo A, with a faster cooling rate, sufficient time for rearrangement and assembly to form α - Al_2O_3 nuclei and crystals was not available before the temperature was reached at which the liquid was saturated with mullite, leading to the nucleation and growth of the elongated mullite crystals. This behaviour supports the concept that α - Al_2O_3 does not nucleate easily unless the aluminosilicate atomic structure becomes saturated with Al_2O_3 molecules.

3.2 Mullite peritectic reaction

Another significant experiment is one that showed



Fig. 3. Microstructures of diffusion zones in couples of sapphire (bottom) and fused silica annealed at 1900°C for 15 min and (A) quenched, (B) cooled at a relatively moderate rate and (C) cooled relatively slowly. Precipitates in diffusion zone in (A) are mullite (light grey), in (B) alumina (light grey needles) and mullite (fine precipitates between alumina needles) and in (C) alumina (light grey needles; precipitates along interface in (B) and (C) are also alumina).

the formation of mullite by a peritectic reaction.¹² A mixture containing 71.8 wt% Al_2O_3 was homogenized in a sealed Mo crucible at 1950°C for 460 min, cooled to 1750°C in 30 min, annealed at 1750°C for 29.4 days, and quenched. A polished cross-section is shown in Fig. 4. The light grey crystals are $\alpha\text{-Al}_2\text{O}_3$ surrounded by medium grey growths of mullite, with a dark grey aluminosilicate glass between the mullite growths. The concentration profiles across the mullite growths correspond to those obtained in $\alpha\text{-Al}_2\text{O}_3/\text{SiO}_2$ diffusion couples at 1750°C. The reactions at the interface are fast and maintain equilibrium compositions for 1750°C at the interfaces. The overall reaction is slow because the rate-determining step is interdiffusion through the forming mullite, which is slow.

The formation of $\alpha\text{-Al}_2\text{O}_3$ crystals which participate in the formation of mullite in a melt of this composition clearly indicates that mullite melts incongruently. If mullite had formed directly from the melt and thus melted congruently, then it would have been impossible to form as a stable phase under the above conditions. It could also be pointed out that if Bowen and Greig,^{2,3} using $\alpha\text{-Al}_2\text{O}_3$ particles as part of their starting materials, did not completely dissolve it into their starting mixture and performed experiments at about 70 wt% Al_2O_3 and temperatures of about 1900°C, $\alpha\text{-Al}_2\text{O}_3$ could not have persisted under these conditions if mullite melted congruently. Concentration profile discontinuities across the phase

boundaries provide very accurate information about the stable composition range of the phase fields.

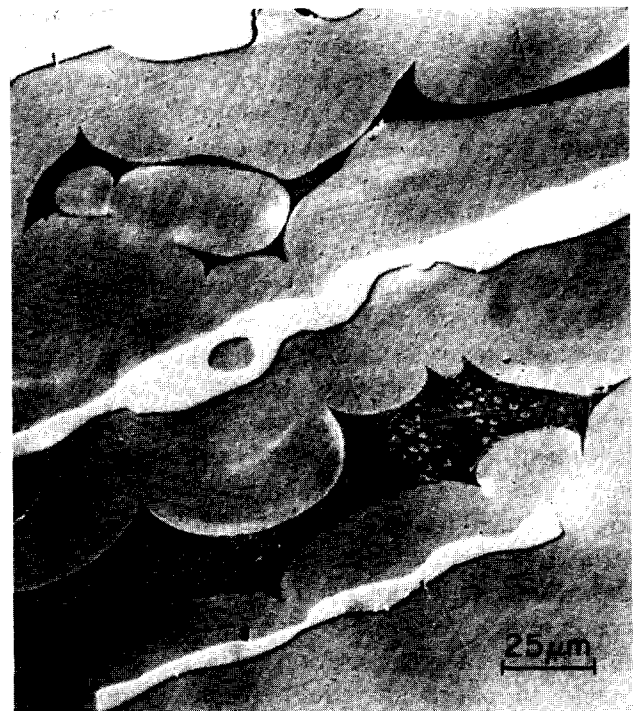


Fig. 4. Microstructure of specimen containing 71.8 wt% Al_2O_3 held at 1950°C for 7.7 h, cooled to 1750°C in 30 min, annealed at 1750°C for 29.4 days, and quenched to room temperature. Light grey precipitates are alumina completely surrounded by layer of mullite. Dark grey portions between mullite layers are glass containing precipitates of mullite formed on quenching. The microstructure formed during the heating schedule indicates a peritectic reaction.

4 Summary and Conclusions

A critical study of the mechanisms and kinetics of the solid-state chemical reactions that take place with different starting materials provides an explanation for the differences that have been reported in the high alumina region of the phase equilibria diagrams for the Al_2O_3 - SiO_2 system. Since the equilibria are formed by reactions, the bond strengths, atomic structures and free energies of the participating phases are critical. The nature of the reactions and their driving forces are the principal factors. Both the source of Al_2O_3 molecules and the nature of the aluminosilicate liquid structures are important in this system.

The Al_2O_3 sources have been either as α - Al_2O_3 particles or chemically-prepared sol-gel aluminosilicates or alkoxides. The α - Al_2O_3 has a high negative free energy of formation. Thus, the energy necessary to break its bonds to provide Al_2O_3 molecules is relatively high. This energy is provided by the aluminosilicate liquid since its free energy is lowered by incorporating Al_2O_3 molecules into its atomic structure. A thermodynamic balance is reached when the free energy change for the overall reaction becomes zero and the chemical potentials for each of the components are equal in both participants at the reacting interface. The source of the phase equilibria differences is the fact that, at this point, equilibria are reached because of insufficient energy to make more Al_2O_3 molecules available. The aluminosilicate liquid at this point, thus, does not become saturated with Al_2O_3 molecules.

In the case of the sol-gel source of Al_2O_3 , the bond strengths are weaker and Al_2O_3 molecules are more readily available. Thus, the aluminosilicate liquid becomes saturated, or near-saturated, with Al_2O_3 molecules. The additional significance of this fact is that in intermediate Al_2O_3 compositions the liquid can be saturated with Al_2O_3 but supersaturated with respect to α - Al_2O_3 . Because of this situation and the high covalency of its bonding, nucleation and growth of α - Al_2O_3 are sluggish in the aluminosilicate liquids.

Consequently, there are two phase equilibria diagrams for the Al_2O_3 - SiO_2 system. The controlling factor is whether α - Al_2O_3 is present or absent throughout the reactions leading to the steady or equilibrium state. In the presence of α - Al_2O_3 , the peritectic composition is 55 wt% Al_2O_3 , mullite corresponds to the 3:2 type and melts incongruently at 1828°C. Its solid solution range remains essentially constant with temperature. In the absence of α - Al_2O_3 , mullite corresponds to the 2:1 type and melts congruently at 1890°C; its solid solution range increases in Al_2O_3 up to 77 wt%

Al_2O_3 but would be expected to vary with the nature of the chemically-prepared source of Al_2O_3 . The 3:1 type of mullite is only formed on quenching homogenized aluminosilicate liquids from above the high temperature α - Al_2O_3 liquidus. This behaviour is the basis of a third phase equilibrium diagram for the Al_2O_3 - SiO_2 system which has not been extensively studied.

Aramaki and Roy²⁷ also performed experiments with ternary mixtures composed of additions of MgO or CaO to Al_2O_3 and SiO_2 . These were used to support the arguments that mullite melted congruently on the basis of the position of the boundary between the primary fields of mullite and α - Al_2O_3 in the corresponding ternary phase equilibrium diagrams. However, since the starting materials were first completely homogenized above the liquidus temperatures, the equilibrium phase compositions were obtained in the absence of α - Al_2O_3 as a starting material.

In summary, the controlling factor in determining the nature of the phase equilibrium diagram for the Al_2O_3 - SiO_2 system is the presence or absence of α - Al_2O_3 during the reactions leading to stable or metastable equilibrium. In the presence of α - Al_2O_3 , the higher temperature α - Al_2O_3 liquidus represents an atomic structure thermodynamically in equilibrium with α - Al_2O_3 but not saturated with Al_2O_3 molecules. In the absence of α - Al_2O_3 as a source of Al_2O_3 molecules, the lower temperature α - Al_2O_3 liquidus represents an atomic structure that is saturated with Al_2O_3 molecules. On cooling, α - Al_2O_3 nucleates and precipitates from liquids when they become saturated with Al_2O_3 molecules. The region between the two liquidus lines represents liquid structures that are supersaturated with respect to α - Al_2O_3 . In order to further differentiate the two conditions, the phase equilibrium diagram derived in the presence of α - Al_2O_3 as one of the starting materials could be identified as the α - Al_2O_3 - SiO_2 system; and in the absence of α - Al_2O_3 , the phase equilibrium diagram could be identified as the Al_2O_3 - SiO_2 system.

References

1. Shepherd, E. S., Rankin G. A. & Wright, W., *Am J. Sci.*, **28** (1909) 301.
2. Bowen, N. L. & Greig, J. W., *J. Am. Ceram. Soc.*, **7** (1924) 238.
3. Bowen, N. L. & Greig, J. W., *J. Am. Ceram. Soc.*, **7** (1924) 410.
4. Bauer, W. H. & Gordon, I., *J. Am. Ceram. Soc.*, **33** (1950) 140.
5. Bauer, W. H. & Gordon, I., *J. Am. Ceram. Soc.*, **34** (1951) 250.
6. Toropov, N. A. & Galakhov, F. Y., *Dokl. Akad. Nauk. SSSR*, **78** (1951) 299.
7. Shears, E. C. & Archibald, W. A., *Iron Steel (London)*, **27** (1954) 26.

8. Welch, J. H., *Nature (London)*, **186** (4724) (1960) 545.
9. Trömel, S., Obst, K. H., Konopicky, K., Bauer, H. & Patzk, L., *Ber. Deut. Keram. Ges.*, **34** (1958) 108.
10. Aramaki, S. & Roy, R., *J. Am. Ceram. Soc.*, **45** (1962) 229.
11. Davis, R. F. & Pask, J. A., *J. Am. Ceram. Soc.*, **55** (1972) 525.
12. Aksay, I. A. & Pask, J. A., *J. Am. Ceram. Soc.*, **58** (1975) 507.
13. Guse, W., *J. Crystal Growth*, **26** (1974) 151.
14. Guse, W. & Mateika, D., *J. Crystal Growth*, **26** (1974) 237.
15. Shindo, I., D.Sc. Thesis, Tohoku University, Japan, 1980.
16. Prochazka, S. & Klug, F. J., *J. Am. Ceram. Soc.*, **66** (1983) 874.
17. Klug, F. J., Prochazka S. & Doremus, R. H., *J. Am. Ceram. Soc.*, **70** (1987) 750.
18. Davis, R. F. & Pask, J. A., *High Temperature Oxides, Part IV*, ed. A. M. Alper, 1971, p. 37.
19. Pask, J. A., *Mullite and Mullite Matrix Composites*, eds S. Somiya, R. F. Davis & J. A. Pask, Am. Ceram. Soc. Trans., Vol. 6, 1990, p. 1.
20. Pask, J. A., *Ceramics Int.*, **9** (1983) 107.
21. Pask, J. A., *Ceramics Developments—Materials Science Forum, Part I*, eds C. C. Sorrel & B. Ben-Nisan, 1988, p. 1.
22. Yoldas, B. E., *Mullite and Mullite Matrix Composites*, eds S. Somiya, R. F. Davis & J. A. Pask, Am. Ceram. Soc. Trans., Vol. 6, 1990, p. 255.
23. Zhang, X. W., Tomsia, A. P., Yoldas, B. E. & Pask, J. A., *J. Am. Ceram. Soc.*, **70** (1987) 704.
24. Sacks, M. D., Lee, H.-W. & Pask J. A., *Mullite and Mullite Matrix Composites*, eds S. Somiya, R. F. Davis & J. A. Pask, Am. Ceram. Soc. Trans., Vol. 6, 1990, p. 167.
25. Risbud, S. H., Draper, V. F. & Pask, J. A., *J. Am. Ceram. Soc.*, **61** (1978) 471.
26. Kriven, W. M. & Pask, J. A., *J. Am. Ceram. Soc.*, **66** (1983) 649.
27. Aramaki, S. & Roy, R., *J. Am. Ceram. Soc.*, **42** (1959) 644.

Formation of Aluminum Rich 9:1 Mullite and its Transformation to Low Alumina Mullite upon Heating

Reinhard X. Fischer,^{a*} Hartmut Schneider^b & Dietmar Voll^b

^aInstitut für Geowissenschaften der Universität, D-55099 Mainz, Germany

^bGerman Aerospace Research Establishment (DLR), Institute for Materials Research, D-51140 Köln, Germany

(Accepted 22 July 1995)

Abstract

The formation of aluminum rich mullites $Al_{4+2x}Si_{2-2x}O_{10-x}$ with $x > 2/3$ has been studied at annealing temperatures between 700 and 1650°C. Calcination of the amorphous precursor at 700°C yields a mullite with 88 mol% Al_2O_3 corresponding to an x -value of 0.809. Simultaneously, a γ -alumina phase is formed. Further increase of the annealing temperature yields an increase in the aluminum incorporation up to 92.1 mol% Al_2O_3 at 1000°C derived from the refined lattice constants. This is the highest amount of Al observed so far in a mullite except the supposed end member ν - Al_2O_3 which, however, has not yet been established unambiguously. Above 1000°C, the aluminum content in mullite is reduced. This is accompanied by a transformation of the spinel-type phase to a superstructure of a θ -alumina like phase. The final product at 1650°C consists of 34 mol% of a 'normal' mullite with $x = 0.32$ and 66 mol% corundum.

1 Introduction

An aluminum rich mullite with 89% Al_2O_3 and lattice constants $a > b$ has been described recently^{1,2} and it was shown that the linear relationship between lattice constant a and the molar content of Al_2O_3 can be extrapolated beyond the crossover point of a and b lattice parameters. In the work described here we show that a sample prepared by sol-gel synthesis exhibits an even higher aluminum content at annealing temperatures below 1000°C. This sample is used to elucidate the crystallization process of mullites at the high alumina end of the solid solution series.

2 Experimental

The sample was prepared as described in Refs 1 and 2. After heating at a rate of 300°C/h, the samples were kept at the respective temperatures for 15 h and subsequently quenched in air. A portion of the sample was retained for the X-ray investigations and the bulk of the sample was further heated to the next temperature step. X-ray powder diffraction data were collected with a Seifert automatic powder diffractometer with CuK_{α} radiation and a graphite monochromator in the diffracted beam. Samples were filled into a flat sample holder with a bottom silicon crystal to diminish background scattering. Background was subtracted by hand with a linear interpolation between consecutive breakpoints in the pattern. Phase analyses were performed by simulation of the mullite powder diagrams using the PC Rietveld plus program.³ Calculated intensities were corrected for automatic divergence slit effects in the Rietveld procedure.⁴ Data were collected in step scan mode between 10 and 100° 2θ with steps of 0.03° and a counting time of 30 s per step, except for the final data set of the 1650°C sample which was measured between 5 and 140° 2θ with 10 s per step.

3 Results and Discussion

Crystallization of mullite starts at about 700°C, together with the formation of a γ -alumina phase (Figs 1(a–d)). High background intensities indicate the presence of a relatively large amount of a coexisting amorphous phase. Mullite formed at 700°C exhibits broad X-ray lines of low intensity. X-ray line intensities gradually increase upon heating accompanied by a sharpening of the line widths, especially at temperatures above 900°C. This indicates an increasing degree of structural order in $a > b$ mullites heat-treated above $\approx 900^\circ C$.

*Present address: Fachbereich Geowissenschaften der Universität, D-28334 Bremen, Germany.

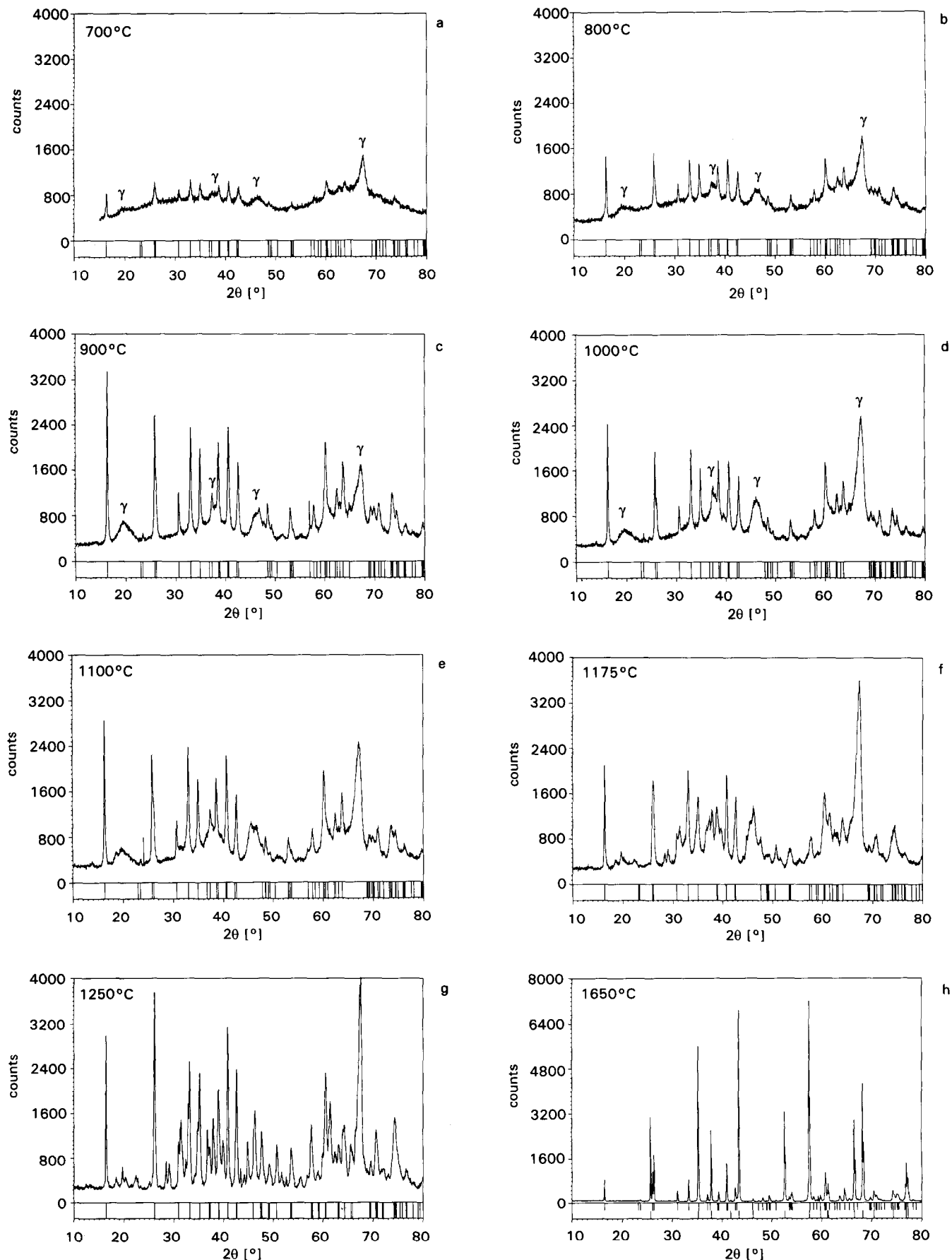


Fig. 1. Observed powder patterns of mullite samples at various annealing temperatures given in the upper left corner of the diagram frames. Mullite reflections are indicated by tickmarks underneath the powder diagrams. The broad peaks belonging to the γ -alumina phase are labeled with the Greek letter γ in Figs 1(a-d). Reflections without tickmarks in Figs 1(e-g) belong to a transformed alumina phase. Fig. 1(h) shows the powder diagrams of mullite (upper row of tickmarks) and corundum, α -alumina (bottom set of tickmarks). The sharp features at $57^\circ 2\theta$ in Fig. 1(c) and at $24^\circ 2\theta$ in Fig. 1(e) are spurious intensities from instrumental effects; they are eliminated in the analyses.

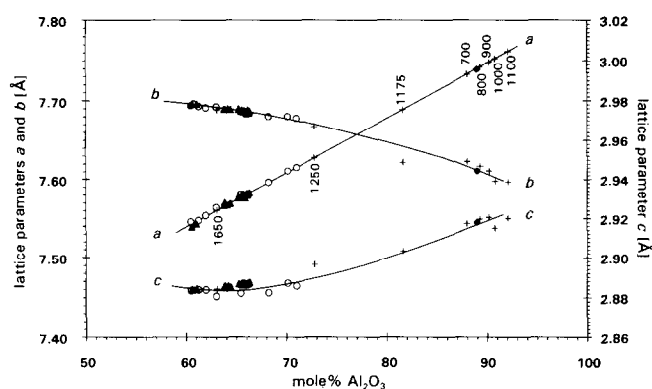


Fig. 2. Lattice parameters a , b , and c of mullites from recent determinations (\blacklozenge Ref. 2, \blacktriangle Ref. 5, \circ Ref. 6) with the additional data points (+) from this work. The straight line for a results from linear regression, the curves for b and c are fitted by hand. Data points of this work are labeled with the respective annealing temperatures ($^{\circ}\text{C}$).

This observation is in agreement with HRTEM studies on $a > b$ mullites prepared at 1000°C which yielded evidence for an ordered sequence of domains with high and low Oc oxygen vacancy concentrations.⁵ The γ -alumina phase has the characteristic broad peaks in the powder diagram at 20 , 46 , and $67^{\circ}2\theta$. Above $\approx 1100^{\circ}\text{C}$ (Figs 1(e–g)), the reflections of the alumina phase become sharper. Splitting of the peaks indicates a phase transition or an ordering of the highly disordered defect spinel. At 1650°C (Fig. 1(h)), the alumina spinel phase transforms to α -alumina (corundum) and mullite exhibits very sharp diffraction peaks.

The chemical composition of the low-temperature mullites were derived from the linear relationship between its lattice constant a and the molar content of Al_2O_3 . Using the more recent data of mullite determinations^{6,7} in the low alumina region extended by the data from the high alumina mullite,² we get the relationships shown in Fig. 2. A linear regression based on these data (represented by the open circles, solid triangles, and the diamond symbol) yields the line drawn for lattice constant a . The curves for lattice constants b and

c are fitted by hand. Slope A and intercept B are derived from the linear regression yielding the relation to calculate the molar content m of Al_2O_3 in mullite

$$a = A \cdot m + B = 0.00692 \cdot m + 7.124$$

and

$$m = 144.5 \cdot a - 1029.5$$

The uncertainties are 0.00008 for A and 0.005 for B yielding an error of about 1.5 mol% for the determination of m with this equation.

Lattice constants were determined by the Rietveld refining method. The accuracy of the refinements depends strongly on the accuracy of the crystal structure parameters which are used for the powder pattern simulation. Therefore, the refinement has been performed iteratively with an average structure of mullite as an initial model. This initial refinement yielded improved lattice constants which were used to redetermine the chemical composition from the curves shown in Fig. 2. The occupation factors of the Al and Si atoms were set to values derived from the x -values according to the formula given below (see also footnote in Table 1). This process was repeated two or three times until the best fit was achieved with the most accurate lattice constants. Regions of the spinel phase in the powder diagrams were excluded from the refinements. The resulting lattice constants, related to the molar content of Al_2O_3 , can be used to derive the x -value in the formula of the mullite chemical composition and, consequently, the occupation factors of the respective atom sites. The x -value is given by

$$x = 10 - 6 \cdot \frac{m + 200}{m + 100}$$

The results are listed in Table 1. The lattice constants are added to Fig. 2 (+ symbols). While the a parameters inevitably lie on the straight line (since they were derived from the linear regression), the parameters b and c give a good measure for the shape of these lattice parameter curves.

Table 1. Lattice constants a , b , c (\AA) from Rietveld refinements, molar content, m of Al_2O_3 (%) from linear regression, and atom site occupancies

$T(^{\circ}\text{C})$	a	b	c	m	x	Number per unit cell			
						Si in T	T^*, Oc^*	T^{**}	Oc
700	7.7328(24)	7.6229(23)	2.9175(6)	88.0	0.809	0.383	1.191	0.426	0
800	7.7419(12)	7.6172(11)	2.9197(3)	89.3	0.830	0.340	1.170	0.489	0
900	7.7480(6)	7.6106(6)	2.9205(2)	90.2	0.845	0.311	1.155	0.534	0
1000	7.7616(9)	7.5969(8)	2.9201(2)	92.1	0.877	0.245	1.123	0.632	0
1100	7.7525(10)	7.5978(9)	2.9150(3)	90.8	0.855	0.289	1.144	0.567	0
1175	7.6889(26)	7.6222(26)	2.9034(6)	81.6	0.697	0.606	1.303	0.091	0
1250	7.6278(20)	7.6671(20)	2.8964(5)	72.8	0.528	0.944	1.056	0	0.416
1650	7.5603(3)	7.6886(3)	2.8843(1)	63.1	0.320	1.360	0.640	0	1.040

Si in T = $2-2x$, $T^*, \text{Oc}^* = 2-x$ for samples with $x > 2/3$ ($700-1175^{\circ}\text{C}$) and $2x$ for samples with $x < 2/3$, $T^{**} = 3x-2$ for samples with $x > 2/3$ else 0, Oc = $2-3x$ for samples with $x < 2/3$ else 0 (see Ref. 2 for explanation).

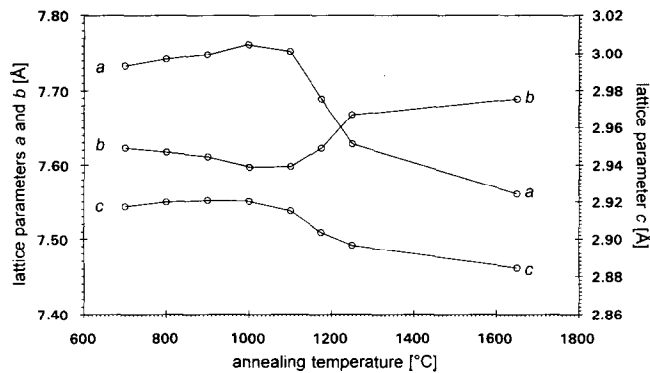


Fig. 3. Plot of lattice constants versus annealing temperature.

The deviations of the parameters of the 1175 and 1250°C samples might be caused by the severe overlap of the mullite reflections with the spinel phase reflections. An improvement in the accuracy of the lattice constant determinations could be achieved by a simultaneous simulation of mullite and γ -alumina. The multiphase refinement could not be performed because of difficulties in the crystal structure determination of the spinel phase. Further work is in progress. However, the results are sufficiently accurate for a discussion of the phase formation. Figure 3 shows a plot of the lattice constants versus the annealing temperature and Fig. 4 shows the corresponding molar relationship derived from data in Fig. 2. It is notable that the lattice constant a , and consequently the molar content of Al_2O_3 , increase upon heating between 700 and 1000°C. In this region, the mullite phase corresponds to the new type of mullite described in Ref. 2 (see also data in Table 1). Above 1000°C, the aluminum content is reduced, rapidly falling to values which represent a 'normal' mullite at 1250°C with lattice constants $a < b$ and with x -values $< 2/3$ corresponding to mullites with less than 80 mol% Al_2O_3 . At the final temperature, at 1650°C, the sample consists of α -alumina (corundum) and a well crystallized mullite with 63% Al_2O_3 . Simultaneously with the reduction in the aluminum content at 1100°C, a transformation of the spinel phase is observed indicated by the narrowing and splitting of the broad reflections at $20^\circ 2\theta$ and $46^\circ 2\theta$ (Fig. 1(e)). At 1250°C, further transformation to a θ -alumina like phase is observed with very sharp reflections indicating a well crystallized product. However, several reflections which do not fit into the monoclinic cell of θ -alumina⁸ indicate a supercell with bigger lattice parameters which has not been observed before for the transition aluminas. We suspect that the reduction of the aluminum content in mullite above 1000°C is directly related to the formation of the new deformed spinel phase. Considering that the spinel phase could incorporate silicon as

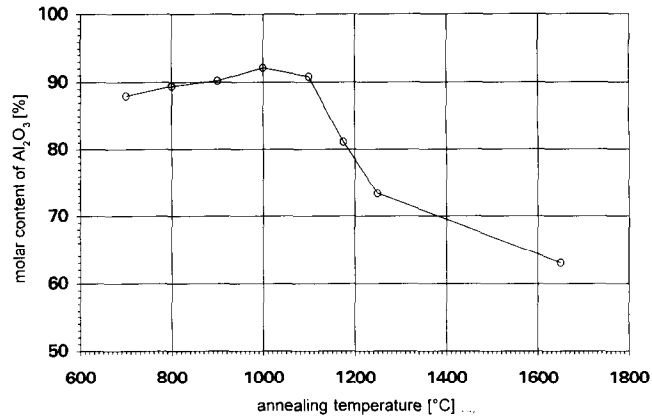


Fig. 4. Plot of molar content of Al_2O_3 versus annealing temperature.

well⁹ a discussion of the exact phase relations in this system is very difficult as long as the structure of the defect spinel has not been determined.

The final product at 1650°C contains 34 mol% mullite ($\text{Al}_{4.64}\text{Si}_{1.36}\text{O}_{9.68}$) and 66 mol% corundum (Al_2O_3) derived from the standardless quantitative Rietveld analysis with an absolute error of about 3%. Here, we assume that the amorphous phase completely disappeared. This corresponds roughly to a Al/Si ratio of 6:1 in the bulk composition of this sample which indicates a loss of silicon in the vigorous hydrolytic reaction of the starting materials with an initial Al/Si ratio of about 4:1.^{1,2}

Acknowledgements

We thank the Deutsche Forschungsgemeinschaft (DFG) for financial support under grant Fi442/2. The award of a Heisenberg fellowship to RXF is gratefully acknowledged. We thank R. D. Shannon for reading the manuscript. Computing facilities were financially supported by the Materialwissenschaftliches Forschungszentrum of the University of Mainz.

References

- Schneider, H., Fischer, R. X. & Voll, D., Mullite with lattice constants $a > b$. *J. Am. Ceram. Soc.*, **76** (1993) 1879–81.
- Fischer, R. X., Schneider, H. & Schmäcker, M., Crystal structure of Al-rich mullite. *Am. Mineral.*, **79** (1994) 983–90.
- Fischer, R. X., Lengauer, C., Tillmanns, E., Ensink, R. J., Reiss, C. A. & Fantner, E. J., PC-Rietveld plus, a comprehensive Rietveld analysis package for PC. *Materials Science Forum* **133–136** (1993) 287–92.
- Fischer, R. X., Divergence slit corrections for Bragg-Brentano diffractometers with rectangular sample surface. *Powder Diffraction*, in press.
- Schneider, H., Okada, Y., Pask, J. A., *Mullite and mullite ceramics*. Wiley & Sons, Chichester, 1994, pp. 33–4.
- Klug, F. J., Prochazka, S. & Doremus, R. H., Alumina-silica phase diagram in the mullite region. *Ceramic Transactions*, **6** (1990) 15–43.

7. Ban, T. & Okada, K., Structure refinement of mullite by the Rietveld method and a new method for estimation of chemical composition. *J. Am Ceram. Soc.*, **75** (1992) 227–30.
8. Zhou, R. -S. & Snyder, R. L., Structures and transformation mechanisms of the η , γ and θ transition aluminas. *Acta. Cryst.*, **B47** (1991) 617–30.
9. Schneider, H., Voll, D., Saruhan, B., Schmücker, M., Schaller, T. & Sebald, A., Constitution of the γ -alumina phase in chemically produced mullite precursors. *J. Europ. Ceram. Soc.*, **13** (1994) 441–8.

The Formation of Mullite from Kaolinite Under Various Reaction Atmospheres

K. J. D. MacKenzie, R. H. Meinhold, I. W. M. Brown & G. V. White

New Zealand Institute for Industrial Research and Development, PO Box 31-310, Lower Hutt, New Zealand

(Accepted 22 July 1995)

Abstract

In addition to its importance as a high-technology ceramic, mullite is also an intermediate phase in the formation of non-oxide ceramics (sialons) by carbothermal reduction of clay minerals. This reaction involved the formation of mullite under non-oxidizing atmospheres and in the presence of carbon. The effect of eight different reaction atmospheres on mullite formation from kaolinite in the presence and absence of carbon was studied by X-ray diffraction, ^{27}Al and ^{29}Si magic angle spinning nuclear magnetic resonance (MAS NMR) spectroscopy. Generally, a greater amount of mullite is formed at 1200°C under vacuum and reducing atmospheres, which also produce mullites that are slightly more silica-rich (as deduced from X-ray lattice parameter measurements) but contain higher proportions of tetrahedral ^{27}Al NMR resonance at ≈ 46 ppm, probably associated with Al^ sites. Reaction systems containing either nitrogen or ammonia in the presence of carbon show NMR evidence of previously unreported early stage formation of Si–O–N bonds. Thermodynamic calculations are presented which suggest that the formation of SiO is an important factor in the complex interactions between the various solid and gaseous reactants.*

1 Introduction

Mullite is an important high-technology ceramic in its own right, especially when prepared in high purity, by contrast with the product generally formed by heating clay minerals. However, the mullite resulting from the thermal reaction of clays plays an important role in the formation of sialons (silicon aluminium oxynitrides), another class of high-technology materials. The synthesis of sialon from natural aluminosilicates involves heating a clay such as kaolinite with carbon in a nitrogen atmosphere, but if other inert atmospheres such as argon are used, equally useful

carbide phases can be formed.¹ The practical importance of such synthesis reactions has led us to study the effect of a number of different reaction atmospheres on the formation of mullite from kaolinite, both in the presence and absence of carbon.

The aim of these studies was to measure the effect of eight different reaction atmospheres on:

- (1) the amount of mullite formed under standard conditions (2 h heating at 1200°C),
- (2) the composition of the mullite formed, and
- (3) the structure of the mullite formed.

The amount and composition of the product was measured by X-ray diffraction (XRD), from peak intensities and unit cell dimensions respectively, while aspects of the bonding and structure were studied by ^{29}Si and ^{27}Al solid-state magic angle spinning nuclear magnetic resonance (MAS NMR) spectroscopy. A thermodynamic analysis was also made, to clarify some of the details of the complex interactions occurring in these reacting systems.

2 Experimental

Kaolinite of high purity and good crystallinity ('Light' grade, supplied by British Drug Houses) was ball milled with an excess (25 wt%) Degussa lampblack under hexane for 16 h, extruded into 2 mm diameter rods, dried and heated in an alumina boat in an electric tube furnace under various flowing gases (flow rate 150 ml min⁻¹). The maximum temperature, at which the samples were held for 10 min, was 1200°C. A parallel set of experiments was also made omitting the carbon. After rapid cooling, maintaining the gas atmosphere, the samples were ground and examined by powder XRD (Philips PW1700 automatic diffractometer with CoK_α radiation) and solid-state nuclear magnetic resonance spectroscopy (Varian Unity 500 spectrometer). All the NMR

spectra were acquired at 11.7 T using a 5 mm Doty magic angle probe spinning up to 12 kHz. The recycle delay time used for the ^{29}Si spectra was 300 s, to allow for the possible presence of species with very long relaxation times.

The thermodynamic calculations were made using a computer program² which uses tabulated thermodynamic data to determine the concentration of the various gas and solid species in complex systems as a function of gas concentration and reaction temperature.

3 Results and Discussion

Figure 1 shows the amount of mullite formation from kaolinite at 1200°C under the various reaction atmospheres, estimated semi-quantitatively from the height of the major mullite XRD peak at 3.4 Å. In the absence of carbon, oxidizing atmospheres produce the least mullite, while reducing atmospheres, which include ammonia and CO_2 , produce the greatest amount. Inert atmospheres are intermediate in their effect. In the presence of carbon the reaction atmosphere clearly changes, with inert gases producing the most mullite, but oxidizing gases still producing the least mullite, due to the fact that the carbon burns off very readily under these conditions.

Figure 2 shows the alumina content of the mullites, estimated from the unit cell dimensions using the relationship of Cameron.³ The unit cells were determined from careful measurements of at least 11 mullite XRD peaks, with angular corrections

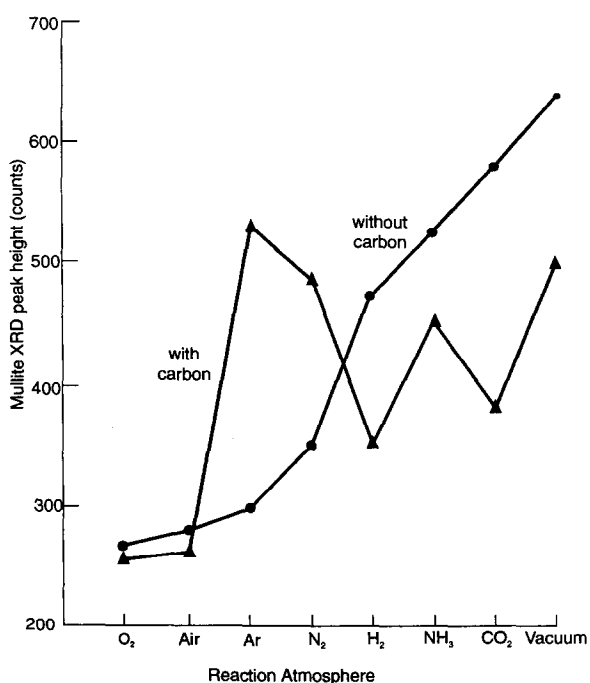


Fig. 1. Mullite formation in kaolinite (1200°C, 10 min) under various atmospheres, with and without carbon.

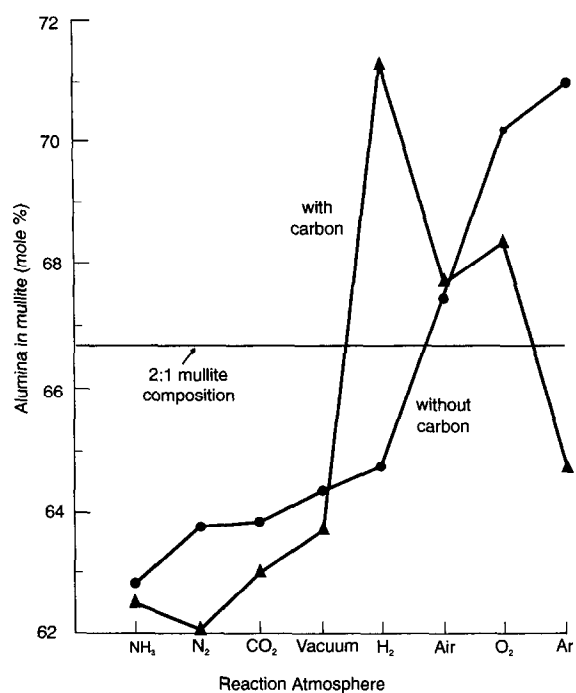


Fig. 2. Composition of mullites formed from kaolinite (1200°C, 10 min) under various atmospheres, with and without carbon.

made using an external silicon standard. In the absence of carbon, the alumina content of the mullite is highest under oxidizing conditions and argon, whereas under reducing conditions and vacuum, the composition is intermediate between 3:2 and 2:1 mullite. A similar situation occurs in the presence of carbon, except that hydrogen atmospheres now produce mullite with the highest alumina content.

Examples of the more interesting ^{29}Si and ^{27}Al spectra are shown in Fig. 3. The ^{29}Si MAS NMR spectra of all the mullites of this study are broad, but show the typical mullite peak at -87 ppm⁴ and a higher-field peak at about -106 ppm due to the free silica which separates from the kaolinite during the reactions preceding mullite formation. However, differences were found in the ^{29}Si spectra of samples heated with carbon in nitrogen (Fig. 3(A)) and heated without carbon in ammonia. In both these spectra there is evidence of broad spectral intensity downfield of the mullite peak. This is in the region of Si-N bonds, and in the spectral simulation of the sample heated in nitrogen (Fig. 3(B)) a peak centred at about -58 ppm could be fitted, the broadness of which suggests the presence of a continuum of nitride and oxynitride species. A similar situation was found in the ^{29}Si spectrum of the sample heated in ammonia, in which two peaks were fitted in this region, their positions (-40 ppm and -68 ppm) consistent with silicon nitride and silicon oxynitride, respectively. Both these samples have experienced the combination of a reducing atmosphere

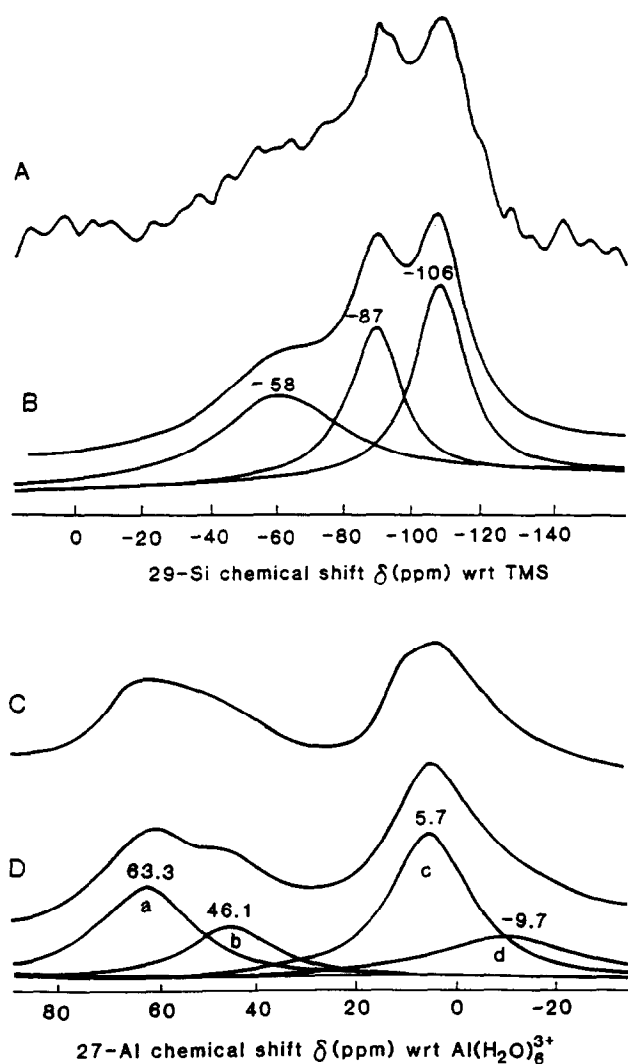


Fig. 3. Observed and simulated solid-state MAS NMR spectra of kaolinite reacted at 1200°C for 10 min: (A) ^{29}Si spectrum of sample containing carbon, in N_2 ; (B) simulation of A; (C) ^{27}Al spectrum of sample containing carbon, in H_2 ; (D) simulation of C.

and nitrogen, which seems to encourage the formation of Si–N bonding even at this low temperature.

The ^{27}Al MAS NMR spectra (Fig. 3(C)) are typical for mullite, containing an octahedral resonance at 1–6 ppm and a tetrahedral resonance at about 59 ppm. The octahedral resonance shows a marked tail on the upfield side which in the simulation of (Fig. 3(D)) has been fitted to a small broad peak (d); this tailing is commonly found in association with octahedral resonances and does not indicate a second site, but arises from electric field gradient (EFG) effects. The tetrahedral resonance at about 59 ppm can also be resolved into two overlapping peaks in a number of the samples (Fig. 3(D)). Following the reasoning of Merwin *et al.*,⁴ the tetrahedral peak at about 46 ppm may be due to the site associated with an oxygen defect. There is no readily discernible relationship between the area of this resonance and factors such as the amount of mullite formed or its total alumina content.

3.1 Thermodynamic calculations for these systems

There is clearly some complex chemistry occurring between the aluminosilicate lattice and the gas atmosphere, which can be modified by the presence of the carbon. Thermodynamic calculations were made in an attempt to interpret the behaviour of the various systems. Although these thermodynamic calculations refer to equilibrium conditions, and the present experiments were conducted under dynamic conditions, it was thought that the calculations could provide an insight into the various processes occurring, provided the results are treated with caution.

For the purpose of the calculations, the system was assumed to be anhydrous, with the composition of kaolinite from which the structural water had been removed (metakaolinite). The thermodynamic calculations predicted that this decomposes to silica and γ -alumina in most cases, with the formation of mullite, which is also taken into account in the calculations. Vacuum conditions were approximated by extremely high concentrations of an inert gas such as Ar, in which the dilution effect mimics the removal of gas by pumping. In all other cases, an ample excess of reactant gas (100 moles) and carbon (10 moles) was assumed. A range of temperatures was calculated, but the greatest attention was paid to the calculations at 1200°C.

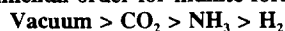
3.2 Reactions in the absence of carbon

Under these conditions at 1200°C, vacuum, CO_2 and reducing atmospheres were found by experiment to be of most assistance to mullite formation. The conclusions of the thermodynamic calculations for these more beneficial atmospheres are summarized in Fig. 4.

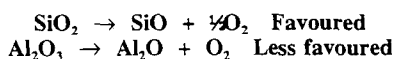
The calculations predict that at 1200°C, vacuum conditions should facilitate the decomposition of the silica to SiO but the alumina component should remain intact. The calculations for the system containing CO_2 indicate that the CO_2/CO equilibrium lies heavily to the left, although under the dynamic gas flow conditions of the experiment it may be shifted more to the right. The resulting CO would also favour the formation of SiO . At 1200°C, ammonia is completely dissociated into H_2 and N_2 ; the resulting hydrogen again facilitates SiO formation but does not form appreciable Al_2O at 1200°C (Fig. 4). Reaction between the silica component and the N_2 in the presence of the dissociated H_2 to form silicon nitride or silicon oxynitride is not predicted, but the formation of AlN from the alumina component is slightly favoured (although not observed experimentally here). Thus, the thermodynamic calculations for all the atmospheres which were found to assist mullite formation suggest that the silica phase is

KAOLINITE WITHOUT CARBON

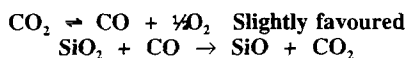
Experimental order for mullite formation:



A. Vacuum



B. Carbon Dioxide



C. Ammonia

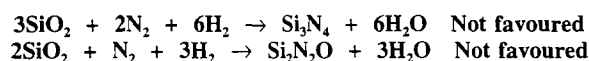
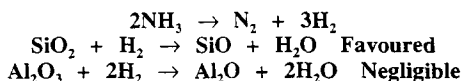


Fig. 4. Conclusions drawn from thermodynamic calculations for aluminosilicate systems reacted at 1200°C in the absence of carbon.

reacting with the gas in all cases, but the alumina component is much more stable.

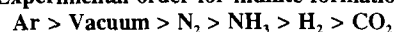
3.3 Reactions in the presence of carbon

In the presence of carbon, the experimental results indicate that reducing conditions again exert a beneficial influence on the formation of mullite, but, by contrast with the results in the absence of carbon, the inert atmospheres Ar and N₂ now also strongly promote mullite formation. The primary action of the inert gases will be to maintain the carbon in its elemental form. The predictions of thermodynamic calculations at 1200°C for the inert and reducing gases in the presence of carbon are summarized in Fig. 5.

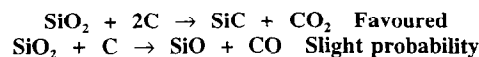
In both argon and vacuum, reaction between the silica component and carbon to form SiC is predicted, although this product was not experimentally observed. Because of its ability to be removed in the gas stream, the formation of SiO is probably more significant than it would be under the equilibrium conditions of the thermodynamic calculations. In nitrogen, the formation of silicon oxynitride from the silica component is strongly favoured in the presence of carbon (Fig. 5), consistent with the ²⁹Si NMR spectrum of this sample (Fig. 3(A)), but the alumina component is predicted to remain unreacted. In ammonia, reaction between the dissociated H₂ and the carbon to form CH₄ is predicted at lower temperatures, but by 1200°C, the equilibrium has shifted back again to the left. Thus, ammonia in the presence of carbon is predicted to form silicon oxynitride, this reaction being confirmed by ²⁹Si NMR. In hydrogen

KAOLINITE WITH CARBON

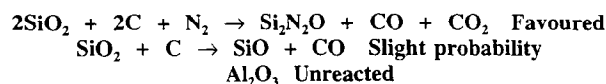
Experimental order for mullite formation:



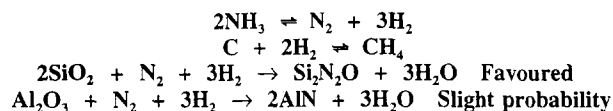
A. Argon and Vacuum



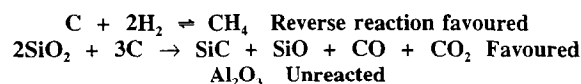
B. Nitrogen



C. Ammonia



D. Hydrogen



E. Carbon Dioxide

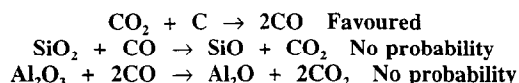


Fig. 5. Conclusions drawn from thermodynamic calculations for aluminosilicate systems reacted at 1200°C in the presence of carbon.

alone, the formation of SiC and SiO is predicted at 1200°C, but the alumina component of the reactant remains unreacted. As with Ar and vacuum atmospheres, the SiC is not experimentally observed. At 1200°C, CO₂ is predicted to react with carbon to form CO, but the thermodynamic probability of further reaction between CO and silica or alumina is low.

Thus, the thermodynamic calculations suggest that both in the presence and absence of carbon, the silica component is most affected by the various atmospheres, especially reducing atmospheres and those with the potential to become reducing. When the free silica in the reacting system has been consumed by the formation of SiO or Si₂N₂O, the silica component of the mullite present will be progressively decomposed by similar reactions (i.e. the formation of SiO, SiC or silicon oxynitrides). Removal of SiO in the gas stream will decrease the silicon concentration of the system unless it is retained by reacting with the alumina-rich components to form further mullite. A relationship between mullite formation and the tendency of the system to form SiO is illustrated in Fig. 6, in which the observed degree of mullite formation is plotted against the calculated SiO concentration for each system.

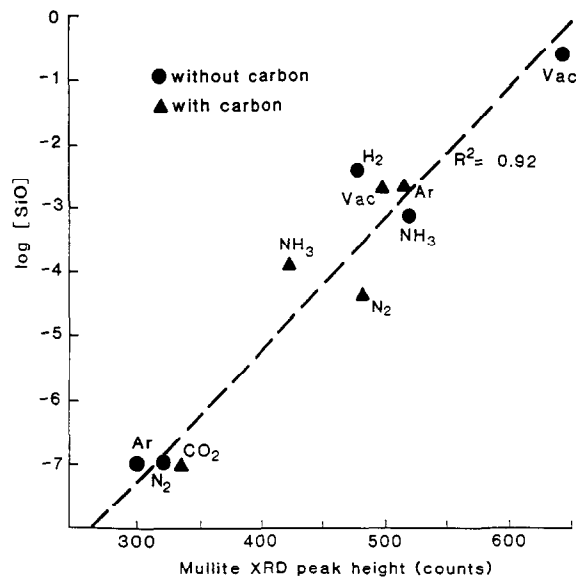


Fig. 6. Calculated SiO concentrations in systems of kaolinite composition, reacted in different atmospheres at 1200°C in the presence and absence of carbon, as a function of the experimentally determined mullite concentration.

The relationship shown in Fig. 6 is better than expected in view of the equilibrium assumptions of the thermodynamic calculations, which are very different from the present experimental conditions. Since the formation of mullite in these systems appears to be closely associated with their tendency to form SiO, the temperature dependence of SiO formation is also of interest (Fig. 7).

Although the calculated thermodynamic predictions of Fig. 7 must again be treated with caution, they indicate very different temperature dependences in the various atmospheres with and without carbon. In all but the two hydrogen-containing systems (H_2 and NH_3), the presence of carbon lowers the onset temperature for SiO formation, and in the case of Ar and N_2 , increases the eventual SiO concentration. These results suggest that the relative behaviour in the various reaction systems (and also the effect on mullite formation) may change markedly with reaction temperature.

The mechanism of mullite formation under reactive atmospheres which decompose the siliceous component to form SiO probably depends on the enhanced reactivity of the gas-phase SiO species for the more alumina-rich components. Alternatively, if discrete SiO is not directly formed, the increased lability of the Si–O bonds in the solid silica or aluminosilicate phases may be sufficient to promote further reaction and an increase in the silica content of the mullite.

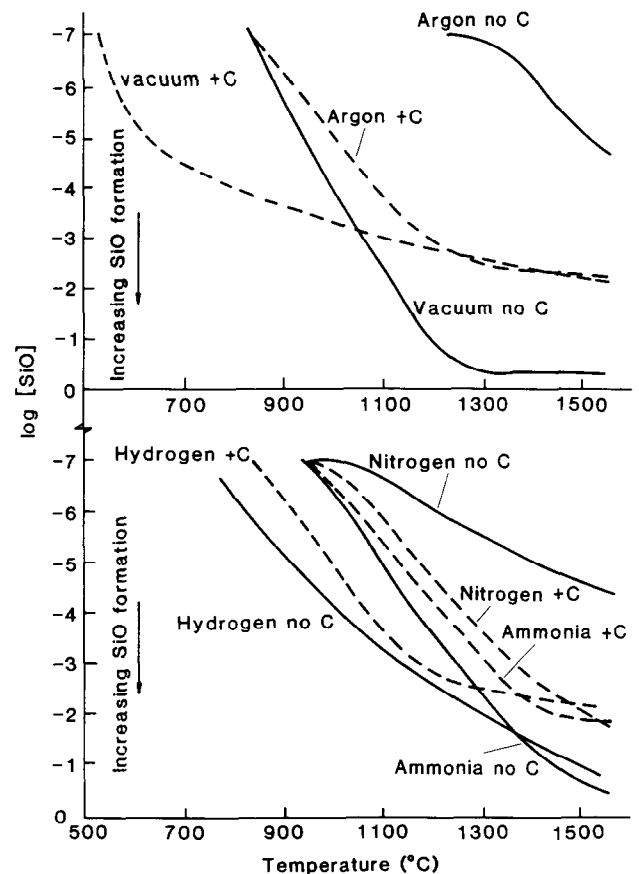


Fig. 7. Temperature dependence of calculated SiO formation in systems of kaolinite composition, under different atmospheres in the presence and absence of carbon.

Although the thermodynamic predictions must be applied with caution to the results of dynamic experiments, they shed interesting light on the relative importance of the various competing reactions occurring in complex gas–solid systems such as mullite-forming systems under various atmospheres.

References

- MacKenzie, K. J. D., Meinhold, R. H., White, G. V., Sheppard, C. M. & Sherriff, B. L., Carbothermal formation of β -sialon from kaolinite and halloysite studied by ^{29}Si and ^{27}Al solid state MAS NMR. *J. Mater. Sci.*, **29** (1994) 2611–19.
- Turnbull, A. G. & Wadsley, M. W., CSIRO Thermochemistry System, Version 5.1, 1988.
- Cameron, W. E., Composition and cell dimensions of mullite. *Am. Ceram. Soc. Bull.*, **56** (1977) 1003–11.
- Merwin, L. H., Sebal, A., Rager, H. & Schneider, H., ^{29}Si and ^{27}Al MAS NMR spectroscopy of mullite. *Phys. Chem. Minerals*, **18** (1991) 47–52.

Mullitization and Densification of $(3\text{Al}_2\text{O}_3 + 2\text{SiO}_2)$ Powder Compacts by Microwave Sintering

P. Piluso, L. Gaillard, N. Lequeux & P. Boch

Laboratoire Céramiques et Matériaux Minéraux, Ecole Supérieure de Physique et de Chimie Industrielles,
10 rue Vauquelin, 75231 Paris Cédex 05, France

(Accepted 22 July 1995)

Abstract

Reaction sintering of $(3\text{Al}_2\text{O}_3 + 2\text{SiO}_2)$ powder compacts was studied using either a conventional electric furnace or a 2.45 GHz microwave furnace. Special attention was paid to temperature measurement within the microwave furnace. The reality of a microwave effect that accelerates the kinetics and therefore, decreases the temperatures of mullitization and densification, remains uncertain. In any case, such an effect does not exceed $\approx 50^\circ\text{C}$, which is in the order of the temperature gradient between the core and the surface of microwave heated specimens.

1 Introduction

Many studies have been devoted to microwave sintering of ceramics.^{1–5} Microwave treatments have been reported to lead to a decrease in the temperature of sintering. In alumina, this decrease was said to be as large as 400°C ,^{6–8} which suggests the existence of a ‘microwave effect’ that accelerates the diffusion kinetics. However, there are large discrepancies in experimental data, and no definitive explanation has been proposed for the microwave effect.

The microwave effect has been most studied for densification without chemical change, but if it is not an artefact it should affect chemical reactions as well. Reaction sintering is a good way of combining reaction mechanisms and densification mechanisms. The present work was devoted to the preparation by reaction sintering^{9–14} of mullite ceramics. The influence of conventional heat treatments was compared to that of microwave treatments in order to investigate the existence of a microwave effect on densification and reaction (mullitization). The evidence of a microwave effect being related to a decrease in the temperature of densification (or of reaction), the accuracy of the

temperature measurements is of major importance. Therefore, special attention was paid to temperature measurement in the microwave furnace.

2 Experimental

2.1 The microwave furnace

The microwave-energy per unit volume (U) that is absorbed within a given material is expressed as:

$$U \approx 2\pi f E_{\text{int}}^2 \epsilon_0 \epsilon'' \quad (1)$$

E_{int} being the microwave electric field within the material, f the frequency, and ϵ'' and ϵ_0 the permittivity of free space and the effective relative loss factor, respectively.

Ceramic oxides such as Al_2O_3 or SiO_2 exhibit low dielectric losses, and are, therefore, difficult to heat in a commercial microwave furnace. We have built a microwave furnace specially designed to heat such low-loss materials.^{10–14} The furnace is shown in Fig. 1. It consists of a 2.45 GHz microwave generator with an adjustable 1.2 kW power output. The microwaves are directed into the applicator (which is a resonant, TE_{10n} single mode cavity) through a waveguide. A coupling iris minimizes the reflected power. The resonance of the cavity is controlled using an adjustable short-circuit. The incident and reflected powers are measured using two microwave-power meters and are recorded via a computer. The specimen is a cylinder of 13 mm in diameter and 3.5 mm thick. Its temperature is measured by a thermocouple (10% Rh–90% Pt/Pt) located in a hole drilled to the center of the specimen. The heating cycle is monitored by a programmable controller that regulates the incident power to follow a programmed temperature-to-time law.

In the absence of a theoretical model for the microwave effect, there is no evident choice for the frequency that would optimize the effect.

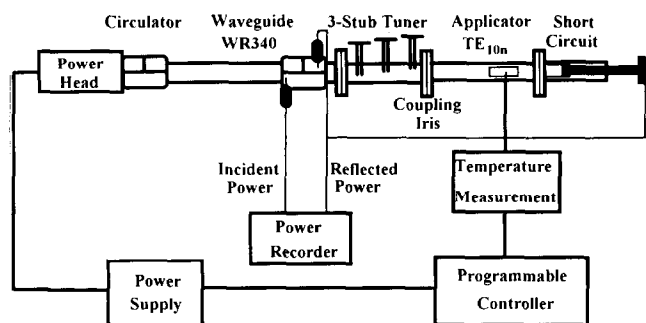
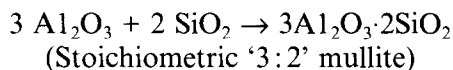


Fig. 1. The microwave furnace.

However, the frequency of 2.45 GHz is practically imposed by international regulations, which severely limit the industrial use of other, (e.g. 28 GHz) frequencies. Any industrial development of microwave sintering should satisfy the regulations and this is the reason why we have chosen a frequency of 2.45 GHz.

2.2 Green body preparation

Mullite ceramics were prepared by reaction sintering of alumina + silica powder compacts:



Alumina was α - Al_2O_3 (CR30 Baikowski[®], 99.99% pure, $d_{50} = 0.5 \mu\text{m}$). Silica was cristobalite (M5000 Sifrac[®], 99% pure, $d_{50} = 1.8 \mu\text{m}$). Powder mixtures were ball-milled for 5 h in a jar with dissociated ZrSiO_4 ($\text{ZrO}_2 + \text{SiO}_2$) balls in alcoholic medium (ethanol) with deflocculant (0.3 wt% of phosphate ester). A binder (3 wt% of polyvinylbutyral) was then added to improve the mechanical strength of the green material. Powders were granulated through a 200 μm sieve, then uniaxially pressed (150 MPa) to form pellets of 13 mm diameter and 3.5 mm thick.

2.3 Heat treatment

The first stage of heat treatment was pyrolysis of organic-binder and pre-sintering (2 h at 1000°C, in a conventional furnace). The resultant relative density (d/d_{th}) was 0.50. The second stage of heat treatment was reaction sintering, in either the

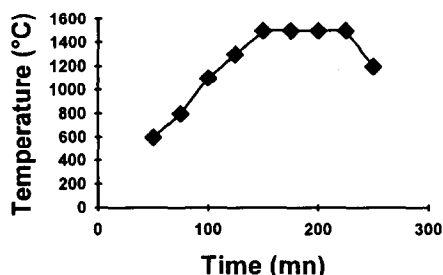


Fig. 2. Temperature versus time for a $(3\text{Al}_2\text{O}_3 + 2\text{SiO}_2)$ powder compact microwave heated to 1500°C.

conventional electric or the microwave furnace. The temperature cycles were similar in both cases: heating at 20°C mn^{-1} from room temperature to the firing temperature (T_f), soaking for 1 h at T_f , then cooling at 20°C mn^{-1} to room temperature. T_f ranged from 1300 to 1600°C. Figure 2 shows a temperature-to-time curve for a $(3\text{Al}_2\text{O}_3 + 2\text{SiO}_2)$ powder compact, microwave heated to 1500°C.

2.4 Characterization of materials

Density of sintered materials was estimated by Archimedes' method. Portions of specimens were diamond sawn, polished with diamond paste, and thermally etched to observe the microstructure by optical and scanning electron microscopy. Microwave reaction-sintered specimens were sawn to cut a slice along the diameter parallel to the thermocouple hole, then the slice was cut into three portions labelled as left, central, and right. X-ray diffraction experiments ($\text{Cu-K}\alpha$ radiation) were performed on those portions and the results were compared to XRD data of reference mixtures of known composition, to analyze the extent of reaction quantitatively. Two ratios of XRD peak areas were considered:

$$\frac{I_{(220)\text{mullite}}}{(I_{(220)\text{mullite}} + I_{(204)\text{alumina}})} \text{ and } \frac{I_{(121)\text{mullite}}}{(I_{(121)\text{mullite}} + I_{(204)\text{alumina}})}$$

3 Results and Discussion

3.1 Temperature calibration

A study of the microwave effect requires that the accuracy of temperature measurement be as accurate as possible. However, temperature measurement is difficult in a microwave furnace. Firstly, microwave heating is a volumetric process that generates temperature gradients that are the opposite of what conventional heating produces, the core being warmer than the surface ('inverse gradients'). Secondly, the dielectric-loss factor of the heated material usually rises very rapidly when temperature exceeds a critical value. This leads to a sudden increase in the temperature of the specimen ('thermal runaway'). Thirdly, the large electromagnetic field inside the applicator can disturb temperature measurement.

Both radiation pyrometers and thermocouples can be used. Pyrometers are best suited to measure the surface temperature of a specimen whereas thermocouples are best suited to measure the core temperature. Pyrometers do not interfere with microwaves whereas metallic thermocouples can disturb the electric field in the cavity or be affected by it. We tried using both radiation pyrometers and thermocouples. Pyrometers require

knowledge of emissivity of the ceramics that were tested, which do not behave as a black body. Thermocouples gave reproducible results if placed perpendicularly to the electric field and protected by a metallic shield. We used thermocouples with small diameters (1 and 0.5 mm) to limit the heat losses by conduction.

The thermocouples were calibrated as follows:

3.1.1 Using 1 mm diameter thermocouples

These were tested using eutectic composition (49.4 wt% CaO + 50.6 wt% Al_2O_3), which melts at $1360^\circ C$,¹⁵ as confirmed by the experiments in the conventional furnace. The assumption was that eutectic melting is not sensitive to any microwave effect. However, the eutectic temperature that was measured in the microwave furnace was $1320^\circ C$. This meant that the temperature in the microwave furnace was under-estimated by about $40^\circ C$ (furnace was at $T \approx 1360^\circ C$) and the discrepancy must be due to heat conduction through the thermocouple. Because conduction decreases when the thermocouple diameter decreases, 0.5 mm thermocouples should behave better than 1 mm ones, as will be confirmed later on.

3.1.2 Using 0.5 mm diameter thermocouples

These were tested by comparison with an IR pyrometer focused on a hole bored into an alumina specimen and shaped to behave as a black body, due to multiple reflections of light. In the conventional furnace, the calibration showed that the emissivity of alumina at $1000^\circ C$ was of about 0.6 whereas that of the 'black-body hole' was of about 0.9 (instead of 1 for a perfect black body). In the microwave furnace, the tip of the 0.5 mm thermocouple was located at the center of the black-body hole in the alumina specimen and the specimen was thermally insulated by alumina fibers. The difference between the temperature given by the thermocouple and that given by the pyrometer was small over all the temperature range. It was of $10^\circ C$ at $T = 1000^\circ C$, to be compared with $40^\circ C$ for the under-estimation induced by the 1 mm thermocouple. This confirms that 0.5 mm thermocouples behave better than 1 mm ones and, therefore, 0.5 mm thermocouples were used for the rest of the study.

3.2 Temperature gradients

Microwave heating is a volumetric process. In the simplest case where the absorbed power is homogeneous across the specimen, the temperature is heterogeneous, the core being warmer than the surface. This is the opposite of what is observed in conventional heating: microwave heating induces 'inverse gradients', instead of the 'normal gradi-

ents' of conventional heating. The absorbed power is not homogeneous across the specimen due to changes in E_{int} and ϵ'' (see Eqn (1)). Usually, the effect of such changes is to increase the (inverse) gradients. To minimize the gradients, the heating rate must be kept at a low value ($\leq 20^\circ C\ mn^{-1}$) to avoid hot spots due to local thermal runaway. This requires a careful control of the microwave power, which must be kept at a low level ($\leq 200\ W$). Moreover, the heated specimen must be situated at the place in the single-mode resonant cavity where the electric field is maximum, and the size of specimen (13 mm in diameter and 3.5 mm thick) must be small in comparison with the wavelength of microwaves ($\lambda \approx 20\ mm$ at 2.45 GHz). Finally, the heated specimen must be thermally insulated using low-conduction alumina fibers. In the absence of such insulation, the temperature difference between the core and the surface of specimen can exceed $500^\circ C$.

3.3 Mullitization

The extent of mullitization was quantified by XRD data obtained for reaction sintered specimens. The conventionally heated specimens were found to be homogeneously mullitized throughout their cross section, which indicated that their temperature had been homogeneous during reaction sintering. Conversely, the microwave heated specimens were found to be heterogeneously mullitized throughout their cross section, which indicated that they had been subjected to inverse temperature gradients during reaction sintering. For those specimens, the 'mullitization index' was determined from XRD data corresponding to the central section of the slice cut parallel to the thermocouple hole.

For a given mullitization index, the difference between the registered temperatures of conventional and microwave treatments was $\leq 65^\circ C$ (Fig. 3). Due to the underestimation of $\approx 10^\circ C$ in the microwave furnace, one sees that the present data are in favor of the existence of a microwave effect on mullitization whose magnitude is $\approx 50^\circ C$.

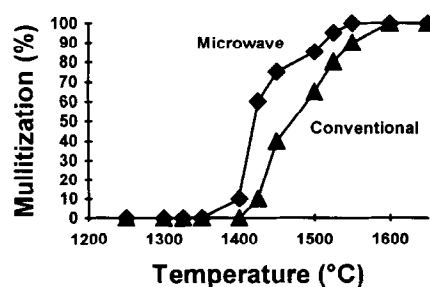


Fig. 3. Mullitization versus temperature (heating rate = $20^\circ C\ mn^{-1}$, soaking time = 1 h), for conventional and microwave heating.

Table 1. Mullitization and estimated temperature in a pellet microwave heated to 1400°C

Portion	Left	Central	Right
Mullitization (wt%)	60	75	60
Measured Temperature (°C)	1360	1400	1360
Estimated			

Mullitization gradients in microwave heated materials were analyzed by XRD, using various portions cut from reaction sintered pellets. For example, a specimen treated at 1400°C was found to be mullitized to 75 wt% in the central zone but to only 60 wt% in the superficial zone.

The mullitization gradients can be used to evaluate the temperature gradients, using reaction-to-temperature plots. Table 1 shows that the difference of temperature between center and surface for a pellet microwave heated to 1400°C is $\approx 40^\circ\text{C}$. This temperature difference is similar to the temperature difference that would correspond to the microwave effect.

3.4 Densification

Theoretical density was estimated from a rule of mixture having found the specimen composition that was given by quantitative XRD phase analysis. Apparent density was determined by averaging data from a whole specimen, which means we were not able to take into account any densification gradient.

Microwave heating seems to accelerate densification in comparison to conventional heating. However, specimens with the same mullitization index show the same densification, whatever the nature of heating. The temperature difference between conventional and microwave heating is a maximum for fully mullitized specimens, where densification is $\approx 75\%$. At its maximum, the microwave effect on densification is $\approx 50\text{--}60^\circ\text{C}$, which corresponds to the microwave effect on mullitization. This temperature difference is much

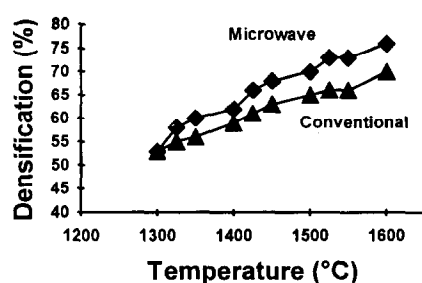


Fig. 4. Densification versus temperature (heating rate = $20^\circ\text{C}\text{mn}^{-1}$, soaking time = 1 h), for conventional and microwave heating.

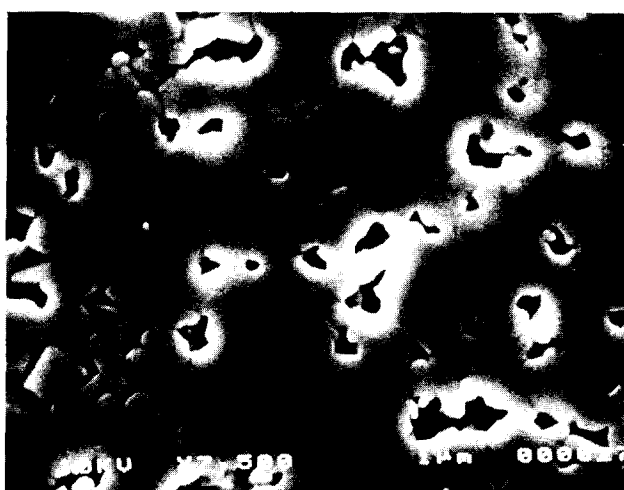


Fig. 5. SEM micrographs of a microwave heated specimen (1580°C , 35 mn): (a) core; (b) surface.

smaller than the difference of $300\text{--}400^\circ\text{C}$ reported by Kimrey *et al.* in 28 GHz microwave sintered alumina.⁶

Microstructural observations confirmed that the microwave heated specimens were heterogeneous. The core exhibits higher densification and larger grain size than the surface (Fig. 5). For a given densification, conventional heated and microwave heated specimens exhibited similar microstructures, with no noticeable difference in grain shape, (i.e. equiaxial versus elongated).

4 Conclusions

The study of reaction sintering of $3\text{Al}_2\text{O}_3 + 2\text{SiO}_2$ powder compacts treated by conventional or microwave heating does not disprove the possibility of a microwave effect, which would slightly accelerate both reaction and densification. However, the decrease in temperature associated with such an effect would be $\approx 50^\circ\text{C}$, at most, which is much lower than what was sometimes claimed. This

temperature difference is in the order of the temperature gradients across the specimens.

It may be that the experimental conditions we used, in particular the choice of a frequency of 2.45 GHz instead of a higher frequency, were not the best to detect the microwave effect. Moreover, results on alumina-plus-silica mixtures cannot be extrapolated to results on ceramic materials having very different electric properties, in particular ionic conductors or semiconductors. However, it is a fact that, from older to newer data,^{1-3,16} the trend is continuously changing toward a decrease in extent of the microwave effect. The present work shows that, for mullitic materials, the microwave effect cannot be expected to accelerate the densification (or reaction) kinetics at a rate sufficient to reimburse the extra cost of sophisticated microwave equipment. This comment refers to the preparation of homogeneous objects. On the other hand, the existence of noticeable 'inverse' gradients and the possibility of changing the heating rate by changing the dielectric properties make microwave heating an excellent technique for producing non-homogeneous objects. Objects with gradients in properties such as in the new family of functional gradient materials (FGM),¹⁷ ceramic-to-ceramic joining, and ceramic-ceramic composites are examples.

Acknowledgements

The authors acknowledge Electricité de France and Ministère de la Recherche for their support to this study.

References

1. Microwave Processing of Materials, eds W. H. Sutton, M. H. Brooks & I. J. Chabinsky, *Mat. Res. Proc.*, **124** Pittsburgh, USA, 1998.
2. Microwave Processing of Materials II, eds W. B. Snyder, W. H. Sutton, M. F. Iskander & D. L. Johnson, *Mat. Res. Proc.*, **189** Pittsburgh, USA, 1991.
3. Microwave: Theory and Applications in Materials Processing, eds D. E. Clark, F. D. Gac & W. H. Sutton, *Ceram. Trans.*, **21**, Am. Ceram. Soc., 1991.
4. Microwave Processing of Materials III, eds R. L. Beatty, W. H. Sutton & M. F. Iskander, *Mat. Res. Proc.*, **269**, Pittsburgh, USA, 1992.
5. Sutton, W. H., Microwave Processing of Materials, *Ceramic Bulletin*, **68**(2) (1989) 376.
6. Janney, M. A. & Kimrey, H. D., Microwave sintering of alumina at 28 GHz. In *Ceramic Powder Science*, eds G. L. Messing, E. R. Fuller & H. Haussner, *Am. Ceram. Soc.*, Westerville, USA, **II**, 1988, 919.
7. Janney, M. A., Kimery, H. D., Schmidt, M. A. & Kiggins, J. O., Alumina grain growth in a microwave field, *J. Am. Ceram. Soc.*, **74**(7) (1991) 1675.
8. Janney, M. A. & Kimery, H. D., Diffusion-controlled processes in microwave-fired ceramics, in Ref. 2, p. 215.
9. Patil, D., Mutsuddy, B. & Garard, R., Microwave reaction sintering of oxide ceramics, *J. Microwave Power and Electromagnetic Energy*, **27** (1992) 49.
10. Boch, P., Lequeux, N. & Piluso, P., Reaction sintering of ceramic materials by microwave heating, in Ref. 3, p. 211.
11. Piluso, P., Lequeux, N. & Boch, P., Microwave sintering of ceramics. In *Euro-Ceramics*, eds G. Ziegler & H. Haussner, Deutsche Keramische Ges. Publ., Köln, Germany, 1993, p. 557.
12. Piluso, P., Lequeux, N. & Boch, P., Microwave reaction-sintering of aluminium titanate and mullite ceramics. In *Third Euro-Ceramics*, eds P. Duran & J. F. Fernandez, Faenza Editrice Publ., San Vicente, Spain, Vol I, 1993 p. 1017.
13. Piluso, P., Lequeux, N. & Boch, P., Reaction and densification of mullite and aluminium titanate ceramics heat-treated in a 2.45 GHz microwave furnace. In *Nanostructure and Properties of Materials*, eds N. Igata & Dimitrov, Annales de Chimie - Science des Matériaux Publ., Paris, France, 1993 p. 101.
14. Piluso, P., Thèse, Etude du frittage réactif de la mullite et du titanate d'aluminium par chauffage micro-onde, Université Pierre et Marie Curie, Paris, France, September 1993, (in French).
15. Nurse, R. W., Welch, J. H. & Majundar A. J., System CaO-Al₂O₃ in a moisture-free atmosphere. In *Phase Diagrams for Ceramists, III*, The Am. Ceram. Soc., Westerville, USA, 1975, p. 103.
16. Microwave Processing of Materials IV, eds M. F. Iskander, R. J. Lauf & W. H. Sutton, *Mat. Res. Proc.*, **347** Pittsburgh, USA, 1994.
17. See *M. R. S. Bulletin*, XX, 1 (1995), for a review on Functionally Gradient Materials.

Characterization of Low Temperature Mullitization

Takayuki Ban, Shigeo Hayashi, Atsuo Yasumori & Kiyoshi Okada

Department of Inorganic Materials, Tokyo Institute of Technology, O-okayama, Meguro, Tokyo 152, Japan

(Accepted 22 July 1995)

Abstract

Anomalously low temperature mullitization was observed in the precursor prepared by the Nishio and Fujiki's method using aluminum nitrate nonahydrate (ANN), aluminum iso-propoxide (AIP), and silicon ethoxide (TEOS) and its mechanism was examined by various methods. The low temperature mullitization was found to occur only when the precursor was once heat-treated at 250°C before heating up to crystallization. The heat-treated precursor showed two-step mullitization with small amounts of mullitization at 450°C and large amount of mullitization at 900°C. On the other hand, the as-prepared precursor showed one-step mullitization at around 900°C. The presence of two small regions with slightly different chemical composition was found in the particles of the heat-treated precursor samples by ^{29}Si nuclear magnetic resonance (NMR) spectra, small angle X-ray scattering (SAXS) and X-ray Rietveld analysis. The low temperature mullitization was considered to occur at the interfaces of the two small regions because they acted as the heterogeneous nucleation sites.

Introduction

Since mullite, $\text{Al}_{4+2x}\text{Si}_{2-2x}\text{O}_{10-x}$, is one of the important ceramic materials, mullitization from various starting materials has been intensively investigated by many workers.^{1,2} Mullite precursors prepared by various methods are known to be grouped into two types of mullitization pathways. One type shows direct mullitization from the amorphous phase at around 1000°C whereas another one shows formation of the spinel phase at similar temperatures and mullitization occurring at higher temperatures, i.e. around 1200°C. The former precursor is considered to be in the homogeneous mixing state for SiO_2 and Al_2O_3 components, whilst the latter precursor is considered to be in an unhomogeneous state.³ On the other hand, some workers recently reported the mullitization which could not be grouped into

these two categories. Mullitization by these precursors occurred at much lower temperatures than those of the mullitization at around 1000°C. Huling and Messing⁴ first reported such low temperature mullitization phenomena. They prepared precursors by drying a sol prepared from ANN and TEOS, followed by aging the gel in a steamed atmosphere at 80°C. The precursor crystallized directly to orthorhombic mullite at 700°C. Fischer *et al.*⁵ reported similarly low temperature mullitization for the precursors prepared from aluminum sec-butylate and silicon chloride. Mullite formed by low temperature mullitization was extremely richer in the Al_2O_3 composition (88 mol%) than the ordinary composition (60 mol%) and its lattice showed $a > b$ relation; the opposite to those of the ordinary mullites. Nishio and Fujiki⁶ prepared mullite long fibers using the sol-gel method. They found that mullite started to crystallize at 600°C from the amorphous state when it was heated, as fibers formed though mullitization occurred at around 1000°C when the powdered sample was heated. We have categorized this as low temperature mullitization in this paper because the mullitization occurred below 900°C.

A different feature was suggested in low temperature mullitization compared with those of the ordinary mullitizations which occur at around 1000°C and/or above 1000°C. However, the mechanisms of low temperature mullitization has not been extensively investigated. The purpose of this study is, therefore, to prepare a precursor which shows low temperature mullitization and to characterize the low temperature mullitization process.

Experimental Procedure

The preparation of precursors used in this study was based on the method reported by Nishio and Fujiki.⁶ In this preparation, ANN was first dissolved in deionized water and AIP and TEOS were added to this solution in that order. The aqueous solution was stirred for 2 days at room temperature, and then gelled and dried at 110°C

for 36 h. This xerogel was designated as the as-prepared sample. A part of the as-prepared xerogel was heat-treated at 250°C for 16 h and was referred as the heat-treated sample. In order to compare the mullitization behavior of these samples, two other samples were prepared the following way. The starting solution was prepared by dissolving ANN in ethanol and then by adding TEOS. It was stirred at room temperature for 3 h. Then, a homogeneous type precursor was prepared by slowly hydrolyzing TEOS and gelling the solution by water included in ANN at 60°C for 4 weeks. An unhomogeneous type precursor was prepared by adding ammonia into the solution which formed a precipitation. The homogeneous and unhomogeneous type precursors were designated as the slowly hydrolyzed (SH) method sample and the rapidly hydrolyzed (RH) method sample, respectively. Chemical composition of all these samples was arranged to $\text{Al}_2\text{O}_3 = 60 \text{ mol}\%$, i.e. $3\text{Al}_2\text{O}_3 \cdot 2\text{SiO}_2$ composition.

High resolution solid state magic angle spinning nuclear magnetic resonance (MAS-NMR) spectra were obtained at 70.26 MHz for ^{27}Al and 53.4 MHz for ^{29}Si using a JEOL GX-270 system. The samples were contained in the zirconia rotor. The ^{29}Si spectra were obtained using a pulse width of 2 μs and a recycle delay of 60 s. The ^{27}Al spectra were obtained using a pulse width of 1 μs and a recycle delay of 10 s. The spinning frequency for the both spectra was 3.8 kHz. The chemical shift (δ) of ^{29}Si spectra was referenced by tetramethylsilane at $\delta = 0.0 \text{ ppm}$, in which the chemical shift was referenced by polydimethylsilane at $\delta = -33.8 \text{ ppm}$. The chemical shift of ^{27}Al spectra was referenced by $\text{Al}_2(\text{SO}_4)_3 \cdot 18\text{H}_2\text{O}$ at $\delta = 0 \text{ ppm}$.

Infrared absorption (IR) spectra were obtained by the KBr disk method using a JEOL JIR-6000 system. A pellet was prepared by mixing 0.01 g of sample with 0.25 g of KBr powder and formed by a uniaxial press. The spectra were measured for a wave number range between 400 and 4000 cm^{-1} . Differential thermal analysis (DTA) curves were measured from room temperature to 1100°C at a heating rate of 10°C/min using about 20 mg of sample. Small angle X-ray scattering (SAXS) measurements were carried out using a glass cell 10 mm in width. The range measured was between 0.1 and 3.0 nm^{-1} in a scattering vector using $\text{Mo K}\alpha$ radiation.

Each sample was fired at 400–1000°C for 1 h and the crystalline phase in their samples were examined by powder X-ray diffraction (XRD) using $\text{Cu K}\alpha$ radiation monochromated by a graphite. The XRD measurements were performed by two scanning methods. Measurements for identification of the crystalline phase were made by

the usual continuous scanning method with a scanning speed of 1°/min for a scanning range from 10–50° in 2θ . Structural parameters for some mullites were refined by the Rietveld method⁷ using the RIETAN program.⁸ The XRD profiles for the Rietveld analysis were measured using the step scanning method with a step scanning width of 0.02° and a fixed time of 20 s for a scanning range from 30 to 100° in 2θ . The details of the structure refinement procedure was reported elsewhere.⁹ The amount of mullite formed was evaluated from the scale factor obtained by the Rietveld analysis.

Results and Discussion

Figure 1 shows the XRD patterns of the as-prepared samples and the heat-treated samples heated at various temperatures. The as-prepared sample heated at 400–800°C showed an amorphous pattern. Mullite and a small amount of spinel phase were observed in the as-prepared sample heated at 1000°C. In contrast, mullite began to crystallize at 450°C in the heat-treated sample.

Mullite formation curves in the as-prepared sample, the heat-treated sample, the SH method

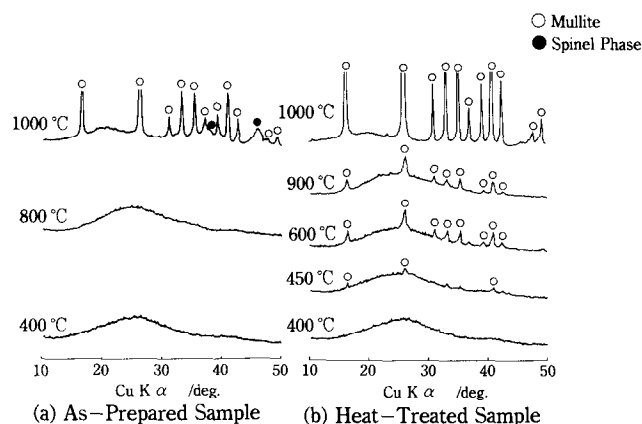


Fig. 1. XRD patterns of the as-prepared sample (a) and the heat-treated sample (b) fired at various temperatures for 1 h.

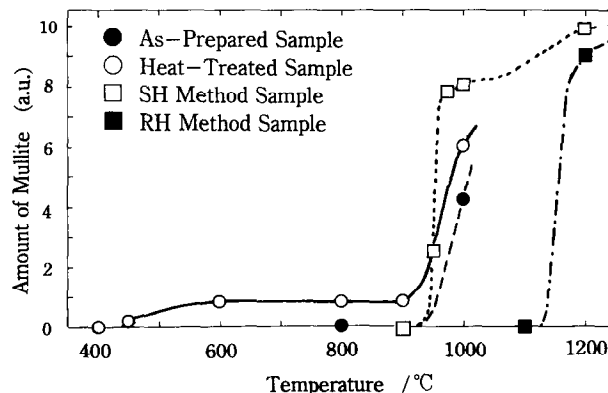


Fig. 2. Formation curves of mullite in the as-prepared sample (●), the heat-treated sample (○), the SH method sample (□) and the RH method sample (■).

sample and the RH method sample are shown in Fig. 2. In the as-prepared sample and the SH method sample, mullite started to crystallize from around 900°C and the amount increased very rapidly by 950°C, especially in the SH method sample. Mullitization in the as-prepared sample was similar to that in the SH method sample. The lower mullite formation content of the as-prepared sample can be interpreted by the co-presence of spinel phase in this sample. In the RH method sample, mullite started to crystallize from around 1100°C and the amount increased very rapidly to around 1200°C. The higher mullitization temperature of this sample was attributed to the formation of the spinel phase at around 1000°C before mullitization. On the other hand, mullite started to crystallize from around 450°C in the heat-treated sample. The amount of formed mullite was, however, very small and did not increase up to 900°C. The amount of mullite rapidly increased from 900°C, and no spinel phase formation was observed at 1000°C as shown in Fig. 1. The mullite formation curve of the heat-treated sample was largely different with respect to the starting temperature of mullitization but was similar with respect to the temperature in which most of the sample crystallized to mullite, i.e. the temperature was at around 1000°C and was similar to those of the as-prepared sample and the SH method sample.

In order to examine the influence of the heating time for the low temperature mullitization, the heat-treated sample was heated at 800°C for 24 h but there was no significant increase in the amount of mullite formed.

Chemical composition of the mullites formed at 600, 800 and 900°C was analyzed by the X-ray Rietveld method. We also evaluated the chemical composition of the mullites from the length of *a*-axis. The chemical compositions of the mullites obtained from both methods were around 66 mol% Al₂O₃. The XRD of these mullites showed the similar pattern with those of the tetragonal-like mullite¹⁰ but did not show the XRD pattern of orthorhombic mullite as reported by Huling and Messing⁴ and also the relation of *a* > *b* as reported by Fischer *et al.*⁵

Figure 3 shows ²⁹Si and ²⁷Al NMR spectra of the heat-treated sample, the SH method sample, and the RH method sample. All the samples were calcined at 600°C for 1 h. The ²⁷Al NMR spectra showed a complex profile and two or three peaks overlapped. Peaks were observed at around 5, 40 and 60 ppm and were assigned to six-, five- and four-coordinated Al atoms, respectively.¹¹ The intensity of the five-coordinated Al peak showed a trend to decrease as the mullitization temperature of the samples increased and no five-coordinated

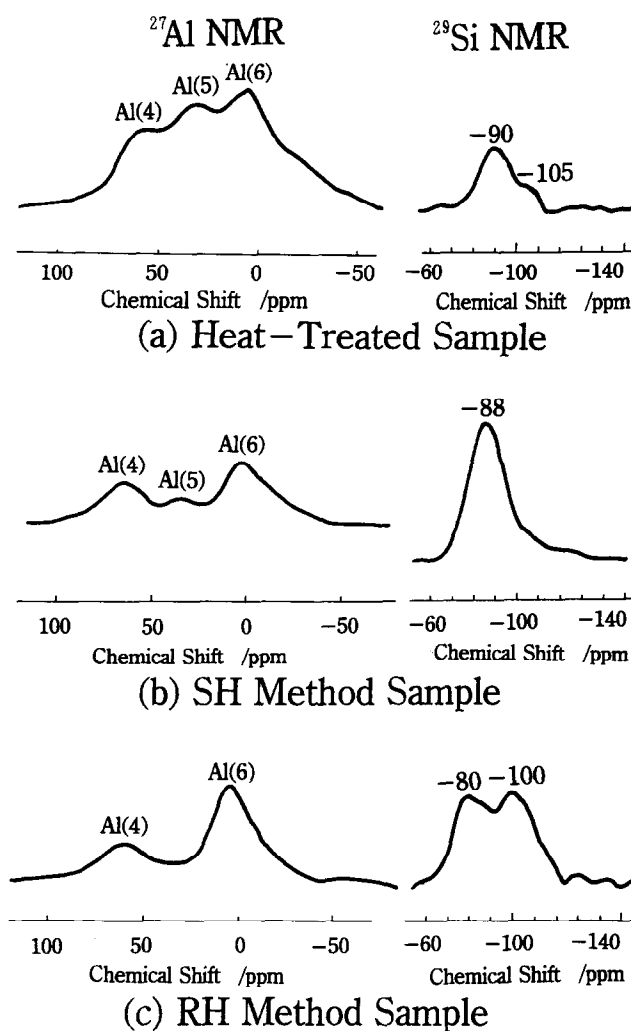


Fig. 3. ²⁹Si and ²⁷Al NMR spectra of the heat-treated sample (a), the SH method sample (b) and the RH method sample (c). All samples were calcined at 600°C for 1 h.

Al peak was observed in the RH method sample. The ²⁹Si NMR spectra showed one or two peaks depending upon the samples. The spectrum of the SH method sample showed only a single peak at around -88 ppm. This peak may be assigned to Q⁴(2Al) or Q⁴(3Al),¹¹ i.e. corresponding to the Q² or Q¹ state for the SiO₄ tetrahedral structure. On the other hand, two peaks at around -80 and -100 ppm were observed in the spectrum of the RH method sample. They may be assigned to the Q⁰ and Q³ or Q⁴ structures, respectively. The spectrum of the heat-treated sample also showed two peaks and they were observed at around -90 and -105 ppm. Therefore, they may be assigned to the Q¹ or Q² and Q³ or Q⁴ structures, respectively.

The following models are proposed for the structure of precursors from the results of ²⁷Al and ²⁹Si NMR spectra. The precursor of the SH method sample has a homogeneous structural state and SiO₂ and Al₂O₃ components are considered to be uniformly mixed at the molecular level. On the other hand, the precursor of the RH method sample consisted of two different structural regions

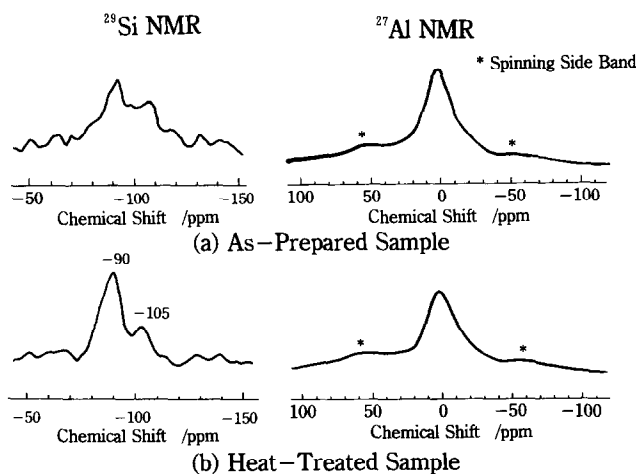


Fig. 4. ^{29}Si and ^{27}Al NMR spectra of the as-prepared sample (a) and the heat-treated sample (b).

which may correspond to an Al-rich and Si-rich chemical composition. Such a separation of chemical composition in the precursor is the reason for the phase change into the spinel phase and amorphous silica at around 1000°C before mullitization.¹ The precursor of the heat-treated sample may also consist of two different composition regions with a slightly Al-rich and Al-poor composition from the starting bulk composition.

In order to elucidate further details of the heat-treated sample, ^{29}Si and ^{27}Al NMR spectra of the heat-treated and the as-prepared samples are compared and are shown in Fig. 4. In the ^{27}Al NMR spectra of both samples, little difference was observed except for some broadening of the six-coordinated Al peak in the heat-treated sample. However, there was a certain difference between their ^{29}Si NMR spectra. The spectrum of the as-prepared sample showed broad complex peaks ranging from -80 to -120 ppm, therefore, they were considered to consist of a number of overlapped peaks. This indicates that there were various polymerization states in SiO_4 tetrahedra of this sample. On the other hand, the spectrum of the heat-treated sample showed two clear peaks at -90 and -105 ppm. These peaks can be assigned to Q^1 or Q^2 and Q^3 or Q^4 structures, respectively. It may indicate that there were two different states in the polymerization structure of SiO_4 tetrahedra of the heat-treated sample. Since this sample shows low temperature mullitization, whereas the as-prepared sample shows no low temperature mullitization, the difference of these polymerization states of SiO_4 tetrahedra is suggested to correspond to the difference of mullitization in the both samples.

Figure 5 shows SAXS curves of the as-prepared sample and the heat-treated sample. In the as-prepared sample, SAXS was observed only in the small scattering vector (q) range of $q < 0.2 \text{ nm}^{-1}$.

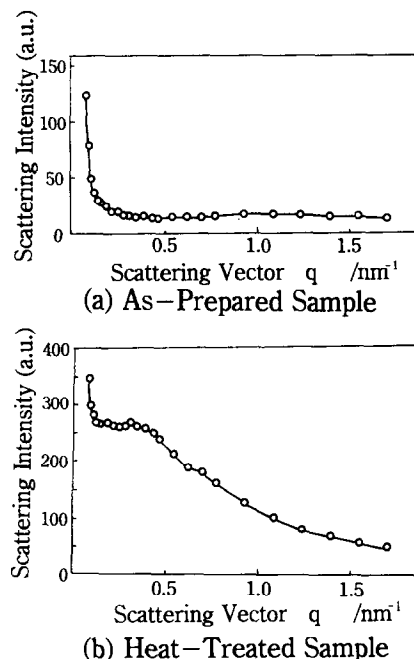


Fig. 5. SAXS curves of the as-prepared sample (a) and the heat-treated sample (b).

It is attributed to scattering from considerably larger scattering species corresponding to the sub-micron size region, in which size corresponds to the particle size of the precursor samples. On the other hand, the SAXS curve of the heat-treated sample showed not only the scattering in the range of $q < 0.2 \text{ nm}^{-1}$ but also the broad scattering in the range of $q > 0.2 \text{ nm}^{-1}$. This broad scattering is attributed to the scattering from relatively smaller scattering species corresponding from angstrom to nanometer order size region. From these SAXS data, we can conclude that the heat-treatment of the sample at 250°C caused very small unhomogeneous structure regions in nanometer size within the precursor particles.

The DTA curves of the as-prepared sample and the heat-treated sample are shown in Fig. 6. Some difference was observed between the two DTA curves. In the DTA curve of the as-prepared sample, endothermic reaction was observed in a wide temperature range from 100 to 400°C . They consisted of some numbers of overlapped endothermic peaks, which were caused due to the various reactions such as dehydration, dehydroxylation and the decomposition of nitrate and alkoxyl groups. On the other hand, the DTA curve of the heat-treated sample differed largely from that of the as-prepared sample and showed a clear single endothermic peak at 360°C . During the heat-treatment at 250°C , a partial thermal decomposition of the hydroxyl groups and the rearrangement of the precursor structure are suggested to occur in the sample. In the DTA curve of the heat-treated sample, a weak and broad exothermic peak was

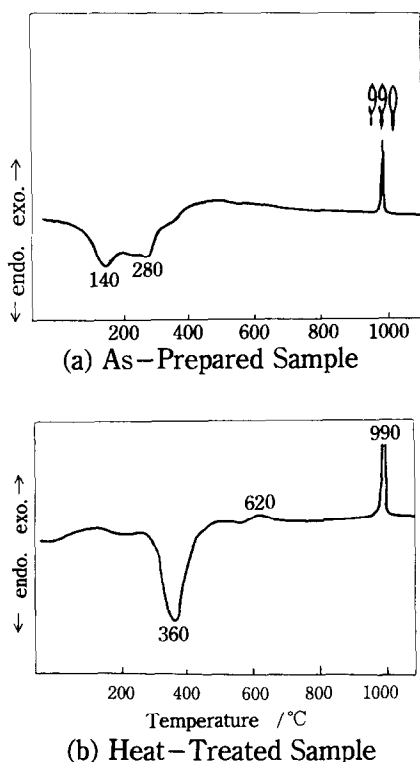


Fig. 6. DTA curves of the as-prepared sample (a) and the heat-treated sample (b).

detected at around 620°C but was not observed in that of the as-prepared sample. This exothermic peak may be corresponding to the low temperature mullitization. On the other hand, the exothermic peak at 990°C was attributed to the crystallization of mullite. Although the intensity of the exothermic peaks in these samples showed little difference, it can be interpreted by the difference of weight loss of the samples with and without heat-treatment at 250°C.

As mentioned in Fig. 1, mullite started to crystallize at 450°C in the heat-treated sample. Therefore, the endothermic peak at 360°C is considered to be important for low temperature mullitization. To examine the structural change by

this endothermic reaction, the heat-treated sample

was further heated at 400°C for 1 h. The IR and NMR spectra of the heat-treated sample and the sample further heated at 400°C are shown in Fig. 7. The ^{27}Al NMR spectrum of the heat-treated sample showed only a single peak at 0 ppm, which is assigned to six-coordinated Al structure. On the other hand, the ^{27}Al NMR spectrum of the sample heated at 400°C showed three peaks at 0, 30, and 60 ppm, which are assigned to six-, five-, and four-coordinated Al structures, respectively. Evolution of the four- and five-coordinated Al structures were found in the sample heated at 400°C and this structural change was considered to be derived from the dehydration of Al-OH. On the other hand, changes in the ^{29}Si NMR spectra was not observed except for a little broadening of the peaks and the two peaks still remained at -90 and -105 ppm in both samples. The broadening of the peaks may be related to the condensation reaction of Si-OH and Al-OH by dehydration. In the IR spectrum of the heat-treated sample, a weak absorption band was observed at 950 cm^{-1} , in which the absorption band resembles that of the OH group in diaspore ($\alpha\text{-AlOOH}$).¹² In the IR spectrum of the sample heated at 400°C the absorption band was not observed, whereas a weak and broad absorption band at 850 cm^{-1} was observed. Since the absorption band at 850 cm^{-1} may be assigned to that of the condensed AlO_4 tetrahedra,¹² it is also a comparable result to explain the condensation reaction of Al polyhedra by heating at 400°C.

We found that heat-treatment at 250°C was very important in causing low temperature mullitization. Structural change during this treatment was characterized by various methods and the following change was observed: dehydration and

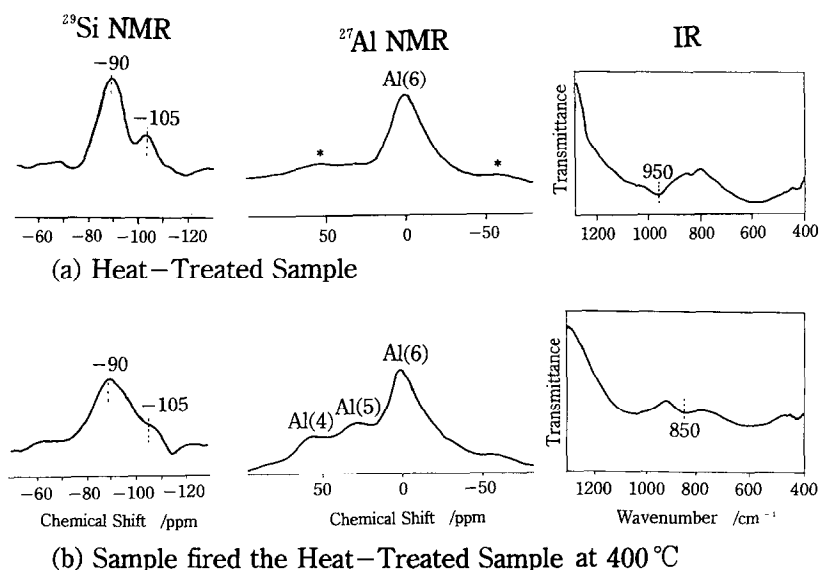


Fig. 7. IR and ^{29}Si and ^{27}Al NMR spectra of the heat-treated sample (a) and the sample further heated the heat-treated sample at 400°C (b).

decomposition of part of the nitrate and alkoxy groups occurred due to the treatment. This change introduced very small unhomogeneous structural regions with a slightly different chemical composition in the precursor particles. These two regions remained even after heating at 400°C, by which temperature condensation and re-arrangement of the precursor were considered. When such small regions with different chemical compositions are present within the particles, the interfaces between them are considered to be energetically active and can act as the heterogeneous nucleation sites. Therefore, low temperature mullitization can occur in the interfaces only by heating at relatively low temperatures. The amount of mullite formed by low temperature mullitization was, however, small because the mullitization occurred only in the interfaces of two regions in the precursor particles. The experimental result was that no apparent increase in the formation amount of mullite occurred, even though the duration at the low mullitization temperature is compatible with the consideration mentioned above.

Conclusions

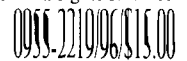
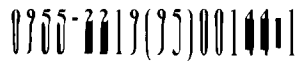
Mullite precursor was prepared from the combination of ANN, AIP and TEOS based on the Nishio and Fujiki's method⁶ and the mullitization process was examined using various methods. The following conclusions were obtained:

- (1) Heat-treatment at 250°C was essentially necessary for the low temperature mullitization and the heat-treated precursor started to show mullitization at 450°C.
- (2) The formation curve of mullite in low temperature mullitization showed a two-step curve with small amount of mullitization at 450°C and large amount of mullitization at 900°C.

- (3) The precursor to show the low temperature mullitization had two small regions with slightly different chemical composition within the precursor particles.
- (4) The interfaces between these two regions in the precursor particles played an important role as the heterogeneous nucleation sites for low temperature mullitization.

References

1. Okada, K., Otsuka, N. & Somiya, S., Review of Mullite synthesis routes in Japan. *Am. Ceram. Soc. Bull.*, **70** (1991) 1633–40.
2. Aksay, I. A., Dabbs, D. M. & Sarikaya, M., Mullite for structural, electronic, and optical applications. *J. Am. Ceram. Soc.*, **74** (1991) 2343–58.
3. Okada, K. & Otsuka, N., Characterization of the spinel phase from SiO₂-Al₂O₃ xerogels and the formation process of mullite. *J. Am. Ceram. Soc.*, **69** (1986) 652–6.
4. Huling, J. C. & Messing, G. L., Chemistry-crystallization relations in molecular mullite gels. *J. Non-Crystall. Solids*, **147/148** (1992) 213–21.
5. Fischer, R. X., Schneider, H. & Voll, D., The crystallization process of high alumina mullites. *J. Eur. Ceram. Soc.*, **16** (1996) 109–13.
6. Nishio, T. & Fujiki, Y., Preparation of mullite fiber by sol-gel method. *J. Ceram. Soc. Jpn.*, **99** (1991) 654–9.
7. Rietveld, H. M., A profile refinement method for nuclear and magnetic structure. *J. Appl. Crystallogr.*, **2** (1969) 65–71.
8. Izumi, F., A software package for the Rietveld analysis of X-ray and neutron diffraction patterns. *Nippon Kessho Gakkaishi*, **27** (1985) 23–31.
9. Ban, T. & Okada, K., Structure refinement of mullite by the Rietveld method and a new method for estimation of chemical composition. *J. Am. Ceram. Soc.*, **75** (1992) 227–30.
10. Schneider, H. & Lipinski, T. R., Occurrence of pseudo-tetragonal mullite. *J. Am. Ceram. Soc.*, **71** (1988) C162–4.
11. Kirkpatrick, R. J., Smith, K. A., Schramm, S. E., Turner, G. & Yang, W. H., Solid-state nuclear magnetic resonance spectroscopy of minerals. *Ann. Rev. Earth Planet. Sci.*, **13** (1985) 29–47.
12. Ryskin, Ya. I., The vibrations of protons in minerals: hydroxyl, water and ammonium. In *The Infrared Spectra of Minerals*, ed. V. C. Farmer. Mineralogical Society, London, 1974, pp. 137–81.



Anisotropic Grain Growth in Seeded and B₂O₃-doped Diphasic Mullite Gels

S.-H. Hong, W. Cermignani & G. L. Messing

Department of Materials Science and Engineering, The Pennsylvania State University, University Park, PA 16802, USA

(Accepted 22 July 1995)

Abstract

Anisotropic grain growth in mullite was investigated in B₂O₃-doped diphasic gels seeded with either mullite particles or whiskers. Anisotropic grain growth was observed in all systems. The largest anisotropic grains were obtained with a system seeded with 2 wt% mullite whiskers and doped with 2 wt% B₂O₃. The mullite whiskers act as sites for multiple nucleation and subsequently as templates for mullite overgrowth. Boria lowered the mullite formation temperature by 150°C and it significantly enhanced anisotropic grain growth independent of the presence of seed particles. This enhancement was attributed to increased dissolution of alumina.

1 Introduction

Anisotropic grain growth is one class of *in situ* reaction that is relatively unexplored but appears to offer significant opportunity for the development of new materials with self-reinforcing microstructures. Silicon nitride (Si₃N₄) is exemplary of how the mechanical properties of a polycrystalline ceramic can be improved by optimizing grain growth of anisotropic β -silicon nitride grains during the α to β -Si₃N₄ phase transformation. Today, silicon nitrides with fracture toughnesses of 10–20 MPa m^{1/2} can be routinely produced. Such highly fracture-resistant materials are a result of extensive experimentation. There is surprisingly little fundamental understanding about the processes leading to growth of anisotropic grains. Although silicon nitride has excellent mechanical characteristics, its low oxidation resistance limits its use in high temperature applications. Clearly, there is a need for oxide ceramics having similar self-reinforcing microstructures.

Mullite (3Al₂O₃·2SiO₂) has been recognised as an important structural and optical material due to its excellent high temperature strength, creep resistance, good chemical and thermal stability,

low thermal expansion coefficient and infrared transparency.^{1–3} The stable crystal structure of mullite is orthorhombic with lattice parameters $a = 7.5456 \text{ \AA}$, $b = 7.6898 \text{ \AA}$ and $c = 2.8842 \text{ \AA}$ (JCPDS Card # 15–776), and is composed of octahedral AlO₆ chains aligned in the c -direction and crosslinked by corner-shared AlO₄ and SiO₄ tetrahedra.⁴ Thus, unrestricted growth parallel to the c -axis favours the development of anisotropic grains.

A number of authors have demonstrated that sol–gel processes can be designed to control the degree of alumina–silica mixing and, consequently, control mullite crystallization kinetics, densification and microstructure evolution.⁵ Several authors^{6–10} have studied microstructural development of aluminosilicates with compositions near the single-phase mullite region. Equiaxed grains in alumina-rich mullites have been attributed to the kinetic limitation of material transport by solid-state diffusion whereas the presence of a liquid phase has been suggested to facilitate the growth of anisotropic grains in silica-rich mullites (i.e. < 74 wt% Al₂O₃). While a sol–gel polymeric mixture resulted in the equiaxed microstructure, variations in local chemical heterogeneity in a sol–gel colloidal mixture lead to anisotropic mullite grains at the same composition (72 wt% Al₂O₃).⁵

In ceramic systems which transform by nucleation and growth, another way to control microstructure evolution is to seed the precursor material. A homogeneous, fine-grained matrix ceramic can be obtained by using seed concentrations > 10¹³ seed particles/cm³ of matrix material. Huling and Messing¹¹ demonstrated that a fully dense, nominally 0.2 μm grain size mullite was obtained by seeding a diphasic gel with 30 wt% polymeric gels. They also reported that a hybrid gel consisting of polymeric and diphasic gels could be designed to control the nucleation frequency, reduce the grain size, and increase the microstructural homogeneity in a manner analogous to particle seeding. Mroz and Laughner¹² utilized

seeding to enhance anisotropic grain growth of mullite and reported that a dense, equiaxed grain structure was developed at a relatively high seed concentration, whereas highly anisotropic, large grains dispersed in a matrix of small, equiaxed grains were obtained at a low seed concentration.

Important factors affecting grain growth processes are: (1) the grain size of the microstructure when the sintered products become fully dense, and able to support grain growth (i.e. free of boundary inhibiting pores); and (2) the transport rate and solubility in systems with liquid phases. A dense, fine-grain microstructure has a large surface free energy associated with the grain boundaries and, thus, a large driving force for grain growth. The importance of a fine initial microstructure for anisotropic grain growth was recently demonstrated in TiO₂-doped alumina obtained by seeding an alumina gel.¹³

In the mullite system, it is known that densification is aided by viscous flow of the amorphous silica phase and that this glass phase also enhances the development of anisotropic grains. The viscosity of the glass phase in mullite can be decreased by several orders of magnitude by adding glass-forming oxides such as boron oxide (B₂O₃) and phosphorous oxide (P₂O₅). Na₂O, which is known to lower the viscosity of silica glasses, did not enhance either the mullite crystallization kinetics or the densification rate.¹⁴ However, the grain size increased and grain morphology changed from equiaxed to anisotropic with increasing Na₂O concentration. When B₂O₃ was added to a mullite precursor, it was reported to react first with alumina to form aluminum borate, 9Al₂O₃·2B₂O₃, a stable crystalline compound,¹⁵ and then to form the mullite phase. Thus, B₂O₃ significantly decreased the temperature of mullite formation.

The crystal structure of aluminum borate (9Al₂O₃·2B₂O₃) is orthorhombic, it has lattice parameters $a = 7.6874(8)$ Å, $b = 15.0127(5)$ Å and $c = 5.6643(6)$ Å (JCPDS Card # 32-3) and it consists of AlO₆ octahedra, AlO₄ tetrahedra, AlO₅ coordination polyhedra and B₂O₃ triangles.¹⁶ Based on similarities in the crystal structure and lattice parameters, it is reasonable to propose that aluminum borate can act as an epitaxial substrate for mullite nucleation and growth. Based on transmission electron microscope analysis, Richards *et al.* reported that the glass-forming oxides such as B₂O₃ or P₂O₅ do not exist as free glassy phases at the grain boundaries in sol-gel derived mullite fibres.¹⁷

While anisotropic grains are often observed in mullite ceramics, there have been few attempts to develop a self-reinforcing mullite microstructure. Also, it is not well understood how boria affects the mullite transformation kinetics and micro-

structural development. In this paper, we report a series of experiments designed to learn how the initial microstructure and the grain boundary chemistry can be adjusted to obtain a self-reinforced mullite microstructure. The objective of these initial studies is to learn about the fundamental factors controlling anisotropic grain growth in mullite.

2 Experimental Procedure

Microstructural development was evaluated for two series of samples. The first series of samples was seeded with either mullite seed particles or mullite whiskers. Any differences between these samples can be attributed primarily to the effect of the seeds on the mullite formation and subsequent microstructure evolution. Boria was added to a second series of samples to investigate the role of phase equilibria and transport on the mullite formation and anisotropic grain growth.

The diphasic sols were prepared from boehmite [γ -AlO(OH)] powder (Catapal D, Vista Chemical Co., Houston, TX) and a silica sol (Ludox AS-40, Du Pont Co., Wilmington, DE). Additional details are described elsewhere.¹¹ All samples contained identical Al₂O₃/SiO₂ ratios prior to calcination and were within the single-phase mullite region (~73 wt% Al₂O₃).

A mullite seed dispersion was prepared by dispersing a commercial mullite powder (Chichibu Cement Co., Ltd, Saitama, Japan) in distilled water adjusted to pH 3 with nitric acid. The dispersion was stirred for 3 days, sonicated and centrifuged at 2000 rev min⁻¹ for 30 min and the particles in suspension were used for seeding. The particle size distribution of the mullite seed particles was measured by a laser scattering technique (Horiba LA-900, Horiba Instrument Inc., Irvine, CA). The mullite whiskers (MW-10, Chichibu Cement Co. Ltd, Saitama, Japan) were dispersed in a manner similar to the mullite powder. The boria was introduced to the sol system as boric acid (H₃BO₃).

After heterocoagulating the boehmite and silica sol, they were gelled at 80°C. The gels were dried for 12 h at 80°C, ground with an alumina mortar and pestle, and sieved to < 74 μ m (-200 mesh). The powder was dry pressed at low pressure and then pellets, 12.7 mm diameter and 3 mm thickness, were cold isostatically pressed at 200 MPa. The pressed pellets were heated in air from 1600 to 1650°C for 1 to 10 h. For microstructure observation, the sintered samples were cut in half, polished with 0.1 μ m diamond paste and thermally etched at 100°C below the sintering temperature.

The micrographs were taken near the centre of the sample. An apparent aspect ratio was measured on the polished surface, but so far we have not attempted to calculate or measure the true aspect ratio.

The mullite formation temperature was determined by differential thermal analysis (DTA) at 10°C min⁻¹ in air (Thermal Analyst 2100, TA Instrument, New Castle, DE). X-ray diffraction (XRD) was used to determine the phases present after calcination, and the apparent density of the sintered samples was measured by the Archimedes method.

3 Results and Discussion

3.1 Mullite particle seeding

As determined by inductively coupled plasma emission spectroscopy (Leeman Labs PS3000UV), the composition of the mullite powder is 71.5 wt% Al₂O₃ and 28.5 wt% SiO₂. This composition is very close to that of 3:2 mullite (~71.8 wt% Al₂O₃). From the XRD measurement of the mullite powder, there was no angular separation of the reflection pair (120)/(210) around 26° 2θ, indicating that the seed particles are pseudotetragonal mullite.¹⁸ The median particle size of the as-received powder was ~1.6 μm and the median size of the mullite seed particles was ~0.14 μm, with the size range from 0.05 to 0.4 μm. The mullite seed particles are spherical and agglomerate-free as confirmed by scanning electron microscopy (SEM).

The mullite formation temperature in the diphasic gels was determined from the DTA exothermic peak maximum. As shown in Fig. 1, the mullite formation temperature decreases from 1345 to 1330°C at 2 wt% seeding. At 10 wt% seeding, the

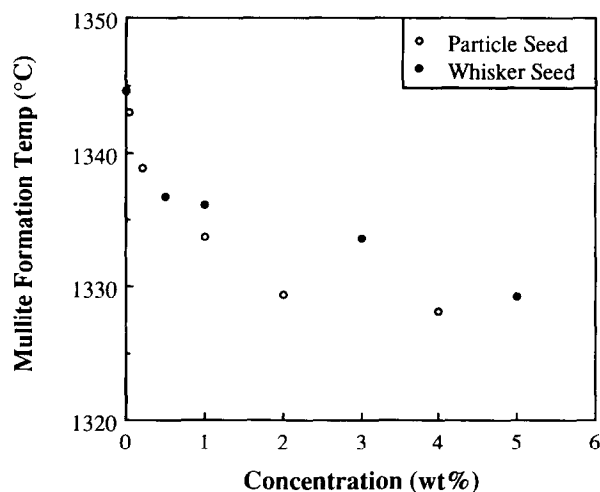


Fig. 1. Temperature of DTA exothermic peak maximum for mullite formation as a function of mullite particle and whisker concentration (heating rate: 10°C min⁻¹).

temperature decreases to 1318°C. The ~30°C decrease in mullite formation temperature relative to the unseeded diphasic gel is comparable to earlier results by Huling and Messing.¹¹ With increasing particle seed concentration, the exothermic mullite formation peak broadens and is obscured by the background. Broadening of the exothermic peak with increasing seed concentration indicates that mullite formation occurs over a wide temperature range. The plateau in mullite formation temperature was shown earlier to be a result of a change in the mullite formation mechanism from nucleation control to interface reaction control.¹⁹

The unseeded and seeded samples were ~97% dense after sintering for 5 h at 1650°C. The microstructures of the unseeded and seeded diphasic gels sintered at 1650°C for 5 h are compared in Fig. 2. In the unseeded samples (Fig. 2(A)), most of the grains are equiaxed with a small number of anisotropic grains whose largest aspect ratio does not exceed 3. The as-received mullite powder, which was sintered at the same sintering condition, yields the same microstructure and approximately the same sintered density as the unseeded colloidal sample. The microstructure of the 0.05 wt% seeded sample (Fig. 2(B)) is similar to the unseeded sample and shows both inter- and intragranular pores. The 0.05 wt% seed concentration corresponds to ~4 × 10¹¹ seed particles/cm³ of mullite powder and is the same order of magnitude as the intrinsic nucleation density in a similar diphasic mullite system.²⁰ In the 2 wt% seeded sample (Fig. 2(C)), anisotropic grains with an aspect ratio of ~5–6 are distributed in a matrix of micrometre-sized grains. Most of the intragranular pores were eliminated as a result of the grain size refinement.¹¹ The aspect ratio in the 10 wt% seeded sample (Fig. 2(D)) does not change much relative to the 2 wt% seeding concentration, but a larger fraction of anisotropic grains was observed. The matrix grains were free of intragranular pores and were ~2 μm in size with rectangular or square shapes. The grains with the polyhedral shapes are most likely end-on views of anisotropic mullite grains.

To determine how the anisotropic grains develop, the 2 wt% seeded samples were sintered at 1600 and 1650°C for 1 to 10 h. After 5 h at 1600°C, the samples are dense with only a few intragranular pores and quite small intergranular pores. The microstructure consists of some anisotropic grains with aspect ratios between 2 and 3 in a matrix of equiaxed, micrometre-sized grains (Fig. 3(A)). A similar microstructure is observed after sintering for 1 h at 1650°C (Fig. 3(B)). Larger anisotropic grains are formed and the aspect ratio increases with increasing sintering

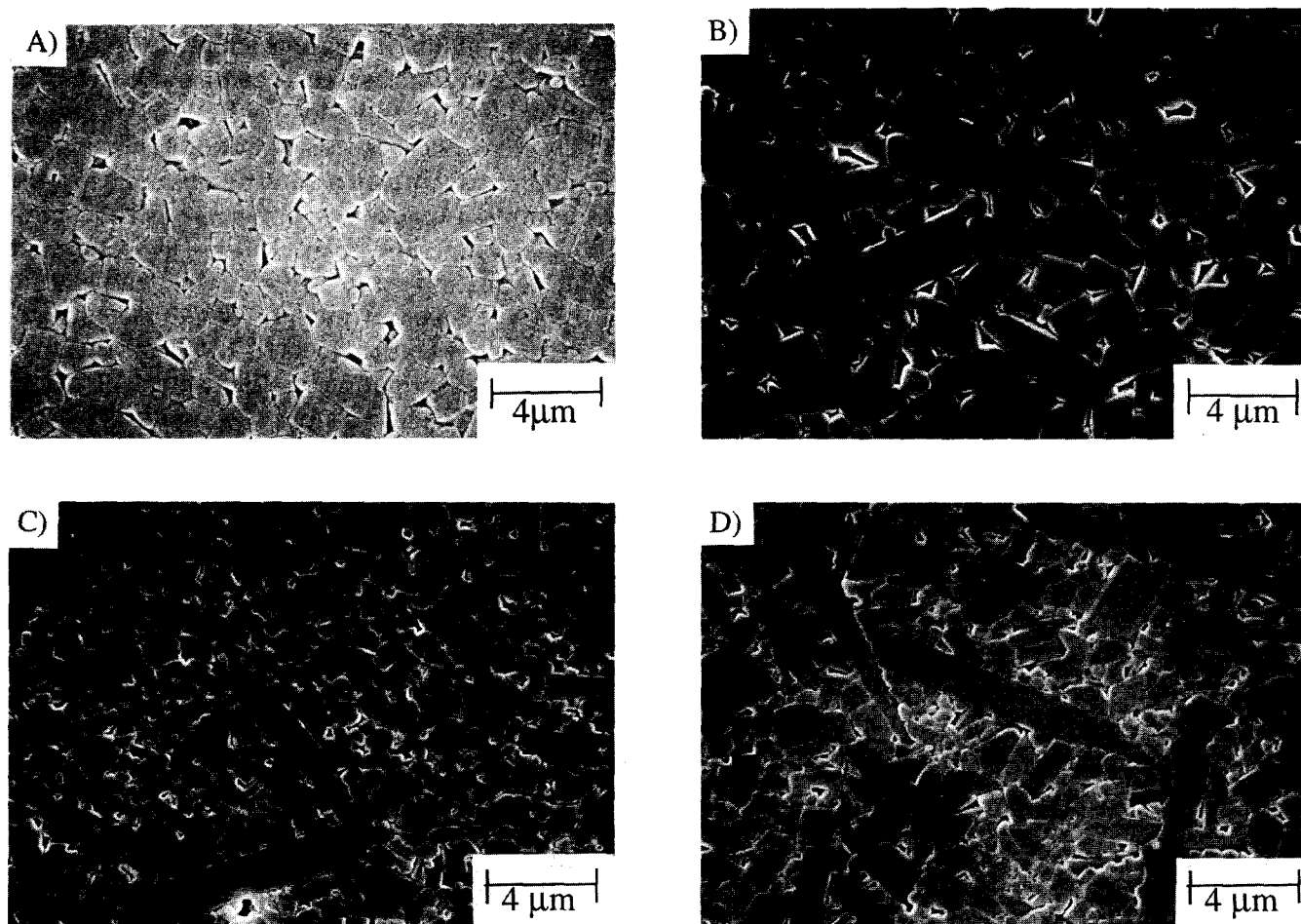


Fig. 2. SEM micrographs of polished diphasic mullite gels heated at 1650°C, 5 h. (A) unseeded; (B) 0.05 wt% mullite seeds; (C) 2 wt% mullite seeds; and (D) 10 wt% mullite seeds.

time and temperature, even though the surrounding equiaxed grains change little. This suggests that the anisotropic grains are nucleated early in the process. With increasing time and temperature, the anisotropic grains impinge and thicken to yield a microstructure of highly anisotropic grains with no intragranular pore.

The evolution of the above microstructure can be explained in terms of the driving force for grain growth and diffusion distance for pore elimination. For low or no seeding, there is a small number of mullite nuclei and grains grow from these nuclei by consuming the amorphous matrix. Thus, as pointed out earlier,²¹ mullite grain boundaries sweep through a larger volume and hence, more pores during the conversion to mullite, thus leaving some of the pores isolated within the grains (Figs 2(A) and 2(B)). In the samples which were seeded above the intrinsic nucleation density, mullite seeds are the active nucleation sites, and thus reduce the grain size after complete mullite conversion. The smaller grains have a large driving force for grain growth. Some grains begin to grow at the expense of the surrounding smaller grains, and these grains become anisotropic (Fig. 2(C)). After a longer sintering time, the anisotropic

grains continue to grow until they impinge. The impinged anisotropic grains cannot grow further, thus these grains begin to thicken. In highly seeded samples (Fig. 2(D)), such as 10 wt% seeding, the grains are initially much finer and the driving force for sintering and grain growth is larger than for lower seeding concentrations. Therefore, samples with a high seed concentration, sintered for a shorter time, develop a microstructure similar to samples with a lower seed concentration, but sintered for a longer time, as shown in Fig. 2(D) and in Fig. 3(D), respectively.

3.2 Mullite whisker seeding

The single crystal mullite whiskers shown in Fig. 4 have an average length of $\sim 5 \mu\text{m}$ and a diameter of $\sim 1 \mu\text{m}$. The chemical composition of the mullite whisker is 73 wt% Al_2O_3 ; the same as that of the diphasic matrix.

The apparent density decreases slightly with increasing whisker seed concentration, and the relative density of 5 wt% whisker seeded samples sintered at 1650°C for 5 h decreased to 95%.

The mullite formation temperature decreases with increasing whisker concentration (Fig. 1). At 5 wt% whisker seed concentration, the mullite

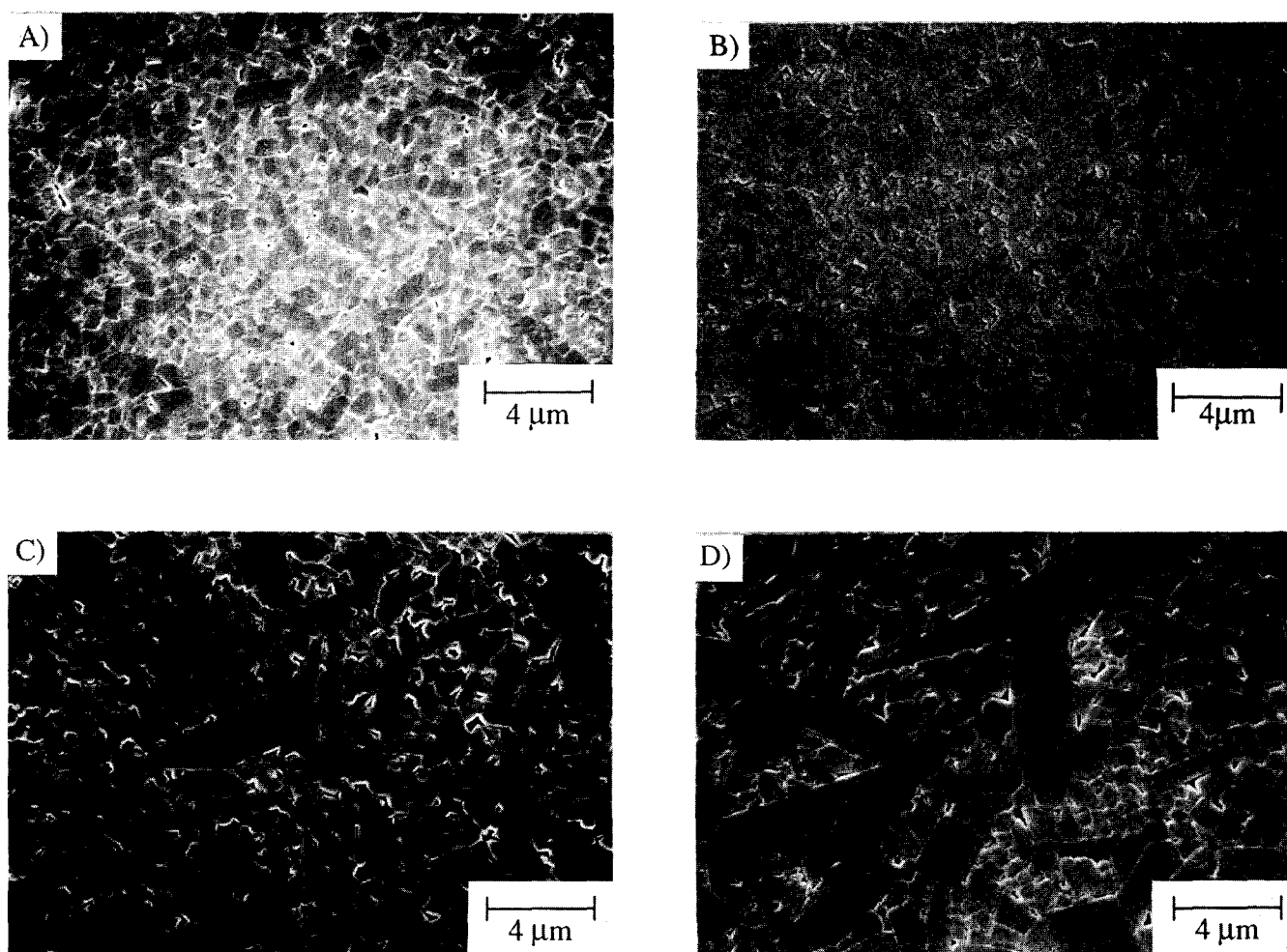


Fig. 3. Effect of time and temperature on the microstructural development of 2 wt% particle seeded mullite gels: (A) 1600°C, 5 h; (B) 1650°C, 1 h; (C) 1650°C, 5 h; and (D) 1650°C, 10 h.

formation temperature decreases by 15°C relative to that of the unseeded sample. In the whisker seeding case, the number of particles per unit weight of seeds is significantly less than in the particle seeding case but interestingly the mullite formation temperature is approximately the same. This suggests that each whisker acts as a site for multiple nucleation.

The micrographs of 1 wt% and 5 wt% whisker seeded samples sintered at 1650°C for 5 h are

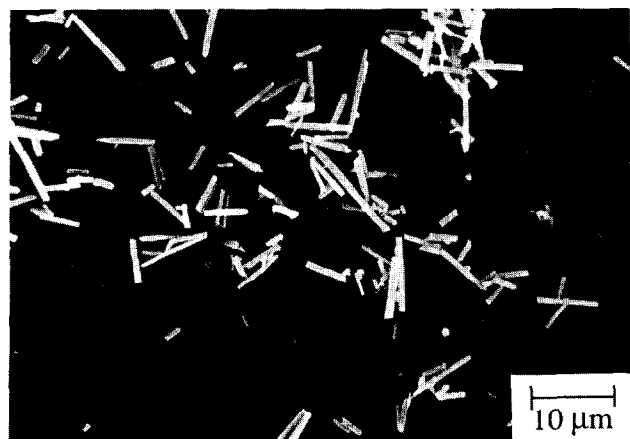


Fig. 4. SEM micrograph of single crystal mullite whiskers.

shown in Fig. 5. As a result of the preparation method, the whisker seeds are randomly distributed. At 1 wt% whiskers, the mullite grains appear to grow more in the axial direction rather than in the radial direction, which leads to an aspect ratio of ~8. At 5 wt% whisker concentration, many randomly distributed, anisotropic grains form and impinge to form a three-dimensionally interlocked microstructure. Again, the whiskers do not continue to grow in the axial direction, but grow in the radial direction, thus thickening the anisotropic grains and reducing the aspect ratio.

The microstructure of the 2 wt% whisker seeded colloidal mullite sample sintered at 1500°C and chemically etched with hydrofluoric acid (HF) for 15 min is shown in Fig. 6. It is evident that the whisker-shaped grain in the centre of the micrograph acted as a site for multiple nucleation. In this sample and many others observed, the anisotropic grains appear to have a mullite whisker core surrounded by an overgrowth layer as demonstrated by the presence of intragranular pores. The intragranular pores in this sample are reduced with increasing temperature and are completely eliminated at 1650°C.

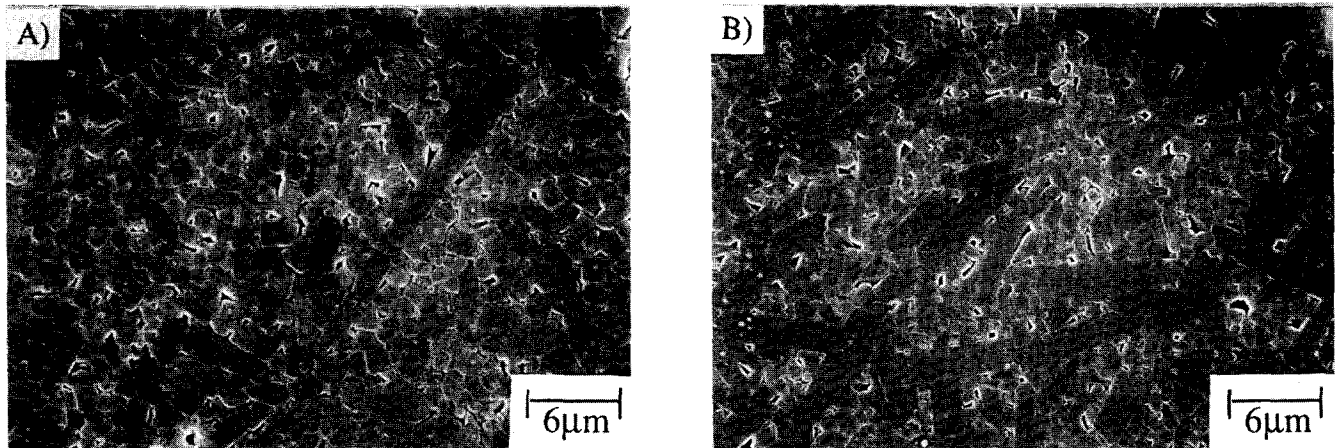


Fig. 5. SEM micrographs of mullite whisker seeded diphasic mullite gels heated at 1650°C for 5 h: (A) 1 wt% mullite whiskers; and (B) 5 wt% mullite whiskers.

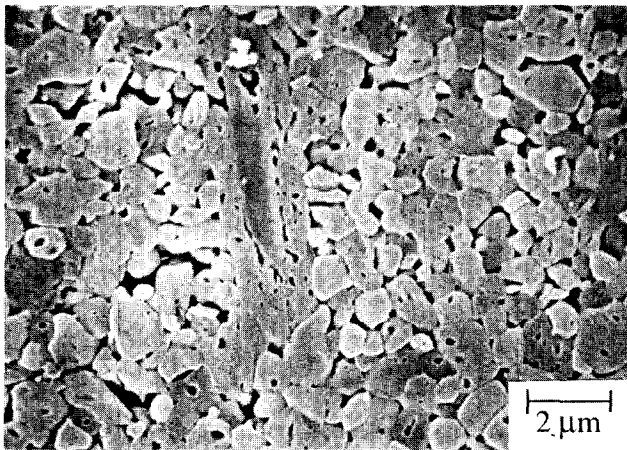


Fig. 6. SEM micrograph of chemically etched, whisker seeded diphasic mullite gel sintered at 1500°C for 5 h.

In both particle seeding and whisker seeding, the same microstructure was developed. However, seeding with whiskers allows for the possibility of aligning the elongated grains: e.g. if another forming method, such as tape casting or extrusion, is used, it is possible to develop a two-dimensionally textured microstructure.^{22,23}

3.3 Boria-doped gels

As expected, the apparent density decreases with increasing boria concentration. For example, the apparent density of the 5 wt% B_2O_3 -doped sample is 2.994 g cm^{-3} . The lower density may be due to the large pores surrounding the anisotropic grains as well as the lower theoretical density of B_2O_3 .

Sowman¹⁵ reported that in the Al_2O_3 - B_2O_3 - SiO_2 system, aluminum borate ($9Al_2O_3 \cdot 2B_2O_3$) forms first in a polymeric gel and then aluminum borosilicate crystalline phase forms by a solid solution reaction with SiO_2 . He attributed the sharp exothermic peak at 885°C to the formation of an aluminum borate compound. Richards *et al.*¹⁷ noted that this composition is not in the

stable mullite phase field and contains a high B_2O_3 concentration (12.5 wt%). In 2 wt% boria-doped sol-gel derived mullite fibre, a sharp exothermic peak at 911°C was confirmed by XRD to be associated with the formation of the spinel phase, and no aluminum borate phase was detected.

In our experiments, up to 5 wt% boria was added to a diphasic gel. However, no sharp exothermic peak was observed around 885°C but a strong exothermic peak was observed between 1200 and 1350°C, which is associated with the mullite formation. No diffraction peaks for aluminum borate or aluminum borosilicate phase were detected before mullite formation, and only mullite was observed after mullite formation. A broad peak at low diffraction angles in the XRD increased with increasing boria concentration, suggesting an increase in glass content with increasing B_2O_3 . The diffraction pattern of the sample sintered at 1650°C for 5 h shows an increase in (1 1 1), (1 2 1) and (3 3 1) peak intensities relative to the undoped mullite sample. This may be due to the incorporation of boron into the mullite, although this is still under investigation.

Based on chemical analysis, 60 wt% of the boria remained in the 5 wt% boria-doped sample after sintering at 1650°C for 5 h. Richards *et al.*¹⁷ reported that after 60 h at 1400°C, 65 wt% of the B_2O_3 in their fibres volatilized. Even though our samples were sintered at higher temperature, a higher percentage of boria remained in the samples. This may be due to differences in sample dimensions and geometry. For example, the diffusion distance from the mullite fibres of Richards *et al.*¹⁷ is significantly less than the bulk pellet samples used in this study.

The mullite formation temperature is plotted in Fig. 7 as a function of boria concentration for both unseeded and 2 wt% mullite particle seeded samples. The mullite formation temperature

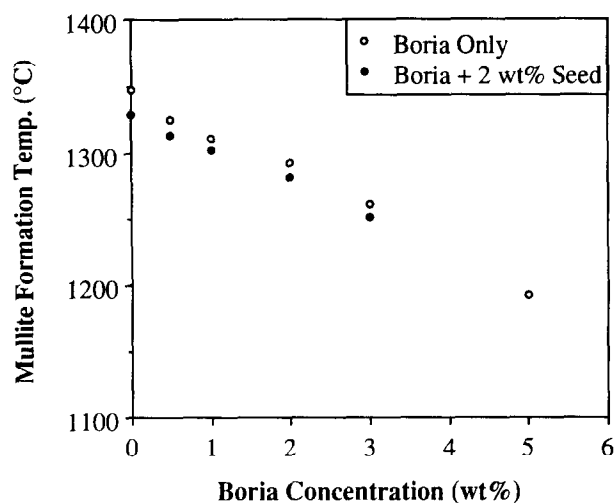


Fig. 7. Temperature of DTA exothermic peak maximum for unseeded and 2 wt% mullite particle seeded diphasic mullite gels as a function of boria addition.

decreases with increasing boria concentration for both samples. At 5 wt% boria, the mullite formation temperature decreases by 150°C relative to the undoped diphasic gel. This indicates that boria has a more dominant effect on the transformation kinetics than seeding. One possibility is that the boroaluminosilicate glass promotes mullite forma-

tion by increasing the solubility of alumina and diffusion rate in the glass phase.

Note that the microstructures of the 2 wt% particle seeded and unseeded samples are similar when B_2O_3 is present. As in the powder seeding and whisker seeding cases, the transformation peak broadened with higher boria concentrations, such that a distinct exotherm could not be observed for the 5 wt% B_2O_3 , 2 wt% particle seeded sample.

Micrographs of the unseeded and 2 wt% particle seeded samples containing B_2O_3 sintered at 1650°C for 5 h are shown in Fig. 8. There is no major difference between the two samples at the same B_2O_3 concentration. In both systems, increasing the boria concentration causes the growth of highly anisotropic grains. At 5 wt% boria, most of the grains are anisotropic and their cross-sections are square or rectangular shaped. There are only a few equiaxed grains. Also, there are several intergranular pores around the anisotropic grain surfaces while there are very few intragranular pores.

3.4 Whisker seeded diphasic mullite with boria

To combine the whisker seeding and boria doping

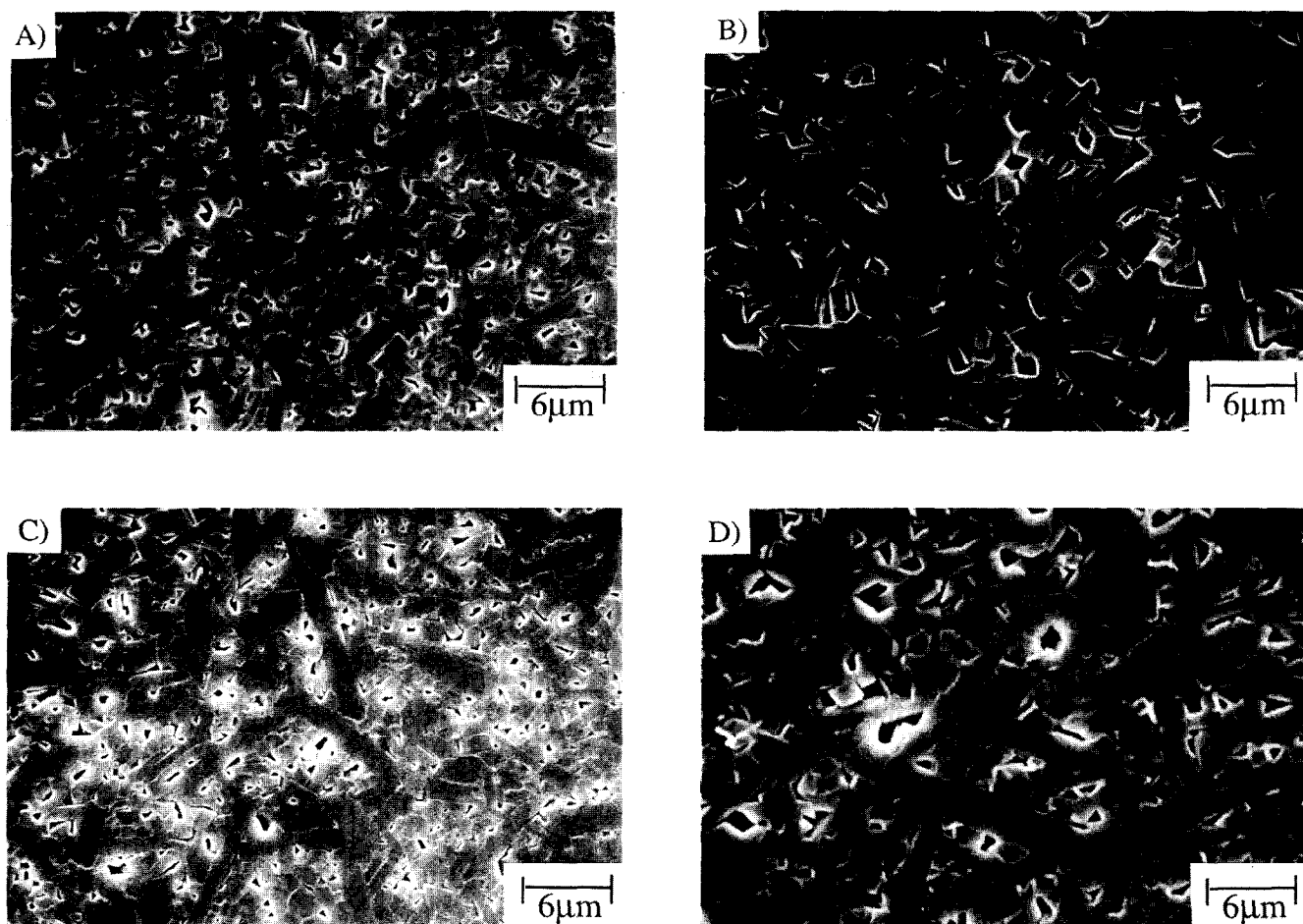


Fig. 8. SEM micrographs of samples heated at 1650°C, 5 h. Diphasic mullite gels doped with: (A) 2 wt% boria; (B) 5 wt% boria; and 2 wt% mullite particle seeded diphasic mullite doped with: (C) 2 wt% boria, (D) 5 wt% boria.

effects, 2 wt% boria was added to 2 wt% whisker seeded diphasic mullite sample. The mullite formation temperature is similar to the 2 wt% boria-doped diphasic mullite. Clearly, a microstructure of three-dimensionally interlocked, anisotropic grains is developed when this system was heated at 1650°C for 5 h (Fig. 9). Some highly anisotropic grains have an aspect ratio of >10 and a length of $>30 \mu\text{m}$.

A model for the microstructure development in whisker seeded and boria-doped diphasic mullite is shown in Fig. 10. Initially, the mullite whiskers are randomly distributed in the amorphous matrix which contains boria (stage A in Fig. 10). The single crystal whiskers provide multiple nucleation sites for overgrowth of mullite. At the same time, intrinsic nucleation occurs in the amorphous matrix (stage B). It is proposed that the boria-containing amorphous matrix facilitates the transport of diffusing ions to their preferred site along the c -axis of the whisker. Thus, the exaggerated, anisotropic grains develop by oriented overgrowth on the whiskers. At the same time, the surrounding grains are only slightly anisotropic at this stage. With further heating, a highly anisotropic microstructure is developed when the matrix grains also undergo anisotropic growth (stage C).

4 Summary

Seeding a diphasic mullite gel with mullite particles results in a decrease in the mullite formation temperature and the development of a fine-grained microstructure. Fine grains have a large driving force for grain growth and promote the preferential growth of mullite along its c -axis by coalescence of the surrounding fine grains to yield an anisotropic grain microstructure. At high seed concentration or at longer sintering time, the aspect ratio is limited by the impingement of the elongated grains and thickening occurs instead.

The mullite whiskers act as multiple nucleation sites for the diphasic precursor to form an 'overgrowth' layer. This overgrowth layer continues to grow with increasing temperature, resulting in highly anisotropic grains. Increasing the whisker concentration results in a gradual decrease in aspect ratio due to earlier impingement of the grains.

The boria-containing matrix enhances the mullite transformation kinetics and decreases the transformation temperature by 150°C compared with unseeded, undoped colloidal samples. The lower temperature appears to result from increased alumina solubility. By seeding with whiskers and doping with boria, highly anisotropic microstructures

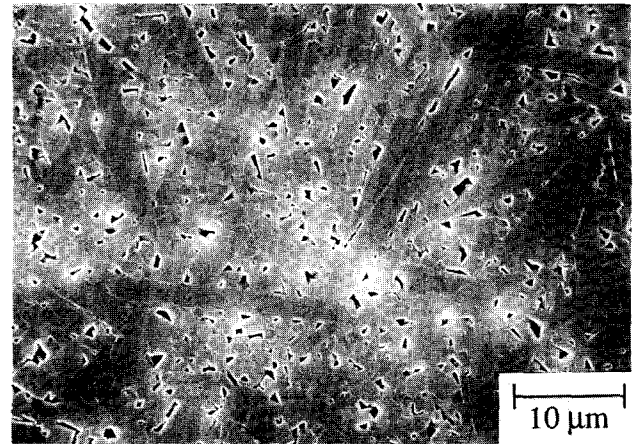


Fig. 9. SEM micrograph of 2 wt% whisker seeded and 2 wt% boria-doped diphasic mullite gel sintered at 1650°C for 5 h.

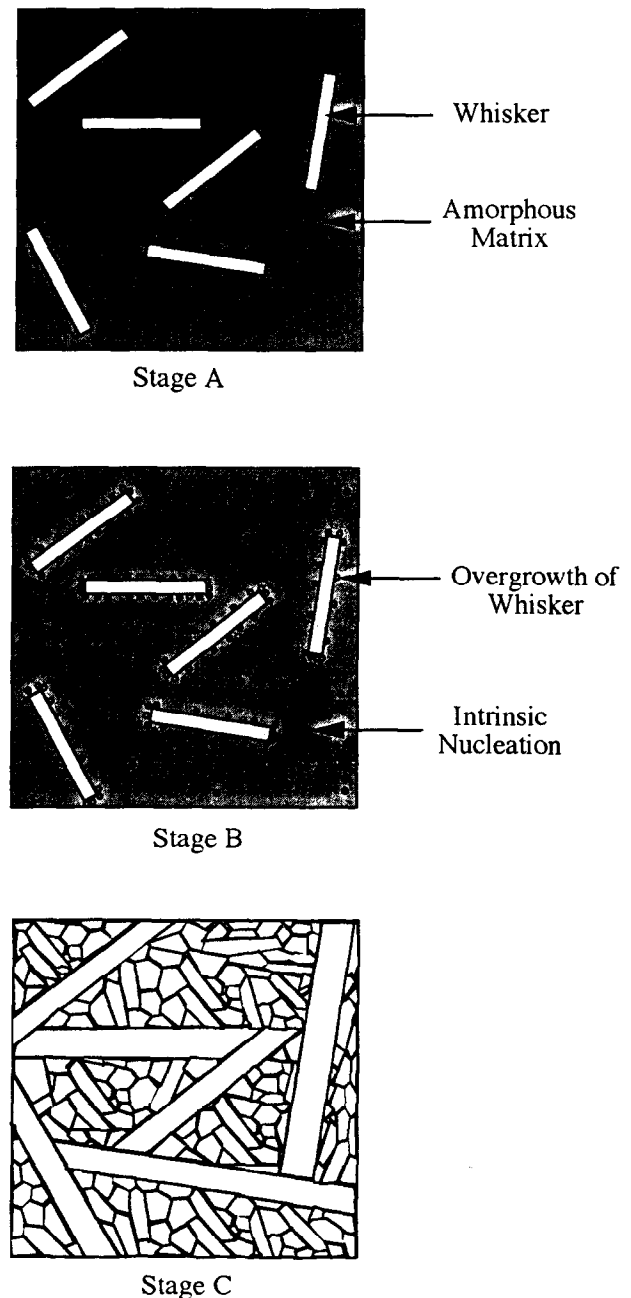


Fig. 10. Schematic model of microstructural development in whisker seeded and boria-doped diphasic mullite gel.

consisting of anisotropic grains with lengths as long as 30 μm and aspect ratios as high as 10 were developed.

Acknowledgements

The authors gratefully acknowledge the support of the Office of Naval Research under grant number N00014-94-1-0007. One of us (W.C.) thanks the Cooperative Research Program of the Center for Advanced Materials at Penn State for support.

References

1. Aksay, I. A., Dabbs, D. M. & Sarikaya, M., Mullite for structural, electronic, and optical applications. *J. Am. Ceram. Soc.*, **74**(10) (1991) 2343–58.
2. Lessing, P. A., Gordon, R. S. & Mazdiyasi, K. S., Creep of polycrystalline mullite. *J. Am. Ceram. Soc.*, **58**(3–4) (1975) 149.
3. Prochazka, S. & Klug, F. J., Infrared-transparent mullite ceramic. *J. Am. Ceram. Soc.*, **66**(12) (1983) 874–80.
4. Yla-Jaaski, J. & Nissen, H.-U., Investigation of superstructures in mullite by high resolution electron microscopy and electron diffraction. *Phys. Chem. Minerals*, **10** (1983) 47–54.
5. Pask, J. A., Zhang, X. W., Tomsia, A. P. & Yoldas, B. E., Effect of sol-gel mixing on mullite microstructure and phase equilibria in the $\alpha\text{-Al}_2\text{O}_3\text{-SiO}_2$ system. *J. Am. Ceram. Soc.*, **70**(10) (1987) 704–7.
6. Von Lohre, W. & Urban, H., Contribution to the morphology of mullite. *Ber. Dtsch Keram. Ges.*, **37** (1960) 249–51.
7. Ismail, M. G. U., Arai, H., Nakai, Z. & Akiba, T., Mullite whiskers from precursor gel powders. *J. Am. Ceram. Soc.*, **73**(9) (1990) 2736–9.
8. Sacks, M. D. & Pask, J. A., Sintering of mullite-containing materials: I, effect of composition. *J. Am. Ceram. Soc.*, **6**(2) (1982) 65–70.
9. Perry, G. S., Microwave dielectric properties of mullite. *Trans. Brit. Ceram. Soc.*, **72** (1973) 279–83.
10. Ohashi, M., Tabata, H., Abe, O., Kanzaki, S., Mitachi, S. & Kumazawa, T., Preparation of translucent mullite ceramics. *J. Mater. Sci. Lett.*, **6** (1987) 528–30.
11. Huling, J. C. & Messing, G. L., Hybrid gels for homoepitactic nucleation of mullite. *J. Am. Ceram. Soc.*, **72**(9) (1989) 1725–9.
12. Mroz, T. J. & Laughner, J. W., Microstructures of mullite sintered from seeded sol-gels. *J. Am. Ceram. Soc.*, **72**(3) (1989) 508–9.
13. Horn, D. S. & Messing, G. L., Anisotropic grain growth in titania-doped alumina. *Mat. Sci. Eng. A.*, **A195** (1995) 169–78.
14. Fahrenholtz, W. G. & Smith, D. M., Densification and microstructure of sodium-doped colloidal mullite. *J. Am. Ceram. Soc.*, **77**(5) (1994) 1377–80.
15. Sowman, H. G., Alumina-boria-silica ceramic fibers from the sol-gel process. In *Sol-Gel Technology for Thin Films, Fibers, Performs, Electronics, and Specialty Shapes*, ed. L. C. Klein, Noyes, Park Ridge, NJ, 1988, pp. 162–82.
16. Ihara, M., Imai, K., Fukunaga, J. & Yoshida, N., Crystal structure of boro-aluminate, $9\text{Al}_2\text{O}_3 \cdot 2\text{SiO}_2$. *Yogyo Kyokaishi*, **33**(2) (1980) 2605–9.
17. Richards, E. A., Goodbrake, C. J. & Sowman, H. G., Reactions and microstructure development in mullite fibers. *J. Am. Ceram. Soc.*, **74**(10) (1991) 2404–9.
18. Schneider, H. & Lipinski, T. R., Occurrence of pseudo-tetragonal mullite. *J. Am. Ceram. Soc.*, **71**(3) (1988) C-162–4.
19. Huling, J. C. & Messing, G. L., Epitactic nucleation of spinel in aluminosilicate gels and its effect on mullite crystallization. *J. Am. Ceram. Soc.*, **74**(10) (1991) 2374–81.
20. Wei, W.-C. & Halloran, J. W., Transformation kinetics of diphasic aluminosilicate gels. *J. Am. Ceram. Soc.*, **71**(1) (1988) 581–7.
21. Huling, J. C. & Messing, G. L., Hybrid gels designed for nucleation and crystallization control of mullite. In *Better Ceramics Through Chemistry IV (Materials Research Society Symposium Proceedings Vol. 180)*, eds B. J. J. Zelinski, C. J. Brinker, D. E. Clark & D. R. Ulrich, Materials Research Society, Pittsburgh, PA, 1990, pp. 515–26.
22. Sabol, S. M., Messing, G. L. & Tressler, R. E., Textured alumina fibers with elongated grains. *HiTemp Review 1992*, Vol. 1, NASA CP-10104, 21–1–14, 1992.
23. Wu, M. & Messing, G. L., Fabrication of oriented SiC whisker-reinforced mullite matrix composites by tape casting. *J. Am. Ceram. Soc.*, **77**(10) (1994) 2586–92.

Single-phase and Diphasic Aerogels and Xerogels of Mullite: Preparation and Characterization

Sridhar Komarneni* & Claire Rutiser

Intercollege Materials Research Laboratory, The Pennsylvania State University, University Park, PA 16802, USA

(Accepted 22 July 1995)

Abstract

Single-phase mullite composition gels have been synthesized using tetraethoxysilane [$\text{Si}(\text{OC}_2\text{H}_5)_4$] and aluminum nitrate nonahydrate as precursors. Diphasic mullite gels have been prepared using colloidal silica and boehmite as precursors. Xerogels and aerogels of both the above gels have been obtained by ordinary drying in air at 60°C and critical point drying in methanol, respectively. Single-phase xerogels show an intense exothermic peak at about 980°C while their counterparts, aerogels, do not show any detectable exotherm by differential thermal analysis (DTA). These results suggest that the structure of single phase gels changed during critical point drying and the structural changes were investigated by solid-state ^{27}Al magic angle spinning nuclear magnetic resonance (MAS NMR) spectroscopy. No differences between diphasic xerogels and aerogels could be detected by DTA because there was little or no effect of drying on the discrete silica and alumina phases. The tetrahedral coordination of Al in single-phase mullite gel changed to octahedral coordination as detected by MAS NMR during critical point drying, which suggests that the alumina component segregated. Both single-phase and diphasic aerogels of mullite composition showed very high surface areas in the temperature range $1000\text{--}1400^\circ\text{C}$ and these may be useful for high temperature catalytic applications.

Introduction

The concept of diphasic nanocomposites for the synthesis of mullite, $\text{Al}_6\text{Si}_2\text{O}_{13}$ and other compositions was first introduced by us.^{1–3} The diphasic mullite gels led to enhanced densification at very low temperatures.^{4–5} The mechanism of nucleation and densification in single and diphasic gels has been studied by numerous investigators.^{6–12} Solid-

state nuclear magnetic resonance studies of ^{27}Al and ^{29}Si have revealed that single-phase gels made from aluminum nitrate and tetraethoxysilane are mixed on an atomic to molecular level while the diphasic gels are mixed on a nanometre scale.^{13–14}

The single-phase gels crystallize to mullite at lower temperatures than the diphasic gels. The rapid crystallization of mullite in the former gels is not conducive for densification while the diphasic gels led to enhanced densification apparently due to densification and crystallization in a very narrow temperature range.¹⁵ The enormous worldwide interest in mullite for high temperature structural applications is due to its high creep and thermal shock resistance as well as its high strength at very high temperatures. For extremely good mechanical properties, the achievement of full densification with fine microstructure and without any glassy phase is imperative. This is the reason why there are numerous studies on mullite densification. The study of porous mullite ceramics for high temperature catalysis, separations, etc., has, however, been neglected. Thus the objectives of this study are (1) to prepare and characterize single-phase and diphasic aerogels and xerogels of mullite and (2) to characterize the porosity characteristics of these mullite gels after sintering to high temperatures.

Experimental

Preparation of mullite single-phase gels

Mullite single-phase gels and diphasic gels were made by the procedure used previously.^{1,4,5} Aluminum nitrate nonahydrate (56.16 g) was mixed with 95% ethyl alcohol (75 ml) and stirred for 1 h. Tetraethylorthosilicate (TEOS) (11.1 ml) was added and the sol was poured into tubes and kept at 60°C until gelation. After gelation, gels were exchanged in methanol for 4–12 days more. Aerogels were made by critical point drying and xerogels were made by drying at 60°C .

*Also with the Department of Agronomy.

Preparation of mullite diphasic gels

Mullite diphasic gels, with excess Al_2O_3 (nominal composition: 86.5% Al_2O_3 –13.5% SiO_2) were made by mixing boehmite (39.34 g) with 160 ml of distilled water for 30 min. Concentrated nitric acid was added to bring the pH to 3. Commercial colloidal silica (Ludox AS40) was added (12.12 g) and the sol was stirred. The sol was poured into glass tubes and gelled. After gelation the diphasic gels were exchanged with methanol. Diphasic mullite aerogels and xerogels were made in the same fashion as those of single-phase mullite gels.

Aerogel preparation by supercritical drying

Both the single-phase and diphasic mullite gels were aged in methanol at room temperature for 4–12 days to exchange residual water out of the pores of the gels. Aerogels were produced by methanol or ethanol critical point drying at 260 or 270°C and 8.27 MPa in a 50 ml Hastalloy C autoclave (Autoclave Engineers). Both single-phase and diphasic mullite gels were run simultaneously so they would have identical drying conditions. The two types of gel in Pyrex tubes were critical point dried in each 4 h run of the autoclave. Two tubes were placed in the autoclave, and 15 ml of alcohol was added to maintain alcohol vapour pressure during the heating period to prevent the premature loss of pore fluid from the gel. An anti-seize compound (Permatex Industrial anti-seize lubricant) was added to the threads, and the vessel was sealed. The autoclave was pre-pressurized with nitrogen to 8.27 MPa, and a three-stage program was activated on the Omega CN 2041 programmable temperature controller. The first stage heated the autoclave from room temperature to 260 or 270°C over 3 h. The pressure was released manually every 15–30 min to maintain the autoclave pressure in the range 8.27 to 8.96 MPa. For the second stage, the pressure was maintained at 8.27 MPa and the temperature was kept at 260 or 270°C. After 15 min into this second stage, the argon valve was opened and the autoclave exhaust valve was opened slightly to purge the supercritical methanol from the chamber. After 15 min of purging, the pressure on the autoclave vessel was released and the temperature was allowed to decrease slowly.

Sintering of aerogels

Sintering was carried out on unground samples. Each individual aerogel sample was sub-sampled for nitrogen BET analysis. Then samples of about 0.1 g each were removed for sintering. The aerogel and xerogel samples were sintered at 900, 1000, 1200 and 1400°C for 2 h. A Lindberg programmable furnace was used with a heating rate of 2°C

min^{-1} ; cooling rates were no greater than 2°C min^{-1} . Samples were weighed before and after sintering to determine weight loss. Sintering was carried out in platinum trays with platinum foil covering the samples.

Characterization of aerogels

The aerogels were characterized to determine thermal stability, analyse the phases present, and measure textural properties. BET nitrogen adsorption analysis was the primary characterization technique for textural properties.

Powder X-ray diffraction of variously treated aerogels and xerogels

Powder X-ray diffraction (XRD) was carried out using a Scintag X-ray diffractometer with Ni-filtered CuK_α radiation. Powders were dispersed on glass slides using ethanol. The diffraction data were analysed using standard commercial software and the standard diffraction data provided by the Joint Committee on Powder Diffraction Standards (JCPDS).

Differential thermal analysis

The xerogels and aerogels were characterized by differential thermal analysis (DTA) with a Perkin–Elmer DTA 1700 instrument using a heating rate of 10°C min^{-1} in air.

^{27}Al magic angle spinning nuclear magnetic resonance (MAS NMR) spectroscopy

The mullite aerogel and xerogel samples were characterized by ^{27}Al MAS NMR spectroscopy using a SDS 360 instrument operating at a Larmor frequency of 94.669 MHz. The samples were spun at 8.5 to 10.5 kHz and the chemical shifts are reported as ppm with respect to $[\text{Al}(\text{H}_2\text{O})_6]^{3+}$ as an external standard.

Scanning electron microscopy (SEM)

An ISI DS-130 scanning electron microscope was used for determining the particle size and morphology of the as-prepared and sintered single-phase and diphasic aerogels.

BET nitrogen adsorption analysis

Surface area analysis and pore size distribution were determined by multi-point BET analysis and by adsorption and desorption isotherms of nitrogen using an Autosorb-1 (Quantachrome, Syosset, New York). As-prepared aerogels and sintered aerogels were ground gently in an agate mortar with a pestle. Powders (0.04 to 0.08 g) were weighed and transferred to glass BET tubes of known weight. The samples were degassed at 60°C for 30 min or longer. The samples were weighed in

BET tubes and true sample weights were calculated, following standard procedures.

Twenty-point adsorption isotherms and 20-point desorption isotherms were obtained for each sample. The multipoint BET surface area was determined using up to eight adsorption points. Pore size distribution was determined using desorption $D(v)dr$ plots. For comparison purposes, a numerical pore size figure was determined by measuring the centre of the peak at half of the maximum peak amplitude.

Results and Discussion

Differential thermal analysis curves of aerogels and xerogels are shown in Fig. 1. The single-phase xerogel shows an intense exotherm at about 980°C (Fig. 1(A)), as expected based on previous studies, due to atomic or molecular scale mixing of alumina and silica components.^{13,14} The single-phase aerogel, however, shows no exotherm (Fig. 1(B)) in the high temperature range 500–1200°C in a similar way to that of a diphasic mullite gel (Fig. 1(C)). The absence of an exotherm at 980°C in single-phase mullite aerogel was unexpected, but it was expected in the case of diphasic mullite aerogel, the latter being based on previous studies

of diphasic xerogels.¹ Thus, the single-phase mullite aerogel is showing a thermal behaviour similar to that of a diphasic aerogel or xerogel. The above implies that the single-phase mullite gel may have altered during methanol critical point drying to a type of diphasic gel, probably due to the segregation and crystallization of alumina phase.

This hypothesis was tested by powder XRD and ²⁷Al MAS NMR spectroscopy. The as-prepared single-phase xerogel and aerogel show somewhat similar XRD patterns (not shown) with little or no crystallinity and, thus, no difference between the two can be detected. Boehmite could not be detected in the as-prepared aerogel by XRD. The as-prepared diphasic aerogel shows boehmite which is one of the starting phases. The amorphous silica sol cannot be detected by XRD, as expected. The segregation and crystallization of alumina phase to boehmite-like phase during critical point drying of single-phase mullite gel at 270°C is uncertain based on these XRD studies. For this reason, ²⁷Al MAS NMR spectra of the three different gels (Fig. 2) were obtained to detect any differences. The single-phase xerogel (Fig. 2(A)) shows two ²⁷Al resonances, one at 54.56 ppm and another at 0.449 ppm which can be attributed to the tetrahedral and octahedral

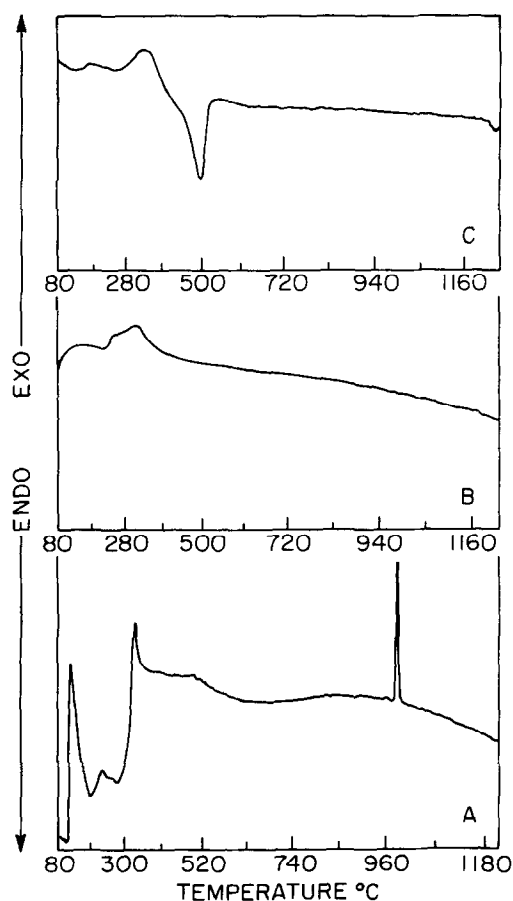


Fig. 1. Differential thermal analysis curves of (A) single-phase mullite xerogel, (B) single-phase mullite aerogel and (C) diphasic mullite aerogel.

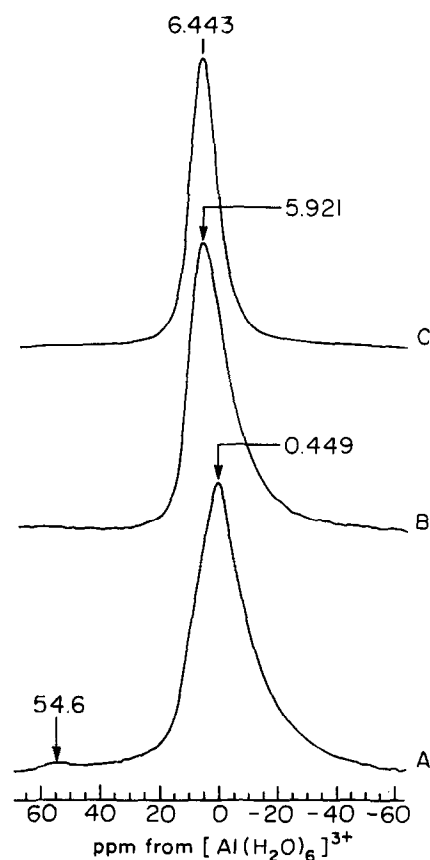


Fig. 2. ²⁷Al MAS NMR spectra of (A) single-phase mullite xerogel, (B) single-phase mullite aerogel and (C) diphasic mullite aerogel. Since these chemical shifts are not corrected for quadrupolar effects, the decimals have no significance.

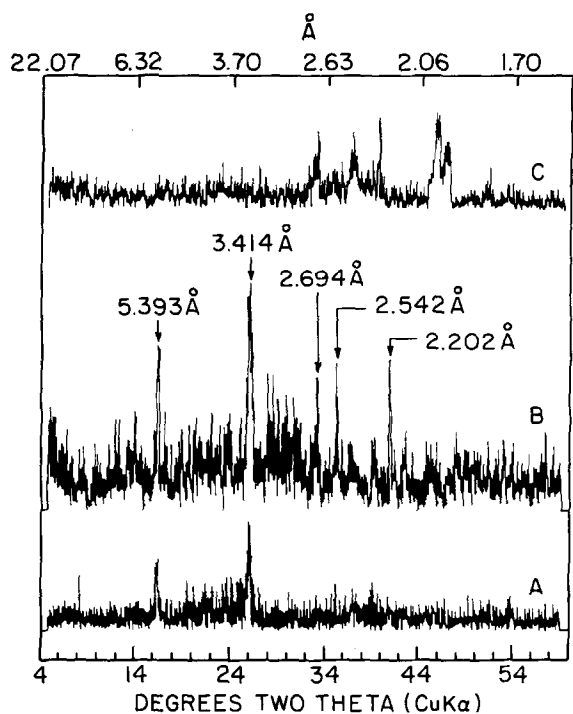


Fig. 3. Powder X-ray diffraction patterns of different mullite gels after DTA run to 1250°C: (A) single-phase xerogel shows mullite peaks, (B) single-phase aerogel shows mullite peaks and (C) diphasic aerogel shows delta alumina peaks.

coordinations, respectively. The tetrahedral coordination of Al implies that part of the Al is in the nearest neighbour environment of silicon due to atomic-scale mixing. When the single-phase gel was dried under supercritical conditions to prepare the aerogel, the ^{27}Al resonance at 54.56 ppm disappeared and only the octahedral ^{27}Al resonance at 5.92 ppm was present (Fig. 2(B)). The diphasic aerogel shows only one resonance at 6.44 ppm (Fig. 3(C)) representing all Al in octahedral coordination because boehmite is one of the starting phases which has Al in octahedral coordination only. Thus the ^{27}Al MAS NMR data show that the alumina component segregated during critical point drying of the single-phase gel to form a boehmite-like phase. These results are supported by the work of Mizushima and Hori,¹⁶ who showed that small boehmite crystals recrystallized to larger crystals during long (72 h) critical point drying of boehmite aerogels.

Powder XRD results of single-phase xerogel and aerogel and diphasic aerogel after heat treatment to 1250°C in the differential thermal equipment shows the formation of mullite in both the single-

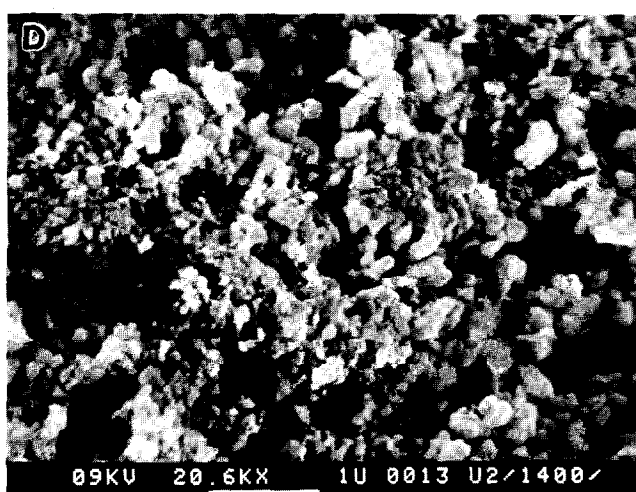
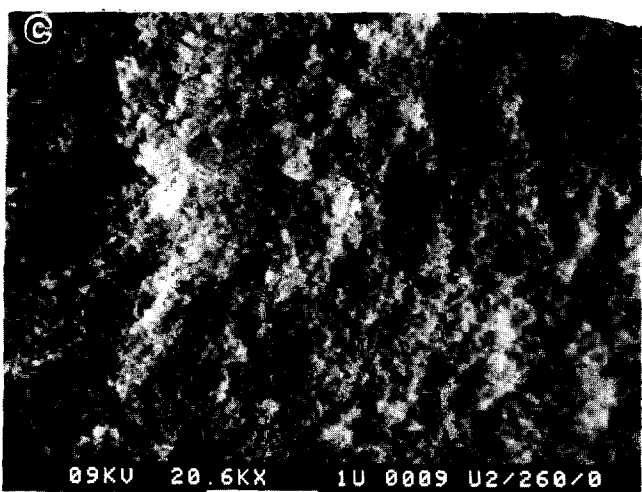
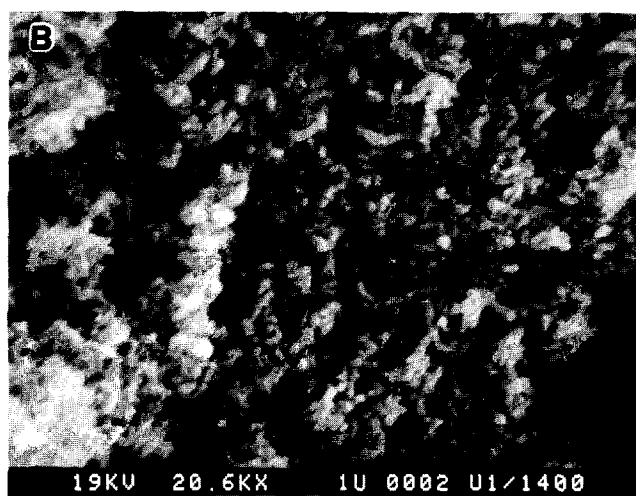
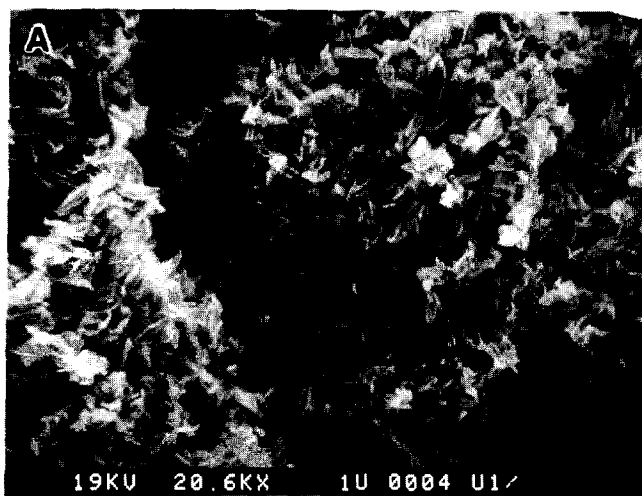


Fig. 4. Scanning electron micrographs of mullite gels: (A) as-prepared single-phase gel, (B) single-phase gel sintered at 1400°C/2 h, (C) as-prepared diphasic gel and (D) diphasic gel sintered at 1400°C 2 h.

Table 1. Surface area and pore sizes of as-prepared and sintered single-phase and diphasic aerogels of mullite composition

	As prepared, 260°C		As prepared, 270°C		Sintered ^d at 1000°C, 2 h		Sintered ^d at 1200°C, 2 h		Sintered ^d at 1400°C, 2 h	
	Surface area (m ² g ⁻¹)	Pore radius (nm)	Surface area (m ² g ⁻¹)	Pore radius (nm)	Surface area (m ² g ⁻¹)	Pore radius (nm)	Surface area (m ² g ⁻¹)	Pore radius (nm)	Surface area (m ² g ⁻¹)	Pore radius (nm)
Single phase	334	1.8; 17 ^b	434	2.1; 13 ^b	309	1.8; 15 ^b	66	nd ^c	27	1.3; 4 ^b
Diphasic	152	13	180	22	148	1.4	93	20	15.7	1.3; 3.2; 26 ^b

^aSintered samples were critical point dried at 260°C.

^bTwo or more numbers indicate different pore radii in the same gel in order of their abundance as determined by the areas of peaks from pore-size distribution plots.

^cNot determined.

phase xerogel and aerogel. The diphasic aerogel, however, shows only delta alumina under the dynamic heating condition (10°C min⁻¹) of the DTA. These results show that the alteration of single-phase gel to diphasic gel during critical point drying can be detected by both DTA and ²⁷Al MAS NMR but not by XRD. Thus DTA and ²⁷Al MAS NMR techniques are more sensitive than XRD in identifying phase segregation in mullite gels.

The scanning electron micrograph of the as-prepared single-phase mullite aerogel shows porosity and an interesting acicular morphology (Fig. 4(A)). This aerogel sample sintered to 1400°C also shows needle-shaped mullite crystals (Fig. 4(B)). The as-prepared diphasic gel shows porosity and a very fine grained structure (Fig. 4(C)) as expected, because of the two mixed sols. The sintered diphasic porous mullite shows equiaxed, submicrometre grains (Fig. 4(D)). All the mullite composition gels showed mullite by XRD after sintering at 1400°C.

The textural properties of the as-prepared and sintered single-phase and diphasic mullite gels are shown in Table 1. The different aerogels of mullite retain high surface areas in the temperature range 1000–1400°C, which suggests that these can be tailored for high-temperature catalytic applications.

Conclusions

Both single and diphasic aerogels of mullite composition exhibit high surface areas after sintering in the temperature range 1000–1400°C. Segregation of the alumina component occurred during critical point drying of single-phase mullite composition gels. Sintered aerogels of mullite composition may be useful for high temperature catalytic applications.

Acknowledgement

This research was supported by the US Department of Energy under Grant No. DE-FGO2-85ER45204.

References

- Hoffman, D. W., Roy, R. & Komarneni, S., Diphasic xerogels, a new class of materials: phases in the Al₂O₃-SiO₂ system. *J. Am. Ceram. Soc.*, **67** (7) (1984) 468–71.
- Hoffman, D. W., Roy, R. & Komarneni, S., Diphasic ceramic composites via a sol-gel method. *Mater. Lett.*, **2** (1984) 245–7.
- Vilmin, G., Komarneni, S. & Roy, R., Crystallization of ThSiO₄ from structurally and/or compositionally diphasic gels. *J. Mater. Res.*, **2** (1987) 489–93.
- Komarneni, S., Suwa, Y. & Roy, R., Application of compositionally diphasic xerogels for enhanced densification: the system Al₂O₃-SiO₂. *J. Am. Ceram. Soc.*, **69**(7) (1986) C-155–6.
- Komarneni, S. & Roy, R., Mullite derived from diphasic gels. In *Mullite and Mullite Matrix Composites*, *Ceramic Transactions*, eds S. Somiya, R. F. Davis & J. A. Pask, The American Ceramic Society, Westerville, OH, Vol. 6, 1990, pp. 209–20.
- Yoldas, B. E. & Partlow, D. P., Formation of mullite and other alumina-based ceramics via hydrolytic polycondensation of alkoxides and resultant ultra- and micro-structural effects. *J. Mater. Sci.*, **23**(5) (1988) 1895–900.
- Columban, Ph, Gel technology in ceramics, glass-ceramics and ceramic-ceramic composites. *Ceramics Int.*, **15**(2) (1989) 23–50.
- Wei, W. C. & Halloran, J. W., Phase transformation of diphasic aluminosilicate gels. *J. Am. Ceram. Soc.*, **71**(3) (1988) 166–72.
- Huling, J. C. & Messing, G. L., Hybrid gels for homoepitactic nucleation of mullite. *J. Am. Ceram. Soc.*, **72**(9) (1989) 1725–9.
- Okada, K., Otsuka, N. & Somiya, S., Recent mullitization studies in Japan. *Am. Ceram. Soc. Bull.*, **70**(10) (1991) 2414–18.
- Wei, W. C. & Halloran, J. W., Transformation kinetics of diphasic aluminosilicate gels. *J. Am. Ceram. Soc.*, **71**(3) (1988) 166–72.
- Wang, Y., Li, D. X. & Thomson, W. J., *Mater. Res.*, **8**(1) (1993) 195–205.
- Komarneni, S., Roy, R., Fyfe, C. A., Kennedy, G. J. & Strobl, H., Solid state ²⁷Al and ²⁹Si Magic-angle spinning NMR of aluminosilicate gels. *J. Am. Ceram. Soc.*, **69** (1986) C42–4.
- Selvaraj, U., Komarneni, S. & Roy, R., Structural differences in mullite xerogels from different precursors characterized by ²⁷Al and ²⁹Si MAS NMR. *J. Solid State Chem.*, **106** (1993) 73–82.
- Pach, L., Iratni, A., Hrabe, Z., Svetik, S. & Komarneni, S., Sintering and characterization of mullite in diphasic gels. *J. Mater. Sci.* (submitted).
- Mizushima, Y & Hori, M., Properties of alumina aerogels prepared under different conditions. *J. Non-Cryst. Solids*, **167** (1994) 1–8.

Effect of Aging Temperature on the Structure of Mullite Precursor Prepared from Tetraethoxysilane and Aluminum Nitrate in Ethanol Solution

Kiyoshi Okada,* Chikako Aoki,† Takayuki Ban, Shigeo Hayashi & Atsuo Yasumori

Department of Inorganic Materials, Tokyo Institute of Technology, O-okayama, Meguro, Tokyo 152, Japan

Abstract

The effect of aging temperature on the structure of mullite precursor prepared by dissolving tetraethoxysilane (TEOS) and aluminum nitrate nonahydrate (ANN) in ethanol was investigated by liquid state ^{29}Si and ^{27}Al nuclear magnetic resonance (NMR) spectroscopy, small angle X-ray scattering (SAXS), powder X-ray diffraction (XRD) and solubility of ANN in ethanol. The aging temperatures examined were from 25 to 60°C. With increasing aging temperature, polymerization of TEOS progressed, size of sol particles increased, and solubility of ANN largely increased but little change occurred in the coordination state of the Al ion. Mullite was obtained as the main crystalline phase only when the precursor solution aged at 60°C was fired at 1000°C, whereas the spinel phase was obtained as the main crystalline phase instead of mullite from the solutions aged at the other temperatures. It was therefore concluded that silica and alumina components in the precursor solution were in an intimately mixed state when the precursor solution was aged at 60°C, but those aged under 60°C were not as intimately mixed as the former. Intimate mixing of both components was achieved in the precursor solution aged at 60°C by trapping of ANN solution in silica gel network.

1 Introduction

Mullite has been actively investigated by many workers during the last decade¹ and its good mechanical properties, especially at high temperature, are recognized. It is, therefore, expected to be a candidate material for high temperature applica-

tions under an oxidizing atmosphere. Various kinds of starting materials and preparation methods were studied as the raw materials for mullite ceramics.¹ Generally, their starting materials are in an amorphous state and mullitization occurs at high temperature before the densification. Although a variety of results on this subject were reported, mullitization pathways can be divided into two types on the whole as reviewed by Okada *et al.*² One type shows direct mullitization from an amorphous state and the other type shows a spinel phase³ formation before mullitization. The former type occurs in the starting materials with a good mixture of silica and alumina components, whereas the latter occurs in starting materials with a poor mixture of silica and alumina components. These two types have been widely accepted by many workers. In Ref. 4, however, we found that the crystalline phase of the thin film fired at 1000°C and prepared by dip-coating the solution by dissolving TEOS and ANN in ethanol varied from mullite to spinel phase by changing the aging time of the same solution at room temperature. In order to elucidate this phenomenon the structural state of the mullite precursor in the solution and the effects of the aging time at room temperature were investigated by liquid state ^{29}Si and ^{27}Al NMR, SAXS and XRD techniques.⁵ The following results were obtained: polymerization of TEOS progressed very quickly and most of the Si atoms formed Q³ and Q⁴ structures within a very short reaction time. Here, the superscript figures in Q represent the number of Si–O–Si bonds per one Si atom. On the other hand, Al atoms showed a monomer state and formed an octahedral structure and it did not change throughout the experimented aging time. It was, therefore, found that the precursor did not form an aluminosilicate complex and silica and alumina components were not so homogeneously mixed in the solution.

In this paper, we investigate the effect of aging

*To whom correspondence should be addressed.

†Now with Japanese Patent Office, 3-4-3 Kasumigaseki, Chiyoda, Tokyo 100, Japan.

temperature on the structure of mullite precursor prepared by dissolving TEOS and ANN in ethanol to further elucidate this subject.

2 Experimental Procedure

Precursor solution with $3\text{Al}_2\text{O}_3\cdot 2\text{SiO}_2$ composition was prepared by dissolving 0.24 mol/l of TEOS and 0.72 mol/l of ANN in ethanol. Since ANN contains $9\text{H}_2\text{O}$ per one Al atom, the $\text{H}_2\text{O}/\text{TEOS}$ is 27 and this amount of water is highly excessive for polymerization of TEOS. The precursor solution was aged at various temperatures in a sealed plastic bottle up to 100 days. The aging temperatures experimented were 25, 40, 50 and 60°C .

Liquid state NMR measurements were performed by JEOL JNM-GSX500 equipment. The spectra of ^{29}Si NMR were recorded at 99.361 MHz using a pulse width of $14.9\ \mu\text{s}$ and a delay time of 1 s. The spectrum was obtained by accumulating 6000 times because the spectrum signal was very weak. A teflon tube instead of a glass tube was used for the measurements to avoid the signal from a glass tube. Chromium acetylacetonate and tetraethoxysilane were added to the solution just before the measurements were made and mixed. The former reagent was used to reduce the spin-lattice relaxation time and the latter one was used as an internal chemical shift standard. The spectra of ^{27}Al NMR were recorded at 130.315 MHz using a pulse width of $1.5\ \mu\text{s}$ and a delay time of 1 s. The spectra were obtained only by accumulating 240 times because the spectrum signal was strong enough in this case. A silica glass tube was used for the measurements. ANN solution was used as an external chemical shift standard.

SAXS measurements were performed by Rigaku RINT-1500 equipment using Ni-filtered $\text{Cu K}\alpha$ radiation (50 kV and 300 mA) through an evacuated beam path. The sample solution was mounted in a glass capillary 3 mm in diameter and $8\ \mu\text{m}$ in thickness. Intensity measurements were made in the scattering angle 2θ from 0.13 to 3.49° with a step interval of 0.02° and a fixed time of 10 s. Since the obtained intensity (I_0) didn't show a linear relation for $\log(I_0)$ versus S^2 (S : scattering vector), the radius of gyration was calculated using the Fankuchen methods.⁶ This value was further recalculated to particle size by assuming sphere shape.⁶ The detection limit of particle size by the present experimental conditions was estimated to be up to around 100 nm.

XRD measurements were performed by Rigaku Geigerflex diffractometer using graphite monochromated $\text{Cu K}\alpha$ radiation (40 kV and 20 mA). The samples for the XRD were prepared by

inserting the precursor solution (2 ml) in an alumina crucible to a furnace kept at 500°C for 15 min to instantly dry and burn out any nitrate and alcohol, and then fired at 1000°C for 6 h.

Solubility of ANN in ethanol at each temperature was measured by a conventional method.

3 Results

3.1 Liquid state ^{29}Si and ^{27}Al NMR

Figure 1 shows ^{29}Si NMR spectra of the precursor solutions aged for 5 days at various temperatures. The spectrum of the solution aged at 25°C showed three peaks at around -91 , -100 and -107 ppm. They are assigned to Q^2 , Q^3 and Q^4 structures,⁷ respectively. With increasing aging temperature, the peaks became weak and broad. The spectrum of the sample aged at 60°C showed no apparent peak and only a halo was observed due to the background signal by the teflon tube. Such a change in the spectra can be related to the hydrolysis and polymerization of TEOS to form a three-dimensional silica framework structure. The lack of peaks in the NMR spectrum can be explained by the formation of sol particles, in which structural information can not be detected by the liquid state NMR technique.

All the ^{29}Al NMR spectra of the precursor solutions aged for 5 days showed very sharp peaks at around 0 ppm. No significant differences were found among these spectra. These peaks are same as that of ANN used as an external standard. Therefore, Al atoms are considered to be in a monomer state with a regular octahedral structure. The spectra showed no change even with the

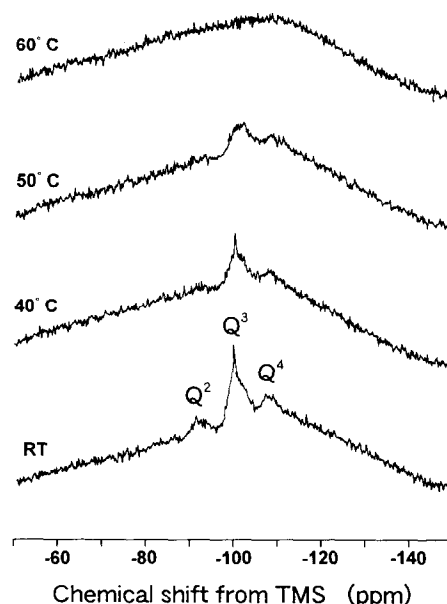


Fig. 1. Liquid state ^{29}Si NMR spectra of the samples aged for 5 days at various temperatures. The superscript figures in Q represent number of Si–O–Si bond per one Si atom.

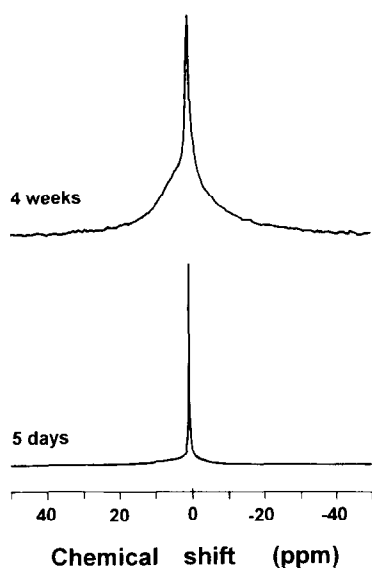


Fig. 2. Liquid state ^{27}Al NMR spectra of the samples aged at 60°C for 5 days and 4 weeks.

longer aging time when they were aged at 40 and 50°C just as in the case of room temperature aging reported before.⁵ On the other hand, a certain change was observed in the spectra when they were aged at 60°C for a long time. The spectra aged at 60°C for 5 days and 28 days are shown in Fig. 2. The full width at half maximum (FWHM) of the peak at around 0 ppm apparently increased and a shoulder also appeared at around several ppm. The increase of FWHM can be attributed to the distortion of octahedra and the shoulder can be assigned to the polymerization of Al-octahedra such as dimer and/or oligomer from a monomer.

3.2 Sol particle size by SAXS

The size of sol particles was measured for the three samples, i.e. aged for 5 days at 25, 50 and 60°C . No clear indication of small angle X-ray scattering was observed for the sample aged at 25°C except for that from the instrument. It was, therefore, unclear whether sol particles were already formed in this solution or not. Even if the sol particles were present in the sample, they were smaller than several nm in size because this was a detection limit of the present experimental conditions. The other two samples showed small angle X-ray scattering corresponding to sol particles. The size of the sol particles was not uniform and had a distribution. By the Fankuchen method,⁶ they were approximated by two particle size distributions for the both samples. Their particle sizes in the sample aged at 50°C were 7 and 14 nm whereas those at 60°C were 9 and 26 nm. Increase of the larger particle size was clear between these two samples and it may correspond to coalescence of small sol particles.

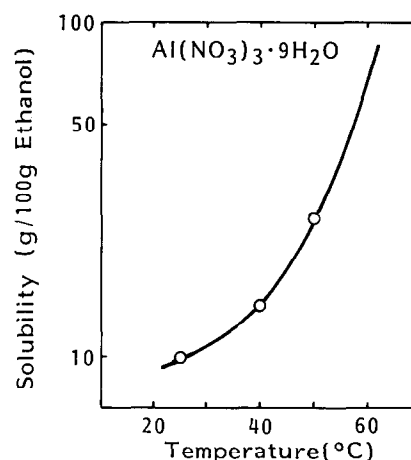


Fig. 3. Solubility curve of aluminum nitrate nonahydrate in ethanol as a function of temperature.

3.3 Solubility of ANN in ethanol

Figure 3 shows the solubility curve of ANN in ethanol. The solubility of ANN at 25°C is around 10 g in 100 g ethanol and is not very high. The solubility increased to 26 g at 50°C . We, however, could not accurately determine the solubility limit of ANN at 60°C because the solution became viscous and evolution of NO_x gas was observed due to the decomposition of nitrate ion.

3.4 Crystalline phase at 1000°C

Intensities for the strongest reflection of mullite, which has fully overlapped peaks of 120 and 210 reflections and 400 reflection of spinel phase were qualitatively measured for the samples fired at 1000°C for 6 h. Their results are shown in Fig. 4. The sample aged at 25°C showed very weak reflections of mullite and spinel phase. Amount of crystalline phases was found to be low compared with the other samples. The samples aged at 40 and 50°C showed relatively intense spinel phase reflections but very weak mullite reflections. On the other hand, only the sample aged at 60°C showed

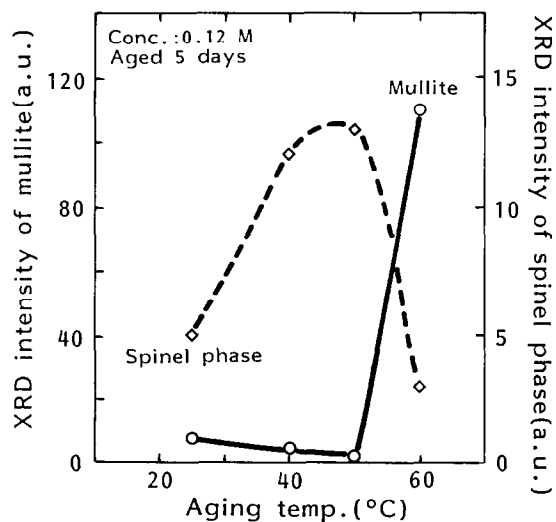


Fig. 4. XRD intensity of crystalline phases in the samples fired at 1000°C for 6 h aged at various temperatures.

strong mullite reflections with only a trace of spinel phase reflections. Thus, the crystalline phases formed by firing the precursor solutions at 1000°C were found to largely differ by the aging temperatures of the samples. Mullite formation was found to be only dominant in the sample aged at 60°C.

The crystalline phase in the samples aged for various times at various temperatures was also examined to clarify the effect of aging time. No dominant mullitization was found in all the samples aged for various times under 60°C. In the samples aged at 60°C, intensity of the mullite reflection of the 1 day aged sample was small. However, the mullite intensity increased with longer aging time and remained constant by aging over 5 days.

4 Discussion

Liquid state NMR data showed that polymerization of TEOS largely progressed but no change occurred in the monomer octahedral coordination of Al atoms with increasing aging temperature. No aluminosilicate complex was detected in the sol solution of the present preparation system. The presence of silica sol particles was also confirmed from the SAXS data. It was, therefore, concluded that the precursor was not in the molecularly mixed state in the solution, though direct mullitization occurred in the samples aged at 60°C. The precursors which show direct mullitization at around 1000°C have been considered to be in a very good mixing state and the silica and alumina components are molecularly mixed.⁸ This may be generally true but it has been found from our results that it is not always necessarily true.

We observed a clear difference in the mullitization pathways between the precursors aged at 60°C and those aged under 60°C. What is the most important point to cause such a difference? Since the precursor did not form an aluminosilicate complex, both components need to be mixed to yield mullite directly. Two things are considered to be important for this. First, it is necessary for polymerized silica to be in small particles and it should form a gel network structure with them. Since the present solution is a very strong acid and contains a high concentration of salt in the present precursor system, the present experimental conditions are considered to be applicable to develop a gel structure rather than particles which is obtained using basic conditions.⁹ The present SAXS data are compatible with this model. Second, the particles of the alumina component, which are considered to be nitrate, are also required to be

small and present around silica gel. As mentioned before, the solubility of ANN in ethanol largely increased with increasing aging temperature. This means that ANN can be dissolved in ethanol up to a very high concentration when they are prepared at higher aging temperature. It is suitable to form a gel structure with a trapped solution of dissolved ANN in the silica gel network structure. The mixed state in silica and alumina is thought to be formed in this way in the sample aged at 60°C and these samples show direct mullitization as a result as has been shown by others previously.^{10,11}

The present and previously reported results,⁴ show that the crystalline phases are found to change not only by the aging conditions of the precursor but also by the firing conditions. The main crystalline phase by firing at 1000°C is mullite in the dip-coated thin films⁴ from the solution aged at room temperature for short time, but it is the spinel phase in the present experiments. In this case the amount of precursor solution for firing is considered to be important and a cause of this difference. A very small amount of precursor was fired in the dip-coating⁴ and was considered to be preferable for mullitization because of the rapid evaporation of the solvent. Recently, Nishio *et al.*¹² reported that the crystallization behaviour of mullite precursor prepared by the solution method changes due to the firing conditions such as the heating rate. We (Ref. 13) also found this and reported similar behavior recently. It is considered that heat treatment under several hundreds °C plays an important role on various reactions such as dehydration and decomposition of nitrates and alkoxyl groups which causes rearrangement of the precursor structure.

5 Conclusions

- (1) With increasing aging temperature, polymerization of TEOS to form silica sol progressed.
- (2) No apparent change was observed for a monomer octahedral structure of Al atoms irrespective of the aging temperature in a short aging time.
- (3) Solubility of ANN in ethanol increased with increasing aging temperature.
- (4) The main crystalline phase obtained by firing at 1000°C is mullite when the precursor solution was aged at 60°C, whereas it is the spinel phase when they were aged under 60°C.
- (5) The mullite precursor in the present system was found not to form aluminosilicate com-

plex and silica and alumina components were not in a molecularly mixed state in the solution. Aging at 60°C was, however, suitable to prepare a well mixed state in silica and alumina components and yielded direct mullitization at 1000°C.

Acknowledgements

We thank Professor I. Ando and Dr. H. Kurosu of Tokyo Institute of Technology for use of the NMR instrument and various fruitful suggestions for the NMR measurements. A part of this study is financially supported by the 1991 Corning Research Grant.

References

1. Schneider, H., Okada, K. & Pask, J. A., *Mullite and Mullite Ceramics*. John Wiley & Sons, London, 1994.
2. Okada, K., Otsuka, N. & Somiya, S., Review of mullite synthesis routes in Japan. *Am. Ceram. Soc. Bull.*, **70** (1991) 1633–9.
3. Brindley, G. W. & Nakahira, M., The kaolinite–mullite reaction series: III. The high-temperature phases. *J. Am. Ceram. Soc.*, **42** (1959) 319–24.
4. Okada, K. & Otsuka, N., Preparation of transparent mullite films by dip-coating method. In *Ceramic Transactions, Vol. 6, Mullite and Mullite Matrix Composites*, eds S. Somiya, R. F. Davis & J. A. Pask. Am. Ceram. Soc., Westerville, OH, 1990, pp. 425–34.
5. Aoki, C., Ban, T., Hayashi, S. & Okada, K., Characterization of polymeric structure of aluminosilicate complex in sol–gel solution. In *Third Euro-Ceramics*, eds P. Duran & J. F. Fernandez. Faenza Editrice Iberica S.L., Madrid, 1993, Vol. 1, pp. 387–92.
6. Nitta, I., *X-ray Crystallography (II)*. Maruzen, Tokyo, 1961, pp. 555–6.
7. Pouxviel, J. C., Boilot, J. S., Beloeil, J. C. & Zallemand, J. J., NMR study of the sol/gel polymerization. *J. Non-Cryst. Solids*, **89** (1987) 345–60.
8. Aksay, I. A., Dabbs, D. M. & Sarikaya, M., Mullite for structural, electronic, and optical applications. *J. Am. Ceram. Soc.*, **74** (1991) 2343–58.
9. Iler, R. K., *The Chemistry of Silica*, John Wiley & Sons, London, 1979, p. 174–6.
10. Hoffman, D., Roy, R. & Komarneni, S., Diphasic xerogels, a new class of materials: phases in the Al_2O_3 – SiO_2 system. *J. Am. Ceram. Soc.*, **67** (1984) 468–71.
11. Komarneni, S., Roy, R., Fyfe, C. A., Kennedy, G. T. & Strokl, H., Solid-state ^{27}Al and ^{29}Si magic-angle spinning NMR of aluminosilicate gels. *J. Am. Ceram. Soc.*, **69** (1986) C42–4.
12. Nishio, T., Kijima, K., Kajiwara, K. & Fujiki, Y., The influence of preparation procedure in the mullite preparation by solution method to the mixing of Al and Si and the crystallization behavior. *J. Ceram. Soc. Jpn*, **102** (1994) 462–70.
13. Ban, T., Hayashi, S., Yasumori, A. & Okada, K., Low temperature mullitization. *J. Eur. Ceram. Soc.*, submitted.

New Aqueous Mullite Precursor Synthesis. Structural Study by ^{27}Al and ^{29}Si NMR Spectroscopy

Isabelle Jaymes & André Douy

CNRS, Centre de Recherches sur la Physique des Hautes Températures 1D, Avenue de la Recherche Scientifique, F-45071 Orléans Cedex 02, France

(Accepted 22 July 1995)

Abstract

A mullite precursor gel is prepared by the slow and homogeneous generation of ammonia inside an aqueous solution of aluminium nitrate and silicic acid, urea being used as the base generator. At 80–100°C a silica gel is rapidly formed, by a catalytic reaction, and then this gel is slowly digested by the partially hydrolysed aluminium atoms which link to silica by Si–O–Al bonds. The structural evolution has been studied by ^{27}Al and ^{29}Si NMR spectroscopy. The first aluminium atoms are incorporated in tetrahedral symmetry and the following ones remain hexacoordinated. The system evolves to soluble aluminosilicate colloids with a local structure close to that of imogolite or allophane: each silicon atom being linked to three AlO_6 hexahedra and a hydroxyl group. By the completion of the hydrolysis the colloids are cross linked to a gel precursor of mullite. With thermal treatment the imogolite-like orthosilicate units arrangement is rapidly lost, but the xerogel remains chemically homogeneous with a random distribution of Al and Si atoms in the lattice, the Al atoms being four-, five- and six-fold coordinated. The xerogel crystallises at 980°C into an alumina-rich mullite and amorphous silica, and the $3\text{Al}_2\text{O}_3 \cdot 2\text{SiO}_2$ stoichiometry is reached at 1300°C by reincorporating the silica in the lattice.

1 Introduction

Due to their excellent high-temperature properties, mullite, $3\text{Al}_2\text{O}_3 \cdot 2\text{SiO}_2$, and mullite-matrix composites have received much attention during the last decade.^{1,2} The chemical synthesis of mullite has been exemplary.³ It is well known that single phase precursors crystallize into mullite at ~980°C while for diphasic precursors this crystallization is delayed to higher temperatures (~1250°C) through transient alumina phases. The synthesis of single

phase aluminosilicate gels has been generally performed by organic processes, using all alkoxides or silicon alkoxide (TEOS) and aluminium nitrate. Aqueous processes, starting with colloids or salts, lead usually to diphasic gels. However chemically homogeneous mullite precursors may also be obtained by aqueous routes. The precursor solution may be conveniently prepared by hydrolysing tetraethoxysilane (TEOS) in a solution of aluminium nitrate. This precursor solution, of aluminium nitrate and silicic acid, may be transformed into chemically homogeneous amorphous materials by an organic gel-assisted process,⁴ by spray-drying⁵ or by rapid precipitation into an alcoholic solution of a base.⁶ While by the addition of a base to hydrolyse the aluminium salt a diphasic precursor is generally obtained, here we present the synthesis of a chemically very homogeneous gel precursor of mullite, by the slow *in situ* generation of ammonia, using urea as the base generator. ^{27}Al and ^{29}Si NMR spectroscopy has been used to study the different steps of the synthesis, from the solution to the ceramic.

2 Experimental

2.1 Synthesis

Tetraethoxysilane (TEOS), $\text{Si}(\text{OC}_2\text{H}_5)_4$ (Merck), was added in the stoichiometric ratio to a stirred 0.6 M aqueous solution of aluminium nitrate nonahydrate (Aldrich). By hydrolysis of TEOS a clear solution was obtained. Urea $\text{CO}(\text{NH}_2)_2$ (Merck) was added (1.8 urea mole per aluminium nitrate mole) and the solution was stored at 80°C. A gel was obtained after a few hours, a clear sol after 3 days, and a second gel after a week. This gel was filtered, washed with water, dried at 100°C, and further calcined to different temperatures. Preparations were also made by adding various quantities of urea to the precursor solution, and storing at 80°C for 20 days or 100°C for 7–10 days. These

preparations corresponded to different degrees of partial hydrolysis of the aluminium cations. For some preparations gadolinium was added from nitrate as a paramagnetic relaxation agent for the ^{29}Si NMR spectroscopy study (0.04 wt% Gd_2O_3 in the final oxide).

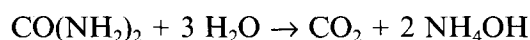
2.2 Characterisation

NMR experiments were recorded on a Bruker MSL 300 spectrometer operating at a magnetic field of 7.04 Tesla. For ^{27}Al a pulse length of 0.6 μs and a recycle time of 1 s were used, and for ^{29}Si a pulse length of 2 μs and a recycle time of 10 s. High resolution solid state MAS-NMR spectra were obtained in zirconia rotors spinning the samples at the magic angle ($54^\circ 44'$) at 15 kHz and 4 kHz respectively for Al and Si. The chemical shifts are given with respect to tetramethylsilane and $[\text{Al}(\text{H}_2\text{O}_6)]^{3+}$ in aqueous aluminium nitrate. The isotropic chemical shift positions (δ_{iso}) and the estimated minimum quadrupolar frequencies (ν_Q) are measured using central and satellite transitions as proposed by Jäger⁷ and Massiot *et al.*⁸

3 Results and Discussion

When TEOS is added to an acidic solution of aluminium nitrate (pH \sim 2) it is hydrolysed into silicic acid. At this pH the rate of hydrolysis is maximum while that of polycondensation of silicic acid is minimum.⁹ If no base is added to this solution the silicic acid will slowly polymerise into silica gel, after several weeks at room temperature or a few days at 100°C. This silica gel may be filtered and carefully washed and dried. By analysis of the gel and the filtrate it is shown that no reaction occurs between the silicated and aluminated species.

Urea has been used as a base generator in the preparation of oxide ceramics.^{10,11} At temperatures higher than 60°C, urea is hydrolysed in aqueous solutions:¹²



For the solution of aluminium nitrate and silicic acid the slow *in situ* generation of ammonia will hydrolyse and polycondense the aluminium species while increasing the pH will result in polycondensation of the silicic acid, although the raising of the pH is significant only at the end of the hydrolysis of the aluminium nitrate. A copolycondensation, or at least a good level of mixing of aluminate and

silicate species may be expected by this reaction. In fact the reaction proceeds by a very different way. When 1.8 mole of urea per mole of aluminium nitrate are added to the solution, that is in slight excess for the complete hydrolysis of aluminium (which would require 1.5 mole of urea), at 80°C a gel is formed within a few hours. Then this gel is slowly desegregated and a clear colloidal sol is obtained after 3 days and a second gel after a week. For the study of the reactions occurring during the synthesis, a series of preparations were made with precise quantities of urea corresponding to partial hydrolyses of aluminium. By storing at 80°C for 20 days or at 100°C for 7–10 days it was considered that practically all the urea had reacted. Even by ageing at 100°C for much longer times the obtained gels or sols did not apparently evolve. In these conditions gels were obtained for degrees of hydrolysis $h = \text{OH}/\text{Al} < 0.7$, clear sols for $0.8 < h < 2.7$ and gels for $h > 2.8$.

3.1 First gels ($h < 0.7$)

The chemical compositions in silicon and aluminium for the first gels and the sols are given in Table 1, determined by EDX analysis on the gels filtered and carefully washed and dried, and on the freeze-dried materials obtained from the concentrated and dialysed sols. The first gel which is formed is probably a pure silica gel; as aluminium is hydrolysed it reacts with this silica gel and is responsible for its digestion to small particles of aluminosilicate species.

The ^{29}Si MAS NMR spectra confirm the nature of the first gels (Fig. 1). For $h = 0.1$ the spectrum is characteristic of polymerised silica with main resonances at -110 ppm (Q^4) and -102 ppm (Q^3). In this Q^n notation,¹³ Q represents a silicon atom in a SiO_4 tetrahedron and n indicates the number of other Q units attached to it. Q^4 denotes three-dimensionally cross-linked tetrahedra, that is fully polymerised silica, and Q^3 chain-branching sites. As the hydrolysis progresses we note a shift of the resonance bands to lower fields. The intensity of the band at -110 ppm decreases and other bands appear at -90 and -78 ppm. Two different phenomena may contribute to this shifting of the resonance lines: the depolymerisation of the silica network and the replacement of silicon by aluminium in the second sphere of coordination of the silicon atoms. Each depolymerisation step (breaking of Si-O-Si to Si-O-OH) results in a shift of ca 10 ppm, while for each replacement of Si-O-Si bonds by Si-O-Al bonds a chemical shift

Table 1. Evolution of the Al/Si ratio in the gels and the colloids with the degree of hydrolysis h of aluminium nitrate

$h = \text{OH}/\text{Al}$	0.2	0.4	0.6	0.8	1.0	1.2	1.5	1.8	2.0	2.4	2.6
Al/Si	0.11	0.21	0.38	0.67	0.82	1.1	1.3	1.7	1.95	2.2	2.55

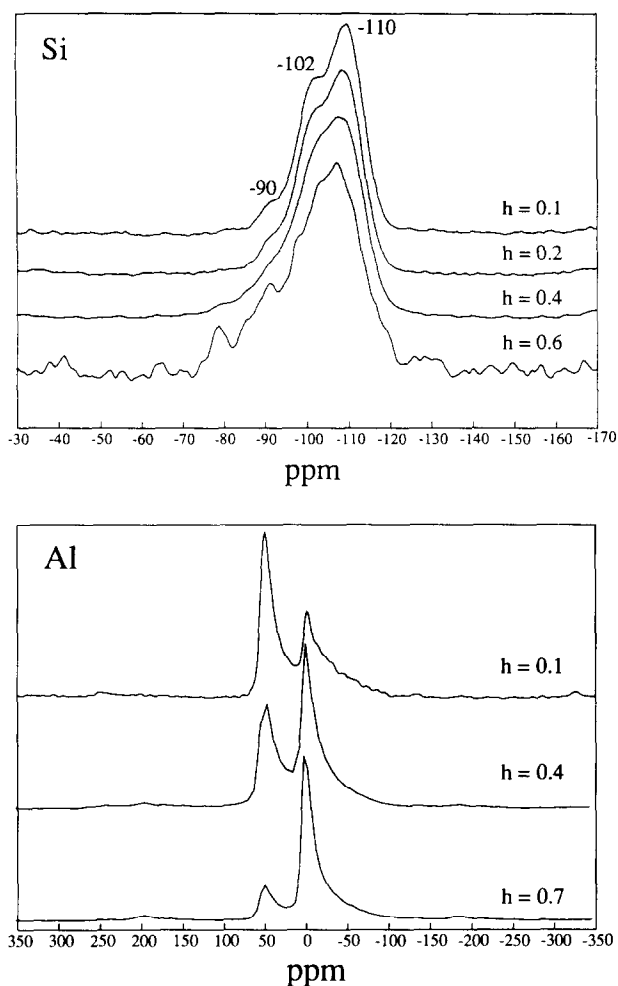


Fig. 1. ^{29}Si and ^{27}Al MAS NMR spectra of the first gels for different degrees of hydrolysis for aluminium.

of ca 5 ppm is expected for the silicon atoms.¹³ The two reactions occur during the hydrolysis and further studies are necessary for precise attribution of the new lines appearing on the NMR spectra.

The first aluminium atoms incorporated in the silica gel are mainly tetraordinated, with the apparent chemical shift at 50 ppm (Fig. 1) for this quadrupolar nucleus, characteristic of AlO_4 tetrahedra. Some Al also occurs in hexacoordinated symmetry, at 0 ppm, characteristic of AlO_6 octahedra. As the hydrolysis progresses the ratio $\text{Al(VI)}/\text{Al(IV)}$ increases and the majority of the aluminium atoms incorporated in the gel are hexacoordinated.

Whatever the quantity of urea added to the precursor solution, a silica gel is always formed in the first step of the reaction. Urea acts as a catalyst in the polycondensation of silicic acid in the presence of aluminium nitrate. The incorporation of the first aluminium atoms in tetrahedral symmetry is in agreement with other reports on silica-rich single phase aluminosilicate gels.¹⁴ When the content in alumina increased the ratio $\text{Al(VI)}/\text{Al(IV)}$ also increased.¹⁵

3.2 Colloidal sols ($0.8 < h < 2.7$)

The ^{29}Si and ^{27}Al NMR spectra of the colloidal sols (Fig. 2) show an evolution of the environments for the silicon atoms. For the ^{29}Si NMR spectroscopy the colloidal sols have been greatly concentrated but remained optically clear. The remaining resonance bands at -110 and -102 ppm, predominant in the first gel progressively disappear and are replaced by lines at -90 and -85 ppm. These lines then disappear in their turn and the evolution is towards a single resonance at -78 ppm for a degree of hydrolysis h slightly higher than 2.4.

The static ^{27}Al NMR spectra show only a band at 0 ppm corresponding to hexacoordinated aluminium atoms, including the non hydrolysed aluminium cations $[\text{Al}(\text{H}_2\text{O})_6]^{3+}$. But due to molecular-weight broadening effects associated with the quadrupolar aluminium nucleus in highly distorted symmetry, many Al species may be not observable by NMR spectroscopy under static conditions.

The size of the colloidal particles has been determined by dynamic light scattering.¹⁶ For a series of colloidal samples aged at 100°C for 10

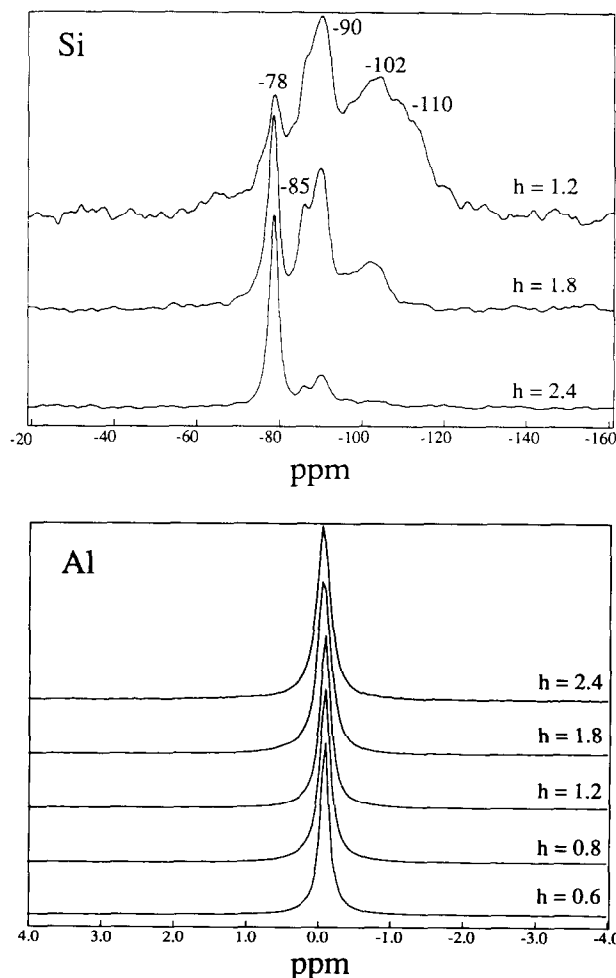


Fig. 2. ^{29}Si and ^{27}Al NMR spectra of concentrated colloidal sols (Si) and colloidal sols (Al) corresponding to different degrees of hydrolysis h for aluminium.

days, the Stokes radius decreases rapidly to values close to 2 nm. A minimum of 1.64 nm is observed around $h = 2.6$, with a narrow size distribution ($+ 0.03$ nm). For higher h values the size of the particles increases sharply just before the second gelation.

3.3 The second gel ($h > 2.8$)

For degrees of hydrolysis higher than 2.8 another gel is obtained, resulting from the cross linking of the colloidal particles by the condensation of the last aluminium atoms being hydrolysed. By further ageing syneresis occurs with cracking of the gel. The gel is filtered and washed to eliminate the ammonium nitrate formed during the hydrolysis and dried. Since no aluminium or silicon were found in the filtrate, this gel is an aluminosilicate gel precursor of stoichiometric 3:2 mullite.

The ^{29}Si and ^{27}Al MAS NMR spectra (Fig. 3) show for silicon atoms a sharp resonance at -78 ppm as in the colloidal sols for high degrees of hydrolysis, and for aluminium atoms practically a single hexacoordinated symmetry at ~ 0 ppm. There remains however some tetrahedrally coordinated atoms (at ~ 50 ppm) not visible in static conditions in the colloidal samples, even though probably present. These local environments for silicon and aluminium atoms are very similar to

those in natural imogolite.¹⁷⁻¹⁹ In this tubular mineral each silicon atom is linked to three hexacoordinated aluminium atoms via oxo bridges and to one hydroxyl group, and the NMR spectrum exhibits a unique resonance band at ~ -78 ppm; and all the aluminium atoms are hexacoordinated. The high degree of similarity in the local structure and the sharpness of resonance bands indicate a very high degree of chemical homogeneity in the colloidal samples before the gelation and in the gel. However the particle size of the colloidal species before gelation, substantially too low for a tubular morphology, and the chemical composition ($\text{Al/Si} = 2.5-3$) are more related to allophane than imogolite. While in imogolite the Al/Si atomic ratio is about 2, for allophanes, very poorly crystalline hydrous aluminosilicates with a hollow spheroidal structure, a much wider range of composition is available.²⁰⁻²² Allophanes usually also possess imogolite-like orthosilicate units giving rise to a sharp resonance at ~ -78 ppm.²²

3.4 Structural evolution with heat-treatment

Heated at $10^\circ\text{C}/\text{min}$ the second gel ($h = 3$) exhibits only a single and strong exotherm at 980°C , on differential scanning calorimetry. By X-ray diffraction this thermal event is checked to be the crystallization into mullite. For the NMR spectroscopy study samples were calcined for 1 h at different temperatures (Fig. 3). There is a strong modification in the local environments of the cations at low temperature treatment, between 100 and 300°C . At 300°C the site distribution for the silicon atoms is much broader than at 100°C , with a shift to higher fields which may result from the condensation of hydroxyl groups. This broad line indicates a random distribution of Si and Al atoms in the lattice. For the aluminium atoms tetrahedral ($\delta_{\text{iso}} = 70-72$ ppm) and 'pentahedral' ($\delta_{\text{iso}} = 41$ ppm) coordinations appear. So the imogolite-like local structure is rapidly lost by heat-treatment. This behaviour is also more characteristic of allophane than imogolite. In imogolite the sharp resonance is still the major band at 400°C (15 min) while in allophane it disappears at about 200°C .^{19,22}

With increasing temperature above 300°C , the structural evolution of this precursor becomes more similar to those of other single phase aluminosilicate gel precursors of mullite.²³⁻²⁶ There is a regular shift of the maximum of the broad resonance for the silicon atoms until 900°C . For the aluminium atoms, the Al(IV) and Al(V) signals increase and are at their apparent maximum intensities at 900°C , before the crystallization temperature.

At 1000°C the sample is crystallised and the environments of the atoms are modified. The 'pen-

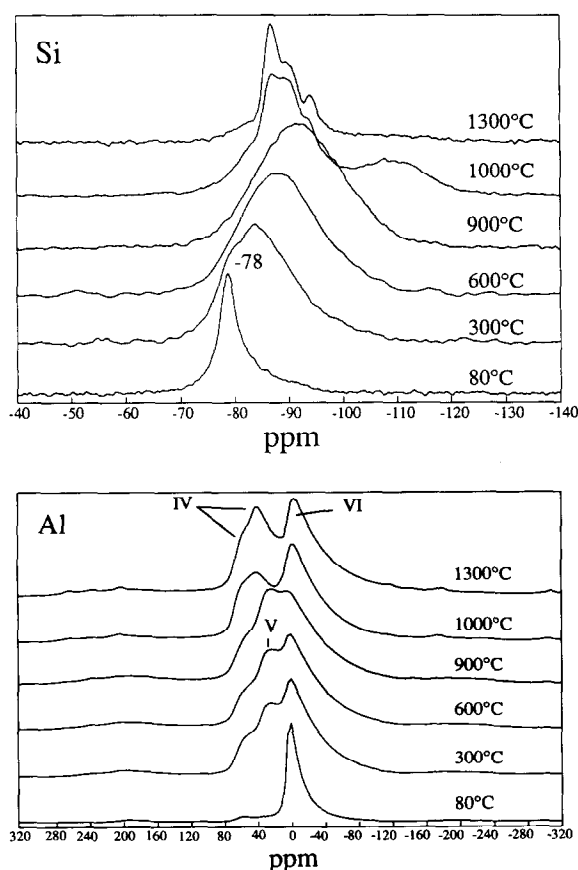


Fig. 3. ^{29}Si and ^{27}Al MAS NMR spectra of the mullite precursor gel to the ceramic after heat treatment for 1 h at different temperatures.

tacoordinated' aluminium atoms have disappeared and there are now three Al sites in mullite: one octahedral ($\delta_{iso} = 10$ ppm) and two tetrahedral, assigned by Merwin and Schneider^{27,28} to T and T* sites of the mullite structure,²⁹ at 70 and 41 ppm respectively for the isotropic positions. T* refers to tricluster distorted Al tetrahedra, explaining the low chemical shift for Al(IV), at a similar isotropic position to the 'pentacoordinated' atoms in the amorphous state. For silicon atoms the broad signal at -90 ppm is replaced by the characteristic resonances of mullite at -86, -90, -94 and -80 ppm, and a broad signal at -110 ppm, characteristic of silica. This reflects the segregation occurring during the crystallization. The crystallised mullite is richer in alumina and a part of silica is expelled from the lattice.

On further heating, to 1300°C, the free amorphous silica has re-entered the mullite structure and the signal at -110 ppm has disappeared. The material is orthorhombic 3:2 mullite.²⁸⁻³⁰ The main resonance at -86 ppm corresponds to Si atoms in a sillimanite-type (Al_2SiO_5) arrangement, while the lines at -90 and -94 ppm reflect a mullite-type Al/Si ordering. The change in the mullite composition from 1000 to 1300°C is accompanied by an apparent increase of the Al(IV)/Al(VI) ratio.

4 Conclusion

This synthesis of mullite precursor proceeds through unexpected reactions. It is shown that a silica gel may be digested by partially hydrolysed aluminium species homogeneously generated inside its network. This leads to aluminosilicate colloids and gels with aluminium and silicon atoms environments close to those in imogolite or allophane. This local arrangement is thermodynamically lost by thermal treatment but a very high degree of mixing of aluminium and silicon atoms is preserved in the amorphous state, and the xerogel crystallises into mullite at low temperature. This synthesis, with the use of urea as a base generator, is well suited to all compositions single phase aluminosilicate gels and especially to mullite precursors.

Acknowledgements

The Région Centre is acknowledged for financial support. The authors are grateful to Dr D. Massiot for NMR discussions, and to Prof. J. P. Busnel for the dynamic light scattering experiments.

References

1. Ceramic Transactions. Vol 6. In *Mullite and Mullite Matrix Composites*, eds S. Somiya, R. F. Davies & J. A. Pask, American Ceramic Society, Westerville, OH, 1990.
2. Proceedings of the Symposium Mullite Processing, Structure and Properties, 43rd Pacific Coast Regional Meeting, The American Ceramic Society, *J. Am. Ceram. Soc.*, **74**(10) (1990).
3. Sacks, M. D., Lee, H. W. & Pask J. A., A review of powder preparation methods and densification procedures for fabricating high density mullite. In ref. 1, pp. 167-207.
4. Douy, A., Organic gels in the preparation of silicate powders. 1. Mullite. *J. Eur. Ceram. Soc.*, **7** (1991) 117-23.
5. Jaymes, I. & Douy, A., Homogeneous mullite-forming powders by spray drying aqueous solutions. *J. Am. Ceram. Soc.*, **75** (1992) 3154-6.
6. Jaymes, I. & Douy, A., Homogeneous precipitation of mullite precursors. *J. Sol-Gel Sci. & Technol.*, **4** (1995) 7-13.
7. Jäger, C., How to get more from ²⁷Al MAS NMR by high speed satellite transition spectroscopy. *J. Magn. Reson.*, **99** (1992) 353-62.
8. Massiot, D., Coté, B., Taulelle, F. & Coutures, J. P., ²⁷Al MAS NMR of crystalline and amorphous materials. In *Applications of NMR to Cement Sciences*, eds P. Colombet & A. R. Grimmer, Gordon and Breach, New York, 1994, pp. 153-69.
9. Iler, P. K., *The Chemistry of Silica*, Wiley, New York, 1979.
10. Kato, A., Inoue, K. & Katatae, Y., Sintering behavior of yttria-stabilized zirconia (YSZ) powder prepared by homogeneous precipitation. *Mat. Res. Bull.*, **22** (1987) 1275-81.
11. Wood, T. E., Siedle, A. R., Hill, J. R., Skarjune, R. P. & Goodbrake, C. J., Hydrolysis of aluminum. Are all gels created equal? *Mat. Res. Symp. Proc.*, **180** (1990) 97-116.
12. Shaw, W. H. R. & Bordeaux, J. J., The decomposition of urea in aqueous media. *J. Am. Chem. Soc.*, **77** (1955) 4729-33.
13. Engelhardt, G. & Mitchell, D., *High Resolution Solid State NMR of Silicates and Zeolites*, Wiley, New York, 1987.
14. Irwin, A. D., Holmgren, J. S. & Jonas, J., ²⁷Al and ²⁹Si NMR study of sol-gel derived aluminosilicates and sodium aluminosilicates. *J. Mat. Sci.*, **23** (1988) 2908-12.
15. Komarneni, S., Roy, R., Fyfe, C. A., Kennedy G. J. & Strobl, H., Solid state ²⁷Al and ²⁹Si magic angle spinning NMR of aluminosilicate gels. *J. Am. Ceram. Soc.*, **69**, (1986) C-42-4.
16. Jaymes, I., Douy, A., Massiot, D. & Busnel, J. P., to be published.
17. Barron, P. F., Wilson, M. A., Campbell, A. S. & Frost, R. L., Detection of imogolite in soils using ²⁹Si NMR. *Nature*, **299** (1982) 616-18.
18. Goodman, B. A., Russel, J. D., Montez, B., Oldfield E. & Kirkpatrick, R. J., Structural studies of imogolite and allophanes by aluminum-27 and silicon-29 nuclear magnetic resonance spectroscopy. *Phys. Chem. Mineral.*, **12** (1985) 342-6.
19. MacKenzie, K. J. D., Bowden, M. E., Brown, I. V. M. & Meinhold, R. H., Structure and thermal transformations of imogolite studied by ²⁹Si and ²⁷Al high-resolution solid-state nuclear magnetic resonance. *Clays & Clay Minerals*, **37** (1989) 317-24.
20. Farmer, V. C., Adams, M. J., Fraser, A. R. & Palmieri, F., Synthetic imogolite: properties, synthesis and possible applications. *Clay Miner.*, **18** (1983) 459-72.
21. Wada, S. I., Eto, A. & Wada, K., Synthetic allophane and imogolite. *J. Soil Sci.*, **30** (1979) 347-55.
22. MacKenzie, K. J. D., Bowden, M. E. & Meinhold, R. H., The structure and thermal transformations of allophanes studied by ²⁹Si and ²⁷Al high-resolution solid-state nuclear magnetic resonance. *Clays & Clay Minerals*, **39** (1991) 337-46.
23. Sanz, J., Sobrados, I., Cavalieri, A. L., Pena, P., de Aza, S. & Moya, J. S., Structural changes induced on mullite

- precursors by thermal treatment: a ^{27}Al MAS NMR investigation. *J. Am. Ceram. Soc.*, **74** (1991) 2398–403.
24. Yoldas, B. E., Effect of ultrastructure on crystallization of mullite. *J. Mat. Sci.*, **27** (1992) 6667–72.
 25. Selvaraj, U., Komarneni, S. & Roy, R., Structural differences in mullite xerogels from different precursors characterized by ^{27}Al and ^{29}Si MAS NMR. *J. Solid State Chem.*, **106** (1993) 73–82.
 26. Jaymes, I., Douy, A., Florian, P., Massiot, D. & Courettes, J. P., New synthesis of mullite. Structural evolution study by ^{17}O , ^{27}Al and ^{29}Si MAS NMR spectroscopy. *J. Sol-Gel Sci. & Technol.*, **4** (1995) 7–13.
 27. Merwin, L. H., Sebal, A., Rager, H. & Schneider, H., ^{29}Si and ^{27}Al MAS NMR spectroscopy of mullite. *Phys. Chem. Miner.*, **18** (1991) 47–52.
 28. Schneider, H., Merwin, L. & Sebal, A., Mullite formation from non-crystalline precursors. *J. Mat. Sci.*, **27** (1992) 805–12.
 29. Angel, R. J. & Previt, C. T., Crystal structure of mullite: a reexamination of the average structure. *Am. Mineral.*, **71** (1986) 1476–82.
 30. Ban, T. & Okada, K., Analysis of local cation arrangement in mullite using ^{29}Si MAS NMR spectra. *J. Am. Ceram. Soc.*, **76** (1993) 291–6.

Germanium Mullite: Structure and Vibrational Spectra of Gels, Glasses and Ceramics

D. Michel,^a Ph. Colomban,^{b*} S. Abolhassani,^{c†} F. Voyron^c & A. Kahn-Harari^c

^aCECM, CNRS UPR 2801, 15 rue G. Urbain, 94407 Vitry, France

^bLASIR, CNRS UPR 2631, 2 rue H. Dunant, 94320 Thiais, France

^cENSCP, URA CNRS 1466, 11 rue P. et M. Curie, 75005 Paris, France

(Accepted 22 July 1995)

Abstract

The Raman spectra of mullite phases in $\text{GeO}_2\text{-Al}_2\text{O}_3$ and $\text{GeO}_2\text{-Ga}_2\text{O}_3$ systems are compared with those of silicon mullite and sillimanite. Replacement of silicon by germanium and aluminium by gallium modifies the wavenumbers of certain lines, especially at high frequency. However, all germanium mullites present similar features which reflect their disordered character. Even for compositions Al_2GeO_5 and Ga_2GeO_5 which are homologous to that of sillimanite, Raman spectra consist of broad bands, as previously observed in silicon mullites. The evolution of spectra is discussed for a series of $\text{Al}_{4+2x}\text{Ge}_{2-2x}\text{O}_{10-x}$ mullite phases with $0 < x < 0.47$. The spectra of amorphous gels and glasses prepared by slow hydrolysis–polycondensation of aluminium and germanium (silicon) alkoxide mixtures show rather narrow bands. This indicates that the polymeric arrangement of molecular entities is less distorted in non-crystalline precursors than in crystalline mullite. Finally, a phase relation diagram is proposed for the sol–gel route.

Introduction

Phases isostructural with silicon mullites exist in the $\text{GeO}_2\text{-Al}_2\text{O}_3$ phase diagram.^{1–5} However, whereas at atmospheric pressure mullite is the only aluminosilicate formed, two other stable compounds exist with germanium: Al_2GeO_5 , isostructural with the high-pressure silicate kyanite,⁴ and $\text{Al}_2\text{Ge}_2\text{O}_7$ in which Al atoms are in five-fold oxygen coordination.⁶ In addition, the metastable phase Al_4GeO_8 , isostructural to $\beta\text{-Ga}_4\text{GeO}_8$, can be obtained.⁷

*To whom correspondence should be addressed.

†Present address: Electron Microscopy Center, University of Lausanne, Bugnon 27, 1005 Lausanne, Switzerland.

As well as $\text{Al}_{4+2x}\text{Si}_{2-2x}\text{O}_{10-x}$ mullites,⁸ Ge mullites have an extended stability range, but the domain of stability differs for germanates and silicates.^{4,8,9} In particular, the Ge mullite range of composition includes Al_2GeO_5 ($x = 0$), which corresponds to that of high-pressure Al_2SiO_5 sillimanite.

An 'ideal' mullite structure ($x = 0$) can be described as a disordered variety of sillimanite in which aluminium and silicon atoms are randomly distributed on the tetrahedral sites.^{10–12} On the contrary, in sillimanite, Al and Si atoms regularly alternate along the tetrahedral chains. This leads to a doubling of the c lattice constant and to a change in the space group from $P6_{3m}$ to $P6_{3mc}$ ($Pnma$ in a standard setting after permutation of axes). In addition to the disorder on tetrahedral sites, $\text{Al}_{4+2x}\text{Si}_{2-2x}\text{O}_{10-x}$ mullites are non-stoichiometric phases with oxygen vacancies when $x \neq 0$. Structure refinements on Si or Ge mullites indicate that the vacancies affect a special set of oxygen positions usually labelled O_c and that the neighbouring cations occupy new sites (Tet*) in order to maintain a tetrahedral environment, as shown in Fig. 1.^{9–14} Consequently, the local structure of mullite is very complex. In particular, various states of order have been observed on germanium mullites depending on composition and thermal treatments.^{15–18}

The present work reports a Raman scattering study on Ge mullites in a large range of composition, $0 < x < 0.47$ (from 50 to 70 mol% Al_2O_3). In addition, the spectrum of mullite Ga_2GeO_5 clarifies the effect of substitution of aluminium by gallium. Results on crystallized mullite ceramics obtained by high temperature processes are compared with those of monoliths prepared from a sol–gel route in order to understand structural changes in glass ceramics and poorly crystallized samples from modifications of their Raman spectra.

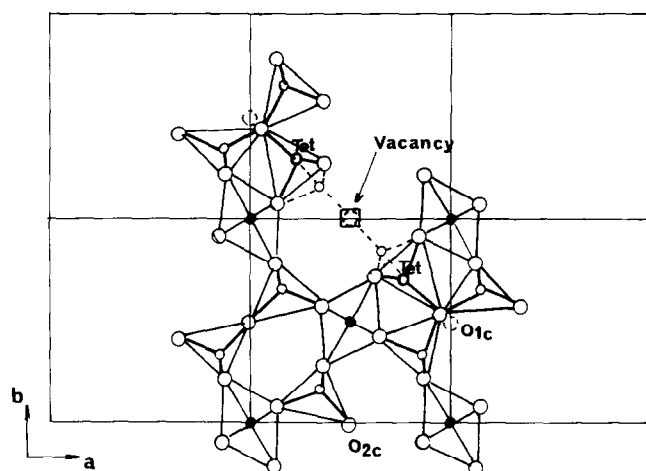


Fig. 1. Projection of the structure of mullite on (001) showing the environment of an oxygen vacancy on O_c positions and occupancy of new tetrahedral sites Tet*.

Experimental Procedure

Samples were prepared by two methods. The first method was used to obtain well-crystallized Al and Ga germanates giving the reference Raman spectra of the various phases. In this case, the synthesis route was coprecipitation with ammonia of mixed germanium oxide (quartz form soluble in hot water) and Al(or Ga)(NO₃)₃·9H₂O aqueous solutions. Atomic absorption analysis on the residual solutions verified that cation losses during the process are negligible. After dehydration, powders were pressed into pellets and heat-treated for 15 h at 1500°C in sealed platinum tubes to prevent GeO₂ volatilization. Then, samples were annealed for 30 h at 1330°C. The characterization of resulting phases and determination of their lattice constants were performed by X-ray diffraction and the results are reported elsewhere.¹⁸ Raman spectra of these samples were recorded with a Jobin-Yvon Ramanor HG2S apparatus with a double monochromator using the blue ($\lambda = 488.0$ nm) or green ($\lambda = 514.5$ nm) lines of an Ar laser. The slit width was kept to about 1–2 cm⁻¹.

The second series of samples was obtained within the framework of studies on mullite formation and sintering using the sol-gel route.^{19–23} In particular, the substitution of germanium to silicon strongly decreases the refractivity and helps to densify mullite composites.²⁴ Monolithic, optically clear gels were prepared by slow hydrolysis (several months) of mixed aluminium secondary butoxide and germanium ethoxide or silicon methoxide diluted in hexane (ratio alkoxide/hexane = 1/5 by volume). Due to the highly hygroscopic nature of the alkoxides, mixture preparation was performed under argon in a glove box free of water traces (H₂O < 20 ppm). Hydrolysis and evacuation of hexane and alcohols resulting from

hydrolysis-polycondensation then proceeds in air through the polyethylene stopper of a glass flask as previously described.²¹ The mixture becomes viscous, gels and, because of its volume contraction, separates from the flask. Heat treatments were then applied in air at various temperatures. Materials remain optically clear up to 1110–1200°C depending on composition. The crystallization process and phase transitions were followed by differential thermal analysis (DTA), dilatometry and X-ray diffraction. The composition and homogeneity were checked by EDX analysis. Hot-pressed pellets were also prepared using graphite dyes and resistors.

The Raman spectra of samples prepared from organic precursors were recorded with a XY Dilor multichannel spectrometer equipped with a Wright 1200-300 CCD detector cooled with nitrogen. Light was collected with an Olympus microscope at a magnification of 1000 ×. Laser excitation was made by the 514.5 nm argon line. Due to the very weak intensity of some spectra, artefacts coming from the collection optics appeared on some spectra around 550 and 1080 cm⁻¹ (broad bands) and 842 and 916 cm⁻¹ (narrow lines). These artefacts are labelled on Fig. 3

Results and Discussion

Relation between spectra of mullite and sillimanite

The Raman spectra of silicon mullites and alumina-silica glass obtained by fast quenching were studied by McMillan and Pirou.²⁵ A complete interpretation of the Raman spectra of sillimanite was made from the study of polarized spectra by Salje and Werneke²⁶ and the effect of pressure was discussed by Mernagh and Liu.²⁷ These results give a useful classification for the Raman modes and have been of considerable help for our interpretation of spectra of germanates with parent structures.

The irreducible representations corresponding to sillimanite are

$$\Gamma = 13 A_g + 13 B_{1g} + 8 B_{2g} + 8 B_{3g} + 11 A_u + 11 B_{1u} + 16 B_{2u} + 16 B_{3u}$$

including the acoustical modes

$$\Gamma_{\text{acoust.}} = B_{1u} + B_{2u} + B_{3u}$$

Therefore, there are 42 Raman active (13 A_g + 13 B_{1g} + 8 B_{2g} + 8 B_{3g}) and 40 infra-red active (10 B_{1u} + 15 B_{2u} + 15 B_{3u}) modes for sillimanite.

For an 'ideal' mullite with no oxygen vacancies ($x = 0$), the irreducible representations decompose as follows :

$$\Gamma = 6 A_g + 6 B_{1g} + 3 B_{2g} + 3 B_{3g} + 5 A_u + 5 B_{1u} + 10 B_{2u} + 10 B_{3u}$$

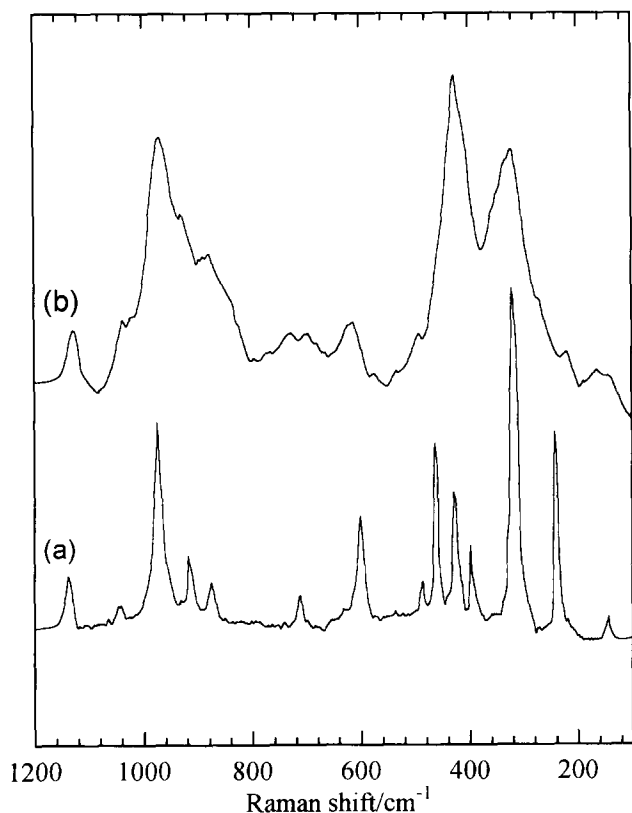


Fig. 2. Raman spectra of: (a) sillimanite from Pinet *et al.*,³⁰ (b) a 55 mol% Al_2O_3 mullite ($x = 0.13$) from McMillan and Piriou.²⁵

including

$$\Gamma_{\text{acoust.}} = B_{1u} + B_{2u} + B_{3u}$$

There are 18 Raman ($6 A_g + 6 B_{1g} + 3 B_{2g} + 3 B_{3g}$) and 22 infra-red ($4 B_{1u} + 9 B_{2u} + 9 B_{3u}$) active modes.

It should be pointed out that in mullite and sillimanite the Al atoms in octahedral sites are on an inversion centre and do not participate in the Raman activity. Scattering coming from cations concerns only tetrahedral Al and Si (or Ge) atoms. For the same reason, the O_c atoms in mullite located at the common corner of two tetrahedra (2a Wyckoff positions) are not involved in the Raman spectra. By symmetry, all the Raman modes of a mullite with $x = 0$ directly derive from degeneracy of sillimanite Raman modes. In particular, mullite modes corresponding to metal and oxygen atoms in 4h Wyckoff positions are split into two for sillimanite. Atoms of type O_c are no longer on an inversion centre in sillimanite and six Raman active modes ($2A_g + 2B_{1g} + B_{2g} + B_{3g}$) are due to vibration of these atoms.

In mullite, the random occupancy of tetrahedral sites by Al and Si, as well as the presence of oxygen vacancies and of new tetrahedral sites when $x \neq 0$, induce breakdown of the translational symmetry of the crystal. In the case of mixed crystals

and solid solutions containing a high content of such massive point defects, the selection rules do not apply and Raman spectra consists of broad bands which tend to reproduce the phonon density of states. A good example can be found in stabilized zirconias, the spectrum of which consists of a broad continuum.^{28,29} Similar features have actually been observed on silicon mullites, as shown in the spectrum of a 55 mol% Al_2O_3 mullite obtained by McMillan and Piriou²⁵ given in Fig. 2(b). Figure 2(a) represents the spectrum of sillimanite obtained by Pinet *et al.*³⁰ Contrary to sillimanite which displays narrow and precisely defined lines, the mullite spectrum consists of broad lines, but each Raman band of mullite can be directly related to corresponding lines in sillimanite. This illustrates well the structural relation between mullite and sillimanite, which possess the same framework of octahedral and tetrahedral chains.

The spectra of Si mullites with compositions $x = 0.25$ and 0.5 prepared from the sol-gel route are given in Fig. 3 and results on mullite and sillimanite spectra are gathered in Table 1. Silicon

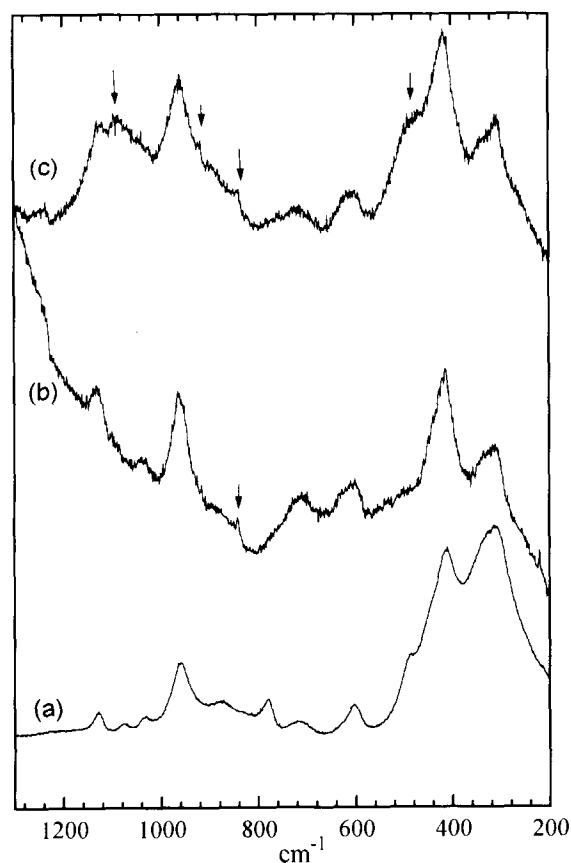


Fig. 3. Raman spectra of silicon mullites with various compositions prepared by a sol-gel route: (a) optically clear nanocrystalline glass-ceramic monolith after 4 days at 1100°C (composition $\text{Al}_2\text{O}_3\text{-}2\text{SiO}_2$); (b) pellet ($x = 0.25$, 60 mol% Al_2O_3) hot-pressed at 1600°C for 2 h (the broad band above 1200 cm^{-1} is due to graphitic precipitates); (c) pellet ($x = 0.5$, 71 mol% Al_2O_3) sintered at 1650°C for 3 h in air (arrows indicate the bands arising from the optics).

Table 1. Raman frequencies of sillimanite and Si-mullites

	$Al_2O_3-2SiO_2$ Sillimanite glass-ceramic, (Ref. 30) sol-gel route, 1100°C	Mullite $x = 0.25$, sol-gel route, 1600°C	Mullite $x = 0.5$, sol-gel route, 1650°C	Mullite (Ref. 25)
144 w				
236 s				
311 vs	310 vs	314 m	308 m	310 s
393 w				
413 w	413 m	415 s	416 s	410 s
423 m				
459 s				
485 w				
597 m	603 w	607 m	607 m	610 w
706 w	715 vw	711 m	718 w	710 w
849 vw	780 w			
874 w	873 w	873 w	875 sh	880 sh
910 w				
966 s	960 m	962 s	960 s	960 s
1036 w	1033 vw	1033 w		1040 m
1060 w	1077 vw	1080 w	1090 w	
1132 w	1129 w	1130 m	1125 w	1160 m

s: Strong; m: medium; w: weak; vw: very weak; sh: shoulder.

mullites, as well as silicon-containing glasses and gels, are generally poor Raman scatterers^{19,20} and this explains the high noise level in the spectra of Figs 2(a), 3(b) and 3(c). However, the spectrum of the nanocrystalline glass-ceramic monolith (Fig. 3(a)) is better resolved. Local arrangements in the first steps of crystallization from gels seem to be less distorted and better defined than after high-temperature treatments.

Spectra of germanium mullites

The Raman spectra of germanium mullites with various compositions, prepared by coprecipitation and by the sol-gel route, are given in Figs 4 and 5, respectively. For the same composition, the Raman spectra of samples prepared by the two methods are very similar. This indicates that the evolution of Raman spectra with composition represents the intrinsic structural change. Corresponding wavenumbers are gathered in Table 2.

All these spectra are very similar to those of silicon mullites except for the wavenumbers, which are shifted towards low values for most lines. For all compositions, the spectra consist of broad lines as for Si mullite. The line width at half maximum amounts to about 40 cm^{-1} , which is more than twice than in sillimanite. In addition, broader bands with asymmetric profiles around 300 and 600 cm^{-1} are probably the envelope of two or more lines. For the Al_2GeO_5 compound where no oxygen vacancies are present ($x = 0$), these features can be only attributed to a disordered distribution of Al and Ge on tetrahedral sites. This confirms previous results obtained by infra-red spectroscopy^{4,31} and by electron and X-ray diffrac-

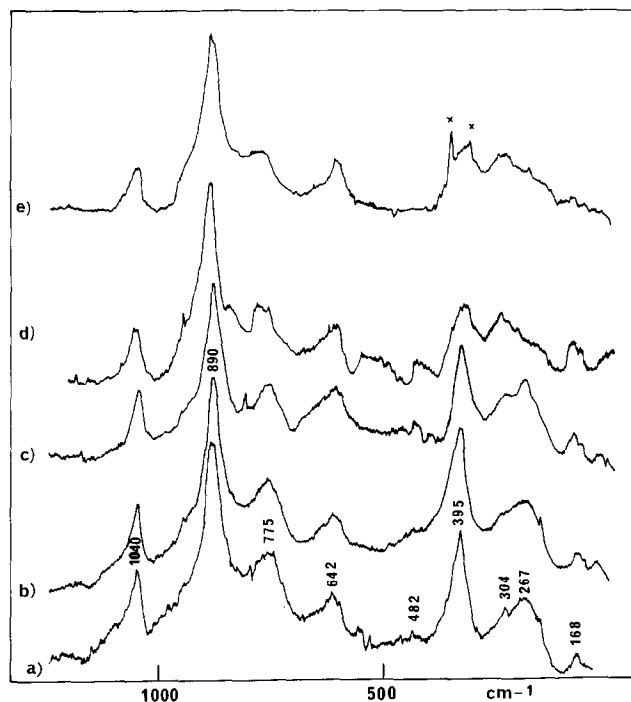


Fig. 4. Raman spectra of $Al_{4+2x}Si_{2-2x}O_{10-x}$ germanium mullites annealed at 1330°C: (a) $x = 0$ (50 mol% Al_2O_3); (b) $x = 0.13$ (55 mol% Al_2O_3); (c) $x = 0.25$ (60 mol% Al_2O_3); (d) $x = 0.40$ (67 mol% Al_2O_3); (e) $x = 0.47$ (70 mol% Al_2O_3). Traces of Al_2O_3 are revealed by the lines at 380 and 417 cm^{-1} indicated by x.

tion patterns, as there is no diffraction spot or diffuse scattering indicating a double periodicity along the c -axis.¹⁷

The general aspect of the spectra remains essentially unchanged with composition for the series of

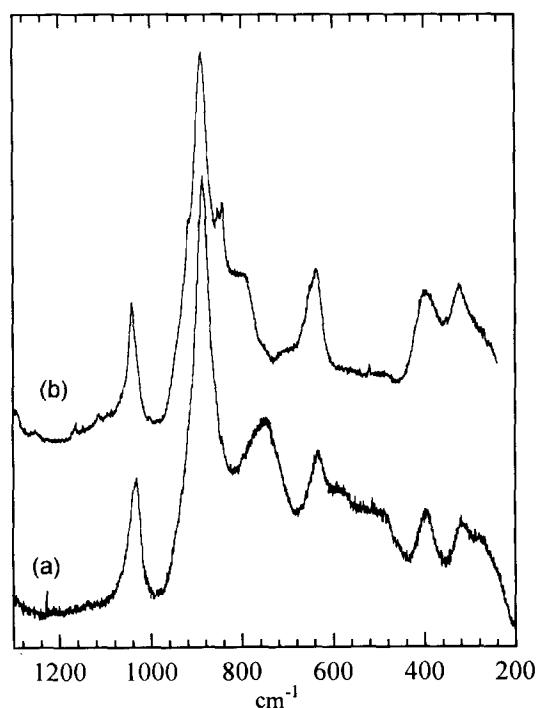


Fig. 5. Raman spectra of $Al_{4+2x}Ge_{2-2x}O_{10-x}$ germanium mullites prepared by sol-gel route: (a) optically clear monolith $x = 0.15$ (56 mol% Al_2O_3) obtained after 3 h at 1000°C; (b) translucent monolith $x = 0.25$ (60 mol% Al_2O_3) obtained at 1250°C.

Table 2. Raman frequencies of $\text{Al}_{4+2x}\text{Ge}_{2-2x}\text{O}_{10-x}$ germanium mullites as a function of composition (mol%). Samples prepared by sol-gel route are indicated by *

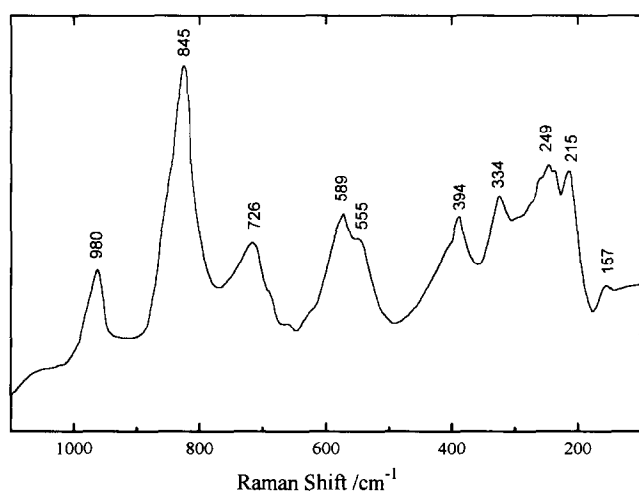
50% Al_2O_3 $x = 0,$ 1330°C	55% Al_2O_3 $x = 0.13,$ 1330°C	56% Al_2O_3 $x = 0.15,$ 1000°C*	60% Al_2O_3 $x = 0.25,$ 1330°C	60% Al_2O_3 $x = 0.25,$ 1250°C*	67% Al_2O_3 $x = 0.40,$ 1330°C	70% Al_2O_3 $x = 0.47,$ 1330°C
170 w	165 w	^a	170 w	^a	170 w	170 w
265 m	270 m	270 w	250 m		260 m	260 m
305 m	305 sh	315 w	300 m	320 m	300 m	310 s
395 s	395 s	395 s	395 s	395 m	395 s	395 m
480 vw	480 vw	490 vw		480 vw	480 vw	
570 vw		580 vw	570 vw		570 vw	
640 m	640 m	635 m	640 m	635 m	640 m	640 m
775 m	780 m	790 m	785 m	790 m	785 m	795 m
890 vs	890 vs	890 vs	890 vs	890 vs	890 vs	890 w
945 sh	945 sh		945 sh		945 sh	950 sh
1040 m	1040 m	1040 m	1045 m	1040 m	1050 m	1055 sh

s: Strong; m: medium; w: weak; vw: very weak; sh: shoulder.

^a Not studied below 200 cm^{-1} .

Fig. 4. However, modification occurs in the shape, intensity or position of certain bands. Wavenumbers are slightly shifted towards lower frequencies as the alumina content increases for two high frequency lines (from 1040 to 1055 cm^{-1} and from 775 to 795 cm^{-1}). On the other hand, the location of the 640 and 395 cm^{-1} lines does not vary, though the 395 cm^{-1} line decreases and broadens as the alumina content increases. Noticeable intensity changes are also observed for the 260 and 310 cm^{-1} lines depending on composition.

The Raman spectrum of a Ga_2GeO_5 mullite ($x = 0$) given in Fig. 6 has a close resemblance with that of Al_2GeO_5 despite a significant shift towards low frequency (about 50 cm^{-1}) for the bands in the region 700–1100 cm^{-1} . Another difference is the better resolution of the broad band between 200 and 350 cm^{-1} for the gallium compound. This result is in agreement with the observation by Schneider³¹ of some band splitting in infra-red spectroscopy which was interpreted in terms of slight ordering.

**Fig. 6.** Raman spectrum of Ga_2GeO_5 mullite.

The high frequency modes of $\text{Al}(\text{or Ga})_2\text{GeO}_5$ mullites (1045, 950, 885 and 785 cm^{-1} with Al and 980, 845 and 726 cm^{-1} with Ga) correspond to the ν_1 and ν_3 internal modes of GeO_4 groups. These modes are found at much higher wavenumbers than for isolated GeO_4 groups. They appear, for instance, in the range 800–700 cm^{-1} in scheelite orthogermanates.³² Salje and Werneke suggested that the coupling with neighbouring Al–O bonds explains the increased frequencies of SiO_4 stretching vibrations in andalusite and sillimanite.²⁶ The frequency difference in Ga and Al compounds that we observed probably results from the weaker Ga–O stretching force constants and the larger unit-cell parameters in Ga_2GeO_5 . In silicon mullites, the corresponding modes are found at higher frequencies, respectively at 1140, 1040, 960 and 880 cm^{-1} ,²⁵ in good agreement with the difference usually observed between Ge–O and Si–O stretching.³³

The asymmetric band at 640 cm^{-1} in Al–Ge mullite may be assigned to Al–O vibrations and those at 555 and 589 cm^{-1} in Ga_2GeO_5 to Ga–O vibrations. Actually, they are located in the same mid-wavenumber region where McMillan and Piriou have suggested to attribute Al–O displacement in mullite.²⁵ Moreover, Mernagh and Liu found lower Gruneisen parameters for the 708 and 594 cm^{-1} sillimanite modes which is indicative of more ionic bonding and may correspond to Al–O vibrations.²⁷

A relatively well-defined line appears at 395 cm^{-1} in Al_2GeO_5 ($x = 0$) in the region corresponding to O–Ge–O bending in orthogermanates.³² This line is severely affected when the alumina content increases and this is attributed to the decrease of the number of GeO_4 tetrahedra at the expense of AlO_4 units. Moreover, a similar line is found in Ga_2GeO_5 practically at the same frequency whereas in silicon mullite this band is at 410 cm^{-1} .

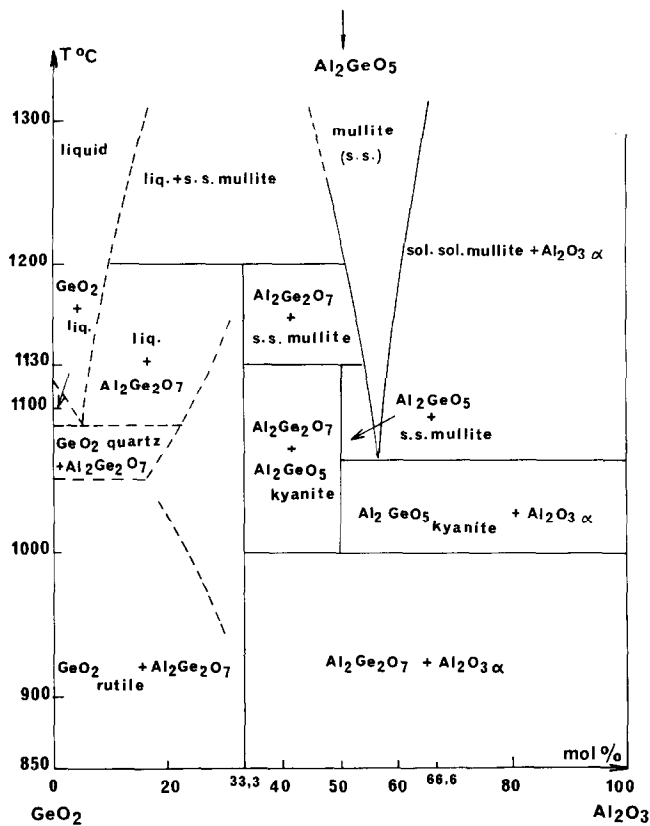


Fig. 7. $\text{GeO}_2\text{-Al}_2\text{O}_3$ phase diagram, after Perez y Jorba.⁴

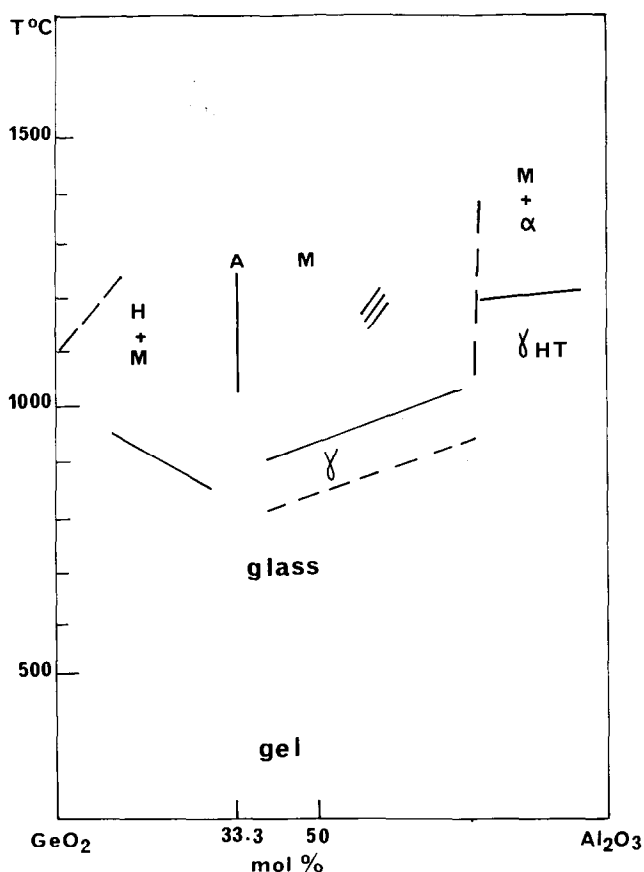


Fig. 8. Phase boundaries observed for gels prepared by slow alkoxide hydrolysis as a function of the composition and thermal treatment (H = hexagonal GeO_2 (quartz-form), M = mullite, α = Al_2O_3 (corundum), γ = disordered phase exhibiting a spinel-like X-ray diffraction pattern, γ_{HT} = spinel phase, A = monoclinic $\text{Al}_2\text{Ge}_2\text{O}_7$, // = metastable Al_4GeO_8).

The new local arrangements formed as the alumina content increases, in particular the groups of three tetrahedra linked by the same corner (Fig. 1), are expected to modify the Raman activity concerning collective vibrations. The observed change in the shape and intensity of bands with the Al/Ge ratio in the region below 380 cm^{-1} , which corresponds to external rotational and translational modes, is probably associated with these modifications.

Mullite formation and $\text{GeO}_2\text{-Al}_2\text{O}_3$ phase diagram

$\text{GeO}_2\text{-Al}_2\text{O}_3$ phase diagrams established by the study of materials prepared solely by solid-state reaction lead to a rather simple diagram, including mullite as the only binary compound similarly to that of $\text{SiO}_2\text{-Al}_2\text{O}_3$.^{2,5} On the contrary, when the composition-temperature range is precisely explored using reactive powders, a more complex phase diagram is achieved (Fig. 7). Similarly, the crystal-

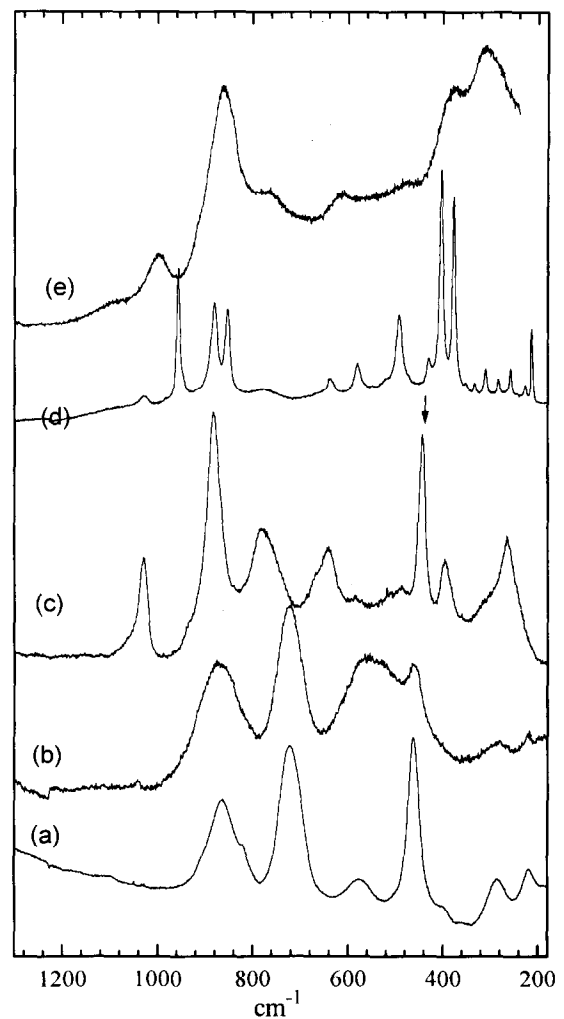


Fig. 9. Evolution of Raman spectra for the composition $2\text{ GeO}_2\text{-Al}_2\text{O}_3$ (33.3 mol% Al_2O_3) depending on temperature: (a) water-containing gel (room temperature); (b) mesoporous glass obtained after heating at 800°C ; (c) crystallized mullite + hexagonal GeO_2 (indicated by arrow) obtained after heating at 1020°C ; (d) monoclinic $\text{Al}_2\text{Ge}_2\text{O}_7$ obtained after heating for 30 min at 1250°C ; (e) high temperature mullite obtained after heating for 3 min at 1450°C .

lization of homogeneous gels leads to a variety of stable or metastable phases. Figure 8 summarizes the results obtained by annealing optically clear $\text{Al}_2\text{O}_3\text{-GeO}_2$ gels and gives the domains where the various phases are formed depending on temperature and the Al/Ge ratio. An example of successive structural changes is shown by Fig. 9, which reports the Raman spectra obtained after heating $\text{Al}_2\text{O}_3\text{-}2\text{GeO}_2\text{-}x\text{H}_2\text{O}$ gels at various temperatures. Corresponding wavenumbers are given in Table 3. In the gel state, the Raman spectrum consists of well-defined bands (Fig. 9(a)) that can be assigned to the vibrations of GeO_4 (460 and 565 cm^{-1}) and GeO_6 (720 and 870 cm^{-1}) entities because this spectrum looks like the superimposition of quartz (443 and 880 cm^{-1}) and rutile (695 and 870 cm^{-1}) germania. Dehydration of this gel leads to a mesoporous glass which possesses the same Raman lines, but which are noticeably broadened. In addition, a very broad band which is characteristic of GeO_2 glass³⁴ is observed around 570 cm^{-1} (Fig. 9(b)). At higher temperature, crystallized phases are obtained, the first of which is mullite with some GeO_2 (quartz form). The Raman lines of this mullite phase (Fig. 9(c)) are relatively well defined. Mullite and GeO_2 quartz then transform into the monoclinic $\text{Al}_2\text{Ge}_2\text{O}_7$ compound. Its Raman spectrum (Fig. 9(d)) contains only very sharp lines in agreement with X-ray results on single crystals which indicated that the structure of $\text{Al}_2\text{Ge}_2\text{O}_7$ is

completely ordered.⁶ The polyhedra present in this compound are Ge_2O_7 groups consisting of two tetrahedra linked by one corner and AlO_5 bipyramids.⁶ According to the phase diagram given in Fig. 7, $\text{Al}_2\text{Ge}_2\text{O}_7$ is the phase stable below 1200°C ; however, crystallization of gels leads first to mullite rather than directly into $\text{Al}_2\text{Ge}_2\text{O}_7$. It is likely that the preparation from hydrolysis-polycondensation favours a connected tetrahedra network and induces crystallization into mullite that contains similar arrangements. At higher temperature, the stable phase mullite appears again, but the significant line width of Raman bands reveals a large amount of disorder (Fig. 9(e)).

Conclusions

Raman scattering studies demonstrated that both silicon and germanium mullites are strongly disordered at the molecular scale. In the case of the $\text{GeO}_2\text{-Al}_2\text{O}_3$ system, in addition to mullites with various degrees of order, (which can be estimated from Raman line width), several phases can be prepared with methods which favour mixing at molecular scale: $\text{Al}_2\text{Ge}_2\text{O}_7$, Al_2GeO_5 (kyanite form), Al_4GeO_8 and spinel-like phases. Furthermore, the lower melting point of GeO_2 enhances the achievement of the stable state at lower temperature than in silicon-containing homologues.

Acknowledgements

The authors are indebted to Drs B. Piriou (CNRS, Ecole Centrale, Chatenay-Malabry) and B. Lasnier (University of Nantes) for helpful discussion and for kindly communicating their results on Raman spectra of silicon mullite and sillimanite.

References

1. Perez y Jorba, M., Tarte, P. & Collongues, R., Structure and properties of alumina-germanium dioxide compounds. *C.R. Acad. Sci.*, **257** (1963) 3417-20.
2. Miller, J. L. Jr., McCormick, G. R. & Ampian, S. G., Phase equilibria in the system $\text{GeO}_2\text{-Al}_2\text{O}_3$. *J. Am. Ceram. Soc.*, **50** (1967) 268-9.
3. Perez y Jorba, M., $\text{GeO}_2\text{-Al}_2\text{O}_3$ and $\text{GeO}_2\text{-Fe}_2\text{O}_3$ systems. Comparison with the silica corresponding systems. *Silicates Industriels*, **1** (1968) 11-7.
4. Perez y Jorba, M., Study of phases between germanium dioxide and some oxides of trivalent elements. *Rev. Int. Hautes Temp. et Refract.*, **6** (1969) 283-98.
5. Prochazka, S., Sintering and properties of dense aluminum germanates, In *Ceramics Powders*, ed. P. Vincenzini, Elsevier, Amsterdam, 1983, pp. 861-70.
6. Agafonov, V., Kahn, A., Michel, D. & Perez y Jorba, M., Crystal structure of a new digermanate $\text{Al}_2\text{Ge}_2\text{O}_7$. *J. Solid State Chem.*, **62** (1986) 402-4.

Table 3. Raman frequencies of the spectra of Fig. 9. Samples prepared by sol-gel route at the composition $2\text{ GeO}_2\text{-Al}_2\text{O}_3$ (33.3 mol% Al_2O_3)

Gel, 20°C	Glass, 800°C	Mullite + GeO_2 , 1020°C	$\text{Al}_2\text{Ge}_2\text{O}_7$, 1250°C	Mullite, 1450°C
			214 m	
220 m	220 vw		228 vw	
		265 m	256 w	
285 m	283 w		284 w	
		312 m	311 w	300 m,b
			334 vw	
			352 vw	
			378 s	
400 vw	400 v w		403 s	390 s,b
		443 s	430 w	
462 s	461 m		492 m	
		487 w	591 w	600 m,b
575 m	570 s,b		638 w	
		641 m		
		670 sh		
722 s	723 s		776 w,b	780 m,b
780 m,b		780 m		
823 sh			854 s	
864 s	869 m,b		881 m	890 s,b
		883 s	957 m	
		1030 m	1030 w	1030 m,b

s: Strong; m: medium; w: weak; vw: very weak; sh: shoulder; b: broad.

7. Kahn, A., Agafonov, V., Michel, D. & Perez y Jorba, M., New gallium germanates with tunnel structures: α -Ga₄GeO₈ and Ga₄Ge₃O₁₂. *J. Solid State Chem.*, **65** (1986) 377–82.
8. Cameron, W. E., Mullite: a substituted alumina. *Am. Mineral.*, **62** (1977) 747–55.
9. Michel, D., Abolhassani, S., Kahn, A., Agafonov, V. & Perez y Jorba, M., Aluminum, gallium and iron (III) germanates with aluminum silicate structures. In *Mullite and Mullite Matrix Composites*, Ceramic Transactions, Vol. 6, eds S. Somiya, R. F. Davies & J. A. Pask, The American Ceramic Society, Westerville, OH, 1990, pp. 159–66.
10. Burnham, C. W., Crystal structure of mullite. *Carnegie Inst. Washington Yearbk*, **63** (1964) 223–7.
11. Burnham, C. W., Composition limits of mullite and the sillimanite–mullite solid solution problem. *Carnegie Inst. Washington Yearbk*, **63** (1964) 227–8.
12. Durovic, S., Isomorphism between sillimanite and mullite. *J. Am. Ceram. Soc.*, **45** (1962) 157–61.
13. Durovic, S. & Fedji, P., Synthesis and crystal structure of germanium mullite and crystallographic parameters of D-mullites. *Silikaty*, **20** (1976) 97–112.
14. Angel, R. J. & Prewitt, C. T., Crystal structure of mullite: a re-examination of the average structure. *Am. Mineral.*, **71** (1986) 1476–82.
15. Saalfeld, H. & Guse, W., Mullite single crystal growth and characterization. In *Mullite and Mullite Matrix Composites*, Ceramic Transactions, Vol. 6, eds S. Somiya, R. F. Davies & J. A. Pask, The American Ceramic Society, Westerville, OH, 1990, pp. 73–101.
16. Perez-Ramirez, J. G., Michel, D. & Portier, J. R., Enhancing of small isolated domains and superstructures in high resolution of oxides. *Mater. Res. Soc. Proc.*, **139** (1989) 321–6.
17. Kahn-Harari, A., Abolhassani, S., Perez-Ramirez, J. G., Michel, D., Mazerolles, L., Portier, R. & Perez-Ramirez, J. G., Observation of ordering in silicon and germanium mullites. *J. Solid State Chem.*, **90** (1991) 234–48.
18. Abolhassani, S., Contribution to the study of mullite-type aluminum germanates. Thesis, University of Paris-Sud, 1991.
19. Colomban, Ph., Structure of oxide gels and glasses by IR and Raman scattering. II, mullites. *J. Mater. Sci.*, **24** (1989) 3011–20.
20. Colomban, Ph., Gel–glass–mullite transition and microstructure as a function of powder preparation, Stoichiometry and Zr(Ti) addition. In *Ceramic Powder Processing Science*, eds H. Hausner, E. R. Fuller & G. D. Messing, The American Ceramic Society, Westerville, OH, 1989, pp. 85–92.
21. Colomban, Ph. & Mazerolles, L., Nanocomposites in mullite–ZrO₂ and mullite–TiO₂ systems synthesized through hydrolysis gel routes. Microstructure and fractography. *J. Mater. Sci.*, **26** (1991) 3503–10.
22. Colomban, Ph., Jones, D. J., Grandjean, D. & Flank, A. M., EXAFS and XANES study of (Si, Ge) mullites gels and glasses prepared by slow hydrolysis of alkoxides. *J. Non-Cryst. Solids*, **147–148**, (1992) 135–40.
23. Colomban, Ph. & Vendange, V., Sintering of alumina and mullites prepared by slow hydrolysis of alkoxides: the role of the protonic species and pore topology. *J. Non-Cryst. Solids*, **147–148**, (1992) 245–50.
24. Colomban, Ph., Lagrange, J. L., Bruneton, E. & Mouchon, E., Sol-gel mullite matrix–SiC 2D woven fabrics composites with and without zirconia interphase. *J. Eur. Ceram. Soc.*, in press.
25. McMillan, P. & Pirou, B., The structures and vibrational spectra of crystals and glasses in the silica–alumina system. *J. Non-Cryst. Solids*, **53** (1982) 279–98.
26. Salje, E. & Werneke, C., The phase equilibrium between sillimanite and andalusite as determined from lattice vibrations. *Contrib. Miner. Petrol.*, **79** (1982) 56–67.
27. Mernagh, T. & Liu, L. G., Raman spectra from the Al₂SiO₅ polymorphs at high pressure and room temperature. *Phys. Chem. Minerals*, **18** (1991) 126–30.
28. Keramidis, V. G. & White, W. B., Raman scattering from Ca_xZr_{1-x}O_{2-x}, a system with massive point defects. *J. Chem. Phys.*, **34** (1973) 1873–8.
29. Michel, D., Perez y Jorba, M. & Collongues, R., Study by Raman spectroscopy of order–disorder phenomena occurring in some binary oxides with fluorite-related structures. *J. Raman Spectrosc.*, **5** (1976) 163.
30. Pinet, M., Smith, D. C. & Lasnier, B., Raman microprobe in gemmology. *Revue de Gemmologie*, (June 1992) 11–60.
31. Schneider, H., Infrared spectroscopic investigation of andalusite and mullite-type structures in the Al₂GeO₅–Fe₂GeO₅ and Al₂GeO₅–Ga₂GeO₅ systems. *N. Jb. Miner. Abh.*, **142** (1981) 11–123.
32. Vandenborre, M. T., Michel, D. & Ennaciri, A., Vibrational spectra and force fields of scheelite-type germanates. *Spectrochim. Acta.*, **45A** (1989) 721–7.
33. Lazarev, A. I., Mirgorodskii, A. P. & Ignatiev, *Vibrational Spectra of Complex Oxides: Silicates and Analogs*, Nauka, Leningrad, 1975.
34. Henderson, G. S., Bancroft, G. M., Fleet, M. E. & Rogers D. J., Raman spectra of gallium and germanium substituted silicate glasses: variation in intermediate order, *Am. Mineral.*, **70** (1985) 946–60.

Infra-red Spectroscopic Investigation in the Mullite Field of Composition: $\text{Al}_2(\text{Al}_{2+2x}\text{Si}_{2-2x})\text{O}_{10-x}$ with $0.55 > x > 0.25$

C. H. Rüscher, G. Schrader & M. Götze

Institut für Mineralogie der Universität Hannover und SFB 173, Welfengarten 1, 30167 Hannover, Germany

(Accepted 22 July 1995)

Abstract

The infra-red absorption of 2:1 and 3:2 mullites, and a series of heat-treated mullite starting materials of nominal composition $3\text{Al}_2\text{O}_3 \cdot 2\text{SiO}_2$ prepared by the sol-gel process, are investigated in the spectral range $400\text{--}1400\text{ cm}^{-1}$ using the KBr powder method. It is shown that the intensity variation of the absorption band in the spectral range $1100\text{--}1200\text{ cm}^{-1}$ provides a useful empirical scale for the determination of mullite compositions. This absorption feature exhibits the superposition of three peaks, which are related to vibrations of the mullite specific tetrahedral units $[\text{SiO}_4]$, $[\text{AlO}_4]$ and $[\text{Al}^*\text{O}_4]$ with frequency maxima at about 1165 , 1130 and 1108 cm^{-1} , respectively.

1 Introduction

Mullite, $\text{Al}_2(\text{Al}_{2+2x}\text{Si}_{2-2x})\text{O}_{10-x}\text{V}_x$, is one of the most important ceramic products. The stability field of mullite depends on the ability to accommodate oxygen vacancies (V), which is commonly described by the exchange reaction $2\text{Si}^{4+} + \text{O}^{2-}$ to $2\text{Al}^{3+} + \text{V}$. Cameron^{1,2} put forward the view of a solid solution in the stability field of mullite. The silica-rich limit has been observed for $x \approx 0.17$, possessing a hypothetical miscibility gap to the structurally closely related mineral sillimanite of $x = 0$ composition. This relationship can be seen by assuming an Al-Si disorder on the tetrahedral sites of the sillimanite structure. The field of solid solution, on the other hand, is implied by the incorporation of oxygen vacancies and the development of the lattice constants on x . The **a**-lattice parameter of the orthorhombic unit cell (*Pbam*) of mullite increases linearly from about $a = 0.754\text{ nm}$ for so-called 3:2 'ideal'¹ sinter mullite ($x = 0.25$) to $a = 0.757\text{ nm}$ for 2:1 melt mullite ($x = 0.4$). Along this route of compositions the **c** and **b** lattice parameters

also vary systematically; however, more smoothly compared with the **a** values ($b \approx 0.768\text{--}0.769\text{ nm}$; $c \approx 0.2886\text{--}0.289\text{ nm}$). The linear increase of the **a** lattice parameter still holds towards higher x values, while the **b** parameter drops down slightly and shows $a = b \approx 0.766\text{ nm}$ for $x \approx 0.67$ ^{1,2} (see also Ref. 3 and references therein). Thus, the empirical rule of the development of the lattice parameters (commonly the **a** lattice constant) can be used for an estimation of the composition of mullite ceramics and powders using X-ray diffraction techniques, as has often been reported (compare Ref. 3).

Another potential technique to estimate the composition of mullite has also been suggested by Cameron.¹ By using KBr diluted pressed pellets of various mullites, Cameron¹ observed a systematic change in the line profile of the infra-red absorption in the spectral range 1100 to 1200 cm^{-1} as a function of Al_2O_3 content. On the other hand, the infra-red technique has been used by various authors to investigate mullite crystallization (compare, e.g., Ref. 4) without, however, exploring the possibility of characterization of the mullite composition in any detail, an oversight which will be addressed in this study.

It is proposed here to follow the crystallization of mullite from base non-crystalline mullites of composition $x = 0.25$ (3:2 mullite), prepared by the sol-gel process with different methods of hydrolysis. The synthesis and structural characterization of these materials (precursor material) have been given in detail previously,^{5,6} and it has been shown that so-called types I, II and III precursors show crystallization of mullite at 900 , 1200 and 1200°C , respectively. It is known that type I precursors show a gradual change from initial mullite with high Al_2O_3 content to mullite of bulk composition $x = 0.25$ (above $\sim 1400^\circ\text{C}$), similar to observations reported by Okada and Otsuka⁷ (see also Refs 3, 5, 6, 8). Type II and III precursors, on the other hand, form $\gamma\text{-Al}_2\text{O}_3$ prior

to the crystallization of mullite.^{3,5,8,9} Thus, by investigating these crystallization processes, information on the applicability of the KBr infra-red spectroscopic technique to the determination of mullite compositions can be expected.

It may be noted that MacKenzie¹⁰ was the first to obtain an assignment of infra-red frequencies of a mullite of composition $x = 0.25$ (3:2 mullite), using simplified structural models in comparison with a KBr powder spectrum. MacKenzie¹⁰ could resolve about eight oscillator frequencies. However, it has been shown recently,¹¹ on the basis of single crystal infra-red investigations of mullite of composition $x = 0.4$ (2:1 mullite), that the spectra show strong anisotropy and that 14, 14 and nine oscillator frequencies can be resolved for the polarizations $E||a$, $E||b$ and $E||c$, respectively. The absorption bands are all close together, distributed mainly in the spectral range 300 to 1000 cm^{-1} and 1100 to 1200 cm^{-1} . This indeed creates serious problems in achieving any accurate determination of oscillator frequencies from KBr powder spectra, a point which will also be discussed here.

2 Experimental

The non-crystalline mullite base materials used in this study were kindly provided by Schneider and co-workers (DLR, Germany). These materials were synthesized starting from tetraethyl orthosilicate (TEOS) and aluminium-sec-butylate (Al-O-Bu). The educts were formulated with the stoichiometric composition $3 \text{Al}_2\text{O}_3:2 \text{SiO}_2$. After different routes of hydrolysis (type I: low water content, slow hydrolysis; types II and III: high water content and fast hydrolysis with pH values of >10 and <10 , respectively), the materials were calcined at 350°C for preservation. Details of the preparation techniques and further characterization of the precursors are given by Schneider and co-workers.^{5,6} A series of samples was prepared from each batch, these samples being subjected to further heat treatments at temperatures between 800 and 1650°C. Each sample (100 mg) was placed in a Pt crucible, heated up to its defined burning temperature at 300°C min^{-1} and quenched by removing the sample from the furnace. The holding time at the burning temperature was 15 h in each case.

The products were investigated by standard X-ray powder methods (Guinier camera) and by infra-red (IR) spectroscopic means (Bruker FTIR IFS88). For the IR measurements the samples were ground to an average particle size of $\sim 1 \mu\text{m}$ and diluted with KBr (sample:KBr = 1:250 wt%; total weight $\approx 1 \text{ g}$). From these mixtures 250 mg were taken and pressed to obtain clear discs for

the measurements. All spectra are plotted in absorption units according to $-\ln(I/I_0)$. I , I_0 = transmitted intensity of the sample plus KBr and pure KBr discs, respectively. For comparison, mullite samples of known 3:2 composition (extracted from sintered mullites) and 2:1 mullites (extracted from melt mullites) were investigated using the same route.

3 Results

KBr powder spectra of pure mullites of known composition $x = 0.25$ ($3\text{Al}_2\text{O}_3 \cdot 2\text{SiO}_2$) and $x = 0.4$ ($2\text{Al}_2\text{O}_3 \cdot \text{SiO}_2$) are shown in Fig 1. Although the line shapes of the spectra look similar, there are characteristic distinctions. The main features observed in the spectrum of the 2:1 mullite are marked by dotted lines. Their vertical extensions are shown for better comparison with the spectrum of the 3:2 mullite. Below about 500 cm^{-1} the spectral line profiles indicate slight differences that are, however, hard to resolve systematically because of experimental difficulties. The peak maximum at $\sim 545 \text{ cm}^{-1}$ in the 2:1 spectrum appears to be shifted to $\sim 575 \text{ cm}^{-1}$ in the 3:2 spectrum. There is a sharper peak structure at $\sim 740 \text{ cm}^{-1}$ in the 3:2 spectrum compared with the 2:1 one. This feature could be related to the difference in intensity of the peak structures at $\sim 810 \text{ cm}^{-1}$ and 895 cm^{-1} . The most prominent spectral difference is observed in the absorption line profile in the spectral range 1100 to 1200 cm^{-1} . The spectrum of the 3:2 mullite is in sufficient agreement with the KBr powder spectrum of a 3:2 mullite reported by MacKenzie.¹⁰ MacKenzie¹⁰ related the peak structure in the spectral range 1100 to 1200 cm^{-1}

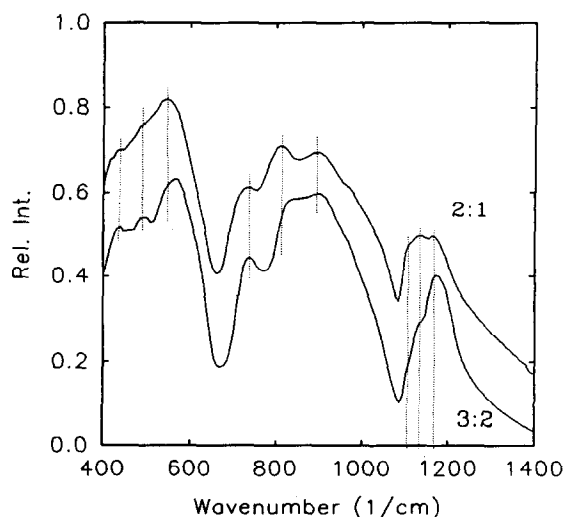


Fig. 1. IR absorption spectra of two mullites of known composition: $2\text{Al}_2\text{O}_3 \cdot \text{SiO}_2$ (2:1 mullite, $x = 0.4$) and $3\text{Al}_2\text{O}_3 \cdot 2\text{SiO}_2$ (3:2 mullite, $x = 0.25$). Dotted vertical lines are given as a guide for the eye, to enable comparison (see text). The spectra are shifted vertically for better comparison.

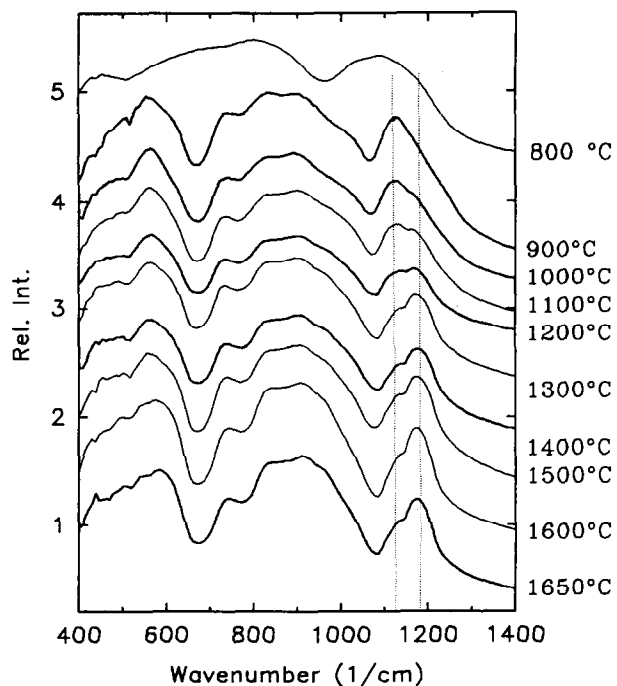


Fig. 2. IR absorption spectra of route of crystallization of type I precursor starting material with the burning temperatures as shown. The spectra are shifted vertically for better comparison. Dotted lines are a guide for the eye.

to a superposition of two peaks of high and low intensity, which were assigned to $[\text{AlO}_4]$ (1165 cm^{-1}) and $[\text{SiO}_4]$ (1125 cm^{-1}) species, respectively. In the spectra shown here, there are three positions marked that will be discussed further below.

The spectra observed for the route of crystallization of type I, II and III precursor starting materials are shown in Figs 2, 3 and 4, respectively. It has been shown earlier⁵ that precursor starting material of type I shows a higher degree of homogeneity than types II and III, i.e. there are larger Al-rich clusters in the type II and III materials.

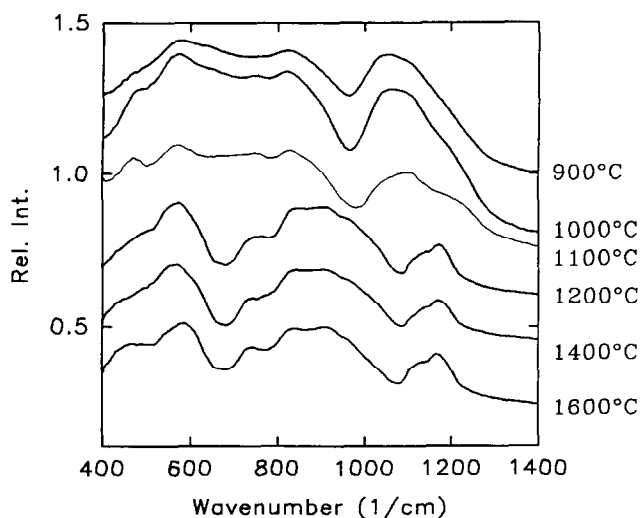


Fig. 3. IR absorption spectra of route of crystallization of type II precursor starting material with the burning temperatures as shown. The spectra are shifted vertically for better comparison.

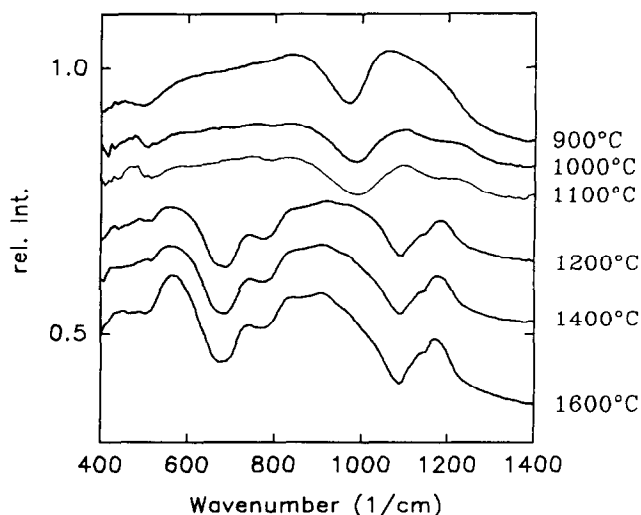


Fig. 4. IR absorption spectra of route of crystallization of type III precursor starting material with the burning temperatures as shown. The spectra are shifted vertically for better comparison.

Therefore, it can be understood that $\gamma\text{-Al}_2\text{O}_3$ crystallizes first⁵ (compare also Ref. 8) in these cases. Inspection of the spectra in Figs 3, 4 and 1 shows that mullite crystallization is proved for the material burned at 1200°C without significant changes in the mullite spectra towards higher burning temperatures. These findings are in agreement with the X-ray results. The changes in the spectra for 900 to 1100°C may be related to prior crystallization ($\gamma\text{-Al}_2\text{O}_3$). In contrast to this, the infra-red absorption spectra show that the formation of mullite for type I precursor material has already occurred at 900°C , with, however, significant changes observed in the 1100 to 1200 cm^{-1} absorption profiles at higher firing temperatures. These changes are in close agreement with observations reported by Cameron¹ for mullites of different Al_2O_3 to SiO_2 ratios ($0.6 < x < 0.25$). It may be noted that the mullite spectra in Fig. 2 also show a systematic decrease of the intensity of the peak structures at 810 cm^{-1} relative to the one at 895 cm^{-1} , but these changes are too small to be followed in detail.

For a first rough determination of the evolution of the absorption profile in the spectral range 1100 to 1200 cm^{-1} , the intensities in the spectra of the series of samples of type I (Fig. 2) were measured at 1130 cm^{-1} and 1170 cm^{-1} relative to the baseline for zero intensity obtained at 2000 cm^{-1} (not shown; note that the spectra are shifted vertically for better comparison). The ratios of the intensities $I(1130 \text{ cm}^{-1})/I(1170 \text{ cm}^{-1})$ are shown in Fig. 5 as a function of the firing temperatures. Also indicated in this figure are the ratios obtained for the 2:1 and 3:1 mullites from Fig. 1. The systematic variation of the data implies that the composition of the mullite changes gradually from Al-rich mullite

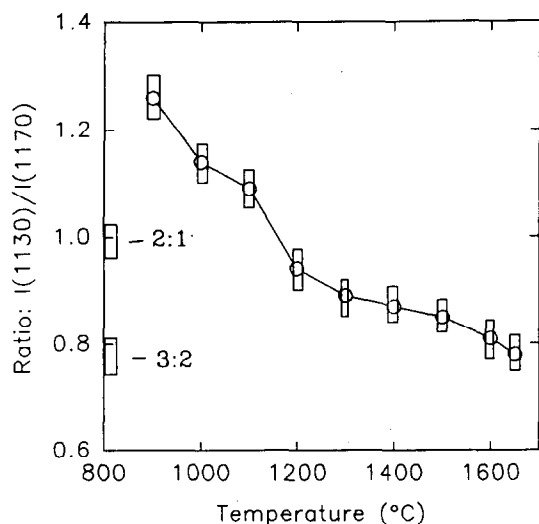


Fig. 5. Ratio of absorption measured at 1130 and 1170 cm^{-1} of the spectra given in Fig. 2 as a function of temperature. Values obtained for ideal 3:2 and 2:1 mullites (Fig. 1) are marked. Boxes indicate the experimental uncertainty. Solid line is a guide for the eye.

to bulk 3:2 mullite as a function of increasing temperature of the firing process. This suggestion is supported by the behaviour of the lattice parameters, which are shown in Fig. 6. Okada and Otsuka⁷ also obtained a similar functional dependence of the lattice constants of so-called 'xerogel' starting materials. These authors were also able to prove the change in Al content of the various mullite products by analytical transmission electron microscopy investigations. A similar phenomenon was also reported by Brown *et al.*¹² in the kaolinite-mullite reaction path, using ²⁹Si and ²⁷Al solid-state nuclear magnetic resonance spectroscopy.

The composition of the mullite products obtained here can be determined by inspecting Fig. 7, in which the intensity ratios are plotted as a function of the *a* lattice parameter. Also shown is the *x*

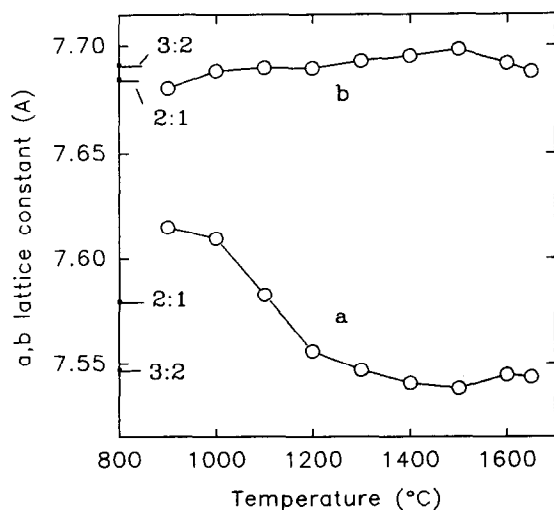


Fig. 6. Refined *a* and *b* lattice constants for the mullite sample according to the firing processes of type I precursors. ($c = 2.888 \pm 0.001 \text{ \AA}$, not shown). *a* and *b* values for the mullites of composition 3:2 and 2:1 are marked by horizontal lines.

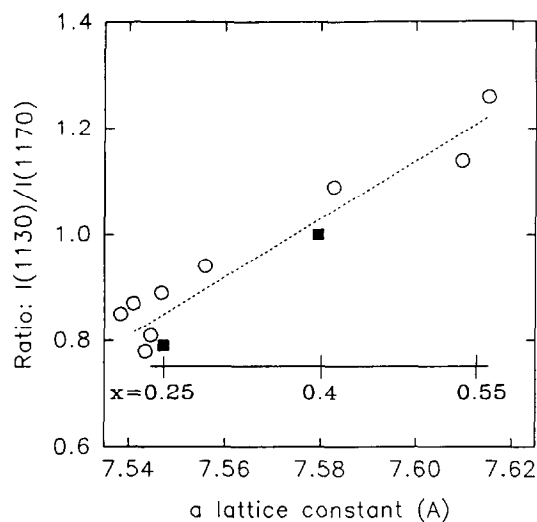


Fig. 7. Intensity ratio $I(1130\text{cm}^{-1})/I(1170\text{cm}^{-1})$ as a function of *a* lattice constants for mullites of composition 3:2 and 2:1 (black squares) and mullites obtained from the firing of type I precursors (open circles), with dotted line as a guide for the eye. Also shown is the linear scale of mullite compositions according to $\text{Al}_2(\text{Al}_{2+2x}\text{Si}_{2-2x})\text{O}_{10-x}$ related on the *a* lattice constants.

scale for the chemical composition $[\text{Al}_2(\text{Al}_{2+2x}\text{Si}_{2-2x})\text{O}_{10-x}]$ according to the linear relationship to the *a* lattice constant. It is of interest to note that this linear dependence holds irrespective of different ordering patterns of the oxygen vacancies,¹³ providing a conclusive measure of the concentration of oxygen vacancies *x*. Thus, the IR data of the intensity ratio $I(1130)/I(1170)$ also imply a quasi linear relationship with the chemical composition of mullite. It may be noted that the absorption ratios $I(1130)/I(1170)$ for the mullite products of type II and III precursors (Figs 3 and 4) would indicate $x \approx 0.25$, i.e. there is no change in composition as a function of firing temperature between 1200 and 1600°C.

IR spectra of mullites in the field of nominal composition $x = 0$ to $x = 0.7$ were also shown by Colombari.⁴ Comparison of the 1100 to 1200 cm^{-1} absorption features to results presented here would tentatively indicate Si-rich mullite ($x < 0.4$) in the presentation in Ref. 4. However, discrimination between mullites of various compositions from the 1100–1200 cm^{-1} absorption characteristics was not considered in that study and therefore will not be discussed further here.

4 Discussion

It has been shown above that the intensity ratio of the absorption $I(1130 \text{ cm}^{-1})/I(1170 \text{ cm}^{-1})$ follows an approximately linear relationship with the composition of mullite $\text{Al}_2(\text{Al}_{2+2x}\text{Si}_{2-2x})\text{O}_{10-x}$. Therefore this ratio might be used as an empirical scale for the determination of mullite compositions. Okada

and Otsuka⁷ and Voll⁹ (compare also Schneider *et al.*³) reported a discontinuous development of the compositional dependence of mullite as a function of the firing process for type I (homogeneous) precursors. These authors observed plateau-like behaviour of the *a* lattice constant (and some anomalies in the *b* and *c* parameters) for temperatures in the range 1000 to 1100°C. However, these features cannot be resolved from the present data and can be disregarded for the further discussion here.

Problems with the use of the empirical scale of the IR absorption in the range 1100 to 1200 cm⁻¹ could be related to the coexistence of an amorphous (glassy) phase with the mullite crystals. This phase has to be considered in the crystallization route of the type I precursor, because SiO₂ or (nSiO₂)(mAl₂O₃) glass phase is known to show an absorption peak in the spectral range 1000 to 1100 cm⁻¹. Thus, with the gradual formation of mullites with *x* ≈ 0.55 at 900°C to *x* ≈ 0.25 above 1300°C, the volume fraction of the residual amorphous phase should gradually decrease, which could be indicated by decrease of the absorption intensity observed at ~ 1130 cm⁻¹ (Fig. 2). On the other hand, there are indications – at least for the formation of mullite from type I precursors above 1000°C – that the volume fractions of the amorphous state show less influence* than the mullite absorption cross-sections. This may be verified by inspecting the absorption profiles of pure phases of 3:2 and 2:1 mullite shown in Fig. 1 and comparing them with the various spectra in Fig. 2. Additionally, this conclusion is supported by the 1100 to 1200 cm⁻¹ absorption spectra for pure mullite phases of different compositions reported by Cameron,¹ where the line profiles show a similar dependence as obtained in Fig. 2.

A deeper understanding of the changes in the absorption line profiles requires a detailed line profile analysis. This is not a simple task for powder-related spectra and anisotropic materials with a high number of atoms per unit cell, like mullite. With simple structural models ([AlO₆], [AlO₄] and [SiO₄] units), MacKenzie¹⁰ calculated the phonon frequencies of nine fundamental vibrations and related them to peak positions of the KBr powder spectra of a 3:2 mullite in the spectral range 400 to 1200 cm⁻¹. On the other hand, the number of IR active modes expected for the average structure of mullite (4B_{1u}, 9B_{2u}, 9B_{3u};¹¹ compare also Ref. 14 from this issue) already indicates that the true number of IR active modes could largely be

enhanced, compared with those resolved by the KBr experiment. The *average structure of mullite* (see, e.g., Refs 15 and 16) can most easily be understood by assuming an idealized half of the sillimanite unit cell (*c*/2 ≈ 2.888 Å) according to a statistical distribution of Al and Si on tetrahedral sites. Edge-sharing [AlO₆] octahedra form chains, which run parallel to the *z*-axis. The centres of these octahedra are at (0, 0, 0) and (1/2, 1/2, 0). The oxygens of the (000) centred octahedra [on O_d sites (*x*, *y*, 0) and (*x*, *y*, 1)] and one oxygen of the second octahedron [O_{ab} at (*x*, *y*, 1/2)] form together with a fourth oxygen (O_c) at (0, 1/2, 1/2) or at (1/2, 0, 1/2) a tetrahedral unit, which is occupied by Si or Al (T₁ site). Thus, two T₁ tetrahedra always have a common O_c oxygen. The *real structure of mullite*, on the other hand, accommodates oxygen vacancies on the O_c sites, which are,

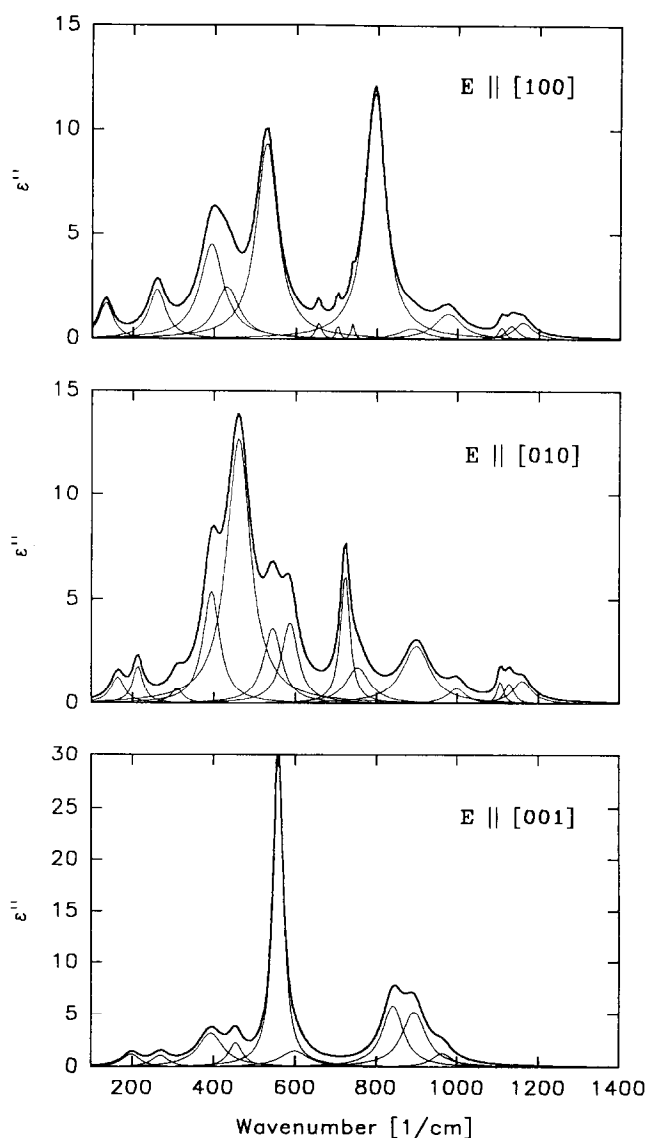


Fig. 8. Imaginary part of the dielectric function obtained by Kramers-Kronig transformation of the single crystal reflectivity of a 2:1 mullite (replotted from Ref. 11). Shown are the results of deconvolution into oscillator terms (thin lines) and their sum thick lines for the different polarizations.

*The contribution of the amorphous (glassy) phase to the IR absorption cross-section has still to be checked more accurately, e.g. by probing the cross-section of the pure phases.

therefore, fractionally occupied. Additionally, charge neutrality requires the substitution of $2\text{Si}^{4+} + \text{O}^{2-} = 2\text{Al}^{3+} + \text{V}$ ($\text{V} = \text{O}_c$ vacancy). These aluminiums can be related to new Al^* tetrahedral sites, creating O_c^* oxygen sites, which are shifted from the O_c positions. Thus, Al^* , O_c , O_c^* and T_1 positions ought all to be fractionally occupied. By taking all atomic positions into account and assuming the rather hypothetical case of full occupation, the number of IR active modes are 13B_{3u} , 13B_{2u} and 6B_{1u} according to polarizations parallel to the a , b and c lattice directions, respectively. For the sake of better comparison, the IR absorption spectra obtained from single crystal investigations of mullite of composition $x = 0.4$ (2:1 mullite) are shown in Fig. 8 (for details see Ref. 11). The deconvolution of these spectra results in 14, 14 and 9 absorption bands with polarizations parallel to the $[100]$, $[010]$ and $[001]$ lattice directions, respectively. According to this it can be concluded that the structural details of mullite result in a large number of modes, that are difficult to resolve in any detail from the KBr powder spectra (see Fig. 1), which sum over all directions of polarizations. However, the triplicate peak structure in the range 1100 to 1200 cm^{-1} can be separated and related back to the peaks in the B_{3u} and B_{2u} related spectra. For comparison, the KBr powder spectrum of 2:1 mullite and the summed single crystal absorption spectrum are shown in Fig. 9 (see also Fig. 1, where the three peak positions are marked). It may be noted that both spectra are in generally good agreement and that small discrepancies have to be related to the different measurement techniques.

Finally, it is interesting to get an assignment for the peak structure used to show the variation in the field of mullite of variable composition. MacKenzie¹⁰ and Cameron¹ suggested only a duplicate peak structure in the spectral range 1100 to

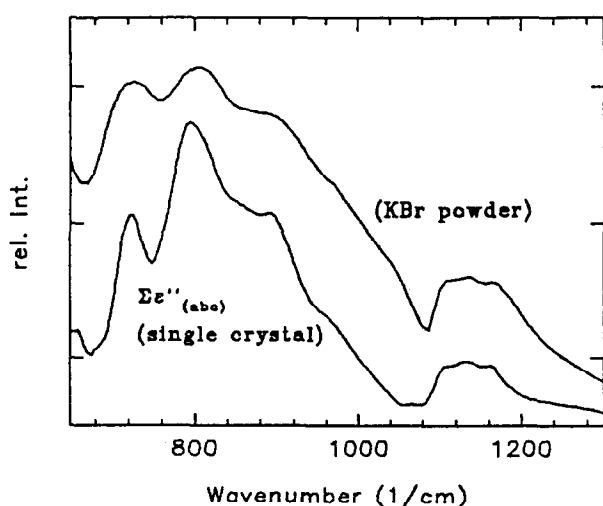


Fig. 9. Comparison of a KBr powder spectra to the summed ϵ'' spectra from Fig. 8.

1200 cm^{-1} in relation to $[\text{AlO}_4]$ and $[\text{SiO}_4]$ structural units. However, it is clear from the present study and from Ref. 11 that a third peak in this spectral range has to be taken into account for mullite, which might be assigned to an $[\text{Al}^*\text{O}_4]$ related tetrahedral vibration. According to this, the chemical variation of mullites $\text{Al}_2^{\text{VI}}(\text{Al}_2^{\text{IV}}\text{Al}_{2x}^*\text{Si}_{2-2x}^{\text{IV}})\text{O}_{10-x}$ should lead to a dependence of the intensity ratio $I(1108 \text{ cm}^{-1})/I(1165 \text{ cm}^{-1})$ as $2x/(2-2x)$, assuming no frequency shifts and no changes of absorption cross-section of each species as a function of x . Similarly, for the ratio $I(1130 \text{ cm}^{-1})/I(1165 \text{ cm}^{-1})$ a dependence according to $2/(2-2x)$ is expected, which increases more smoothly as a function of x than does the former. This increase seems to be justified by the observed dependence for the crystallization of type I precursors (see Fig. 7). However, for better information about this, the observed line profiles in the spectral range 1100 to 1200 cm^{-1} have to be deconvoluted quantitatively, which will be the task of further studies.

Acknowledgements

The authors would like to express their thanks to Dr H. Schneider and co-workers (German Aerospace Establishment, Köln) for preparing the precursor starting materials for the present study. Professor E. Eberhard is gratefully acknowledged for his encouragement of this study and for many helpful discussions. Finally, we express our thanks to Professor K. J. D. MacKenzie for many helpful comments on the manuscript.

References

1. Cameron, W. E., Composition and cell dimensions of mullite. *Am. Ceram. Soc. Bull.*, **56** (1977) 1003–11.
2. Cameron, W. E., Mullite: a substituted alumina. *Am. Mineral.*, **62** (1977) 747–55.
3. Schneider, H., Okada, K. & Pask, J. A., *Mullite and Mullite Ceramics*, John Wiley and Sons, 1994, p. 31.
4. Colomban, Ph., Structure of oxide gels and glasses by infra-red and Raman scattering. *J. Mater. Sci.*, **24** (1989) 3011–20.
5. Schneider, H., Saruhan, B., Voll, D., Merwin, L. & Sebald, A., Mullite precursor phases. *J. Eur. Ceram. Soc.*, **11** (1993) 87–97.
6. Schneider, H., Voll, D., Saruhan, B., Sanz, J., Schrader, G., Rüscher, C. H. & Mosset, A., Synthesis and structural characterization of non-crystalline mullite precursors. *J. Non-Crystalline Solids*, 178 C19.
7. Okada, K. & Otsuka, N., Change in chemical composition of mullite formed from $2\text{SiO}_2 \cdot 3\text{Al}_2\text{O}_3$ xerogel during the formation process. *J. Am. Ceram. Soc.*, **70** (1987) C245–47.
8. Li, D. X. & Thomson, W. J., Tetragonal to orthorhombic transformation during mullite formation. *J. Mater. Res.*, **6** (1991) 819–24.
9. Voll, D., Mullitprecursoren: Synthese, temperaturabhängige

- Entwicklung der strukturellen Ordnung und Kristallisationsverhalten. Dr Thesis, University Hannover, 1994.
10. MacKenzie, K. J. D., Infrared frequency calculations for ideal mullite ($3\text{Al}_2\text{O}_3 \cdot 2\text{SiO}_2$). *J. Am. Ceram. Soc.*, **55** (1972) 68–70.
 11. Rüscher, C. H., Lattice vibrations of 2 : 1 mullite in infra-red and Raman spectra. Submitted.
 12. Brown, I. W. M., MacKenzie, K. J. D., Bowden, M. E. & Meinhold, R. H., Outstanding problems in the kaolinite–mullite reaction sequence investigated by ^{29}Si and ^{27}Al solid state nuclear magnetic resonance: II, high-temperature transformations of metakaolinite. *J. Am. Ceram. Soc.*, **68** (1985) 298–301.
 13. Eberhard, E., Private communication, 1994.
 14. Michel, D., Colombari, Ph., Abolhassani, S., Voyron, F. & Kahn-Harari, A., Germanium mullite: structure, phase relations and vibrational spectra of gels, glasses and ceramics. *J. Eur. Ceram. Soc.*, **16** (1996) 161–8.
 15. Sadagana, R., Tokonami, M. & Takeuchi, Y., The structure of mullite, $2\text{Al}_2\text{O}_3 \cdot \text{SiO}_2$, and relationship with the structure of sillimanite and andalusite. *Acta Crystallogr.*, **15** (1962) 65–8.
 16. Angel, R. J. & Prewitt, C. T., Crystal structure of mullite: a reexamination of the average structure. *Am. Mineral.*, **71** (1986) 1476–82.

Interpretation of Mullite Real Structure via Inter-vacancy Correlation Vectors

S. H. Rahman,^a S. Strothenk,^a C. Paulmann^b & U. Feustel^a

^aInstitut für Mineralogie, Universität Hannover, Welfengarten 1, 30167 Hannover, Germany

^bMineralogisch-Petrographisches Institut, Universität Hamburg, Grindelallee 48, 20146 Hamburg, Germany

(Accepted 22 July 1995)

Abstract

High resolution electron microscopy (HREM) results yield that the oxygen vacancies in mullite form domains with higher oxygen vacancy concentrations and specific preferred directions. The domains are more or less statistically distributed in a disordered matrix. In the (010) plane the oxygen vacancies are arranged along [102] and [10 $\bar{2}$] over two to four unit cells. In addition, ordered domains with higher amounts of vacancies exhibit a doubling of the c-axis which can already be seen in h0l diffraction patterns. Vacancy arrangements in the (100) plane are characterized by preferred orientations along [012] and [01 $\bar{2}$] and [001], resulting in an average direction parallel to [013] and [01 $\bar{3}$]. Columns with higher vacancy concentrations usually reveal distances of 1.5b and 5 to 6c.

Considering the above-mentioned HREM results, the real structure configuration of 2:1 mullite has been established using the videographic two-dimensional and three-dimensional simulation method. The ordering scheme of the oxygen vacancies can be described via inter-vacancy correlation vectors (short-range order vectors $1\ m\ n$; $l = a/2$, $m = b/2$, $n = c$). It has been confirmed that the inter-vacancy correlation vectors $\langle 111 \rangle$, $\langle 201 \rangle$ and $\langle 310 \rangle$ are preferred but a complete structure description can only be obtained by considering the correlation vectors $\langle 022 \rangle$, $\langle 330 \rangle$, $\langle 130 \rangle$, $\langle 401 \rangle$, $\langle 113 \rangle$, $\langle 040 \rangle$, $\langle 222 \rangle$, $\langle 223 \rangle$, $\langle 600 \rangle$ and $\langle 312 \rangle$ additionally. These inter-vacancy vectors, especially $\langle 022 \rangle$ and $\langle 330 \rangle$, play an important role for the formation of the diffuse scattering in the h0l and 0k1 plane.

Introduction

Deviations from the ideal periodic arrangement (point defects, modulations, short-range order, domain boundaries, etc.) strongly influence the physical properties of crystalline solids. Hence,

determination of the real structure becomes a major task in examining the influence of structural disorder on the physical behaviour of materials.

Characteristic features in diffraction patterns of disordered crystals are diffuse scattering and/or satellite reflections apart from the Bragg reflections, the latter being attributed to the average structure. Diffuse scattering, caused by short-range ordering, cannot be directly interpreted by known structural disorder theories^{1,2} which mainly deal with discrete satellite reflections. However, Monte Carlo methods in conjunction with optical or computer-based Fourier transforms yield information about deviations from the average structure. Besides this, high resolution electron microscopy (HREM) in combination with contrast simulations of predefined structure models is the most important real space method to achieve information about certain types of structural disorder on the atomic scale.

The above-mentioned methods have been applied to characterize the ordering phenomena of oxygen vacancies in the non-stoichiometric aluminosilicate mullite ($\text{Al}_2[\text{Al}_{2+2x}\text{Si}_{2-2x}]\text{O}_{10-x}$) which shows a complex scheme of satellite reflections and diffuse scattering throughout reciprocal space (Fig. 1).

HREM investigations of mullite mainly deal with beam directions parallel to [001]³⁻⁷ and [010].⁸⁻¹⁰ Recently, Paulmann *et al.*¹¹ performed 200 kV and 300 kV HREM investigations along [010] and [100]. They found preferred vacancy orientations in domains with higher vacancy concentrations, distributed in a matrix with minor degree of order.

Early investigations of the satellite reflections with optical Fourier transforms were performed by Saalfeld¹² for the h0l plane. Tokonami *et al.*¹³ examined the diffuse scattering in $hk\frac{1}{2}$ and $hk\frac{2}{5}$ planes and derived a model of the vacancy arrangement in large domains. Monte Carlo simulations of structural models together with their Fourier transforms were presented by Welberry

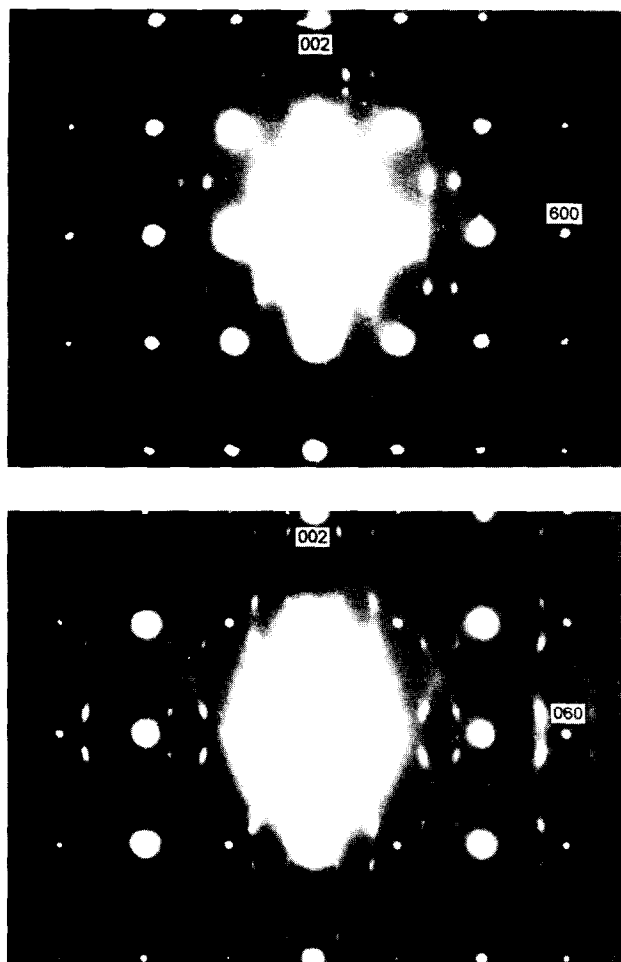


Fig. 1. Electron diffraction patterns of mullite: top, $h0l$; bottom, $0kl$.

and Withers¹⁴ to explain the diffuse scattering in $hk\frac{1}{6}$, $hk\frac{1}{4}$, $hk\frac{1}{3}$, $hk\frac{1}{2}$.

Taking the results of HREM investigations into consideration, a specific distribution scheme of inter-vacancy vectors in the (001) plane was presented by Rahman,^{15,16} Rahman and Paulmann,¹⁷ Paulmann *et al.*¹⁸ and Paulmann *et al.*¹¹ Butler *et al.*¹⁹ recently carried out a three-dimensional (3-D) real structure simulation by taking interaction pair energies into account, the latter having been obtained by Padlewski *et al.*²⁰ Variation and addition of pair energies led to relatively good agreement of Fourier transforms with the experimental diffraction patterns of the $hk\frac{1}{3}$ and $hk\frac{1}{2}$ reciprocal planes, whereas the Fourier transforms for $hk\frac{1}{6}$ and $hk\frac{1}{4}$ differed slightly from the experimental patterns.

Until now, Monte Carlo simulations of the mullite real structure have mostly dealt with the diffuse scattering in reciprocal planes from $hk0$ to $hk\frac{1}{2}$, taking neither the position of satellite reflections nor the diffuse scattering in $h0l$ and $0kl$ diffraction patterns into account. Additionally, no next nearest inter-vacancy correlation vectors were considered,²¹ although these vectors may play an important role in the exact interpretation of the

additional diffraction phenomena in the $h0l$ and $0kl$ planes.

Consequently, the aim of the present study is to combine results from a quantitative investigation of HREM images by contrast simulations and digital image processing methods with videographic real structure simulations²² to receive a 3-D description of the oxygen vacancy arrangement in mullite via inter-vacancy correlation vectors.

Experimental

The investigated specimens of 2:1 mullite grew as single crystals ($3 \times 3 \times 10$ mm) in ingots of commercially produced mullite bricks which were synthesized by heating a mixture of kaolinite and Al_2O_3 with an arc furnace and casting the melt at 2000°C. Several microprobe analyses of crystals with well-developed $\{110\}$ faces and growth direction along $[001]$ gave a chemical composition of 75.9 wt% Al_2O_3 and 23.8 wt% SiO_2 ($x = 0.39$), close to the ideal value of 0.40.

Electron microscope investigations (diffraction, HREM) were performed using Hitachi H-800 and H-9000 microscopes with LaB_6 cathodes, operating at 200 and 300 kV accelerating voltage, respectively.

Preparation of crystallites was carried out by conventional crushing with propanol in an agate mortar and transferring the suspension to carbon-coated copper grids.

The computer system for videographic real structure simulations comprised of an IBM-AT with a special array processor and graphic adaptor boards interconnected by a fast external port and to the host computer through the AT-bus interface. The configuration permitted calculation of fast Fourier transforms (FFT) of 1024×1024 pixels and 8-bit colour depth within 8 s.

HREM Investigations

HREM investigations of real structures require contrast simulations with predefined structure models to permit a correct interpretation of the contrast patterns. A detailed study with beam directions along $[010]$ and $[100]$ was recently carried out by Paulmann *et al.*¹¹ since the satellite reflections, indicating an incommensurate modulation of the mullite structure, are best visible in $h0l$ and $0kl$ diffraction patterns. A projection of the structure along these directions shows a dense packing of atoms with different scattering potentials. Nevertheless, extensive contrast simulations of supercells with more than 2000 atoms revealed

striking changes of the contrast pattern in the immediate vicinity of projected vacancy positions. This fact can be attributed to associated cation shifts near an oxygen vacancy which result in a remarkable change of the scattering potential. Both planes are characterized by contrast enhancements at vacancy positions, whereas in the (001) plane⁴ an intensity decrease of dots located clockwise next to a vacancy position is observed. Through-focus series of the (010) and (100) planes gave characteristic defect-induced contrast patterns at defocus values of -30 , -65 , -75 nm and -35 , -45 , -65 , -75 nm, respectively. More details about the applied supercells and simulation parameters are given elsewhere.^{11,16} Special attention should be paid to a defocus range of -25 to -35 nm where dots in the contrast pattern directly coincide with the vacancy position (*ac*-plane) or cause an elongated and enhanced dot (*bc*-plane).

Figure 2 shows 200 kV HREM images along [010] and [100] at approximate defocus values of -30 nm. Closer inspection of the images reveals intensity variations of dots which can be attributed to higher vacancy concentrations along the incident beam.¹¹ Further investigations with different vacancy concentrations and different arrangements yield a linear dependence of defect-induced intensity enhancements and the concentration of oxygen vacancies along the beam direction. Furthermore, concentrations of only 20% still cause a detectable change of the contrast pattern.

In order to determine preferred vacancy arrangements in the (010) and (100) planes, digitized HREM images were investigated by image processing methods. After determining the greyscale area of the contrast patterns (8 bit) in Fig. 2, a progressive filtering procedure of selected greyscale areas was performed. As the stepwise filtering progresses, a continuous decrease of the observable maxima can be detected [Figs 3(a)–(e) and 4(a)–(e)], which enables the determination of O_c columns with different concentrations of vacancies and domains with specific ordering schemes. Detailed analyses were carried out for selected areas [rectangles in Figs 3(a) and 4(a)] and the results are presented in Figs 3(f) and 4(f), respectively.

A striking feature of (010) HREM images are linear arrangements of higher vacancy concentrations along [102] and [10 $\bar{2}$] over two to four unit cells. In addition, ordered domains with higher amounts of vacancies exhibit a doubling of the *c*-axis which can already be seen in *h0l* diffraction patterns. Combining the arrangements along [102] and [10 $\bar{2}$] and the twofold periodicity along [001] yields a centred pattern with columns of higher oxygen vacancy concentrations, frequently

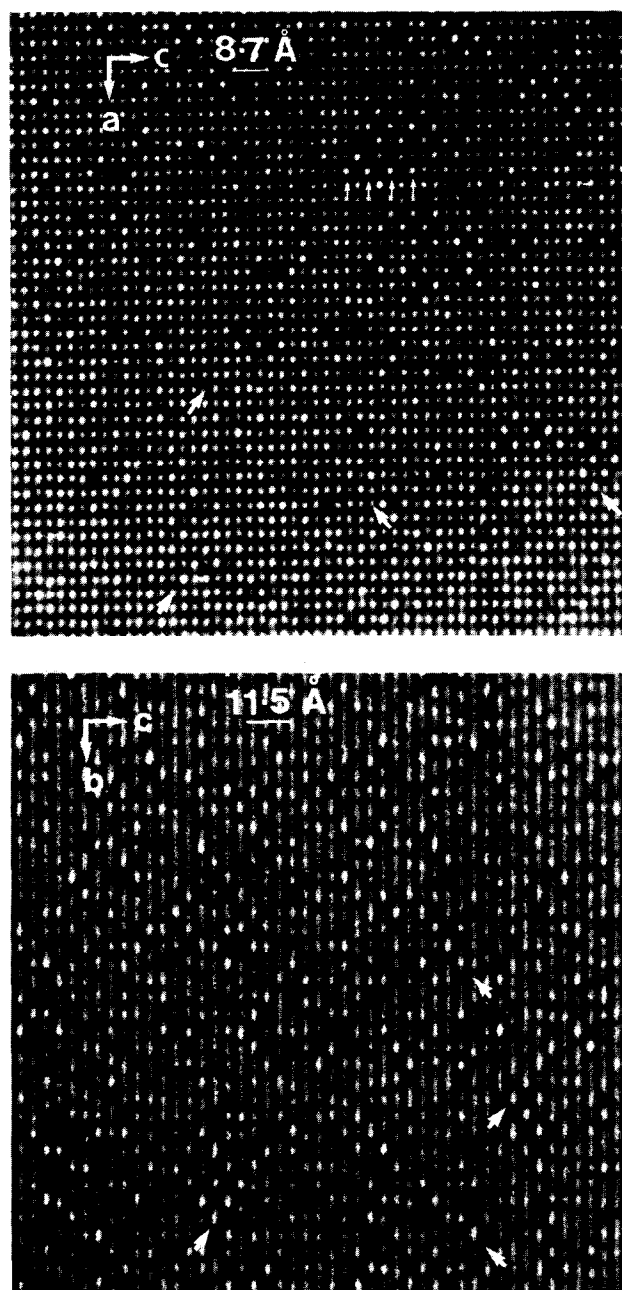


Fig. 2. 200 kV HREM images of 2:1 mullite: top, (010) plane; bottom, (100) plane.

building up an antiphase relationship. The pattern closely resembles those of Al-rich mullites ($x \geq 0.48$)⁹ but does not show long-range ordering. Vacancy arrangements in the (100) plane are characterized by preferred orientations along [012], [01 $\bar{2}$] and [001], resulting in an average direction parallel to [013] and [01 $\bar{3}$]. O_c columns with higher vacancy concentrations usually reveal distances of $1.5b$ and 5 to $6c$.

Summarizing the HREM results, the oxygen vacancies in mullite form domains with higher defect concentrations and specific preferred directions. The domains are more or less statistically distributed in a disordered matrix. A schematic representation of the vacancy arrangements in the main crystallographic planes is presented in Fig. 5.

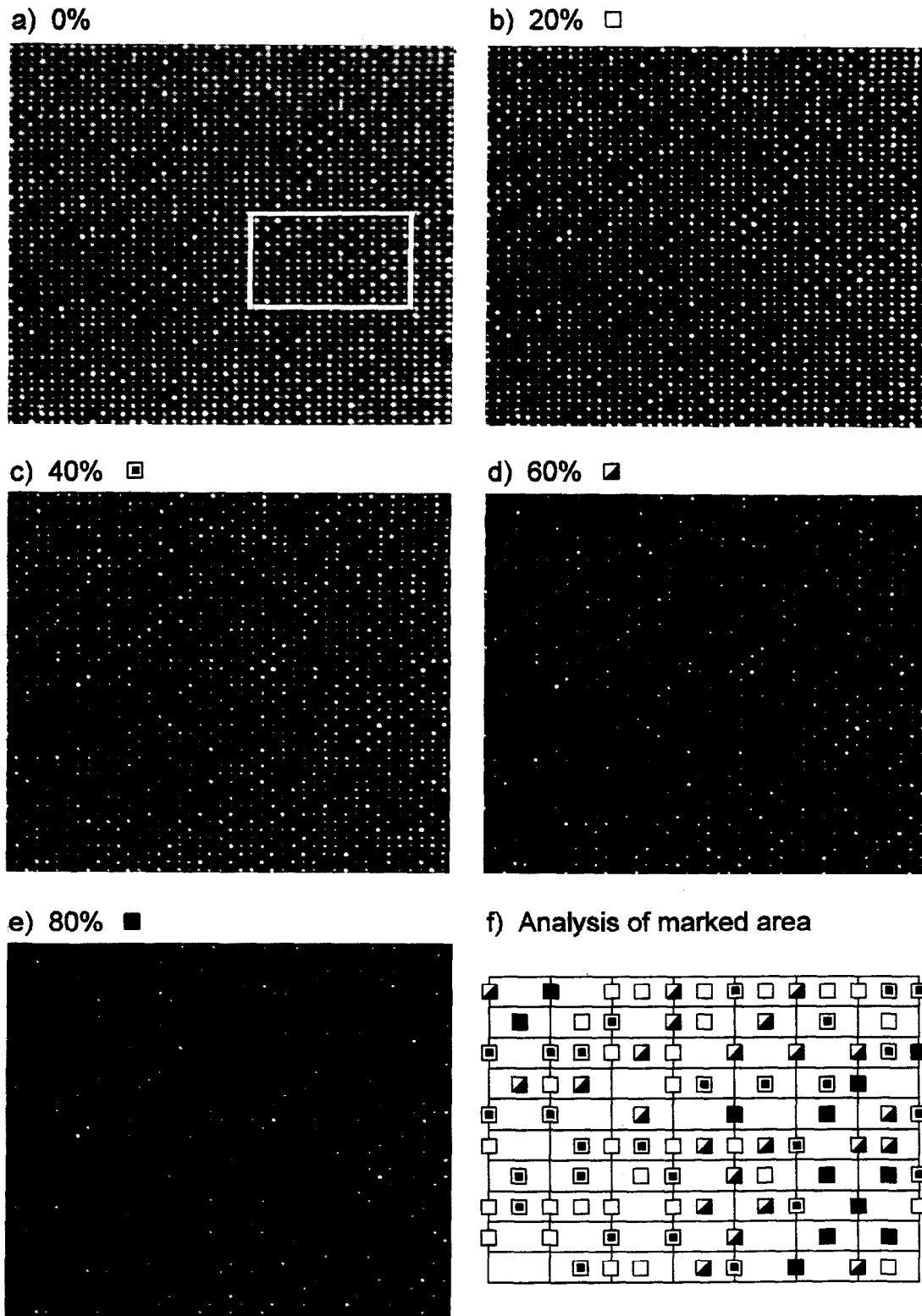


Fig. 3. Digital image processing of a 200 kV HREM image of the (010) plane. (a)–(e) Continuous filtering of dot greyscale in %. (f) Analysis of marked area in (a). a -Axis horizontal, c -axis vertical.

Although HREM investigations yield valuable information about preferred vacancy arrangements, one has to deal with some restrictions regarding the 3-D interpretation of the contrast patterns, since they are caused by a projection of the structure along the incident beam. However, the HREM results in the three main crystallographic directions give valuable parameters for

two-dimensional (2-D) and 3-D videographic real structure simulations.

2-D Videographic Real Structure Simulations

The videographic method is a procedure for the determination of real structures and employs a

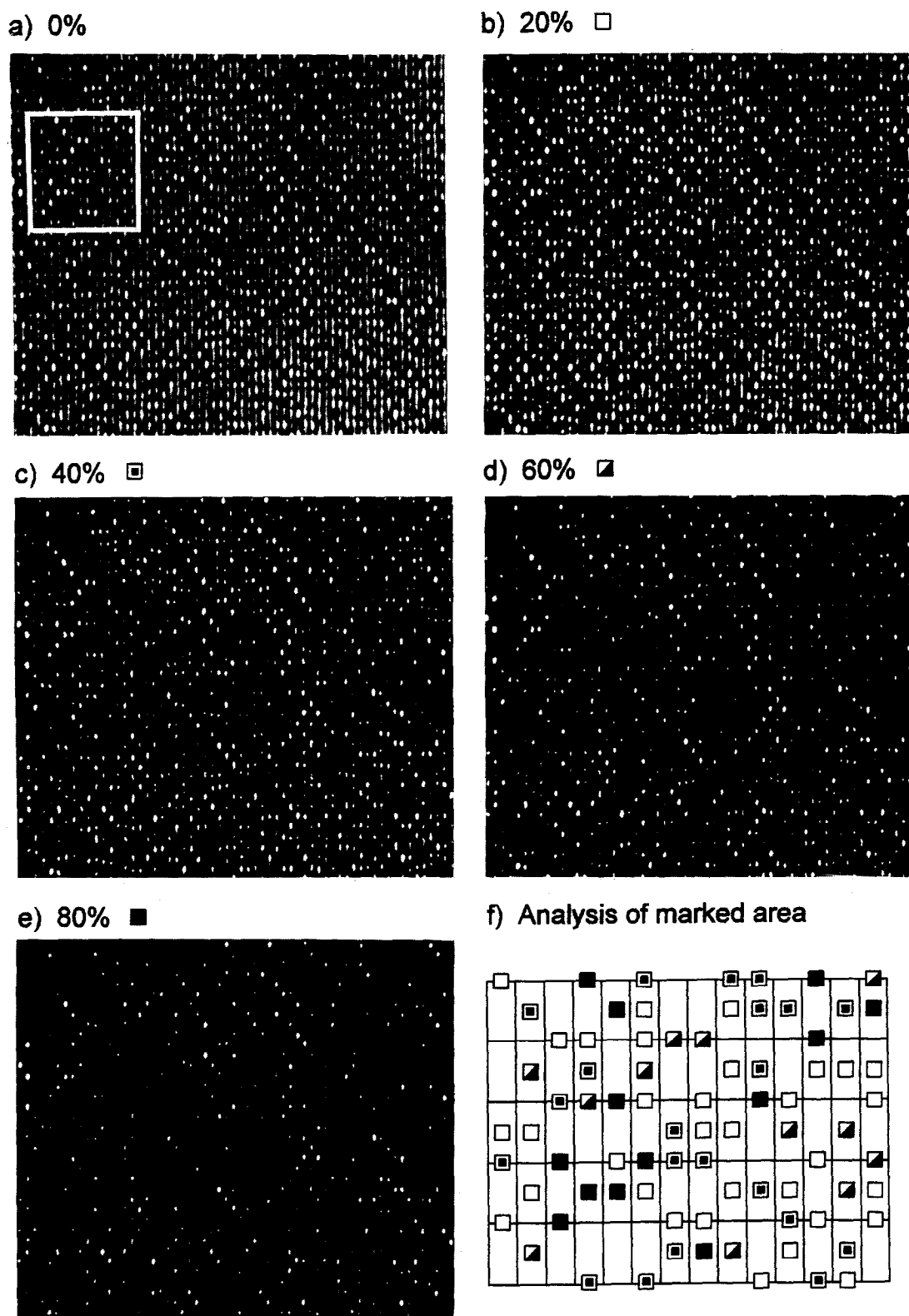


Fig. 4. Digital image processing of a 200 kV HREM image of the (100) plane. (a)–(e) Continuous filtering of dot greyscale in %. (f) Analysis of marked area in (a). *c*-Axis horizontal, *b*-axis vertical.

statistical mathematical approach and computer graphics to aid the interpretation of diffuse scattering from a disordered crystal.²² The video-graphic method replaces atoms of different scattering power by pixels with varying grey levels. Instead of calculating the diffraction pattern by a time-consuming real space summation, the method offers the opportunity of using the fast FFT

algorithm for Fourier transforming a real structure image (superstructure) which consists of structure variants, derived from the average structure.

Determinations of mullite average structure^{23–29} revealed the space group *Pbam* with chains of edge-sharing AlO_6 octahedra along [001] which are crosslinked by (Si, Al) tetrahedral double chains [Fig. 6(a)]. Introduction of oxygen vacancies on

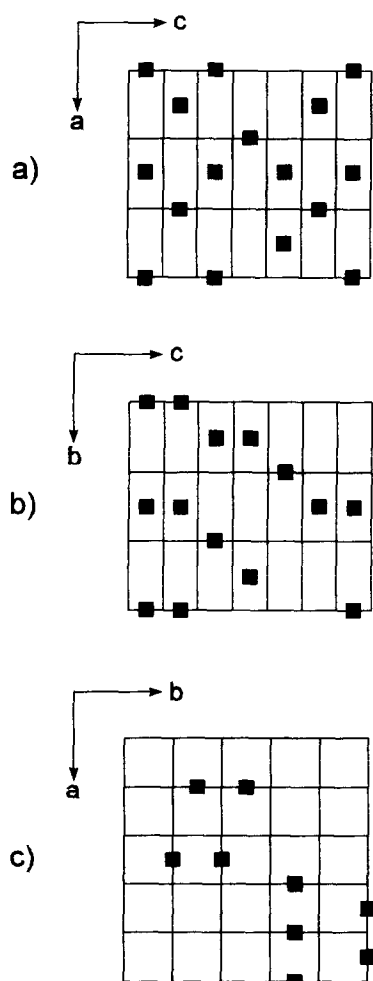


Fig. 5. Schematic representation of ordering schemes: (a) (010) plane; (b) (100) plane; (c) (001) plane.

O_c sites drives adjacent cations to occupy a new tetrahedral Al^* site to preserve a fourfold coordination. Additionally, neighbored O_c atoms shift towards a less symmetric O_c^* site [Fig. 6(b)]. According to Rahman,²² the average structure can be described as a superposition of a number of structure variants which are usually derived by taking crystal chemical rules into account. For a deconvolution of the mullite average structure the following arguments were applied.

$Si/Al-O_c^*$ bond lengths of 0.173 and 0.178 nm lead to a tetrahedral occupation by Al, whereas 0.167 nm for the $Si/Al-O_c$ bond gives an Si occupation of the tetrahedron in agreement with calculations of Padlewski *et al.*²⁰ Considering these rules and different O_c and O_c^* occupations, it is possible to derive 34 structure variants from the mullite average structure which are represented in Fig. 7. Each four variants (1–4, 5–8, 9–12, 13–16) exhibit an oxygen vacancy on the same cell edge and different O_c/O_c^* occupations on the remaining three edges. Numbers 17 to 32 are vacancy-free only with a variation on the O_c/O_c^* sites. Variants 33 and 34 represent the silica-free $\nu-Al_2O_3$ modification proposed by Saalfeld.³⁰ The distribution of

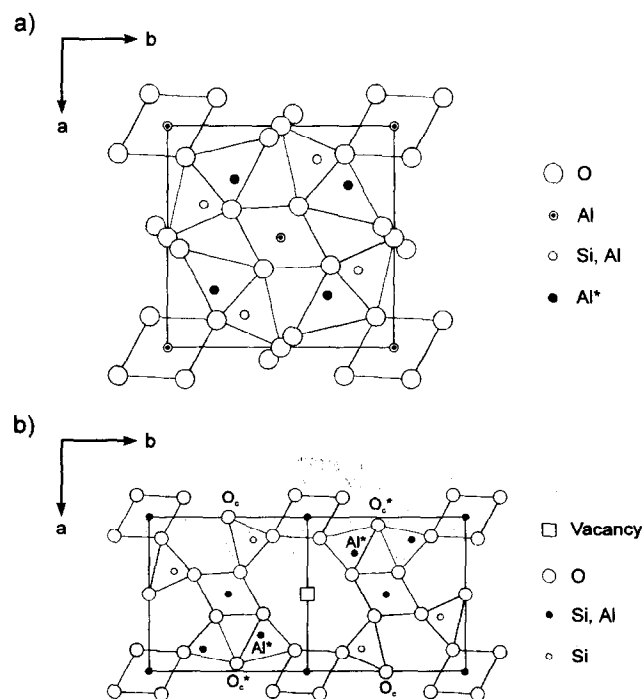


Fig. 6. (a) Average structure of mullite. (b) Atomic displacements around an oxygen vacancy.

the structure variants is performed using joint probabilities (nearest neighbours) and correlation vectors (next nearest neighbours, over next nearest) as described in more detail by Rahman²² and Rahman and Rodewald.³¹

For the 2-D videographic real structure simulations, the following preferred vacancy arrangements, obtained from HREM investigations and interpretation of diffraction patterns,¹¹ were taken into consideration.

(001) plane: Linear arrangements along [100] and [010] occasionally separated by $1.5b$ and $1.5a$, respectively.

(010) plane: Arrangements along [102] and [10-2] with an incommensurate modulation of $\approx 1.5a$ and twofold periodicity along [001].

(100) plane: Arrangements along [012], [01-2] and [001] with an incommensurate modulation of $\approx 1.5b$ and approximate fivefold modulation along [001].

Extended videographic simulations³² with different structure variants represented by 8×8 and 16×16 pixel grids per structure variant yielded the preference of only a few correlation vectors to be responsible for the main features of the diffuse scattering in experimental X-ray diffraction patterns. The intensity distribution at higher scattering angles is mainly affected by an appropriate representation of the O_c/O_c^* shift in the videographic structure image, whereas the Al/Si occupation of the tetrahedral sites only plays a negligible role. Figure 8 (top) shows a diffraction

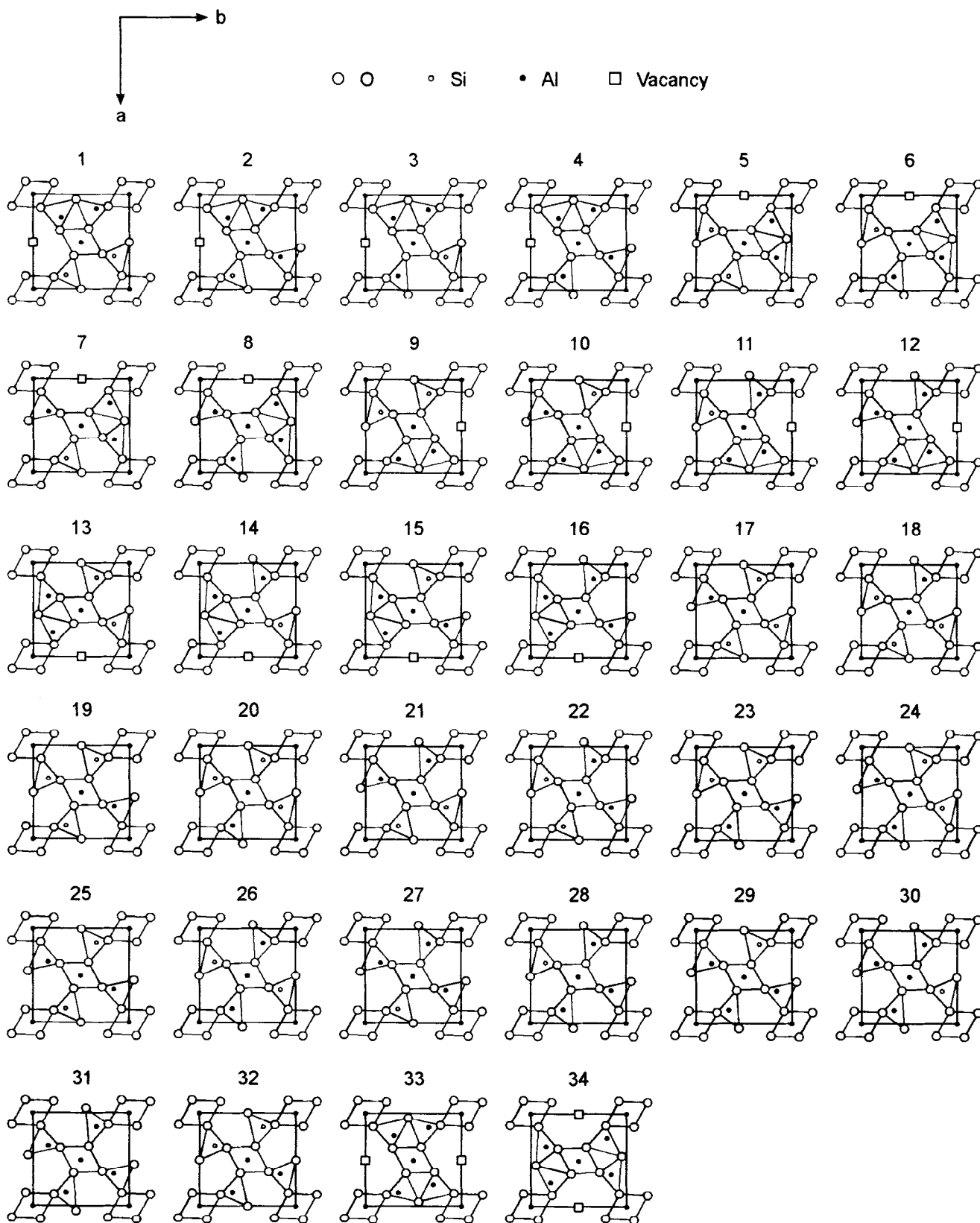


Fig. 7. 34 structure variants of mullite.

pattern of the $hk\frac{1}{2}$ plane which has been reconstructed from a digitized Weissenberg pattern with additional background correction and contrast enhancement of the weak diffuse scattering. Comparison with a Fourier transform [Fig. 8 (middle)] of the videographic structure image [Fig. 8 (bottom)] reveals good agreement because the application of

a 16×16 grid allows the representation of all atomic positions with sufficient accuracy.

For an analysis of the structure image, the unit lengths of the correlation vectors (lmn) were chosen to be $l = \frac{1}{2}a$, $m = \frac{1}{2}b$ and $n = c$. An analysis of the simulation field shows a higher frequency of $\langle 310 \rangle$, $\langle 130 \rangle$, $\langle 330 \rangle$, $\langle 020 \rangle$ and $\langle 200 \rangle$

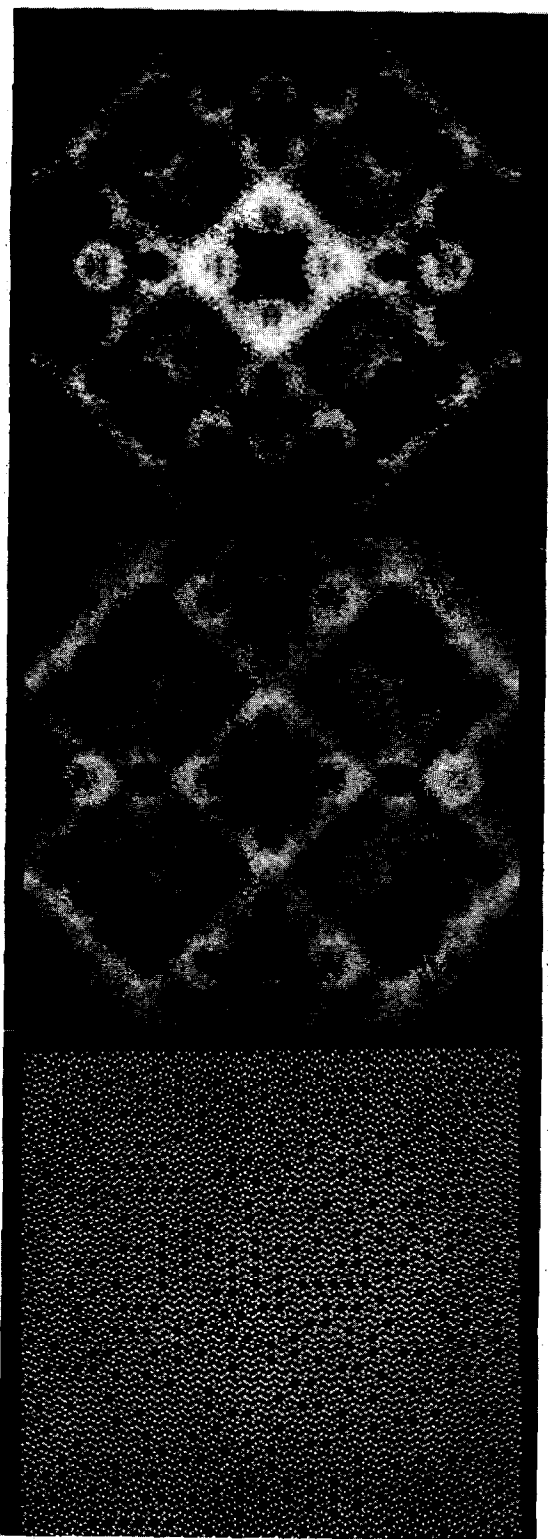


Fig. 8. 2-D videographic investigations of the $hk\frac{1}{2}$ plane: top, processed Weissenberg image; middle, Fourier transform of videographic structure image; bottom, small portion of videographic structure image. b -Axis horizontal, a -axis vertical.

short-range correlation vectors, where $\langle 330 \rangle$ results from a combination of $\langle 310 \rangle$ and $\langle 020 \rangle$ or $\langle 130 \rangle$ and $\langle 200 \rangle$.

Further investigations confirmed that $\langle 130 \rangle$ and $\langle 310 \rangle$ are mainly responsible for the diffuse circles at the 01 and 10 positions [Fig. 8 (middle)], whereas the exact shape is caused by longer corre-

lation vectors. Resulting from a combination of $\langle 130 \rangle$ and $\langle 310 \rangle$, an equal number of $\langle 240 \rangle$, $\langle 420 \rangle$, $\langle 440 \rangle$, $\langle 260 \rangle$, $\langle 620 \rangle$, $\langle 060 \rangle$ and $\langle 600 \rangle$ gives an exact circular shape of the diffuse scattering. In contrast, a higher frequency of $\langle 440 \rangle$ results in a rhombic form with edges along $\langle 110 \rangle^*$. Preferring $\langle 020 \rangle$ and $\langle 310 \rangle$ against $\langle 200 \rangle$ and $\langle 310 \rangle$ yields a diffraction pattern similar to the X-ray diffraction pattern of $hk\frac{1}{2}$.

Considering the above mentioned preferences, 2-D videographic real structure simulations were also performed for the (010) and (100) planes. By comparison, the satellite positions in the Fourier transforms of the videographic simulations are in close agreement with $h0l$ and $0kl$ electron diffraction patterns,³² respectively. Analysis of the 2-D simulations yielded most frequent correlation vectors of $\langle 002 \rangle$, $\langle 300 \rangle$, $\langle 101 \rangle$, $\langle 201 \rangle$, $\langle 501 \rangle$ and $\langle 302 \rangle$ for the (010) plane. The (100) plane revealed a higher frequency of $\langle 030 \rangle$, $\langle 022 \rangle$, $\langle 005 \rangle$, $\langle 023 \rangle$, $\langle 006 \rangle$ and $\langle 013 \rangle$ correlation vectors.

Before proceeding with 3-D videographic simulations, some valuable information about the ordering scheme can be already obtained from the 2-D investigations. The 1.5-fold modulations along [100] and [010] in $h0l$ and $0kl$ diffraction patterns are caused by a preference of $\langle 130 \rangle$, $\langle 310 \rangle$ and $\langle 330 \rangle$ correlation vectors. Furthermore, it can be assumed that the twofold period along [001] in $h0l$ patterns originates from more frequent $\langle 022 \rangle$ inter-vacancy correlation vectors which already appear in (100) HREM images as preferred arrangements along the $\langle 012 \rangle$ crystallographic directions (Fig. 2). Thus, a projection of the $\langle 022 \rangle$ vectors onto (010) results in a twofold period along [001].

3-D Videographic Real Structure Simulations

By comparing the frequencies of the correlation vectors in the 2-D simulations, a scheme of the 3-D vacancy distribution can be derived. The preferred vacancy arrangements along [102], [10-2], [012] and [01-2] (crystallographic directions) observed in HREM images can be achieved by a preference of the $\langle 111 \rangle$ correlation vector, in agreement with the 2-D simulation of the (010) plane with the high frequency of the $\langle 101 \rangle$. The preference of $\langle 201 \rangle$ in the 3-D simulation corresponds to the $\langle 201 \rangle$ in the 2-D simulation of the (010) plane and – in projection on (100) – to a vacancy arrangement along [001] which appears in (100) HREM images. In addition, the correlation vectors $\langle 312 \rangle$, $\langle 131 \rangle$, $\langle 113 \rangle$ and $\langle 223 \rangle$ are preferred in the 3-D simulations.

After projecting the 3-D videographic simulation field along the main crystallographic directions, the correctness of the simulated structure model was tested by comparing its Fourier transforms with experimental diffraction patterns (Fig. 1). The Fourier transforms of the (010) and (100) planes are given in Fig. 9. The positions and intensities of the satellites are in close agreement to the experimental diffraction patterns of the $h0l$ and $0kl$ planes. It can be concluded that the input parameters for the simulation field resemble the vacancy distribution in 2:1 mullite. The most frequent 15 inter-vacancy correlation vectors determined by analysing the simulation field are presented in Table 1 together with those measured by Butler and Welberry.²¹ Further calculations showed that slight changes in the frequencies and order of the correlation vectors do not influence the positions of the satellites but only have influence on the shape of the satellites and the

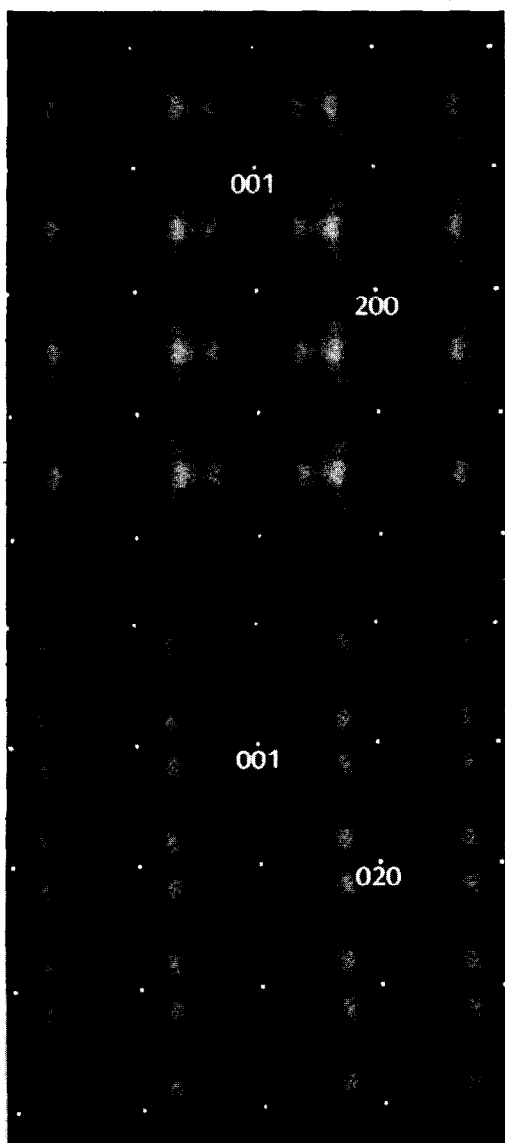


Fig. 9. Fourier transforms of the 3-D simulation field projected on (010) and (100).

Table 1. The most frequent 15 inter-vacancy vectors lmn ($l=a/2$, $m=b/2$, $n=c$) calculated from the 3-D simulation field [p = probability in %, a = short-range order parameter, a_{BW} = short-range order parameter determined by Butler & Welberry²¹]

lmn	p	a	a_{BW}
$\langle 022 \rangle$	28.25	0.103	—
$\langle 310 \rangle$	28.00	0.100	0.141
$\langle 111 \rangle$	27.09	0.089	0.109
$\langle 201 \rangle$	24.98	0.062	0.113
$\langle 330 \rangle$	24.90	0.061	—
$\langle 130 \rangle$	24.21	0.053	0.077
$\langle 401 \rangle$	23.24	0.040	—
$\langle 113 \rangle$	23.24	0.040	—
$\langle 040 \rangle$	23.12	0.039	—
$\langle 004 \rangle$	22.79	0.035	0.047
$\langle 131 \rangle$	22.72	0.034	0.058
$\langle 222 \rangle$	22.71	0.034	—
$\langle 223 \rangle$	22.56	0.032	—
$\langle 600 \rangle$	22.19	0.027	—
$\langle 312 \rangle$	21.88	0.024	—

intensity of streaks. It must be noted that the most frequent inter-vacancy vector $\langle 022 \rangle$ belongs to the second shell and plays an important role for the formation of the diffuse scattering in the $h0l$ and $0kl$ planes together with $\langle 330 \rangle$, $\langle 310 \rangle$ and $\langle 130 \rangle$. The correlation vector $\langle 022 \rangle$ can be obtained by a certain sequence of two $\langle 111 \rangle$ vectors (e.g. $[111]$ followed by $[-111]$ or $[1-11]$ followed by $[-1-11]$, etc.) However, it is unlikely that the occurrence of $\langle 022 \rangle$ is only caused by the combination of $\langle 111 \rangle$ since the frequencies of $\langle 111 \rangle$ and $\langle 022 \rangle$ are nearly the same.

Short-range order parameters (correlation vectors) are usually used to describe the real structure of intermetallic alloys above the critical temperature, T_c . In most cases, the first three short-range order parameters are adequate to describe the short-range ordered state. In mullite, with T_c above the melting point, the three shortest correlation vectors are not sufficient to describe the oxygen vacancy ordering scheme. In this case, higher order inter-vacancy correlation vectors (Table 1) are important for complete interpretation of the real structure.

Acknowledgement

The authors gratefully acknowledge financial support of the Deutsche Forschungsgemeinschaft.

References

1. Korekawa, M., Theorie der Satellitenreflexe. Habilitationsschrift, Universität München, 1967.

2. Böhm, H., Eine erweiterte Theorie der Satellitenreflexe und die Bestimmung der modulierten Struktur des Natriumnitrits. Habilitationsschrift, Universität Münster, 1977.
3. Schryvers, D., Srikrishna, M. A. & Thomas, G., An electron microscopy study of the atomic structure of a mullite in a reaction-sintered composite. *J. Mater. Res.*, **3** (1988) 1355–66.
4. Rahman, S. H. & Weichert, H.-T., Interpretation of HREM images of mullite. *Acta Crystallogr.*, **B46** (1990) 139–49.
5. Epicier, T., O'Keefe, M. A. & Thomas, G., Atomic imaging of 3:2-mullite. *Acta Crystallogr.*, **A46** (1990) 948–62.
6. Epicier, T., Benefits of high-resolution electron microscopy for the structural characterization of mullites. *J. Am. Ceram. Soc.*, **74** (1991) 2359–66.
7. Rahman, S. H., Interpretation of mullite HREM images using the potential-exchange-method. *Z. Kristallogr.*, **203** (1993b) 67–72.
8. Nakajima, Y., Morimoto, M. & Watanabe, E., Direct observation of oxygen vacancy in mullite, $1.86\text{Al}_2\text{O}_3\cdot\text{SiO}_2$ by high resolution electron microscopy. *Proc. Jpn. Acad.*, **51** (1975) 173–8.
9. Ylä-Jääski, J. & Nissen, H.-U., Investigation of superstructures in mullite by high resolution electron microscopy and electron diffraction. *Phys. Chem. Minerals*, **10** (1983) 47–54.
10. Kahn-Harari, A., Abolhassani, S., Michel, D., Mazerolles, L., Portier, R. & Perez-Ramirez, J. G., Observation of ordering in silicon and germanium mullites. *J. Solid State Chem.*, **90** (1991) 234–48.
11. Paulmann, C., Rahman, S. H. & Strothenk, S., Interpretation of mullite HREM images along [010] and [100]. *Phys. Chem. Minerals*, **21** (1994) 546–54.
12. Saalfeld, H., The domain structure of 2:1-mullite. *N. Jb. Min. Abh.*, **134** (1979) 305–16.
13. Tokonami, M., Nakajima, Y. & Morimoto, N., The diffraction aspect and a structural model of mullite. *Acta Crystallogr.*, **A36** (1980) 270–6.
14. Welberry, T. & Withers, R. L., An optical transform and Monte Carlo study of the diffuse X-ray scattering in mullite $\text{Al}_2(\text{Al}_{2+2x}\text{Si}_{2-2x})\text{O}_{10-x}$. *Phys. Chem. Minerals*, **17** (1990) 117–24.
15. Rahman, S. H., Die Videographische Methode: Ein neues Verfahren zur Simulation und Rekonstruktion fehlgeordneter Kristallstrukturen. Habilitationsschrift, Universität Hannover, 1991.
16. Rahman, S. H., The real crystal structure of mullite. In *Mullite and Mullite Ceramics*, eds H. Schneider, K. Okada & J. A. Pask, Wiley and Sons, England, 1994, pp. 4–31.
17. Rahman, S. H. & Paulmann, C., Sauerstoffleerstellenverteilung in Mullit $\text{Al}_2[\text{Al}_{2+2x}\text{Si}_{2-2x}]\text{O}_{10-x}$. 25. DGE Tagung in Darmstadt, *Optik Supplement 4*, Vol. 88, 1991, Abstract 018.
18. Paulmann, C., Rahman, S. H. & Weichert, H.-T., Ordering scheme for oxygen vacancies in mullite. *Electron Microscopy EUREM92*, Granada, Spain, Vol. 2, 1992, pp. 445–6.
19. Butler, B. D., Welberry, T. R. & Withers, R. L., Oxygen vacancy ordering and the incommensurate structure of mullite. *Phys. Chem. Minerals*, **20** (1993) 323–32.
20. Padlewski, S., Heine, V. & Price, G. D., The energetics of interaction between oxygen vacancies in sillimanite: a model for the mullite structure. *Phys. Chem. Minerals*, **19** (1992) 196–202.
21. Butler, B. D. & Welberry, T. R., Analysis of diffuse scattering from the mineral mullite. *J. Appl. Crystallogr.*, **27** (1994) 742–54.
22. Rahman, S. H., The videographic method: a new procedure for the simulation and reconstruction of real structures. *Acta Crystallogr.*, **A49** (1993) 56–68.
23. Sadanaga, R., Tokonami, M. & Takeuchi, Y., The structure of mullite $2\text{Al}_2\text{O}_3\cdot\text{SiO}_2$ and relationship with the structures of sillimanite and andalusite. *Acta Crystallogr.*, **15** (1962) 65–8.
24. Burnham, C. W., The crystal structure of mullite. *Carn. I. Wash. Yb.*, **62** (1963) 158–62.
25. Burnham, C. W., Crystal structure of mullite. *Carn. I. Wash. Yb.*, **63** (1964) 223–7.
26. Durovic, S., Refinement of the crystal structure of mullite. *Chem. Zvesti*, **23** (1969) 113–28.
27. Angel, R. J. & Prewitt, C. T., Crystal structure of mullite a re-examination of the average structure. *Am. Mineral.*, **71** (1986) 1476–82.
28. Angel, R. J. & Prewitt, C. T., The incommensurate structure of mullite by Patterson synthesis. *Acta Crystallogr.*, **B43** (1987) 116–26.
29. Angel, R. J., McMullan, R. K. & Prewitt, C. T., Substructure and superstructure of mullite by neutron diffraction. *Am. Mineral.*, **76** (1991) 332–42.
30. Saalfeld, H., A modification of Al_2O_3 with sillimanite structure. *Transactions VIII International Ceramic Congress*, Copenhagen, (1962) pp. 71–4.
31. Rahman, S. H. & Rodewald, M., Simulation of short-range order in FCC-alloys. *Acta Crystallogr.*, **A51** (1995) 153–8.
32. Rahman, S. H., Strothenk, S. & Rodewald, M., Paper in preparation.

Local Structural Information of Mullite Obtained from Diffuse X-ray Scattering

T. R. Welberry & B. D. Butler*

Research School of Chemistry, Australian National University, Canberra, ACT 0200, Australia

(Accepted 22 July 1995)

Abstract

A full reciprocal space volume of diffuse scattering data from a single crystal of the mineral mullite, $Al_2(Al_{2+2x}Si_{2-2x})O_{10-x}$, $x = 0.4$, has been collected. These data were analysed using least-squares techniques by writing an equation for the diffuse scattering which involves only the local order between vacancies on specific oxygen sites in the material. The effect of the large, but predictable, cation shifts on the diffuse intensity was taken account of in the coefficients to the oxygen vacancy short-range order intensities. This analysis shows that in addition to the absence of defects separated by the vectors $\frac{1}{2}\langle 110 \rangle$ and $[110]$ (which results from the simplifying assumptions that were made), there is also a strong tendency to avoid defects separated by $\langle 001 \rangle$ and a moderately strong tendency to avoid pairs of defects separated by $\langle 003 \rangle$, $\langle 011 \rangle$, $[1-10]$ and $\frac{1}{2}\langle 312 \rangle$. The most common inter-defect vectors found were $\frac{1}{2}\langle 310 \rangle$, $\langle 101 \rangle$, $\frac{1}{2}\langle 112 \rangle$, $\langle 012 \rangle$, $\frac{1}{2}\langle 130 \rangle$, $\frac{1}{2}\langle 132 \rangle$ and $\langle 022 \rangle$.

Introduction

Conventional crystal structure determination involves measurement of the intensities of Bragg reflections – the sharp diffraction peaks that occur at integral points of reciprocal space. Analysis using this information leads to a description of the *average* structure of the material. For a disordered material such as mullite, this may include such information as the coordinates of different atomic sites in the average unit cell, site occupancies and mean-square atomic displacements. This latter information may result from the thermal motion of the atoms or may be related to a spatial average of a static distribution in which atoms in different unit cells lie on positions distributed about the mean.

*Current address: National Institute of Standards & Technology, A325 Broadway, Boulder, CO 80303, USA.

Bragg-scattering thus provides only information about *single* site properties of the material. On the other hand, *diffuse X-ray scattering*, the much weaker broadly distributed scattering occurring at general points in reciprocal space, contains information concerning *pairs* of sites and is thus potentially a rich source of information regarding local chemical and displacement correlations and can be employed to aid the understanding of locally ordered materials such as mullite. Unfortunately, the extraction of correlation fields from diffuse diffraction data has proved to be a difficult task even for relatively simple systems and success in obtaining such information has mostly been limited to alloys and simple oxides (see, for example, Refs 1–3). At first sight mullite appears to be of such significantly greater complexity than these simple systems that success in extracting quantitative correlation information would seem unlikely. In this paper we describe how, by making certain simplifications based on chemical considerations, the diffuse X-ray scattering from mullite can be analysed to reveal a much more complete description of the structure than is possible from Bragg analysis.

The Average Structure

Details of the average structure of mullite of composition $Al_2(Al_{2+2x}Si_{2-2x})O_{10-x}$ where $x = 0.4$, as revealed by the Bragg scattering,⁴ are shown in Fig. 1. The structure is similar to that of sillimanite, $Al(AlSi)O_5$. Chains of edge-sharing AlO_6 octahedra, running parallel to the crystallographic c-axis, are crosslinked by $(Al,Si)O_4$ tetrahedra. In sillimanite the tetrahedrally coordinated cations are bridged by a single oxygen atom and are ordered in such a way that the bridging anion always connects an Si-containing tetrahedron with an Al-containing tetrahedron. In mullite some fraction, x , of these bridging oxygen sites are vacant. To preserve charge balance, each of the O^{2-} vacancies are accommodated by the exchange

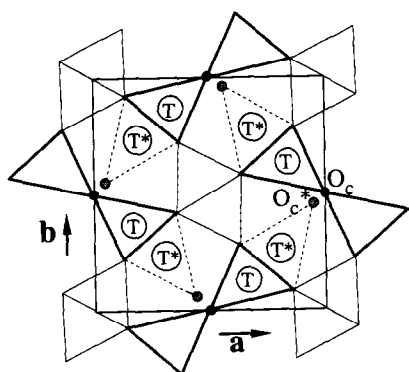


Fig. 1. The average structure of mullite seen in projection down the crystallographic c -axis. The sites labelled O_c and O_c^* contain oxygen atoms which bridge two or more tetrahedra. In an $x = 0.4$ mullite the T , T^* sites are disordered such that 80% of the T sites and 20% of the T^* sites are occupied by Al or Si. 40% of the O_c sites and 20% of the O_c^* sites are occupied.

of $2Al^{3+}$ for $2Si^{4+}$. Because the tetrahedrally coordinated Al and Si are no longer present in the ratio of 1:1 these sites necessarily become chemically disordered. Furthermore, crystal structure analysis has identified the presence of a second tetrahedral site – displaced from the original by approximately 1.3 \AA – that is presumably occupied by cations which have lost bridging oxygen atoms. The bridging oxygen atom was also found to occasionally occupy a site displaced 0.5 \AA from its normal position and appears to be associated with the displaced tetrahedral site. In Fig. 1 the (Al,Si) tetrahedral sites are labelled T and T^* and the bridging anion sites are labelled O_c and O_c^* where * indicates the displaced positions mentioned above. It should be stressed that it is only *presumed* that the T^* sites are occupied by cations which have lost bridging oxygen atoms and that the displaced O_c^* sites are directly associated with them. The Bragg experiment only reveals the overall average occupancies.

The Diffuse Diffraction Data

The diffuse intensity data were collected on an instrument specially designed for the rapid collection of planar sections of single crystal diffraction patterns. The apparatus is an electronic version of a Weissenberg camera utilizing flat-cone geometry in which a curved linear (gas filled) position sensitive detector (PSD) is used to collect data normal to the Weissenberg cylinder axis. A monochromated, sealed tube, $Cu K_\alpha$ source is employed. With this geometry a series of scans taken as the crystal is rotated through 360° produces a flat, two-dimensional section of the diffraction pattern normal to the crystal rotation axis. Several scans can be made using different goniometer settings to

construct a three-dimensional image of the diffraction space as a series of two-dimensional sections. Further details about the instrument can be found elsewhere.⁵

Although the data recorded in this way provide quantitative measurements at points in reciprocal space, it is convenient for display purposes to present the data as grey-scale images. We prefer this method to the often used practice of drawing contour plots. In Fig. 2 we show such plots of data from six different reciprocal sections. Each pattern consists of $\sim 180 \times 180$ pixels. Each pixel corresponds to an increment in the Miller indices Δh_1 , $\Delta h_2 = 0.05$. This resolution is rather poorer than the resolution that the instrument can provide, but the data were binned at this resolution to provide a manageable number of independent measurements. Eleven sections in $\Delta h_3 = 0.05$ increments from $h_3 = 0.5$ to 1.0 were measured, yielding in excess of 130 000 independent measurements.

The plots of data in Fig. 2, which are all made on the same scale, demonstrate the rich detail that is present in the diffuse data. Many different features may be seen, varying from the relatively

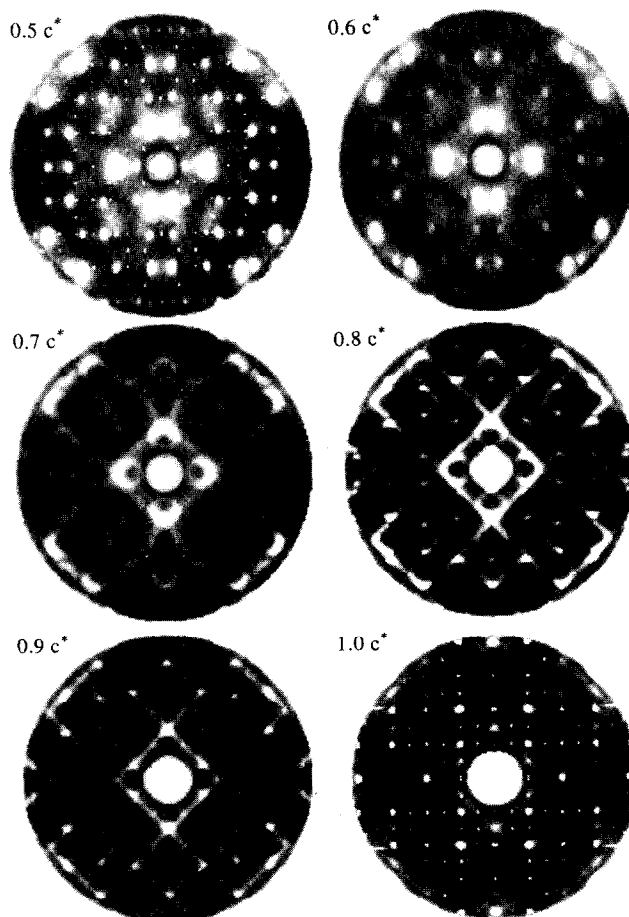


Fig. 2. Diffuse X-ray diffraction data. The data were collected digitally but are displayed on a grey scale so that the full range of diffuse features can be seen. Only six of the 11 diffuse planes that were used in the analysis are displayed. The small single pixel peaks seen in the $0.5c^*$ and $1.0c^*$ sections are Bragg peaks caused by $\lambda/2$ contamination of the beam.

sharp incommensurate peaks visible in the $0.5\mathbf{c}^*$ section to the more diffuse circular features in the $0.7\mathbf{c}^*$ section and the narrow lines of the $0.9\mathbf{c}^*$ section. Although in the past much interest has centred on the incommensurate peaks, these patterns reveal that these are just an integral part of the continuous diffuse distribution. The total integrated intensity in each of the different recorded sections is fairly constant.

Theory

A general description of diffuse scattering that allows for both short-range compositional (chemical) order and local atomic displacements can be obtained by expanding the exponential in the kinematic scattering equation in powers of displacement.

$$\begin{aligned}
 I &= \sum_{n=1}^N \sum_{m=1}^M f_m f_n \exp[i\mathbf{k} \cdot (\mathbf{R}_m + \mathbf{u}_m - \mathbf{R}_n - \mathbf{u}_n)] \\
 &\approx \sum_{n=1}^N \sum_{m=1}^M f_m f_n \exp[i\mathbf{k} \cdot (\mathbf{R}_m - \mathbf{R}_n)] \\
 &\quad \times \left\{ 1 + i\mathbf{k} \cdot (\mathbf{u}_m - \mathbf{u}_n) - \frac{1}{2} [\mathbf{k} \cdot (\mathbf{u}_m - \mathbf{u}_n)]^2 \right. \\
 &\quad \left. - \frac{i}{6} [\mathbf{k} \cdot (\mathbf{u}_m - \mathbf{u}_n)]^3 + \dots \right\} \quad (1)
 \end{aligned}$$

Here I is the scattered intensity and f_m is the scattering factor of the atom m associated with the lattice site at the location \mathbf{R}_m and which is displaced from its site by a small amount \mathbf{u}_m . $\mathbf{k} = h_1\mathbf{a}^* + h_2\mathbf{b}^* + h_3\mathbf{c}^*$ is the scattering vector. Eqn (1) expresses the fact that the intensity distribution may be written as the sum of component intensities: the first term being independent of the displacements, the second term dependent on the first moment of displacements, the third term on the second moment, etc.

$$\mathbf{I}_{\text{Diffuse}} \approx \mathbf{I}_0 + \mathbf{I}_1 + \mathbf{I}_2 + \mathbf{I}_3 + \dots \quad (2)$$

It is usual in analyses of alloys and simple oxides to truncate this Taylor expansion at second order, although recently we have shown that for cubic-stabilized zirconias the third and higher order terms are also important. These components can be shown to have the following forms,

$$\mathbf{I}_0 = - \sum_{ij} \sum_{lmn} c_i c_j f_i f_j^* \alpha_{lmn}^{ij} \cos\{2\pi(h_1 l + h_2 m + h_3 n)\} \quad (3)$$

$$\begin{aligned}
 \mathbf{I}_1 &= -2\pi \sum_{ij} \sum_{lmn} c_i c_j f_i f_j^* (1 - \alpha_{lmn}^{ij}) [h_1 \langle X_{lmn}^{ij} \rangle \\
 &\quad + h_2 \langle Y_{lmn}^{ij} \rangle + h_3 \langle Z_{lmn}^{ij} \rangle] \\
 &\quad \times \sin\{2\pi(h_1 l + h_2 m + h_3 n)\} \quad (4)
 \end{aligned}$$

$$\begin{aligned}
 \mathbf{I}_2 &= -2\pi^2 \sum_{ij} \sum_{lmn} c_i c_j f_i f_j^* (1 - \alpha_{lmn}^{ij}) \\
 &\quad \times [h_1^2 \{ \langle (X_{lmn}^{ij})^2 \rangle - (1 - \alpha_{lmn}^{ij})^{-1} \langle (X_z^{ij})^2 \rangle \} \\
 &\quad + h_2^2 \{ \langle (Y_{lmn}^{ij})^2 \rangle - (1 - \alpha_{lmn}^{ij})^{-1} \langle (Y_z^{ij})^2 \rangle \} \\
 &\quad + h_3^2 \{ \langle (Z_{lmn}^{ij})^2 \rangle - (1 - \alpha_{lmn}^{ij})^{-1} \langle (Z_z^{ij})^2 \rangle \} \\
 &\quad + 2h_1 h_2 \{ \langle (X_{lmn}^{ij} Y_{lmn}^{ij}) \rangle + 2h_1 h_3 \langle (X_{lmn}^{ij} Z_{lmn}^{ij}) \rangle \\
 &\quad + 2h_2 h_3 \{ \langle (Y_{lmn}^{ij} Z_{lmn}^{ij}) \rangle \} \\
 &\quad \times \cos\{2\pi(h_1 l + h_2 m + h_3 n)\} \quad (5)
 \end{aligned}$$

The first term \mathbf{I}_0 is the intensity component due to short-range order and is not dependent on displacements. There is one term in this summation for every different interatomic vector lmn along which significant correlation may be present. Each term in the sum involves a short-range order parameter, α_{lmn}^{ij} , defined by

$$\alpha_{lmn}^{ij} = 1 - P_{lmn}^{ij}/c_j \quad (6)$$

where P_{lmn}^{ij} is the conditional probability of finding an atom with label j at the end of a vector \mathbf{r}_{lmn} given that there is an atom with label i at its origin. \mathbf{I}_1 and \mathbf{I}_2 , which involve displacements, similarly also have terms for every different interatomic vector. For a simple binary system \mathbf{I}_1 has six terms for each interatomic vector and \mathbf{I}_2 has 18. Fitting equations of this form with such large numbers of parameters is a formidable task even for simple systems, but for a system as complex as mullite it is quite prohibitive. Consequently we look for a means by which the problem may be simplified.

A Simplified Model

The simplification we adopt consists of making two assumptions. First we assume that only the distribution of oxygen vacancies is important, and that the shift of cations from the \mathbf{T} to the \mathbf{T}^* sites and the shift of the oxygens from \mathbf{O}_c to \mathbf{O}_c^* follow from these as a direct consequence [see Fig. 3(a)]. Secondly, we assume that certain local configurations, which are chemically implausible, do not occur at all in the structure. These are shown in Figs 3(b) and 3(c). In Fig. 3(b) the presence of two vacancies separated by $\frac{1}{2}\langle 110 \rangle$ causes the cation 'M' to have no bridging oxygen atom to bond with. In Fig. 3(c) the presence of two vacancies separated by $[110]$ causes four tetrahedral cations to share the same bridging oxygen.

A description of the mullite structure based on the occupancy of the bridging oxygen sites alone can then be formulated as follows. When a bridging

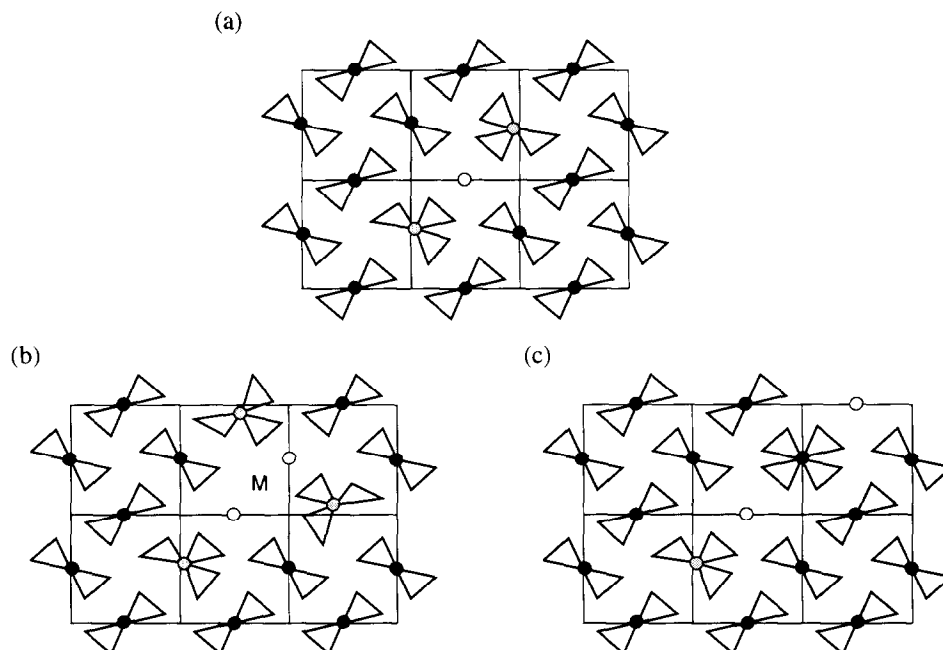


Fig. 3. In all the figures a black circle represents an oxygen atom on the O_c site, a grey circle an oxygen atom on the O_c^* site and an open circle represents a vacancy. (a) Shows the effect of introducing an oxygen vacancy into the mullite structure. Two nearby cations transfer from T sites to the alternative T^* sites and the two O_c oxygens, which now are bonded to three cations, move to the O_c^* sites. (b) and (c) Show two configurations that are assumed never to occur in the disordered structure. In (b) the cation 'M' is left without a bridging O_c atom to bond with. In (c) four cations are forced to share one bridging oxygen.

site is occupied by an oxygen atom we 'decorate' that site with one O_c oxygen atom and two T cations. When the site is vacant we decorate with two T^* cations, two neighbouring O_c^* oxygen atoms and *subtract* two neighbouring O_c oxygen atoms. Note that as long as the ordering rules stated above are obeyed and all the bridging sites have been 'filled' with either an oxygen atom or a vacancy, the positions of all tetrahedrally coordinated cations and all of the bridging oxygen atoms will have been specified. The 'negative' O_c oxygen atoms that are included with an oxygen vacancy are used as a means to displace O_c atoms from their normal positions to positions labelled O_c^* while still preserving the total number of oxygen atoms in the crystal. Once the entire lattice has been decorated in this way there will be no remaining 'negative' oxygen atoms.

With this formulation we can discard the intensity components, I_1 and I_2 , and use only the short-range order (SRO) term I_0 , in which we replace the atomic scattering factor by structure factors for the chemical motifs of an occupied or a vacant site. This simplification merely incorporates the displacements which would normally appear in I_1 and I_2 into I_0 , but in doing so automatically dictates that the displacements when they occur are always of exactly the same magnitude. The scattering power of an occupied (O) and vacant (V) O_c site can be calculated as a simple structure factor of the chemical motifs described above:

$$\begin{aligned}
 F_O^1 &= f_O + 2f_{Al} \cos \{2\pi(x_T h_1 + y_T h_2)\} \\
 F_V^1 &= 2f_O \cos \{2\pi(x_{O_c^*} h_1 + y_{O_c^*} h_2)\} \\
 &\quad + 2f_{Al} \cos \{2\pi(x_T h_1 + y_T h_2)\} \\
 &\quad - 2f_O \cos \{2\pi(x_{O_c} h_1 + y_{O_c} h_2)\} \quad (7)
 \end{aligned}$$

Here, f_O, f_{Al} are the atomic scattering factors of O and Al; x_T, y_T etc. are the fractional coordinates of the T, T^* , O_c and O_c^* sites measured relative to the O_c site in question; h_1, h_2, h_3 are continuous reciprocal space coordinates; and the superscript on the structure factors indicates the sublattice upon which the oxygen atom or vacancy resides. Sublattice 1 refers to the O_c site at $(\frac{1}{2}0\frac{1}{2})$ and translationally equivalent sites, while sublattice 2 refers to the O_c site at $(0\frac{1}{2}\frac{1}{2})$. Equation (7) gives the expressions for motifs centred at sites on sublattice 1. Similar, symmetry-related, expressions may be written for motifs centred on sublattice 2.

Replacing the atomic scattering factors in Eqn (3) by the structure factors of the chemical motifs we obtain, after some manipulation (see Butler & Welberry⁶ for further details), the following expression for the SRO diffuse scattering in mullite:

$$I_{SRO}^{mullite} = \mu_1 I_1 + \mu_2 I_2 + \mu_{12} I_{12} \quad (8)$$

where

$$I_1 = \sum_{l,m,n} \alpha_{lmn}^{O,V_1} \cos(h_1 l + h_2 m + h_3 n)$$

l, m, n integer

$$I_2 = \sum_{\substack{lmn \\ l, m, n \text{ integer}}} \alpha_{lmn}^{O_2V_2} \cos(h_1l + h_2m + h_3n)$$

$$I_{12} = \sum_{\substack{lmn \\ l = \text{int} + 1/2 \\ m = \text{int} + 1/2 \\ n = \text{int}}} \alpha_{lmn}^{O_1V_2} \cos(h_1l + h_2m + h_3n) \quad (9)$$

and,

$$\begin{aligned} \mu_1 &= c_O c_V (F_{O_1} - F_{V_1})^2 \\ \mu_2 &= c_O c_V (F_{O_2} - F_{V_2})^2 \\ \mu_{12} &= 2c_O c_V \Re\{(F_{O_2} - F_{V_2})(F_{O_2} - F_{V_2})^*\} \end{aligned} \quad (10)$$

The three intensities, I_1 , I_2 , and I_{12} , are periodic functions in reciprocal space with a repeat that is commensurate with the first Brillouin zone and the coefficients μ_1 , μ_2 and μ_{12} are continuous functions in reciprocal space. I_1 and I_2 involve only correlations between sites on the same sublattice (1 and 2 respectively), while I_{12} involves cross-correlations between the two different sublattices. In Fig. 4 we show plots of the functions, μ_1 , μ_2 , μ_{12} , which are calculated from the fractional coordinates of the average structure obtained from the Bragg reflections. It should also be noted that since \mathbf{T} , \mathbf{T}^* , \mathbf{O}_c and \mathbf{O}_c^* all have the same z -coordinate in the structure, the functions μ_1 , μ_2 and μ_{12} are virtually independent of h_3 , the reciprocal coordinate in the c^* -direction. The variation of the intensity distribution with reciprocal section thus results entirely from the Warren short-range

order parameters, α_{lmn} , appearing in the three intensity components I_1 , I_2 and I_{12} .

Results

A value for each of the three intensity components can be obtained for a given point inside the first Brillouin zone by gathering together several measurements of the diffuse intensity from points in the reciprocal space that are related by symmetry with this point. The set of measurements related by symmetry in this way is commonly referred to as an *associated set* and the point inside the minimum repeat volume is referred to as a *minimum volume point*.⁷ For example, if the point (h_1, h_2, h_3) , lies inside the first Brillouin zone, then the points $(1 - h_1, h_2, h_3)$, $(h_1, 2 + h_2, h_3)$, $(2 + h_1, 3 - h_2, 1 + h_3)$, etc. form the associated set of the minimum volume point (h_1, h_2, h_3) . Each of the intensity components I_1 , I_2 and I_{12} have the same numerical magnitude (but not necessarily sign) for all points inside a particular associated set but the coefficients μ_1 , μ_2 and μ_{12} vary predictably in a way that does not repeat commensurately with the underlying reciprocal lattice. Any collection of three or more measurements in an associated set can therefore be used to solve for the three intensity components at one minimum volume point. In the present case, upwards of 30–40 measurements were available in each associated set and with only three intensity components to solve for the problem is highly overdetermined. Standard least-squares procedures were used to solve for the three intensity components at each of 1331 points in the minimum volume.

When this had been done for every point in the minimum volume, the Warren short-range order parameters α_{lmn} were extracted from each of the three component intensities by simple Fourier inversion of Eqn (9). The most significant of these are given in Table 1. Assuming that the three SRO intensities derived this way are the only significant

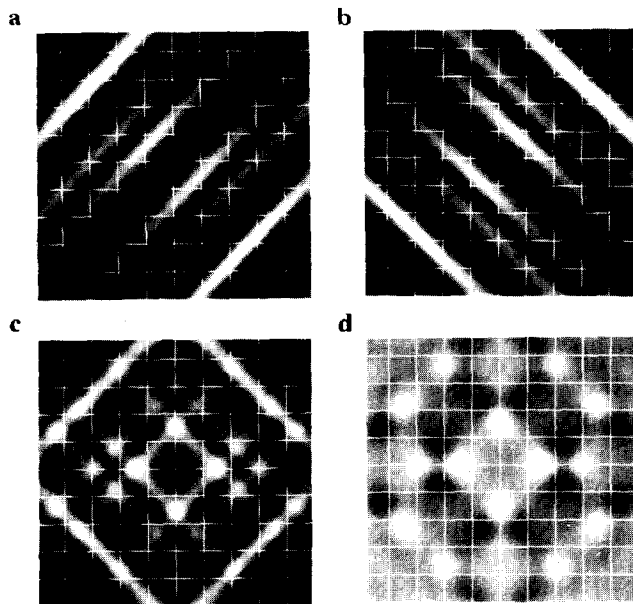


Fig. 4. Plots in the $(hk0)$ plane of the coefficients μ_1 , μ_2 and μ_{12} which occur in Eqn (8). These coefficients are constant functions calculated from the coordinates obtained from the average structure analysis. (a) μ_1 . (b) μ_2 . (c) $\mu_1 + \mu_2$. (d) μ_{12} . μ_1 and μ_2 are positive everywhere but μ_{12} varies from negative (black) to positive (white). The white lines drawn on the figures indicate where h_1 and h_2 are integral.

Table 1. Local order parameters for mullite determined from the least-squares analysis

Interatomic vector, lmn	Short-range order parameter, α_{lmn}	Interatomic vector, lmn	Short-range order parameter, α_{lmn}
$\frac{1}{2}\langle 110 \rangle$	-0.250	$\langle 011 \rangle$	-0.122
$[110]$	-0.250	$[111]$	-0.079
$[1-10]$	-0.081	$[1-11]$	+0.000
$\langle 001 \rangle$	-0.227	$\frac{1}{2}\langle 112 \rangle$	+0.109
$\langle 100 \rangle$	-0.004	$\frac{1}{2}\langle 310 \rangle$	+0.141
$\langle 010 \rangle$	+0.015	$\frac{1}{2}\langle 130 \rangle$	+0.077
$\langle 002 \rangle$	-0.019	$\frac{1}{2}\langle 312 \rangle$	-0.092
$\langle 003 \rangle$	-0.124	$\frac{1}{2}\langle 132 \rangle$	+0.058
$\langle 004 \rangle$	+0.047	$\langle 012 \rangle$	+0.088
$\langle 101 \rangle$	+0.113	$\langle 022 \rangle$	+0.051

contributions to the total diffuse intensity in mulite, then the oxygen-vacancy SRO parameters obtained by this procedure will contain all the information that the diffuse part of the diffraction pattern can provide.

The intensity R factor

$$R = [\sum (I_{\text{obs}} - I_{\text{calc}})^2 / \sum I_{\text{calc}}^2]$$

for a typical least-squares solution of one of the 1331 minimum volume points was approximately 35%. This obvious quantitative discrepancy may seem very high by conventional crystallographical standards but the resulting least-squares fit is not as bad as this figure implies. When all 1331 independent solutions are used, together with the μ_1 , μ_2 , μ_{12} coefficients, to obtain a 'best-fit' calculated diffraction pattern for visual comparison with the observed patterns, the results are really rather convincing (see Fig. 5).

Both Figs 2 and 5 are reproduced on the same scale so that the grey shades can be compared to see how the two agree. There are a few obvious differences. For instance, in the $0.7c^*$ reciprocal layer the measured intensities near the origin and

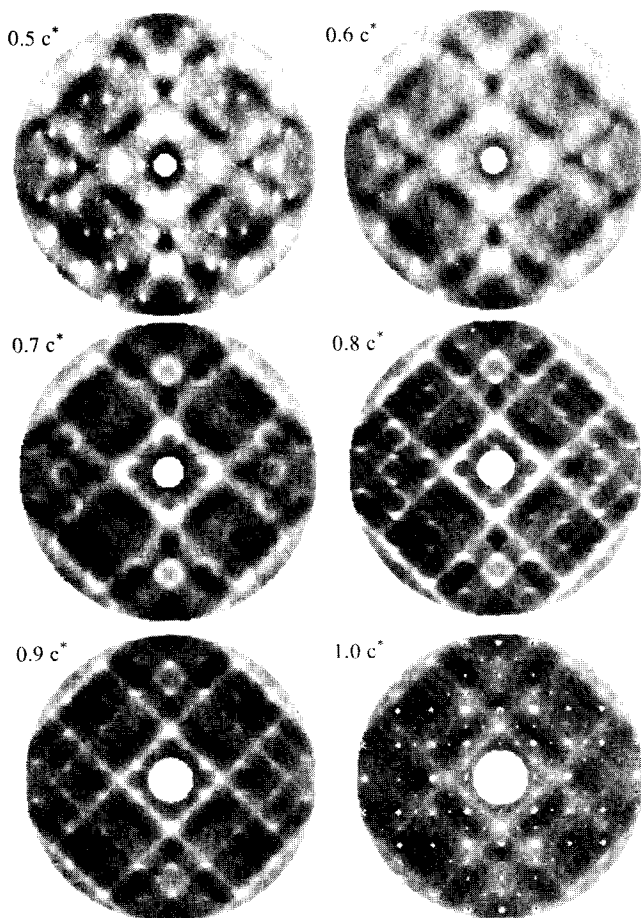


Fig. 5. Diffraction patterns calculated from the least-squares fit of the model to the observed data. The least-squares solution provided three intensity components at each of 1331 points inside the first Brillouin zone. The entire pattern was generated by multiplying these component intensities by the appropriate coefficients μ_1 , μ_2 , μ_{12} and adding.

at large scattering angles are noticeably higher than in the calculated pattern, whereas at intermediate angles this situation is reversed. There are also distinct diagonal dark bands visible in the $0.5c^*$ layer of the calculated pattern that are much less distinct in the data. These differences may indicate minor short-comings in the model used to derive Eqn (8) which does not allow for atom displacements other than those included in the simple chemical motifs described.

The most significant values for the Warren short-range order parameters, α_{lmn} , obtained from the analysis are shown in Table 1. For a vacancy concentration of 0.2 the most negative value of α_{lmn} feasible is $\alpha_{lmn} = -0.25$, which corresponds to complete avoidance of defect pairs separated by the vector lmn . Thus we see that, in addition to the absence of defects separated by the vectors $\frac{1}{2}\langle 110 \rangle$ and $[110]$ (which results from the simplifying assumptions that were made), there is also a strong tendency to avoid defects separated by $\langle 001 \rangle$ and a moderately strong tendency to avoid pairs of defects separated by $\langle 003 \rangle$, $\langle 011 \rangle$, $[1-10]$ and $\frac{1}{2}\langle 312 \rangle$. The most common inter-defect vectors found were $\langle 101 \rangle$, $\frac{1}{2}\langle 112 \rangle$ and $\frac{1}{2}\langle 310 \rangle$.

Conclusion

Comparison of Figs 2 and 5 demonstrates convincingly that, for this seemingly complicated mineral, the diffuse scattering can be described simply as the sum of three component short-range order diffuse intensities. Two of these components involve correlations between the basic defects on each of the two different sublattices (symmetry-related) and the third involves correlations between the two sublattices. Although there are quantitative discrepancies indicating some short-comings in the fine detail of the model, there is no doubt that the model is essentially correct.

The basic defect consists of a vacant O_c site together with a transfer of its two neighbouring tetrahedral cations from a T to a T^* site. Each T^* cation then shares a further bridging oxygen which shifts from O_c to O_c^* [see Fig 3(a)]. An integral part of the model was the necessity to assume that two chemically implausible configurations [shown in Figs 3(b) and 3(c)] were forbidden. If two defects were separated by $\frac{1}{2}[110]$ the intervening cation would be left without a bridging O_c atom, while if two defects were separated by $[110]$ it would be necessary for four cations to share the same bridging O_c atom. The analysis revealed that defect pairs separated by $\langle 001 \rangle$ were strongly avoided, and that defects separated by $\langle 003 \rangle$,

$\langle 011 \rangle$, $[1-10]$ or $\frac{1}{2}\langle 312 \rangle$ also tended to be avoided, although rather less strongly. The most common inter-defect vectors found were $\frac{1}{2}\langle 310 \rangle$, $\langle 101 \rangle$, $\frac{1}{2}\langle 112 \rangle$, $\langle 012 \rangle$, $\frac{1}{2}\langle 130 \rangle$, $\frac{1}{2}\langle 132 \rangle$ and $\langle 022 \rangle$.

References

1. Hayakawa, M. & Cohen, J. B., *Acta Crystallogr.*, **A31** (1975) 635–45.
2. Matsubara, E. & Cohen, J. B., *Acta Metall.*, **33** (1985) 1945–55.
3. Reinhard, L., Robertson, J. L., Moss, S. C., Ice, G. E., Zschack, P. & Sparks, C. J., *Phys. Rev. B*, **45** (1992) 2662–76.
4. Angel, R. J. & Prewitt, T., *Am. Mineral.*, **71** (1986) 1476–82.
5. Osborn, J. C. & Welberry, T. R., *J. Appl. Crystallogr.*, **23** (1990) 476–84.
6. Welberry, T. R. & Butler, B. D., *J. Appl. Crystallogr.*, **27** (1994) 742–54.
7. Wu, T. B., Matsubara, E. & Cohen, J. B., *J. Appl. Crystallogr.*, **16** (1983) 407–14.

Time-Resolved Fluorescence Spectroscopy of Cr^{3+} in Mullite

Bernard Piriou,^a Helmut Rager^b & Hartmut Schneider^c

^aPCM/URA 1907-CNRS, Ecole Centrale de Paris, F-92295 Châtenay-Malabry Cedex, France

^bInstitut für Mineralogie, Universität Marburg, D-35032 Marburg, Germany

^cGerman Aerospace Research Establishment, Institute for Materials Research, D-51140 Köln, Germany

(Accepted 22 July 1995)

Abstract

Mullites doped with Cr_2O_3 concentrations ranging from 2 to 10 wt% were investigated by both time-resolved emission spectroscopy and site-selective excitation. The emission decays are non-exponential. They depend on Cr concentration and emission frequency and, hence, it is possible to distinguish different kinds of Cr^{3+} sites: at least two different types of low field site, one type of high field site and one intermediate field site. The emission decay time for Cr^{3+} in intermediate field sites was found to be the longest. In Cr_2O_3 -poor mullites Cr^{3+} occurs dominantly at high field sites, i.e. at structural $M(1)$ positions replacing Al^{3+} , whereas in Cr_2O_3 -rich mullites the majority of Cr^{3+} is incorporated in interstitial sites.

1 Introduction

In recent years, mullite has attracted much interest because of its favourable high temperature properties such as low thermal expansion and conductivity, and because of its excellent creep resistance up to 1400°C.¹ Furthermore, chromium-doped mullite transparent glass-ceramics are promising compounds for tunable solid-state lasers. Mullite is able to incorporate a variety of transition metal cations into its structure. Among these ions Cr^{3+} is of special interest since it can be used as local probe for optical and electron paramagnetic resonance (EPR) investigations. Previous optical studies of chromium-doped mullite were carried out on glass-ceramics having Cr^{3+} concentrations between 0.1 and 0.05 wt% Cr_2O_3 .^{2–7}

The energy levels of $\text{Cr}^{3+}(\text{d}^3)$ in an octahedral field are given by a Tanabe–Sugano diagram: some levels such as ${}^4\text{T}_2(\text{t}_2^2\text{e})$, ${}^4\text{T}_1(\text{t}_2^2\text{e})$ and ${}^4\text{T}_1(\text{t}_2\text{e}^2)$ depend strongly on the crystal field strength Dq . If Dq is larger than $\sim 1550 \text{ cm}^{-1}$ ($Dq/B = 2.1$) the low-

est excited state is ${}^2\text{E}(\text{t}_2^2\text{e})$ and Cr^{3+} is located in so-called high field sites (HFS). With $Dq < 1550 \text{ cm}^{-1}$, ${}^4\text{T}_2$ becomes the lowest state and Cr^{3+} is located in so-called low field sites (LFS). The ground state is ${}^4\text{A}_2(\text{t}_2^3)$. Depending on Dq , the HFS transition ${}^2\text{E} \Rightarrow {}^4\text{A}_2$ and the LFS transition ${}^4\text{T}_2 \Rightarrow {}^4\text{A}_2$ can be observed by emission spectroscopy. The LFS transition leads to a broad band decaying in a few μs . In crystalline phases the HFS transition exhibits two sharp R-lines with lifetime in the ms region. The intensity is low because the transition is spin-forbidden. The breaking of the selection rule is due to spin–orbit coupling and phonon–electron interaction which admixes the ${}^4\text{T}_2$ wave function into the ${}^2\text{E}$ state and vice versa. In aluminosilicates, glasses and in more or less ordered crystalline compounds this mixing is stressed because Dq lies in the crossing region of the ${}^4\text{T}_2$ and ${}^2\text{E}$ states, leading to a strong distortion of oscillator strength and of the lifetime of the excited levels.^{2,8–12}

Luminescence measurements of solids are helpful in the study of laser material and the search for new phosphors, because information is provided about the local structure of optically active ions in the host material, e.g. point group symmetry and crystal field strength can be inferred. In structurally disordered materials such as glasses and compounds with ion vacancies, the site-selective excitation technique is able to develop the individual response of optically different ions from an inhomogeneously broadened luminescence spectrum. Moreover, overlapping bands can often be discriminated by time-resolved spectroscopy provided the emitting levels have different decay times. In the investigation of ceramics, it was shown that the application of both techniques is suitable to follow the martensitic transformation in partially stabilized zirconia.¹³

This paper presents time-resolved fluorescence measurements of mullite with chromium concen-

trations between 2 and 10 wt% Cr₂O₃ using both these techniques, to determine structurally different Cr sites in mullite.

2 Experimental

2.1 Sample synthesis

Mullite samples were prepared by reaction sintering. Chemically pure powders of α -Al₂O₃ (62 - x wt%), SiO₂ (38 wt%) and $x = 2, 5, 7.5$ and 10 wt% Cr₂O₃ were used for the syntheses. After grinding the starting powders with ethyl alcohol in an agate mortar, the mixture was annealed in a PtRh crucible at 1650°C for 10 days. The glass phase present after the reaction sintering process was leached with an HF/HCl acid solution. The chemical composition and the lattice parameters of the samples are compiled in Table 1. Samples are designated as CR2, CR5, CR7.5 and CR10, according to their bulk Cr₂O₃ contents. The acid-treated mullite powders are green in colour. Samples were checked prior to spectroscopic measurements with a polarizing microscope and by X-ray diffraction. Neither impurity minerals nor glass was observed in the samples. Therefore, the acid-treated material is considered to be single-phase mullite.

2.2 Luminescence measurements

The fluorescence spectra were measured with a 80 cm double grating spectrometer (Coderg Co., Pho model) equipped with an R 928 Hamamatsu photomultiplier. The signals were processed by a Tektronix 2430 digital oscilloscope and a BFM 187 personal computer. Time-resolved measurements were performed by ultraviolet (UV) pulsed excitation using a nitrogen laser (Jobin Yvon ISA, LAO4 model). Selected excitation in the visible region was performed by a dye laser (Jobin Yvon, EIT model) pumped by a nitrogen laser. Usual dyes, coumarins, rhodamines and blue Nile, were used.

Each fluorescence decay, following the excitation pulse, was analysed in real time while simultaneously scanning the wavelength of the The signals were numerically integrated in different time gates, each one defined by a given delay and

width. Using up to six time gates the corresponding time-resolved emission spectra could be recorded during one scan. Each spectrum was normalized to its main band. The spectra were not corrected for the spectral sensitivity of the optical set-up. Since the cut-off of the spectrometer is near 11 000 cm⁻¹, the signals below 12 000 cm⁻¹ did not have the true line shape. In order to reduce the energy transfer between chromium ions, most of the measurements were carried out at 77 K. Moreover, from this set-up, decay profiles were obtained by averaging over some hundred decay measurements.

3 Results

As reference for a Cr³⁺ high field site spectrum, the optical absorption of ruby was measured. The ⁴A₂ ⇒ ⁴T₂ and ⁴A₂ ⇒ ⁴T₁ transitions were observed as broad bands at 18 300 and 25 000 cm⁻¹, respectively. Weak narrow features in the spectrum correspond to spin-forbidden transitions from the ground state to the states ²E, ²T₁ and ²T₂. In the absorption spectra of the samples investigated here two doublets can be distinguished. Their intensities correspond to the Cr concentration. The two doublets occur at 16 280/22 440 cm⁻¹ and 18 520/24 520 cm⁻¹, respectively. By comparison with the ruby spectrum they were assigned to both low field site and high field site transitions.

Under UV pulsed excitation using a wavelength of 337 nm (29 674 cm⁻¹) all samples show a broad emission band designated as E (Fig. 1). The maximum lies at about 21 300 cm⁻¹ and the line width is ~5000 cm⁻¹. The time decay of band E is < 50 ns. Below 15 000 cm⁻¹ the intensity of the emission spectra depends slightly on the Cr concentration. This was not observed for sample CR2. Therefore, the concentration quenching seems to start with Cr₂O₃ contents > 2 wt%. Sample CR2 exhibits further an emission spectrum in the low energy range which differs in some details from the spectra of the samples with higher Cr content. For delay times ranging from 2 to 500 μ s, two bands centred around 12 550 and 13 950 cm⁻¹, labelled as A and C respectively, were observed; band A exhibits the

Table 1. Chemical composition and lattice parameters of Cr₂O₃-doped mullites

Sample	Chemical composition (wt%)			Lattice parameters (\AA)			
	Al ₂ O ₃	SiO ₂	Cr ₂ O ₃	a	b	c	v (\AA^3)
CR2	68.8 (3)	28.9 (4)	2.3 (2)	7.5498 (7)	7.6951 (7)	2.8867 (2)	167.71 (1)
CR5	65.7(4)	28.5 (4)	5.7 (2)	7.5561 (2)	7.7006 (2)	2.8921 (1)	168.281 (5)
CR7.5	62.8 (4)	28.4 (3)	8.6 (2)	7.5624 (4)	7.7067 (5)	2.8973 (2)	168.861 (1)
CR10	60.0 (4)	28.4 (3)	11.5 (2)	7.5674 (5)	7.7089 (7)	2.9010 (2)	169.23 (2)

The chemical composition refers to electron microprobe analyses. Values in parantheses are standard deviations. Data were taken from Rager *et al.*⁷

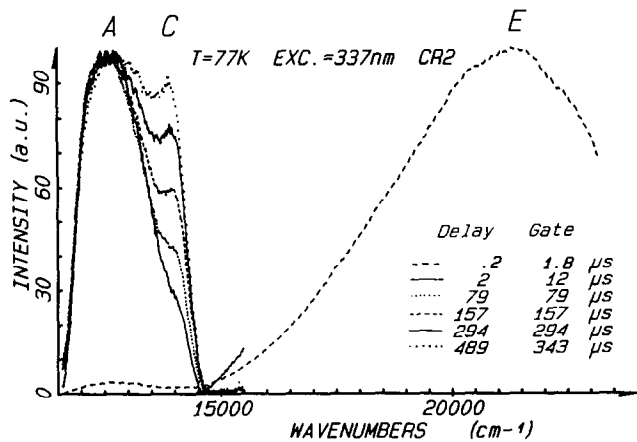


Fig. 1. Time-resolved emission spectra of sample CR2 at 77 K obtained with different delay and gate times. Excitation at 29 674 cm⁻¹.

shorter decay time. Similar bands at 12 500 and 14 325/14 300 cm⁻¹ were also reported from transparent mullite glass ceramics with Cr concentrations < 0.1 wt% Cr₂O₃.^{2,3,5}

Band A occurs in all our samples. Except for sample CR2, it is shifted towards lower energy by increasing the delay time from 0.1 to ~20 μ s (Fig. 2). The shift occurs mainly within the first 10 μ s. It depends also on the Cr concentration, i.e. it increases from sample CR5 to sample CR10. In the emission spectra of samples CR5 and CR7.5, additionally, a shoulder appeared at delay and gate times of 150 μ s. It corresponds probably to band C observed in sample CR2 (Fig. 1). On increasing the delay and gate times further, another shoulder designated as B appears at about 13 600 cm⁻¹ (Fig. 3). In the spectrum of sample CR10, however, no indication for the shoulders B and C could be observed when delay and gate times were > 150 μ s.

The decay profiles of all samples were recorded at room and liquid nitrogen temperatures; decay profiles of sample CR2 were recorded also at 22 K. The decay profiles depended on Cr concentration, temperature and observation frequency

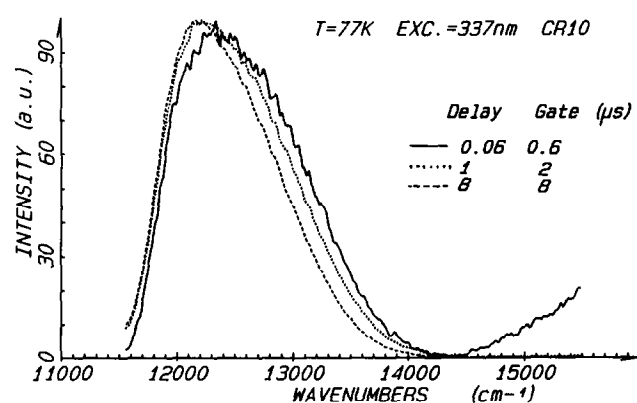


Fig. 2. Time-resolved emission spectra of band A in sample CR10 observed with short delay times. Excitation at 29 674 cm⁻¹.

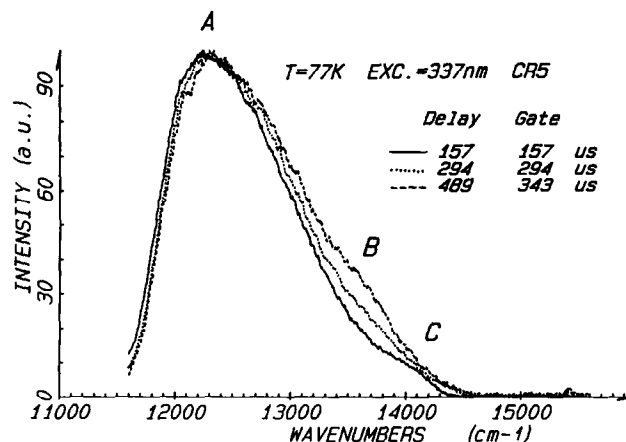


Fig. 3. Time-resolved emission spectra in sample CR5 observed with long delay times. Excitation at 29 674 cm⁻¹.

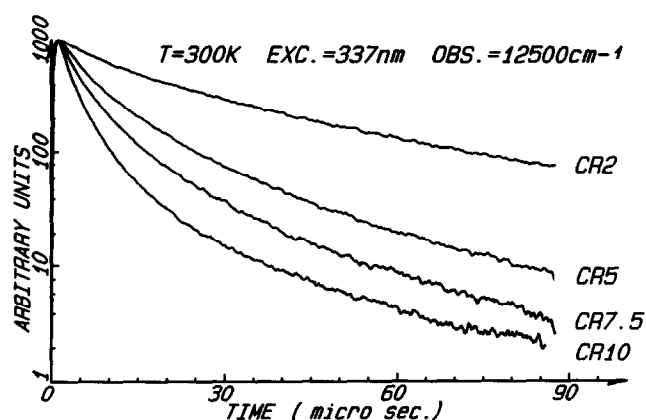


Fig. 4. Fluorescence decay profiles of band A in the different samples. Excitation at 29 674 cm⁻¹; observation at 12 500 cm⁻¹.

(Figs 4 and 5) but only slightly on the excitation frequency. All decays are non-exponential and, hence, can be characterized by a short and a long lifetime component. The short component corresponds to an average lifetime in the first e-folding while the long-lived component governs the last recorded e-folding. Both lifetime components decrease with increasing Cr content and increase with decreasing temperature. For example, in samples

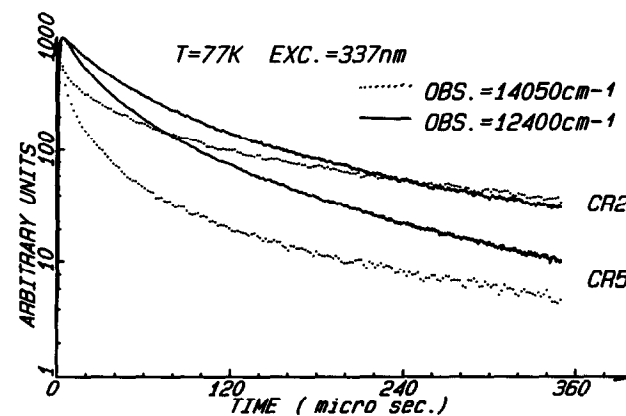


Fig. 5. Dependence of the fluorescence decay profiles on observation frequency and Cr³⁺ content at 77 K. Excitation at 29 674 cm⁻¹; observation at 14 050 cm⁻¹ (dotted lines) and 12 400 cm⁻¹ (full lines).

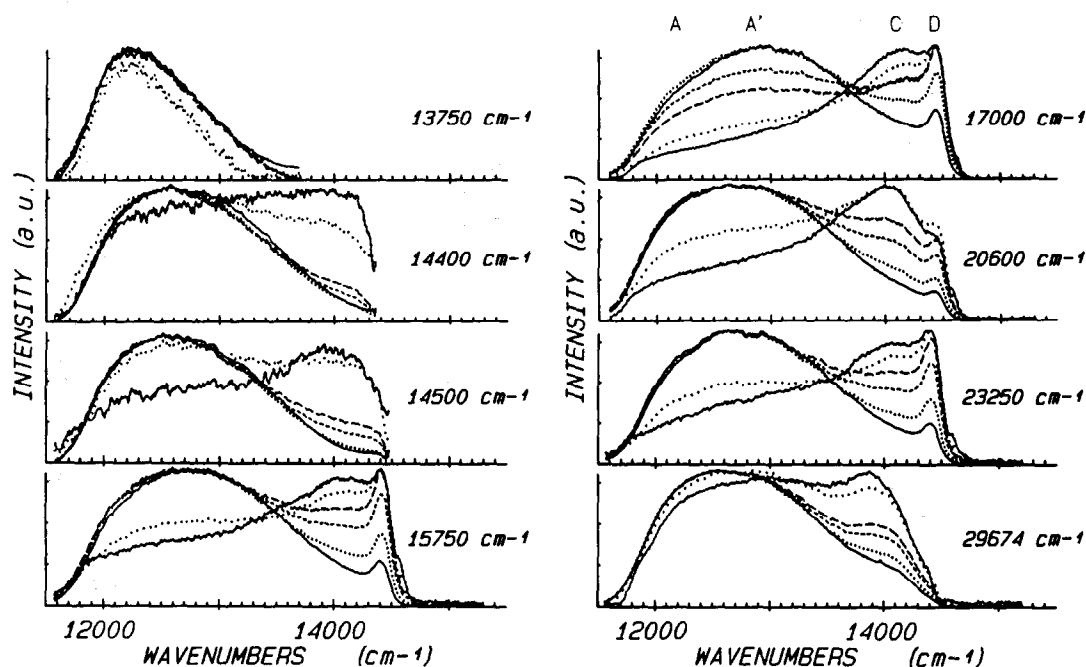


Fig. 6. Time-resolved emission spectra of sample CR2 as a function of the excitation frequency at 77 K. Gate/decay times in μs are: —, 10/50; 50/100; ---, 100/170; - · - · - ·, 150/150; ○○○○○○, 300/300; and — · — · — ·, 500/300.

CR2 and CR10 the short lifetime components of band A are ~ 15 and $3 \mu\text{s}$, respectively, at 300 K, and 30 and $5 \mu\text{s}$ at 77 K. The long lifetime components for CR2 and CR10 are 45 and $35 \mu\text{s}$, respectively, at room temperature and 70 and $54 \mu\text{s}$ at 77 K. The non-exponential behaviour of the decay profiles does not change very much with temperature and becomes almost constant below 100 K.

Below 15000 cm^{-1} the emission spectrum of sample CR2 is strongly time-dependent. Therefore, it was investigated in detail at 77 K varying the excitation energy from 29674 to 13750 cm^{-1} (Fig. 6). To compare the spectra the time-resolved emissions during each scan were recorded with the same set of delays and gates, i.e. with 10/50, 50/100, 100/170, 150/150, 300/300 and 500/350 μs . Four bands centred at 12350 (A), 12800 (A'),

14100 (C) and 14480 (D) cm^{-1} could be resolved. The intensity ratio of these bands depends on both the time elapsed after the excitation pulse and the excitation frequency. Due to the strong deviation from an exponential decay, the lifetimes could not be determined. The bands were, therefore, classified in the sequence A', A, D and C according to their increasing decay time. The decay times range from some hundred μs to ms.

Band A could still be excited at 13700 cm^{-1} , which indicates a Stokes shift of $\sim 1500 \text{ cm}^{-1}$. The lowest excitation frequency for band A' was not determined since A and A' were not time-resolved under excitation in the 13700 – 15000 cm^{-1} range. The width of the A–A' signal, however, is enlarged with increasing excitation energy. In contrast to the fast-decaying bands A and A', the Stokes shift of

Table 2. Summary of experimental data. Band frequencies are given in cm^{-1}

Material	${}^3\text{E} \Rightarrow {}^4\text{A}_2$	${}^4\text{A}_2 \Leftrightarrow {}^4\text{T}_2$		${}^4\text{A}_2 \Leftrightarrow {}^4\text{T}_1$		Assignment	Reference
	Emission	Emission	Absorption	Emission	Absorption		
Glasses*		12000–12600	15200–15900		22600–23300	LFS	2, 3, 10, 14, 15
Mullites**	14280–14390	13300–13700 [†]	16700–17200		≈ 25000	HFS	2, 3, 4, 5, 15
Kyanite	14180		≈ 17150		≈ 23900	HFS (A)	9
	14210	13250	≈ 16240		≈ 23150	HFS (B)	9
Sillimanite		12400				LFS (C)	9
Ruby	14417–14446		18300		25000	LFS	8
CR2	14480 (D)		18520	>21300	24520	HFS	This work
CR2		14000 (C)				IFS	This work
CR5, CR7.5		13600 (B)				IFS	This work
CR2		12350 (A)	16280	<21300	22440	LFS	This work
CR2		12800 (A')	16280			LFS	This work

*Silicate and other oxide glasses.

**Cr poor mullites originated in crystallization of aluminoborosilicate glasses.

[†]Band maximum depends on excitation frequency, attributed to IFS.

the two long-lived bands, C and D, was estimated to be $< 300 \text{ cm}^{-1}$ because these bands could still be excited at 14400 and 14500 cm^{-1} , respectively. The intensity of the long-lived and narrow band D runs through a minimum at the excitation frequency of 21000 cm^{-1} . It could not be excited at the energy of 29674 cm^{-1} . The spectroscopic data are listed in Table 2 and compared with literature data of some reference samples.

4 Discussion

The fast-decaying, high frequency emission band E was observed in all samples. It is assigned to the ${}^4T_1 \Rightarrow {}^4A_2$ spin-allowed transition and corresponds to the main absorption band at 24520 cm^{-1} . The Stokes shift is $\sim 3000 \text{ cm}^{-1}$. This value is of the same order as observed for ${}^4T_2 \Rightarrow {}^4A_2$ transitions in silicate glasses.¹³ For both these transitions, which occur between the t_2^3e and t_2^3 configurations, electron-phonon coupling has to be taken into account. The Stokes shift of 3000 cm^{-1} includes (i) twice the maximum frequency of the involved phonons (relevant to the Huang-Rhys parameter) and (ii) the inhomogeneous broadening of the zero phonon line due to a distribution of Cr sites for which the crystal field continuously varies. This interpretation is supported by the band width of 5000 cm^{-1} , which indicates a convolution of the state density of the involved phonons with the inhomogeneous zero phonon band. Moreover, both high and low field chromium sites may contribute to the unusual broadening of the zero phonon band. Because of the lack of spectral and time resolution inside the E band, the above-mentioned contributions cannot be separated. A similar band width for the ${}^4A_2 \Rightarrow {}^4T_2$ absorption was reported for transparent mullite glass-ceramics.¹⁵

In sample CR10 only band A is observed. According to its low energy, this fast-decaying band is ascribed to ${}^4T_2 \Rightarrow {}^4A_2$ transitions of Cr³⁺ in low field sites. The shoulder B, clearly observable only when the delay times were $> 500 \mu\text{s}$ and occurring only in the spectra of samples CR5 and CR7.5, is difficult to assign. The long decay time could be indicative of high field sites; however, the band width and the energy of the shoulder rules out this possibility. Band C appears at intermediate delay times of $\sim 150 \mu\text{s}$ and does not occur at other delay times. Regarding the intensities of the bands A, B and C, the dominant band A suggests that predominantly low field sites of Cr³⁺ exist in the samples CR5, CR7.5 and CR10.

In spite of the energy transfer due to different non-radiative relaxation processes, the emission spectra of CR2 show a significant degree of site

selection which is emphasized by the kinetic behaviour as shown in the spectra of Fig. 6. The time-resolved spectra reveal the presence of two bands, A and A', in the low energy range. The decay of A and A' is fast and, hence, they are assigned to ${}^4T_2 \Rightarrow {}^4A_2$ transitions of two families of chromium low field sites. In previous investigations,^{3,5,15} only one band at about 12500 cm^{-1} was observed in this energy range. As for the E band this interconfigurational transition ($t_2^3e \Rightarrow t_2^3$) is phonon-assisted. The Stokes shift of 1500 cm^{-1} for band A was estimated from the limit of the site-selective excitation. It is significantly smaller than the Stokes shift of band E. This may be explained by assuming that only a small fraction of Cr³⁺ centres within a given distribution of low field sites was excited. In such a case the band width may be reduced to its homogeneous width. Furthermore, the excitation can still occur with low energy phonons, i.e. close to the zero phonon line.

The sharp long-lived band D at 14480 cm^{-1} is close to the ruby R-lines at 14417 and 14446 cm^{-1} . It is, therefore, attributed to transitions between the states 2E and 4A_2 which belong to Cr³⁺ ions at high field sites. The transition ${}^2E \Rightarrow {}^4A_2$ occurs within the t_2^3 configuration and is not vibronically broadened. Its inhomogeneous width of about 120 cm^{-1} indicates a certain variation of high field sites. The low fluorescence efficiency and the strong diffuse reflectance did not allow to observe resonantly this transition, but close to the excitation at 14500 cm^{-1} the emission band appears at 14400 cm^{-1} . Thus, the Stokes shift of $\sim 100 \text{ cm}^{-1}$ or even less indicates a weak phonon coupling.

The A/A' and D bands are usually encountered in silicate and aluminosilicate ceramics as well as in the corresponding glasses.^{2,4,5,14,15} They were identified without difficulty. In contrast, the origin of the C band around 14000 cm^{-1} is not clear. So far this band has not yet been mentioned in the literature, except for a band at 13700 cm^{-1} in a transparent glass-ceramic.¹⁴ The decay of C band is longer than the decay of high field site transitions between 2E and 4A_2 . The maximum frequency as well as the band width of about 800 cm^{-1} classify it just between LFS and HFS emissions. It is still present under a 14400 cm^{-1} excitation, which indicates a Stokes shift of $\sim 400 \text{ cm}^{-1}$. We ascribe it, therefore, to intermediate field sites (IFS) of Cr³⁺ for which the crystal field parameters lies in the crossing region of the 4T_2 and 2E states. Nevertheless, the long decay and the small Stokes shift are not well understood. A distribution of Cr³⁺ at intermediate field sites was already mentioned by some authors^{5,15} and, hence, an emission from both 4T_2 and 2E states may be expected. The intermediate field sites of Cr³⁺ are not restricted to

centres which obey the condition $\Delta E = {}^4T_2 - {}^2E = 0$. Cr^{3+} energy states which differ at 77 K from the above condition by less than $\pm 100 \text{ cm}^{-1}$ may be activated thermally to emit from the two levels. Further, the states 4T_2 and 2E should be in thermal equilibrium and, thus, emission from both levels should occur with the same decay. However, this consideration may not apply to bands D and C because they show a different time behaviour. Moreover, as pointed out by Andrews *et al.*,¹⁵ a two-level thermally equilibrated system could not be applied to the data obtained for Cr^{3+} in transparent glass-ceramics in the temperature range 77 to 298 K. A more sophisticated model,¹¹ with adequate parameters, and which includes spin-orbit and vibronic coupling effects in the crossing region, is needed to explain the nature of the C band. The admixture of wave functions with predominant 2E character, for example, could explain the long lifetime. Furthermore, a certain separation between the 2E and 4T_2 branches in the coupling region may explain the lowering of the emitting level with respect to the pure 2E level and the fact that no emission from the upper level occurs.

The intensity calibration of the time-resolved emission spectra was difficult because the intensities of the dye lasers are wavelength-dependent. Seven different dyes were required for the excitation beam to cover the range from 13 500 to 23 500 cm^{-1} . Further, reproducibility of the optical set-up was hard to achieve. Therefore, the selectivity of the spectra with respect to the individual chromium sites in mullite was estimated by the intensity ratios $(I_{14480}/I_{12900})_2$ and $(I_{14000}/I_{12900})_4$ of the bands D, C and A'. The subscripts 2 and 4 denote the second and fourth gates (see Fig. 6) through which bands D and C could best be resolved. The ratios (Fig. 7) reflect the spectral selectivity of the long-lived bands with respect to the fast-decaying bands, i.e. HFS/LFS ratios. The curves in Fig. 7 correspond roughly to the absorption spectrum of both high and low field chromium sites. Although the experimental accuracy of these plots is not high, two small dips at 14 600 and 14 800 cm^{-1} should be noted. A similar fine structure also appeared in the ${}^4A_2 \Rightarrow {}^4T_2$ absorption band in Cr-doped glasses.^{10,14} The most probable interpretation is a Fano anti-resonance between the 4T_2 vibrational quasi-continuum and the 2T_1 and 2E discrete levels.

In the mullite sample with the lowest Cr_2O_3 content, bands D and C indicate high and intermediate field sites and bands A and A' two kinds of low field site. This corresponds to the observations in mullite glass-ceramics with low Cr contents which exhibit high and low field sites, though the major part of Cr^{3+} may occur in high

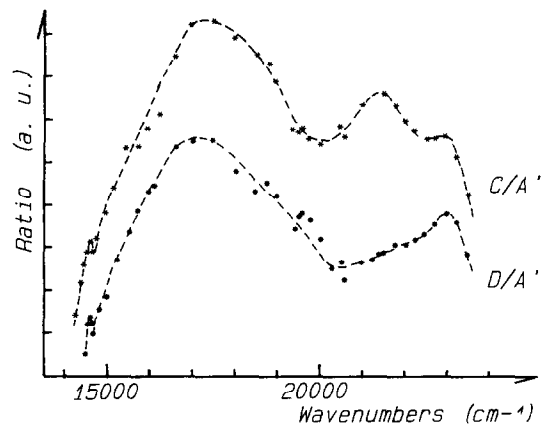


Fig. 7. Spectrum of the excitation ratios C/A' and D/A' bands in sample CR2 at 77 K.

field site domains.⁴ In mullites with intermediate and high Cr_2O_3 contents only the band A can be clearly observed. The results are interpreted in the following way: at low Cr_2O_3 contents the predominantly high field Cr sites are explained by Cr^{3+} at octahedral M(1) positions (position (2a) in the space group *Pham* of mullite). With increasing Cr concentration in the mullite structure, low field Cr sites predominate which are described as distorted interstitial Cr sites. The fluorescence spectroscopic results presented here, i.e. the occurrence of at least two different structural Cr sites in mullite, agree well with spectroscopic investigations by electron paramagnetic resonance (EPR) and by optical absorption.^{1,7}

Finally, we would like to comment on the non-exponential behaviour of the band decays observed in all samples. This observation is not surprising because it was likewise reported for transparent mullite glass-ceramics.^{5,15} It is explained by an excitation transfer between the Cr^{3+} ions which increases with increasing Cr content and temperature. An energy transfer mechanism from HFS to LFS was proposed in the literature.³ However, other transfer mechanisms among Cr sites of the same kind cannot be excluded. Thus, for band A of sample CR10 (Fig. 2), which was identified as ${}^4T_2 \Rightarrow {}^4A_2$ transitions of low field chromium sites, a transfer from high to low energy sites within a distribution of low field sites could explain the observed shift towards lower energy as the delay time increases. Generally, excitation transfers are assumed to be responsible for the poor selectivity when applying site-selective excitations, as can be seen in Fig. 6.

5 Conclusion

In this work time-resolved fluorescence spectroscopy was applied in a wide time range to investi-

gate Cr sites in heavy doped mullite. ${}^4T_2 \Rightarrow {}^4A_2$, ${}^4T_2 \Rightarrow {}^4A_2$ and ${}^2E \Rightarrow {}^4A_2$ emissions were separated. As in low Cr content mullite glass-ceramics, high and low field chromium sites have been detected. The further findings are summarized as follows.

1. At least two types of low field chromium site occur in the mullite structure.
2. In addition to the 14480 cm⁻¹ band which is attributed to high field chromium sites, another band at 14000 cm⁻¹ with the longest observed decay time appears. It is assigned to intermediate field chromium sites. The 2E character of the emitting level of this band is retained despite its unusual low energy.
3. In mullites containing high Cr₂O₃ contents, Cr³⁺ ions are mostly located in low field sites with a certain variation of their crystal fields. All sites have the 4T_2 state as the lowest level.
4. High field Cr sites are predominant in Cr₂O₃-poor mullites. They are correlated with incorporation of Cr³⁺ at octahedral M(1) positions replacing Al³⁺. Upon increasing the Cr₂O₃ content Cr³⁺ favourably enters the highly distorted low field sites, which are attributed to interstitial lattice positions in the mullite structure.
5. Strong deviation from an exponential decay is observed for all emission bands at room and low temperatures (22 K). This may be explained by an energy transfer between different Cr sites which occurs even at low temperatures.

References

1. Schneider, H., Okada, K. & Pask, J. A., *Mullite and Mullite ceramics*, John Wiley and Sons, Chichester, 1994.
2. Wojtowicz, A. J. & Lempicki, A., Luminescence of Cr³⁺ in mullite transparent glass ceramics (II). *J. Lumin.*, **39** (1988) 189–203.
3. Knutson, R., Liu, H., Yen, W. E. & Morgan, T. V., Spectroscopy of disordered low-field sites in Cr³⁺: mullite glass ceramic. *Phys. Rev. B*, **40** (1989) 4264–70.
4. Liu, H., Knutson, R. & Yen, W.M., Saturation-resolved-fluorescence spectroscopy of Cr³⁺ mullite glass ceramic. *Phys. Rev. B*, **41** (1990) 8–14.
5. Liu, H., Knutson, R., Jia, W., Strauss, E. & Yen, W. M., Spectroscopic determination of the distribution of Cr³⁺ sites in mullite ceramics. *Phys. Rev. B*, **41** (1990) 12888–94.
6. Schneider, H., Transition metal distribution in mullite. *Ceram. Trans.*, **6** (1990) 135–58.
7. Rager, H., Schneider, H. & Graetsch, H., Chromium incorporation in mullite. *Am. Mineral.*, **75** (1990) 392–7.
8. Wojtowicz, A. J. & Lempicki, A., Luminescence of Cr³⁺ in sillimanite. *Phys. Rev. B*, **39** (1989) 8695–701.
9. Wojtowicz, A. J., Luminescence of Cr³⁺ in kyanite. *J. Lumin.*, **50** (1991) 221–30.
10. Brawer, S. A. & White, W. B., Optical properties of trivalent chromium in silicate glasses: a study of energy levels in the crossing region. *J. Chem. Phys.*, **67** (1977) 2043–55.
11. Donnelly, C. J., Healy, S. M., Glynn, T. J., Imbush, G. F. & Morgan, G. P., Spectroscopic effects of small 4T_2 - 2E energy separations in 3d³-ion systems. *J. Lumin.*, **42** (1988) 119–25.
12. Wojtowicz, A. J., Grinberg, M. & Lempicki, A., The coupling of 4T_2 and 2E states of Cr³⁺ ion in solid state materials. *J. Lumin.*, **50** (1991) 231–42.
13. Piriou, B., Dexpert-Ghys, J., Bastide, B. & Odier, P., Martensitic transformation of TZP investigated by site selective spectroscopic method. *Proceedings of Zirconia 88*, 17 November 1988, Bologna.
14. Andrews, L. J., Lempicki, A. & McCollum, B. C., Spectroscopy and photokinetics of chromium (III) in glass. *J. Chem. Phys.*, **74** (1981) 5526–38.
15. Andrews, L. J., & Lempicki, A., Luminescence of Cr³⁺ in mullite transparent glass ceramics. *J. Lumin.*, **36** (1986) 65–74.

EXAFS Studies of Cr-doped Mullite

K. R. Bauchspieß,^{a,*} H. Schneider^b & A. Kulikov^c

^aSchool of Mathematical and Physical Sciences, Murdoch University, Perth, WA 6150, Australia

^bGerman Aerospace Research Establishment (DLR), Institute for Materials Research, D-51140 Köln, Germany

^cInstitute of Chemistry, Russian Academy of Sciences, Vladivostok 690022, Russia

(Accepted 22 July 1995)

Abstract

Mullites doped with 7.3 (Cr 6) and 11.5 wt% Cr₂O₃ (Cr 10) were synthesized by reaction sintering of Al₂O₃, SiO₂ and Cr₂O₃ powder compacts at 1650°C in air. Prior to the spectroscopic analyses, the powder samples were HF/HCl-washed in order to remove coexisting glassy phases. According to X-ray diffractometry all samples consisted of mullite only.

Measurements of the extended X-ray absorption fine structure (EXAFS) of the Cr K edge of mullite were performed at the Photon Factory, National Laboratory of High Energy Physics (KEK), in Tsukuba, Japan. The measured spectra were normalized by first subtracting a pre-edge background and then fitting a smoothly varying cubic-spline background in the region of the EXAFS. For all measured spectra the magnitude of the Fourier transform, which is related to the pair distribution function (PDF) and similar to it, is characterized by two pronounced peaks. The first peak is ascribed to oxygen making up the octahedra surrounding the Cr atoms and the second peak is assumed to be due to Al. It turned out that the second peak could not be fitted satisfactorily with one Al coordination shell alone. The discrepancy can be reduced by assuming that there is an additional contribution from Cr atoms that do not occupy regular lattice sites but are displaced by some amount. The existence of such displaced Cr atoms is known from EPR and crystal field spectroscopy experiments. Since these Cr atoms are not in the center of the Al coordination shell, the Al PDF seen by these Cr atoms is broadened and also slightly asymmetric. From our data analysis we find the displacement of the Cr atoms from the center of their surrounding aluminum coordination shell to be 0.50 Å.

1 Introduction

Mullite has the general composition Al_{4+2x}Si_{2-2x}

O_{10-x} (0.25 ≤ x ≤ 0.4).¹ The orthorhombic crystal structure of mullite contains chains of edge sharing AlO₆ octahedra running parallel to the crystallographic *c*-axis. Octahedral columns are crosslinked by tetrahedra double chains with randomly distributed Al and Si atoms. Tetrahedra double chains also run parallel to *c*. Some O atoms bridging adjacent tetrahedra are removed and as a consequence a new tetrahedral site is formed, in which the bridging O atoms belong to three tetrahedra (e.g. Refs 2–4).

Earlier work on the doping of mullite with Cr was performed by Gelsdorf *et al.*,⁵ Murthy and Hummel,⁶ and Rager *et al.*⁷ It has been stated that up to 12 wt% Cr₂O₃ is incorporated in mullite. A detailed study of the crystal chemistry of Cr-doped mullites prepared by reaction sintering of Al₂O₃, SiO₂ and Cr₂O₃ (0.5–11 wt%) powders, was performed by Rager *et al.*¹³ Rager *et al.* found a reciprocal and equimolar dependence between Cr₂O₃ and Al₂O₃ in mullite, but not between Cr₂O₃ and SiO₂ contents. They concluded that Cr³⁺ is incorporated by replacement of Al³⁺. The structural state (*x*-value) of Cr-doped mullite, which corresponds to that of 3/2-type mullite, indicates that the variation of Cr incorporation is not correlated with a change of the amount of O(C) oxygen vacancies in mullite.

Electron paramagnetic resonance (EPR) studies provided information on the structural distribution of Cr in mullite:⁷ Cr-doped mullites exhibit two sharp EPR signals near $g_{\text{eff}} = 5$, and a broad signal near $g_{\text{eff}} = 2.2$. The peaks near $g_{\text{eff}} = 5$ were assigned to Cr³⁺ in slightly distorted octahedral Al chain positions in mullite. The broad, slightly asymmetric signal near $g_{\text{eff}} = 2.2$ may indicate coupling between localized magnetic moments, and was associated with interstitial Cr³⁺ incorporation in mullite. According to the EPR peak intensities the entry of Cr³⁺ into the regular AlO₆ octahedra is favoured at low bulk Cr₂O₃ contents of mullite, whereas interstitial incorporation with formation of Cr clusters becomes more important at higher Cr₂O₃ contents. Unpolarized crystal field spectra

*To whom correspondence should be addressed.

measured by Ikeda *et al.*⁸ in the wavelength range from 340 to 1540 nm by reflection from mullite powders with about 8 wt% Cr₂O₃ yielded further evidence for the structural distribution model of Cr³⁺ developed by Rager *et al.*⁷

2 Sample Material

Samples were prepared from about 4 g of chemically pure Al₂O₃ (VAW, 302), SiO₂ (Ventron, 88316), and Cr₂O₃ (Merck, 2483) powders, with 62-*x* wt% Al₂O₃, 38 wt% SiO₂, and *x* wt% Cr₂O₃ (*x* = 6, 10; designated as samples Cr 6 and Cr 10). The mixtures were pressed into disks of 20 mm diameter and 5 mm thickness in a pressing mold using uniaxial pressure loading, in a laboratory furnace in air at 1650°C. Prior to the EXAFS measurements the samples were HF/HCl-washed in order to leach the coexisting glassy phase. According to X-ray diffractometry all HF/HCl-treated samples consisted of mullite only. The actual chemical compositions of acid washed mullites determined by microprobe analysis were: Cr 6: Al₂O₃:64.1 wt%, SiO₂:28.5 wt%, Cr₂O₃:7.3 wt%, and Cr 10: Al₂O₃:60.0 wt%, SiO₂:28.4 wt%, Cr₂O₃:11.5 wt % (see Ref. 7).

3 EXAFS Measurements

3.1 Basic considerations

EXAFS spectroscopy measures the pair distribution function with respect to the absorbing atom as center. The pair distribution function $P(R)$ about the X-ray absorbing atom is defined through

$$N(R) = 1 + \int_0^R P(\tilde{R}) d\tilde{R} \quad (1)$$

$N(R)$ is the number of atoms contained in a sphere of radius R centered at the X-ray absorbing atom. Hence, integrating $P(R)$ yields the number of atoms in the system. (The radial distribution function $g(R)$ is obtained via $g(R) = P(R)/(4\pi\nu R^2)$, where ν is the number density.) In a solid the atoms can be grouped in coordination shells about a given atom and $P(R)$ can be written as a sum over S coordination shells:

$$P(R) = \sum_{j=1}^S P_j(R) \quad (2)$$

The EXAFS function, $\chi(k)$, is given by the following expression:

$$\chi(k) = S_0^2 \cdot \sum_{j=1}^S \frac{1}{k_j} \int_0^{\infty} \frac{dR}{R^2} |f_{b,j}(k_j, R, \pi)| \cdot \exp \quad (3)$$

$$(-2R/\lambda_j(k_j)) \cdot P_j(R) \cdot \sin(2k_j R + \delta_c(k_j) + \delta_{b,j}(k_j, R, \pi))$$

R is the distance from the absorbing atom (Cr) and k_j is the magnitude of the wavevector of the photoelectron. The atoms of different coordination shells may experience different potentials and therefore the photoelectron wavevector k_j of a coordination shell must be adjusted. k_j is related to the wavevector k of the data by means of an adjustable energy shift ΔE_j :

$$k_j = \sqrt{k^2 - \Delta E_j/\gamma} \text{ with } \gamma \equiv \frac{h^2}{8\pi^2 m_e} \cong 3.81 \text{ eV\AA}^2 \quad (4)$$

$|f_{b,j}(k_j, R, \pi)|$ and $\delta_{b,j}(k_j, R, \pi)$ are magnitude and phase of the complex backscattering amplitudes $f_{b,j}(k_j, R, \pi)$, and $\delta_c(k_j)$ is the central-atom phaseshift (of Cr) for K-shell absorption. $\lambda_j(k_j)$ is the inelastic mean free path of the photoelectron. S_0^2 is an overall amplitude reduction factor due to multi-electron excitations. Since the R -dependence of $f_{b,j}(k_j, R, \pi)$ is weak, R can be replaced by its average value R_j for shell j , as far as the backscattering amplitude is concerned, and eqn (3) becomes:

$$\chi(k) = S_0^2 \cdot \sum_{j=1}^S \frac{|f_{b,j}(k_j, R_j, \pi)|}{k_j} \int_0^{\infty} \frac{dR}{R^2} \exp$$

$$(-2R/\lambda_j(k_j)) \cdot P_j(R) \cdot \sin(2k_j R + \delta_c(k_j) + \delta_{b,j}(k_j, R_j, \pi)) \quad (5)$$

In the harmonic approximation it is assumed that the pair distribution functions $P_j(R)$ are Gaussians:

$$P_j(R) = \frac{N_j}{\sigma_j \sqrt{2\pi}} \exp(-(R-R_j)^2/2\sigma_j^2) \quad (6)$$

N_j is the number of atoms in shell j . Inserting eqn (6) into eqn (5) one obtains the standard EXAFS formula:

$$\chi(k) = S_0^2 \cdot \sum_{j=1}^S \frac{N_j}{k_j R_j^2} |f_{b,j}(k_j, R_j, \pi)| \cdot \exp(-2R_j/\lambda_j(k_j)) \cdot \exp(-2\sigma_j^2 k_j^2) \cdot \sin(2k_j R_j + \delta_c(k_j) + \delta_{b,j}(k_j, R_j, \pi)) \quad (7)$$

From the measured EXAFS data one can obtain a first guess at the pair distribution function by calculating the Fourier transform. This is done according to:

$$H(R) = \frac{1}{\sqrt{\pi}} \int_{-\infty}^{\infty} w(k) \chi(k) k^p e^{+i2kR} dk \quad (8)$$

Here the term k^p was introduced in order to compensate for the decrease of $\chi(k)$ with k . $w(k)$ is a Hamming window function⁹ and is applied in

order to suppress sidelobes in the Fourier transform. $w(k)$ vanishes everywhere except on the interval $k_{\min} \leq k \leq k_{\max}$ where it is given by:

$$w(k) = 0.54 + 0.46 \cos(2\pi k/\Delta k) \text{ with } \Delta k = k_{\max} - k_{\min} \quad (9)$$

$H(R)$ is a complex function whose magnitude is related, but not equal, to the pair distribution function. In order to extract quantitative information from the data one has to employ curve fitting techniques.

3.2 Experimental procedure

The EXAFS experiments were carried out at Beamline 7C of the Photon Factory, National Laboratory for High Energy Physics, Japan. The positron storage ring was operating at 2.5 GeV and had a beam lifetime of about 70 h. The average positron current during the measurements was 270 mA. Measurements of the Cr K edge EXAFS were performed on mullite samples doped with 7.3 and 11.5 wt% Cr_2O_3 (samples Cr 6 and Cr 10, see Section 2). Samples with an absorption thickness product of about 2 in the region just after the edge were mounted on Scotch Tape. The spectra were measured in transmission, with the first ion chamber filled with N_2 gas and the second filled with a mixture of 25% Ar and 75% N_2 . In order to suppress harmonics in the X-ray beam the Si(111) double-crystal monochromator was detuned from parallelism such that the output intensity decreased by at least 50%.

4 Results of EXAFS Data Analysis

The EXAFS was extracted from the measured X-ray absorption spectra by normalizing the spectra in the usual way. First, the pre-edge region was fitted to a Victoreen-type background: $A_0 + A_3/E^3 + A_4/E^4$. E is the X-ray energy. The background was then extended into the edge and post-edge region and subtracted from the whole spectrum.

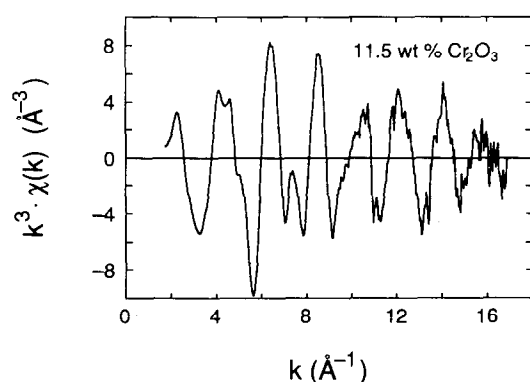


Fig. 1. k^3 -multiplied normalized EXAFS spectrum for the Cr 10 sample (~ 11.5 wt% Cr_2O_3) measured at 300 K.

After converting the spectrum above the energy E_{edge} of the absorption edge to the wavevector scale k according to $k = \sqrt{(E - E_{\text{edge}}) \cdot 8\pi^2 m_e / h^2}$ a second background was fitted to the EXAFS region of the spectrum. This background consisted of a smoothing spline $s(k)$ using cubic polynomials¹⁰. The EXAFS, $\chi(k)$ was then obtained by forming the difference between the data $y(k)$ and the background and dividing by the height D of the absorption step at the edge: $\chi(k) = (y(k) - s(k))/D$. One such normalized spectrum is shown in Fig. 1. The spectrum has been multiplied by k^3 in order to compensate for the decrease of the envelope with k . The data analysis is carried out using three different models, labelled 1, 2 and 3 and described below.

4.1 Model 1

For the samples investigated in this work, the magnitude of the Fourier transform, calculated according to eqn (8) and for $p = 3$, is dominated by two peaks (Fig 2(a)). The first peak is due to the nearest-neighbour (NN) O atoms that surround the Cr atoms. The second peak is assumed

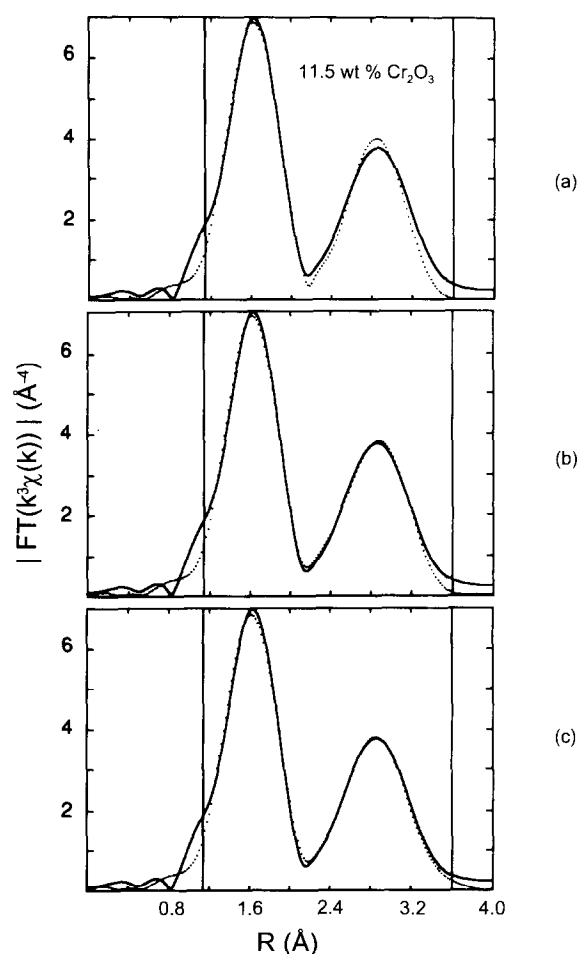


Fig. 2. Fourier transform magnitude for the Cr 10 sample (~ 11.5 wt% Cr_2O_3) measured at 300 K (solid line) and fit data (dotted line) from a simultaneous fit to three datasets: (a) with two coordination shells (O and Al) each; (b) with three coordination shells each; (c) with three coordination shells each, but taking the displacements of Cr atoms explicitly into account.

to be due to a next-nearest neighbour (NNN) coordination shell consisting of Al and/or Si atoms. It is impossible in EXAFS spectroscopy to distinguish between backscattering from Al and from Si atoms because Al and Si are too close in atomic number. Hence, it was assumed that the NNN coordination shell consisted of Al atoms only. In order to obtain quantitative information, the O and Al shells were curve fitted using a program developed by one of the authors.¹¹ The spectra were first fitted according to the standard EXAFS formula (eqn 7). Amplitudes and phases of the shells were calculated using the single-scattering version of the FEFF code (version 3.1.1).¹² In a fit using the harmonic approximation there are four parameters that can be varied for each coordination shell: ΔE_j , R_j , σ_j^2 and N_j . Least-squares fits to both coordination shells were carried out simultaneously to the real and imaginary parts of the Fourier transform. The Fourier transform of $k^3\chi(k)$, with $\chi(k)$ according to eqn (7), was fitted to the Fourier transform of the k^3 -multiplied data. The data that was fitted was for the Cr10 sample measured at 300 and at 150 K, and for the Cr 6 sample measured at 300 K. Three such datasets were fitted in real space simultaneously. By fitting multiple spectra one is able to include constraints on the fitting parameters and reduce the number of variable parameters per dataset. For example, one can exploit the fact that the energy corrections ΔE are identical for each atom type and that the coordination numbers are temperature independent. A typical fit carried out in this way is shown in Fig. 2. The fit interval is indicated by the vertical lines, and 16 variable fit parameters were employed for the simultaneous fit to three datasets with two shells each. There is a shoulder, which could not be fitted, at about 1 Å at the low R side of the oxygen peak. Assuming two oxygen shells could not reduce the discrepancy and thus only one O shell will be used.

The spectra had been fitted ignoring the amplitude reduction factor S_0^2 . Therefore, the coordination numbers had come out too low. From the absence of a peak just before the Cr K absorption edge one knows that the immediate Cr environment has inversion symmetry¹³ and one can thus assume that each Cr atom is octahedrally coordinated. With 6 oxygen atoms around each Cr atom, but only 4.3 atoms obtained from the data analysis, we conclude that for the data in Table 1 $S_0^2 = 0.72$. Values of S_0^2 are usually around 0.7. For Fe, which is near to Cr in the periodic table, a value of 0.69 is reported.¹⁴ Using $S_0^2 = 0.72$ one obtains for the Al coordination numbers $N_{Al} = 6.9$.

Special attention has been given to error estimation. Using a method outlined in Ref. 15, the

Table 1. Results of a simultaneous fit to three datasets with two coordination shells each

	R_O ΔR_O (Å)	σ_O^2 $\Delta\sigma_O^2$ (10^{-4} Å ²)	N_O ΔN_O	R_{Al} ΔR_{Al} (Å)	σ_{Al}^2 $\Delta\sigma_{Al}^2$ (10^{-4} Å ²)	N_{Al} ΔN_{Al}
7.3 wt%	1.985	34	6	3.258	42	6.9
300 K	± 0.004	± 4	± 0	± 0.007	± 7	± 0.6
11.5 wt%	1.984	33	6	3.261	47	6.9
300 K	± 0.004	± 4	± 0	± 0.007	± 7	± 0.6
Cr 10	1.984	28	6	3.258	36	6.9
150 K	± 0.004	± 4	± 0	± 0.006	± 6	± 0.6

$$\Delta E_O = 0.6 \text{ eV} \pm 1.0 \text{ eV}; \Delta E_{Al} = -10.4 \text{ eV} \pm 1.1 \text{ eV}; S_0^2 = 0.72 \pm 0.04.$$

error of a variable parameter in an n parameter fit was determined by giving this parameter fixed values around the optimum and for each given value performing an $n-1$ parameter fit with the remaining fit parameters. This method is computationally intensive but properly takes into account all parameter correlations. The error bars were obtained from the width of the minima of the residual sums of squares (χ^2) curves. In order to determine up to which value χ_{\max}^2 along each χ^2 curve to go, it is assumed that the error for ΔE_O for the first coordination shell (O) is ± 1.0 eV. This determines χ_{\max}^2 and all other errors are then determined from the parameter values where χ^2 becomes equal to χ_{\max}^2 . For S_0^2 the error is determined from the fit error for the number N_O of atoms in the first coordination shell (O). All error bars were found to be approximately symmetric. The error bars given here do not include systematical deviations resulting from the procedure of calculating the scattering phases and amplitudes. Hence the EXAFS results are precise but not necessarily accurate. The methods described here to estimate S_0^2 and to determine the errors of the fit parameters are used throughout this work.

The PDF that is shown in Fig. 3(a) was calculated according to eqn (6) and corresponds to the fit shown in Fig. 2(a). The position of the Al peak (~ 3.26 Å) corresponds to Cr atoms occupying regular lattice sites in the mullite structure. Closer inspection of the data reveals that the second peak (Al) is not fitted very well. This is not because only Al, and not also Si, was considered here. Instead, the discrepancy might be due to asymmetry in the pair potential of Cr and Al atoms. A cumulant analysis,¹⁶ including C_3 for the phase and C_4 for the amplitude, was attempted. However, no conclusive results could be obtained because there was not enough EXAFS signal available at the high- k end of the spectrum (Fig. 1), which is important for determining any cumulant terms. Considering the possible presence of other Cr atoms in the vicinity of the Cr absorber could

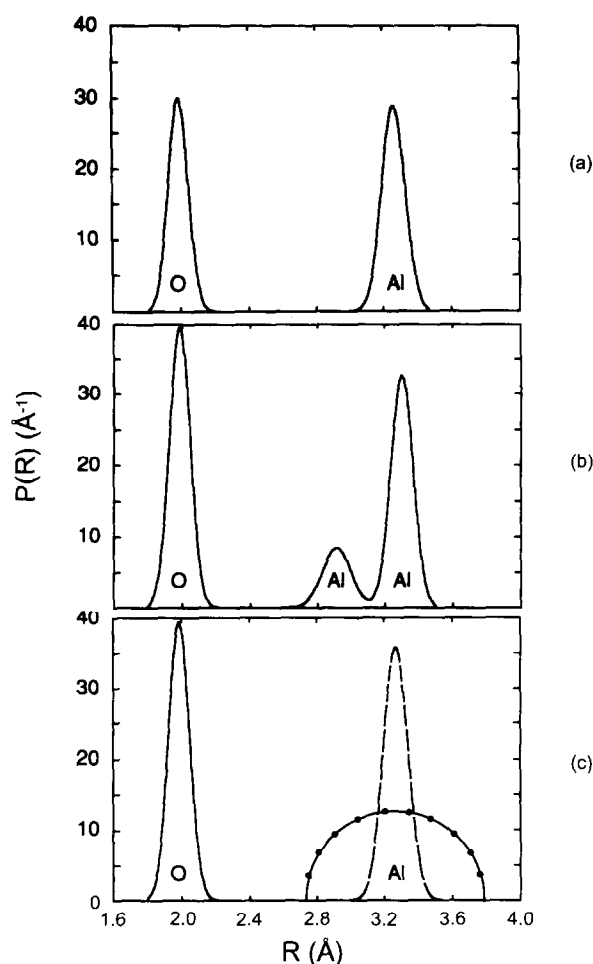


Fig. 3. Pair distribution function corresponding: (a) to the fit shown in Fig. 2(a); (b) to the fit shown in Fig. 2(b); (c) to the fit shown in Fig. 2(c); dashed line: Cr atoms in regular Al(1) sites, dotted line: Cr atoms in random interstitial sites.

not explain the discrepancy either and thus it had to be accounted for in other ways.

4.2 Model 2

The discrepancy can be reduced by including a third coordination shell, also consisting of Al atoms and close to the other Al shell. Again, three datasets were fitted simultaneously and the number of variable parameters is reduced by incorporating the constraints that all energy corrections ΔE are identical for each atom type and that the coordination numbers of each coordination shell

are the same for each dataset, that is, the coordination numbers are assumed to be independent of temperature and of Cr_2O_3 content. The simultaneous fit to three spectra, with three coordination shells each, had then 23 variable parameters for the 9 coordination shells. The fit for the Cr 10 sample measured at 300 K is shown in Fig. 2(b) and the fit results are listed in Table 2.

Comparing these results with those shown in Table 1 one finds that the total number of Al atoms about the absorbing Cr atoms is almost the same (7.2 compared to 6.9) except that they are now distributed over two coordination shells. Figure 3(b) shows the PDF corresponding to the fit of Fig. 2(b). The Al peak at ~ 2.9 Å probably describes the environment of the interstitial Cr atoms and the Al peak at ~ 3.3 Å describes the environment of the Cr atoms at the regular lattice sites. The asterisks in place of error bars for σ_{Al}^2 and N_{Al} for the coordination shell at ~ 2.9 Å indicate that the error was either very large or that it could not be determined because the minima of the χ^2 curves for σ_{Al}^2 and N_{Al} were too shallow. This means that σ_{Al}^2 and N_{Al} for the first Al coordination shell are not well defined.

For the 11.5 wt% Cr_2O_3 sample it can be seen from the table that the radius of the first Al shell decreases with increasing temperature. This anomalous behaviour could indicate an asymmetric PDF. However, taking asymmetry for this Al coordination shell into account is not practical because the correlation of the fit parameters becomes too large.

4.3 Model 3

In a third model, we now consider besides the Cr atoms occupying regular lattice sites, the effect of a large disorder of the interstitial Cr positions. These Cr atoms, with their NN oxygen octahedra, are assumed to be surrounded by an Al coordination shell of radius R_{O} but the average position of the Cr–O octahedra is off center by an amount ζ ($\zeta \geq 0$) as indicated in Fig. 4. The Al atoms are assumed to be continuously distributed over the coordination shell indicated in the figure. Neglecting atomic

Table 2. Results of a simultaneous fit to three datasets with three coordination shells each

	R_{O}	σ_{O}^2	N_{O}	R_{Al}	σ_{Al}^2	N_{Al}	R_{Al}	σ_{Al}^2	N_{Al}
	ΔR_{O}	$\Delta \sigma_{\text{O}}^2$	ΔN_{O}	ΔR_{Al}	$\Delta \sigma_{\text{Al}}^2$	ΔN_{Al}	ΔR_{Al}	$\Delta \sigma_{\text{Al}}^2$	ΔN_{Al}
	(Å)	(10^{-4}Å^2)		(Å)	(10^{-4}Å^2)		(Å)	(10^{-4}Å^2)	
7.3 wt%	1.985	37	6	2.92	64	1.8	3.30	40	5.4
300 K	± 0.004	± 4	± 0	± 0.04	*	*	± 0.02	± 20	± 1.6
11.5 wt%	1.984	37	6	2.91	73	1.8	3.30	40	5.4
300 K	± 0.004	± 4	± 0	± 0.04	*	*	± 0.02	± 20	± 1.6
11.5 wt%	1.984	31	6	2.93	54	1.8	3.29	35	5.4
150 K	± 0.004	± 4	± 0	± 0.03	*	*	± 0.02	± 15	± 1.6

$$\Delta E_{\text{O}} = 0.6 \text{ eV} \pm 1.0 \text{ eV}; \Delta E_{\text{Al}} = -3 \text{ eV} \pm 3 \text{ eV}; S_0^2 = 0.76 \pm 0.04.$$

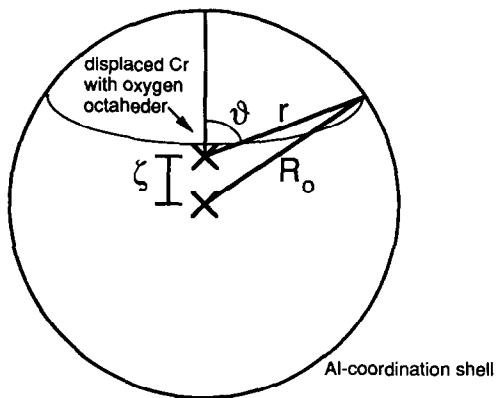


Fig. 4. Sketch of the displaced Cr atoms, octahedrally coordinated by six O atoms, but displaced from the center of the coordination sphere by the amount ζ . The Al atoms are assumed to be distributed continuously over the sphere.

vibrations for the moment, the distribution for the interstitial (displaced) Cr atoms ranges from $r = R_0 - \zeta$ to $r = R_0 + \zeta$. The number of Al atoms at distance r from a Cr atom displaced with its oxygen octahedra by ζ from the center of the Al coordination shell is proportional to the length $2\pi r \sin\vartheta(r)$ of the circle subtended by the angle ϑ (Fig. 4). The PDF for the Al atoms about the Cr atoms displaced by ζ is then:

$$P^*(r) = N_{\text{Al}} \frac{2\pi r \sin \vartheta(r)}{2\pi \int_{R_0 - \zeta}^{R_0 + \zeta} r \sin \vartheta(r) dr} \quad (10)$$

; $R_0 - \zeta \leq r \leq R_0 + \zeta$; $\zeta \geq 0$

The denominator is a normalization constant so that the total number of Al atoms in the coordination shell is N_{Al} . By eliminating $\vartheta(r)$, $P^*(r)$ can be brought into the form:

$$P^*(r) = N_{\text{Al}} \cdot \frac{1}{C} \cdot \sqrt{[1 - (r - R_0)^2/\zeta^2] \cdot [(r + R_0)^2/\zeta^2 - 1]} \quad (11)$$

where the normalization constant C is given by:

$$C = \int_{R_0 - \zeta}^{R_0 + \zeta} \sqrt{[1 - (r - R_0)^2/\zeta^2] \cdot [(r + R_0)^2/\zeta^2 - 1]} dr \quad (12)$$

The function $P^*(r)$ looks like a slightly asymmetric semicircle and is very broad compared to Gaussian widths. No disorder of the Al atoms, which will modify $P^*(r)$, has been considered because its effect will only lead to a negligible broadening of $P^*(r)$. The same applies to the distribution of ζ values. This was confirmed by numerically convolving $P^*(r)$ with distributions for R_0 and ζ . Hence, $P^*(r)$ is employed as in eqns (11) and (12), without any convolution. Since $P^*(r)$ is not Gaussian the harmonic approximation cannot be used and eqn (5) is employed instead in order to calculate the EXAFS corresponding to $P^*(r)$. In addition to the constraints imposed for the previous model it is assumed that the ratio of ζ/R_0 is the same for the three datasets. This assumption is justified because it had turned out in preliminary fits, where ζ and R_0 had been varied independently, that ζ/R_0 was approximately the same for each of the three datasets. A fit to three datasets simultaneously has then 21 variable parameters. The fit result for the sample with a Cr_2O_3 content of 11.5 wt% and measured at 300 K is shown in Fig. 2(c) and numerical values are given in Table 3.

Now there are no problems with the estimation of the errors. We plot the PDFs for both types of Cr atoms separately using these results. Figure 3(c) shows the PDF corresponding to the Cr atoms at regular lattice sites. There are 6.5 Al atoms at ~ 3.27 Å from the absorbing Cr atoms. The contribution from Cr atoms at random interstitial positions is also shown in Fig. 3(c) for the same sample. The Al peak is modified, according to the model presented here, and there are 10.1 Al atoms about the displaced Cr atoms. The average displacement is $\zeta = 0.50$ Å and the ratio ζ/R_0 is 0.154 ± 0.007 . It is apparent that the radii of the Al coordination shell around the Cr–O octahedra are also about 3.27 Å, just like the Al shell radii for the Cr atoms at regular sites. The number of Al atoms around the interstitial Cr atoms is now much higher than estimated in the previous model, where two Gaussian Al peaks were assumed (10.1 versus 1.8). This difference is possibly

Table 3. Results of a simultaneous fit to three datasets according to the third model

	R_0 ΔR_0 (Å)	σ_{O}^2 $\Delta \sigma_{\text{O}}^2$ (10^{-4}Å^2)	N_{O} ΔN_{O}	R_{Al} ΔR_{Al} (Å)	σ_{Al}^2 $\Delta \sigma_{\text{Al}}^2$ (10^{-4}Å^2)	N_{Al} ΔN_{Al}	$R_{\text{Al}} \equiv R_0$ ΔR_{Al} (Å)	ζ $\Delta \zeta$ (Å)	N_{Al} ΔN_{Al}
7.3 wt%	1.984	38	6	3.267	50	6.5	3.24	0.50	10.1
300 K	± 0.004	± 4	± 0	± 0.007	± 10	± 0.9	± 0.02	± 0.02	± 2.4
11.5 wt%	1.984	37	6	3.268	50	6.5	3.26	0.50	10.1
300 K	± 0.004	± 4	± 0	± 0.008	± 10	± 0.9	± 0.03	± 0.02	± 2.4
11.5 wt%	1.984	32	6	3.264	40	6.5	3.28	0.50	10.1
150 K	± 0.004	± 4	± 0	± 0.007	± 10	± 0.9	± 0.03	± 0.02	± 2.4

$$\Delta E_{\text{O}} = 0.4 \text{ eV} \pm 1.0 \text{ eV}; \Delta E_{\text{Al}} = -9.1 \text{ eV} \pm 1.1 \text{ eV}; S_{\text{O}}^2 = 0.76 \pm 0.04.$$

due in part to the uncertainty of N_{Al} in the previous model.

It should be noted that for the second and third model the small additional contributions to the Fourier transform is resulting from quite different PDFs. In the second model the additional Al coordination shell has only a few atoms (1.8) and therefore the contribution to the EXAFS or its Fourier transform is small. The third model results in a very broad distribution of Al atoms and the corresponding EXAFS is almost averaged out. However, due to the large number of Al atoms (10.1) a finite small contribution to the Fourier transform still remains.

5 Conclusions

The C–Al distances obtained using one Gaussian peak for the PDF of Al appear to be reasonable for Cr atoms located at regular octahedral lattice sites in the mullite structure (Model 1) though a simple fit with one coordination shell does not agree with the measured data sufficiently. In order to improve the fit, an additional Al coordination shell may be considered (Model 2). The error analysis for the data revealed, however, that σ_{Al}^2 and N_{Al} for the added coordination shell are not well defined, and therefore this model is not suitable. A better way of improving Model 1 is given by another model, where a displacement of Cr atoms is taken into account (Model 3). In this model, only 21, rather than 23, variable parameters are used, the residual sum of squares, χ^2 , is 25% smaller than in the second model, and the parameters are all well defined. We believe that these Cr atoms occur at distorted positions at interstitial lattice sites. For the Cr atoms an average displacement of $\zeta = 0.50 \text{ \AA}$ is obtained. This value is an approximation because the angular positions of the Al atoms, which influence the amount and direction of the deduced displacement, were not taken into account. A detailed evaluation of crystal structure data and using present EXAFS data of Cr-doped mullite may allow to define possible sites for the interstitial Cr atoms. Favourable sites for an interstitial incorporation of Cr^{3+} into the mullite structure may be O vacancies or the structure channels running parallel to the crystallographic *c*-axis.⁷

Acknowledgements

One of the authors (KRB) acknowledges with thanks the financial support by the Japan Society for the Promotion of Science (JSPS) through a fellowship during which some of this work was carried out. The work was also supported in part by grants from the Australian Research Council. Another author (AK) is grateful for a fellowship from the Japanese Ministry of Education (Monbusho).

References

1. Cameron, W. E., Mullite: a substituted alumina. *Am. Mineral.*, **62** (1977) 747.
2. Burnham, C. W., *Crystal structure of mullite*. Carnegie Inst., Washington Yearb., **63** (1964) 223.
3. Saalfeld, H. & Guse, W., *Structure refinement of 3:2-mullite ($3\text{Al}_2\text{O}_3 \cdot 2\text{SiO}_2$)*. Neues Jahrb. Mineral. Monatsh., 1981, p. 145.
4. Angel, R. J. & Prewitt, C. T., Crystal structure of mullite: a re-examination of the average structure. *Am. Mineral.*, **71** (1986) 1476.
5. Gelsdorf, G., Müller-Hesse, H. & Schwiete, H. E., Einlagerungsversuche an synthetischem Mullit und Substitutionsversuche mit Galliumoxid und Germaniumoxid. *Teil II Arch. Eisenhüttenwesen*, **29** (1958) 513.
6. Murthy, M. K. & Hummel, F. A., X-ray study of the solid solution of TiO_2 , Fe_2O_3 and Cr_2O_3 in mullite ($3\text{Al}_2\text{O}_3 \cdot 2\text{SiO}_2$). *J. Am. Ceram. Soc.*, **43** (1960) 267.
7. Rager, H., Schneider, H. & Graetsch, H., Chromium incorporation in mullite. *Am. Mineral.*, **75** (1990) 392.
8. Ikeda, K., Schneider, H., Akasaka, M. & Rager, H., Crystal-field spectroscopic study of Cr-doped mullite. *Am. Mineral.*, **77** (1992) 251.
9. Harris, F. J., On the use of windows for harmonic analysis with the discrete Fourier transform. *Proceedings of the IEEE*, **66** (1978) 51.
10. Bauchspieß, K. R., EXAFS background subtraction using splines. *Physica B*, **208** & **209** (1995) 183.
11. Bauchspieß, K. R., EXAFIT: a curve-fitting program for EXAFS. *Jpn. J. Appl. Phys.*, **32** (Suppl. 32–2) (1993) 131.
12. Rehr, J. J., Albers, R. C. & Mustre de Leon, J., Single scattering curved wave XAFS code, *Physica B*, **158** (1989) 417.
13. Grunes, L. A., Study of the K edges of 3d transition metals in pure and oxide form by X-ray-absorption spectroscopy. *Phys. Rev.*, **B27** (1983) 2111.
14. Stern, E. A., Theory of EXAFS, in X-ray Absorption, In *Chemical Analysis*, Vol. 92, eds D. C. Koningsberger & R. Prins, Wiley, New York, 1988, Chap. 1, p. 40.
15. Bauchspieß, K. R., Alberding, N. & Crozier, E. D., Comment on simple method for the evaluation of bond length from data. *Phys. Rev. Lett.*, **60** (1988) 468.
16. Bunker, G., Application of the ratio method EXAFS analysis to disordered systems, *Nucl. Instr. and Meth.* **207** (1983) 437.

Electron Paramagnetic Resonance and Optical Absorption Studies on Cr-doped Mullite Precursors

H. Schneider,^a K. Ikeda,^b B. Saruhan^a & H. Rager^c

^aInstitute for Materials Research, German Aerospace Research Establishment, 51140 Köln, Germany

^bDepartment of Advanced Material Science and Engineering, Yamaguchi University, 755 Ube, Japan

^cDepartment of Geosciences, University of Marburg, 35032 Marburg, Germany

(Accepted 22 July 1995)

Abstract

Mullite precursors doped with 3 wt% Cr₂O₃ were investigated with X-ray diffractometry (XRD), electron paramagnetic resonance (EPR) and optical absorption spectroscopy. The development of phase assemblages occurs over three temperature ranges. In the first temperature field (450–600°C) the precursors are amorphous, and in the second field (800–1100°C) small amounts of γ -Al₂O₃ and crystalline Cr₂O₃ can be observed. Finally, in the third field ($\geq 1250^\circ\text{C}$) mullite forms, and simultaneously γ -Al₂O₃ and crystalline Cr₂O₃ disappear.

The EPR measurements reveal different temperature-controlled structural types of short-range order of Cr in the precursors, which go along with phase developments. Between 450 and 800°C EPR spectra appear with a main signal at $g_{\text{eff}} \approx 1.96$, most probably resulting from Cr⁵⁺. Between 800 and 1250°C, the Cr EPR signal is similar to that of Cr-containing glasses, and above 1250°C the typical Cr³⁺ EPR spectrum of Cr-doped mullite appears.

Optical absorption spectroscopy yields evidence for the occurrence of Cr⁶⁺, Cr⁵⁺ and Cr³⁺ in the mullite precursors, the concentrations of the different oxidation states being dependent on the calcination temperature: Cr⁶⁺ and Cr⁵⁺ contents are high at low temperatures (450°C), but gradually decrease with temperature. Simultaneously, increasing amounts of Cr³⁺ can be detected. At temperatures $> 1100^\circ\text{C}$, Cr⁶⁺ and Cr⁵⁺ cations completely disappear and optical absorption and EPR spectra of samples gradually approach to those of Cr-doped mullite. Although starting materials consist of Cr³⁺, slow hydrolysis kinetics of Cr³⁺ causes formation of polyanions which contain Cr⁶⁺. Deprotonation on heating results in reduction of [Cr⁶⁺O₇]²⁻ species to form Cr₂O₃.

Introduction

Syntheses of high purity and ultra-reactive sol-gel mullite precursor powders have become important for the fabrication of advanced mullite ceramics.^{1,2} These materials exhibit outstanding mechanical, optical and electrical properties suitable for high temperature optical windows, for substrates in multilayer computer packaging, for high temperature insulating devices, and for high temperature structural applications in aircraft turbine engines and space vehicles.^{3,1}

Previous studies have shown that three different types of mullite formation processes can be distinguished in precursors of stoichiometric 3:2 mullite composition (72 wt% Al₂O₃, 28 wt% SiO₂), designated as mullite precursor types I, II and III.⁴ Type I and type III precursors are amorphous at room temperature and remain so up to 900°C. Above this temperature, type I precursors crystallize to Al₂O₃-rich mullite, while precursors of type III transform to γ -alumina and, consequently, mullite formation follows at temperatures $\geq 1200^\circ\text{C}$. Type II precursors consist of poorly crystalline pseudo-boehmite at room temperature which transforms to γ -alumina above $\sim 350^\circ\text{C}$. Mullite crystallization occurs at temperatures $\geq 1200^\circ\text{C}$.^{4,5} The different crystallization behaviours of mullite precursors were attributed to different structural short-range orders prior to mullite formation.

The aim of this study was to provide knowledge on the temperature-dependent development of the structural order of mullite precursors which are doped with paramagnetic and optically absorbant Cr ions. A specific goal was to investigate local structures of the precursors using Cr ions occurring in different oxidation states as probes. For that purpose X-ray diffractometry (XRD),

electron paramagnetic resonance (EPR) and optical absorption spectroscopy were applied.

Experimental Methods

Sample preparation

Cr-doped precursors were synthesized from purely organic starting materials. Tetraethoxysilane (TEOS) and aluminium-sec-butylate ($\text{Al}(\text{OBU}^{\text{S}})_3$) were separately diluted with isopropanol and then admixed in proportions corresponding to 3:2 mullite (72 wt% Al_2O_3 , 28 wt% SiO_2). Chromium(III) acetate was dissolved in ethanol at $\sim 80^\circ\text{C}$. The solution was homogenized for 1 h using a magnetic stirrer and was added to the alcoholic mixed solution of TEOS and $\text{Al}(\text{OBU}^{\text{S}})_3$. The addition of Cr corresponds to 3 wt% Cr_2O_3 in the final product. After further homogenization, hydrolysis was carried out by addition of deionized acidic water. Its pH was adjusted to 1.5 with HCl. Gelation took place immediately after hydrolysis. The gel was dried over several hours in a sandbath at 110°C and a very fine and greenish precursor powder was obtained. The precursor was calcined in a temperature range between 450 and 1750°C (Table 1).

X-ray diffractometry (XRD)

X-ray powder diffractometry studies were carried out with a computer-controlled Siemens D5000 powder diffractometer using Ni-filtered $\text{Cu } K_\alpha$ radia-

tion. Diffraction patterns were recorded in the 10 to $80^\circ 2\theta$ range, in the step scan mode (3 s/ 0.02° , 2θ).

Electron paramagnetic resonance spectroscopy (EPR)

EPR measurements were performed on powder samples at room temperature. The spectra were recorded at both X-band (9.5 GHz) and Q-band (35 GHz) frequency, using a magnetic modulation of 100 kHz and 5×10^{-4} T. Some selected samples were also measured at low temperatures down to 50 K in order to check unknown paramagnetic species in the precursor samples.

Optical absorption spectroscopy

Unpolarized diffuse reflectance spectra were recorded for the precursor series in the wavelength range 290 nm ($34\,400\text{ cm}^{-1}$) to 1538 nm (6500 cm^{-1}). A Hitachi 323S automatic recording spectrophotometer with an integrating globe was used. BaSO_4 was taken as reference material. Reading the original analogous spectra by a digitizer in 100 cm^{-1} intervals, digital spectra were obtained, and stored in a computer. The Kubelka–Munk function was applied. Before evaluation of the spectra a baseline correction in both the infra-red (IR) and ultraviolet (UV) region was carried out using Gaussian curves with centres around 3400 and $34\,000\text{ cm}^{-1}$. Around these wavenumbers, vibronic bands of H_2O and M–O charge transfer bands occur. Overtone bands of adsorbed H_2O appearing around 6900 cm^{-1} were corrected by a smoothing procedure. On the basis of known crystal field absorption bands of Cr^{3+} in Cr_2O_3 – SiO_2 gels and glasses,⁶ the obtained spectra were fitted with a Gaussian peak fitting procedure. Bands due to Fe^{2+} around $10\,000\text{ cm}^{-1}$ were included into the fitting procedure. High energy absorption bands of Cr^{3+} originating from the crystal field P term were also taken into account. These extra bands are labelled R, F, U, 9 and 10 (Table 2). All spectra fittings were carried out assuming a cubic crystal field.

Table 1. Heat treatments of Cr-doped mullite precursors

Sample key	Temperature ($^\circ\text{C}$)	Duration (h)	Colour of powder
CR3-450	450	15	Yellow
CR3-600	600	15	Greenish yellow
CR3-800	800	15	Pale green
CR3-900	900	15	Greyish pale green
CR3-950	950	15	Greyish pale green
CR3-1100	1100	15	Greyish pale green
CR3-1650	1650	15	Grey
CR3-1750	1750	2	Grey

Table 2. Optical absorption band peak positions of Cr-doped mullite precursors heat-treated at different temperatures

Sample key	Absorption band (cm^{-1})														σ
	R	F	1	2	3	4	5	6	7	8	9	10	U		
CR3-450	3400	10 500	—	—	—	—	23 850	—	27 050	30 200	—	—	33 600	0.94	
CR3-600	3400	10 500	—	—	—	—	23 850	—	27 050	30 200	—	—	33 700	0.99	
CR3-800	3400	10 500	16 000	—	22 100	—	23 850	—	27 050	30 200	34 900	—	34 000	0.96	
CR3-900	3400	10 600	14 800	17 000	20 100	22 450	—	26 000	27 050	30 200	32 000	36 300	34 000	1.62	
CR3-950	3400	10 600	14 900	17 000	20 100	22 500	—	26 000	27 050	30 200	32 100	36 300	34 200	0.82	
CR3-1100	3400	10 800	14 950	17 050	20 350	22 700	—	26 000	27 050	30 200	32 400	36 500	33 900	0.75	
CR3-1650	3400	11 000	15 600	18 200	22 500	24 900	—	—	—	—	35 100	39 500	34 200	0.75	
CR3-1750	3400	11 000	15 600	18 200	22 500	25 100	—	—	—	—	35 100	39 700	34 200	0.56	

R, IR band of adsorbed H_2O ; F, impurity ferrous; U, M–O charge transfer; 5, Cr^{5+} bands; 6, Fe^{3+} bands (impurities); 7 and 8, Cr^{6+} bands; 1, 3 and 9, low field Cr^{3+} bands; 2, 4 and 10, high-field Cr^{3+} bands. σ , standard deviation of fitting in %; all bands in cm^{-1} . For the sample key see Table 1.

Results

X-ray diffractometry (XRD)

The mullite precursors are amorphous up to 600°C (Fig. 1). Above this temperature, weak reflections appear in the XRD patterns which are due to some small amount of crystalline Cr_2O_3 . The Cr_2O_3 phase is present up to 1000°C. At 900°C, $\gamma\text{-Al}_2\text{O}_3$ forms, and becomes the only crystalline phase at 1100°C. The formation of mullite starts at 1250°C, as $\gamma\text{-Al}_2\text{O}_3$ disappears. XRD spectra taken from samples heat-treated above 1250°C show only the reflections of mullite. At 1750°C, besides mullite, a very low amount of $\alpha\text{-Al}_2\text{O}_3$ can be detected.

Electron paramagnetic resonance spectroscopy (EPR)

Precursors calcined in the temperature range between 450 and 800°C show a strong and sharp EPR signal at $g_{\text{eff}} \approx 1.96$ and a weak feature extending from $g \approx 5$ to $g \approx 2$ (Fig. 2), the former becoming anisotropic at Q-band frequencies. The

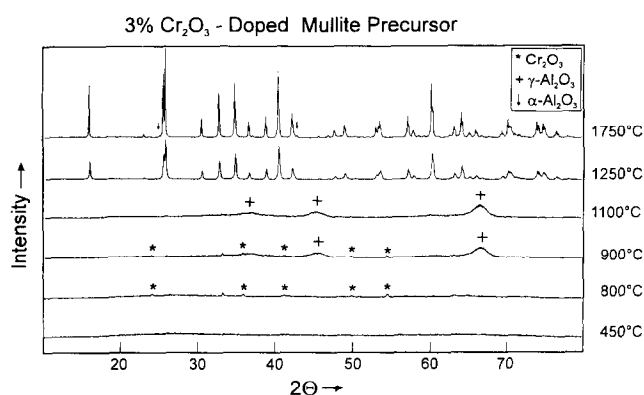


Fig. 1. Evolution of X-ray diffraction patterns of Cr-doped (3 wt%) mullite precursor with heat treatment temperature.

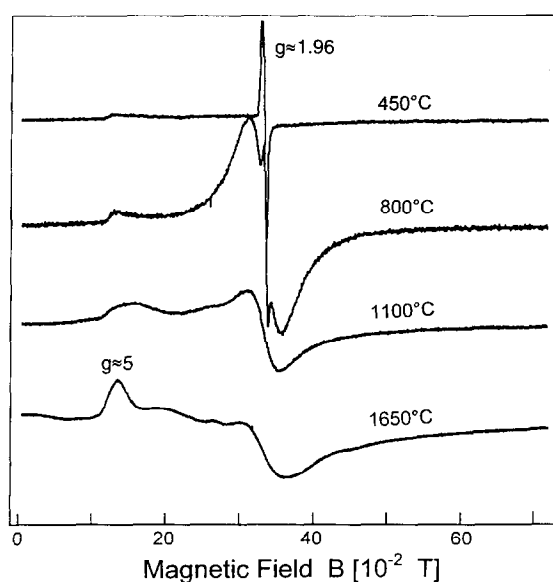


Fig. 2. Powder EPR spectra of Cr-doped (3 wt%) mullite precursors, heat-treated at 450, 800, 1100 and 1650°C. The spectra were taken at room temperature and 9.520 GHz.

strong signal near $g_{\text{eff}} = 1.96$ disappears at calcination temperatures $> 800^\circ\text{C}$. Between 900 and 1000°C a glass-like Cr^{3+} EPR spectrum appears. Development of the typical Cr^{3+} EPR spectrum of mullite with characteristic features near $g_{\text{eff}} = 5$ is visible at higher temperatures ($\geq 1250^\circ\text{C}$).

In the temperature range between 800 and 1100°C, an isotropic and broad EPR signal centred at $g_{\text{eff}} \approx 2$ can be additionally detected (Fig. 2). The intensity of this signal increases, if the EPR spectra are recorded at temperatures ≥ 310 K, due to the occurrence of crystalline Cr_2O_3 .⁷

No additional EPR signal was detected down to 50 K, indicating the absence of additional Cr-bearing phases in the mullite precursors.

Optical absorption spectroscopy

As shown in Fig. 3, the optical absorption spectra of the precursors calcined between 450 and 1650°C were fitted by Gaussian curves. The differentiated peaks were labelled with numbers from 1

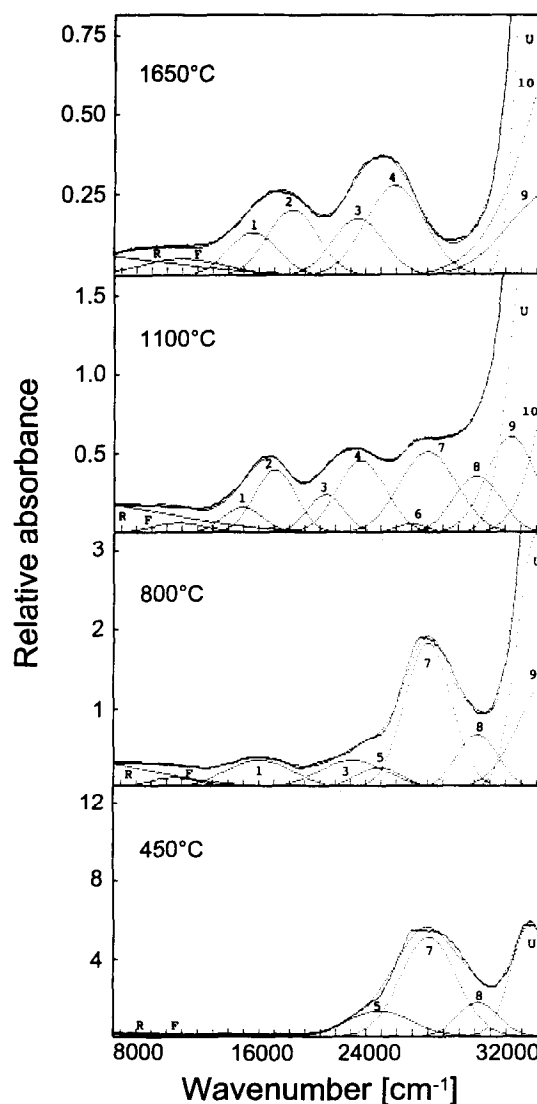


Fig. 3. Peak-fitted optical absorption spectra of Cr-doped (3 wt%) precursors, heat-treated at 450, 800, 1100 and 1650°C. For attribution of peak numbers see the text and Table 2.

to 10 (see the pattern of the 1100°C sample). They are listed in Table 2. Peaks 5, 7 and 8 are characteristic for the low temperature (450°C) sample, and are assumed to be the result of charge transfer transitions of Cr⁶⁺. The corresponding EPR spectrum at this temperature, however, shows the presence of Cr⁵⁺ in the precursor. The electron configuration of Cr⁶⁺ and Cr⁵⁺ ions are 3d⁰ and 3d¹, respectively. Cr⁵⁺ has an electron spin of $S = 1/2$ and is paramagnetic. It can therefore easily be detected by EPR. However, Cr⁶⁺ is diamagnetic and, hence, is not detectable by EPR. We believe that peak 5 belongs to Cr⁵⁺, and peaks 7 and 8 to Cr⁶⁺, which is in agreement with the yellow colour of the 450°C sample. The colour of precursors calcined at temperatures $\geq 800^\circ\text{C}$ turns to green due to the appearance of Cr³⁺. Above this temperature the intensities of optical absorption peaks 7 and 8, assigned to Cr⁶⁺, decrease as the intensity of peak 5, assigned to Cr⁵⁺, totally disappears.

Octahedrally coordinated Cr³⁺ generally displays two optical absorption peaks in the visible region due to the splitting of the F term. Sometimes an additional Cr³⁺ peak occurs in the UV region which results from the P term. This actually has been observed in the samples heat-treated at $\geq 800^\circ\text{C}$. The precursors calcined at 1650 and 1750°C have grey colour and their absorption spectra are equal to those of octahedrally coordinated Cr³⁺, occurring in high and low field sites.⁸ High and low field occupations of Cr³⁺ have also been observed in samples heat-treated between 900 and 1100°C, suggesting the evolution of a mullite-type short-range order in the precursors. However, Racah parameters (see below) show that this actually is not the case. Furthermore, peak 6 (Table 2) resolved in the spectra of these samples is believed to be due to impurity Fe³⁺ ions.⁹

Discussion

The EPR signal at $g_{\text{eff}} \approx 1.96$, appearing at calcination temperatures $\leq 1100^\circ\text{C}$, is connected with Cr doping, because it is not observed in undoped mullite precursors. The spin of the paramagnetic centre is assumed to be $S = 1/2$ and the g value indicates an electron centre. This signal is, there-

fore, assigned to Cr⁵⁺. A paramagnetic centre with $S > 1/2$, e.g. Cr³⁺ with $S = 3/2$, can be excluded, because the Cr³⁺ EPR should not display a single line spectrum around $g_{\text{eff}} \approx 2$. The Cr⁵⁺ signal at $g_{\text{eff}} \approx 1.96$ can be simulated at both 9.5 and 35 GHz using an axial g tensor with $g_{x,y} = 1.960$ and $g_z = 1.946$, an effective spin $S = 1/2$ and a constant line width of 25×10^{-4} T. The frequency-independent line width indicates that Cr⁵⁺ occurs in a non-random environment. According to the EPR data only one type of coordination exists for Cr⁵⁺.

Optical absorption spectra suggest that Cr⁵⁺ is present in larger amounts in the samples calcined at temperatures $< 900^\circ\text{C}$, while Cr⁶⁺ persists up to $\leq 1100^\circ\text{C}$. Taking into account the ionic radii of Cr⁶⁺ (0.38 Å) and Cr⁵⁺ (0.43 Å),¹⁰ both cations should be fourfold coordinated in these precursors. Substitution of Al³⁺ or Si⁴⁺ cations by Cr⁵⁺ or Cr⁶⁺ produces a charge surplus in the oxygen network which may be balanced by octahedral cation vacancies.

Although the Cr³⁺ EPR signal around $g_{\text{eff}} = 5$ is already present in the sample heat-treated at 450°C, its intensity is significant only at calcination temperatures $> 800^\circ\text{C}$. This is in accordance with optical absorption data. Furthermore, from the absorption spectra a certain variation of slightly different distorted octahedral Cr³⁺ sites in the precursors can be deduced as high and low field sites.

The crystal field parameters $10 Dq$ and B for Cr³⁺ and Cr⁵⁺ cations in the Cr-doped precursors (Table 3) are in general agreement with literature data.⁸ Racah parameters B of all samples are small, indicating a partly covalent bonding character of Cr³⁺ in the precursor matrix. The Racah parameter B of Cr³⁺ should be larger for high field and smaller for low field sites, respectively. This actually becomes true for samples heat-treated at 1650°C and at 1750°C, which comprise Cr-doped mullites. However, it does not hold for samples heat-treated in the temperature range between 900 and 1100°C where the formal application of the fitting procedure yielded high and low field sites with nearly the same Racah parameter ($\approx 518 \text{ cm}^{-1}$). Therefore, we assume that strongly distorted Cr³⁺ sites which do not allow a

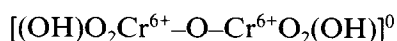
Table 3. Crystal field parameters $10 Dq$ and B of Cr-doped mullite precursors heat-treated at different temperatures

	Sample key							
	CR3-450	CR3-600	CR3-800	CR3-900	CR3-950	CR3-1100	CR3-1650	CR3-1750
Oct. Cr ³⁺ $10 Dq$	—	—	16 000	14 800/17 000	14 900/17 000	14 950/17 050	15 600/18 200	15 600/18 200
B	—	—	601	513/515	500/521	524/537	717/654	717/679
Tet. Cr ⁵⁺ $10 Dq$	23 850	23 850	23 850	—	—	—	—	—

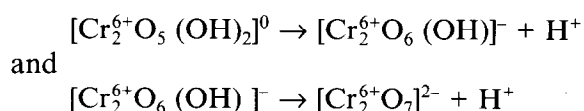
Slash indicating both of high-field and low-field in cm^{-1} . Oct. = octahedral, Tet. = tetrahedral.

differentiation between high and low field Cr³⁺ positions can explain the above observations.

It is interesting to discuss the temperature-dependent mechanisms of Cr incorporation into the mullite precursors. The literature data on the hydrolysis behaviour of trivalent Cr³⁺ indicates that the kinetics of hydrolysis with Cr³⁺ are slow.¹¹ Slower kinetics facilitate occurrence of the gel network which results in the formation of polyanions by oxidation of Cr³⁺ to Cr⁶⁺.¹¹



On heating, deprotonation of the dimer occurs, yielding a gradual development of:



Reduction of [Cr₂⁶⁺O₇]²⁻ species at temperatures ≥ 800°C may result in the formation of crystalline Cr₂³⁺O₃, as is observed by XRD of the calcined Cr-doped precursors.

Cr-doping of mullite precursors has a significant influence on the crystallization behaviour of the material. Undoped precursors prepared in exactly the same way as the Cr-doped precursors are amorphous up to ≈900°C. At this temperature they crystallize to mullite and some small amount of γ-Al₂O₃. The nearly exclusive formation of mullite indicates that a small degree of phase separation into Al₂O₃- and SiO₂-rich areas occurred before mullite crystallization. Addition of chromium acetate in alcoholic solution, how-

ever, promotes this phase separation to such an extent that intermediate phases of γ-Al₂O₃ and Cr₂O₃-rich non-crystalline SiO₂ form prior to mullitization, similar to the case of type III mullite precursors.⁴

References

- Hoffman, D., Roy, R. & Komarneni, S., Diphasic xerogels, a new class of materials: phases in the Al₂O₃-SiO₂ system. *J. Am. Ceram. Soc.*, **67** (1984) 468-71.
- Komarneni, S., Suwa, Y. & Roy, R., Application of compositionally diphasic xerogels for enhanced densification: the system Al₂O₃-SiO₂. *J. Am. Ceram. Soc.*, **69** (1986) C-155-C-156.
- Schneider, H., Okada, K. & Pask, J. A., *Mullite and Mullite Ceramics*. John Wiley & Sons, Chichester, 1994.
- Schneider, H., Saruhan, B., Voll, D., Merwin, L. & Sebald, A., Mullite precursor phases. *J. Eur. Ceram. Soc.*, **11** (1993) 87-95.
- Schneider, H., Voll, D., Schmücker, M., Saruhan, B., Schaller, T. & Sebald, A., Constitution of the γ-alumina phase in chemically produced mullite precursors. *J. Eur. Ceram. Soc.*, **13** (1994) 441-8.
- Tanaka, K. L. & Kamiya, K., Electron spin resonance and optical absorption spectra of chromium in silica gels and glasses prepared by the sol-gel method. *J. Mater. Sci. Lett.*, **10** (1991) 1095-7.
- Rager, H., Schneider, H. & Graetsch, H., Chromium incorporation in mullite. *Am. Mineral.*, **75** (1990) 392-7.
- Ikeda, K., Schneider, H., Akasaka, M. & Rager, H., Crystal-field spectroscopic study of Cr-doped mullite. *Am. Mineral.*, **77** (1992) 251-7.
- Marfunin, A. S., *Spectroscopy, Luminescence and Radiation Centers in Minerals*. Springer, Berlin, 1979.
- Whittaker, E. J. W. & Muntus, R., Ionic radii for use in geochemistry. *Geochim. Cosmochim. Acta*, **34** (1970) 945-56.
- Brinker, C. J. & Scherer, G. W., *Sol-Gel Science*. Academic Press, San Diego, CA, 1990.

Mechanical Properties of Mullite Materials

M. I. Osendi & C. Baudín

Instituto de Cerámica y Vidrio (CSIC), E-28500, Arganda del Rey, Madrid, Spain

(Accepted 22 July 1995)

Abstract

The mechanical behaviour of two $3\text{Al}_2\text{O}_3\cdot 2\text{SiO}_2$ dense mullite materials with the same level of impurities but different in nature has been studied. Microstructure has been characterized by SEM and TEM. Toughness, bend strength and Young's modulus have been determined from room temperature up to 1400°C . Dependence of toughness on strain rate has been investigated. Special attention has been paid to correlate the trend of the mechanical parameters to fractographic observations by SEM.

1 Introduction

Nowadays, highly reactive, homogeneous and pure mullite powders that allow us to obtain high density structural $3\text{Al}_2\text{O}_3\cdot 2\text{SiO}_2$ mullite materials are available.¹ In these materials, the mullite phase is the 3:2 one. Even though the starting powders are highly pure, small amounts of impurities, whose nature depends on the synthesis route,² are always present. When powders are obtained by sol-gel methods the main contaminants come from the milling media, (eg. ZrO_2), whilst when mullite powders are fabricated from raw materials, the main impurities are alkalis and alkaline-earths. Some impurities, like iron oxide and titania,³ can enter in solid solution in mullite in rather large quantities or, like zirconia, remain mostly as isolated particles⁴ while others, like alkaline oxides can form liquids at rather low temperatures, (eg. $T \sim 1000^\circ\text{C}$ for Na_2O).⁵ After sintering of the mullite materials, a certain amount of liquid remains as glassy phases. Softening temperature and viscosity of these residual amorphous phases dramatically depend on their composition.^{6,7} Moreover, quantity and distribution of these glassy phases in the material should depend on sintering temperature, and content and nature of the impurities.

From a mechanical point of view, the most studied property of mullite materials at high temperature has been creep.^{8–12} A variety of mechanisms, from solid-state diffusion to viscous flow,

and activation energies, ranging from 500 KJ/mol^{8,9} to 1300 KJ/mol,¹⁰ have been reported for mullite creep. This diversity in the data, in spite of the similar ranges of test temperatures and loads, could be attributed to slight differences in the impurity contents and their nature. In fact, small amounts of additives greatly change not only the viscosity of liquids⁶ but, certainly, their wetting characteristics. Distribution of remaining glassy phases, along grain boundaries or forming isolated pockets, will influence creep mechanisms at high temperatures.

On the other hand, probably due to its inherent brittleness, fracture properties of mullite have been analyzed less.^{13,14} In fact, most of the work has been devoted to establishing the relationships between mullite stoichiometry and parameters such as toughness and modulus of rupture.^{15–20}

In the present work, the mechanical behaviour of two mullite materials with the same level of impurities but different in nature has been studied. The selected parameters have been toughness, bend strength, and Young's modulus. Variations of these parameters with temperature and strain rate have been obtained. Special attention has been paid to correlate the parameter trends to the aspect of the fracture surfaces.

2 Experimental

Two kinds of mullite materials henceforth labelled as MS0 and MB0 have been prepared from commercial powders* as previously described.⁴ MS0 was processed from a commercial gel type mullite ($1.5 \mu\text{m}$ of average particle size), that was spray dried, isostatically pressed and sintered at 1660°C for 2 h. MB0 powders were coarse grain commercial mullite, that were attrition milled with mullite balls down to $0.8 \mu\text{m}$, before isostatically pressing and sintering at 1630°C for 4 h. Fundamental

*MS0: Chichibu Cement Co., supplied by Scimareck Ltd. Tokyo, Japan.

MB0: Baikowski Chimie, France.

Table 1. Main characteristics of the mullite materials

Material	Dynamic Young's Modulus (GPa)	Density (g/cm ³)	Average grain size (μm)	Al ₂ O ₃ /SiO ₂ ratio (wt%)
MS0	202 ± 2	3.05 ± 0.02	1.2 ± 0.9	2.66
MB0	195 ± 4	3.01 ± 0.02	0.7 ± 0.5	2.75

Table 2. Impurity contents in the mullite materials

Material	Fe ₂ O ₃ + TiO ₂ + Y ₂ O ₃ (wt%)	Na ₂ O + CaO + MgO + K ₂ O (wt%)	ZrO ₂ (wt%)
MS0	0.17	0.13	0.33
MB0	0.11	0.30	0.02

characteristics of the materials are collected in Table 1. Main impurities of these mullites are shown in Table 2.

Although the total level of impurities in both mullites is similar (<0.65 wt% in MS0 and <0.45 wt% in MB0) chemical compositions are quite different. The main impurity in MS0 is ZrO₂, followed far behind by TiO₂. Conversely, the more abundant impurities in MB0 are Na₂O and Fe₂O₃. The large amount of ZrO₂, found in MS0, is attributable to the powder milling procedure of the supplier.

Figure 1 shows representative microstructures (SEM) of the studied mullite materials. In MS0 some exaggerated grain growth and pore trapping have taken place whereas MB0 has a more uniform microstructure and mainly intergranular porosity.

In Fig. 2 the main characteristics of grain boundaries in MS0 samples are observed (TEM). Zirconia remains as particles (≈200 nm) located at triple points (Fig. 2(a)) while glassy pockets at grain junctions are scarcely observed (Fig. 2(b)). Figure 3 shows glassy pockets at triple points that are often present in MB0, where alkaline impurities concentrated as EDX analysis revealed. At the level of resolution employed no glassy phase films were observed along grain boundaries in any sample.

All mechanical and elastic tests were performed in an universal load testing machine with an electrically heated furnace, using 4-point bending fixtures made of SiC or Al₂O₃, with inner and outer spans of 20 and 40 mm.

Bend strength test measurements at temperatures ranging from RT to 1400°C were performed on 4 × 3 × 50 mm bars that were diamond machined from the sintered compacts, polished and chamfered on the tension surface. At least 5 bars were tested at each temperature.

Static Young's modulus (RT–1400°C) was calculated from the central point deflection of bend bars measured using a SiC probe attached to a LVDT through an alumina tube. Three bars were tested at each temperature. For bend strength and Young's

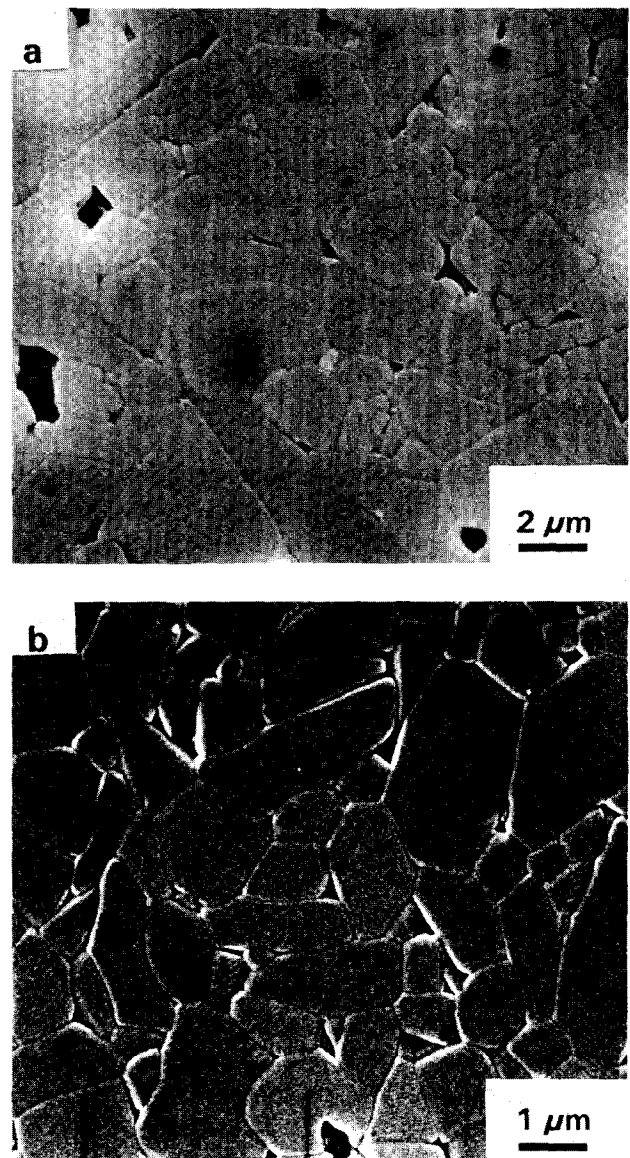


Fig. 1. Representative SEM microstructures of the studied mullite materials: (a) MS0; (b) MB0.

modulus measurements, load was applied at 1000 N/min.

Toughness was determined by the SENB method using five bars for each temperature. Bars of dimension 4 × 6 × 50 mm were machined and

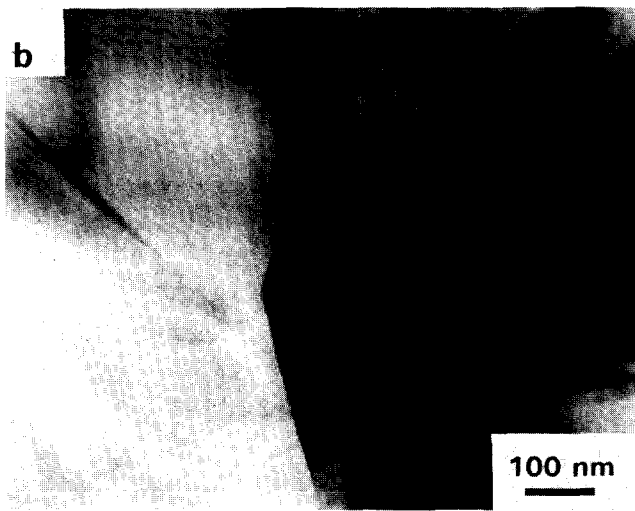


Fig. 2. TEM microstructures of MS0. The main characteristics of the grain boundaries are observed: (a) Zirconia located at triple points; (b) glassy pockets at grain junctions.

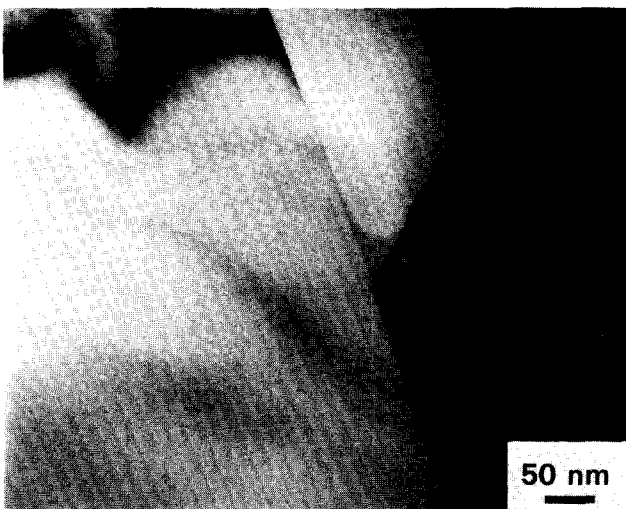


Fig. 3. TEM microstructure of MB0. Glassy pockets at triple points are observed.

notches were introduced with a thin diamond disc. Notches were 3 mm long and 200 μm width. The actuator rates ranged from 0.005 to 5 mm/min.

Polished and thermally etched (1500°C) samples

and ‘as fractured’ surfaces were observed by SEM. Specimens were thinned, dimpled and Ar milled in order to be analyzed by TEM.

3 Results

In Fig. 4 static Young’s modulus versus temperature is depicted. Room temperature values are the same for both materials and a slight decrease with temperature is observed.

Bend strength as a function of temperature is shown in Fig. 5. Values are always lower for MS0 although data trends are the same for both mullites, showing peaks in strength at $T = 1200\text{--}1300^\circ\text{C}$.

Toughness values obtained using an actuator speed of 0.05 mm/min are represented in Fig. 6. Room temperature values are almost the same for

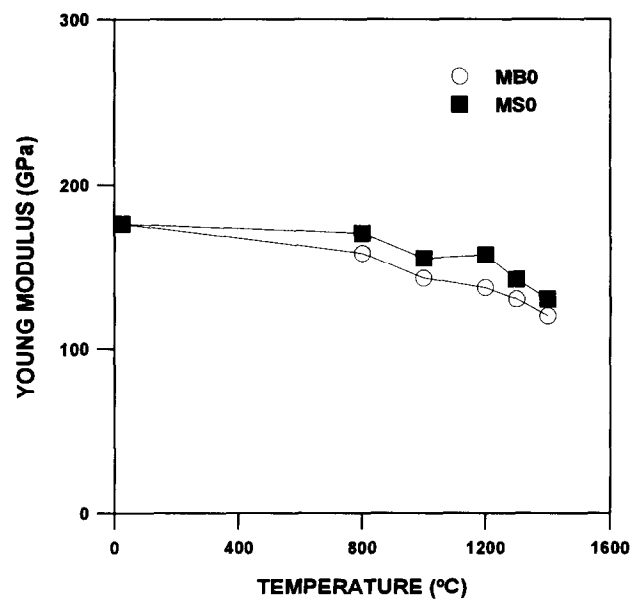


Fig. 4. Static Young’s modulus versus temperature.

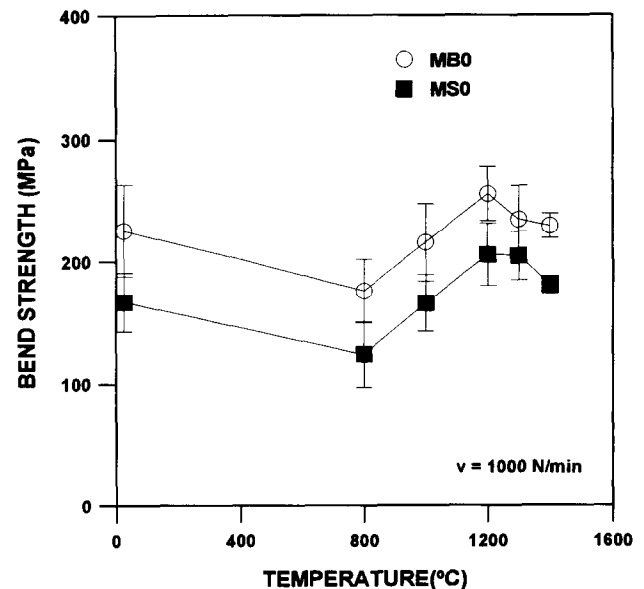


Fig. 5. Bend strength versus temperature.

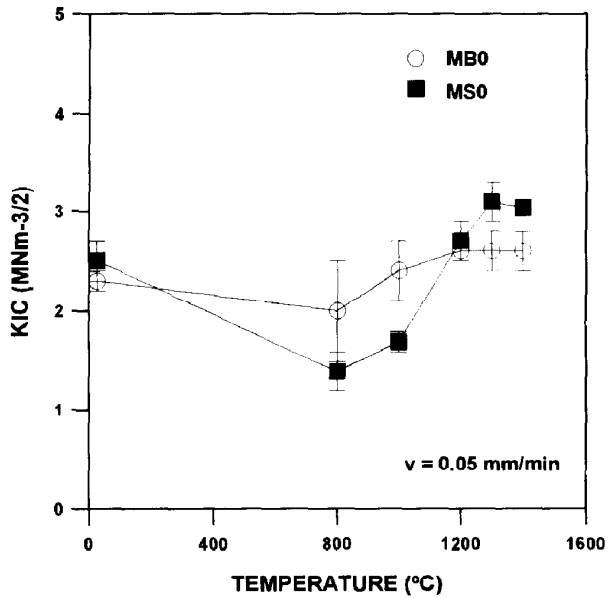


Fig. 6. Toughness values versus temperature obtained using an actuator speed of 0.05 mm/min.

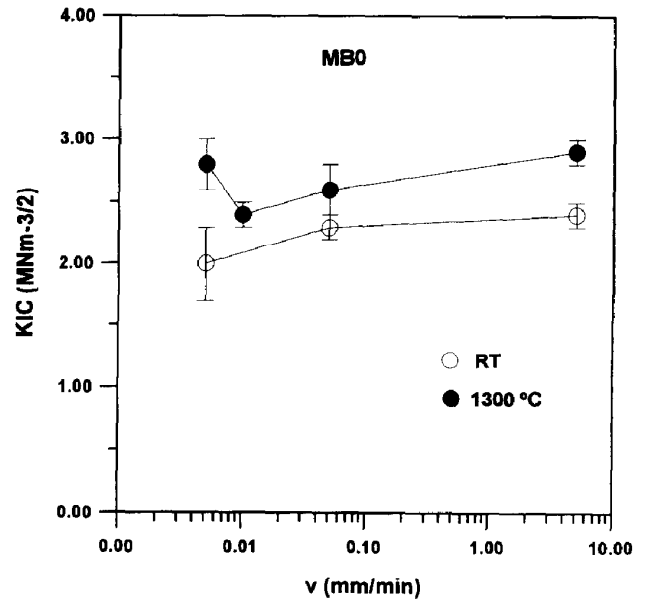


Fig. 8. K_{IC} data at room temperature and 1300°C as a function of the actuator speed for MB0.

both materials although toughness dependence on temperature is more marked for MS0, showing a decrease from room temperature up to 800 followed by a sudden increase.

Figures 7 and 8 show K_{IC} data as a function of the actuator speed for MS0 and MB0. Tests were performed at room temperature and 1300°C. At room temperature, K_{IC} increases with strain rate for MS0 whereas K_{IC} is practically constant for MB0. At 1300°C, toughness values diminish as strain rate increases for MS0. The dependence of toughness on strain rate is not monotonous for MB0: maximum values are obtained using the slowest strain rate (0.005 mm/min) and a minimum is found for a strain rate of 0.01 m/min.

In Fig. 9 room temperature fracture surfaces of

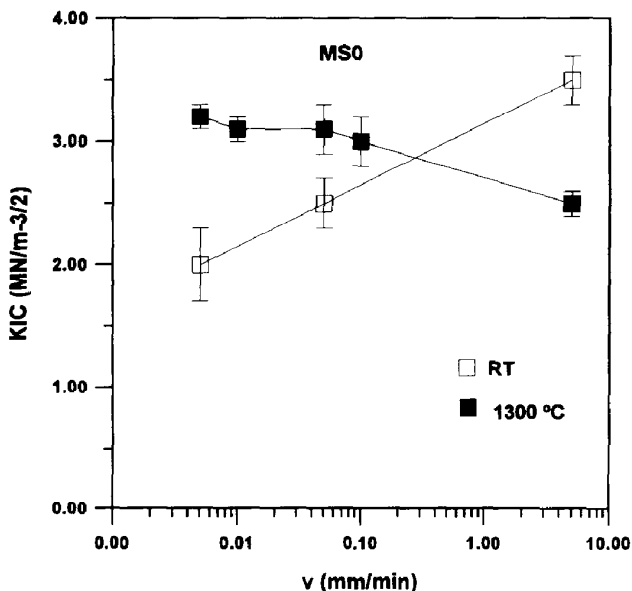


Fig. 7. K_{IC} data at room temperature and 1300°C as a function of the actuator speed for MS0.

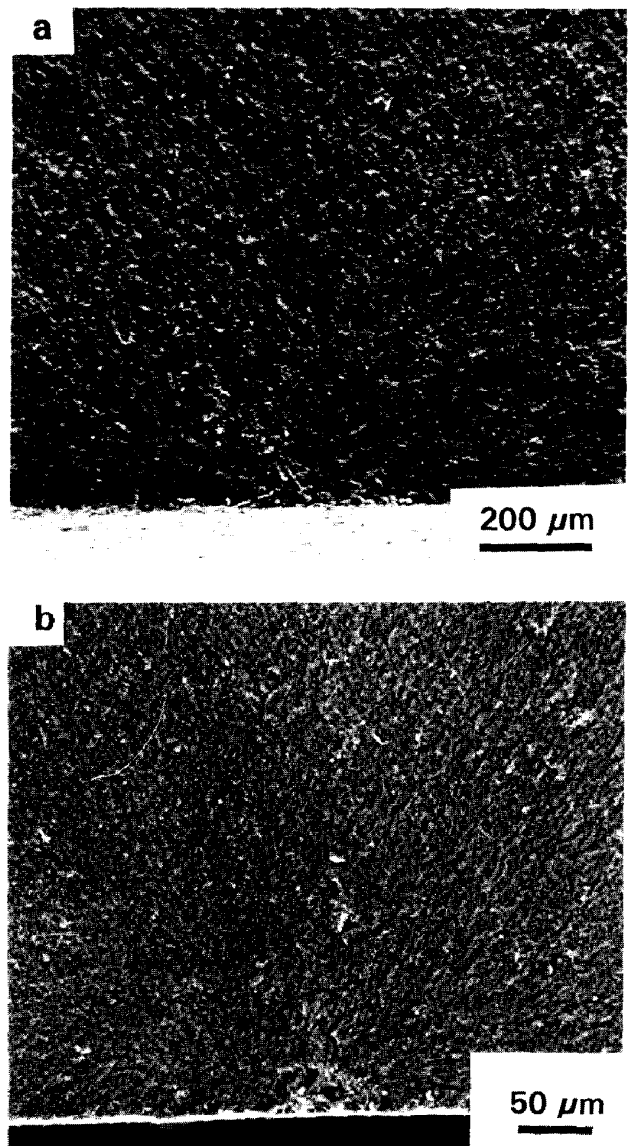


Fig. 9. Room temperature fracture surfaces of bend bars (SEM): (a) MS0; (b) MB0.

bend strength bars are displayed. In MS0, fracture origins are not well defined, but a characteristic semielliptical feature (diameter $\approx 150 \mu\text{m}$) close to the tension surface is usually detected (Fig. 9(a)). Most of fracture origins in MB0 samples are pores (diameter $\approx 30 \mu\text{m}$) as the one in Fig. 9(b).

Figure 10 shows typical fracture surfaces of MS0 notched bars after toughness testing. At room temperature, as well as at 1300°C , differentiated zones close to the notch exist (Fig. 10(a, b)). The size of these zones increased as strain rate decreased and as temperature increased. Higher magnification (Fig. 10(c)) shows that intergranular fracture predominates in these zones for tests done at room temperature. In parallel, in the samples tested at 1300°C the main features of the zone close to the notch are large areas ($d \approx 200 \mu\text{m}$ for the slowest strain rate) at both surfaces of the crack that have crept, sliding one against the other, coexisting with intergranular fracture (Fig. 10(d)).

Fracture surfaces of MB0 toughness specimens are collected in Fig. 11. No special features are

observed in the room temperature samples, being the fracture mainly transgranular through the whole specimen (Fig. 11(a, c)). Conversely, at 1300°C a differentiated zone close to the notch exist (Fig. 11(b)). Higher magnification (Fig. 11(d)) reveals a sharp transition from intergranular to transgranular fracture at the boundary of this zone. The size of this zone varies with loading rate and is minimum for samples tested at 0.005 mm/min .

4 Discussion

4.1 Room temperature mechanical behaviour

In order to explain the difference in the room temperature bend strength values, lower for MS0, whereas toughness values are about the same for both materials (Figs 5 and 6) the following equation should be considered:

$$\sigma_f = \frac{Z}{Y} \frac{K_{IC}}{\sqrt{c}}$$

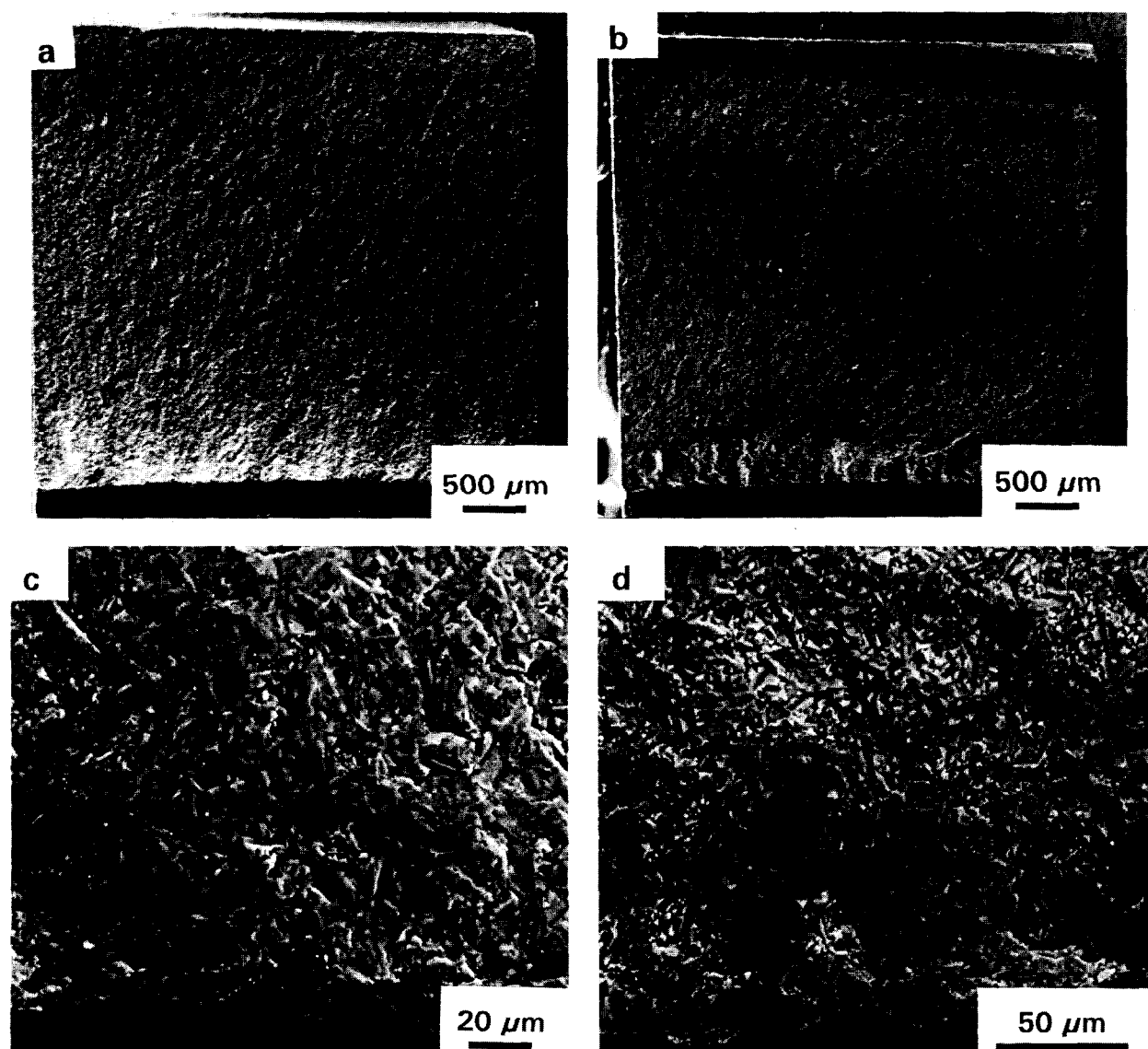


Fig. 10. Fracture surfaces of MS0 notched bars after toughness testing: (a) and (c) room temperature; (b) and (d) 1300°C .

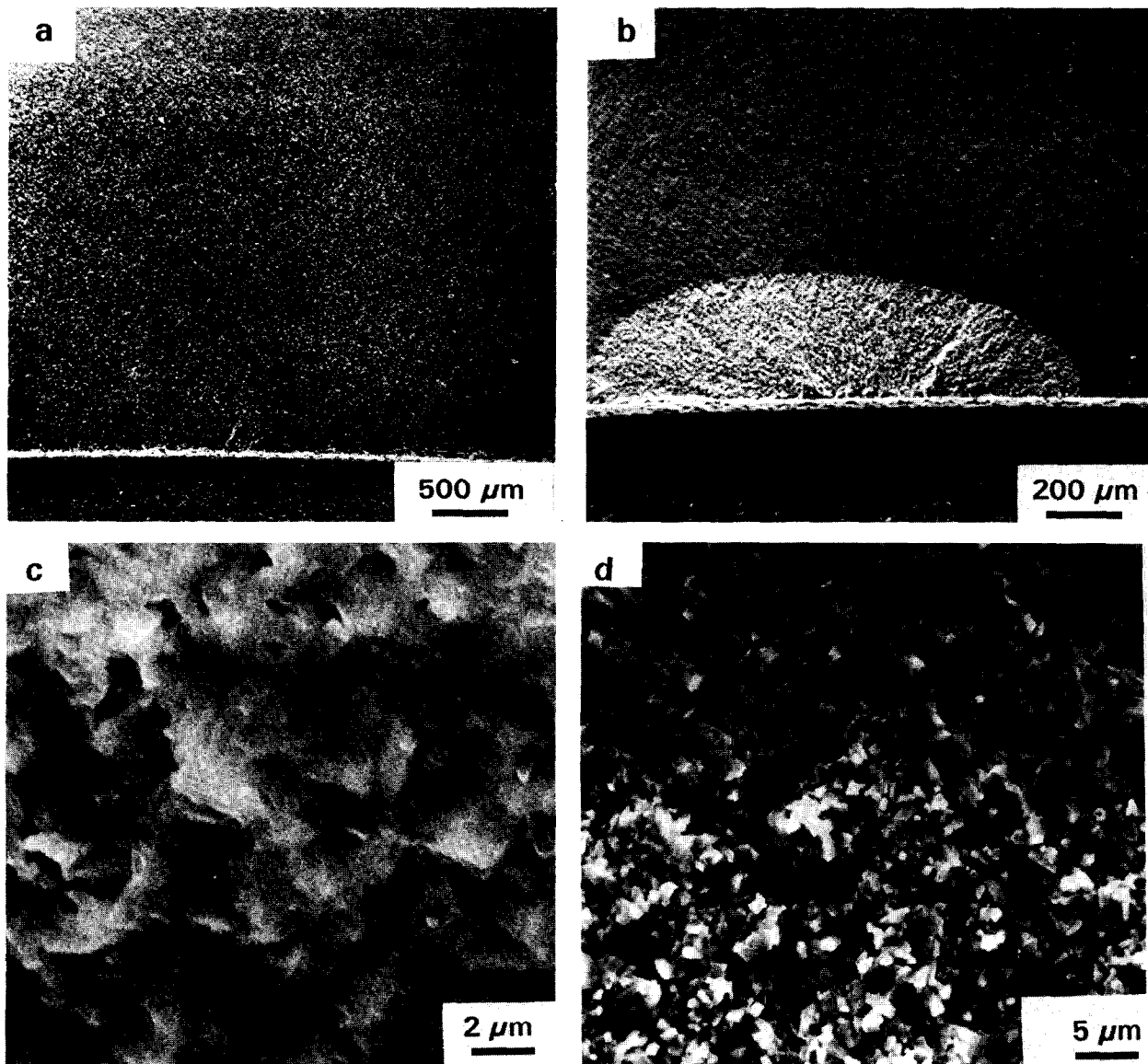


Fig. 11. Fracture surfaces of MB0 notched bars after toughness testing: (a) and (c) room temperature; (b) and (d) 1300°C.

Substituting the constant values for a semielliptical ($Z = 1.6$) surface ($Y = 2$) crack of radius c^{21} and introducing K_{IC} and σ_f limiting values into the expression, critical defect sizes ranging from 100 to 276 μm for MS0 and from 40 to 112 μm for MB0 are obtained.

In the case of MS0 specimens, these calculated critical flaw sizes agree well with the sizes of the semielliptical features observed close to the tension surfaces, as shown in Fig. 10(a). These semielliptical zones seem to develop from smaller processing defects by subcritical crack growth. Subcritical crack growth zones, defined by intergranular fracture mode, were also apparent on fracture surfaces of K_{IC} specimens tested at room temperature, as shown in Fig. 11(a,c). Moreover, toughness values determined using the slowest rate are much lower than those obtained at the fastest rate (Fig. 7). This trend of K_{IC} with loading rate also support subcritical crack growth in MS0.

Observing the fracture surfaces of MB0 specimens (Fig. 9(b)) fracture origin dimensions agree with the previous calculations. In fact, no dependence of room temperature K_{IC} values on loading rate occurs (Fig. 8) and no subcritical crack growth zone is observed close to the notch in toughness specimens (Fig. 11(a, c)). It is interesting to note that the range of loading rates that have been used is very large, thus apparently, no easy paths for crack growth exist in MB0.

The existence of subcritical crack growth at room temperature in MS0 and not in MB0 implies that grain boundaries are weaker in MS0 than in MB0. As mentioned in Section 2, no glassy films along grain boundaries were observed with the available techniques in neither mullite. Nevertheless, its presence in MS0 sample can be assumed considering the level of impurities and sintering temperatures. Furthermore, thin glassy films of ≈ 10 nm have been observed by other authors at

the mullite–mullite interfaces by HRTEM in the eutectic systems ZrO_2 -mullite²² and also in mullite materials doped with small amounts of ZrO_2 .²³ These facts support the evidence that the glassy phase is preferentially located along grain boundaries in MS0, in agreement with TEM observations in which triple point glassy pockets were scarcely observed in MS0. Conversely, large amounts of glassy pockets were observed in MB0 comparatively to MS0, which suggests that glassy phase is preferentially located at triple points in agreement to the lack of subcritical crack growth at room temperature in MB0 mullite.

4.2 Mechanical behaviour up to 1400°C

The decrease in Young's moduli with temperature for both mullites (Fig. 4) is the expected one considering the rather high loading rate used. At this rate, materials remain linear elastic through the load cycle at each testing temperature.

In terms of bend strength, both mullites present the usual behaviour of ceramic materials with small glassy phase amounts (Fig. 5). The initial decrease is related to elastic bond relaxation as temperature increases as discussed above. The increase at temperatures higher than 1000°C can be associated to the softening of the residual glassy phases in the range of testing temperatures, which could lead to healing of the critical flaws or an increase in apparent toughness.

For each mullite, toughness and bend strength dependences on temperature (Figs 5 and 6) show only slight differences that can be attributed to differences in strain rates between both tests. Both mullites experience K_{IC} and σ_f peak values in the interval 1200–1300°C. Therefore, the increase in bend strengths at high temperature can easily be associated to the toughness behaviour.

Most ceramics, like the mullites studied here, contain remaining glassy phases that have been formed during sintering. In materials such as alumina, silicon nitride and glass ceramics,^{24,25} peaks in strength and toughness with temperature have been associated with several phenomena derived from the softening of those remaining glassy phases.^{26,27} A variety of mechanisms, from blunting of critical flaws to grain boundary sliding, crack branching or formation of crack bridges by viscous flow during crack propagation have been proposed.²² Probably, not a single mechanism takes place but an interaction of several ones occurs depending on composition and distribution of the glass, testing temperature and strain rate.

In order to discern which of those mechanisms are predominant in the present mullite materials, K_{IC} data as a function of strain rate at two limiting temperatures RT and 1300°C were analyzed.

Considering first the MS0 samples, the increase in K_{IC} with strain rate at room temperature (Fig. 7) is due to subcritical crack growth through the easy paths provided by the glass phase as above discussed. The toughness behaviour at 1300°C is also attributed to the glassy phase, but the mechanism seems to be quite different. Actually, viscous flow at slow strain rates favors sliding between grains or agglomerates as can be observed on the micrographs of fracture surfaces at 1300°C (Fig. 10(b, d)). This grain boundary sliding phenomenon, and its related plastic deformation effect, produce higher apparent K_{IC} at slow strain rates, while at the very high strain rate it does not take place. Due to the lack of energy dissipative mechanisms at high strain rates, toughness values at high temperature are lower than at room temperature because of the decrease of the elastic modulus (Fig. 4), as experimentally observed in Fig. 7.

For MB0, K_{IC} values at 1300°C are always larger than at room temperature for each strain rate (Fig. 8) but, the energy absorbing mechanisms in this mullite are more complex than in MS0. In fact, the trend of K_{IC} values for MB0 samples with strain rate (Fig. 8) is opposite to that shown by MS0 and there is one point that does not follow the general trend ($v = 0.005$ mm/min). The K_{IC} fracture surfaces of MB0 samples (Fig. 1(b, d)) show process zones close to the notch, in which a total decohesion of the mullite grains is evident. This microstructural aspect could be due to migration of the low viscosity liquid phase during loading. The energy absorbing mechanisms associated to the liquid phase occur in MB0 through the whole range of strain rates, even at the very high one, but their effectiveness depend on time.

From post mortem observations of MB0 samples, the energy absorbing mechanism associated to the liquid can only be speculated. At medium-high loading rates, it might act as crack bridges, more effective for high loading rates due to its low viscosity (high alkaline content). For the lowest strain rate, microstructural changes such as solution-precipitation and/or crystallization phenomena at the crack tip could take place leading to an increase of toughness.

5 Conclusions

The mechanical behaviour of two structural mullites with the same levels of impurities but different nature strongly depends on strain rate. This dependence shows different trends at room temperature and at high temperatures (1300°C).

Fracture behaviour at room temperature is determined by the distribution of the residual glassy phase:

- (a) The glassy phase along grain boundaries leads to subcritical crack growth.
- (b) When the glassy phase remains at triple points no subcritical crack growth takes place.

Fracture behaviour at high temperature is determined by the nature of the residual glassy phase which softens during testing:

- (a) Decohesion of grains and liquid migration take place in mullite with higher alkali content (0.3%) due to the formation of low viscosity liquids.
- (b) Grain boundary sliding is the main mechanism in mullite with low alkali content (<0.1%) due to a higher viscosity of the liquids formed.

Acknowledgement

This work has been supported by CICYT, Project no. MAT 499-91.

References

1. Somiya, S. & Hirata, Y., Mullite Powder Technology and Applications in Japan. *Ceram. Bull.*, **70** (1991) 1624-32.
2. Sacks, M. D., Lee, H. W. & Pask, J. A., A Review of Powder Preparation Methods and Densification Procedures for Fabricating High Density Mullite. In *Mullite and Mullite Matrix Composites*, Ceramic Transactions, Vol. 6, The American Ceramic Society Inc., Ohio, 1990, pp. 167-213.
3. Baudin, C., Osendi, M. I. & Moya, J. S., Solid Solution of TiO₂ in Mullite. *J. Mater. Sci. Lett.*, **2** (1983) 185-7.
4. Baudin, C., Miranzo, P. & Osendi, M. I., High Temperature Mechanical Behaviour of 3Al₂O₃:2SiO₂ Mullite Based Materials. In *Third Euro-Ceramics V-3*, Faenza Editrice Ibérica S.L, Spain, 1993, pp. 369-75.
5. Osborn, E. F. & Muan, A., plate no. 501, *Phase Diagrams for Ceramists*, The Am. Ceram. Soc. Inc., Ohio, USA, 1964.
6. Urbain, G., Cambier, F., Deletter, M. & Anseau, M. R., Viscosity of Silicate Melts. *Trans. J. Br. Ceram. Soc.*, **80** (1981) 139-41.
7. Fernandez Navarro, J. M., *El Vidrio*, Consejo Superior de Investigaciones Científicas, Spain, 1991, pp. 337-50.
8. Lessing, P. A., Gordon, R. S. & Mazdizyasny, K. S., Creep of Polycrystalline Mullite. *J. Am. Ceram. Soc.*, **58** (1975) 149.
9. Dokko, P. C., Pask, J. A. & Mazdizyasny, K. S., High Temperature Mechanical Properties of Mullite under Compression. *J. Am. Ceram. Soc.*, **60** (1977) 150-5.
10. Okamoto, Y., Fukudome, H., Hayashi, K. & Nishikawa, T., Creep Deformation of Polycrystalline Mullite. *J. Eur. Ceram. Soc.*, **6** (1990) 161-8.
11. Hynes, A. P. & Doremus, R. H., High Temperature Compressive Creep of Polycrystalline Mullite. *J. Am. Ceram. Soc.*, **74** (1991) 2469-75.
12. Ashizuka, M., Honda, T. & Kubota, Y., Effects of Grain size on Creep of Mullite Ceramics, *J. Ceram. Soc. Jpn. Int. Edition*, **99** (1991) 282-5.
13. Mah, T. I., Mazdizyasny, K. S., Mechanical Properties of Mullite. *J. Am. Ceram. Soc.*, **66** (1983) 699-703.
14. Yamade, Y., Kawaguchi, Y., Takeda, N. & Kishi, T., *J. Ceram. Soc. Jpn. Int. Edition*, **99** (1991) 452-7.
15. Kanzaki, S., Tabata, H., Sintering and Mechanical Properties of Stoichiometric Mullite. *J. Am. Ceram. Soc.*, **68** (1985) C6-7.
16. Ismail, M. G. M. U., Nakai, Z. & Somiya, S., Microstructure and Mechanical Properties of Mullite Prepared by Sol-Gel Method. *J. Am. Ceram. Soc.*, **70** (1987) C7-8.
17. Ohnishi, H., Maeda, K., Nakamura, T. & Kawanami, T., High Temperature Mechanical Properties of Mullite Ceramics, in Ref. 2, pp. 605-12.
18. Mizuno, M., Shiraishi, M. & Saito, H., Microstructure and Bending Strength of Highly Pure Mullite Ceramics, in Ref. 2 pp. 413-24.
19. Mizuno, M., Microstructure, Microchemistry and Flexural Strength of Mullite Ceramics. *J. Am. Ceram. Soc.*, **74** (1991) 3017-22.
20. Kaumazawa, T., Ohta, S., Nagaoka, T., Yasuoka, M. & Kanzaki, S., Influence of Powder Characteristics on Sinterability and Mechanical Properties of Silica-Alumina Ceramics (74 wt% Al₂O₃). *J. Ceram. Soc. Jpn. Int. Edition*, **99** (1991) 1191-6.
21. Bansal, G. K., Effect of Flaw Shape on Strength of Ceramics. *J. Am. Ceram. Soc.*, **59** (1976) 87-8.
22. Notis, M. R., Dravid, V. P. & Lyman, C. E., AEM and HRTEM Studies of the Eutectic System Zirconia-Mullite, in Ref. 2, pp. 528-39.
23. Torrecillas, R., Comportamiento Mecánico de Mullita y Mullita-Circona obtenida por sinterización reactiva, PhD Thesis. UNED, Madrid (Spain), 1990.
24. Cheeseman, C. R. & Groves, G. W., The Mechanism of Peak in Strength and Toughness at Elevated Temperatures in Alumina Containing a Glass Phase, *J. Mater. Sci.*, **20** (1985) 2614-22.
25. Rief, C. & Kromp, K., Fracture Toughness Testing. In *Mechanical Testing of Engineering Ceramics at High Temperatures*, Elsevier Applied Science, 1989, pp. 209-25.
26. Oda, I., Matui, M. & Sowa, T., High Temperature Fatigue Failure in Pressureless Sintered Silicon Nitride, In *Progress in Nitrogen Ceramics*, Martinus Nijhoff Publisher, The Netherlands 1983, pp. 501-6.
27. Kriz, K., Fracture Behaviour of Hot Pressed Silicon Nitride between Room Temperature and 1400°C, in Ref. 26 pp. 523-8.

Mechanical Properties of High Purity Mullite at Elevated Temperatures

H. Ohira,^a M. G. M. U. Ismail,^a Y. Yamamoto,^a T. Akiba^a & Shigeyuki Sōmiya^b

^aKumagaya Factory, Ceramics Business Div., Chichibu Onoda Cement Corp., 5310 Mikajiri, Kumagaya, Saitama 360, Japan

^bFaculty of Science and Engineering, The Nishi-Tokyo University, Uenohara, Yamanashi 409-01, Japan

(Accepted 22 July 1995)

Abstract

Microstructures and mechanical properties of stoichiometric mullite (71.8 wt% Al_2O_3 /28.2 wt% SiO_2) sintered at different temperatures (1650–1750°C) were studied. Maximum bulk density was obtained by sintering at 1675°C and the density slightly decreased with temperature above 1700°C. Grain size increased with sintering temperature from 1.8 μm at 1650°C to 4.0 μm at 1750°C, and a microstructure comprising a little glassy phase with large elongated grains was observed over 1725°C by scanning electron microscopy. Flexural strength measured below 1500°C decreased with sintering temperature, but creep resistance at 1550°C increased with sintering temperature. Plastic deformation was accompanied by fracture at elevated temperatures.

1 Introduction

High purity mullite is now considered as a prime candidate material for high temperature structural applications because of its excellent high temperature properties. Its flexural strength at room temperature is 300–400 MPa and it is maintained up to 1400°C.^{1,2} Excellent creep resistance is also reported.^{3–7} But it is reported that the existence of a glassy phase at the grain boundaries has a strong influence on its microstructure and mechanical properties.⁸

As for the stability of mullite at elevated temperature, Prochazka and Klug⁹ have suggested that stoichiometric mullite is not stable above a certain temperature. This implies that the microstructure and mechanical properties of stoichiometric mullite will be affected by the sintering temperature.

High purity stoichiometric mullite powder is now produced commercially via the sol–gel process.¹⁰ In the present investigation, the microstructures,

flexural strengths and creep resistance of high purity mullite bodies were studied as a function of sintering temperature.

2 Experimental Procedure

Commercial stoichiometric mullite powder (MP40, Chichibu Onoda Cement Corp., Japan) derived via the sol–gel process was used as starting material. Table 1 shows its standard characteristics and Fig. 1 presents a scanning electron micrograph of the as-received MP40. The powder was uniaxially pressed into 50 × 30 × 8 mm blocks and cold isostatically pressed under 200 MPa for 5 min. The blocks were then sintered at 1650, 1675, 1700, 1725 and 1750°C for 2 h in air. Bulk density of the sintered specimens was determined by the liquid displacement method. The sintered bodies were cut into 4 × 3 × 40 mm samples and polished for flexural strength and creep measurements.

Flexural strength and creep resistance were measured by the three-point bending method (Autograph DCS-5000, Shimadzu Corp., Japan) with span of 30 mm. Flexural strength was measured at room temperature, 1400, 1500 and 1600°C with crosshead speed of 0.5 mm min⁻¹ in air.

Creep resistance was measured at 1550°C and the strain rate, $\dot{\epsilon}$, and the stress exponent, n , were calculated by following equations:¹¹

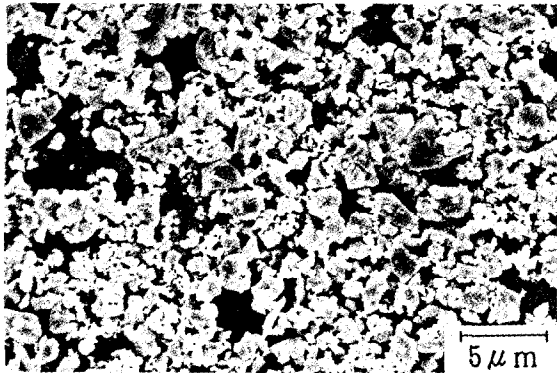
$$\sigma = \frac{3 P L}{2 b d^2} \cdot \frac{2 n + 1}{3 n} \quad (1)$$

$$\dot{\epsilon} = \frac{2 b (n + 2)}{L^2} \dot{y} \quad (2)$$

where σ is the maximum stress, P is the applied load, L is the span length, b is the width of the specimen, d is the thickness of the specimen and \dot{y} is the deflection rate at the load point.

Table 1. Standard characteristics of starting mullite powder (MP40)

Composition (wt%)	Al ₂ O ₃	71.8
	SiO ₂	28.2
Impurities (wt%)	TiO ₂	<0.1
	Fe ₂ O ₃	<0.01
	Na ₂ O	<0.01
Average particle size (μm)		1.4
Surface area (BET) (m ² g ⁻¹)		8

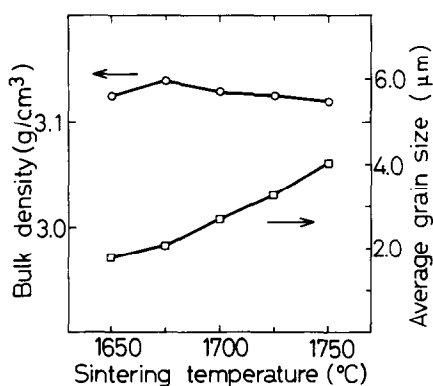
**Fig. 1.** Scanning electron micrograph of starting mullite powder (MP40).

The microstructure of the specimens was observed by scanning electron microscopy (SEM) (model SIGMA-V, Akashi Seisakusho Co., Ltd., Japan) after polishing and thermal etching. Average grain size was determined by the intercept method.¹²

3 Results and Discussion

3.1 Effects of sintering temperature on density and microstructure

Figure 2 shows the variation of bulk density and average grain size with respect to sintering temperature. Bulk density increased with sintering temperature, reaching a maximum value of 3.14 g cm⁻³ at 1675°C, and then decreased slightly with increase of sintering temperature above 1700°C. The average grain size was 1.8 μm in the 1650°C-sintered

**Fig. 2.** Variation of bulk density and average grain size of high purity mullite with sintering temperature (duration: 2 h).

specimen and gradually increased with sintering temperature, growing to 4.0 μm at 1750°C.

Representative microstructures of specimens sintered at different temperatures are shown in Fig 3. In the 1650°C-sintered specimen, many small pores remained, the grains were relatively equiaxial and few elongated grains were observed. However, with the increase of sintering temperature above 1675°C, the grain morphology changed from equiaxial to elongated with the disappearance of the pores. Sintering above 1725°C caused the exaggerated growth of elongated grains, which reached 30 μm in certain cases. Also, small equiaxial grains grew gradually, and a phase separation resulting in the formation of a small amount of glassy phase was observed at the grain boundaries (Fig. 4). The exaggerated grain growth promoted the formation of large pores between the grains and small pores within the grains. The existence of glassy phase at the grain boundaries and the large elongated grain growth suggest that a phase may shift from stoichiometric mullite to high-Al₂O₃ mullite within the solid solution limit and that a liquid phase consisting mainly of SiO₂ may be formed by the phase separation. Prochazka and Klug⁹ suggested in their studies on the Al₂O₃-SiO₂ phase diagram that 3:2 mullite is not stable above a certain temperature, and that it forms high alumina mullite with a liquid phase. Thus our present results are consistent with theirs, even though the temperature at which phase separation was observed by SEM in this study was a little higher than the value reported by them.

3.2 Effects of sintering temperature on flexural strength

Figure 5 schematically illustrates load-displacement curves measured at different temperatures for the 1725°C-sintered specimens. The specimen tested at 1400°C showed brittle fracture and little plastic deformation prior to failure. At 1500°C, however, the fracture was brittle but evidence of slight plastic deformation was observed prior to failure. At 1600°C, the specimen fractured with considerable plastic deformation.

Figure 6 shows the variation of flexural strength at room and elevated temperatures as a function of sintering temperature. The data measured at 1600°C were excluded because of significant plastic deformation during the measurements, as shown in Fig. 5. It was evident that the flexural strength decreased with both testing temperature and sintering temperature. As for the relationship between flexural strength and sintering temperature, the strength at room temperature decreased from 400 MPa for the 1675°C-sintered specimen to 300 MPa for the 1750°C-sintered specimen. The

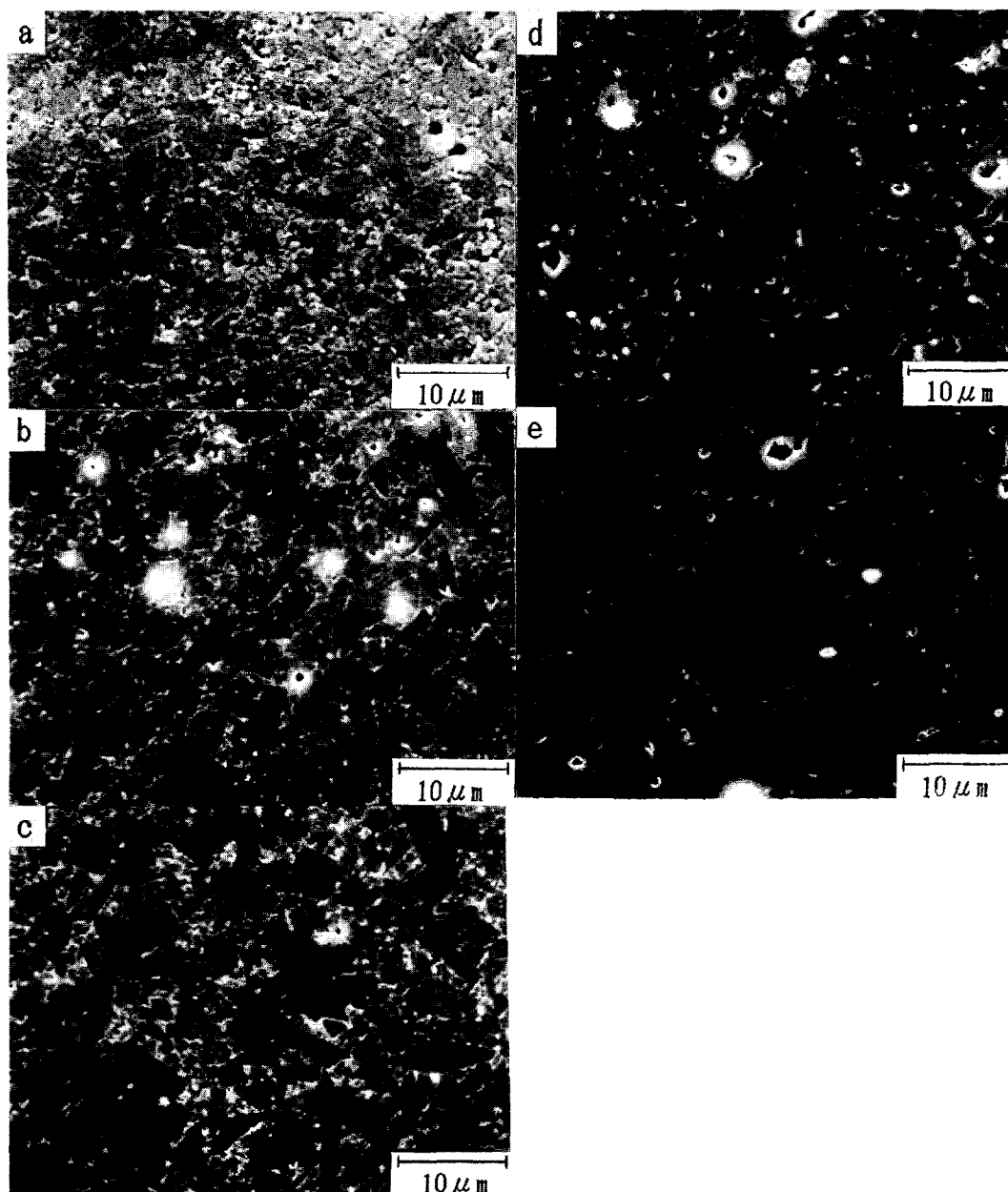


Fig. 3. Scanning electron micrographs of high purity mullite sintered at (a) 1650°C, (b) 1675°C, (c) 1700°C, (d) 1725°C and (e) 1750°C for 2 h (thermally etched at 1550°C).

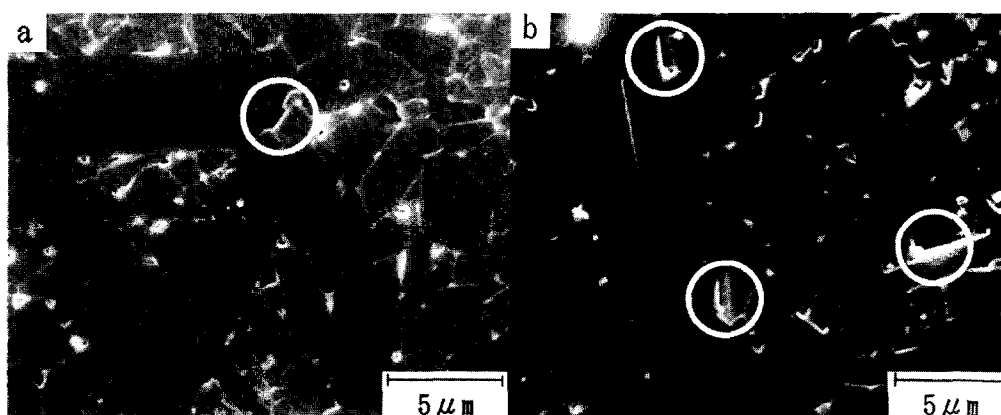


Fig. 4. Scanning electron micrographs of high purity mullite sintered at (a) 1725°C and (b) 1750°C, showing small glassy areas (thermally etched at 1550°C).

strength at 1400°C also decreased from 360 MPa for the 1650°C-sintered specimen to 280 MPa for the 1750°C-sintered specimen. The reason for this

strength degradation could be the grain growth, as discussed later. Strength degradation at 1500°C, however, became smaller than those of strength at

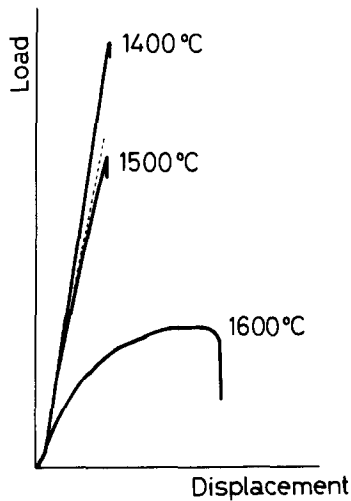


Fig. 5. Schematic illustration of load-displacement curves measured at elevated temperatures for the specimen sintered at 1725°C for 2 h (three-point bending, crosshead speed 0.5 mm min⁻¹).

room temperature and 1400°C. This observation could be explained by the relation between plastic deformation and the glassy phase. If glassy phase exists at the grain boundaries, plastic deformation at fracture will occur at elevated temperature and the calculated fracture stress will be higher than the real fracture stress. As previously shown in Figs 3 and 4, more glassy phase at grain boundaries was observed at higher sintering temperature. And also, more significant plastic deformation at fracture was observed at higher testing temperature as shown in Fig. 5. Therefore the effects of glassy phase on the fracture stress would be higher for the specimens sintered at higher temperature and, as a result, the strength degradation at 1500°C would become smaller.

Figure 7 shows the relationship between fracture stress and grain size. The relationship followed a Hall-Petch type equation,

$$\sigma_f = \sigma_0 + k d^{-1/2} \quad (3)$$

where σ_f is the fracture stress, σ_0 is the stress axis

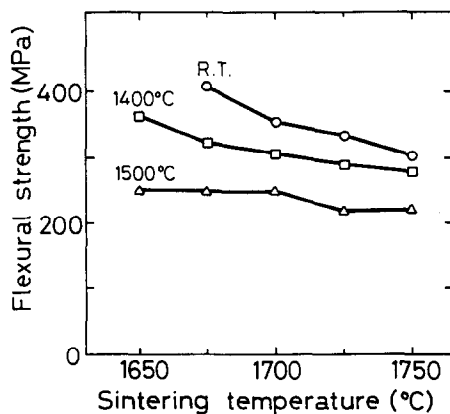


Fig. 6. Variation of flexural strength at different temperatures as a function of sintering temperature.

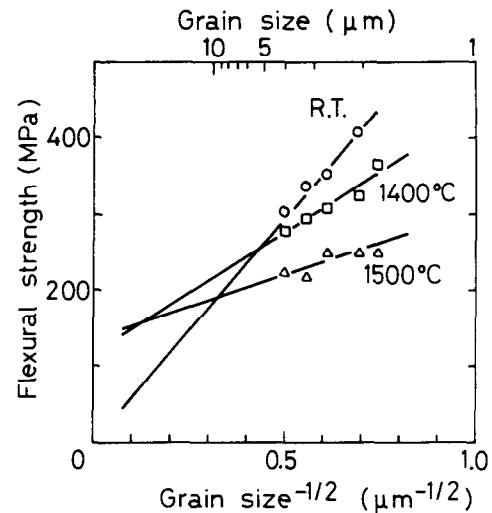


Fig. 7. Variation of flexural strength at different temperatures as a function of average grain size.

intercept, k is a constant and d is the grain size. Flexural strength at room and elevated temperatures obeyed a Hall-Petch relationship although the intercepts and gradients of the curves differed. The stress-axis intercept of the data at room temperature was close to zero and equation (1) can be expressed as,

$$\sigma_f = k' d^{-1/2} \quad (4)$$

where k' is a constant. Equation (4) is equivalent to the Griffith equation by assuming that the critical flaw size is proportional to the grain size, i.e.

$$c = \alpha d \quad (5)$$

where c is the critical flaw size and α is a constant. This implies that the specimens would fracture in the brittle manner at room temperature. On the other hand, the fracture stresses measured at 1400 and 1500°C follow Eqn (3) which has been confirmed for a variety of polycrystalline strength phenomena.¹³⁻¹⁵ This suggests that fracture at elevated temperatures could be accompanied by plastic flow, although little plastic deformation was observed from the load-displacement curves as shown in Fig. 5. That is, the stress at the crack tip becomes very high at fracture as a result of stress concentration, therefore plastic flow would occur even at 1400°C.

3.3 Effects of sintering temperature on creep

Figure 8 shows the steady-state creep rate vs. stress from 10 to 100 MPa at 1550°C as a function of sintering temperature. Creep resistance increased with sintering temperature, i.e. with the grain size. The stress exponent, n , of the 1675°C-sintered specimen was 1.3 and that of 1700°C-sintered specimen was 1.2. These similar values suggest that the same creep mechanism was operative in this tem-

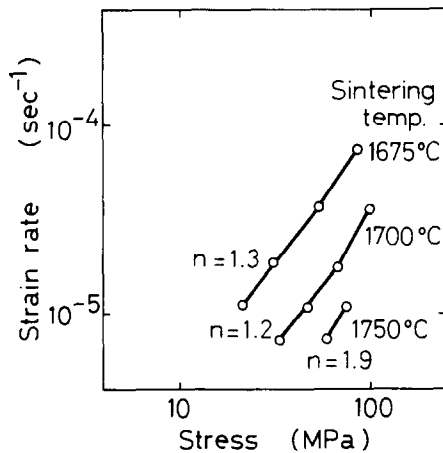


Fig. 8. Steady-state creep rate vs. stress at 1550°C by three-point bending as a function of sintering temperature.

perature region. Some researchers^{3,5,6} have reported that the stress exponents of stoichiometric mullite measured by the bending technique are 0.95–1.3 at 1400 and 1500°C, and that the deformation mechanism is diffusional creep. Results of the present study are similar to these reported values, therefore the deformation mechanism for the 1675°C- and 1700°C-sintered specimens of this study may also be diffusional creep although the testing temperature was higher than in previous reports. For the specimen sintered at 1750°C, however, a higher n value of 1.9 was obtained, suggesting that a different creep mechanism was operative. As shown in Fig. 4, the microstructure of this specimen was a little different and a small amount of glassy phase was observed at grain boundaries by SEM observation. Therefore this glassy phase would have influenced the creep behaviour of this specimen.

4 Conclusions

Microstructures and mechanical properties of stoichiometric mullite (71.8 wt% Al₂O₃/28.2 wt% SiO₂) sintered at different temperatures (1650–1750°C) have been studied and following results obtained.

1. Maximum bulk density is obtained by sintering at 1675°C and decreases slightly upon sintering above 1700°C. Grain size increases with sintering temperature from 1.8 μm at 1650°C to 4.0 μm at 1750°C, and a little glassy phase and large elongated grains are observed above 1725°C by SEM.
2. Flexural strength measured below 1500°C decreases with sintering temperature. Plastic

deformation is accompanied by fracture even at the temperature of 1400°C, although little plastic deformation prior to failure is observed in load–displacement curves.

3. Creep resistance increases with sintering temperature. The creep mechanism of specimens sintered at 1675 and 1700°C is considered to be diffusional creep, but a different creep mechanism may also be operative for the specimen sintered at 1750°C.

References

1. Kanzaki, S., Tabata, H., Kumazawa, T. & Ohta, S., Sintering and mechanical properties of stoichiometric mullite. *J. Am. Ceram. Soc.*, **68**(1) (1985) C-6–7.
2. Ismail, M. G. M. U., Nakai, Z., Ohira, H. & Sōmiya, S., Preparation and characterization of mullite containing materials. In *Ceramic Powder Science II B*, eds G. R. Messing, E. R. Fuller & H. Hausner, The American Ceramic Society, Inc., Westerville, OH, 1988, pp. 1108–14.
3. Lessing, P. A., Gordon, R. S. & Mazdiyasn, K. S., Creep of polycrystalline mullite. *J. Am. Ceram. Soc.*, **58**(3–4) (1975) 149.
4. Dokko, P. C., Pask, J. A. & Mazdiyasn, K. S., High temperature mechanical properties of mullite under compression. *J. Am. Ceram. Soc.*, **60**(3–4) (1977) 150–5.
5. Ohnishi, H., Maeda, K., Nakamura, T. & Kawanami, T., High temperature mechanical properties of mullite ceramics. In *Mullite and Matrix Composites*, eds S. Sōmiya, R. F. Davis & J. A. Pask, The American Ceramic Society, Inc., Westerville, OH, 1990, pp. 605–12.
6. Okamoto, Y., Fukudome, H., Hayashi, K. & Nishikawa, T., Creep deformation of polycrystalline mullite. *J. Eur. Ceram. Soc.*, **6** (1990) 161–8.
7. Ohira, H., Shiga, H., Ismail, M. G. M. U., Nakai, Z., Akiba, T. & Yasuda, E., Compressive creep of mullite ceramics. *J. Mater. Sci. Lett.*, **10**(14) (1991) 847–9.
8. Kumazawa, T., Kanzaki, S., Ohta, S. & Tabata, H., Influence of chemical composition on the mechanical properties of SiO₂–Al₂O₃ ceramics. *Yogyokukai-shi*, **96**(1) (1988) 85–91.
9. Prochazka, S. & Klug, F. J., Infrared-transparent mullite ceramic. *J. Am. Ceram. Soc.*, **66**(12) (1986) 874–80.
10. Ismail, M. G. M. U. & Nakai, Z., Properties of high-purity mullite prepared by the sol–gel method. In *Mullite II*, ed. S. Sōmiya, Uchida Rokakuho Publishing Co., Tokyo, Japan, 1987, pp. 69–80.
11. Hollenberg, G. W., Terwillinger, G. R. & Gordon, R. S., Calculation of stresses and strains in four-point bending creep tests. *J. Am. Ceram. Soc.*, **54**(4) (1971) 196–9.
12. Underwood, E. E., *Quantitative Stereology*. Addison-Wesley, 1970.
13. Sinha, M. N., Lloyd, D. J. & Tangri, K., Microyield and fracture in polycrystalline MgO. *J. Mater. Sci.*, **8** (1973) 116–22.
14. Tressler, R. E., Langensiepen, R. A. & Bradt, R. C., Surface-finish effects on strength-vs-grain-size relations in polycrystalline Al₂O₃. *J. Am. Ceram. Soc.*, **57**(5) (1974) 226–7.
15. Bradt, R. C., Dulberg, J. L. & Tressler, R. E., Surface finish effects and the strength-grain size relationship in MgO. *Acta Metall.*, **24** (1976) 529–34.

Microstructure and Mechanical Properties of Mullite/Zirconia Composites Prepared from Alumina and Zircon under Various Firing Conditions

T. Koyama,^a S. Hayashi,^a A. Yasumori,^a K. Okada,^a
M. Schmucker^b & H. Schneider^b

^aDepartment of Inorganic Materials, Tokyo Institute of Technology, O-okayama, Meguro, Tokyo 152, Japan

^bGerman Aerospace Research Establishment (DLR), Institute for Materials Research, D-51140 Koln, Germany

(Accepted 22 July 1995)

Abstract

Zirconia-dispersed mullite composites were prepared by reaction sintering of alumina and zircon powders under various firing conditions. Mullite formed by firing at 1635°C apparently contained > 60 mol% Al₂O₃ and incorporated a small amount of zirconia. This transient mullite composition changed to the normal composition by treatments such as long firing time, annealing, two-step firing and/or seeding. Mullite/zirconia composites at room temperature showed good strength and fracture toughness, but these properties decreased significantly at high temperature because glassy phase in the grain boundaries. Mechanical strength at high temperature could be improved by those firing treatments which reduced the amount of glassy phase, especially by two-step firing and seeding methods.

1 Introduction

As a means to enhance the mechanical properties of mullite ceramics, mullite/zirconia composites have been investigated extensively by many workers.^{1–5} Mullite/zirconia composites can be prepared via various methods: (1) sintering of mullite and zirconia, (2) reaction sintering of alumina and zircon, and (3) reaction sintering of alumina, silica and zirconia. We⁶ prepared mullite/zirconia composites by these methods and found that composites prepared by method (2) had some unique characteristic features compared with those by the other methods, e.g. higher fracture toughness. We considered that the reason could be attributed to the characteristic microstructure.⁶ We also found

that the chemical composition of mullite formed in the route (2) composites was richer in alumina than the expected composition of 60 mol%. The reason for these characteristic features of the composites are not clear yet.

In this work, we prepared mullite/zirconia composites from reaction sintering of alumina and zircon under various firing conditions and examined changes of the microstructure, the chemical composition of mullite and their mechanical properties.

2 Experimental Procedure

Fine and high purity alumina (TM-DAR, Taimei Chemicals), zircon (Tosoh) and mullite (MP-20, Chichibu Cement) powders were used for the experiments. The powders were mixed by wet ball milling in ethanol using a polyethylene pot and yttria-stabilized tetragonal zirconia balls of 2 mm in diameter. The mixtures were dried by stirring with a hot stirrer at 80°C. Pellets were compacted by uniaxial pressing at 400 MPa. They were fired under various firing schedules. The firing schedules are shown schematically in Fig. 1 and can be summarized as follows: (1) ordinary firing: fired with a heating rate of 15 K min⁻¹, firing temperature 1570–1635°C for 0–156 h and a cooling rate of 30 K min⁻¹; (2) annealing: fired in two steps, i.e. firing at 1635°C for 12 h and annealing at 1570°C for 12–144 h; (3) re-firing: fired in three steps, i.e. firing at 1635°C for 12–144 h, annealing at 1570°C for 12–144 h and re-firing at 1635°C for 12–144 h; (4) optimized firing: fired by a two-step firing profile at 1570°C for 2 h and subsequently at

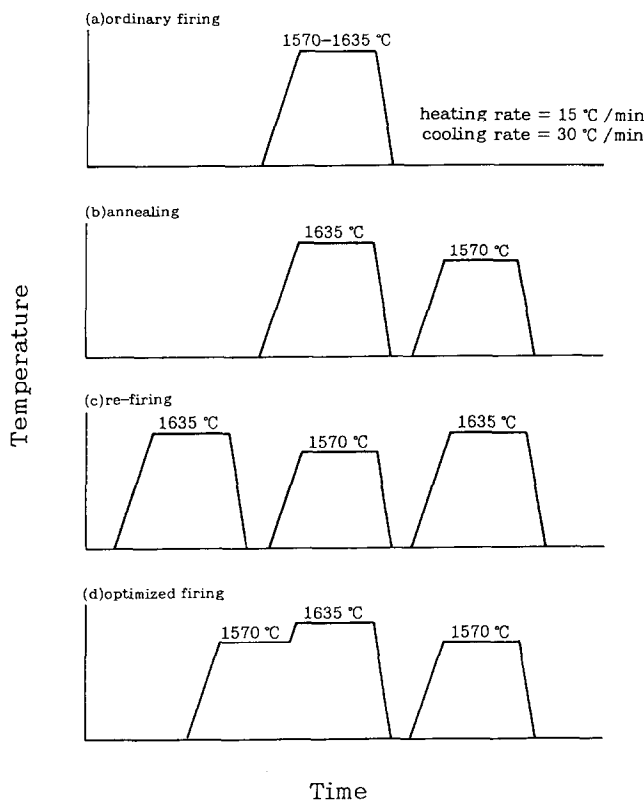


Fig. 1. Scheme of the firing schedules.

1635°C for 72 h, and then annealing at 1570°C for 72 h. Additionally, samples seeded with 5 and 20 vol% of mullite particles (average particle size 1.76 μm) were also prepared and fired with the optimized firing schedule.

X-ray diffraction (XRD) patterns of the samples were measured using a powder X-ray diffractometer (Geigerflex, Rigaku) with monochromated $\text{CuK}\alpha$ radiation. Seven mullite reflections in the powdered samples were precisely measured using an internal standard of Si powder. Lattice constants of mullite were calculated by the least-squares method. Microstructure of the fired samples was observed by transmission electron microscopy TEM (JEM 200CX, Jeol) using thin-sectioned samples. Chemical composition of mullite was analysed by EDX (Northern) with the TEM instrument and calculated by the K -factor method.

Four-point bending strengths of the samples were measured from room temperature to 1500°C using a testing instrument (Instron 4302) with a crosshead speed of 0.5 mm min^{-1} for a test bar of $3 \times 4 \times 36 \text{ mm}^3$ (JIS R 1601). The samples used for the measurements were > 98% of relative density and were polished by #800 diamond paste.

Table 1. Lattice parameters of mullite in the variously fired samples

Sample no.	Temp. ($^{\circ}\text{C}$)/duration (h)	Lattice parameter (nm)		
		a-axis	b-axis	c-axis
(1) Ordinary firing				
1	1570/12	0.75609(10)	0.76877(14)	0.28853(05)
2	1600/12	0.75640(20)	0.76872(16)	0.28862(01)
3	1635/0	0.75619(13)	0.76890(05)	0.28850(05)
4	1635/6	0.75684(05)	0.76877(16)	0.28852(06)
5	1635/12	0.75701(11)	0.76876(04)	0.28863(01)
6	1635/18	0.75655(11)	0.76882(07)	0.28852(01)
7	1635/24	0.75648(11)	0.76882(12)	0.28861(03)
8	1635/84	0.75636(07)	0.76882(12)	0.28861(03)
(2) Annealing				
9 No. 5 \rightarrow	1570/12	0.75643(18)	0.76876(05)	0.28853(02)
10 No. 5 \rightarrow	1570/72	0.75592(07)	0.76879(07)	0.28855(07)
11 No. 5 \rightarrow	1570/144	0.75533(07)	0.76892(05)	0.28846(02)
(3) Re-firing				
12 No. 9 \rightarrow	1635/12	0.75622(03)	0.76870(01)	0.28856(04)
13 No. 10 \rightarrow	1635/72	0.75512(02)	0.76906(05)	0.28850(04)
14 No. 11 \rightarrow	1635/144	0.75486(11)	0.76907(01)	0.28851(04)
(4) Optimized firing				
15	1570/2,1635/12,1570/72	0.75472(06)	0.76911(04)	0.28839(03)
16	1570/12,1635/12,1570/12	0.75475(28)	0.76909(13)	0.28846(04)
5 Vol% mullite seeded				
17	1570/12	0.75602(07)	0.76909(05)	0.28844(07)
18	1600/12	0.75602(19)	0.76890(13)	0.28851(05)
19	1635/12	0.75607(18)	0.76893(16)	0.28853(04)
20 Vol% mullite seeded				
20	1570/12	0.75512(04)	0.76912(21)	0.28844(03)
21	1600/12	0.75504(08)	0.76910(19)	0.28852(04)
22	1635/12	0.75505(09)	0.76904(14)	0.28847(04)
23	1570/02,1635/12,1570/72	0.75456(09)	0.76911(06)	0.28846(03)

Standard derivations are in parentheses and refer to last decimal place.

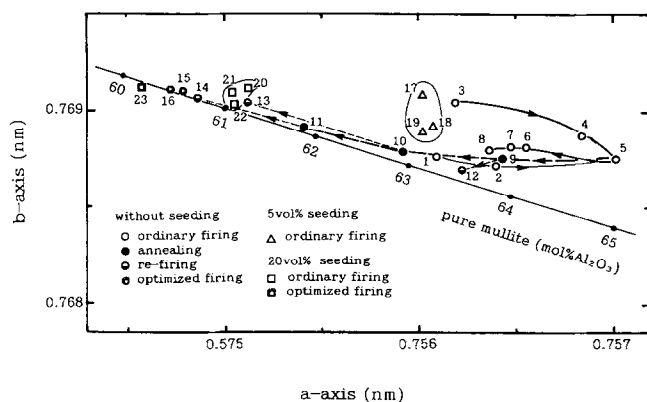


Fig. 2. Relation between the lengths of the a - and b -axes of mullite in the samples prepared under various conditions (see text and Table 1 for details).

Edges were chamfered with a diamond disc. Fracture toughness was determined using an indentation microcrack method⁷ with a load of 49 N.

3 Results and Discussion

3.1 Ordinary firing

In these experiments, the samples were prepared with two series of firing conditions. In the first series, the samples were fired for a constant duration of 12 h with firing temperatures from 1570 to 1635°C. In the second series, the samples were fired at a constant temperature of 1635°C with duration varying from 0 to 156 h. Lattice constants of mullite in these samples are listed in Table 1. The correlation between the lengths of the a - and b -axes is shown in Fig. 2. In the first series, the length of the a -axis of mullite increased with higher firing temperature while the lengths of the b - and c -axes did not change significantly (samples 1, 2, 5). The change was especially large between the mullite fired at 1600°C and that at 1635°C (samples 3–8). Due to this increase of the length of the a -axis, the lattice constant data of the mullite fired at 1635°C deviated from the relation reported for pure mullite, which is also depicted in Fig. 2. This deviation of the data

Table 2. Chemical analysis of mullite by EDX

Sample no.	Chemical composition (mol %)			
	Al_2O_3	SiO_2	ZrO_2	Al_2O_3/SiO_2
3	61.3(13)	37.5(13)	1.2(04)	1.63
5	63.4(09)	35.5(09)	1.1(05)	1.79
8	63.8(10)	36.1(07)	1.1(04)	1.77
11	62.9(09)	36.5(09)	0.6(02)	1.73
21	60.7(07)	38.8(07)	0.5(02)	1.56

Standard derivations are in parentheses and refer to last decimal place.

suggests incorporation of ZrO_2 into the mullite structure. A second series of experiments was, therefore, made in order to elucidate this phenomenon.

The lengths of the a - and b -axes for the second series samples (3–8) are also shown in Fig. 2. With longer firing time, the cell edges changed on a line parallel to the composition line of pure mullite, indicating increasing Al_2O_3 contents. This trend continued up to 12 h. Since this line runs parallel

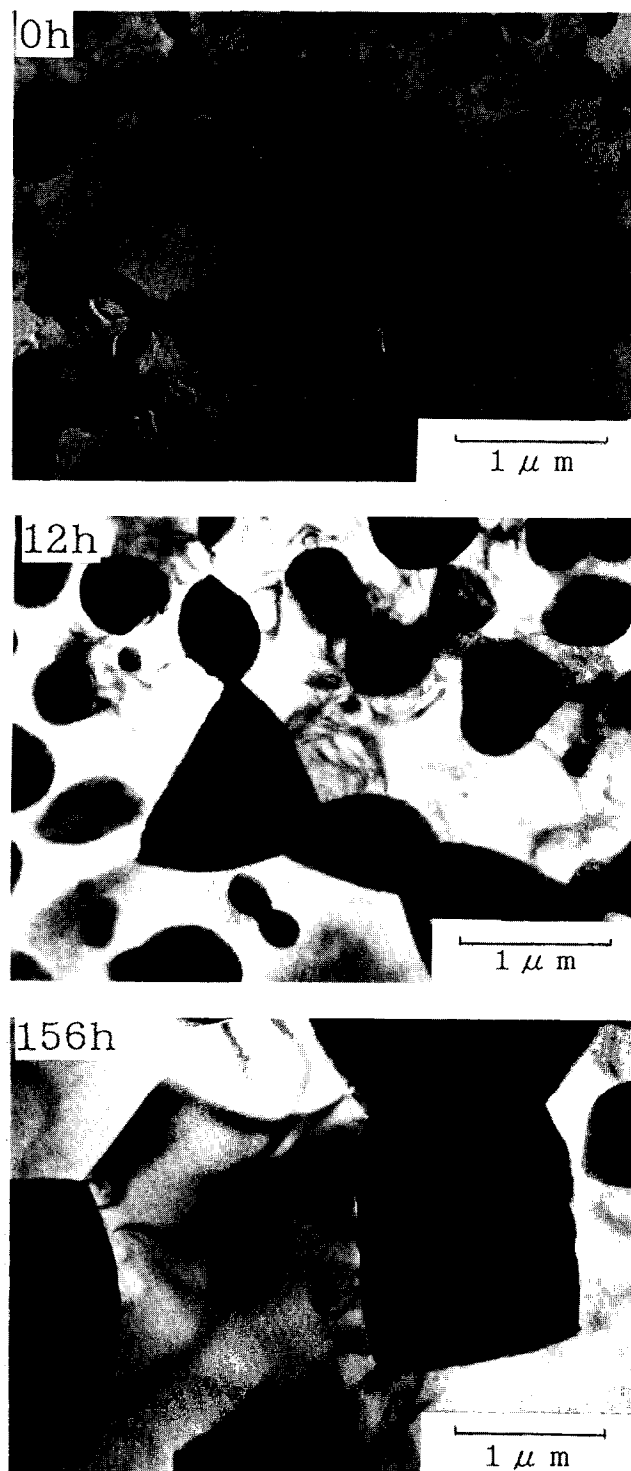


Fig. 3. TEM photographs of the 'ordinary firing' samples with various firing times.

to the pure mullite line, it is suggested that a small amount of zirconia is incorporated in these mullites. With firing times longer than 12 h, the a -axis became shorter again. This new trend approached the pure mullite line but stopped at a certain stage intermediate between pure mullite and the line given by samples 3, 4 and 5. Chemical compositions of some mullites were analysed by EDX and are listed in Table 2. From these data, it is confirmed that a small amount of zirconia was incorporated in the mullites (samples 3 and 5).

Figure 3 shows the microstructural changes in the samples fired at 1635°C for different times. With longer firing time, the grain size of the zirconia drastically increased and the thickness of a glassy grain boundary phase also increased. As the XRD and EDX results indicated, the mullites were richer in alumina than the expected composition of 60 mol%. Therefore, some excess silica should be exsolved and be present in the samples. Indeed, a thick amorphous film was observed in the grain boundaries as shown in Fig. 4. This amorphous film totally covered the mullite grains. The amorphous film was, therefore, considered to be silica-rich in composition. The liquid phase from which this amorphous film was formed is considered to have evolved transiently at high temperature because of the peculiar mullite formation reaction in this system, i.e. silica formed by the decomposition of zircon reacted with alumina to form mullite at high temperature. With higher firing temperature, the amount of the liquid phase

apparently increased. Therefore, the chemical composition of mullite changed transiently towards the $2\text{Al}_2\text{O}_3\cdot\text{SiO}_2$ composition and incorporated some amount of zirconia due to the rapid mullitization in the presence of the liquid phase. However, this transit state then gradually changed to the apparently stable state at that temperature with longer firing time and the transiently formed mullite changed its chemical composition towards the apparently stable state and exsolved zirconia as a result. (This apparently stable state does not mean really equilibrium stable state.) Similar transient zirconia incorporation in mullite was also reported in the crystallization of mullite in rapidly quenched mullite/zirconia composites by Yoshimura *et al.*⁸

3.2 Annealing and re-firing

With longer firing times up to 156 h at 1635°C in the ordinary firing method described above, the chemical composition of mullite became almost constant at some intermediate state as reported in the previous section. Although the sample (5) showed a very high fracture toughness of 6.9 MPa $\text{m}^{1/2}$ and good four-point bending strength of 310 MPa at room temperature, the existence of a silica-rich amorphous phase in the grain boundaries was anticipated to be detrimental for high temperature mechanical properties of the composites. Hence, an annealing treatment was attempted at 1570°C in order to crystallize the grain boundary phase by a reaction between the amorphous phase and the alumina-rich mullite. This reaction should also

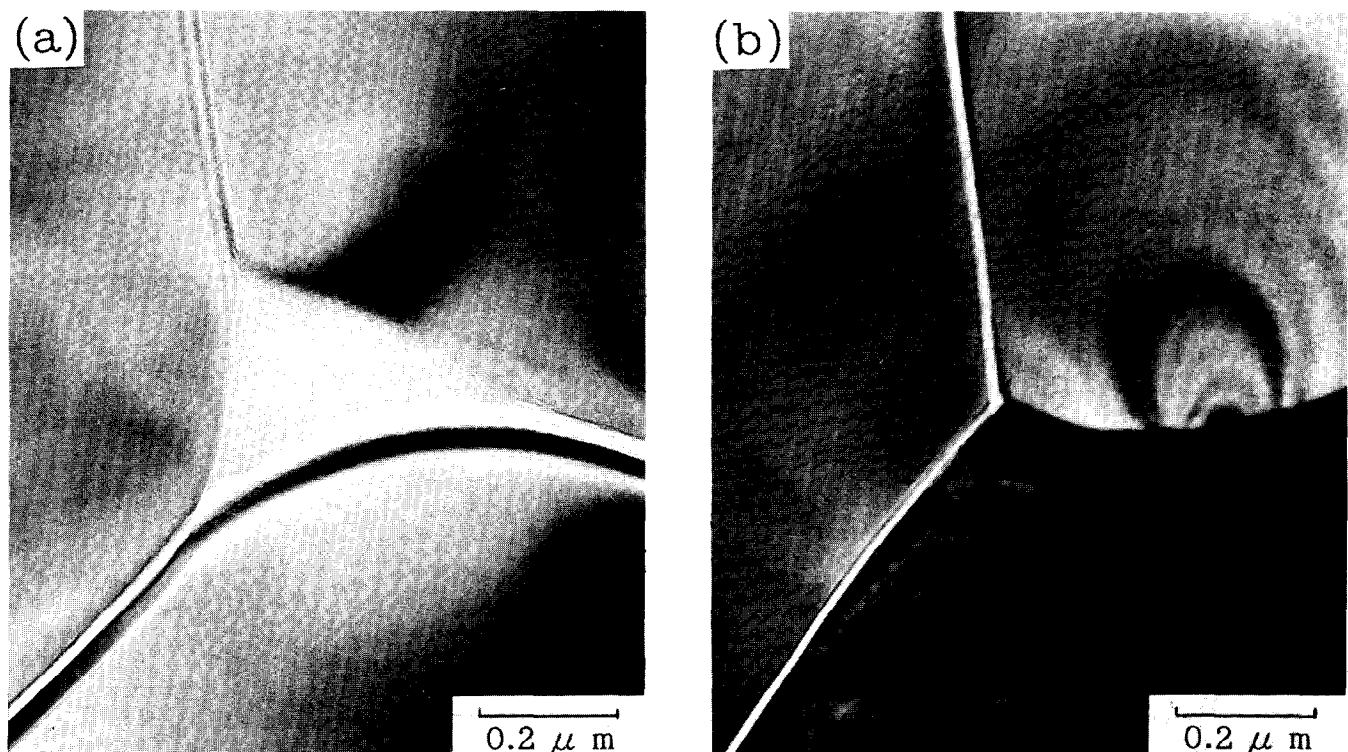


Fig. 4. TEM photographs of the grain boundaries of the 'ordinary firing' samples: (a) fired at 1635°C for 1 h; (b) for 156 h.

change the chemical composition of mullite to 60 mol% Al_2O_3 . The lattice parameter changes resulting from the annealing treatment are also shown in Fig. 2 (samples 9–11). With longer annealing time at 1570°C, the chemical composition of mullite indeed shifted and approached the expected value of 60 mol% Al_2O_3 . As is evident from Fig. 2, zirconia was mostly expelled from mullite by this treatment. This was also confirmed by EDX analysis listed in Table 2. The annealing treatment at 1570°C was found to be effective to change the chemical composition of mullite to the expected value. Further, annealing experiments were performed at 1520 and 1450°C but they were found to be less effective than those at 1570°C.

In the next step, we re-fired the annealed samples again at 1635°C. The lattice constants of mullite changed again upon this treatment, indicating that the chemical composition further approached 60 mol% Al_2O_3 . This implies that no liquid phase was formed during this re-firing even though it was fired at the same firing temperature as that of the 'ordinary firing', where a transient metastable liquid phase had formed. The reaction that occurred in the re-firing treatment was, therefore, considered to approach stable state at this temperature. In the case of the ordinary firing at 1635°C, the change of the lattice constants showed limitation and stopped at some intermediate stage even after long firing times. Comparing with this result, the change of the lattice constants of mullite was accelerated in the annealing and re-firing treatments. The driving force for this change is, however, uncertain at present.

3.3 Optimized firing

From the previous results, we found that the chemical composition of mullite formed by the ordinary firing was alumina-rich and yielded a silica-rich amorphous film in the grain boundaries. This type of microstructure is anticipated to lead to degradation of mechanical properties at high temperature. In order to avoid the formation of alumina-rich mullite, we considered two counterplans.

The first counterplan was firing the samples by a two-step firing schedule, which was first proposed by Claussen and Jahn.² The concept of this process was to separate the densification stage and the reaction stage. In the present study, we attempted to form mullite at a temperature lower than 1635°C to avoid alumina-rich mullite formation. Therefore, mullitization was done by holding at 1570°C for 2–12 h and then the samples were sintered at the higher temperature of 1635°C. Indeed, mullite formed by this firing schedule was much closer in composition to 60 mol% Al_2O_3

than in the samples made by the 'ordinary firing'. The samples were then further annealed at 1570°C as shown in Fig. 1. By this firing schedule (d), the chemical composition of mullite in the composites became very close to the expected composition of 60 mol% Al_2O_3 as shown in samples 15 and 16 of Fig. 2. The difference between the results of this firing schedule (samples 15 and 16) and the annealing schedule (samples 13 and 12) was quite considerable. This is attributed to the difference of their mullitization temperature. Apparently the chemical composition of firstly formed mullite is very important for the ability of the mullite to reach the final equilibrium composition close to 60 mol% Al_2O_3 .

Our second counterplan was the seeding method. Composites seeded with 5 and 20 vol% of mullite particles were prepared. As is apparent from the data of samples 17–22 in Fig. 2, the chemical composition of the mullite formed depended on the amount of seeding but was almost independent of the firing temperatures. Therefore, we combined the two counterplans of two-step firing and seeding methods and found that the mullite thus formed (sample 23 in Fig. 2) showed a composition very close to 60 mol% Al_2O_3 .

3.4 Temperature dependence of bending strength

Figure 5 shows the four-point bending strength of the mullite/zirconia composites from room temperature to 1500°C. The bending strength of the 'ordinary firing' sample (5) was fairly high (310

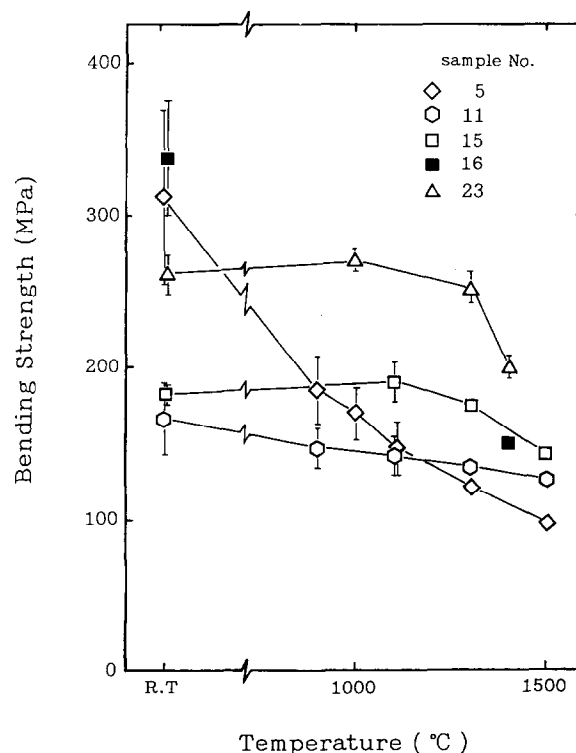


Fig. 5. Temperature dependence of the four-point bending strength different samples (see Table 1 for processing details).

MPa) at room temperature. However, it decreased linearly with temperature and was only 100 MPa at 1500°C. This large degradation of the strength was considered to be due to the presence of a thick and continuous silica-rich amorphous film in the grain boundaries as shown in Fig. 4. To avoid this degradation of strength at high temperature, the amorphous phase was crystallized by annealing at 1570°C for 144 h. The bending strength of the annealed sample (11) was, however, very low at room temperature. Since a jagged pattern was observed in the stress-strain curve of this sample, microcracking in the annealed sample was considered to be the main reason for the low bending strength. Many cracks along the grain boundaries were indeed observed by TEM. The cracks were considered to occur by the crystallization of mullite from the reaction of alumina-rich mullite and silica-rich amorphous phase in the grain boundaries. Therefore, crystallization of the grain boundaries was found not to be effective in these composites although this technique was reported to be effective to enhance the mechanical properties of silicon nitride.⁹

To avoid the formation of glassy phase and microcracks in the samples, we adopted the two-step firing and annealing treatments. Sample (15) showed a fair enhancement of the bending strength for the whole temperature range compared with the annealed sample (11). This enhancement of bending strength was considered to be due to the shorter firing time, that is, decreased grain size. However, the grain size of this sample was still much larger than that of the 'ordinary firing' and the bending strength at room temperature was also lower. With shorter annealing time, the bending strength (sample 16) was found to increase to around 340 MPa at room temperature but it was not improved at high temperature because of the residual glassy phase. On the other hand, the seeded sample (23) showed an improvement of high temperature strength compared with the previous sample (16). Since the firing schedule was the same for these two samples, the seeding with mullite particles was found to be effective to improve high temperature strength. This also confirms that seeding is very effective to control the chemical composition of mullite formed in the reaction sintering of alumina and zircon.

Torretilas *et al.*¹⁰ and Kubota *et al.*¹¹ examined the high temperature mechanical properties of zirconia-dispersed mullite composites and also zirconia- and alumina-dispersed mullite composites prepared by reaction sintering of alumina and zircon. Torretilas *et al.*¹⁰ considered the formation of liquid phase at high temperature. Recently,

Ebinuma *et al.*¹² showed direct evidence of liquid phase formation at high temperature in the reaction sintering of alumina and zircon. Torretilas *et al.*¹⁰ and Kubota *et al.*¹¹ shifted the bulk chemical composition towards an alumina-rich composition to avoid the liquid phase formation. These composites showed little degradation of high temperature strength because of almost glass-free grain boundaries, but lowering of creep properties was inevitable due to co-existence of alumina. Comparing with their data, the bending strengths of the seeded sample in the present study were similar or a little higher for all temperatures from room temperature to high temperature.

4 Summary

Zircon-dispersed mullite composites were prepared via reaction sintering of alumina and zircon with various firing schedules. The following results were obtained.

In the 'ordinary firing' schedule, the chemical composition of the mullite formed was extraordinarily alumina-rich and a small amount of zirconia was incorporated. This caused continuous thick glassy films in the grain boundaries. Incorporation of zirconia was transient and expelled by longer firing time. By long duration of annealing at 1570°C, zirconia was also exsolved from mullite and some change was observed in the chemical composition of mullite by the crystallization of the glassy grain boundaries. However, it was insufficient for complete crystallizing of the glassy grain boundaries. Further progress was made by the re-firing treatment but this treatment was still insufficient for complete crystallization. The two-step firing treatment to form mullite at 1570°C was effective to avoid the formation of alumina-rich mullite. Seeding with 20 vol% of mullite particles accelerated the mullitization at that temperature. The 'ordinary firing' samples showed good four-point bending strength and fracture toughness at room temperature but showed degradation of the mechanical properties at high temperature. This was attributed to the continuous and thick glassy phase in the grain boundaries.

Four-point bending strength of the samples could not be improved when they were prepared by long firing time at high temperature because grain growth and microcracking occurred by these treatments. High temperature strength was improved, however, by reducing the silica-rich amorphous glassy phase in the grain boundaries. Seeding with mullite particles combined with two-step firing were most effective to obtain high strength from room temperature up to 1500°C.

Acknowledgements

We are grateful to Mr T. Mori of Tosoh Company, Japan for supplying the zircon powder and Dr C. Yamagishi of Nippon Cement Company, Japan for the measurement of bending strength.

References

1. Prochazka, S., Wallace J. S. & Claussen N., Microstructure of sintered mullite-zirconia composites. *J. Am. Ceram. Soc.*, **66**(8) (1983) c125-7.
2. Claussen, N. & Jahn J., Mechanical properties of sintered in-situ reacted mullite-zirconia composites. *J. Am. Ceram. Soc.*, **63**(3-4) (1980) 228-9.
3. Moya, J. S. & Osendi, M. I., Microstructure and mechanical properties of mullite/ZrO₂ composites. *J. Mater. Sci.*, **19** (1984) 2909-14.
4. Ismail, M. G. M. U., Nakai, Z. & Somiya, S., Properties of zirconia-toughened mullite synthesized by the sol-gel method. *Adv. Ceram.*, **24** (1988) 119-26.
5. Rundgren, K., Elfving, P., Tabata, H., Kanzaki, S. & Pompe, R., Microstructures and mechanical properties of mullite-zirconia composites made from inorganic sols and salts. *Ceram. Trans.*, **6** (1990) 553-66.
6. Koyama, T., Hayashi, S., Yasumori, A. & Okada, K., Contribution of microstructure to the toughness of mullite/zirconia composites. *Proc. Ceram. Process. Sci. Technol.*, in press.
7. Niihara, K., Evaluation of K_{IC} by indentation microfracture method. In *Abstracts 21st Symposium of Basic Science of Ceramics*, (1983) B-15.
8. Yoshimura, M., Hanaue, Y. & Somiya, S. Non-stoichiometric mullites from Al₂O₃-SiO₂-ZrO₂ amorphous materials by rapid quenching. *Ceram. Trans.*, **6** (1990) 449-56.
9. Hecht, N. L., McCullum, D. E. & Graves, G. A., In *Proc. 3rd Int. Symp. on Ceramic Materials and Components for Engines*, ed V. J. Tennery, Am. Ceram. Soc. Inc., 1989 pp. 806-17.
10. Torrecillas, R., Moya, J. S., De Aza, S., Gross H. & Fantozzi, G., Microstructure and mechanical properties of mullite-zirconia reaction-sintered composites. *Acta Metall. Mater.*, **41**(6) (1993) 1647-52.
11. Kubota, Y., Yamamoto, S., Mori, T., Yamamura, H. & Mitamura, T., Changes of microstructure and high-temperature strength of ceramic composite in the mullite-ZrO₂-Al₂O₃ system using an in-situ reaction between synthetic zircon and Al₂O₃. *J. Ceram. Soc. Jpn.*, **102**(1) (1994) 93-8.
12. Ebinuma, T., Hamano, K. & Okada, S., Preparation of alumina-zirconia-mullite composite on solid-phase reaction between alumina and zircon. In *Proc. 7th Autumn Symp.*, Sapporo, 1994, p. 66.

Phase Transformation and Grain Coarsening of Zirconia/Mullite Composites

Wen-Cheng J. Wei, H. C. Kao & M. H. Lo

Institute of Materials Science and Engineering, National Taiwan University, Taipei, Taiwan 106, Republic of China

(Accepted 22 July 1995)

Abstract

*ZrO₂/mullite composites (ZMC) with homogeneously dispersed ZrO₂ grains were prepared from colloidal or sol-gel processes of the precursors, which were a mixture of colloidal pseudo-boehmite (γ -AlOOH), zirconia and silicic acid gel, or prepared from dissociated zircon with alumina powder. After pressureless sintering of the ZMCs, their microstructure was examined by means of X-ray diffractometry, scanning electron microscopy and analytical transmission electron microscopy techniques. The microstructure of the ZMCs showed a difference in scale. ZrO₂ and mullite grains grown in the gel matrix were formed at temperatures as low as 1100 and 1300°C, respectively. Experimental results indicated that heat treatment from 1300 to 1600°C influences the growth of mullite and fine ZrO₂ grains in ZMCs, especially for the composite prepared from sol-gel methods in which the ZrO₂ grew from tens of nanometres to micrometre size. The effects of the presence of ultra-fine ZrO₂ on retarding the grain growth of mullite and the increase of metastable *t*-phase ZrO₂ are also discussed. The growth of fine ZrO₂ grains in a mullite matrix belongs to a mechanism of coalescence.*

1 Introduction

The appropriate selection of a matrix phase and the addition of various zirconia grains to form ceramic composites with better strength and toughness has become widely recognised as a method for producing materials for engineering applications. ZrO₂ in alumina,¹ Si₃N₄² and mullite³ have been reported to form composite systems that are effective in strengthening and toughening the ceramic matrix. Garvie⁴ also found that the addition of 10% tetragonal (*t*) zirconia enhanced the thermal shock resistance of zircon-zirconia composite. The retained strength of zirconia-zircon composites could be as high as 90% of the

original after quenching from 600°C. In addition, other advantages included less deterioration as a result of the tetragonal to monoclinic (*m*) phase transformation of zirconia grains at high temperature and in high humidity environment, and more economically feasible materials owing to lower costs. However, some disadvantages were also recognised: the zirconia particles coarsened in the alumina matrix⁵ as soon as the ceramic matrix densified. Also, thermal expansion mismatch of ZrO₂ with the ceramic matrix resulted in thermal stresses, either tensile or compressive, as the zirconia composite was cooled from sintering temperature. These would trigger the '*t*-to-*m*' transformation, thereby degrading mechanical properties.

High quality mullite can be made from various sources, alkoxides or other high purity chemicals, through the sol-gel or co-precipitation method.⁶ The method allows the addition of zirconia for making zirconia-toughened mullite (called ZMC in this paper) composites. In addition, the composites can also be made by the reaction sintering of zircon and alumina,^{7,8} by the co-sintering of fine zirconia/mullite mixture,⁹ or by directly sintering the mixture of alumina, silica and zirconia.

High temperature densification above 1450°C with sintering aids is currently used to densify the zirconia-mullite composite. TiO₂,³ MgO^{10,11} and Ca¹² can facilitate the formation of a liquid phase to achieve viscous sintering. These additives were reported to have a profound influence on the high temperature properties of ZMC⁸ and on the formation of glassy and grain boundary phases.¹⁰

The additives, including ZrO₂ and sintering aids, may dissolve in the mullite matrix to some extent. A microanalysis experiment to determine the ZrO₂ content in mullite grains was conducted by Dinger *et al.*,¹³ who found the presence of an apparent solid solution on the crust of mullite grains. This gave a grain boundary of mullite in a state of expansion, thereby improving the toughness of the composite. Other oxide dopants, including Ti, V, Mn, Fe and Co oxides,¹⁴ incorporated into

the mullite structure were determined as being preferentially located in oxygen octahedral sites. The upper limit of solubility is controlled by cation radii and the valence state of cations. This work was partially motivated by the report that the amount of ZrO_2 solid solution in mullite composites was of the order of few per cent up to 20%,¹³ which was thought to be quite influential in determining the grain growth mechanism of ZrO_2 .

Since the toughness and high temperature stability of ZMC are dependent upon the reactions between zirconia and mullite phases, gel-derived precursors and high purity zircon reacted with alumina are used here with and without sintering additives. This research attempts to characterize the transformation of ZrO_2 and the microstructural features, as well as determine the coarsening phenomenon of zirconia and mullite. Thus, rationalizing the parameters which govern the grain growth phenomenon is of interest, thereby permitting the development of an appropriate quantitative model.

2 Experimental

2.1 Sample preparation

2.1.1 Gel-derived (GD-) ZMC

The solution prepared for gelation included 50 wt% tetraethyl orthosilicate (TEOS; Merck Chemical Co., Germany), 30 wt% dry alcohol (reagent grade; Showa Chemicals Co., Ltd, Tokyo, Japan) and 20 wt% 0.018 N HCl (diluted from reagent grade 0.1 N HCl; Merck Chemical Co., Germany). The three chemicals were first mixed and then maintained in a water bath at 50°C for 3 h, so as to obtain a well-mixed silicic acid solution.⁶ Next, pseudo-boehmite sol (Remet Co., NY, USA) and ZrO_2 sol (Johnson Matthey Co., MA, USA) were slowly added to the solution. After mixing for 30 min, the viscosity of the solution increased until gelation. The gel was dried at 80°C for several days until no further weight loss was measured. The aerogel was crushed and sieved through 325 mesh. The Al_2O_3 and SiO_2 ratio was at the mullite stoichiometry and the volume fraction of added ZrO_2 was 24, 9 or 3 vol%. ZMC powders were die-pressed at a pressure of 160 MPa. Sintering of the specimens was conducted at 800 to 1600°C for 2 to 6 h.

2.1.2 Reaction-sintered (RS-) ZMC

Two types of RS-ZMC mixture were selected as comparative cases.¹⁵ One was a mixture of dissociated zircon (supplied by Z-Tech Corp.; impurities included 0.36% Al_2O_3 , 0.08% TiO_2 , 0.03% Fe_2O_3 , and 0.11% free SiO_2) and alumina (A-16SG; Alcoa

Corp., USA) powders. The other consisted of ground zircon sand, alumina and 4 wt% CeO_2 as a sintering aid. They are named DZ-ZMC and RS(CeO_2)-ZMC, respectively. The zircon/alumina mixtures were in a molar ratio of 2:3, subsequently yielding 24 vol% ZrO_2 . These powders were initially dispersed in distilled water with 1 wt% dispersant (based on solid phase; Darvan C, supplied by R.T. Vanderbilt Co., USA), then turbo-mixed for 2 h. The solid fraction of the slurry was 30 vol%. After being cast and dried on a plaster mould, the CeO_2 -doped RS-ZMC was sintered between 1400 to 1550°C for 2 h; however, the DZ-ZMC was sintered at higher temperatures, from 1400 to 1700°C (which is higher than the dissociation temperature of zircon) for 30 min. The heating rate of the sintering was 10°C min⁻¹. Nearly fully-dense DZ-ZMC and RS-ZMC samples were obtained, then heat-treated at temperatures from 1400 to 1700°C.

2.2 Characterization

Densification of the ZMCs was examined by a dilatometer (Theta Industries, Inc., USA) up to 1500°C. Crystalline phases were determined by X-ray diffractometry (XRD; PW 1729, Philips Electronics Instruments, Inc., USA). Microstructural and micro-chemical analyses were performed by using scanning electron microscopy (SEM; Philips 515) and transmission electron microscopy (TEM; JEOL 100CXII and 2000FX, JEOL Inc., Japan), the latter equipped with EDAX (Tracer Northan Co., USA). The densities of the sintered specimens were obtained by Archimedes' method.

3 Results and Discussion

3.1 Transformation sequence

The XRD patterns of three ZMC powders were analysed and are summarized in Table 1. GD-ZMC appeared to have no crystalline phases when sintered at 800°C for 2 h. Tetragonal- ZrO_2 and mullite phases appeared at 1100 and 1300°C, respectively. The peak width of the *t*-phase ZrO_2 at 1100°C in Fig. 1 is apparently broader than the diffraction peaks of *t*- ZrO_2 at temperatures $\geq 1200^\circ C$. This implies that the zirconia has a fine grain size. After sintering at temperatures of 1600°C or above, a large portion of ZrO_2 transforms to *m*-phase in the GD-ZMC. As for the RB-ZMC, only about one-third of the ZrO_2 was found to be the tetragonal phase at sintering temperatures above 1450°C, but this quantity decreased with increasing sintering temperature and CeO_2 additive, as shown in Fig. 2. This decrease could be due to grain growth of the

Table 1. Phases detected in ZMCs prepared from three different sources and sintered at temperature shown for 2 h

GD-ZMC phase/temp.	1000	1100	1200	1300	1400	1500	1600 (°C)
Zircon	—	—	*	*	*	—	—
Mullite	—	—	—	*	*	*	*
<i>t</i> -ZrO ₂	**	**	**	**	**	*	*
<i>m</i> -ZrO ₂	—	—	—	—	—	*	**
<i>RS-ZMC (without additive)</i>							
phase/temp.	1400	1450	1500	1550 (°C)			
Zircon	**	**	*	*			
Mullite	—	—	*	*			
<i>t</i> -ZrO ₂	—	—	*	*			
<i>m</i> -ZrO ₂	—	—	*	**			
<i>RS-ZMC (with 4 wt% CeO₂ additive)</i>							
phase/temp.	1400	1450	1500	1550 (°C)			
Zircon	**	*	*	*			
Mullite	—	*	*	*			
<i>t</i> -ZrO ₂	—	—	*	—			
<i>m</i> -ZrO ₂	—	*	*	**			

Note —, * and ** means that the X-ray diffraction intensity of the phase is not detectable, detectable and in large quantity, respectively.

ZrO₂, lack of phase stabilizer such as CaO or MgO, and thermal stress induced transformation. However, the amount of *t*-ZrO₂ finally became stable at a level of 20% (Fig. 2) when the heat treatment was extended up to 4 h at 1450°C. This occurrence is explained later by means of microstructural observations (in Section 3.3), in which the *t*-ZrO₂ is possibly intragranular and holds a submicrometre size.

The formation temperatures of these zirconia and mullite phases in GD-ZMC are apparently lower than the RS-ZMCs, as shown in Table 1, and are also lower than those reported by Low and McPersonal.¹⁶ GD-ZMC underwent this transformation at a temperature 200°C lower than that for RS-ZMC.¹⁷ This lower transformation is due to the reaction kinetics, enhanced by the fact of the diminutive gel structure in GD-ZMC.

Zircon, as a reaction product of zirconia and silica, forms as a transition phase in the gel-

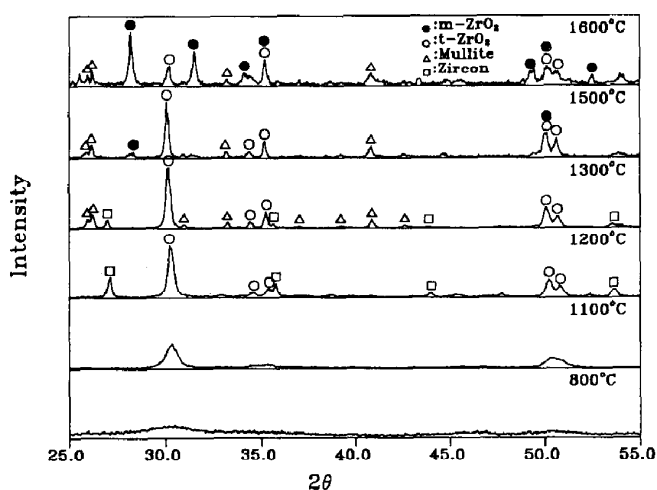


Fig. 1. XRD patterns for GD-ZMC samples after sintering at 800 to 1600°C for 2 h.

derived ZMC in the range between 1200 and 1500°C. If the temperature increases, the amount of zircon phase decreases and is accompanied by the appearance of mullite phase. The formation and diminishing of zircon phase in a similar ZMC

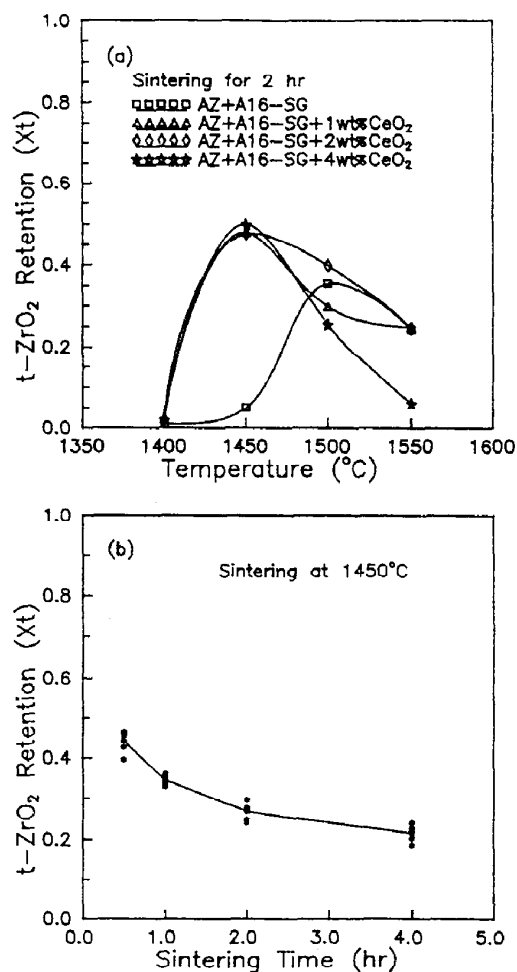


Fig. 2. Weight fraction of *t*-phase zirconia in reaction-sintered RS-(CeO₂)-ZMC as a function of (a) sintering temperature and (b) sintering time at 1450°C.

was also reported by Holmstron *et al.*,¹⁸ who used Al_2O_3 , SiO_2 and ZrO_2 as raw materials to prepare a reaction-sintered ZMC. The zircon appeared at temperatures between 1450–1560°C when the ZrO_2 content was >15 vol%. In this study, the spray-dried powders were found to have phase transformation sequences similar to those of the powders prepared from grinding.

3.2 Densification of ZMCs

Dilatometric data of the ZMCs are shown in Fig. 3 plotted as a function of sintering temperature up to 1500°C. The changes in the dimensions of die-pressed GD-ZMC at temperatures around 300 and 550°C correspond to the sintering of extremely fine pores, in which the contained volatile species evaporate readily. Those nm size pores are densified at 600°C or lower temperatures, as reported previously.⁶ Testing at higher temperature unveils that the next densification of GD-ZMC starts at 900°C and exhibits the fastest densification rate at 1200°C. In comparison, DZ- or RS-ZMC specimens undergo less densification and at higher temperature starting from 1100°C. The densification rate of RS-ZMC can be enhanced by the addition of CeO_2 , as revealed by the densification curve of the RS(CeO_2)-ZMC in Fig. 3. The GD-ZMC shows a lower sintering temperature and more shrinkage than the other two ZMCs.

3.3 Microstructural evolution

Figure 4 shows SEM micrographs of polished and thermally-etched RS- and DZ-ZMC samples. The micrographs show dense and well reacted ZMCs, which have a relative density of >95% TD (theoretical density). The densified ZMCs show very stable microstructural features, most of the intergranular ZrO_2 being 3 μm in size (Fig. 5), as they are post-annealed at temperatures of 1400 to

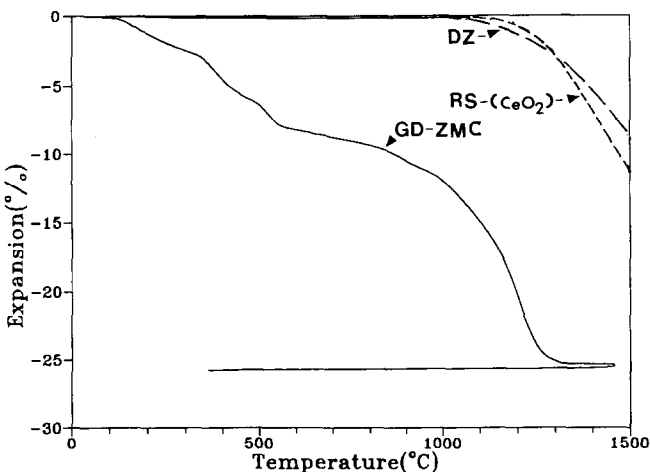


Fig. 3. Dilatometric curves of gel-derived (GD), reaction-sintering with 4 wt% CeO_2 (RS-(CeO_2)-) and DZ-ZMC specimens plotted as a function of temperature.

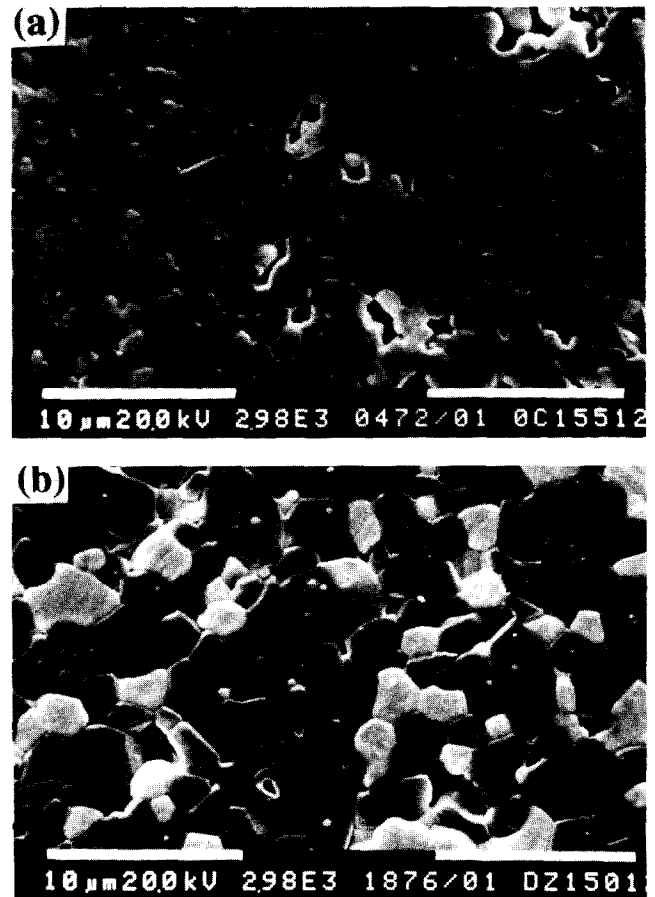


Fig. 4. SEM micrographs of (a) RS-ZMC without doping additive sintered at 1550°C for 12 h; (b) DZ-ZMC sintered at 1700°C for 30 min, then annealed at 1500°C for 12 h. The samples were all polished and thermally etched.

1600°C for up to 24 h. The grain sizes of mullite and ZrO_2 change within the range of experimental error, so that their grains are considered not to coarsen during the heat treatment. Some fine and submicrometre-sized zirconia grains are observed

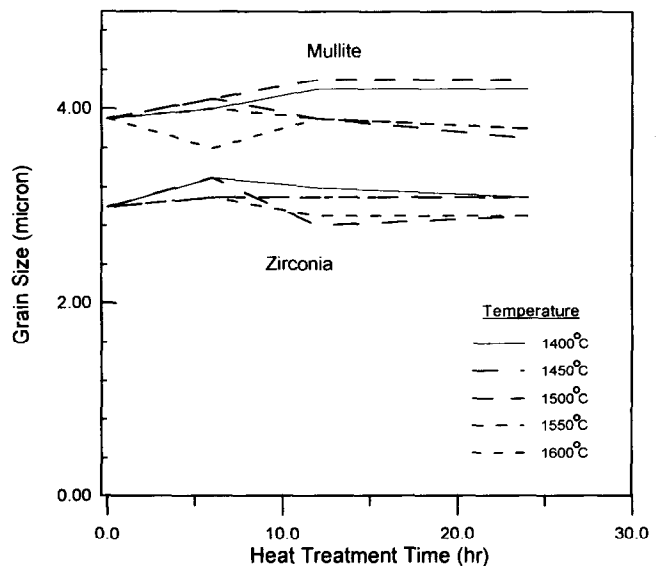


Fig. 5. Average grain sizes (μm) of intergranular zirconia and mullite grains of DZ-ZMC samples with 24 vol% ZrO_2 sintered at 1700°C for 30 min following various heat treatments.

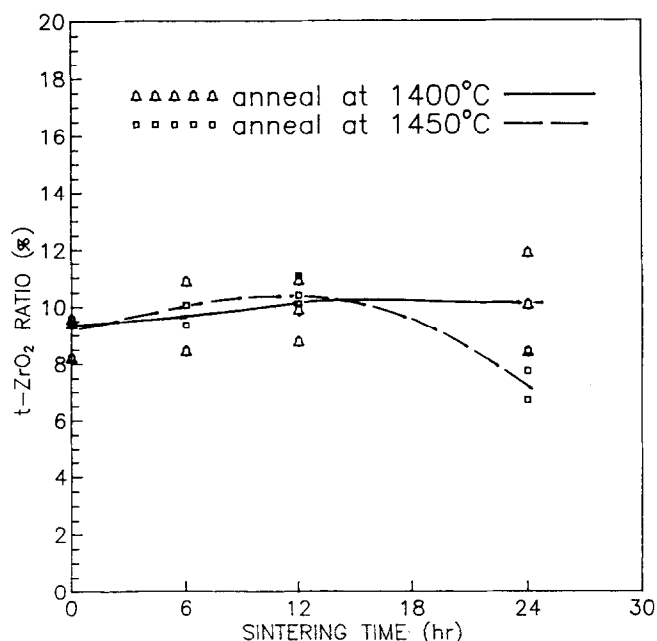


Fig. 6. Weight percentage of *t*-ZrO₂ phase to all ZrO₂ in DZ-ZMC vs. annealing period at 1400 or 1450°C.

that are nearly spherical and engulfed in mullite grains (Fig. 4). These intragranular ZrO₂ grains are the major part of *t*-phase ZrO₂ which is not transformable even following the same post-annealing at 1400 or 1450°C as long as 24 h (Fig. 6). The microstructures of the RB-ZMCs are stable at high temperatures (>1400°C). However, the reaction-sintering process for the preparation of ZMC cannot offer the microstructure with finer ZrO₂ and submicrometre-sized mullite grains.

GD-ZMC samples sintered at 1400, 1500 or 1600°C for 2 h were carefully polished and thermally-etched at the conditions 1350°C for 2 h, 1475°C or 1500°C for 30 min, respectively. The GD-ZMC sample sintered at 1600°C [Fig. 7(c)] has a similar microstructure to the previous RS-ZMCs. A small fraction of fine-grained zirconia is enclosed in the mullite grains, which are of the order of a few micrometres in size. Figures 7(b) and (c) clearly show that ZrO₂ grains are either intergranular or intragranular; the grain size of intergranular ZrO₂ increasing with sintering temperature. The intragranular ZrO₂ in the 1400°C and 2 h sintered sample is <0.1 μm. If sintered at 1600°C for 2 h, it grows to 2.3 μm and becomes intergranular. Increasing the size of ZrO₂ grains has been shown previously to instantly transform ZrO₂ to *m*-phase.⁵ The analysis of XRD patterns in Fig. 1 reveals several strong diffraction peaks of the *m*-phase in the pattern of the 1600°C sintered samples; however, the *m*-phase is rarely detected in the GD-ZMC processed at 1500°C or lower temperatures.

It is noted that the amount of intragranular ZrO₂ decreases with increasing sintering tempera-

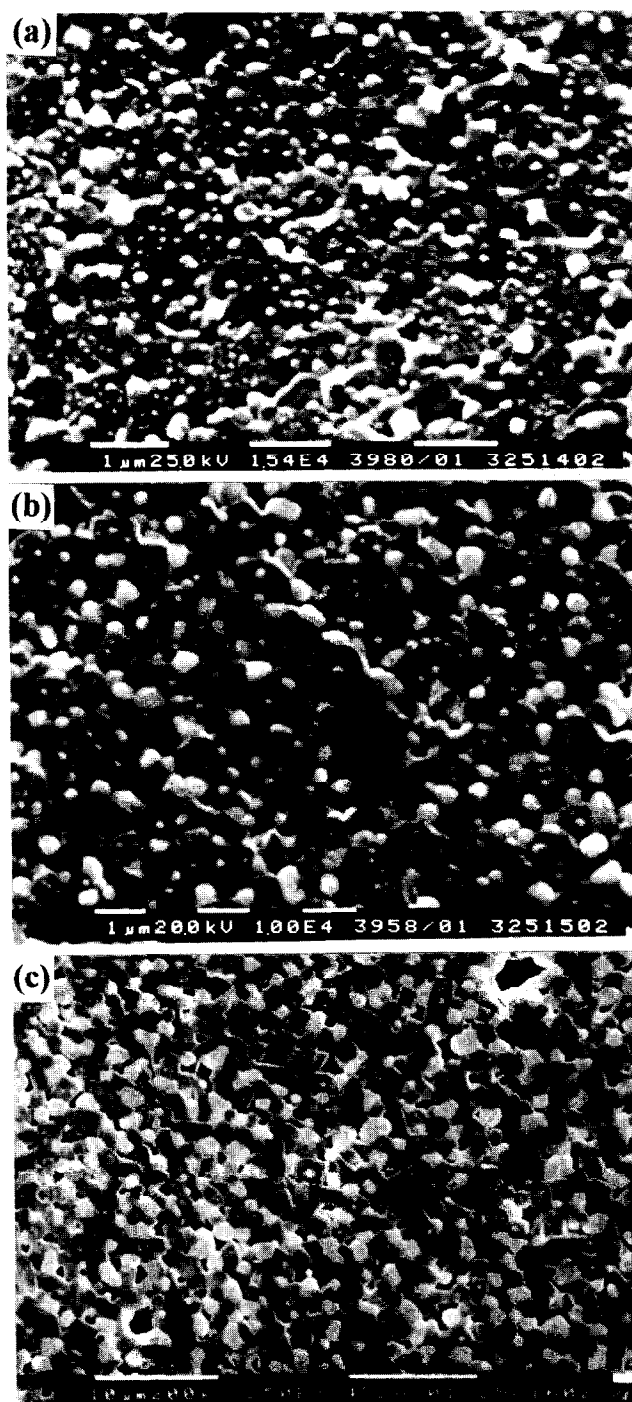


Fig. 7. SEM micrographs of polished and thermally etched GD-ZMC specimens sintered at (a) 1400°C, (b) 1500°C and (c) 1600°C for 2 h.

ture. Meanwhile, the average grain sizes of the intergranular ZrO₂ and matrix mullite grow larger. The grain size data, obtained from SEM and TEM micrographs, reveal that the intergranular ZrO₂ and matrix mullite grains scarcely grow from 1300 to 1500°C. However, both phases grow rapidly in size when the sintering temperature rises from 1500 to 1600°C.

TEM bright-field (BF) and centred-dark-field (CDF) micrographs of a GD-ZMC sample sintered at 1300°C for 2 h are shown in Fig. 8. The BF image shows that the ZrO₂ grains in dark

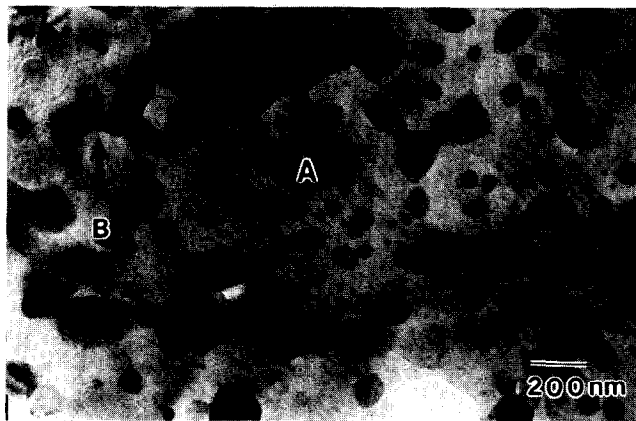


Fig. 8. TEM BF micrograph of GD-ZMC (with 24 vol% ZrO_2) sintered at 1300°C for 2 h.

contrast are uniformly dispersed within the mullite matrix. For sintering at higher temperature, a few large ($0.3 \mu\text{m}$ or larger) intergranular ZrO_2 grains are occasionally found in the 1400°C sintered GD-ZMC. The twinning features of these grains (Fig. 9) are characteristic of *m*-phase ZrO_2 . The boundaries of each ZrO_2 lath in the large *m*- ZrO_2 grains exhibit interfacial microcracks, as denoted by arrows A and B in Fig. 9. In addition to the microcracks, strain fringes (arrow C) occurring next to large ZrO_2 grains are produced by thermal mismatch, and represent internal stresses.¹⁹ These features, i.e. microcracks and strain fringes, are possibly caused by the phase transformation of *t*- ZrO_2 to *m*- ZrO_2 and thermal expansion mismatch between mullite and ZrO_2 .

SEM and TEM analyses indicate that GD-ZMC has a smaller grain size than DZ- or RS-ZMC when sintering at the same temperature. For 24 vol% ZrO_2 samples, the average grain size of the intergranular ZrO_2 in GD-ZMC is 98 nm and the size of the mullite grains is 600 nm, which is

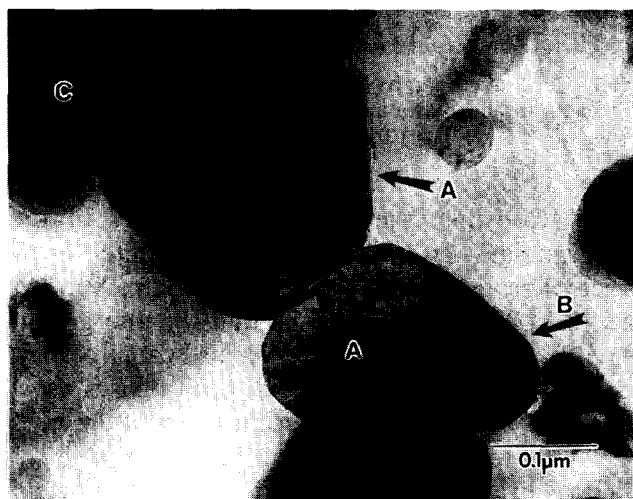


Fig. 9. Microcracks (A and B) and strain fringes (C) around two overgrowth *m*- ZrO_2 grains, imaged with TEM BF conditions. The GD-ZMC was sintered at 1400°C for 2 h.

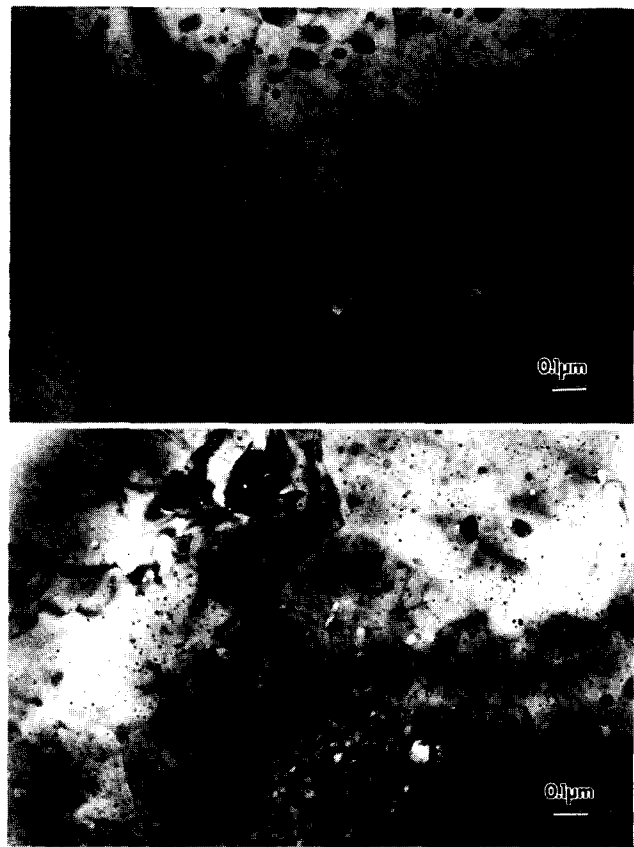


Fig. 10. TEM micrographs of GD-ZMC samples with (a) 9 vol% and (b) 3 vol% of ZrO_2 sintered at 1400°C for 2 h.

several times less than the size of mullite grains measured in a pure aluminosilicate gel system.⁶ However, the mullite grows to a larger size if sintered at a higher temperature or the composition contains less ZrO_2 . Figure 10 presents TEM micrographs of GD-ZMC samples containing either 9 or 3 vol% ZrO_2 . Their ZrO_2 grains are mostly intragranular, and have an average grain size, 30 or 9 nm, which is several times less than that of GD-ZMC with 24 vol% ZrO_2 . The mullite grains in Fig. 10 grew to larger size, near $1 \mu\text{m}$, and had straight grain boundaries. The dragging of mullite grain boundaries by ZrO_2 grains is apparently dependent upon the volume fraction and size of the ZrO_2 , which is similar to the behaviour reported by Lange and Hirlinger²⁰ and Prochazka *et al.*⁹ An illustrative example, i.e. the 1300°C-sintered GD-ZMC sample, is given in Fig. 8; the mullite grains exhibit crooked boundaries which trap several larger ZrO_2 grains (larger than the average size of intragranular ZrO_2). This demonstrates the likelihood that the growth of mullite grains is inhibited by ZrO_2 grains.

3.4 Grain growth of zirconia and mullite

The results of previous SEM and TEM micrographs are reported in Fig. 11, from which it can be seen that the grain sizes of mullite and ZrO_2 in

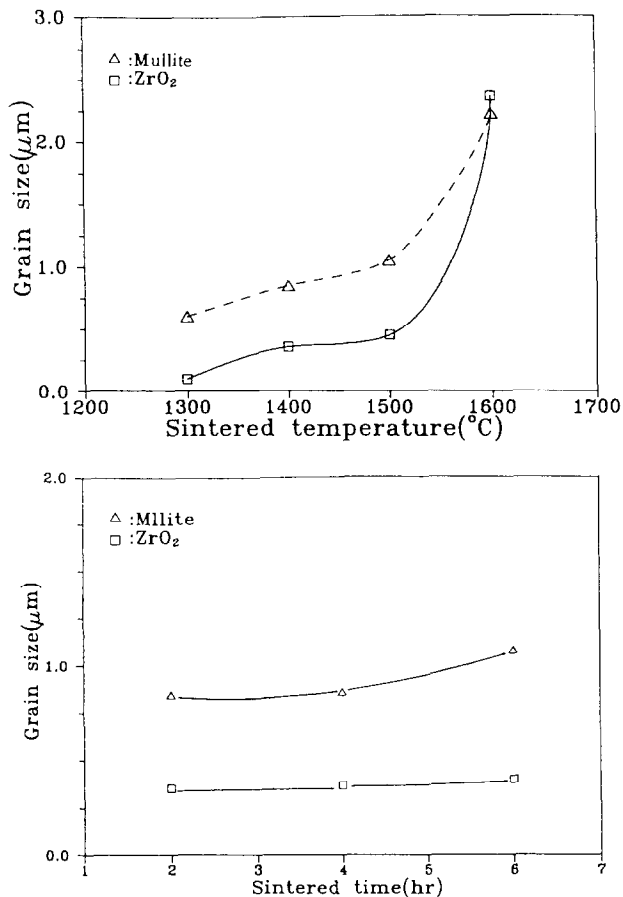


Fig. 11. Grain sizes of mullite and intergranular ZrO₂ in various GD-ZMC samples with 24 vol% ZrO₂: (a) sintered at 1300 to 1600°C for 2 h; (b) sintered at 1400°C for 2 to 6 h.

various gel-derived ZMCs increase as the sintering temperature and sintering time increase. The application of Zener's relationship²¹ to the above cases illustrates the relationship between the mean grain radius (R) of the mullite matrix, the mean radius (r) of the ZrO₂ inclusions and the volume fraction (f) of the inclusion:

$$R = 4r/(3f) \quad (1)$$

This relationship provides a calculated R value for the 1400°C-sintered GD-ZMC that is comparable with the measured R (Table 2). However, the measured mullite grain size increases as the amount of zirconia decreases, and the zirconia inclusions are not all spherical and uniformly distributed (Fig. 10), leading to differences between measured and calculated R values. In addition, the relationship does not hold true for mullite grains in the GD-

Table 2. Calculated and measured mean radius (R) of mullite in GD-ZMC determined from the volume fraction (f) and grain radius (r) of zirconia phase

f	r (nm)	Calculated R (nm)	Measured R (nm)
0.24	49	272	300
0.09	15	222	~600
0.03	4.5	200	~750
Pure mullite ²²	—	—	~1250

ZMC sintered at temperatures >1500°C [Fig. 11(a)]. The growth of the mullite grains is accompanied by the coarsening of ZrO₂ inclusions. Two phases are growing inter-affected.

The second-phase ZrO₂ in the mullite matrix can ripen either by Ostwald ripening or by coalescence. The processes are well documented in a similar ceramic composite system,⁵ in which Ostwald ripening is driven by the variation of solubility of ZrO₂ with various particle sizes, and the composite grows larger ZrO₂ particles at the expense of smaller ZrO₂ particles. Coalescence of ZrO₂ particles occurs by the dragging of matrix mullite boundaries. The phenomenological evidence for the former process was a particle-free zone at matrix grain boundaries despite the fact that the diffusion rate along the mullite grain boundaries is faster than that in the mullite lattice. Alternatively, the latter case is particle clustering at grain boundaries. In this study, the micrographs revealed no grain boundary particle-free zone.

It was reported by Dinger *et al.*¹³ that a 2% solid solution of ZrO₂ near interface grain boundaries of mullite has been detected. They sintered the sample at 1570°C for 2 to 16 h. Mullite with an extensive amount of zirconia solid solution should be expected at temperature >1570°C. But a quite controversial result was reported later by the same research group,¹⁰ that >20 wt% of ZrO₂ was found in the mullite grains. This seems *not to be the case* for our ZMC. Figure 12 shows a DZ-ZMC sample that has been sintered at 1700°C for 30 min. The zirconia grains either intergranularly or intragranularly are of size 50 nm to 3.5 μm, as shown in Fig. 12. Scanning transmission electron microscopy with micro-beam EDS analysis reveals that the ZMC has a non-detectable zirconia concentration in the mullite grains, as shown in the EDS spectra obtained from spots 2 and 4. That implies that *no zirconium forms a solid solution in mullite*. This finding is consistent with the recent measurement given by Moya²³ that <0.1 wt% zirconia solid solution is measured in zirconia-toughened mullite. This implies that ripening through grain boundary diffusion was not occurring in ZMC. Many intergranular ZrO₂ particles are actually in the form of clustering at triple grain boundaries, and exhibit larger grain size. We believe that such particle clustering is good evidence for coarsening by the coalescence of ZrO₂. The zirconia in GD-ZMC is apparently ripening intergranularly while being treated above 1300°C in this experiment.

4 Summary

Three types of ZMC prepared either from gel

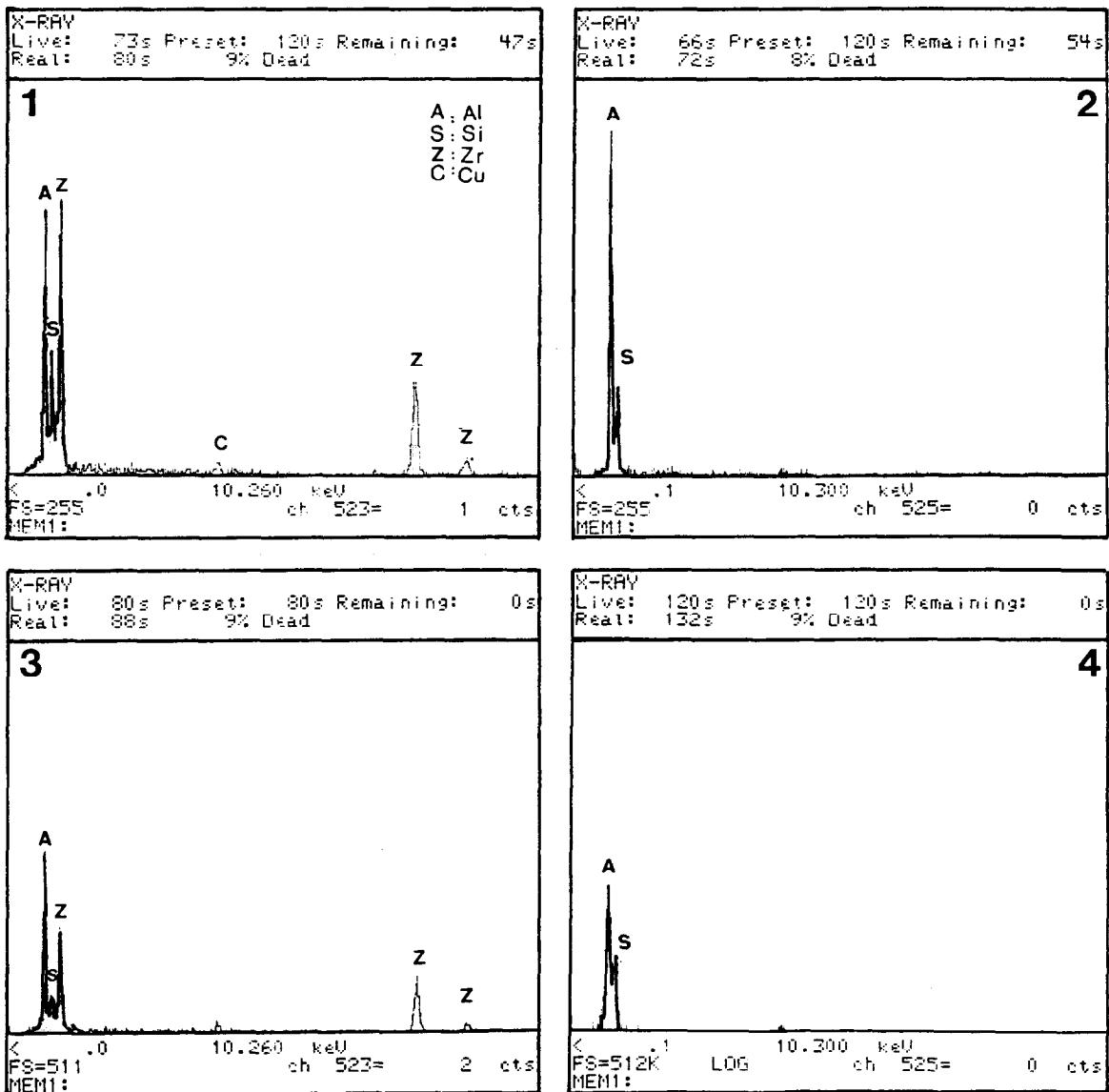


Fig. 12. TEM BF micrograph and EDX results of the intergranular and intragranular zirconia grains (1 and 3) and their mullite neighbourhood (2 and 4). The DZ-ZMC was sintered at 1700°C for 30 min.

precursors or solid powder mixtures were investigated in this study. Quantitative analysis on the micro-structural evolution of ZrO_2 and mullite

matrix grains was conducted, and correlated with the processing temperature and the content of ZrO_2 .

The solid solution of ZrO_2 in the mullite matrix was undetected and ZrO_2 particle-free zones were not observed in the GD- and DZ-ZMC samples, including the one with the longest heat treatment (1600°C for 24 h). This implies that the growth of ZrO_2 grains in mullite matrix cannot proceed via the process of Ostwald ripening. Grain clustering of intergranular ZrO_2 was observed, suggesting the coalescence of the ZrO_2 can occur at temperatures above 1300°C. Coarsening of intergranular and intragranular ZrO_2 particles in the mullite matrix is triggered by the mullite grain growth. The dragging of mullite grain boundaries by ZrO_2 is apparent for samples sintered at temperatures of 1400°C and above. The relationship between the grain growth of mullite and the volume fraction and size of ZrO_2 inclusions can be verified, but not well described by Zener's equation.

The advantages of the gel-process over reaction-sintering to prepare ZMCs with fine microstructure are clearly revealed in this work. A lower sintering temperature offers a higher densification rate and smaller grain size, thereby resulting in more *t*-phase zirconia and smaller grain size of mullite.

Acknowledgement

This work was supported by National Science Council in Taiwan under contract numbers NSC 81-0405-E002-25 and 82-0405-E002-245.

References

1. Claussen, N. & Ruhle, M., Design of transformation-toughened ceramics. In *Science and Technology of Zirconia III*, Advances in Ceramics, Vol. 24, eds S. Somiya, N. Yamamoto & H. Yanagida, The American Ceramics Society, Westerville, OH, 1988, p. 137.
2. Lange, F. F., Low thermal conductivity silicon nitride/zirconia composite ceramics. US Patent 4 640 902, 3 Feb. 1987.
3. Rincon, J. M. & Moya, J. S., Microstructural study of toughened ZrO_2 /mullite ceramic composition obtained by reaction sintering with TiO_2 . *Br. Ceram. Trans. J.*, **85** (1986) 201–6.
4. Garvie, R. C., Improved thermal shock resistant refractories from plasma-dissociated zircon. *J. Mater. Sci.*, **14** (1979) 817–22.
5. Kibbel, B. W. & Heuer, A. H., Ripening of inter- and intragranular ZrO_2 particles ZrO_2 -toughened Al_2O_3 . In *Science and Technology of Zirconia II*, Advances in Ceramics, Vol. 12, The American Ceramics Society, Westerville, OH, 1984, pp. 415–24.
6. Wei, W., Ph. D. Thesis, Case Western Reserve University, July 1986.
7. Wallace, J. S., Petzow, G. & Claussen, N., Microstructure and property development of in situ-reacted mullite- ZrO_2 composites. In *Science and Technology of Zirconia II*, Advances in Ceramics, Vol. 12, The American Ceramics Society, Westerville, OH, 1984, pp. 436–42.
8. Descamps, P., Sakaguchi, S., Poorteman, M. & Cambier, F., High-temperature characterization of reaction-sintered mullite-zirconia composites. *J. Am. Ceram. Soc.*, **74**(10) (1991) 2476–81.
9. Prochazka, S., Wallace, J. S. & Claussen, N., Microstructure of sintered mullite-zirconia composites. *J. Am. Ceram. Soc.*, **66** (1983) C125–7.
10. Miranzo, P., Pena, P., de Aza, S., Moya, J. S., Ma Rinco, J. & Thomas, G., TEM study of reaction-sintered zirconia-mullite composites with CaO and MgO additions. *J. Mater. Sci.*, **22** (1987) 2987–92.
11. Leriche, A., Mechanical properties and microstructures of mullite-zirconia composites. In *Mullite and Mullite Matrix Composites*, Ceramic Transactions, Vol. 6, eds S. Somiya, R. F. Davis & J. A. Pask, The American Ceramics Society, Westerville, OH, 1990, pp. 541–52.
12. Pena, P., Miranzo, P., Moya, J. S. & de Aza, S., Multi-component toughened ceramic materials obtained by reaction sintering, Part I—System ZrO_2 - Al_2O_3 - SiO_2 -CaO. *J. Mater. Sci.*, **20** (1985) 2011–22.
13. Dinger, T. R., Krishnan, K. M., Thomas, G., Osendi, M. I. & Moya, J. S., Investigation of ZrO_2 /mullite solid solution by energy dispersive X-ray spectroscopy and electron diffraction. *Acta Metall.*, **32**(10) (1984) 1601–7.
14. Schneider, H., Transition metal distribution in mullite. In *Mullite and Mullite Matrix Composites*, Ceramic Transactions, Vol. 6, eds S. Somiya, R. F. Davis & J. A. Pask, The American Ceramics Society, Westerville, OH, 1990, pp. 135–58.
15. Ho, Y. F. & Wei, W. J., Reaction sintering of zirconia-mullite composites. In *Proc. 1992 Annual Conf. Chinese Soc. for Mater. Sci.*, 24–26 April 1992, pp. 470–1.
16. Low, I. M. & McPersonal, R., Crystallization of gel-derived mullite-zirconia composites. *J. Mater. Sci.*, **24** (1989) 951–8.
17. Shiga, H., Katayama, K., Tsunatori, H. & Ismail, G. M. U., Sol gel synthesis and sintering of oxide-doped mullite- ZrO_2 composite powders. *Ceram. Powder Sci. IV*, (1990) 457–62.
18. Holmstrom, M., Chartier, T. & Boch, P., Reaction-sintered ZrO_2 -mullite composites. *Mater. Sci. Eng.*, **A109** (1989) 105–9.
19. Mader, W., On the electron diffraction contrast caused by large inclusions. *Phil. Mag. A*, **55**(1) (1987) 59–83.
20. Lange, F. F. & Hirlinger, M. M., Hindrance of grain growth in Al_2O_3 by ZrO_2 inclusion. *J. Am. Ceram. Soc.*, **67**(3) (1984) 164–8.
21. Reed-Hill, R. E., *Physical Metallurgy Principles*, Van Nostrand, Princeton, NJ, 1973, p. 138.
22. Wei, W. & Halloran, J. W., Transformation kinetics of diphasic aluminosilicate gels. *J. Am. Ceram. Soc.*, **71**(7) (1988) 581–7.
23. Moya, J. S., Private communication, September 1994.

Mullite–Aluminosilicate Glassy Matrix Substrates Obtained by Reactive Coating

J. Requena,^a J. F. Bartolomé,^a J. S. Moya,^a S. de Aza,^a F. Guitian^b & G. Thomas^c

^aInstituto de Cerámica y Vidrio (CSIC), Arganda del Rey, Madrid, Spain

^bInstituto de Cerámica, Universidad de Santiago, Spain

^cDepartment of Materials Science and Mineral Engineering, University of California, Berkeley, CA 94720, USA

(Accepted 22 July 1995)

Abstract

Layered kaolinite–alumina composites have been obtained by a sequential slip casting technique. The interfacial reaction as well as the microstructure of different layers have been studied in laminates fired at 1650°C. The results are discussed on the basis of the $\text{SiO}_2\text{--Al}_2\text{O}_3\text{--K}_2\text{O}$ equilibrium diagram. Taking into account these results, a new low-cost ceramic substrate for electronic applications — reinforced by mullite whiskers and with controlled closed porosity, low permittivity value ($\epsilon \approx 4$ at 1 MHz) and thermal expansion coefficient close to that of silicon ($3.8 \times 10^{-6} \text{ }^\circ\text{C}^{-1}$) — has been developed starting from conventional kaolinite powder.

Introduction

Recently, Liu *et al.*^{1,2} have studied mullite formation in the alumina–kaolinite system. By X-ray diffraction (XRD) and transmission electron microscopy (TEM) analysis, they have clearly shown the formation of monosized primary mullite in plate-like kaolinite at 1300°C. At higher temperatures bimodal mullite crystals were detected, indicating formation of secondary mullite by nucleation and primary mullite growth. This secondary mullite is formed mainly by a solution–precipitation mechanism. Both types of mullite have a different composition and different morphologies. Primary mullite is needle-like with [00 1] being the crystallographic growth direction.³ The secondary mullite has a higher content of alumina and no preferential growth direction.

In the present work kaolinite has been spatially separated from alumina by means of a layered structure obtained by sequential slip casting. In this configuration, the interfacial reaction, microstructure development into the layers and morphological

aspects of the fired composites have been studied. On the basis of the results obtained, a new substrate with low permittivity value is proposed for electronic applications.

Experimental

The following starting materials have been used: (1) high-purity kaolinite (Caobar S.A., Spain) with an average particle size of 3 μm and a specific surface area of 9.2 $\text{m}^2 \text{g}^{-1}$, with mica and quartz as minor constituents; and (2) commercial submicronic alumina (Alcoa CT 3000 SG) with an average particle size of 0.5 μm and a specific surface area of 8.0 $\text{m}^2 \text{g}^{-1}$. The results of wet chemical analysis (wt%) of both materials are (1) Caobar kaolinite: SiO_2 (48.4), Al_2O_3 (37.0), Fe_2O_3 (0.25), TiO_2 (0.002), Na_2O (0.13), K_2O (0.46), CaO (0.31), MgO (0.05) and (2) α -alumina: Al_2O_3 (99.2), Na_2O (0.12), SiO_2 (0.08), MgO (0.1) and Fe_2O_3 (0.03). Aqueous suspensions were prepared of alumina and kaolinite, using an alkali-free organic poly-electrolyte in the case of alumina and sodium silicate and sodium carbonate in the case of kaolinite. Both suspensions were dispersed in alumina ball mills for 4 h. The suspensions showed Newtonian flow behaviour and low viscosity values (i.e. 11 and 15 mPa s^{-1} for Al_2O_3 and kaolinite, respectively).

Multilayer alumina–kaolinite composites were obtained by alternately casting alumina and kaolinite suspensions in plaster of Paris moulds according to the flow chart shown in Fig. 1.

Microstructural analysis was performed on polished cross-sections with and without chemical etching (10% HF solution) using optical microscopy (Zeiss Axiophot, Germany) with an image analyser, and scanning electron microscopy (SEM) with EDS and WDS (Jeol JMS-6400, Japan).

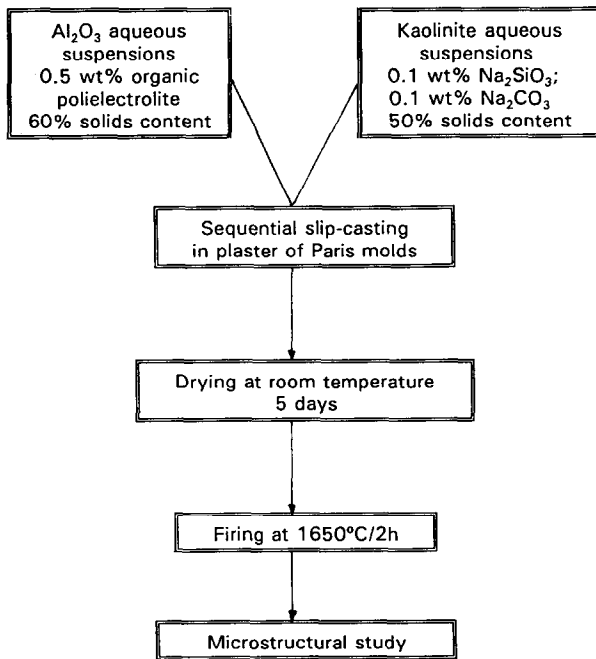


Fig. 1. Processing flow chart for layered composites.

Results and Discussion

Layered composites

The cross-section of a layered composite after firing is shown in Fig. 2. As observed, the morphology of the laminate is built up of dense alumina layers and porous aluminosilicate (original kaolinite) layers. Cracks due to the thermal expansion mismatch are visible.

SEM micrographs of polished and chemically etched surfaces are shown in Fig. 3. It is seen that the interface is formed by a $\sim 5 \mu\text{m}$ layer of secondary mullite which penetrates into the alumina

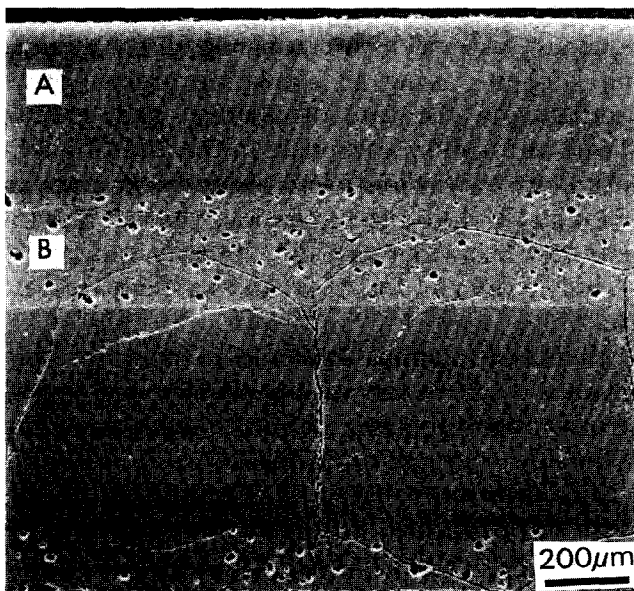


Fig. 2. SEM micrographs of the alumina-kaolinite multilayer composite fired at 1650°C: (A) alumina layer; (B) original kaolinite layer.

Table 1. Quantitative microprobe (WDX) analysis (wt%)

	Al_2O_3	SiO_2	K_2O
Primary mullite	72.0 ± 0.5	26.6 ± 0.3	—
Secondary mullite	73.5 ± 0.3	27.8 ± 0.3	—
Glassy matrix*	26.4 ± 0.7	73.88 ± 0.56	1.47 ± 0.05

*CaO and Fe_2O_3 impurities have not been considered.

layer, entrapping alumina grains. The original kaolinite layer transforms into a silica-rich glassy matrix containing aluminium, potassium, calcium and iron, as can be seen in the corresponding EDS pattern, and prismatic primary mullite crystals. EDS spectra corresponding to primary and secondary mullite are also shown.

This particular microstructure can be explained by means of the SiO_2 - Al_2O_3 - K_2O equilibrium phase diagram.⁴ In Fig. 4 the silica-alumina-rich portion of this diagram is plotted. The theoretical composition of metakaolinite as well as the composition of the calcined Caobar kaolinite have also been plotted. In this plot only the K_2O impurity has been taken into account. According to this equilibrium diagram, on heating, Caobar kaolinite will develop a liquid phase at the eutectic temperature (985°C) which corresponds to the invariant point of the subsystem silica-mullite-potash feldspar. As the temperature increases, the composition of the glassy phase will move along the cristobalite-mullite boundary until reaching a temperature close to 1470°C . Then the cristobalite disappears and the liquid phase moves away from the binary boundary following the tie-line which joins the Caobar kaolinite composition with the silica-rich mullite composition, until reaching the isothermal line corresponding to 1650°C , the final firing temperature. This liquid is in equilibrium with primary mullite. In a subsequent step this liquid will react with the alumina layer, giving alumina saturated with secondary mullite.

Quantitative microprobe analysis (WDS) of the primary mullite, secondary mullite and glassy matrix corresponding to the layered composites fired at 1650°C is reported in Table 1. As can be observed, these data are in good agreement with the previous synopsis.

Layered substrates for electronics

One basic requirement for electronic ceramics that support high frequency circuitry,⁵ is to have a low permittivity value (ϵ), to provide short signal transmission delay time (t_d):

$$t_d = \frac{\sqrt{\epsilon s}}{c}$$

where s = signal pass length and c = velocity of light.

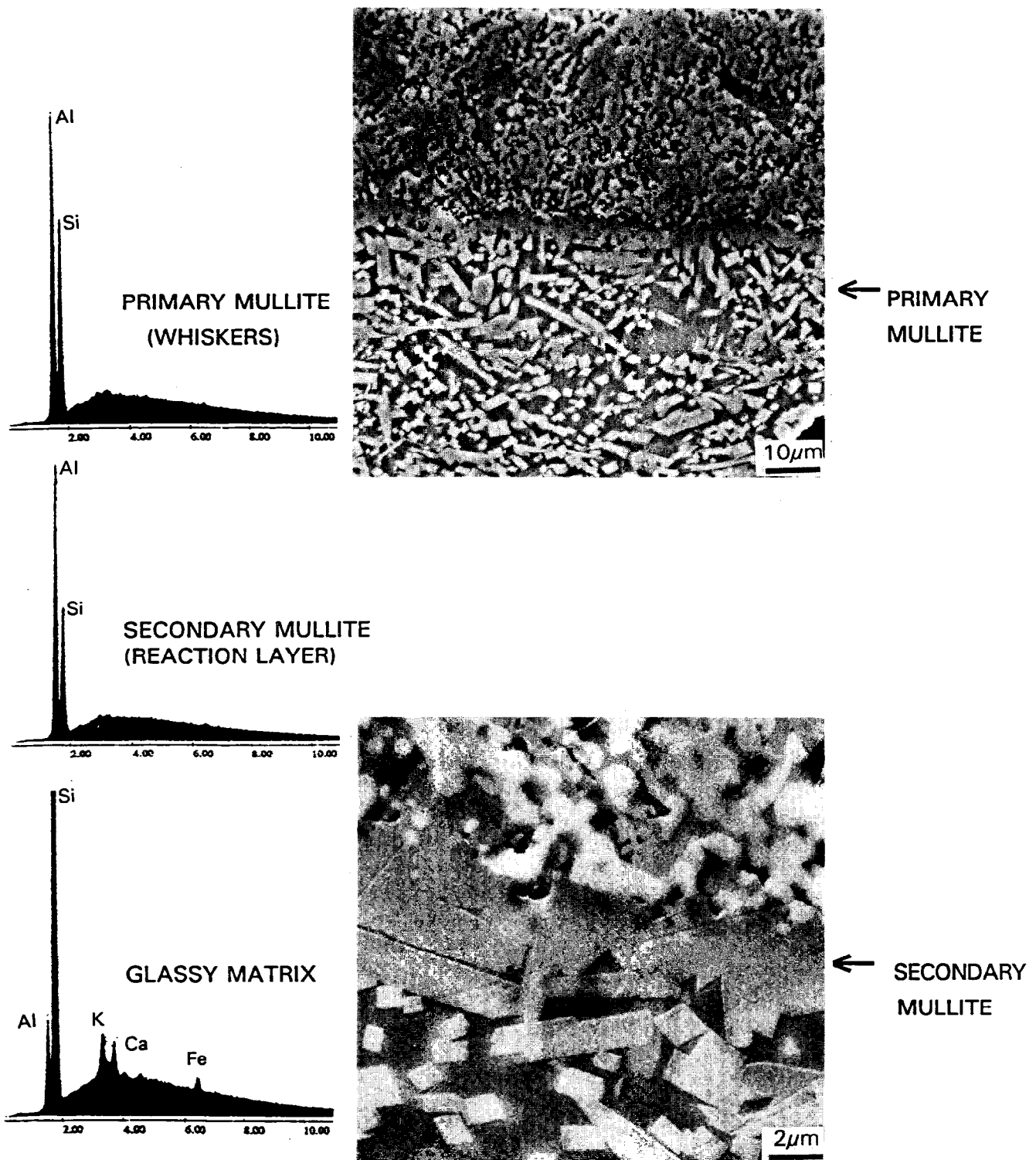


Fig. 3. SEM micrograph of polished and HF-etched cross-section of the alumina–kaolinite layered composite. The EDS spectra corresponding to primary mullite, secondary mullite and glassy matrix are also shown.

The major problems for large-scale production of mullite silica glass substrate are:^{6,7}

- (i) high cost of starting materials;
- (ii) porosity control;
- (iii) formation of cristobalite;
- (iv) low mechanical properties.

Taking into account the results obtained in the layered composites as previously reported, it should be possible to design a silicoaluminate

glassy matrix reinforced with mullite whiskers and with controlled porosity starting from low-cost kaolinite raw materials.

The idea consists of coating a prefired kaolinite block with a sufficiently thin layer of alumina in order to develop, during final firing (at 1650°C), an electrical insulator layer of secondary mullite, avoiding the cracks formed because of the thermal expansion mismatch between alumina and silicoaluminate layers (Fig. 2).

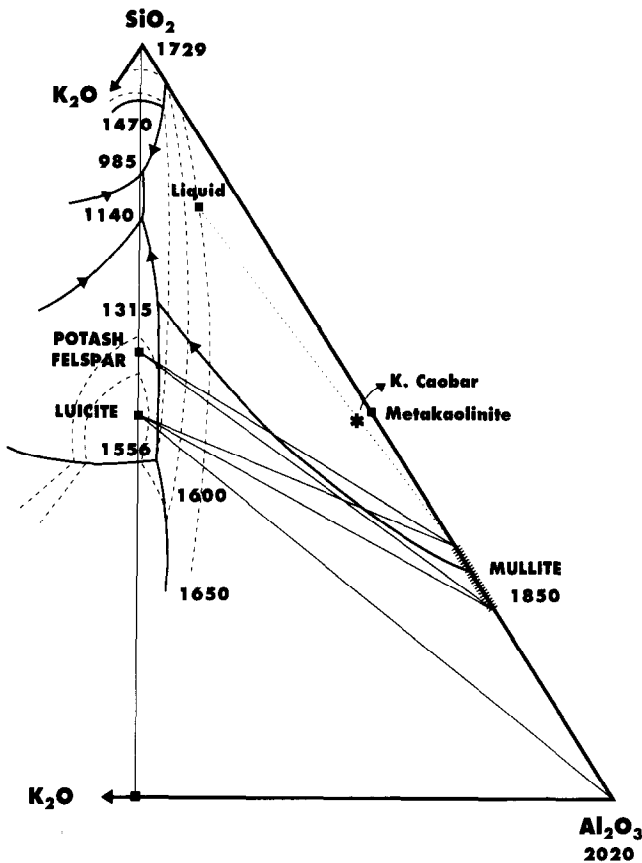


Fig. 4. The $\text{SiO}_2\text{-Al}_2\text{O}_3\text{-K}_2\text{O}$ equilibrium diagram.

According to the equilibrium diagram plotted in Fig. 4 as well as the time-temperature-transformation curves reported by Liu *et al.*² for Caobar kaolinite (Fig. 5), if firing is made at $T > 1470^\circ\text{C}$ no cristobalite is present. In this case only mullite and glassy phases are formed, as has been observed in the present case. In this sense, a processing-flow chart, as shown schematically in Fig. 6, has been followed.

Figure 7 shows an optical micrograph of the cross-section of the fired substrate. As observed, closed pores $< 40 \mu\text{m}$ are present. The total porosity has been determined by image analysis on micrographs and found to be $8 \pm 1 \text{ vol}\%$.

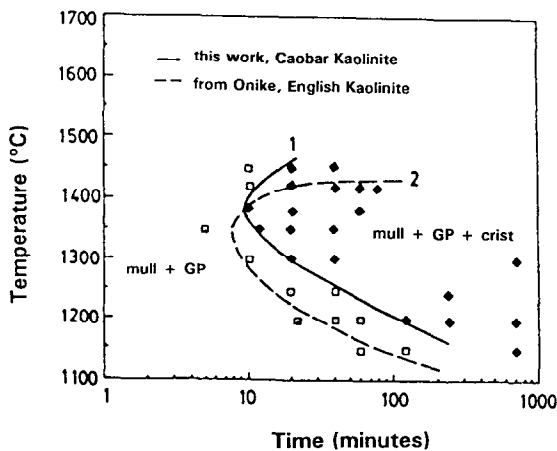


Fig. 5. Time-temperature-transformation curves of cristobalite nucleation for Caobar Kaolinite and English Kaolinite.

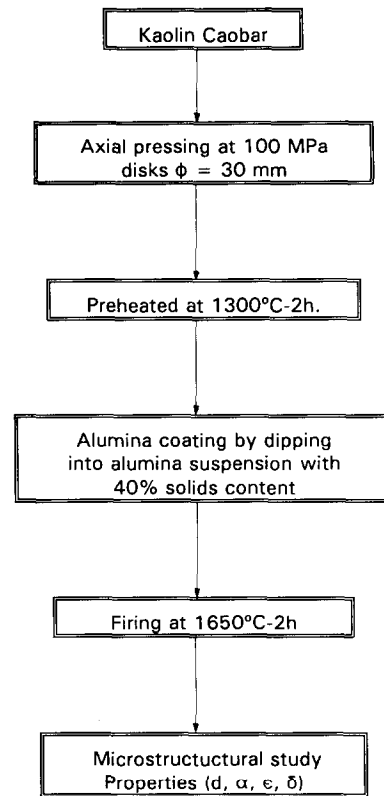


Fig. 6. Substrates processing flow chart.

The micrograph of an HF etched polished cross-section shows the presence of $5 \mu\text{m}$ thick coating of a secondary mullite layer and a bulk formed by continuous glassy matrix reinforced by primary mullite whiskers. These are of length $20 \pm 5 \mu\text{m}$ and width $2 \pm 0.5 \mu\text{m}$, having an aspect ratio of 10 ± 2 (Fig. 8). The content of the primary mullite needle-like single crystals has been determined by quantitative XRD analysis and found to be 60 wt%. These data are in agreement with that calculated from Fig. 4 at 1650°C ($60 \pm 5\%$).

The specific gravity of the fired substrate has

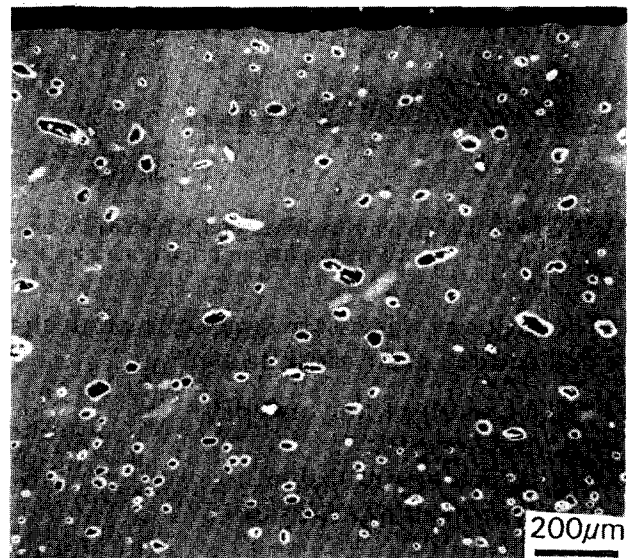
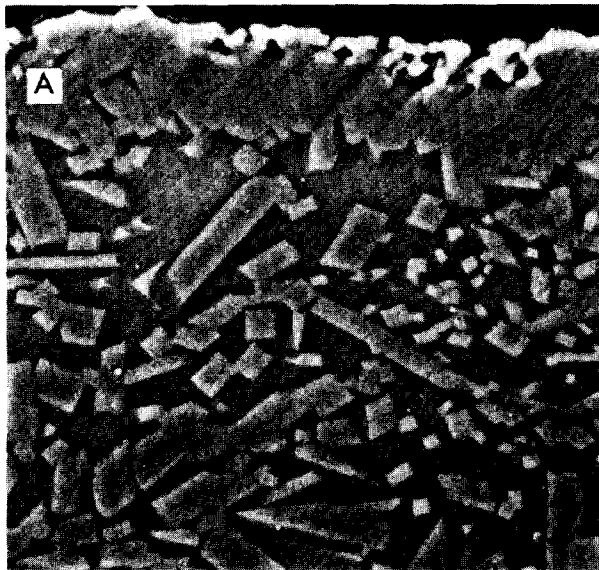
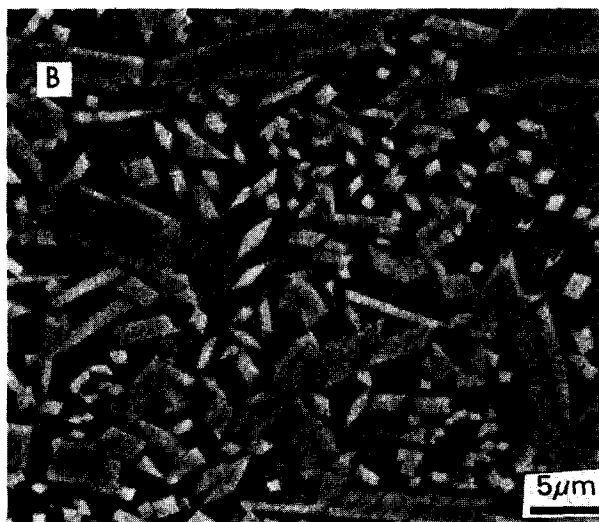


Fig. 7. Optical micrograph of the cross-section of a substrate, showing closed porosity.



SECONDARY MULLITE
LAYER



PRIMARY MULLITE WHISKERS
REINFORCE GLASSY MATRIX

Fig. 8. SEM micrographs of the cross-section of a substrate fired at 1650°C: (A) secondary mullite top layer; (B) glassy matrix reinforced with primary mullite whiskers.

been determined using Archimedes' method in Hg and has been found to be $2.75 \pm 0.06 \text{ g cm}^{-3}$.

The thermal expansion of the substrate has been determined by dilatometry using a sample of 1 cm length, giving $\alpha_{20-500} = 3.8 \times 10^{-6} \text{ }^\circ\text{C}^{-1}$. As can be observed in Fig. 9, the thermal expansion of the substrate matches that of silicon in the temperature interval ranging from 20 to 600°C.

The dielectric constant and dielectric loss were determined on discs 25 mm in diameter and 2 mm height with parallel flat surfaces coated by Ag (70 wt%) + Pd (30 wt%), the discs being heated at 200°C for 30 min prior to measurements. A Hewlett-Packard 4192 ALF impedance analyser at 1 kHz to 10 MHz at 0.1–0.2 mV was used. The results obtained were: $\epsilon = 4$ at 1 MHz; $\delta = 0.01$ at 1 MHz.

Tummala⁸ has pointed out that for high performance ceramic packaging, the two main requirements are: (i) less interconnect delay and (ii) larger chip. To meet the first requirement ceramic

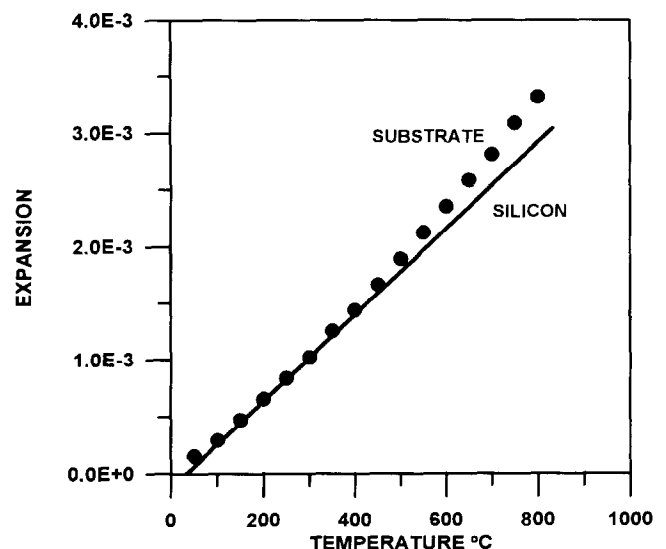


Fig. 9. Thermal expansion curve of the substrate. That of silicon is also shown for comparison purposes.

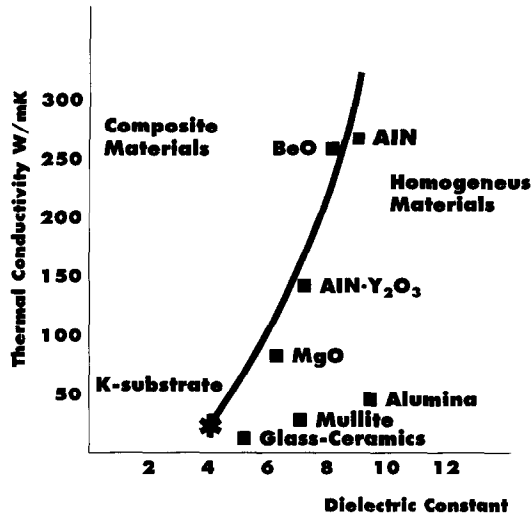


Fig. 10. Thermal conductivity versus dielectric constant for several materials used in electronic packaging. The value corresponding to the kaolinite-based substrate is also plotted (*).

substrates with lower dielectric constant and higher packaging density are necessary. The second one is met by decreasing the thermal expansion mismatch between substrate and silicon.

The kaolinite substrate prepared as described in this paper, has the lowest permittivity value obtained to date (Fig. 10) and a thermal expansion very close to that of silicon (Fig. 9). Because of these facts and the low cost of the starting raw materials, this substrate may be of potential interest for the electric and electronic industries.

Conclusions

Layered kaolinite-alumina ceramics obtained by

sequential slip casting have proved to be a useful model to design new ceramic materials.

A new low-cost ceramic substrate for electronic applications, reinforced by mullite whiskers and with controlled closed porosity, low permittivity value ($\epsilon \approx 4$ at 1 Mhz) and thermal expansion coefficient close to that of silicon ($3.8 \times 10^{-6} \text{ }^\circ\text{C}^{-1}$), has been developed starting from conventional kaolinite powder.

Acknowledgement

This work was supported by CYCIT Spain under contract MAT-94-0974.

References

1. Lui, K. C., Thomas, G., Caballero, A., Moya, J. S. & de Aza, S., Mullite formation in kaolinite- Al_2O_3 . *Acta Metall. Mater.*, **42**(2) (1994) 489-95.
2. Lui, K. C., Thomas, G., Caballero, A., Moya, J. S. & de Aza, S., Time-temperature-transformation curves for kaolinite- α -alumina. *J. Am. Ceram. Soc.*, **77** (1994) 1545-52.
3. Katsuki, H., Furuta, S., Ichinose, H. & Nakao, H., Preparation and some properties of porous ceramics sheet composed of needle-like mullite. *J. Ceram. Soc. Jpn. Int.*, **96** (1988) 1056-61.
4. Leving, E. M., Robbins, C. R. H. & McMurdie, H. F., in *Phase Diagrams for Ceramists*, ed. R. K. Reser, American Ceramics Society, Columbus, OH, 1964, Fig 407.
5. Tummala, R. R., & Rymaszewski, E. J., *Microelectronics Packaging Handbook*, Van Nostrand Reinhold, New York, 1989.
6. Kanzaki, S., Ohashi, M. & Tabata, H., Mullite ceramics for insulating substrates. *Ceram. Trans.*, **6** (1990) 389-99.
7. Giess, E. A., Roldan, J. M., Bailey, Ph. J. & Goo, E., Microstructure and dielectric properties of mullite ceramics. *Ceram. Trans.*, **15** (1990) 167-77.
8. Tummala, R. R., Ceramics in microelectronic packaging. *Am. Ceram. Soc. Bull.* **64**(4) (1988) 752-8.

Fabrication of Low-to-Zero Shrinkage Reaction-Bonded Mullite Composites

Dietmar Holz,^a Sonja Pagel,^a Chris Bowen,^b Suxing Wu^c & Nils Claussen^d

^aPhilips WEB, 22419 Hamburg, Germany

^bUniversity of Leeds, School of Materials, Leeds, UK

^cLehigh University, Materials Research Center, Bethlehem, USA

^dTechnische Universität Hamburg-Harburg, Advanced Ceramics Group, 21071 Hamburg, Germany

(Accepted 22 July 1995)

Abstract

The technology of reaction bonding Al_2O_3 (RBAO) can be modified by the use of Si-containing additives to yield low-to-zero shrinkage mullite composites. In the present work, SiC particles were added to the Al/ Al_2O_3 precursor mixture. During air heat-treatment, first Al oxidizes to Al_2O_3 at 300–900°C, thereafter SiC converts to SiO_2 (900–1200°C). Both phases form mullite ($3Al_2O_3 \cdot SiO_2$) at temperatures >1400°C. Depending on the hold time at 900–1200°C, the extent of SiC oxidation, hence the ratio of mullite to dispersed SiC can be controlled. Since both oxidation reactions and the mullitization are associated with volume expansions, the sintering shrinkage can either be fully or partially compensated for. The process parameters amount of Al and SiC, green density and degree of SiC oxidation can be utilized to fabricate low-to-zero shrinkage mullite composites.

1 Introduction

In recent years, the development of high-strength mullite for engineering and electronic applications has become a new area of ceramic research. This is due to many advantageous properties like high melting point, good creep resistance, low thermal expansion, low dielectric constant, and good corrosion resistance.¹ However, the mechanical properties of plain mullite are low (bending strength: ≈ 250 MPa, fracture toughness: ≈ 2.5 MPa m^{1/2}) when compared to other ceramics.² Therefore, several mullite composites have been fabricated to improve the mechanical properties, e.g. by adding ZrO_2 as well as platelets, whisker, or fibers.^{3–7} The

fabrication of these improved mullite composites often requires new processing routes, such as sol-gel techniques combined with hot pressing, which limits the shape and size of the product and reduces the economy of the process.

The Reaction Bonding of Aluminum Oxide (RBAO) technology,^{8–10} provides a new processing route to fabricate low-to-zero shrinkage high-strength mullite composites.^{11–13} The plain RBAO process, which results in a product consisting only of Al_2O_3 , starts from intensively milled Al/ Al_2O_3 precursor powder mixtures. Heating powder compacts in oxidizing atmosphere (usually air) up to temperatures of $\sim 900^\circ C$ results in complete oxidation of Al to Al_2O_3 . Due to very small 'new' Al_2O_3 crystallites, sintering starts at $\sim 1100^\circ C$. The Al oxidation results in a 28% volume expansion partially compensating for the sintering shrinkage. Therefore, low shrinkage (5–15%) Al_2O_3 ceramics are readily fabricated. In order to further reduce the shrinkage even to zero, the RBAO process can be modified in various ways by incorporating other metal or ceramic additives that exhibit volume expansions on oxidation which further compensate for the sintering shrinkage.

In this work, SiC additions are utilized to form mullite ceramics. Because of the large volume expansion associated with both the oxidation of SiC to SiO_2 (108%) and with the mullite ($3Al_2O_3 \cdot SiO_2$) formation (4.2%), the sintering shrinkage is effectively compensated. In this respect, 26 vol.% in the precursor powder composition is necessary to fabricate pure mullite.¹¹ Therefore, the heat treatment should be set ensuring complete oxidation of SiC. If the heat treatment is selected such that the SiC particles are not completely oxidized, various mullite/ Al_2O_3 /SiC composites result. The aim of this paper is to describe and to discuss the formation of low-to-zero shrinkage mullite composites obtained by the RBAO technology.

2 Experimental

Powder compositions and sources of raw materials used are listed in Table 1. The notations for the compositions contain the SiC content in vol.% in the precursor composition and a small letter defining the SiC particle size (c for coarse and f for fine). The powder mixtures were attrition-milled in acetone for 7 h with TZP (3Y-ZrO₂) milling media. The amount of ZrO₂ introduced into the powder was estimated from qualitative phase analyses of the reaction-bonded samples. After milling, the powder was dried and sieved with a 200 μm mesh. Green bodies were produced by uniaxial pressing at 50 MPa followed by cold isostatic compaction (CIP) at pressures of 300 and 900 MPa. Oxidation and sintering was carried out in a box furnace in air using the heating cycle shown in Fig. 1. At 1150°C, a dwell time of 15 h (coarse SiC) and 10 h (fine SiC) was selected to ensure complete oxidation of SiC. This temperature was chosen because sintering is not yet significant, hence the powder compacts still contain open porosity. Therefore, the carbon monoxide produced by the SiC oxidation can diffuse outwards. Sintering was carried out at 1550°C for 1 h. The density of the final products was measured by the Archimedes method. Reaction products were identified by X-ray diffraction (XRD). Qualitative phase compositions were determined by Rietveld analysis. Microstructures were investigated by transmission electron microscopy (TEM).

Table 1. RBAO precursor powder compositions

	SC30c	SC30f	SC45f
¹ Al	40	40	40
² Al ₂ O ₃	30	30	15
SiC	³ 30	⁴ 30	⁴ 45

¹Alcan 105, <50 μm, globular, Alcan International, Canada.

²Ceralox HPA-0.5, ≈0.8 μm, Condea Chemie GmbH, Brunsbüttel, Germany.

³F1000, 2.5–3.5 μm, Norton AS, Lillesand, Norway.

⁴Ultra-fine, 0.27 μm, Ibiden Co., Ogaki, Japan.

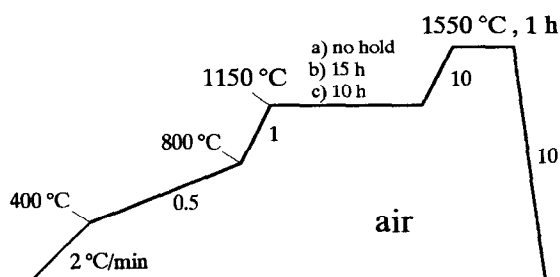


Fig. 1. Heat treatment cycles: (a) without and (b, c) with oxidation holds for SiC.

3 Results and Discussion

3.1 Phase development

The XRD diagrams (Fig. 2) of composition SC30c at 1150°C without and with 15 h hold show that, for both temperature cycles, all Al has been completely oxidized, and that a large amount of ZrO₂ is introduced (12–15%) during milling. It originates from wear debris of the TZP balls and discs. Composition SC30f (fine SiC) contains somewhat less ZrO₂ (~10%) which is due to the reduced aggressiveness of the smaller SiC particles. When using coarse SiC, it is impossible to get complete oxidation, even after 15 h hold, while with finer SiC (SC30f), even 10 h at 1150°C are sufficient. The oxidation product is amorphous SiO₂ not detectable by XRD. It has been shown previously¹¹ that crystalline SiO₂ (α-cristobalite) does not form until ~1200°C.

Phase compositions of samples SC30c and SC30f after sintering at 1550°C for 1 h are shown in Fig. 3. Sample SC30c without holding at 1150°C (SC30c1550/0, left bar) consists of mullite/Al₂O₃/SiC/

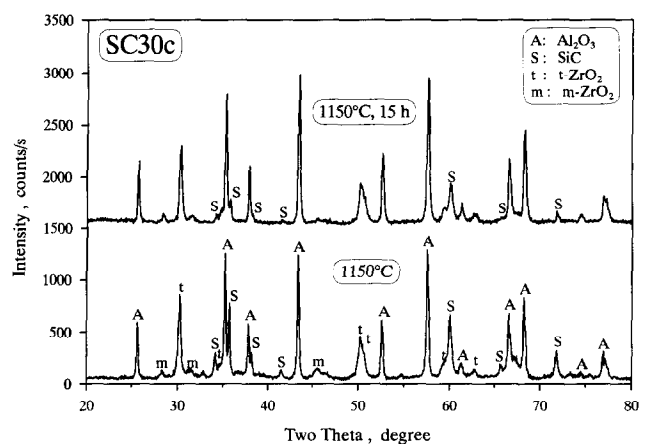


Fig. 2. XRD diagrams of sample SC30c without and with hold for 15 h at 1150°C.

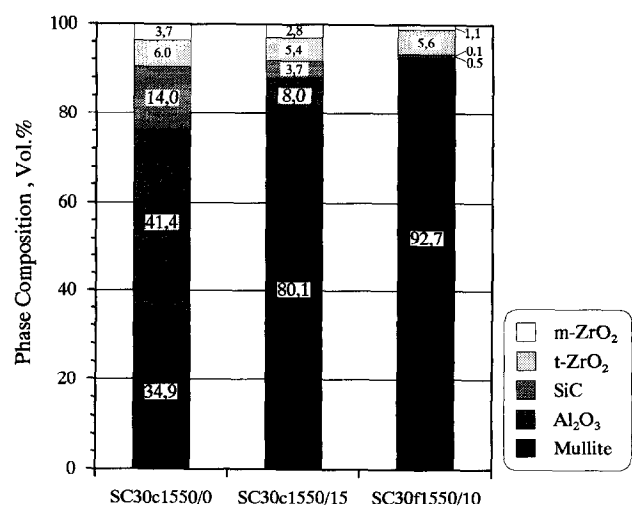


Fig. 3. Phase compositions of samples SC30c and SC30f after sintering at 1550°C for 1 h.

t-ZrO₂/m-ZrO₂(34.9/41.4/14.0/6.0/3.7 vol.%). After holding at 1150°C for 15 h (SC30c1550/15) before sintering, the sample still contains mullite/Al₂O₃/SiC/t-ZrO₂/m-ZrO₂ (80.1/8.0/3.7/5.4/2.8 vol.%). Due to the higher degree of SiC oxidation though, the amount of mullite is strongly increased and correspondingly the content of Al₂O₃ and SiC is lower. When coarse SiC is used neither dwell time nor heat-up time to the sintering temperature (heating rate is 10°C/min) are sufficient to allow complete SiC oxidation. However, sample SC30f after holding at 1150°C for 10 h before sintering (SC30f1550/10, Fig. 3 right bar) consists mainly of mullite and ZrO₂ (92.7/6.7 vol.%). Only traces of Al₂O₃ and SiC are left (<0.5 / <0.1 vol.%).

It is interesting to note that, at temperatures >1400°C in air, samples with non-completely oxidized SiC always have a white outer layer consisting of mullite and Zircon (ZrSiO₄). This effect is attributed to preferred densification in the surface region due to oxidation of SiC and mullite formation. These reactions are associated with a volume increase enhancing surface layer densification and thus hindering oxygen diffusion inwards thereby preventing further oxidation in the interior. The formation of Zircon can be explained by an excess of SiC leading to a reaction of SiO₂ with ZrO₂. With progressing densification, the trapped gas inside of the sample, due to further SiC oxidation, diffuses outwards resulting in a higher porosity of the outer layer which remains even after sintering. Prevention of this layer can be achieved by initially oxidizing the SiC and Al in air and sintering the body in an inert atmosphere.

3.2 Microstructural development

The TEM micrograph (Fig. 4) of sample SC30c after holding at 1150°C for 15 h demonstrates that, when using coarse SiC particles, the heat treatment used is not sufficient for complete oxidation of all SiC particles. For this heating schedule, the critical SiC particle size after milling for complete oxidation is ~0.3–0.4 μm. The amorphous oxide layer thickness around SiC particles larger than this critical size is ~0.15–0.2 μm.

Figure 5 shows microstructures of samples SC30f after sintering at 1550°C for 1 h (a) without and (b) with hold at 1150°C for 10 h. The microstructure of the sample without hold (Fig. 5(a)) consists of mullite, Al₂O₃, SiC, and ZrO₂ (cf. Section 3.1). The grain sizes of all phases are ≤ 1 μm. Mullite and Al₂O₃ grains cannot be distinguished optically, only by EDX. SiC as well as ZrO₂ particles are mostly located at mullite or Al₂O₃ grain boundaries. SiC show the typical polytype structure. Some small SiC particles are located within the mullite grains. In contrast to XRD

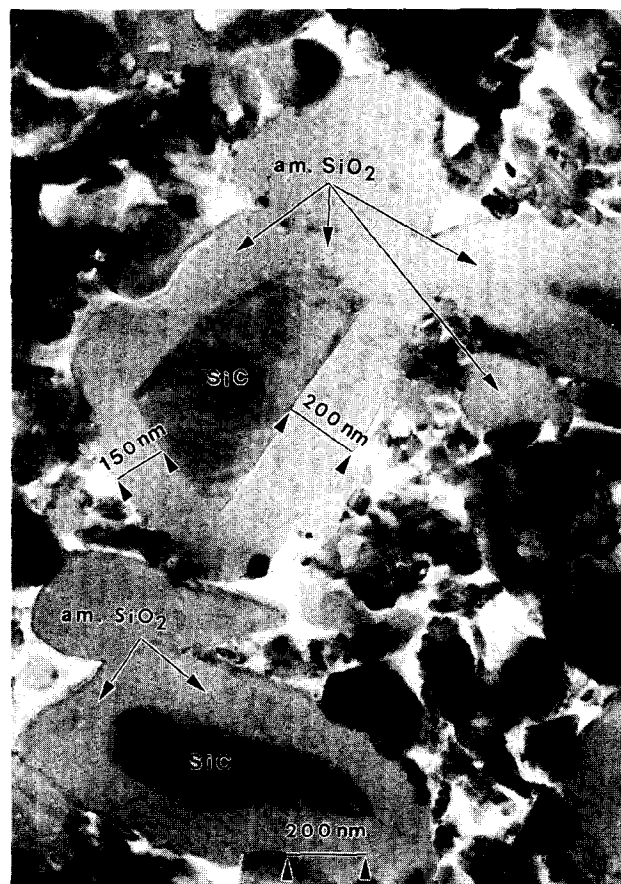


Fig. 4. TEM micrograph demonstrating the effect of SiC oxidation at 1150°C for 15 h.

results, ZrO₂ is in monoclinic crystal symmetry. The tetragonal-to-monoclinic phase transformation is attributed to TEM sample preparation.

The microstructure of SC30f in Fig. 5(b) after sintering at 1550°C with hold at 1150°C for 10 h (complete SiC oxidation) is characterized by a dense and homogeneous mullite matrix with ZrO₂ dispersions at grain boundaries and Al₂O₃ particles inside mullite grains. Some tiny SiC particles are also found within mullite grains. The survival of these SiC particles can be explained by reduced oxygen access in the final state of densification. Consequently, also some small Al₂O₃ particles survive embedded in mullite during grain growth. The density of this mullite/ZrO₂ sample is somewhat higher (96%) than that shown in Fig. 5(a) (94.5%). This is due to the increased SiC content which is known to hinder densification of Al₂O₃.^{14,15}

3.3 Zero-shrinkage conditions

The shrinkage calculation of mullite composites requires the knowledge of: (a) the fraction of Al oxidized during milling (f); (b) the fraction of ZrO₂ introduced by milling wear (V_{ZrO_2}); (c) the degree of SiC oxidation during reaction bonding (Ψ) and (d) green (ρ_0) and final density (ρ). The

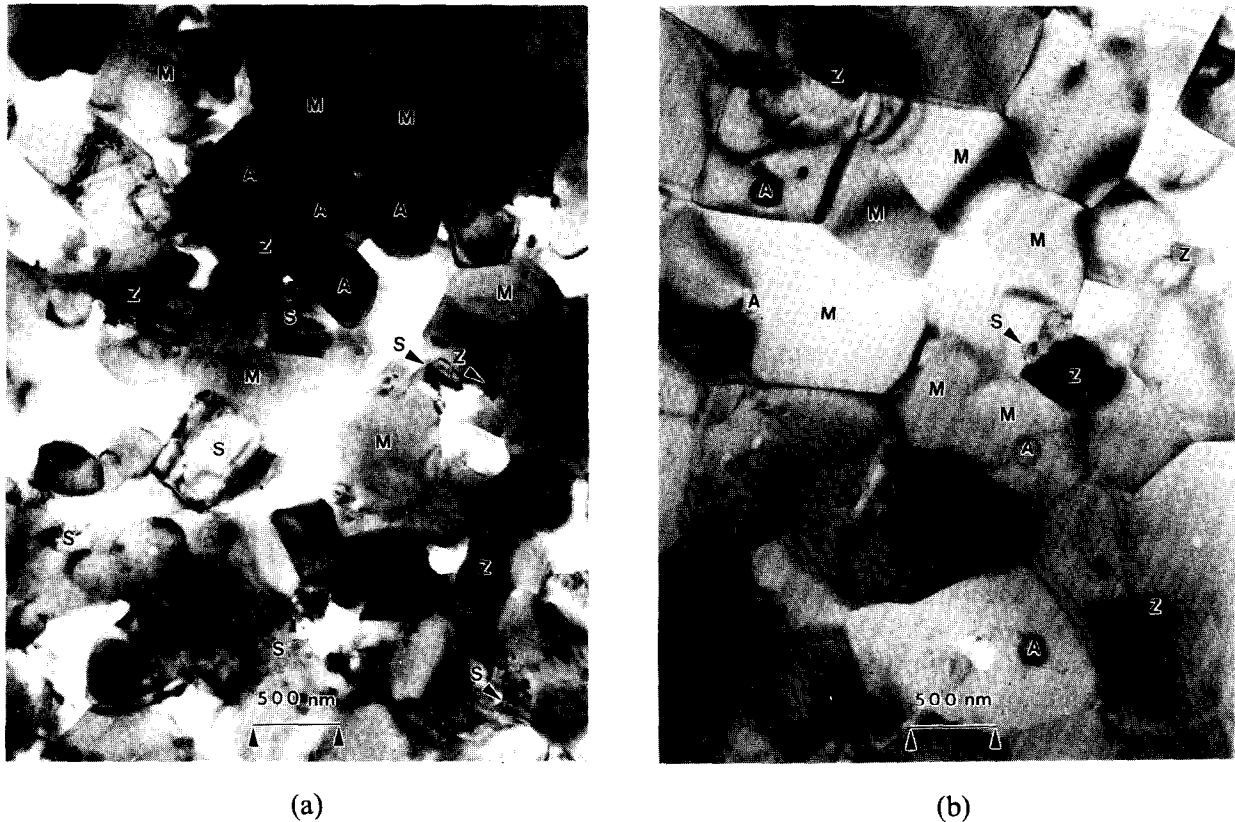


Fig. 5. TEM micrographs showing composition SC30f after sintering at 1550°C for 1 h: (a) without and (b) with hold at 1150°C for 10 h (M: Mullite, A: Al₂O₃, S: SiC, Z: ZrO₂).

determination of f has been described elsewhere⁹ and can be done by quantitative X-ray or thermogravimetric analyses. Typical values for f are 0.3–0.5. V_{ZrO_2} can be determined by different methods: (a) XRD analysis of the milled powder (difficult because of the amorphous Al₂O₃); (b) weighing the milling discs and balls before and after milling (not very accurate), and (c) quantitative XRD phase analysis of reaction-bonded bodies. Method (c), e.g. Rietveld analysis, enables the exact determination of phase composition after reaction bonding, however, phase composition depends strongly on the degree of SiC oxidation. Therefore, exact calculation of V_{ZrO_2} requires the determination of the ZrO₂ content of a sample with completely oxidized SiC ($\psi = 1$). V_{ZrO_2} can then be calculated considering the ZrO₂ volume fraction in the final composition ($V_{\text{ZrO}_2}^{\#}$) and the volume expansion during reaction bonding.¹⁰

$$V_{\text{ZrO}_2} = \frac{\left(\frac{1 + 0.28V_{\text{Al}} + 1.125V_{\text{SiC}}}{1 + 0.60fV_{\text{Al}}} \right) \cdot V_{\text{ZrO}_2}^{\#}}{1 - V_{\text{ZrO}_2}^{\#}} \quad (1)$$

Thereby, 0.28 and 1.125 are the volume expansions associated with the Al oxidation (0.28) and the combination of SiC oxidation (1.08) and mullite formation (0.042), and V_{Al} and V_{SiC} the respective volume fractions. 0.60 is the volume expansion

associated with the oxidation of Al to amorphous Al₂O₃ (density ~3.2 g/cm³) during milling.¹⁰

Exact shrinkage calculations require the reevaluation of the true volume fractions of each phase after milling (V_i^*). The true volume fraction is given by the ratio of volume fraction before milling (V_i) to increased total volume after milling (formation of amorphous Al₂O₃ and ZrO₂ wear debris).

$$V_i^* = \frac{V_i}{1 + 0.60fV_{\text{Al}} + V_{\text{ZrO}_2}} \quad (2)$$

Equation (2) also enables the differentiation between the volume fraction of Al left after milling (V_{Al}^*) and the volume fraction of Al oxidized to amorphous Al₂O₃ (V_{amorph}^*). In this case, V_i for Al is equal to $(1-f)V_{\text{Al}}$ and for amorphous Al₂O₃ equal to $1.60fV_{\text{Al}}$, respectively. Generally speaking, the volume increase during reaction bonding due to oxidation of Al can be calculated either by considering V_{Al} and f (see also Ref. 10) or by the real volume fractions, as demonstrated in eqn (3). Thereby, -0.20 is the volume decrease associated with the phase transformation of amorphous Al₂O₃ to α -modification. However, in case when for shrinkage calculations also wear debris has to be considered always the real volume fractions have to be determined.

$$\frac{1 + 0.28V_{Al}}{1 + 0.60fV_{Al}} = 1 + 0.28V_{Al}^* + 0.20V_{amorph}^* \quad (3)$$

To determine the degree of SiC oxidation during reaction bonding (ψ), the SiC phase content after reaction bonding ($V_{SiC}^\#$) has to be measured, e.g. by Rietveld analysis. $V_{SiC}^\#$ is also given by the volume ratio of non-oxidized SiC ($(1-\psi)V_{SiC}^*$) to total volume after reaction bonding.

$$V_{SiC}^\# = \frac{(1-\psi)V_{SiC}^*}{1 + 0.28V_{Al}^* - 0.20V_{amorph}^* + 1.125\psi V_{SiC}^\#} \quad (4)$$

Rearranging eqn (4) gives:

$$\psi = \frac{1 - \frac{V_{SiC}^*}{V_{SiC}^\#} (1 + 0.28V_{Al}^* - 0.20V_{amorph}^*)}{1 + 1.125V_{SiC}^\#} \quad (5)$$

The shrinkage calculation also requires the knowledge of relative green (ρ_0) and final (ρ) density. Therefore, theoretical green and final density have to be calculated considering the true volume fractions. A modified equation predicting the total dimensional linear change, S , during reaction bonding of SiC-containing RBAO ceramics is then given by

$$S = \left[(1 + 0.28V_{Al}^* - 0.20V_{amorph}^* + 1.125\psi V_{SiC}^\#) \frac{\rho_0}{\rho} \right]^{\frac{1}{3}} - 1 \quad (6)$$

Following eqn (6), the conditions for low-to-zero shrinkage are high Al and SiC contents, complete oxidation ($\psi = 1$), low fraction of Al oxidized during milling (V_{amorph}^* small), and high green and

low final densities. In composition SC30, the Al and SiC content is given with 40 and 30 vol.% in the precursor powder. Calculations according to eqn (6) for low-to-zero shrinkage conditions assuming $\psi = 1$ (complete SiC oxidation) and $V_{ZrO_2}^\# = 10$ vol.% together with general trends mentioned before are given in Fig. 6. A low-to-zero shrinkage range can be defined for samples with 90% final density and $f = 0$ as an upper limit and with 100% final density and $f = 0.5$ as a lower limit. The dashed line represents samples with 100% final density and $f = 0$.

A green machined sample of composition SC30 was fabricated with a linear shrinkage of 0.6%, 96% TD final density, and a ZrO_2 content of 6.7 vol.% (see Fig. 7). The green density was 68% TD (CIP pressure: 900 MPa), $f \sim 0.3$, and SiC completely oxidized. According to eqns (1) and (2), the phase composition in the powder mixture after milling has been calculated to be 23.7/16.2/25.2/25.2/19.7 vol.% (Al, amorphous Al_2O_3 , Al_2O_3 , SiC, and ZrO_2), respectively. Calculating the linear dimensional change according to eqn (6) and considering the true phase composition gives a shrinkage of 2.1% which is higher than the experimental value. This can be explained by an increased volume of the porous outer layer consisting of mullite and Zircon (see Section 3.1). Neglecting the change of phase composition due to ZrO_2 wear debris gives a linear shrinkage of 1.4% which is similar to that considering $V_{ZrO_2}^*$. The calculated and experimentally determined shrinkage values are also presented in Fig. 6.

In order to reduce the required green density for zero-shrinkage behavior, SiC contents > 26 vol.% may be used to further increase the oxidation expansion. However, when more than 26 vol.% SiC is used, an excess of SiO_2 remains. Therefore, the volume expansion due to SiC oxidation (ΔV_{SiC}) has to be modified considering the

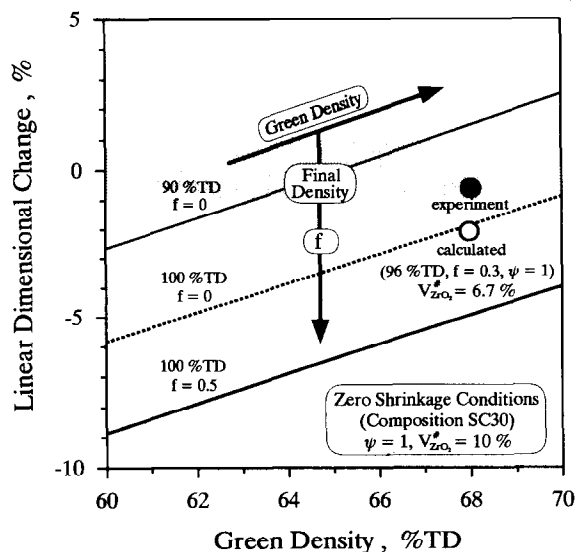


Fig. 6. Calculated linear dimensional change (according to eqn (1)) of composition SC30 for 90 and 100% final density. Experimental and calculated data points for composition SC30 (68 and 96% green and final density, $f = 0.3$) are also given.

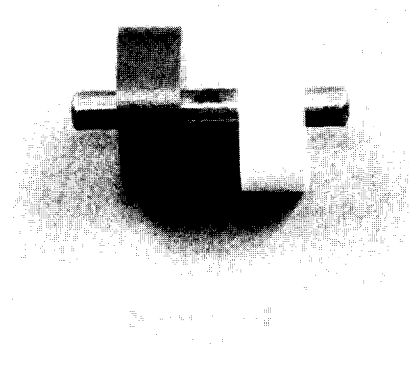


Fig. 7. Photograph demonstrating zero-shrinkage of a part made from composition SC30. The inner diameter of the green (dark) and reaction-bonded part (white) did not change.

amount of remaining SiO_2 . ΔV_{SiC} is then a combination of only SiC oxidation ($\Delta V_{\text{SiC} \rightarrow \text{SiO}_2} = 1.08$) and SiC oxidation plus mullitization ($\Delta V_{\text{SiC} \rightarrow \text{mullite}} = 1.125$). A composition consisting of 40/15/45 vol.% Al/ Al_2O_3 /SiC (SC45) was fabricated and a shrinkage of 1% (97% final density) was observed using a CIP pressure of only 300 MPa. The presence of SiO_2 would possibly reduce the high temperature strength of the composite.

4 Conclusions

- (1) The RBAO process can be modified by adding SiC to the precursor powder mixture to fabricate low-to-zero shrinkage mullite/ Al_2O_3 /SiC/ ZrO_2 composites. Attrition-milling of RBAO precursor powders is normally carried out with TZP balls and discs which introduces, when SiC is present, a substantial amount of ZrO_2 wear debris into the mixture (10–15%). ZrO_2 is not necessary for the RBAO process, however, it improves the microstructural development.⁸
- (2) The phase ratio of mullite to SiC in the final composition can be varied by adjusting the degree of SiC oxidation.
- (3) The exact calculation of the linear dimensional change during reaction bonding requires the determination of the true volume fractions of each phase in the green and sintered state considering the fraction of Al oxidized during milling, the ZrO_2 wear debris, and the degree of SiC oxidation.
- (4) To achieve zero shrinkage, high SiC contents (>26%), high green densities (>65%) and complete SiC oxidation are required. Therefore, small SiC powders (<1 μm) and intensive milling are recommended.
- (5) In order to reduce the required green density for zero shrinkage, SiC contents >30% should be used to further increase the oxidation expansion. However, when >26% SiC is used, excess SiO_2 remain in the body.
- (6) At temperatures >1400°C, a white porous outer layer consisting of mullite and Zircon (ZrSiO_4) is produced. Prevention of this layer can be achieved by initially oxidizing the SiC and Al in air and sintering the body in an inert atmosphere.
- (7) Reaction-bonded mullite/ Al_2O_3 /SiC/ ZrO_2 com-

posites exhibit superior mechanical properties. These results are published elsewhere.¹²

Acknowledgements

The authors thank Deutsche Forschungsgemeinschaft (DFG) for financial support under contracts No. Cl 52/12-2 and Cl 52/23-1. Thanks are also due to D. Thiele for Rietveld analyses.

References

1. Schneider, H., Okada, K. & Pask, J. A., *Mullite and Mullite Ceramics*, John Wiley & Sons, Chichester, 1994.
2. Kanzaki, S., Tabata, H., Kumazawa, T. & Ohta, S., Sintering and mechanical properties of stoichiometric mullite. *J. Am. Ceram. Soc.*, **68** (1985) C6–7.
3. Claussen, N. & Jahn, J., Mechanical properties of sintered *in situ*-reacted mullite/ ZrO_2 composites. *J. Am. Ceram. Soc.*, **63** (1980) 229.
4. Wei, G. C. & Becher, P. F., Development of SiC-whisker-reinforced ceramics. *Am. Ceram. Soc. Bull.*, **64** (1985) 298–304.
5. Liu, H. Y., Claussen, N., Hoffmann, M. J. & Petzow, G., Fracture sources and processing improvements of SiC-whisker-reinforced mullite (ZrO_2) composites. *J. Eur. Ceram. Soc.*, **7** (1991) 41–7.
6. Nischik, C., Seibold, M., Travitzky, N. A & Claussen, N., Effect of processing on mechanical properties of platelet-reinforced mullite composites. *J. Am. Ceram. Soc.*, **74** (1991) 2464–8.
7. Niihara, K., New design concept of structural ceramics–ceramic nanocomposites. *J. Ceram. Soc. Japan, Int. Ed.*, **99** (1991) 945–52.
8. Wu, S., Holz, D. & Claussen, N., Mechanisms and kinetics of reaction-bonding Al_2O_3 (RBAO) ceramics. *J. Am. Ceram. Soc.*, **76** (1993) 970–80.
9. Holz, D., Wu, S., Scheppokat, S. & Claussen, N., Effect of processing parameters on phase and microstructure evolution in RBAO ceramics. *J. Am. Ceram. Soc.*, **77** (1994) 2509–17.
10. Claussen, N., Wu, S. & Holz, D., Reaction bonding of aluminum oxide (RBAO) composites: Processing, reaction mechanisms, and properties. *J. Eur. Ceram. Soc.*, **14** (1994) 97–109.
11. Wu, S. & Claussen, N., Fabrication and properties of low-shrinkage reaction-bonded mullite. *J. Am. Ceram. Soc.*, **74** (1991) 2460–3.
12. Wu, S. & Claussen, N., Reaction bonding and mechanical properties of Mullite/SiC composites. *J. Am. Ceram. Soc.*, **77** (1994) 2898–904.
13. Brandt, J. & Lundberg, R., Processing of mullite-based long-fiber composites via slurry routes and by oxidation of an Al:Si alloy powder. *J. Eur. Ceram. Soc.*, **16** (1996).
14. Nakahira, A. & Niihara, K., Sintering behaviors and consolidation process for Al_2O_3 /SiC nanocomposites. *J. Ceram. Soc. Japan, Int. Ed.*, **100** (1992) 448–53.
15. Stearns, L. C., Zhao, J. & Harmer, M. P., Processing and microstructure development in Al_2O_3 -SiC 'nanocomposites'. *J. Eur. Ceram. Soc.*, **10** (1992) 473–7.

Processing of Mullite-based Long-fibre Composites via Slurry Routes and by Oxidation of an Al–Si Alloy Powder

J. Brandt^a & R. Lundberg^b

^aSwedish Ceramic Institute, Box 5403, S-402 29 Göteborg, Sweden

^bVolvo Aero Corporation, S-461 81 Trollhättan, Sweden

(Accepted 22 July 1995)

Abstract

A novel technique to synthesize mullite by the oxidation of Al–Si alloy powder was used for the manufacture of Al₂O₃ long-fibre reinforced mullite composites. It included (1) slurry infiltration/fibre winding of continuous Al₂O₃ yarns (ALMAX) and (2) slurry infiltration/slip casting of sapphire fibres (Saphikon). The nonaqueous slurry used consisted of an Al–Si alloy, mullite and additives. During reaction-bonding of green matrices, the Al–Si alloy oxidized and was fully converted to mullite after 1 h at 1430°C in air. The oxidation caused an internal volume expansion, resulting in reduced fibre/matrix shrinkage stresses during reaction-bonding of composites, which minimized the sensitivity to crack formations. For the ALMAX-based composites, the fracture was non-catastrophic. Regarding the sapphire-based composites, an interfacial space between the fibres and the matrix gave the desired fibre pull-out.

1 Introduction

Ceramic long-fibre reinforced composites are being considered as future materials for gas turbine hot parts.¹ However, there are still some obstacles to overcome before this group of materials are mature enough for turbine applications, where there are high demands on long-term, high-temperature stability in the oxidizing environment. For instance, it has been difficult to produce dense ceramic long-fibre composites with adequate high temperature properties, including good oxidation resistance, for use at over 1400°C. This is especially true for nonoxide materials, where both fibres, matrix and interface material are nonoxides and consequently oxidize to form a strong fibre/matrix bond leading to brittle fracture behaviour.²

One possible solution is to develop composites consisting of high temperature oxide matrices and fibres and maybe even allow some open porosity in the final material.³

Mullite (Al₆Si₂O₁₃) is of particular interest as matrix material among the binary metal oxide ceramics.⁴ This refractory possesses good creep resistance and excellent oxidation resistance.⁵ However, the drawbacks of mullite are the low fracture toughness ($K_{Ic} = 2\text{--}3 \text{ MPa}\cdot\text{m}^{1/2}$) and the poor sinterability, mainly due to the low interdiffusion rates of silicon and aluminium ions in crystalline mullite.⁶ However, if this material is reinforced with high-temperature oxide long-fibres, and if some porosity could be accepted, then mullite could definitely be a competitive, moderate cost material for high-temperature structural applications. The fibres also facilitate the production of large thin-walled, complex-shaped components.⁷

A new technique to synthesize mullite has been developed, particularly, in view of the manufacture of mullite-based long-fibre composites.⁸ The technique is described in this paper. In short, a mixture of an Al–Si alloy and oxide powders is milled and formed into a powder compact, after which the alloy is oxidized and reaction-bonded to its corresponding ceramic composition, i.e. mullite. The brittle Al–Si is effectively comminuted during milling, avoiding the formation of undesired large, flat agglomerates by cold welding, as is the case with pure Al powder.^{9,10} Consequently, when long-fibre composites are processed, fibre tows are more easily infiltrated. Because of the fine metal distribution in the alloy, the transformation to mullite, during oxidation and reaction-bonding, is favoured. Another advantage is that the oxidation causes an internal volume expansion of the matrix.¹¹ This minimizes the sensitivity to crack formation due to reduced shrinkage stresses between the fibres and the matrix.^{12,13}

2 Experimental

2.1 Materials

A commercially available, gas-atomized Al–Si alloy with a weight-ratio of 75:25 (Al75/Si25 (hypereutectic compound)), particle size $<150\ \mu\text{m}$, (AL146010, GoodFellow, UK) was selected. The Al–Si ratio is close to the one necessary for the formation of stoichiometric mullite ($3\text{Al}_2\text{O}_3 \cdot 2\text{SiO}_2$) during reaction-bonding. Between 577 and 760°C, the Al75/Si25 alloy is melted to a liquid phase of a eutectic composition (Al88/Si18) plus a solid phase of large Si grains.¹⁴ On oxidation, the theoretical weight increase is 95%. If full conversion to mullite is achieved (including some excess Al_2O_3), the volume expansion is 59%. In addition to the alloy, the oxide powders used were mullite (SACR193, Baikowski Chimie, France), Al_2O_3 (AKP-30, Sumitomo, Japan) and MgO (Merck, Germany) as an oxidation catalyst. Extra Al_2O_3 was added to form mullite of otherwise unreacted, free SiO_2 — an excess of Al_2O_3 was preferred in the final material.

Two kinds of ceramic long fibres were used for the manufacture of the composites: (1) polycrystalline, continuous α - Al_2O_3 yarn with 1000 filaments per yarn (filament diameter $10\ \mu\text{m}$) and without any sizing (ALMAX Y-1010S-N, Mitsui Mining Material, Japan) and (2) single crystal, continuous α - Al_2O_3 sapphire fibres with a diameter of $130\ \mu\text{m}$ (Saphikon, USA). Whereas the ALMAX polycrystalline fibres showed limited resistance to heat in earlier experiments, the sapphire fibres have excellent high temperature properties.^{15,16} The ALMAX fibres should thus be considered as a model material.

For the preparation of the slurry, an organic, non-polar solvent, with a high boiling point, and a suitable dispersant, KD-3 (ICI, USA), were used.

2.2 Specimen preparation

One master slurry was prepared for all the experiments. A batch with a composition by weight of 30% Al75/Si25, 63% mullite, 5% Al_2O_3 and 2% MgO was mixed in the organic solvent with 3% KD-3 (on powder), resulting in a solid loading of 73.0 wt% (40.3 vol%). After prolonged ball milling, the slurry was wet-sieved through a $20\ \mu\text{m}$ cloth.

Bars with the dimensions $60 \times 9 \times 8\ \text{mm}^3$ were slip cast onto a plaster mould, both with and without a few sapphire fibres suspended parallel in the middle of the mould. In addition, long-fibre composites with the ALMAX fibre yarn were prepared by slurry infiltration/fibre winding. To keep the filament together during the fibre winding procedure, the fibre yarn bobbin was soaked with

organic solvent. The yarn was then passed through the slurry, with a thread tension of 0.08 N and a speed of 2 m/min, and wound on a quadrangular take-up spool ($65 \times 65\ \text{mm}^2$). When the soaked yarn came into contact with the slurry, the organic solvent had evaporated enough for the yarn, via capillary forces, to become fully impregnated by the slurry. In fact, the solvent residue improved the wettability of the yarn. All specimens were carefully dried, burned out in nitrogen at 500°C and subsequently stored in a dry atmosphere.

The specimens were reaction-bonded and partly densified in flowing air with heating rates of 10°C/min to 450°C and 2°C/min to maximum temperatures of 1430–1600°C with dwelling periods of 5–240 min.

2.3 Evaluation

The effect of ball milling was verified by means of specific surface area (BET) measurements and micrographs of the particles, before and after milling. The weight and the dimensional changes during the reaction-bonding process were recorded with a thermobalance (TGA) and a dilatometer (TDA). Phase compositions were determined by X-ray diffractometry (XRD), and microstructures were studied by scanning electron microscopy (SEM). Densities of reaction-bonded specimens were estimated by Archimedes' principle of volume displacement. Fracture strength and Young's modulus were measured at room temperature in a universal testing machine in four-point bending (20/40 mm span). Only a few test specimens (dimensions: $55 \times 6 \times 2\ \text{mm}^3$) were prepared.

3 Results and Discussion

3.1 Specimen preparation

As can be seen in Fig. 1, the particle size was considerably reduced after milling and there are no large, flat agglomerates present. These micron-sized, round-shaped particles favour a more homogeneous particle distribution in the powder compacts and facilitate the infiltration of fibre tows. A number of as-received, spherical Al–Si alloy particles are shown in the left micrograph.

The milling result was also checked by BET specific surface area measurements, which gave 2.7 m^2/g before milling and 8.8 m^2/g after milling.

The bulk density of the slip cast green bodies was 58.0% of theoretical density (TD). Presumably, the green density of the matrix in the fibre wound composites was slightly less, due to non-optimized particle packing. By light microscope studies, no cracks could be found in the green composites.

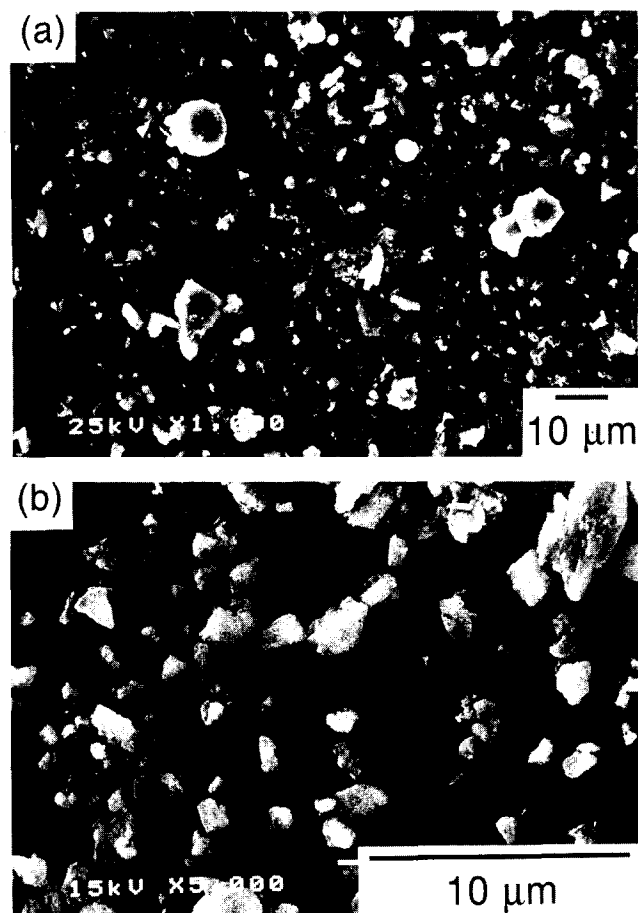


Fig. 1. Scanning electron micrographs of particles from the batch before (a) and after milling (b).

3.2 Oxidation/reaction-bonding behaviour

Thermogravimetry (TGA) and dilatometry (TDA) were used to determine the oxidation and reaction-bonding behaviour of slip cast, green bodies. In Fig. 2, the dimensional change, degree of

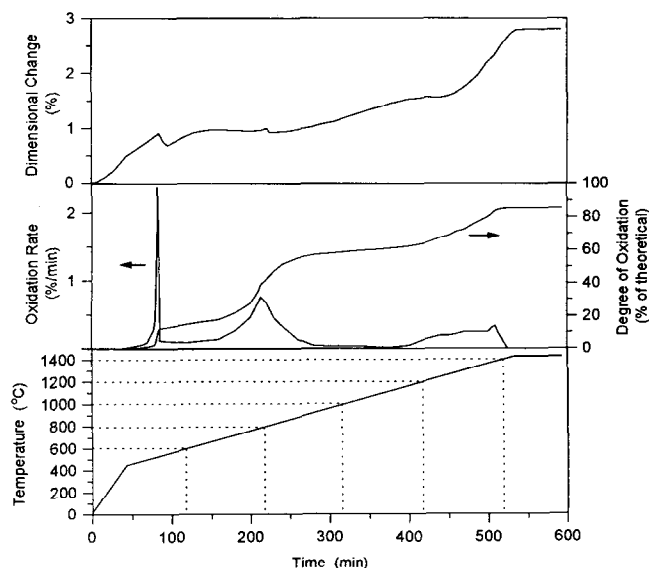


Fig. 2. Dimensional change, degree of oxidation and oxidation rate of a slip cast and burned out powder compact (without fibres) as a function of the reaction-bonding cycle, in flowing air. The total cycle time, including cooling, was 10 h.

oxidation and oxidation rate during the reaction-bonding cycle are shown.

The oxidation rate curve in Fig. 2, shows a sharp oxidation peak at 528°C, where surface oxidation of solid Al particles takes place. This reaction is strongly exothermal and probably causes local temperature increase. Since the alloy starts to melt at 577°C, this intermittent increase is expected to be high enough to partly melt the alloy, enabling a certain particle rearrangement. This may explain the minor shrinkage in the TDA at 530°C. In addition, the fine-grained Al_2O_3 that is formed reacts with the added MgO to form spinel (MgAl_2O_4), which presumably further favours the oxidation of Al in this temperature region.¹⁷ Approximately 15% of the Al in the alloy appears to oxidize by solid state/gas reaction.

After further heating, the oxidation of Al slows down considerably. At about 680°C, though, the process accelerates, with an oxidation rate maximum at 797°C. The thermal expansion of the melt presumably results in a rupture of the oxide shell so that the melt leaks out, resulting in a more rapid oxidation.^{12,18} This causes, once again, a shrinkage of the powder compact because of the particle rearrangement. This is consistent with the dilatometer analysis, with the shrinkage starting at 680°C, followed by an intermediary expansion peak at 805°C, then a small drop, before the expansion continues.

As the Al in the melt is consumed, the phase composition of the alloy is shifted towards the Si corner.¹⁴ The liquidus temperature (when also the Si grains melt) increases gradually. An oxidation rate of 0.2 %/min (based on TGA) for the Al corresponds to an increase in the liquidus temperature of approximately 1°C/min. The Si will thus be supersaturated and precipitate, which has been verified by calculations. Consequently, the primary solid Si grains will not dissolve at the liquidus temperature of Al₇₅/Si₂₅ of 760°C.

The increasing oxidation rate at ~ 1180°C indicates that Si begins to oxidize in order to form α -cristobalite (SiO_2). In spite of the fact that there is a large volume increase involved when Si oxidizes (114%), the TDA shows no expansion from 1200 up to 1240°C. One possible explanation is that the previously formed, fine α - Al_2O_3 crystals to some extent sinter. Above 1240°C, however, the oxidation of Si prevails and the expansion curve rises steeply as expected until all the Si has been oxidized. The small oxidation rate peak at 1395°C is related to the melting temperature of Si (1410°C), which may be lowered due to impurities. It is interesting to note the high degree of conversion (85.5% of the theoretical weight gain), implying that less than 15% of the alloy was

oxidized during milling. This is one of the significant advantages when employing an alloy instead of pure Al (for which up to 40 wt% premature oxidation has been reported^{11,18}). There is another advantage during reaction-bonding due to the sluggish oxidation of Si: The homogeneously distributed Si in the alloy, which encloses the reactive Al, improves the oxidation controllability and the oxidation rate can thus be increased.

All oxidation experiments were carried out in air. During this process a large amount of oxygen is consumed. According to a rough estimate (assumptions: an average pore volume of 40% in the green bodies, pores filled with oxygen batchwise at an average oxidation temperature of 800°C), the pore network has to be refilled 17 000 times with oxygen from the surrounding air to completely oxidize the specimens. This leads to a substantial reduction of the partial oxygen pressure, especially in the interior part, since the surface layer reacts with most of the inflowing oxygen. However, to avoid a runaway oxidation because of the strongly exothermal nature of the oxidation reaction, low partial oxygen pressure is necessary.

The conversion to mullite ($3\text{Al}_2\text{O}_3 + 2\text{SiO}_2 \rightarrow \text{Al}_6\text{Si}_2\text{O}_{13}$) begins below 1400°C. Table 1 shows the resulting crystalline phases before and after oxidation at 1430°C in flowing air.

Practically all Si and SiO_2 have reacted with Al_2O_3 to form mullite already after 5 min at 1430°C. In addition, an intermediate phase of cordierite ($2\text{MgO} \cdot 2\text{Al}_2\text{O}_3 \cdot 5\text{SiO}_2$) has formed. Cordierite is an undesirable final product, since two of the ternary eutectic compositions including cordierite in the $\text{MgO}-\text{Al}_2\text{O}_3-\text{SiO}_2$ system melt at 1345 and 1360°C, respectively. Fortunately, the cordierite turns into mullite and a Mg-, Al-spinel during extended heating at 1430°C. Yet to be explored is if cordierite favours the mullitization process.

According to Table 1, after oxidation/reaction-bonding at 1430°C for 60 min in flowing air, the predominant phase was mullite, but there was also some Al_2O_3 , due to the surplus alumina added, together with traces of cordierite. The total linear dimensional change for the specimen above was 2% in expansion.

3.3 Microstructure and mechanical properties of composites

Figure 3 shows micrographs of sapphire fibre reinforced mullite, reaction-bonded at three different temperatures. The effect of increasing the maximum reaction temperature can clearly be observed. First, the obvious increase of the density of the matrices: the density was after reaction-bonding at 1430°C (5 min) 65.6%, 1430°C (60 min) 66.5%, 1500°C (60 min) 80.2% and at 1600°C (60 min) 94.1% of theoretical density. The 1600°C matrix had only closed porosity. This can also be seen by comparing the SEM micrographs, where the open, fine-distributed pore network in Figs 3(a-d) have changed into enlarged close pores in Figs 3(e,f).

Images of the sapphire fibre/matrix interfaces in Fig. 3(b,d) indicate that there are spaces between the fibres and the matrices, whereas in Fig. 3(f), no space can be observed. Instead, surrounding cracks in the matrix are seen. These phenomena are due to the expansion coefficient mismatch of alumina ($8.8 \times 10^{-6} \text{ K}^{-1}$) and mullite ($5.3 \times 10^{-6} \text{ K}^{-1}$). Thus, during cooling, the sapphire fibres shrink more than the mullite matrices, causing a widening of the interface spaces. According to calculations, the space width should theoretically be $0.35 \mu\text{m}$. At the higher temperature (Fig. 3(f)), the matrix may react with the fibres to form a strong bond. The cooling stresses then lead to cracking of the adjacent matrix and even of the fibres.

One role of the fibres is to increase the fracture toughness of the material.¹⁹ As suggested by Davis *et al.*,²⁰ the interfacial debonding energy should be about one quarter of the fibre fracture energy, resulting in high-energy sliding when the fibres are pulled out. Figure 4 shows a sapphire fibre pull-out in a matrix of mullite, but whether this composite, reaction-bonded at 1430°C for 60 min, has the appropriate energy ratio has not yet been examined. A possibility is to coat the fibres with an interfacial, debonding layer, for instance ZrO_2 ,^{20,21} and thus enable sintering of the composite at higher temperatures.

In Fig. 5, an ALMAX fibre reinforced mullite composite is shown. For all composites based on ALMAX fibres, the reaction-bonding cycle was

Table 1. Crystalline phases of the green and the reaction-bonded matrices, by X-ray diffraction.

Temp. (°C)	Time (min)	$\text{Al}_6\text{Si}_2\text{O}_{13}$ (mullite)	Al_2O_3	Al	Si	SiO_2	MgO	$2\text{MgO} \cdot 2\text{Al}_2\text{O}_3 \cdot 5\text{SiO}_2$ (cordierite)
Green body		m	w	s	s	w	vw	—
1430	5	s	w/m	—	—	vw	—	w
1430	60	s	w	—	—	—	—	vw

s = strong; m = medium; w = weak; vw = very weak.

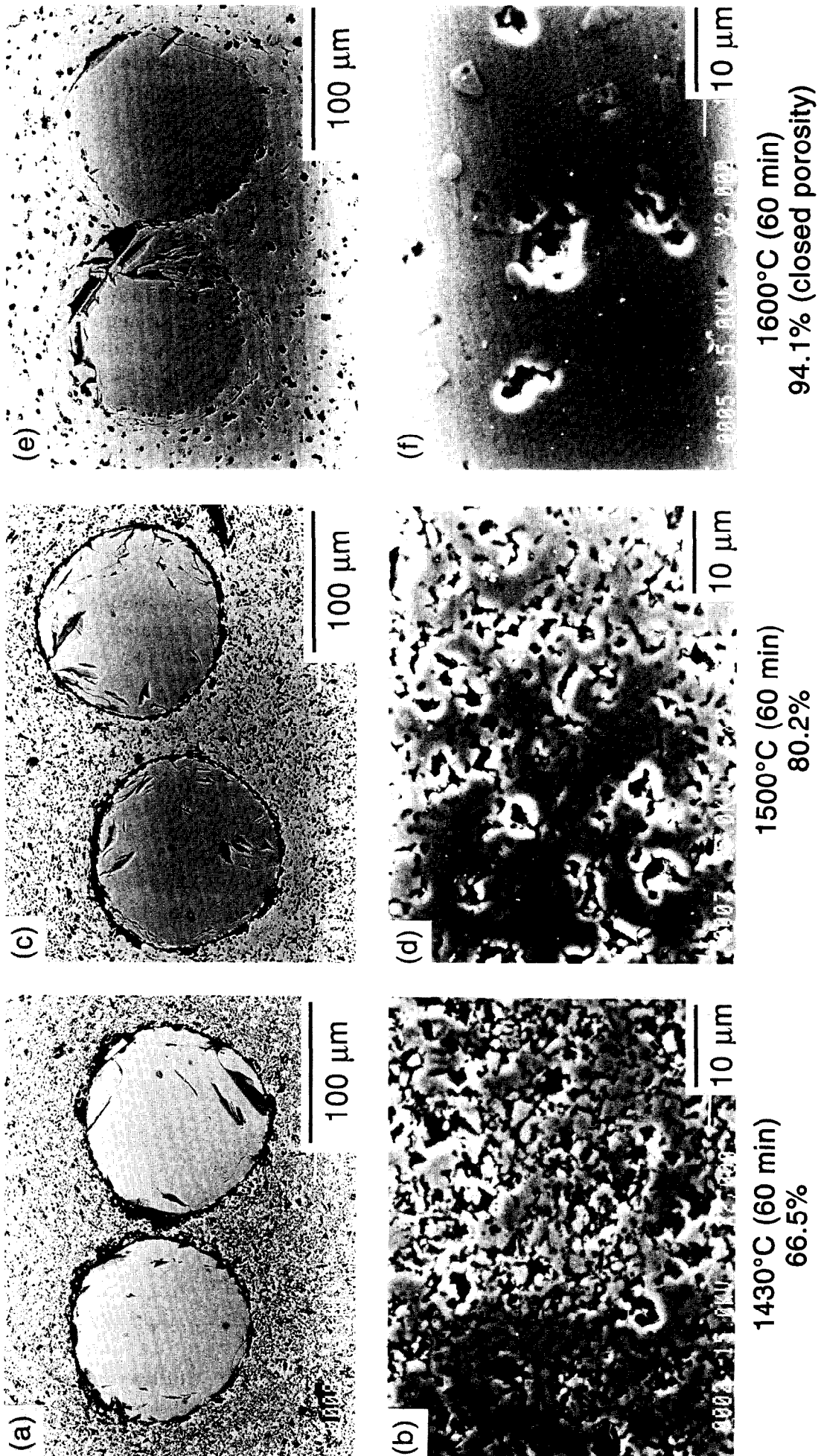


Fig. 3. Scanning electron micrographs of sapphire fibre reinforced mullite, reaction-bonded at 1430 (a, b), 1500 (c, d) and 1600°C (e, f), respectively, for 60 min. The graphs underneath are close-ups of the matrices above.

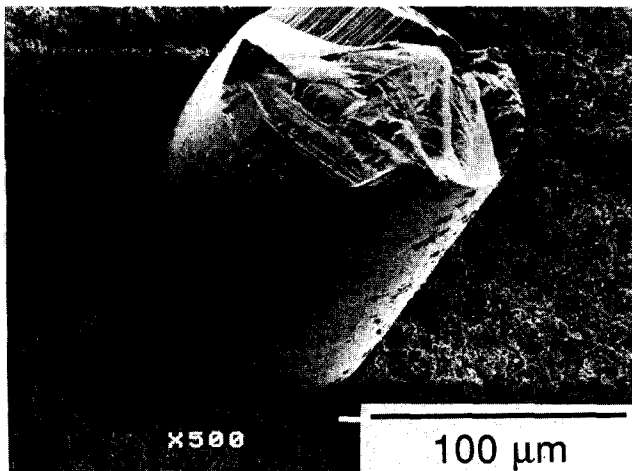


Fig. 4. Scanning electron micrograph of the fracture of a sapphire fibre reinforced mullite specimen, reaction-bonded at 1430°C for 60 min, showing a fibre pull-out.

limited to 1430°C for 5 min. This because the polycrystalline ALMAX fibres may degrade at elevated temperatures, as mentioned previously.

From the close-up (Fig. 5(b)), it is clear that the slurry has properly infiltrated the fibre tows and no fibres are in contact with each other. In addition, no cracks can be detected. The absence of cracks is probably due to the internal volume

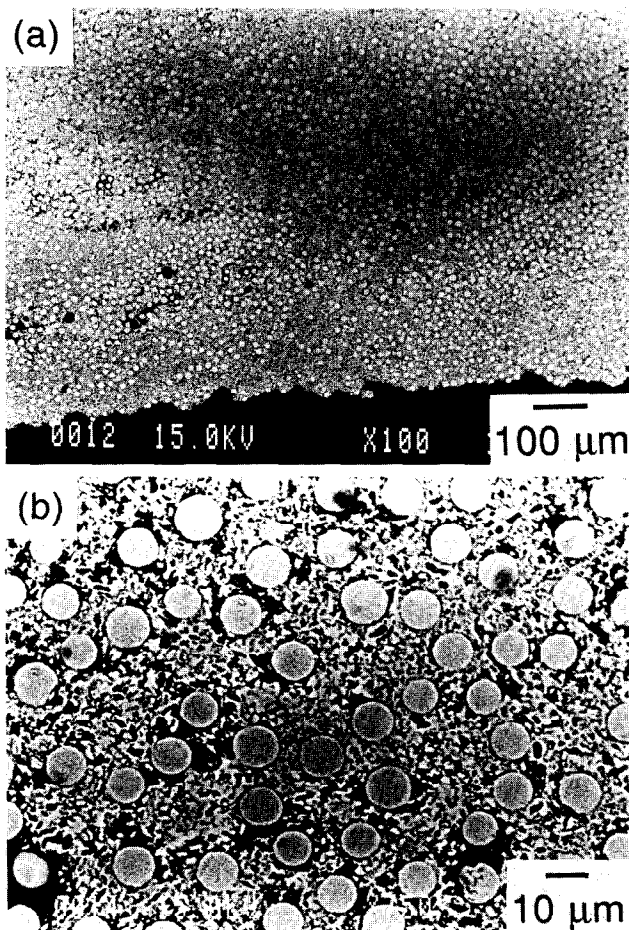


Fig. 5. Scanning electron micrographs of ALMAX fibre reinforced mullite, prepared by slurry infiltration/fibre winding followed by reaction-bonding at 1430°C for 5 min. The fibres are approximately 10 µm in diameter.

expansion of the matrix on oxidation, which reduces the fibre/matrix stresses. Unfortunately, the overview graph shows regions where there are almost no fibres present, indicating that too much slurry has covered the tows during winding and hence obstructed a homogeneous fibre distribution.

The fracture behaviour of an as-reaction bonded ALMAX fibre/mullite matrix composite is illustrated in Fig. 6. As the test specimens were not machined, this test only gives an indication of the strength potential for these composites. For the charted one, which was reaction-bonded at 1430°C for 5 min, the strength was 120 MPa. As can be seen, there was no catastrophic failure; on the contrary, a partial load-transfer took place. Even after testing, the broken parts held together. The Young's modulus was calculated for the first straight slope; with a thickness of the specimen of 2 mm it was roughly 90 GPa.

4 Conclusion

Composites of reaction-bonded long-fibre reinforced mullite were prepared by means of a new reaction-bonding technique. Both the technique, in which an Al-Si alloy in a powder compact during oxidation converts to mullite, as well as the preparation of the composites via a slurry route were demonstrated.

Starting with an Al-Si alloy, instead of Al and Si as separate components, resulted in a more effective milling, a better distribution of the two reactants, less undesired oxidation during milling and improved control of the oxidation during the reaction-bonding cycle. Furthermore, there was neither Si nor SiO₂ in the final matrix material, reaction-bonded at 1430°C for 1 h.

The long-fibres, including also fibre tows, were properly infiltrated by the Al-Si-based slurry. After reaction-bonding at 1430°C for 5 min, the

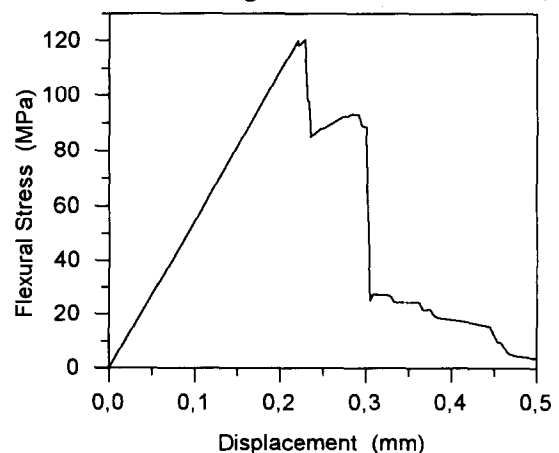


Fig. 6. Plot of the flexural stress at room temperature as a function of the displacement of an ALMAX fibre reinforced mullite test specimen, reaction-bonded at 1430°C for 5 min.

ALMAX-based composites showed no matrix cracks. The flexural test gave non-catastrophic failure characteristics. For the sapphire-based composites, reaction-bonded at 1430 and 1500°C, for 1 h, there were void spaces between the fibres and the mullite, due to a thermal expansion mismatch on cooling.

Acknowledgements

We wish to thank Lars Eklund for all SEM micrographs, Annika Kristoffersson for assistance in fibre winding and Robert Pompe for valuable discussions and constructive criticism of this paper.

References

- Butler, E. G. & Lewis, M. H., Prospects for ceramics in airborne gas turbine engines. In *Proceedings of the 4th International Symposium on Ceramic Materials and Components for Engines*, eds R. Carlsson, T. Johansson & L. Kahlman, Elsevier Applied Science, London, 1991, pp. 32–49.
- Brandt, J., Rundgren, K., Pompe, R., Swan, H., O'Meara, C., Lundberg, R. & Pejryd, L., SiC continuous fiber-reinforced Si₃N₄ by infiltration and reaction bonding. *Ceram. Eng. Sci. Proc.*, **13** (1992) 622–31.
- Kristoffersson, A., Warren, A., Brandt, J. & Lundberg, R., Reaction bonded oxide composites. In *Proceedings of the 6th European Conference on Composite Materials (EACM), High Temperature Ceramic Matrix Composites*, eds R. Naslain, J. Lamon & D. Doumeingts, Woodhead Publishing Ltd, Abington Cambridge, UK, 1993, pp. 151–9.
- Aksay, I. A., Dabbs, D. M. & Sarikaya, M., Mullite for structural, electronic, and optical applications. *J. Am. Ceram. Soc.*, **74** (1991) 2343–58.
- Dokko, P. C., Pask, J. A. & Mazdiyasi, K. S., High-temperature mechanical properties of mullite under compression. *J. Am. Ceram. Soc.*, **60** (1977) 150–5.
- Sacks, M. D., Lee, H. & Pask J. A., A review of powder preparation methods and densification procedures for fabricating high density mullite. In *Proceedings of the International Conference on Mullite*, Vol. 6, American Ceramic Society, Westerville, OH, USA, 1990, pp. 167–207.
- Ko, F. K., Preform fiber architecture for ceramic-matrix composites. *Am. Ceram. Soc. Bull.*, **68** (1989) 401–14.
- Brandt, J. & Lundberg, R., Synthesis of mullite materials by oxidation of metal alloy powder compacts. In *Third Euro-Ceramics, Vol. 1 Processing of Ceramics*, eds P. Duran & J. F. Fernández, Faenza Editrice Ibérica S.L., Spain, 1993, pp. 169–76.
- Milling of brittle and ductile materials. *Metals Handbook*, Vol 7, 9th Edition, ASM International, Materials Park, OH, 1984, 56–70.
- Claussen, N., Le, T. & Wu, S., Low-shrinkage reaction-bonded alumina. *J. Eur. Ceram. Soc.*, **5** (1989) 29–35.
- Wu, S. & Claussen, N., Fabrication and properties of low-shrinkage reaction-bonded mullite. *J. Am. Ceram. Soc.*, **74** (1991) 2460–3.
- Claussen, N., Wu, S. & Holz, D., Reaction bonding of aluminium oxide (RBAO) composites: processing, reaction mechanisms and properties. *J. Eur. Ceram. Soc.*, **14** (1994) 97–109.
- Thompson, I. & Witt, M. C., Fabrication of continuous fibre ceramic matrix composites via slurry routes. In *British Ceramic Proceedings No. 49, Special Ceramics 9*, The Institute of Ceramics, Stoke-on-Trent, 1992, pp. 269–78.
- Specific metals and alloys. *Metals Handbook*, Vol 2, 10th Edition, ASM International, Materials Park, OH, 1990, pp. 124.
- Corman, G. S., High-temperature creep of some single crystal oxides. *Ceram. Eng. Sci. Proc.*, **12** (1991) 1745–66.
- Haggerty, J. S., Wills, K. C. & Sheehan, J. E., Growth and properties of single crystal oxide fibres. *Ceram. Eng. Sci. Proc.*, **12** (1991) 1785–801.
- Newkirk, M. S., Urquhart, A. W. & Zwicker, H. R., Formation of Lanxide™ ceramic composite materials. *J. Mater. Sci.*, **1** (1986) 81–9.
- Wu, S., Holz, D. & Claussen, N., Mechanism and kinetics of reaction-bonded aluminium oxide ceramics. *J. Am. Ceram. Soc.*, **76** (1993) 970–80.
- International Encyclopedia of Composites*. Vol. 1, eds Lee, S. M., VCH Publishers, Inc., New York, 1990, pp. 267–77 and 297–318.
- Davis, J. B., Löfvander, J. P. A. & Evans, A. G., Fiber coating concepts for brittle-matrix composites. *J. Am. Ceram. Soc.*, **76** (1993) 1249–57.
- Hay, R., Fiber-matrix interfaces for oxide fiber-oxide matrix composites. In *Proceedings of the 6th European Conference on Composite Materials, High Temperature Ceramic Matrix Composites*, eds R. Naslain, J. Lamon & D. Doumeingts, Woodhead Publishing Ltd, Abington Cambridge, UK, 1993, pp. 385–9.

Preliminary Results on a Novel Fabrication Route for α -Al₂O₃ Single Crystal Monofilament-reinforced Reaction-bonded Mullite (RBM)

B. Saruhan, W. Luxem & H. Schneider

German Aerospace Research Establishment (DLR), Institute for Materials Research, D-51140 Köln, Germany

(Accepted 22 July 1995)

Abstract

Owing to their excellent properties, continuous-fibre reinforced mullite-matrix composites are good candidates for applications in which oxidation resistance and damage tolerance at high temperatures (>1000°C) are required. To avoid fibre damage, near net-shape fabrication techniques of the composite are required. This has been achieved by using the reaction-bonding process which benefits the oxidation of metal powders producing volume expansion, and hence fully or partially compensating for the sintering-induced shrinkage. Starting materials include Al–Si alloy (80:20), Si metal, α -Al₂O₃ and mullite precursor powders. Due to the variety of starting compounds with different reaction and sintering kinetics, composite fabrication becomes a complex process. Differential scanning calorimetry (DSC) measurements, scanning electron microscopy (SEM) observations, and X-ray diffractometry (XRD) data show that effective milling of metal powder leads to a high degree of mullite formation (\approx 84%) at temperatures as low as 1500°C, although densification of the ceramic compacts remains rather low (\approx 45% of theoretical density).

Single crystal α -Al₂O₃ monofilaments were used to reinforce the reaction-bonded mullite (RBM) matrix. Although no intense reaction between the matrix and the fibres was observed at process temperature, strong bonding develops between uncoated fibres and the matrix. In order to produce a weaker fibre–matrix interface, which is necessary for improvement of the damage tolerance, the fibres were coated with ZrO₂ by means of high frequency sputtering. Microstructural observations of the fibre surfaces before and after the reaction-bonding process indicate that thick coatings (>10 μ m) produce very weak bonding, insufficient for matrix–fibre load transfer due to shrinkage of the low density ZrO₂ layers. Thinner layers (1 μ m) produce a better interfacial relation with suitable pull-out of fibres.

1 Introduction

Mullite is an excellent candidate for ceramic components requiring high temperature oxidation resistance.^{1,2} However, due to the low strength and fracture toughness of mullite, continuous-fibre reinforcement is required if the material should be damage tolerant under cycling temperature conditions.

Fabrication of ceramic composites with continuous fibres is a complicated process, since volume shrinkage of the matrix during processing can give rise to fibre damage. Reaction bonding of metal powders has been suggested to be a suitable method to acquire near net-shape production of ceramics. Reaction-bonded silicon nitride (RBSN) and aluminium oxide (RBAO) are the best known examples of such materials, in which sintering-induced shrinkage is at least partially compensated by nitridation or oxidation yielding volume expansion of the starting metals and alloys.^{3,4} Recently, some studies were devoted to fabricating mullite ceramics with this method (reaction bonded mullite; RBM), using Al–Si alloys or Al and Si metal and SiC powders as starting compounds.^{3,4,7}

The aim of the present study was to produce continuous-fibre reinforced mullite matrix composites with long-term oxidation resistance, good high-temperature stability (\geq 1250°C), good thermal shock behaviour, and low creep rate. As a matrix, mullite meets these requirements. One possible way to increase the damage tolerance of the brittle mullite matrix is to use polymer-derived oxide-based fibres. However, most of the commercially available fibres are stable only up to 1250°C for long-term and up to 1400°C for short-term use.⁵ Another approach to solve this problem is to use single crystal fibres. The present paper presents preliminary results on the fabrication of α -Al₂O₃ single crystal monofilament-reinforced mullite composites, making use of a modified reaction-bonding technique.

2 Materials and Experimental Methods

2.1 Processing of composites

2.1.1 Starting materials

Starting materials for mullite reaction bonding were Al–Si (80:20) alloy (24 wt%), mullite precursor (60 wt%), α -Al₂O₃ (14 wt%) and Si metal powders (2 wt%). The laboratory produced (nitrogen-atomized) Al–Si metal powder (Toyal, Osaka, Japan) had a particle size of $d_{av} = 60 \mu\text{m}$. To decrease the mullitization temperature of the system, a commercial mullite precursor produced from colloidal starting materials (Siral, Condea Chemie, Hamburg, Germany) was added. The as-received precursor was a nanometre-sized powder. It was calcined at 400°C in order to burn out the organic species and thereby reduce weight loss during composite processing. α -Al₂O₃ was a sub-micrometre-sized powder (99.995% Al₂O₃, AKP-50, Sumitomo, Tokyo, Japan), while the Si powder had an average particle size of 3 μm (Starck, Goslar, Germany).

For reinforcement of the composite, commercial single crystal corundum (α -Al₂O₃) continuous monofilaments ($d = 125 \mu\text{m}$), with the fibre axis being parallel to the crystallographic c -axis of α -Al₂O₃, were used (Saphikon, Milford, USA).

2.1.2 Coating of fibres

Fibres were coated with ZrO₂. Coatings were produced in argon atmosphere at about 150°C by using commercial ZrO₂ (+ 3% HfO₂) targets in a high frequency sputtering equipment (Balzers, Lichtenstein, Germany). For the coating procedure fibres were mounted between metal grids and were rotated (50 rev min⁻¹). Two types of coating experiment were carried out on the α -Al₂O₃ fibres, one having a duration of 15 min and the other a duration of 4 h. After a coating time of 15 min, the layer thickness was about 1 μm ; it reached about 12–15 μm after 4 h of sputtering.

2.1.3 Composite fabrication

The principles of mullite matrix development and composite fabrication are given in Fig. 1. Mullite precursor, α -Al₂O₃ and Si metal powders were mixed with organic pressing aids in alcohol and wet-milled overnight. The Al–Si alloy powder was milled separately according to three different schedules in order to achieve a high degree of oxidation of the Al–Si metal powder at low temperature during reaction bonding:

- wet-planetary milling of the Al–Si alloy powder together with the other reactants;
- separate dry ball-milling of the Al–Si alloy

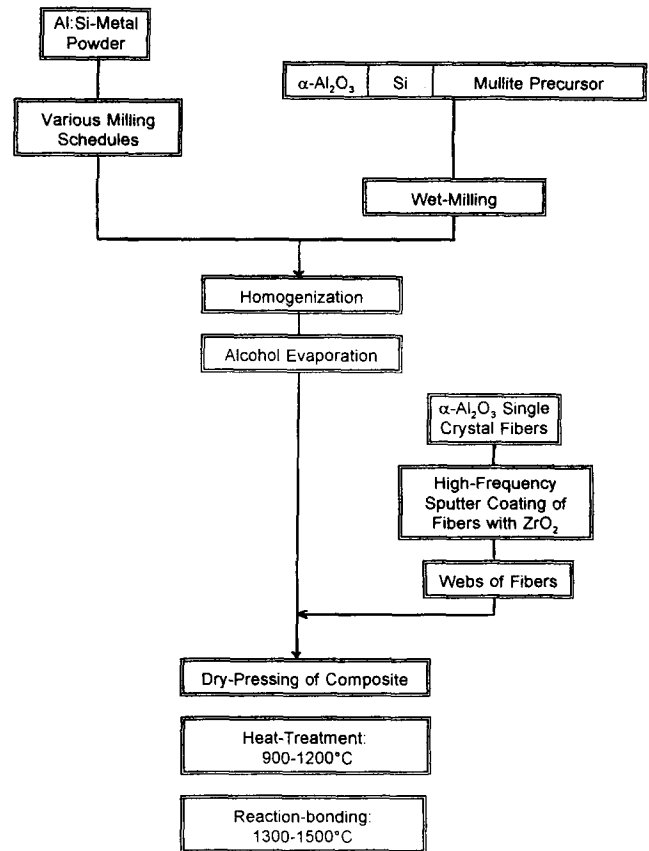


Fig. 1. Processing flow chart of reaction-bonded mullite matrix composites.

powder, prior to mixing with the other reactants. To avoid the danger of flaming, the alloy powder was previously calcined in air at 350°C;

- dry ball-milling of the calcined Al–Si alloy powder as described above but after an attrition milling step in alcohol.

After homogenization of the powder mixtures, alcohol was evaporated in each case by a rotary evaporator. Fibres were arranged in webs by using a fixture which consisted of fine grooves of 100 μm . The fibre webs were fixed with glue at the fibre ends. Composite samples were prepared by uniaxial pressing of the fibre webs, which had been filled with the powder mixtures.

Composite powder compacts were heat-treated (300°C h⁻¹) at 900 and 1200°C for 5 h to promote volume oxidation of Al and Si particles. Reaction-bonding was performed at 1500°C (60°C h⁻¹) for 1 h.

2.2 Characterization methods

2.2.1 X-ray diffractometry (XRD)

X-ray powder diffraction studies were carried out at room temperature with a computer-controlled Siemens D5000 powder diffractometer using Cu K_{α} radiation. Diffraction patterns were recorded in the 2θ range of 10 to 80°, in a step scan mode (3 s / 0.02°, 2θ).

2.2.2 Differential scanning calorimetry (DSC)

DSC data were collected by a computer-controlled Netsch DSC 404 equipment with respect to a sapphire reference material considering baseline corrections of the DSC curves. Measurements were carried out in air up to 1400°C, with a heating rate of 10°C min⁻¹.

2.2.3 Microstructural investigations

Microstructural investigations were performed with a Philips 525M scanning electron microscope (SEM) on fracture surfaces of uncoated and ZrO₂-coated α -Al₂O₃ fibres and composites.

3 Results and Discussion

The investigation on the fabrication of α -Al₂O₃ single crystal monofilament-reinforced mullite composites was focused on two main activities: (i) development of the reaction-bonded mullite matrix and (ii) coating of α -Al₂O₃ single crystal monofilaments and subsequent fabrication of composites.

3.1 Development of the reaction-bonded mullite matrix

The main aims of matrix development were to achieve near net-shape production, low Al-Si alloy oxidation and low mullitization temperatures, homogeneous microstructures, and suitable densities. Near net-shape production requires compensation of the sintering-induced shrinkage of the green body by volume expansion of the starting metal powder caused by oxidation of the alloy and subsequent reaction of Al₂O₃ and SiO₂ to mullite.

The present study used an Al-Si metal alloy with an Al:Si ratio of 80:20, which is near to that of mullite (75:25). DSC measurements showed that the as-received Al-Si alloy powder melts at 584°C, whereas surface oxidation of particles starts immediately after melting and reaches to maximum at about 620°C. The sudden oxidation

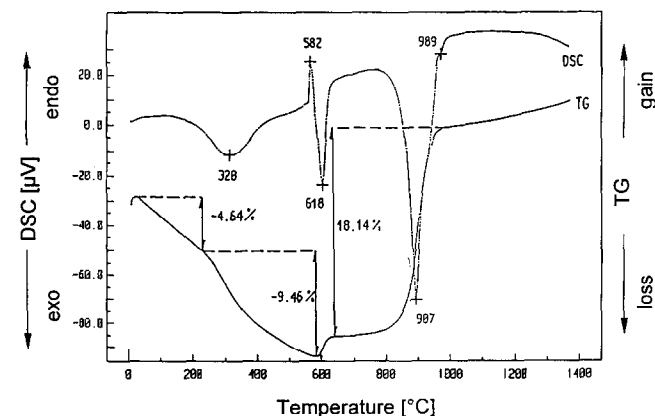


Fig. 2. DSC measurement and thermal gravimetry analysis (TGA) on powder wet-milled in air up to 1400°C (10°C min⁻¹) mixtures.

results in the formation of an oxide layer which slows down further oxidation of the Al-Si alloy particles. Volume oxidation of the Al-Si alloy takes place at about 900°C (Fig. 2). Si oxidizes in turn above 1200°C.⁴

Microstructural observations show that the melting of Al-Si alloy particles prior to oxidation is highly unfavourable, since this produces large, channel-like pores. We believe that the initial exothermal surface oxidation primarily forms a shell structure around the Al-Si alloy particles and consequently causes local temperature increase and melting of the Al-Si alloy left in the core. The melt diffuses out of the oxidized shell through grain boundaries and microcracks and wets the other existing particles, causing large voids in the shell centres. This may be prevented by achievement of complete oxidation of Al-Si particles prior to melting. Literature data report that this is possible if very fine ($\leq 1 \mu\text{m}$) metal powders are used.⁷ Furthermore, addition of α -Al₂O₃ enhances oxidation of metal powders probably due to an increased oxygen partial pressure provided by alumina.³

DSC and XRD investigations showed that the milling procedure of the Al-Si alloy powders has a significant influence on the oxidation behaviour and on reaction processes. According to DSC measurements, wet-milling of the metal powder together with the other reactants has no significant effect on the oxidation behaviour (Fig. 2). Dry-milling of the precalcined metal powders prior to mixing with the other reactants results in an increase of particle surface area. In this case, the rates of surface and volume oxidation are similar (Fig. 3). Surface oxidation becomes more significant if metal powder is attrition-milled. Thereby, the melting and oxidation temperatures of the alloy have also been reduced to 578°C and 600°C, respectively (Fig. 3).

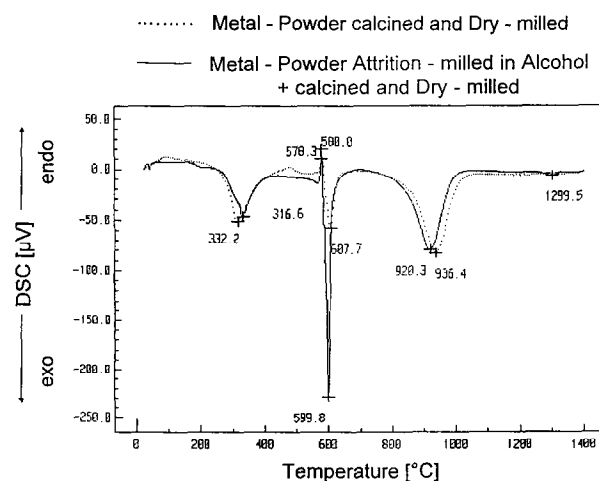


Fig. 3. DSC measurement on metal alloy, ceramic, precursor powder mixtures in air up to 1400°C (10°C min⁻¹), after dry-planetary and attrition-milling of metal powders.

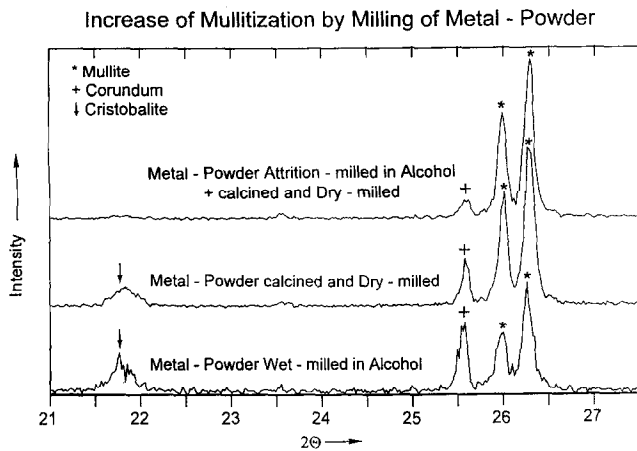


Fig. 4. XRD traces of metal alloy, ceramic and precursor powder compacts after various milling schedules and reaction-bonding processes at 1500°C.

XRD data show that the milling of Al-Si alloy powders greatly affects the rate of mullitization. Best results were obtained by attrition-milled metal powders (Fig. 4). Powder compacts, prepared by attrition-milling and subsequent reaction bonding at 1500°C, contain high mullite (84%) and low corundum (16%) contents. Dry- and wet-milled powders have lower mullite-to-corundum ratios and contain same cristobalite (Fig. 4).

Non-crystalline mullite precursors, transforming to mullite at temperatures above about 1200°C, were added to the starting powders. These low temperature-produced mullite crystals may act as nuclei for reaction-bonding induced mullitization, thus increasing the mullite formation rate at a given temperature with respect to samples without precursor addition in the starting material. Precursor additions to the green bodies also have a strong influence on the volume stability during processing. Precursor additions of 40 wt% led to a slight total volume expansion of the sintered samples (2–15 vol%). Precursor additions of > 60 wt% produce volume shrinkages (~10–16 vol%). In order to achieve a near-zero volume shrinkage, precursor contents between 45 and 55 wt% may be considered. The experiments also showed that the processing temperature of the RBM compacts can be reduced by more than 100°C, by addition of ~40 wt% mullite precursor. This may be an essential point, if polycrystalline fibres are used for the reinforcement instead of α -Al₂O₃ single crystal fibres, since the former are unstable at processing temperatures \geq 1300°C.

3.2 Coating of α -Al₂O₃ single crystal fibres and fabrication of composites

Preliminary experiments were carried out to identify the fibre stability, during processing, and to develop suitable fibre coatings. Fibre coatings are essential to produce the necessary fibre-matrix

interaction which on the one hand enables load transfer from the matrix to the fibre, and on the other gives rise to energy-consuming crack deflection and pull-out effects. Frequently used coating materials are SiC, C or graphite-type BN, which may initiate favourable fibre debonding by sliding processes parallel to the respective {001} crystallographic planes.⁸ However, due to poor oxidation resistance, these coatings are not suitable for long-term use in oxidizing atmospheres.

In this study α -Al₂O₃ fibres were coated with ZrO₂ by using high frequency sputtering technique. After 4 h of high frequency sputtering, the thickness of the ZrO₂ layers on the fibres was ~12–15 μ m. The layers exhibit columnar microstructure with ZrO₂ growing perpendicular to the fibre surface (Fig. 5). Between individual ZrO₂ columns small pore-like channels occur. The webs of coated fibres were compacted with matrix powder mixture and die-pressed prior to reaction bonding at 1500°C. After processing the thickness of ZrO₂ layers was reduced to 7 to 8 μ m, due to sintering of the low density ZrO₂ coatings. This

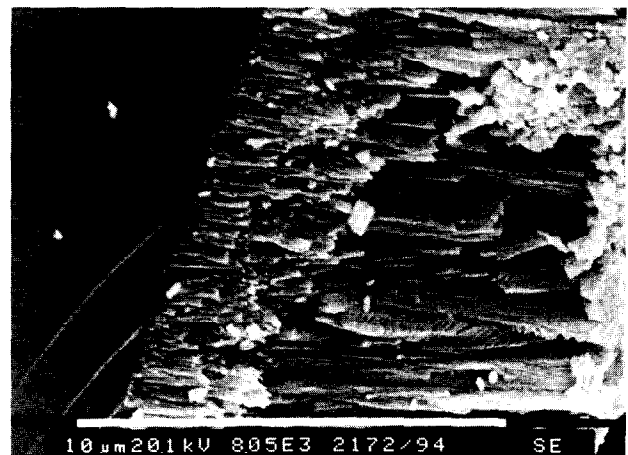


Fig. 5. High frequency sputtered ZrO₂ layer (4 h) on single crystal α -Al₂O₃ fibres, before reaction bonding.



Fig. 6. High frequency sputtered ZrO₂ layer (4 h) on single crystal α -Al₂O₃ fibre, after reaction bonding at 1500°C.

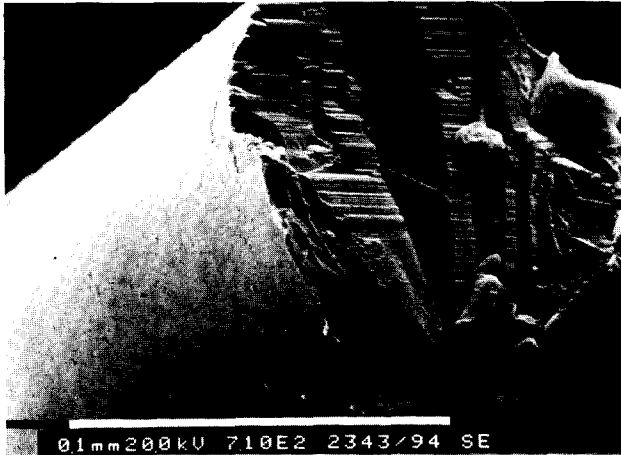


Fig. 7. High frequency sputtered ZrO₂ layer (15 min) on single crystal α -Al₂O₃ fibre, before reaction-bonding process.

effect is reinforced by the strong thermal contraction of ZrO₂ (higher expansion coefficient), caused by cooling down the composite from processing to room temperature (Fig. 6). Thereby, gaps up to 5 μ m wide are formed between the fibres and matrix, producing low or even insufficient interfacial fibre–matrix bonding at room temperature.

Short time high frequency sputtering experiments (15 min) deposit thin ZrO₂ layers (\approx 1 μ m) on the α -Al₂O₃ fibres (Fig. 7). The interfacial gaps produced by shrinkage of the ZrO₂ coating after processing in this case are almost negligible. In spite of the very thin ZrO₂ layers on the fibres, no reaction between the fibres and the matrix has been observed.

Our preliminary study on the fabrication of the ZrO₂-coated α -Al₂O₃ single crystal monofilament-reinforced mullite composite stresses its potential as a high temperature oxidation resistant, damage tolerant material. However, further intensive work

is needed in order to improve RBM matrices, fibre coatings and related fibre–matrix interactions, and the fabrication of composites. These investigations should include a careful mechanical characterization of the composites, extending to strength measurements, damage tolerance studies and fibre push-out tests at room temperature and at high temperatures.

Acknowledgements

The authors gratefully thank Ms G. Paul for DSC measurements and Mr H. Gedanitz for high frequency sputtering of fibres.

References

1. Aksay, A., Dabbs, D. M. & Sarikaya, M., Mullite for structural, electronic and optical applications. *J. Am. Ceram. Soc.*, **75**(10) (1991) 2343–58.
2. Schneider, H., Okada, K. & Pask, J. A., *Mullite and Mullite Ceramics*, John Wiley and Sons, Chichester, 1994.
3. Wu, S. & Claussen, N., Fabrication and properties of low-shrinkage reaction-bonded mullite. *J. Am. Ceram. Soc.*, **74** (1991) 2460–3.
4. Brandt, J. & Lundberg, R., Synthesis of mullite materials by oxidation of metal alloy powder compacts. *Third Euro Ceramics, Vol. 1*, eds P. Durán & J. F. Fernández, Faenza Editrice Ibérica S.L., 1993, pp. 169–76.
5. Schmücker, M., Flucht, F. & Schneider, H., High temperature behaviour of polycrystalline aluminium silicate fibres with mullite bulk composition. I. Microstructure and strength properties. *J. Eur. Ceram. Soc.*, **16** (1996) 281–5.
6. Schneider, H., Saruhan, B., Voll, D., Merwin, L. & Sebal, A., Mullite precursor phases. *J. Eur. Ceram. Soc.*, **11** (1993) 87–94.
7. Claussen, N., Private communication.
8. Ha, J.-S., Chawla, K. K. & Engdahl, R. E., Effect of processing and fibre coating on fibre–matrix interaction in mullite fibre–mullite matrix composites. *Mater. Sci. Eng.*, **A161** (1993) 303–8.

Effects of Composition and Atmosphere on Reactive Metal Penetration of Aluminium in Mullite

Eduardo Saiz,^a Antoni P. Tomsia,^a Ronald E. Loehman^b & Kevin Ewsuk^b

^aCenter for Advanced Materials, Lawrence Berkeley Laboratory, Berkeley, CA, USA

^bSandia National Laboratories, Albuquerque, NM, USA

(Accepted 22 July 1995)

Abstract

Ceramic–metal composites can be made by reactive penetration of dense ceramic preforms by molten Al. Molten Al will reduce mullite to produce a composite of Al₂O₃, Si and Al. The reaction can be written as $3Al_6Si_2O_{13} + (8 + x)Al \rightarrow 13Al_2O_3 + Al_xSi_y + (6 - y)Si$. The penetration is driven by the strongly negative Gibbs free energy for reaction. In order to assess the influence of atmosphere and temperature in the penetration process, reaction couples of molten Al on mullite were heated at temperatures from 950 to 1150°C, and at $p(O_2)$ from $\sim 10^{-10}$ to $\sim 10^{-20}$ atm. In this range $p(O_2)$ has little influence on reaction kinetics; the reaction rate is controlled by the rate of Si diffusion out of the preform to the external Al source.

Introduction

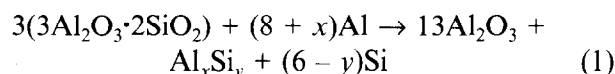
The development of ceramic/metal composites offers an opportunity to produce ceramics with significantly improved properties. Advanced ceramic composites are potential structural materials with improved strength, stiffness and toughness, and thus are more resistant to failure.^{1,2}

Techniques for making ceramic/metal composites by reactive synthesis have been under development for a number of years. Processes that involve a gas-phase reactant include chemical vapour infiltration (CVI), gas-phase reaction bonding and the direct oxidation of molten metal.^{3,4} Reactive processing of condensed phases to make composites include infiltration of reactive liquids into porous preforms, self-propagating high temperature synthesis (SHS) and *in situ* displacement reactions.^{3–5}

Recently, several research groups have reported techniques for making ceramic/metal composites by reaction between molten metals and dense glass or ceramic preforms.^{6–8} In these techniques, a dense oxide preform is converted to a composite

as an oxidation–reduction reaction front moves into the preform. For example, reaction synthesis of composites in the SiO₂/Al system has recently been reported by Matsuo and Inabe⁶ and by Breslin *et al.*^{7,8} Matsuo and Inabe⁶ made Al₂O₃/Al/Si composite bodies by reacting amorphous silica and molten aluminum at 900–1000°C. The reaction product was a mutually interpenetrating structure of ~70 wt% alumina and ~25 wt% Al with reported improvements on bend strength and other physical properties. Breslin *et al.*^{7,8} also reacted amorphous silica with molten aluminium to give similar composites.

In contrast to the work just cited, the ceramic–metal composites discussed in this paper are synthesized from dense ceramic preforms rather than from amorphous silica. Al reacts and penetrates dense ceramic mullite preforms according to the reaction:



The reaction product has the form of an interpenetrating diphasic composite of alumina and an Al/Si alloy (Fig. 1). The reactive metal penetration technique has the advantage of producing complex ceramic parts with near net-shape and very low porosity. It appears that the mechanism for reactive penetration of polycrystalline ceramics such as mullite^{9,10} is completely different from that for the glass preforms described above.^{6–8} Thus the method discussed in this paper can be expected to have its own specific advantages for synthesis of ceramic/metal composites.

If reactive metal penetration is to be a commercially useful way of composite fabrication, it must be economical, reliable and designed to produce the adequate microstructures that will optimize critical properties. The main objective of this work was to study the processing variables that affect Al wetting and reaction with mullite substrates, with particular emphasis on the effects of temperature and $p(O_2)$.

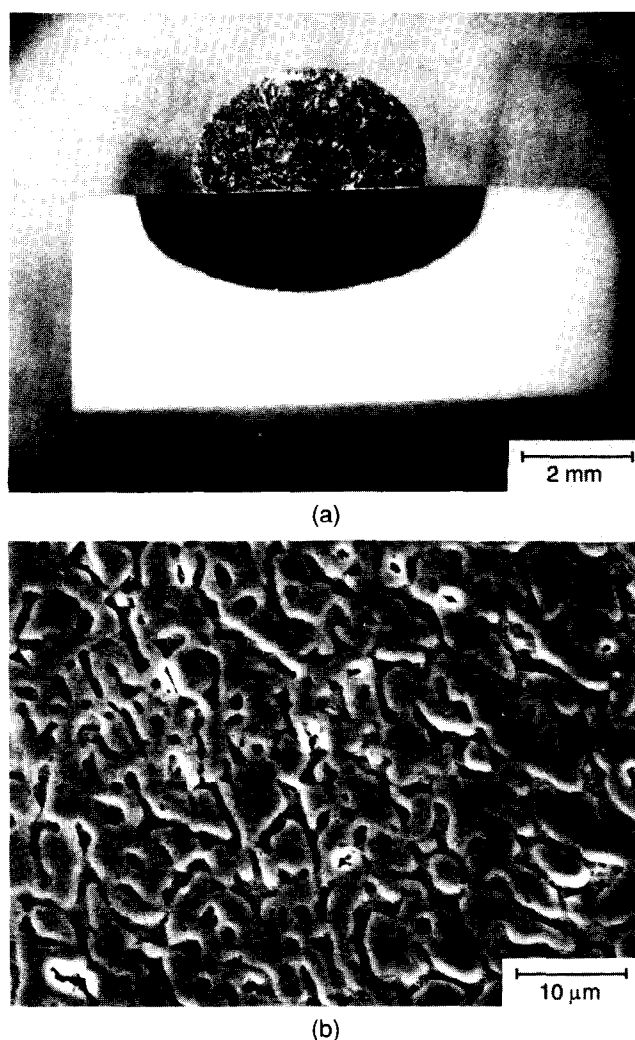


Fig. 1. (a) Al drop on mullite substrate after reaction for 60 min at 1100°C. The reaction zone under the Al drop is a composite of Al and Al_2O_3 . (b) Micrograph of the composite reaction zone showing the interpenetrating Al/ Al_2O_3 microstructure.

Experimental

Mullite substrates for the wetting and infiltration experiments were made using Chichibu MP40 mullite powder (Scimarec Co., Ltd., Tokyo, Japan). Mullite ceramic pellets were formed by cold isostatic pressing at ~ 200 MPa and sintering in vacuum ($\sim 6.7 \times 10^{-4}$ Pa) at 1600–1650°C for 2 h. The final compacts (~ 200 g) had a density $\rho \geq 95\%$ theoretical. Mullite substrates ($\sim 2 \times 2 \times 0.5$ mm) were cut using a diamond saw and were subsequently surface finished using a 800 grit resin-bonded diamond wheel.

Contact angle measurements of molten Al on mullite were made by placing Al cylinders (0.2–0.3 g) on the substrates, and the assemblies were heated in 30 min to the test temperature (950–1150°C) in a furnace with a tubular metal resistance heating element. The contact angle was monitored through a porthole in the furnace and recorded as a function of time using a telegoniometer. The tempera-

ture was recorded with a calibrated Pt–Pt10Rh thermocouple. After the test, the sample was cooled in 10 min to 900°C and in 300 min from 900°C to room temperature. Al/Si alloys for wetting studies were made *in situ* by placing Si chips over the Al cylinders.

The tests were performed in two kinds of atmospheres.

- (a) High $p(\text{O}_2)$: Ar (99.998%) flow (0.5 l min^{-1}) with a Pt tube resistance heating element, $p(\text{O}_2) \sim 10^{-10}$ atm.
- (b) Low $p(\text{O}_2)$: Ar (99.998%) gettered with Ti/Zr chips at 900°C, flowing (0.5 l min^{-1}) with a Ta tube resistance heating element lined inside with Zr foil, $p(\text{O}_2) \sim 10^{-20}$ atm.

In both cases the $p(\text{Ar})$ was kept slightly higher than 1 atm.

After the tests, the samples were mounted in an epoxy resin and cut perpendicular to the metal/ceramic interface. The cross-sections were then polished to $1/4 \mu\text{m}$ diamond finish. The thickness and volume of the reaction layer and its microstructure were measured using reflected light optical microscopy (RLOM) and scanning electron microscopy (SEM). Elemental analysis and X-ray mapping were performed both by energy dispersive (EDS) and wavelength dispersive (WDS) methods.

Results and Discussion

Figure 2 shows the contact angles and reaction layer thicknesses vs. time for wetting experiments carried out at 1100°C, for times up to 150 min in both high and low $p(\text{O}_2)$ atmospheres. In the high $p(\text{O}_2)$ atmosphere ($\sim 10^{-10}$ atm) a thick oxide layer developed on the surface of the Al drop, making the contact angle measurement unreliable. In low $p(\text{O}_2)$ ($\sim 10^{-20}$ atm) the drop surface was shinier and measurements were reproducible. Even after 150 min an equilibrium contact angle was not reached. Despite the differences in contact angles, the microstructures and thicknesses of the reaction layers were practically the same for both atmospheres. The microstructure is that of an Al_2O_3 –Al/Si (alloy) composite. The reaction layer thickness did not follow a $t^{1/2}$ law as would be expected for a diffusion driven process (Fig. 2).

Contact angle measurements carried out for 60 min at temperatures ranging from 950 to 1150°C in low $p(\text{O}_2)$, Fig. 3, show an equilibrium contact angle value of 140° at 950°C. At 1000°C there is a sudden decrease, from $\sim 140^\circ$ to $\sim 110^\circ$, after 25–30 min. For higher temperatures the contact angle decreases with time to values down to $\sim 90^\circ$. Measurements of the reaction layer thickness after

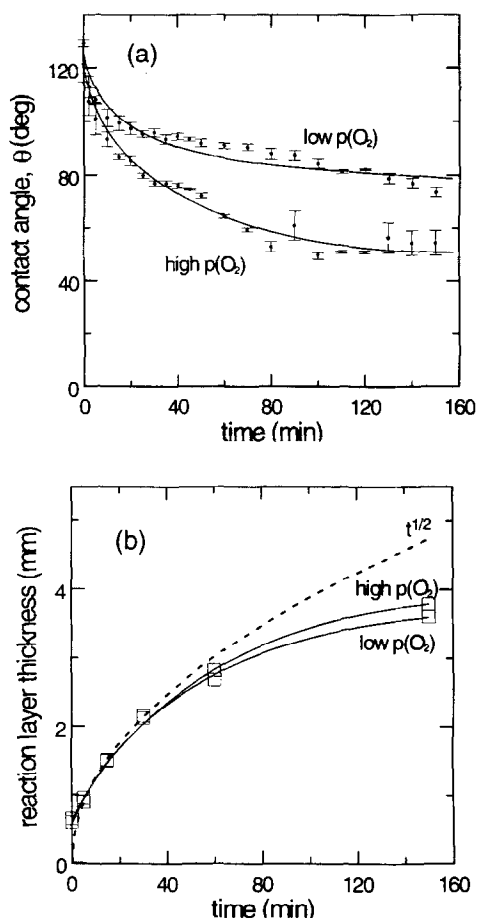


Fig. 2. (a) Contact angle vs. time for aluminium on mullite in different atmospheres ($T = 1100^\circ\text{C}$). (b) Reaction layer thickness vs. time after the wetting experiments ($T = 1100^\circ\text{C}$).

the experiments show a maximum around 1100°C (Fig. 3).

Si mapping and EDS analysis in the reaction layer revealed a lower Si content than that corresponding to the original mullite substrate (Fig. 4). This decrease is due to Al–Si interdiffusion during the test. Large silicon crystals can be observed in the drop (darker crystals in Fig. 5) and metallic Al/Si alloy in the reaction layer after the experiment. There is a small gradient in the Si content in the reaction layer, reaching a maximum at the interface between reaction layer and mullite. The Si content at that interface increases with time at the reaction temperature (Fig. 4).

Wetting experiments between pure Al and mullite were also performed using larger Al drops. In Fig. 6 it can be observed that when the test is done using a 1.43 g drop the contact angle is larger than the one corresponding to the small drops (0.2–0.3 g), and the reaction layer is thicker with the larger Al drop. The thicknesses corresponding to reactions for 0, 5 and 15 min with the small drop and 150 min with the big one fit to a $t^{1/2}$ law.

In order to further assess the role of Al–Si interdiffusion and Si dissolution into Al, a wetting

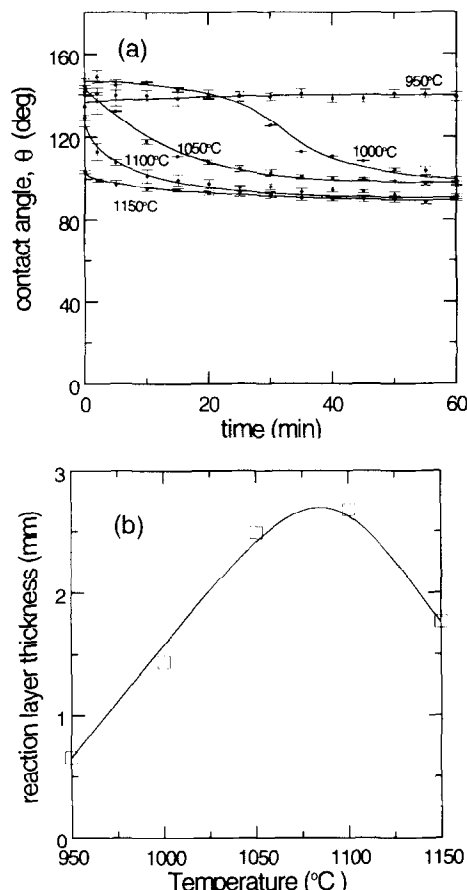


Fig. 3. (a) Contact angle vs. time at different temperatures for Al on mullite at low $p(O_2)$. (b) Reaction layer thickness after wetting experiments at different temperatures in a low $p(O_2)$ atmosphere.

experiment was carried out at 1100°C in a low $p(O_2)$ atmosphere using a Al/Si (40/60 wt%) liquid alloy already saturated with silicon at the test temperature (saturation value at 1100°C is 56 wt% Si¹¹). The contact angle of the Al/Si alloy reached an equilibrium value of 55° (Fig. 6) and the corresponding reaction layer thickness is $180\ \mu\text{m}$ (~ 20 times smaller than for pure Al).

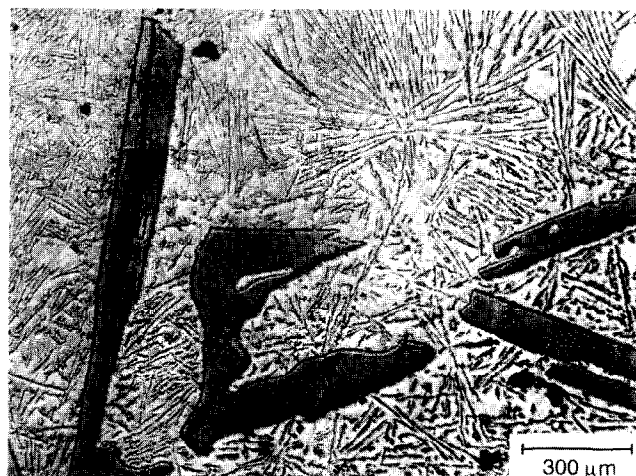


Fig. 4. Micrograph of Al drop after reacting with mullite substrate for 60 min at 1100°C . The needle-like crystals are from Si that diffuses into the molten Al drop during reaction.

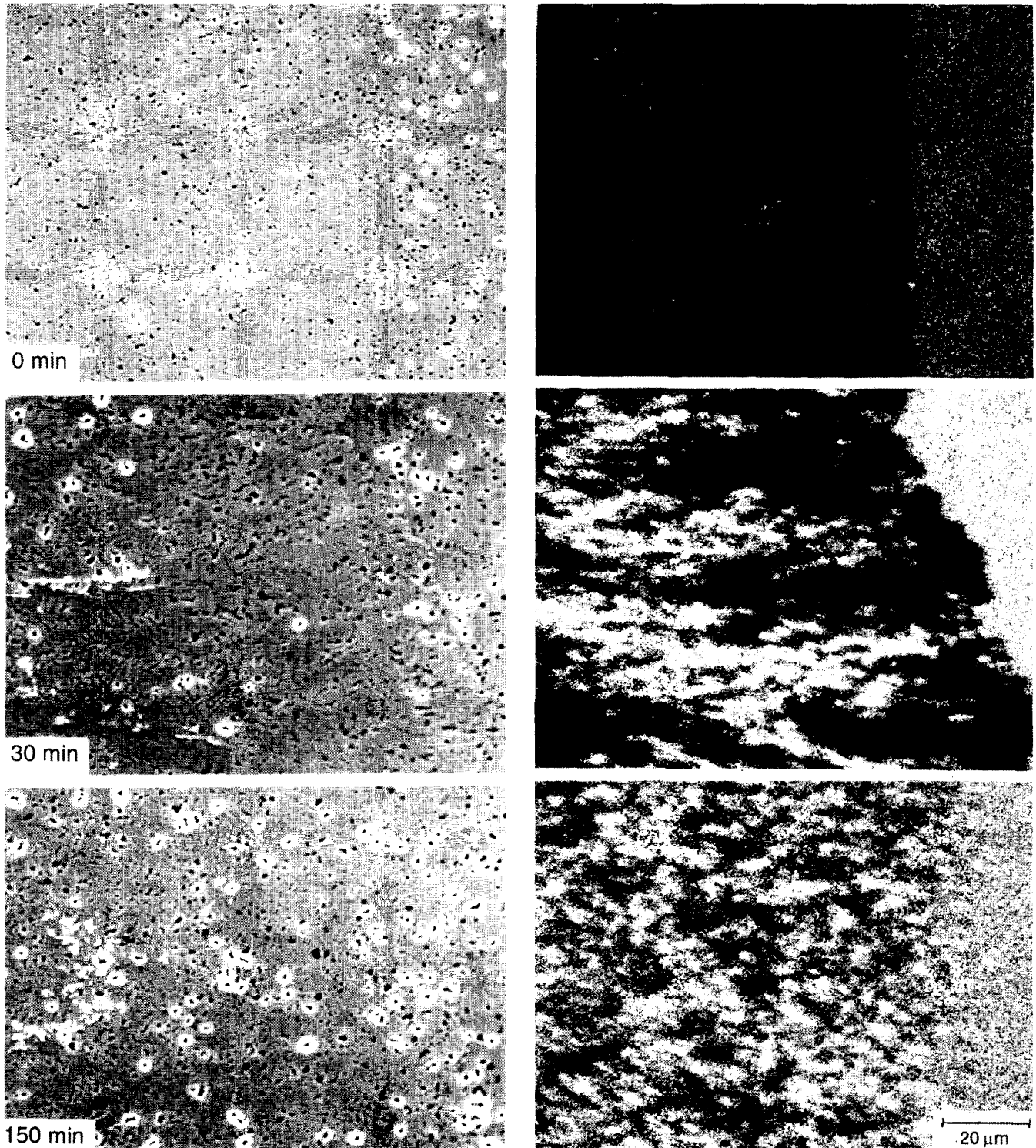


Fig. 5. Micrographs of interface between Al/Al₂O₃ composite and unreacted mullite after 0, 30 and 150 min at 1100°C. The right-hand photos are X-ray compositional maps of Si.

Table 1. Free energy values corresponding to Eqns (3) and (5), y (wt%) value corresponds to Si saturation at each temperature, ΔG_2 is calculated taking $N = 6/y$ (Refs 13 and 14).

Temperature (°C)	ΔG_1 (kJ)	y (Si solubility in Al) ¹¹	ΔG_2 (kJ)	ΔG_R (kJ)
950	-952	0.42	-46	-998
1000	-933	0.46	-44	-977
1050	-914	0.52	-39	-953
1100	-895	0.56	-35	-930
1150	-876	0.62	-29	-905

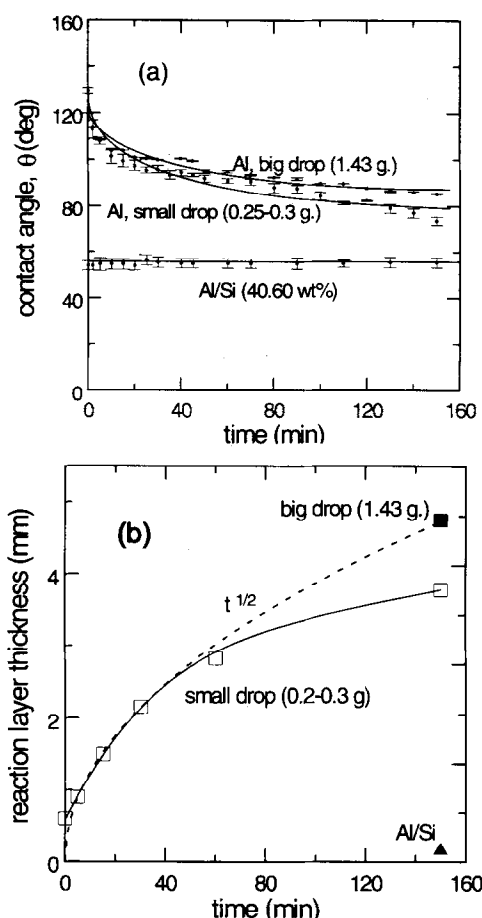
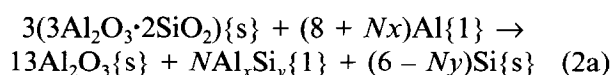


Fig. 6. (a) Contact angle vs. time for different sizes of Al drop and Al/Si alloy on mullite. (b) Corresponding reaction layer thicknesses.

As has been reported by Brennan and Pask,¹² under most conditions there is always an Al_2O_3 layer present on the surface of aluminium. Those authors report that temperatures higher than 950–1000°C are necessary to break that layer and expose fresh Al to the furnace atmosphere. This effect could explain the invariant contact angle of Al on mullite at 950°C in low $p(\text{O}_2)$, see Fig. 3. The sudden decrease in contact angle at 1000°C is probably related to the breakup of this alumina layer.

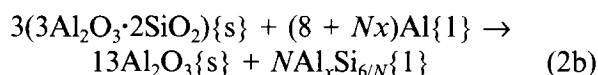
At $T \leq 1000^\circ\text{C}$ the presence of an Al_2O_3 passivating layer on the metal drop surface inhibits the contact of fresh Al and the mullite substrate, consequently reduced reaction rates are observed (Fig. 3). At $T > 1000^\circ\text{C}$, and once the passivating layer breaks, fresh Al is in contact with the ceramic; the reaction front seems isolated from the furnace atmosphere and reaction kinetics together with reaction layer microstructure and composition do not depend on $p(\text{O}_2)$ (Figs 3 and 4).

At the test temperature, the net reaction (1) between mullite and Al can be rewritten to show the effect of the starting amount of Al on Si precipitation:



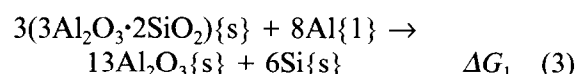
where $x + y = 1$ and where y , the solubility of Si in Al, depends on temperature. Nx represents the excess of Al with respect to the amount necessary for mullite reduction.

With an excess of Al (no Si precipitates, $N > 6/y$):

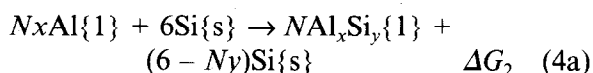


ΔG_R , the change in free energy corresponding to the reactions (2a) and (2b), must be negative in order for the reactions to proceed as written.

The reactions (2a) and (2b) are made up of two partial reactions, Eqns (3) and (4a), (4b):



The second partial reaction can be written in two ways, depending on whether the Si concentration is high enough to give precipitates. For $N \leq 6/y$ [Eqn (2a)], Si precipitates:



For $N > 6/y$ [Eqn (2b)], no Si precipitates:



Then, depending on whether the concentration of Si exceeds the solubility limit at the processing temperature or not:

$$\Delta G_R = \Delta G_1 + \Delta G_2 \quad \text{or} \quad \Delta G_R = \Delta G_1 + \Delta G_3 \quad (5)$$

Table 1 shows some of the ΔG_R , ΔG_1 , ΔG_2 and y values at different temperatures. It can be seen that the contribution of Si dissolution to the total free energy of the reaction is relatively low.

The corresponding change in the volume of solids at the test temperature is:

$$\% \Delta V = [13V_{\text{Al}_2\text{O}_3} + (6 - Ny)V_{\text{Si}} - 3V_{3\text{Al}_2\text{O}_3 \cdot 2\text{SiO}_2}] \times 100 / 3V_{3\text{Al}_2\text{O}_3 \cdot 2\text{SiO}_2} \quad (6)$$

where $V_{\text{Al}_2\text{O}_3}$ ($25.7 \text{ cm}^3 \text{ mol}^{-1}$), V_{Si} ($12.1 \text{ cm}^3 \text{ mol}^{-1}$) and $V_{3\text{Al}_2\text{O}_3 \cdot 2\text{SiO}_2}$ ($135 \text{ cm}^3 \text{ mol}^{-1}$) are correspondingly the molar volumes of alumina, silicon and mullite. If the liquid does not dissolve any of the Si that originates from the mullite reduction, $y = 0$ and $\% \Delta V \approx 0$, Al and mullite must then react by solid-state diffusion through an $\text{Al}_2\text{O}_3/\text{Si}$ layer. On the other hand, if there is a Si dissolution, $y > 0$ and $\% \Delta V < 0$ ($\% \Delta V = -17\%$ for $y = 6/N$), space is created through which the Al/Si liquid can penetrate into the reaction front and the reaction can progress at a faster pace than the one corresponding to solid-state diffusion driven processes. When the experiment is performed using Al/Si alloy already saturated in Si, the liquid does not dissolve any silicon coming from mullite reduction; then, on one hand, there is a reduction in the total free energy of the reaction because the inverse of Eqn

(4a), for $N = 6/y$, takes place, while on the other hand, the liquid does not dissolve Si and does not create space to penetrate fast into the reaction front. These can explain the lower reaction rate observed for the Al saturated with Si at the test temperature (Fig. 6).

In the case of the small drop, the concentration of Si in the Al drop increases noticeably after 30–60 min, consequently the diffusion rate of Si decreases and so does the reaction rate. In the case of the large drop the Si concentration remains low and the diffusion rate of Si remains constant, consequently the reaction rate is higher and exhibits a $t^{1/2}$ law corresponding to a diffusion-driven process. The calculated diffusion coefficient, $D \approx 2 \times 10^{-5} \text{ cm}^2 \text{ s}^{-1}$, is in the order of diffusion coefficients observed in liquid metals.¹⁵

These results indicate that Si/Al interdiffusion is the kinetic limiting step for the reaction/penetration of molten Al into dense mullite ceramics.

It can also be observed that the contact angle does not decrease when the reaction layer thickness increases (the bigger drop has a bigger reaction layer). It seems that the decrease in contact angle as the reaction goes on is more related to the increase in Si concentration in the drop.

Conclusions

The results presented in this paper indicate that the kinetic limiting step for the reactive penetration of molten Al into dense mullite substrates is the diffusion of Si out of the composite. In the range of $p(\text{O}_2)$ studied the oxygen partial pressure does not affect appreciably either the penetration rate or the microstructure of the reaction layer.

These data suggest that processing conditions can be adjusted to make this a practical system for

the fabrication of metal/ceramic composites by reactive metal penetration.

Acknowledgements

This work was supported by the US DOE Office of Industrial Technologies and the US DOE under contract No. DE-AC04-94AL85000. E. Saiz wishes to acknowledge Fulbright Foundation and MEC (Spain) for financial support.

References

- Harrigan, W. C. Jr, in *Metal Matrix Composites Processing and Interfaces*, eds R. K. Everett & R. J. Arsenault, Academic Press, New York, 1991, Vol. 1.
- Ashby, M. F., *Acta Metall. Mater.*, **41**[5] (1993) 1313.
- Chiang, Y., Haggerty, J. S., Messner, R. P. & Demetry, C., *Ceram. Bull.*, **68**[2] (1989) 420.
- Claussen, N., *J. de Physique IV, Colloque C7*, **3** (1993) 1327.
- Hilling, W. B., *Ceram. Bull.*, **73**[4] (1994) 56.
- Matsuo, S. & Inabe, T., *Tokyo Ceramics*, (1991) 222.
- Breslin, M. C., Rignalda, J., Seeger, J., Marasco, A. L., Daehn, G. S. & Fraser, H. L., *Ceram. Eng. Sci. Proc.*, **15**[4] (1994) 104.
- Breslin, M. C., US Pat. No 5 214 011, 25 May 1993.
- Tomsia, A. P., Loehman, R. E. & Ewsuk, K., *J. Am. Ceram. Soc.*, submitted.
- Fahrenholtz, W. G., Ewsuk, K. G., Loehman, R. L. & Tomsia, A. P., in *In Situ Reactions for Synthesis of Composites, Ceramics and Intermetallics*, eds E. B. Berrera, F. D. S. Marquis, W. E. Frazier, S. G. Fishman, N. N. Thadhani & Z. A. Munir, The Minerals, Metals and Materials Society, Warrendale, PA, 1995.
- Binary Alloy Phase Diagrams*, ed. T. B. Massalski, ASM International, Metals Park, OH, 1990.
- Brennan, J. J. & Pask, J. A., *J. Am. Ceram. Soc.*, **51**[10] (1968) 569.
- Kubachevsky, O. & Alcock, C. B. (eds), *Principles of Metallurgical Thermodynamics, 5th Edn*, Pergamon Press, New York, 1979.
- HSC Chemistry for Windows, Outokumpu Research.
- Smithells, C. J. (ed.), *Metals Reference Book*, Butterworth & Co, London, 1976.

High Temperature Behaviour of Polycrystalline Aluminosilicate Fibres with Mullite Bulk Composition. I. Microstructure and Strength Properties

M. Schmücker, F. Flucht & H. Schneider

German Aerospace Research Establishment (DLR), Institute for Materials Research, D-51140 Köln, Germany

(Accepted 22 July 1995)

Abstract

Temperature-dependent microstructure/strength relations of commercial aluminosilicate fibres with near-stoichiometric mullite bulk composition are investigated.

As-received Nextel 440TM fibres (70 wt% Al₂O₃, 28 wt% SiO₂, 2 wt% B₂O₃), consisting of nanometre-sized γ -Al₂O₃ and a minor amount of amorphous phase, have tensile strength of 2100 MPa. Heat treatment at 1200°C causes transformation into fine-grained mullite (mean grain size: 80 nm). The remaining tensile strength is 1600 MPa. Heat treatment at higher temperatures leads to considerable reduction of strength (1100 MPa after firing at 1400°C) attributed to mullite grain coarsening (mean grain size at 1400°C: 135 nm).

Altex 2K fibres (72 wt% Al₂O₃, 28 wt% SiO₂) consist of single-phase mullite with a mean grain size of 115 nm. Tensile strength is comparatively low (1250 MPa). Annealing at 1000°C causes a significant increase in strength (1600 MPa). Above 1200°C mullite coarsening and strength reduction are similar to those of Nextel 440 fibres.

1 Introduction

Aluminosilicate fibres are used in a wide variety of high temperature applications, e.g. for thermocouple insulations, furnace seals and filter bags.¹ Another promising application of aluminosilicate fibres is the reinforcement of ceramic matrices in composites (see, for example, Ref. 2). Aluminosilicate fibres of mullite bulk composition may consist of non-crystalline precursor states, of nanocrystalline γ -Al₂O₃ plus SiO₂ phase assemblages or of microcrystalline mullite. Due to their phase compositions and/or small crystal sizes, the microstructures of these fibres are not stable thermodynamically: by heat treatment at sufficiently high temperature, phase transformations and grain

coarsening occur which in most cases are harmful for the mechanical properties of the fibres. Detailed knowledge of the temperature-dependent microstructures and strengths is therefore essential for the prediction of possible applications of the fibres in high temperature composites.

2 Experimental

2.1 Sample material

Two types of technical aluminosilicate fibres were investigated: Nextel 440TM (3M, St. Paul, MN, USA) with 70 wt% Al₂O₃, 28 wt% SiO₂, 2 wt% B₂O₃¹ and Altex 2K (Sumitomo Chemical Inc., Osaka, Japan) with 72 wt% Al₂O₃ and 28 wt% SiO₂. Nextel 440 fibres have elliptical cross-sections with 7 and 12 μ m diameters and consist of transition alumina (designated as γ -Al₂O₃ in the following) and silica-rich glassy phase. Sumitomo Altex 2K fibres have circular cross-sections with a mean diameter of 12 μ m, and consist of single-phase mullite. Both fibre materials were annealed in air in an induction heated laboratory furnace at 1000, 1100, 1150, 1200, 1300, 1400, 1500, 1600°C for 4 h in each case.

2.2 Single fibre tensile strength measurements

Room temperature strengths of the fibres annealed for 4 h at various temperatures were determined, based on at least 30 individual measurements in each case. Single fibres were glued on a paper bridging the centre of a circular hole (diameter \approx 5 mm). On both sides of the hole the paper was separated and bridged by a polymer fibre. The arrangement was installed in a tensile testing equipment with a load cell for very small loads. After fixing the holder the polymer fibres were melted and special care was taken that the test fibre was not damaged by this procedure. Tensile tests were performed under a constant crosshead speed of 0.2 mm min⁻¹. Actual tensile strength

values of fibres were then calculated considering individual fibre cross-sections measured by scanning electron microscopy. Elliptical cross-section areas of Nextel fibres were determined according to the procedure described by Fernando *et al.*³

2.3 Microstructural characterization of fibres

Due to the small grains occurring in all fibres, microstructures were examined by transmission electron microscopy (TEM, Philips EM 430) with an accelerating voltage of 300 kV. Electron transparent areas in long sections of the fibres were achieved by Ar-ion beam milling. Based on TEM photographs, grain area distributions of starting materials and of heat-treated fibres were calculated by means of a Synoptics-Semper 6 image processing system using at least 100 grain area values. Diameter distributions and mean grain sizes for each sample were calculated neglecting intersectional effects.

Information on the temperature-dependent phase compositions were obtained by X-ray powder diffractometry. Studies were carried out with a computer-controlled Siemens D 5000 powder diffractometer using Ni-filtered CuK_α radiation. Diffraction patterns were recorded in the 2θ range from 10 to 80°, in step scan mode.

3 Results

3.1 Tensile strengths of fibres

Tensile strengths of Nextel and Altex fibres as-received and heat-treated at 1000, 1200 and 1400°C are given in Table 1 and Fig.1. The tensile strength of Nextel fibres in the as-received state is >2 GPa. This value remains nearly constant up to 1000°C heat treatment. At higher annealing temperatures, however, the tensile strength decreases. Tensile strength of as-received Altex 2K fibres is significantly lower than that of Nextel 440 fibres. The strength of the Altex fibres annealed at 1000°C significantly increases with respect to the starting material, whereas the value of the 1200°C sample is similar to that of the as-received material. Distinct strength reduction is observed in Altex 2K fibres heat-treated at 1400°C. Above 1400°C, both fibres become so brittle that handling with regard to the testing facilities was not possible, which indicates drastic decrease in strength.

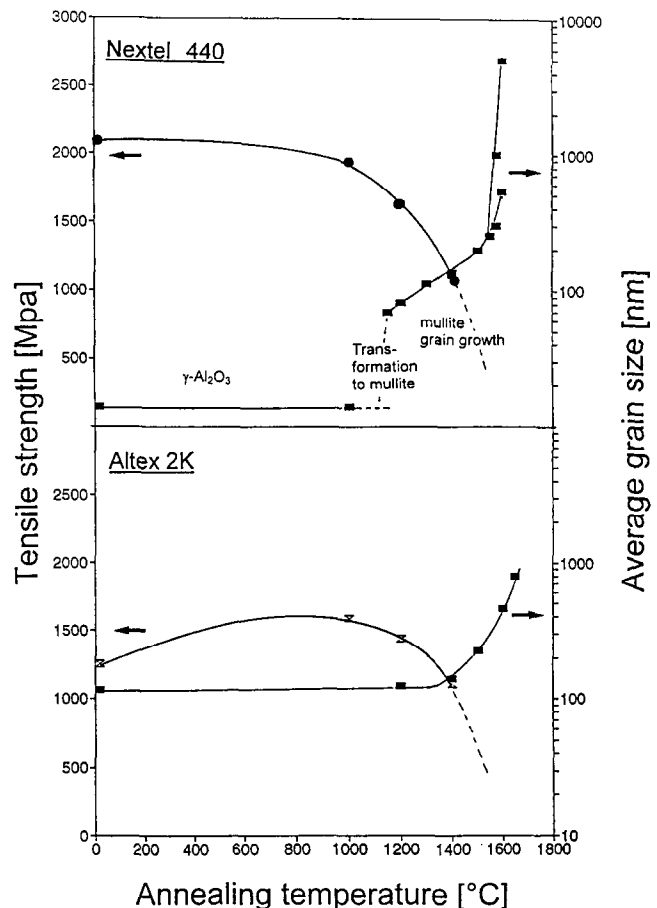


Fig. 1. Grain size and strength of Nextel 440 and Altex 2K fibres heat-treated between 1000 and 1600°C.

3.2 Phase content and microstructural development of fibres

3.2.1 Nextel 440 fibres

According to phase content and microstructure, the temperature-dependent development of the Nextel 440 fibres can be subdivided into three stages (Fig. 1): ' $\gamma\text{-Al}_2\text{O}_3 + \text{SiO}_2$ stage'; ' $\gamma\text{-Al}_2\text{O}_3 + \text{SiO}_2$ to mullite transformation stage'; and 'mullite grain growth stage'.

(a) $\gamma\text{-Al}_2\text{O}_3 + \text{SiO}_2$ stage. The $\gamma\text{-Al}_2\text{O}_3 + \text{SiO}_2$ region extends from the as-received state up to $\approx 1100^\circ\text{C}$. A typical microstructure of this stage is given in Fig. 2, showing equiaxed $\gamma\text{-Al}_2\text{O}_3$ crystallites with an average grain size of 15 nm. Annealing up to 1100°C causes no coarsening of the $\gamma\text{-Al}_2\text{O}_3$ nanocrystals.

Table 1. Tensile strength of Nextel and Altex 2K fibres as-received and heat-treated at different temperatures

	as-received		1000°C		1200°C		1400°C	
	Nextel	Altex	Nextel	Altex	Nextel	Altex	Nextel	Altex
σ_m (MPa)	2086	1253	1954	1594	1635	1439	1117	1108
Weibull parameter, m	4.9	6.1	6.0	5.8	4.6	5.1	6.1	5.7

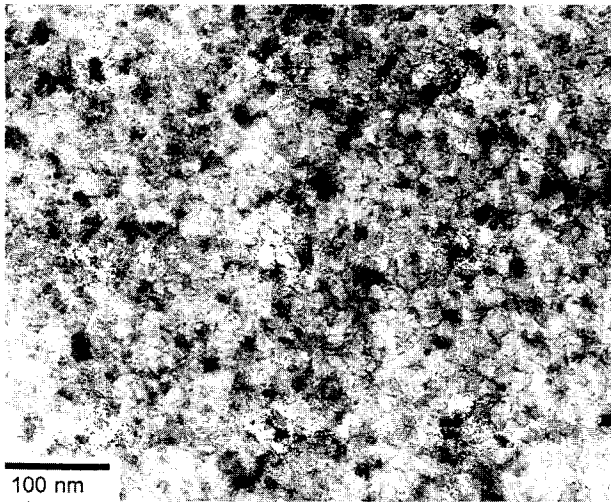


Fig. 2. Micrograph (TEM) of as-received Nextel 440 fibres: nanosized $\gamma\text{-Al}_2\text{O}_3$ crystals.

(b) $\gamma\text{-Al}_2\text{O}_3 + \text{SiO}_2$ to mullite transformation stage. The $\gamma\text{-Al}_2\text{O}_3 + \text{SiO}_2$ to mullite transformation region extends from ≈ 1100 to 1200°C . In samples heat-treated at 1100°C small mullite crystals are occasionally detected by means of convergent beam diffraction or lattice fringe imaging (Fig. 3). With increasing temperature the mullite content gradually increases. A detailed analysis of the $\gamma\text{-Al}_2\text{O}_3 + \text{SiO}_2$ to mullite transformation behaviour is presented in the second part of this study.⁴

(c) *Mullite grain growth stage.* This region refers to annealing temperatures $> 1200^\circ\text{C}$, where distinct mullite grain coarsening occurs. Microstructures of Nextel 440 fibres completely transformed to mullite by heat treatments at 1200, 1400 and 1600°C are shown in Figs 4 to 6. Firing at 1200°C leads to irregular-shaped mullite crystals with an average grain size of 80 nm (Fig. 4). After firing at 1400°C the mean grain size of mullite has increased to 135 nm and the crystals develop more

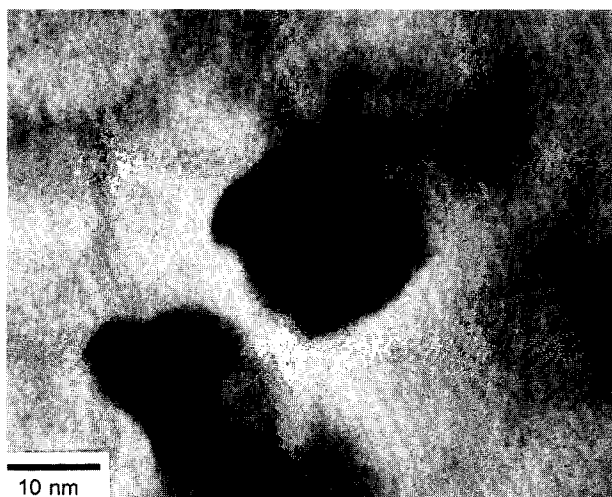
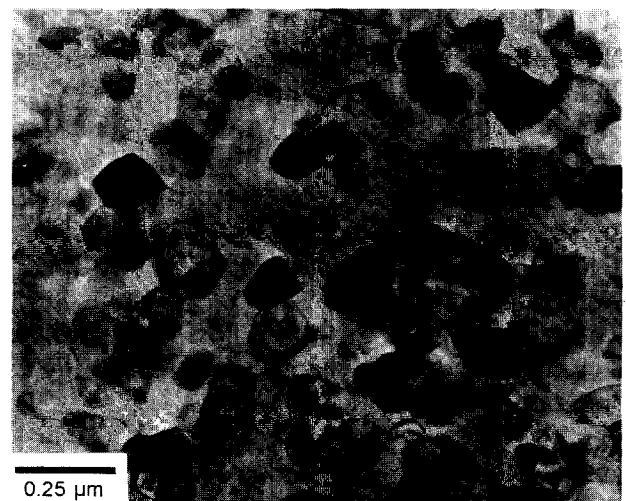


Fig. 3. Micrograph (TEM) of Nextel 440 fibres heat-treated at 1100°C , 4 h: small mullite crystal with (100) lattice fringes.

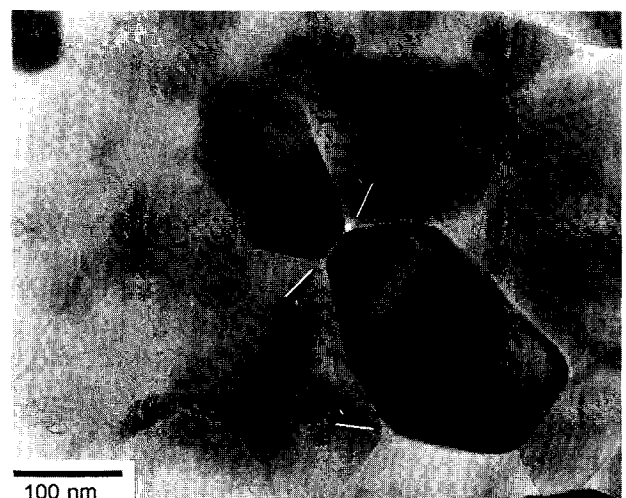


Fig. 4. Micrograph (TEM) of Nextel 440 fibres heat-treated at 1200°C , 4 h: irregular-shaped mullite grains.

regular polygonic shapes [Fig. 5(a)]. At triple grain junctions glassy phase is detected [Fig. 5(b)]. Above 1550°C exaggerated grown mullite crystals



(a)



(b)

Fig. 5. Micrographs (TEM) of Nextel 440 fibres heat-treated at 1400°C , 4 h: (a) coarsened polygonic mullite grains; (b) glassphase at triple grain junctions (arrows).



Fig. 6. Micrograph (TEM) of Nextel 440 fibres heat-treated at 1600°C, 4 h: secondary grain growth of mullite.

are observed which are embedded in a finer grained matrix (Fig. 6). The bimodal grain size distribution leads to the split grain size curve at $\geq 1550^\circ\text{C}$ (Fig. 1): the upper branch corresponds to the large secondary mullite grains, while the lower one represents the unconsumed primaries.

3.2.2 Altex 2K fibres

The microstructure of the as-received Altex 2K fibres is similar to that of Nextel 440 heat-treated at 1200°C, i.e. containing irregular-shaped mullite grains with a mean grain size of ≈ 115 nm. Heat treatments at 1000°C and 1200°C cause no distinct microstructural change, but above 1200°C moderate grain coarsening occurs (Fig. 1). The average grain sizes and strengths of Altex fibres fired at 1400°C are very similar to those of Nextel 440 fibre heat-treated under the same conditions. However, secondary growth of mullite grains does not occur in Altex 2K fibres even at 1650°C.

4 Discussion

Only $\gamma\text{-Al}_2\text{O}_3$ could be detected by TEM in the as-received Nextel 440 fibres, although, according to the bulk composition, SiO_2 is present at 28 wt%. Though a certain amount of SiO_2 is known to be incorporated in the alumina phase,⁵ a remaining fraction must occur, presumably as very thin (~ 1 nm) non-crystalline layers which are not detectable by our TEM analyses of the nanocrystalline material.

These amorphous films surrounding the transition alumina grains may explain the stability of the nanocrystalline microstructure up to 1100°C: obviously the high Si–O bond strength⁶ within the SiO_2 films may cause them to act as diffusion barriers, thus preventing crystal coarsening. On the other hand, the occurrence of amorphous films

enveloping $\gamma\text{-Al}_2\text{O}_3$ crystallites considerably reduces the mechanical strength and creep resistance at elevated temperature by viscous flow mechanisms.

Between about 1100 and 1200°C the nanometre-sized $\gamma\text{-Al}_2\text{O}_3 + \text{SiO}_2$ phase assemblage transforms to mullite. The phase transformation is associated with a strong increase of mean grain size and leads to a distinct reduction of tensile strength. Heat treatments of Nextel 440 fibres between 1200 and 1400°C cause a drastic decrease in strength, attributed to grain coarsening. According to the reciprocal relationship between grain size and strength:⁷

$$\sigma \propto d^p$$

(where σ is strength, d is grain size and $p \approx 0.5$), it turns out that the coarsening of small grains in particular has a strong influence on strength. A strength reduction of 23% (380 MPa) is estimated considering Nextel grain growth data between 1200 and 1400°C. The slightly higher strength loss of 31% (520 MPa) found experimentally may be caused by changes in grain morphology. Strong agglomerations of micropores or glassy phase are assumed if the irregular-shaped mullite crystals develop planar interfaces at high temperature. Obviously the increasing flaw density reduces the mechanical strength.

Above 1550°C exaggerated grain growth takes place in Nextel 440 fibres. Presumably secondary grain growth is assisted by the existence of grain boundary glassy phase separating the surfaces of the small and large grains.⁸ Low viscosity glassy phase occurring at high temperature is related with the B_2O_3 content of the fibres. Retention of B_2O_3 in fired Nextel 440 fibres is deduced from very small weight loss ($< 1\%$) after heat treatment at 1600°C.¹

As-received Altex 2K fibres exhibit similar microstructures to Nextel 440 fibres in the temperature range just beyond the $\gamma\text{-Al}_2\text{O}_3 + \text{SiO}_2$ to mullite transformation (1200°C). We assume therefore that the Altex fibres were produced in this temperature range. This suggestion fits well with the observation that there is no significant change of the microstructure up to 1200°C. Moreover, no glassy phase is detected, probably due to the lack of B_2O_3 flux in Altex 2K fibres. The probable lack of a grain boundary glass phase accounts for the better creep resistance of Altex 2K fibres than of Nextel 440, although the room temperature strength of Altex 2K is comparatively low. The increase of tensile strength of Altex 2K fibres after annealing at 1000°C is attributed to the reduction of residual stresses. Residual stresses may be caused by rapid cooling of the fibres during the fabrication process, due to anisotropy of the thermal expansion coefficients of mullite ($\sim 3.9 \times 10^{-6} \text{ K}^{-1}$ || a -axis and $\sim 7 \times 10^{-6} \text{ K}^{-1}$ || b -axis)⁹.

The present study of the two commercial polycrystalline aluminosilicate fibres with near-stoichiometric mullite composition shows that fibres consisting of nanocrystalline $\gamma\text{-Al}_2\text{O}_3 + \text{SiO}_2$ in the as-received state are suitable for high strength applications at low or moderate temperatures. For applications at higher temperatures ($> 1100^\circ\text{C}$), fibres consisting of polycrystalline mullite without any coexisting glass phase will be more favourable due to the higher creep resistance and resistance against creep-induced fracture.

Moreover, it has been shown that suitable mechanical properties for high temperature applications of the fibres demand homogeneous and extremely fine-grained microstructures and that the content of non-crystalline grain boundary phase should be as low as possible. However, fulfilment of both requirements simultaneously is difficult. For instance, addition of B_2O_3 to a diphasic aluminosilicate starting material causes high nucleation density of mullite, leading to a favourable fine-grained microstructure.⁴ On the other hand, due to B_2O_3 addition, the tendency of forming amorphous grain boundary phases is increased which has a negative influence on the high temperature mechanical properties.

Another result of the investigation is that grain coarsening at elevated temperatures does reduce the strength of the fibres drastically. Therefore

further developments of mullite fibre should have the aim of grain growth reduction. A possible way to be successful is doping the starting materials with vanadium or chromium, both of which have a negative influence on the mullite grain growth rate.¹⁰

References

1. *Nextel Keramische Fasern*, 3M technical data, 1989.
2. Schneider, H., Okada, K. & Pask, J., *Mullite and Mullite Ceramics*. John Wiley & Sons, Chichester, 1994, p. 186.
3. Fernando, J. A., Chawla, K. K., Ferber, M. K. & Coffey, D., Effect of boron nitride coating on the tensile strength of Nextel 480TM fibre. *Mater. Sci. Eng.*, **A154** (1992) 103–8.
4. Hildmann, B. O., Schneider, H. & Schmücker, M., High temperature behaviour of polycrystalline aluminosilicate fibres with mullite bulk composition. II. Kinetics of mullite transformation. *J. Eur. Ceram. Soc.*, **16** (1996) 287–92.
5. Schneider, H., Voll, D., Saruhan, B., Schmücker, M., Schaller, T. & Sebald, A., Constitution of the γ -alumina phase in chemically produced mullite precursors. *J. Eur. Ceram. Soc.*, **13** (1993) 441–8.
6. *Ullmann's Encyclopedia of Industrial Chemistry*, Vol. 23A. VCH Publishers, Inc., Weinheim, 1993, p. 586.
7. Kingery, W. D., Bowen, H. K. & Uhlmann, D. R., *Introduction to Ceramics*, 2nd edn. John Wiley & Sons, New York, 1976, p. 794.
8. Kingery, W. D., Bowen, H. K. & Uhlmann, D. R., *Introduction to Ceramics*, 2nd edn. John Wiley & Sons, New York, 1976, p. 465.
9. Schneider, H. & Eberhard, E., Thermal expansion of mullite. *J. Am. Ceram. Soc.*, **73** (1990) 2073–6.
10. Schneider, H., Transition metal distribution in mullite. *Ceram. Trans.*, **6** (1990) 135–58.

High Temperature Behaviour of Polycrystalline Aluminosilicate Fibres with Mullite Bulk Composition. II. Kinetics of Mullite Formation

B. O. Hildmann, H. Schneider & M. Schmücker

German Aerospace Research Establishment (DLR), Institute for Materials Research, D-51140 Köln, Germany

(Accepted 22 July 1995)

Abstract

Kinetics and mechanisms of mullite formation in technical diphasic aluminosilicate fibres (Nextel™ 440), consisting of transition alumina and a non-crystalline silica-rich phase, were studied by quantitative X-ray phase analysis. The as-received fibres were heat-treated in the temperature and time ranges from 1130 to 1215°C and from 7.5 min to 32 h. The overall mullitization process can be described by an Avrami reaction law, or alternatively, by a simple exponential reaction law with a temperature-dependent induction period. Early stages of mullite formation with a low mullitization degree ($\alpha = 0.02$) are characterized by an activation energy of $\sim 650 \text{ kJ mol}^{-1}$, whereas the apparent activation energy of the overall transformation reaction is $\sim 900 \text{ kJ mol}^{-1}$. Both activation energies are significantly lower than those described in the literature for other diphasic aluminosilicate gels. The relatively low activation energies of mullite formation in Nextel 440 fibres are attributed to the small B_2O_3 content of the as-received fibres. The presence of B_2O_3 may be responsible for the decrease of viscosity of the coexisting non-crystalline SiO_2 -rich phase, by which diffusion, and mullite nucleation and growth is accelerated.

1 Introduction

Nextel™ 440 aluminosilicate fibres in the as-received state are diphasic and consist of nanocrystalline transition alumina ($\gamma\text{-Al}_2\text{O}_3$) and a non-crystalline silica-rich phase, which contains 2 wt% B_2O_3 . Above 1100°C these fibres transform into mullite which is associated with a distinct drop of tensile strength from about 2.0 to 1.6 GPa. A detailed description of the temperature-dependent microstructural development and related mechanical properties is presented in Part I of this study.¹

Mullite formation processes from diphasic gels in the system $\text{Al}_2\text{O}_3\text{-SiO}_2$ have been investigated by several groups (e.g. Refs 1–7). Wei and Halloran⁴ studied reaction kinetics and phase transformation mechanisms of a diphasic gel by quantitative X-ray diffraction of annealed samples and described the kinetics by an Avrami equation with an average time exponent $\langle n \rangle = 1.3(2)$ and a temperature-dependent induction period. Li and Thomson⁵ analysed the kinetic mechanisms from different sol-gel precursors using dynamic X-ray diffraction and differential thermal analysis (DTA) methods and found a significant change in the Avrami exponent n . Huling and Messing⁶ investigated ‘hybrid’ gels and analysed the influence of various seedings on the crystallization of aluminosilicate phases. However, no information is available so far on phase transformations in technical Nextel 440 fibres containing some B_2O_3 . Information on transformation kinetics and mechanisms is valuable for evaluation of the temperature application range of the fibres, and may also help to understand the microstructural developments of the fibres.

2 Experimental

2.1 Sample material

Continuous Nextel 440 fibre bundles (3M Inc., St. Paul, MN, USA) were used for this study. The chemical composition of the fibres is 70 wt% Al_2O_3 , 28 wt% SiO_2 and 2 wt% B_2O_3 .⁸ The as-received fibres have elliptical cross-sections (mean diameters are 7 and 12 μm), and consist of transition alumina (designated as ‘ $\gamma\text{-Al}_2\text{O}_3$ ’ in the following) and a coexisting silica-rich, non-crystalline phase.

2.2 Annealing experiments

Annealing experiments were performed in an induction heated laboratory furnace with SiC

susceptor tube at 1128, 1148, 1166, 1183, 1192 and 1215°C under normal air atmosphere conditions. The annealing times ranged between 7.5 min and 32 h with about six different time intervals for each temperature. Furnace temperatures were controlled using a conventional PID controller and a Pt₁₀₀/Pt₉₀Rh₁₀ thermocouple located close to the sample. By means of an additional reference thermocouple, the accuracy of measurements was estimated to be better than $\pm 3^\circ\text{C}$. For the annealing experiments a sample of ~ 1 g fibre was loaded in a small Al₂O₃ crucible and placed into the hot induction furnace. Special care was taken to bring the samples immediately to the annealing temperatures and to quench to room conditions at the end of annealing time.

2.3 X-ray diffraction (XRD)

XRD studies were performed with a computer-controlled Siemens D 5000 diffractometer, equipped with a graphite monochromator in front of the counter. Diffraction patterns were recorded at room temperature with CuK α radiation in the 2θ range between 25 and 71°. To reduce scattered background intensity, flat silicon single crystal sample holders were used, orientated in such a way that no Si reflection appeared over the 2θ scan region. Following standard procedures in quantitative X-ray analysis^{9,10} for determining weight fractions of transformed mullite, calibration XRD reference measurements were recorded from defined mixtures of as-received fibres (not transformed) and fibres that had been heat-treated at 1230°C (completely transformed into the mullite phase). Calibration curves were obtained from integrated intensities of the mullite reflection doublets 120/210, 121/211, 230/320 and from the integrated diffraction intensity of the 400 reflection of transition alumina ($\gamma\text{-Al}_2\text{O}_3$). Based on these calibration curves, the degree of transformation could be determined with an estimated error of $\pm 1\%$.

3 Results and Discussion

According to X-ray diffraction spectra and transmission electron microscopic observations, the as-received fibres consist of transition alumina ($\gamma\text{-Al}_2\text{O}_3$) and a non-crystalline SiO₂-rich phase, containing 2 wt% B₂O₃. The phase assemblage directly transforms to mullite in a temperature interval extending from ~ 1100 to $\sim 1230^\circ\text{C}$ without forming any other transient crystalline phase. The experimentally determined transformation levels α (α = weight fraction of newly formed mullite) are plotted vs. annealing time at different annealing

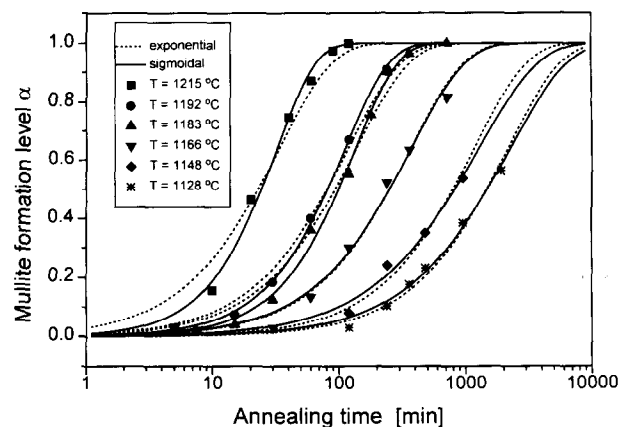


Fig. 1. Experimentally determined mullite formation levels α (weight fraction) plotted as function of annealing time on a logarithmic time scale. Dotted and solid lines correspond to exponential and sigmoidal approximations, respectively, assuming no induction periods ($\tau = 0$) (see Section 3.2).

temperatures in Fig. 1 in a semi-logarithmic scale. The fitted curves represent both simple exponential and sigmoidal functions and will be discussed in Section 3.2.

3.1 Early stages of reaction

Independent from any particular kinetic law, early reaction stages of mullite formation were evaluated by analysing time intervals τ required to attain small, but definite transformation levels α . Though being of major interest, precise determination of formation time intervals τ for very small conversion levels ($\alpha < 0.02$) turned out to be difficult, due to the lack of precisely measured data at the very beginning of the transformation processes. Therefore reaction time intervals necessary for the formation of 2, 5 and 10 wt% mullite ($\alpha = 0.02$, 0.05 and 0.10) were determined from isothermal data sets by interpolating between zero and the first measured data points using linear, polynomial and sigmoidal interpolation functions. Transformation time intervals $\tau_{\alpha=0.02}(T)$, $\tau_{\alpha=0.05}(T)$ and $\tau_{\alpha=0.10}(T)$ belonging to mullite formation levels $\alpha = 0.02$, 0.05 and 0.10, respectively, are plotted in an Arrhenius diagram in Fig. 2. From the slopes of the fitted straight lines slightly increasing activation energies are obtained with the increase of the transformation level: $\Delta E(\tau_{\alpha=0.02}) = 644(18)$ kJ mol⁻¹, $\Delta E(\tau_{\alpha=0.05}) = 679(12)$ kJ mol⁻¹, and $\Delta E(\tau_{\alpha=0.10}) = 696(17)$ kJ mol⁻¹.

Formation time intervals $\tau_{\alpha=0.02}(T)$ certainly cover the early (induction) stages of the transformation processes, including the period of stable nuclei formation and beginning of grain growth. The activation energy of initial mullite formation in Nextel 440 fibres at transformation level $\alpha = 0.02$ [$\Delta E(\tau_{\alpha=0.02}) = 644(18)$ kJ mol⁻¹] is significantly lower than the corresponding value

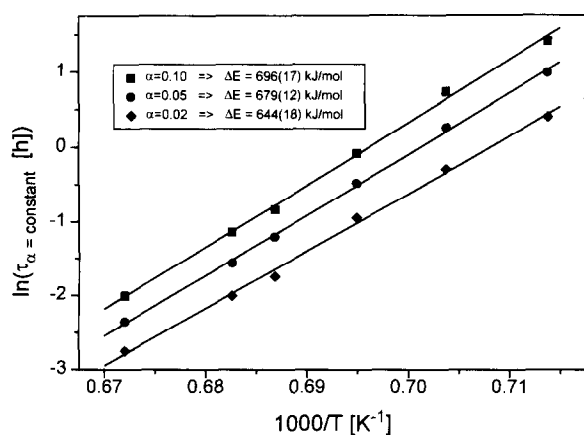


Fig. 2. Arrhenius plot of mullite formation times $\tau_{\alpha=0.02}(T)$, $\tau_{\alpha=0.05}(T)$ and $\tau_{\alpha=0.10}(T)$ required to attain mullite formation levels $\alpha = 0.02, 0.05$ and 0.10 , respectively. An activation energy of $\sim 650 \text{ kJ mol}^{-1}$ is determined for the early mullite formation stages.

obtained under the same conditions by Wei and Halloran [$\Delta E(\tau_{\alpha=0.02}) = 987(15) \text{ kJ mol}^{-1}$]⁴ for the transformation of diphasic aluminosilicate gels to mullite. The large difference of almost 350 kJ mol^{-1} between both ΔE values can be explained by different nucleation characteristics: a very high nucleation density of about $2 \times 10^{15} \text{ cm}^{-3}$ is observed in Nextel 440 fibres,¹ which is four orders of magnitude higher than that in diphasic gels, $\sim 2 \times 10^{11} \text{ cm}^{-3}$.⁴ The high nucleation density in the Nextel 440 fibres may be caused by the occurrence of a non-crystalline silicate phase of low viscosity in the transformation interval due to the presence of $\sim 2 \text{ wt\% B}_2\text{O}_3$. Thereby diffusion processes are accelerated by liquid phase assisted mechanisms.

Aksay¹¹ investigated the diffusion of Si and Al in mullite (and other aluminosilicates) and found that the activation energy for the diffusion of Si and Al species alone amounts to $\sim 700 \text{ kJ mol}^{-1}$ which is slightly higher than our experimentally obtained value for the initial processes in Nextel 440 fibres. A conclusion is either that in our case

(1) the additional activation energy term for nuclei formation is negligibly small, or (2) diffusion barriers play a less important role than they do usually in the initial stages of mullite formation, due to the presence of B_2O_3 .

3.2 Overall transformation laws

In the discussion of the kinetics of the overall mullite formation processes, we used rate equations of the general form:¹²

$$K(T) \cdot (t - \tau) = f(\alpha) \quad (1)$$

with α = transformation level (weight fraction of newly formed mullite), K = reaction rate parameter, t = annealing time and τ = induction period.

In a first approach the kinetic data were fitted using a simple exponential function (index e). Such transformation laws are characteristic for chemical first-order reactions and have often been used to describe diffusion controlled grain growth processes:

$$K_e(T) \cdot (t - \tau) = -\ln(1 - \alpha) \quad (2)$$

The dashed curves in Fig. 1 are least-squares fits using Eqn (2), but without considering any induction period ($\tau = 0$). In a $\ln(1 - \alpha)$ vs. t diagram, not shown here, linear regression lines are obtained documenting a reasonable fit of measured and calculated data. Refined values for K_e are summarized in Table 1.

A closer look at the kinetic data shows that the transformation curves do not really follow the simple kinetic law of Eqn (2) with $\tau = 0$, but display sigmoidal shapes (index s). Transformation curves of this type are described by a modified Avrami kinetic law:¹²

$$K_s(T) \cdot (t - \tau) = [-\ln(1 - \alpha)]^{1/n} \quad (3)$$

Compared with Eqn (2), Eqn (3) has a time exponent n (real number) as an additional freely

Table 1. Kinetic data evaluation of the overall mullite formation: reaction rate coefficients K and exponents n for one exponential and two sigmoidal approximations of the kinetic Avrami law in the general form $K \cdot (t - \tau) = [-\ln(1 - \alpha)]^{1/n}$. In one sigmoidal approximation induction periods $\tau = \tau_{\alpha=0.02}$ were assumed. The numbers in parenthesis represent standard deviations from least-squares refinements and refer to the last digits.

Annealing temperature, T ($^{\circ}\text{C}$)	Exponential approximation ($n = 1$): $\ln(1 - \alpha) = -K_e \cdot t$		Sigmoidal approximations ($n \neq 1$): $\ln[-\ln(1 - \alpha)] = n \cdot \ln(K_s) + n \cdot \ln(t - \tau)$				
	No induction period, $\tau = 0$		No induction period, $\tau = 0$		Induction period, $\tau = \tau_{\alpha=0.02}$		
	K_e	$\ln(K_e)$	$n \cdot \ln(K_s)$	n	$n \cdot \ln(K_{s\tau})$	n_{τ}	$\tau_{\alpha=0.02}$ (h)
1215	2.27(10)	0.82	0.87(18)	1.59(13)	0.869(52)	1.11(3)	0.064
1192	0.585(15)	-0.54	-0.83(10)	1.373(84)	-0.502(36)	0.98(3)	0.135
1183	0.539(21)	-0.62	-1.113(63)	1.367(63)	-0.671(56)	1.03(4)	0.175
1166	0.1498(64)	-1.90	-2.20(19)	1.23(13)	-1.511(36)	0.88(2)	0.39
1148	0.0504(23)	-2.99	-3.00(31)	1.03(16)	-2.46(12)	0.82(7)	0.75
1128	0.02727(95)	-3.60	-3.94(27)	1.15(12)	-2.907(31)	0.81(2)	1.5
mean of n				1.29(20)		0.94(12)	

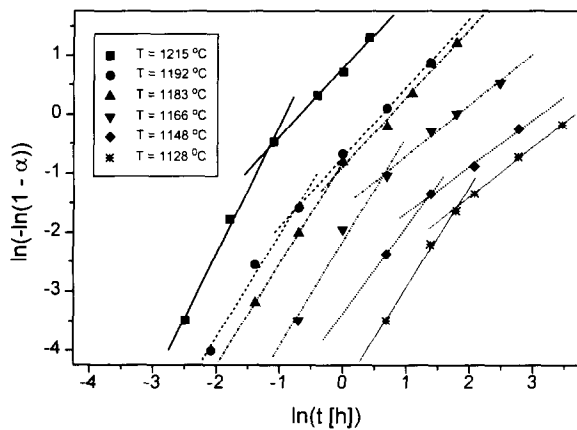


Fig. 3. Mullite formation levels α plotted in the form $\ln[-\ln(1 - \alpha)]$ vs. $\ln(t)$ without considering any induction period [$\tau = 0$]. It is obvious that the measured data is not well fitted by one straight line, but 'initial' and 'final' regions can be distinguished.

refined parameter, and an induction period τ . The solid lines in Fig. 1 are least-squares fits using Eqn (3), again without considering any induction period ($\tau = 0$). Compared with the exponential approach the sigmoidal functions represent better numerical approximations. Refined values for n [average $\langle n \rangle = 1.3(2)$] and $n \cdot K_s(T)$ are listed in Table 1.

If the measured raw data are plotted in double logarithmic plots, $\ln[-\ln(1 - \alpha)]$ vs. $\ln(t)$, it becomes obvious that one single straight line for each isothermal data set does not fit the data well (see Fig. 3). Instead, two straight lines with significantly different slopes n referring to an 'initial' (index 1) and a 'final' (index 2) transformation region* can be distinguished ('split model'). Linear regression fits for the two transformation regions lead to values $n_1 \cdot \ln(K_1)$ and n_1 [average $\langle n_1 \rangle = 1.81(18)$] and to $n_2 \cdot \ln(K_2)$ and n_2 [average $\langle n_2 \rangle = 1.00(20)$], respectively.

Several possible explanations for the change of slopes n were discussed in the literature. Arguments are based on the ideas that (1) nucleation sites are consumed in the 'initial' region,¹³ (2) variable nucleation and growth rates occur in different grains,¹⁴ and (3) impingement of growing grains takes place in the 'final' region.¹⁵ Li and Thomson described a significant change in the Avrami slope for a diphasic gel⁵ (from $\langle n_1 \rangle = 2$ to $\langle n_2 \rangle = 0.5$) and a somewhat smaller change for a single-phase gel¹⁶ (from $\langle n_1 \rangle = 1$ to $\langle n_2 \rangle < 0.4$). Li and Thomson⁵ explained the change of n in the diphasic gel by impingement of grains in the 'final' region using the model of Rosen *et al.*,¹⁵ who analysed the recrystallization of pure iron and

*The 'initial region' extends up to a transformation level of 20 to 35 wt%. It should not be mixed up with the term 'induction period', which characterizes the early beginning of the reaction ($\alpha < 0.02$).

suggested preferred impingement of grains in the axial direction causing the grains to grow only in the transverse direction. Impingement of grains effectively leads to a reduction of growth dimensionality, and thus of slope n , due to restrictions in normal growth directions. Huling and Messing⁶ also attributed lower n values to effectively lower dimensional growth, e.g. due to combinations of growth along and normal to the interfaces in diphasic 'hybrid' 75M_I gels. In Nextel 440 fibres reduction of growth dimensionality may also take place due to impingement of grains and, thus, explain the change of n . Here, however, the difference of n values between 'initial' and 'final' region [$\langle n_1 \rangle = 1.81(18)$ and $\langle n_2 \rangle = 1.00(20)$] is smaller than the values reported in the literature.

Another way to treat the change of slopes n is based on the consideration of induction periods $\tau(T)$, which have not been taken into account in our data analyses up to this point and have also not been considered by Li and Thomson.^{5,16} In order to check for linearity in $\ln[-\ln(1 - \alpha)]$ vs. $\ln(t)$ plots, induction periods $\tau(T)$ were introduced prior to numerical data evaluation. It should be kept in mind that precise estimations of $\tau(T)$ values are required, and that slight variations of τ sensitively influence the shape of the reaction curves. Such a precise determination of τ from the measured raw data at early reaction stages is difficult (see also Section 3.1). Following the procedure of Wei and Halloran,⁴ formation time periods $\tau_{\alpha=0.02}(T)$, required to attain a mullite formation level $\alpha = 0.02$, were arbitrarily considered as induction periods τ to correct the time axis of the measured isothermal raw data before subsequent calculations. Starting from this point, data sets of $\alpha(T)$ were numerically approximated via least-squares techniques using Eqn (3) in the form

$$\ln[-\ln(1 - \alpha)] = n(T) \cdot \ln[K_s(T)] + n(T) \cdot \ln[t - \tau_{\alpha=0.02}(T)] \quad (4)$$

Induction time periods $\tau_{\alpha=0.02}(T)$ and freely refined parameters $n_{\tau} \cdot K_{s\tau}$ and n_{τ} are listed in Table 1. Mullite formation levels α presented in double logarithmic plots now yield straight lines. The lines have slightly different slopes $n_{\tau}(T)$ ranging around a mean value of $\langle n_{\tau} \rangle = 0.94(12)$ (see Fig. 4). Since n_{τ} is close to 1 in each case mullite formation can be equally well described by a first-order reaction ($n = 1$), if correct temperature-dependent induction periods $\tau_0(T)$ are taken into account. Finally, refinements with fixed $n = 1$ and slightly changed induction periods $\tau_0(T)$ confirm this conclusion. We believe that this simple kinetic model is best suited to describe the mullite formation processes in Nextel 440 fibres.

Arrhenius plots fitted on the basis of least-squares regressions of experimentally determined

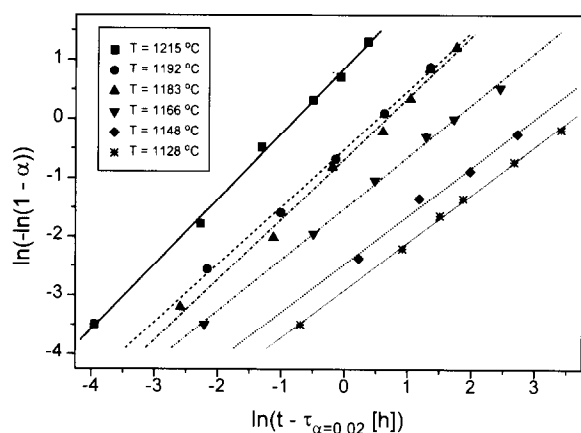


Fig. 4. Mullite formation levels α plotted in the form $\ln[-\ln(1 - \alpha)]$ vs. $\ln(t - \tau)$. Induction times $\tau = \tau_{\alpha = 0.02}(T)$ were used to correct the time axis prior to numerical fitting. Linear regression fits yield values $n_r \cdot \ln(K_{s,r})$ and n_r listed in Table 1 (compare with Fig. 3).

rate coefficients $\ln(K_c)$ and $\ln(K_{s,r})$ are shown in Fig. 5 (see Table 1). From the slopes of the straight lines apparent activation energies of the overall mullite formation processes can be derived. Based on reaction rate coefficients K_c and $K_{s,r}$, the values $\Delta E_c = 914(56)$ kJ mol⁻¹ and $\Delta E_{s,r} = 903(54)$ kJ mol⁻¹ are obtained, respectively. An Arrhenius plot of $n \cdot \ln(K_s)$ leads to the energy value 939(56) kJ mol⁻¹. From Arrhenius plots of $\ln(K_1)$ and $\ln(K_2)$ of the 'split model', apparent activation energies $\Delta E_1 = 727(59)$ kJ mol⁻¹ and $\Delta E_2 = 908(64)$ kJ mol⁻¹ were calculated. Compared with the activation energy of the initial stages of reaction (derived from Arrhenius plots of formation times $\tau_{\alpha = 0.02}$, see Section 3.1), the apparent activation energies for the overall mullite forming processes [derived from Arrhenius plots of the reaction coefficients $\ln(K)$] are clearly higher. This indicates that processes associated with initial nucleation

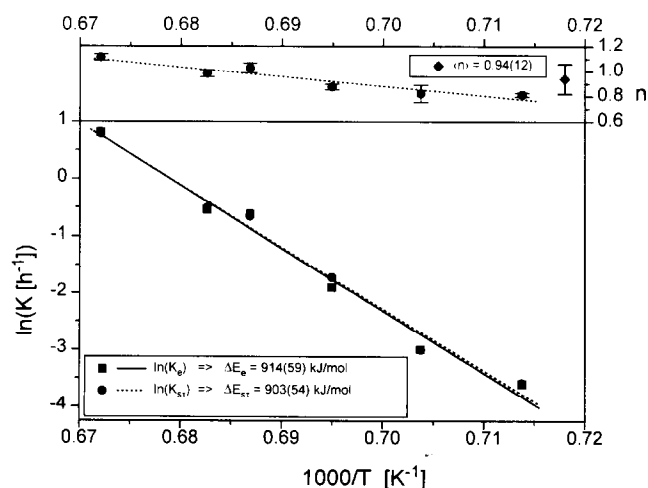


Fig. 5. Arrhenius plot of $\ln(K_c)$ (exponential approximation) and $\ln(K_{s,r})$ (sigmoidal approximation considering induction periods $\tau = \tau_{\alpha = 0.02}$) for the overall mullite transformation. The different slopes give apparent activation energies of $\Delta E_c = 914(56)$ kJ mol⁻¹ and $\Delta E_{s,r} = 903(54)$ kJ mol⁻¹. The average value of the exponent n is 0.94(12).

and grain growth are characterized by smaller energy barriers than those related to final formation and grain growth.

The mean values of the apparent mullite activation energies of Nextel 440 fibres are lower than the mean values of diphasic gels reported in the literature (e.g. Wei and Halloran:⁴ $\Delta E = 1070(200)$ kJ mol⁻¹; Li and Thomson:⁵ $\Delta E = 1028(37)$ kJ mol⁻¹; and Huling and Messing:⁶ $\Delta E = 987(71)$ kJ mol⁻¹ for the hybrid gel 25M₁). It must be emphasized that Wei and Halloran obtained their value from an Arrhenius plot of $n_r \cdot \ln(K_{s,r})$ considering induction periods $\tau = \tau_{\alpha = 0.02}$ before data evaluation, whereas Huling and Messing obtained theirs from an Arrhenius plot of $\ln(K_s)$ without considering an induction period. Li and Thomson obtained their value from DTA measurements. The differences between apparent activation energies of mullitization between the present study and literature data may have similar reasons as already discussed for the initial stages of reaction (see Section 3.1). A suitable explanation is that atomic diffusion, which is the rate-controlling process for both nucleation and growth, is enhanced in Nextel 440 fibres by the presence of the viscous glassy phase containing B₂O₃, which, according to our observations, is retained in the bulk of the fibres at least up to 1400°C. Our own preliminary studies have also shown that diphasic fibres without B₂O₃ (Nextel™ 550, Altex from Sumitomo Chemical Inc.) transform into mullite in a similar way as do, for example, Wei and Halloran's diphasic (but B₂O₃-free) gels, thus supporting the suggestion that B₂O₃ content has a transformation-controlling influence.

References

- Schmücker, M., Flucht, F. & Schneider, H., High temperature behaviour of polycrystalline aluminosilicate fibres with mullite bulk composition. I. Microstructure and strength properties. *J. Eur. Ceram. Soc.*, **16** (1996) 281–5.
- Hoffmann, D. W., Roy, R. & Komarneni, S., Diphasic xerogels, a new class of materials in the system Al₂O₃–SiO₂. *J. Am. Ceram. Soc.*, **67** (1984) 468–71.
- Wei, W. & Halloran, J. W., Phase transformation of diphasic aluminosilicate gels. *J. Am. Ceram. Soc.*, **71** (1988) 166–72.
- Wei, W. & Halloran, J. W., Transformation kinetics of diphasic aluminosilicate gels. *J. Am. Ceram. Soc.*, **71** (1988) 581–7.
- Li, D.X. & Thomson, W. J., Kinetic mechanisms for mullite formation from sol–gel precursors. *J. Mater. Res.*, **5** (1990) 1963–9.
- Huling, J. C. & Messing, G. L., Epitactic nucleation of spinel in aluminosilicate gels and its effect on mullite crystallization. *J. Am. Ceram. Soc.*, **74** (1991) 2374–81.
- Voll, D., Mullitprecursoren: Synthese, temperaturabhängige Entwicklung der strukturellen Ordnung und Kristallisationsverhalten. PhD thesis, University of Hannover, 1994.

8. 3M Company, *Properties of NextelTM 440 ceramic fibers*. Technical data, 3M Ceramic Materials Department, 1993.
9. Klug, H. P. & Alexander, L. E., *X-ray Diffraction Procedures*. John Wiley, New York, 1954.
10. Cullity, B. D., *Elements of X-ray Diffraction*. Addison-Wesley, London, 1956.
11. Aksay, I. A., Diffusion and phase relationship studies in the alumina silica system. PhD Thesis, University of California, Berkeley, CA, 1973.
12. Bamford, C. H. & Tipper, C. F. H., *Chemical Kinetics—Reactions in the Solid State*. Elsevier Scientific, Amsterdam, 1980, Vol. 22.
13. Avrami, M., Kinetics of Phase Changes II. Transformation-time relations for random distribution of nuclei. *J. Chem. Phys.*, **8** (1940) 212–24.
14. Rollet, A. D., Srolovitz, D. J., Doherty, R. D. & Anderson, M. P., Computer simulation of recrystallization in non-uniformly deformed metals. *Acta Metall.*, **37** (1989) 627–39.
15. Rosen, A., Burton, M. S. & Smith, G. V., Recrystallization of high-purity iron. *Trans. AIME*, **230** (1964) 205–15.
16. Li, D. X. & Thomson, W. J., Mullite formation kinetics of a single-phase gel. *J. Am. Ceram. Soc.*, **73** (1990) 964–9.

Processing, Structure, and Properties of Mullite Fiber/Mullite Matrix Composites

K. K. Chawla, Z. R. Xu & J.-S. Ha

Department of Materials and Metallurgical Engineering, New Mexico Institute of Mining and Technology, Socorro, New Mexico 87801, USA

(Accepted 22 July 1995)

Abstract

Oxide fiber/oxide matrix composites form an important and very attractive subpart of ceramic matrix composites because of their inherent stability in oxidizing atmospheres at high temperature. In particular, mullite fiber/mullite matrix composites have the potential of high temperature usage in oxidizing atmospheres.

The interface in mullite fiber/mullite matrix was engineered by using thick BN (1 μm) or BN/SiC double coating on mullite fibers, such that deformation mechanisms conducive to toughness enhancement could be brought to play. Significant improvements in the room temperature mechanical properties of these mullite fiber/mullite matrix composites could be achieved by incorporation of these interfacial coatings and by using a colloidal processing route to make dense mullite matrix.

Introduction

Ceramic matrix composites (CMCs) capable of maintaining excellent strength and fracture toughness are required for high temperature structural applications. Many of these applications require exposure to an oxidizing environment, as such the thermodynamic stability and oxidation resistance of CMCs become important issues. Nonoxide fiber/nonoxide matrix composites generally show good low temperature strength, but oxidation resistance is a major limitation.^{1,2} Nonoxide fiber/oxide matrix composites or oxide fiber/nonoxide matrix composites do not have high oxidation resistance because the permeability constant for the diffusion of oxygen is high, resulting in rapid oxygen permeation through the oxide matrix.³ It would thus appear that in applications where stability in air at high temperature is a prime objective, oxide fiber/oxide matrix composites should be considered because they are inherently stable in air.

Some oxide/oxide matrix composite systems have been investigated.^{4–7} A strong fiber/matrix bond forms in the oxide matrix reinforced with uncoated oxide fibers, such as in the like/like systems, (e.g. mullite/mullite)^{4,5} or in the mixed systems, (e.g. $\text{Al}_2\text{O}_3/\text{SiO}_2$)⁶ where additional compound(s) could form at the interface, and the overall mechanical properties of those composites were not much improved. As a consequence, a barrier layer is generally introduced to prevent fiber/matrix interaction, and thus, prevent strong interfacial chemical bonding. Carbon barrier coating has been frequently used in oxide/oxide composites.⁸ In this work on mullite/mullite composites, we have used BN and BN/SiC duplex coatings as interphase materials. We recognize that both BN and SiC are nonoxides, but are more oxidation resistant than carbon. Ideally, one would like to incorporate an oxide coating, but in this preliminary work we wish to explore the basic idea of mullite/mullite composites. If we can produce such composites with a BN or BN/SiC interphase without surface cracks, then oxygen ingress will be inhibited. The use of a BN coating is desirable because of its ease of sliding along the basal planes.⁹

Objective

The objectives of this work were to use an interface engineering approach, involving fiber coating, microstructure characterization of the interface, mechanical test and fractography study, in mullite/mullite systems to weaken the interfacial bond in order to achieve oxide/oxide composites with high work of fracture and a noncatastrophic failure mode.

Materials and Experimental Procedure

Mullite fibers, Nextel 480 and Nextel 550, both of 3M Co., were used in mullite matrix composites.

Table 1. Properties of fibers, mullite matrix, and fiber coatings

Properties	Nextel 480	Nextel 550	Mullite matrix ($3Al_2O_3-2SiO_2$)	Boron nitride (<i>h</i> -BN)	Silicon carbide (β -SiC)
Composition	70wt% Al_2O_3 28wt% SiO_2 2wt% B_2O_3	73wt% Al_2O_3 27wt% SiO_2	—	—	—
Melting point ($^{\circ}C$)	1850	1850	1850	3000	2220
Density (g/cm^3)	3.03	3.03	3.17	2.27	3.21
Strength [†] (MPa)	1900 [#] (Tensile)	2000 [#] (Tensile)	128–185	80–110	255–465*
Young's Modulus (GPa)	220	193	181	60–80*	440–470*
Coefficient of thermal expansion ($10^{-6}/^{\circ}C$)	4–5	4–5	4–5	5	4.8
Diameter (μm)	8×12	8×12	—	—	—
Reference	10	11	12–14	15–17	12, 18

[†]: At room temperature.

[#]: 51 mm gauge length.

*: Data of CVD materials.

Nextel 480 is a polycrystalline mullite fiber, while the as-received Nextel 550 is not crystalline mullite but a mixture of α -alumina and amorphous silica with mullite composition, which can be transformed to mullite when heated above 1200 $^{\circ}C$. Fiber coating of BN on Nextel 480 was applied by at Synterials Co. (Herndon, VA) using a proprietary CVD technique, and the double coating of BN/SiC on Nextel 550 was applied by 3M Co. (St. Paul, MN) via a proprietary CVD technique. In the double coating, the outer layer was SiC.¹⁰ The nominal compositions and some properties of the materials used are summarized in Table 1.^{11–19}

Conventional mullite powders need temperatures above 1500 $^{\circ}C$ for considerable densification because of the low interdiffusion rates of silicon

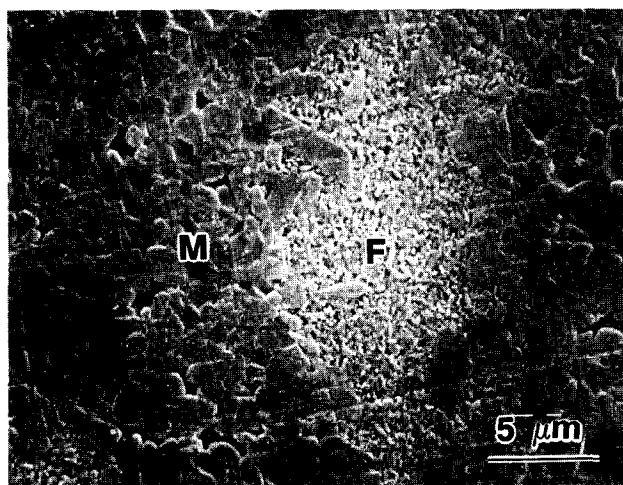


Fig. 1. Etched surface of uncoated Nextel 480/mullite composite fabricated with a commercial mullite powder as the matrix material. Note the extensive fiber (F)/matrix (M) interaction and fiber deformation.

and aluminum ions in crystalline mullite.^{18,19} Such high processing temperatures could cause severe damage on the fibers.⁴ The composite fabricated from the commercial mullite powder with uncoated Nextel 480 fiber showed fiber deformation and extensive interaction between the fiber and matrix, see Fig. 1. Note that large matrix grains had grown into the fiber due to the high processing temperature and pressure required for densification of the commercial mullite powders. The mullite matrix used in this work was obtained via a powder synthesized in our laboratory by a diphasic gel route using a boehmite ($AlOOH$) powder (Dispal 11N7, Remet Chemical Corp., Chadwicks, NY) and an amorphous silica sol (SP-30, Remet Chemical Corp.) as precursors. The gel was prepared by dispersing the boehmite powder in distilled water to get a boehmite sol, which was then mixed with the silica sol to have the stoichiometric mullite composition (71.8 wt.% Al_2O_3 and 28.2 wt.% SiO_2), followed by gelling at room temperature. The gel obtained was dried at 70 $^{\circ}C$ and ground into powder form. All the composites were fabricated by slurry impregnation method.²² Consolidation of composites was done by hot-pressing. The composites were fabricated by infiltrating uncoated and coated fibers, Nextel 480, with a slurry of the matrix powder prepared with isopropanol and an organic binder, and unidirectionally laying the infiltrated fibers on mylar tapes. After drying, the prepared tapes were cut, stacked, and heated at 700 $^{\circ}C$ for 2 h in air to remove the binder and the hydroxyl in the boehmite. Consolidation of composites was done by hot-pressing at 1300 $^{\circ}C$ and 35 MPa for 1 h in vacuum. A part of the hot-

pressed composite was cut and heat treated at 1320°C for 1 h in N₂, to cause produce complete crystallization of the mullite matrix, since it was found that the matrix in the as-hot-pressed composite did not crystallize. The details of processing have been reported elsewhere.^{23,24}

Optical and scanning electron microscopes were used for general characterization of the microstructure of the composites. Secondary ion mass spectrometry (SIMS) was used to identify the coatings in composites. Strength of composites was measured in three-point bend tests at room temperature using rectangular bar-shaped specimens with fiber direction parallel to the length of the specimen. Work of fracture (WOF) and the critical stress intensity factor of the composites were measured at room temperature using Chevron-notched bar specimen in three-point bend tests. The frictional shear stress in the BN coated Nextel 480/mullite composite was measured using an interfacial testing system (ITS). The details of this method have been published in Ref. 25.

Results and Discussion

Characterization of the interface

Figure 2(a) shows the cross-section of the BN coated Nextel 480 fiber, with coating thickness being about 1 μm . SIMS characterization verified that there was boron present, see Fig. 2(b). BN structure was turbostratic.²⁶ The microstructure of the BN/SiC coated Nextel 550 fiber, Fig. 3(a), shows that the fiber was fairly uniformly coated with two layers, BN and SiC, with thickness of about 0.1 and 0.2 μm , respectively. SIMS characterization also illustrated the presence of the double coating in the composites, Fig. 3(b and c). Such a thick (1 μm) BN coating was used to survive the processing conditions in order to provide a desired weak interface. By the same token, the outer SiC coating was used to protect the BN inner layer from oxidation during composite fabrication.

Typical raw load versus fiber-end displacement curves from single fiber pushout tests are shown in Fig. 4 (a and b). Note that after fiber pushout, which coincides with load drop, the curve rises with upward concavity. This is because the 10 μm flat-bottomed indenter is very close in dimension to the minor axis of the fiber and soon after fiber pushout the indenter starts loading the matrix. Figure 5 shows the stress versus fiber-end displacement curve after correcting for the contribution of the load train compliance to the total measured displacement. The load train compliance is determined from load versus displacement curves

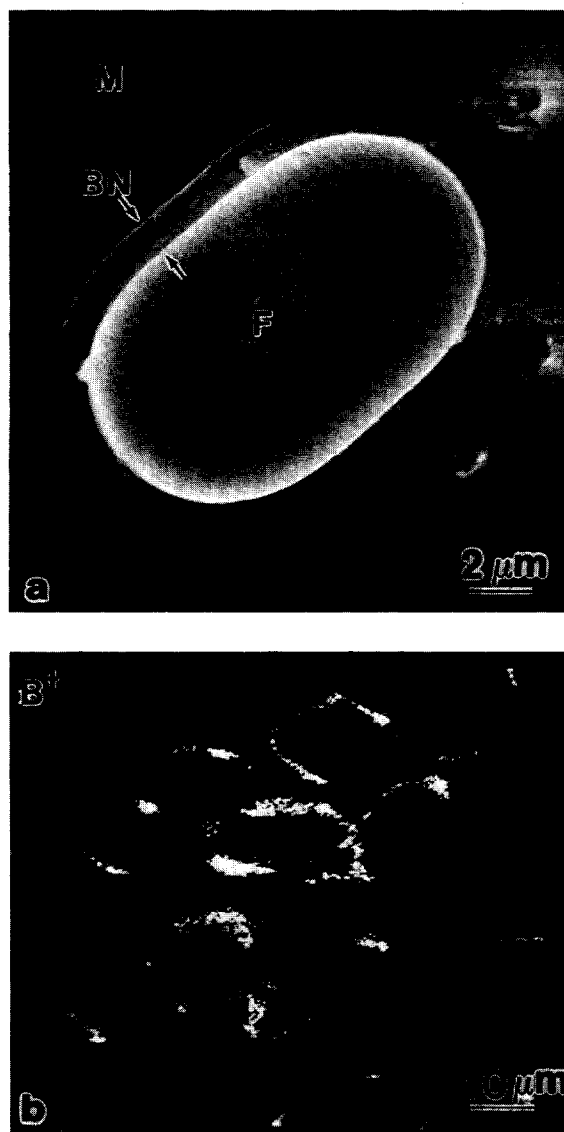


Fig. 2. (a) Cross-section of a BN-coated Nextel 480 fiber, showing the coating thickness 1 μm , (M: matrix, F: fiber); (b) B⁺ mapping by SIMS in a BN-coated Nextel 480/mullite composite.

obtained by subjecting the sample to compression at various points along the wedge by means of a 500 μm diameter stainless steel rod. Typical values for the compliance of the ITS system and wedged continuous fiber reinforced ceramic composite sample are between 4 and 6 $\mu\text{m}/\text{N}$.²⁷ Also shown is the best fit of the data (from the initiation of debonding to the point of fiber pushout) using the progressive fiber debonding and sliding model of Hsueh.²⁸ It should be pointed out that the predictions of the strength-based model of Hsueh are equivalent to those of the energy-based model of Kerans and Parthasarathy.^{27,29} The frictional shear stress in the present system was about 50 MPa.

Mechanical properties

The density, fiber volume fraction, and phases of the composites are listed in Table 2. It can be seen from this table that the matrix in the as-hot-



Fig. 3. (a) Cross-section of a SiC/BN coating Nextel 550 fiber, showing the double coating, (M: matrix, F: fiber); (b and c) SIMS analysis of the surface of a SiC/BN-coated Nextel 550/mullite composite, showing the presence of boron and silicon.

pressed composites did not transform to crystallize mullite at the hot pressing temperature. However, a complete mullite crystallization of the mullite matrix was achieved after the heat treatment (see the section on Materials and Experimental Procedure).

The bend strength, work of fracture, and criti-

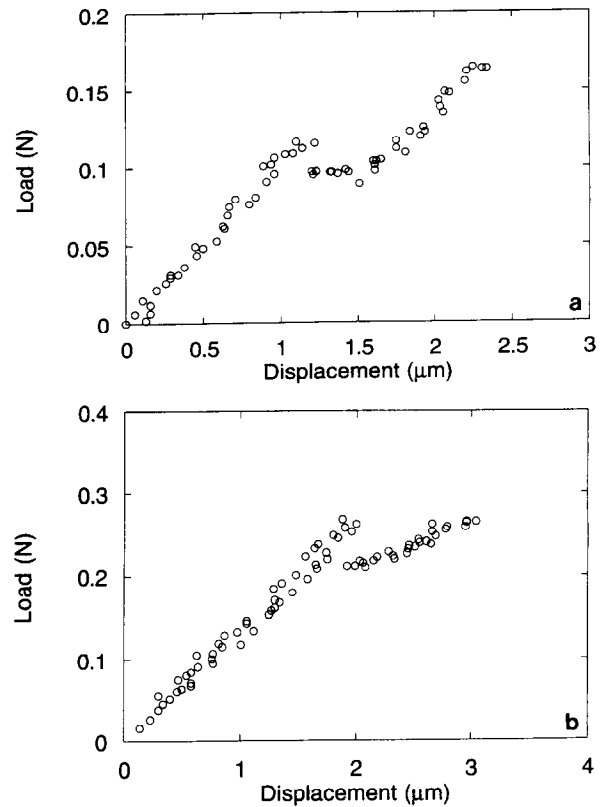


Fig. 4. (a and b) Typical raw load versus fiber-end displacement curves from single fiber pushout tests. Note that after the fiber pushout, which coincides with load drop, the curve rises with upward concavity. This is because soon after debonding the indenter starts loading the matrix.

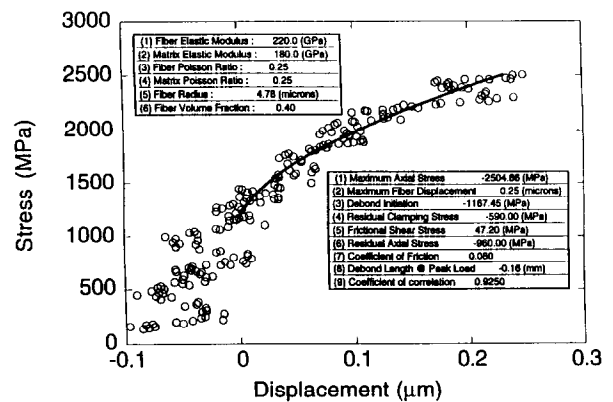


Fig. 5. Stress versus fiber-end displacement curve after correcting for the contribution of the load train compliance to the total measured displacement. Also shown is the best fit of the data (from the initiation of debonding to the point of fiber pushout) using the progressive fiber debonding and sliding model of Hsueh.²⁵

cal stress intensity factors for mullite/mullite composites are listed in Table 3. As can be seen, significant improvements, especially in fracture toughness, were obtained in the interface engineered mullite/mullite composites.

The composite with 1 μm BN coated Nextel 480 exhibited damage tolerant characteristics with a load-bearing capacity even beyond the maximum load, as indicated by a gradual load drop which continued up to a significant amount of displace-

Table 2. Density, fiber volume fraction, and phases of the composites

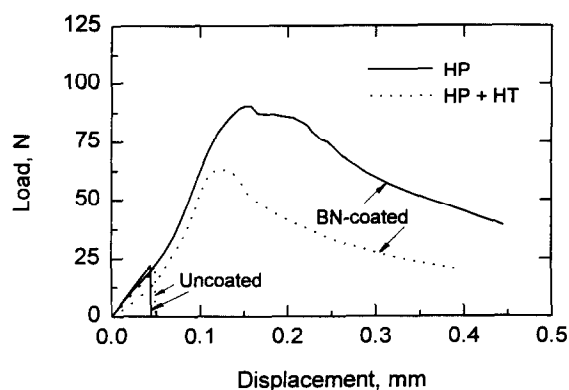
	Nextel 480/BN/mullite	Nextel 550/BN/SiC/mullite
Density(%) [#]	90	85
Fiber volume fraction, V_f	0.41	0.33
Phase		
As-HP [†]	$a + s + m^*$	$a + s^*$
HP+HT [‡]	Mullite	Mullite

[#]Relative densities to the theoretical composite densities calculated using a rule of mixture.

[†] As hot pressed.

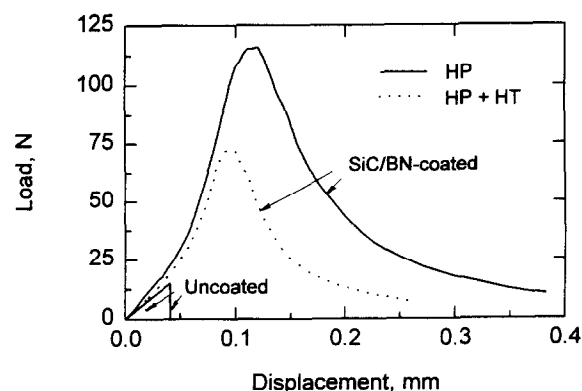
[‡] As hot pressed and heat treated.

* a , s and m denote δ -alumina, amorphous silica, and mullite, respectively.

**Fig. 6.** Load-displacement curves obtained in Chevron-notch tests for Nextel 480/BN/mullite composites in as hot-pressed and hot-pressed + heat-treated conditions.

ment without complete failure during the test, as seen in Fig. 6. After heat treatment leading to complete mullite crystallization of the matrix, this composite still showed a non-catastrophic failure, also shown in Fig. 6. The loss of fiber strength resulted from the heat treatment was responsible for the load drop to a certain level after heat treatment.

Similar to the composite with 1 μm BN coated Nextel 480 fibers, the composite with SiC/BN

**Fig. 7.** Load-displacement curves obtained in Chevron-notch tests for Nextel 550/BN/SiC/mullite composites in as hot-pressed and hot-pressed + heat-treated conditions.

double coated Nextel 550 fibers showed a non-brittle failure, see Fig. 7.

Scanning electron micrographs of the fracture surfaces obtained in three-point bend test of the mullite/mullite composites are shown in Figs 8, 9 and 10. The BN coating in Nextel 480/mullite was found on the pulled-out fiber surface with some peeling-off or separation from the fiber, see Fig. 8. This indicates that both the interfaces of matrix/coating and coating/fiber were weakly bonded. This is not surprising inasmuch as hexagonal BN shears easily. The pulled-out fiber surfaces in the BN/SiC coated Nextel 550/mullite composite were mostly clean and smooth, see Fig. 9. An SEM picture, Fig. 10, showing one of the holes formed in the matrix of Nextel 550/mullite composite as a result of the fiber pullout, reveals that the SiC and BN layers were intact in the matrix and a strong bonding was formed between the matrix and the SiC coating. This can be attributed to a relative strong bonding between SiC and matrix. Also, the BN thickness in double coating is very thin ($\sim 0.1 \mu\text{m}$). This indicates that, unlike Nextel 480/BN/mullite in which the fiber pullout could occur at

Table 3. Mechanical properties of the composites

Composite		V_f	σ_{max} (MPa)	WOF (J/m^2)	K_{IC} ($\text{MPa m}^{1/2}$)
Nextel 480/mullite:					
Uncoated	As-HP	0.45	104	56	1.8
	HP+HT	0.45	106	47	1.9
BN-coated	As-HP	0.41	322	2410	11.6
	AP+HT	0.41	258	1630	8.5
Nextel 550/mullite:					
Uncoated	As-HP	0.47	87	18	1.5
	HP+HT	0.47	71	12	1.4
BN-coated	As-HP	0.33	182	733	7.1
	HP + HT	0.33	223	308	6.0

As-HP: as hot pressed; HP+HT: as hot pressed and heat treated.

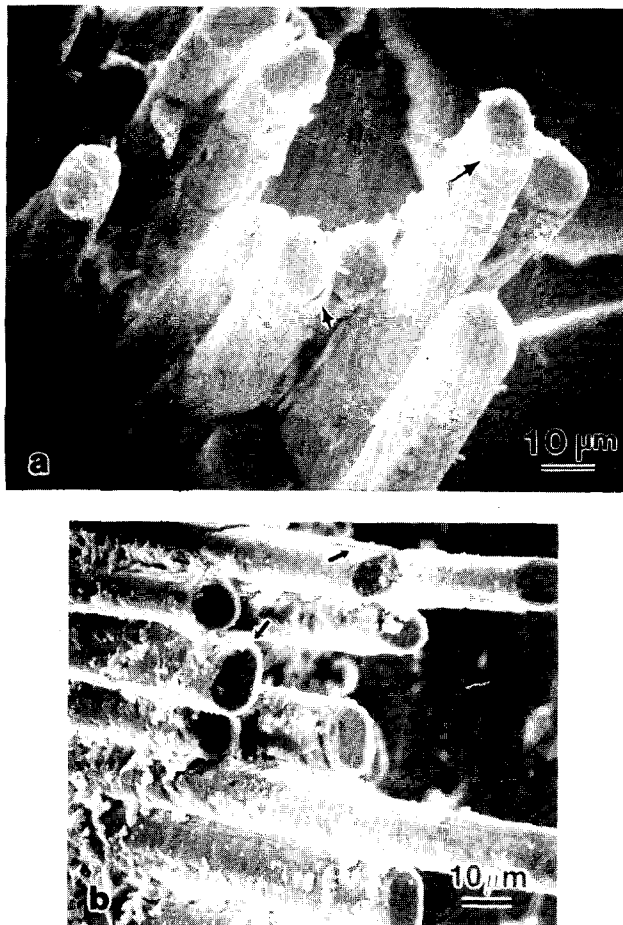


Fig. 8. Fracture surface of BN-coated Nextel 480/mullite composites: (a) hot-pressed and (b) hot-pressed + heat-treated, arrows showing the separation or peeling off of the BN coating.

the interfaces of either matrix/coating or coating/fiber, the fiber pullout occurred along the interface of the fiber and BN coating only.

Conclusions

The fiber/matrix interaction in mullite fiber/mullite matrix composites during processing can be effectively controlled by interface engineering approach. These engineered interfaces consisting of thick BN or a double BN/SiC coating coupled with the colloidal processing to consolidate the mullite matrix at a relatively low temperature, allowed us to make mullite fiber/mullite matrix composites showing high work of fracture and a noncatastrophic failure mode at room temperature.

Acknowledgements

This work was supported by the office of Naval Research, Contract No. N0014-89-J1459 and was monitored by Dr S. G. Fishman.

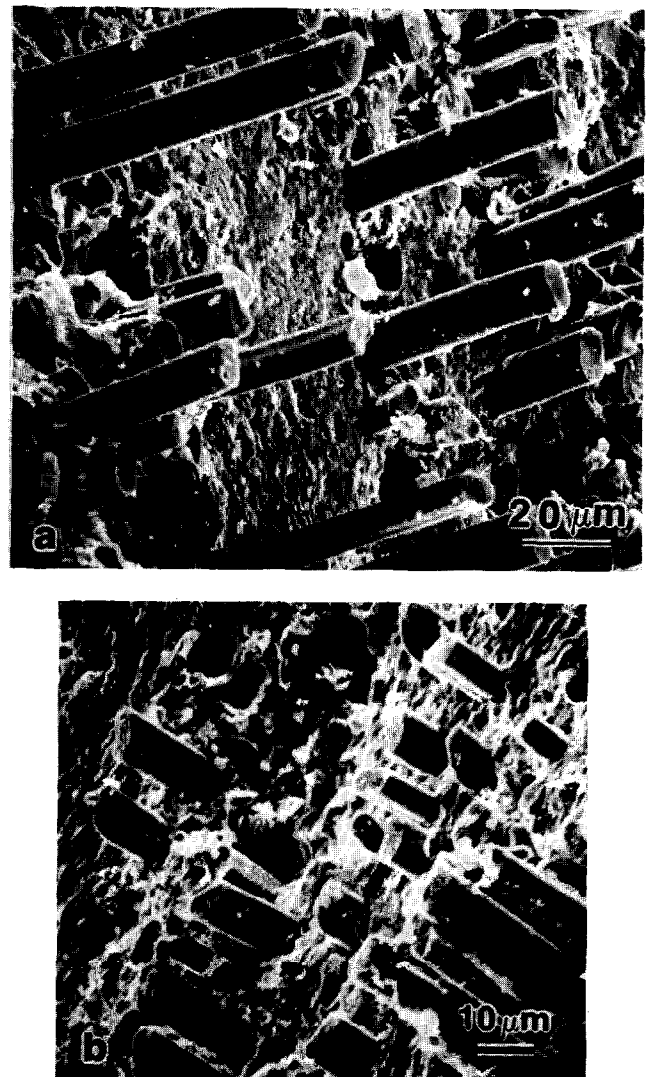


Fig. 9. Fracture surface of BN/SiC coated Nextel 550/mullite composites: (a) hot-pressed and (b) hot-pressed + heat-treated.

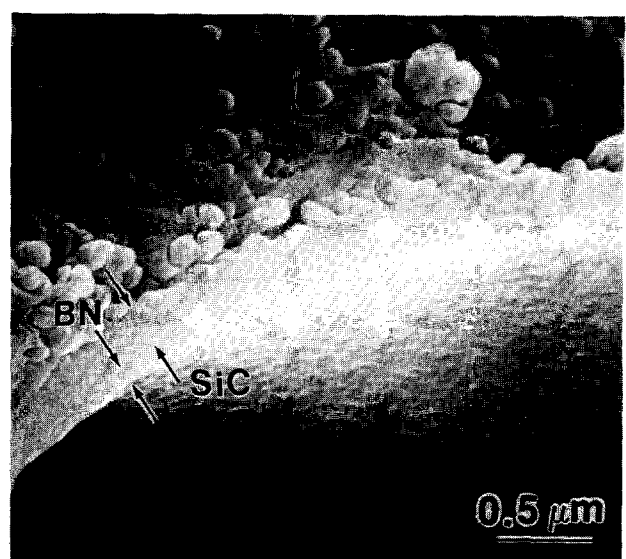


Fig. 10. Fracture surface of SiC/BN coated Nextel 550/mullite composite showing a hole formed in the matrix as a result of fiber pullout. Note the double coating left in the matrix during fiber pullout and the strong bonding between the matrix and the SiC coating.

References

- Prewo, K. M. & Batt, J. A., The oxidative stability of carbon fibre reinforced glass-matrix composites. *J. Mater. Sci.*, **23** (1988) 523–7.
- Mah, T., Hecht, N. L., McCullum, D. E., Hoenigman, J. R., Kim, H. M., Katz, A. P. & Lipsitt, H. A., Thermal stability of SiC fibres (Nicalon). *J. Mater. Sci.*, **19** (1984) 1191–201.
- Hermes, E. E. & Kerans, R. J., Degradation of non-oxide reinforcement and oxide matrix composites. *Mat. Res. Soc. Symposium Proceedings*, **125** (1988) 73–8.
- Singh, R. N. & Brun, M. K., Effect of boron nitride coating on fiber-matrix interactions. *Ceram. Eng. Sci. Proc.*, **8** (1987) 636–43.
- Yehekel, O., Balmer M. L. & Cranmer, D. C., Interfacial chemistry of mullite/mullite composites. *Ceram. Eng. Sci. Proc.*, **9** (1988) 687–94.
- Michalske, T. A. & Hellmann, J. R., Strength and toughness of continuous-alumina-fiber-reinforced glass-matrix composites. *J. Am. Ceram. Soc.*, **71** (1988) 725–31.
- Fitzer, E. & Schlichting, J., Fiber-reinforced refractory oxides. *High Temperature SiC*, **13** (1980) 149–72.
- Lehman, R. L. & Doughan, C. A., Carbon coated alumina fiber/glass matrix composites. *Comp. Sci. & Tech.*, **37** (1990) 149–64.
- Rice, R. W., BN coating of ceramic fibers for ceramic matrix composites. *US Patent*, **4**, 642,271, Feb. 10, 1987.
- Ha, J.-S., Chawla, K. K. & Engdahl, R. E., Effect of processing and fiber coating on fiber-matrix interaction in mullite fiber–mullite matrix composites. *Mater. Sci. & Eng.*, **A161** (1993) 303–8.
- Johnson, D. D., Hiltz, A. R. & Grether, M. F., Properties of Nextel 480 ceramic fibers. *Ceram. Eng. Sci. Proc.*, **8** (1987) 744–54.
- Experimental Product Data Sheet, Ceramic Materials Department, 3M Co., St. Paul, Minnesota.
- Ceramic Sources, Vol. 1, American Ceramic Society, 1985 pp. 336 and 350.
- Skoog, A. & Moore, R., Refractory of the past for the future: mullite and its use as a bonding phase. *Am. Ceram. Soc. Bull.*, **67** (1988) 1180–5.
- Kumazawa, T., Ohta, S., Kanzaki, S., Sakaguchi, S and Tabata, H., Elastic properties of mullite ceramics at elevated temperature. *J. Mater. Sci.*, **8** (1989) 47–8.
- Blocher, Jr, J. M., Nitrides. In *High-Temperature Materials and Technology*, Chap. 11, eds I. E. Campbell & E. M. Sherwood, John Wiley & Sons, New York, 1967, p. 379.
- Williams, D. S., Elastic stiffness and thermal expansion coefficient of boron nitride films. *J. Appl. Phys.*, **57** (1985) 2340–2.
- Hampshire, S., Engineering properties of nitrides. In *Engineered Materials Handbook*, Vol. 4: Ceramics and Glasses, ed. S. J. Schneider, ASM International, 1991, p. 819.
- Shaffer, P. T. B., Engineering properties of carbides. In *Engineered Materials Handbook*, Vol. 4: Ceramics and Glasses, ed. S. J. Schneider, ASM International, 1991, p. 808.
- Sacks, M. D., Lee, H.-W. & Pask, J. A., A review of powder preparation methods and densification procedures for fabricating high density mullite. In *Ceramic Transactions*, Vol. 6: Mullite and Mullite Matrix Composites, Eds S. Somiya, R. F. Davis and J. A. Pask, American Ceramic Society, Westerville, OH, 1990, p. 167.
- Aksay, A., Dabbs, D. M. & Sarikaya, M., Mullite for structural, electronic and optical applications. *J. Am. Ceram. Soc.*, **74** (1991) 2343–58.
- Chawla, K. K., *Ceramic Matrix Composites*, Chapman & Hall, London, 1993, p. 128.
- Ha, J.-S. & Chawla K. K., The effect of precursor characteristics on the crystallization and densification of diphasic mullite gels. *Ceramics International*, **19** (1993) 299–305.
- Ha, J.-S. & Chawla, K. K., Effect of SiC/BN double coating on fibre pullout in mullite fibre/mullite matrix composites. *J. Mater. Sci. Lett.*, **12** (1993) 84–6.
- Chawla, K. K., Xu, Z. R., Ha, J.-S., Lara-Curzio, E., Ferber, M. K. & Russ, S., Interfacial characteristics of mullite fiber/BN/coating/mullite matrix composites. In *Pro. Advanced Ceramic Matrix Composites*, ed. J. P. Singh, Amer. Ceram. Soc., 1994, p. 779.
- Chawla, K. K., *Ceramic Matrix Composites*, Chapman & Hall, London, 1993, p. 325.
- Lara-Curzio, E. & Ferber, M. K., *J. Mater. Sci.*, 1994, in press.
- Hsueh, C.-H., Evaluation of interfacial properties of fiber-reinforced ceramic composites using a mechanical properties microprobe. *J. Am. Ceram. Soc.*, **76** (1993) 3041–50.
- Kerans, R. J. & Parathasarathy, T. A., Theoretical analysis of the fiber pullout and pushout tests. *J. Am. Ceram. Soc.*, **74** (1991) 1585–96.

Sol-gel Mullite Matrix-SiC and -Mullite 2D Woven Fabric Composites with or without Zirconia Containing Interphase: Elaboration and Properties

Ph. Colomban,^{a*} E. Bruneton,^{a,b} J. L. Lagrange^a & E. Mouchon^a

^aONERA-OM, BP 72, 92322 Chatillon, France

^bCNRS-CECM, 15 rue G. Urbain, 94407 Vitry-sur-Seine, France

(Received September 1994; accepted 30 October 1995)

Abstract

The properties of composites made with fabrics of Nicalon[®] NLM202 SiC or Nextel[®] 440 mullite fibers are reported. The method used to make composites is a three stages sol-gel process: (i) in situ gelation of a mixture of alkoxides in a ceramic fiber fabric; (ii) the deposit of a matrix precursor onto the impregnated fabrics and (iii) hot-pressing of the stacked fabrics in a carbon mold. The composites have been studied by SEM and TEM. Three point flexural strength has been measured at room temperature and at 900°C in air. Local Young's modulus, microhardness and interfacial shear stress have been determined at RT. Micro-Raman spectra and X-ray microanalysis have been used to study the fiber-interface reactions. Using a mixture of aluminium-silicon ester and tributylborate as interface precursor, we obtained a carbon film free SiC-mullite sliding interface. The use of a complementary ZrO₂-GeO₂ gel interface precursor allows us to obtain dense composites at a low temperature exhibiting good mechanical properties (linear behaviour up to ~180 MPa, even after annealing in air). The effects of a zirconia interphase on the mechanical properties of mullite-mullite composite are also discussed.

Introduction

Many advanced aerospace systems require or would benefit from new low density materials for structural applications. Ceramic materials could replace existing metals and alloys, especially in corrosive environments. This is particularly true of those applications requiring materials working

at temperatures above 800°C, e.g. aircraft engine parts. For these applications the most promising class of new materials is ceramic woven fabric-reinforced ceramic matrix composites. The use of monolithic ceramics is limited by their intrinsic inability to tolerate mechanical damage without brittle rupture due to their polycrystalline state and the nature of the chemical bonds existing in these compounds. The use of long, continuous ceramic fibers embedded in a refractory ceramic matrix results in a composite material exhibiting enhanced toughness through a specific micromechanism at the fiber-matrix interface: the cracks appearing in the matrix are deflected, dissociated and then stopped at the fiber-matrix interface. Thus the composite materials exhibit a pseudo-plastic fracture easily observed in the load-strain plots. Calculations with safety coefficients would thus be possible for parts made of ceramic matrix composites as well the manufacture of complex architectures. For aerospace applications requiring high reliability, it is necessary to use woven ceramic fibers as reinforcement. At present, Nicalon[®] NLM202 SiC fibers are considered to be the most convenient fibers but mullite fibers such as Nextel[®] 440 also present some potential advantages in the preparation of composites exhibiting both good thermomechanical properties and oxidation resistance. One of the most interesting matrices is mullite. The interest in the mullite matrix arises from its superb thermal and chemical stability and from its relatively low temperature expansion, comparable with that of the fibers. Furthermore, its mechanical properties, up to 1300–1500°C are retained. Also, its low toughness and Young's modulus can be improved by zirconia dispersion.

Improvements can be made using the sol-gel method, which allows refractory oxide matrices such as mullite, alumina, zirconia^{1,2} to be processed

*To whom correspondence should be addressed. Also at CNRS-LASIR, 2 rue Henry Dunant, 94320 Thiais, France.

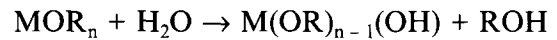
at relatively low temperatures (1000–1300°C) and fine grained ceramics to be produced with regular submicronic zirconia dispersion.³ Finally, as these matrices are free of alkali- or alkaline-earth ions, there is no formation of a carbon rich interface at the boundary of the Nicalon SiC fiber.⁴ This absence of a carbon film prevents rapid thermal degradation in oxidizing atmospheres. The reaction between the oxide fiber and the matrix has to be controlled in order to prevent the formation of a strong interfacial bond. In spite of the potential interest of mullite as a matrix for use in more or less oxidizing atmospheres, attempts to prepare long fiber reinforced mullite matrix composites remain limited. Jones *et al.*⁵ and Qui & Pantano⁶ have prepared mullite matrix composites using long SiC and carbon fibers. To date no work has been reported on the preparation and properties of woven fabric reinforced mullite matrix composites, except our preliminary reports of Refs 4 and 7.

In this paper we compare the properties of ceramic composites consisting of Nicalon[®] NLM202 (Nippon Carbon) SiC or with Nextel[®] 440 (3M) mullite fibers in mullite matrices, before and after annealing in air at temperatures between 900 and 1300°C. Emphasis is given on understanding the mechanical behaviour of each composite component: the fiber, the matrix and the fiber/matrix interface and interphases.

Experimental

Composite preparation

Our preparation process of two-dimensional (2D) woven fabric reinforced composites is based on the hydrolysis–polycondensation of alkoxides according to the following reaction



The resulting material is a gel (composition: $\text{MO}_{n-2x}(\text{OH})_x \cdot m\text{H}_2\text{O}$) which is converted by thermal treatment into a meso/microporous ‘glass’ and then, after the departure of the last OH^- , densification leads to a glass, a glass-ceramic or a ceramic depending on composition.^{1,2,8} The CMC’s preparation process takes place in three stages (Fig. 1):

- (i) impregnation of the fiber yarn of the fabrics with an interface fiber–matrix precursor (a liquid alkoxide mixture which slowly hydrolyses and polycondenses, *in situ* by reaction with air moisture into a gel);
- (ii) deposition of the fine amorphous and reactive–matrix precursor (a gel powder which has been converted by thermal treatment at ca. 600–800°C in a mesoporous xerogel in order to evacuate most of the water in the polymeric network and hence to reduce the shrinkage). This powder precursor is deposited onto the interface precursor impregnated fabric in the form of a suspension in chlorobenzene, with addition of PMMA;

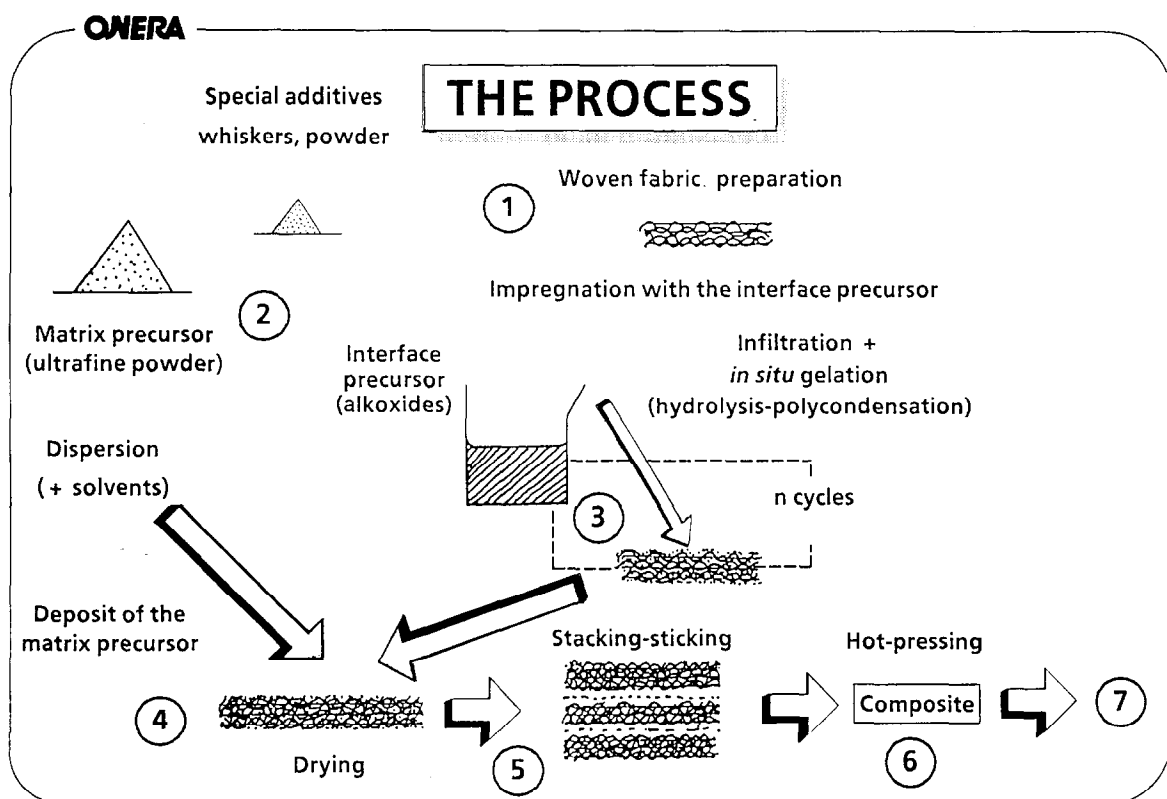


Fig. 1. Flowchart of the sol-gel route for the manufacture of ceramic fiber woven fabric-ceramic matrix composites.

- (iii) hot pressing of the impregnated and stacked fabrics in a graphite mold at a temperature between 1000 and 1400°C.

Details on the manufacturing technology are given in Ref. 9.

The problems arising in the preparation of refractory matrix dense composites leads to the difficulty of achieving an open porosity below 8–10%. The fiber must be thoroughly embedded in the matrix and the matrix must be incorporated through the voids between fibers (a few microns or less, in size). This is possible by infiltration of liquid or gaseous precursors for which the ceramic yield is necessarily low. It results in considerable shrinkage which generates new voids: the presence of the woven fabrics inhibits the coherent shrinkage of the matrix. The ceramic precursor can infiltrate the yarns reducing the porosity and the shrinkage creates voids. In the case of two-dimensional reinforcement: this dilemma is solved by the use of a very reactive matrix precursor in association with a liquid interface precursor which polycondenses within the fiber yarns into a gel. On heating, the gel is converted in glass-ceramic and gives rise to a temporary liquid sintering aid at the same temperature at which the matrix densification occurs.⁸ The liquid phase contributes to the densification by mass transport (liquid assisted sintering) but also helps to lubricate the powder rearrangement under pressure and to achieve a good contact between the grains coming from the matrix precursor and/or from the interface precursor despite the presence of a fiber network (Fiber volume: ~30–40%).

The matrix precursor is prepared by rapid hydrolysis of an alkoxide mixture diluted in propanol with very strong stirring.¹ The resulting gel is dried under IR bulbs and heated up to 750°C to reach the amorphous state. Densification occurs at about 1000°C for mullite with the dehydroxylation–nucleation–densification reaction.^{8,10,11}

Woven fabrics

Nicalon[®] NLM202 fibers (Nippon Carbon Co.) were woven by CRST (21350 Gisse, France) along four directions in the plane to give a ~1 mm thick fabric (surface mass: $76 \times 10^{-3} \text{ g/cm}^{-1}$). The SiC fiber diameter is ~15 μm and the thermal expansion of fiber is about $3\text{--}3.5 \times 10^{-6} \text{ K}^{-1}$.¹⁰ Yarns contain ~500 fibers.

Nextel[®] 440 mullite fiber (3M Co) were woven by Ets Cotton Frères (France) along two directions, within the plane to give a ~0.4 mm thick satin (surface mass: $22 \times 10^{-3} \text{ g/cm}^2$). The mullite fiber diameter is about 11 μm and a yarn contains 390 fibers. The thermal expansion is about $5 \times 10^{-6} \text{ K}^{-1}$.

Interface precursors

Different kinds of interface precursors (so-called because the fiber–matrix interface will result from the reaction between the fibers and the precursor) may be used, solely or in combination, depending on the matrix and the fibers.^{9,12} In the case of mullite matrix composites three different precursors are used:

- (i) a mixture of $(\text{OEt})_2\text{Al-O-Si}(\text{OEt})_2$ ester (ref. SiAl084 Dynasyl, from formerly Dynamit Nobel, now Hüls-France) and tributylborate (TBB, from Alfa-Ventron, ref. 10691), or tributylphosphate $\text{PO}(\text{O}_i\text{C}_4\text{H}_9)_3$ (TBP from Fluka, ref. 10138);
- (ii) pure zirconium i-propoxide (ZP, ref. 88733 from Fluka);
- (iii) a mixture of ZP and tetra-ethoxy-germane (TEOGe, prepared at the laboratory).

The transient liquid sintering aid results from the melting of B_2O_3 (~600°C), Ge and of GeO_2 (~1100°C), both liquids being eliminated by volatilization during the hot-pressing cycle or incorporated in the matrix. It is important that no traces remain present at the grain boundaries in order to maintain good mechanical properties at high temperatures or in water-rich atmospheres.

Mullite matrix

A mullite matrix reinforced with a dispersion of zirconia is prepared by instant hydrolysis of a mixture of ZP and aluminum isobutoxide and silicon methoxide diluted in propanol as described in Ref. 13. A submicronic dispersion of tetragonal zirconia is obtained, (Fig. 2). The great advantage of the alkoxide route is that it blends the liquid gel-formers very homogeneously and keeps this homogeneity up to the nucleation at about 1000°C.^{1,3} The steady size of the precipitates whatever the thermal treatment time is due to the low diffusion coefficient in the mullite glass-ceramic below 1400°C. The equilibrium between the crystallites and the host amorphous or spinel-like matrix depends only on temperature and composition.^{3,11,14}

Hot pressing

Pressure sintering is performed under vacuum up to 400°C, a N_2 atmosphere (1 atm) being applied above 400°C. The heating rate is 250°C/h up to 600°C and increased to 350°C/h up to the dwell temperature. A pressure of 2.5 MPa is applied at the beginning of the hot-pressing cycle in order to get a good contact between the fiber yarns and the interphase and matrix precursors. The applied pressure is then raised to 20 MPa between 600 and 900°C, this maximum value being reached before the beginning of the mullite intrinsic shrinkage (~850°C), related to the dehydroxylation–

nucleation reaction,^{8,11} the pressure is removed just before the end of the dwelling time. Cooling is complete after 5 h.

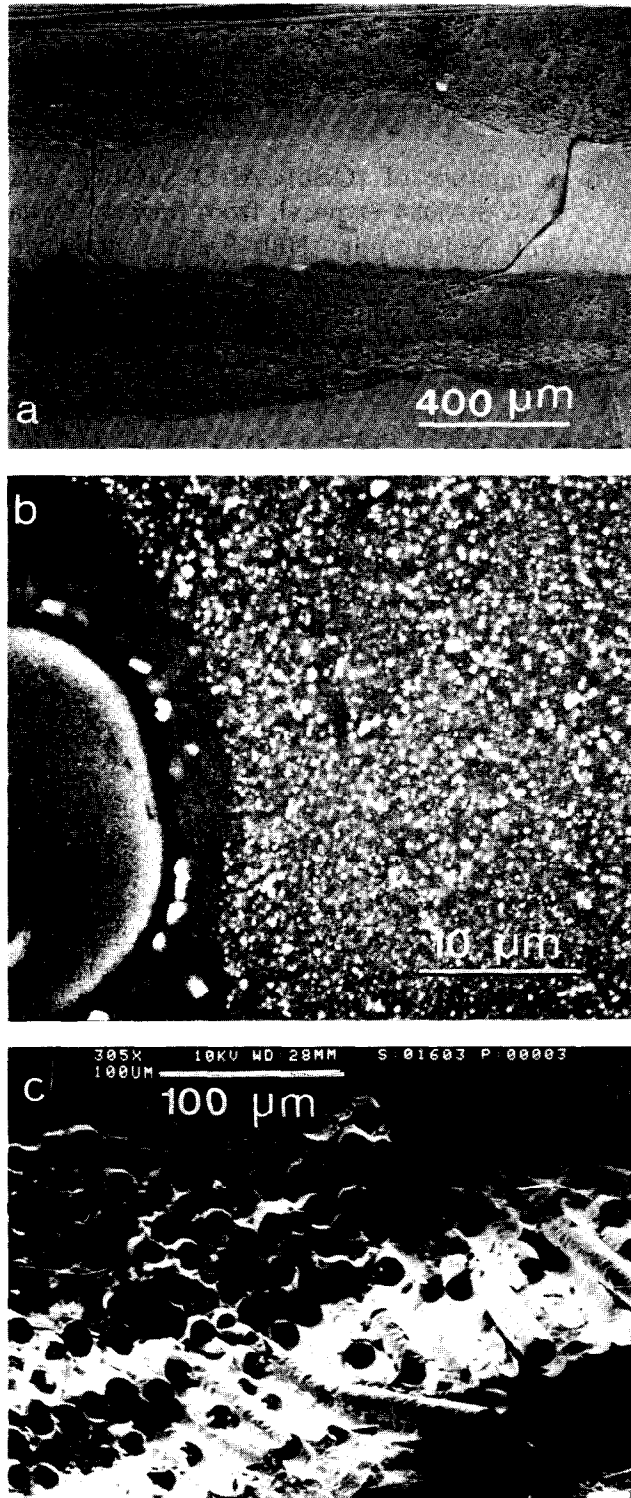


Fig. 2. Photomicrograph of a Nicalon NL202[®] SiC fiber woven fabric-mullite matrix composites pressure sintered at 1350°C: (a) polished section: a regular $3\text{Al}_2\text{O}_3\cdot 2\text{SiO}_2$ matrix cracking pattern is observed, mean intercrack distance ~ 1 mm; (b) detail of the fiber-matrix interface; the zirconia precipitates of the matrix appear in white (mean matrix composition: $6\text{Al}_2\text{O}_3\cdot 4\text{SiO}_2\cdot \text{ZrO}_2$). The zirconia-free interphase around the SiC fiber arises from the transformation of the interface precursor deposit TBB+3SiAl (mean composition: $\text{Al}_2\text{O}_3\cdot 2\text{SiO}_2$ with B_2O_3 traces); (c) fracture of a Nextel 440 fiber fabric-mullite matrix composite pressure sintered at 1200°C (interface precursor: TBP+SiAl).

Interface precursor-matrix precursor reaction

Figure 2 gives an illustration of the interphase formation between the fiber and the matrix. The matrix composition was chosen to be $6\text{Al}_2\text{O}_3\cdot 4\text{SiO}_2\cdot \text{ZrO}_2$. The interface precursor is the mixture of TBB and SiAl ester (oxide composition: $\text{Al}_2\text{O}_3\cdot 2\text{SiO}_2\cdot n\text{B}_2\text{O}_3$). We can observe the homogeneous, submicronic dispersion of zirconia precipitates in the mullite matrix and a zirconia free contour around the SiC fiber can be observed (zirconia appears white in the SEM photomicrograph due to the high number of electrons of Zr). The contour corresponds to a silica-rich mullite glass-ceramic with nanometric mullite crystals created by the pyrolysis of the interface precursor gel. However, some zirconia crystals are observed at the fiber periphery because of zirconia precipitation through reaction with the temporary liquid sintering aid.

Techniques

The expansion measurement was achieved using an Adamel Lhormargy DI24 apparatus (Instrument SA, Longjumeau, France) with silica glass rod and support. Dilatometric curves were drawn under vacuum at heating and cooling rates of 5°C/min from room-temperature up to 900°C. Sample dimensions were $25 \times 10 \times 10$ mm³.

Flexural strength was recorded by three point bending tests using a bar specimen (35 or 50 mm length) over a 30 mm span at a cross-head speed of 0.1 mm/min. Tests were performed at room temperature and at 900°C in air after 30 min stabilization (heating rate 300°C/h). Typically three samples were broken for each composition at both temperatures.

Fracture surfaces and sliced or polished sections of the samples were observed using an optical microscope or by scanning electron microscopy (Cambridge Scan 200 KV). TEM investigations were performed using 200 KV microscopes (Jeol 2000 FX and Topcon 002-B) both equipped with EDX analysis with optimal 5 nm spatial resolution. The standardless metallurgical thin film (SMTF) method was used to determine the local composition.

Local Young's modulus, microhardness and interfacial frictional stress (IFS: τ) were determined using a home-made Vickers microindenter instrument and models described in Ref. 15. The load cell measures loads up to 1 N with an accuracy of about 500 μN . The capacitive displacement gauge has an accuracy of some nanometers. The loading rate is load-controlled and varies from 7 to 30 mN/s. The position of the indenter relative to the polished surface of the sample and the applied

load were measured continuously during testing. This enables the hardness and Young's modulus to be determined without the need for direct imaging of the indentation. However, the size and shape of the indentation were always checked afterwards and the indentation axis position was checked using the method described in Ref. 15.

Micro-Raman spectra were recorded at the 514.5 nm exciting wavelength of an Ar⁺ laser using a XY Dilor multichannel microprobe (Lille, France) equipped with a liquid nitrogen cooled Wright CCD (1200-300) array detector.

Results and Discussion

Porosity and macroscopic mechanical properties

SiC-mullite composites

Preliminary work has shown that 2D fabric SiC fiber/mullite matrix composites prepared by the above method exhibit a RT dissipative fracture (Fig. 3) and a rather good linear limit of strength behavior when a 1TBB + 3SiAl (volume ratio) interface precursor was used.⁷ On the other hand, the deposit only the TBB precursor leads to a brittle composite.¹⁶ Optimisation of the enduction process lowers the open porosity to about 9% and

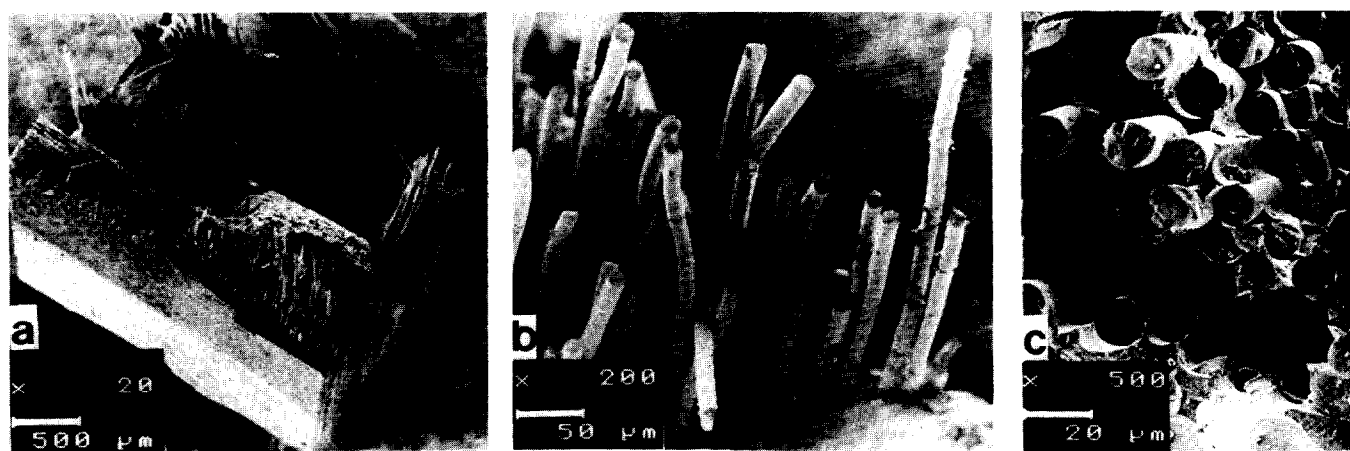


Fig. 3. Photomicrograph of a SiC fiber woven fabric-mullite matrix composite pressure sintered at 1350°C (TBB+3SiAl interface precursor). Fiber volume: 0.3; open porosity: 12%: (a) fracture at RT; (b) detail of the fiber pull-out at RT, and (c) after 900°C.

Table 1. Open porosity (*P*) and flexural strength (σ) of composites prepared using various interface and matrix precursors

Fabrics (fibers)	Matrix	Interface precursors ^c (volume ratio)	Sintering temperature and dwell-time	σ (MPa) ^d	P (%)
4 dir (NLM202) ^a	3Al ₂ O ₃ ·2SiO ₂	TBB	1350°C (45 min)	<100 (brittle) ^e	~15
	6Al ₂ O ₃ ·4SiO ₂ ·ZrO ₂	1TBB	1350°C	~120–130 (100) ^f	9–14
		3SiAl	45 min	(dissipative) ^e ~150–180 (120) ^f	9
			90 min	(dissipative) ^e 150 μm	
Satin (Nextel 440) ^b	3Al ₂ O ₃ ·2SiO ₂ ·0.1TiO ₂	1ZP	1300°C	RT ~260 ± 30	3 ± 0.5
		1TEOGe + 1TBB	90 min	900°C ~280 ± 20 (190) ^f	
		3SiAl		(dissipative) ^e 500–2000 μm	
Satin (Nextel 440) ^b	3Al ₂ O ₃ ·2SiO ₂ ·0.1B ₂ O ₃	1SiAl + 1TBP	1200°C	100 (brittle)	8%
		ZP	1200°C	70 (dissipative) ^e 50–100 μm	20%

^aNicalon[®], Nippon Carbon; the volume of fiber is about to 35–40%.

^b3M Co.

^cTBB: tributylborate; SiAl: SiAl 084 Dynasyl ester; ZP: zirconium i-propoxide. TBP: tributylphosphate; TEOGe: tetraethoxygermane.

^dIn air, at RT or at 900°C.

^eFracture behaviour, fiber pull-out.

^fLinear limit.

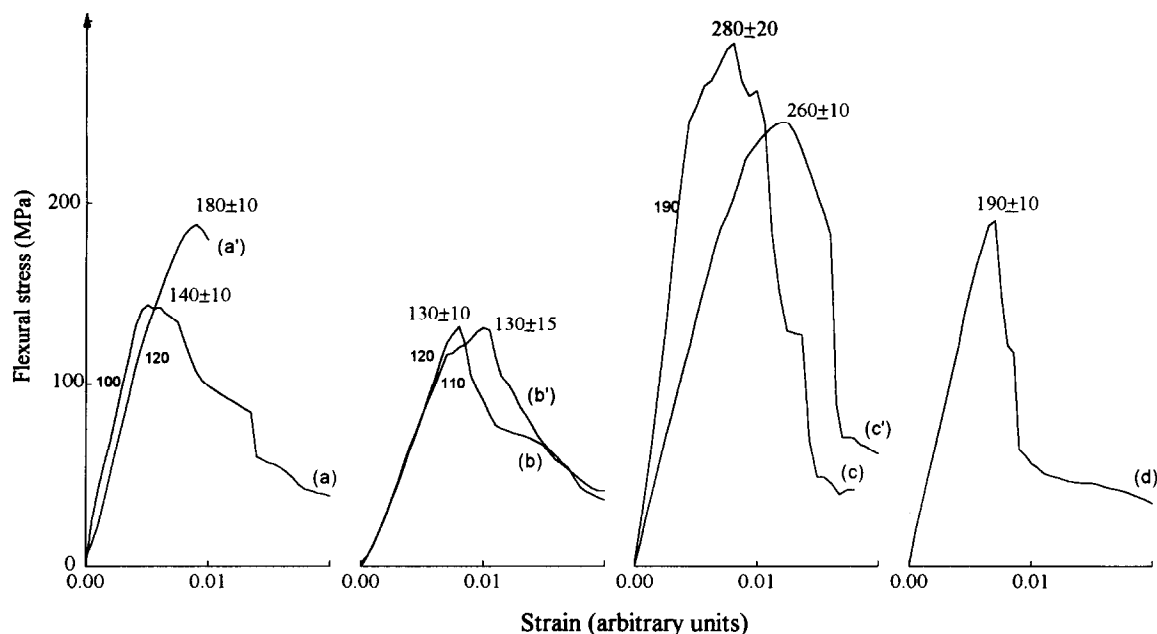


Fig. 4. Flexural stress–strain plots for various composites made with a $6\text{Al}_2\text{O}_3\cdot 4\text{SiO}_2\cdot \text{ZrO}_2$ matrix. Curves are recorded at RT (a, b, c, d) or at 900°C (a', b', c') in air. Samples are made with the TBB+3SiAl interface precursor, with (c, c', d) or without (a, a', b, b') addition of zirconium propoxide and tetra-ethoxygermane. The samples were sintered for 90 min at 1300°C (a, a', c, c', d) or at 1350°C with a 5 min excursion to 1450°C (b, b'). Curve d was recorded at RT after 30 h annealing at 1200°C , in air. Arbitrary relative scales are used in x-axis: the comparison is made for similar bar specimens (same number of fabrics sheets, same thickness).

the corresponding ultimate strength reaches 150 MPa at RT and at 900°C (Table 1 and Fig. 4) for zirconia containing mullite matrices. The calculated strain values are close to 0.5%. Decreasing the sintering temperature from 1350 to 1300°C is possible without increase of the porosity if the dwelling time is increased to 90 min. At the same time, the linear strength limit is increased up to 120 MPa. With the addition of $\text{ZrO}_2\text{-GeO}_2$ interface precursor, the densification begins below 800°C (instead of 950°C) and open porosity of ~3% is obtained after hot-pressing at 1300°C . The ultimate strength reaches 250 MPa at RT and 300 MPa at 900°C , in air. Furthermore, the equivalent strain calculated for the fibers located in the medium plane is ~0.9% at the ultimate strength which corresponds to the typical value measured for SiC fibers heated at $1200\text{--}1300^\circ\text{C}$. The linear limit is close to 180 MPa and is not lowered after 30 h annealing in air at 1200°C (Fig. 4, size of annealed samples: $35 \times 5 \times 4$ mm). Good mechanical properties are thus observed for 2D SiC fiber and mainly tetragonal zirconia particulates–reinforced mullite matrix composites.

Mullite–mullite composites

Using mullite fiber woven fabrics, the achievement of low porosity composites without fiber–matrix reaction is much more difficult due to the high reactivity of the mullite fibers. When the interface precursor consisted of a mixture of SiAl ester and TBP as sintering aid, a rather good densification

of the composite is obtained (open porosity ~8%). Neither matrix microcracking nor fiber pull-out can be deduced from the stress–strain plots (a straight line up to the failure); however fiber pull-out, typically in the range of $5\text{--}50\ \mu\text{m}$, can be observed in the fracture micrograph (Fig. 2). In order to prevent reaction between the matrix and the reinforcing fibers, we deposited an inert layer between the mullite matrix and the mullite fibers. This interphase may be selected from refractory compositions which should remain stable during the hot-pressing and at the working temperature. Thus zirconia has been chosen as interphase.

A significant work of fracture is observed on the strain–stress plot measured at samples consisting of the Nextel® 440 satin coated with ZrO_2 interphase in a B_2O_3 doped mullite matrix. X-ray diffraction patterns indicate that the zirconia interphase has monoclinic symmetry. The mechanical performances remain poor ($\sigma \sim 70$ MPa, Table 1) because of the high open porosity (~20%) and the low fiber volume fraction (~30%). Further work is needed to know whether the remaining porosity promotes or inhibits the dissipative character of the fracture, and to improve the mechanical strength.

Matrix, fiber and interphase characterization methodologies

The measurement of local mechanical properties is an important step in the understanding of the macroscopic behaviour of composites. The indentation hardness test is probably the simplest

Table 2. Local Young's modulus (E) and Vickers microhardness (H_v) of various mullite samples and fibers

Samples	E (GPa)	H_v (GPa)	Remarks
$3Al_2O_3 \cdot 2SiO_2$	180 ± 17	12.4 ± 2	Hot-pressed — 1600°C (porosity <0.5%)
$3Al_2O_3 \cdot 2SiO_2^a$ with zirconia precipitates (10%, molar)	240 ± 15	16 ± 2	Hot-pressed — 1600°C (porosity <0.5%)
$3Al_2O_3 \cdot 2SiO_2 \cdot 0.1B_2O_3$ (matrix of a composite)	160 ± 20	12.5 ± 5	Hot-pressed — 1350°C (composite porosity ~12%)
$6Al_2O_3 \cdot 4SiO_2 \cdot ZrO_2^b$ (matrix of a composite)	150 ± 20	17 ± 3	Hot-pressed — 1300°C (composite porosity ~9%)
$6Al_2O_3 \cdot 4SiO_2 \cdot ZrO_2^b$ (matrix of a composite)	200 ± 20	18 ± 3	Hot-pressed — 1350°C (composite porosity ~9%)
$Al_2O_3 \cdot 2SiO_2$ (interphase of a composite)	90 ± 10	8 ± 2	Hot-pressed — 1350°C (composite porosity ~9%)
SiC fiber in composite pressure sintered at			
1000–1200°C	210 ± 20	25 ± 0.5	
1350°C	200 ± 30	20 ± 1	
1350°C ^d		17.5 ± 1	

^aMicron dispersion; ^bSubmicron dispersion; ^cMeyer law: $h = \alpha F^\beta$ with $\alpha = 0.1 \pm 0.01$ and $\beta = 0.623 \pm 0.03$ (F in g, d in μm); ^da 180 min annealing at 900°C in air was performed after preparation.

method of measuring the mechanical properties of materials. The use of load-controlled depth-sensing hardness tester which operates in the (sub)micron range enables the study of each component of the composite. Following the work of Loubet *et al.*,¹⁷ we extract Young's modulus (E) and the Vickers microhardness (H_v) from the load–displacement

plot during the unloading displacement.¹⁵ Results are given in Table 2. Typical applied load–penetration depth plots are shown in Fig. 5 for the indentation of the silica-rich interphase and of the tetragonal zirconia reinforced mullite matrix. E and H_v values are calculated using Loubet's model:

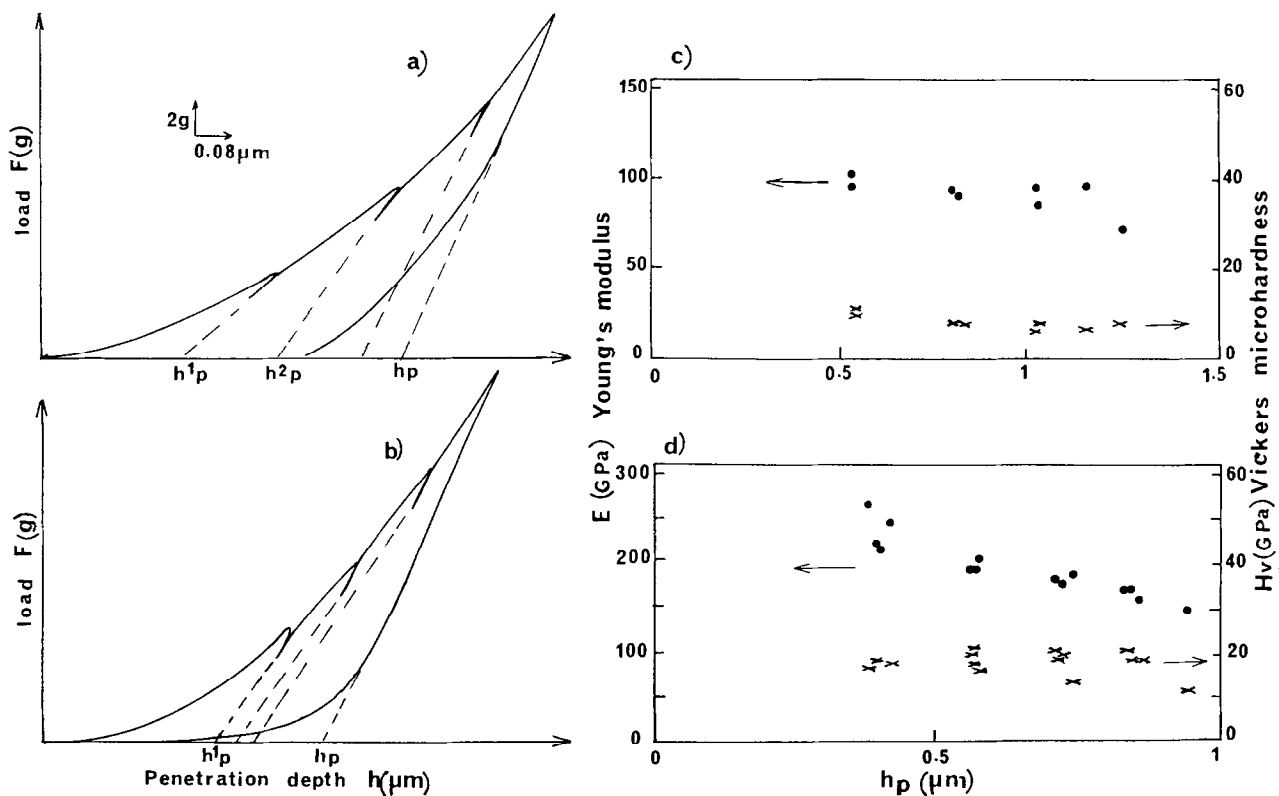


Fig. 5. $6Al_2O_3 \cdot 4SiO_2 \cdot ZrO_2$ mullite matrix; Indentation plots of applied load (F) against penetration depth (h) for (a) the fiber matrix interphase (TBB+3SiAl interface precursor, mean composition after sintering: $Al_2O_3 \cdot 2SiO_2$) and (b) the matrix (mean composition $6Al_2O_3 \cdot 4SiO_2 \cdot ZrO_2$) region for a composite pressure sintered at 1350°C. Partial unloadings are made in order to determine the microhardness H_v and the Young's modulus E for different loads as described in Ref. 15. The H_v and E values are deduced from the plateau observed in the plots given in (c) and (d) for the interphase and the matrix, respectively.

$$E = \frac{\partial F}{\partial h} \left(\frac{\pi}{2} \right)^{1/2} \frac{1}{2 \sqrt{2h_p \tan \theta}} \text{ and } H_v = \frac{F \cos^2 \theta}{4h_p^2 \sin \theta}$$

2θ being the angle of the Vickers pyramidal indenter and h_p the plastic depth deduced from the intersection between the extrapolation of the straight line occurring when the load is lowered (unloading cycle) and the abscissa. At very small penetration depth the measurement error is large due to the diamond tip defect and the difficulty of determining the contact point ($F = 0$ origin). At high penetration depth cracks may occur deforming the unloading trace.¹⁵ Thus the observation of a plateau is needed to determine the true E and H_v values (Fig. 5 (c,d)).

Comparison is made with pure mullite and zirconia reinforced mullite monolithic ceramics hot-pressed at 1600°C for 1 h (Table 2). The local mechanical properties of mullite matrices sintered at 1350°C are very similar to those of dense hot-pressed monoliths. A large increase in the E and

H_v values is observed for zirconia containing samples. The Young's modulus of the silica-rich mullite glass surrounding the fibers, arising from the thermal treatment of the alumino(boro)silicate interface precursor is much lower: ~90 GPa (H_v ~8 GPa). This low value corresponds to that usually measured for glass-ceramics.¹⁸

Indentation of the fiber allows one to observe the degradation of the fiber properties as a function of the processing and the thermal ageing. No degradation is evident in composites prepared below 1300°C: E and H_v values remain unchanged. On the other hand, the indentation of fibers of composites sintered above 1300°C indicates a lowering of both Young's modulus and micro-hardness. Similar conclusions can be made after air annealing at 900°C (Table 2).

Examination of the indentation figures shows that fiber fractures are numerous and if the applied load exceeds the threshold load (F_s) (Fig. 6), the fiber slides within the matrix and a black circle

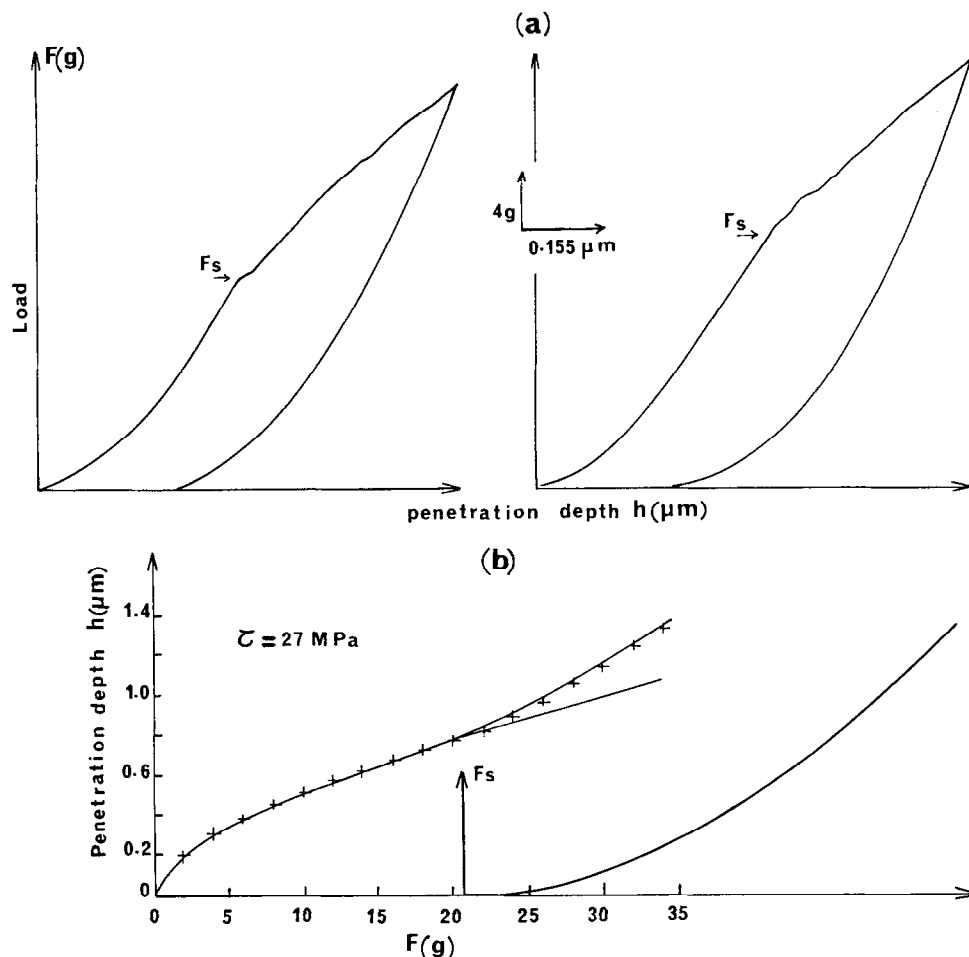


Fig. 6. (a) Typical indentation plots of applied load (F) against penetration depth (h) for various SiC fibers embedded in a silica rich-mullite glass-ceramic matrix. The steps (arrows) correspond to the debonding and the onset of the sliding regime. (b) Example of the calculation of the interfacial shear stress (τ). Crosses: experimental data from the indentation plots. Lines: calculations. The results are interpreted using a Meyer law ($h = \alpha F^\beta$) which describes the fiber hardness before the threshold load (F_s) plus the Marshall model in the sliding regime, after the threshold:

$$F > F_s : h = \alpha F^\beta + \frac{(F - F_s)^2}{4\pi^2 r^3 E \tau}$$

(E : fiber Young's modulus, r : fiber radius).

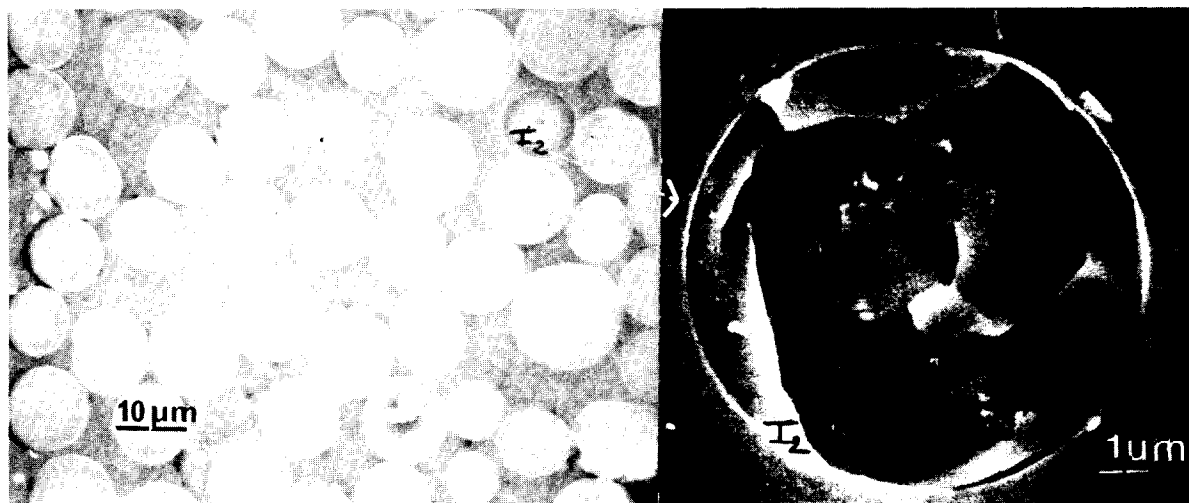


Fig. 7. SEM photomicrographs (secondary electron mode) showing SiC Nicalon[®] indented fibers (left); see the white contour due to the fiber debonding and the remaining step (right).

becomes visible at the fiber periphery (Fig. 7) due to the step formation: part of the fiber push-down is permanent.

Comparison of the thermal expansion coefficient measured parallel or perpendicularly to the woven fabrics gives further information about the composite. The parallel value corresponds to that imposed by the SiC fibers whereas the perpendicular value is the mean of the thermal expansion of the matrix and that of the SiC fibers. Thermal expansion coefficients are given in Table 3. A rather good agreement is obtained. No significant discrepancies are observed for zirconia-free and zirconia reinforced matrix. On the other hand, a slight shrinkage is observed above 900°C, perpendicularly, which could indicate some softening of the glassy mullite-like second phase.

Fiber/matrix interface

Figure 8 compares the line scan profiles across SiC fibers in two composites prepared using the TBB+3SiAl interface precursor with or without the addition of the ZP+TEOGe interface precursor.

In both cases, we observe that some aluminium ions replace silicon ions at the fiber periphery (penetration depth $\sim 3 \mu\text{m}$ after 45 min sintering at 1350°C). Germanium is present in the fiber periphery.

Typical transmission electron microscopy thin film micrographs are shown in Fig. 9. Four interphases are found in the interfacial region. The SiC fiber (phase no. 1) is identified by its typical electron diffraction pattern which exhibits the 111, 220 and 311 rings of the cubic βSiC structure. EDX spectra show a 5% atomic aluminum concentration. This result confirms the 'macroscopic' electron microprobe analysis of Fig. 8. The fiber crust near the interface is enriched in oxygen and depleted in silicon and carbon. Moreover, we notice in Fig. 8 that the oxygen peak of the macroscopic line scan is more intense at the fiber periphery corresponding to the Si depleted region. This indicates a superficial oxidation of the fiber. At a very fine scale the transmission electron microscope image shows an external (phase no. 2), amorphous layer of several tens of nanometers

Table 3. Mean thermal expansion coefficients (α) of 4 dir SiC fiber^a-mullite matrix composites

Sintering ^b temperature	Open porosity (%)	$\alpha_{25 \text{ } 800^\circ\text{C}} (10^{-6} \text{ } ^\circ\text{C}^{-1})$		$\alpha_{25 \text{ } 1000^\circ\text{C}} (10^{-6} \text{ } ^\circ\text{C}^{-1})$	
		//	\perp	//	\perp
1300 ^c	12	3.7	3.2	3.7	2.6
1350 ^d	13.5	3.5	3.1	3.4	2.3
1300 ^e (30 h in air at 1200°C)	3	4	— ^f	3.8	— ^f

^aNicalon NLM202[®], the fibers are woven along four directions in a plane.

^bDwell-time: 30 min.

^cMatrix :6Al₂O₃·4SiO₂·ZrO₂, interface precursor: 1TBB+3SiAl (see Table 1 for definition).

^dMatrix 3Al₂O₃·2SiO₂·0.1B₂O₃, interface precursor: 1TBB+3SiAl.

^eMatrix 6Al₂O₃·4SiO₂·ZrO₂, 1TBB+3SiAl and ZP+TEOGe interface precursors are simultaneously used.

^fNot measured.

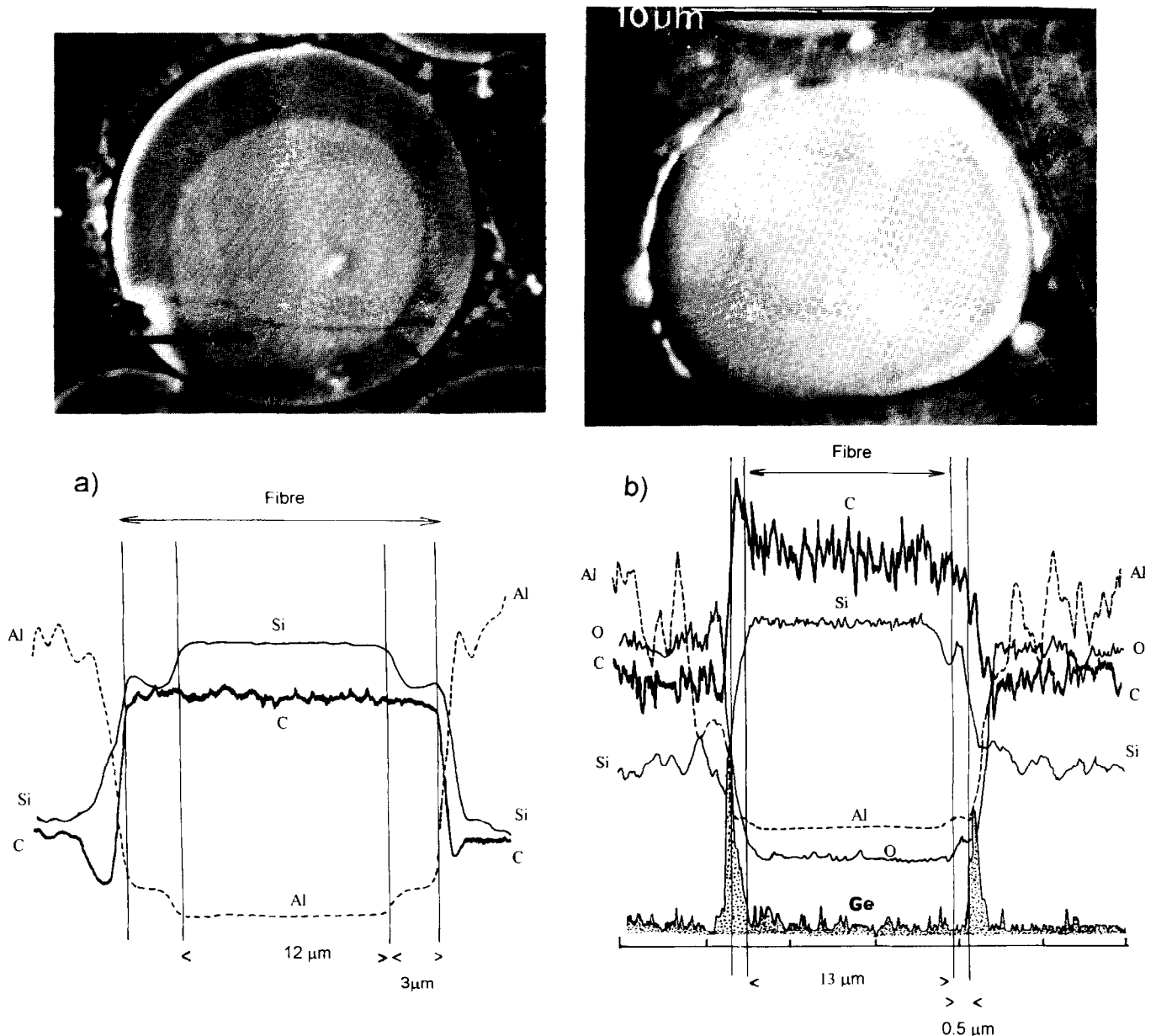


Fig. 8. SEM photomicrographs and X-ray line scan profiles recorded with a CAMEBAX electron microprobe across SiC Nicalon[®] fiber sections of composites prepared using the TBB+3SiAl interface precursor without (a) or with (b) addition of the ZP+TEOGe interface precursor. Al, Si, C, O, Zr and Ge profiles are measured (sintering temperature: (a) 1350°C; (b) 1300°C).

thickness. This oxide phase contains about 10 at% Al and 90% Si, respectively. Only carbon traces are detected by EDX and electron diffraction and this zone did not display the 'white' layer and the corresponding rings of graphitic carbon as observed in many other composites.^{4,19-21} The interface precursor leads to small acicular $3\text{Al}_2\text{O}_3 \cdot \text{SiO}_2$ mullite crystals (phase no. 3) dispersed in a glassy phase (phase no. 4). The composition of this last phase is 60 mol% SiO_2 , 40 mol% Al_2O_3 with a relatively intense carbon signal (the size of the analyzed area is about $10 \times 10 \text{ nm}^2$). The origin of the relatively high carbon content of this phase can be found in the organic traces arising from the pyrolysis of the interface precursor. Incompletely hydrolyzed branches often remain in the *in situ* gelled interface precursor. The interfaces appear to be free of a carbon

film. However, these observations do not exclude the presence of a few atomic carbon planes around the SiC fibers, as observed at the interface of SiC whiskers.²² The carbon film, if such a film is present, is thinner than that usually observed in composites made with alkali or earth-alkali-containing matrices.¹⁹⁻²¹ Furthermore, TEM examination of the fiber/matrix interface of a composite annealed for a few hours in air at 1470°C (Fig. 9(b)) shows that the main changes are: (i) the growth of the mullite crystals; (ii) the punctuation of the SiC fiber rings which indicates the onset of the crystallization.

Fiber/matrix sliding properties

The high strength and toughness of glass-ceramic matrix composites result directly from the low

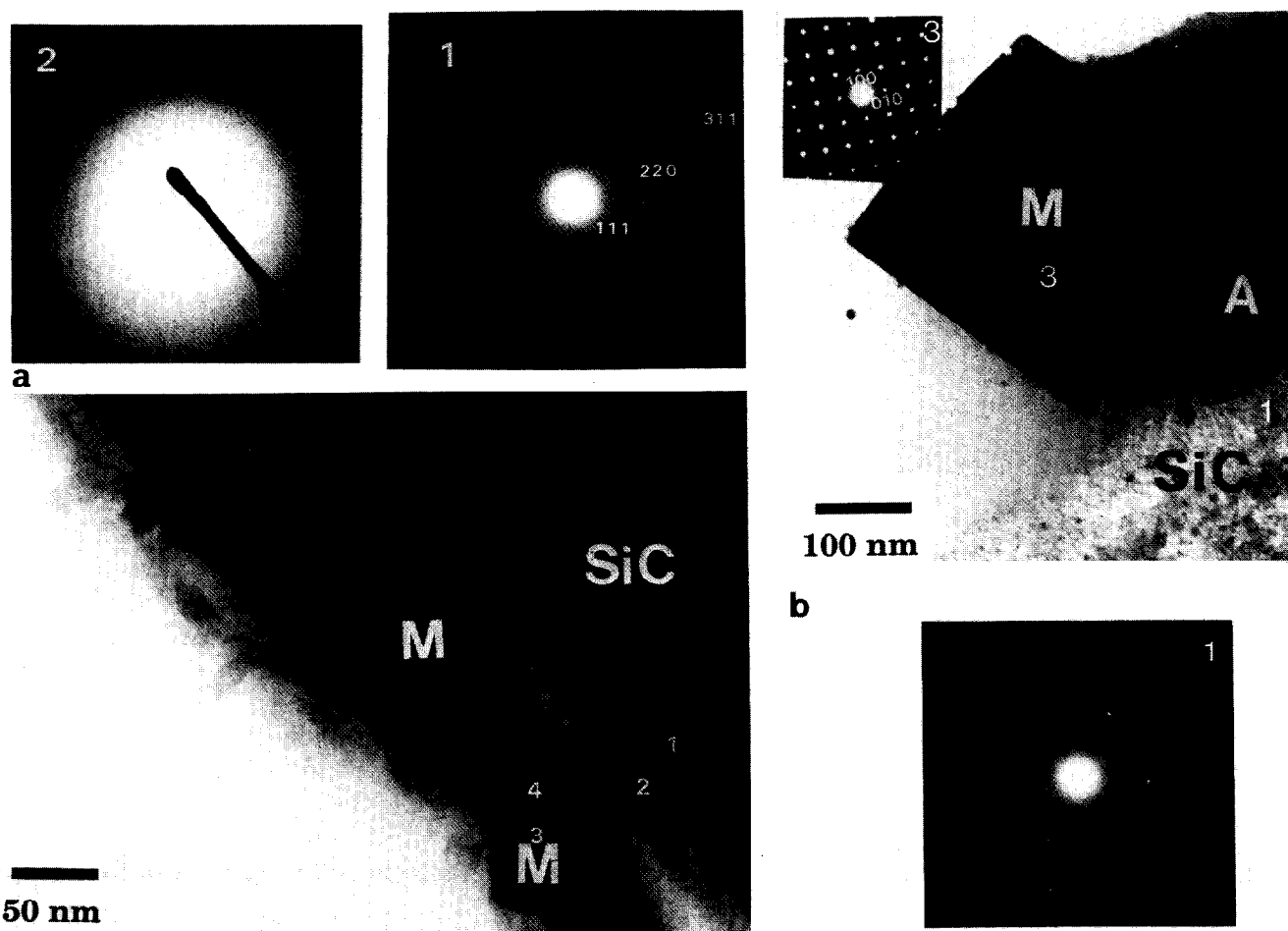


Fig. 9. TEM image of a SiC Nicalon[®] NLM202 fiber woven fabric-embedded in $(3\text{Al}_2\text{O}_3 \cdot 2\text{SiO}_2 \cdot 0.1\text{B}_2\text{O}_3)$ mullite matrix composite elaborated using the TBB+3SiAl interface precursor and pressure sintered at 1350°C . (a) Interfacial regions are: (1) fiber; (2) external region; (3) mullite crystal; (4) amorphous aluminosilicate phase. (b) After annealing for 3 h at 1470°C , in air.

fiber/matrix bonding originates in the processing. Usually, a reaction between SiC Nicalon fibers and an alkali- or earth-alkali-containing matrix leads to the formation of a thin carbon-rich interfacial layer (~ 100 nm) referred to as the carbon interphase.^{19–21} This interphase acts as a ‘fuse’, deflecting the matrix microcracks parallel to the fiber axis and thus avoiding the early failure of the fibers. This interphase is formed *in situ* during the hot-pressing as a result of the fiber/matrix chemical reaction or results from the deposit of a thin coating of C or BN when non-reactive matrices are used.²³

Another important parameter controlling the fiber/matrix bonding is the sign and the level of the residual mechanical stresses in the composite after processing arising from the thermal coefficient expansion mismatch. Too high a radial compressive residual stress increases the fiber/matrix bonding and is usually detrimental.

The sliding strength is usually measured on 1D composites using instrumented or non-instrumented micro-hardness tester following the method of Marshall.^{24–26} The fiber to be tested is selected

with regard to its axial position (circular section) and to have a uniform arrangement of distances from neighbouring fibers. Its diameter is measured after indentation. If the indent is not centered or if there is the least sign of fiber splitting, the measurement is rejected. Examples of applied load indenter/tip displacement are given in Fig. 6. Three regions are clearly distinguished on the load (F)–depth (h) plots:

- (i) the first polynomial regime $h = \alpha F^\beta$ related to the fiber indentation and its elastoplastic deformation under the sharp indenter (see above, Loubet’s model, $F < F_s$),
- (ii) a region characterized by a lower rate of load increase, a few steps often being observed at the limit between the elastoplastic response of the fiber and the debonding-plus-sliding regime ($F \sim F_s$),
- (iii) a third region can be observed when the pyramidal diamond tip comes into contact with the matrix ($F > F_s$).

The interfacial frictional stress (τ) related to sliding may be measured in 2D material if the fiber curvature is larger than the debonding length

induced by fiber sliding. The very large yarn curvature in 4-direction woven fabrics (curvature radius > a few tens of centimetres whereas debonding length ranges between 50 and 500 μm , typically e.g. see Fig. 3) makes possible experiments and calculations.

The calculation of the interfacial stress (or sliding strength) τ is made using Marshall's uniaxial model. The elastoplastic contribution of the fiber before the sliding threshold (F_s : threshold load) is assumed to follow a Meyer law:¹⁵

$$h = \alpha F^\beta \quad (\forall F \leq F_s)$$

h : penetration depth, F : applied load

In the sliding regime $\forall F > F_s$:

$$h = \alpha F^\beta + \frac{(F - F_s)^2}{4\pi^2 r^3 E \tau} \quad (1)$$

E : Young's modulus, r : radius of the fiber, respectively.

A more accurate model has been proposed:¹⁵

$$h = \alpha F^\beta + \frac{F^2 - F_s^2}{4\pi^2 r^3 E \tau} \quad (2)$$

This last model gives a τ -value 2–3 times larger than that calculated from model 1. In fact, it is very difficult to determine the true interfacial frictional stress and to compare the τ values calculated by different authors. Only comparative studies using the same model—and the same apparatus—are significant. The main results are summarized in Table 4 and typical curves are shown in Fig. 6. Comparison of the experimental data with the calculation (model no. 1) shows a rather good agreement. A similar agreement is obtained using model no. 2. A criterion for choosing between model no. 1 and model no. 2 is the height of the residual step after indentation.¹⁵ However, the measurement is difficult and the thermally induced stress should also be taken into consideration.²⁶ Our τ values may be considered as comparative data. The τ value is rather constant whatever the sintering temperature (1350–1450°C temperature range). On the other hand, the threshold load

is lowered when zirconia reinforced mullite is used as matrix. Comparison with experiments (using the same model and instrument) on SiC/LAS (or MLAS) matrix composites shows that our F_s values remain large ($\tau_{\text{LAS}} \sim 3\text{--}8$ Mpa). The fibers can be initially debonded in the LAS (MLAS) matrix ($F_2 \leq 2$ g).¹⁵ A large increase in the τ value is observed after annealing in air. This is consistent with the decrease in the area of the strain–stress plot (Fig. 4) and with the TEM examination: the fiber/matrix boundary is well-defined in the 1350°C sintered sample whereas a corrugated front is observed in the sample annealed for 3 h at 1470°C (Fig. 9). Benoit *et al.*²⁷ have demonstrated that the interface sliding behaviour is controlled by the difference between the roughness induced misfit and the thermally induced gap. The lack of a visible C film in our SiC-mullite composites could explain why our τ values remain 4–5 times larger than those measured on composites exhibiting a well-defined carbon-rich interface (e.g. SiC/LAS matrix composite). This also explains why the thermally induced degradation is slower in SiC/mullite composites than for example in SiC/LAS composites.

Thermal degradation of the matrix and fiber/matrix interphase

TEM investigation and microindentation analysis have demonstrated that the fibre–matrix interface changes after thermal annealing. Transformations are also seen in the matrix. Figure 10 shows micro-Raman spectra recorded in different places for a germanium containing composite annealed for 30 h at 1200°C in air. This annealing being performed on a very small sliced rod, it represents a brutal thermal ageing. After annealing, we observe that zircon (ZrSiO_4) replaces the (tetragonal and monoclinic) zirconia precipitates in the matrix. The complete disappearance of tetragonal zirconia indicates that the smaller grains have been first transformed into zircon, even though the heating temperature is lower than the usual limit for the reaction mullite + zirconia \rightarrow zircon + alumina ($> 1300^\circ\text{C}$). The germanium phase exhibiting the strong 300 cm^{-1} Raman peak remains present (white

Table 4. Interfacial shear stress (τ) and threshold load (F_s) of SiC fiber/mullite matrix composites^a

Matrix	Sintering temperature	F_s (g)	τ_1^c (MPa)	τ_2^c (MPa)
$3\text{Al}_2\text{O}_3 \cdot 2\text{SiO}_2 \cdot 0.1\text{B}_2\text{O}_3$	1350°C	15–25	20 ± 5	~50
$6\text{Al}_2\text{O}_3 \cdot 4\text{SiO}_2 \cdot \text{ZrO}_2$	1350°C	10–18	22 ± 5	~50
	+2 h		≥ 80	≥ 200
	at 900°C in air			
	1450°C	15–25	24 ± 7^b	~50

^aAt least 12 fibers are studied.

^bMany fibers are crushed under indentation

^c τ_1 : model of eqn (1); τ_2 model of eqn (2).

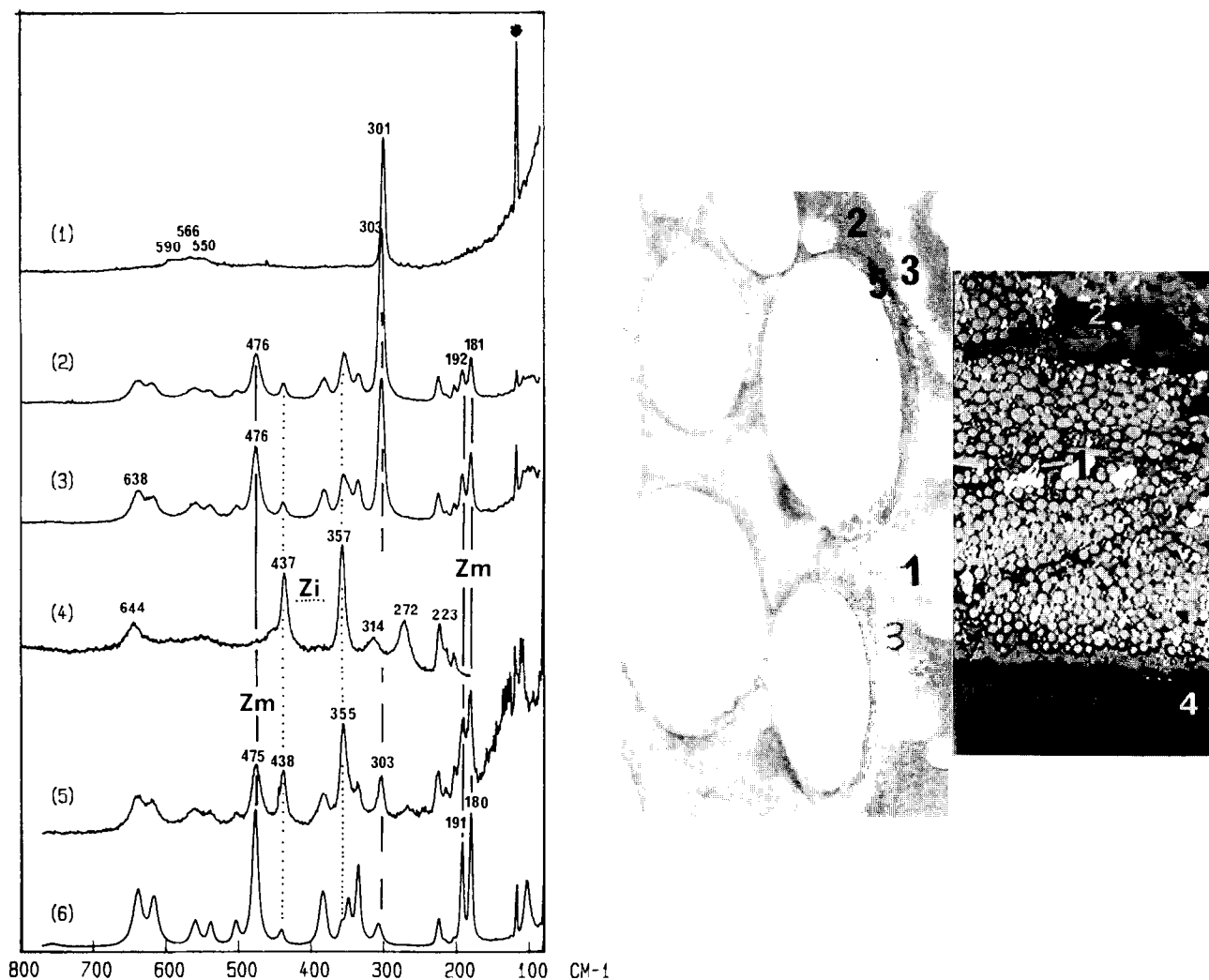


Fig. 10. Optical photomicrographs showing the reaction contour at the SiC fiber periphery in composite prepared using the ZP+TEOGe interface precursor and annealed for 30 h at 1200°C in air. The corresponding micro-Raman spectra are given: (1) Ge rich 'white' precipitate; (2) black region (main phases: Ge+Zm+Zi); (3) grey region (Zm+Zi+Ge); (4) matrix surface (Zi); (5) region around the fiber. Zm: monoclinic zirconia, Zi: zircon; (6) comparison is made with Raman spectra recorded before annealing or after annealing below 800°C (star: laser line).

grains). The interphase at the fiber contour is made of monoclinic zirconia and of zircon. This zircon crust can be formed by reaction with silicon evolving from the fiber as observed in many composites.⁴

Conclusions

From the results which have been presented and discussed the following conclusions can be drawn:

- (i) Almost fully dense woven fabric mullite matrix composites have been prepared by a prepreg sol-gel route using tailored interface precursors compatible with SiC Nicalon NLM202[®] and/or mullite Nextel 440[®] fibers. Low porosity SiC-mullite composites are obtained with the help of transient liquid sintering aids (first a B₂O₃ rich phase and then a Ge/GeO₂ containing phase). The porosity of oxide fiber/mullite

composites remains high and further work must be done to improve their densification.

- (ii) In the as-processed composite the matrix composition changes gradually from the intersheet region to the fiber environment due to the use of two kinds of precursors, the interface and the matrix precursors. This accommodates the thermal expansion coefficient mismatch. Multilevel reinforcement is achieved (fibers, particulates).
- (iii) Good (bending) mechanical properties are obtained for SiC/mullite composites (~300 MPa at RT and at 900°C). The high linear limit (180 MPa) is maintained after 30 h annealing in air. However, a gradual transformation of the zirconia precipitates into zircon is observed. The mechanical properties of mullite-mullite composites show the potential interest of such materials in air if the porosity can be lowered.

(iv) The SiC Nicalon NLM202[®] fiber/silica-rich mullite interphase appears to be free of a carbon film. This behaviour is consistent with the rather good preservation of sliding behaviour at the fiber/matrix interface after air annealing. On the other hand the interfacial shear stress is 3–4 times larger than that measured when the usual carbon interface is present (e.g. SiC/LAS composite). These carbon-film-free SiC-mullite composites as well as the mullite–mullite composites are promising materials for structural applications at medium temperature in an oxidizing atmosphere.

Acknowledgements

Dr D. Michel is kindly acknowledged for his help for the TEM examination. Dr M. Parlier is acknowledged for fruitful discussions.

References

- Colomban, Ph., *Ceramics Int.*, **15** (1989) 23–50.
- Klein, L. C., *Sol-Gel Technology*, Noyes Publication, New Jersey, 1988.
- Colomban, Ph. & Mazerolles, L., *J. Mater. Sci.*, **26** (1991) 3503–10.
- Bruneton, E., Michel, D. & Colomban, Ph., *J. de Physique IV*, **C7** (1993) 1937–40.
- Guney, V., Jones, F. R., James, P. F. & Bailey, J. E., *Int. Phys. Conf. Ser. III*, IOP Publishing Ltd, 1990, pp. 217–26; Chen, M., Jones, F. R., James, P. F. & Bailey, J. E., *ibid.* 227–37.
- Qui, D. & Pantano, C. G., *3rd Int. Conf. Ultrastructure Processing of Ceramics, Glasses and Composites*, eds J. D. Mackenzie & D. R. Ulrich, 1987, pp. 635–44.
- Colomban, Ph. & Mouchon, E., *High Temperature Ceramic Matrix Composites*, Proc. HT-CMC1, 20–24 Sept. 1993, Bordeaux, eds R. Naslain, J. Lamon & D. Doumeingts, Woodhead Publ. Ltd, Abington, Cambridge, 1993, pp. 159–66.
- Colomban, Ph. & Vendage, V., *J. Non-Crystalline Solids*, **147/148** (1992) 245–50.
- Colomban, Ph., Menet, M., Mouchon, E., Courtemanche, C. & Parlier, M., French patent 2672283 (1991), European patent 92400235.5, US patent 07/8303510.
- Prewo, K. M., *Ceram. Bull.*, **68** (1989) 395–401; Lipowitz, J., *ibid.* **70** (1991) 1888–92.
- Colomban, Ph., *Ceramics Today—Tomorrows Ceramics*, ed. P. Vincenzini, Elsevier, Amsterdam, 1991, pp. 599–605.
- Colomban, Ph. & Mouchon, E., *Solid State Ionics*, **73** (1994) 209–20.
- Colomban, Ph., *J. Mater. Sci.*, **24** (1989) 3011–20.
- Low, I. M. & MacPherson, R., *J. Mater. Sci.*, **24** (1989) 926–35.
- Lagrange, J. L., Passilly, B., Parlier, M. & Colomban, Ph., *Proc. JNC-8 (8èmes Journées Nationales sur les Composites)*, 16–18 Nov. 1992, Palaiseau, France, eds O. Allix, J. P. Favre & P. Ladevèze, AMAC, Paris, 1992, pp. 241–52.
- Parlier, M., Grenier, T., Renevey, S., Passilly, B., Mouchon, E., Bruneton, E. & Colomban, Ph., *Proc. 4th Int. Symp. on Ceramic Materials and Components for Engines*, 10–12 Jun. 1992, eds R. Göteborg, Carlsson, T. Johansson & L. Kahlmann, Elsevier Appl. Sci. Ltd, UK, 1992, pp. 440–8.
- Loubet, J. L., Georges, J. M., Marchesini, O. & Meille, G., *J. Tribology*, **106** (1984) 43–8; Loubet, J. L., Georges, J. M. & Meille, G., *Microindentation Techniques in Materials Science and Engineering*, eds J. P. Blau & B. R. Lawn, ASTM STP 889, Philadelphia, 1980, pp. 72–89.
- Ashcroft, I. A., Lawrence, C. W., Weihs, T. P. & Derby, B., *J. Am. Ceram. Soc.*, **75** (1992) 1284–6.
- Cooper, R. F. & Chyung, K., *J. Mater. Sci.*, **22** (1987) 3148–60.
- Brennan, J. J., *Fiber-reinforced Ceramic Composites, Materials, Processing and Technology*, ed. K. S. Mazdiyasn, 1990, pp. 223–59; Colomban, Ph. & Mouchon, E., *High Temperature Ceramic Matrix Composites*, Proc. HT-CMC1, 20–24 Sept. 1993, Bordeaux, eds R. Naslain, J. Lamon & D. Doumeingts, Woodhead Publ. Ltd, Abington, Cambridge, 1993, pp. 269–83.
- Bleay, S., Scott, V. D., Harris, B., Cooke, R. G. & Habis, F. A., *J. Mater. Sci.*, **27** (1992) 2811–22.
- Lin, F., Moriels, T., Morrone, A. & Nutt, S., *Mat. Res. Symp. Proc.*, **120** (1988) 323.
- Naslain, R., *JNC-8 (8èmes Journées Nationales sur les Composites)*, 16–18 Nov. 1992, Palaiseau, France, eds O. Allix, J. P. Favre & P. Ladevèze, AMAC, Paris, 1992, pp. 199–212.
- Marshall, D. B., *J. Am. Ceram. Soc.*, **67** (1984) C259–60.
- Marshall, D. B. & Evans, A. G., *J. Am. Ceram. Soc.*, **68** (1985) 225–31.
- Sudre, O., Passilly, B. & Parlier, M., *Proc. 17th Ann. Conf. Composites and Adv. Ceramics*, Cocoa Beach, FL, 10–15 Jan. 1993, *Ceram. Eng. Sci. Proc.*, (1994), July–August, 1994, pp. 180–7.
- Benoit, M., Brenet, P. & Rouby, D., *High Temperature Ceramic Matrix Composites*, Proc. HT-CMC1, 20–24 Sept. 1993, Bordeaux, eds R. Naslain, J. Lamon & D. Doumeingts, Woodhead Publ. Ltd, Abington, Cambridge, 1993, pp. 329–36.

Processing and Mechanical Properties of Laminated Composites of Mullite/Woven Fabrics of Si–Ti–C–O Fibers

Yoshihiro Hirata,^a Manabu Matsuda,^a Kumiko Takeshima,^a Ryoko Yamashita,^a Masaki Shibuya,^b Martin Schmücker^c & Hartmut Schneider^c

^aDepartment of Applied Chemistry and Chemical Engineering, Faculty of Engineering, Kagoshima University, 1-21-40 Korimoto, Kagoshima 890, Japan

^bTyranno Fiber Development Project, Ube Industries, Ltd, 1978–10 Kogushi, Ube 755, Japan

^cGerman Aerospace Research Establishment, (DLR), Institute for Materials Research, D-51140 Köln, Germany

(Accepted 22 July 1995)

Abstract

A sol-gel-processed mullite powder and Si–Ti–C–O fiber woven fabrics were formed into laminated composites by filtration or doctor blade method using aqueous mullite suspensions containing polyacrylic ammonium (PAA) and methyl cellulose (MC) at pH 8.5. The laminate green composites with 6 and 10 vol% fabrics were hot-pressed to near full density at 1500–1650°C for 1 h under a pressure of 39 MPa in a N₂ atmosphere. However, the composites with 20 and 30 vol% fabrics resulted in delaminated porous ones after hot-pressing due to the exfoliation of filament yarn in woven fabrics. A linear relation of stress–displacement in fracture behavior of monolithic mullite changed to a non-linear relation in the composites with 10–30 vol% of Si–Ti–C–O fabrics and hot-pressed at 1650°C. Addition of Si–Ti–C–O fabrics decreased the four point flexural strength of monolithic mullite (328 MPa) to 292 MPa at 6 vol%, 271 MPa at 10 vol% and 59–78 MPa at 20–30 vol% of fabrics whereas the fracture toughness by the single edge precracked beam (SEPB) method increased from 1.6 MPa m^{0.5} for the monolithic mullite to 4.7 MPa m^{0.5} for the composites with 10 vol% of Si–Ti–C–O fabrics. Enhancement of the mechanical properties can be interpreted by the partial decomposition of Si–Ti–C–O fibers during hot-pressing at 1500–1650°C, which caused the diffusion of C and Ti elements of fibers to the interfaces between the fibers and mullite matrix. The diffusion of Al from mullite matrix into fibers was also observed. The change of composition, microstructure and strength at the interfaces would increase debonding or pull-out effect of fibers.

1 Introduction

Mullite (3Al₂O₃·2SiO₂) is a candidate oxide for high temperature structural applications because of a high melting point, a low thermal expansion coefficient, good thermal shock fracture resistance, a low true density and high creep resistance. For increase of mechanical reliability of mullite ceramics with a low fracture toughness (1–2 MPa m^{0.5}), some papers reported the increase of fracture toughness by addition of SiC whiskers, long carbon or Si–Ti–C–O fibers to mullite matrix.^{1–5} Especially, the long fiber-reinforced mullite matrix composites are attractive materials because this type of composites show usually high fracture toughness and non-linear fracture behaviour of stress–displacement curves, along with remarkably high fracture energy. A typical mullite composite reinforced by 35 vol% of uniaxial carbon fiber showed significantly high strength above 800 MPa and high fracture toughness reaching 29 MPa m^{0.5} at 1200°C.³ The most important factor in the processing of fiber-reinforced composites would be the control of strength of interface between fiber and matrix. An adequate interface strength that is not too strong or too weak can lead to the excellent mechanical properties of composite materials.^{6–8} The objective of this research was to study the processing, mechanical properties, and microstructure of the laminated mullite/woven fabric composites with high fracture toughness and high strength. In this study, mullite green sheets formed by doctor blade of aqueous mullite suspensions and woven fabrics of Si–Ti–C–O long fibers were laminated to sinter by hot-pressing at 1500–1650°C. The Si–Ti–C–O long fibers show

high tensile strength (3.2 GPa), high oxidation resistance, and good wettability to oxide ceramics.⁹

2 Experimental Procedure

2.1 Starting materials and colloidal processing

A sol-gel-processed mullite powder (Fig. 1(a)) was mixed with aqueous solutions to form thick green sheets or to pour into the spaces separated with the woven fabrics of Si-Ti-C-O fibers. The mullite powder used was supplied from Chichibu Cement Co., Ltd, Japan. It has the following properties: particle size distribution: 0.1–1.5 μm , specific surface area: 3.2 m^2/g (equivalent diameter of spherical particle: 0.59 μm), chemical composition: 71.80 mass% Al_2O_3 , 28.05 mass% SiO_2 , 0.10 mass% TiO_2 , and 0.01 mass% Na_2O . The Si-Ti-C-O woven fabrics of 270 μm thick (Ube Industries, Ltd, Yamaguchi, Japan), were made of long fibers with an average diameter of 8.5 μm (Fig. 1(b)), and a chemical composition of 50.4 mass% Si, 29.7 mass% C, 17.9 mass% O, and 2.0 mass% Ti. The surface characteristics of the mullite and crushed Si-Ti-C-O fibers in dilute aqueous suspensions (0.02 mass%) were studied by measuring the electrophoretic mobility. The pH of each suspension was adjusted using 0.01N HCl and 0.01N NH_4OH solutions. Electrosterically stabilized mullite suspensions of 40 vol% solid at pH 8.5 were prepared by adding 0.75 mass% of polyacrylic ammonium (PAA, $(\text{HCOONH}_4\text{CH}_2)_n$, average molecular weight: 10000) and 2.0 mass% of methyl cellulose (MC) against the weight of mullite to give flexibility and strength for handling of thick films formed.

The suspensions were stirred for 24 h and ultrasonic vibration at 20 kHz was applied for an additional 5 min to disperse particle agglomerates. Air bubbles in the suspensions were eliminated in a bell jar connected to a vacuum pump. These suspensions were formed into thick films by doctor blade of a blade clearance of 500 μm at a transfer rate of 15 cm/min of polyethylene carrier tape (DP-100, Tsugawa Seiki Seisakusho, Tokyo, Japan). In the preparation of composite with 6 vol% fabrics, the mullite suspensions of 52 vol% solid containing 0.75 mass% of PAA at pH 8.5–8.8 were poured into the rectangular spaces separated at 2.7 mm intervals of four Si-Ti-C-O fabric sheets (thickness, 270 μm , 38 mm long and 25 mm wide) which were set on a gypsum mold.

2.2 Hot-pressing and measurement of mechanical properties

Before hot-pressing in a N_2 atmosphere, a set of 5–7 layers of a mullite sheet (thickness, 200–250 μm) and one layer of Si-Ti-C-O fabric sheet, (thickness, 270 μm , 38 mm long and 25 mm wide) were alternately laminated to 10–12 mm in thickness. The green laminated composites of 6–30 vol% Si-Ti-C-O fabrics were pressed with a carbon die under a pressure of 39 MPa at room temperature and heated to 1500 or 1650°C at the rate of 10°C/min, and sintered for 1 h in a N_2 atmosphere (FVH-5 type, Fuji Denpa Kogyo Co., Osaka, Japan). The densities of hot-pressed composites were measured in distilled water by the Archimedes method. A hot-pressed sample was cut into five test specimens 38 mm long, 3–4 mm wide and 4–7.5 mm thick, parallel to the hot-pressing direction.

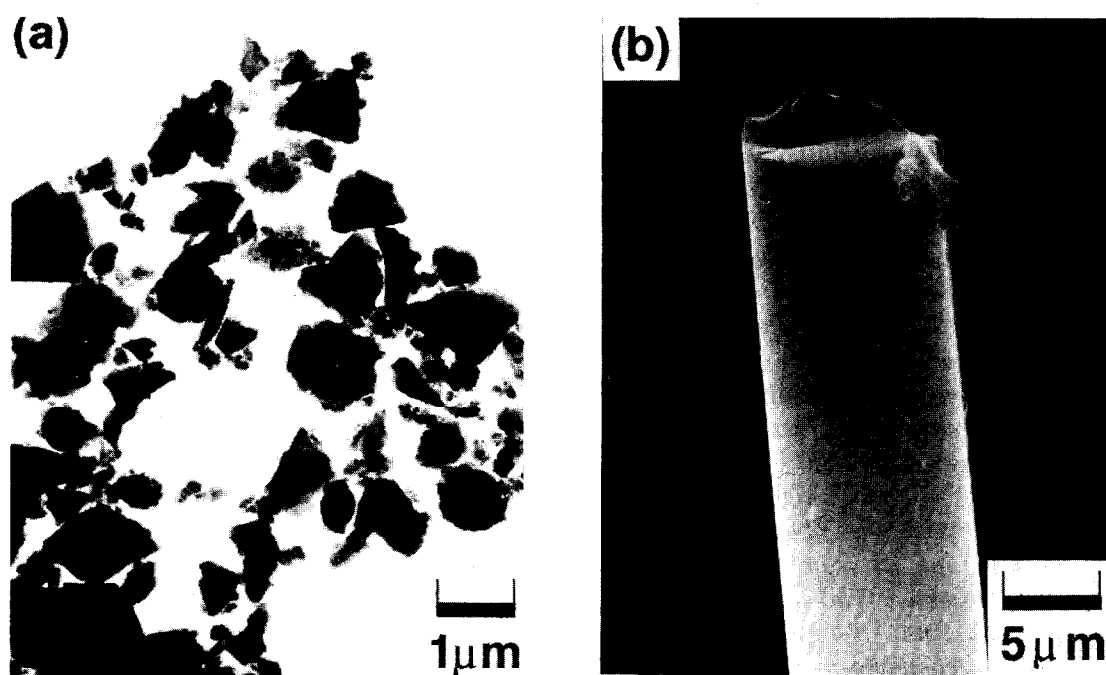


Fig. 1. Photographs of: (a) sol-gel-processed mullite powder and (b) Si-Ti-C-O long fiber.

The flexural strength of test specimens parallel to the hot-pressing direction was measured at room temperature by the four-point flexural method over spans of 30 mm (lower span) and 10 mm (upper span) at a crosshead speed of 0.5 mm/min. The test specimens were prepared by grinding with a No. 400 diamond wheel and finished with No. 2000 abrasive paper. The average strength was calculated from the data for 3–4 specimens. The fracture toughness was evaluated by single edge precracked beam (SEPB) method. The strengths of the flexural specimens, precracked by a Vickers indenter (model MVF-K, Akashi Seisakusho Co., Tokyo, Japan) of 98 N to induce microcracks, were measured by three-point loading over a span of 30 mm at a crosshead speed of 0.5 mm/min, and then calculated to fracture toughness.¹⁰ Data for 3–4 test specimens were used to calculate the average fracture toughness. Microstructures of the composites were observed by scanning electron microscopy with energy dispersive X-ray spectroscopy (EDX: S-5000 Type, Hitachi Co., Tokyo, Japan) and analytical transmission electron microscopy (TEM: EM430, Philips Co., Eindhoven, Netherlands).

3 Results and Discussion

3.1 Forming of laminated composites

As shown in Fig. 2, the isoelectric points for the suspensions of the mullite particles and crushed Si-Ti-C-O fibers were pH 4.9 and 3.5, respectively. The electrophoretic mobility of both of the negatively charged powders reached the maximum values of -4 – $-5 \mu\text{m s}^{-1} \text{V}^{-1} \text{cm}$ in the pH range of 8–10. The above result suggests that: (1) the mullite particles are to be dispersed due to the strong electric repulsion at high pH and (2) strong repulsive interaction is also formed between the negatively charged mullite particles and Si-Ti-C-O fibers at

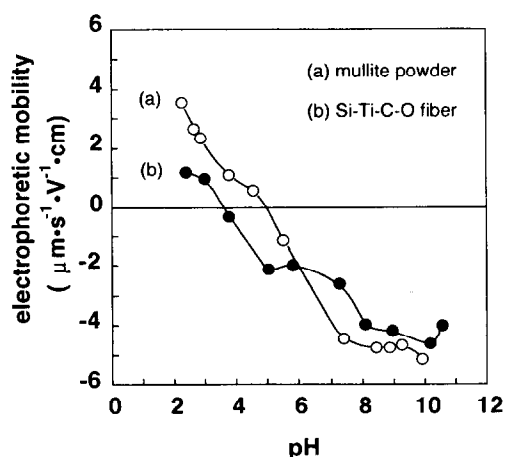


Fig. 2. Electrophoretic mobility of: (a) mullite particles and (b) Si-Ti-C-O fibers in aqueous suspensions.

high pH. Thus, the mullite suspensions in this experiment were adjusted at pH 8.5 to enhance the dispersion state of mullite powder. In the doctor blade method, 2.0 mass% of MC and 0.75 mass% of PAA against the weight of mullite were added to the suspensions to give an apparent viscosity of 45.1 Pa s at a shear rate of 3.83 s^{-1} . For the preparation of laminated composites with 6 vol% fabrics by filtration of the mullite suspension in the space separated with Si-Ti-C-O fabrics, 0.75 mass% of PAA was added to the concentrated mullite suspensions of 52 vol% solid at pH 8.5–8.8.⁵ This electrosterically stabilized mullite suspensions behaved as a Newtonian flow and the viscosity was 122 mPa s. The green compacts obtained from this suspension was 63% of the theoretical density (TD).¹¹

3.2 Hot-pressing and mechanical properties of laminated composites

The monolithic mullite and mullite/Si-Ti-C-O fiber fabric (6 and 10 vol%) composites were densified to near full densities (99.7–99.9% TD) at 1500 to 1650°C for 1 h by hot-pressing under a pressure of 39 MPa. However, the composites with 20 and 30 vol% fabrics resulted in delaminated porous bodies and the filament yarns in the woven fabrics exfoliated. The density of the composites with 30 vol% fabrics was 64% TD. Since the Si-Ti-C-O fabrics introduce a high porosity, the increase of fabrics content may cause the insufficient packing of mullite particles in the open spaces of fabrics. The above phenomenon indicates a limit of fiber loading in this type of laminated composites.

Figure 3 shows the stress–displacement curves

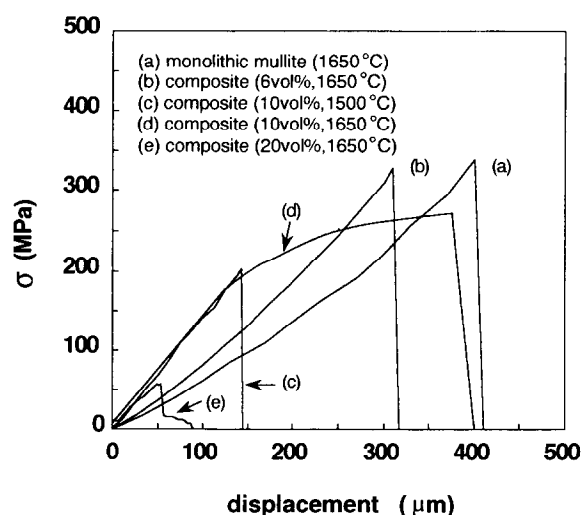


Fig. 3. Stress–displacement curves at room temperature for: (a) monolithic mullite hot-pressed at 1650°C; (b) mullite/Si-Ti-C-O fabrics composites with 6 vol% fabrics hot-pressed at 1650°C; (c) composites with 10 vol% fabrics hot-pressed at 1500°C; (d) composites with 10 vol% fabrics hot-pressed at 1650°C and (e) composites with 20 vol% fabrics hot-pressed at 1650°C.

for monolithic mullite and mullite/Si-Ti-C-O fabric composites. The fracture behavior of composites was affected by two factors, i.e. hot-pressing temperature and Si-Ti-C-O fabrics content. The stress-displacement curve of the composites with 10 vol% fabrics hot-pressed at 1500°C was similar to that of mullite hot-pressed at 1650°C. This result suggests that the inserted fabrics behaved like a part of mullite matrix and they fractured in the clear absence of pseudoplastic behavior. Increase in the hot-pressing temperature of the composites with 10 vol% fabrics to 1650°C caused a non-linear fracture behavior with a high fracture energy as seen in Fig. 3(d). This effect of hot-pressing temperature may be corresponding to decrease in strength of interface between the mullite matrix and Si-Ti-C-O fabrics. Increase in the Si-Ti-C-O fabric content from 6 to 10 vol% in the composites hot-pressed at 1650°C was effective to achieve the non-linear fracture behavior and to increase fracture energy as shown in Fig. 3. On the other hand, the delaminated porous composites with 20–30 vol% fabrics showed a non-linear fracture behavior with a low fracture strength. It is also noted that the composites with 10 vol% fabrics hot-pressed at 1650°C and precracked by a Vickers indenter of 98 N showed a clear non-linear fracture behavior as shown in Fig. 4, indicating a high damage tolerance. However, the precracked composite with 6 vol% fabrics fractured with a linear relation of stress-displacement.

Figure 5 summarizes the mechanical properties of mullite/Si-Ti-C-O fabric composites hot-pressed at 1650°C. Increase of the Si-Ti-C-O fabric content caused a slight decrease of flexural strength up to 10 vol% fabrics but gave a drastic decrease at 20 and 30 vol% fabrics. The fracture toughness that was calculated at the highest stress

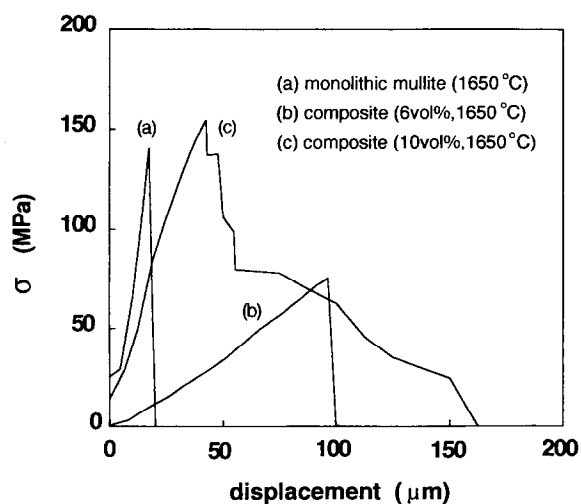


Fig. 4. Stress-displacement curves for: (a) monolithic mullite; (b) composites with 6 vol% fabrics and (c) composites with 10 vol% fabrics, precracked by a Vickers indenter of 98 N.

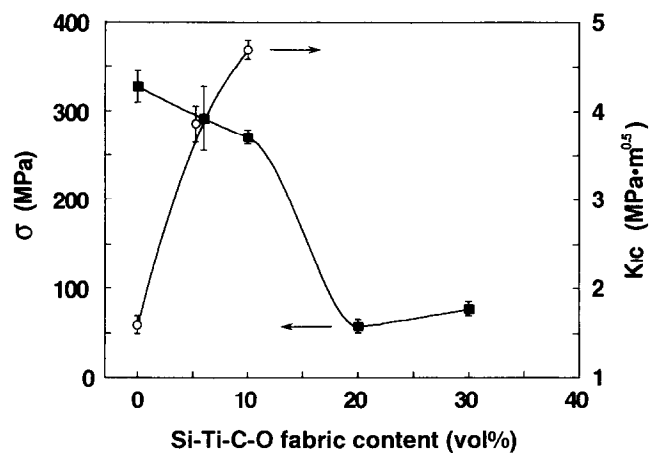


Fig. 5. Dependence of flexural strength and fracture toughness on Si-Ti-C-O fabric content for composites hot-pressed at 1650°C.

of samples with precracks in SEPB method, increased from 1.6 $\text{MPa}\cdot\text{m}^{0.5}$ for monolithic mullite to 4.7 $\text{MPa}\cdot\text{m}^{0.5}$ for the composite with 10 vol% fabrics. That is, it was possible to increase fracture toughness of the laminated composites significantly with a comparable strength to monolithic mullite.

Figures 6 and 7 show the SEM photographs

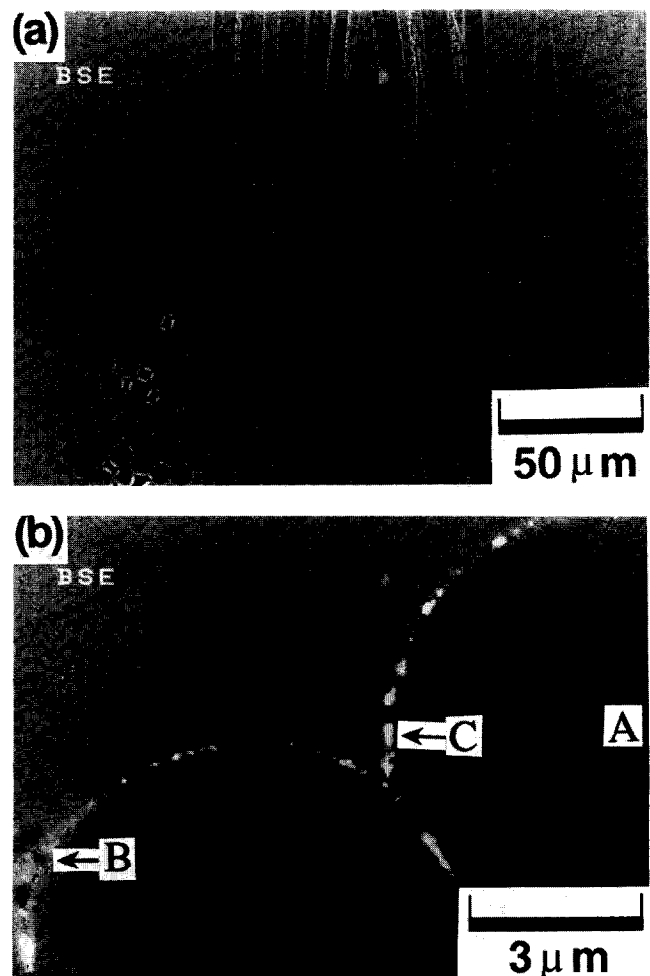


Fig. 6. SEM photographs of composites with 10 vol% fabrics hot-pressed at 1650°C.

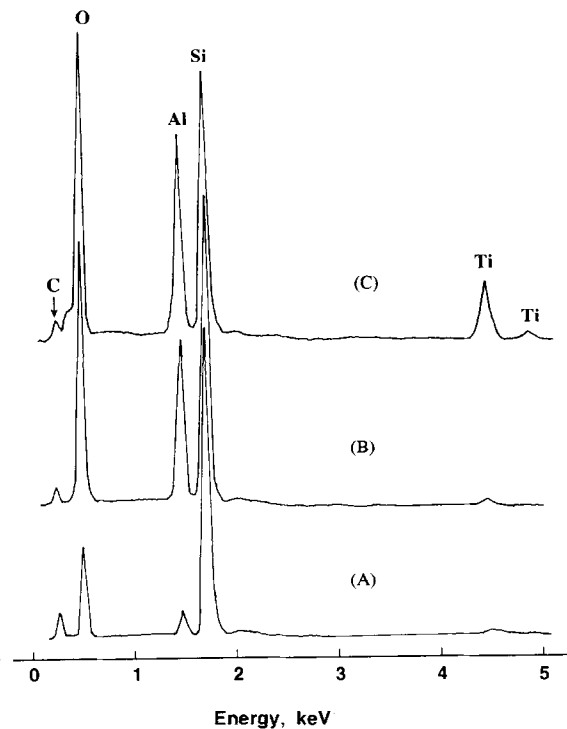


Fig. 7. EDX analysis of Si-Ti-C-O fiber (point A) and interface (points B and C).

and corresponding EDX spectra of the composites with 10 vol% fabrics hot-pressed at 1650°C. Pore-free microstructure was observed in the mullite matrix of the composites. A few pores remained in the spaces surrounded by the Si-Ti-C-O fibers (Fig. 6(a)). The interface between the mullite matrix and Si-Ti-C-O fibers contained a light colored precipitate (Fig. 6(b)). The EDX analysis for Si-Ti-C-O fibers and the interface indicates that: (1) the inside of Si-Ti-C-O fibers contained the elements of Si, C, O and Al; (2) the chemical composition of the interface without precipitate was more enriched in Al and O than that of the center of Si-Ti-C-O fiber and (3) the light color precipitate in the interface contained a relatively high concentration of Ti in addition to the elements of Si, Al, O and C. The above results suggest that Ti in fibers diffused into interfaces and Al in mullite diffused into fibers during hot-pressing. Similar EDX spectra were measured in the composites with 10 vol% fabrics hot-pressed at 1500°C but the interfaces were enriched in C than the inside of fibers. These results can be explained by the thermal decomposition of Si-Ti-C-O fibers in the mullite matrix above 1500°C.¹² In the observation of the interfaces of the mullite/Si-Ti-C-O fabric (6 vol%) composites hot-pressed at 1650°C by transmission electron microscopy (Fig. 8), the following phenomena were shown: (1) formation of thin graphite layer (30–50 nm) at interface and (2) formation of fine SiC particles (<50 nm) in the Si-Ti-C-O fiber. The basal planes of graphite

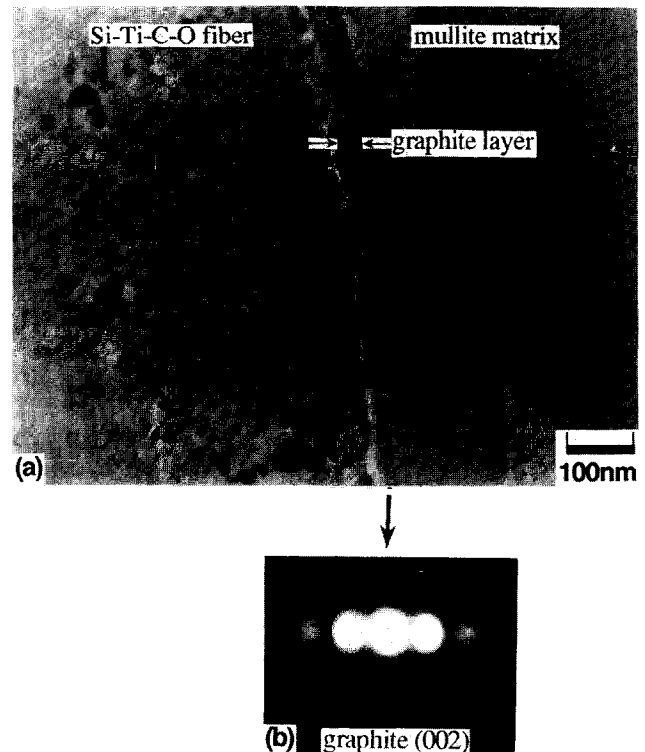


Fig. 8. TEM photograph (a) and selected area electron diffraction pattern (b) at the interface between Si-Ti-C-O fiber and mullite matrix of composites hot-pressed at 1650°C.

were parallel to the interface. The observation of graphite layer was also reported by Sato *et al.*⁴ in the interfaces of the composites of mullite/chopped Si-Ti-C-O fiber hot-pressed at 1650°C. In respect to the thermal stability of Si-Ti-C-O fiber, Yamamura *et al.*^{13,14} reported that: (1) the oxygen content of Si-Ti-C-O fibers hot-pressed in Ar atmosphere decreases above 1500°C and reaches below 1 mass% at 1800–2100°C and (2) the atomic ratio of C/(Si + Ti) decreases from 1.5 to 1.0. Decomposition of Si-Ti-C-O fiber to form SiC-TiC fiber, therefore, releases excess carbon at the interfaces of the composites above 1500°C. The graphite layer formed would reduce the interface strength and enhance the debonding or pull-out effect of Si-Ti-C-O fibers. The precipitate enriched with Ti and the compositional gradient of Al element at the interfaces may also contribute to the improvement of mechanical properties.

Figure 9 shows a transmission electron micrograph of the mullite grains in the composites hot-pressed at 1650°C. The mullite matrix consisted of granular-shaped grains of 0.8–1.1 μm in size. Since the granular shape of mullite grains is correlated to little existence of glassy phase in the grain boundaries,^{15,16} it may be expected to show high possibility of mechanical strength at high temperatures.



Fig. 9. TEM photograph showing granular-shaped mullite grains in the matrix of composites hot-pressed at 1650°C.

4 Conclusions

Laminated green compacts of mullite/Si-Ti-C-O fiber fabrics (6–30 vol%) were formed by the doctor blade method or filtration of aqueous mullite suspensions (40–52 vol% solid) containing 0.75 mass% of polyacrylic ammonium and 2.0 mass% of methyl cellulose against the weight of mullite at pH 8.5. These green compacts with 6–10 vol% fabrics were densified to nearly full density (>99% of theoretical density) by hot-pressing under a pressure of 39 MPa in a N₂ atmosphere at 1500–1650°C. Increase of the fabric content to 20 or 30 vol%, however, resulted in a delaminated porous composite. The fracture toughness of monolithic mullite hot-pressed at 1650°C (1.6 MPa m^{0.5}) was enhanced to 4.7 MPa m^{0.5} in the composites with 10 vol% Si-Ti-C-O fabrics which showed a non-linear fracture behavior at room temperature. The strength of monolithic mullite (328 MPa) at room temperature decreased slightly with addition of Si-Ti-C-O fabrics to 292 MPa at 6 vol% and to 271 MPa at 10 vol% of fabrics. The composites with 20–30 vol% fabrics showed a non-linear fracture behavior but their strengths were significantly lower (59–78 MPa) compared to the strength of monolithic mullite. The improvement of mechanical properties in the mullite/Si-Ti-C-O fabric composites was interpreted by the thermal decomposition of Si-Ti-C-O fibers

above 1500°C, which caused the diffusion of C and Ti from the fibers to the interfaces between Si-Ti-C-O fibers and mullite matrix of granular-shaped grains (~1µm). The diffusion of Al from mullite matrix to fiber was also observed. These change of composition, microstructure, and strength of the interface would enhance the debonding or pull-out effect of Si-Ti-C-O fibers in the composites.

References

1. Kumazawa, T., Ohta, S., Tabata, H. & Kanzaki, S., Mechanical properties of mullite-SiC whisker composites. *J. Ceram. Soc. Japan*, **97**(9) (1989) 895–902.
2. Becker, P. F. & Tieg, T. N., Toughening behavior involving multiple mechanisms: whisker reinforcement and zirconia toughening. *J. Am. Ceram. Soc.*, **70**(9) (1987) 651–4.
3. Somiya, S. & Hirata, Y., Mullite powder technology and application in Japan. *Am. Ceram. Soc. Bull.*, **70**(10) (1991) 1624–32.
4. Sato, M., Shibuya, M., Ohtsubo H., Hiratsuka, T., Harada, Y. & Yamamura, T., Properties of ceramic matrix composite using chopped Si-Ti-C-O fibers. In *Proceedings of 2nd International SAMPE Symposium*, 1991, pp. 844–51.
5. Hirata, Y. & Takeshima, K., Colloidal processing for preparation of laminated composites of mullite/woven fabrics of Si-Ti-C-O fibers. *Mater. Lett.*, **17**(6) (1993) 374–8.
6. Prouhet, S., Camus, G., Labrugere, C., Guette, A. & Martin, E., Mechanical characterization of Si-C(O) fiber/SiC(CVI) matrix composites with a BN interphase. *J. Am. Ceram. Soc.*, **77**(3) (1994) 649–56.
7. Bender, B. A. & Jessen, T. L., Comparison of the interfaces development and ultimate strength between nicalon and Tyranno silicon carbide-fiber-reinforced zirconia titanate matrix composites. *Ceram. Eng. Sci. Proc.*, **14**(7–8) (1993) 931–8.
8. Jessen, T. L., Powers, J. & Bender, B. A., The effect of fiber arrangement on the mechanical properties of an unidirectional CFCC. *Ceram. Eng. Sci. Proc.*, **14**(7–8) (1993) 991–7.
9. Mah, T., Mendiratta, M. G., Katz, A. P. & Mazdiyasi, K. S., Recent development in fiber-reinforced high temperature ceramic composites. *Am. Ceram. Soc. Bull.*, **66**(2) (1987) 304–8.
10. Japanese Industrial Standard, JIS R-1607-1990. Testing methods for fracture toughness of high performance ceramics.
11. Hirata, Y. & Takeshima, K., Effect of particle classification on colloidal processing of mullite. *Mater. Lett.*, **16**(4) (1993) 169–74.
12. Yamamura, T., Ishikawa, T., Shibuya, M., Tamura, M., Nagasawa, T. & Okamura, K., A new type of ceramic matrix composite using Si-Ti-C-O fiber. *Ceram. Eng. Sci. Proc.*, **10**(7–8) (1989) 736–47.
13. Jero, P. D., Parthasarathy, T. A., Kerans, R. J., A comparison of single and multi-fiber pushout techniques. *Ceram. Eng. Sci. Proc.*, **14**(7–8) (1993) 147–55.
14. Wereszczak, A. A., Feber, M. K. & Lowden, R. A., Development of an interfacial test system for the determination of interfacial properties in fiber reinforced ceramic composites. *Ceram. Eng. Sci. Proc.*, **14**(7–8), (1993) 156–67.
15. Pask, J. A., Zhag, X. W., Tomsia, A. P. & Yoldas, B. E., Effect of sol-gel mixing on mullite microstructure and phase equilibria in the α -Al₂O₃-SiO₂ system. *J. Am. Ceram. Soc.*, **70**(10) (1987) 704–7.
16. Ismail, M. G. M. U., Nakai, Z. & Somiya, S., Microstructure and mechanical properties of mullite prepared by the sol-gel method. *J. Am. Ceram. Soc.*, **70**(1) (1987) C-7–8.

Editorial

The cohesive characteristics of Ceramic Science and Technology are well evident in the relationship between the processing of materials, their microstructure, and their chemical and physical properties. The more recent strict requirements for the design and application of ceramics brought about a specific demand upon characterization of the microstructure. This is a complex topic comprising the distribution of phases, the nature of grain boundaries, the chemical composition of phases, the shapes and sizes of individual crystallites, the nature and morphology of defects and the morphological and elemental composition of interfaces. Therefore it is evident that the significance of ceramic microstructures is a key topic which demands special attention. Moreover, the tools and techniques of microstructural analyses have virtually exploded in number and capabilities over the last few decades.

The increasing interest on microstructural and microanalytical characterization of ceramic materials suggested the opportunity of organizing a special session on 'The Modern Applications of Electron and Scanning Probe Microscopies to Ceramics' at the European Ceramic Society Fourth Conference, Riccione, Italy, 2-6 October 1995. World-reknowned Scientists were invited to present the state of the art in this field, emphasizing the aspect of the application of transmission electron microscopy (including atomic resolution imaging) and related microanalytical techniques to advanced ceramics, metal/ceramic interfaces and superconductors.

A. Armigliato, CNR LAMEL

A. Bellosi, CNR IRTEC

(Co-chairs of Special Session)

Electron Microscopy and Microanalysis of Ceramics

Gareth Thomas

Department of Materials Science and Mineral Engineering, University of California, Berkeley, CA 94720-1760, USA;
and Materials Sciences Division, Lawrence Berkeley Laboratory, 1 Cyclotron Road, Berkeley, CA 94720, USA

(Received 1 June 1995; revised version received 22 June 1995; accepted 28 June 1995)

Abstract

We live and work in a world that depends on materials and their performance. The science of materials has developed to a position of great understanding, such that materials can be microscopically tailored to provide specific sets of properties. The practical applications of newly designed materials depend on market interest and costs. In the final analysis it is the processing of materials that remains the key factor. In order to facilitate technical advances, the relationships between processing, microstructure, and performance must be established. This task is generic to all materials whether for mechanical or physical property goals. Central to such understanding is the role played by electron optical, diffraction and analytical methods of characterization in their specificity to synthesis almost to the atomic level.¹⁻³ This paper provides some examples of such applications to several ceramic systems, and attempts to indicate the generic nature of many problems to be solved.

1 Introduction

Materials science is concerned with the understanding of the relationships between *processing–structure–properties* as shown schematically in Fig. 1(a). Electron microscopy, diffraction and microanalysis are especially important for characterizing materials because of their specificity and high spatial resolution, as is now very well known. In the last decade or so the number of investigations using these techniques for characterizing ceramics has increased greatly and many examples of such are in the ceramics and electron microscopy literature.⁴

There is a wealth of information about structure, microstructure, chemical composition, etc., obtainable from state-of-the-art instruments as indicated in Fig. 1(b). It is clear that no materials research laboratory can function properly without such facilities.

In this paper no attempt will be made to review the vast field of applications to ceramics. Instead, some general points will be discussed relevant to electron imaging, diffraction and spectroscopy techniques, and the paper will be illustrated by representative examples, mostly drawn from research programs at U.C. Berkeley.

2 General Remarks

2.1 Interpretation of results: resolution

While excellent commercial microscopes are now generally available with capabilities of better than 2 Å interpretable resolution, and which provide data as is illustrated in Fig. 1(b), a word of caution is needed. With a good thin specimen it is relatively easy to obtain excellent images, diffraction and spectroscopic data. However, the *interpretation*, especially, of high resolution images *must* be done with the appropriate matching calculations.² As shown in Fig. 2, structure images are very sensitive to microscope conditions, especially objective lens defocus and specimen thickness.³ Thus, the materials scientist must know the instrumental conditions from source to image recording in order to sensibly utilize the images. Without calculations, publications of micrographs are, to put it bluntly, almost useless. In fact it is necessary to interpret all the data with suitable computer simulations/calculations. Programs for these purposes are available from several laboratories.⁵

When instruments, specimens and simulations are optimized and effectively used, then electron microscopy becomes a unique tool. For example, it is possible to do structure analysis on nanocrystals in real space from images in different orientations. Figure 3 is an example for mullite.³ Clearly, large-angle tilt specimen holders ($\pm 45^\circ$) are a necessity with the requirement to maintain the resolution over the complete tilt range. A clear application of such work is in the analysis of nanostructures or small second phases which

Materials Science Iterative Tetrahedron

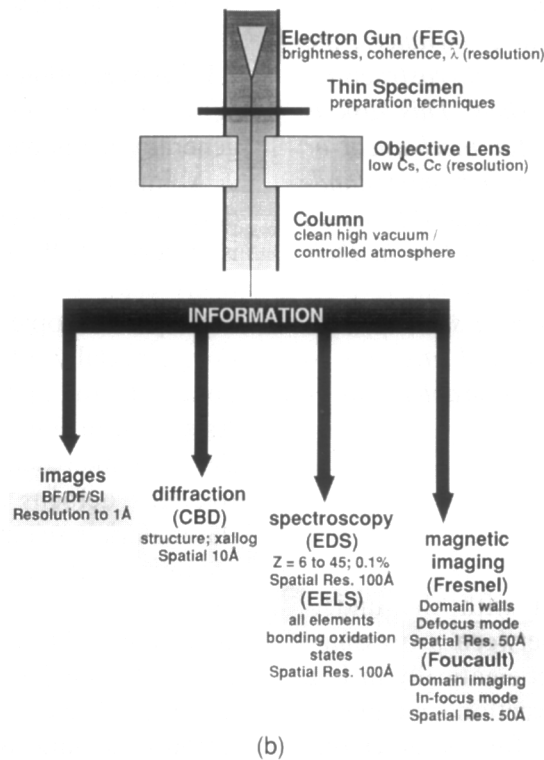
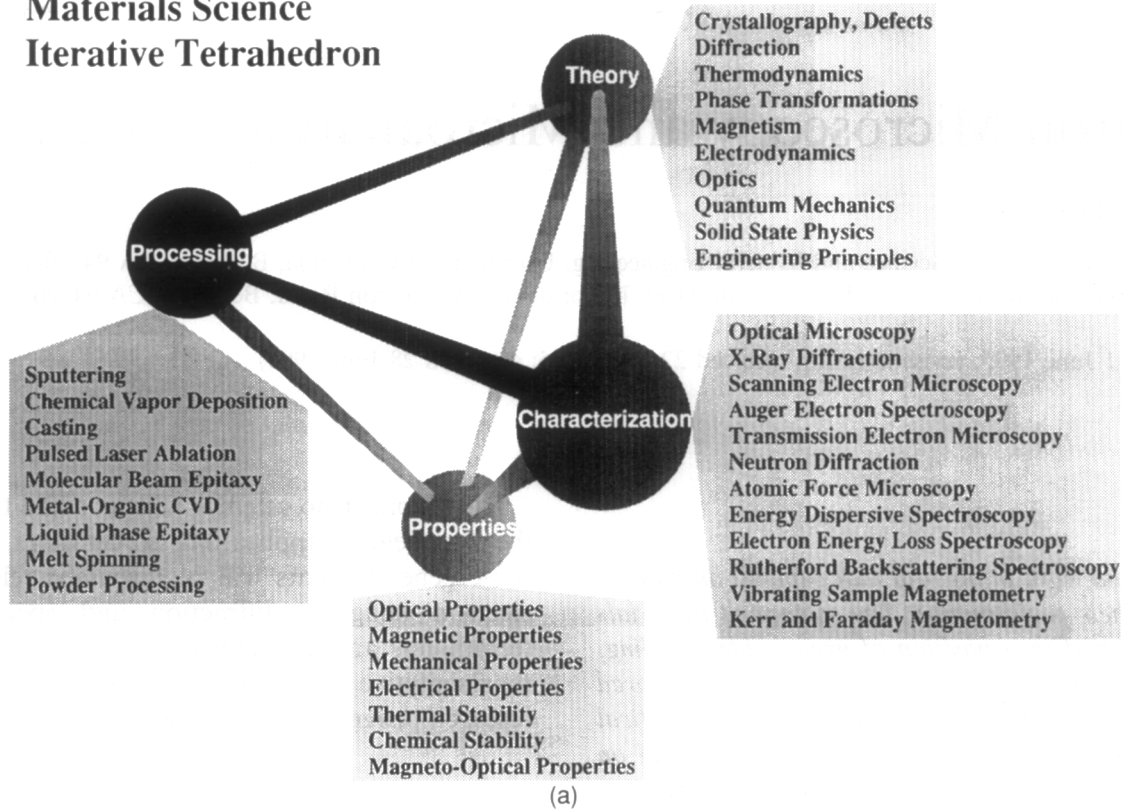


Fig. 1. (a) Scheme showing the iterations involved in materials science and engineering research. (b) Schematic showing the wide range of high resolution information available from modern electron optical facilities.

would not be amenable to traditional X-ray studies.

The question of resolution is very important for ceramics. Until recently, instruments did not have the resolution capable of interpreting the positions of small anions in structures; and to increase resolution by lowering the wavelength (raising voltage) increases the probability of displacement radiation damage. Consequently, a new generation of high

resolution (HREM) instruments are now becoming available at moderate voltages (300–400 kV), by developing low aberration objective lenses (operated with large magnetic fields) and/or incorporating holographic capabilities. In addition, and essential for improved analytical resolution, intense coherent electron sources by field emission are finally becoming generally available. Figure 4, using essentially a weak phase object analysis,

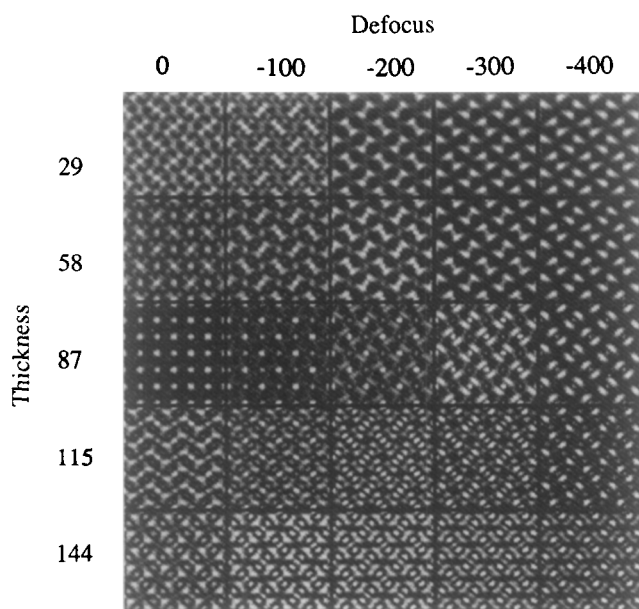


Fig. 2. 001 projected images computed for mullite $3\text{Al}_2\text{O}_3 \cdot 2\text{SiO}_2$ as a function of specimen thickness and objective lens defocus. Experimental images must match these conditions to be interpretable (Ref. 3).

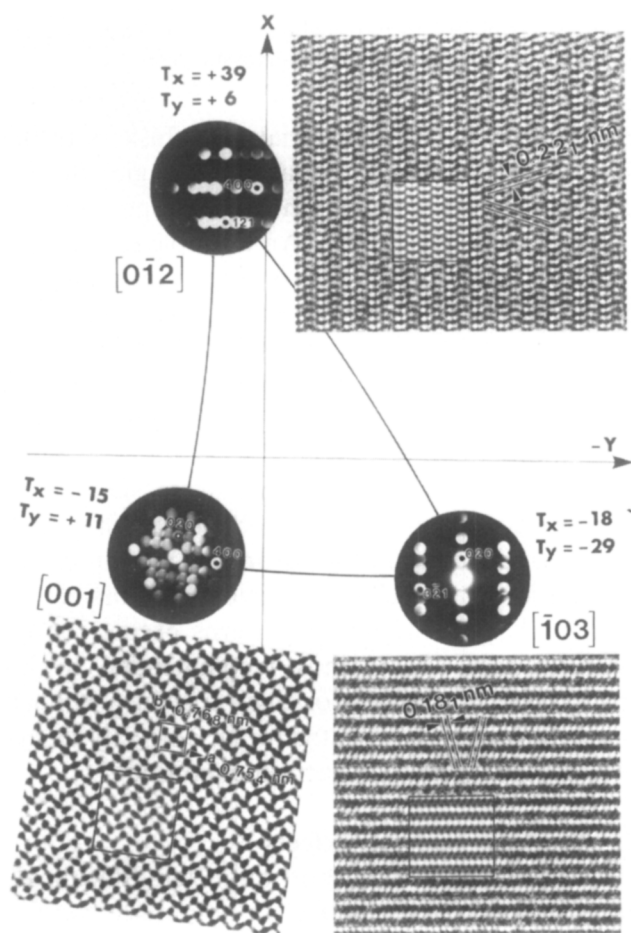


Fig. 3. Structure images obtained in the Berkeley ARM microscope for a crystal of mullite. Three different orientations allow the orthorhombic structure to be verified when images match simulations (inset rectangles). Point-to-point resolution is 1.6 \AA (courtesy T. Epicier).

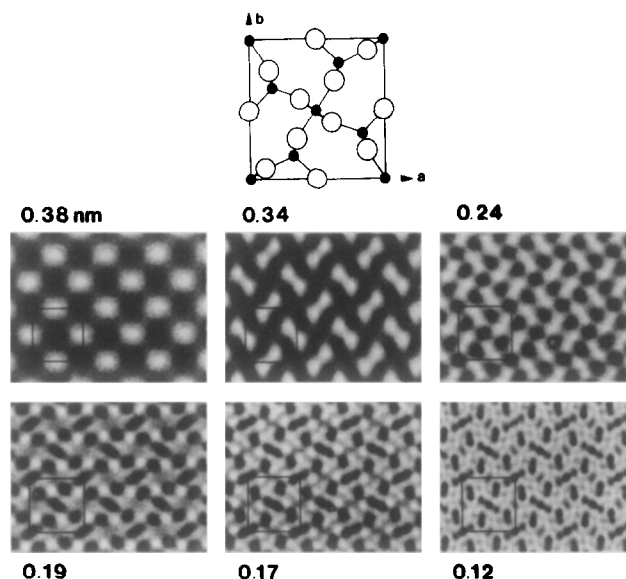


Fig. 4. Simulations of the 1.2 \AA resolution required to distinguish oxygen from the Al, Si cations in the [001] projection of orthorhombic mullite (courtesy M. O'Keefe).

shows that an instrument of resolution better than 1.2 \AA is needed to distinguish oxygen in the 001 projection of mullite. Such instrument development allows materials scientists to probe materials at or near atomic levels. Image information at 1 \AA is now possible with computer-assisted deconvolution of sequential recording, e.g. the work at Antwerp (G. Van Tendeloo, reported at this session).

However, electron microscopy is not only a problem of instrumental resolution and interpretation, it is also a problem of specimen preparation. For example, glasses and glassy films are very important in ceramics, as will be illustrated below. In order to resolve the structure of even a simple SiO_2 glass, assuming a random network, Fig. 5 indicates the specimen must be less than 10 \AA thick, and this is obviously a terrible restriction.

2.2 Convergent beam diffraction (CBD)

This diffraction method probes the three-dimensional structure (Fig. 1) providing three-dimensional reciprocal space data which in turn allow the researcher to fix the crystal structure and point/space symmetries.⁶ The development of convergent beam diffraction, which is a powerful analytical technique, has enabled detailed crystallographic analyses to be done on nanostructured materials and within very small volumes. In addition, high resolution analyses of large-angle lines in the patterns allow very accurate lattice parameter measurements to be made. Typical applications include studies of phases, e.g. the so-called morphotropic boundary in ferroelectric systems such as lead zirconate titanate,⁷ indicate that both the rhombohedral and tetragonal phases exist over a very narrow composition range, so that the

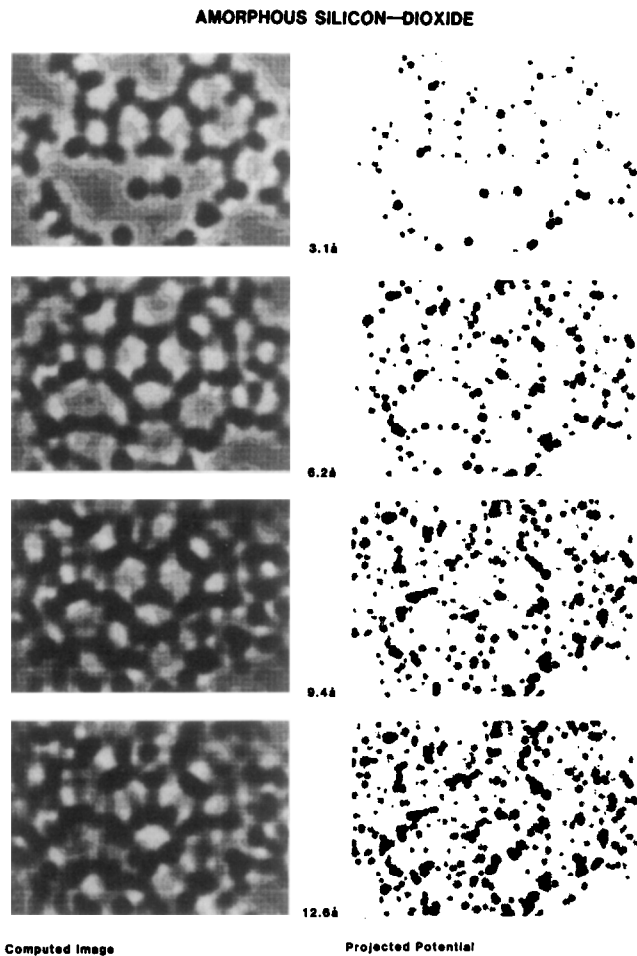


Fig. 5. Random network model of SiO_2 glass showing projected potentials and corresponding image simulations. Notice that the images become very difficult to interpret when the specimen is $\geq 10 \text{ \AA}$ thick (courtesy M. O'Keefe).

'phase diagram' normally utilized is not correct. In another application the CBD method has been essential in helping to analyze the oxygen problem in AlN, as has been published recently.⁸ In this system spectroscopic analyses are confused because of the presence of surface oxide films, so that CBD seems the only way to probe the oxygen content and its variability from grain to grain and at/across grain boundaries. However, this can be achieved only when the relationship between lattice parameter and (dissolved) oxygen has already been established, and the appropriate computer simulations have been carried out to interpret the CBD measurements. This particular case illustrates that problem solving should involve utilization of all the available techniques⁹ and not just any one technique.

Ceramic materials are generally more complex than metallic systems and often have low crystal symmetries. Mullite close to $3\text{Al}_2\text{O}_3:2\text{SiO}_2$ is orthorhombic, yet when prepared as whiskers can also occur in the metastable tetragonal structure.¹⁰ Such discoveries would not be possible without analytical techniques, such as CBD, capable of

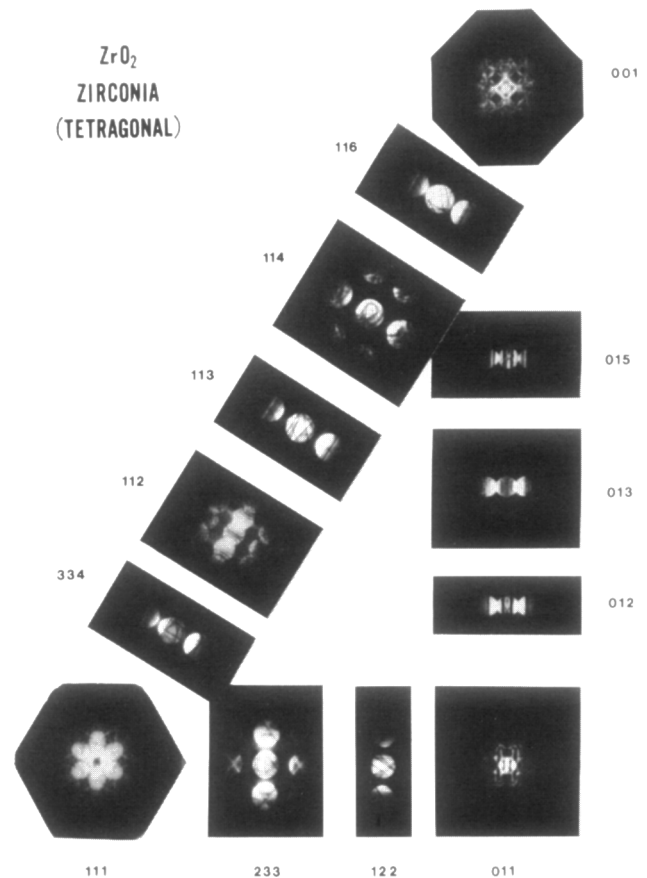


Fig. 6. CBD reciprocal space map for tetragonal ZrO_2 . Such maps are useful for structure analysis, orientation determination, and general crystallographic data.

resolving small sized materials — whiskers in this case. In combinations of large tilt angles the full crystal structure-orientation can be represented as CBD (or Kikuchi) maps.⁹ An example for tetragonal ZrO_2 is shown in Fig. 6. Such maps can also be simulated by using the appropriate computing software. These maps are also useful for controlling the orientation for many situations, e.g. selecting the correct diffraction conditions for high resolution imaging,² contrast analyses,⁹ lattice parameter or strain measurements, etc.⁶ Due to the complexity of diffraction problems arising from multiple scattering in low symmetry structures and orientations, it becomes almost impossible to recognize spot diffraction patterns except for the simplest cases. It is thus recommended to use microdiffraction (CBD) or thick specimen Kikuchi maps to assist the investigator in correctly assessing the appropriate diffraction conditions.⁹

2.3 Contrast analyses: defects

Defect analysis is important but often difficult due to the reasons given above. In amplitude contrast analysis the contrast depends on the phase factor $2\pi\vec{g} \cdot \vec{R}$ where \vec{g} is the operating diffraction vector and \vec{R} is the displacement vector.⁹ \vec{R} can be quite complex, especially in non-isotropic systems. Also, the magnitude of $\vec{g} \cdot \vec{R}$, which must shift the inten-

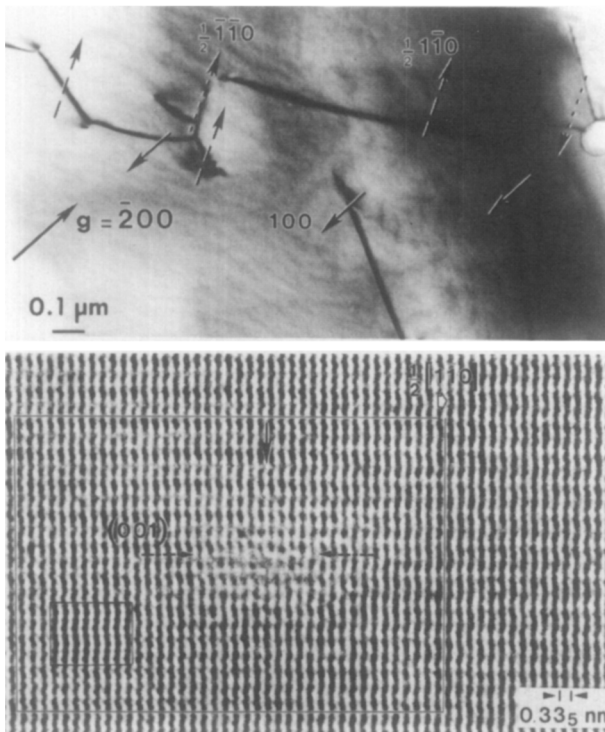


Fig. 7. Al_2TiO_5 : Simplified Bravais lattice showing shortest translation vectors. Top RH: amplitude contrast image to set dislocations with $\bar{b} = \frac{1}{2}\langle 001 \rangle$ invisible. Lower RH: structure imaging—closure circuit shows $\bar{b} = \frac{1}{2}[001]$ directly (Ref. 11).

sity by at least $\pm 10\%$ over background for visibility, may be too small to evaluate \bar{R} , (e.g. for interface dislocations whose \bar{R} vector may be \ll lattice vectors). In general, dislocations in crystals

are expected to be those of smallest Burgers vectors (lowest energies). Figure 7 is an example of dislocation Burgers vector analysis in AlTiO_5^{11} (space group Cmc m , $a = 0.35$ nm, $b = 0.94$ nm, $c = 0.96$ nm), in which the simplified Bravais lattice indicates the expected Burgers vectors to be the shortest vectors in the close-packed planes ($a < b < c$). One of several $\bar{g} \cdot \bar{b}$ conditions is shown, alongside a structure image. The analysis of Burgers vectors and habit planes is consistent with elementary crystallographic considerations: $[100]$ and $\frac{1}{2}[110]$ -type translation vectors are the shorter ones (0.36 and 0.53 nm respectively), and (011) and (001) are two of the densest planes; these planes are probably glide planes. The HREM approach is very useful when $(\bar{g} \cdot \bar{R})$ is very small (dislocations not visible), and can be effectively used in studying defects and structural aspects of interfaces and grain boundaries which contain structural defects with displacements not equal to the lattice vectors.

Many other examples of defect analysis could be given, but space is limited. Therefore, we mention just one other case for planar faults which have importance in several technically important ceramics, e.g. nitrogen ceramics,¹²⁻¹⁴ superconductors,¹⁵ minerals, etc. These are the 'composition' faults which occur to adjust to compositional changes, and are properly described as polytypoids—to be distinguished from polytypic faults which affect structure but not composition (SiC is

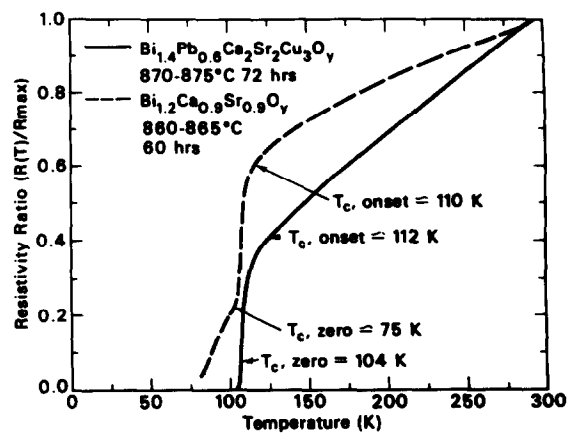
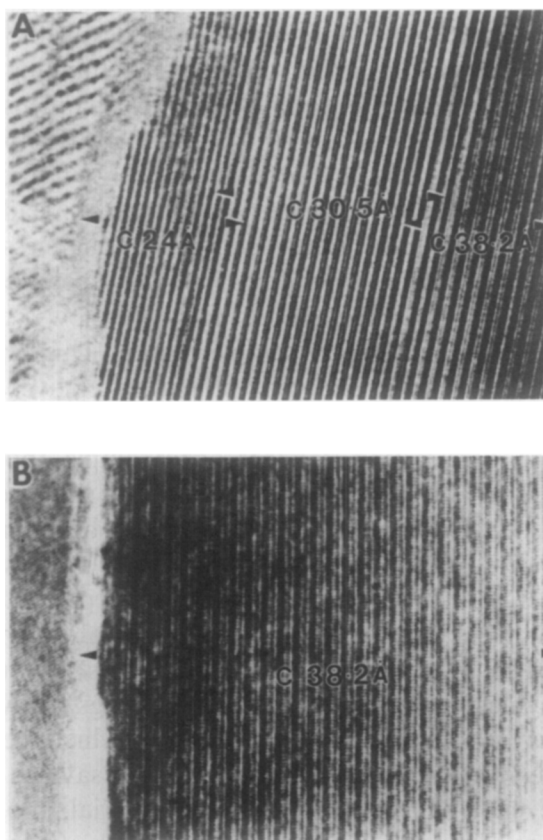


Figure (above)
Plot of resistivity versus temperature for led (—) and the unled (---) samples of Bi-containing superconducting materials. Note the presence of a step in the resistivity plot for the unled sample resulting in a lower T_c . (XBL 884-7341)

Figure (above, left)
High resolution lattice fringe electron micrograph of the unled sample showing the decrease in c -parameter close to the grain boundary. The 24Å spacing polytypoid has a T_c of 20K, the 30.5Å polytypoid a T_c of 75K and the 38.2Å polytypoid a T_c of 110K.

Figure (left)
High resolution lattice fringe image from the led sample showing the uniform c -parameter of 38.2Å up to the grain boundary.

Fig. 8. Showing polytypoids near grain boundary in alkaline earth superconductors; caption as indicated.

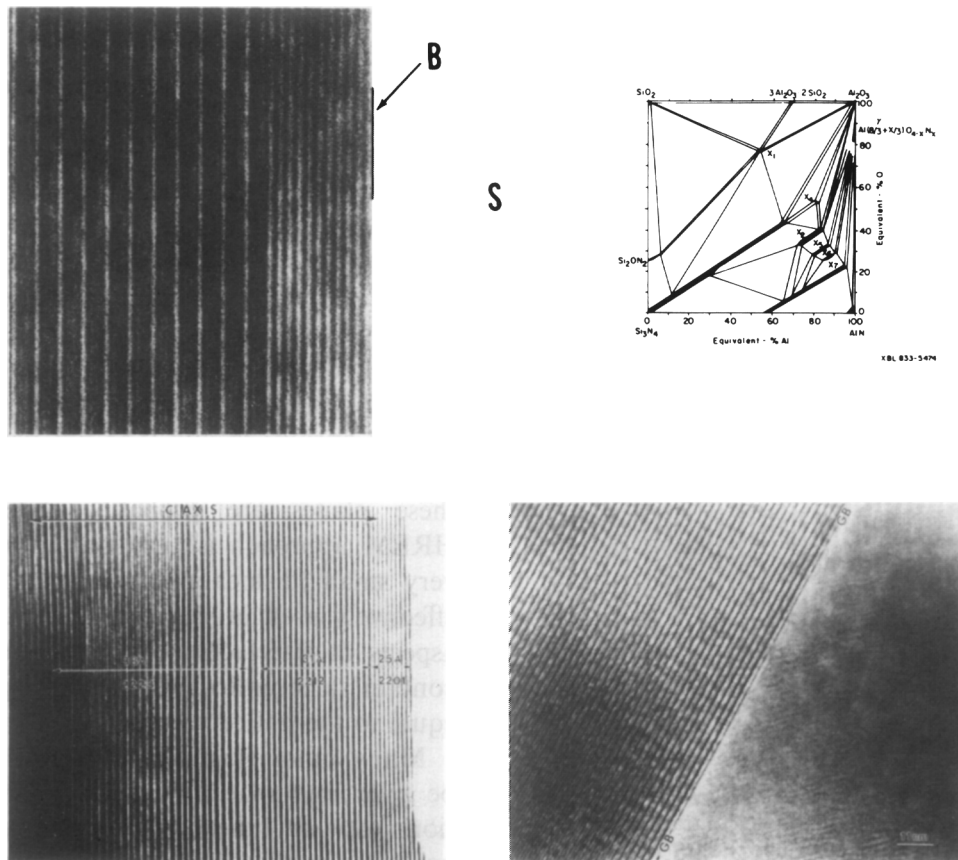


Fig. 9. Polytypoids in MgSiAlON and a section of the phase diagram; due to composition changes (Mg/Si ratios) the polytypoid spacing changes: each $|c|$ axis parameter corresponds to a unique composition and thus indirectly provides compositional data (courtesy D. R. Clarke).

a well known example). In the electron microscope, such polytypoids can be considered as projections of compositional images, as each structure has a unique cation: anion ratio.

In superconductors the faulting associated with Cu–O layers has a strong effect on physical properties, especially the critical temperature. Compositional changes near grain boundaries can locally generate polytypoids of low T_c , as shown in Fig. 8. Suitable sintering aids (in this case PbO) can alleviate these structural problems and hence reduce the problem of grain boundary resistivity and lack of connectivity. This example typifies the need to closely monitor processing–microstructure relationships. Shown for comparison to Fig. 8 is Fig. 9, with similar structural polytypoids due to changes in Mg/Si/O ratios in MgSiAlON ‘alloys.’

2.4 High voltage TEM — penetration

HVEM (>300 kV) is useful not only because of improved resolution (shorter wavelength) and reduced ionization damage (but increased knock-on damage for voltages > threshold), but also for increased penetration up to 1 meV.⁹ The latter benefit is useful in dealing with complex materials such as composites, coated fibres, etc. in which specimen thinning for 200 kV transparency is particularly difficult.¹⁶

An example is that for BN coated fibres. Preparation of TEM specimens of composite materials can be complicated by the mere fact of the existence of two or more different phases in the material. For instance, ion-beam thinning can preferentially remove one phase if it happens to be softer than the other. In the case of SiC fiber/SiC matrix specimens, the fiber–matrix interface has been deliberately engineered to be weak, leading to a material with improved fracture toughness. This leads to difficulty in preparing thin specimens for TEM, as the fibers tend to fall out below a certain thickness, leading to sample failure. This problem has been circumvented by preparing relatively thick specimens of the composite and observing them at high accelerating voltages. The sample shown in Fig. 10 was observed at 1500 kV. It shows clearly the circumferential cracking in the boron nitride coating on the fiber. Such cracking increases the energy of propagation of a crack perpendicular to the fibers, leading to improved material toughness.

The use of ceramic components in turbine engines could lead to weight savings as well as increases in operating temperature, which increases fuel efficiency. The potential dollar savings could be enormous. One candidate material, molybdenum disilicide,¹⁷ has relatively high creep rates above 1000°C. A possible solution is to use a rein-

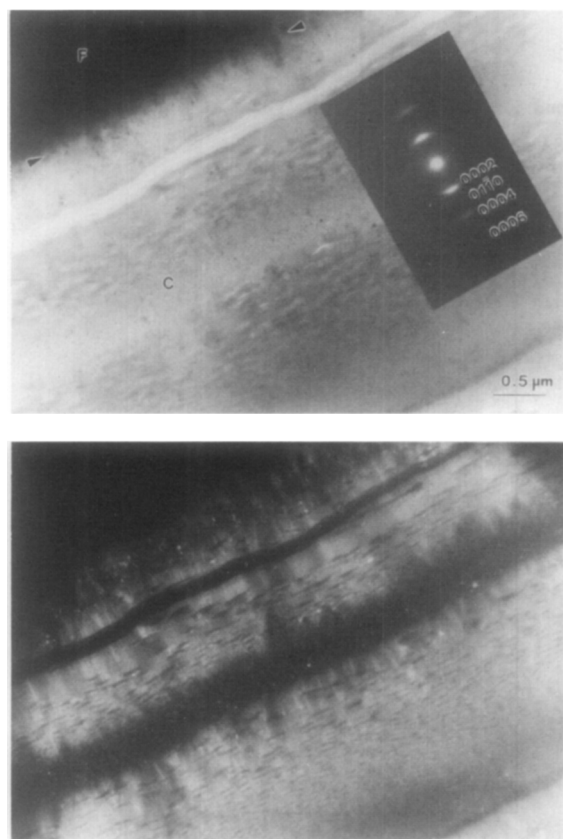


Fig. 10 Bright field (a) and dark field (b) pair of TEM micrographs showing circumferential crack (labeled 'C') in BN coating of SiC fiber in ceramic composite. Cracking in the coating increases the composite toughness. Imaging at 1500 kV (courtesy A. McFayden).

forcement with a very low creep rate, in this case mullite.¹⁸ Improvement in creep performance depends upon the formation of a strong interface between the two materials. Diffuse dark field imaging, shown in Fig. 11, indicates the presence of a small amount of glassy phase at the interface prior to creep deformation. Current experiments indicate increased creep resistance, implying a change in the interphase glass—possibly devitrification. Clearly crept specimens will be examined carefully by HREM and AEM to investigate this interesting situation.

2.5 Microanalyses

Figure 1 also illustrates the information available by microanalysis (AEM). AEM is now a widely accepted technique.¹⁹ X-ray spectroscopy spatial resolutions of 10 nm capable of identifying elements from $Z = 6$ to $Z = 60$ by EDS have become almost routine. Detection limits are about 0.1% with field emission sources, depending on the signal-to-noise ratio, detector efficiency, and data retrieval from small volumes. Again, it should be pointed out that intense sources, (e.g. FEG) can give rise to problems such as heating, radiation damage and even decomposition, such as loss of nitrogen from nitride ceramics.

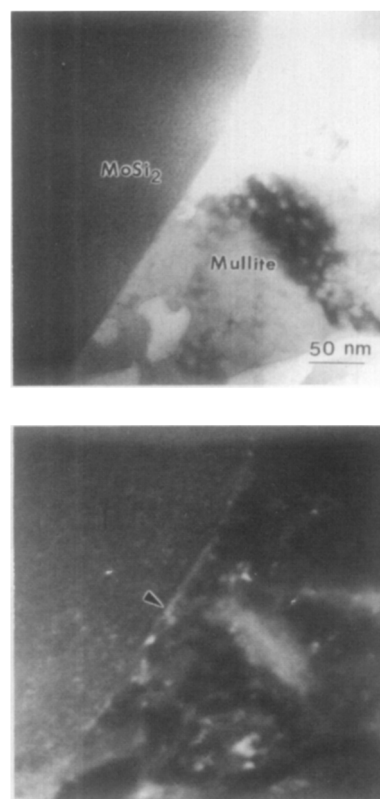


Fig. 11. Bright field (a) and diffuse-dark field (b) pair of TEM micrographs showing glassy layer (arrow) between MoSi_2 and mullite phases in ceramic composite. The creep resistance of the composite is dependent on the morphology and composition of this layer. Imaging at 120 kV (courtesy A. McFayden).

Energy loss spectroscopy, EELS, is also progressing mainly as a qualitative method useful for light elements, and should be used more widely, especially coupled with high resolution imaging studies of ceramics. It is also very effective in analyzing bonding relationships from details of the fine structure near the absorption edge. It is possible to detect graphite with diamond in 50 Å particles,²⁰ as shown in Fig. 12. With image analysis it is a very powerful addition to the battery of electron optical techniques available in modern microscopes.

2.6 Magnetic structure

Magnetic structure and properties also depend on microstructure and local composition. Examples include domain wall pinning of soft ferrites, which raises coercivity but lowers permeability. The problem with magnetic imaging is that to obtain high resolution, one needs objective lenses of low aberrations. This means working at very high magnetic fields in the objective, e.g. up to 2 or more Tesla. Such fields saturate magnetic specimens in the microscope, rendering them useless for magnetic structure imaging. Thus, unless special instruments are available for observing specimens in zero field environments, one is restricted to turning off the objective lens, so limiting observation to

Spatial Resolution

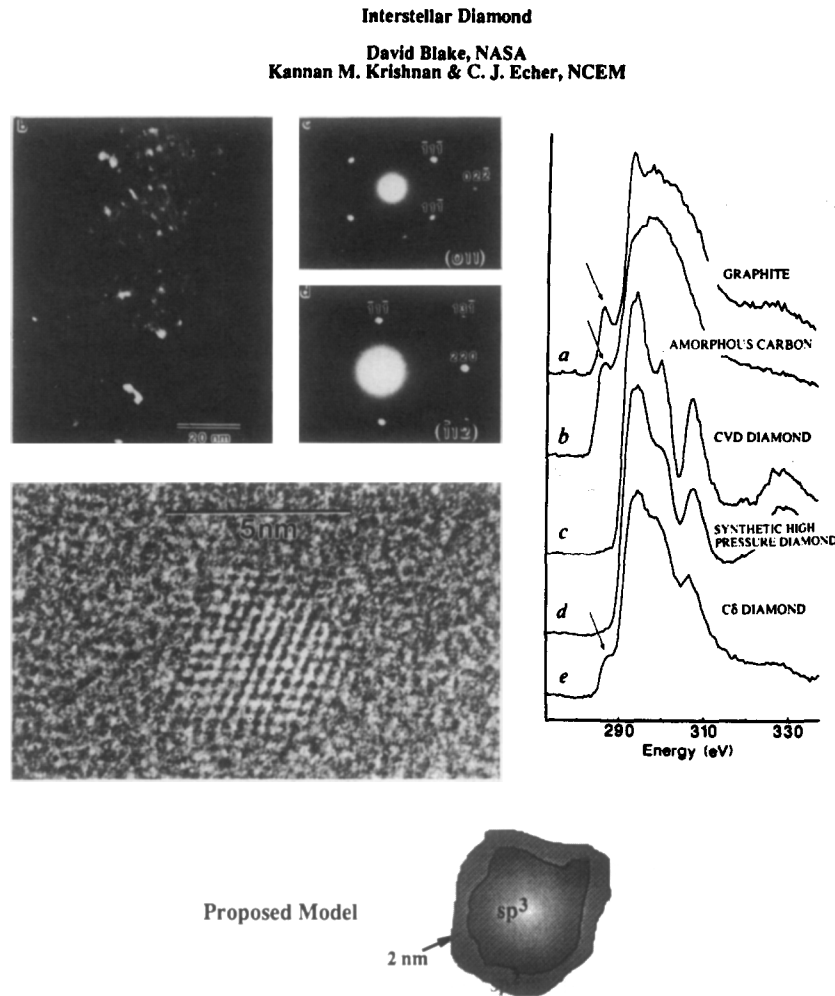


Fig. 12. EELS studies of nanocrystalline meteoric diamond. The HREM lower left dark field image shows the small particles of meteoric diamond. The EELS spectra on the RH side are from carbon phases near the absorption edge (K). The sp_2 graphite transition can be seen in the $C\delta$ spectrum from the diamond particle shown. It is concluded that the diamonds are coated with a graphite layer (Ref. 20). (Courtesy K. Krishnan.)

low-resolution Lorentz imaging.^{9,21} If, however, a high voltage instrument is available with free lens control, it is possible to obtain 10 nm or less resolution, as has been demonstrated recently in our laboratory. Figure 13 shows an example of such research, in which particles of Co, some being single-domain at <100 nm diameter, are magnetically imaged in a gold matrix. The size and morphology of these Co particles have a major effect on giant magnetoresistance and this effect is of great interest for magnetic recording. For soft ferrites, Fig. 14 is an example of low resolution 'conventional' imaging of domain walls, which indicates the pinning power of grain boundaries on the domain walls in Mn/Zn ferrites.²² Microanalyses by AEM and CBED proved that such pinning is associated with CaO impurity segregation and its associated lattice distortion, and results in poor permeability properties. This result again shows the importance of material purity and processing on microstructure-property relationships.

3 Representative Examples

Representative examples of the use of electron microscopy in ceramics can be drawn from the tremendously important problem of grain boundaries, interfaces, and interphase interfaces,²³ as many examples will be given in this symposium. Grain boundary engineering is quite generic and is required to control many mechanical and physical properties. Figure 15 is a schematic to illustrate this point and Fig. 8 is one example for electronic conduction in superconductors.

3.1 Properties and intergranular phases: Si_3N_4

In the case of many ceramics whose bonding characteristics require the use of sintering aids to achieve densification, the resulting materials often contain residual, glassy phases at grain boundaries (Fig. 15). Silicon nitride is a typical example. These amorphous phases, depending on their composi-

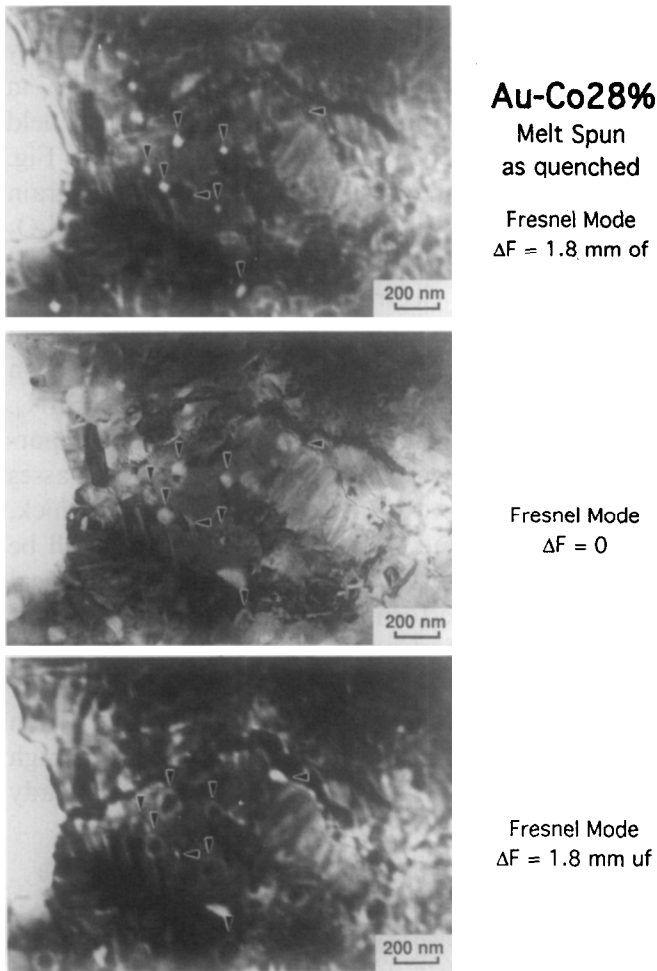


Fig. 13. Au 28at%Co alloy as quenched and imaged at 800 kV (in Berkeley ARM) in the diffraction mode. The arrows show changes in contrast for particles with similar direction of magnetization, and the central figure ($\Delta f = 0$) shows the particles with no magnetic contrast (courtesy J. Bernardi).

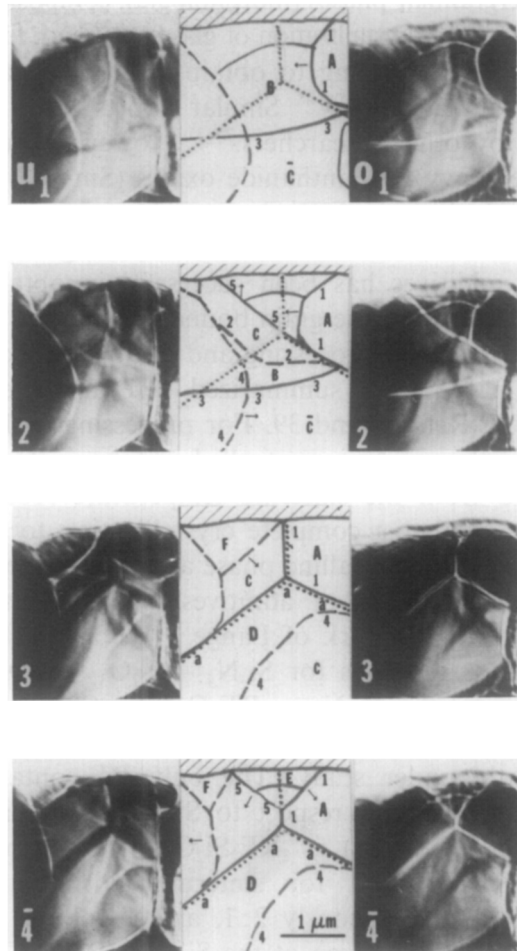


Fig. 14. MnZn ferrites Lorentz imaging for under- and over-focused conditions. Center column is sketch to indicate how grain boundary regions pin magnetic domain walls. The effective field is changed by specimen tilt. A large field reversal is needed to release the domain walls, hence decreasing permeability (Ref. 22).

tion, viscosity, etc. can deteriorate mechanical properties. A basic understanding of such intergranular and interphase interfaces is therefore essential if improvements in performance are to be

achieved. A program towards this end has been under way at Berkeley for some 15 years. In the course of this program, techniques were developed for high resolution electron optical characterization

Some Generic Microstructures: Ceramics

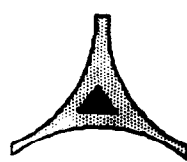
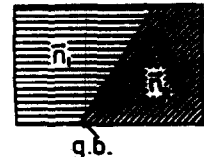
<u>Grain boundaries / interfaces</u>	<u>Examples</u>	<u>Properties limited</u>
	Amorphous films	Creep
	Partly crystalline films	Creep
	Additives / impurities	Permeability
		Voltage drop required
	Si_3N_4	Na^+ conduction
	Some Sialons	Conduction a-b plane
	Ferrites	Affects T_c and J_c
	Varistors	
	β Na alumina	
	$\text{YBa}_2\text{Cu}_3\text{O}_{7-x}$	
	$\text{Bi}_2\text{Sr}_2\text{Cu}_n\text{Ca}_{n-1}\text{O}_y$	
	polytypoids of low T_c	
	ZrO_2 / mullite	
	composites	Varied (creep, etc.)

Fig. 15. Schematic to indicate importance of grain boundaries and interphases on many properties of ceramics.

of intergranular phases (morphologies, composition), studies²⁴⁻²⁶ of crystallization of glasses²⁷⁻²⁹ and, finally, successful processing to obtain mostly crystalline intergranular phases.²⁸ Similar efforts have been made by other researchers.²⁹⁻³⁷ However, the use of the heavy RE lanthanide oxides (Sm→Tb) has received little attention outside our current research. In all materials studied, sintering with RE oxide additives has been successful in obtaining RE₂Si₂O₇ crystalline grain boundary phases.³⁷⁻⁴⁰

The materials processing and testing procedures used in the work summarized here are given in detail in Refs 38 and 39. For processing with the rare-earth oxides, controlled cooling through 1400°C from the sintering temperature (1600°C) results in almost complete crystallization to form the RE₂Si₂O₇ crystalline phase at the grain boundaries. The choice of additives is based on the phase diagram work of Lange.³⁰ We assume that the phase relations for Si₃N₄ – Y₂O₃ – SiO₂ are similar to the Si₃N₄ – RE₂O₃ – SiO₂ systems, where RE represents Y, Sm, Gd, Dy, Er, and Yb, currently under study. The only RE-containing phase stable with respect to SiO₂ (the oxidation product of Si₃N₄) is RE₂Si₂O₇. The ratios of SiO₂:RE₂O₃ used for sintering aids to form RE₂Si₂O₇ are obviously 2:1, and a volume fraction of ~0.2, as given at the Si₃N₄ – RE₂Si₂O₇ tie line, is chosen so as to ‘cover’ all grain boundaries. Previous researchers have used Y₂O₃ – Al₂O₃ sintering aids,²⁹ but later work^{27,28} indicated that the glassy phase was stabilized by partitioning of Al and N during crystallization.

Figures 16 and 17 show electron micrographs of the sintering products using Yb₂O₃+SiO₂. High aspect ratio grains of Si₃N₄ are surrounded by intergranular pockets (dark contrast in Fig. 16(a), (b)) of crystalline RE₂Si₂O₇ phase. These high

aspect ratio matrix grains are important in crack deflection, and such materials gave reasonably good K_{IC} fracture toughness values, e.g. ~8 MPa√m in compact tension tests.⁴¹ The diffuse dark field image in Fig. 15(d) and the HREM image in Fig. 16 show that some residual glass remains at grain boundaries, and at the interfaces between RE₂Si₂O₇ crystal phases and Si₃N₄ at triple points. Preliminary analytical electron microscopy (AEM) indicates that these glassy regions contain several cationic impurities, notably Ca,²⁴ and research on this is continuing.⁴² Impurities (from the Si₃N₄, SiO₂, and RE₂O₃ starting powders) play an important role in glass retention. Although such glasses are often only two to three molecular layers thick, their viscosity and thus composition could still be the limiting factor in high temperature mechanical behavior and performance. In only rare instances are glass-free interfaces found,⁴⁰ e.g. Fig. 18. Auger and sputtering experiments on Si₃N₄ and AlN show that oxide layers form very quickly (within seconds) on the surface after removal from high vacuum. Thus, it may be that powders already

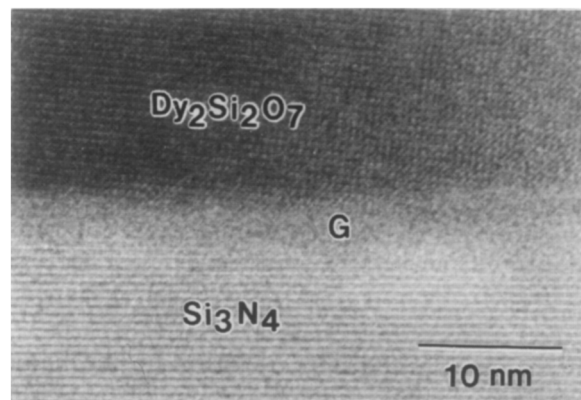


Fig. 17. Lattice image of Si₃N₄–Yb₂O₃ sintered sample showing intergranular amorphous phase (Ref. 40).

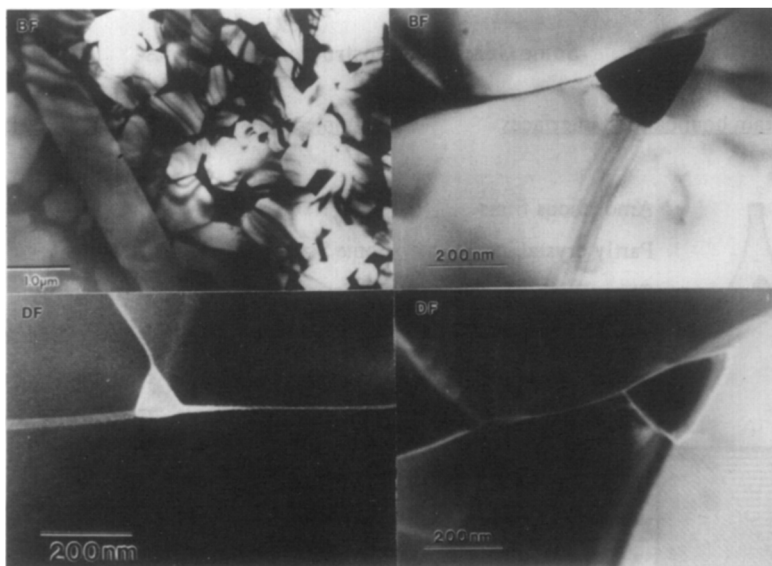


Fig. 16. Electron microscopy analyses of intergranular phases, crystalline and amorphous, in Si₃N₄ sintered with Yb₂O₃ (Ref. 40). Lower left is dark field image of RE silicate phase, lower right is diffuse dark field imaging showing glassy phase at grain boundaries.



Fig. 18. Lattice imaging showing a rare case of a glass-free $\text{Si}_3\text{N}_4/\text{Si}_3\text{N}_4$ interface (Ref. 40).

contain surface oxide, which on processing react to form intergranular monolayer glassy films.

These results of sintering silicon nitride with heavy rare-earth oxides to produce stable $\text{RE}_2\text{Si}_2\text{O}_7$ crystalline phases at grain boundaries are very encouraging. A summary of the main results obtained to date is given in Fig. 19. Sintering with $\text{RE}_2\text{Si}_2\text{O}_7$ produces material at nearly 99% theoretical density with a crystalline intergranular phase. Figure 19³⁸⁻⁴⁰ shows that these ceramics have greatly improved high temperature strength, creep and oxidation resistance. Results of fatigue behavior, Fig. 19(d), show no detrimental effects of the intergranular crystalline phase on fatigue behavior, probably because there is nearly always a glassy interface present.⁴¹ It is these interfaces that favor preferred crack propagation paths in both stable and fast fracture. Thus, the immediate crack tip environment may not be much affected by crystallization of the bulk intergranular phases. Greater differences are expected for high temperature testing where glasses become 'fluid.' The research is continuing, with emphasis on optimizing the sintered microstructures and more controlled fatigue experiments, especially at high temperatures. A detailed statistical survey of grain boundary films by HREM and AEM by Kleebe *et al.*⁴² showed that the glassy phase thickness at grain boundaries in Si_3N_4 sintered with Yb_2O_3 , Al_2O_3 and CaO depends on film chemistry. More work still is needed, however, especially high resolution microanalysis (including EELS).

3.2 Magneto-optical garnet heterostructures

The huge effort put into the development of a green-blue range diode laser has been coupled lately with a sustained effort in the study and production of magneto-optical (MO) materials that

respond to the blue radiation.⁴³ The MO materials already on the market are amorphous Tb-Fe-Co films with a decent response in the infrared region of the EM spectrum. Their response dies fairly quickly with an increase in radiation frequency. The idea behind the reduction of the wavelength is the increase in storage density (bit size is dependent on the resolution of the writing laser focused spot, which in turn is diffraction limited, controlled by the wavelength). By the end of the year, the thermo-magneto-optical media are expected to have about 25% of the optical memories market (reaching production of 12 million disks with a profit of \$300 million⁴³). The impact on the computer/memory industry is expected to increase when comparing the 10^8 bits/cm² of the MO disks with the 10^6 bits/cm² of the magnetic systems.

The best candidates considered for the next generation of MO materials are the garnets (particularly Bi substituted iron garnets; Bi increases the Faraday rotation), the ferrites, and the Co/Pt multilayers.⁴⁴ Of these, the garnets have the highest MO response in the blue-green range (our films have up to 54000 deg/cm in normal incidence reflective Faraday measurements).

Our effort has concentrated on the development of epitaxial heterostructures in collaboration with Belcore and IBM's Almaden Laboratory. Heterostructures of Bi-Fe-garnet and Y-Fe-garnet (BIG/YIG) as well as Eu-Bi-Fe-garnet and Y-Fe-garnet (EBIG/YIG) have been grown by pulsed laser ablation.⁴⁵ Experiments performed up to the present indicate increased MO performance and coercivities (up to 1.2 kOe for some films) with higher EBIG content of the films, as well as in improved MO response with a decrease of the total thickness of the films. The thick films (1.3-2.4 μm) showed rotations up to 13000 deg/cm, while the thin films (0.3-0.9 μm) go up to 54000 deg/cm. The increased performance of the thinner films raises the suggestion that magnetic coupling of the EBIG layers occurs through the YIG layers. The addition of Eu to the BIG structure has shown a change in the anisotropy of the films from in-plane to out-of-plane (all MO systems use perpendicular anisotropy for increased density and improved MO responses from the media).

Initial work by HREM-TEM indicates that while the YIG layers tend to grow epitaxially on the Gd-Ga-garnet (GGG) substrates (with high coherence of the interface, e.g. Fig. 20), the next layer (EBIG), although maintaining the apparent coherence, has to develop microstructural defects to accommodate the lattice mismatch with the YIG layer. Figure 21 is an example. Because the stresses induced in the material by the lattice mismatch tend to increase with the thickness of the layers,

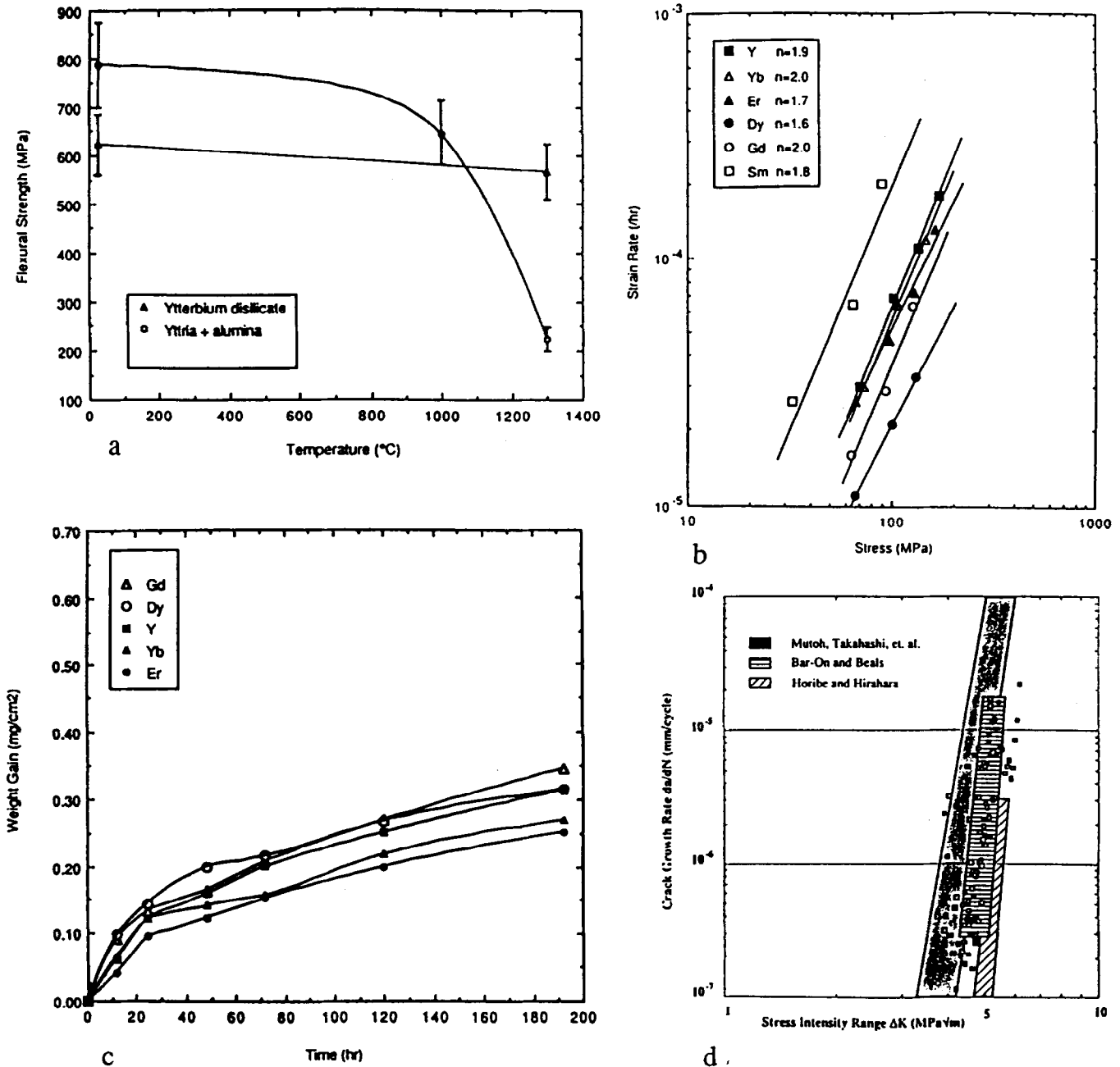


Fig. 19. Composite showing main mechanical properties of sintered Si_3N_4 : (a) Plot of flexural strengths from 25 to 1300°C; note the improvement for the Yb_2O_3 sintered material (Ref. 38; courtesy *J. Am. Ceram. Soc.*); (b) plot of steady state creep strain rates with applied stress at 1400°C in air. The exponents are shown in the inset (Ref. 38; courtesy *J. Am. Ceram. Soc.*); (c) plot of oxidation rates (weight gain) at 1400°C (Ref. 39; courtesy *J. Am. Ceram. Soc.*); (d) fatigue crack growth data for $\text{RE}_2\text{Si}_2\text{O}_7\text{-Si}_3\text{N}_4$ samples (data points) compared to published data (shaded) for room temperature tests; shows very little difference in crack growth rates (Ref. 41; courtesy Acta Met Inc.).

the thin films are probably prone to lower densities of such microstructural defects, and this may lead to improved MO responses. Such a relationship is speculative at this point and has to be proven by systematic microstructural characterizations of all the films in the series, followed by a coupling of these data with the magnetic and MO properties.

3.3 Multilayer mirrors: X-ray optics and interface roughness

The interest in multilayer mirrors in the soft X-ray regime is mainly twofold: (1) for X-ray lithography for digital devices requiring finer features and (2)

for X-ray microscopy for studying living biological specimens at high resolution. Such multilayers consist of alternating films of low density and high density materials, e.g. glass and heavy metal. The thickness of the layers is ideally quarter-wavelengths so as to optimize the reflected intensity. The roughness of the interface is important in affecting X-ray reflectivity and intensity.⁴⁶ Figure 22 is an example for Mo/SiO_2 formed by magnetron sputtering using two fixed guns and a rotating substrate holder. It can be seen that the metal layer is very defective. Stress relaxation can occur by elastic/plastic/fracture mechanisms. In

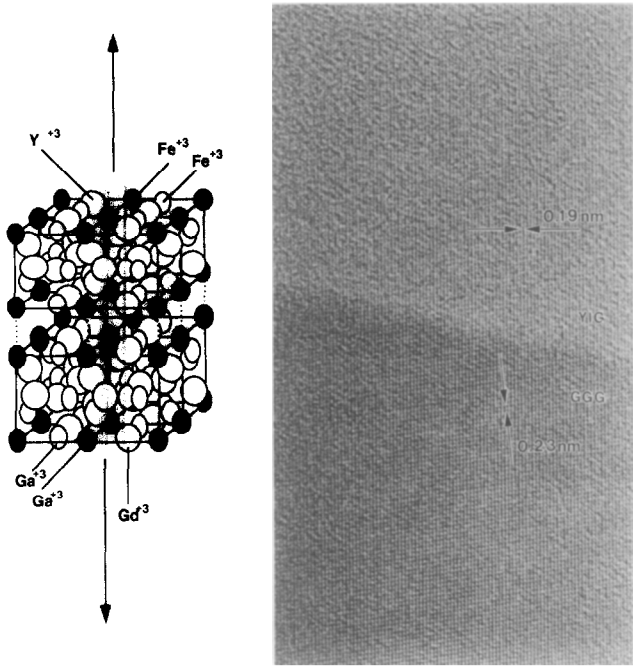


Fig. 20. Half unit cell diagrams indicating the substrate (GGG)/film (YIG) interface, and a high resolution image showing a GGG/YIG interface. The coherence of the interface indicates epitaxial growth. The image is taken in the $[-1 \ -5 \ 3]$ zone axis. The lattice spacings indicated correspond to one (026) plane - 0.19 nm and one (510) plane - 0.23 nm.

this case microtwinning can be resolved, and such twins produce surface shear steps which contribute to roughness during or after sputtering and can be independent of the smoothness of the substrate.

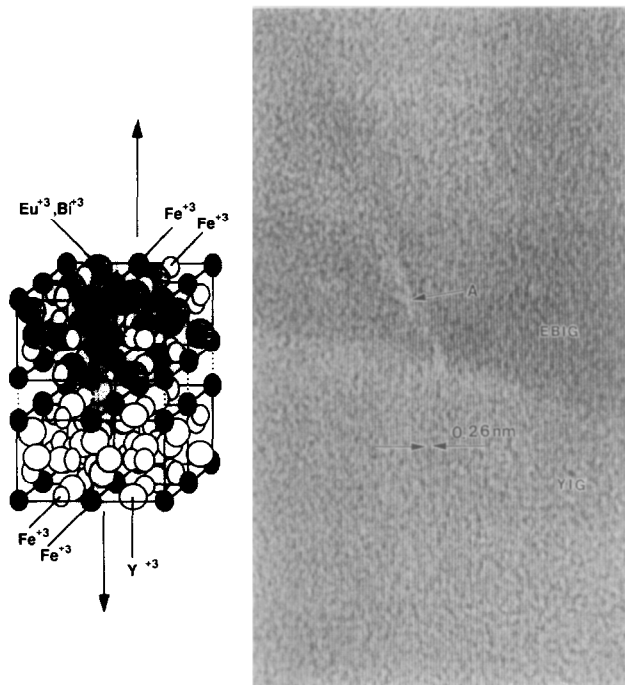


Fig 21. Half unit cell diagrams indicating the template (YIG)/film (EBIG) interface, and a high resolution image showing a YIG/EBIG interface. The coherence of the interface indicates epitaxial growth. At this second interface a number of defects can be observed (A). The image is taken in the $[-1 \ -5 \ 3]$ one axis. The lattice spacing indicated corresponds to (224) planes. The lattice mismatch between the two films is of 0.96%.

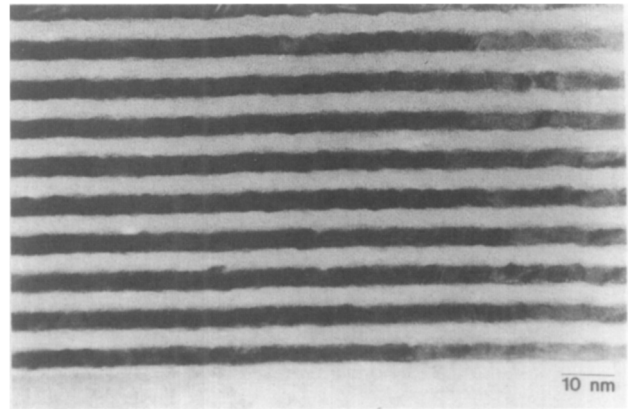


Fig. 22. Multilayer SiO_2/Mo films formed by magnetron sputtering. Notice high defect density in the Mo layers leading to interfacial roughness (courtesy C. Walton).

3.4 Multilayer magnetic oxides: roughness and coupling

Interfacial roughness is also an important factor which can affect electronic and magnetic properties. One example is ferromagnetic-antiferromagnetic coupling, which is effective in improving signal recording (noise reduction) in recording systems. One such system being studied in our group, in collaboration with Professor A. E. Berkowitz of U.C. San Diego,⁴⁷⁻⁴⁹ is coupling between ferromagnetic permalloy and antiferromagnetic NiO/CoO. The latter can be grown as a CoO-NiO alloy or multilayered NiO/CoO superlattices by sputtering on a suitable substrate, e.g. $\alpha\text{-Al}_2\text{O}_3$ [0001], to achieve [111] epitaxial growth.

As the schematic diagram of Fig. 23 shows, steps at the interface can interfere with the magnetic coupling. In addition to the similar task for preparing smooth multilayers for X-ray optics, the films must not deform plastically or else twin/slip steps are generated and rough interfaces can develop during or subsequent to film growth. Clearly, a study needs to be made of the accommodation of these films to strains, e.g. in terms of orientation, epitaxy, thickness, and heat treatment. Of course steps in the substrate surface can be propagated into the growing layer(s), so this first layer must be atomically smooth and clean to start.

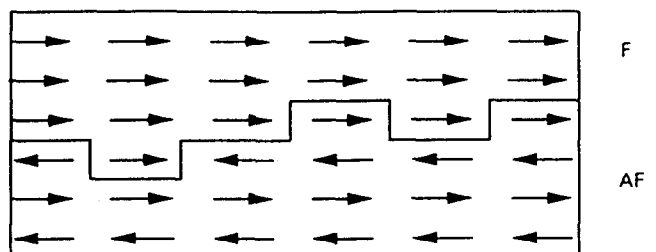


Fig. 23. Schematic of antiferromagnetic/ferromagnetic coupling. Notice now the roughness of the interface can affect the magnetic spin orientations and hence their interactions.

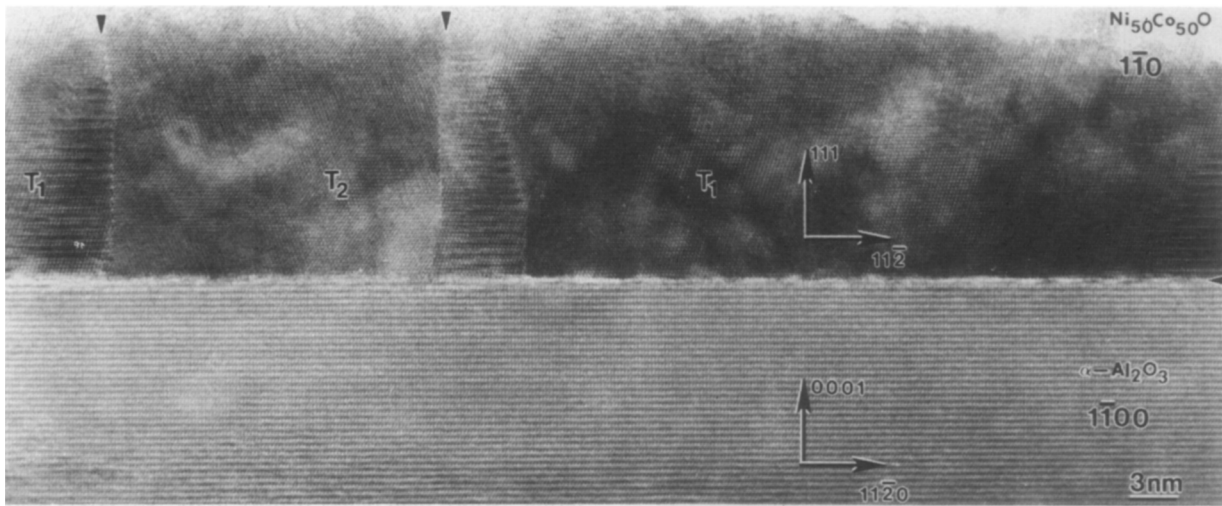


Fig. 24. Cross-section showing high resolution image of the epitaxial interface for CoONiO alloy sputtered onto [0001], α -Al₂O₃. Notice twins in the antiferromagnet (Ref. 47).

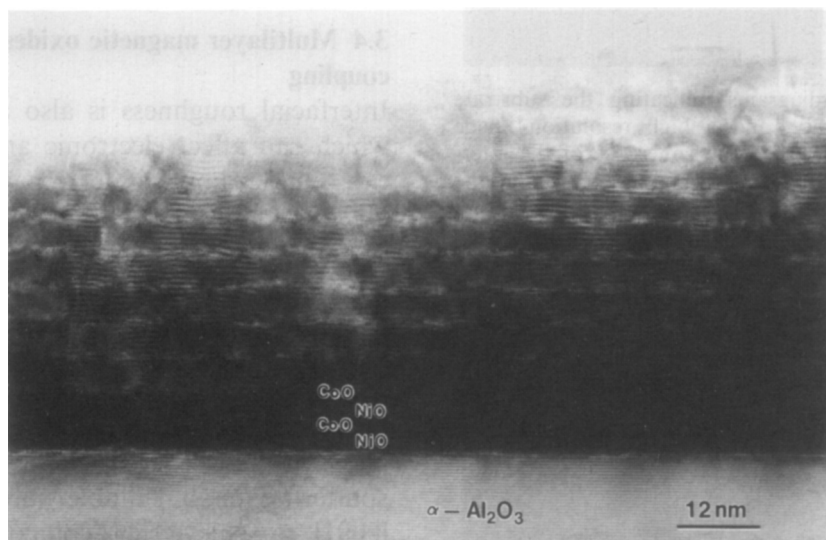


Fig. 25. Similar to Fig. 24 but with CoO/NiO multilayer sputtering. The CoO shows defect structures but no twins (Ref. 48).



Fig. 26. Cross-section of NiO/CoO and Fe/Ni interface which is very rough, resulting in poor magnetic coupling (courtesy W. Cao).

Figures 24 and 25 show these interfaces and Fig. 26 shows a poor permalloy–NiOCoO coupled interface.

4 Summary

Modern electron optical diffraction and analytical techniques are essential to understand ceramic (and *all*) materials. A major characterization difficulty is that of high resolution light element analysis, but ARM and PEELS hold great promise. Nevertheless, it is not too difficult to design ideal structures for specific property performance. The real challenge is the task of processing and consistent economical manufacturing practices, in order to produce the desired microstructures.

Acknowledgements

The research on magnetic recording materials is partially supported by National Science Foundation Grant No. DMR-90-10908 under a joint program with the Center for Magnetic Recording Research, University of California at San Diego (Professor A. E. Berkowitz). The work on structural ceramics and the electron microscopy facilities at the National Center for Electron Microscopy, Lawrence Berkeley Laboratory, are supported by the Director, Office of Basic Energy Sciences, Division of Materials Sciences of the United States Department of Energy under Contract No. DE-AC03-76SF00098. Work at Belcore/University of Maryland is supported by the Office of Naval Research. We acknowledge the cooperation of many groups, especially Professor R. Ramesh (Belcore and now University of Maryland), Dr. J. Petrovic at Los Alamos National Laboratory (MoSi₂), Mr Y. Goto of Toshiba (Si₃N₄ fibers), Dr E. Marinero (IBM Almaden Laboratory, San Jose, California), members of my research group, and co-authors of many of the examples cited in this short review.

References

1. Thomas, G., *Electron Microscopy and materials science. Acta Microscop.*, **1** (1) (1992) 1–19.
2. Spence, J. C. H., *Experimental High Resolution Electron Microscopy*, 2nd ed., Oxford University Press, UK, 1988.
3. Epicier, T., O'Keefe, M. A. & Thomas, G., Atomic imaging of 3:2 mullite. *Acta Cryst.*, **A46** (1990) 948–62.
4. See, for example, the annual proceedings of the Microscopy Society of America, and the proceedings of the International and Regional Electron Microscopy Congresses held every four years.
5. For example, M. O'Keefe, National Center for Electron Microscopy, Lawrence Berkeley Laboratory, Berkeley, California 94720, USA.
6. Steeds, J. W., Convergent beam electron diffraction. In *Introduction to Analytical Electron Microscopy*, eds J. J. Hren, T. J. Goldstein & D. C. Joy, Plenum, New York, 1979, pp. 387–422.
7. Dass, M. L. A., Bielicki, T. A. & Thomas, G., Convergent beam studies on lead zirconate titanate ceramics. In *Proceedings of the Electron Microscopy Society of America*, ed. G. W. Bailey. San Francisco Press, 1986, pp. 482–3.
8. Callahan, D. L. & Thomas, G., Convergent beam diffraction analysis of lattice shifts in AlN. *J. Am. Ceram. Soc.*, **75** (5) (1992) 1092–6.
9. Thomas, G. & Goringe, M. J., *Transmission Electron Microscopy of Materials*, J. Wiley & Sons, New York, and Tech Books, Fairfax, VA, 1981.
10. Merk, N. & Thomas, G., Structure and composition of submicroscopic mullite whiskers. *J. Mat. Res.*, **6** (4) (1991) 825–34.
11. Epicier, T. A., Wohlfromm, H. & Thomas, G., Dislocation analysis in Al₂TiO₅. In *Proceedings of the Electron Microscopy Society of America*, ed. G. W. Bailey. San Francisco Press, 1989, pp. 422–3.
12. Van Tendeloo, G., Faker, K. T. & Thomas, G., Characterization of long period polytypoids in AlN ceramics. *J. Mat. Sci.*, **18** (1983) 525–7.
13. Krishnan, K. M., Rai, R. S., Thomas, G., Corbin, N. D. & McAuley, J. W., Characterization of long period polytypoids in Al₂O₃–AlN System. In *Mat. Res. Soc. Symp. Proc.*, **60** 1986, pp. 211–20.
14. Shaw, T. M. & Thomas, G., Electro microscopy study of Be₃N₂–BeSiN₂ systems. *J. Sol. State Chem.*, **33** (1) (1980) 63–82.
15. Ramesh, R., Green, S. M. & Thomas, G., Microstructure property relationships in ceramic superconductors. In *Studies of High Temperature Superconductors*, Vol. 5, ed. Anant Narlikar. New York, Nova Science Publishers (4) 1989, pp. 361–403.
16. McFayden, André, Mullite-whisker reinforced molybdenum disilicide composites. PhD thesis. University of California, Berkeley, CA, 1995.
17. Vasudevan, A. K. & Petrovic, J. J., A comparative overview of molybdenum disilicide composites. *Mater. Sci. Eng.*, **A155** (1992) 1–17.
18. Lessing, P. A., Gordon, R. S. & Mazdiyasi, K. S., Creep of polycrystalline mullite. *J. Am. Ceram. Soc.*, **58** (1975) 149.
19. Williams, D. B., *Practical Analytical Electron Microscopy in Materials Science*, Verlag Chemie Int., 1984.
20. Blake, D. F. *et al.* Nature and origin of interstellar diamond. *Nature*, **332** (1988) 611–13.
21. *Proceedings of Symposium on Magnetic Imaging*, Microscopy Society of American, eds G. W. Bailey & C. L. Rider, San Francisco Press, 1993, pp. 1010–53.
22. Lin, I-Nan, Mishra, R. K. & Thomas, G., TEM study of structure and composition of MnZn ferrites. In *Proceedings of Advanced Materials Characterization*, Plenum, New York, 1983, pp. 351–8.
23. Thomas, G., High resolution analyses and interfacial design of inorganic materials. *Scripta Metall Mater.*, **31** (1994) 953–8.
24. Clarke, D. R. & Thomas, G., Microstructure of Y₂O₃ fluxed hot pressed silicon nitride. *J. Am. Ceram. Soc.*, **61** (1978) 114–18.
25. Thomas, G., Grain boundaries and interfaces. In *Ceramic Microstructures '86*, eds J. A. Pask & A. G. Evans. Plenum, New York, 1988, pp. 55–72.
26. Thomas, G., Ahn, C. & Weiss, J., Characterization and crystallization of Y–Si–Al–O–N glasses. *J. Am. Ceram. Soc.*, **65** (1982) C185–8.
27. Dinger, T. R., Rai, R. S. & Thomas, G., Crystallization behavior of a glass in the Y₂O₃–SiO₂–AlN system. *J. Am. Ceram. Soc.*, **71** (1988) 236–44.
28. Cinibulk, M. K., Thomas, G. & Johnson, S. M., Fabrication and secondary phase crystallization of RE disilicate–Si₃N₄ ceramics. *J. Am. Ceram. Soc.*, **75** (1992) 2037–43.

29. Tsuge, A., Nishida, K. & Komatsu, M., Effect of crystallizing grain boundary phase on high temperature strength of hot pressed Si_3N_4 ceramics. *J. Am. Ceram. Soc.*, **58** (1975) 323–6.
30. Lange, F. F., Singhal, S. C. & Kuznicki, R. C., Phase relations and stability studies in Si_3N_4 - SiO_2 - Y_2O_3 pseudoternary system. *J. Am. Ceram. Soc.*, **60** (1977) 249.
31. Loehman, R. E., Preparation and properties of oxynitride glasses. *J. Non-Cryst. Solids*, **56** (1983) 411–16.
32. Clarke, D. R., Lange, F. F. & Schnittgrund, G. D., Strengthening of sintered Si_3N_4 by a post-fabrication heat treatment. *J. Am. Ceram. Soc.*, **65** (1982) C51–2.
33. Bonnell, D. A., Tien, T.-Y. & Rühle, M., Controlled crystallization of the amorphous phase in silicon nitride ceramics. *J. Am. Ceram. Soc.*, **70** (1987) 460–5.
34. Cinibulk, M. K., Thomas, G. & Johnson, S. M., Grain boundary phase crystallization and strength of Si_3N_4 sintered with YAlSiO_3 glass. *J. Am. Ceram. Soc.*, **73** (1990) 1606–14.
35. Sanders, W. A. & Mieskowski, D. M., Strength and microstructure of sintered Si_3N_4 with RE oxide additions. *J. Am. Ceram. Soc.*, **64** (1985) 304–9.
36. Lewis, M. H., Reed, C. J. & Baker, N. D., Pressureless sintered ceramics based on $\text{Si}_2\text{N}_2\text{O}$. *Mat. Sci. Eng.*, **71** (1985) 87–94.
37. Wiederhorn, S. M. & Tighe, J. J., Structural reliability of Y_2O_3 doped hot pressed Si_3N_4 at elevated temperatures. *J. Am. Ceram. Soc.*, **66** (1983) 884–9.
38. Cinibulk, M. K., Thomas, G., & Johnson, S. M., Strength and creep behavior of RE disilicate - Si_3N_4 ceramics. *J. Am. Ceram. Soc.*, **75** (1992) 2050–5.
39. Cinibulk, M. K., Thomas, G. & Johnson, S. M., Oxidation behavior of RE disilicate — Si_3N_4 ceramics. *J. Am. Ceram. Soc.*, **75** (1992) 2044–9.
40. Goto, Y. & Thomas, G., Microstructure of Si_3N_4 ceramics sintered with RE oxides. *Acta Metall. Mater.*, **43** (1995) 923–30.
41. Cornelissen, B. E., Dauskart, R. H., Ritchie, R. O. & Thomas, G., Cyclic fatigue behavior and fracture toughness of Si_3N_4 ceramics sintered with RE oxides. *Acta Metall. Mater.*, **42** (1994) 3055–64.
42. Kleebe, H.-J., Cinibulk, M. K., Cannon, R. M. & Rühle, M., Statistical analysis of the intergranular film thickness in silicon nitride ceramics. *J. Am. Ceram. Soc.*, **76** (1993) 1969–77.
43. Hall, C. W., Magneto-optic media. In *Storage and Recording Systems*, Conference Publication 402. London, Institute of Electrical Engineers, 1994, pp. 137–9.
44. Lin, C. J., Co/Pt multilayers for magneto-optical recording. In *High Density Recording*, ed. K. H. J. Buschow, NATO ASI Series, 1993, pp. 461–81.
45. Simion, B. M., Ramesh, R., Keramidis, V. G., Pfeffer, R. L., Thomas, G. & Marinero, E., Magnetic characterization of epitaxial $\text{Y}_5\text{Fe}_3\text{O}_{12}/\text{Bi}_3\text{Fe}_5\text{O}_{12}$ and $\text{Y}_5\text{Fe}_3\text{O}_{12}/\text{Eu}_1\text{Bi}_2\text{Fe}_5\text{O}_{12}$ heterostructures grown by pulsed laser deposition. In *Epitaxial Oxide Thin Films and Heterostructures*, eds D. K. Fork, J. M. Phillips, R. Ramesh & R. M. Wolf, Pittsburgh, *Mat. Res. Soc.*, 1994, pp. 65–72.
46. Hütten, A., Cao, W., Walton, C. & Thomas, G., Structural properties of multilayer thin films. In *Proceedings of 13th Congress on Electron Microscopy*, 2A, Paris, French Society for Electron Microscopy, 1994, pp. 231–2.
47. Cao, W., Thomas G., Carey, M. J. & Berkowitz, A. E., Characterization of epitaxially sputtered $\text{Ni}_x\text{Co}_{1-x}$ thin films on $\alpha\text{-Al}_2\text{O}_3$ using TEM. *Scripta Metall. Mater.*, **25** (1991) 2633–8.
48. Carey, M. J., Spada, F. E., Berkowitz, A. E., Cao, W. & Thomas, G., Preparation and structural characterization of sputtered CoO/NiO thin epitaxial films. *J. Mat. Res.*, **6** (1991) 2680–7.
49. Fullerton, E. E., Cao, W., Thomas, G., Schuller, I. K., Carey, M. J. & Berkowitz, A. E., Quantitative characterization of epitaxial superlattices by X-ray diffraction and HREM. *Appl. Phys. Lett.*, **63** (1993) 482–8.

Transmission Electron Microscopy of Microstructures in Ceramic Materials

Hans-Joachim Kleebe,^a Wolfgang Braue,^b Hans Schmidt,^a Giuseppe Pezzotti^c & Günter Ziegler^a

^aUniversity of Bayreuth, Institute of Materials Research, Ludwig-Thoma-Str. 36B, D-95447 Bayreuth, Germany

^bGerman Aerospace Research Establishment (DLR), Materials Research Institute, Linder Höhe, D-51147 Cologne, Germany

^cToyohashi University of Technology, Department of Materials Science, Hibarigaoka, Tempaku-cho 1-1, Toyohashi 441, Japan

(Received 4 July 1995; accepted 10 September 1995)

Abstract

Based on selected examples from the area of Si_3N_4 ceramics, the value of utilizing transmission electron microscopy (TEM) as a technique to study ceramic microstructures as well as a characterization tool for the development of new materials is demonstrated. In the field of 'new ceramics', one Si_3N_4 -based composite is discussed, which was processed via pyrolysis of liquid precursors (polysilazanes). Moreover, it is shown that TEM in general can helpfully accompany ceramic processing techniques. This applies to the characterization of ceramic starting powders as well as to the study of densified materials. The investigation of Si_3N_4 powders, in particular the influence of the addition of sintering aids via organometallic precursors, which leads to a homogeneous distribution of sintering additives in the powder compact, in contrast to the use of metal oxide powders, is shown. The variation of microstructures during the densification process of liquid assisted sintering is also demonstrated. The most common application of the TEM technique is to characterize dense ceramic components in the as-processed (as-sintered) state. Post-sintering heat treatment can initiate secondary phase crystallization. However, the very important aspect of microstructure integrity at elevated temperatures, e.g. the stability of microstructures under severe service conditions, is also addressed. Emphasis is placed on the fact that ceramic microstructures, which are typically thought to be rather stable, can undergo serious microstructural changes when temperature and stress is applied simultaneously, which strongly limits potential applications of these materials.

1 Introduction

It is well established that transmission electron

microscopy (TEM) is a very helpful and powerful technique to characterize microstructures of materials in detail. It is way beyond the scope of this paper to review all major contributions in materials science which are related to TEM, however, it should be emphasized that this technique allows the gathering of a wide variety of different information with respect to microstructure and/or composition with high spatial resolution.^{1,2} The main areas of information covered by TEM investigations are: (i) conventional imaging; (ii) electron diffraction; (iii) chemical microanalysis—EDX, EELS; (iv) high-resolution imaging and (v) magnetic structure imaging—Lorentz microscopy. Apart from diffractive data, obtained by either selected area (SAD) or convergent beam electron diffraction (CBED) techniques,^{3,4} which allow phase identification as well as space group determination or residual stress analysis, one of the major contributions of TEM to materials science is the enlarged understanding of materials performance.^{5–8} This is based on the correlation between microstructural features observed during TEM inspection and bulk material properties. In order to tailor materials to meet specific requirements such as high temperature performance, the relationship between processing, microstructure, and mechanical behaviour has to be known. Therefore, this paper intends to underline the importance of TEM analysis to materials science in general and, in particular, to the processing and development of ceramics. However, it should be emphasized that the information obtained by TEM with respect to the overall ceramic microstructure is the final result of a number of processing steps involved, each of which plays an important role during microstructure development.^{9,10} Hence, materials characterization can be rationalized in terms of: (i) powder processing; (ii) powder compacts; (iii) development during

sintering — temperature and time dependence; (iv) as-sintered microstructure and (v) variation of microstructure under service conditions.

The studies reported here focus on Si_3N_4 -based ceramics as one representative of the important materials group of structural ceramics for technical and engineering applications. Emphasis is placed on the fact that TEM is a favourable technique to characterize the materials along the different processing steps involved in the production of dense components. In addition to the microstructural development of Si_3N_4 -based materials, processed via the two major processing routes utilized today, i.e. powder processing and organometallic precursors, the variation of microstructure under service conditions, as observed by TEM, is also discussed. Hence, processing of Si_3N_4 ceramics is characterized from its origin, the powder particle and doping of starting powders with sintering aids, through the formation of a dense body to the performance of the final product at elevated temperatures and higher local stresses. It should be noted here that the observed degradation in microstructure stability under testing conditions seemingly suggests a rather limited potential of Si_3N_4 ceramics for high-temperature performance.

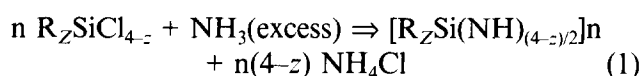
2 Experimental Procedures

2.1 Materials preparation

Processing of different silicon nitride-based ceramics was accompanied by transmission electron microscopy studies, in order to characterize microstructural development during subsequent processing steps. Incorporation of sintering additives was made by both mixing/milling of the Si_3N_4 powders with the metal oxide, (e.g. Y_2O_3 , HC-Starck) and by utilizing soluble organometallic compounds (Y-ethanolate, Aldrich) which react with the surface silanol groups in a non-aqueous solvent. In case of organometallic doping, the corresponding metal oxide is formed after calcination at an elevated temperature of approximately 800°C . The respective processing steps involved to form dense sintered (SSN) or dense post-sintered reaction bonded Si_3N_4 materials (SRBSN) via gas-pressure sintering (GPS) are reported in detail elsewhere.¹¹ GPS usually follows four distinct dT/dt ramps. The increase from RT to 1100°C was achieved in about 1 h, followed by two 30 min intervals for the ramps between 1100 and 1300°C and between 1300 and 1875°C . To ensure the formation of closed porosity within the presintered body, the experiment was held for 20 min at 1875°C ($p_{\text{N}_2} = 1.5 \text{ MPa}$). Thereafter, the N_2 -pressure was increased to 10 MPa with the temperature raised to 1925°C

and held for 60 min. During gas-pressure sintering, a dilatometer was attached to the specimen surface in order to register both linear shrinkage and densification rate during sintering.

Processing of Si_3N_4 -based ceramics via organometallic precursors was performed by the synthesis of polycarbosilazanes at room temperature by the ammonolysis of substituted chlorosilanes $\text{R}_z\text{SiCl}_{4-z}$ ($\text{R} = \text{H}$, alkyl, $\text{CH} = \text{CH}_2$). The reaction which is given in (1) was



carried out in dry toluene.¹² After removing both ammonium chloride and solvent the remaining liquid polysilazanes yields 75–85%. Purity and structure of the precursors were determined spectroscopically and by chemical analysis.¹³ Precursor synthesis, processing and characterization were performed in an inert gas atmosphere (Schlenk technique, glove box) to avoid the incorporation of oxygen. Crystallization as well as reaction behaviour of the materials were investigated at temperatures up to 1600°C .*

2.2 Microstructure characterization, TEM studies

The overall microstructural characterization of the Si_3N_4 materials investigated was performed by transmission electron microscopy (TEM) utilizing a Philips CM20FEG (field emission gun) microscope fitted with both an ultra-thin window Ge energy dispersed X-ray (EDX) detector and a PEELS spectrometer. Operating at 200 kV, the instrument reveals a point resolution of 0.24 nm. TEM-foil preparation followed standard techniques commonly used for ceramic materials which involve diamond cutting, ultra-sound drilling, mechanical grinding, dimpling, Ar-ion thinning to perforation, and light carbon coating to minimize electrostatic charging under the electron beam. In addition to conventional TEM analysis, high-resolution electron microscopy (HREM) imaging was performed to study two-grain boundaries ($\text{Si}_3\text{N}_4/\text{Si}_3\text{N}_4$ interfaces) utilizing a JEOL JEM 4000EX (top entry) operating at 400 kV with a point resolution of 0.18 nm.[†]

Surface analysis of commercially available Si_3N_4 powders (direct nitridation: Denka SN-9FW, diimide precipitation: Tosoh TS-10) was performed by XPS (Perkin Elmer PHI 5600) and FT-IR spec-

*The material investigated was fabricated by Dr H. Schönfelder at the Max-Planck-Institute in Stuttgart under the assistance of Prof. R. Riedel and Prof. F. Aldinger.

†The high-resolution electron microscope is located at the Max-Planck-Institute in Stuttgart and the HREM work presented in Figs 6 and 7 was performed with the support of Prof. M. Rühle.

trospectroscopy (Digilab FTS 15/80; reflection mode). Qualitative phase analysis from bulk materials was determined by standard powder X-ray diffraction (Seifert XRD3000P) techniques. In addition to TEM studies, quantitative microstructure analysis was performed using an image processing system (Quantimet 5000). The evaluation of the microstructure was based on CF_4 plasma-etched cross sections of the corresponding materials obtained by scanning electron microscopy (SEM) using a Jeol JSM-6400 instrument operating at 30 kV. The K_{1c} -values of the different Si_3N_4 materials were determined by Vickers hardness indentation measurements (10 kg, 10 s, 0.5 mm/min) as well as Chevron notch experiments. In addition, crack propagation studies were performed by SEM and correlated to the grain-boundary chemistry (sintering aid composition) in these materials.

2.3 Microanalysis, EELS characterization

Electron energy-loss spectroscopy (EELS) studies were performed utilizing a PEELS spectrometer (Gatan, 666) with parallel detection, which is fitted to the Philips CM20FEG (field emission gun) microscope operating at 200 kV. Under optimized working conditions, an energy resolution of 0.75–0.80 eV was achieved, which also allows for energy-loss near edge structure (ELNES) analysis. It should be noted that during EELS measurements of the glass phase, present at triple-grain pockets as well as along interfaces, these amorphous residues can easily be damaged since a high energy field emission gun is utilized. In order to limit possible changes in the local chemistry owing to beam damage, which would exclude quantitative chemical analysis, a slightly defocused and spread beam was used during acquisition of the different spectra. These only slightly altered acquisition conditions do not influence the energy resolution of the spectrometer.

3 Results and Discussion

3.1 Characterization of starting powders

In general, there are two major routes regarding processing of ceramic components: (i) the classic way of utilizing crystalline ceramic starting powders to shape powder-compact preforms, which are subsequently densified via liquid assisted sintering and (ii) the utilization of liquid, highly viscous precursors (commonly polysilazanes), which are heat treated after initial cross-linking to form amorphous pre-ceramics that can finally be transformed into fully crystalline ceramics with a low oxygen content.^{14–16} In this section, only the characterization of crystalline Si_3N_4 starting powders

by TEM is presented since polymer-derived powders are typically amorphous. However, the microstructure development of such amorphous pre-ceramics during subsequent heat treatment up to 1600°C is discussed in more detail in the following section.

3.1.1 Particle-surface chemistry (organometallic doping)

Apart from the characterization of crystalline powders, which commonly focuses on the determination of intrinsic defects and the imaging of amorphous oxidized surface films, the influence of the oxygen distribution and chemical bonding state as well as the particle shape and surface chemistry (OH-group versus fluorine occupation) on both the doping via organometallic precursors and the densification rate of the powder compacts was investigated.^{17–20} Two Si_3N_4 powders, processed via direct nitridation (Denka) and diimide precipitation (Tosoh), were studied. Photoelectron spectroscopy (XPS) studies revealed a lower oxygen concentration at the Si_3N_4 particle surface for the Denka powder SN-9FW compared to the Tosoh powder TS-10, (see Fig. 1(b)). In addition, a high fluorine concentration was observed in the Denka powder. The low oxygen content is closely related to the high fluorine content since the powder, processed via direct nitridation, was subsequently HF leached, which reduces the continuous silica layer on the Si_3N_4 particle surface and, furthermore, introduces fluorine into the powder and reduces the amount of surface OH-groups. Infrared spectroscopy (FT-IR) revealed an increasing height of the absorption peak of the OH-stretching vibration at 3750 cm^{-1} for the Tosoh powder in contrast to the Denka Si_3N_4 powder, as depicted in Fig. 1(a).

Comparing TEM micrographs of the two different synthesized starting powders, the data obtained by spectroscopic means are consistent with the TEM observations of the particle surfaces with high spatial resolution.²⁰ Moreover, densification studies performed by *in situ* dilatometry during gas-pressure sintering showed a clear difference between the two starting powders investigated. By adding sintering aids via organometallic compounds, a higher densification rate was monitored for the Tosoh powder (diimide precipitation, high OH-group occupancy). It is thought that a homogeneous coverage of the Si_3N_4 particle surface with the sintering aid in combination with a continuous SiO_2 layer leads to a higher density of contact points, where liquid can locally be formed at elevated sintering temperatures, which results in the observed enhanced densification rate. Therefore, the use of organometallic compounds is

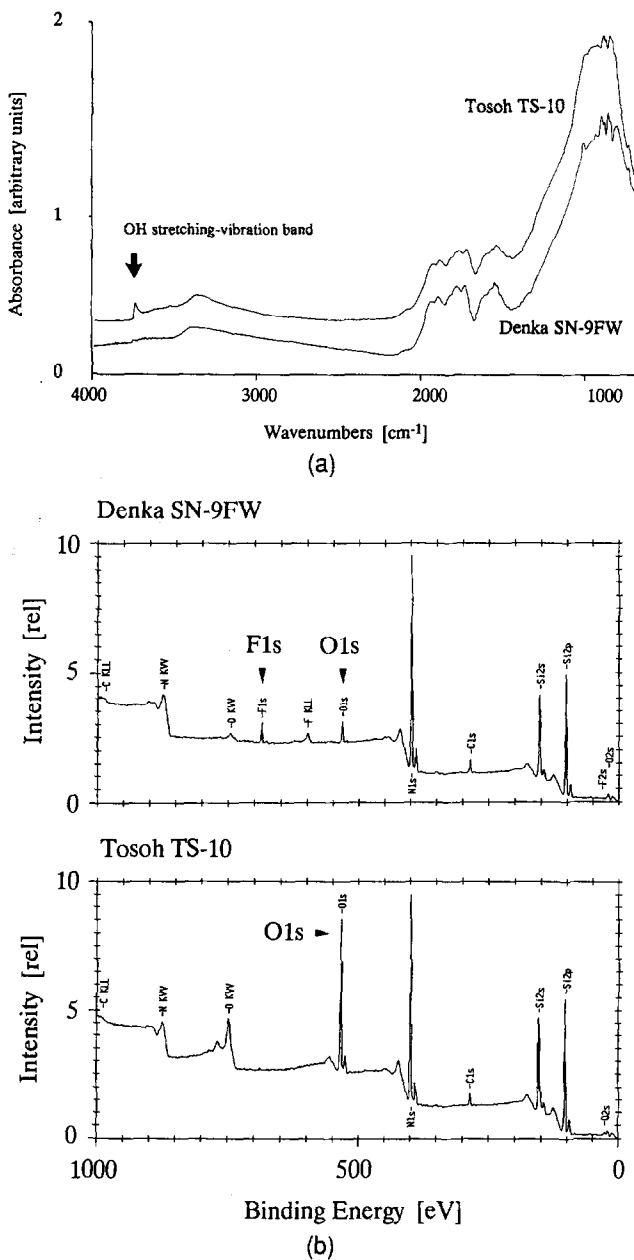


Fig. 1. (a) FT-IR spectra of the undoped Tosoh TS-10 (diimide process) and Denka SN-9FW (direct nitridation) Si_3N_4 powders. Note the higher OH-stretching vibration intensity at 3750 cm^{-1} for the Tosoh powder indicating a higher OH-group occupancy which favours doping via organometallic precursors. (b) XPS spectra for both Si_3N_4 powders showing strong variations in the surface oxygen and fluorine content.

favourable for Si_3N_4 processing, however, it should be noted that this potential advantage strongly depends on the particle-surface chemistry of the powder (oxygen content, fluorine content, OH-groups). XPS in addition to FT-IR studies clearly revealed that a high OH-group occupancy, a high surface oxygen content (not the total oxygen content), and a low fluorine concentration, as given for the Tosoh TS-10 powder, are necessary requirements in order to fully exploit the potential of chemical doping.

In contrast, Fig. 2 also reveals an inhomogeneous distribution of Y_2O_3 addition (via organo-

metallic precursors) for the Denka Si_3N_4 powder with a relatively low OH-group occupancy and a thin amorphous oxidized layer on the particle surface. This study unequivocally showed that particle-surface chemistry strongly affects the distribution of sintering aids dispersed within the Si_3N_4 -powder compact as well as the densification behaviour of the material. Moreover, it should be emphasized that a distinction between surface oxygen and bulk oxygen (partially dissolved in the crystal lattice) has to be made.

3.2 Microstructure development during densification

3.2.1 Powder derived ceramics (transient crystalline phases)

Densification behaviour of ZrO_2 -fluxed SRBSN was monitored by *in situ* dilatometry and correlated to the microstructural development of the material using conventional TEM, HREM and AEM. Two distinct densification events were observed at $1730\text{--}1750^\circ\text{C}$ and at $1900\text{--}1920^\circ\text{C}$. The densification rate during the first dilatometer maximum was relatively low with $0.5\text{ }\mu\text{m}/\text{min}$ compared to the second maximum which was strongly pronounced with $70\text{ }\mu\text{m}/\text{min}$. The low densification rate of the first dilatometer event can be related to the formation of a silica-rich highly viscous liquid phase, which mainly promotes rearrangement of the matrix grains. Conventional TEM investigations of TEM-foils which corresponded to the two dilatometer maxima showed marked differences regarding both crystalline phase assemblage and microstructure development, as reported in more detail elsewhere.²¹

The low-temperature sintered body consisted of homogeneously fine-grained $\beta\text{-Si}_3\text{N}_4$ particles with a relatively high amount of residual porosity of approximately 10 vol%, as estimated by TEM. As opposed to the fully dense material, no elongated large $\beta\text{-Si}_3\text{N}_4$ grains were present at this stage of microstructural development. However, some extended aggregates of the crystalline ZrO_2 secondary phase (up to $5\text{ }\mu\text{m}$ in diameter), which are presumably due to agglomeration during powder processing, were occasionally observed. It is important to note that these agglomerates are only present under the conditions of the first dilatometer maximum and were not observed in the densified SRBSN materials. This indicates that the unstabilized zirconia addition does not (or only in a very limited amount) contribute to the liquid-phase formation process within the low-temperature densification regime.

Apart from the large agglomerates crystalline ZrO_2 secondary phases are present at three- and four-grain junctions. In addition to the ZrO_2 ,

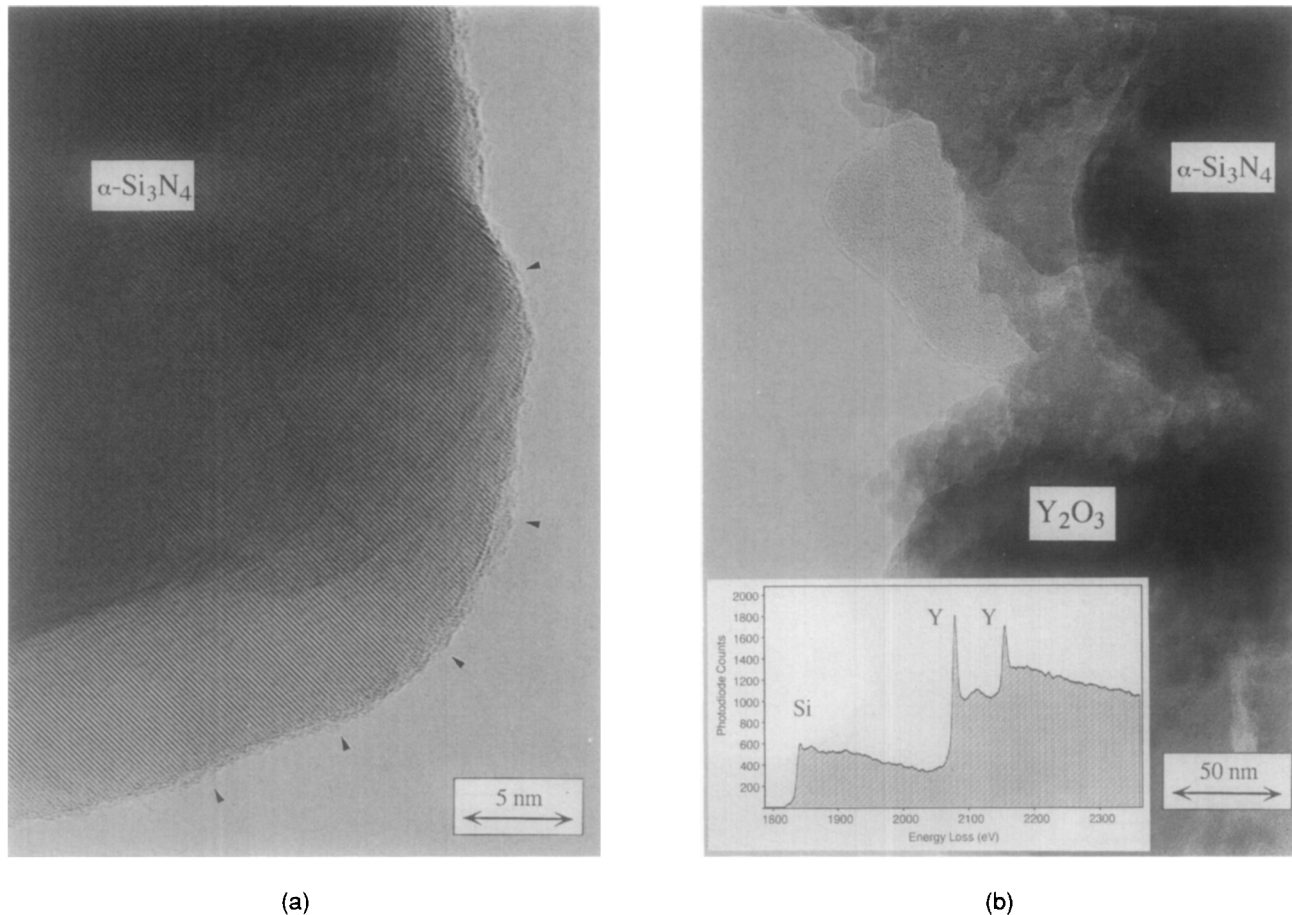
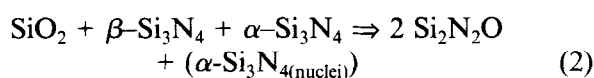


Fig. 2. TEM bright field images of (a) the Tosoh TS-10 powder homogeneously covered by a thin amorphous ytria layer (organo-metallic doping) and (b) the Denka SN-9FW powder, where an inhomogeneous precipitation of amorphous ytria is shown. Note that the inhomogeneity in sintering aid distribution is based on the particle surface chemistry, i.e. the relatively low OH-group occupancy and the high fluorine content of the nitrided powder.

$\text{Si}_2\text{N}_2\text{O}$ was also observed in the material which corresponds to the first low-temperature sintering event. Although, with respect to its thermal stability, $\text{Si}_2\text{N}_2\text{O}$ is a transient secondary phase in the $\text{Si}_3\text{N}_4\text{-ZrO}_2$ system, it plays an important role during liquid phase sintering of Si_3N_4 ceramics. This becomes evident comparing the characteristic microstructural features of $\text{Si}_2\text{N}_2\text{O}$ microcrystals from the $\text{Si}_3\text{N}_4\text{-ZrO}_2$ material with other liquid-phase sintered Si_3N_4 -based materials, e.g. the $\text{SiO}_2\text{-Si}_3\text{N}_4$ binary system.²² As shown in Fig. 3, $\text{Si}_2\text{N}_2\text{O}$ contains numerous small spherical intragranular inclusions which were identified as $\alpha\text{-Si}_3\text{N}_4$ by means of HREM, CBED and small probe microanalysis. This is in agreement with recent observations obtained from $\text{Si}_2\text{N}_2\text{O}$ microcrystals formed during liquid-phase sintering in the system $\text{SiO}_2\text{-Si}_3\text{N}_4$.²³ Based on the TEM observations, the reaction scheme which is given in (2) is proposed.



In the ZrO_2 -fluxed SRBSN materials an eutectic SiO_2 -rich liquid is formed at approximately 1680°C and, since the α/β Si_3N_4 phase transformation is not yet completed, $\text{Si}_2\text{N}_2\text{O}$ is formed

surrounding $\alpha\text{-Si}_3\text{N}_4$ particles. It is important to note that $\text{Si}_2\text{N}_2\text{O}$ is a transient phase in the temperature range of $1700\text{--}1800^\circ\text{C}$ and will decompose at higher sintering temperatures, which influences the densification behaviour of the material. Therefore, the relatively low densification rate of the first dilatometer maximum of $5 \mu\text{m}/\text{min}$ can be related to the formation of a SiO_2 -rich eutectic liquid enhancing particle rearrangement. Moreover, the results suggest that the formation of $\text{Si}_2\text{N}_2\text{O}$ grains during the first dilatometer maximum influences further densification, because the SiO_2 content in the liquid phase present at elevated temperatures is changed. With increasing sintering temperature and duration of the experiment, the SiO_2 content and hence the amount of liquid is lowered by the $\text{Si}_2\text{N}_2\text{O}$ formation, which strongly retards further densification.

Upon sintering, the material was fully densified and no large secondary-phase agglomerates were observed. Moreover, $\text{Si}_2\text{N}_2\text{O}$ is no longer present in the microstructure, owing to the thermal degradation of $\text{Si}_2\text{N}_2\text{O}$ above 1830°C ²² releasing additional SiO_2 and Si_3N_4 and, therefore, increasing the liquid-phase amount in the $\text{Si}_3\text{N}_4\text{-ZrO}_2$ system. Thus, both $\text{Si}_2\text{N}_2\text{O}$ and ZrO_2 participate in the

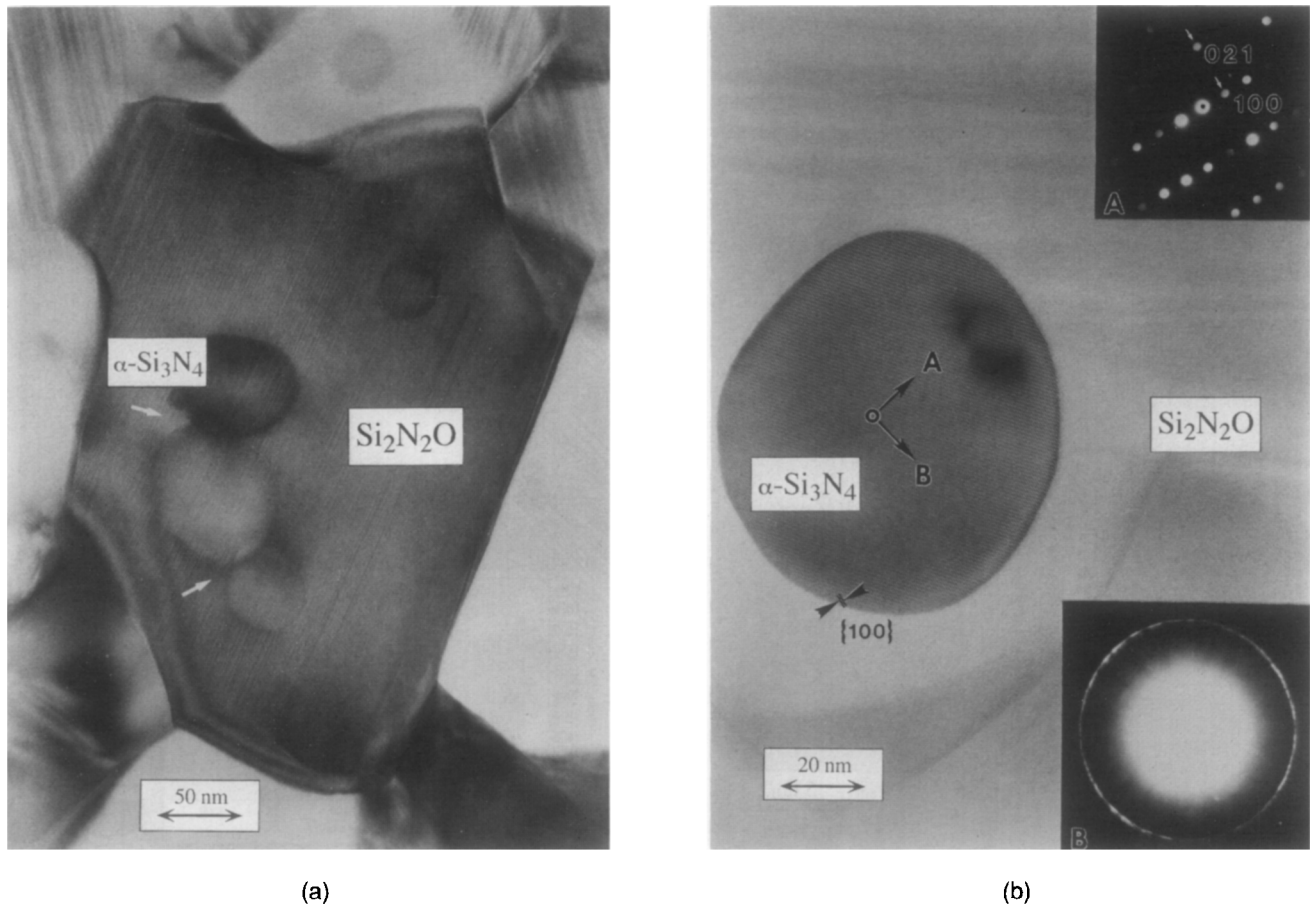


Fig. 3. (a) TEM bright field image and (b) HREM micrograph of a similar area showing an $\text{Si}_2\text{N}_2\text{O}$ crystal with intergranular spherical $\alpha\text{-Si}_3\text{N}_4$ inclusions (arrowed). The image is taken from the ZrO_2 -doped SRBSN microstructure equivalent to the first low-temperature dilatometer maximum. Note the high density of planar defects in the $\text{Si}_2\text{N}_2\text{O}$ grain. At higher sintering temperatures, $\text{Si}_2\text{N}_2\text{O}$ is no longer observed in the microstructure (transient phase).

liquid-phase formation and give rise to the strongly pronounced densification, as observed in the second dilatometer maximum. It should be noted that the microstructure development of dense ceramic materials can only be understood in light of the transient crystalline phases which form and subsequently decompose during the densification process.

3.2.2 Polymer derived ceramics (crystallization)

In the Si-C-N system, synthesis of polymer-based precursors was performed with respect to optimization of viscosity, wettability, long-term stability and maximum ceramic yield.^{13,16} Improved thermal behaviour as one aim of the development of such polymer-derived ceramics was investigated in the temperature range up to 1600°C in air.²⁴ Heat treatment at 1400°C in N_2 -atmosphere results in a nearly completely amorphous silicon carbonitride matrix phase $\text{Si}_{3+x}\text{N}_4\text{C}_{x+y}$. TEM observations revealed that, in contrast to XRD analysis, small precipitates of $\alpha\text{-Si}_3\text{N}_4$, $\alpha\text{-SiC}$, and graphite are already present within the amorphous matrix. The amount of these phases is, however, below the detection limit of the XRD measurement. On further oxidizing annealing above 1400°C, the amorphous material continues to crys-

tallize. The $\alpha\text{-Si}_3\text{N}_4$ crystals continuously grow, forming large microcrystals, as depicted in Fig. 4.

$\alpha\text{-SiC}$ continues to crystallize as well, but no-enhanced grain growth was observed. The overall SiC crystallite size is approximately 10–20 nm. Apart from Si_3N_4 (microcrystals) and SiC (nano-sized crystallites) residual graphite was also observed in the material. The presence of graphite is consistent with the chemical composition of the polysilazane precursor. It can be concluded that the phase assemblage within the material did not change during heat treatment up to 1600°C in air. The material studied underwent complete crystallization during oxidation at 1600°C for 50 h. No residual amorphous phase was observed during TEM investigations. The oxidation resistance of this covalently bonded ceramic micro-nanocomposite is related to the formation of a passivating SiO_2 -surface layer. It should be noted that the composition of such materials may be changed in a relatively wide range ($\text{Si}_3\text{N}_4\text{-SiC-C}$) via chemical modifications. Moreover, it is thought that by changing maximum pyrolysis temperature, heating rate, holding time, and annealing atmosphere, the resulting microstructure (micro/nano) can also be markedly changed. Thus, tailoring of microstruc-

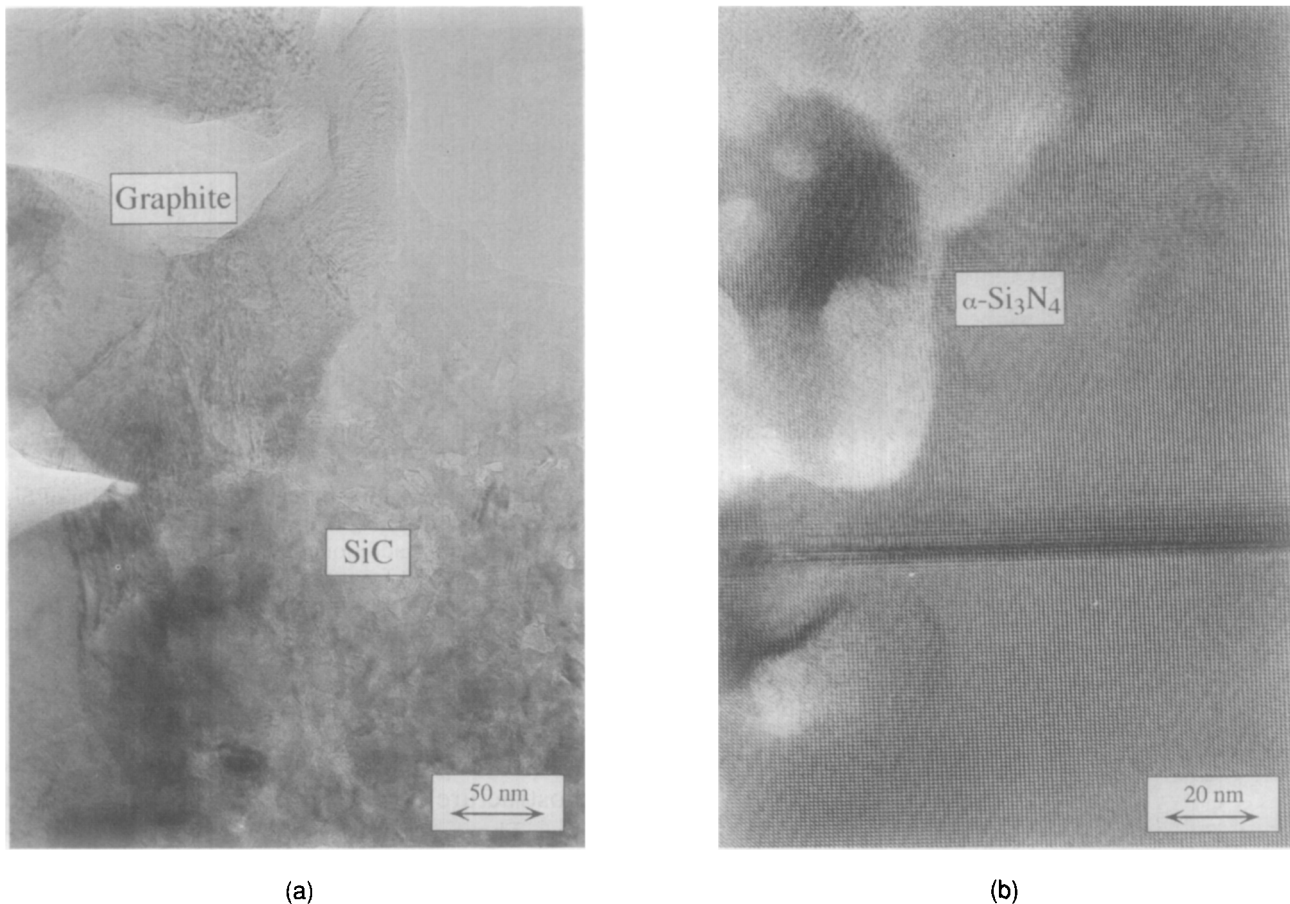


Fig. 4. (a) TEM bright field and (b) HREM image of the micro-nanocomposite formed after oxidizing annealing at 1600°C for 50 h of the amorphous silicon carbonitride matrix $\text{Si}_{3+x}\text{N}_4\text{C}_{x+y}$. Note that large $\alpha\text{-Si}_3\text{N}_4$ microcrystals are formed opposite to the occurrence of nanosized $\alpha\text{-SiC}$ crystallites. Graphite is only rarely observed. The phase assemblage is consistent with the phase diagram (starting composition).

tures becomes possible by applying specific crystallization procedures, which could be controlled by TEM observations.

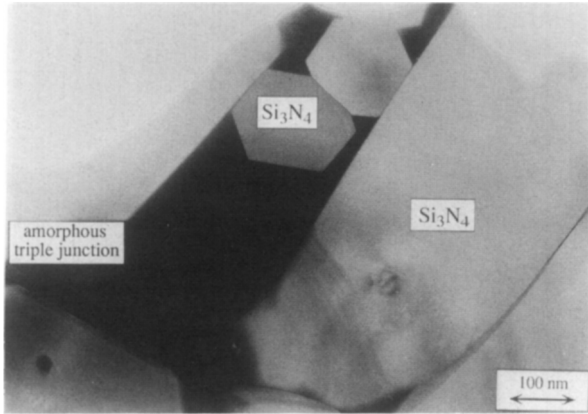
3.3 Dense ceramic microstructures

3.3.1 Microstructure characterization (secondary phase crystallization)

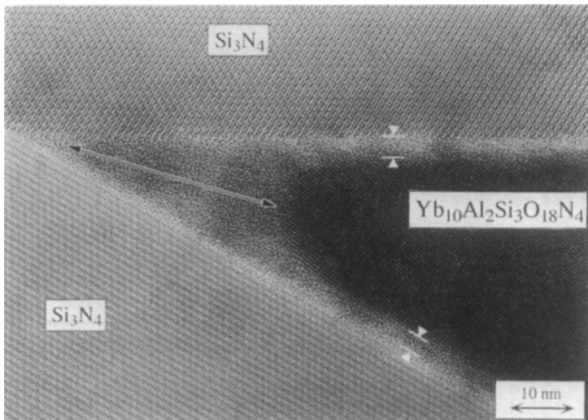
Since silicon nitride cannot be fully densified by classical solid-state sintering mechanisms due to its high covalent bonding character (incongruent decomposition of Si_3N_4) and low self-diffusivity, the addition of sintering aids is a prerequisite to promote liquid-phase assisted sintering in order to achieve nearly complete densification.^{25–27} During sintering, the metal oxides such as Y_2O_3 react with $\text{Si}_3\text{N}_4 + \text{SiO}_2$ forming an eutectic liquid which promotes both particle rearrangement and solution–reprecipitation processes.²⁸ Upon cooling, the liquid phase formed at high temperatures is present as an amorphous residue at triple-grain junctions and along grain and phase boundaries. Large amounts of sintering additives result in the well-known detrimental effects on high-temperature mechanical properties, e.g. creep behaviour and flexural strength, thus requiring a significant reduction in

their volume fraction.^{29,30} In most systems, the amorphous phase present at three- and four-grain junctions can be partially crystallized via subsequent heat-treatment. Another approach to improve high-temperature properties takes advantage of the refractory properties of rare-earth and transition element based oxides, which influence the viscosity of the liquid phase formed.^{31,32} Therefore, a microstructural and microchemical characterization of the secondary phases formed after cooling or upon additional heat treatment is required.

The overall microstructure of Yb_2O_3 -containing Si_3N_4 consisted of elongated $\beta\text{-Si}_3\text{N}_4$ grains, and triple-point pockets filled with remains of the liquid that formed during sintering. The multi-grain regions are homogeneously distributed throughout the material. Virtually all of the triple-point pockets were amorphous in the as-sintered material with 5 vol% Yb_2O_3 addition. The amorphous triple-grain regions were interconnected by thin amorphous grain-boundary films covering the Si_3N_4 particles. Figure 5 depicts a triple pocket which is filled with the amorphous secondary phase. Chemical analysis by EDS showed that the glass contained approximately an equal amount of both Yb and Si, a high level of oxygen, but no



(a)



(b)

Fig. 5. TEM bright field image of (a) SSN doped with 5 vol% Yb_2O_3 after sintering and (b) SSN with 10 vol% Yb_2O_3 addition (as-sintered). In the material with the low volume fraction of sintering aid only amorphous residue is present at triple pockets while about 70% of the multi-grain junctions are already crystallized within the material containing 10 vol% Yb_2O_3 (+ 0.5 vol% Al_2O_3) forming an interconnected network of the $\text{Yb}_{10}\text{Al}_2\text{Si}_3\text{O}_{18}\text{N}_4$ phase.

nitrogen could be detected. After the heat treatment for 12 h at 1250°C , however, approximately 80% of the prior amorphous triple-grain pockets were crystalline. Both XRD and selected area diffraction (SAD) indicated that the secondary crystalline phase formed was $\text{Yb}_2\text{Si}_2\text{O}_7$. No other crystalline secondary phases were observed.

The microstructure of the material with 10 vol% Yb_2O_3 additives (which also contained about 0.5 vol% Al_2O_3 as an impurity) was substantially different compared to the material with 5 vol% Yb_2O_3 addition. After sintering, approximately 70% of the secondary phase was already crystallized in the triple junctions. $\text{Yb}_{10}\text{Al}_2\text{Si}_3\text{O}_{18}\text{N}_4$ existed as large grains extending up to several microns in size. One example of such a crystal of the interconnected secondary phase network is also shown in Fig. 5. After a post-sintering heat treatment, the secondary phase material within the triple pockets was completely crystallized. The previously large secondary-phase particles which extended over

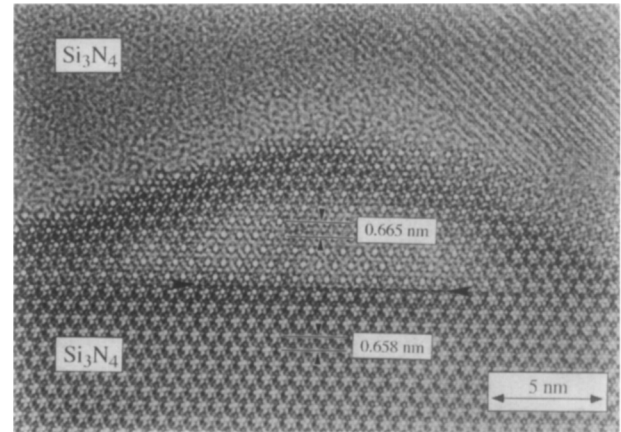


Fig. 6. HREM micrograph of an epitaxial deposition of Si_3N_4 onto a pre-existing Si_3N_4 matrix grain owing to the second phase change upon additional heat treatment. The rejection of Si and N (and Al) from the triple pockets is related to the change in composition of the secondary phase. Note that the lattice parameters of the epitaxial deposition (SiAlON phase) also change compared to the host crystal.

several triple pockets (observed in the as-sintered microstructure) were broken up into smaller grains. There was also a phase change upon heat treatment. The new secondary phase formed after heat-treating was Yb_2SiO_5 with an additional small amount of about 20% of the $\text{Yb}_2\text{Si}_2\text{O}_7$ secondary phase. The formation of these two phases is in accordance with the starting compositions in the Si_3N_4 - Yb_2O_3 - SiO_2 phase diagram. HREM studies along triple-grain pockets indicated an epitaxial deposition of Si_3N_4 onto pre-existing Si_3N_4 matrix grains.³³ Owing to the secondary phase change during post-sintering heat treatment, Si and N must be rejected from the triple-point pockets forming Si_3N_4 which is deposited epitaxially during the heat-treatment process. Such a deposition is shown in the HREM micrograph given in Fig. 6.

3.3.2 Fracture toughness (matrix grains versus secondary phases)

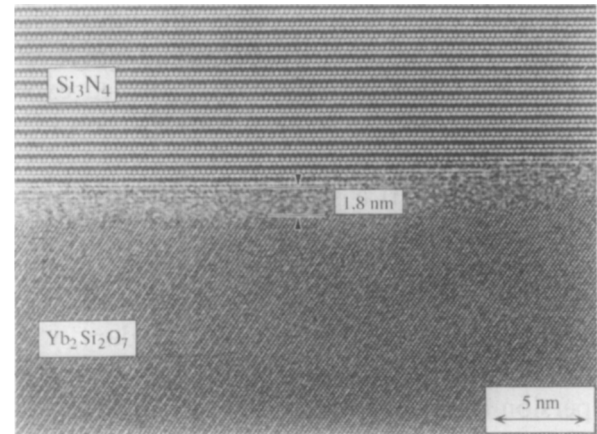
The overall microstructure in Si_3N_4 ceramics is commonly studied by scanning electron microscopy (SEM) of CF_4 plasma-etched cross sections. Quantitative microstructure analysis via image analysis allows a correlation between microstructure and bulk properties such as fracture toughness of the material. It is well established that for Si_3N_4 materials the resulting fracture resistance scales with the square root of the grain diameter, in particular, when a bimodal grain-size distribution is observed (*in situ* toughening).³⁴⁻³⁶ However, quantitative microstructure analysis in combination with TEM analysis revealed that, in addition to the influence of the matrix grains, secondary phase crystallization can also influence fracture

toughness.³⁷ In case of ZrO_2 addition, the martensitic $t \rightarrow m$ - ZrO_2 phase transformation results in the formation of local compressive stresses within the matrix. These residual stresses can cause a slight improvement in fracture resistance since the propagating crack tends to avoid such highly stressed regions. It was shown that the utilization of Sc_2O_3 as a sintering aid also resulted in an improvement in fracture resistance. Upon cooling, the material contained $Sc_2Si_2O_7$ as the only crystalline secondary phase. This phase tends to crystallize completely into the tip of the triple pockets (compare also Fig. 5(b)) and, hence, no residual glass was observed in these regions. Therefore, upon crack propagation, crack branching was often observed by SEM and TEM inspection. It is concluded that apart from matrix grain morphology and grain diameter, the crystallization of secondary phases, located at multi-grain pockets, can also affect the propagation of the crack and, therefore, influence fracture toughness. Moreover, it should be noted that grain-boundary chemistry was found to also affect fracture resistance. Depending on the interface chemistry and the resulting grain boundary bonding character, trans-granular fracture is favoured compared to the commonly observed intergranular fracture mode. Strong interface bonding, as observed for the addition of $ZrO_2 + Al_2O_3$ as sintering aids, leads to a marked reduction in fracture toughness since predominantly transgranular fracture occurred.³⁸

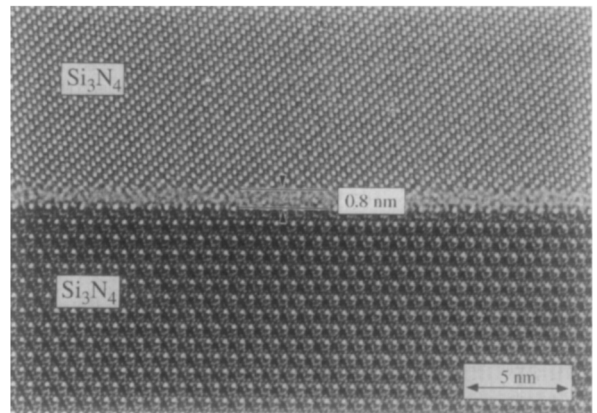
3.3.3 Characterization of interfaces (amorphous grain-boundary films)

Apart from characterizing secondary phase crystallization, high-resolution electron microscopy (HREM) was utilized to study Si_3N_4 interfaces. Owing to the liquid phase involved during sintering at elevated temperatures, amorphous residue of this liquid is commonly present at multi-grain regions (see also Fig. 5). Moreover, Si_3N_4 -grains are always separated by a continuous amorphous intergranular film with the only exception being low-energy grain boundaries.³⁹ Such intergranular films are present at both homophase (Si_3N_4/Si_3N_4) and heterophase (Si_3N_4 /crystalline secondary phase) boundaries. The film thickness of hetero-phase boundaries was shown to always be greater than the thickness observed along homophase boundaries, as depicted in Fig. 7. The presence of such amorphous interfacial glass profoundly affects the mechanical properties of Si_3N_4 -based ceramics, particularly at high service temperatures. Therefore, a control of these films is most desirable with respect to materials performance.

It is important to note that these interfacial glassy films revealed a constant thickness within



(a)



(b)

Fig. 7. HREM micrographs (400 kV) of (a) $Yb_2Si_2O_7/\beta$ - Si_3N_4 phase boundary observed in the annealed SSN doped with 5 vol% Yb_2O_3 and (b) β - Si_3N_4/β - Si_3N_4 grain boundary found in a MgO-fluxed silicon nitride. Note that the intergranular film thickness along phase boundaries is typically wider compared to the width at grain boundaries.

each of the materials investigated. In general, different TEM techniques can be applied for the detection and evaluation of the intergranular film thickness. The measurement of the film thickness by diffuse dark-field imaging resulted in values 50–100% larger than those determined by HREM imaging. Defocus Fresnel fringe imaging is an indirect method of obtaining intergranular film width. With this method the film thickness was overestimated by about 20–35%, with the largest error stemming from the uncertainty in the exact location of the Fresnel fringe maxima. Therefore, high-resolution lattice imaging is a method capable of the resolution necessary to obtain detailed information of the boundary and the intergranular phase itself. It was shown to be applicable to quantitatively evaluate the intergranular film thickness in Si_3N_4 materials with an accuracy of ± 0.1 nm.^{40–42}

Model experiments on high-purity Si_3N_4 materials with and without a low amount of CaO addition seemingly support the model first presented by Clarke^{43,44} on the equilibrium thickness of

amorphous intergranular films in liquid-phase sintered Si_3N_4 ceramics. Statistical analyses of a number of grain-boundary films provided experimental verification of these theoretical considerations.⁴² The model involves the influence of two repulsive forces: (i) a steric force which is caused by the steric hindrance of SiO_4 tetrahedra present in the silicate films and (ii) a force produced by an electrical double layer along the interface owing to the segregation of cations at the boundary, which is thought to balance the attractive van der Waals dispersion force that acts across the interface. This force balance results in the observed formation of an equilibrium film thickness. Si_3N_4 materials with different rare-earth and transition-element oxide additions as well as variations in volume content of sintering aids were studied. HREM studies in conjunction with analytical electron microscopy (AEM) revealed that differences in grain-boundary film thickness are related to changes in chemical composition of the intergranular films, which depends on the material analyzed, i.e. its densification aid and impurity content (see also Fig. 7).

The results clearly show a dependence of intergranular film thickness on chemical composition. No clear dependence on volume fraction of additives was found. Upon post-sintering heat treatment crystalline secondary phases form at triple-grain regions. Depending on the secondary phases formed (crystal chemistry), interface chemistry can be altered and hence grain-boundary film thickness will also be markedly changed.

3.3.4 Microanalysis (electron energy-loss spectroscopy)

In order to study, apart from cation concentration, the influence of anions at the interface on the intergranular film thickness and the resulting mechanical properties, a Si_3N_4 material was fabricated via hot-isostatic pressing without the addition of commonly used sintering aids. However, a small amount of fluorine was added to the system via powdered teflon.⁴⁵ The incorporation of fluorine into the material was deliberately chosen, in order to weaken the interfaces. Electron energy-loss spectroscopy (EELS) revealed the presence of fluorine both at the triple-grain junctions and the grain-boundary films. Through the determination of the F/O-ratio for the spectra obtained from triple pockets and interface regions, no major compositional changes were detected, which seemingly suggests a homogeneous secondary phase composition within the material. Assuming a constant grain-boundary chemistry, a constant film thickness is expected. In contrast, with respect to the incorporation of fluorine into the SiO_2 -glass structure, a small increase in film thickness ($\delta =$

0.1 nm) was also expected in comparison to the pure silica containing material (1.0 nm). This is due to the fact that the replacement of oxygen by fluorine, which have almost identical ionic radii with 140 pm and 133 pm for O^{2-} and F^- , respectively, requires two fluorine ions to allow for charge balance (compare also Fig. 8). The HREM observations are consistent with the obtained EELS results and, in addition, that the grain-boundary structure is also influenced by the anion concentration, i.e. the fluorine content at the interface. Preliminary results showed an enhanced intergranular fracture of the F-doped material compared to the undoped sample as well as a lower creep resistance.⁴⁶ This latter result is consistent with the lower HIPing temperature needed in the F-doped system to achieve full densification. The variation in mechanical response of the F-doped samples compared to the undoped materials is attributed to changes in the glass structure (glass chemistry), owing to the incorporation of fluorine.

3.4 Dynamic microstructures

In this section, the variation of ceramic microstructures, which are commonly thought to be very stable even under service conditions, is investigated after their exposition to high temperatures and high local stresses. Emphasis is placed on the structural and chemical changes in Si_3N_4 ceramics doped with m- ZrO_2 which are observed after cyclic fatigue testing of the material.⁴⁷ Before testing, a typical Si_3N_4 microstructure with m- ZrO_2 present at multi-grain pockets was observed by TEM, as depicted in Fig. 9.

Upon mechanical testing, one unexpected result which emerges from the microstructural characterization of the m- ZrO_2 doped Si_3N_4 ceramic was the formation of newly formed amorphous phase owing

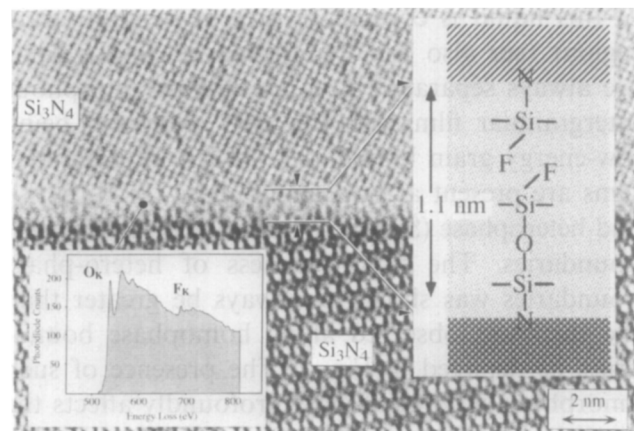
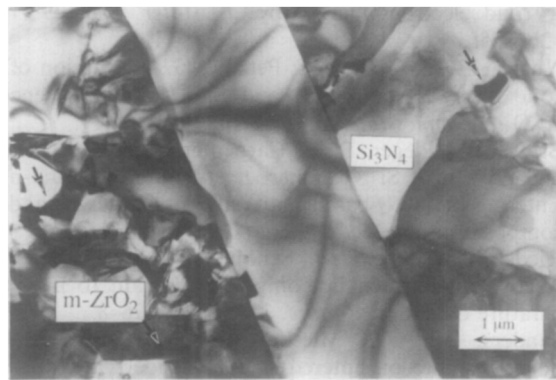
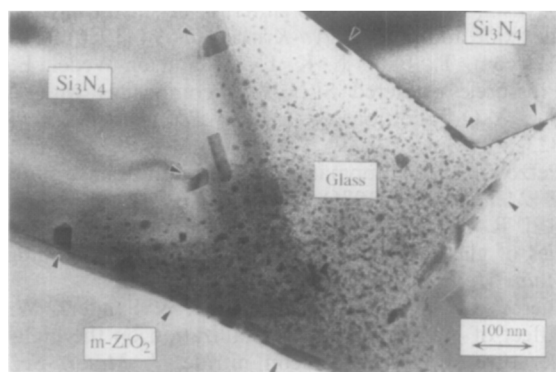


Fig. 8. HREM image (400 kV) of an intergranular film present in fluorine-doped Si_3N_4 HIPed without the addition of sintering aids. Note that F could be detected along the interface by EELS measurements (see inset). The variation of the glass structure due to the incorporation of F (replacing the bonding O) is schematically indicated in the inset on the right.



(a)



(b)

Fig. 9. TEM bright field images of ZrO_2 -doped SRBSN (a) as-sintered microstructure with $m-ZrO_2$ homogeneously distributed at triple pockets. (b) Microstructural changes observed after cyclic fatigue at $1100^\circ C$. Note that the $m-ZrO_2$ dissolved in the residual glass and, upon cooling, started to reprecipitate in the glass pocket as well as along the phase boundaries (epitaxy) owing to supersaturation of the glass.

to the local dissolution of zirconia in the pre-existing glass, as shown in Fig. 9(b). This surprising observation of the partial decomposition of $m-ZrO_2$ at rather low testing temperatures seemingly suggests that the potential application of this 'high-temperature ceramic' is well below $1200^\circ C$. Moreover, it should be borne in mind that crystallization of residual glass pockets via post-sintering heat treatments in these materials is, in general, believed to overcome the problem of degradation of high-temperature properties. Since the replacement of amorphous triple pockets by crystalline secondary phases, e.g. the formation of $m-ZrO_2$ with a high thermal stability, would strongly reduce the amount of glass which softens at elevated temperatures. Therefore, high temperature properties are commonly thought to improve with secondary phase crystallization. However, the results presented clearly show that even the formation of $m-ZrO_2$ does not allow for a sufficient material performance above $1100^\circ C$. This is due to the formation of additional residual glass (newly formed) owing to the local dissolution of ZrO_2 under the applied temperature and stress. It is concluded that high-temperature performance of Si_3N_4 -based ceramics can only

be improved by post-sintering heat treatment when the formation of secondary phases can be initiated, which are stable even under the applied high temperature and high local stresses, i.e. the occurrence of newly formed residual glass has to be suppressed.

4 Conclusions

The results presented were thought to underline the importance of the TEM technique for a detailed characterization of ceramic microstructures with high spatial resolution. The TEM technique can be applied, in addition to spectroscopic methods, in most of the relevant steps involved during ceramic processing such as:

- Powder processing; organometallic doping (powder surface chemistry);
- Microstructure development during densification (transient crystalline phases);
- Crystallization of polymer derived ceramics (micro/nanocomposites);
- Secondary phase crystallization (phase change upon post-sintering heat treatment);
- As-sintered microstructures (amorphous intergranular films);
- Microstructural changes under service conditions (formation of new glass).

Transmission and analytical electron microscopy is hence shown to be a very helpful characterization tool which allows us to expand our understanding of the development of ceramic microstructures. This technique can be: (i) applied in order to investigate the formation process of complex ceramic microstructures such as polymer-derived pre-ceramics and, based on the understanding of microstructure formation, (ii) used to influence materials processing. This enables the direct influence of materials fabrication with respect to tailoring ceramic microstructures for potential application requirements.

Acknowledgements

C. Kunert, University of Bayreuth, is acknowledged for her excellent preparation of the delicate TEM-foils. Dr J. Göring, German Aerospace Research Establishment (DLR), is thanked for cyclic fatigue testing of ZrO_2 -doped SRBSN. We are greatly indebted to Prof. M. Rühle who strongly supported the work presented on HREM studies of interfaces in Si_3N_4 ceramics during the stay of the primary author at the Max-Planck-Institute in Stuttgart.

References

- Reimer, L., *Transmission Electron Microscopy*, 3rd Edition, Springer-Verlag, Berlin, 1993.
- Spence, J. C. H. & Zuo, J. M., *Electron Microdiffraction*, Plenum Press, New York, 1992.
- Braue, W., Konvergente Elektronenbeugung in der analytischen Elektronenmikroskopie keramischer Werkstoffe – eine Anleitung für die Praxis. *Mat.-wiss. u. Werkstofftech.*, **21** (1990) 72–84.
- Redjamimia, A. & Morniroli, J. P., Application of microdiffraction to crystal structure identification. *Ultramicroscopy*, **53** (1994) 305–17.
- Greil, P. & Weiss, J., Evaluation of the microstructure of β -SiAlON solid solution materials containing different amounts of amorphous grain boundary phase. *J. Mater. Sci.*, **17** (1982) 1571–8.
- van Tendeloo, G., Anders, L. & Thomas, G., Electron microscopy investigation of the ZrO_2 -ZrN system. II: Tetragonal and Monoclinic ZrO_2 Precipitation. *Acta Met.*, **31** (1983) 1619–25.
- Bonnell, D. A., Tien, T.-Y. & Rühle, M., Controlled crystallization of the amorphous phase in silicon nitride ceramics. *J. Am. Ceram. Soc.*, **70**(7) (1987) 460–5.
- Rühle, M., Ma, L. T., Wunderlich, W. & Evans, A. G., TEM studies on phase stabilities of zirconia ceramics. *Physica B*, **150** (1988) 86–98.
- Falk, L. K. L. & Dunlop, G. L., Crystallization of the glassy phase in an Si_3N_4 material by post-sintering heat treatments. *J. Mater. Sci.*, **22** (1987) 4369–76.
- Cinibulk, M. K., Thomas, G. & Johnson, S. M. Grain-boundary-phase crystallization and strength of silicon nitride sintered with a YSiAlON glass. *J. Am. Ceram. Soc.*, **73**(6) (1990) 1606–12.
- Kleebe, H.-J. & Ziegler, G., Influence of crystalline secondary phases on densification behaviour of reaction-bonded silicon nitride during post-sintering under increased nitrogen pressure. *J. Am. Ceram. Soc.*, **72**(12) (1989) 2314–17.
- Schönfelder, H., Silicon carbonitride ceramics from polysilazane. Ph.D. Thesis, University of Stuttgart, Germany, 1992.
- Laine, R. M., Babonneau, F., Blowhowiak, K. Y., Kennish, R. A., Rahn, J. A., Exarhos, G. J. & Waldner, K., The evolutionary process during pyrolytic transformation of poly(N-methylsilazane) from a preceramic polymer into an amorphous silicon nitride/carbon composite. *J. Am. Ceram. Soc.*, **78**(1) (1995) 137–45.
- Mocaer, D., Pailler, R., Naslain, R., Richard, C., Pillot, J. P., Dunogues, J., Gerardin, C. & Taulelle, F., Si-C-N ceramics with a high microstructural stability elaborated from the pyrolysis of new polycarbosilazane precursors. *J. Mater. Sci.*, **28** (1993) 2615–31.
- Riedel, R., Passing, G., Schönfelder, H. & Brook, R. J., Synthesis of dense silicon-based ceramics at low temperatures. *Nature*, **355** (1992) 714–16.
- Hapke, J. & Ziegler, G., Synthesis and pyrolysis of liquid organometallic precursors for advanced Si-Ti-C-N composites. *Adv. Mater.*, **7** (1995) 380–4.
- Rahaman, M. N., Boiteux, Y. & De Jonghe, L. C., Surface characterization of silicon nitride and silicon carbide powders. *Am. Ceram. Soc. Bull.*, **65**(8) (1986) 1171–6.
- Wang, C. M. & Riley, F. L., Alumina-coating of silicon nitride powder. *J. Europ. Ceram. Soc.*, **10** (1992) 83–93.
- Joshi, P. N. & McCauley, R. A., Metal-organic surfactants as sintering aids for silicon nitride in an aqueous medium. *J. Am. Ceram. Soc.*, **77**(11) (1994) 2926–34.
- Schmidt, H., Nabert, G., Ziegler, G. & Gorezki, H., Characterization and surface chemistry of uncoated and coated silicon nitride powders. *J. Europ. Ceram. Soc.*, **15** (1995) 667–74.
- Kleebe, H.-J., Braue, W. & Luxem, W., Densification of SRBSN with unstabilized zirconia by means of dilatometry and electron microscopy. *J. Mater. Sci.*, **29** (1994) 1265–75.
- Huang, Z. K., Greil, P. & Petzow, G., Formation of silicon oxynitride from Si_3N_4 and SiO_2 in the presence of Al_2O_3 . *Ceramics International*, **10** (1984) 14–17.
- Braue, W., Pleger, R. & Carpenter, R. W., Nucleation and growth of Si_2N_2O microcrystals during liquid-phase sintering of Si_3N_4 -based materials with different additive compositions. *J. Mater. Res.*, (1995) in press.
- Riedel, R., Kleebe, H.-J., Schönfelder, H. & Aldinger, F., A covalent micro/nano-composite resistant to high temperature oxidation. *Nature*, **374** (1995) 526–8.
- Sanders, W. A. & Mieskowski, D. M., Strength and microstructure of sintered silicon nitride with rare-earth oxide additions. *Am. Ceram. Soc. Bull.*, **64** (1985) 304–9.
- Tani, E., Nishijima, M., Ichinose, H., Kishi, K. & Umebayashi, S., Gas-pressure sintering of silicon nitride with an oxide addition. *Yogyo-Kyokai-Shi*, **94** (1986) 300–5.
- Ekström, T., Falk, L. K. L. & Knutson-Wedel, E. M., Pressureless-sintered Si_3N_4 - ZrO_2 -composites with Al_2O_3 and Y_2O_3 additions. *J. Mater. Sci. Letters*, **9** (1990) 823–6.
- Petzow, G. & Huppmann, W. J., Liquid phase sintering. *Z. Metallkd.*, **67** (1976) 579–90.
- Raj, R. & Lange, F. F., Crystallization of small quantities of glass (or a liquid) segregated in grain boundaries. *Acta Met.*, **29** (1981) 1993–2000.
- Pierce, L. A., Mieskowski, D. M. & Sanders, W. A., Effect of grain-boundary crystallization on the high-temperature strength of silicon nitride. *J. Mater. Sci.*, **21** (1986) 1345–8.
- Cinibulk, M. K., Thomas, G. & Johnson, S. M., Strength and creep behaviour of rare-earth disilicate-silicon nitride ceramics. *J. Am. Ceram. Soc.*, **75**(8) (1992) 2050–5.
- Lee, W. E. & Hilmas, G. E., Microstructural Changes in β -silicon nitride grains upon crystallizing the grain-boundary glass. *J. Am. Ceram. Soc.*, **72**(10) (1989) 1931–7.
- Vetrano, J. S., Kleebe, H.-J., Hampp, E., Hoffmann, M. S. & Rühle, M., Epitaxial deposition of silicon nitride during post-sintering heat treatment. *J. Mater. Sci. Letters*, **11** (1992) 1249–52.
- Tani, E., Umebayashi, S., Kishi, K., Kobayashi, K. & Nishijima, M., Gas-pressure sintering of Si_3N_4 with concurrent addition of Al_2O_3 and 5 wt% rare earth oxide: high fracture toughness Si_3N_4 with fiber-like structure. *Am. Ceram. Soc. Bull.*, **65**(9) (1986) 1311–15.
- Mitomo, M. & Uenosono, S., Gas-pressure sintering of β -silicon nitride. *J. Mater. Sci.*, **26**, (1991) 3940–4.
- Padture, N. P., *In situ* toughened silicon carbide. *J. Am. Ceram. Soc.*, **77**(2) (1994) 519–23.
- Unger, S., Influence of microstructure development on fracture toughness in silicon nitride. Thesis, University of Bayreuth, Germany, 1994.
- Kleebe, H.-J., Meißner, E. & Ziegler, G., Influence of Si_3N_4 interface chemistry on both grain morphology and fracture toughness. *J. de Physique IV*, **3** (1993) 1393–7.
- Schmid, H. & Rühle, M., Structure of special grain boundaries in SiAlON ceramics. *J. Mater. Sci.*, **19** (1984) 615–28.
- Kleebe, H.-J., Hoffmann, M. J. & Rühle, M., Influence of secondary phase chemistry on grain-boundary film thickness in silicon nitride. *Z. Metallkd.*, **83**(8) (1992) 610–17.
- Cinibulk, M. K., Kleebe, H.-J. & Rühle, M., Quantitative comparison of TEM techniques for determining amorphous intergranular film thickness. *J. Am. Ceram. Soc.*, **76**(2) (1993) 426–32.
- Kleebe, H.-J., Cinibulk, M. K. & Rühle, M., Statistical analysis of the intergranular film thickness in silicon nitride ceramics. *J. Am. Ceram. Soc.*, **76**(8) (1993) 1969–77.
- Clarke, D. R., On the equilibrium thickness of intergranular glass phases in ceramic materials. *J. Am. Ceram. Soc.*, **70**(1) (1987) 15–22.

44. Clarke, D. R., Shaw, T. M., Philipse, A. P. & Horn, R. G., Possible electrical double layer contribution to the equilibrium thickness of intergranular glass phases in polycrystalline ceramics. *J. Am. Ceram. Soc.*, **76**(5) (1993) 1201–4.
45. Kleebe, H.-J., Pezzotti, G. & Nishida, T., Transmission electron microscopy characterization of a fluorine-doped Si₃N₄. *J. Mater. Sci. Letters*, (1995) in press.
46. Pezzotti, G., Matsuchita, K., Kleebe, H.-J., Okamoto, Y. & Nishida, T., Viscous behaviour of grain and phase boundaries in fluorine doped Si₃N₄-SiC composites. *Acta Metall.*, (1995), in press.
47. Göring, J., Braue, W. & Kleebe, H.-J., Microstructural response of ZrO₂-doped Si₃N₄ during static loading. In *Silicon Nitride-Based Ceramics*, Stuttgart, 4–6 October, 1993, eds M. J. Hoffmann, P. F. Becher & G. Petzow, Trans Tech Publications, Switzerland. Key Engineering Materials, **89–91**, 1994, pp. 641–6.

Structure and Composition of Metal/Ceramic Interfaces

Manfred Rühle

Max-Planck-Institut für Metallforschung, Institut für Werkstoffwissenschaft, Seestrasse 92, D-70174 Stuttgart, Germany

(Received 11 September 1995; revised version received 31 October 1995; accepted 7 November 1995)

Abstract

The structure and composition of metal/ceramic interfaces play an important rôle for the properties of composites, for the bonding of bulk metals (or metallic alloys) to bulk ceramics, in electronic packaging, and for the properties of oxide scales on metals (or metallic alloys) formed after high-temperature corrosion. In this paper the possibilities of high-resolution transmission electron microscopy (HRTEM) and analytical electron microscopy (AEM) will be summarized and recent developments discussed. Those advancements encompass quantification of HRTEM data by image processing and studies of specific components of the interfaces by investigations of the near-edge fine structures (ELNES) of energy loss spectra. The techniques will be applied to the Nb/Al₂O₃ and Cu/Al₂O₃ interfaces, respectively.

1 Introduction

Metal/ceramic interfaces (MCI) belong to heterophase boundaries.¹ Those boundaries exist between two crystals which possess different structures and/or compositions. In contrast, a homophase boundary separates two crystals of the same material with the same composition (see Fig. 1). Recently, heterophase boundaries and MCIs were the subject of intense research and of several conferences.^{2–4} The great interest in MCIs results from the high potential of application of those components: (i) for the bonding of metals to ceramics; (ii) as an important component of composites; (iii) electronic packaging systems used in information processing; (iv) thin film technology and (v) high-temperature oxidation of metals and metallic alloys. The MCIs must typically sustain mechanical and/or electrical forces without failure. Consequently, interfaces exert an important, sometimes controlling influence on performance for the components mentioned above.

A basic understanding of the properties of the interfaces requires a knowledge of the different

structures and compositions of the MCIs. The structures should be available to the atomic level and the coordinates of atoms at or near to the interface have to be determined with high precision. At the interface between two dissimilar materials, segregation of impurities and/or the formation of reaction products may occur.^{5–7} Those processes lead to a modification of the properties of the system. Therefore, it is essential to also study the composition and possible reactions at the MCI.

In this paper, results will be reported with respect to structural studies by quantitative high-resolution transmission electron microscopy (QHRTEM) as well as investigations on chemical processes and bonding across the interface by analytical electron microscopy (AEM), with emphasis on electron energy loss spectroscopy (EELS), and studies of the energy loss near edge structures (ELNES). The techniques will be applied to the Nb/Al₂O₃ and Cu/Al₂O₃ interface.

2 Remarks on Bonding Across Metal/Ceramic Interfaces

The free energy per unit area, γ , of an interface represents the most fundamental thermodynamic property of an interface. The free energy is correlated to the measurable work of adhesion W_{ad} by the Dupré equation⁸

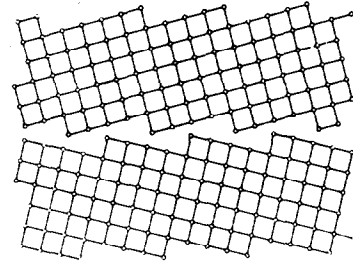
$$W_{ad} = \gamma_m + \gamma_c - \gamma \quad (1)$$

with γ_m = surface energy of the metal and γ_c = surface energy of the ceramic. Attractive interaction between the two constituents (metal, ceramic) results in $W_{ad} > 0$.

The measurement of W_{ad} is not easy. Jilavi⁹ determined W_{ad} by measuring contact angles at (equilibrium) pores present at the MCI following a suggestion by Fischmeister *et al.*¹⁰ Jilavi determined W_{ad} for Nb/Al₂O₃ interfaces by TEM cross-sections of equilibrium pores in solid state bonded bicrystals. W_{ad} ranges from 0.5 to 1.5 J/m² depending on the relative orientation of the Nb single crystal with respect to the sapphire crystal.

homophase boundaries

grain boundaries
twins
domain boundaries
stacking faults



heterophase boundaries

M(I) / M(II)
ZrO₂ (t) / ZrO₂ (c)
Metal / Ceramic
Metal / Semiconductor
Metal / Polymer

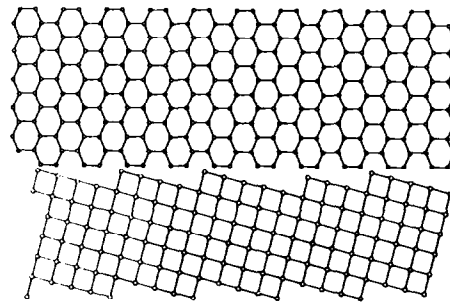


Fig. 1. Homophase boundaries and heterophase boundaries. Homophase boundaries limit on both sides materials of the same composition and same structure, whereas at heterophase boundaries the structure and/or composition of both components is different.

The evaluation is made by assuming an isotropic behaviour of all quantities in eqn (1). This is, however, not correct for most crystalline materials. Nevertheless, the measured data⁹ result in the correct order of magnitude of W_{ad} . Furthermore, the anisotropy of the interface energies alone cannot explain the measured variation of W_{ad} .⁹

A theoretical description of W_{ad} on the atomic level requires the knowledge of the interatomic potential at the interface. At the MCI a *qualitative* change in the bonding across the interface occurs. There exist appropriate models for describing interatomic forces in the metal and in the ceramics, respectively.¹¹ However, an interatomic potential between a metal and a ceramic cannot be derived easily. Geometrical arguments do, in general, not lead to a correct description of the dependence of W_{ad} on orientation,¹² as suggested previously.¹³ Cluster calculations¹⁴ predicted the trend of W_{ad} for several MCIs, however, no quantitative or even semi-quantitative values of W_{ad} can be deduced from those simple calculations.

The phenomenological considerations are contrasted by recent fundamental calculations of the bonding across MCIs. *Ab initio* calculations of rather small cells containing the interface allow the determination of the bonding at MCIs. Those calculations were performed for Ag/MgO¹⁵⁻¹⁷ and Nb/Al₂O₃.¹⁸⁻²⁰ In the calculations the Schrödinger equation is being solved without any input parameter but basic atomic data and an assumed structure of the selected cell containing up to about 50 atoms (ions) only. No structural relaxations are possible in the calculations. Therefore, the calculations have to be performed for different atomic

arrangements and the energy determined. The lowest energy configuration represents the most likely configuration of the system. The calculations result in the electronic band structure of the ground state at 0 K.

In a first step, Kruse *et al.*²⁰ calculated the equilibrium structure of a Nb monolayer on a (0001) sapphire surface. Figure 2 shows the Nb positions of the different starting configurations used in the calculations. After different runs in the computer for different atomic configurations it could be proven that the absolute energy minimum of the Nb/Al₂O₃ interface occurs with Nb in the A position (Fig. 2). This result agrees with HRTEM observations of MBE grown Nb over layers on (0001) Al₂O₃.²¹⁻²⁴

Basically the same result is obtained for bulk Nb (3–5 atomic layers of Nb on top of the (0001) sapphire surface).^{18,19} The positions of all atoms (ions) can be calculated for the lowest energy configuration (Fig. 3). The results of the first-principles calculations allow detailed analysis of the bonding at the Nb/Al₂O₃ interface. Charge density plots (Fig. 4) reveal that the Nb atoms are partially ionized. At the same time, electron density accumulates between Nb and O atoms. Detailed analysis of the electron density distribution reveal that the increase of charge density is mainly an overlap of atomic orbitals, rather than delocalization of electrons into a molecular orbital.¹⁹ This analysing leads to the conclusion that the bonding between Nb (monolayer and bulk) and sapphire is predominantly ionic. Charge is being transferred from the metal to the oxide leading to ionic bonding. Similar results are obtained for Ag/MgO.¹⁵⁻¹⁷

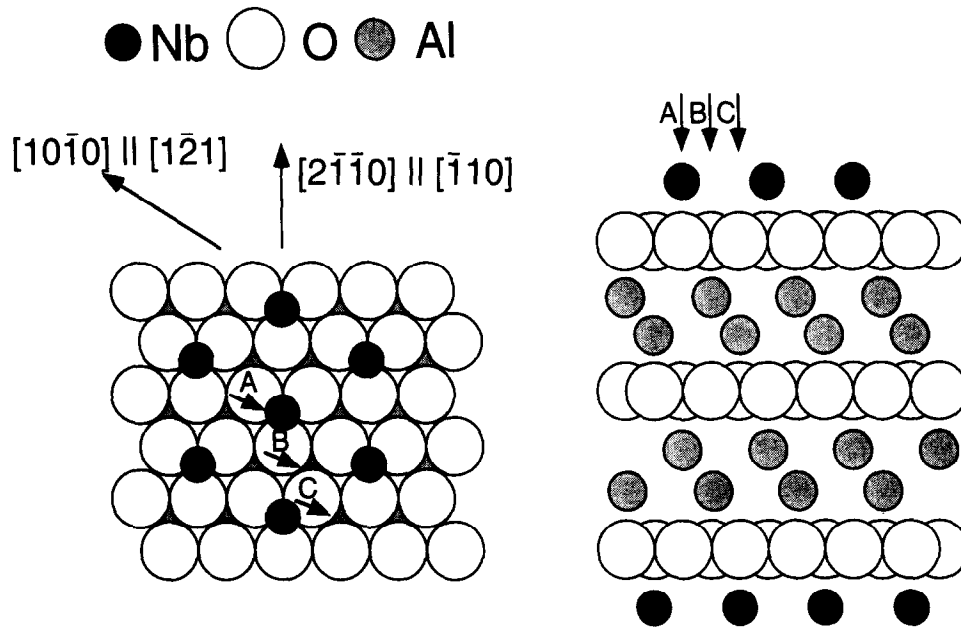


Fig. 2. Model of a Nb monolayer on the (0001) surface of sapphire used for the first-principles calculations of Kruse *et al.*¹⁸⁻²⁰ A, B and C denote those different positions of the Nb atoms for which the calculations have been done. (a) and (b) show the model in plan view and in cross-section, respectively.²⁰

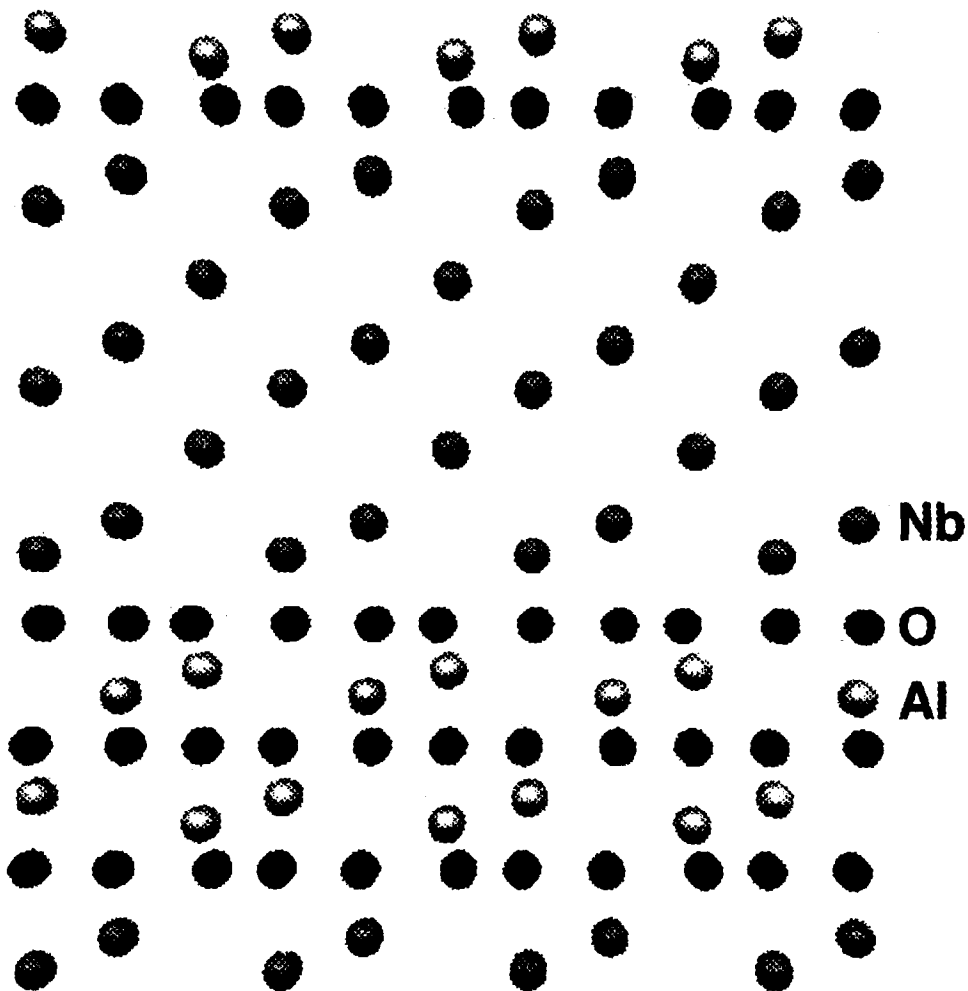


Fig. 3. Model of 'bulk' Nb on the (0001) surface of sapphire. A layer of 3 (or 5) Nb atoms on top of sapphire can be handled by the computer. A small kink in the 2nd Nb layer indicates the attractive forces on the Nb by Al_2O_3 .¹⁹

So far *ab initio* calculations can only be performed for less than about 50 atoms. In these small supercells it is assumed that the metal (Nb, Ag) fits coherently to the oxide substrate. The

mismatch between the two lattices (metal and ceramics, respectively) can so far not yet be treated on the same basic level since the required supercell cannot be calculated by today's computers.

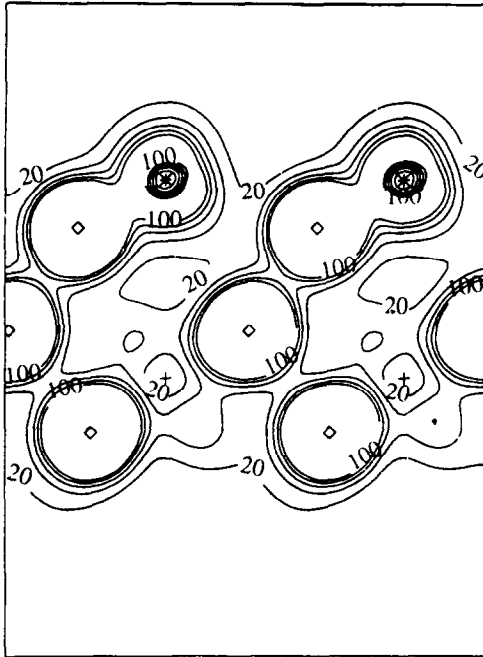


Fig. 4. Charge density (in units of $0.003 \text{ e}^- \text{ \AA}^{-3}$) of a Nb monolayer on a (0001) sapphire slab, according to a self-consistent *ab initio* band structure calculations. The projection direction corresponds to $(2\bar{1}\bar{1}0)$ in sapphire. O, Al and Nb atoms (ions) are indicated by O, + and *, respectively (C. Kruse *et al.*^{18,20}).

Empirical interatomic potentials have to be used for modelling of the structure and misfit dislocations and the dislocation networks.²⁵ Experimentally, so far, different results are obtained by different authors.^{26,27}

Korn *et al.*^{28,29} have shown experimentally that the level of the bonding energy at the interface between Nb and Al_2O_3 can be strongly influenced by impurities and chemical processes occurring at

the interface. However, no fundamental (basic) theory can so far explain the measured changes. Empirical models have to be used.

3 Transmission Electron Microscopy

The different possibilities offered by modern transmission electron microscopy are summarized schematically in Fig. 5.³⁰ Conventional TEM techniques (CTEM) involve bright field (BF) and dark field (DF) imaging and selected area diffraction (SAD). CTEM is being used for morphological analyses, the identification of different phases and for the analysis of lattice defects.³¹ Spectroscopy can be performed in an analytical TEM with high spatial resolution.³² The probe size in a scanning transmission electron microscopy (STEM) ranges from less than 1.0–50 nm. Energy dispersive spectroscopy (EDS) uses X-rays emitted from the specimen for a chemical characterization,³² while characteristic energy losses can be used for identifying qualitatively and quantitatively the different elements present in the specimen by electron energy loss spectroscopy (EELS).³³ EELS has so far most successfully been applied for the analysis of light elements. The surroundings of atoms can be probed by extended energy-loss fine structure studies (EXELFS) whereas energy-loss near-edge structure (ELNES) investigations result in information on the distance, bonding and bonding states to neighbouring atoms.³⁴ ELNES has been successfully applied to interfaces.³⁵ High-resolu-

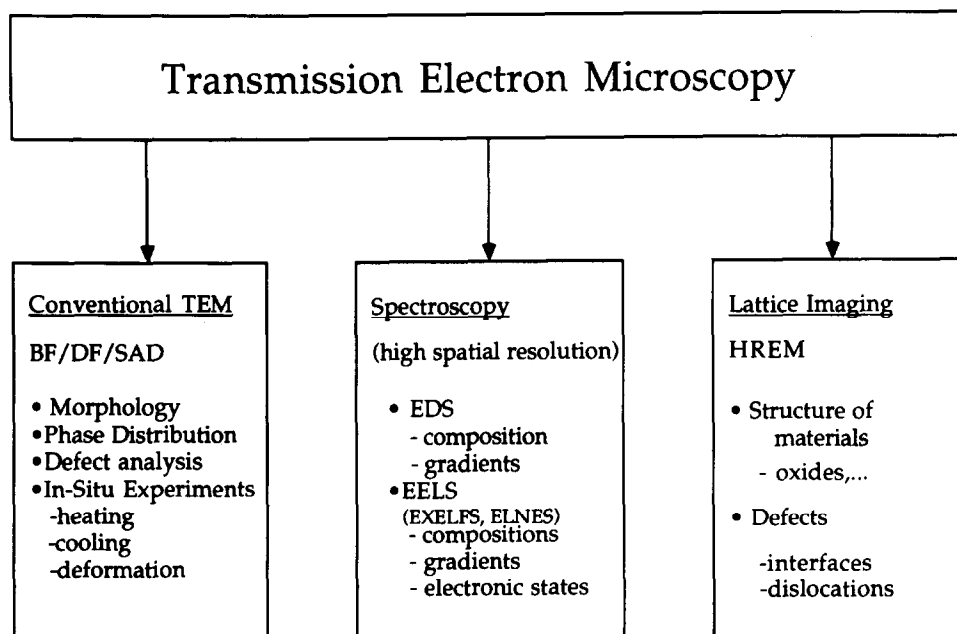


Fig. 5. Schematic illustrations of different TEM techniques. (a) Conventional TEM (CTEM), only one beam is used for imaging (BF: bright field imaging; DF: dark field imaging; SAD: selected area diffraction). (b) Spectroscopy utilizes the inelastic scattering processes of electrons in the specimen for a chemical characterization with high spatial resolution (EDS: energy dispersion spectroscopy; EELS: electron energy loss spectroscopy; EXELFS: extended energy-loss fine structure; ELNES: electron energy loss near-edge structure). (c) Lattice imaging. The direct and scattered beam from the image (HRTEM: high resolution transmission electron microscopy).

tion transmission electron microscopy (HRTEM) studies result in structure images^{36–38} of small perfect and/or defected regions in crystal.

In this paper we concentrate on quantitative high-resolution transmission electron microscopy and advanced analytical electron microscopy studies. This emphasis should, however, not diminish the important role that conventional TEM still plays in materials science: most results obtained so far in electron microscopy are done in the area of CTEM.

4 Determination of Atomic Structure of Metal/Ceramic Interfaces by Quantitative High-Resolution Transmission Electron Microscopy

The resolution of commercially available transmission electron microscopes has improved significantly. The point-to-point resolution of medium high-voltage electron microscopes with an acceleration voltage of 300–400 kV results in ~0.17 nm. The new generation of high-voltage high-resolution instruments pushes the resolution limit to ~0.1 nm.³⁹

The major obstacle in applying HRTEM routinely in materials science is caused by the fact that experimentally obtained micrographs cannot be interpreted in a 'naive way', which means that, for example, dark spots on a micrograph correspond to the position of a column of atoms in the investigated specimen.^{36,37} On the contrary, the contrast on a micrograph is formed by a complex scattering procedure which usually excludes the naive interpretation.

If one assumes that a completely coherent plane wave enters the specimen at the upper specimen surface then the amplitude and phase of the wave field at the exit surface can be calculated following well established procedures. The dynamical scattering of electrons is complex and highly nonlinear which means that the wavefield does not depend linearly on any experimental parameter such as specimen thickness and specimen orientation and positions of atoms or columns of atoms.^{36,37}

Furthermore, the HRTEM image depends on several instrumental parameters such as: (i) the coherency of the illumination system. (ii) The spherical aberration of rotational symmetric lenses which cannot be corrected. This aberration results in a change of the phase of the electron wave scattered even under small angles ($\leq 1^\circ$, depending on the instrument). This alteration may lead to a modification of the experimentally recorded micrograph. (iii) The exact position of the imaging plane (with respect to the exit surface of the specimen), the defocus value Δf , is an additional parameter which can be adjusted and has to be known

rather accurately for a proper interpretation of the experimental micrograph. (iv) Finally, the recording medium (photographic film, CCD camera, etc.) influences also the registered micrograph.

Another important, although nearly trivial aspect is that a HRTEM micrograph represents a two-dimensional (2D) projection of a three-dimensional (3D) object. Detailed information can be obtained if the specimen is crystalline and is oriented so that the incoming electron beam is parallel to a low-order Laue zone. A determination of the coordinates of an atom in a specimen requires experimental studies in (at least) two different orientations ('electron tomography'⁴⁰). For one HRTEM analysis of crystalline materials, the number and location of the positions of atom column rows can be established. For the analysis it is assumed that the lattice to be investigated is periodic in the direction of the incoming beam. The analysis of the atomistic structure of an interface requires that a low indexed zone axis of both crystals adjacent to the interface and the interface itself are parallel to the incoming electron beam. (See Fig. 7).

The amplitude and intensity distribution in the image plane depends critically on the spherical aberration of the objective lens. The geometrical beam path is shown in Fig. 6(a). In the image plane of the objective plane, an image of the object is formed by the interference of the transmitted beam with all diffracting beams. A better physical description of the image-forming processes can be performed by using wave optics (Fig. 6(b)). A transmission function $q(x, y)$ leaves the exit surface of the crystalline specimen. This

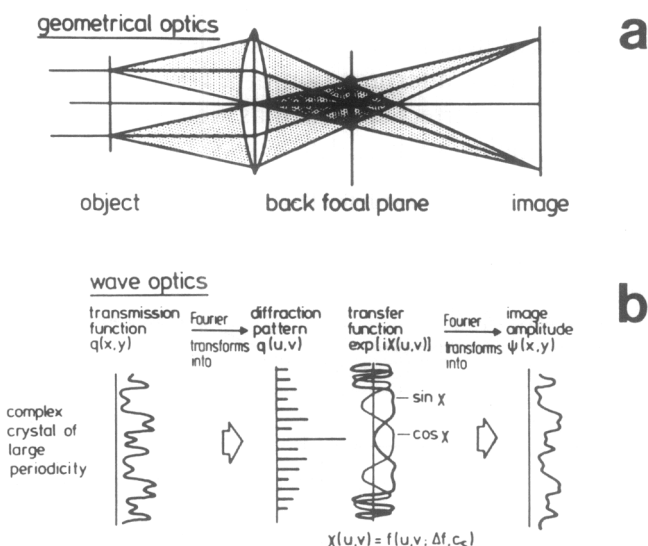


Fig. 6. Image formation by the objective lens of a transmission electron microscopy. (a) Geometric optical path diagram (b) Wave optical description (see text for explanation). Contrast transfer $CTF = \exp(i\chi(u,v))$, with $\chi(u,v) = f(u,v, \Delta f, C_s)$. u, v : Coordinates in the diffraction plane, Δf : defocus distance (= distance between lower specimen surface and imaging plane); C_s : constant of spherical aberration.

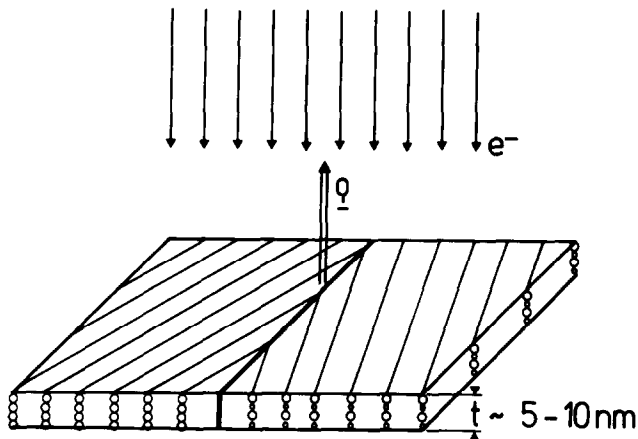


Fig. 7. Direct imaging of an interface by HRTEM. The crystalline specimen must be adjusted so that the direction of the incoming electron beam coincides with the orientation of atomic columns. The schematic drawing includes an interface. HRTEM can successfully be performed at such an interface if the interface normal lies perpendicular to the direction of the incoming beam (or the interface plane parallel to the direction of the incoming beam). Note that the foil thickness has to be in the range of 5–10 nm. The foil thickness should be constant over the investigated area.

function $q(x, y)$ can be periodic or non-periodic. The wave field moves through the objection lens and the amplitude distribution in a diffraction pattern $Q(u, v)$ is formed by a Fourier transformation of $q(x, y)$. The intensity distribution in the diffraction plane $Q(u, v)$ is being modified according to the exact shape of the contrast transfer function (CTF) of the microscope.³⁶ A Fourier back transformation of the modified amplitude distribution $Q(u, v)$ leads to the amplitude and intensity distribution in the image plane of the objective plane. Owing to the strong modifications caused by the CTF the amplitude and plane distribution in the image plane can be dramatically altered compared to the wave field leaving the specimen.

Quantitative interpretation of a HRTEM micrograph of the perfect specimen as well as of a specimen containing a lattice defect (such as an interface)

requires two independent steps (Fig. 8). Firstly, experimental micrographs have to be taken under well defined imaging conditions and the electron microscope has to be aligned and the contrast transfer function (CTF) has to be determined.⁴¹ The interpretation of the micrographs requires the knowledge of the exact thickness of the specimen. This is usually done by comparing the experimental micrographs (taken under different focus values) with simulated images (for different thicknesses and defocus values). A quantitative comparison results in both values, the thickness and the defocus distance Δf . Often it is helpful to reduce the noise on the micrograph. This can best be done by an adaptive Fourier filtering technique.⁴²

The second step covers the quantitative analysis of the nature and position of atomic columns at or near the defect such as an MCI. The analysis requires that a series of micrographs is taken under different, well defined defocus values. The experimental micrographs have to be compared to simulated image. For the simulated images a model configuration of the atomistic structure of the crystal (including the lattice defect) has to be assumed.

The simulated images have to be compared to experimental micrographs. So far most authors made the comparison with a visual inspection. The experimental micrograph and the simulated image are shown side by side. Sometimes, the mounting of an inlet of the simulated image into an experimental micrograph should demonstrate the 'good agreement'. This evaluation is, however, not quantitative. The accuracy of critical parameters (volume increase at an interface, positions of atomic columns at or near defect) cannot be determined objectively.

Recently, techniques for a quantitative evaluation of HRTEM micrographs have been developed.^{43,44} These techniques use advanced image processing techniques for the evaluation of HRTEM micrographs. Firstly, the experimental micrograph is noise reduced.⁴² Then the experimental micrograph as well as the simulated image are stored in a computer pixel by pixel (usually 1024×1024 pixels). After aligning and bringing both images to the same magnification, the two images are subtracted from each other. If there would be full agreement between the experimental micrograph and the simulated image, then the sum of intensity differences in corresponding pixels would be zero. This is usually not the case. There exists always a residual intensity (difference intensity). It is essential that this difference intensity does not contain any structural information and consists completely of noise. If the residual intensity of the difference image is significantly different from zero, then the positions of columns

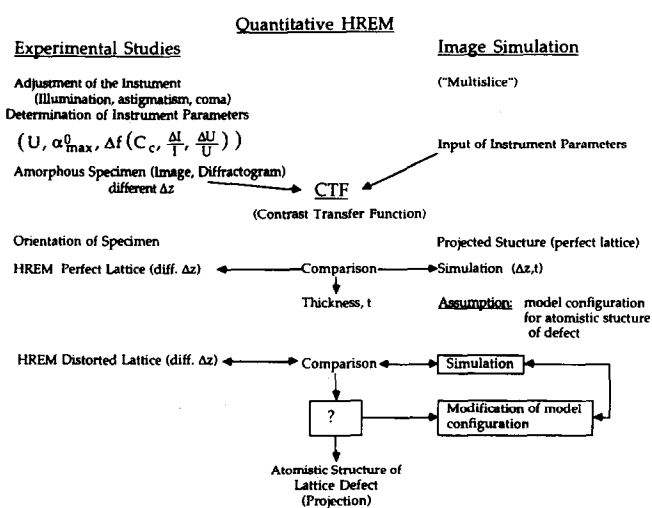


Fig. 8. A flow chart for quantitative high-resolution transmission electron microscopy (QHRTEM).

in the atomistic model are varied, an image is simulated and the difference image is formed again by subtracting the modified simulated image from the experimental micrograph. This procedure is continued until best agreement between the experimental micrograph and simulated image is reached.^{43,44}

There exists different measures of agreement between two micrographs.⁴⁵ The normalized Euclidean distance (NED) is an excellent measure for comparing two images. NED is defined as

$$NED = \frac{\sqrt{\sum_p \{I_1(p) - I_2(p)\}^2}}{\sqrt{\sum_p I_1(p)^2} \cdot \sqrt{\sum_p I_2(p)^2}} \quad (2)$$

where the summations contain the intensities I of the pixels labelled p . The subscript 1 corresponds to the experimental micrograph and the subscript 2 to the simulated image. Best agreement is reached when the NED is as small as possible (ideally equal to zero). Information on the accuracy can be obtained from the value of NED.⁴⁴ This technique was applied for the determination of the structure of unknown materials as well as of the structure of grain boundaries and MCIs. The procedure requires a lot of computer time.

5 Analytical Electron Microscopy

When an electron beam passes through a specimen there exists always a nonvanishing cross-section for inelastic scattering processes which leads to an energy distribution of the electrons passing through the specimen. The energy losses can be subdivided into the zero-loss region ($0 < \Delta E < \text{eV}$), plasmon region ($\Delta E < 100 \text{ eV}$) and core-loss region. From the different regions one can get information on the chemistry and bonding of the specimen.^{33,34} Plasmon losses result from the collective excitation of electrons, whereas the core-loss regions (edges) result from energy losses caused by the excitation of electrons from inner shells. The minimum energy required to eject an electron from an inner shell is specific for every element. Therefore, this energy can be used for a characterization of elements present in the specimen. Techniques exist for the quantification of the data.³²⁻³⁴ In addition, the fine structure of edges (ELNES) allows the determination of the bonding and distances to nearest neighbour atoms.³⁴

6 Case Study 1: Structure of Nb/Al₂O₃ Interface

The interface between Nb and sapphire serves as a model system for MCIs since both constituents

are representative materials: Nb as a bcc metal and Al₂O₃ as a technologically important ceramic. Since Al and O are highly soluble in Nb, no reaction products form at the interface. Thermal stresses can be neglected because the thermal expansion coefficients of Nb and sapphire are about the same.

The accommodation of the lattice mismatch between a thin film and its substrate is an important concern in thin film technology. The lattice mismatch can be compensated by straining the lattice of the film or by misfit dislocations. Straining the epilayer leads to coherent interfaces, whereas the presence of misfit dislocations leads to semicoherent interfaces. At semicoherent interfaces, coherent regions exist between the misfit dislocations. The atomistic structure of the coherent regions and the misfit dislocations were studied by quantitative HRTEM. Additional information on bonding at the interface can be obtained by ELNES studies (see Section 6.3).

6.1 Experimental details and results

The Nb layers were grown in a MBE growth chamber as described elsewhere.^{46,21,23,24} During the growth of the Nb films the substrate was heated to 1123 K and a vacuum of 10^{-6} Pa was maintained. A typical growth rate was 1 monolayer/s. The film thicknesses ranged from 12 to 100 nm. Most HRTEM studies were performed at a JEOL 4000 EX with a point resolution of 0.17 nm. Some studies were performed at the Berkeley ARM²¹ and the Stuttgart ARM.²³

X-ray and electron diffraction revealed that a unique orientation relationship exists between the Nb and the Al₂O₃ lattices for all investigated interfaces. The orientation relationship can be described by the following sets of parallel directions in the two crystals: $[0001]_S \parallel [111]_{Nb}$ and $[2\bar{1}\bar{1}0]_S \parallel [1\bar{1}0]_{Nb}$ ($S = \text{sapphire}$). The lattice planes in the Nb and sapphire lattice, which are parallel to the interface, are thus given by the orientation relationship and the chosen substrate surface: $(0001)_S \parallel (111)_{Nb}$, $(01\bar{1}0)_S \parallel (11\bar{2})_{Nb}$, $(2\bar{1}\bar{1}0)_S \parallel (1\bar{1}0)_{Nb}$ and $(01\bar{1}2)_S \parallel (001)_{Nb}$. The different interfaces are referred to as system 1, system 2, system 3 and system 4, respectively, in the following text.

6.2 Atomistic structure of the coherent regions

The quantitative evaluation of the HRTEM micrographs of the interfaces shows that the atomistic structure in the coherent regions of all four interfaces can be described by the same building principle. Two simple rules characterize the building principle for these interfaces. As an example, the evaluation of a HRTEM micrograph of the interface of system 1 is described. Figure 9(a) shows a

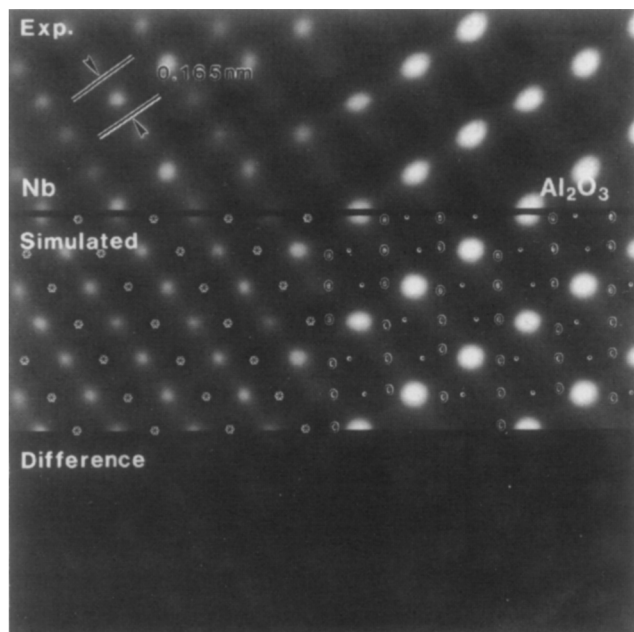


Fig. 9. HRTEM micrograph of the Nb/Al₂O₃ interface. (a) Experimental micrograph, I_e . (b) Simulated image based on the interface shown in Fig. 10(a), I_s . (c) Difference image $D = |I_e - I_s|$. The positions of columns of atoms (ions) can be determined quantitatively. Summary of results, see Table 1.

HRTEM micrograph of the interface of system 1 taken along the $[2\bar{1}\bar{1}0]_S$ and $[1\bar{1}0]_{Nb}$ directions. The intensity distribution on the micrograph is given by $I(x, y)_e$, where x and y are the coordinates of pixels on the experimental micrograph. Figure 9(b) represents a simulated image of the interface model of Fig. 10(a). The corresponding calculated intensity distribution is given by $I(x, y)_s$. Figure 9(c) contains the difference image $D = |I_e - I_s|$. The sum of the intensities in all pixels in D is minimized by the procedure described in Section 4 (eqn (2)). The experimentally determined structure is shown in Fig. 10(a) and the determined parameters are summarized in Table 1.

All Nb atoms at this interface occupy Al lattice sites. The translation vector T (Fig. 10) is thus a lattice vector of the sapphire lattice. The Nb atoms at the interface of all other systems also continue the Al lattice of the sapphire. This leads to the first rule, which states that a maximum of Al lattice sites is occupied by Nb atoms. This rule

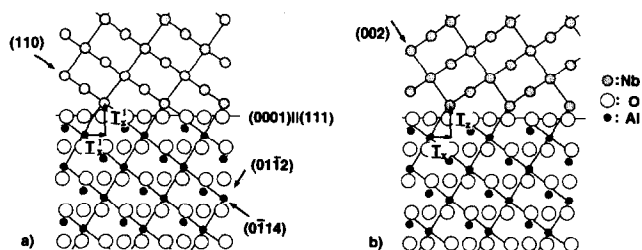


Fig. 10. (a) Nb/Al₂O₃ interface model which results in the best agreement between simulated image and experimental micrograph. (b) Interface model with the Nb lattice in a twin orientation with respect to the Nb lattice of Fig. 10(a).

Table 1. Structure of Nb/Al₂O₃ interface — results by quantitative HREM

Translation state (perfect Nb to perfect Al ₂ O ₃)	$T = (-0.1, -0.1) \text{ \AA}, \pm 0.1 \text{ \AA}$
Terminating layer of Al ₂ O ₃	Oxygen
Relaxation of first Nb layer	$R_1 = (-0.2, -0.1) \text{ \AA}, \pm 0.1 \text{ \AA}$
Relaxation of other Nb layer i	$R_i = (0.0) \text{ \AA}, \pm 0.1 \text{ \AA}$
Kink in Nb lattice	No

is confirmed by the coincidence of the morphological unit cell of sapphire,⁴⁷ which is rhombohedral ($a = 85.7^\circ$, $a = 0.35 \text{ nm}$) and constructed by connecting Al lattice sites, and the bcc unit cell of Nb ($a = 0.33 \text{ nm}$).²⁴ If only the position of the Nb atoms of the first layer were determined, then twins should occur in the Nb lattice of system 1 and 2. These twins have never been observed. Figure 10(b) shows an interface model for system 1 with the Nb lattice in a twin orientation with respect to the Nb lattice as shown in Fig. 9 and Fig. 10(a). Thus the position of the Nb atoms in the second layer must be fixed. The second rule states that the Nb atoms of the second layer occupy positions, which are close to the Al lattice sites of a continued Al lattice of the sapphire. The second rule also explains the rotation of the Nb lattice of system 4 in a specific direction.²⁴ It is interesting that so far the theoretically predicted kink in the second Nb layer (see Fig. 3) cannot be observed experimentally by HRTEM. Further theoretical and experimental studies have to be performed.

A quantitative evaluation of the HRTEM micrographs does not reveal unequivocally the nature of the terminating plane of sapphire. The terminating layer could either be composed of Al or Nb. Both would agree with the HRTEM micrograph analysed so far. As will be shown in the next section, ELNES studies support the model with an oxygen terminating layer.

6.3 Electron energy loss near edge structures (ELNES) studies

ELNES studies of characteristic edges have been performed⁴⁸ for the energy losses close to an energy edge. Using a dedicated scanning transmission electron microscope (STEM) Bruley *et al.*⁴⁸ record EELS spectra at high spatial resolution. A spectrum of a 'box' with a size of $3 \times 4 \text{ nm}^2$ is taken from areas including the interfaces and then a spectrum is taken from pure Nb and sapphire. It is assumed that the signal of the total spectrum $I_T(\Delta E)$ which, taken from the area which includes the interface, is linearly composed of components resulting from the two crystals adjacent to the interface (I_{Nb} and I_S , respectively) and from the interface area itself, I_I .

$$I_T(\Delta E) = a I_I(\Delta E) + b \cdot I_{Nb}(\Delta E) + c \cdot I_S(\Delta E). \quad (3)$$

The interface-specific component of the ELNES was obtained by using the spatial difference technique as described in Section 6.3.⁴⁸ For this method three spectra were acquired, one from a region containing the interface and two in the adjacent bulk materials. The interface spectrum contained not only the signal from the interfacial atoms but also contributions from the surrounding bulk materials. The extraction of the interfacial ELNES requires the removal of the contributions from the bulk materials. The reference spectra taken in the bulk materials were scaled and then subtracted from the interface spectrum. The remaining difference spectrum represents the ELNES arising from the interfacial atoms with an environment or oxidation state different from both bulk materials. The scaling of the reference spectra is necessary because different numbers of bulk atoms are irradiated during the acquisition of the interface and reference spectra respectively. The scaling factors were determined by trial and error applying the following guidelines: Selection of an energy-loss region containing strong and characteristic features for the bulk materials and minimizing these contributions in the difference spectrum. In the case that a chemical shift occurs, the intensity directly above the edge onset is eliminated. Care was taken that the subtraction of the reference spectra did not lead to negative intensities which are physically not allowed.

The quantities a , b , c are constants which have to be determined from reference spectra.⁴⁸ The O–K-edge and the Nb–M-edge were studied. (Fig. 11) It could be concluded that the interface term I_I con-

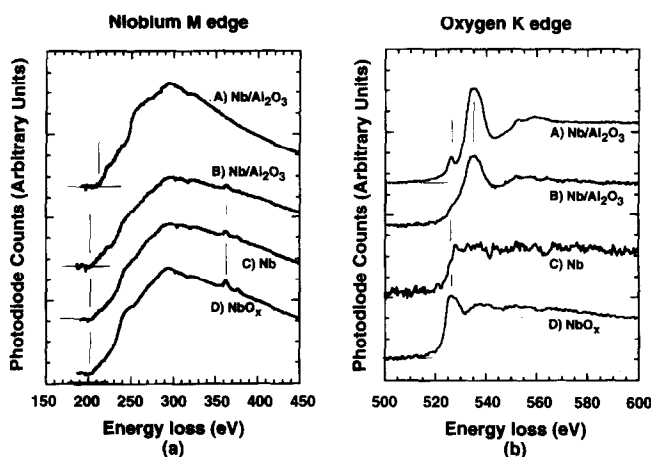


Fig. 11. Energy loss near edge structure (ELNES) of the regions at or close to the Nb/Al₂O₃ interface. (a) O–K-edge. The different spectra are recorded at various locations across the interface. A reference spectra for NbO_x and Nb is shown. The little peak visible at the spectrum taken from the interface region is indicative of Nb³⁺. Nb must form the terminating layer. (b) Al₂O₃, L-edge. There exist no difference the ELNES of the interface and bulk A indicating that Al atoms ‘feel’ always the same environment. Al does not terminate the sapphire.

tains a signal which must result from Nb being in an oxidized state (Nb³⁺) whereas Al exists only with Al³⁺ configuration. Those investigations suggest that sapphire is terminated by an oxygen layer and the first Nb layer (of the Nb crystal) consists of oxidized Nb. Those observations are in agreement with the results of *ab initio* calculations.^{18–20}

6.4 Misfit dislocations at the interface

The Burgers vector of the misfit dislocations are determined by a Burgers circuit in the HRTEM micrograph. An example for a Burgers circuit around a misfit dislocation of system 4 is shown in Fig. 12. The Burgers circuit results in a Burgers vector of $1/2 [11\bar{1}]$. The edge component $1/2 [110]$ is parallel to the interface and accommodates the lattice mismatch. The edge component $1/2 [00\bar{1}]$ is perpendicular to the interface and causes the rotation of the Nb lattice. Due to the rotation of the Nb lattice, the (001)_{Nb} planes are not parallel to the (01 $\bar{1}2$)_S interface plane. Table 2 summarizes the experimental results for all systems.^{23,27} Burgers vector components, which do not accommodate any lattice mismatch, are in general compensated in these networks. In the network of system 2 and 4, these components are compensated by an alternating sequence of misfit dislocations with the same line direction but different Burgers vectors. Only the $1/2 [00\bar{1}]$ Burgers vector component of the misfit dislocations of system 4 with line direction $[1\bar{1}0]$ is not compensated. In the network of system 1, the edge component b_{perp} perpendicular to the interface of one array of dislocations is compensated by the b_{perp} component of the second array.

The Burgers vector of the misfit dislocations has been determined with HRTEM due to the small average distance d_{MD} between the misfit dislocations. If d_{MD} is smaller than $1/3$ of the extinction

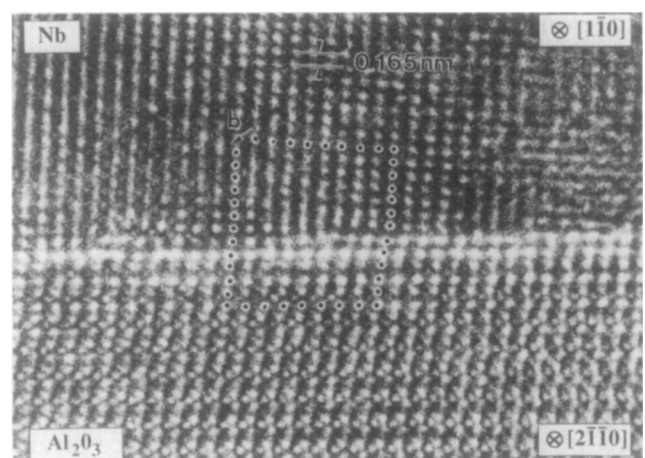


Fig. 12. HRTEM micrograph of a misfit dislocation at the Nb/Al₂O₃ interface of system 4. A Burgers circuit is marked around a misfit dislocation. The micrograph is not yet evaluated quantitatively.

Table 2. Summary of the dislocation networks

System	Line direction	Burgers vector	Edge dislocation	Geometry	d_{MD}
System 1 (0001) (111)	$\xi_1 = [1\bar{1}0]$	$\vec{b}_1 = 1/2[11\bar{1}]$	+	rhombic	21 nm
	$\xi_2 = [01\bar{1}]$	$\vec{b}_2 = 1/2[1\bar{1}1]$	+		21 nm
System 2 (01\bar{1}0) (11\bar{2})	$\xi_1 = [1\bar{1}0]$	$\vec{b}_1 = 1/2[111]$	+	rectangular	2.4 nm
	$\xi_2 = [111]$	$\vec{b}_{2a} = 1/2[1\bar{1}1]$	-		12.1 nm
System 3 (2\bar{1}\bar{1}0) (1\bar{1}0)	$\xi_1 = [11\bar{2}]$	$\vec{b}_1 = 1/2[111]$	+	rectangular	14 nm
	$\xi_2 = [112]$	$\vec{b}_2 = 1/2[1\bar{1}1]$	+		2.5 nm
System 4 (01\bar{1}2) (001)	$\xi_1 = [1\bar{1}0]$	$\vec{b}_{1b} = 1/2[111]$	+	rectangular	2.7 nm
	$\xi_2 = [110]$	$\vec{b}_{2a} = 1/2[1\bar{1}1]$	+		12.1 nm
		$\vec{b}_{2b} = 1/2[1\bar{1}1]$	+		

distance ξg , then it is impossible to distinguish between the contrast of a dislocation network and a moiré pattern.⁴⁹ The extinction distance $\xi[110]$ for Nb is 26 nm.

7 Case Study 2: The Copper/Sapphire Interface

7.1 The structure of the Cu/Al₂O₃ interface

Cu films were deposited on Al₂O₃ substrates in a MBE machine. During the growth of the crystal reflection high energy electron diffraction patterns could be observed. It was quite interesting that at a growth temperature of 473 K only a ring pattern could be revealed (with reflection from {111}, {200}, {220}, {311} and {422} Cu planes). After depositing a certain thickness of Cu the crystallites reorient and form a single crystalline film. The diffraction ring pattern remains unchanged up to an effective film thickness of about 10 nm. But for thicknesses beyond 10 nm the RHEED pattern develops sharp diffraction streaks characteristic of single crystal films. The close packed planes and the close-packed directions in the two crystals are parallel:

$$(111)_{Cu} \parallel (0001)_S \text{ and } \langle 110 \rangle_{Cu} \parallel [10\bar{1}0]_S \quad (4)$$

Edge-on bright field imaging of the Cu/Al₂O₃ interface reveals a sharp transition between the sapphire substrate and the Cu layer. No chemical reaction on interdiffusion has occurred at the interface during crystal growth. Theoretical calculations¹⁴ indicate that Cu bonds to surface oxygen atoms (ions) of sapphire. The approximate 7% difference between the corresponding spacing of the adjacent lattices raises the question of coherence at the Cu/Al₂O₃ interface.

Either the lattice strain of the film is relaxed by a network of misfit dislocations, or contact of the two phases does not introduce any lattice strain. For the case of a semicoherent interface, two different hexagonal misfit dislocation networks are possible.⁵⁰ One network consists of 60° dislocations with $\langle 110 \rangle_{Cu}$ line vectors which should be

observable end-on in a HRTEM lattice image such as Fig. 13. This HRTEM micrograph of the Cu/Al₂O₃ interface was obtained with the incident beam parallel to $[10\bar{1}0]_{Al_2O_3}$ and $\langle 110 \rangle_{Cu}$, respectively. The dominant periodicity of sapphire in the lattice image corresponds to the spacing of $(2\bar{1}\bar{1}0)_{Al_2O_3}$ and $(0003)_{Al_2O_3}$ planes. The $(0003)_{Al_2O_3}$ planes are parallel to the $\{110\}_{Cu}$ planes. Since the copper lattice is slightly twisted about $[111]_{Cu}$, the contribution of the $\{1\bar{1}1\}_{Cu}$ planes is weak whereas $(002)_{Cu}$ planes are dominant. The experimental image does not reveal localized misfit dislocations, thus the less likely case of a 60° misfit dislocation network is excluded.

The other possible misfit dislocation network has edge type dislocations with a $_{Cu}/2 \langle 110 \rangle_{Cu}$ Burgers vectors and line vectors along $\langle 211 \rangle_{Cu}$ directions. Thus a network will be visible by imaging the Cu/Al₂O₃ interface edge-on the $[211]_{Cu}$ direction. In order to resolve the $\{220\}_{Cu}$ planes with a lattice spacing of 1.28 Å, the experimental image shown in Fig. 13 was obtained on the Stuttgart-ARM.³⁹ The resolved $(022)_{Cu}$ planes do not reveal any trace of strain fields caused by the proposed dislocation network. Additionally, no periodicity between the terminating copper and sapphire planes is found. Therefore, the investigated Cu/Al₂O₃ interfaces can be described by a rigid lattice model possessing an incoherent interface. The weak adhesion of copper on sapphire based on non-covalent bonding¹⁴ and also the absence of localized misfit dislocations for internally oxidized copper/alumina interfaces,⁵⁰ agrees well with the results of these investigations.⁵¹

7.2 Energy loss spectroscopy at the Cu/Al₂O₃ interface

Each absorption edge in EELS is associated with an energy-loss near-edge structure (ELNES) which contains information on bonding and electronic structure.³⁴ Different oxidation states of metals can be distinguished either by a change in the energy onset of a particular edge (a so called chemical shift) and/or by a change in the shape of the ELNES. The latter is also sensitive to the local

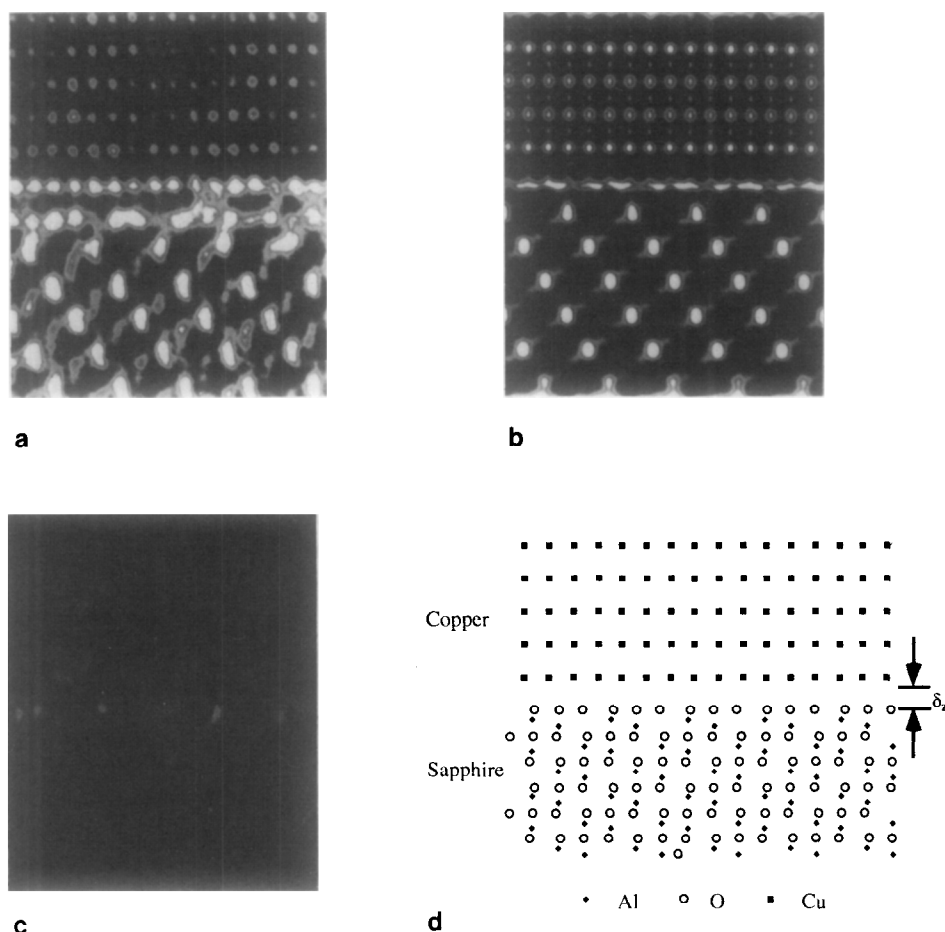


Fig. 13. (a) HRTEM micrograph of the Cu/Al₂O₃ interface. (ARM Stuttgart). The (022) planes of Cu can readily be seen (0.12 nm distance). A detailed analysis revealed that a fixed orientation relationship exists between Cu and Al₂O₃. The interface is, however, incoherent. (b) Simulated micrograph assuming the atomistic model of Fig. 13(d). (c) Difference image $D = |I_c - I_s|$. (d) Model used for image shown in Fig. 13(b) (G. Dehm, unpublished work).

coordination of the atomic species. In this section, results on ELNES of Cu/Al₂O₃ interfaces are reported. The same specimens as for the structural studies were used.

The measurements were carried out with a VG HB 501 dedicated STEM spectrometer (Gatan 666 PEELS) as described in Section 6.3. Scanning the beam enables simultaneous imaging of the interface and allows a manual correction of specimen drift. All spectra were corrected for dark current and readout-pattern of the parallel detector. The pre-edge background was extrapolated by a power law $A \times E^{-r}$ ³³ and subtracted from the original data.

The interface-specific component of the ELNES was obtained by using the spatial difference technique as described in Section 6.3.⁴⁸ For this method three spectra were acquired, one from a region containing the interface and two in the adjacent bulk materials. The interface spectrum contains not only the signal from the interfacial atoms but also contributions from the surrounding bulk materials. The extraction of the interfacial ELNES requires the removal of the contributions from the bulk materials. The reference spectra taken in the bulk materials were scaled

and then subtracted from the interfaces spectrum. The remaining difference spectrum represents the ELNES arising from the interfacial atoms with an environment or oxidation state different from both bulk materials. The scaling of the reference spectra is necessary because different numbers of bulk atoms are irradiated during the acquisition of the interface and reference spectra respectively. The scaling factors were determined by trial and error applying the following guidelines: selection of an energy-loss region containing strong and characteristic features for the bulk materials and minimizing these contributions in the difference spectrum. In the case that a chemical shift occurs, the intensity directly above the edge onset is eliminated. Care was taken that the subtraction of the reference spectra did not lead to negative intensities which are physically not allowed.

The Cu-L_{2,3} edge spectra recorded in the bulk copper and at the Cu/Al₂O₃ interface are shown in Fig. 14. The spectrum taken in the bulk sapphire is omitted because there is only a smooth background in this energy-loss region. Subtraction of the Cu-L_{2,3} edge spectrum of bulk copper from the interface spectrum yields a difference spectrum

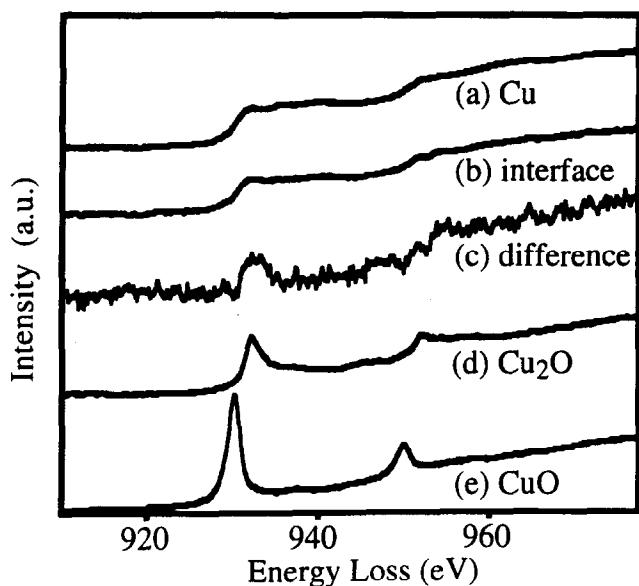


Fig. 14. ELNES studies at Cu/Al₂O₃ interface. Cu-L_{2,3} edge of (a) Cu; (b) the interface containing region; (c) the extracted difference spectrum; (d) Cu₂O and (e) CuO. The position and shape of the maximum in (c) is similar as in (d) suggesting that at the interface Cu¹⁺ exists. (C. Scheu, unpublished results).

with an ELNES different from the pure metal (Fig. 14). The difference spectrum shows a shape similar to the reference spectra taken from cuprous oxide (Cu₂O) and cupric oxide (CuO) (Fig. 14(d, e)). No chemical shift, typical for Cu²⁺, was observed, which indicates that Cu exists at the interface in a Cu¹⁺ oxidation state.

The ELNES of the Al-L_{2,3} edge in bulk sapphire (onset 78 eV) and the Cu-M_{2,3} edge in bulk copper (onset 74 eV) overlap. Therefore, the spectrum measured at the interface contains contributions from both bulk materials. The intensity of the calculated difference spectrum is zero within the detection limits set by noise. This indicates that the Al atoms are not involved in the bonding and that no noticeable change in the local coordination of the Al atoms occurs. From the results of the Cu-L_{2,3} edge one might expect a change of the Cu-M_{2,3} ELNES which was not observed.

The results of the investigation of the Cu-L_{2,3} and Al-L_{2,3} edge indicate an interaction between the Cu and the O atoms, whereas the Al atoms are not affected by the presence of the interface. This is supported by the existence of a difference spectrum at the O-K edge. The interface-specific component shows a slight downward shift of the edge onset and a broadening of the main peak at 540 eV compared to the O-K edge in the sapphire matrix.

Using the basic formulae for the quantification of an EELS absorption edge^{33,34}

$$S = J_0 N \sigma \quad (5)$$

(S = characteristic inner-shell signal; J_0 = total transmitted intensity; N = number of atoms per

unit area, and σ = cross section) it is possible to obtain the number of atoms affected by the interface. The interfacial width is the region containing these interfacial atoms with a coordination or oxidation state different from both bulk materials. From the ratio of the signal of the difference spectrum and the as-acquired interface spectrum both integrated over an energy-loss region of 30 eV above the edge onset a width of 0.36 ± 0.04 nm is obtained (averaged over ten measurements in two different specimens). This corresponds to 1.6 monolayers when compared to the 0.21 nm spacing of the Cu (111) planes which are parallel to the interface.

The ELNES of the Cu-L_{2,3}, O-K and Al-L_{2,3} edge of the Cu/Al₂O₃ interface indicate bonding between copper and the oxygen sublattice of α -Al₂O₃ with a charge transfer from copper to oxygen. The oxidation state of copper at the interface is +1. The aluminium atoms do not alter their coordination compared to bulk α -Al₂O₃. The results show that the investigation of the interfacial ELNES is a useful method to study the bonding and electronic structure of metal/ceramic interfaces.

If segregated atoms exist at the MCIs interfaces they could be identified by AEM. For example, it is readily possible to determine segregation of components by EDS technique and EELS. The detection limit is in the order of 1.

Acknowledgements

The author acknowledges many helpful discussions with J. Bruley, G. Dehm, F. Ernst, M. W. Finnis, G. Gutekunst, C. Kruse, J. Mayer, C. Scheu and H. Müllejans. The work was supported by the Volkswagen Foundation (contract monitor Dr H. Steinhardt) under contract no. I/66 791.

References

1. Cahn, J. W. & Kalonji, G., *Solid-solid phase transformation*, ed. H. I. Aaronson, American Society for Metals, Metals Park/OH, 1982, p. 1.
2. Rühle, M., Evans, A. G., Ashby, M. F. & Hirth, J., (eds), *Metal/Ceramic Interfaces, Acta-Scripta Metall. Proc. Series Vol. 4*, Pergamon Press, Oxford, 1989.
3. Rühle, M., Heuer, A. H. & Ashby, M. F., Metal/ceramic interfaces. Suppl. *Acta Metall. Mater.*, **40** (1992)S1-368.
4. Knowles, K. M., Microscopy of interface in composites. *J. Microscopy*, **169** (1993) 95; **177** (1995) 187.
5. Trumble, K. P. & Rühle, M., *Acta Metall. Mater.*, **39** (1991) 1915.
6. Ernst, F. & Rühle, M., *Materials Science Forum*, **155/156** (1994) 331.
7. Ernst, F., *Mat. Sci. Eng.*, **R14** (1995) 97.
8. Klomp, J. T., *Ceramic Microstructure 86: Role of Interfaces*, eds J. A. Pask & A. G. Evans, Plenum Press, New York, 1986, p. 307.

9. Jilavi, M., Ph.D. Thesis, Universität of Stuttgart, 1995.
10. Fischmeister, H. F., Navara, E. & Easterling, K. E., *Mat. Sci.*, **6** (1972) 211.
11. Sutton, A. P. & Balluffi, R. W., *Interfaces in Crystalline Materials*, Clarendon Press, Oxford (1995).
12. Sutton, A. P. & Balluffi, R. W., *Acta Metall. Mater.*, **35** (1987) 2177.
13. Fecht, H. J. & Gleiter, H., *Acta Metall. Mater.*, **33** (1985) 557.
14. Johnson, K. H. & Pepper, S. V., *J. Appl. Phys.*, **53** (1982) 6634.
15. Li, R., Wu, Q., Freeman, A. J. & Fu, C. L., *Phys. Rev.*, **B48** (1993) 8317.
16. Schönberger, U., Andersen, O. K. & Methfessel, M., *Acta Metall. Mater.*, **40** (1992) S1.
17. Hong, T., Smith, J. R. & Srolovitz, D. J., *Acta Metall. Mater.*, **43** (1995) 2721.
18. Kruse, C., Ph.D Thesis, Universität Stuttgart, 1994.
19. Finnis, M. W. & Kruse, C., *Materials at High Temperatures*, **12** (1994) 189; *Proc. Mat. Res. Soc. Symp.*, **357** (1995) 427.
20. Kruse, C., Finnis, M. W., Milman, V. Y., Payman, M. C., Vita, A. D. & Gillan, M. J., *J. Am. Cer. Soc.*, **77** (1994) 431.
21. Mayer, J., Flynn, C. P. & Rühle, M., *Ultramicroscopy*, **33** (1989) 51.
22. Mayer, J., Gutekunst, G., Möbus, G., Dura, J., Flynn, C. P. & Rühle, M., *Acta Metall. Mater.*, **40** (1992) S227.
23. Gutekunst, G., Mayer, J. & Rühle, M., *Scripta Metall. Mater.*, **31** (1994) 1097.
24. Gutekunst, G., Mayer, J. & Rühle, M., *Atomic Structures of Epitaxial Nb/Al₂O₃ Interfaces: I. Coherent Regime*, to be published.
25. Vitek, V., Gutekunst, G., Mayer, J. & Rühle, M., *Phil. Mag.*, **A71** (1995) 1219.
26. Tricker, D. M. & Stobbs, W. M., *Phil. Mag.*, **A71** (1995) 1037 & 1051.
27. Gutekunst, G., Mayer, J. & Rühle, M., *Atomic Structure of Epitaxial Nb/Al₂O₃ Interfaces: II. Misfit Dislocations*, to be published.
28. Elßner, G., Korn, D. & Rühle, M., *Scripta Metall. Mater.*, **31** (1994) 1037.
29. Korn, D., Elßner, G. & Rühle, M., to be published.
30. Rühle, M., *Fundamentals of Metal-Matrix Composites*, eds S. Suresh, A. Mortensen & A. Needleman, Butterworth-Heinemann, Boston, 1993, p. 81.
31. Hirsch, P. B., Howie, A., Nicholson, R., Pahsley, D. W. & Whelan, M. J., *Electron Microscopy of Thin Crystals*, Krieger Publishers Company, Malabar/FL, USA
32. Joy, D. C., Ronnig, Jr., A. D. & Goldstein, J. I. (eds), *Principles of Analytical Electron Microscopy*, Plenum Press, New York, 1979.
33. Egerton, R. F., *Electron Energy-Loss Spectroscopy*, Plenum Press, New York, 1986.
34. Disko, M. M., Ahn, C. C. & Fultz, B., (eds.), *Transmission Electron Energy Loss Spectroscopy in Materials Science*, The Minerals, Metals and Materials Society, Warrendale, 1992.
35. Bruley, J., *Microsc. Microanal. Microstruc.*, **4** (1993) 23.
36. Spence, J. C. H., *Experimental High-Resolution Electron Microscopy*, 2nd ed., Oxford University Press, New York and Oxford, 1988.
37. Busek, P., Cowley, J. & Eyring, L. (eds), *High-Resolution Transmission Electron Microscopy*, Oxford University Press, New York and Oxford, 1988.
38. Horiuchi, S., *Fundamentals of High-Resolution Electron Microscopy*, North Holland Publishing Company, Amsterdam, (1993).
39. Phillipp, F., Höschen, R., Möbus, G., Osaki, M. & Rühle, M., *Ultramicroscopy*, **56** (1994) 1.
40. Frank, J. (ed.), *Electron Tomography*, Plenum Press, New York and London, 1992.
41. Möbus, G. & Rühle, M., *Optik*, **93** (1993) 108.
42. Möbus, G., Necker, G. & Rühle, M., *Ultramicroscopy*, **49** (1993) 46.
43. Hofmann, D. & Ernst, F., *Ultramicroscopy*, **56** (1994) 54.
44. Möbus, G. & Rühle, M., *Ultramicroscopy*, **56** (1994) 54.
45. Frank, J., *Computer Processing of Electron Microscopy Images*, ed. P. W. Hawkes, Springer-Verlag Berlin, 1980, p. 235.
46. Durbin, S. M., Cunningham, J. E., Mochel, M. E. & Flynn, C. P., *J. Phys.*, **F11** (1981) L223.
47. Lee, W. E. & Lagerlöf, K. P. D., *J. Electron. Microsc. Tech.*, **2** (1985) 247.
48. Bruley, J., Brydson, R., Müllejans, H., Mayer, J., Gutekunst, G., Mader, W., Knauss, D. & Rühle, M., *J. Mater. Res.*, **9** (1994) 2574.
49. Thölen, A. R., *Phys. Stat. Sol. (a)*, **2** (1970) 537.
50. Ernst, F., Pirouz, P. & Heuer, A. H., *Phil. Mag.*, **A63** (1990) 259.
51. Dehm, G., Rühle, M., Ding, G. & Raj, R., *Phil. Mag.*, **A71** (1995) 1111.

HREM of Ceramic High T_c Superconductors

G. Van Tendeloo & T. Krekels

EMAT, University of Antwerp (RUCA) Groenenborgerlaan 171, B-2020 Antwerp, Belgium

(Received 18 April 1995; revised version received 18 October 1995; accepted 24 October 1995)

Abstract

High resolution electron microscopy (HREM) is a real space technique, able to provide structural information complementary to the reciprocal space techniques such as X-ray or neutron diffraction. While the latter produce average information, HREM provides local information down to atomic scale. For ceramic high temperature superconductors not only the perfect structure is of importance, but particularly the defect structure or local structure. Physical properties such as critical current or superconducting volume fraction are strongly influenced by the deviations from perfection. We will further show that light element configurations—such as oxygen ordering or the incorporation of carbonate groups in the material—can be identified on atomic resolution images.

1 Introduction

Structural defects in materials strongly influence a large number of physical properties. Different techniques allow us to detect or characterize these defects in a direct or an indirect way. We may subdivide them in reciprocal space techniques, such as X-ray or neutron scattering, and real space techniques such as the different microscopy techniques.

The strength of reciprocal space techniques has been strongly improved recently because of synchrotron radiation sources; they allow a higher resolution and need smaller amounts of material. Neutron as well as X-ray diffraction are highly quantitative and detailed analyses of intensity maxima and peak widths allow us to draw far-reaching conclusions on the perfection of the material, deviations from stoichiometry, and the average defect density. However no direct visualization of these imperfections is possible and therefore important information such as a correlation between defects, Burgers vectors of dislocations, local deviations from perfection is not available. The presence of mesoscopic or nano-

sized secondary phases as well as weak modulations in the structure can be easily overlooked.

Real space microscopy techniques can be subdivided into surface techniques and bulk techniques; both have their merits and specific application fields. Optical microscopy, scanning electron microscopy, scanning tunneling microscopy and atomic force microscopy for example belong to the former and give detailed, eventually atomic scale information on the surface perfection, surface reconstruction and surface adsorption. Information from the bulk can be obtained by a number of techniques such as acoustic microscopy, infra-red microscopy, X-ray tomography or others. Although most of these bulk techniques have their specific merits, the spacial resolution of the information is in general very limited however.

Electron microscopy not only has the advantage of being able to resolve structural details down to the atomic level, it also allows us to switch—with a single push-button—to electron diffraction, i.e. to reciprocal space. This combination of real space and reciprocal space information makes electron microscopy a unique technique for the study of solid state materials. As with all other techniques, it has its shortcomings and limitations, but electron microscopy can provide structural information that no other technique is able to produce.

We will illustrate the possibilities of HREM for several superconducting materials and we will emphasize especially the imaging of light elements such as oxygen and carbonate or sulphite groups.

2 Structural Defects in YBCO-Based Materials

The high temperature superconductor $\text{YBa}_2\text{Cu}_3\text{O}_7$ has been the first to be studied in detail by EM. The coherent twin fragmentation on (110) planes resulting from the tetragonal to orthorhombic phase transition was discovered by means of diffraction contrast electron microscopy and electron diffraction.^{1,2} From a microstructural point

of view, $\text{YBa}_2\text{Cu}_3\text{O}_{7-\delta}$ is an interesting compound. It allows a large number of oxygen vacancies ($0 \leq \delta \leq 1$) on the oxygen sublattice. Depending on their concentration these vacancies tend to occur into various ordering schemes.³⁻²¹ The $2a_0$ superstructure (Ortho II) in non-stoichiometric $\text{YBa}_2\text{Cu}_3\text{O}_{7-\delta}$, due to the alternation along the a_0 direction of filled and empty CuO chains in the CuO layers was also discovered by electron diffraction and electron microscopy.^{3,17,18} The oxygen ordering occurs within nanometer size domains and is generally highly faulted; therefore it can hardly be detected by X-rays or neutrons. On the other hand these small dimensions make them eligible for flux pinning centra.

Another important feature of the YBCO compound is its susceptibility to allow elemental substitutions on most of its sublattices, without substantially altering the structure, but inducing quite different physical and chemical properties. We will focus here on those aspects where electron microscopy and electron diffraction have played an important role in elucidating the structure and bridging the gap between physical properties and structural data.

2.1 Oxygen-vacancy ordering in the CuO-plane of $\text{YBa}_2\text{Cu}_3\text{O}_{7-\delta}$

It is well-established that, at room temperature and atmospheric pressure, within the range $0 \leq \delta \lesssim \delta_t$ the structure of $\text{YBa}_2\text{Cu}_3\text{O}_{7-\delta}$ is orthorhombic and within the range $\delta_t \lesssim \delta \leq 1$, it is tetragonal. Values for δ_t vary around 0.65.^{4,23-27} In

experiments where δ is fixed the transition temperature T_t increases linearly with δ .²⁸ Reported values for the $O \rightarrow T$ transition temperature range between 110°C at $\delta = 0.67$ and 680°C at $\delta = 0.34$.

On cooling from the high temperature tetragonal phase, a spontaneous strain, proportional to the orthorhombicity of the material is introduced. This strain can be released by the introduction of coherent twinning on (110) planes. The microstructure then consists of slabs of two orientation variants of the orthorhombic phase. The (110) twinning is a reaction to a *macroscopic* orthorhombic strain. This, in contrast to the case of 'tweed' which seems to be triggered by *local* orthorhombic deformations. It is important to note that twinning as well as tweed are effects related to the orthorhombic range of the phase diagram. By non-local techniques such as X-ray or neutron diffraction, tweed textured material has often been described as tetragonal.

In the tetragonal phase, the oxygen atoms in the CuO-layer are distributed quasi randomly, with an equal occupation of the O(1)- and O(5)-sublattices. The sublattices consist of the oxygen sites between every two copper atoms in the plane, the O(1) sites lying along one direction (defined as a), the O(5) sites along the other (see Fig. 1). The formation of short CuO-segments along both basic directions of the CuO-chain plane is likely to cause local orthorhombic strains that lead to the pre-transition tweed texture.

The presence of short range ordering of oxygen and vacancies is revealed in electron diffraction

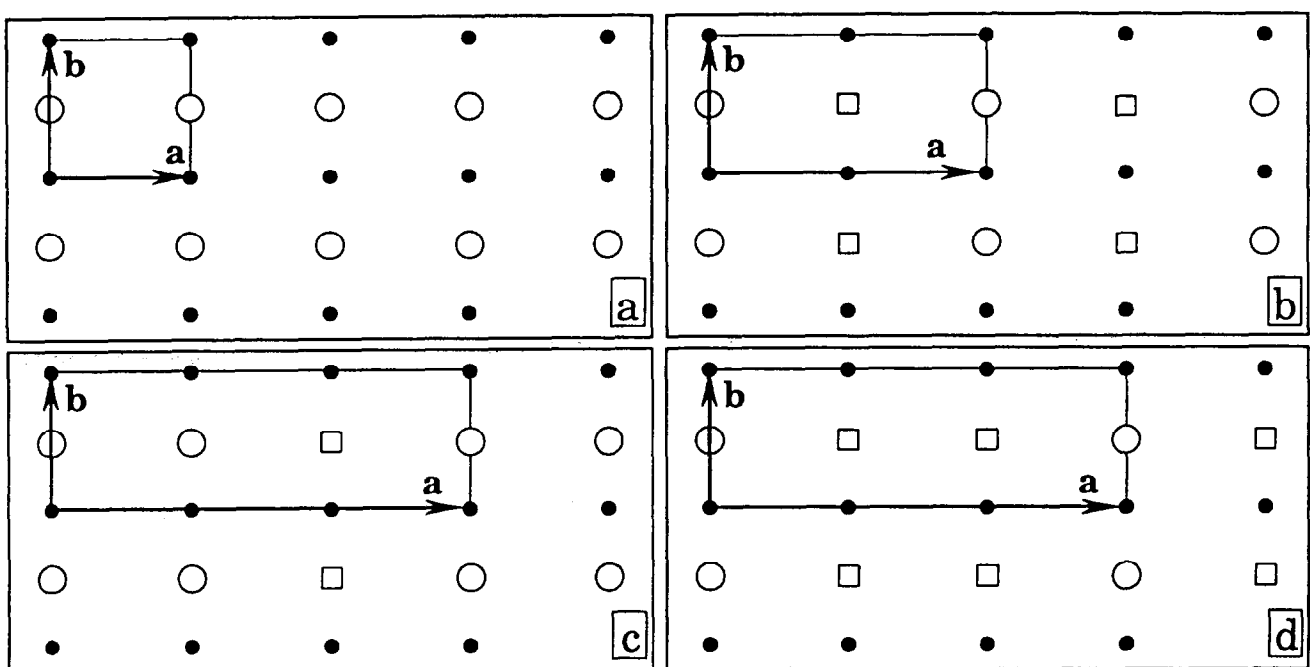


Fig. 1. (a) Schematic representation of the CuO-plane Ortho-I ordering. (b) Model of the Ortho-II ordering. Along a CuO and Cu-vacancy chains alternate. (c) and (d) are representations of ordering leading to tripled a -parameters: (c) represents the Ortho-III phase with an oxygen content 6.667; (d) represents a symmetric phase where roles of vacant and filled chains are reversed, that occurs at oxygen contents 6.333.

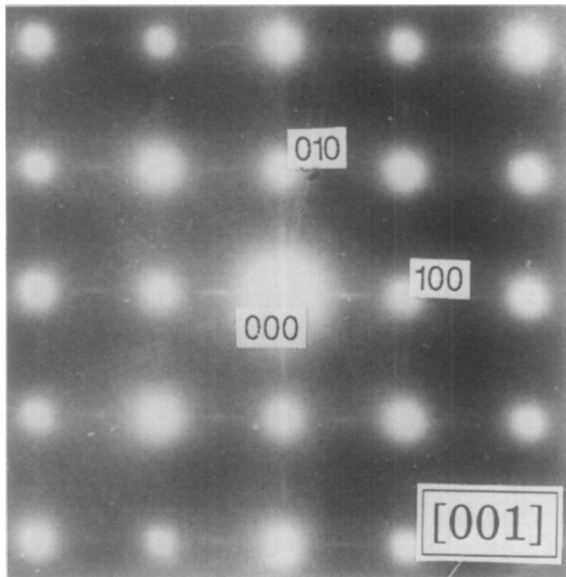


Fig. 2. Electron diffraction pattern along the [001] zone, in a tetragonal sample. *In situ* heating and cooling causes disorder reflected in the presence of diffuse scattering along the basic directions.

patterns by the occurrence of diffuse intensities. The diffuse streaks observed in the [001]-zone diffraction pattern of Fig. 2 are due to the presence of irregularly spaced, short segments of CuO-chains. Short range order is commonly observed in highly oxygen deficient samples and can be induced in oxygen-rich materials by a thermal disordering by an *in situ* heating treatment.

The orthorhombic phase that corresponds to $\text{YBa}_2\text{Cu}_3\text{O}_7$ ($\delta = 0$), is termed 'Ortho-I'. The CuO-plane in the Ortho-I phase has all O(1)-sites filled and all O(5)-sites vacant. CuO-chains run along b (Fig. 1(a)). As a result, for the Ortho-I phase $a_o < b_o$. A second phase, termed Ortho-II, has every other b -oriented chain evacuated of oxygen and has an ideal composition $\text{YBa}_2\text{Cu}_3\text{O}_{6.5}$ ($\delta = 0.5$). (Fig. 1(b)) The oxygen content range over which the Ortho-II phase is observed stretches over $0.3 < \delta \leq 0.5$. The new unit mesh that can be defined on the ordered $\text{CuO}_{1-\delta}$ -plane has dimensions $a_{II} = 7.668 \text{ \AA} \approx 2a_p$, $b_{II} = 3.869 \text{ \AA} \approx b_p$. (based on ref. 3). The Ortho-II-phase is easily recognized in [001] ED patterns (Fig. 3); it produces superstructure spots at positions $h + \frac{1}{2} k l$, characteristic for a doubling of the a -parameter. Often however, in such patterns also the b -parameter seems doubled by the appearance of spots at positions $h k + \frac{1}{2} l$ as well. These spots are due to the basic (110) twinning of the orthorhombic matrix, the resulting diffraction pattern (Fig. 3) being the overlap of the two identical patterns, with a rotation difference of about 90° . In ref. 29 it is shown that a disordered array of line defects gives rise to Lorentzian-shaped diffraction spots, with a position associated with the mean spacing of the scat-

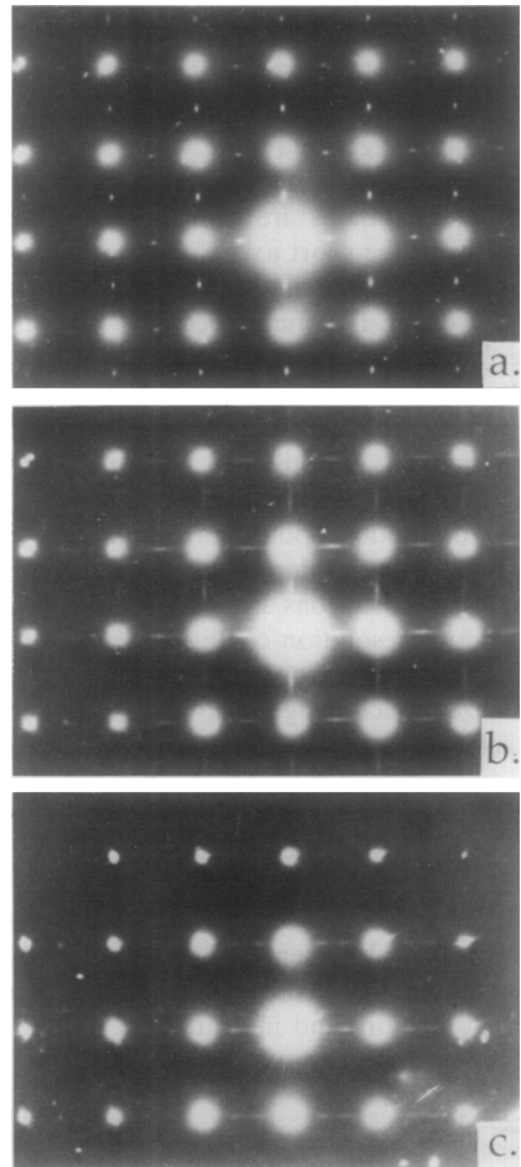


Fig. 3. (a) [001] zone diffraction pattern with sharp superstructure reflections at positions $h + \frac{1}{2} k l$ appearing in well-ordered Ortho-II material. Since the material is twinned, spots seem to appear along both basic directions. (b) [001] zone diffraction pattern with streaked superstructure intensity, corresponding to domains that are short range ordered along a , occurring at oxygen contents at the slopes above and below the Ortho-II plateau. (c) [001] zone diffraction pattern with spots at positions $h + \frac{1}{2} k l$ and $h + \frac{2}{3} k l$ due to an Ortho-III structure occurring in samples with oxygen contents around 6.8.

tering elements. When chains in the CuO-plane are irregularly spaced with a mean spacing of $2a_p$, Lorentzian shaped diffraction spots at positions $h + \frac{1}{2} k l$ are expected. When the average periodicity increases, the superstructure reflections will become more elongated. (Fig. 3(b)). A second factor influencing the superstructure reflection shape is the Ortho-II domain shape, small domain dimensions leading to elongated reflections. Intensity and sharpness of the superstructure reflections can thus be considered as indices of the domain size and the ordering quality of the phase. Whereas an ideal Ortho-II domain has an oxygen deficiency

$\delta = 0.5$, the strongest and sharpest Ortho-II electron diffraction intensity occurs at an oxygen deficiency of only $\delta = 0.4$.³⁰ The domain size and the ordering quality thus are apparently maximized at $\delta = 0.4$.

Dark field images allow the visualisation of the oxygen ordered domains. The images show that the Ortho-II domains are elongated or lenticular in shape, with the short axis along the a -direction. Largest Ortho-II domains (4×20 nm) and a maximal total Ortho-II volume, occur at oxygen deficiencies $\delta = 0.4$. For the $\delta = 0.4$ sample of ref. 5, from measurements of the Ortho-II peak surface in a [100] electron densitogram, the Ortho-II volume fraction was an estimated 50%, in accordance with our results. Samples showing elongated Ortho-II diffraction spots, correspondingly show Ortho-II domains in dark-field images (Fig. 4(b)) with reduced dimensions along a (size: 1×20 nm).

Under high resolution conditions, imaged along the [100] direction, the ordered domains can be easily visualized. Such images also allow us to deduce the stacking of the vacancy rows in successive $\text{CuO}_{1-\delta}$ planes along the c -axis (Fig. 5). The normal stacking of these rows is vertical, but small domains of a staggered stacking of successive 2D-ordered CuO-planes are no exception. The ordered domains also reveal anti-phase boundaries with a displacement vector $\mathbf{R} = \frac{1}{2} [100]_{\text{Ortho-II}}$. This is best visible under grazing angles along the [001] direction, and indicated by a white line, broken at the defects.

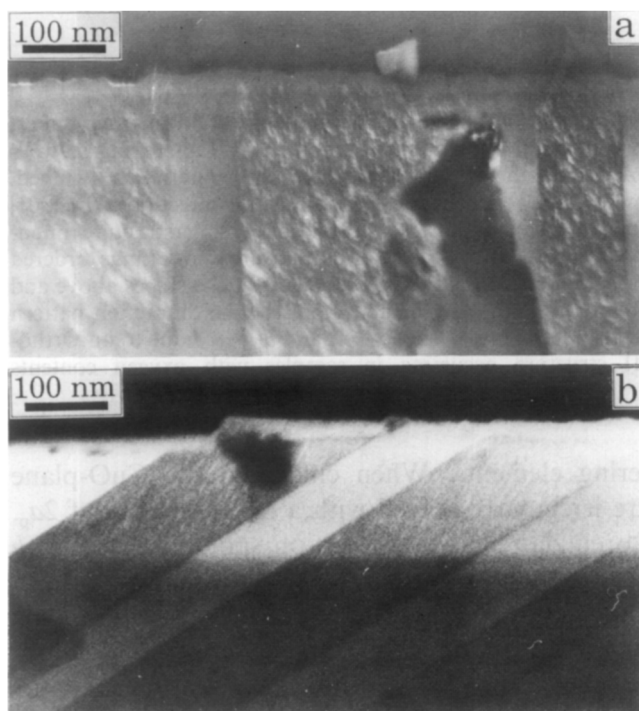


Fig. 4. (a) Dark field image showing Ortho-II ordered domains in bright. The corresponding diffraction pattern is shown in Fig. 3(a). (b) Dark field image corresponding to Fig. 3(b). Domain size is short along a and large along the CuO-chain direction b . The band structure in these images is due to twinning.

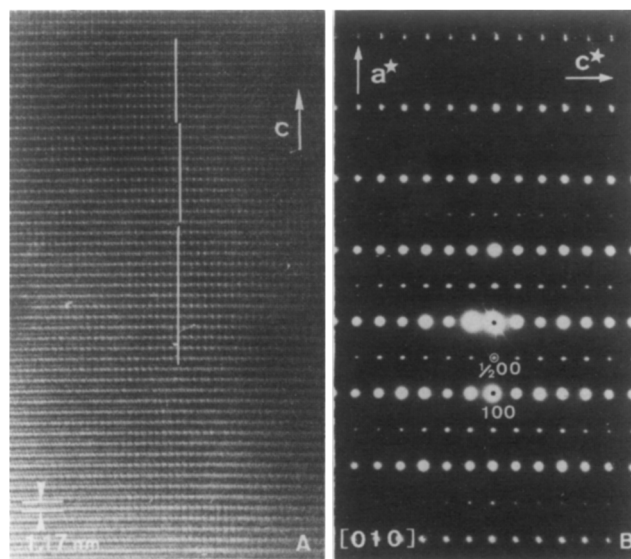


Fig. 5. (a) High resolution image along the [010]-axis, of the Ortho-II phase. The cell doubling can be seen by the white dots that appear every $2a_p$. In this view along the chains, chains are stacked vertically along c . Note the presence of anti-phase boundaries with displacement vector $\mathbf{R} = \frac{1}{2} [100]$. (b) Diffraction pattern along the [010] zone axis. Note the splitting of the outer spot rows due to twinning.

Instead of a doubling of the unit cell due to oxygen vacancy ordering along the b -axis, one can imagine different ordering schemes, introducing tripling, quadrupling, ... of the basic Ortho-I structure. Electron microscopic observations of the Ortho-III-phase have been reported (Fig. 3(c)), but much less and more ill defined than the Ortho-II phase.^{10,31,32} Due to the short structural coherence length of this phase, their presence could not be detected neither by X-ray, nor by neutron diffraction. The Ortho-III phase ideally appears at an oxygen deficiency $\delta = \frac{1}{3}$, (or $\frac{2}{3}$) and compared to the Ortho-I phase, one out of three Cu_1O_1 -chains is depleted of oxygen (Fig. 2(c)). Superstructures with longer periodicities of $4a_p$ and $5a_p$ have also been observed by electron microscopy.^{33,34} These phases appear on very local scales (a few unit cells wide), and therefore have only been observed by means of high resolution electron microscopy. Identifying these phases as (Cu-O)-chain ordered phases, they should probably be considered as metastable phases at oxygen contents, intermediate to that of the stable Ortho-I, Ortho-II and Ortho-III phases. Theoretical studies seem to support this conclusion.^{35,36}

2.2 (001) planar defects in YBCO-based material

The presence of (001) planar defects consisting of a double CuO-layer, replacing the normal single layer, was first demonstrated by means of electron microscopy³⁷ (Fig. 6). This observation has led to the development of a superconducting mixed layer Y-Ba-Cu-O family containing regular arrange-

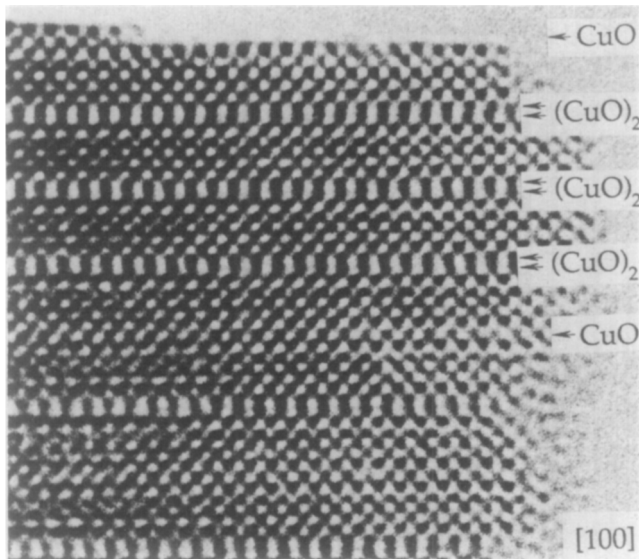


Fig. 6. HREM image showing the presence of double CuO planes in the $\text{YBa}_2\text{Cu}_3\text{O}_7$ structure.

ments of single and double CuO layers. Members of this family are the so called 1-2-4 phase ($\text{YBa}_2\text{Cu}_4\text{O}_8$)^{38,39} and the 2-4-7 phase ($\text{Y}_2\text{Ba}_4\text{Cu}_7\text{O}_{15}$).⁴⁰ 1-2-4 and 2-4-7 can be regarded as members of a series of 'shear structures' derived from the 123 basic structure by the periodic insertions of supplementary CuO-layers. Representing the number of 123 unit cells separating these supplementary CuO-layers by an integer, the 124 and 247 structures are represented by the stacking symbols $1\bar{1}$

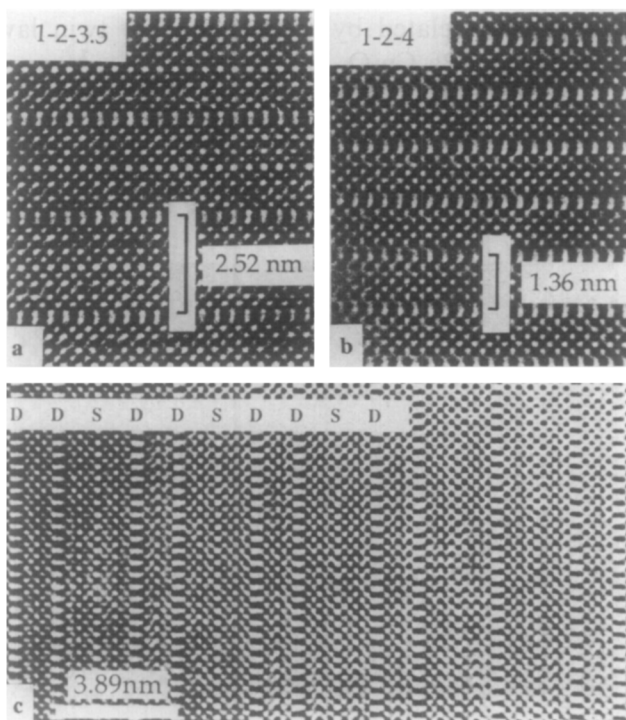


Fig. 7. [010] HREM image of: (a) the $\text{Y}_2\text{Ba}_4\text{Cu}_7\text{O}_{15}$ structure (2-4-7); the double $(\text{CuO})_2$ layer is introduced every two unit cells; (b) the $\text{YBa}_2\text{Cu}_4\text{O}_8$ structure (1-2-4); the double $(\text{CuO})_2$ layer is introduced every unit cell; (c) a complex sequence of double and single CuO layers.

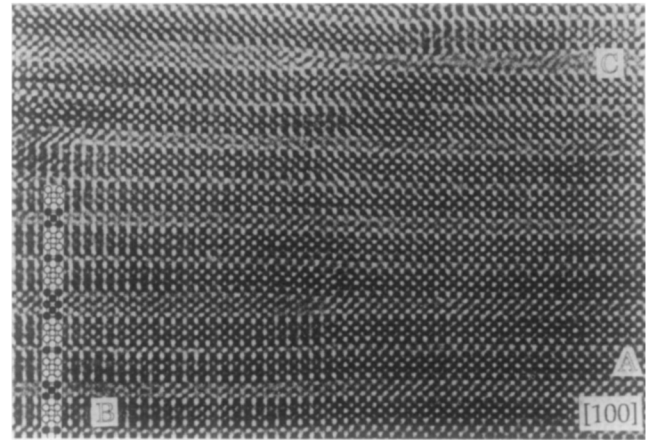


Fig. 8. Heavily distorted part of a 2-4-7 grain with all double $(\text{CuO})_2$ layers replaced by triple ones (area A) or by quintuple ones (area B).

and $2\bar{2}$.^{41,42} The minus sign is introduced to indicate that the presence of a double CuO layer causes a lateral offset between successive 123 blocks over $\frac{1}{3}[010]$. High resolution images along the [010] direction of the perfect 124 and 247 structure are reproduced in Fig. 7(a, b). The double chain layers are characterized by intense rows of elongated double white dots. Changing the initial composition does not alter the stoichiometry of the outcoming material, one does however stabilize to some extent different phases such as $2\bar{2}$ and $3\bar{3}$ over limited areas. Figure 7(c) shows an example of a complex polytypoid over a limited region. Apart from this series of phases being a mixture of 1-2-3 and 1-2-4 where periodically double $(\text{CuO})_2$ layers are introduced, a different series of Cu-rich phases was discovered, in which successive perovskite blocks are separated by triple $(\text{CuO})_3$ layers.⁴³ An example is reproduced in Fig. 8 together with a schematic inset where the CuO layer configuration is represented by black dots. In some parts of the crystal even isolated CuO multilayers consisting of as much as five CuO layers have been observed in a matrix of essentially 2-4-7 material.⁴¹

2.3 Cu substitution in YBCO 1-2-3 superconductors

Although it seems well established that superconductivity is to be associated with the CuO_2 layers, doping of the CuO-layers seems to play an important role in determining the concentration and the type of carriers. Also the critical temperature T_c is related to the composition of the CuO layer. It could for instance be shown that the 60 K plateau in the curve relating T_c to the oxygen content in this layer is associated with the presence of the $2a_0$ structure, i.e. with the material with ideal composition $\text{YBa}_2\text{Cu}_3\text{O}_{6.5}$.⁴⁴⁻⁴⁶ It was attempted to replace copper in the CuO-layers, either completely or partly by other metallic ions such as iron, cobalt,

zinc, gallium. Also complex ions such as CO_3^{2-} or SO_4^{2-} were incorporated in the CuO-layer, carbon and sulphur occupying copper sites in the CuO chains. Iron substitution is found to induce a 'tweed' texture, the geometry of which could be assessed by assuming that iron occurs in the CuO layers in two types of oxygen coordination: octahedral and tetrahedral. The tetrahedrally coordinated iron ions induce microtwinning by the nucleation of CuO chains along mutually perpendicular directions which causes the tweed microtexture (ref. 47 and references therein). Cobalt substitutions in small concentrations has a rather similar aspect.⁴⁸

The substitution of all copper ions in the CuO layers by gallium or cobalt ions ($\text{YSr}_2\text{Cu}_2\text{MO}_{7-x}$) leads to the formation of rows of corner sharing CoO_4 (or GaO_4) tetrahedra along the $[110]$ direction of the basic perovskite structure, replacing in a sense the CuO_4 strings of square planar configurations along the b_0 direction. The tetragonal symmetry is hereby reduced to an orthorhombic one.^{49,50} The strings of tetrahedra can moreover adopt two mutually perpendicular directions giving rise to two twin related orientation variants of the orthorhombic structure. It was moreover shown that period doubling (also tripling) occurs in the (001) plane along the direction normal to the chains of tetrahedra. This could be rationalized by noting that the parallel chains can adopt two different configurations, differing by the sense of rotation of the coupled tetrahedra along a string. Period doubling can then be attributed to the regular alternation of these two types of chains in a parallel set.

In case of carbonate substitutions for Cu(1) in the $\text{YSr}_2\text{Cu}_3\text{O}_7$ compound, the CO_3 triangles align in chains along the perovskite b -axis.⁵¹ We will discuss here a recent and similar substitution, the substitution by tetrahedral SO_4 -groups in compounds with composition $[\text{Y}_{1-y}\text{Sr}_y]\text{Sr}_2[\text{Cu}_{3-x}(\text{SO}_4)_x]\text{O}_{7-\delta}$, where $y = 0.16$ and $x = 0.22$. The electron diffraction patterns of this material confirm this average structure determined by neutrons^{52,53} but strong satellites are associated with every basic reflection. The $[010]$ and $[001]$ zone diffraction patterns of Fig. 9 shows the presence of bright first order satellites (Fig. 9(a)) and weaker second order satellites (Fig. 9(a, b)); the length of the satellite- q -vector is 1 nm^{-1} . The structure can therefore be considered as modulated with the wavevector in the (010) plane, inclined over an angle α ($\alpha \approx 32^\circ$) with respect to the $[100]$ -direction and with a wavelength $\lambda \approx 1 \text{ nm}$. Although the observed modulation is orthorhombic, most $[001]$ observed diffraction patterns show tetragonal symmetry, with superstructure spots along a^* as well as along b^* . This is due to the presence of two orthorhombic

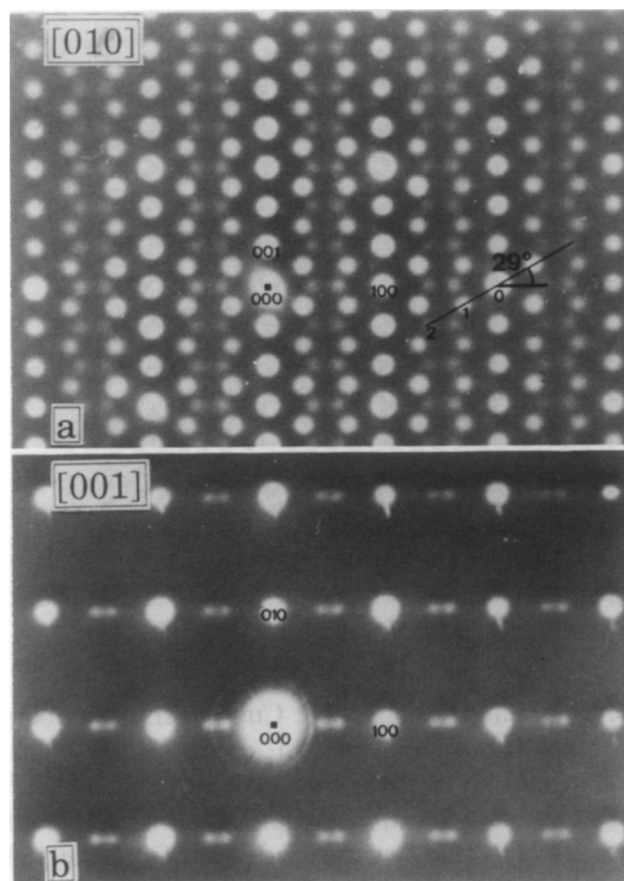


Fig. 9. Electron diffraction patterns of $[\text{Y}_{0.84}\text{Sr}_{0.16}]\text{Sr}_2\text{Cu}_{2.78}(\text{SO}_4)_{0.22}\text{O}_{6.12}$: (a) $[010]$ pattern showing satellites at every basic spot; numbers indicate spot order, the angle indicated is $\alpha = 29^\circ$; (b) $[001]$ pattern with only the weaker second order spots; indexing of both patterns refers to the basic unit cell.

variants, related by the usual (110) twin law common in $\text{YBa}_2\text{Cu}_3\text{O}_{7-\delta}$.

High resolution images along the $[010]$ -zone (Fig. 10), show the presence of a modulation corresponding to the satellites in the corresponding diffraction pattern of Fig. 9(a). The image is more

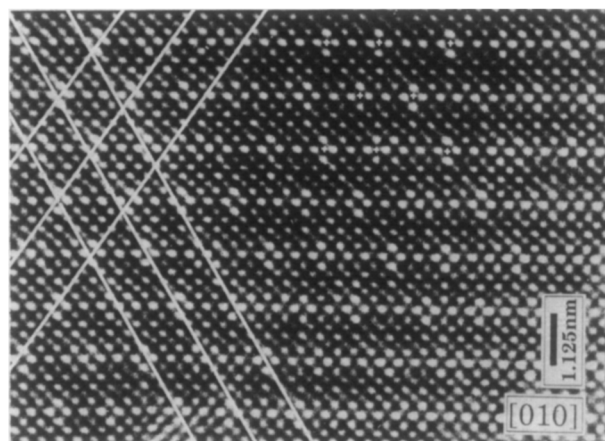


Fig. 10. High resolution image along the $[010]$ -zone showing S-rich columns as brighter squares of four dots centered on the Cu(1)-S-O-layers. The maxima of the modulating wave, easily seen under grazing angles, are stressed by two sets of heavy lines in the image. The brighter dot configurations are indicated in part of the image by small crosses.

or less the same as that of the undoped $\text{YBa}_2\text{Cu}_3\text{O}_7$ material, however every three or four repeat distances along the a -direction, squares of more intense dots are present. According to image simulations, this is to be associated with the presence of SO_4 -groups in the Cu-O(1) layer. Along the c -direction the stacking of these columns or 'chains' is usually staggered in such a fashion that their configurations in every second Cu(1)-S-O-plane coincide vertically. Within a single Cu(1)-S-O-plane the alternation is incommensurate but the intensity maxima are spaced roughly as $\dots - 4a_0 - 3a_0 - 3a_0 \dots$. Looking along the directions indicated by heavy lines in Fig. 10, planes containing a high density of SO_4 -clusters are revealed by a modulation in dot intensity. These planes can be considered as the maxima of a planar concentration wave. The normal to this concentration wave makes an angle α of about 30° with the $[100]$ -direction and the length of the wavevector is about 1 nm.

These observations can be explained by a simple model of SO_4 -chain formation and ordering. The $[001]$ high resolution image suggests the presence of chains oriented along the b -direction, the nature of which must differ from that of CuO chains by their S content. The stacking-rule of the SO_4 -rich chains can be derived from the observation of the concentration waves in Fig. 10:

- (1) The SO_4 -chains substitute these sites of the Cu(1)-sublattice which are closest to the maxima of the concentration waves.
- (2) The integer l -coordinates of the second order satellites as well as direct observations in high resolution images suggest that the SO_4 -chain-stacking coincides vertically in every second plane along the $[001]$ direction.

These observations allow us to propose an atomistic model for the modulation in $[\text{Y}_{1-y}\text{Sr}_y]\text{Sr}_2$

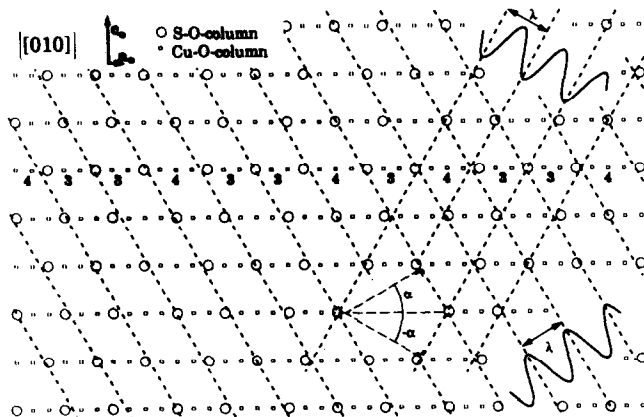


Fig. 11. Schematic representation of the incommensurate modulation of the Cu(1)-column-sublattice. Squares represent the Cu(1)-column sublattice, circles represent SO_4 -chains and are located on Cu(1)-column-sites closest to the maxima of a SO_4 -occupancy wave with wavevector inclined over α with respect to $[100]$ and with wavelength λ .

$[\text{Cu}_{3-x}(\text{SO}_4)_x]\text{O}_{7-\delta}$. In the schematic representation of Fig. 11 only the Cu(1) sublattice is shown; dashed lines are the maxima of the concentration waves with angles $\alpha = \pm 30^\circ$ and $\lambda \approx 1$ nm. Due to the incommensurability of the basic lattice with the modulation, the ordering along the a -direction is essentially aperiodic, which is in agreement with the absence of periodic superstructure spots in the diffraction patterns. A physical explanation for the observed SO_4 -chain arrangement is not straightforward but certainly involves a strain component. The chains occupied by SO_4^{2-} -ions cause cylindrically symmetrical stress fields as a consequence of the difference in size of the sulphur-ions and the copper-ions that they replace. Parallel chains thus interact by mutually repulsive elastic forces which depend on the separation r as $1/r$. The equilibrium configuration of such a set of repelling parallel chains, when confined to a finite area, or with a specified concentration, consists of a triangular array. With the restriction that the SO_4 -chains can only be located at positions in the Cu(1)O-chain layers, the observed distribution of SO_4 -chains is the one that yields the largest average separations between different chains.

3 Superconducting Bi-, Tl- or Hg-compounds

The Bi-compounds with general formula $\text{Bi}_2\text{Sr}_2\text{Ca}_n\text{Cu}_{n+1}\text{O}_{6+2n}$ were the first to present T_c values above 100 K. They can be considered as a family of mixed layer compounds '2 2 n n + 1' and there is a clear correlation between the chemical formula and the values of T_c ; 20 K for $n = 0$, 80 K for $n = 1$ and 105 K for $n = 2$.⁵⁴⁻⁵⁷ The existence of such a family was initially predicted based on HREM observations of singular lamellae containing a number of CuO_2 layers deviating from the bulk composition. All of the Bi-compounds moreover exhibit an incommensurate one-dimensional deformation modulation, localized mainly within the BiO layers.⁵⁸ The modulation was attributed primarily to the misfit between the perovskite blocks and the BiO layers and the particular lone pair electronic configuration of the Bi^{3+} .⁵⁹ The one-dimensional modulation reduces the point symmetry of the compound from tetragonal to monoclinic in the 2201 compound and to orthorhombic in the 2212 or 2223 compound. As a result defects, i.e. modulation twins caused by the modulation and related by the lost symmetry elements may arise. The effect of the substitution of bismuth by lead on the modulation period and on the geometrical features of the modulation wave, resulting in a stabilization of the 2212 or the 2223 structure, has been studied almost exclusively by

means of EM. The modulated structure in the lead substituted compounds, differs from that in the pure Bi-compounds; whereas the modulation waves in successive layers are in anti-phase in the pure Bi-compounds, they are in phase in the lead substituted compounds. Figure 12 compares the modulation along the [010] zone axis for the undoped (Fig. 12(a)) and the Pb doped compound (Fig. 12(b)).

Recently several higher-order members of the Hg-based superconducting family $\text{HgBa}_2\text{Ca}_{n-1}\text{Cu}_n\text{O}_{2n+2+\delta}$ have been synthesized recently; the critical temperature reaches a maximum of 133.5 K for the $n = 3$ member of the family,⁶⁰ while for larger n values, T_c seems to decrease.⁶¹ It was furthermore shown (not very unexpectedly) that T_c increases steadily with pressure at a rate of more or less 1 K/GPa. In this way Chu *et al.*⁶² and Nunez-Regueiro *et al.*⁶³ were able to reach values such as 164 and 155 K (T_c onsets) for the Hg-1223 compound respectively. This strong pressure effect suggests that by the appropriate chemical doping, which would introduce a chemical pressure, T_c

values of the order of 150 K would not be excluded at normal-external-pressure. Several substitutions in the Hg-plane as well as at the Ba- or the Ca-positions have been tried by the Caen group; they have led to the discovery of a series of new Hg-based superconducting compounds, which can be prepared under ambient pressure and which have a T_c up to 110 K.⁶⁴⁻⁶⁸

The structure of all members is similar; they contain rock salt like slabs $[(\text{BaO})(\text{HgO}_\delta)(\text{BaO})]$, alternating with perovskite slabs of the type $[(\text{CuO}_2)(\text{Ca})]_{n-1}(\text{CuO}_2)$. The structure for different n -compounds is represented in Fig. 13; for increasing n -values an extra $[(\text{CuO}_2)(\text{Ca})]$ slab is inserted, leaving the rest of the average structure unaltered. Although there is a strong similarity between the Hg- and the Tl-series, the occupation of the oxygen sites in the Hg-layers and the corresponding one in the Tl layers, are quite different.

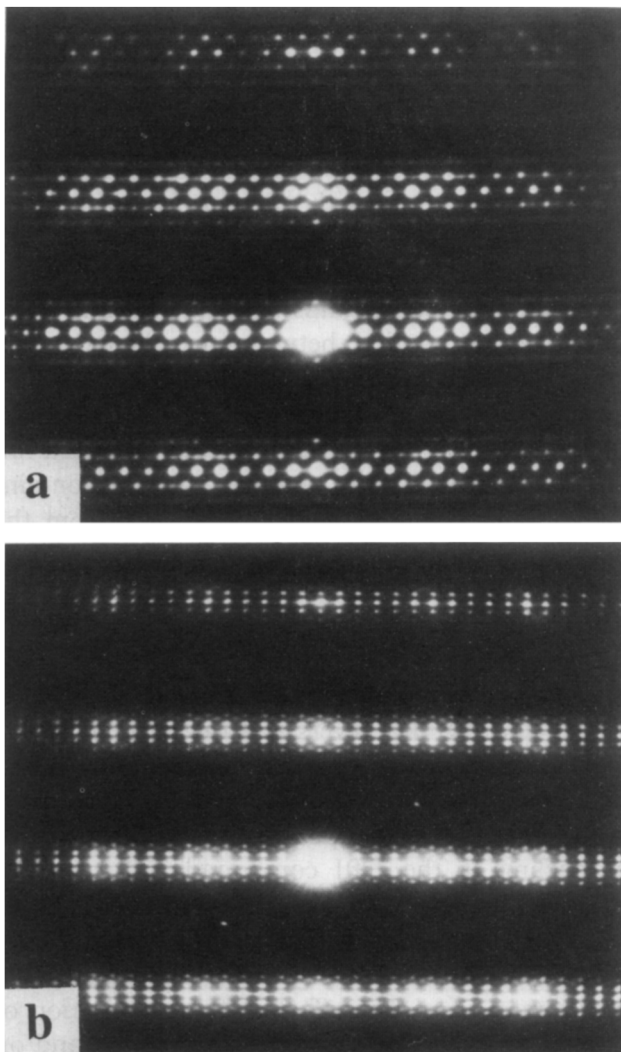


Fig. 12. [010] diffraction pattern of: (a) the undoped $\text{Bi}_2\text{Sr}_2\text{Ca}_1\text{Cu}_2\text{O}_{8+\delta}$ compound; (b) the Pb doped compound $(\text{Bi}_{2-x}\text{Pb}_x)\text{Sr}_2\text{Ca}_1\text{Cu}_2\text{O}_{8+\delta}$.

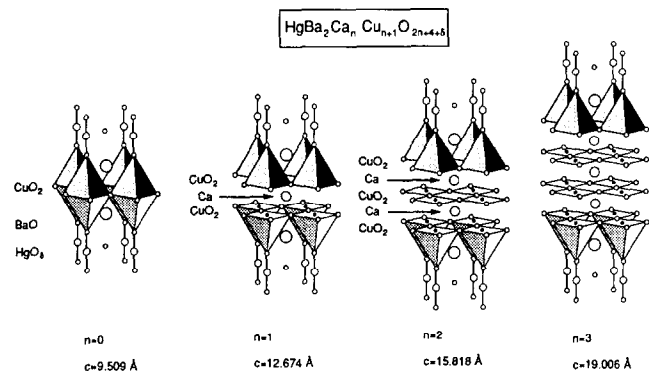


Fig. 13. Schematic representation of several members of the structural family $\text{HgBa}_2\text{Ca}_{n-1}\text{Cu}_n\text{O}_{2n+2+\delta}$.

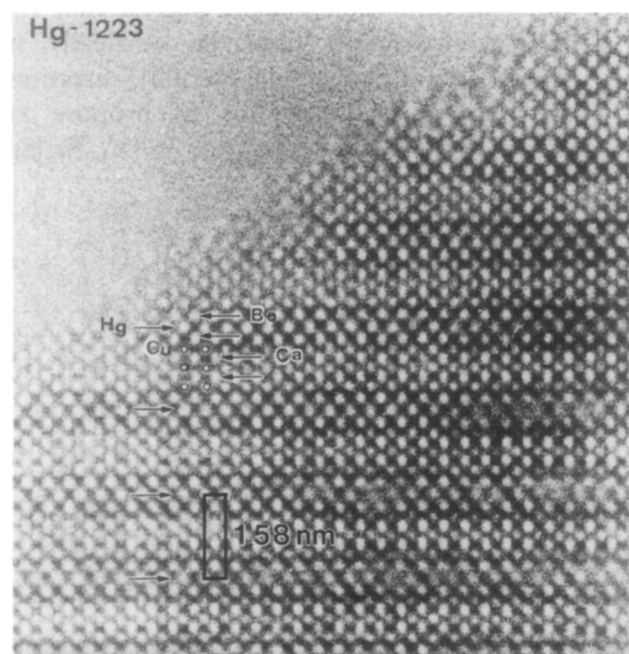


Fig. 14. High resolution image along [100] of $\text{HgBa}_2\text{Ca}_2\text{Cu}_3\text{O}_{8+\delta}$. In this contrast the heavy ions are imaged as bright dots; the imaging code as well as the unit cell is indicated in the figure.

HREM images of the different members of the family are obtained, particularly along the [100] zone, which is the most instructive one. An example for the 1223 compound is shown in Fig. 14; the cation configuration can be readily identified from symmetry considerations. There is clearly a one to one correspondence between the white dot configuration of the HREM image and the cation configuration of Fig. 13. This semi-intuitive interpretation has of course to be confirmed by computer simulations;⁶⁹ they will allow us to analyse in detail the atomic structure of planar defects in these compounds. The most common defect encountered, particularly for higher order members of the family, is the intergrowth of different n -members; they occur as isolated defects and are well known from other homologous series. Periodicities up to $n = 8$ have been seen to occur locally, although no single phase material could be produced.⁶⁹ A most remarkable defect in this structure is the occasional occurrence of a double (HgO_δ) layer instead of the usual sequence of three layers $[(\text{BaO})(\text{HgO}_\delta)(\text{BaO})]$. The occurrence of such defects with a double (HgO_δ) layer suggested the feasibility to produce '2 2 $n-1$ n ' type materials; such '2 2 $n-1$ n ' compounds have indeed been produced by replacing some of the Hg by Pr or Cu⁷⁰ or some of the Ca by a trivalent element such as e.g. Y.⁷¹

When Hg deficient compounds $\text{Hg}_{1-x}\text{Ba}_2\text{Ca}_{n-1}\text{Cu}_n\text{O}_{2n+2+\delta}$, with $x \approx 0.3$ are prepared and carbon is introduced on the sublattice, T_c will decrease⁷² and the carbonate groups will or substitute randomly for the Hg, as in the present compound or occur in an ordered way in related compounds.⁷³⁻⁷⁵

Electron diffraction as well as HREM of $\text{Hg}_{1-x}\text{Ba}_2\text{Ca}_2\text{Cu}_3\text{O}$ reveal the perfect 1223 structure, with no traces of superstructure or imperfections (see Fig. 15(b)). In the HREM image of Fig. 15 all

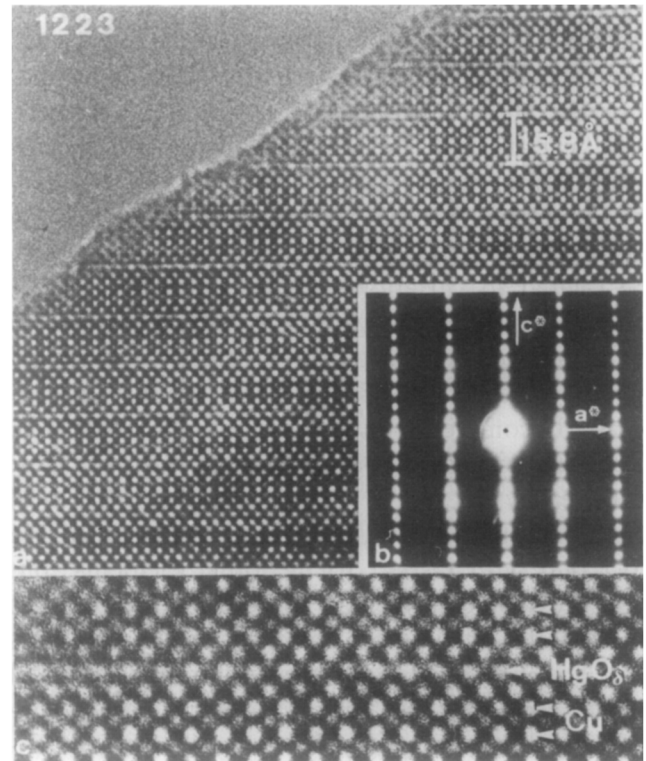


Fig. 15. (a) High resolution image along [010] of the Hg-1223 compound, showing the individual cation columns as bright dots. No extended defects are observed. (b) Corresponding electron diffraction pattern. (c) High magnification of part of (a); note that in the HgO_δ layer the intensity of the individual dots is not homogeneous.

cations are revealed as bright dots and the HgO_δ layer can easily be identified as the more diffuse layer; this follows by comparison with computer simulated images. Along this layer, however, we do see variations in the intensities of the different bright dots (see Fig. 15(c)) which is an enlargement of part of Fig. 15(a). We can quantify these variations by making densitometer traces along the HgO_δ layer as well as along one of the neighbouring CuO_2 layers. The results are shown in

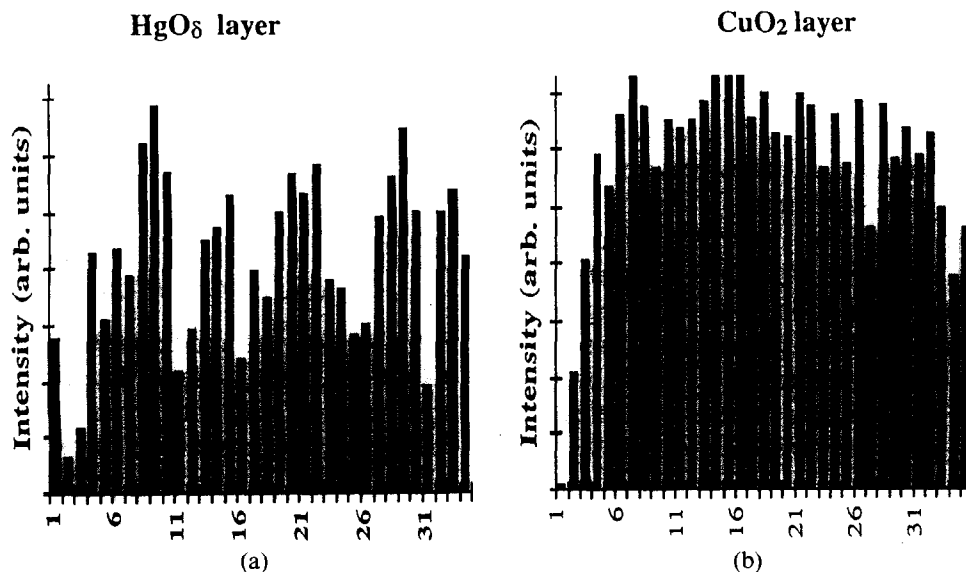


Fig. 16. Intensity measurement of individual dots from Fig. 15(c): (a) along the HgO_δ layer; (b) along the neighbouring CuO_2 layer.

Fig. 16(a), where we have plotted the intensity for different 'bright dots' along a single HgO_8 row; the intensities are corrected for the background. For the HgO_8 layer there is a clear, pseudo-periodic variation in the intensity (Fig. 16(a)), such variation is not observed in the corresponding measurement for the surrounding BaO or CuO_2 layer (Fig. 16(b)). These intensity variations are to be related to variations in the occupation of the Hg-sublattice. If the variations were not random but periodic, they would give rise to weak superstructure reflections visible in the diffraction patterns. If complete columns, or even a single one, were occupied by carbonate groups, this would be detected by HREM.^{75,76} Measurements of the local composition by EDX, reveals a deficiency of Hg (0.7–0.8) with respect to the other elements, but no excess of Cu. We can therefore conclude that the Hg-deficiency is not compensated by an excess Cu. The missing Hg-ions are randomly distributed on the Hg-sublattice; they are most probably occupied by carbonate groups, by vacancies or by a mixture of both; this cannot be decided from EM only.

4 Superconducting Oxycarbonates

A wide variety of novel superconducting materials has recently been prepared by incorporating complex ions such as carbonate, phosphate or sulphate groups in the perovskite-like structures of existing high T_c cuprates; for an overview and further references we refer to refs 77 and 78. Carbonate groups can be substituted into the mercury or thallium based cuprates of the type $\text{Hg}_{1-x}\text{Tl}_x\text{Sr}_{4-y}\text{Ba}_y\text{Cu}_2\text{CO}_3\text{O}_{7-\delta}$. The incorporation of these groups produces interesting modulated structures. Related compounds of the type $\text{ASr}_{4-y}\text{Ba}_y\text{Cu}_2\text{CO}_3\text{O}_{7-\delta}$ where $A = \text{Tl}$, Hg or $\text{Hg}_{0.5}\text{Pb}_{0.5}$ were also found to exhibit remarkable long period interface modulated structures. The modulation vector is along the [010] perovskite direction in the samples with $A = \text{Tl}$ and along the $[110]_p$ direction in the samples with $A = \text{Hg}$ or $A = \text{Hg}_{0.5}\text{Pb}_{0.5}$. The wavelength is mostly incommensurate but varies between 6 and 8 times the basic perovskite unit.

High resolution electron microscopy of the compound $\text{Hg}_{1-x}\text{Tl}_x\text{Sr}_{4-y}\text{Ba}_y\text{Cu}_2\text{CO}_3\text{O}_{7-\delta}$, is able to directly image the modulation (Fig. 17). Together with the electron diffraction information (inset of Fig. 17) one can also deduce the origin of the modulation and the building blocks of the complex structure. The prominently bright dot sequences image columns of carbon and oxygen atoms which are the lightest atoms in the compound. The carbonate groups clearly substitute on the (Hg-Tl)-sublattice, in agreement with previous

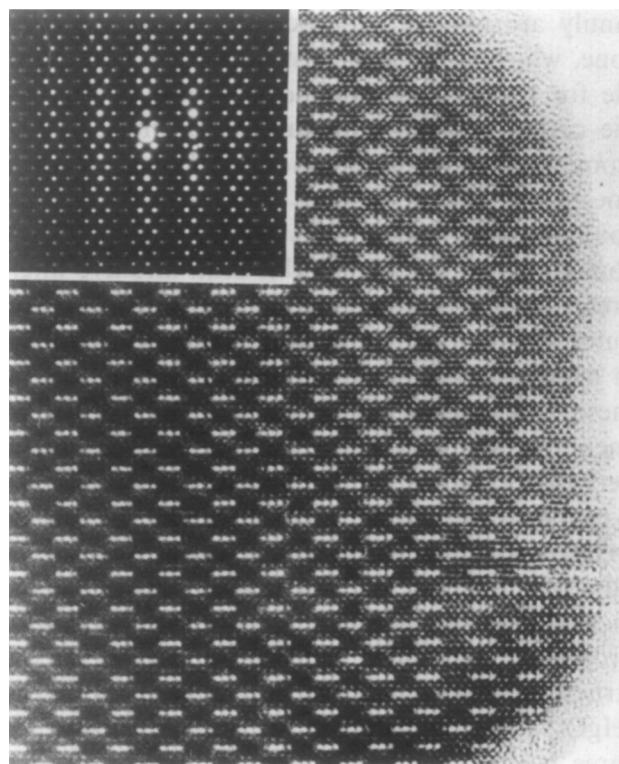
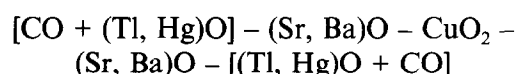


Fig. 17. HREM image of $\text{Hg}_{0.3}\text{Tl}_{0.7}\text{Sr}_{1.5}\text{Ba}_{2.5}\text{Cu}_2\text{CO}_3\text{O}_{7.6}$ along [100]; the carbonate groups are imaged as particularly white features. The corresponding diffraction pattern is shown as an inset.

findings. The carbonate sequences contain either three or four dots. Bright and dark dot sequences alternate in anti-phase in successive layers, leading to a centered rectangular arrangement. The corresponding [100] zone diffraction pattern (Fig. 17) consists of main reflections, which can be indexed on a tetragonal lattice and weaker satellite reflections, which decrease in intensity with distance from the main reflections. The pattern looks commensurate, however careful measurements show that it is in fact incommensurate, the period being slightly smaller than $8b_p$. Actually the periodicity of the modulation can vary between $6b_p$ and $8b_p$, depending on a number of parameters, which will not be discussed here.

The high resolution images of these compounds not only suggest a model for the stacking along the c -direction:



but also for the modulated structure within the $[\text{CO} + (\text{Tl}, \text{Hg})\text{O}]$ -plane. Incommensurate diffraction patterns originate from a structure in which commensurate carbonate strips of two different widths (3 and 4 times the perovskite unit) are uniformly mixed. The high resolution images (e.g. Fig. 17) give evidence for sequences such as 3434... or 334334....

As to the -near- future of HREM and the imaging of light elements in electron microscopy, we can announce that we have just installed a new CM30-FEG-Ultra twin microscope at the EMAT laboratory in Antwerp, which is able to produce structural information down to the 1.1 Å level. The interpretation of such images in function of the projected crystal potential is certainly not straightforward, but with the help of CCD recording and computer treatment of the data, we are starting real quantitative HREM.⁷⁹

Acknowledgements

We are most grateful to S. Amelinckx (Antwerp) for common research on the YBCO-based compounds and to M. Huvé (now in Lille), M. Hervieu, C. Michel and B. Raveau (Caen), C. Chaillout and M. Marezio (Grenoble), C. Greaves (Birmingham) and E. V. Antipov (Moscow) for valuable discussions and use of common results on the Hg-based compounds and the oxycarbonates.

References

1. Van Tendeloo, G., Zandbergen, H. W. & Amelinckx, S., *Solid State Comm.*, **63** (1987) 389.
2. Zandbergen, H. W., Van Tendeloo, G., Okabe, T. & Amelinckx, S., *Phys. Stat. Sol. (a)*, **103** (1987) 45.
3. Cava, R. J., Hewat, A. W., Hewat, E. A., Batlogg, B., Marezio, M., Rabe, K. M., Krajewski, J. J., Peck, Jr., W. F., Rupp, Jr., L. W., *Phys. C*, **165** (1989) 419–33.
4. Ourmazd, A. & Spence, J. C. H., *Nature*, **329** (1987) 425–7.
5. Lin, Y. P., Greedan, J. E., O'Reilly, A. H., Reimers, J. N., Stager, C. V. & Post, M. L., *J. Sol. Stat. Chem.*, **84** (1990) 226–36.
6. Chaillout, C., Alario Franco, M. A., Capponi, J. J., Chenavas, J., Hodeau, J. L. & Marezio, M., *Phys. Rev. B*, **36** (1987) 7118–20.
7. Zhu, Y., Moodenbaugh, A. R., Suenaga, M. & Taftø, J., *Physica C*, **167** (1990) 363–8.
8. Chen, C. H., Werder, D. J., Schneemeyer, L. F., Gallagher, P. K. & Waszczak, J. V., *Phys. Rev. B*, **38** (1988) 2888–91.
9. Rao, C. N. R., Nagarajan, R., Ganguli, A. K., Subbana, G. N. & Bhat, S. V., *Phys. Rev. B*, **42**(4) (1990) 6765–8.
10. Burmester, C. P., Quong, S., Wille, L. T., Gronsky, R., Ahn, B. T., Lee, V. Y., Beyers, R., Gür, T. M. & Huggings, R. A., *Mat. Res. Soc. Symp. Proc.*, **183** (1990) 369–74.
11. Hodeau, J.-L., Bordet, P., Capponi, J.-J., Chaillout, C. & Marezio, M., *Phys. C*, **153–155** (1988) 582–5.
12. Beyers, R., Ahn, B. T., Gorman, G., Lee, V. Y., Parkin, S. S. P., Ramirez, M. L., Roche, K. P., Vazquez, J. E., Gür, T. M. & Huggings, R. A., *Nature*, **340** (1989) 619–21.
13. Alario-Franco, M. A., Chaillout, C., Capponi, J. J. & Chenavas, J., *Mat. Res. Bull.*, **22** (1987) 1685–93.
14. Alario-Franco, M. A., Chaillout, C., Capponi, J. J., Chenavas, J., & Marezio, M., *Phys. C*, **156** (1988) 455–60.
15. Hou, C. J., Manthiram, A., Rabenberg, L. & Goode-nough, J. B., *J. Mater. Res.*, **5** (1990) 9–16.
16. Chaillout, C., Alario Franco, M. A., Capponi, J. J., Chenavas, J., Strobel, P. & Marezio, M., *Sol. Stat. Comm.*, **65**(10) (1987) 283–6.
17. Hervieu, M., Domengès, B., Raveau, B., Post, M., McKinnon, W. R. & Tarascon, J. M., *Mat. Lett.*, **8** (1989) 73–82.
18. Hervieu, M., Domengès, B., Michel, C., Provost, J. & Raveau, B., *J. Sol. State Chem.*, **71** (1987) 263.
19. Van Tendeloo, G., Zandbergen, H. W. & Amelinckx, S., *Sol. Stat. Comm.*, **63** (1987) 603–6.
20. Fleming, R. M., Schneemeyer, L. F., Gallagher, P. K., Batlogg, B., Rupp, L. W. & Waszczak, J. V., *Phys. Rev. B*, **37** (1988) 7920–3.
21. You, H., Axe, J. D., Kan, X. B., Hashimoto, S., Moss, S. C., Liu, J. Z., Crabtree, G. W. & Lam, D. J., *Phys. Rev. B*, **38** (1988) 9213–6.
22. Zeiske, T., Holhwein, D., Sonntag, R., Kubanek, F. & Wolf, T., *Phys. C*, **194** (1992) 1–8.
23. Nakazawa, Y. & Ishikawa, M., *Phys. C*, **158** (1989) 381–4.
24. Nakazawa, Y. & Ishikawa, M., *Phys. C*, **162–164** (1989) 83.
25. Ueda, Y. & Kosuge, K., *Phys. C*, **156** (1988) 281–5.
26. Cava, R. J., Batlogg, B., Chen, C. H., Rietman, E. A., Zahurak, S. M. & Werder, D., *Phys. Rev. B*, **36** (1987) 5719.
27. Strauven, H., Locquet, J. P., Verbeke, O. B. & Bruynser-aede, Y., *Sol. Stat. Comm.*, **65** 293–6 (1987).
28. Gerdanian, P., Picard, C. & Touzelin, B., *Physica C*, **182** (1991) 11.
29. Van Dyck, D., Condé, C. & Amelinckx, S., *Phys. Stat. Sol. (a)*, **56** (1979) 327–34.
30. Krekels, T., Van Tendeloo, G., Amelinckx, S., Wagener, D., Buchgeister, M., Hosseini, S. M. & Herzog, P., *Physica C*, **196** (1992) 363–8.
31. Yang, S., Claus, H., Veal, B. W., Wheeler, R., Paulikas, A. P. & Downey, J. W., *Phys. C*, **193** (1992) 243–52.
32. Rusiecki, S., Bucher, B., Kaldis, E., Jilek, E., Karpinski, J., Rossel, C., Pümpin, B., Keller, H., Kündig, W., Krekels, T. & Van Tendeloo, G., *J. Less Common Metals*, **164–165**, (1990) 31–8.
33. Reyes-Gasga, J., Krekels, T., Van Tendeloo, G., Van Landuyt, J., Amelinckx, S., Brugginck, W. H. M. & Verweij, H., *Phys. C*, **159** (1989) 831–48.
34. Van Tendeloo, G. & Amelinckx, S., *J. El. Mic. Tech-nique*, **8** (1988) 285–95.
35. Khachatryan, A. G. & Morris, J. W., *Phys. Rev. Lett.*, **61** (1988) 215–8.
36. de Fontaine, D., Ceder, G. & Asta, M., *Nature*, **343** (1990) 544–6.
37. Zandbergen, H. W., Gronsky, R., Wang, K. & Thomas, G., *Nature*, **331** (1988) 569.
38. Morris, D. E., Asmar, N. G., Nickel, J. H., Sid, R. L., Wei, J. Y. T. & Post, J. E., *Physica C*, **159** (1989) 287.
39. Karpinski, J., Kaldis, E., Jilek, E., Rusiecki, S. & Bucher, B., *Nature*, **336** (1988) 660.
40. Bordet, P., Chaillout, C., Chenavas, J., Hodeau, J. L., Marezio, M., Karpinski, J. & Kaldis, E., *Nature*, **334** (1989) 596.
41. Krekels, T., Van Tendeloo, G., Amelinckx, S., Karpinski, J., Ruisiecki, S., Kaldis, E. & Jilek, E., *Physica C*, **178**, (1991) 383.
42. Krekels, T., Van Tendeloo, G., Amelinckx, S., Karpinski, J., Kaldis, E. & Ruisiecki, S., *Solid State Comm.*, **79**, (1991) 607.
43. Ramesh, R., Jin, S. & March, P., *Nature*, **346** (1990) 420.
44. Beyers, R., Ahn, B. T., Gorman, G., Lee, V. Y., Parkin, S. S. P., Ramirez, M. L., Roche, K. P., Vasquez, J. E., Gür, T. M. & Huggings, R. A., *Nature*, **340** (1989) 619.
45. Poulsen, H. F., Andersen, N. H., Andersen, J. V., Bohr, H. & Mauritsen, O. G., *Nature*, **349** (1991) 594.
46. Krekels, T., Zou, H., Van Tendeloo, G., Wagener, D., Buchgeister, M., Hosseini, S. M. & Herzog, P., *Physica C*, **196** (1992) 363.

47. Krekels, T., Van Tendeloo, G., Broddin, D., Amelinckx, S., Tanner, L., Mehbod, M., Vanlathem, E. & Deltour, R., *Physica C*, **173** (1991) 361.
48. Schmahl, W. W., Punis, A., Salje, E., Freeman, P., Graeme-Barber, A., Jones, R., Singh, K. K., Blunt, J., Edwards, P. P., Loram, J. & Mirza, K., *Phil. Mag. Lett.*, **60** (1989) 341.
49. Krekels, T., Milat, O., Van Tendeloo, G., Amelinckx, S. Babu, T. G. N., Wright, A. J. & Greaves, C., *J. Sol. State Chem.*, **105** (1993) 313.
50. Van Tendeloo, G. & Amelinckx, S., *Advanced Materials*, **5** (1994) 620.
51. Miyazaki, Y., Yamane, H., Ohnishi, N., Kajitani, T., Hiraga, K., Morii, Y., Funahashi, S. & Hirai, T., *Physica C*, **198** (1992) 7.
52. Slater, P. R., Greaves, C., Slaski, M. & Muirhead, C. M., *Physica C*, **208** (1993) 193.
53. Krekels, T., Milat, O., Van Tendeloo, G., Van Landbuyt, J., Amelinckx, S., Slater, P. R. & Greaves, C., *Physica C*, **210** (1993) 439.
54. Michel, C., Hervieu, M., Borel, M. M., Grandin, A., Deslandes, F., Provost, J. & Raveau, B., *Z. Physik B*, **68** (1987) 421.
55. Hazen, R. M., Prewitt, C. T., Angel, R. J., Ross, N. L., Finger, L. W., Hadjidakos, C. G., Veblen, D. R., Heaney, P. J., Hor, P. H., Meng, R. L., Sun, Y. Y., Wang, Y. Q., Xue, Y. Y., Huang, Z. J., Gao, L., Bechtold, J. & Chu, C. W., *Phys. Rev. Lett.*, **60** (1988) 1174.
56. Maeda, H., Tanaka, Y., Fukitoki, M. & Asano, T., *Jpn. J. Appl. Phys.*, **27** (1988) L205.
57. Zandbergen, H. W., Huang, Y. K., Menken, M. J. V., Li, J. N., Kadowaki, K., Menovsky, A. A., Van Tendeloo, G. & Amelinckx, S., *Nature*, **322** (1988) 620.
58. Zandbergen, H. W., Groen, W. A., Van Tendeloo, G., Van Landuyt, J. & Amelinckx, S., *Solid State Comm.*, **66** (1988) 397.
59. Zandbergen, H. W., Groen, W. A., Mijlhoff, F. C., Van Tendeloo, G. & Amelinckx, S., *Physica C*, **156** (1988) 325.
60. Schilling, A., Cantoni, M., Guo, J. D. & Ott, H. R., *Nature*, **363** (1993) 56.
61. Antipov, E. V., Loureiro, S. M., Chaillout, C., Capponini, J. J., Bordet, P., Tholence, J. L., Putilin, S. N. & Marezio, M., *Physica C*, **215** (1993) 1.
62. Chu, C. W., Gao, L., Chen, F., Huang, Z. J., Meng, R. L. & Xue, Y. Y., *Nature*, **365** (1993) 323.
63. Nunez-Regueiro, M., Tholence, J. L., Antipov, E. V., Capponi, J. J. & Marezio, M., *Science*, **262** (1993) 97.
64. Maignan, A., Van Tendeloo, G., Hervieu, M., Michel, C. & Raveau, B., *Physica C*, **212** (1993) 239.
65. Hervieu, M., Van Tendeloo, G., Maignan, A., Michel, C., Goutenoire, F. & Raveau, B., *Physica C*, **216** (1993) 264.
66. Pelloquin, D., Hervieu, M., Michel, C., Van Tendeloo, G., Maignan, A. & Raveau, B., *Physica C*, **216** (1993) 257.
67. Martin, C., Huve, M., Van Tendeloo, G., Maignan, A., Michel, C., Hervieu, M. & Raveau, B., *Physica C*, **212** (1993) 274.
68. Maignan, A., Michel, C., Van Tendeloo, G., Hervieu, M. & Raveau, B., *Physica C*, **216** (1993) 1.
69. Van Tendeloo, G., Chaillout, C., Capponi, J. J., Marezio, M. & Antipov, E. V., *Physica C*, **223** (1994) 219.
70. Martin, C., Hervieu, M., Van Tendeloo, G., Goutenoire, F., Michel, C., Maignan, A. & Raveau, B., *J. Sol. State Comm.*, (1995) 53.
71. Radaelli, P. G., *et al. Physica C*, (1995) in press.
72. Kopnin, E. M., Antipov, E. V., Capponi, J. J., Bordet, P., Chaillout, C., de Brion, S., Maerzio, M., Bobylev, A. P. & Van Tendeloo, G., *Physica C*, (1995) 222.
73. Alario-Franco, M., Chaillout, C., Capponi, J. J., Souletie, B. & Tholence, J. L., *Physica C*, **222** (1994) 52.
74. Uehara, M., Sahoda, S., Nakata, H., Akimitsu, J. & Matsui, Y., *Physica C*, **222** (1994) 27.
75. Matusi, Y., Kawashima, T. & Takayama-Muromachi, E., *Physica C*, **235-240** (1994) 166.
76. Huvé, M., Van Tendeloo, G., Hervieu, M., Maignan, A. & Raveau, B., *Physica C*, **231** (1994) 15.
77. Hervieu, M., Michel, C., Van Tendeloo, G., Martin, C., Maignan, A. & Raveau, B., *Physica C*, **235-240** (1994) 25.
78. Raveau, B., Michel, C., Hervieu, M., Van Tendeloo, G., Martin, C. & Maignan, A., *Superconductivity*, **7** (1994) 9.
79. Van Dyck, D., Op de Beeck, M. & Coene, W., *Optik*, **93** (1994) 103.

Modern Applications of a New 300 kV Field Emission Transmission Electron Microscope to the Study of Advanced Materials

Y. Bando, K. Kurashima & S. Nakano

National Institute for Research in Inorganic Materials, 1-Namiki, Tsukuba, Ibaraki 305, Japan

(Received 18 April 1995; revised version 19 May 1995; accepted 22 May 1995)

Abstract

Some instrumental features of a new 300 kV analytical transmission electron microscope with a field emission gun and its applications to structure and composition analysis of advanced materials at nanometer scales are given. In the new microscope, a fine electron probe of about 0.5 nm in size with a probe current of about 0.1 nA can be routinely applied for elemental analysis in combination with high resolution lattice imaging. A crystal structure of 33R-AlN polytype is determined from the single atomic layer level analysis using energy dispersive X-ray spectrometry (EDS). It is also shown that a new cubic B–C–N compound is identified to be a diamond-like structure from the observation of lattice image and electron energy loss spectrometry (EELS).

1 Introduction

In recent years, analytical transmission electron microscopes have become a most useful tool in materials science. Energy dispersive X-ray spectrometry (EDS) and electron energy loss spectrometry (EELS) which are attached to the microscope column, can be successfully applied to perform quantitative and qualitative analysis from small volumes in thin specimens.^{1–2} The relations between structures and compositions in local areas are then well determined. However, the conventional transmission electron microscope having a thermal emitter of LaB₆ is not always powerful to carry out high spatial resolution chemical analysis at nanometer level regions, because the brightness of the electron source emitter is very limited and then corresponding electron probe current for the nanometer scale probes is too small to perform the elemental analysis.

Since the brightness of the field emission gun is

approximately 100 times larger than that of the thermal LaB₆ emission gun, the analytical transmission electron microscope with the field emission gun is very powerful to carry out high spatial resolution analysis at nanometer scales. In the field emission microscope, the very fine electron beam of about 1 nm size with a high current density of about 1 nA can be obtained.^{3–5}

In 1993, at the National Institute for Research in Inorganic Materials (NIRIM), a new 300 kV medium voltage analytical transmission electron microscope with a field emission gun was constructed and the high spatial resolution analysis of advanced materials such as silicon nitride and InFeO₃(ZnO)₁₃ has been carried out.^{6–8} In this paper, the important features of the new microscope are briefly summarized. Also, some applications in the structure and composition analysis of advanced materials, such as aluminum nitride and boron nitride containing carbon, are given. It is shown that the high spatial resolution elemental analysis with EDS and EELS techniques using the fine electron probe of about 0.5 nm diameter are successfully carried out in combination with high resolution lattice imaging. The results of the crystal structure analysis of the 33R-AlN polytype and the new cubic B–C–N compound are described.

2 A New 300 kV Field Emission Analytical Transmission Electron Microscope at NIRIM

2.1 Principal specifications

The main purpose for constructing the new 300 kV analytical transmission electron microscope with a field emission gun, is to carry out ultra high spatial resolution analysis at subnanometer to nanometer scales in combination with high resolution lattice imaging. Some characteristic instrumental features of the new microscope have been already described.⁹ The principal specifications of

the new 300 kV field emission microscope are shown as follows:

- (1) A stable field emission gun working at 300 kV is required.
- (2) In order to reduce vibration of electron microscope, both high voltage generator and field emission power supply is placed in one tank.
- (3) A probe size can be maintained constant at different probe currents.
- (4) A minimum probe size must be smaller than 0.5 nm size having a probe current of about 0.1 nA.
- (5) A point-to-point resolution must be better than 0.2 nm, in which a double tilt specimen holder can be tilted up to $\pm 30^\circ$.
- (6) In order to increase the detection sensitivity for EDS analysis, the X-ray solid angle is larger than 0.20 str.
- (7) The peak to the background ratio of the EDS spectra using the Fiori method must be higher than 3700 at 300 kV.
- (8) In order to reduce the X-ray cut-off effect due to the specimen holder, a new specimen holder with a Be mount base is designed.
- (9) An energy resolution of a zero loss peak must be better than 0.6–0.8 eV at 300 kV.
- (10) The image resolution of the scanning transmission electron microscope (STEM) is about 0.34 nm.
- (11) Using a liquid helium specimen holder and a high temperature specimen holder, the image resolution at low temperature (15 K) and at high temperature (1300 K) is about 0.23 nm.

The principal specifications described above have been successfully confirmed by experimental observations.^{6,9}

2.2 Probe sizes and probe currents produced by thermally assisted type and Schottky type field emission guns

It is well known that there are three types of field emission guns such as the cold-type, the Schottky-type and the thermally assisted-type, which are now used in transmission electron microscopes. The emitter cathodes for the cold-type, the thermally assisted type and the Schottky type were single crystals of a tungsten $\langle 310 \rangle$ oriented chip, a tungsten $\langle 100 \rangle$ chip and a tungsten $\langle 100 \rangle$ chip coated with zirconium oxide, respectively. In the Schottky type and the thermally assisted type of the field emission guns, the cathode chips were heated at high temperatures of about 1400–1800 K. It is characteristic of these guns that stable emission currents with high total emission currents can

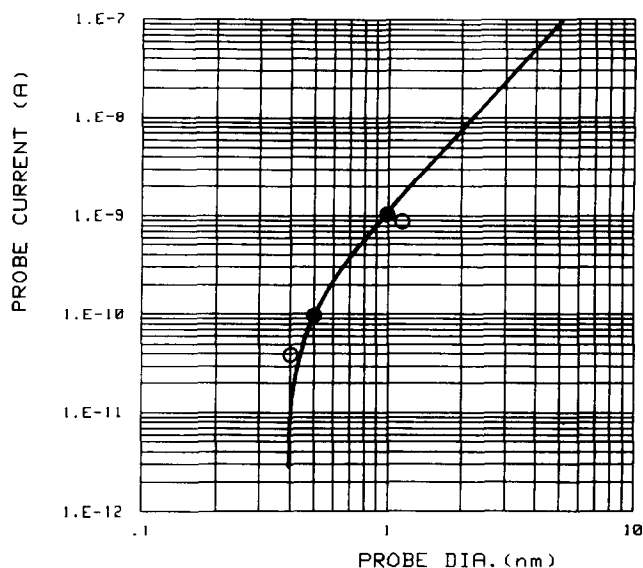


Fig. 1. A calculated probe diameter as a function of probe current at 300 kV. Brightness of electron source for the thermally assisted type and Schottky type field emission gun was considered as 7×10^8 A/cm²str. The minimum probe size was assigned to be 0.4 nm. The observed probe currents for the 0.5 and 1.0 nm probe sizes for the thermally assisted type they were measured as about 0.1 and 1.0 nA, respectively, and for the Schottky type were 0.07 and 0.9 nA for 0.4 and 1.1 nm probe sizes, respectively, in which observed values are marked by dark circles (thermally assisted type) and open circles (Schottky type), respectively.

be produced for a long use over a long period of time. In the new microscope, we used the thermally assisted type field emission gun in a first installment and then the gun was changed to the Schottky type.

The electron probe diameter, D at the specimen point were calculated by the following equations.

$$D = (D_g^2 + D_{Cs}^2 + D_{Cc}^2 + D_d^2)^{1/2}$$

Here D_g , D_{Cs} , D_{Cc} and D_d indicate the Gaussian image of the emitter source, the minimum disk broadening caused by a spherical aberration (Cs), a chromatic aberration (Cc) and a diffraction aberration (d), respectively. A result of the calculation of the probe diameter as a function of the probe current is shown in Fig. 1. In the calculation, the brightness of the field emission gun is considered as 7×10^8 A/cm² str at 300 kV for both the thermally assisted type and the Schottky type. The minimum probe size was assigned to be about 0.4 nm at 300 kV.

Figure 2 shows a profile of a minimum probe size for the Schottky type field emission gun. The total emission current was 130–150 μ A with an extraction electrode potential of 3.1 kV, an electrostatic lens potential of 6.6 kV, a filament heating current of 2.3 A. A half-width of the minimum probe size recorded was about 0.4 nm. The minimum probe size for the thermally assisted type was also observed to be 0.4 nm. These observa-

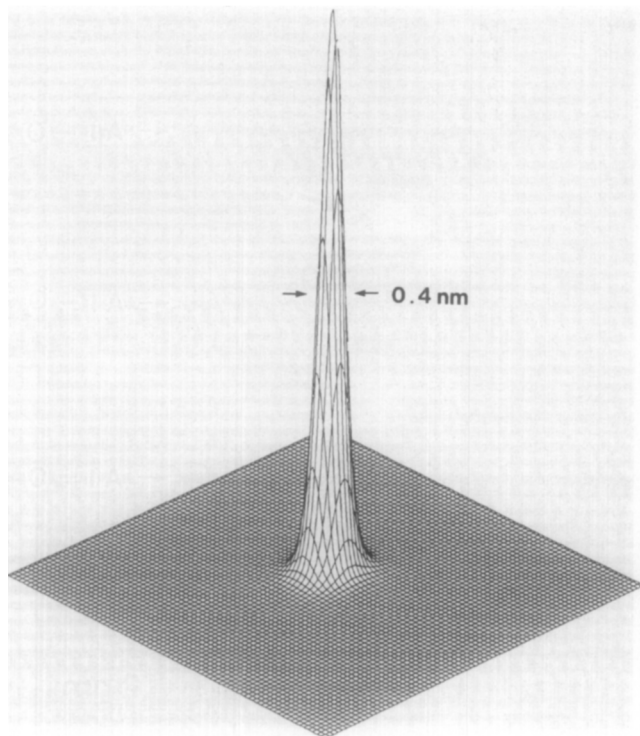


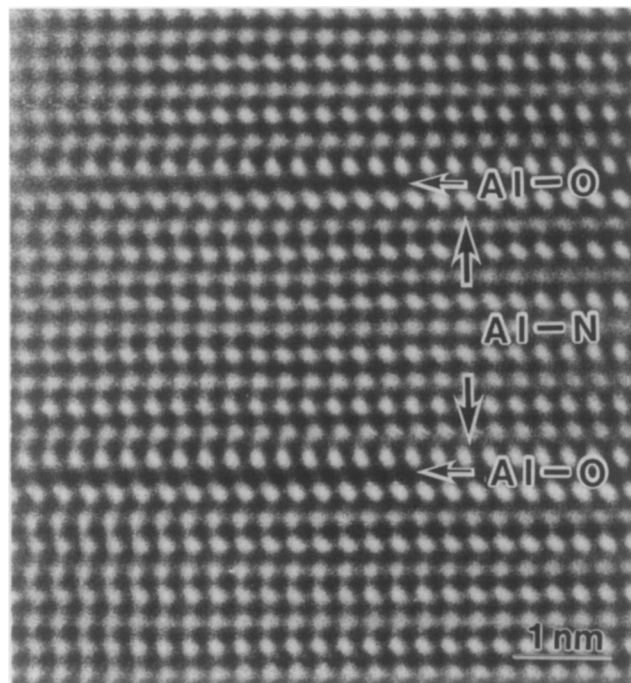
Fig. 2. A profile of minimum probe size for the Schottky type field emission gun, recorded by an imaging plate. The minimum probe size was observed to be about 0.4 nm.

tions agreed well with the calculation of Fig. 1. The probe currents were also measured by using a Faraday cup. The probe currents for the Schottky type were about 0.07 nA and 0.9 nA for the probe sizes of 0.4 nm and 1.1 nm, respectively and for the thermally assisted type they were about 0.1 nA and 1.0 nA for the probe sizes of 0.5 nm and 1.0 nm, respectively. These observed values are indicated in Fig. 1. The probe currents between the two different guns were almost the same in such small probes.

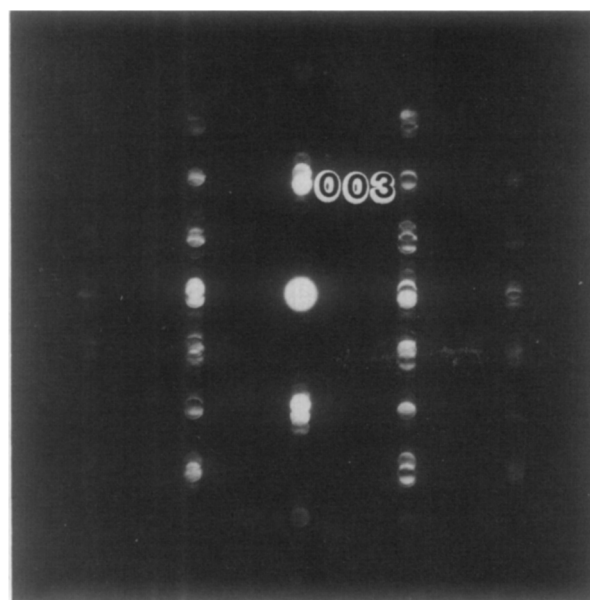
3 Applications in the Study of Advanced Materials

3.1 Monolayer level analysis of AlN polytype

Aluminum nitride (AlN) is a very useful material for the use of substrate in LSI devices instead of alumina, since it shows a high thermal conductivity. This compound reacts easily with oxygen at high temperatures to form aluminum oxynitride or aluminum silicon oxynitride, which are known as compositional polytypes or polytypoids.^{10,11} It is characteristic of present polytypes that the composition varies with a periodicity of the *c*-axis. In the AlN–Al₂O₃ system, polytypes such as 12H, 15R, 33R, 39R and 32H have been already observed^{12–14} and its composition was considered as a general chemical formula of *m*AlN–Al₂O₃, where *m* is an integer. From the X-ray powder diffraction study, the structure is considered to be AlN₄ (Al–N)



(a)



(b)

Fig. 3. A crystal structure image of 33R-9AlN–Al₂O₃ (a) and corresponding nano-area electron diffraction pattern (b). The image was observed at Scherzer defocus. The incident electron beam was normal to the (110) plane. Each of the Al atoms was well resolved as dark dots in the image, but the N and O atoms were not imaged.

tetrahedral layers interleaved with AlO₆ (Al–O) octahedral layers. It is speculated that a part of the nitrogen atoms is replaced by oxygen atoms to form Al–O layers. Since identification between oxygen and nitrogen atoms is difficult in X-ray diffraction, their distribution is not well understood.

Figures 3(a) and (b) shows a crystal structure image of 33R polytype and its corresponding nano-area electron diffraction pattern, respectively. The structure image was observed at

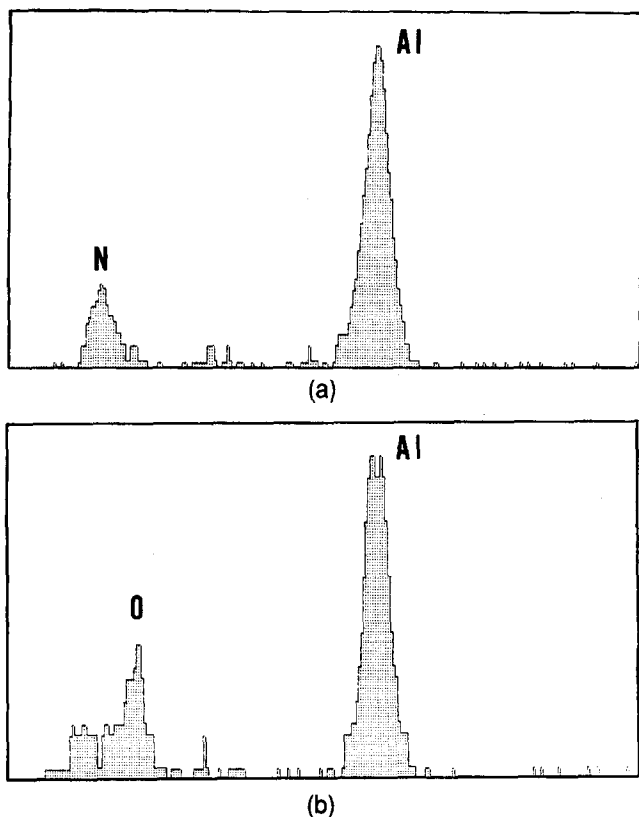


Fig. 4. EDS spectra, obtained from one of the atomic layers marked as Al-N (a) and Al-O (b) in Fig. 3. The probe size was 0.5 nm and the exposure time was 20–30 s.

Scherzer defocus of about 56 nm. The incident electron beam was normal to the (110) plane. The results of electron diffraction indicates that the crystal is 33R type with lattice parameters $a = 0.308$ nm and $c = 8.69$ nm. In the image, each of the aluminum atoms site appeared as dark dots, while those of the N and O atoms were not imaged. The separation between the dark dots normal to the c -axis is 0.26 nm.

A chemical analysis using the EDS method was carried out in combination with high resolution lattice image, where the fine electron probe of about 0.5 nm size was focused on each single atomic layer as indicated in the figure. Figures 4(a) and (b) show EDS spectra, obtained from the layers marked as Al-N and Al-O, respectively. The acquisition time was about 20–30 s. Every 10 s, the focused probe position was confirmed to be constant during the observation. In the spectrum in Fig. 4(a), nitrogen and aluminum X-ray peaks were clearly observed and almost no oxygen peaks were detected. While in the spectrum in Fig. 4(b), the oxygen peak was identified as well as the aluminum peak with a the weak nitrogen peak. This elemental analysis confirms that oxygen atoms are not randomly distributed among the nitrogen layers, but they are ordered to form Al-O layers.

The crystal structure of 33R type is then derived. The 33R aluminum oxynitride polytype

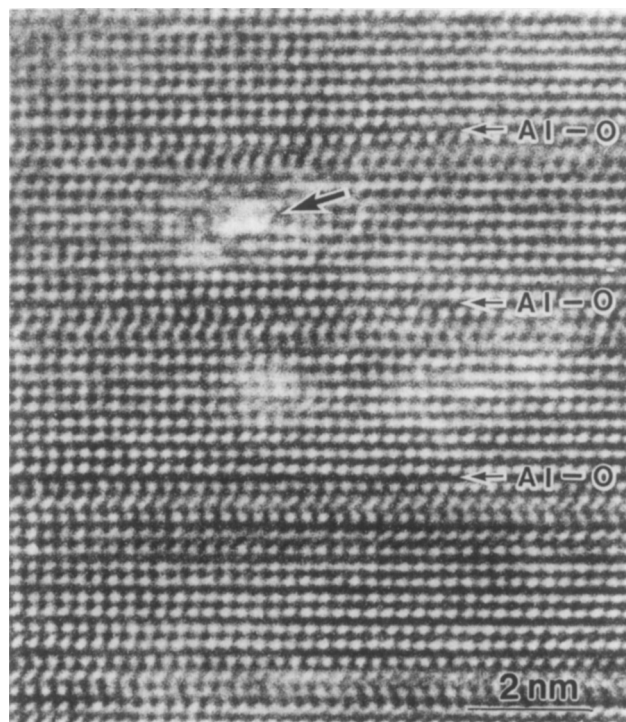


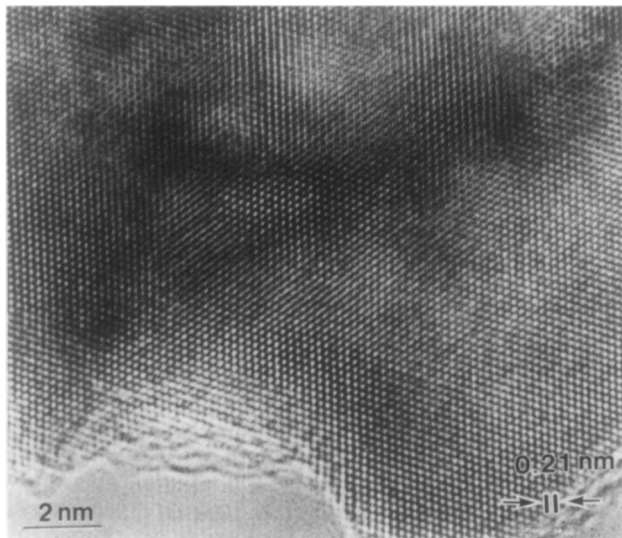
Fig. 5. Radiation damage of the 33R-9AlN- Al_2O_3 . A small hole of about 1 nm diameter, which is marked by an arrow was selectively formed with the layers of Al-N during the observation of the EDS point analysis.

consists of 9 layers of AlN_4 tetrahedral layers interleaved with 2 layers of AlO_6 octahedral layers along the c -axis. From the rhombohedral symmetry, the structure unit is repeated three times to give a total of 33 layers. The chemical composition is then assigned to be $9\text{AlN}-\text{Al}_2\text{O}_3$, which is consistent with the general chemical formula of $m = 9$.

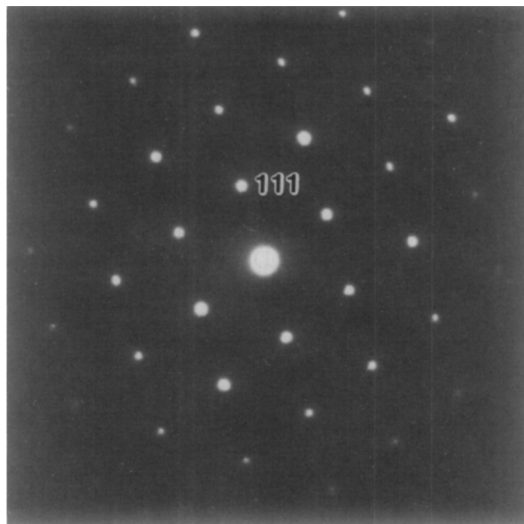
During the observation, the specimen often suffered radiation damage due to a focused strong beam irradiation. Figure 5 shows a high resolution lattice image of 33R type after the radiation damage. After about 30 s exposure of the fine electron beam to the specimen, small holes measuring a few nanometers were formed. These small holes were only introduced into the areas of Al-N layers and no holes were formed at the layers of Al-O. This means that selective mass loss has occurred due to electron beam irradiation effect. The Al-N layers are more easily attacked than those of Al-O by the electron beam bombardment.

3.2 Identification of a cubic B-C-N compound

Recently, one of the present authors prepared a cubic phase of B-C-N compound under the conditions of high pressure (7×7 GPa) and high temperature (2150–2400°C).¹⁵ A graphite BC_2N compound was transformed into the cubic B-C-N phase with minor phases of cubic BN and diamond under such conditions without using an additive. However, no direct evidence of the cubic B-C-N phase has been obtained.



(a)



(b)

Fig. 6. A high resolution lattice image of a new B-C-N crystal (a) and its corresponding electron diffraction pattern (b). The crystal was assigned to be cubic with lattice parameter $a = 0.36$ nm. The lattice separation of about 0.21 nm corresponds to cubic (111) plane.

The specimens contained small crystal fragments of a few tens nanometer scales. Figures 6(a) and (b) show a high resolution image of the specimen fragment and its corresponding electron diffraction pattern, respectively. The electron diffraction pattern was assigned to be cubic (110) plane. It is then concluded that the crystal is cubic with lattice parameter $a = 0.36$ nm. In the high resolution image of Fig. 6(a), a cubic packing of white dots having a separation of about 0.21 nm was well observed. This lattice separation corresponded to the cubic (111) plane. The result of the lattice image also suggests that the crystal is a diamond-like structure.

In order to confirm the chemical composition of the specimens, an EELS spectrum was obtained from the specimen fragment as shown in Fig. 6. The result is shown in Fig. 7. In the spectra, loss

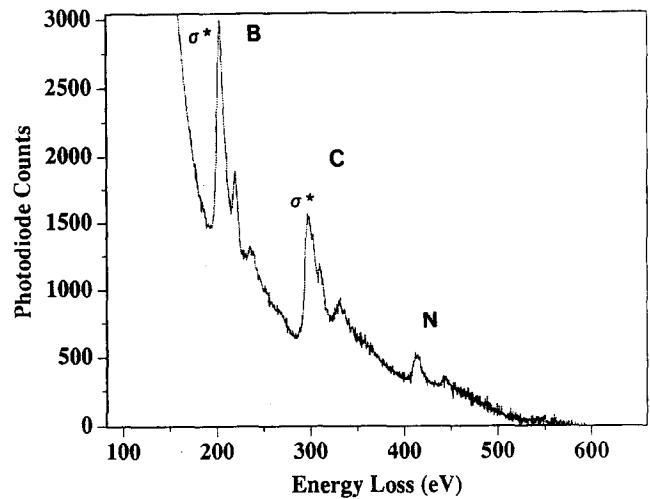


Fig. 7. An EELS spectrum, obtained from the edge part of the specimen as shown in Fig. 6. The δ^* edges were clearly observed with the absence of π^* edges. The crystal was then assigned to be B-C-N compound with a diamond-like structure.

peaks located at about 188, 283 and 402 eV corresponded to k edges of boron (B), carbon (C) and nitrogen (N), respectively. The characteristic δ^* peaks were present and π^* peaks were not observed at the near edges of B and N. This indicates that the crystal is not a graphite-like but a diamond-like structure.

During the observation, the present cubic B-C-N phase transformed into a hexagonal phase due to heating effect by strong beam irradiation. Figure 8(a) shows a high resolution lattice image of the B-C-N crystal showing the cubic to hexagonal transformation. The specimen was the same as that of Fig. 6. After the strong beam irradiation, the graphite-like structure having the separation of 0.34 nm of (002) lattice plane was newly formed. It grew from the edge part of the fragment. An EELS spectrum, observed from the graphite-like structure is shown in Fig. 8(b). Its fine structure is very different from that of Fig. 7 and the characteristic π^* peak corresponding to the graphite-like structure was clearly observed, suggesting that the specimen is the hexagonal B-C-N compound. It is very characteristic in the image that the graphite-like layers were very irregular and curled, where the edge dislocation is indicated by an arrow in the figure. These features correspond to a turbostatic layered structure.

It should be noted that the hexagonal B-C-N have an epitaxial relation with the cubic B-C-N phase. From the observation of the lattice image as shown in Fig. 8(a), the lattice relations between them are as follows.

$$\begin{aligned} &^{(101)}\text{hexagonal} \parallel ^{(111)}\text{cubic} \\ &^{[010]}\text{hexagonal} \parallel [110]\text{cubic} \end{aligned}$$

A detailed analysis of the cubic B-C-N crystal will be published elsewhere.

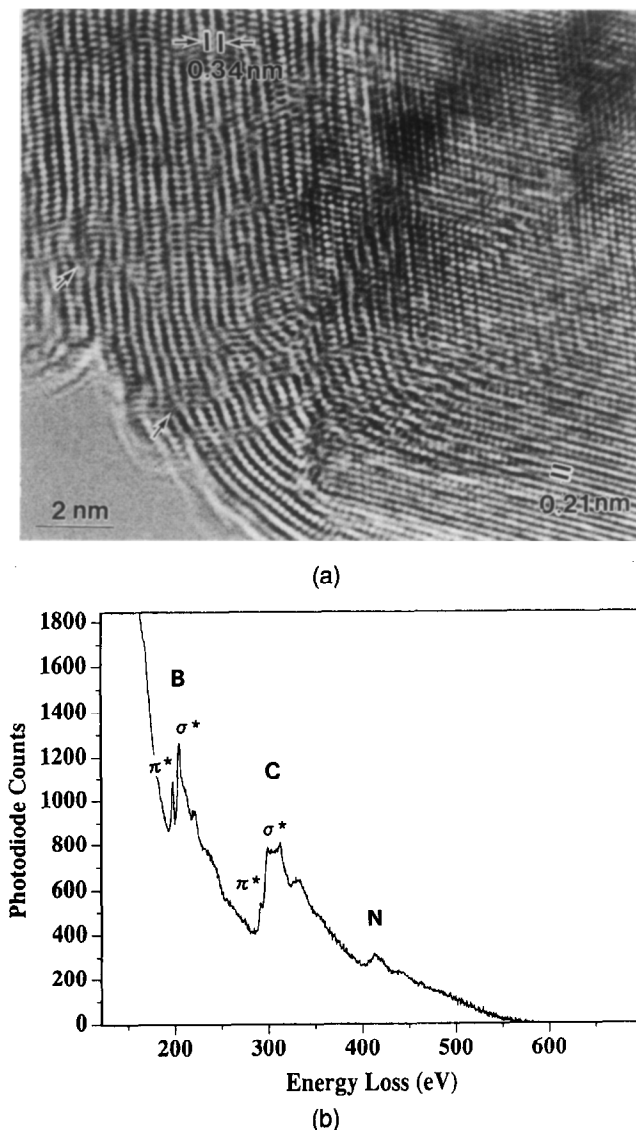


Fig. 8. A high resolution lattice image of the B-C-N crystal (a), where the cubic structure changed into the hexagonal structure after the radiation damage, and its corresponding EELS spectrum (b). The specimen was the same as that of Fig. 6. After the beam heating by the strong beam irradiation, the graphite-like structure having 0.34 nm lattice separations was newly formed. The edge dislocation is indicated by an arrow. The characteristic π^* peak was well observed in (b).

4. Conclusion

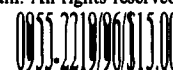
The new 300 kV analytical transmission electron microscope with a field emission gun, which has been recently developed in NIRIM, is successfully applied to carry out high spatial resolution analysis of advanced materials at subnanometer to nanometer level using EDS and EELS techniques. The crystal structure of 33R polytype was determined in the combination of the lattice image and the point analysis of the EDS. The new phase of cubic B-C-N was also identified from the EELS observation.

Acknowledgements

The authors thank Drs M. Akaishi, T. Sasaki and S. Yamaoka for supplying the specimens and also valuable discussions. They also thank Mr Y. Kitami, NIRIM, and Mr M. Tomita and K. Kawasaki, JEOL, for the support of the experiment.

References

1. Bando, Y., Analytical transmission electron microscopy of materials in Japan. *J. Electron Microsc.*, **S58** (1989) 81-9.
2. Bando, Y., Analytical transmission electron microscopy in materials science. *Mater. Trans. JIM*, **31** (1990) 538-44.
3. Isakozawa, S., Sato, Y., Kashikura, Y., Kubo, T., Hashimoto, T., Takahashi, T., Ichihashi, M. & Murakoshi, H., Development of 200 kV field emission TEM. In *Proc. 47th Annual Meeting Electron Microscopy Society of America*, Ed. The Organizing Committee, San Francisco Press, San Francisco, 1989, 112-13.
4. Tomita, T., Katoh, S., Kitajima, H., Kokubo, Y. & Ishida Y., Development of field emission gun for high voltage electron microscope. In *Proc. XIIth Int. Congr. for Electron Microscopy*, Ed. The Organizing Committee, San Francisco Press, San Francisco, 1990, 94-5.
5. Coene, W., De Jong, A. F., Lichite, H., Op de Beek, M., Tietz, H. & Van Dyck, D., FEG-TEM: The route to HRTEM. In *Proc. 50th Annual Meet. Electron Microscopy of America*, Ed. The Organizing Committee, San Francisco Press, San Francisco, 1992, 100-1.
6. Bando, Y., Kitami, Y., Tomita, T., Honda, T. & Ishida Y., A newly developed 300 kV field-emission analytical transmission electron microscope. *Jpn. J. Appl. Phys.* **32** (1993) L1704-6.
7. Bando, Y., Subnanometer level analysis by 300 kV FE-ATEM. In *Proc. 13th Int. Congr. for Electron Microscopy*, Ed. The Organizing Committee, Les editions de physique, Paris, 1994, 591-4.
8. Bando, Y., Suematsu, H. & Mitomo, M., Grain boundary phase analysis of silicon nitride by a newly developed 300 kV field emission electron microscope. In *Mat. Res. Soc. Symp. Proc. Vol. 346*, 1994 Materials Research Society, 1994, 733-8.
9. Bando, Y., Kitami, Y., Kurashima, K., Tomita, T., Honda, T. & Ishida, Y., Development and application of 300 kV field emission analytical transmission electron microscope, *Microbeam Analysis*, **3** (1994) 276-86.
10. Jack, K. H., Nitrogen ceramics. *Trans. J. Brit. Ceram. Soc.*, **72** (1973) 376-84.
11. Bando, Y., Mitomo, M., Kitami, Y. & Izumi, F., Structure and composition analysis of silicon aluminum oxynitride polytypes by combined use of structure imaging and microanalysis. *J. Microscopy*, **142** (1986) 235-46.
12. Sakai, T., Hot-pressing of the AlN-Al₂O₃ system, *Yogyo-Kyokai-Shi*, **86** (1978) 125-30.
13. Bartram S. F. & Slack, G. A., Al₁₀N₈O₃ and Al₉N₇O₃, two new repeated-layer structures in the AlN-Al₂O₃ system. *Acta Cryst.*, **B35** (1979) 2281-3.
14. Van Tendeloo, G., Faber K. T. & Thomas, G., Characterization of AlN ceramics containing long-period polytypes. *J. Mater. Sci.*, **18** (1983) 525-32.
15. Nakano, S., Akaishi, M., Sasaki, T. & Yamaoka, S., Segregative crystallization of several diamond-like phases from the graphitic BC₂N without an additive at 7.7 GPa, *Chem. Mater.*, **6** (1994) 2246-51.



S 0 9 5 5 - 2 2 1 9 (9 6) 0 0 0 4 3 - X

Editorial

Elsevier Science is pleased to announce a new service for authors and readers, ContentsDirect, which will provide previews of forthcoming issues of the *Journal of the European Ceramic Society*.

ContentsDirect is a free alerting service, which is available to all those with an e-mail address. 'Subscribers' will be e-mailed the table of contents of each issue of the Journal, between two and four weeks prior to publication. The table of contents consists of paper titles, authors and page numbers, giving readers useful information regarding upcoming articles. We believe authors will also benefit, as ContentsDirect will increase awareness of each issue's subject matter, and so stimulate interest in authors' research.

To register for this free service, please complete a copy of the application form published at the end of this issue, and return it to Elsevier Science Ltd, Marketing Department, The Boulevard, Langford Lane, Kidlington, Oxford OX5 1GB, UK or to Elsevier Science Inc., Marketing Department, 660 White Plains Road, Tarrytown, NY 10591-5153, USA.

If you have any queries or comments on this service, please do not hesitate to contact me at i.salusbury@elsevier.co.uk, or by telephone (+44 1865 843425) or fax (+44 1865 843931).

Ian Salusbury
Publishing Editor
Elsevier Science Ltd
The Boulevard, Langford Lane
Kidlington
Oxford OX5 1GB
United Kingdom

Injection Moulding of Polysiloxane/Filler Mixtures for Oxycarbide Ceramic Composites

S. Walter, D. Suttor, T. Erny, B. Hahn & P. Greil

Friedrich-Alexander University of Erlangen–Nuernberg, Institute of Materials Science, Glass and Ceramics, 91058 Erlangen, Germany

(Received 1 June 1995; revised version received 6 July 1995; accepted 14 July 1995)

Abstract

A complex shaped preceramic part has been prepared from polysiloxane/MoSi₂ mixtures via the injection moulding process. Processing of the system requires granulation of the powders prior to injection moulding through a separate extrusion step and the addition of carboxylic acids as surfactants to adjust the viscosity. Polymerization temperatures are effected through catalytic behaviour of the filler particles. Viscosity measurements have been applied to determine an appropriate viscosity, temperature and time-frame for this novel thermosetting system. The presence of Mo³⁺ oxidation states on the filler surface and interaction with the carboxyl groups of the carboxylic acids were detected.

1 Introduction

Injection moulding is a suitable method for economic manufacturing of complex shaped ceramic parts.¹ Usually organic binder systems are added to the ceramic powder to obtain a mouldable mixture with the appropriate viscosity. The binder system usually consists of the major binder, a minor binder, a plasticizer/lubricant (or hardener) and a surfactant for particle wetting. The organic binder has to be removed very carefully to avoid the creation of porosity afterwards.^{2–5} The minor binder is burned out at a lower temperature to provide pore channels for the escape of gaseous species produced on decomposition of the major binder. The green body is then sintered with typical linear shrinkages of up to 20%. Especially complex geometries are susceptible to tolerance deviations due to inhomogeneities and the large degree of sintering shrinkage, leading to increased machining costs or even rendering the part useless.⁷ The development of easily removable binder systems and lowering the sintering shrinkages are therefore important issues.

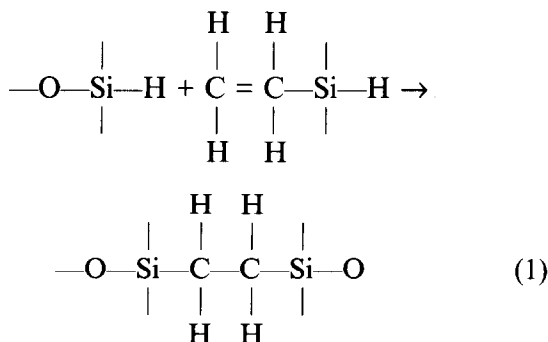
Recently, Zhang and Evans⁸ reported on the

properties of a ceramic injection moulding suspension which is based on an organometallic polymer. A ceramic suspension was prepared by adding a fine sinterable silicon carbide powder to a polycarbosilane vehicle which had been modified by additions of paraffin wax to make it suitable for plastic forming operations.

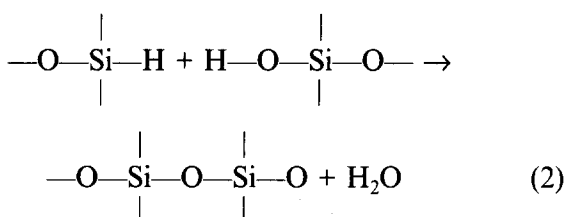
By using organometallic polymers like polysiloxanes, polysilazanes or polycarbosilanes as a binder no binder burn-out is necessary, since these polymers are converting into SiO₂/SiC, Si₃N₄, SiC or Si–O–C–(N) glasses upon pyrolysis depending on the pyrolysis temperature.⁹ Large weight loss and corresponding shrinkage, porosity formation and fragmentation upon pyrolysis are obstacles for the realization of monolithic ceramic parts from pure organometallic polymers. The addition of reactive fillers like the transition metals of groups IV–VI is a possibility to obtain samples with structural integrity. When sintered in a reactive atmosphere like N₂, the filler components react with the decomposition products of the polymer and the atmosphere to constitute a ceramic matrix consisting of the corresponding metal carbides and nitrides and a Si–O–C–(N) glass.^{10–12} By appropriate choice of the amount and type of the polymer and filler component, a positive volume change upon carburization or nitridation can be achieved, leading to very low shrinkages.¹³

The use of organometallic polymers necessitates thermosetting systems, thereby retaining the shape during the early stages of the pyrolysis. Another requirement with respect to processing is the handling of the polymer in an ambient atmosphere, making hydrolysis sensitive silazanes difficult binder candidates. Polysiloxanes are easy to handle and are commercially available in a large variety of forms, and have thus been chosen for this work. The crosslinking mechanism is of importance, depending on the forming methods. Using pressureless forming methods like moulding, a polymer which undergoes crosslinking via an addition mechanism is the choice, since no gaseous products

are evolved, which would lead to bloating of the part. The most common reaction is based on the hydrosilylation of a vinyl group:¹⁴⁻¹⁶



In the case of the injection moulding process, polycondensating systems, giving off water during polymerization, can be used as well due to the applied pressure. The reaction involves two silanol groups:



Compensation of the shrinkage during pyrolysis depends on the filler loading and, in general, filler loadings are of the order of 40–60 vol% depending on the filler type. The use of solid polymeric precursors in powder form with a defined melting point simplifies the processing as compared to liquid precursors and enables high filler loadings, since filler and polymer can be dry mixed and granulated in a separate extrusion step before injection moulding.

Pyrolysed polysiloxane/MoSi₂ mixtures have shown the potential for high temperature applications with excellent oxidation stability and creep resistance up to 1550°C. This paper summarizes the processing of such a preceramic part with complex geometry through injection moulding, i.e. a screw 70 mm in length with a diameter of 8 mm and a fine thread (M8 with respect to DIN 601).

2 Experimental Procedures

A commercially available solid polycondensating polymethylsiloxane (NH 2100, Hüls Corp., Germany) with a melting point of 54°C and a setting temperature of 230°C was chosen as the polymeric precursor. This polymer exhibits a high ceramic yield of 90 wt% and is decomposing with the evolution of environmentally uncritical species like hydrogen and methane. MoSi₂ (Grade C, HC Starck Corp., Germany) ($d_{50} = 2.0 \mu\text{m}$) was used as the reactive filler. Citric acid (CA) and tartaric acid (TA) (Merck Corp., Germany) (1–5 wt%) were used as surfactants.

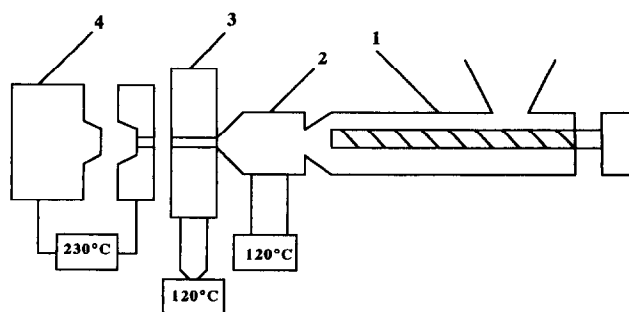


Fig. 1. Set-up of modified injection moulding unit: 1, injection moulding unit; 2, nozzle; 3, thermal barrier; 4, injection moulding die.

Polymer (60 vol%), filler (40 vol%) and surfactant were dry mixed and homogenized in a polyethylene bottle with Al₂O₃ milling media for 12 h. Preliminary experiments had shown that direct feeding of the powder mixture into the injection moulding unit was inappropriate due to electrostatic charging of the polymer powder and subsequent inhomogeneous melting and homogenization. It was therefore necessary to prepare a granulate by extruding the powder mixture through a double-screw extruder (LSM 30.34.GI, Leistritz Corp., Germany) at 120°C. The surfactant was either added as a powder to the mixture or directly precipitated on to the filler surface by dissolving the acid in acetone, adding the filler, ultrasonically dispersing the powder and evaporating the acetone. The granulate was then fed into a modified injection moulding machine (ES 200/50, Engel Corp., Germany). A thermal barrier was installed between the injection unit and the die to prevent thermal flux from the die (230°C) to the injection unit tip (120°C); Fig. 1. The injection velocity was chosen as 5 mm s⁻¹ at a maximum injection pressure of 16 MPa, a post-pressure of 4 MPa, post-pressure time of 250 s and curing time of 400 s.

The viscosities of the polymer/filler mixtures were measured with a cone/plate system (SR 200, Bohlin Corp., UK) in the dynamic mode (shear rates of: 2.9×10^{-3} – 2.7 cm^{-1}) at shear stresses ranging from 100 to 3000 Pa and temperatures ranging from 100 to 240°C to determine an appropriate η - t - T -frame. A viscosity range of 100–100000 Pa s, a temperature range of 100–140°C and a time-frame of 60 min were used.

The effect of the carboxylic acids on the catalytic behaviour of MoSi₂ and the rheology was examined by EPR spectroscopy (B-K 70, Bruker Corp., UK). The microwave frequency (9.67 GHz), microwave power (63.6 mW) and measurement time (335 s) were kept constant, while the magnetic field strength was varied between 33.0×10^6 and 37.5×10^6 T.

Thermogravimetric analysis (Model 409, Netzsch

Inc., Selb, Germany) was employed to monitor the oxidation behaviour. Density and porosity were determined using a helium pycnometer (AccuPyc 1330, Micromeritics Inc., Germany) by measuring the pressure change in a calibrated volume. The electrical conductivity was examined by impedance spectroscopy (4192A LF Impedance Analyser, Hewlett-Packard, USA). The pyrolysed samples were tested in four-point-flexure with a universal testing machine (Instron, UK) and a fixture with a 24 mm outer span and 12 mm inner span. A constant displacement rate of 1 mm min^{-1} was used. Creep behaviour was monitored by a compression test with a constant load of 100 MPa at 1500°C in air.

3 Results and Discussion

3.1 Rheology

Figure 2 shows the viscosity as a function of temperature of the filler-free polysiloxane. Figure 3 shows the thermosetting temperature T^* as a function of filler loading. A minimum of the viscosity is observed at 230°C with $\eta \sim 1 \text{ Pa s}$. At higher temperatures the viscosity increases, again due to crosslinking of the polymer. With a solid loading of 20 vol% MoSi_2 the viscosity increased by five orders of magnitude and the polymerization temperature decreased by more than 120°C . Although a viscosity drop can be expected, the polymerization temperature should remain constant. From catalysis, however, it is known that transition metals and transition metal compounds, especially oxides, can act as catalysts in various polymerization processes.¹⁷ Molybdenum oxides are widely used for such purposes.

With 40 vol% solid loading it was therefore necessary to inhibit the catalytic effect and to decrease the viscosity in order to adjust the system to the desired η - t - T -frame. Carboxylic acids can be used as surfactants which react with the filler surface via the carboxyl groups. Furthermore, it was expected that the carboxyl groups would

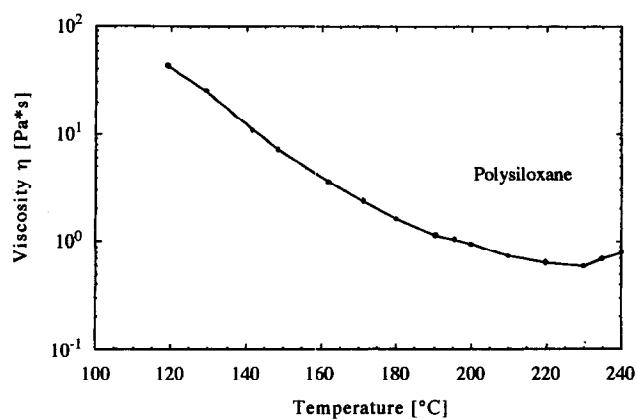


Fig. 2. Viscosity as a function of temperature of the filler-free polysiloxane measured with a constant shear rate of 5.15 cm^{-1} .

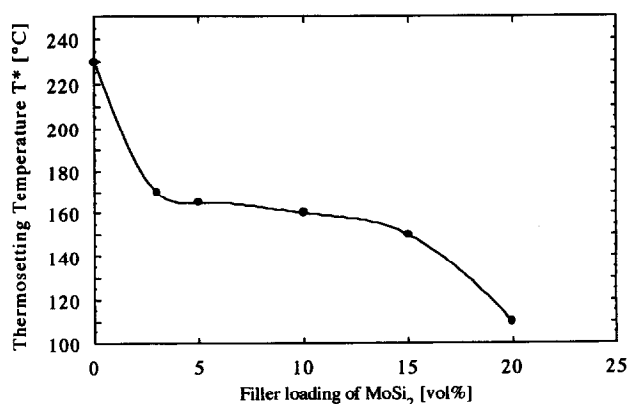


Fig. 3 Thermosetting temperature T^* as a function of filler loading between 0 and 20 vol% MoSi_2 .

reduce the catalytic effect of the filler. The effect of adding 3 wt% CA on the η - T dependency is shown in Fig. 4. The polymerization temperature increases by more than 40°C to 150°C , which is close to the decomposition temperature of the acid ($T_{\text{dec}} = 153^\circ\text{C}$). At the same time the viscosity decreased to $3 \times 10^4 \text{ Pa s}$. The η - t dependency at constant shear stress (2200 Pa) and temperature (120°C), i.e. the stability of the mixture in the injection unit, is shown in Fig. 5.

Immediately after remelting of the mixture, an overlapping of two processes is noticed: (1) a decrease of the viscosity due to homogenization of the melting mixture and (2) an increase of the viscosity due to the onset of thermosetting. With increasing CA content (from 3 to 5 vol%) the time-frame (time until polymerization commences) increases from 17 to 25 min. The addition of 3 vol% TA instead of CA further decreases the viscosity by an order of magnitude and prolongs the time-frame to 30 min; Fig. 6. Coating of the filler surfaces with 1 wt% TA is sufficient to achieve a constant viscosity of 50000 Pa s for at least 1 h at 120°C and a shear stress of 2200 Pa.

Figure 7 shows the viscosity as a function of temperature with increasing shear stress of a mixture containing 20 vol% filler (1 wt% CA). A decrease in

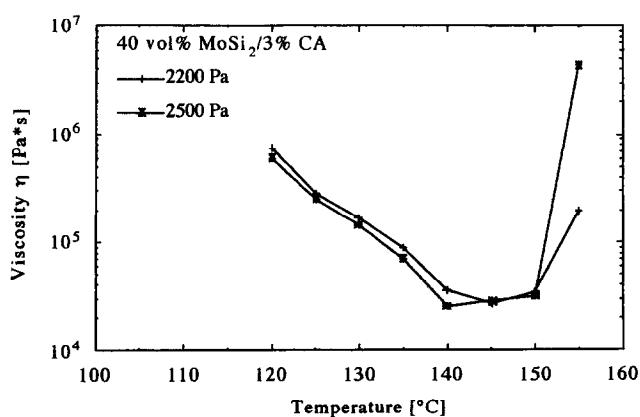


Fig. 4. Viscosity as a function of temperature for 40 vol% solid loading with 3 wt% CA, shear stresses of 2200 and 2500 Pa and shear rates of 2.9×10^{-3} - $1.1 \times 10^{-2} \text{ cm}^{-1}$.

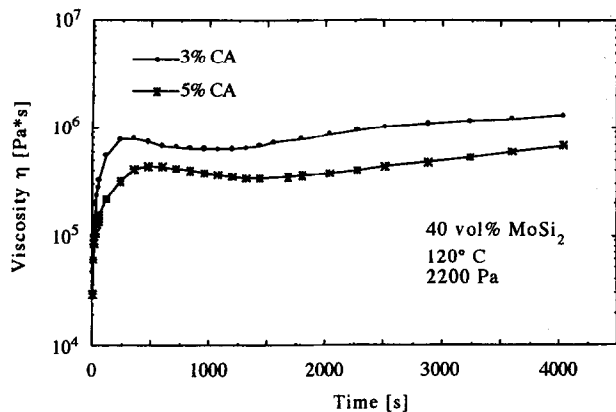


Fig. 5. Viscosity as a function of time for 40 vol% solid loading with 3 and 5 wt% CA, shear stress of 2200 Pa and constant temperature of 120°C.

viscosity is noted for increasing temperatures and increasing shear stresses. The temperature-dependent viscosity minimum is shifted to lower temperatures with increasing shear stresses. This behaviour is observed for filler loadings higher than 30 vol%. High filler loadings result in frictional heat and hence decreasing polymerization temperatures. This behaviour has been confirmed by viscosity measurements in the oscillation mode (frequency 20 Hz), where only small volume elements are moved in the gap of the cone/plate system. In the oscillation mode the real polymerization temperature can be determined. High filler loadings beyond the percolation limit and subsequent enhanced shear stresses are therefore responsible for local frictional heat and apparently lower polymerization temperatures. An oil tempered injection moulding nozzle was subsequently installed in the injection moulding unit tip to absorb the frictional heat from the polymer mixture during remelting and homogenization of the granulate.

The first injection moulding trials were performed by injecting the granulate in the heated die at 250°C. These parts showed a distinct core-shell structure, whereby the outer parts, which are in direct contact with the die wall, had undergone

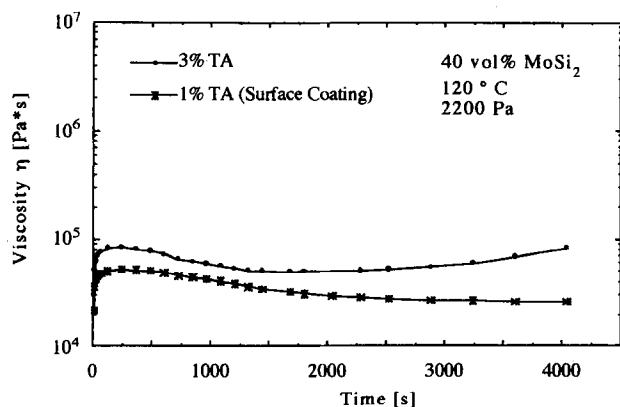


Fig. 6. Viscosity as a function of time for 40 vol% solid loading with 1 (surface coating) and 3 wt% TA, shear stress of 2200 Pa and constant temperature of 10°C.

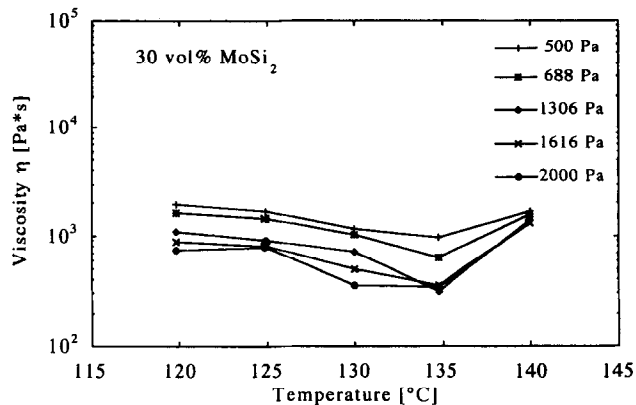
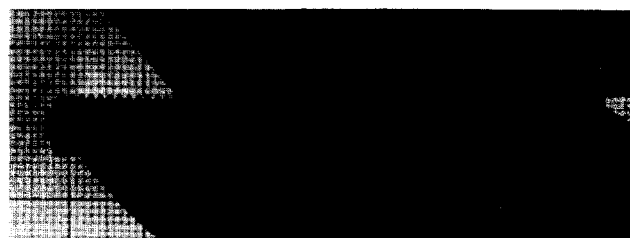


Fig. 7. Viscosity as a function of temperature and different shear stresses (500–2000 Pa) for 30 vol% solid loading with 1 wt% CA and shear rate of 2.5×10^{-1} – 2.7×10^{-1} cm⁻¹.

instantaneous crosslinking, while the inner parts were still fluid. Consequently, the parts usually showed distinct fracture lines along the interface of the outer and inner region. Subsequently the die temperature was reduced to 230°C, enabling more homogeneous crosslinking across the screw cross-section. Figure 8(a) shows the screw and Fig. 8(b) a magnification of the thread part, demonstrating the well-defined contours.

3.2 Filler surface coating

EPR spectrum of MoSi₂ powders is shown in Fig. 9. The narrow peak at 34.5×10^6 T corresponding to a g -value of 2.003 may be attributed to dangling bonds¹⁸ of free carbon.¹⁹ Carbon is used for the synthesis of MoSi₂.²⁰ The broad



(a)



(b)

Fig. 8. (a) Injection moulded screw with 40 vol% solid loading. The screw was cured at 230°C for 400 s. (b) Magnification of the screw thread

absorption between 35.0×10^6 and 36.0×10^6 T is assigned to pentavalent Mo^{5+} oxidation states in the MoSi_2 powder, because the determined g -value of ~ 1.95 is typical for Mo^{5+} .²¹

Transition metal compounds of groups IV–VI (V, Nb, Ta, Cr, Mo), mainly Cr-complexes, are used for catalytic processes in the chemical industry. They are all capable of catalysing the reactions of hydrogen and olefins, alkynes and polymerization reactions.²² The determined g -value confirms the presence of Mo^{5+} oxidation states.²¹ Further investigations of monoalkene polymerization²³ showed that the valence states and the structures of the transition metal active centres of Cr^{5+} -complexes are responsible for the polymerization process. Based on these observations, we suggest that Mo^{5+} shows similar catalytic behaviour to Cr^{5+} and is therefore (unless other active sites are present) responsible for decreasing the thermosetting temperature of the polysiloxane/filler mixture.

The mechanisms of surface adsorption of carboxylic acids from liquid solutions have been discussed previously.^{24–26} The adsorbate molecules are amphiphilic, i.e. they contain both a hydrophobic non-polar part (aliphatic chain) and a hydrophilic polar ionic carboxyl group. Depending on the relative magnitude of the hydrophobic part and the polarity or non-polarity of the particle surface and of the solvent, these solutes may be adsorbed primarily either due to the hydrophobic effect or by electrostatic or co-ordinative interaction (attraction between functional groups of the solute and the particle surface).²⁷

The first step in the adsorption mechanism of tartaric acid in acetone on MoSi_2 is orientation of the hydrophilic group of the surfactant (carboxyl groups) towards the particle surface; Fig. 10. Similar to the adsorption mechanism of stearic acid in cyclohexane on AlN [Fig. 10(a)] for making AlN powders²⁷ or benzoic acid on Al_2O_3 [Fig. 10(b)]^{28,29}

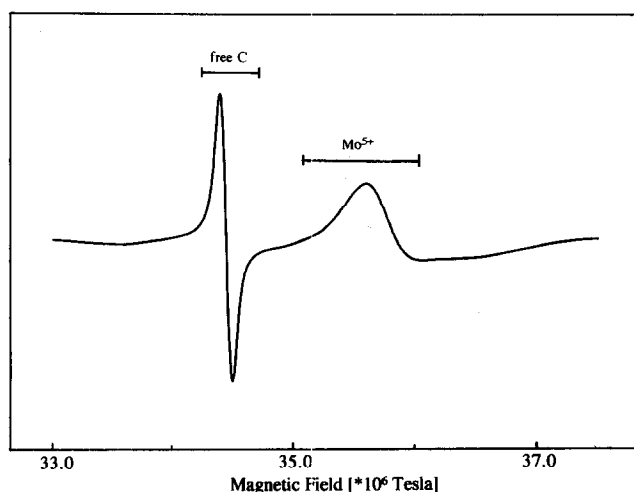
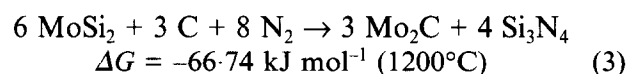


Fig. 9. EPR spectra of dry MoSi_2 powder with $d_{50} = 2.0 \mu\text{m}$ at a microwave frequency of 9.67 GHz.

hydrophobic, such behaviour can be related to the adsorption of tartaric acid on polar surfaces [Fig. 10(c)] and is in agreement with the chemisorption hypothesis.³⁰ Tartaric acid is a dipolar molecule, with two carboxyl groups and the two hydroxyl groups. Due to inductive effects and electrostatic interactions, the acidity of the carboxyl groups is stronger than that of the hydroxyl groups.³¹ The carboxyl groups are orientated towards the polar particle surface and the weak hydroxyl groups act as hydrophobic units. Since tartaric acid is a two-teeth ligand, two positive surface charges will be compensated.

3.3 Pyrolysis

The injection moulded parts are easily transformed into ceramic composites by subsequent pyrolysis using a N_2 atmosphere (99.99% purity, 0.1 mPa). The samples were heated to 1200°C at a rate of 5 K min^{-1} , held at temperature for 4 h, and then cooled to room temperature at a rate of 10 K min^{-1} . The reaction of the active filler MoSi_2 can be described by:



Through the large volume expansion of 67 vol% for eqn (3) the inherent polymer shrinkage can be significantly reduced; using a volume content of 40 vol% MoSi_2 filler phase a linear shrinkage of 5% results after pyrolysis at 1200°C . The microstructure of the ceramic composite consists mainly of Mo_2C and Si_3N_4 particles which are embedded in a nanocrystalline oxycarbide/oxynitride matrix; Fig. 11. Residual pores due to insufficient solvent removal, however, were frequently found in the pyrolysed screws. To avoid surface cracking as a result of inhomogeneous shrinkage during pyrolysis a uniform curing process throughout the cross-section of the screw is required.

Due to the formation of a protective SiO_2 layer on the sample surface, the ceramic composites reveal an excellent oxidation resistance. Thermogravimetric experiments showed a small weight increase of 0.30 wt% after oxidation at 1500°C for 100 h. Furthermore, the pyrolysis samples (density 4300 kg m^{-3} , porosity 8 vol%) show excellent creep behaviour ($\epsilon_{\text{sec}} = 1 \times 10^{-7} \text{ s}^{-1}$, 100 MPa, 1500°C) and a high electrical conductivity of $\sigma = 0.1 \times 10^6 \text{ S m}^{-1}$ at 1400°C . The pyrolysed material exhibits a four-point bending strength of $\text{MOR} = 390 \pm 10 \text{ MPa}$, a fracture toughness of $K_{\text{IC}} = 3.2 \text{ MPa m}^{1/2}$ and an average linear thermal expansion coefficient of $\bar{\alpha} = 8.2 \times 10^{-6} \text{ K}^{-1}$ (RT– 1000°C). These properties, in combination with the shaping capabilities, offer a high potential for net shape production of low cost ceramic bulk materials for high temperature applications such as heating

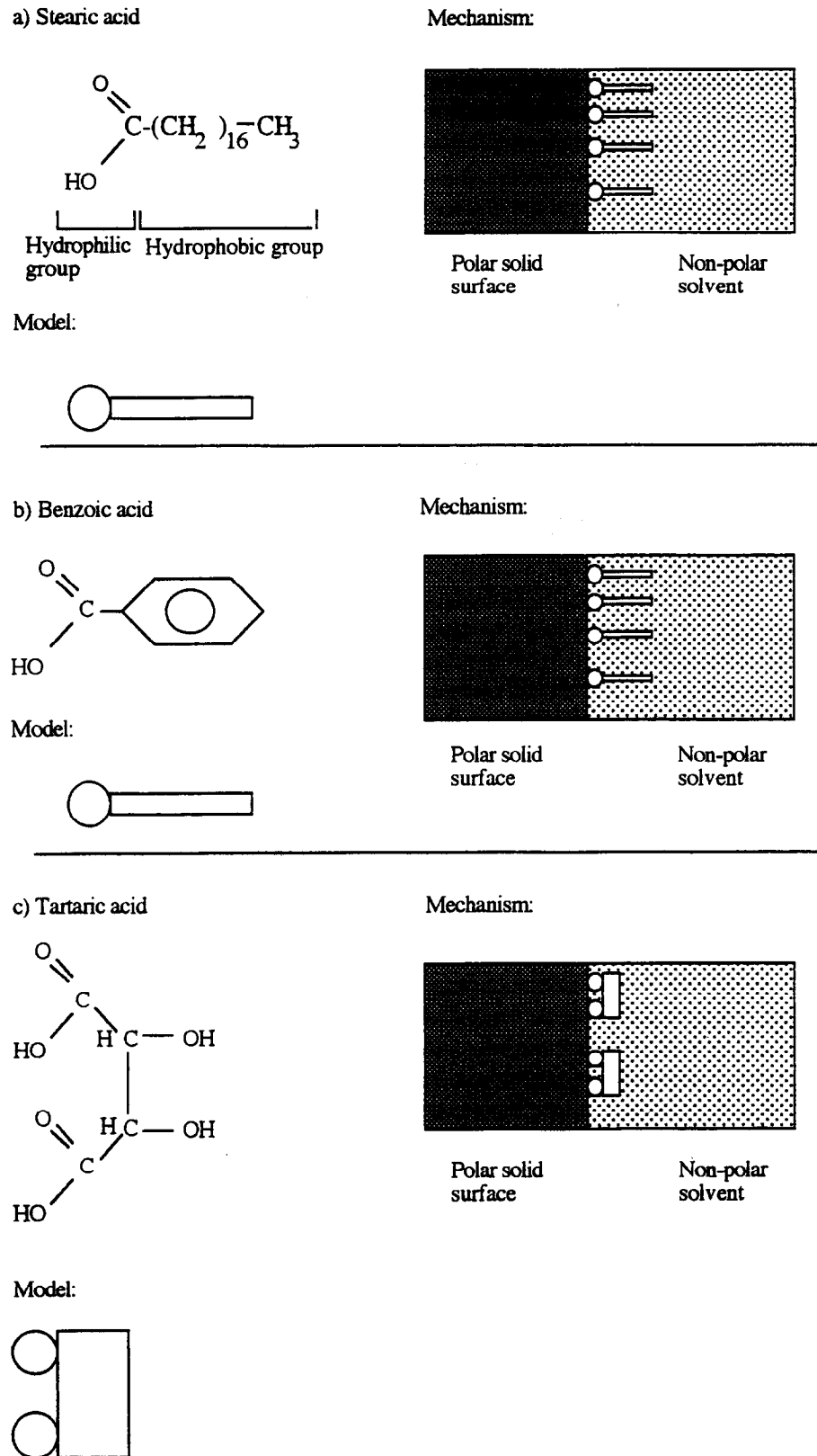


Fig. 10. Adsorption mechanisms of carboxylic acids: (a) Stearic acid; (b) benzoic acid; (c) tartaric acid.

elements, high temperature electrical contacts, wear resistant coatings and thermal barriers.

4 Conclusions

Polysiloxane/MoSi₂ mixtures can be injection moulded into complex preceramic parts. Filler

surface chemistry has a strong impact on polymerization temperatures and viscosity/time and viscosity/temperature dependencies due to catalytic effects. Processing requires the granulation of powdery polymer/filler mixtures in a separate extrusion step before injection moulding. Mo⁵⁺ oxidation states are suggested to account for the catalytic behaviour of MoSi₂, leading to charging

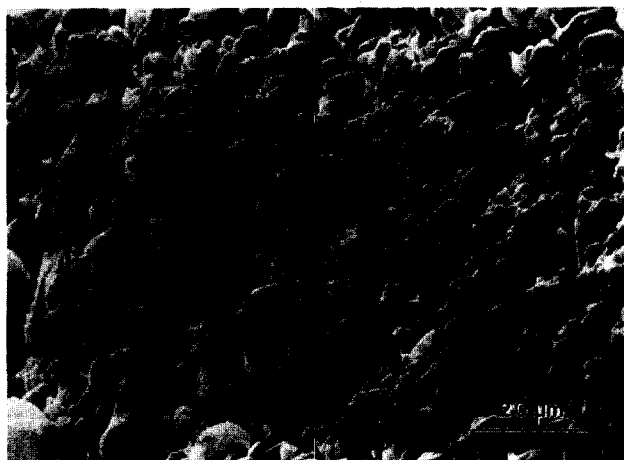


Fig. 11. SEM micrograph of composite microstructure (fracture surface) with 40 vol% MoSi₂ after pyrolysis in N₂ atmosphere at 1500°C.

effects on the surface and causing interaction with the hydroxyl groups of the polymer. Positive surface charges were compensated by shielding with carboxylic acids, which was achieved by coating the filler surface. Appropriate surfactants are citric acid and tartaric acid. They are most effective if precipitated on to the filler surface, enabling high filler loadings by lowering the viscosity and increasing the polymerization temperatures.

Acknowledgements

A. Weber, K. Kuhmann and G. Ehrenstein (Institute of Polymer Engineering, Friedrich–Alexander University of Erlangen–Nürnberg) are gratefully acknowledged for providing the injection moulding facilities.

References

- Edirisinghe, M. J. & Evans, J. R. G., Fabricating engineering ceramics by injection moulding. I. Materials; II. Technologies. *Int. J. High Tech. Ceram.*, **2** (1986) 249.
- Carlström, E., Sjöstedt, M., Mattson, B. & Hermansson, L., Binder removal from injection moulded ceramic turbocharger rotors. In *Science of Ceramics*, Vol. 14, ed. D. Taylor. Butter & Tanner, London 1988, p. 199.
- Hennicke, H. W. & Neuenfeld, K., Spritzgußtechnik als Formgebungsverfahren in der Keramik. *Ber. Dtsch. Keram. Ges.*, **45**(9) (1968) 469.
- Quackenbush, Q. L., Smith J. T., Neil, J. T. & French, K. W., Sintering, properties and fabrication of Si₃N₄ + Y₂O₃ based ceramics. In *Progress in Nitrogen Ceramics*, ed. F. L. Riley. Martinus Nijhoff Publishers, 1983, p. 669.
- Mangels J. A., Fabrication of complex shaped ceramic articles by slip casting and injection moulding. In *Progress in Nitrogen Ceramics*, ed. F. L. Riley. Martinus Nijhoff Publishers, 1983, p. 711.
- Reed J. S., *Principles of Ceramic Processing*. John Wiley & Sons, New York 1987.
- Johnson, A., Carlström, E., Hermansson, C. & Carlson, R. Minimization of the extraction time for injection moulded ceramics. *Proc. Brit. Ceram. Soc.*, **33** (1983) 139.
- Zhang, T. & Evans, J. R. G., The properties of a ceramic injection moulding suspension based on a preceramic polymer. *J. Europ. Ceram. Soc.*, **7** (1991) 405.
- Wells, R. R., Markle, R. A. & Mukherjee, S. P., Siloxanes, silanes and silazanes in the preparation of ceramic glasses. *Am. Ceram. Soc. Bull.*, **62**(8) (1983) 904.
- Erny, T., Seibold, M., Jarchow, O. & Greil, P., Microstructure development of oxycarbide composites during active filler controlled pyrolysis. *J. Am. Ceram. Soc.*, **76** (1993) 207.
- Seibold, M. & Greil, P., Thermodynamics and microstructural development of ceramic composite formation by active filler controlled pyrolysis. *J. Europ. Ceram. Soc.*, **11** (1993) 105.
- Greil, P., Seibold, M. & Erny, T., Microcrystalline ceramic composites by active filler controlled pyrolysis of polymers. In *MRS Symposium Proceedings 27: Submicron Multiphase Materials*, 1992, p. 155.
- Greil, P. & Seibold, M., Modelling of dimensional changes during polymer-ceramic conversion for bulk component fabrication. *J. Mater. Sci.*, **27**(9) (1992) 1053.
- Renlund, G. M., Prochazka, S. & Doremus, R. H., Silicon oxycarbide glasses: Part I. Preparation and chemistry. *J. Mater. Res.*, **6** (1991) 2716.
- Renlund, G. M., Prochazka, S. & Doremus, R. H., Silicon oxycarbide glasses: Part II. Structure and properties. *J. Mater. Res.*, **6** (1991) 2723.
- Hurwitz, F. I., Heimann P., Farmer, S. C. & Hembree Jr, D. M., Characterization of the pyrolytic conversion of polysilsesquioxanes to silicon oxycarbides. *J. Mater. Sci.*, **28** (1993) 6622.
- Bond, G. C., *Catalysis by Metals*. Academic Press, Inc., London, 1964.
- Marshik, B., Meyer, D. & Apple T., Electron-spin-resonance studies of vapor-grown carbon fibers. *J. Appl. Phys.*, **62** (1987) 3947.
- Lipowitz, J. & Turner, G. L., *Solid State NMR of Polymers*, ed. L. Mathias. Plenum Press, New York, 1991, p. 305.
- Jeng, Y. L. & Lavernia, E. J., Review, processing of molybdenum disilicide. *J. Mater. Sci.*, **29** (1994) 2557.
- Abdo, S., Lojacoc, M., Clarkson, R. B. & Keith Hall, W., The Environment of Mo(V) in supported molybdena catalysts. *J. Catal.*, **36** (1975) 330.
- Kiselev, V. F. & Krylov, O. V., *Adsorption and Catalysis of Transition Metals and their Oxides*. Springer-Verlag, Berlin, 1988.
- Tait, P. J. T. & Watkins, N. D., *Monoalkene Polymerization Mechanism: Comprehensive Polymer Science Vol. 4*. Pergamon Press, Oxford, 1989.
- Valenzuela, D. P. & Myers, A. L., *Adsorption Equilibrium Data Handbook*. Prentice-Hall, Englewood Cliffs, New York, 1989, p. 253.
- Hunter, R. J., *Colloid Science, Vol. 2: Zeta Potential in Colloid Science - Principles and Applications*. Academic Press, London, 1981, p. 308.
- Ulrich, H. J., Stumm, W. & Cosovic, B., Adsorption of aliphatic acids on aquatic interfaces. *Environ. Sci. Technol.*, **22** (1988) 37.
- Hotza, D., Sahling, O. & Greil, P., Hydrophobing of aluminium nitride powders. *J. Mater. Sci.*, **30** (1995) 127.
- Wolfrum, S. M. & Ponjee, J. J., Surface modification of powders with carboxylic acids. *J. Mater. Sci. Lett.*, **8** (1989) 667.
- Horn, R. G., Surface forces and their action in ceramic materials. *J. Am. Ceram. Soc.*, **73** (1990) 1117.
- Kipling, J. J. & Wright, E. H. M., Adsorption on carbon black from solution of monocarboxylic acids: the higher members. *J. Chem. Soc.* **23** (1963) 3382.
- Streitwieser Jr, A. & Heathcock, C. H., *Organische Chemie*. VCH Verlagsgesellschaft, Berlin, 1986.

Preparation of Glass-Impregnated Isotropic Graphite and its Gas Permeability

Toshiaki Sogabe & Takashi Matsumoto

Toyo Tanso Co., Ltd, Ohnohara Technical Development Center, 2181-2 Ohnohara-cho, Mitoyo-gun, Kagawa-ken, 769-16, Japan

(Received 7 November 1994; revised version received 21 June 1995; accepted 14 July 1995)

Abstract

Two kinds of borosilicate glass, T1 (SiO_2 : 38%, B_2O_3 : 36%, Na_2O : 21%, Al_2O_3 : 5%, softening point 620°C) and T2 (SiO_2 : 50%, B_2O_3 : 30%, Na_2O : 15%, MgO : 5%, softening point 639°C), were impregnated into a high-density isotropic graphite block. Achieved impregnation depths were 50 and 24 mm for glasses T1 and T2, respectively, with typical impregnation conditions of 1200°C and 15 MPa pressure for 1 h. Around 90% of the open pore volume of the original graphite was occupied by the glass. Gas permeability of the T1- and T2-impregnated graphites was reduced to 6.2×10^{-5} and $1.8 \times 10^{-6} \text{ cm}^2 \text{ s}^{-1}$, respectively, from $1.3 \times 10^{-1} \text{ cm}^2 \text{ s}^{-1}$ for the original untreated material. Glass impregnation was shown to be more effective in reducing gas permeability than phenolic resin. It was suggested that gas permeability could be much reduced by minimizing the machining of the glass-impregnated blocks.

1 Introduction

Isotropic graphite materials are widely used because of their fine texture, high strength and excellent thermal stability. However, they are gas permeable due to the pores which are unavoidably created in the production process. There is a strong demand to make isotropic graphite impermeable to gases for many applications. Impregnation of synthetic resins and metals with low melting point into the pores of graphite has been commonly performed in order to lower permeability.¹ It can be important to impregnate the graphite with high melting point materials for applications where thermal stability is required, though this needs high pressures and temperatures. Impregnation of borosilicate glass into a low-density graphite electrode nipple has, for example, been reported.² We have tried to impreg-

nate borosilicate glasses into dense carbon and graphite materials by using an autoclave capable of high pressures and temperatures.^{3–5}

In the present paper, we investigate the process and conditions for the impregnation of two kinds of borosilicate glass into a high-density isotropic graphite to provide gas impervious materials.

2 Experimental Procedures

2.1 Materials

A high-density isotropic graphite, grade IG-11 manufactured by Toyo Tanso Co., Ltd, was used as a graphite substrate. Its properties are tabulated in Table 1. It was made from a petroleum coke with average grain size of $10 \mu\text{m}$, and its open porosity was $\sim 15\%$ with a mean pore radius of $1.7 \mu\text{m}$. Two kinds of borosilicate glass, which are here termed T1 and T2, were selected for impregnation. Their composition and physical properties are summarized in Table 2. The composition of these glasses was designed so that they would have a reasonably small difference in thermal expansion coefficient from graphite. The temperature dependence of viscosity for these glasses is shown in Fig. 1. A higher content of SiO_2 in glass T2 results in higher thermal and chemical stabilities, and also in higher viscosity than for T1.

2.2 Apparatus and conditions for impregnation

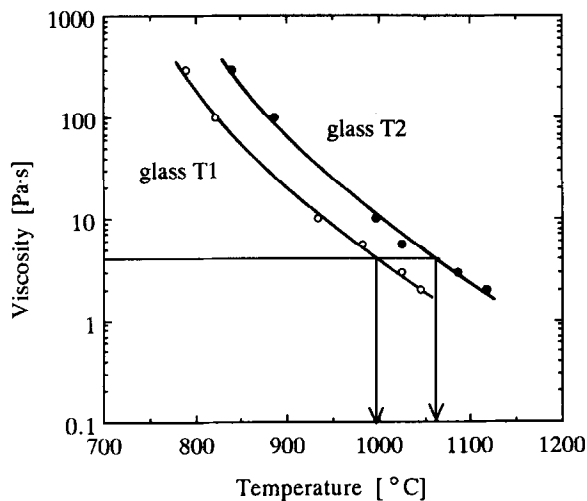
An apparatus for glass impregnation is illustrated in Fig. 2. This facility is capable of working either in vacuum or under a pressure of up to 15 MPa nitrogen gas and at temperatures up to 1500°C . The impregnant is loaded in a crucible and the pieces of graphite are placed in a sagger attached to the upper lid. Raising and lowering of the lower actuator allows the pieces to be immersed or separated from the molten impregnant. A flow chart of the impregnation procedure employed in the present work is shown in Fig. 3(a).

Table 1. Mechanical properties of the original and borosilicate glass-impregnated graphites

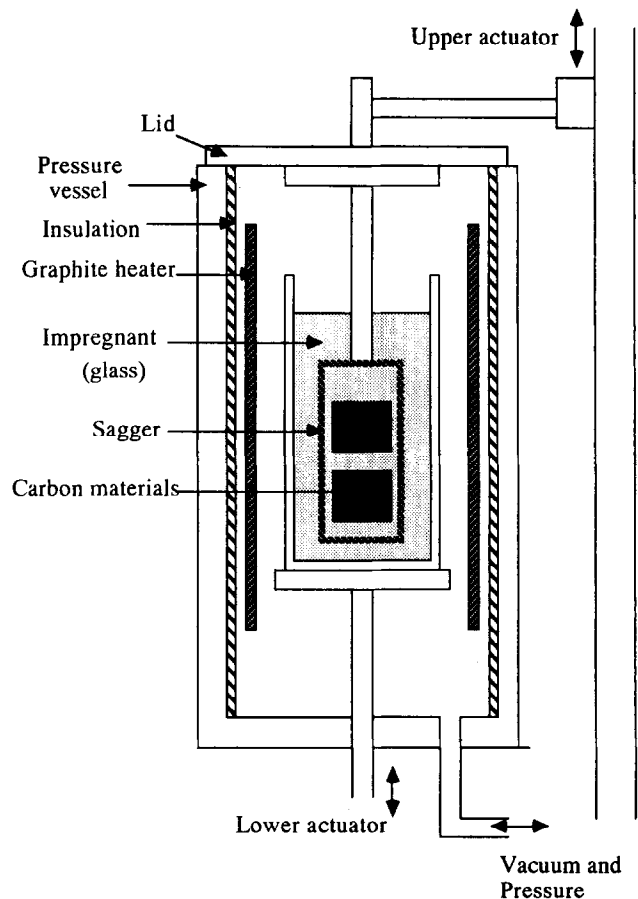
	Bulk density ($g\ cm^{-3}$)	Shore hardness	Bending strength (MPa)	Compressive strength (MPa)	Young's modulus (GPa)	Thermal expansion coefficient ($10^{-6}\ K^{-1}$), 350–450°C
Original graphite (IG-11)	1.78	56	40	77	10.5	4.6
Glass T1-impregnated	2.08	70	58	147	17.3	5.8
Glass T2-impregnated	2.09	68	61	154	17.7	5.5

Table 2. Composition and properties of borosilicate glasses for impregnation

Glass	Composition (mass %)					Glass transition point (°C)	Softening point (°C)	Thermal expansion coefficient ($10^{-6}\ K^{-1}$), 50–300°C	True density ($g\ cm^{-3}$)
	SiO ₂	B ₂ O ₃	Na ₂ O	Al ₂ O ₃	MgO				
T1	38	36	21	5	—	513	620	9.6	2.49
T2	50	30	15	—	5	521	639	9.3	2.50

**Fig. 1.** Temperature dependence of viscosity of borosilicate glasses for impregnation.

The impregnation of glass T1 into graphite IG-11 was carried out at temperatures of 1000, 1100 and 1200°C under a pressure of 15 MPa for 1 h. The impregnation of glass T2 was carried out at a temperature of 1200 °C under the same pressure as in the case of T1. A typical temperature programme during impregnation is shown in Fig. 3(b). The autoclave was kept in a vacuum ~ 0.13 kPa in order to evacuate gas from the graphite blocks and glass. The ramp-up rate was slowed down from $400^\circ\ h^{-1}$ to $200^\circ\ h^{-1}$ at 800°C to promote smooth gas evacuation. The final temperature was held for 1 h to produce a uniform temperature distribution in the molten glass before immersing the sample graphite. After the immersion of the graphite blocks into the molten glass by raising the crucible, the pressure was increased to 15 MPa and held at this value for 1 h. To study the impregnation depth of the glass into the graphite, a cubic block of $100 \times 100 \times 100\ mm^3$ size was used, two opposite faces of which were protected from glass impregnation by a carbon sheet. After impregnation, the block was cut into

**Fig. 2.** Autoclave for glass impregnation.

two pieces and the depth of glass impregnation was measured by spreading grease on the cut surface of one piece; after wiping it off with an organic solvent, the non-impregnated surface gave different results from that of the impregnated part. Mechanical properties of the impregnated samples were measured by conventional methods and the open porosity was also determined by mercury porosimetry. Test specimens for the measurements were taken from the glass-impregnated graphite, after the surface layer of about 5–10 mm had been cut off.

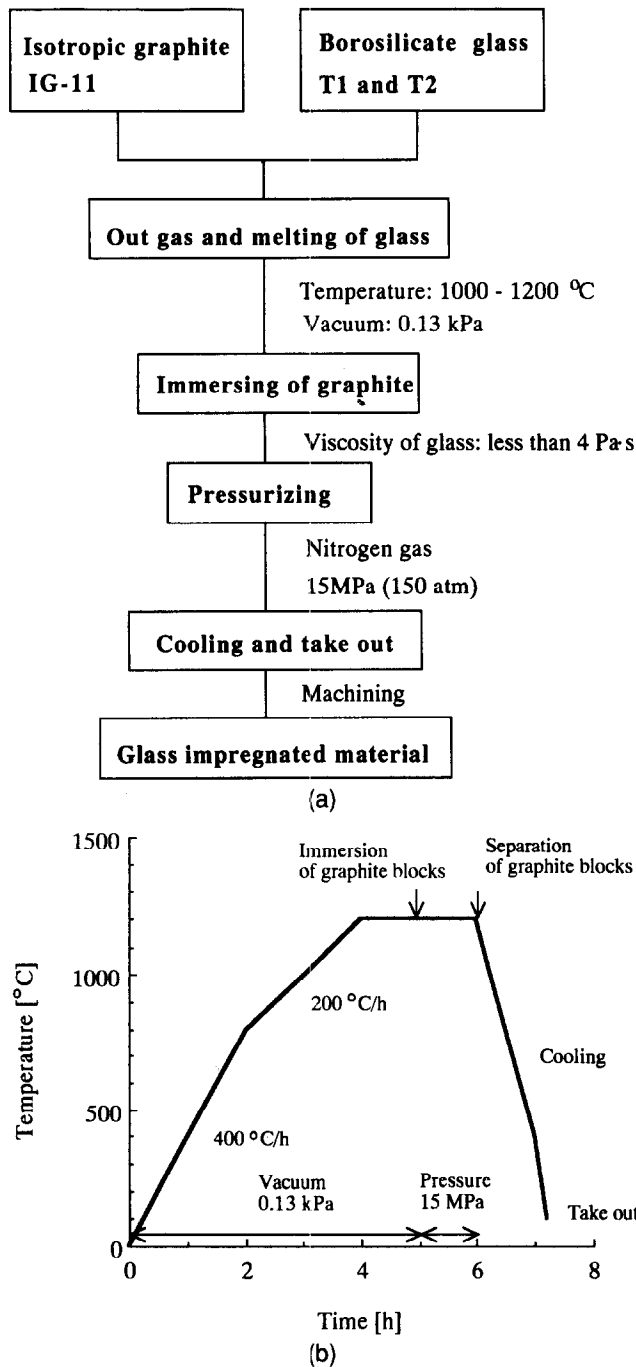


Fig. 3. (a) Flow chart of glass impregnation procedure. (b) Typical temperature programme for glass impregnation.

Impregnation of phenolic resin into the graphite substrate was also carried out. Curing of the resin was done at 200°C. A hollow cylindrical test specimen with an inner diameter of 5 cm, an outer diameter of 8 cm and 4 cm length was taken from a phenolic resin-impregnated block. A second impregnation was conducted on the test specimen, and no machining was done because no resin remained on the surface after the impregnation.

2.3 Measurement of gas permeability

Gas permeability K [$\text{cm}^2 \text{s}^{-1}$] was calculated from the following equation:^{6,7}

$$K = QL / \Delta PA \quad (1)$$

where Q [$\text{Pa cm}^3 \text{s}^{-1}$] is the flow rate of permeated gas, L [cm] is the thickness of the specimen, ΔP [Pa] is the pressure difference in the two chambers separated by the specimen and A [cm^2] is the cross-sectional area for gas permeation. The value Q was determined by the rate of pressure rise and by the volume of the secondary chamber into which gas permeated through the specimen from the primary chamber, which was kept at 100–600 kPa. Details of the equipment used for the present measurements have been reported elsewhere.^{8,9}

In the present work, the permeability specimens were cut from 100 mm cubic glass-impregnated blocks and the size of the specimen is a disc, 3 cm in diameter and 0.7 cm in thickness. In the present equipment, the gas permeation diameter is set at 2 cm, so that A is 3.14 cm^2 and L is 0.7 cm in eqn (1). The measurement was done at room temperature using nitrogen gas of high purity.

The gas permeability K of graphite materials has been reported to be approximated by the following relation:^{6,7}

$$K = (B_0/\eta) P_m + (4/3)K_0(8RT/\pi M)^{1/2} \quad (2)$$

where B_0 [cm^2] is the viscous flow permeability, K_0 [cm] is the molecular flow coefficient permeability, η [Pa s] is the viscosity of the gas, P_m [Pa] is the mean pressure of the two chambers, R [$\text{cm}^3 \text{Pa mol}^{-1} \text{K}^{-1}$] is the gas constant, T [K] is the temperature and M [kg mol^{-1}] is the molecular weight of gas. The contribution of molecular flow gas permeation through pores in the specimen was assessed from the relation between K and P_m .

To see the effect of machining, a hollow cylindrical graphite block with an inner diameter of 5 cm, an outer diameter of 8 cm and 4 cm in length was also impregnated by glass T1. The impregnation was carried out at a temperature of 1200°C under a pressure of 15 MPa for 1 h. After impregnation, the glass adhering to the surface was removed carefully by using a file and sandpaper and the surface skin of ~0.05 cm was cut off using a lathe. In the gas permeability measurement with the cylindrical specimen, gas permeated from the outer wall to the inner wall. In eqn (1), A was taken as the logarithmic mean of the inner and the outer wall surface area, and L is the thickness of the cylinder. Both nitrogen and helium gases were used for this measurement.

3 Results and Discussion

3.1 Glass impregnation

It was found that the viscosity of the molten glass should be lower than 4 Pa s to allow smooth mechanical immersion of the sagger into the molten

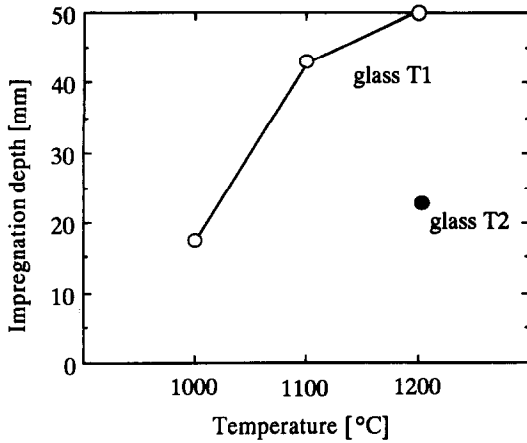


Fig. 4. Relations between impregnation depth into IG-11 graphite and temperature for glass impregnation (pressurized at 15 MPa for 1 h).

glass. For glass T1, a temperature above 1000°C where its viscosity becomes ~ 4 Pa s was necessary, as shown in Fig. 1. The maximum temperature was limited to 1200°C to avoid chemical reactions between the glass and the metal crucible. Impregnation depth for the two kinds of glass is plotted against temperature in Fig. 4. Impregnation depth of glass T1 increased significantly with elevation of temperature. At 1200°C, the depth became > 50 mm, which was the measurement limit because the graphite block has a size of 100 mm. However, the impregnation depth for glass T2 was only 24 mm.

The effect of mean pore radius on impregnation depth for glass T1 and T2 into some carbon substrates has been studied in our previous work³ and is shown in Fig. 5 in the form of curves. Impregnation depths observed on the present substrate IG-11 are also plotted against mean pore radius in Fig. 5, where the impregnation were carried out at a temperature of 1200°C under a pressure of 15 MPa for 1 h. The present data are almost on the

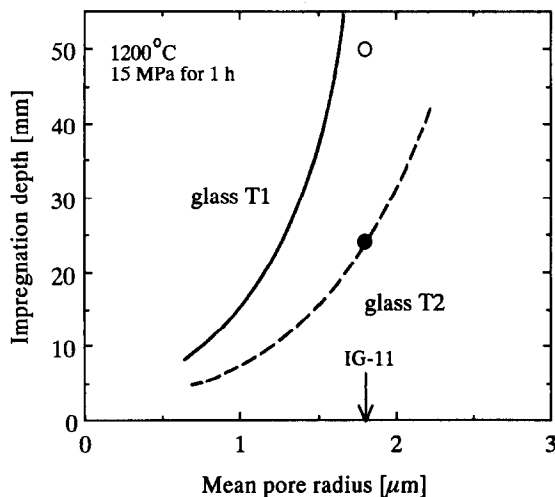


Fig. 5. Relations between glass T1 and T2 impregnation depth and mean pore radius of carbon materials. Impregnation was carried out at 1200°C under a pressure of 15 MPa for 1 h. Open and filled circles are data quoted from Fig. 4.

curves. This indicates that impregnation depth is very dependent on the pore radius of the materials. Impregnation depth decreases rapidly as the pore radius become small, which suggests that it may be difficult for a material to be fully or deeply impregnated by glass if the pore size is less than 1 μm.

Micrographs from scanning electron microscopy (SEM) of the polished surface of the original and glass-impregnated graphites are shown in Fig. 6.

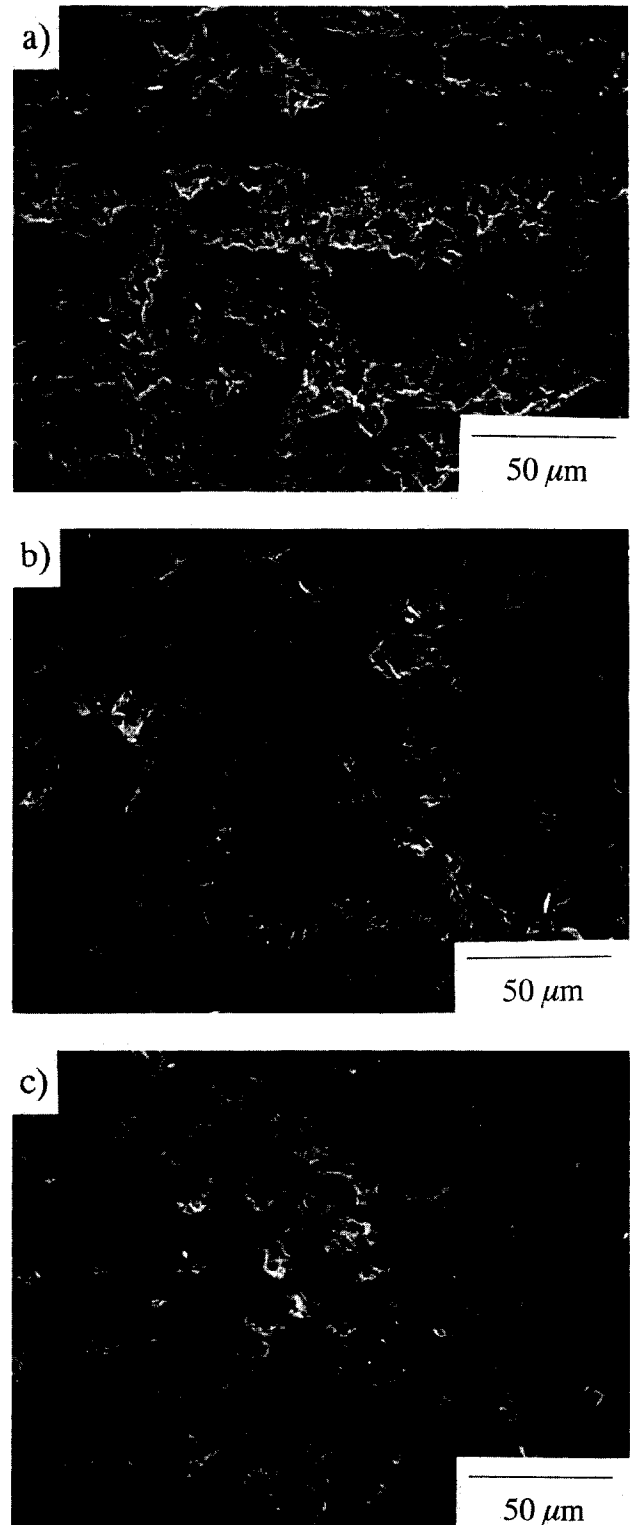


Fig. 6. SEM micrographs of polished surface of the original (a), glass T1-impregnated (b) and glass T2-impregnated (c) graphites.

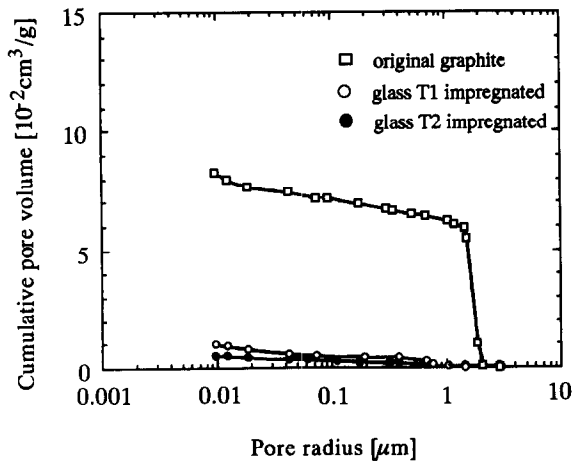


Fig. 7. Effects of glass T1 and T2 impregnation into the isotropic graphite substrate, IG-11, on pore distribution.

Mechanical properties of the glass-impregnated IG-11 are shown in Table 1. The cumulative pore volume of the original and glass-impregnated graphites are determined by mercury porosimetry. These values are plotted against pore radius in Fig. 7.

The SEM micrographs designate that pore regions were much reduced by glass T1- and T2-impregnation. Bending and compressive strengths at room temperature are improved about 1.5 and 2 times by impregnation of the glass, respectively. The Young's modulus becomes about 1.7 times higher than that of the original. A good wettability between glass and graphite is considered to be the main reason for this improvement. Pores of radius $> 1 \mu\text{m}$ disappeared from the graphite substrates following impregnation with both glass T1 and T2. This result means that the size of residual crack-initiating flaws became small. The improvement in bending strength was smaller than that in compressive strength, probably because of the brittleness of the glass. There was no significant difference in mechanical properties between the two glass-impregnated materials. The slightly low thermal expansion coefficient of the T2-impregnated graphite is probably due to the lower thermal expansion coefficient of glass T2 than that of T1.

The volume impregnation ratio was calculated from total open pore volume and density of each material and substrate. About 90% of the open pore volume of the graphite substrate was found to be occupied by the glass.

The voids of $\sim 10\%$ seemed to be mostly pores whose radius was less than $0.7 \mu\text{m}$. In the original graphite, the pore volume consisting of pores with radii less than $0.7 \mu\text{m}$ was $\sim 20\%$ of the total, so that roughly half that region was impregnated. The main reason for residual unoccupied space may be that small pores are difficult to impregnate, as shown in Fig. 5. Also, the larger thermal

expansion of these glasses in comparison to that of the graphite substrate results in the creation of space during cooling. It may be noticed that impregnated glass was extruded to a certain extent during cooling by hot gas still confined in the pores; this phenomenon may be more likely to happen if the viscosity of the impregnated molten glass is lower.

The volume impregnation ratio for glass T2 was found to be 93%, which is a little higher than the value of 86% for T1. This finding is probably due to the relatively low thermal expansion coefficient of glass T2 and the relatively high viscosity of glass T2 at the impregnation temperature compared with T1. It was found that glass T2, having a higher viscosity, is more difficult to impregnate deeply, but the impregnated part achieves a slightly higher volume impregnation ratio than T1.

3.2 Gas permeability

The plots of gas permeability K against mean pressure P_m of the original and glass-impregnated graphites are shown in Fig. 8. The K values of the glass T1-impregnated cylindrical specimen whose surface layer was removed to 0.05 cm after impregnation are plotted against P_m in Fig. 9. The viscous flow permeability B_0 and molecular flow coefficient permeability K_0 determined by eqn (2) are summarized in Table 3. In this table, glass-impregnated graphites are compared with phenolic-resin impregnated specimens.

The impregnation of glass T1 and T2 reduced the gas permeability by four and five orders, respectively, from $10^{-1} \text{ cm}^2 \text{ s}^{-1}$ for the original. The low gas permeability of the T2-impregnated graphite seems to result from the high occupation of the open pores by glass T2. It is found that glass impregnation reduces gas permeability more effectively than that with phenolic resin. This is probably due to the fact that condensation gas from the resin creates open pores in the course of curing. By double impregnation of resin, gas permeability was reduced down to $10^{-7} \text{ cm}^2 \text{ s}^{-1}$, and was independent of pressure; the pore radius being so small that gas flow only by slip on the pore surface is possible.

The gas permeability of the cylindrical specimen was $10^{-7} \text{ cm}^2 \text{ s}^{-1}$ which was lower by two orders of magnitude than that of the T1-impregnated disc after machining. It is supposed that in the vicinity of the surface, glass is well impregnated into the much smaller pores than in the inner part of the block, as Fig. 5 indicates the high dependence of pore radius on impregnation depth. Also, the contribution of the viscous flow of gas for this specimen became much smaller than that of the

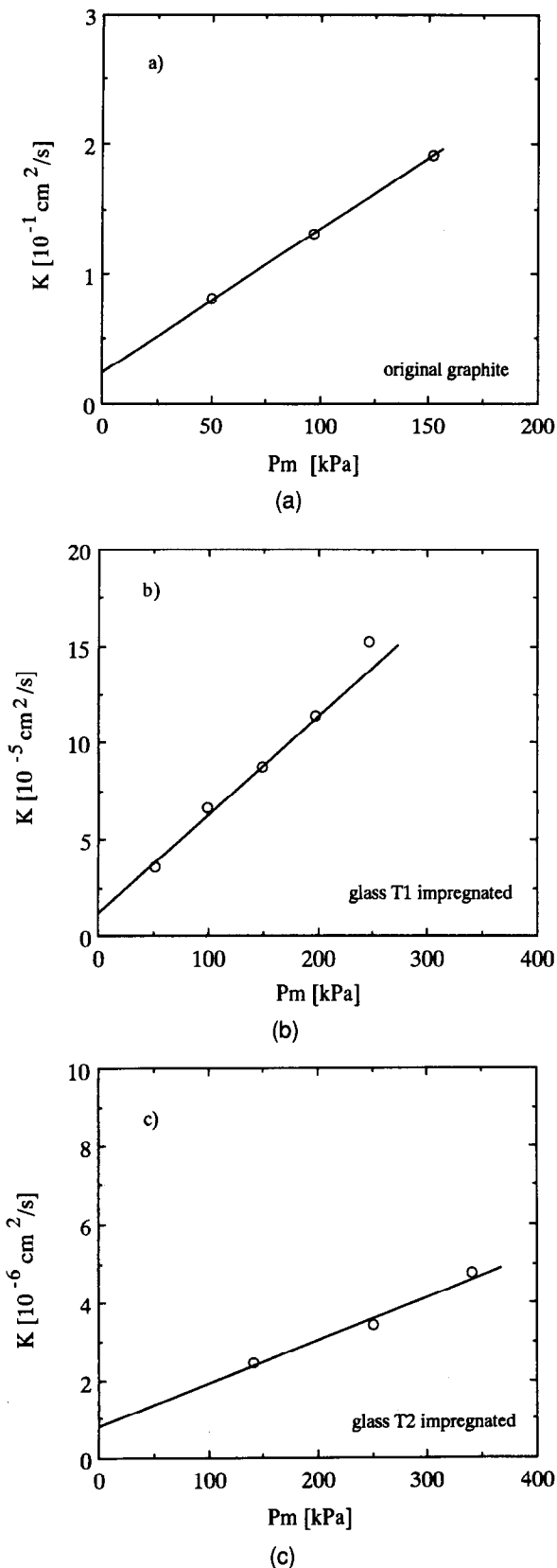


Fig. 8. Relations between gas permeability K and mean pressure P_m of nitrogen gas for the original (a), glass T1-impregnated (b) and glass T2-impregnated (c) graphites.

machined specimen; the molecular flow coefficient permeability was close to that of the double resin impregnated specimen, which indicates that the radii of the pores are very small, at least in the vicinity of the surface of the specimen. The gas

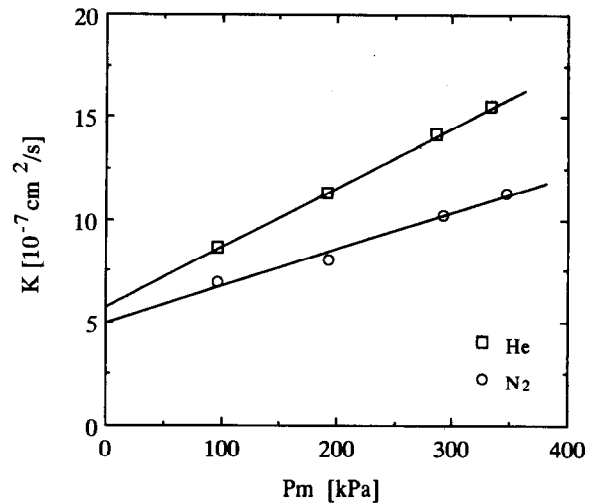


Fig. 9. Relations between gas permeability K and mean pressure P_m of nitrogen and helium gas for a cylindrical specimen whose surface layer was cut off only 0.05 cm after impregnation.

Table 3. Gas permeability and its parameters under nitrogen gas at 25°C for various graphites

	Gas permeability, K ($\text{cm}^2 \text{ s}^{-1}$) ($P_m = 98 \text{ kPa}$)	Viscous flow permeability, B_0 (cm^2)	Molecular flow permeability, K_0 (cm)
Original			
IG-11 graphite	1.3×10^{-1}	1.9×10^{-11}	1.4×10^{-5}
Impregnated			
Glass T1	6.2×10^{-5}	9.2×10^{-15}	4.5×10^{-9}
Glass T2	1.8×10^{-6}	2.0×10^{-16}	3.5×10^{-10}
Glass T1-cylinder*	6.6×10^{-7}	3.2×10^{-17}	2.4×10^{-10}
Phenolic resin once	2.8×10^{-4}	4.2×10^{-14}	2.0×10^{-8}
Phenolic resin twice	2.6×10^{-7}	—	1.3×10^{-10}

*Surface layer was cut off only 0.05 cm after glass T1 impregnation.

permeability of helium gas was a little larger than that of nitrogen gas. Gas permeability at constant temperature is only a function of the molecular weight of the gas in the molecular flow dominant region, as indicated in eqn (2), and it follows that helium gas with smaller molecular weight appears to permeate through a porous medium more readily than nitrogen gas. It can be concluded that minimizing of machining is very effective in reducing gas permeability.

Acknowledgements

The authors would like to thank Professor M. Inagaki of Hokkaido University and Dr K. Kuroda of Toyo Tanso Co., Ltd for their helpful discussions and encouragement.

References

- Paxton, R., *Manufactured Carbon: A Self-lubricating Material For Mechanical Devices*. CRC Press, Inc., Boca Raton, FL, 1979.

2. Ikeda, S., Hori, S., Eguchi, K., Fujii, R., Matsuo, K., Zaima, H. & Gamada, Y., Trial production of carbon materials impregnated with glass. *TANSO*, **124** 1986 2.
3. Matsumoto, T., Sogabe, T., Matsuo, K., Fujii, R., Ikeda, S. & Eguchi, K., Features of glass-impregnated carbon material. In *Proceedings of 16th Annual Meeting of the Carbon Society of Japan*, Tokyo Japan, 1989, p. 202.
4. Sogabe, T., Matsumoto, T. & Matsuo, K., Some properties of glass-impregnated carbon materials, *FC Report No. 7*. Japan Fine Ceramics Association, 1989, p. 243.
5. Ikeda, S., Nakamura, O., Sogabe, T. & Matsumoto, T., Improvement of mechanical strength of isotropic graphite by glass impregnation. *Chemistry Express*, **8**(7) (1993) 515–8.
6. Hewitt, G. F., Gaseous mass transport within graphite. In *Chemistry and Physics of Carbon* Vol. 1. ed. P. L. Walker Jr. Merceel Dekker, New York, 1965, p. 73.
7. Jenkins, T. R. & Roberts, F., Gas permeability studies on some artificial graphites. In *Proceedings of 5th Carbon Conference*, Pennsylvania, 1961, p. 335.
8. Sogabe, T., Gas permeability measurement on carbon materials. *Zairyou-kagaku*, **30** (1993) 159–64.
9. Kamiyama, M. & Sogabe, T., The relationship between gas permeability and open pore of carbon. In *Abstracts of Int. Symposium on Carbon. New Processing and New Applications*, Tsukuba, Japan, November 1990, p. 296.

Influence of Boron Nitride and Carbon Additives on the Behaviour of Sintered AlN in a Steel-Making Environment

A. Amadeh, J. C. Labbe,* A. Laïmeche & P. Quintard

Laboratoire de Matériaux Céramiques et Traitements de Surface (CNRS URA 320), Université de Limoges, 123 av. Albert Thomas, 87060 Limoges, France

(Received 7 June 1995; revised version received 10 July 1995; accepted 14 July 1995)

Abstract

In an earlier work we showed that the corrosion of pure aluminium nitride by steels takes place via an attack on the grain boundary Al/O/N phases and through AlN decomposition, with oxidation of aluminium by the dissolved oxygen. To reduce this type of corrosion, we tried to remove alumina and Al/O/N phases from the grain boundary by adding to the initial powders a small quantity of BN or carbon. The quantity of added BN must be in strict accordance with the quantity necessary to clean the grain boundaries. Best results were obtained with 10 wt% of BN. Carbon addition, which helps to improve the thermal shock resistance as well, produces the same result, but through a different mechanism. Best results were obtained with quantities between 5 and 10 wt% of carbon.

1 Introduction

For economic reasons and to optimize their mechanical, thermal and thermochemical properties, the refractory parts and ceramic coatings used in the iron and steel industry are composed of a mixture of different materials. For example, carbon is added to improve the resistance to thermal shock of certain ceramic parts. In our earlier work¹ we have shown the importance of grain boundary phases in the behaviour of AlN against liquid steels. Here we have tried to improve the corrosion resistance of AlN by systematically adding BN or carbon, while verifying their influence on the properties of AlN each time.

*To whom correspondence should be addressed.

2. Experimental

2.1 Preparation of sintered samples of AlN–BN and AlN–C ceramic materials

Initial powder mixtures were prepared by magnetic agitation in ethanol–acetone for 2–3 h in order to obtain homogeneous dispersions. These powders were kept in an oven at 100°C for 1 h and then milled once again before placing them in a graphite mould.

In the case of the AlN–BN mixture, only the 66% AlN–34% BN mixture could be densified to 88% of its theoretical density. We did not succeed in densifying the other compositions (50% AlN–50% BN and 34% AlN–66% BN) sufficiently to carry out experiments (Table 1). In the case of AlN–C a relatively low densification was obtained, compared to AlN–BN. The low density of AlN–BN and AlN–C substrates could be due to the reactivity of BN and C towards oxynitrides and oxides^{2–5} which are present in the AlN powder: their influence has previously been proved in the sintering of AlN.⁶

The X-ray patterns of the AlN–BN and AlN–C substrates, obtained after the sintering process, show only the peaks corresponding to AlN, BN and C, which confirm the purity of the sintering products and the absence of any reaction between the materials.

2.2 Steels

We worked with three type of steel: A, extra mild low carbon; B, treated SiCa; and C, IFS ultra-low carbon steel. The chemical composition of these steels is given in Table 2.

3 Study of AlN–BN Behaviour with Respect to Steels

The study of the AlN reaction with steels A, B and C in the liquid state,¹ has shown that AlN presents weak corrosion resistance against these steels, and

Table 1. Sintering conditions of AlN–BN and AlN–C mixtures

AlN rate (% mass)	66	50	34	95	90	80
BN rate (% mass)	34	50	66	0	0	0
Carbon rate	0	0	0	5	10	20
Temperature (°C)	1830	1850	1850	1820	1825	1830
Pressure (MPa)	23	23	23	28	29	30
Time (min)	30	35	40	60	60	60
d/d_{th} (%)	88	—	—	82	80	78

Table 2. Chemical composition of steels in p.p.m. by weight

Steels	A	B	C
C	430	1000	60
Si	120	3430	50
Al	450	250	440
Ti	0	110	670
N	46	36	26
Mn	1940	13730	1850

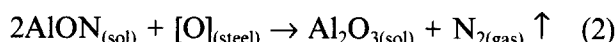
that the steels A and B show a wetting character over AlN substrates.

This corrosion is the result of strong reactivity at the solid–liquid interface, during the wettability experiments, through a complex mechanism which can be divided into two stages:

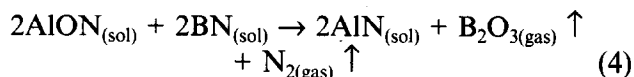
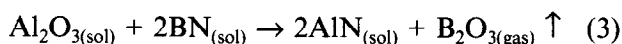
- (1) Thermal decomposition of aluminium nitride⁷ and oxidation of the resulting aluminium by oxygen dissolved in steels:



- (2) Grain boundary attack through oxidation of AlON phases which are present at the grain boundaries:



The boron nitride added to the AlN matrix reacts with Al_2O_3 and AlON phases during the sintering process^{2,3} according to reactions (3) and (4), which helps in the removal of these parasite phases and in the cleaning of AlN grain boundaries:

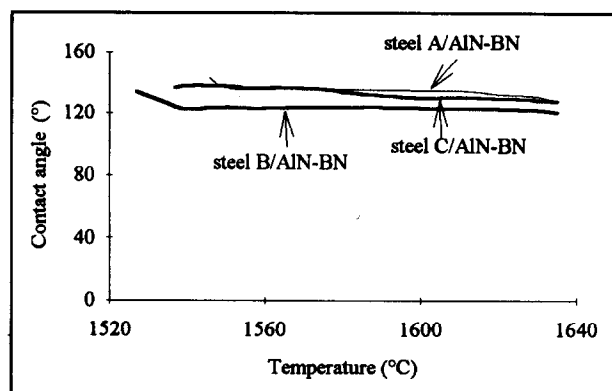
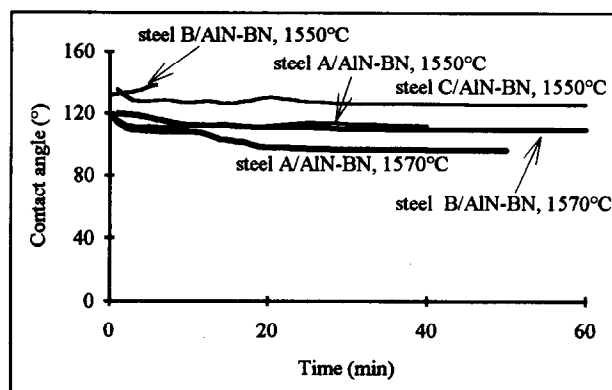


3.1 Wettability of AlN–BN substrates by steel

Experiments were performed using the sessile drop method, between 1520 and 1635°C, using the apparatus already described in Ref. 8. The metallic sample is kept under vacuum up to 1490°C (25–40°C before the melting point), at which point argon is introduced in the furnace with a little overpressure¹.

3.2 Contract angle

The contract angle between the steel drops and

**Fig. 1.** Evolution of contract angle with temperature.**Fig. 2.** Contract angle as a function of time.

AlN–BN solid substrate remains constant and non-wetting, in the temperature range between drop formation and 1635°C (Fig. 1).

The contract angle also remains constant as a function of time, at a given temperature, as shown in Fig. 2. For the system steel B/AlN–BN, a strong swelling of the liquid drop was observed at 1550°C, which made contact angle measurement almost impossible. The values for this system shown in Fig. 2, at 1570°C, are approximate because the measurement was made between two swellings.

3.3 Solid–liquid surface tension

Calculations for solid–liquid surface tension were obtained using Young's equation¹ while keeping σ_{sv} constant between the considered temperatures. We fixed $\sigma_{sv} = 1000 \text{ mN m}^{-1}$, which is the value generally used by other authors.^{9,10} This means that our observations only concern the variation of σ_{SL} and not its absolute value.

The solid–liquid surface tension for the systems of steels A and B over AlN–BN substrates, as a function of temperature, decreases immediately after liquid drop formation and stabilizes afterwards (Fig. 3); in the system steel C/AlN–BN, it slightly decreases between the temperature of drop formation and 1620°C.

At constant temperature, σ_{SL} for the system C/AlN–BN decreases rapidly during the first 10 min, which shows strong interaction between the

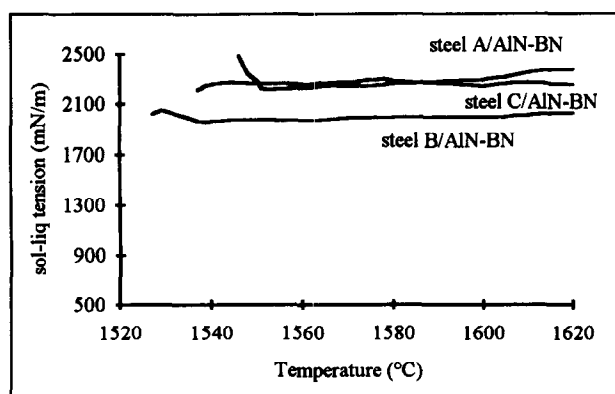


Fig. 3. Solid-liquid tension as a function of temperature.

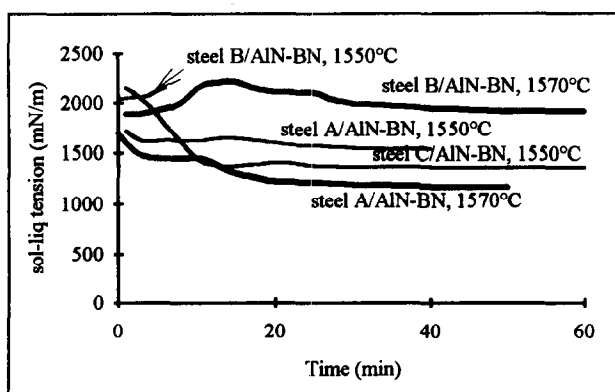


Fig. 4. Solid-liquid tension as a function of time.

steel and substrate at 1550°C (Fig. 4). At 1570°C the liquid drop started swelling, which made contact angle measurement impossible. The same type of behaviour was obtained in the case of A/AlN-BN, where stabilization was obtained after 20 min contact time. In all cases, this decrease in σ_{SL} value was more pronounced as the temperature was increased.

The results obtained by the dipping method (Table 3) have shown that the corrosion of AlN-BN is less than that of pure AlN, thus proving the effect of BN addition to the AlN matrix.

4 Discussion and Interpretation of Results

The addition of BN in the AlN matrix modifies considerably the wetting behaviour of steels A and B. We observe contact angles of 110 and 120° at 1550°C, respectively, with AlN-BN, whereas in

Table 3. Corroded thickness of AlN-BN and AlN small bars after contact with liquid steel for 1 h (in mm)

Substrate	Pure AlN ¹ (d/d _{th} = 90%)		66% AlN-34% BN (d/d _{th} = 88%)		90% AlN-10% BN (d/d _{th} = 89%)
	1550°C	1650°C	1550°C	1650°C	1650°C
A	0.06	>0.2	0.01	—	<0.01
B	0.048	0.2	0.026	—	<0.01
C	0.02	0.19	<0.01	0.1	<0.01

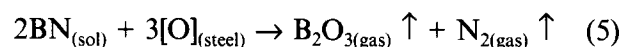
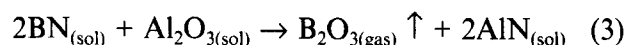
Table 4. Decrease in the solid-liquid tension of steels over AlN and AlN-BN substrates, at 1570°C, during the first 10 min

Steels	$\Delta\sigma_{SL}$ (mN m ⁻¹)	
	AlN ¹	AlN-BN
A	1000	300
B	2000	100
C	400	0

the case of pure AlN (89% densified) these angles were 50° and 40°. At a higher temperature, 1570°C, the same difference exists. The same effect is observed in the variation of solid-liquid surface tension, where the form of the curves in the two cases remains the same, while the value of $\Delta\sigma_{SL}$ varies (Table 4). These values can be assimilated approximatively as the free enthalpy of interaction at the solid-liquid interface per unit surface area ($\Delta G/S$).¹¹

The fact that the contact angle of liquid steels over the AlN-BN substrates varied slightly (Figs 1 and 2) with temperature and time appears to be paradoxical, if we only consider the reactivity of AlN,^{12,13} since in the AlN-steel systems the oxidation of the ceramic was the principal reason for the diminution of contact angle. To explain this behaviour we must consider the presence of BN and its reactivity with oxygen and alumina, which was certainly the origin of this non-wetting behaviour of steels. Compared to pure AlN, in the latter case, we have a competition between two chemical reactions:

- AlN oxidation through dissolved oxygen (1); and
- BN oxidation through alumina, the product of the AlN oxidation reaction (3).



Globally the reaction resulted in the oxidation of BN. Thus the intervention of BN takes place:

- during the sintering through reaction with Al₂O₃ and AlON, which gives AlN according to reaction (3), and cleans the grain boundaries;
- during contact with the liquid steel, where it consumes oxygen according to the global reaction (5) at the interface, and reduces the risk of AlN oxidation.

While eliminating the parasite secondary phases, boron nitride also eliminates the oxidation reaction at the interface and thus prevents the contact angle evolution.

We note also that the steels do not wet the AlN–BN ceramic and have relatively high values of σ_{LV} (1600 mN m^{-1}), which helps to avoid capillary penetration. Whereas, in the case of pure AlN, the steels have a wetting character which facilitates capillary penetration, while increasing the reactive surface. In all cases, these reactions give nitrogen and B_2O_3 at the given temperature. This phenomenon promotes the swelling of liquid drops, which is mentioned earlier. Another negative effect of these reactions is the appearance of porosity at the interface, which possibly helps the liquid to penetrate to new surfaces. Thus the quantity of BN should be sufficient to clean the grain boundaries, to consume the oxygen during sintering, but it should not be more than the required value, to avoid the formation of porosity as well as the liquid steel penetration. The results have helped us to determine an optimum value, which is 10% by weight.

AlN–BN samples prepared under these conditions show very little corrosion compared to pure AlN (Table 3). In the case of steel B at 1550°C , for example, we found through the dipping method, a corroded thickness of $60 \mu\text{m}$ for pure AlN and $10 \mu\text{m}$ for AlN–BN (34% BN) ceramic, whereas this value became almost zero for AlN–BN (10% BN).

5 Study of AlN–Carbon Mixture Behaviour Towards Steel B

5.1 Contract angle

The contract angle of steel B over AlN–C substrates depends upon the carbon content (expressed here in wt%). At 5% carbon, the contact angle remains constant and non-wetting ($120 < \theta < 140^\circ$) between 1540 and 1630°C . With 10% carbon, the contact angle decreases rapidly with temperature, its values were 110° and 70° at 1550°C and 1570°C , respectively.

With 20% carbon, the wetting angle decrease is still more important than in the second case. We found that the wetting starts just after 1550°C . At

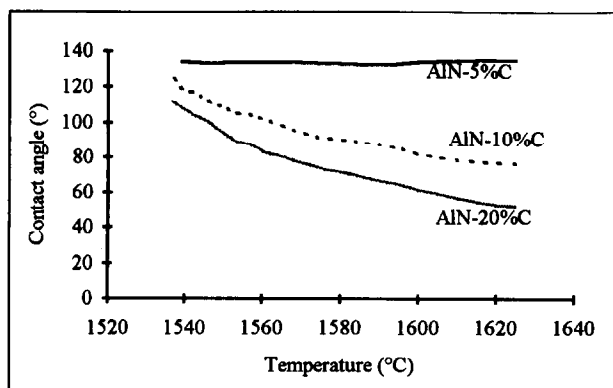


Fig. 5. Contract angle as a function of temperature.

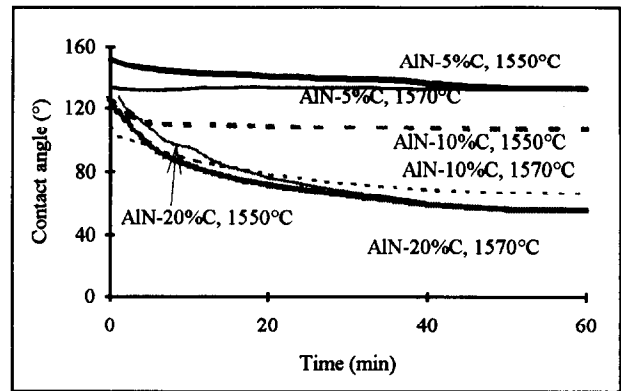


Fig. 6. Contract angle as a function of time.

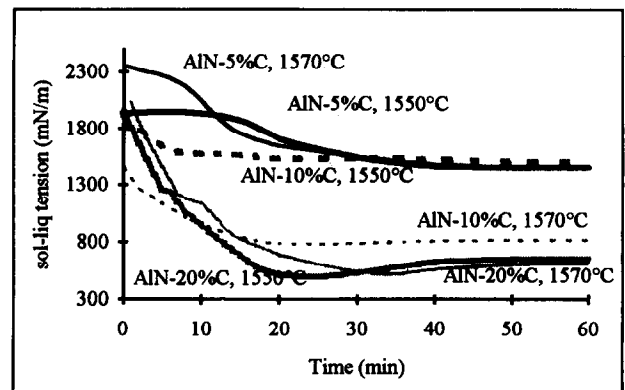


Fig. 7. Solid–liquid tension as a function of time.

constant temperature, the contact angle decreases rapidly during the first 10 min and then stabilizes at $\sim 60^\circ$ (Figs 5 and 6).

5.2 Solid–liquid surface tension

With 5% carbon the solid–liquid surface tension decreases with time and becomes constant after 40 min. The σ_{SL} curve for the compositions with 10 and 20% carbon passes from a minimum value, with respect to the temperature. This minimum is more important for higher concentrations of carbon. This type of behaviour is characteristic of a chemical interaction at the solid–liquid interface,¹¹ and is particularly important at higher carbon concentrations.

6 Interpretation of Results

Overall, whatever the carbon concentration may be, the contact angle remains superior compared to pure AlN or carbon (Table 5). In the case of pure AlN or C, the angle is controlled through chemical reactions at the interface:

- In the case of pure AlN, these reactions start by the decomposition of AlN and oxidation of Al through oxygen present in the steel and by a grain boundary attack on the AlON phases.¹
- In the case of pure carbon, the interaction takes

place by the dissolution of carbon in the steel, which promotes the formation of a low melting point liquid phase¹⁴ around 1200°C (whereas the melting point of steel B is 1515°C). This interaction is probably the origin of the contact angle evolution and the corrosion of the substrate through liquid penetration.

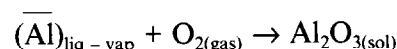
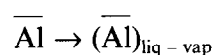
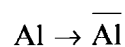
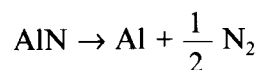
The decrease in the melting point of steel due to the carbon dissolution was still more important for higher carbon concentrations (Table 5).

Thus for carbon concentrations between 5 and 20% the dissolution of carbon in the liquid steel seems to be the cause for the contact angle decrease.¹¹ This dissolution locally reduces the steel and decreases the oxygen content in the steel, which in turn reduces or slows down the oxidation of Al formed during the decomposition of AlN. The corrosion in this case takes place by AlN dissolution in the liquid steel. This mechanism explains the decrease in the corroded thickness of the substrates having higher carbon concentrations, whereas the effect of this phenomenon over the contact angle is an inverse one because the angle is controlled by the carbon dissolution (Table 5).

EDAX microanalysis confirms that the steel which penetrated into the substrate is rich in aluminium and Raman spectrometry detects the presence of carbon flakes in the corroded thickness. The presence of carbon in the AlN matrix greatly modifies the corrosion behaviour of the substrate towards steel B compared to the substrate with pure AlN:¹

- (1) During sintering, as in the case of BN addition, carbon reacts with AlON phases releasing CO, stable at high temperature,¹⁵ which: (a) discourages densification during sintering, and thus a high porosity of 20% is obtained after sintering; and (b) eliminates the grain boundary attack when the substrate is in contact with liquid steel.
- (2) The oxygen in the contact zone is eliminated by its reaction with dissolved carbon, and the resulting CO produces a small reducing atmosphere around the interface, which avoids direct oxidation of AlN through dissolved oxygen.¹⁶
- (3) The only possible reaction is aluminium nitride

decomposition, and dissolution of aluminium in steel. This dissolution takes place without alumina formation, due to the absence of oxygen at the interface, but the formation of alumina takes place on the liquid drop surface:



The release of gas at the solid-liquid interface is due to the decomposition reaction (N₂) and also due to CO release, resulting from the reaction between dissolved oxygen and carbon. These gases promote swelling of the liquid drop and cavity formation at the interface, and result in the σ_{LV} values being superior to those pure iron.

7 Conclusions

The addition of BN or carbon in an aluminium nitride matrix improves its corrosion resistance qualitatively and quantitatively, against different types of liquid steel and against type B steel in the case of AlN-C substrates.

The mixtures AlN-BN and AlN-C give comparable results but through different mechanisms. In the two cases we eliminate the AlON phase from the grain boundaries during sintering, through a reaction between BN and AlON with B₂O₃ release in the case of AlN-BN and through a reaction between carbon and AlON with CO release in the case of the AlN-C substrate.

In both cases the wetting angle increases compared to that obtained with pure AlN substrate (particularly in the case of 5 and 10% carbon) and the grain boundary attack is largely reduced.

Finally, in the two cases we reduce the presence of solid impurities in the liquid steel, because the identified reaction at a given temperature gives: 1, volatile B₂O₃ for BN addition; and 2, gaseous CO in the case of C addition. Only in the case of carbon dissolution at high temperatures can the initial carbon content in the steel be modified.

The rapid and preferential consumption of BN and C during the reaction, helps us to optimize their concentration in the mixtures:

- The quantity of BN should be just enough to clean the AlN grain boundaries and to participate in the consumption of dissolved oxygen. The optimum value was found to be 10% by weight (Table 3).

Table 5. Influence of carbon content on corrosion of AlN matrix

wt% of C	T _m (°C)	Corroded thickness (μm)	θ (°)
0	1515	300	40
5	1515	550	140
10	1500	450	110
20	1490	150	65
100	1200	1000	60

- The optimum carbon quantity should be calculated while keeping in mind the decrease in corrosion due to carbon presence and the reactivity of carbon with steels. Values of 5–10% were found to be optimum considering the corrosion and wettability results.

References

1. Labbe, J. C. & Laïmeche A., *J. Eur. Ceram. Soc.* in press.
2. Labbe, J. C. & Jeanne, A., *Ceram. Int.*, **18** (1992), 81–4.
3. Turpin-Launay, D., Goeriot, P., Orange, G., Thevenot, F. & Fantozzi G., *Rev. Int. Htes. Tempér. Réfract. Fr.*, **20** (1983) 147–58.
4. Marty, F., Thesis of University of Limoges, 1988.
5. Rankel, F., *Z. Electrochem.*, **19** (1913) 361.
6. Ado, G., Bernache, D., Billy, M., Han, K. S. & Lefort, P., *Rev. Chim. Min.*, **22** (1985) 473–83.
7. Yefsah, S., Billy, M., Jarrige, J. & Mexmain, J., *Rev. Int. Hautes Temp. Réfract. Fr.*, **18** (1981) 167–72.
8. Labbe, J. C., Lachau-Durand, A., Laïmeche A., Paulyou, V. & Tétard, D., *High. Temp. Chem. Process.*, **1** (1992) 151–6.
9. Dalannay, F., Froyen, L. & Duruyttere, A., *J. Mater. Sci.*, **22** (1987) 1–16.
10. Chatain, D., Rivollet, I. & Eustathopoulos, N., *J. Chim. Phys.*, **83** (1986) 560–7.
11. Aksay, I. A., Hoge, C. E. & Pask, J. A., *J. Phy. Chem.*, **78**(12) (1974) 1178–83.
12. Lavrenko, V. A. & Alexeev, A. F., *Ceram. Int.*, **12** (1986) 25–31.
13. Podobeda, L. G., Tsapuk, A. K. & Buravov, A. D., *Sov. Pow. Met. Ceram.*, **15**(9) (1976) 696.
14. Anderson, J. C., Leaver, K. D., Rawlings, R. D. & Alexander, J. M., *Mater. Sci.*, 3rd edn. Van Nostrand Reinhold, UK, 1985, p. 268.
15. Richardson, F. D. & Jeffes, J. H. E., *J. Iron and Steel Inst.*, **160** 11 (1948) 261.
16. Mouradoff, L., Lachau-Durand, A., Demaison, J. & Labbe, J. C., *J. Eur. Ceram. Soc.*, **13** (1994) 323–8.

In-situ Synthesized TiB₂ Toughened SiC

G. J. Zhang,^a X. M. Yue,^a Z. Z. Jin^a & J. Y. Dai^b

^aChina Building Materials Academy, Beijing 100024, China

^bInstitute of Metal Research, Academia Sinica, Shenyang 110015, China

(Received 23 March 1995; revised version received 13 June 1995; accepted 28 June 1995)

Abstract

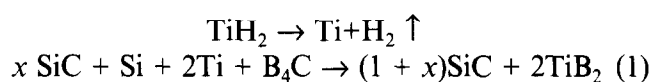
A new process of preparing SiC–TiB₂ particulate-reinforced composite by in-situ synthesis has been developed. TiB₂ particles were formed in situ by chemical reaction between TiH₂, Si and B₄C; the particle size of the TiB₂ is usually about 2 μm. The composite containing 30 vol% TiB₂ exhibited a fracture toughness of 6.21 MPa m^{1/2} and a flexural strength of 400 MPa. It was suggested that the main toughening mechanisms are the thermal residual stress field, crack bridging by TiB₂ particles and crack deflection around TiB₂ particles.

1 Introduction

SiC ceramics have many good properties and are prospective structural materials. But their low fracture toughness make them very sensitive to defects and less reliable. Prior studies found that by adding a second phase particle, such as TiC^{1,2} or TiB₂,^{3–5} into the SiC matrix, the strength and fracture toughness can be greatly improved. The above authors considered that the main toughening mechanism is crack deflection caused by the second phase particles via induced residual stresses. Taya *et al.*⁶ reasonably explained the experimental results by calculating and theoretically analysing the residual stress toughening mechanisms. Table 1 shows the main physical properties of TiB₂ and SiC.⁷

The above discussed SiC matrix composites were all prepared by directly adding the second phase particles. By internally synthesizing TiB₂, Tani and Wada^{8,9} obtained SiC–TiB₂ ceramic composites from the chemical reactions TiN + 2B → TiB₂ + 0.5N₂ ↑ and TiO₂ + 0.5B₄C + 1.5C → TiB₂ + 2CO ↑. This kind of processing avoids the difficulties of treating TiB₂ powders (owing to their slow reaction with water), and the internally synthesized TiB₂ particles are finer and more uniformly distributed. The reactant B simultaneously improved the sintering of the SiC matrix. Accord-

ing to the above reactions, there are gases such as N₂ and CO released in the reaction processes, which prevent sintering to some extent. So the following *in situ* chemical reaction was developed to internally synthesize TiB₂:



According to this reaction, when no extra SiC is added, the phase composition of the product is 28.89 vol% SiC and 71.11 vol% TiB₂, and the volume content of the second phase TiB₂ can be conveniently adjusted by adding extra SiC. This paper describes the effect of the TiB₂ content on the mechanical properties and the toughening mechanisms. The mechanism of the above reaction has been discussed elsewhere.¹⁰

2 Experimental Procedure

The raw materials were used as-received. They are α-SiC (6H) (particle size ~ 1 μm, BET specific surface area 7.5 m² g⁻¹, major impurity = oxygen at < 0.5 wt%), Si (≥ 99% phase pure, particle size < 45 μm) and TiH₂ (≥ 99.5% phase pure, particle size < 45 μm), B₄C (> 99% phase pure, particle size 5–8 μm). There were three composites, designated ST-1 (monolithic SiC), ST-2 (containing 15 vol% TiB₂) and ST-3 (containing 30 vol% TiB₂). According to the content of SiC, 1 wt% C and 1 wt% B₄C were added as sintering additives. After being ball-milled with a WC-Co media in alcohol for 4 h and dried, the mixed powders were hot pressed at 2000°C in Ar for 60 min under 30 MPa, and a disc of φ60 × 5 mm was then obtained.

The densities of the hot pressed specimens were obtained by liquid displacement. X-ray diffraction (XRD) was used to determine the phase composition of the fabricated bodies. The microstructure was examined by scanning electron microscopy (SEM), transmission electron microscopy (TEM) and HREM. Vickers hardness was tested at a load of 98 N. The fracture toughness K_{IC} was measured

Table 1. Properties of TiB_2 and SiC

Property	SiC	TiB_2
Density ($g\ cm^{-3}$)	3.21	4.52
Melting point ($^{\circ}C$)	2540*	2790
Thermal expansion coefficient ($\times 10^{-6}\ ^{\circ}C^{-1}$)	4.0	8.1
Poisson's ratio	0.14	0.28
Elastic modulus (GPa)	414	529
Vickers hardness (GPa)	25.5	34

*Decomposition temperature.

on bars ($2 \times 4 \times 20\ mm$) machined from the hot-pressed specimens by the SENB method (notch width $<0.2\ mm$, depth $\sim 1.6\ mm$, load speed $0.5\ mm\ min^{-1}$). The flexural strength σ_f was measured on bars ($3 \times 4 \times 36\ mm$) by the three-point bending method (span $30\ mm$, load speed $0.5\ mm\ min^{-1}$).

3 Results and Discussion

According to the XRD pattern of sample ST-2, as shown in Fig. 1 (to which that of ST-3 is similar) it can be seen that there are only phases of SiC and TiB_2 , and no other phase existed, indicating that the high temperature reaction was in accordance with reaction (1). The SiC formed from reaction (1) was β -SiC,¹⁰ but the starting powder of SiC was α -SiC, thus the SiC existing in the samples was a mixture of α - and β -SiC.

The relative densities of the hot-pressed specimens are shown in Fig. 2. It can be seen that the density was obviously improved by increasing the volume content of TiB_2 . The relative density of sample ST-3 was 99.33%, indicating the reactants simultaneously improved the density of the SiC matrix. Figure 3 shows the flexural strength and fracture toughness versus volume content of TiB_2 . It can be seen that the properties of sample ST-3 were relatively better; its fracture toughness was $6.21 \pm 0.59\ MPa\ m^{1/2}$ and fracture strength was $392 \pm 30\ MPa$. The 'lower' properties of monolithic SiC and sample ST-2 may be mainly due to their low sintering densities. So, the following discussion is based on the ST-3 specimen.

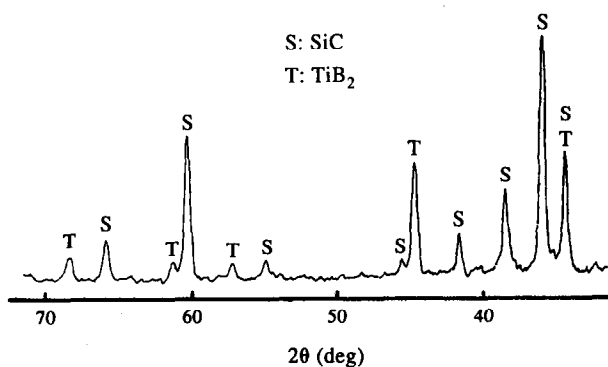


Fig. 1. XRD pattern of specimen ST-2 (CuK α).

Figure 4 is the TEM micrograph of sample ST-3. It can be seen that the particle size of TiB_2 formed *in situ* is $\sim 2\ \mu m$. Figure 5 is the HREM image of the interface between an *in situ* synthesized TiB_2 particle and the α -SiC matrix, which shows that the interface is 'clean' and free from any interfacial phase. Such a characteristic is attributed to the high surface energy of the newly formed TiB_2 by *in situ* reaction and indicates that

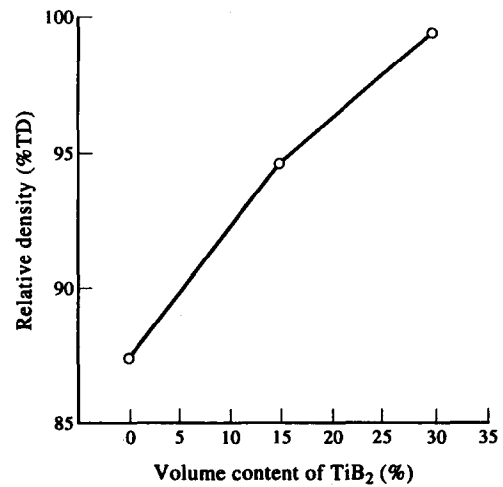


Fig. 2. Relative density of specimen versus volume content of TiB_2 .

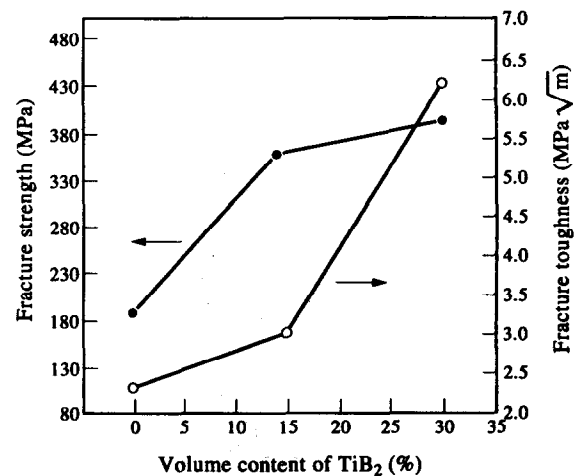


Fig. 3. Flexural strength and fracture toughness versus volume content of TiB_2 .

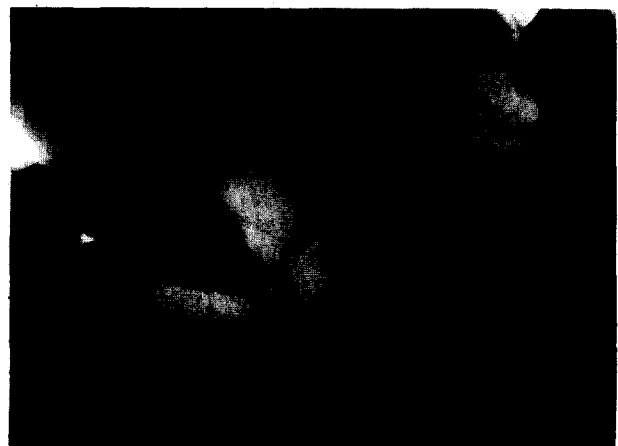


Fig. 4. TEM micrograph of sample ST-3. The dark phase is TiB_2 and the grey phase is SiC.

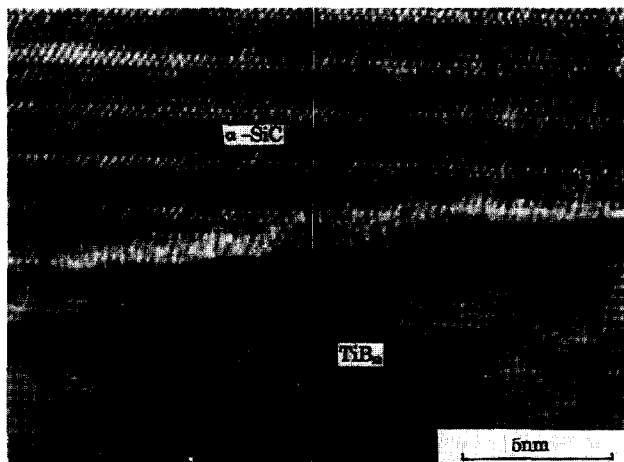


Fig. 5. HREM image of α -SiC– TiB_2 interface.

the second phase particles formed *in situ* directly connect with the matrix and the interfacial connection will be strong; which is markedly different from the weak TiB_2 –SiC interface of the composites produced by directly adding TiB_2 particles.^{4,11}

The mismatch between the linear thermal expansion coefficient (α) and elastic moduli (E) in the SiC matrix and the TiB_2 particle results in the generation of residual stresses in the particles and around the matrix (tensile residual stress and compressive tangential stress).¹ A crack would be expected to propagate in a direction parallel to the axis of the local compressive stress and perpendicular to the axis of the local tensile stress in the matrix surrounding the particle, which will induce crack deflection.

Figure 6 shows the crack interaction with TiB_2 particles on the polished surface of sample ST-3. It can be seen that the crack deflected around the TiB_2 particles and crack branching occurred. Figure 7 shows crack bridging by a TiB_2 particle at the crack tip. Because the interfaces between the *in situ* synthesized TiB_2 particles and SiC matrix are strong, TiB_2 particulate bridging is easily formed. According to the crack bridging toughening mechanism,¹² higher interfacial strength will induce a better toughening effect.



Fig. 6. Crack deflection by TiB_2 particles in sample ST-3.

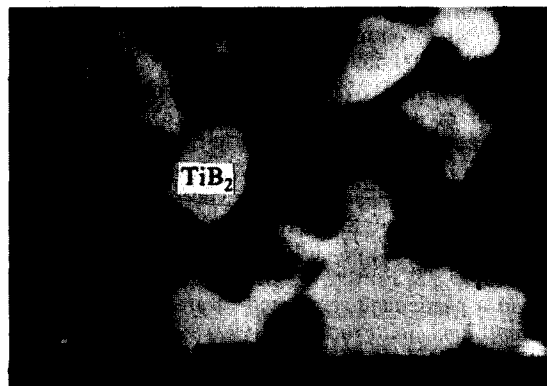


Fig. 7. Crack bridging by TiB_2 particle. The light-grey phase is TiB_2 and dark-grey phase SiC.

According to the calculation method proposed by Taya *et al.*,⁶ the calculated average residual stresses for the SiC matrix and TiB_2 particle in composite ST-3 are (using the data in Table 1 and setting ΔT , the temperature range over which stresses are not relieved, to be 1200 K):

$$\langle \sigma \rangle_{SiC} = -595 \text{ MPa}, \quad \langle \sigma \rangle_{TiB_2} = +1388 \text{ MPa}$$

This compressive stress in the SiC matrix will increase the fracture toughness according to the thermal residual stress toughening mechanism.⁶ As discussed above, it was suggested that the toughening mechanisms for the ST-3 composite were the thermal residual stress field, crack bridging by TiB_2 particles and crack deflection around TiB_2 particles.

4 Conclusions

- (1) TiB_2 can be synthesized *in situ* in a SiC matrix by the chemical reaction of TiH_2 , Si and B_4C . The particle size of TiB_2 is generally $\sim 2 \mu\text{m}$.
- (2) The reactant simultaneously improved the densification of the SiC matrix.
- (3) The fracture toughness and flexural strength of SiC–30 vol% TiB_2 were, respectively, $6.21 \pm 0.59 \text{ MPa m}^{1/2}$ and $392 \pm 30 \text{ MPa}$. The toughness was twice as high as that of monolithic SiC ceramics. It was suggested that the main toughening mechanisms were the thermal residual stress field, crack bridging by TiB_2 particles and crack deflection around TiB_2 particles.

References

1. Wei, G. C. & Becher, P. F., Improvements in mechanical properties in SiC by the addition of TiC particles. *J. Am. Ceram. Soc.*, **67** (1984) 571–4.

2. Li, B. W., Yano, T. & Iseki, T., High-temperature toughening mechanism in SiC / TiC composites. *J. Ceram. Soc. Jpn.*, **100** (1992) 509–13.
3. Janney, M. A., Mechanical properties and oxidation behavior of a hot-pressed SiC-15 vol% TiB₂ composite. *Am. Ceram. Soc. Bull.*, **66** (1987) 322–4.
4. McMurtry, C. H., Bcocker, W. D. G., Seshadri, S. G., Zanghi, J. S. & Garnier, J.E., Microstructure and material properties of SiC-TiB₂ particulate composite. *Am. Ceram. Soc. Bull.*, **66** (1987) 325–9.
5. Brett, R. L. & Bowen, P., Micromechanisms of toughening in a particulate reinforced ceramic matrix composite. *Ceram. Eng. Sci. Proc.*, **7/8** (1992) 99–107.
6. Taya, M., Hayashi, S., Kobayashi, A. S. & Yoon, H. S., Toughening of a particulate-reinforced ceramic-matrix composite by thermal residual stress. *J. Am. Ceram. Soc.*, **73** (1990) 1382–91.
7. Zhang, G. J., He, Y. & Jin, Z. Z., Study on SiC matrix composites reinforced with *in situ* synthesized TiB₂. *J. Chinese Ceram. Soc.*, **23** (1995) 134–40.
8. Tani, T. & Wada, S., SiC matrix composites reinforced with internally synthesized TiB₂. *J. Mater. Sci.*, **25** (1990) 157–60.
9. Tani, T. & Wada, S., Pressureless-sintered and HIPed SiC-TiB₂ composites from SiC-TiO₂-B₄C-C powder compacts. *J. Mater. Sci.*, **26** (1991) 3491–6.
10. Zhang, G. J., Jin, Z. Z. & Yue, X. M., Reaction synthesis of TiB₂-SiC composites from TiH₂-Si-B₄C. *Mater. Lett.* in press.
11. de Mestral, F. & Thevenot, F., Ceramic composites: TiB₂-TiC-SiC, Part I., Properties and microstructures in the ternary system. *J. Mater. Sci.*, **26** (1991) 5547–60.
12. Becher, P. F., Microstructural design of toughened ceramics. *J. Am. Ceram. Soc.*, **74** (1991) 255–69.

Liquid Phase Sintering of Silicon Carbide

F. K. van Dijen & E. Mayer

Jestettenerstrasse 6, 79802 Baltersweil, Germany

(Received 13 August 1993; revised version received 3 July 1995; accepted 14 July 1995)

Abstract

It is shown that the decomposition reactions during the sintering of liquid phase silicon carbide (SiC) can be described well by thermodynamics. This allows for an optimization of the sintering parameters. The use of carbon as a sintering additive, together with, for instance, yttria plus alumina, is of advantage. When C is used, SiO₂ will not occur in the liquid phase during sintering or in the amorphous and crystalline phases after sintering. The microstructure of sintered samples is described.

1 Introduction

Liquid phase sintered silicon carbide (LP-SiC) has the potential to become an alternative, commercially attractive, sintered SiC material, because it can be ('pressureless') sintered without a powder bed and because relatively cheap raw materials and sintering additives can be used. The literature on LP-SiC is scattered, with the main topics of interest being the sintering process, the microstructure of the sintered material and the resulting properties.^{1–16} References for the individual topics are indicated in the following paragraphs.

The most important factors which control the liquid phase sintering of SiC are: the specific surface area of the SiC powder, the sintering atmosphere (N₂ or Ar), the amount and composition of the liquid phase, the use of a powder bed, the sintering time, the sintering temperature and, of course, the processing methods used prior to firing. The usual sintering additives are alumina + yttria with an alumina:yttria weight ratio >1.¹ Typically 5–15 wt% of the sintering additives are used. The higher the amount of sintering additives, the higher the sintering rate.² Other sintering additives instead of yttria + alumina are: magnesia + alumina,³ other rare earth metal oxides + alumina,⁴ alumina,⁵ sialon⁶ or yttria + aluminium nitride.⁷

We carried out a literature survey, as well as experiments to verify the results presented in the

literature, resulting in an assessment of the state-of-the-art for LP-SiC, as presented below.

The sintering temperature in Ar is ~1900°C.^{3,4,8,9} The sintering temperature in N₂ is ~2100°C.^{1,4} We found a sintering time of ~2 h. A few per cent weight loss of the sample is always observed. We observed a higher weight loss upon sintering in N₂ than in Ar. We also observed more grain growth upon sintering in N₂ than in Ar. These phenomena can be explained by the higher sintering temperature required in N₂, compared to Ar. The use of closed containers and a powder bed reduces the weight losses.^{9,10} We observed that the material sintered in N₂ picks up ~1 wt% N and that weight loss is related to a reduction of the oxygen content of the material. A SiC powder with a specific surface area of >5 m² g⁻¹ has to be used; for instance a SiC powder with a specific surface area of 10 or 15 m² g⁻¹.¹¹ We found that the higher the specific surface area of the SiC powder, the higher the sintering rate. It was shown that good mixing of the SiC powder with the sintering additives is necessary. We discovered that CeO₂ is a cheaper but less effective sintering additive, compared to yttria. La₂O₃ proved to be a cheaper and effective sintering additive. By using La₂O₃ instead of yttria, one has to increase the sintering temperature in Ar by ~50°C.

The microstructure of LP-SiC is characterized by the absence of exaggerated grain growth and by a small average grain size.^{7,11,12} By annealing the sintered material, the grain boundary phase can be completely removed from the grain boundaries and crystallized at the triple points.^{8,11,12} By good processing, the presence of large pores can be prevented. Sintered densities of more than 3.15 g ml⁻¹ are obtained.

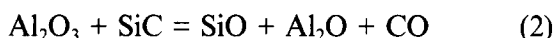
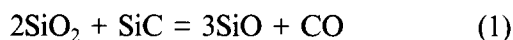
Compared to SiC sintered with B and C, LP-SiC has a strength which is twice as high.^{5,7,8,12} This high strength is related to the much higher fracture toughness and to a change from transcrystalline to intercrystalline fracture behaviour.^{5,8,10,12} We obtained a material with a K_{Ic} value of 6–7 MPa m^{1/2}, as determined by the indentation technique. The microhardness is ~26 GPa, which is

similar to that of SiC sintered with B and C. Little has been published on the properties of LP-SiC and the relations between the different microstructures and the properties.

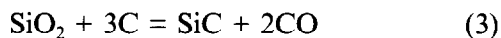
The goal of the present work is to optimize the processing and sintering of LP-SiC. The microstructures of the sintered materials that have been obtained are shown and discussed.

2 Theoretical Aspects

The liquid phase sintering of SiC in Ar is influenced by the phase relations between SiC and the sintering additives, for instance yttria + alumina, by the extent of wetting of the SiC by the liquid phase and by the solubility of SiC in the liquid phase. As will be shown, SiO₂ present as surface silica on the SiC powder plays a very different role in the sintering process compared to the surface silica on Si₃N₄ powder. There is competition between the sintering and decomposition reactions which result in weight losses. The most important decomposition reactions are:



Reaction (1) can be prevented by adding carbon, as in the sintering of SiC with B and C. By adding carbon the following reaction will occur:



To remove the 1 wt% oxygen present as surface silica on the SiC particles, one has to add 1.13 wt% carbon relative to the SiC powder. SiC powder typically contains ~0.1 wt% oxygen (m² g⁻¹)⁻¹.¹³ The changes in Gibbs free energy for reactions (1)–(3) are:

$$G^\circ_T = 384\,400 - 165.4 T \text{ (J)} \quad (4)$$

$$G^\circ_T = 1\,369\,700 - 551.6 T \text{ (J)} \quad (5)$$

$$G^\circ_T = 604\,000 - 339.4 T \text{ (J)} \quad (6)$$

The total gas pressure resulting from reactions (1)–(3) can be calculated from eqns (4)–(6). The results of these calculations are given in Table 1.

Table 1. Total gas pressure (in bar) as a function of temperature, according to reactions (1)–(3)

Temperature (°C)	Reaction					
	1	2	3	1*	2*	3*
1600	0.53	0.002	2.8	0.17	0.002	0.87
1800	0.96	0.038	18	0.30	0.030	5.7
2000	1.6	0.39	84	0.50	0.30	27
2200	2.4	2.7	306	0.75	2.2	97

*The activity of alumina is taken as 0.5 and the activity of silica is taken as 0.1.

For these calculations, the activity of the solids (SiC, SiO₂, Al₂O₃ and C) is taken as 1. One set of calculations is made with an activity for alumina of 0.5 and an activity for silica of 0.1, to allow for the case where an alumina–yttria–silica compound is the reactant instead of pure alumina or silica.

From Table 1 it can be seen that, from a thermodynamic point of view, reaction (3) is favoured over reaction (1). Reaction (2) becomes very important at temperatures higher than about 2000°C, which is the sintering condition in N₂. Reaction (2) will play a less significant role when the material is sintered in Ar, a process which is carried out at 1900°C. The addition of carbon should result in a significantly lower weight loss when the material is sintered in Ar because SiO should not be formed. The addition of carbon is also an advantage from the processing point of view, as it acts as a lubricant in shaping methods such as dry pressing and extrusion. From Table 1 it also becomes clear that some weight loss cannot be prevented, since reactions (1) and (3) will always occur (the total gas pressure is higher than 1 bar under the sintering conditions). This also shows that most, if not all, of the originally present silica will be lost from the sintered material. Reactions (1) and (3) must be allowed to finish before the pores close, otherwise large pores and even cracks may form in the sintered material.

The rare earth metal oxides seem stable, from a thermodynamic point of view, under the sintering conditions. However, magnesia seems less stable. When the material is sintered in N₂ the following reaction may occur:



Sintering in Ar is consequently favoured over sintering in N₂; the proper amount of carbon should also be used as a sintering additive.

The crucial aspect of the microstructure of LP-SiC, besides the absence of exaggerated grain growth, seems to be the presence or absence of a grain boundary phase. Such a phase would be expected to influence the oxidation resistance, the high-temperature strength, the creep resistance and the electrical conductivity of LP-SiC.¹⁴ As mentioned before, this grain boundary phase can be removed by an annealing process after sintering.^{8,11} Due to the absence of silica, crystalline phases are expected to form at the triple points, because silica is well known as the main vitrifying component.

3 Experimental Procedures

As SiC powder, UFB-10 from Lonza-Werke, Waldshut, Germany was used. This powder has a

specific surface area of $10 \text{ m}^2 \text{ g}^{-1}$ and contains ~ 1.0 wt% oxygen and 0.2 wt% aluminium. The yttria powder was from Sassoon, Brussels, Belgium, the alumina powder, type CS 400, from Martinswerk, Bergheim, Germany and the carbon black, type FW-18, from Degussa, Hanau, Germany. The SiC powder was mixed with the sintering additives in demineralized water using a polyurethane-lined grinder and sintered SiC media with a diameter of 3 mm. Dispersing agents (Triton X-100, Union Carbide, 3 wt% and triethanolamine, Merck, 2 wt%), an antifoam agent (SE-34, Wacker Chemie, 0.5 wt%) and a lubricant (polyethyleneglycol-400, Hoechst, 3 wt%) were also added. The percentages are relative to the SiC plus sintering additives. After mixing, the suspension was dried at 100°C overnight. The dried cake was broken in a mortar and screened over a 0.3 mm screen. The granulate was uniaxially pressed at 100 MPa and organic additives were removed by heating the tablets at 300°C for 8 h in air. The green density of the tablets after removal of the organic additives was 1.70 g ml^{-1} .

Next, the tablets were sintered in a closed graphite crucible, using the powder bed technique. The powder bed consisted of 61 wt% SiC UFB-10, 32 wt% BN, 3 wt% yttria and 4 wt% alumina. The other experimental conditions are listed in Table 2. After sintering the density and the weight loss of the sintered tablets were measured. The sintered tablets were cut, ground and polished using diamond tools. The Vickers microhardness was determined using a 100 g load. The polished samples were plasma-etched and the microstructure was

studied using SEM at the Max Planck Institut für Metallforschung, Stuttgart, Germany. This technique reveals the grain size distribution in the sintered material. The sintered samples were cut, thinned and investigated using TEM with EDX at the University of Technology, Zürich, Switzerland. This method shows, amongst other aspects, the presence of a grain boundary phase. Samples were observed after sintering with XRD to reveal the crystalline phases present.

4 Results

The results of the experiments are summarized in Table 3. They indicate that the density and microhardness are similar for all experiments. The tablets sintered in N_2 at 2100°C show a higher weight loss than the tablets sintered in Ar at 1900°C . The sample sintered in Ar with C as a sintering additive shows less weight loss than the sample sintered in Ar without C. The materials sintered in N_2 at 2100°C have larger grains than the material sintered in Ar at 1900°C .

Figures 1–4 show scanning electron micrographs of the sintered materials. A quantitative microstructural analysis revealed clear differences in average grain size between the samples (Table 3).

Table 2. Most important experimental parameters

Experiment	Composition (wt%)			Sintering time (h)	Temperature ($^\circ\text{C}$)	Atmosphere
	Y_2O_3	Al_2O_3	C			
1	4	6	1	2	1900	Ar
2	4	6	—	2	1900	Ar
3	4	6	1	2	2100	N_2
4	4	6	—	2	2100	N_2

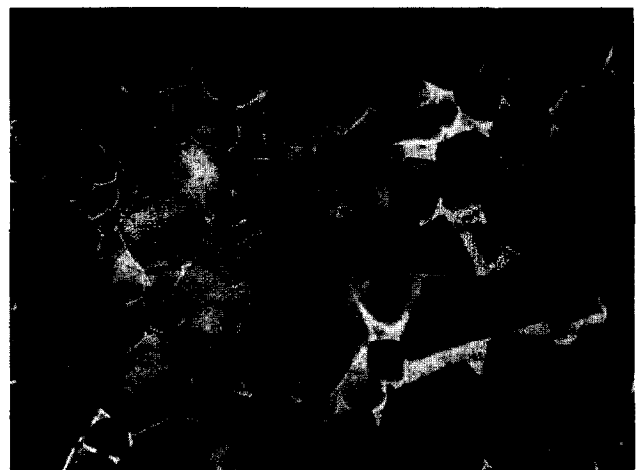


Fig. 1. Electron micrograph of sample 1, for material sintered with C in Ar at 1900°C . The length of the bar is $2 \mu\text{m}$.

Table 3. Results of experiments

Experiment	Weight loss (wt%)	Density (g ml^{-1})	Hardness (GPa)	Grain size (μm)	Average grain size (μm)	Second-phase material
1	2.5	3.20	26.4	<4	2.0	YAG Y-Al-O-C
2	3.5	3.18	26.4	<4	1.9	YAG Y-Al-Si-O
3	7.0	3.21	26.4	<6	3.4	Y_2O_3 , YAG AlN
4	7.5	3.18	26.0	<4	3.0	Y_2O_3 , YAG AlN



Fig. 2. Electron micrograph of sample 2, for material sintered without C in Ar at 1900°C. The length of the bar is 2 μm .

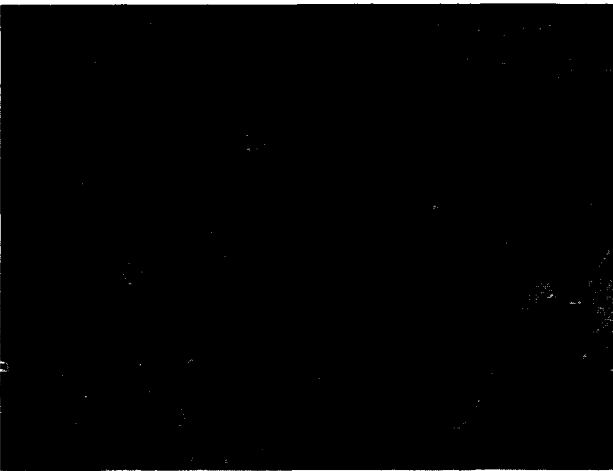


Fig. 3. Electron micrograph of sample 3, for material sintered with C in N_2 at 2100°C. The length of the bar is 2 μm .



Fig. 4. Electron micrograph of sample 4, for material sintered without C in N_2 at 2100°C. The length of the bar is 2 μm .

Figures 5–14 show transmission electron micrographs of the sintered materials. Figure 5 shows the rounded grains in sample 1. Figure 6 shows a triple point in sample 1. Note the poor wetting of the SiC grains by the second phase, as indicated by an angle between 50 and 80°. ¹⁴ The second



Fig. 5. Transmission electron micrograph of sample 1, for material sintered with C in Ar at 1900°C, showing rounded grains. The length of the bar is 3.1 μm .



Fig. 6. Transmission electron micrograph of sample 1, for material sintered with C in Ar at 1900°C, showing a triple point. The length of the bar is 120 nm.

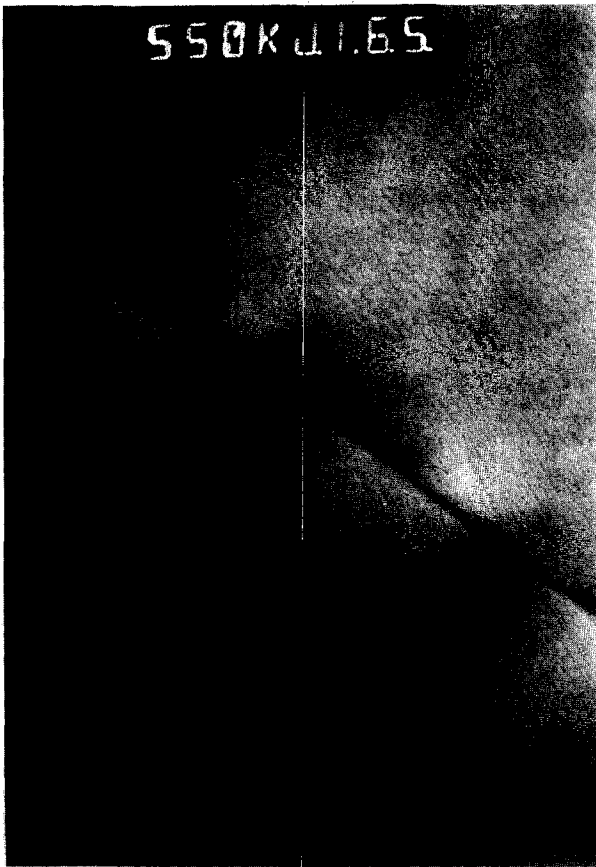


Fig. 7. Transmission electron micrograph of sample 1, for material sintered with C in Ar at 1900°C, showing the grain boundary phase. The length of the bar is 46 nm.



Fig. 9. Transmission electron micrograph of sample 2, for material sintered without C in Ar at 1900°C, showing a triple point. The length of the bar is 120 nm.



Fig. 8. Transmission electron micrograph of sample 2, for material sintered without C in Ar at 1900°C, showing rounded grains. The length of the bar is 3.1 μm .



Fig. 10. Transmission electron micrograph of sample 3, for material sintered with C in N_2 at 2100°C, showing SiC grains. The length of the bar is 3.1 μm .

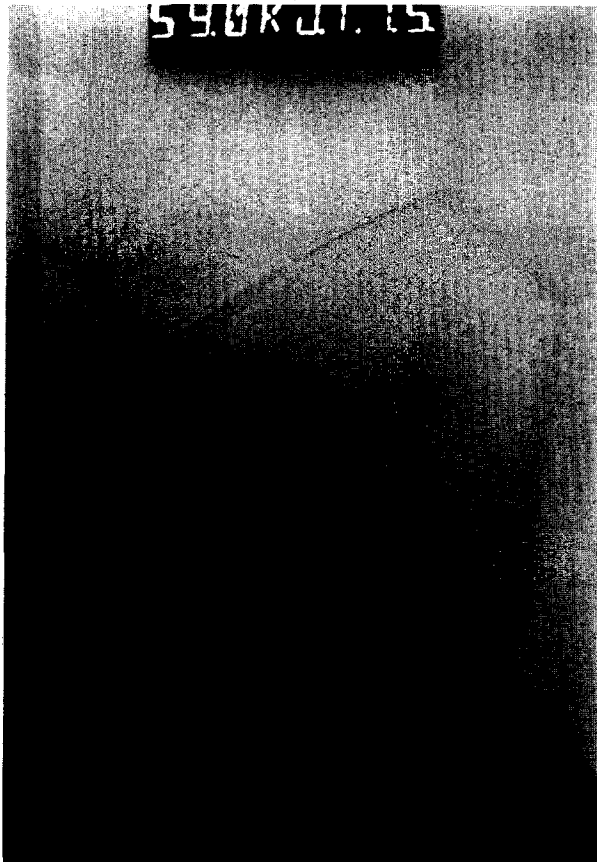


Fig. 11. Transmission electron micrograph of sample 3, for material sintered with C in N_2 at 2100°C , showing triple points. The length of the bar is 420 nm.



Fig. 13. Transmission electron micrograph of sample 4, for material sintered without C in N_2 at 2100°C , showing SiC grains. The length of the bar is $3.1\ \mu\text{m}$.

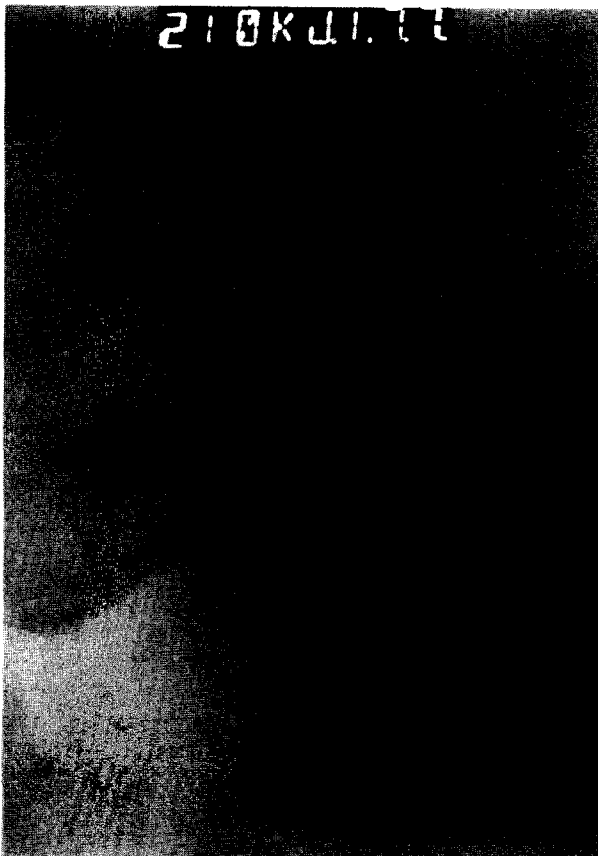


Fig. 12. Transmission electron micrograph of sample 3, for material sintered with C in N_2 at 2100°C , showing an inclusion at the grain boundary. The length of the bar is 120 nm.

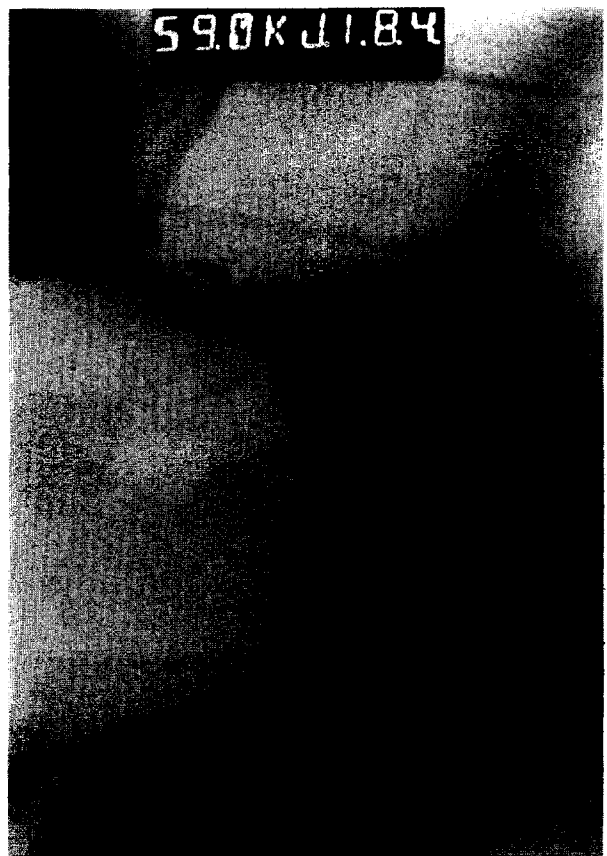


Fig. 14. Transmission electron micrograph of sample 4, for material sintered without C in N_2 at 2100°C , showing triple points. The length of the bar is 420 nm.

phase can partially penetrate the grain boundaries. EDX revealed that the second phase consists of Y–Al–O and Y–Al–O–C. This means that the second phase is free of Si or, more accurately, that the silicon content is lower than the detection limit of 3 wt%. Figure 7 shows a grain boundary in sample 1. No second phase is detected at the grain boundary.

Figure 8 shows the rounded grains of SiC in sample 2. Figure 9 shows a triple point in sample 2. Note the improved wetting of the SiC by the second phase, as indicated by an angle of 40–50°. EDX revealed that the second phase consists of Y–Al–Si–O. The silicon content is between 5 and 10 wt%, which is just above the detection limit. No second phase is detected at the grain boundary.

Figure 10 shows the SiC grains in sample 3. Note that some of the triple points contain a second phase, while other triple points are free from second-phase material. This is shown even better in Fig. 11. EDX showed that the second phase is yttria and Y–Al–O. No second phase is observed at the grain boundary. However, many small inclusions are observed at the grain boundary. EDX revealed that they are yttria and AlN. Figure 12 shows such an inclusion.

Figure 13 shows the SiC grains in sample 4. Except for the grain size, no differences between samples 3 and 4 are observed. Some of the triple points contain a second phase, while other triple points are free from second-phase material, as shown in Fig. 14. EDX showed that the second phase is yttria and Y–Al–O. No second phase is detected at the grain boundary phase. Some small inclusions of yttria and AlN are observed at the grain boundary. XRD performed on sample 2 showed the phases SiC and YAG.

5 Discussion

There is excellent agreement between the theoretical aspects and experimental results. When sintering in Ar at 1900°C, weight loss can be limited by the use of carbon as a sintering additive; very little aluminium vaporizes off. The use of carbon as a sintering additive has no negative effect on sintering rate or the microstructure of the sintered material. It is suggested that the liquid phase is free of silica when carbon is used as a sintering additive. Similar remarks hold for the crystalline phases after cooling of the sintered material. No amorphous phases were found in the material after sintering in Ar at 1900°C with C. Owing to the absence of silica, this is to be expected. Therefore, liquid phase sintering of SiC is more similar

to the sintering of AlN to the sintering of Si₃N₄. This is in agreement with the literature.¹¹

When sintering in N₂, AlN is formed and will dissolve in the SiC grains during sintering, as known from the phase diagram of SiC–AlN.⁷ Upon cooling the AlN leaves the SiC grains and precipitates at the grain boundaries.

By using a SiC powder with a specific surface area of 10 m² g⁻¹, mixed with 4 wt% yttria and 6 wt% alumina (sample 2), it is possible to sinter the material in a closed graphite crucible without a powder bed at 1900°C in Ar for 2 h with ~6% weight loss. This weight loss is generally acceptable.

Especially by using carbon as an additive, an interesting SiC material is obtained. The microhardness is 26 GPa, which is similar to sintered SiC prepared with B and C as dopants. The production costs of parts made from LP-SiC should be equal to those made of SiC sintered with B and C.

6 Conclusions

LP-SiC is an excellent material, especially when carbon is used as a sintering additive. Sintering in Ar at 1900°C is recommended. When C is used, the second phase is free of silica, crystalline and less weight loss during sintering is observed. The second phase is present at the triple points and no grain boundary or glassy phases are detected. Excellent high temperature properties are anticipated.

Acknowledgement

A grant from the EU is gratefully acknowledged.

References

- Omori, M. & Takei, H., *J. Am. Ceram. Soc.*, **65** (1982) C-92.
- Kostic, E., *Powder Metall Int.*, **20** (1988) 28–9.
- Trigg, M. B., Australian Patent 00518, 1990.
- Omori, M. *et al.*, US Patent 4 564 490, 1986.
- Suzuki, K., *Silicon Carbide Ceramics Vol 2*, eds S. Somiya and Y. Inomata. Elsevier Applied Science, London, 1991, pp. 163–82.
- Trigg, M. B., Australian Patent 00271, 1988.
- Böcker, W. D. G., European Patent 419271 A2, 1990.
- Hamming, R., Krüner, H. & Böcker, W., *J. Hard Mater.*, **3** (1992) 93–107.
- Mulla, M. A. & Krstic, V. D., *Ceram. Bull.*, **70** (1990) 439–43.
- Cutler, R. A. & Jackson, T. B., *Ceramic Materials and Components for Engines*, ed. V. J. Tennery. American Ceramic Soc. Inc., Columbus, OH, 1989, pp. 309–18a.
- Böcker, W. & Hamming, R., *Inter-ceram*, **40** (1991) 520–5.

12. Private communication with the Carborundum Company in Niagara Falls on Hexoloy SX.
13. Private communication within Lonza-Werke Waldshut on ultra-fine SiC powders.
14. Kingery, W. D., Bowen, H. K. & Uhlmann, D. R., *Introduction to Ceramics*, 2nd edn. J. Wiley and Sons, Inc., New York, 1976.
15. Komp, G., PhD Thesis, University of Technology, Berlin, 1991.
16. Cutler, R. A. *et al.*, US Patent 4 829 027, 1989.

Viscous Phase Sintering of Particle-Reinforced Glass Matrix Composites

M. Ferraris & E. Verné

Dipartimento di Scienza dei Materiali e Ingegneria Chimica, Politecnico di Torino, C.so Duca degli Abruzzi 24, I-10129 Torino, Italy

(Received 20 February 1995; revised version received 20 June 1995; accepted 28 June 1995)

Abstract

The aim of this work is the optimization of the sintering process of particle-reinforced glass matrix composites to obtain densities as close as possible to the theoretical value and improved mechanical properties in comparison with the parent glass matrix. A pressureless sintering process has been studied by means of heating-microscopy, differential scanning calorimetry and dilatometry on glass powders and mixtures of glass and reinforcement powders. The chosen glass matrix composites have the following compositions: (1) 5, 10 and 20 wt% Ti particle-reinforced ZnO–B₂O₃–PbO based glasses; and (2) 5, 10 and 20 wt% Ti particle-reinforced TiO₂–ZnO–B₂O₃–PbO based glasses. These glasses are suitable as 'model' glasses, but the method can be extended to any other matrix.

1 Introduction

Glass and glass-ceramic matrix composites (GMC, GCMC) are promising materials for structural and functional applications in the fields of automotive, aerospace and biomedical industries. They are low cost, low density, highly thermal and chemically resistant materials, compared with metal and ceramic matrix composites. The matrices are common silicate glasses or glass-ceramics, toughened by metal or ceramic fibres, platelets or particles.^{1,2}

One of the main drawbacks of these materials is the difficulty in obtaining full density bodies with low cost preparation techniques (e.g. pressureless sintering). In order to focus the subject of this work, the discussion will be limited to metal particle-reinforced GMC and the optimization of a pressureless sintering process.

There are several preparation processes for GMC and GCMC materials: firstly, 'green' bodies (i.e. not sintered) can be prepared by uniaxial or

isostatic cold pressing or slip casting methods. Then, there are three main sintering methods: greens can be sintered by uniaxial hot pressing or isostatic hot pressing or pressureless sintering. This last method is very attractive from an economical point of view as well as for its industrial feasibility; moreover, pressureless sintering allows the densification of larger and more complex shapes compared with expensive hot pressing or isostatic methods.

Due to the peculiarity of the glass matrix, these composites can be subjected to pressureless sintering in a viscous phase process (VPP), at temperatures well below the melting point and without any sintering aids. The key is to operate within the softening range of the glass and at the maximum temperature allowed *without any crystallization and with minimum viscosity*. The sintering time t is proportional to the ratio η/γ , as can be deduced from:

$$(x/a)^2 = (3/2)(\gamma/\eta)(1/a) t$$

where x is the neck radius between two particles, a is the particle radius, η is the viscosity and γ the surface tension of the glass, at the sintering temperature.^{3–10} A pressureless method is effective when the surface tension is high and the viscosity is low, i.e. when the glass is at its lower viscosity, without any crystallization process in action.⁵ If crystallization occurs, the process does not follow VPP behaviour, but other sintering theories come into play, e.g. solid or liquid phase sintering processes.

The presence of a second phase (metal particles, in this case) can interfere with the above described model: the second phase causes internal stresses in the matrix during the sintering process and the resulting sintering rate is decreased. This effect is less dramatic for the VPP of composites, because the internal stresses are almost completely absorbed by the matrix in the viscous state, but the sintering time and temperature should be *increased*

proportionally with the second phase volume fraction.⁶⁻¹⁰ The rule of mixtures does not work above 15–20% volume fraction; above this limit, the glassy phase is not enough to guarantee a pressureless viscous phase sintering process.^{6,8,11}

Furthermore, the presence of a crystalline second phase enhances the heterogeneous nucleation rate of the glass: as any crystallization during the sintering process is to be avoided,⁵ the best compromise between the highest sintering rate and the lowest crystallization level needs to be determined. Moreover, by operating at the lowest possible temperature, the interfaces will be less reactive and can be designed to fulfil the composite requirements: a good interface between reinforcement and matrix is the main factor in determining the mechanical behaviour of brittle matrix composites. A subsequent heat treatment can be done to 'ceramize' the matrix and to obtain a glass-ceramic matrix composite with a low percentage of residual glassy phase.

The aim of this work is to optimize the pressureless sintering of glasses and composites with various percentages of titanium particles as the second phase, by differential scanning calorimetry (DSC) simulation of the sintering process, to find out the maximum sintering temperature, without encountering crystallization of the matrix, for both glasses and composites. To verify the effectiveness of this method a morphological and microstructural characterization was performed, and some preliminary mechanical tests were carried out on samples with a higher density, as a check on the improved mechanical properties of the composites in comparison with the parent glasses.

2 Experimental Procedure

Two glass matrices have been prepared by melting mixtures of ZnO, B₂O₃, PbO and TiO₂. The molar compositions are shown in Table 1. The addition of TiO₂ to the glass matrix modifies the interface between the titanium particles and the glass.^{14,15}

The glasses have been powdered in a ball-mill and sieved to 100–140 mesh. Part of the powders were mixed with 5, 10 and 20 wt% of Ti particles (PlasmaTechnik, 99.99%) (sieved to 100 mesh). The thermal properties of the glass powders and of the mixtures of glass plus Ti were studied by means of heating microscopy (Leitz mod.II A),

Table 1. Mol% composition of the two glass matrices

Sample	ZnO	PbO	B ₂ O ₃	TiO ₂
ZPB	45	15	40	—
TZPB	45	8	40	7

dilatometry (Netzsch 402) and differential scanning calorimetry (Perkin-Elmer DSC 7). The linear shrinkage versus temperature of the two glasses has been measured by heating-microscopy on cubes of pressed glass powder (heating rate 10°C min⁻¹).

Isothermal heating of the powders (glasses and glasses plus titanium) has been carried out by DSC, in the range of temperature between T_g (glass transition) and T_{x1} (first crystallization) with a 10°C min⁻¹ heating rate, for 150 min under flowing Argon, in graphite crucibles. After the isothermal treatment, each sample was submitted to a scan in the temperature range 400–700°C to verify if the isothermal treatment has caused total, partial or no crystallization of the glass. The highest temperature after which the isothermally heated and scanned sample ('iso and scan' in the following text) still shows T_g and both crystallization peaks has been chosen as the maximum sintering temperature allowed for a viscous flow sintering process.

On the basis of this calorimetric study, a pressureless sintering process has been tested on greens of glass and glass plus Ti particles, under Ar flow. Greens have been prepared by uniaxial pressing, using pressures from 4 to 6 tons cm⁻², with the aid of liquid binders (isopropyl alcohol).

The sintered samples were characterized by X-ray diffraction (XRD, Philips PW 1710), scanning electron microscopy (SEM, Philips 525 M), compositional analysis (EDAX, Philips 9100), porosimetry (Carlo-Erba 2000 mod. 120), density measurements (Archimedean method) and mechanical tests: Young's modulus measurements (Grindosonic-Lemmens Elektronica), K_{IC} (indentation technique^{16,17}) and Vickers induced crack propagation.

3 Results

Table 2 shows the characteristic temperatures (°C) and the thermal expansion coefficients (10⁻⁶ °C⁻¹) of the two glasses, obtained by DSC and dilatometry, respectively.

Figure 1 represents the percentage linear shrinkage versus temperature for ZPB (a) and TZPB (b) greens, obtained by heating microscopy. The two glasses show rapid shrinkage above 500 and 550°C, respectively, and their crystallizations occur

Table 2. Characteristic temperatures (°C) and linear expansion coefficients (10⁻⁶ °C⁻¹) of the two glasses

Sample	T_g	T_{x1}	T_{x2}	α
ZPB	479	612	653	7.96
TZPB	523	625	650	5.02

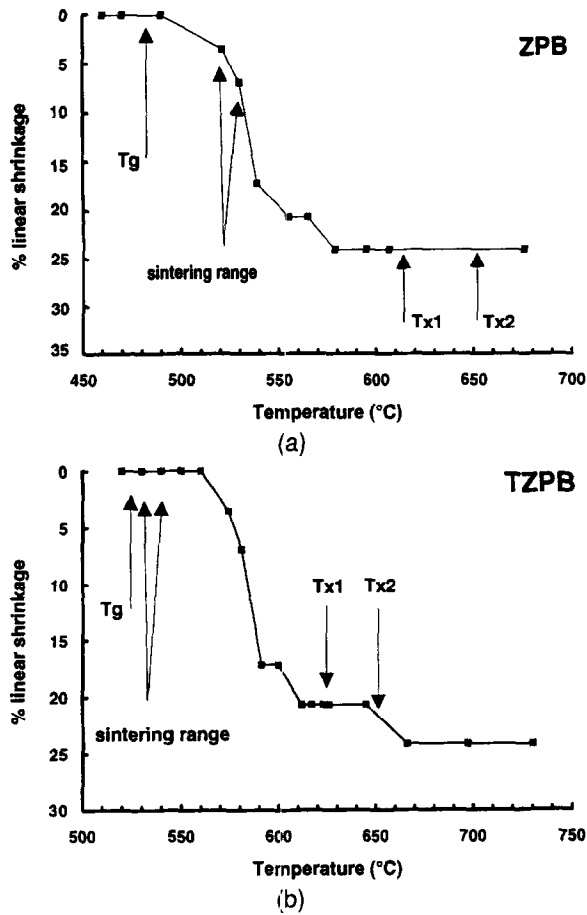


Fig. 1. Per cent linear shrinkage versus temperature for (a) ZPB and (b) TZPB greens (heating rate $10^{\circ}\text{C min}^{-1}$).

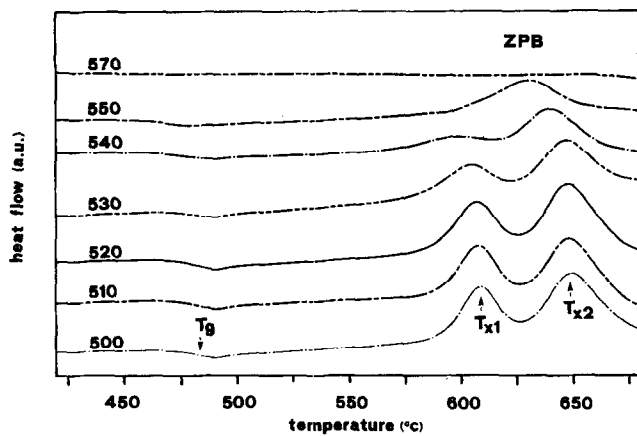


Fig. 2. DSC curves of 'iso and scan' ZPB (heating rate $10^{\circ}\text{C min}^{-1}$).

with any volume increase. The arrows refer to the characteristic temperatures (T_g , T_{x1} and T_{x2}) obtained by DSC and to the sintering temperature chosen after DSC 'iso and scan', as described below.

Figures 2–5 show the DSC curves of ZPB (Fig. 2), ZPBT20 (ZPB powders plus 20 vol% Ti) (Fig. 3), TZPB (Fig. 4), and TZPBT20 (TZPB powders plus 20 vol% Ti) (Fig. 5): each 'iso and scan' curve represent a DSC scan made on the same powder previously heated at the temperature labelled on the curve.

The DCS scans on ZPB samples after the

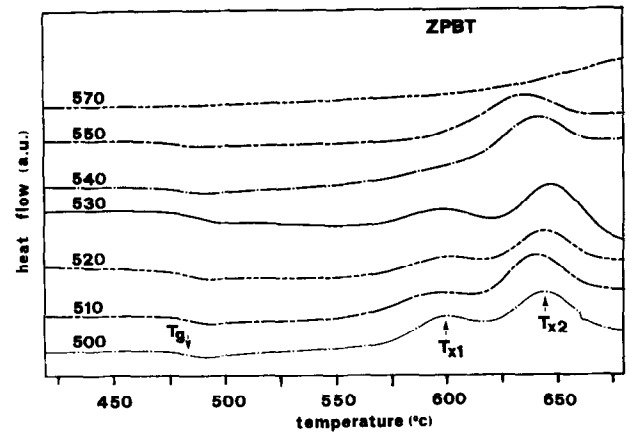


Fig. 3. DSC curves of 'iso and scan' ZPBT20 (heating rate $10^{\circ}\text{C min}^{-1}$).

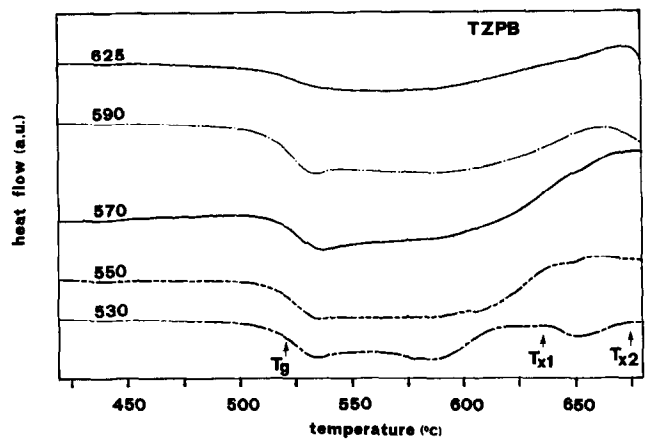


Fig. 4. DSC curves of 'iso and scan' TZPB (heating rate $10^{\circ}\text{C min}^{-1}$).

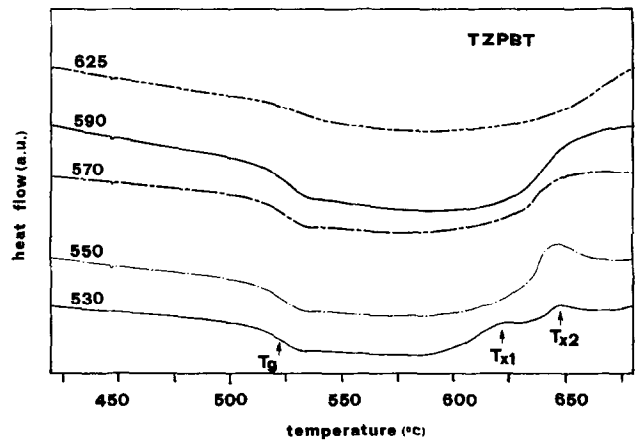


Fig. 5. DSC curves of 'iso and scan' TZPBT20 (heating rate $10^{\circ}\text{C min}^{-1}$).

isothermal heatings (150 min) at 510, 520 and 530°C (Fig. 2) do not reveal any difference from the DSC of the as-prepared glass.¹⁸ On the contrary, for the isothermal heatings at higher temperatures (from 540°C upwards), the DSC results are markedly modified: the two crystallization peaks and the T_g progressively disappear, up to the limit situation of the curve labelled 570°C, where only the melting temperature was detectable (above 700°C), which is not represented here.

Approximately the same behaviour has been found for the ZPBT20 composite (Fig. 3), where some modification of the 'iso and scan' occur from 540°C onwards.

The TiO₂ modified glass, TZPB, (Fig. 4) changes from the starting DSC 'iso and scan' curve from 550°C onwards, and the same has been found for the composite TZPBT20 (Fig. 5).

The following sintering temperature ranges have been chosen on the basis of the thermograms shown in Figs 2–5, as described above:

ZPB and ZPBT: 520–530°C
TZPB and TZPBT: 530–540°C

The composites have been sintered at temperatures about 10°C higher than the respective matrices. The per cent densities (measured density/theoretical density × 100) of the sintered glasses and composites are summarized in Tables 3 and 4. All the densities exceed 92%, with higher values for pure glasses and 5%-reinforced composites (98%) and lower values for 10- and 20%-reinforced composites.

SEM observations and porosimetric analysis confirm the density results. Figure 6 shows a polished cross-section of a ZPBT20 composite: the interfaces between Ti particles and the glass matrix are continuous and deflect a crack propagation obtained by Vickers indentation (at 5 kg; see arrows). EDS compositional results of the numbered zones are showed in Fig. 6 and its caption (1 = Ti, 2 = Pb, 3 = matrix). The values found for the glass matrix (45.4% Zn and 54.6% Pb) are in agreement with the theoretical ones (48.6% Zn and 51.4% Pb, calculated taking into account that EDS only detects metallic Zn and Pb in this glass and that the technique is semi-quantitative).

A similar behaviour pattern has been found for TZPBT composites, except for the Pb growth around Ti particles, due to a redox reaction between PbO and Ti (as described in Ref. 14).

XRD analysis on the sintered samples showed an amorphous background, with Ti and Pb signals for ZPBT composites and just Ti for TZPBT

Table 3. Densities of bulk and sintered glasses

Sample	Bulk	Sintered	% Density
ZPB	4.43	4.35	98.20
TZPB	4.02	3.94	98.34

Table 4. Theoretical and experimental densities of sintered samples

Sample	ZPBT			TZPBT		
	5	10	20	5	10	20
Theoretical density (g cm ⁻³)	4.43	4.44	4.44	4.04	4.07	4.12
Measured density (g cm ⁻³)	4.35	4.29	4.09	3.99	3.87	3.85
% Densities	98.2	96.9	92.2	98.8	95.1	93.4

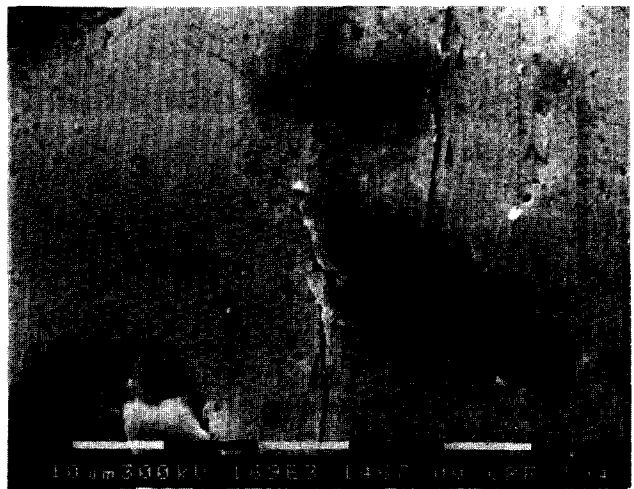


Fig. 6. SEM micrograph of ZPBT20 composite; showing induced crack propagation after Vickers indentation (1 = Ti, 2 = Pb, 3 = matrix).

ones. The XRD instrumental detection limit is about 5% crystallinity; which means that less than 5% crystals could be present in the samples, but would not be revealed by XRD. In fact, with another kind of analysis, scanning electron microscopy (SEM), some 20%-reinforced composites revealed the presence of a few crystalline phase (approximately below 5 vol%).

The Young's moduli (E) have been measured for the as-prepared bulk glasses (70 and 80 GPa for ZPB and TZPB, respectively) and for the sintered glasses and composites having comparable densities. The obtained values for the composites are in good agreement with the theoretical ones, calculated by the following equations:¹⁹

$$E_c = E_m E_p / (V_m E_p + V_p E_m) \quad (\text{lower limit})$$

$$E_c = E_m V_m + E_p V_p \quad (\text{upper limit})$$

where: $E_c = E$ of the composite, $E_m = E$ of the sintered matrix, $E_p = E$ of the Ti particles, $V_m =$ matrix volume fraction and $V_p =$ Ti particles volume fraction. The measured Young's modulus for the sintered ZPB is 61 GPa, and it is higher (62.5 GPa) for the corresponding composites having 5 wt% Ti particles (calculated lower and upper moduli for the composite: 62.45 and 63.37 GPa). It is 55 GPa for the sintered TZPB and 56.4 GPa for the 5 wt%-reinforced composite (calculated lower and upper moduli for the composite: 56.4 and 57.38 GPa).

The K_{IC} values (calculated as reported in Refs 16 and 17) for the sintered glasses are, respectively; 0.574 MPa m^{1/2} (ZPB) and 0.578 MPa m^{1/2} (TZPB). The K_{IC} value for the 5 wt%-reinforced TZPBT composite is about twice the matrix one: 1.027 MPa m^{1/2}.

4 Discussion

The ZPB glass matrix is a typical non-silica based 'soft' glass,^{12,13} chosen in this work for its low characteristic temperatures suitable for a DSC based study; the glass composition has been modified by adding 7 mol% TiO₂ to change the interfacial reactivity between the matrix and Ti particles in the composites, as discussed in a previous paper¹⁴ and in Ref. 15. The aim of this work is to find the suitable temperature range for a viscous-phase pressureless sintering process for glasses and composites: crystallization of the samples during sintering is to be avoided, otherwise the sintering temperatures should be increased and a certain pressure required to obtain full density; furthermore, the crystalline phases could have different expansion coefficients with respect to the matrix and cause cracks or voids in the sintered sample.

The first useful information about the sintering behaviour is given by the per cent linear shrinkage versus temperature (Figs 1(a) and (b)): ZPB and TZPB could be sintered from 575 and 650°C onwards, respectively (maximum value of % shrinkage). This information, the same as is obtainable by dilatometric studies, must be completed, for glasses, with other considerations: as indicated by the arrows, 575 and 650°C are very close to or above the crystallization temperatures (T_{x1} and T_{x2}). As the sintering process requires isothermal treatment of the sample at these temperatures, it must be pointed out that the sample will not be in the glassy state during the entire process, but is transformed to a partially or totally crystallized sample during the process. It must also be pointed out that a glass of the same system (ZnO–PbO–B₂O₃) starts with homogeneous surface crystallization after 1 h at 420°C.¹² The linear shrinkage versus temperature gives us initial rough information about the sintering behaviour, but it is not representative of the actual sintering process. In particular, it does not take into account the kinetics of crystallization: the maximum shrinkage temperature recorded with a heating rate of about 10°C min⁻¹ can not be immediately transferred to a sintering process which requires a prolonged isothermal step. During this time the sample could partially or totally crystallize. A more realistic way to simulate the sintering process could be to

consider several isothermal heatings at different temperatures inside the heating-microscope, but the choice of temperatures could require several time-consuming experimental runs.

The alternative way proposed in this work takes into account the high sensitivity of the DSC in detecting glass transition and crystallization in glasses: the 'iso and scan' method is more representative of the sintering process than a heating-microscopy or dilatometric study, it does not require the preparation of greens and it is very attractive from an experimental (runs versus time) point of view.

In order to know exactly if the sample is still amorphous or crystalline after an isothermal heating, the 'iso and scan' curves of Figs 2–5 are of immediate utility: if the 'iso and scan' curve shows any modification from the previous one, it means that something is happened during the isothermal heating at that temperature, so that temperature may be too high to sinter in a pure glassy state. This method also takes into account the nucleating effect of TiO₂ and of Ti particles in composites: in these cases, suitable temperatures to work in the glassy state must be lowered, because crystallization is favoured by the presence of these substances.

The nucleating effect of TiO₂ can be noted by comparing Figs 2 and 4 (ZPB and TZPB 'iso and scan' curves, respectively): the stability of the titania-containing glass matrix is decreased by ~100°C ($T_{x1} - T_g$). By comparing Figs 2 and 3 (ZPB and ZPBT 'iso and scan' curves, respectively), the nucleating effect of Ti can be noted by the decreasing crystallization onset in the composite with respect to the pure glass matrix. The same is true for Figs 4 and 5 (TZPB and TZPBT 'iso and scan' curves, respectively). Titanium particles also have an opposite effect: the sintering temperature of the composites must be increased with respect to the matrix one, proportionally to the volume fraction of the second phase.^{3–8}

The 'iso and scan' curves gave an immediate answer to sample modification (with or without a different percentage of second phase) during the sintering process. Figures 2–5 show the two extremes of behaviour (pure glass matrices and 20% Ti composites, the 5 and 10% Ti composites being similar to the former and latter case, respectively).

The chosen sintering temperature ranges, indicated by arrows in Figs 1(a) and (b) for ZPB and TZPB glasses, respectively, stress the above discussed differences between heating-microscopy and DSC study of the process: ZPB glass starts to sinter at 520–530°C, but it reaches its constant shrinkage values after 575°C. 'Iso and scan' curves for ZPB (Fig. 2) show that already, after an

isothermal heating at 530°C, the sample starts to show modifications from the glassy state. In fact, a pressureless sintering process at 520°C gave 98.20% density (Table 3), whereas higher sintering temperatures gave lower density values. Even more dramatic is the kinetic factor for TZPB (Fig. 1(b)) where, apparently, the DSC derived sintering range (530–540°C) is below the shrinkage curve slope onset temperature. In this particular case, the presence of a nucleating agent such as titania causes an early nucleation and crystallization during the isothermal heating of the glass, well below the recorded crystallization temperature onset! In this last case, as well as for the composites, the 'iso and scan' method revealed its effectiveness: TZPB sintered at 530°C showed the maximum density obtained (98.34%) (Table 3).

For the composites, the two opposite effects of Ti particles (the sintering temperature for the glassy state must be decreased because of its nucleating effect, but also increased because of its second phase effect) are clearly evident in Table 4: the 'iso and scan' method proved to be effective for 5 and 10% Ti composites, but fails at 20%. In this last case, 92–93% density is the maximum value obtainable by pressureless sintering in the glassy state: by increasing the sintering time or temperature, a partial crystallization of the samples has been observed. The process is not a VPP and the use of pressure could be useful to obtain a full density vitreous composite.

Obtaining high density composites allows their mechanical characterization, in order to verify their improved mechanical properties with respect to the matrix. Figure 6 shows a polished cross-section of a ZPBT composite (20% Ti): the Vickers induced crack (see arrows) is made to deviate by Ti particles (bridging). This energy-consuming mechanism is responsible for composite toughening, compared with the sintered glass matrix. In fact, the measured Young's moduli, as well as the calculated K_{IC} values, are higher for composites than for pure matrices, confirming that the interfaces between the matrix and reinforcements are continuous and act as a load transfer zone between the brittle matrix and ductile particles, leading to toughening of the material.

5 Conclusions

These first results let us show that pressureless sintering of glass matrix composites must occur in the glassy state; the sintering temperature must be chosen as high as possible to minimize the viscosity and the sintering time, *always being in the glassy state*. If any crystallization begins, the

viscosity of the system abruptly increases, and the sintering time and temperature must be prolonged and the use of hot-pressing techniques could be required to obtain fully densified samples. Furthermore, the use of higher temperatures is normally considered detrimental for interfacial reactivity and consequently for the mechanical properties of the composites (i.e. the formation of thick reaction layers between particles and matrix could occur).

The 'iso and scan' curves are an effective method to identify a sintering temperature range in the glassy state, taking into account some fundamental factors such as the decreasing sintering rate, and the nucleation effect of the reinforcement, as well as the kinetic contribution occurring during the sintering process.

Acknowledgements

The authors wish to thank Dr. P. Lemoine and Professor M. Montorsi for their remarkable scientific contribution and friendly collaboration, and FIAT Research Centre (CRF — Orbassano, Torino) for the SEM-EDS facilities.

References

1. Bleay, S. M. & Scott, V. D., Microstructure and micro-mechanics of the interface in carbon fibre reinforced Pyrex glass. *J. Mater. Sci.*, **26** (1991) 3544–52.
2. Hegeler, H. & Brueckner, R., Mechanical properties of carbon fibre-reinforced glasses. *J. Mater. Sci.*, **27** (1992) 1901–7.
3. Pastor, H., La cinétique du frittage sous pression. *Rev. Int. Hautes Temp. et Réfract.* (1972) 251–64.
4. Exner, H. E. & Petzow, G., Shrinkage and rearrangement during sintering of glass spheres. In *Sintering and Related Phenomena, Materials Science Research*, ed. Kuczynski. Plenum Press, New York, 1973, Vol. 6, pp. 279–93.
5. Panda, P. C. & Raj, R., Sintering and crystallization of glass at constant heating rate. *J. Am. Ceram. Soc.*, **72**(8) (1989) 1564–6.
6. Bordia, R. & Raj, R., Analysis of sintering of composite with glass or ceramic matrix. *J. Am. Ceram. Soc.*, **69**(3) (1989) C55–7.
7. Scherer, G. S., Sintering with rigid inclusions. *J. Am. Ceram. Soc.*, **70**(10) (1987) 719–25.
8. Rahaman, M. N. & De Jonghe, L. C., Effect of rigid inclusions on the sintering of glass powder compacts. *J. Am. Ceram. Soc.*, **70**(12) (1987) C348–51.
9. Jean, J. H. & Gupta, T. K., Liquid-phase sintering in the glass-cordierite system. *J. Mater. Sci.*, **27** (1992) 1575–84.
10. Fan, C. L. & Rahaman, M. N., Factors controlling the sintering of ceramic particulate composites: I. conventional processing. *J. Am. Ceram. Soc.*, **75**(8) (1992) 2056–65.
11. Dutton, R. E. & Rahaman, M. N., Sintering, creep, and electrical conductivity of model glass-matrix composites. *J. Am. Ceram. Soc.*, **75**(8) (1992) 2146–54.
12. Shinkai, N. R., Bradt, C. & Rindone, G. E., Elastic modulus and fracture toughness of ternary PbO–B₂O₃–ZnO glasses. *J. Am. Ceram. Soc.*, **65**(2) (1982) 123–6.
13. Rabinovich, E. R., Crystallization and thermal expansion

- of solder glass in the PbO-B₂O₃-ZnO system with admixtures. *Ceram. Bull.*, **58**(6) (1969) 595-8.
14. Ferraris, M., Badini, C. & Couzinet, B., Interfacial equilibria in titanium particle/glass ceramic composites. *Composites*, **25**(7) (1994) 494-8.
 15. Donald, I. W., Preparation, properties and chemistry of glass- and glass-ceramic-to-metal seals and coatings. *J. Mater. Sci.*, **28** (1993) 2841-86.
 16. Anstis, G. R., Chantikul, P., Lawn, B. R. & Marshall, D.B., A critical evaluation of indentation techniques for measuring fracture toughness: I, direct crack measurements. *J. Am. Ceram. Soc.*, **64**(9) (1981) 533-8.
 17. Breder, K., Zeng, K. & Rowcliffe, D. J., Indentation testing of an Al₂O₃/SiC whisker composite. *Ceram. Eng. Sci. Proc.*, **10**(7-8) (1989) 1005-13.
 18. Montorsi, M., Ferraris, M., Verné, E. & Lemoine P., Sintering of glass-ceramic matrix composites: an approach to the process optimisation. In *Proceedings of The 1995 IChemE Research Event*, ed. by the Institution of Chemical Engineers, Warwickshire, 1995, pp. 814-16.
 19. Callister, W. D. Jr, *Materials Science and Engineering, an Introduction*. John Wiley & Sons, New York, 1990.

Synthesis of Hydroxyapatite-Based Powders by Mechano-Chemical Method and their Sintering

M. Toriyama,^b A. Ravaglioli,^a A. Krajewski,^a G. Celotti^a & A. Piancastelli^a

^aInstitute for Technological Research on Ceramics of the Italian National Research Council, via Granarolo 64, 48018 Faenza (Ravenna), Italy

^bNational Industrial Research Institute of Nagoya (NIRIN), 1-1 Hirate-cho, Kita-ku, Nagoya-shi 462, Japan

(Received 18 April 1995; revised version received 28 June 1995; accepted 14 August 1995)

Abstract

Ceramic hydroxyapatite (HA) is on the way to gaining credit as one of the most promising and diversified materials for employment in surgery, thanks to its good characteristics of biocompatibility and bioadaptability. The main and probably unique deficiency of these materials obtained by traditional methods consists in its weak mechanical resistance, that does not allow their use when even low loading is involved. To improve the mechanical properties of HA-based ceramic bodies additions are normally necessary.

In this paper the authors propose a method to prepare powders and composite ceramic bodies with a matrix comprising HA. The powders are produced by the utilization of a simple and economic mechano-chemical method. The composite ceramic bodies are easily obtained by simple firing of the powders at a suitable temperature (1250°C). The powders, after sintering, give products that show a flexural strength of more than 100 MPa in standard samples. This value is significantly higher than that usually attainable with present commercially available powders (60 MPa). The transformation in the components (HA and β -tricalcium phosphate) of the composite ceramic arises from the nature of the powders, consisting of highly defective HA.

The mechano-chemical process is described together with the employed procedures specifically followed for reactive milling of starting powders. The preparation conditions of defective HA powders and properties acquired through such a method are reported. By this method an intimate mixing of β -tricalcium phosphate (β -TCP) inside the HA matrix is obtained that easily allows the preparation of ceramic bodies with reproducible properties, with no necessity for additions and mixing procedures, that could lead to inhomogeneity.

1 Introduction

Hydroxyapatite (HA) is the main inorganic com-

pound of hard tissues such as bones and teeth of vertebrate animals and humans. Consequently HA was readily considered as a bioactive material for artificial bone substitution because of its biocompatibility, and chemical and biological affinity with bone tissue. In the past many different methods were proposed to manufacture HA by chemical synthesis. Particular care was given to wet synthesis starting from separate precursor compounds containing Ca^{2+} and PO_4^{3-} , respectively (see, for example, Refs 1–4).

Many other methods of HA preparation were devised: in the search for an extremely simple one, for β -tricalcium phosphate (β -TCP)⁵ and then for HA, a new synthesis method based on dynamic grinding was developed. This method, applied to HA, is the subject of this work and allows us to synthesize a defective HA powder simply by wet-milling a mixed slurry of $\text{CaHPO}_4 \cdot 2\text{H}_2\text{O}$ and CaCO_3 . The amount of defects depends on the ratio of the reacting powders and on the physical condition of synthesis. A particular choice of these two physico-chemical conditions has led in the past to workers obtaining a calcium-deficient HA⁶ by a mechano-chemical method which, for crystallization by firing at $\sim 720^\circ\text{C}$, led to a total transformation in β -TCP.⁷ This initial work on HA synthesis showed that defective powders of HA can be easily obtained by mechano-chemical methods.

The principle on which dynamic synthesis during grinding is founded, relates to the energy provided by the impaction that mill balls exert on powder grains constrained towards the internal wall of the jar, making them react through the setting up of either an interdiffusion mechanism among different grains or intimate chemical reaction of molecules among themselves. The mechano-chemical method is based on the deep squeezing and crushing of powders in the limited surface area of the spherical segment adjacent to the contact point of any milling ball on the container wall (the jar). The physico-chemical conditions needed to

shift a chemical reaction towards the required products can be the change of two fundamental parameters: temperature and/or pressure.

In the mechano-chemical process no high variation of temperature is implied, but high values of pressure are reached by that fraction of powder caught between the wall of the jar and the contact area of each milling sphere. The pressure exercised on the bottom part of a cylindrical section of the rotating jar arises mainly by the load coming from gravity forces of all the balls that are arranged in this cylindrical section. Centrifugal force is not practically implied because of the low rotation speed. In order to start the reaction process, it is quite likely that a threshold pressure value should be attained, below which the reaction cannot occur.

In this work we synthesized defective HA by a mechano-chemical method with specific physico-chemical conditions, different from those of a previous paper,⁷ to obtain a non-calcium-deficient apatitic compound. The final target was to obtain defective HA-based powders mechano-chemically to give rise to an intimate HA/ β -TCP composite ceramic after sintering. To show the importance of the intimate powder mixture on the strengthening of the final ceramic material obtained, the deliberate addition of Al₂O₃ and SiO₂ was also carried out.

2 Materials and Methods

To produce HA, the starting materials were brushite (CaHPO₄·2H₂O) and anhydrous calcium carbonate (CaCO₃) powders. The reagents were selected from the commercial market (Carlo Erba, Milan). The milling device for the mechano-chemical reaction consisted of a Teflon jar and zirconia (ZrO₂) balls. For this study a milling jar made with Teflon was utilized because they are cheaper than zirconia ones utilized in previous papers⁵⁻⁸ and are easily produced 'in house'.

An 800 g batch of balls was utilized for the usual ball mill (280 r.p.m.), while 340 g were employed for the planetary ball mill. At the usual

ball mill, the milling process continued for 48 h, whereas for the planetary ball mill only 4 h are needed. The powders extracted from the mill were placed in a drying oven for a drying period of ~12 h at 90°C. The obtained powders were submitted to microcalorimetric examinations, to X-ray diffraction (XRD) and to infrared spectrometric (IR) analyses, after having fired them at different temperatures.

Table 1 summarizes the main operative parameters, that were chosen from among many experimental ones as those which brought the best results of bending strength of the manufactured ceramic samples prepared in a standardized manner using the obtained powders. All the powders were prepared maintaining a Ca/P molar ratio of 1.67. This table reports only a limited number of different powders, each one specifically coded, obtained under the different conditions described, including the most significant ones. In this paper the authors have used the die pressing method to prepare the samples in the physico-mechanical tests.

To test the quality of the obtained powders, bar-shaped samples were produced by the pressing method with all the synthesized powders: the pressing conditions were 444 kg_f cm⁻² applied on a 45 × 4 × 3 mm die. The bars were fired at temperatures between 1000 and 1400°C for 1 h. Flexural strength tests on the as-fired samples were performed by a four-point bending method (Instron 1195).

3 Results

A Teflon jar was employed to produce HA mechano-chemically synthesized powders for this work. It was observed that the synthesis with this kind of jar requires a time (48 h) twice that necessary when using the zirconia jar. The Teflon jar undergoes a certain degree of surface erosion during rotation. Most of it sublimates with pyrolytic decomposition over 400°C, as thermogravimetric analyses have shown. However no traces of fluorine were detected by micro-chemical analyses

Table 1. Preparation condition of hydroxyapatite powders

Powder code	Apparatus	Container jar material	Milling balls material	Milling time (h)	Introduced water (wt%)	Powder content of slurry (%)	Distinguishable phases by XRD*
A-2	Ball mill	Teflon	ZrO ₂	24	80	20	a-HA, DCPD, CaCO ₃
H0TP	Ball mill	Teflon	ZrO ₂	48	87	13	a-HA
D-1	Ball mill	Porcelain	Al ₂ O ₃	24	80	20	DCPD, CaCO ₃
C-4	Planetary ball mill	Teflon	ZrO ₂	4	80	20	a-HA
C-10	Planetary ball mill	Porcelain	ZrO ₂	3	80	20	a-HA, m-ZrO ₂ c-ZrO ₂ , DCPD

*a-HA = Large band peaks of hydroxyapatite; m-ZrO₂ = monoclinic zirconia; c-ZrO₂ = cubic zirconia; DCPD = CaHPO₄·2H₂O.

on the obtained powders heated over 600°C. Consequently, the calcination process must completely remove it. Teflon debris, if present, can be easily sieved off before any thermal treatment. The powders obtained after synthesis are characterized by low crystallinity, with XRD spectra that exhibit large band peaks (1° wide on a 2θ scale) clearly belonging to apatite alone. We have coded this quasi-amorphous or low crystalline system as *a*-HA. However, it is not possible to exclude the presence of other calcium phosphate-carbonate compounds in the amorphous state, which are not detectable by XRD analysis. This uncertain state goes on till about 600°C. The samples are characterized by a high specific surface area: after optimal calcination (700°C, 1 h) they appear perfectly crystalline but still extremely fine-grained (Table 2).

XRD analysis on powders calcined at different temperatures up to 1350°C allowed us to evaluate the crystallographic degree of purity of the obtained calcium phosphate system. By comparison of the overlapping peaks (0.2.10) and (217) having $d = 2.880 \text{ \AA}$ belonging to β -TCP with the $d(211) = 2.814 \text{ \AA}$ one belonging to HA, it was possible to calculate intensity ratios. By comparison with samples prepared by intimate mixing of β -TCP and HA in known proportions, it was possible to define the percentage ratios reported in the curve of Fig. 1. The trend for this curve is not constant

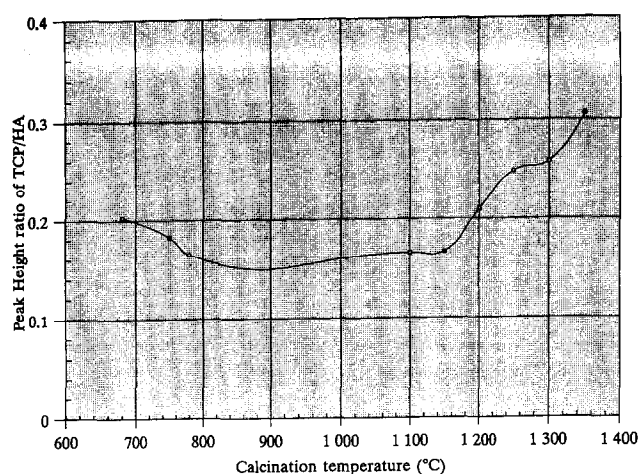


Fig 1. Relationship between XRD intensity ratios of TCP/HA and calcination temperature.

and the ratio β -TCP/HA changes with temperature. The minimum level of β -TCP arising from the heated mechano-chemical defective HA powders prepared for this work is exhibited, approximately, in the range 700–1160°C, as shown in Fig. 1. The minimum fraction of β -TCP is produced at 1150°C. The maximum amount of TCP was evaluated to be ~30% on powders heated at 1350°C.

On the same powders calcined at various temperatures, FTIR spectroscopic analysis was also performed: the IR spectra obtained at the most significant temperatures are reported in Fig. 2. As

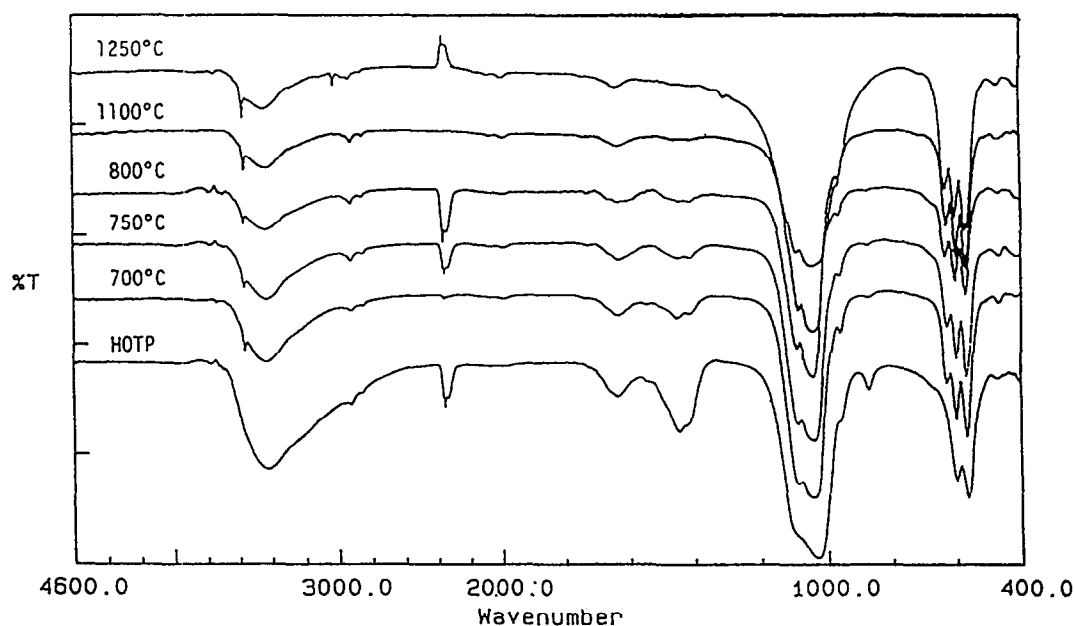


Fig. 2. IR spectra of mechano-chemically synthesized hydroxyapatite powders: starting powder and calcined powders at the most significant temperatures.

Table 2. Properties of H0TP powders prepared by mechano-chemical method, as obtained and after calcination (700°C, 1 h)

Calcination temperature (°C)	Specific surface area ($\text{m}^2 \text{g}^{-1}$)	Particle diameter (nm)	Distinguishable phases by XRD*
As prepared	168.8	< 12	<i>a</i> -HA
700	43.9	43	HA, β -TCP

**a*-HA = Large band peaks of hydroxyapatite; HA = hydroxyapatite; β -TCP = β -tricalcium phosphate.

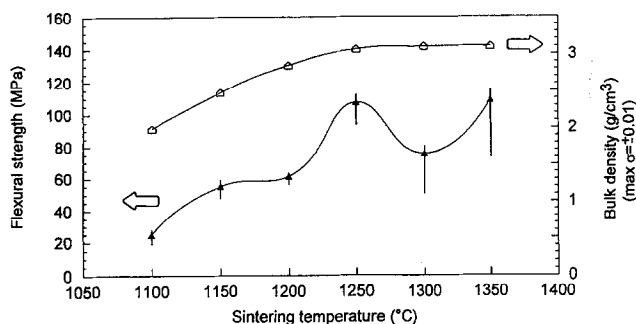
Table 3. Optimum synthetic conditions of production of hydroxyapatite H0TP powders by mechano-chemical method

Mechano-chemical reaction				
Apparatus	Milling media	Milling time (h)	Reaction temperature	Powder content of slurry
Teflon jar (70 × 100 mm)	Zirconia balls (15 mm, 800 g)	48 (280 r.p.m.)	Room temperature (25°C)	13 wt% CaHPO ₄ ·2H ₂ O = 14.413 g CaCO ₃ = 5.587 g H ₂ O = 150.000 g
Calcination conditions				
Calcination temperature (°C)		Calcination time (h)		
700		1		

we were interested in the mechanical properties of the ceramic bodies obtained using the proposed powders, an accurate determination of these was carried out to identify the specific conditions of preparation for the powders corresponding to the best results for mechanical resistance obtained on ceramized samples.

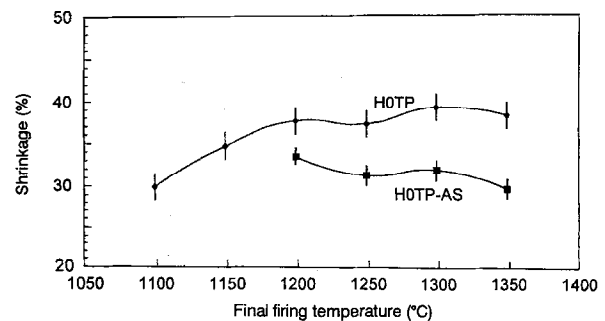
Among the systems examined, the best results were obtained using the raw material proportions and operative conditions reported in Table 3: the corresponding powder is that already coded H0TP in Table 1. The physical characteristics of H0TP powders are summarized in Table 2.

The density, mechanical strength and fracture toughness (Chevron-notched beam method) of samples produced by die pressing non-calcined

**Fig. 3.** Flexural strength and bulk density as a function of firing temperature.

H0TP powders are summarized in Table 4. Flexural strength and bulk density as a function of sintering temperature are also reported in Fig. 3. Shrinkage values at the different final firing temperatures are reported in Fig. 4.

Further experiments performed with the powders produced via the same mechano-chemical procedure, but employing porcelain jars according to the parameters of Table 1, surprisingly showed good results (Table 4; C-10). Since in the case of production of β -TCP in previous work,⁸ the addition of Al₂O₃ and SiO₂ was demonstrated to produce strengthening effects on the obtained ceramics, the supposition was made that valuable results obtained with HA samples ground in porcelain jars

**Fig. 4.** Linear shrinkage trend during sintering of green bars made with H0TP and H0TP-AS by die pressing until indicated final firing temperature.**Table 4.** Mechanical properties of mechano-chemically synthesized hydroxyapatite ceramics by die pressing

Powder code	Optimum sintering temperature °C	Flexural strength* (MPa)	Fracture toughness† K _{IC} MPa m ^{1/2}	Bulk density g cm ⁻³	Distinguishable phases by XRD (proportional intensity) [‡]
H0TP	1250	107.2	0.93	3.07	HA(80%), β -TCP(20%)
C-4	1300	35.3	—	2.41	HA(85%), β -TCP(15%)
C-10 [‡]	1300	101.6	1.71	2.95	HA(34%), β -TCP(66%)
H0TP-AS [§]	1250	130.4	1.64	3.04	c-ZrO ₂ , m-ZrO ₂ HA(13%), β -TCP(X7%)

*Four-point bending method.

†Chevron-notched beam method.

‡Contamination with 15 wt% ZrO₂, 15 wt% SiO₂, 9 wt% Al₂O₃ and 1 wt% K₂O (from jar release).

§Deliberate addition of 2 wt% Al₂O₃ and 6 wt% SiO₂ (no crystalline traces of either visible by XRD).

¶HA = Hydroxyapatite; β -TCP = β -tricalcium phosphate; c-ZrO₂ = cubic zirconia; m-ZrO₂ = monoclinic zirconia.

could come from aluminosilicates released by the container during the milling. Therefore experiments were performed with the deliberate addition of Al_2O_3 (Alcoa A-16) and SiO_2 (Cab-O-Sil M-5, CABOT Co., Ravenna, Italy).

The mechanical properties measured for all these samples are shown in Table 4: the maximum value of flexural strength was found for a sintering temperature of 1250°C and for addition of 2 wt% Al_2O_3 and 6 wt% SiO_2 . In this case, however, a body similar to 'vitreous porcelain' with poor mechanical properties is obtained at 1350°C , and a very large degree of transformation to β -TCP was observed. A marked reduction of mechanical properties is also shown by the samples made with H0TP powders fired above 1350°C .

4 Discussion

The variations in the mechanical properties of the obtained ceramics for the various operative conditions for manufacturing the powders mechano-chemically is the basis of the supposition of a close cause and effect connection between starting conditions (and amount of defects) in the preparation of HA powder and final mechanical properties of the resulting ceramics. Among the possible variables that could play a role in determining the physical state under which the mechano-chemical process is carried out, there are the dimensions and the nature of the milling balls.

In the case of using Al_2O_3 balls as the grinding medium, $\text{CaHPO}_4 \cdot 2\text{H}_2\text{O}$ does not react with CaCO_3 (Table 1, D-I). The authors have formulated the hypothesis that with parity of dimensional (radius) distribution of the milling balls, the specific gravity of those made with Al_2O_3 (3.96) is not sufficient to reach the above mentioned threshold pressure that is reached when using ZrO_2 balls, with their higher value of density (6.05). Moreover, despite the large number of attempts to modify the dimensional distribution of Al_2O_3 balls, the expected reaction was never achieved. H0TP powder proved to be the most suitable for giving rise to ceramic bodies with high mechanical performance. Therefore the discussion deals mainly with this type of powder.

IR spectra analysis carried out on H0TP powder heated at various temperatures suggests that large levels of CO_3^{2-} groups are involved in the lattice of this defective HA, mainly instead of PO_4^{3-} at this site. This content of CO_3^{2-} inside HA strongly decreases towards 1250°C . With respect to OH^- groups, taking into account the limited decrease in intensity of their indicative peaks, it does not seem that they undergo an easy condensation

process leading to H_2O elimination, at least up to 1250°C (Fig. 2).

The calcinated H0TP powder contains some fractions of β -TCP; nevertheless its Ca/P atomic ratio is always 1.67, not far from the theoretical value of pure stoichiometric HA, a value imposed by the chosen ratio of the raw materials in the synthesis of H0TP powders. Whereas an increasing trend in mechanical properties is exhibited by the ceramic samples fired at increasing temperatures, a loss of mechanical properties is observed in the range of firing temperature from 1250 to 1350°C , a change not justified by the evolution of the corresponding density of the obtained ceramics (Fig. 3). This mechanical 'failure', shows a minimum centred at 1300°C , when flexural strength values are larger for both lower and higher sintering temperatures. Such 'failure' cannot be ascribed to accidental or random causes because many series of measurements on many sets of samples confirm this trend. On the other hand it cannot be ascribed to a failure in the density of the material (Fig. 3). The same correlation could be identified in the trends of mechanical properties (Fig. 3) and shrinkage after firing (Fig. 4). One drawback is that the associated standard deviation (σ) hides the observed fluctuations of shrinkage with temperature.

To justify the surprising existence of this mechanical 'failure' in a temperature range where maximum values were expected, a variety of concomitant reliable physical circumstances can be considered: (a) intergranular phases; (b) grain growth; (c) diffusion effects; (d) release of gaseous components; (e) phase transformation of phosphate compounds; (f) chemical transformation of phosphate compounds; (g) a trend towards alignment and epitaxial rearrangement of crystallographic planes belonging to adjacent grains; (h) mobility of defects and vacancies; and (i) micro-porosity distribution. Those factors related to (a), (b), (d), (e) and (i) are certainly adverse to sintering, making the ceramic product brittle. Those reported in (g) and (h) tend, on the contrary, to favour hardness and mechanical toughness. With regard to the problem of diffusion effects (c), this can contribute to the stabilizing of the crystal lattice by arranging the different ionic species in energy levels as low as possible and helping intergranular phase reabsorption, which usually increases below 1300°C , while enormously decreasing above this.

The intergranular phase reabsorption is probably in equilibrium with the defects and vacancies of HA, which would justify the observed trend of the TCP/HA ratio of Fig. 1. This equilibrium is possible because of the intimate contact and distribution of the arising β -TCP that is largely

expected to become part of the intergranular phase, just for this invoked mechanism. Control of the kinetics of this equilibrium is performed by the circumstances reported in points (g) and (h). For each temperature a 'best intergranular composition' exists. A contribution to the amount of microporosity and intergranular cavity reabsorption is also expected from the presence of this equilibrium which, on the other hand, is adversely influenced when other equilibria take place concerning, for example, phase transformations to other phosphate compounds and crystalline phases, mainly concerning the $\beta \rightarrow \alpha$ change of TCP (Table 5) that takes place starting from about 1180°C for pure β -TCP.⁷

Taking into account the non-negligible presence of β -TCP in heated synthesized powders, α -TCP could play a very important role in determining the mechanical 'failure' in the observed range of temperature (Fig. 3) due to the involved molecular volume increase, and consequent microcrack formation due to the back-transformation to β -TCP during cooling of the ceramic body of a fraction of α -TCP, that leads to some grain-grain detachments. The shift towards higher temperatures of formation of the first significative amount of α -TCP inside these samples (Table 5) is probably due to the interference brought about by the mentioned equilibrium.

By increasing the sintering temperature, the amount of intergranular phase decreases, while simultaneously the grains grow and the diffusion effects are enhanced. The decrease in intergranular phase and in diffusion phenomena tends to favour mechanical strength, while grain growth is adversely affected. Phenomena at points (g), (h) and (i) increase with sintering temperature and therefore mechanical strength is promoted more and more. Those at points (d), (e) and (f) play an adverse role at the temperatures of their respective occurrences.

Considering the involved phenomena overall, among the favourable and adverse ones, competition would arise, and one can think in terms of results characterized by one or more maximum and minimum in mechanical strength with respect to temperature. Since most phenomena bringing

collapse of the mechanical properties (mainly phase and chemical transformations) occur in the temperature range between 1150 and 1300°C, the presence of the above mentioned mechanical 'failure' just inside this interval is justified. The corresponding temperature value (and those of the two related maxima) can vary according to the nature and morphology of the powders, and the specific HA composition and eventual presence of other concomitant compounds.

The formation of such a 'failure' (or discontinuity in the mechanical strength behaviour as a function of sintering temperature) is however by no means new, as there was observed, on different HA powders in the past, the existence of a maximum in mechanical resistance at 1230°C, followed by an inversion in this tendency at higher temperatures (at least up to 1250°C).⁹ The temperature range between 1150 and 1250°C was then considered critical: it was stated that in such an interval the main part of the HA transformations occurred. The transformation hypotheses in the literature are manifold and forecast the formation of other calcium phosphates, mainly pyrophosphate and tricalcium phosphate.¹⁰⁻¹² Different types of pyrophosphates were proposed by Newesely,¹³ while recent investigations¹² showed that HA at the highest temperatures decomposes with the formation of TCP and $\text{Ca}_4(\text{PO}_4)_2\text{O}$.

Moreover, the formation of oxyapatite was supposed, while others had mainly described the transformation as being a consequence of hydroxyl group release. In particular, it was hypothesized that in dehydration by hydroxylic condensation, the final material could be considered as an oxyhydroxyapatite with vacancies related to hydroxyl sites.¹⁴

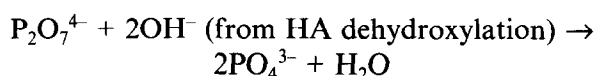
From firing experiments on various types of HA powders, it was observed that in such a temperature range unpredictable transformations can occur, often not revealable by XRD, and in some cases with the formation of different phases. This could depend first of all on HA stoichiometry (the content in replaced ions, CO_2 , H_2O , etc.), and moreover on the presence, even in extremely reduced quantities, of other phosphate phases which could induce a trend towards one or another phosphate

Table 5. Per cent molar proportions of calcium phosphate compounds present inside the ceramic bodies made with H0TP powders at different firing temperatures, after cooling at room temperature

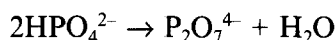
Phase (mol%)*	Firing temperature (°C)					
	1100	1150	1200	1250	1300	1350
HA	85	85	83	80	76	73
β -TCP	15	15	17	20	20	20
α -TCP	0	0	0	0	4	7

*HA = Hydroxyapatite; β -TCP = β -tricalcium phosphate; α -TCP = α -tricalcium phosphate.

species, to be formed in the transformation. Consequently physical and chemical parameters and conditions are important in imprinting on the starting powders the physico-chemical characteristics that greatly influence the obtainable sintered products. Moreover, an investigation performed by some of the authors on commercially available HA powders,¹⁵ showed evidence that many HA 'raw' materials contain, in general, 1–5% of $\text{Ca}_2\text{P}_2\text{O}_7$ in crystalline phase, easily disclosed by XRD. The presence of pyrophosphate can induce the reaction:



with subsequent β -TCP formation, that can already occur at temperatures between 650 and 750°C.¹⁶ On the other hand, defective HA that may contain HPO_4^{2-} can also undergo the following transformation:



which comes to the previous reaction and consequently represents a possible example of the above mentioned equilibrium between β -TCP and defects or vacancies of HA grains.

The dehydroxylation of HA already begins to take place in the temperature range 850–900°C. At lower temperatures it does not interfere with sintering, while at higher temperatures (above 1150°C) it hinders sintering and causes the decrease in density, flexural strength and hardness of the obtained sintered compact ceramics. Knoop hardness of sintered HA shows a maximum of ~2000 MPa near 1130°C, while at lower and higher temperatures it quickly falls to ~480 MPa.¹⁷ Similar behaviour is exhibited by flexural strength (Fig. 3).

In the H0TP powders, prepared in the present work, large chemical transformations are not identified except that deducible from IR spectra, which should produce HA through a CO_2 releasing reaction, besides the parallel one of hydroxyl condensation. In previous work on β -TCP,⁷ an optimum sintering temperature of β -TCP powders synthesized by a mechano-chemical method was decreased some 50–100°C lower than that of β -TCP powders obtained by another synthetic methods. But a similar effect was not found in powders synthesized in this work by the mechano-chemical method, in spite of the particle diameter of the grains of the powder being smaller than that of β -TCP. For samples of β -TCP calcined over 720°C, the absorption peaks of CO_3^{2-} completely disappeared.⁶ On the other hand, even if the calcination temperature was increased above 800°C, these peaks remain in the case of HA powders. IR absorption peaks gradually tend to become sharper

with increase in temperature, except for a broadening between 1100 and 1250°C, which clearly indicates lattice deformations in the calcined grain mass.

Experiments performed with Al_2O_3 and SiO_2 additions show that for particular relative proportions of these compounds, good mechanical results are obtained, partially due to the formation of aluminium phosphate (with satisfactory mechanical properties). No crystalline phases were observed by XRD analysis of compounds containing these two added oxides. The supposition that aluminium phosphate is involved comes from the literature.⁸ However their presence widely shifts the above-mentioned equilibrium existing between β -TCP and defective HA, as shown by the resulting per cent proportion of these in Table 4 (H0TP-AS samples), compared to the untreated ones (H0TP samples). In this case a very high amount of β -TCP arises at the expense of HA, and evidently the additions play a different role with respect to that involved when the matrix is completely made up of β -TCP only.⁸

Everything considered, we can pick out the temperature of 1250°C as the best for sintering H0TP powders to obtain the maximum mechanical resistance. This temperature is the same for powders with additions of Al_2O_3 and SiO_2 . The temperature of 1250°C is chosen to produce ceramic bodies since it was revealed to be the maximum limit before formation of α -TCP. The corresponding values of fracture toughness (K_{IC}) of ceramics made with H0TP powders are shown to be practically equal to that of ceramic samples prepared with conventional powders. The fracture toughness of ceramics made with H0TP-AS powders (containing Al_2O_3 and SiO_2) are shown to be higher, probably influenced by close cohesion between the matrix and foreign compound grains. Having ceramic materials with practically only a microcrack propagation step, from the K_{IC} value of ceramics coming from H0TP powders the time of resistance to cyclic loading should be expected to be equal to that of a HA ceramic prepared with conventional powders; whereas from the K_{IC} value of ceramics coming from H0TP-AS powders, longer times are expected.

5 Conclusions

This work has shown the feasibility of using powders produced by a mechano-chemical method to constitute HA-based bioceramics. The described procedure concerns a product that contains β -TCP in a proportion estimated at around 10–12 wt% (20–23 mol%). The obtained ceramic exhibits very good flexural strength. The presence of Al_2O_3 and

SiO₂ additives leads to an increase in the mechanical properties but at the same time to a complete transformation of the nature of the matrix from HA to β -TCP. All the transformations observed during firing suggest that originally powders of defective HA give rise to HA and β -TCP in equilibrium at every temperature.

The existence of a critical temperature range was confirmed, in which a whole range of transformation phenomena occur associated with a decrease in the mechanical properties for sintered bodies. On the basis of previous experiences too, it is possible to state that such a critical temperature interval is not really fixed, but exhibits a certain degree of variability depending on the chemical quality and physical characteristics of the powders and their thermal treatments. For samples obtained by pressing H0TP powders elaborated in this work and produced through a mechanochemical method, the above mentioned 'failure' was found at 1300°C (with adjacent maxima at 1250 and 1350°C). A number of factors can, theoretically, contribute to the presence of such an interval of temperatures in which an adverse trend of the mechanical properties is observed. Certainly important among these are the grain growth and the development of anisotropy, but the authors consider the $\beta \rightarrow \alpha$ phase transformation of TCP to represent the main contribution, as evidenced by XRD results. CO₂ and H₂O losses are practically negligible and should not cause any considerable modification in the HA lattice.

Acknowledgements

The authors wish to thank Dr Stefano Guicciardi

for his kind help and interest in the mechanical measurements.

References

1. Jarcho, M., Bolen, C. H., Thomas, M. B., Bobick, J., Kar, J. F. & Doremus, R. H., *J. Mater. Sci.*, **11** (1976) 2027–35.
2. Peelen, J. G. J., Rejda, B. V. & De Groot, K., *Ceram. Int.*, **4** (1978) 71.
3. Rejda, B. V., Peelen, J. G. J. & De Groot, K., *J. Bioeng.*, **1** (1977) 93.
4. Akao, M., Aoki, H. & Kato, K., *I Zai Ken Po*, **15** (1981) 17–22.
5. Toriyama, M. & Kavamura, S., *Yogyo-Kyokai-shi*, **94** (1986) 1004–8.
6. Toriyama, M., Kavamura, S., Ito, Y. & Nagae, H., *J. Ceram. Jpn Int. Ed.*, **97** (1989).
7. Toriyama, M. & Kawamura, S., *J. Ceram. Soc., Jpn Int. Ed.*, **95** (1987) 698–702.
8. Toriyama, M., Kavamura, S., Ito, Y., Nagae, H. & Toyama, I., *J. Ceram. Soc., Jpn Int. Ed.*, **96** (1988) 815–19.
9. Krajewski, A., Ravaglioli, A., Riva di Sanseverino, L., Marchetti, F. & Monticelli, G., *Biomaterials*, **5** (1984) 105–8.
10. Bredings, M. A., Frank, H. H. & Fuedner, H., *Z. Elektrochem.*, **39** (1933) 959.
11. Trombe, J. C. & Montel, G., *J. Inorg. Nucl. Chem.*, **40** (1978) 15, 23 and 27.
12. Denissen, H., De Groot, K., Vandijk, H. J. & Gehering, A. P., *Proc. 3rd Conf. on Materials for Use in Medicine and Biology*, Keele University, UK, September 1978.
13. Newesley, H., *Proc. 3rd Conf. on Materials for Use in Medicine and Biology*, Keele University, UK, September 1978.
14. Kijima, T. & Tsutsumi, M., *J. Am. Ceram. Soc.*, **62** (1979) 455.
15. Ravaglioli, A., Krajewski, A., Piancastelli, A. & Martinetti, R., *Bioceramics and the Human Body*, eds A. Ravaglioli and A. Krajewski. Elsevier Science Publishers Ltd, London, 1992, pp. 203–5.
16. Ishikawa, K., Ducheyne, P. & Radin, S., *J. Mat. Sci.: Mat. in Medicine*, **4** (1993) 165–8.
17. Wang, P. E. & Chaki, T. K., *J. Mat. Sci.: Mat. in Medicine*, **4** (1993) 150–8.

Preparation of Ultrafine Zirconia Powder by Emulsion Method

L. Gao, H. C. Qiao, H. B. Qiu & D. S. Yan

State Key Laboratory on High Performance Ceramics and Superfine Microstructure Studies, Shanghai Institute of Ceramics, Chinese Academy of Sciences, 1295 Dingxi Road, Shanghai 200050, China

(Received 13 March 1995; revised version received 16 June 1995; accepted 28 June 1995)

Abstract

Ultrafine 14 nm 3 mol% Y_2O_3 stabilized tetragonal ZrO_2 powder was prepared by emulsion processing. The obtained particles were weakly agglomerated into polyhedral or spherical shaped powders. The powder characteristics were investigated by using X-ray diffraction (XRD), X-ray fluorescence (XRF), inductively coupled plasma spectroscopy (ICP), nitrogen adsorption (BET model) and thermal analysis (DTA–TG). The experiments indicated that the heterogenous distillation used in the process was an effective method to remove residual water in the gel-precipitate and reduce the formation of strong agglomerates. The powder presented good formability and sinterability.

1 Introduction

Ceramic materials which consist of 100% yttria-doped tetragonal zirconia polycrystals (Y-TZP) exhibit a high strength and toughness compared to other ceramics. The ceramic powder characteristics of particle size, shape, size distribution and agglomeration state have very important influences on the sintering behaviour and final microstructure. In order to obtain dense and pure tetragonal zirconia ceramics with small grain sizes, special requirements must be fulfilled by the powders used for the sintering process. These ceramic powders must be homogeneous in composition and highly sinter-active (low sintering temperature) in order to decrease grain growth during sintering. Previous studies have shown that ultrafine, unagglomerated, soft powders can lower sintering temperature and produce fine grain microstructure.¹

With a drastic decrease in the grain size and, subsequently, increasing of interfacial surface areas, some improved or new properties of ceramic materials could be expected. For instance,

if the grain sizes of ceramics are decreased down to the nanometre scale, the higher fraction of atoms located in the grain boundary regions will result in the rapid diffusivities, enhanced solubilities and low temperature ductility.²

Recently, considerable effort has been given to the chemical synthesis of ultrafine ceramic powders via both aqueous and vapour phase routes.³ A noteworthy problem is that the ultrafine powders could easily contain hard agglomerates, which would postpone the densification process. To solve this problem, Kanai⁴ and Ramamurthi⁵ have reported on emulsion methods for the preparation of ultrafine and unagglomerated powders.

In this paper, the synthesis of ultrafine ZrO_2 –3 mol% Y_2O_3 powder using the emulsion method has been described. In this method, water droplets containing zirconium ions are suspended and stabilized in an organic non-polar solvent by addition of an appropriate surfactant. The emulsion droplets are gelled by ammonia gas, and the gel droplets are then stabilized by removing water during heterogeneous distillation. The powder characteristics and its sintering properties have also been investigated.

2 Experimental Procedure

Zirconyl nitrate, $ZrO(NO_3)_2 \cdot nH_2O$ and yttrium nitrate $Y(NO_3)_3 \cdot 6H_2O$ (both with purities > 99%) were selected for the preparation of Y-TZP powders and dissolved in distilled water. $ZrO(NO_3)_2 \cdot nH_2O$ was chosen over $ZrOCl_2 \cdot nH_2O$, since nitrogen-containing compounds lead to cleaner and easier burn-out compared with chloride-containing compounds. The concentrations of Zr^{4+} and Y^{3+} in the above two solutions were exactly determined by chemical analysis in order to precisely control the chemical compositions of the prepared powders.

The mixed solution was poured into a 5000 ml

beaker which was charged with xylene. The volume ratio of solution to xylene was 1:10. A surfactant, Tween 80 with 0.2 vol% of xylene, was slowly added to the beaker while stirring. Small solution droplets were thus developed and an emulsion was formed in which the droplets were stabilized by the surfactant present. The emulsion was magnetically stirred for 45 min. Ammonia gas was bubbled through the suspension using a glass tube for 10 min to gel the emulsion droplets. The suspension was then transferred to a flask for distillation using the apparatus shown in Fig. 1. The temperature of the suspension was increased by heating and maintained at 144°C which is the boiling point of xylene. At this time, the distillate was xylene only. The distillation treatment was finished after the temperature had stabilized at 144°C for about 45 min. The powder was isolated by filtering, dried at 160°C for 12 h and calcined at 600°C for 1 h and 700°C for 1 h. The whole process is summarized in Fig. 2.

Powder calcined at 700°C was cold isostatically pressed at 200 MPa into pellets (7.2 mm in diameter, 1–2 mm in thickness) with the use of PVA. Sintering was conducted at 1250°C for 30 min. The grain size was determined by scanning electron microscope (SEM) observation and the sintered densities were measured by the Archimedes method in distilled water.

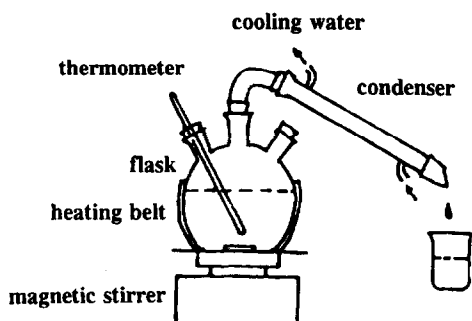


Fig. 1. Apparatus used for heterogeneous distillation.

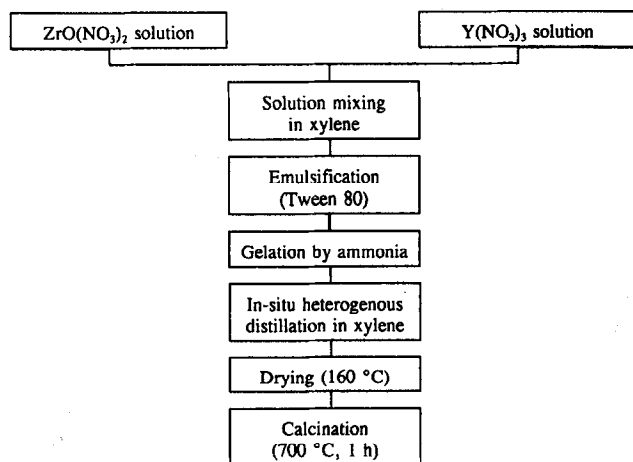


Fig. 2. Processing diagram of powder preparation by emulsion method.

3 Results and Discussion

3.1 Powder characteristics

The chemical compositions of the powder, as determined by X-ray fluorescence spectroscopy (XRF) and inductively coupled plasma spectroscopy (ICP), are given in Table 1. The yttria composition of the prepared powder showed a small amount of deviation from the designed composition by the XRF method. The X-ray diffraction study on the powder identified the tetragonal phase after calcination.

The morphology of the particles was observed by transmission electron microscopy (TEM). It was found that the prepared powders were composed of nanometre-sized crystallites, which in turn were loosely attached together to form powders of polyhedral or spherical shape, as seen from Fig. 3. The specific surface area of the powder calcined at 700°C measured by the BET

Table 1. Chemical analysis results of prepared powder

Y_2O_3 content by XRF (mol%)	Impurities measured by ICP (wt%)			
Y_2O_3	SiO_2	MgO	HfO_2	CaO
2.8	0.022	<0.007	0.78	0.47

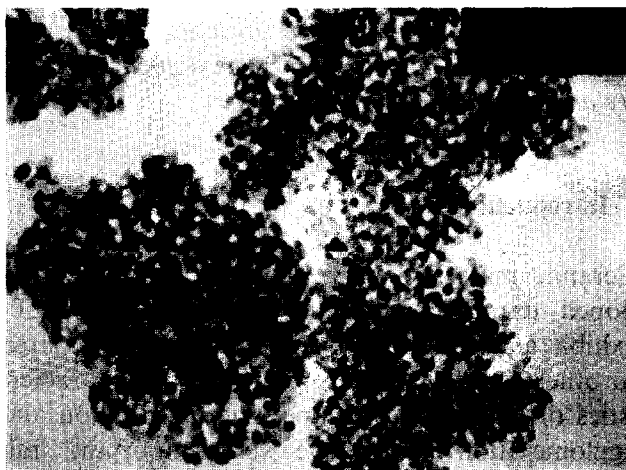


Fig. 3. TEM micrograph of the prepared powder.

method was $52.5 \text{ m}^2 \text{ g}^{-1}$ which was equivalent to an 18.7 nm crystallite.

This result was in good agreement with the

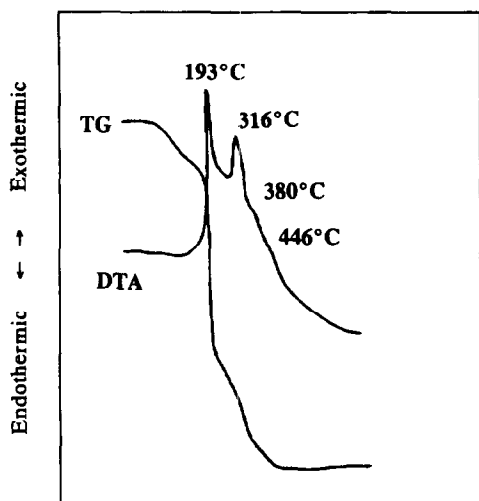


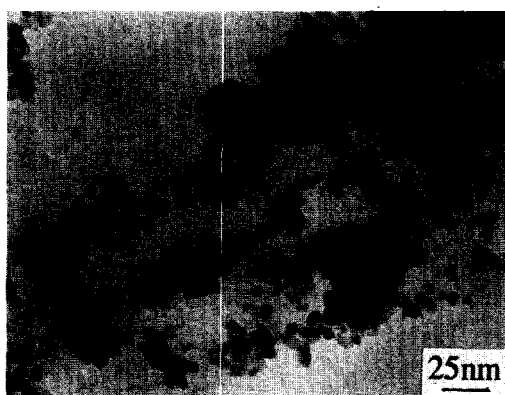
Fig. 4. DTA-TG traces of the prepared powder.

average crystallite size of 14 nm obtained from the TEM micrograph in Fig. 5(D). From this fact, it could be concluded that the agglomeration strength among the crystallites in the powder was very weak and the formation of hard agglomerates was basically avoided.

The thermal processing and crystallization behaviour of the powder were investigated by using DTA-TG methods as shown in Fig. 4. Two obvious exothermic peaks were found at 193 and 316°C and they could be attributed to the organic substance burn-out and nitrate decomposition. Another two small exothermic peaks around 380 and 446°C could be related to the debonding of oxyhydrogen groups and the beginning of crystallization, respectively.

3.2 Effects of solution concentration and calcination temperature on crystallite size

Figure 5 shows TEM micrographs of the powder



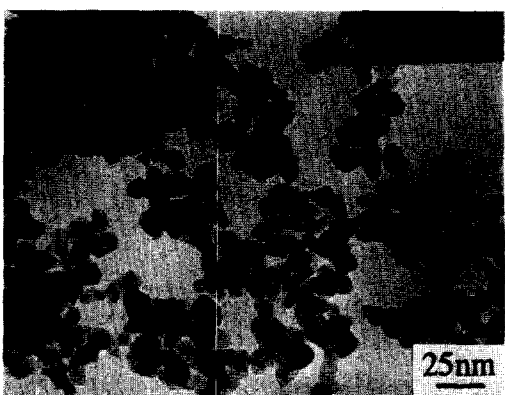
(A). Solution concentration: 0.25 M

Calcined at: 600 °C



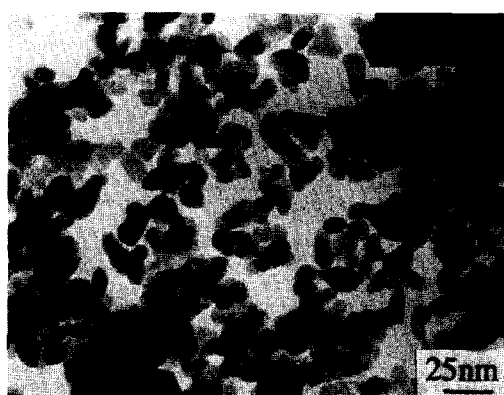
(B). Solution concentration: 0.5 M

Calcined at: 600 °C



(C). Solution concentration: 0.25M

Calcined at: 700 °C



(D). Solution concentration: 0.5 M

Calcined at: 700 °C

Fig. 5. The effects of solution concentration and calcination temperature on crystallite size.

prepared with different solution concentrations and at different calcination temperatures. The average crystalline size in Figs 5(A) and (B) was about 8–10 nm, while that in Figs 5(C) and (D) ranged from 12 to 14 nm. From this observation, it could be suggested that the crystallite size is mainly dependent upon the calcination temperature rather than the solution concentration.

3.3 Sintering behaviour

High green densities of over 50% TD were obtained after pressing. Sintering was performed using the following schedule: ambient to 800°C at 10°C min⁻¹; 800 to 1100°C at 6°C min⁻¹; 1100 to 1250°C at 3°C min⁻¹; holding at 1250°C for 30 min and then cooled naturally. Sintered zirconia in 100% tetragonal phase with a density of 97% TD and an average grain size of 0.22 μm was obtained.

4 Conclusions

Ultrafine Y₂O₃ stabilized tetragonal ZrO₂ powder

was successfully prepared by the emulsion method. The prepared powders take advantage of forming weak agglomerates in the preparation process which facilitate the compaction of nanometre-scale primary particles. Experimental results showed that the calcination temperature had a significant influence on the crystallite size. Preliminary sintering studies indicated good sinterability of the powder.

References

1. Rhodes, W. H., *J. Am. Ceram. Soc.*, **64**(1) (1981) 191.
2. Birringer, R., *Mater. Sci. Eng.*, **A117** (1989) 33.
3. Johnson, D. W. Jr, in *Ceramic Powder Science: Advances in Ceramics*, Vol. 21, eds G. L. Messing, K. S. Mazdizyani, J. W. McCauley and R. A. Haber. The American Ceramic Society, Inc., 1987, p. 3.
4. Kanai, T., Rhine, W. E. & Bowen, H. H., in *Ceramic Powder Science II: A, Ceramic Transactions* Vol. 1, eds G. L. Messing, E. R. Fuller Jr and H. Hausner. The American Ceramic Society, Inc., 1988, p. 119.
5. Ramamurthi, S. D., Xu, Z. & Payne, D. A., *J. Am. Ceram. Soc.*, **73**(9) (1990) 2760.

Thermomechanical Behaviour of Mullite–Zirconia Composite

M. Hamidouche,^a N. Bouaouadja,^a H. Osmani,^a R. Torrecillas^b & G. Fantozzi^b

^aLaboratoire des Matériaux, IOMP Université de Sétif, Sétif 19000, Algeria

^bLaboratoire GEMPPM, UA 341, INSA de Lyon, France

(Received 24 January 1994; revised version received 26 March 1995; accepted 9 June 1995)

Abstract

Mullite is one of the most widely used compounds in many industrial products. It has been shown that addition of zirconia to mullite improves its mechanical properties, particularly at high temperature. Some investigations have been attempted to explain the fracture toughening of this material. In this paper, the mechanical properties of mullite–zirconia composite have been determined from room temperature up to 1400°C. The thermomechanical behaviour of this material is sensitive to the phase transformation of zirconia. The obtained results are presented and discussed.

1 Introduction

It is generally accepted that mullite ($MAl_2O_3-NSiO_2$ with M/N ratio varying from 3:2 to 2:1) is one of the most widely encountered and important compounds found in many industrial ceramic products.^{1,2} However, mullite is difficult to consolidate into fully dense single-phase bodies. To optimize its mechanical properties, some investigations have been attempted using different processing techniques such as hot-pressing, hot-isostatic pressing and sol-gel processing.^{3,4}

Claussen and Jahn⁴ showed that significant toughening could be obtained by incorporating zirconia particles (ZrO_2) in a mullite matrix. Different mechanisms are involved in the toughening of mullite composite with zirconia additions: stress-induced transformation, microcracking, crack bowing and crack deflection.⁵ In all cases, the operative toughening mechanism depends on such variables as matrix stiffness, zirconia particle size, chemical composition, temperature and strength.

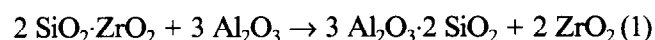
There are three main processing routes for producing mullite–zirconia composites,⁶ each leading to a special microstructure and then to specific properties. Mullite–zirconia material can be pro-

duced by conventional sintering of mechanical mixtures of fused mullite or reactive pre-mullite and zirconia powders. It can also be produced by an *in situ* reaction process between zircon ($ZrSiO_4$) and alumina to form mullite with dispersed zirconia. The third technique is based on sintering the mullite precursors (SiO_2 and Al_2O_3) with different zirconia contents.

The aim of this work is to determine the mechanical properties of a mullite–zirconia composite from ambient temperature up to 1400°C. Fracture toughness, fracture strength, elastic modulus and thermal shock are characterized and discussed in terms of the effect of zirconia at high temperature.

2 Experimental Procedure

The following compounds were used as starting materials: zircon fine powder (Ceraten SA, Spain) with 1 μm average particle size, and α -alumina powder (CT 3000 SG; Aleoa, Germany) with 0.5 μm mean particle size. Zircon and alumina are formed according to the following reaction:



The powder mixtures were ball-milled for 2 h using alumina balls and containers with isopropyl alcohol as milling medium. After evaporation of the liquid, the powder was cold-isostatically pressed at 200 MPa. The mullite–zirconia blocks were treated at 1600°C for 4 h. From these blocks, bars with dimensions 40 × 6 × 4 mm³ were sawn for mechanical tests. The tensile surface was polished using a slurry containing 1 μm diamond grains.

Flexural strength measurements were made on samples of rectangular section (6 × 4 mm²) using four-point bending tests (inter/outer span: 10/35). The tests were carried out in air, from ambient temperature up to 1400°C, using an Instron testing machine equipped with a high temperature

furnace. The crosshead speed was 0.1 mm min^{-1} . Fracture toughness (K_{Ic}) was determined using single-edge notched beam (SENB) samples, tested in a three-point bending test. The ratio of notch depth to specimen width (a/W) was ~ 0.4 for all samples. The effect of crosshead speed on fracture toughness was observed using speeds of 0.2, 0.05 and $0.005 \text{ mm min}^{-1}$.

Thermal shock resistance was determined by flexural strength measurements after quenching in water (20°C) from different temperatures. The dilatometric curve has also been determined.

3 Results and Discussion

3.1 Chemical composition and phases

The bars were annealed for 12 h at 1200°C . Chemical composition (Table 1) was determined at room temperature by spectral analysis made with the 'Tracor' analyser of the Jeol scanning electron microscope (SEM).

Microscopic observation of the mullite-zirconia composite reveals a complex microstructure which contains three phases: mullite, zirconia and zircon (Fig. 1). The mullite grains are formed from agglomerates of about $10 \mu\text{m}$ size. Two types of zirconia grain are observed: spherical grains of $1 \mu\text{m}$ mean particle size which are located in the triple points, and rounded grains of about $3 \mu\text{m}$ mean grain size which are located normally in contact with zircon grains. Zircon grains are also present in the microstructure. The degree of dissociation

Table 1. Chemical composition obtained by spectral analysis for mullite-zirconia

	Al_2O_3	SiO_2	ZrO_2
Composition (wt%)	42.40	16.00	41.46



Fig. 1. Microphotographs of the structure of mullite-zirconia showing the scattering of zirconia particles.

of zircon is strongly dependent on the alumina fraction present in the initial mixture. Reaction sintering in the $\text{ZrSiO}_4\text{-Al}_2\text{O}_3$ system proceeds by atomic solution-diffusion-precipitation.⁷ The SiO_2 phase, which is always present on the zircon grains, primarily forms a residual glass phase situated in the grains boundaries of ZrSiO_4 and at zirconia-mullite interfaces, but not at mullite-mullite grain boundaries. This distribution most likely results from interfacial energy differences. The heat-treated sample exhibits a fractional content of 0.2 tetragonal and 0.8 monoclinic zirconia. The rounded appearance of the zirconia particles results from thermal etching, as revealed on fracture surfaces where the particles have the normal faceted morphology. The addition of zirconia promotes densification and retards grain growth. Compared with bodies produced by natural sintering of mixtures of mullite and zirconia powders,³ our materials present a higher amorphous phase for a corresponding zirconia volume fraction. This difference can be understood on the basis of the microstructural formation. It is evident that at high temperature, the strength of this material is affected by the viscosity of the glassy phase.

3.2 Mechanical behaviour

The mechanical characteristics of the studied material (fracture strength R , elastic modulus E , fracture toughness K_{Ic} , thermal shock resistance ΔT_c and linear expansion coefficient α) determined at room temperature are listed in Table 2. The effect of crosshead speed (s) on K_{Ic} values at room temperature is presented in Table 3. Thermal shock resistance is determined by the critical quenching temperature ΔT_c which leads to severe cracking of the composite, and then to low

Table 2. Mechanical characteristics obtained at room temperature ($T = 20^\circ\text{C}$) for mullite-zirconia composite

σ_f (MPa)	E (GPa)	K_{Ic} ($\text{MPa m}^{1/2}$)	ΔT_c ($^\circ\text{C}$)	$\alpha \times 10^6$ ($^\circ\text{C}^{-1}$)
215	150	4.2	300	1.62

Table 3. K_{Ic} values obtained at high temperature with three different crosshead speeds

$T(^\circ\text{C})$	$s \text{ (mm min}^{-1}\text{)}$		
	0.2	0.05	0.005
20	4.2 ± 0.3	4.0 ± 0.3	3.2 ± 0.4
800	3.6 ± 0.3	4.1 ± 0.4	2.9 ± 0.2
900	3.8 ± 0.2	4.2 ± 0.3	3.1 ± 0.2
1000	3.5 ± 0.5	3.8 ± 0.4	3.1 ± 0.3
1100	3.9 ± 0.2	4.0 ± 0.1	3.0 ± 0.1
1200	3.5 ± 0.1	3.0 ± 0.3	2.5 ± 0.3
1300	2.2 ± 0.3	2.8 ± 0.2	—

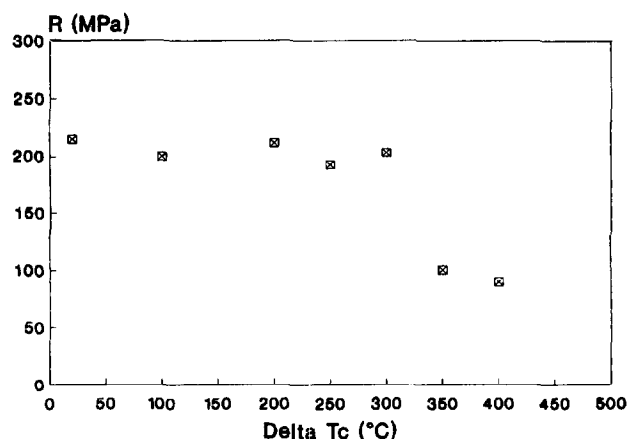


Fig. 2. Thermal shock curve of mullite-zirconia.

strength values. The obtained behaviour is plotted in Fig. 2. This mullite-zirconia composite shows better thermal shock resistance than pure mullite.⁸ The strength, after thermal shock, increased considerably in systems containing additions from 10 to 20 vol% of ZrO_2 .

3.2.1 Dilatometric behaviour

To study the dilatometric behaviour, a test was carried out from ambient temperature up to 1400°C. Figure 3 shows the thermal expansion curve of a rectangular mullite-zirconia specimen ($10 \times 5 \times 4 \text{ mm}^3$), which exhibits an average linear expansion of $1.6 \times 10^{-6} \text{ }^\circ\text{C}^{-1}$ with temperatures up to 1100°C. The hysteresis exhibited during this test indicates that there is a zirconia phase transformation. These results contrast with the data of Ruh *et al.*,⁹ who did not observe the transformation in mullite with 35% ZrO_2 and 1.5% Y_2O_3 . This is reasonable because our samples present a great amount of monoclinic phase (~80%). The curve shows a phase transformation corresponding to a zirconia compound. This phase transformation occurs at 1100°C during heating (monoclinic \rightarrow tetragonal) and at 785°C during cooling (tetragonal \rightarrow monoclinic).

3.2.2 Flexural strength

Fracture strength values, established at different temperatures up to 1400°C, are plotted in Fig. 4. At room temperature our mullite-zirconia pre-

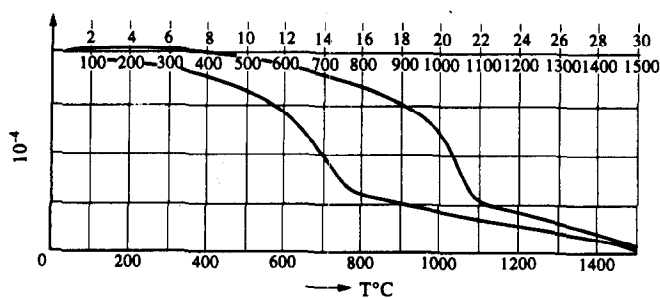


Fig. 3. Dilatometric curve of mullite-zirconia.

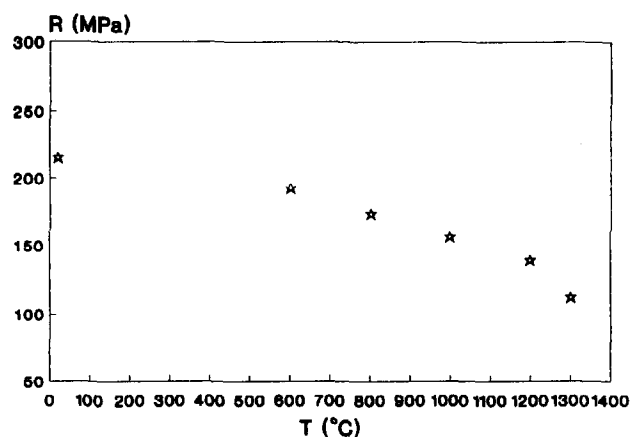


Fig. 4. Variation of fracture strength versus temperature.

sents a fracture strength of about 215 MPa, which is half the value found by Claussen and Jahn⁴ for a mullite-zirconia elaborated by reaction sintering and having approximately the same zirconia content. This wide difference can be explained by the differences in density (3.71 g cm^{-3} in our case, compared with 3.76 g cm^{-3}) and grain sizes of the mullite matrix and zirconia which are more than twice Claussen and Jahn's values (10 and $3 \mu\text{m}$ respectively in our case, compared with 4 and $1 \mu\text{m}$). The sintering time was 4 h in our case instead of 1 h in Claussen and Jahn's study made at the same temperature, giving them smaller grain sizes of zirconia and mullite. The authors explain the good mullite-zirconia characteristics by the separation of the sintering and reaction steps,⁴ which has not been done in our case.

From room temperature to 1400°C there is a slow and continuous decrease of flexural strength. Up to 1200°C, the load-displacement curves exhibit linear behaviour with limited apparent plasticity. The flexural strength R at 1200°C is half its room temperature value. The amorphous phase is probably the cause of this decrease in R .

It has been demonstrated that corrosion at the crack tip results in the formation of a surface layer of amorphous SiO_2 and viscous flow of the grain-boundary glass phase, the driving force for which is minimization of the surface energy. A further increase of temperature decreases the viscosity of the glassy phase for this material, resulting in a loss in fracture strength.

3.2.3 Elastic modulus

Elastic modulus was determined using a static method from load-displacement curves (Fig. 5). At room temperature, E is about 150 GPa. This value is in good agreement with results reported by Qi-Ming *et al.*¹⁰ for a mullite-zirconia composite with 25 vol% ZrO_2 (average grain size of $1 \mu\text{m}$). The variation of E with temperature seems regular

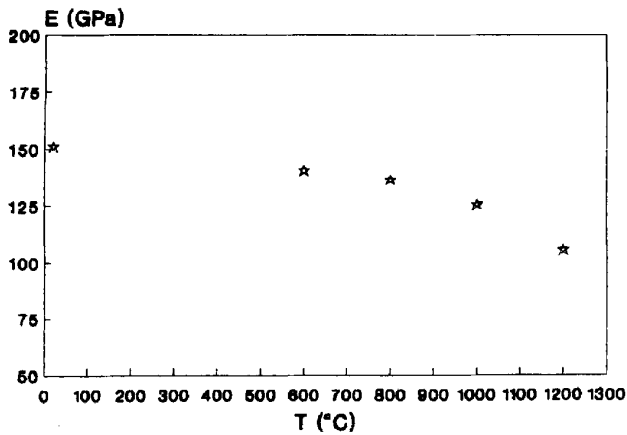


Fig. 5. Variation of Young's modulus versus temperature.

up to 900°C, beyond which there is a sensitive decrease of the curve. Elastic modulus reaches 105 GPa at 1050°C. As temperature increases, the stiffness of atomic linking decreases as a consequence of thermal agitation. The elastic modulus decrease is regular as far as the phenomenon is governed by these mechanisms. However, at a limit temperature value, intergranular phases become sufficiently viscous and generate sliding in the grain boundaries. Consequently, there is a sensitive decrease of elastic modulus.

3.2.4 Fracture toughness

The critical stress intensity factor is calculated using the equation:

$$K_{Ic} = \sigma_f Y \sqrt{a} \quad (2)$$

with

$$\sigma_f = 3 P_f L / 2 B W^2 \quad (3)$$

where Y is the geometric correction factor, a is the crack length, P_f is the maximum load, L is the span (three-point bending test), B and W are respectively the width and depth of the SENB samples.

The fracture toughness value (4.2 MPa m^{1/2})

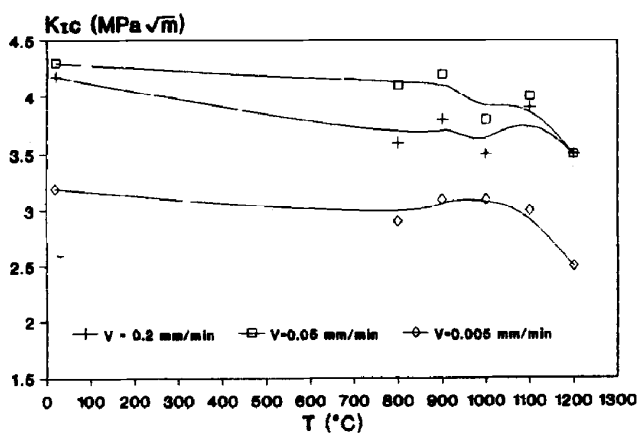


Fig. 6. Variation K_{Ic} versus temperature at three different crosshead speeds.

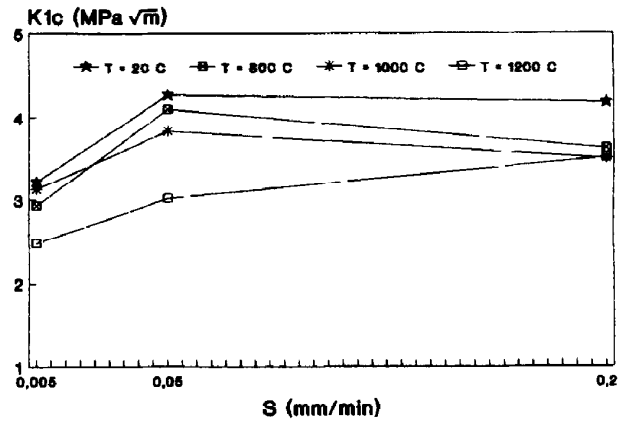


Fig. 7. Variation K_{Ic} versus crosshead speed at different temperatures.

found at room temperature is of the same order as values reported by Claussen and Jahn (4.5 MPa m^{1/2})⁴ and Ruh *et al.* (4.2 MPa m^{1/2}).⁹ The average K_{Ic} values established at high temperature with three different crosshead speeds are given in Table 3. The K_{Ic} versus temperature curves established at three different crosshead speeds, and the K_{Ic} versus crosshead speed S curves established at different temperatures, are shown in Figs 6 and 7, respectively.

When considering the fracture toughness values at room temperature and in the range 800–900°C it appears that the fracture mechanism is the same; i.e. fracture occurs by unstable crack extension from critical flaws. The fracture is typically transgranular (Fig. 8). K_{Ic} decreases linearly as the temperature increases according to the reduction of fracture energy. To determine which mechanisms are responsible for the toughness behaviour observed in this material, it is necessary to take into account the effects of the zirconia toughening and the microstructure.

In the case of mullite–zirconia composite, the monoclinic → tetragonal transformation occurs at about 1070°C. This phase modification explains

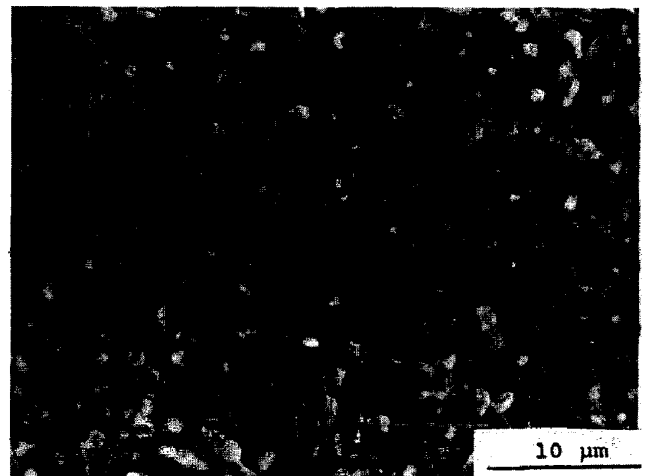


Fig. 8. Fracture facies showing transgranular cracks ($T = 800^\circ\text{C}$).

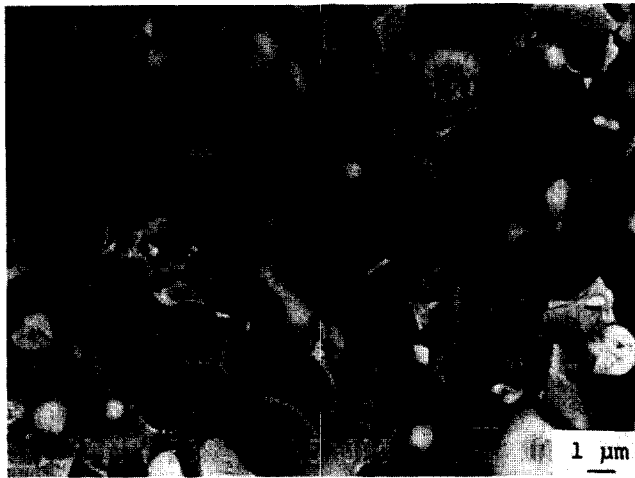


Fig. 9. Fracture facies showing intergranular cracks ($T = 1100^{\circ}\text{C}$).

the observed decrease of K_{Ic} values. Above 900°C , the glassy phase becomes more fluid. Consequently, sliding in grain boundaries becomes more important than plastic relaxation and can lead to the formation of cracks and debonding of the matrix which, in turn, leads to a decrease of K_{Ic} values. In this domain of temperature, the load–displacement curves exhibit some plasticity and the fracture is typically intergranular (Fig. 9).

The mullite matrix presents mainly an intergranular fracture. The zirconia particles present three kinds of fracture mode: some show a single fracture plane, the largest and most irregularly shaped particles show several differently oriented cleavage planes and the largest round particles are surrounded by the crack. The same mechanisms have been observed in an other ceramic composite by Baudin *et al.*¹¹

3.2.5 Effect of crosshead loading speed on K_{Ic}

Crosshead speed is a parameter which has a sensitive effect on fracture toughness values (see Fig. 7). At low crosshead loading speed ($S = 0.005 \text{ mm min}^{-1}$), the low crack growth phenomenon prevails in the grain boundaries (reaction in crack front). This leads to crack increase and to low K_{Ic} values. At intermediate speed ($S = 0.05 \text{ mm min}^{-1}$), the material responds globally to the applied loading. The microstructure is strengthened because of the damage zone at the crack tip. On the other hand, upon a further increase in crosshead speed ($S = 0.2 \text{ mm min}^{-1}$), the phenomena described previously do not have sufficient time to grow. This leads to brittleness of the material.

4 Summary and Conclusions

- (1) Phase transformation of zirconia (monoclinic \rightarrow tetragonal) occurs at 1100°C during heating and at 785°C during cooling (tetragonal \rightarrow monoclinic).
- (2) The thermal shock resistance of mullite–zirconia is $\sim 300^{\circ}\text{C}$.
- (3) Young's modulus decreases linearly with temperature. It is 150 GPa at room temperature and 105 GPa at 1050°C .
- (4) At low temperature, the zirconia phase exhibits a positive effect on fracture strength.
- (5) At high temperature, phase transformation of the zirconia marked the fracture toughness decrease
- (6) The K_{Ic} maximum versus crosshead loading speed is shifted towards high temperature when crosshead speed increases.

References

1. Torrecillas, R., De Aza, S., Moya, J. S., Epicier, T. & Fantozzi, G., Improved high temperature mechanical properties of zirconia doped mullite. *J. Mater. Sci. Lett.*, **9** (1990) 1400–2.
2. Skoog, A. J. & Moore, R. E., Refractory of the past for the future: mullite and its use as a bonding phase. *Ceram. Bull.*, **67** [7] (1988) 1180–4.
3. Prochazka, S., Wallace, J. S. & Claussen, N., Microstructure of sintered mullite–zirconia composites. *Commun. J. Am. Ceram. Soc.*, (1983) C125–C127.
4. Claussen, N. & Jahn, J., Mechanical properties of sintered in situ-reacted mullite–zirconia composites. *J. Am. Ceram. Soc.*, **63** [3–4] 228–9.
5. Deportu, G. & Henney, J. W., The microstructure and mechanical properties of mullite–zirconia composites. *Brit. Ceram. Trans. J.*, **83** (1984) 69–72.
6. Orange, G., Fantozzi, G., Cambier, F., Leblud, C., Anceau, M. R. & Leriche, A., High temperature mechanical properties of reaction sintered mullite–zirconia composites and mullite–alumina–zirconia composites. *J. Mater. Sci.*, **20** (1985) 2533–40.
7. Di Rupo, E. & Anceau, M. R., Solid state reactions in the $\text{ZrO}_2\text{-SiO}_2\text{-}\alpha\text{-alumina}$ system. *J. Mater. Sci.*, **15** (1980) 114–8.
8. Hamidouche, M., Comportement thermomécanique de la mullite et de la mullite–zirconie. Magister thesis, IOMP University of Sétif, 1992.
9. Ruh, R., Mazdiyasn, K. S. & Mendiratta, M. G., Mechanical and microstructural characterization of mullite and mullite–SiC whisker and ZrO_2 toughened-mullite–SiC whisker composites. *J. Am. Ceram. Soc.*, **71** [6] (1988) 503–12.
10. Qi-Ming, Y., Jia-Qi, T. & Zhen-Guo, J., Preparation and properties of zirconia-toughened mullite ceramics. *J. Am. Ceram. Soc.*, **69** [3] (1986) 265–7.
11. Baudin, C., Cambier, F. & Delaey, L., Fractographic and acoustic emission of mullite–alumina–zirconia composites prepared by reaction sintering. *J. Mater. Sci.*, **22** (1987) 4398–402.

Localization of Oxygen Cathodic Reduction Zone at Lanthanum Manganite/Zirconia Interface

H. Lauret & A. Hammou

Laboratoire d'Ionique et d'Electrochimie des Solides de Grenoble (INPG-UJF), Associé au CNRS (URA 1213), ENSEEG, BP 75, 38402 Saint-Martin d'Hères Cédex, France

(Received 30 March 1995; revised version received 29 June 1995; accepted 14 July 1995)

Abstract

The electrochemical properties of $\text{La}_{0.45}\text{Sr}_{0.55}\text{MnO}_3$ have been studied under steady state polarization. The $I-\eta$ curves have been obtained for three point electrodes with three different values of surface area of contact with the electrolyte, which is yttria-stabilized zirconia. The results obtained in the 0 to 160 mV overpotential range exhibit a current proportional to the length of the triple contact between the gas phase, the point electrode and the electrolyte. For higher cathodic overpotentials no direct proportionality between the current and the length of the triple contact nor the surface area of the contact between the electrode and the electrolyte was found. These facts were interpreted in terms of the progressive extension of the reaction zone from the triple contact line to the surface of the contact between the electrode and the electrolyte at conditions under which the electrode material exhibits mixed conductivity.

1 Introduction

Solid oxide fuel cells (SOFCs) are electrochemical devices in which much interest has been shown over recent decades. They are considered to have potential for electric power generation with high grade by-product heat. Furthermore, they are among the more desirable systems to reduce the environmental impact caused by fossil fuel consumption. SOFCs operate in the 800–1000°C temperature range and may be described by the following electrochemical chain: fuel gas, Ni-yttria-stabilized zirconia cermet anode / yttria-stabilized zirconia electrolyte / ceramic oxide cathode, air.

Perovskite-type oxides $\text{La}_{1-x}\text{M}_x\text{MnO}_3$ ($\text{M} = \text{Sr}, \text{Ca}$) have been selected as cathodes for their high electrical conductivity, their electrocatalytic properties for oxygen reduction and their thermal and chemical compatibility with the electrolyte mate-

rial (yttria-stabilized zirconia). The major part of the power losses in these cells are due to the cathodic material. Therefore, many studies have been carried out to define the relationship between the cathodic overpotential, the oxygen reduction pathway and the intrinsic properties of these materials (e.g. microstructure, porosity). The oxygen reaction mechanism is still unknown.¹

This work is an attempt to define where the oxygen reduction takes place (contact area or triple contact line) in order to modify the cathode microstructure accordingly. The material studied belongs to the strontium-doped lanthanum manganite (LSM) family. $\text{La}_{0.45}\text{Sr}_{0.55}\text{MnO}_3$ was chosen because of its high electrical conductivity among this family.² It is known that no solid state reaction involving the formation of new phases takes place at the manganite/zirconia interface at temperatures below 1100°C.³

2 Experimental Procedures

For the electrolyte, discs of yttria-stabilized zirconia (9% Y_2O_3) were prepared. Highly pure (>99.99%) Y_2O_3 and ZrO_2 reactant powders were mixed in appropriate amounts in ethanol, filtered, dried and sieved. The resulting powder were calcined at 900°C then compacted in the shape of a cylinder and pressed isostatically at 1500 bar. The sintering process was carried out in a reducing atmosphere at 1350°C for 2 h. During cooling the atmosphere was air. The sample had a density more than 95% of the theoretical density. The sample grain size was in the range 2–3 μm . The dense cylinder was cut into discs of 200 μm thickness.

The solid state reaction route was chosen for the Sr-doped lanthanum manganite sample preparation. The starting components were high purity SrCO_3 , MnCO_3 and La_2O_3 . The powders were dried at 80°C for several days to avoid hydration due to their hygroscopic nature. The appropriate

amounts of powders were ball-milled with ethanol in an agate mortar, then dried and compacted. The resulting cylinder was calcined at 1400°C for 4 h. During the increase of temperature carbonates were destroyed in a step between 850 and 1050°C; between these two temperatures the temperature increase was only 50°C h⁻¹ instead of 100°C h⁻¹ elsewhere. The sample was then ground and compacted into a cylinder in a uniaxial press at 200 bar and isostatically pressed at 3000 bar. The cylinder was sintered at 1400°C for 4 h. The grinding/compacting/sintering cycle was repeated twice.

After each cycle, X-ray measurements were performed to verify that no product other than the classical perovskite phase was present. The chemical analysis of the sample was performed by plasma emission spectroscopy. The results confirmed the expected composition. The cylinders obtained were dense enough (higher than 95% of the theoretical density) that machining into pin-shaped samples was feasible. Three point electrodes were prepared. Their ends were polished to obtain three different values of the surface area of contact with the electrolyte. This polishing operation was performed using a zirconia disc to avoid any chemical contamination.

We will call 'electrode material' the perovskite part of the 'electrode' which is, in fact, the perovskite material, the electrolyte and the surrounding atmosphere. The cell configuration is shown in Fig. 1. The cell was made in such a way that three working electrodes could be placed in the furnace and could be studied in parallel under the same conditions. They were arranged in an equilateral triangle. On the other side of the electrolyte the counter-electrode was annular and large enough to cover the area directly opposite the working electrodes. The reference electrode was central and its surface area was much smaller than that of the counter-electrode. The counter- and reference elec-

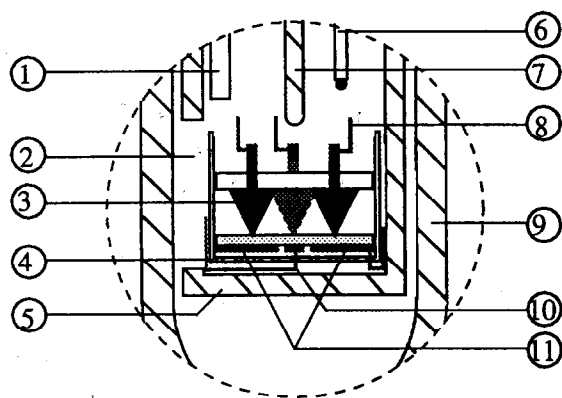


Fig. 1. Cell configuration. 1, Air entry tube; 2, alumina support; 3, electrode material; 4, alumina cup; 5, alumina sample holder tube; 6, thermocouple; 7, alumina tightening rod; 8, Pt wire; 9, alumina furnace tube; 10, reference electrode; 11, counter-electrode.

trodes were made of a porous platinum coating (Degussa 308A). Platinum leads were cemented to the electrode materials with the same platinum paste. The cell temperature was controlled by a Pt/PtRh thermocouple placed close to the working electrode. The experiments were performed at 960°C in air.

Potentiostatic and impedance spectroscopy measurements were carried out with a Tacussel Z-Computer potentiostat/impedance spectroscopy analyser, which allowed simultaneous polarization and impedance spectroscopy measurements in the frequency range 10⁵–10⁻⁴ Hz. We limited the studied domain to 10⁵–10⁻² Hz. The ohmic drop in the cell was calculated using the high frequency intercept of the impedance diagram with the real axis. This high frequency intercept was corrected, if necessary, by taking into account the self-induction of the circuit (typically 10⁻⁶ H). The steady state polarization curves were drawn point by point for the three electrodes, one point a day in general, and an impedance spectroscopy measurement taken at each point.

3 Results and Discussion

3.1 Determination of surface contact area between electrode material and electrolyte

Two types of determination were made for evaluation of the surface contact area between the electrode material and the electrolyte. First, micrographs of the point electrode areas were taken before and after the experiment. We also took micrographs of the zirconia disc surface after the experiment. The electrode material left black spots of perovskite on the disc. The spot area allowed us to evaluate the minimum surface contact area.

The Newmann equation⁴ was used as a second method for determination of the surface contact area. This equation is:

$$R_{el} = \frac{1}{4r\sigma_{el}}$$

where R_{el} is the electrolyte resistance determined by impedance spectroscopy and σ_{el} is the electrolyte conductivity determined with large electrodes

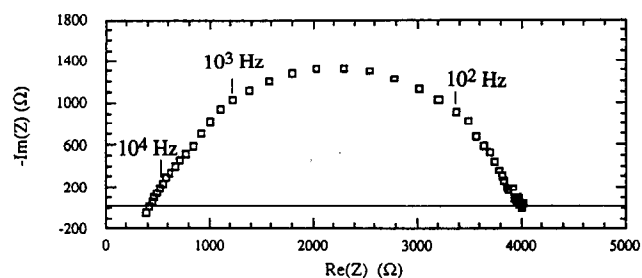


Fig. 2. Typical impedance spectra obtained on electrode C at 66 mV cathodic polarization.

Table 1. Geometrical parameters of the LSM/YSZ interface determined by microscopic observation

		Electrode A	Electrode B	Electrode C
Electrode observation*	S (cm ²)	3.8×10^{-4}	5.6×10^{-4}	6.1×10^{-3}
	L (cm)	0.07	0.14	0.28
Spot observation†	S (cm ²)	$2.9A \times 10^{-3}$	6.85×10^{-3}	2.3×10^{-3}
	L (cm)	0.19	0.26	0.16
Newmann calculation	S (cm ²)	2.0×10^{-3}	4.4×10^{-3}	1.1×10^{-3}
	L (cm)	0.16	0.23	0.11

*Electrodes before use.

†Spot left by the electrode on ceramic electrolyte after use.

fully covering two sides of an electrolyte disc. In the present work, the value determined for the latter term was $9.6 \times 10^{-2} \text{ S cm}^{-1}$ at 960°C . r is the electrically determined average radius of the equivalent disc of the same area. From the r value we can deduce the surface contact area and the length of the contact if its shape is close to a disc. Table I shows the results of the microscopic observations and the electrical calculations. A typical impedance spectrum is shown in Fig. 2. From these results we see that there is no correlation between the observed contact area of the point electrodes before their use and the effective contact area. Actually, the electrode material may be badly placed so that the whole observed surface is not in contact with the electrolyte. This is the case for electrode C. Furthermore, the ceramic material may be slightly squashed in the case of the finest pin-shaped electrodes. This is the case for electrodes A and B.

Good agreement between the Newmann calculation and the observation of the spot left on the electrolyte by the electrode material was found. It is reasonable to give more credit to the Newmann formula than to the microscopic observations, because the latter enabled us to follow the values of the geometrical parameters during the experiment, even if these were changed accidentally.

3.2 Cathodic polarization results in the 0–160 mV domain

The steady state polarization curves are shown in Fig. 3. The currents are not normalized using the geometrical parameters. It can be seen, in particular, that the relative values of the current follow the geometrical parameters, the higher current being obtained with the point electrodes having the largest area, i.e. electrode B. In Fig. 4 these curves are normalized using the geometrical parameters. The normalization with respect to the optically determined parameters gives no conclusive results, as expected; the reliability of these parameters being low as mentioned before. On the other hand, the Newmann parameters give better

results: a direct correlation between the oxygen reduction current and the contact perimeter is found with good accuracy.

Whereas the discrepancies between the three curves are within 4000 and 1000% in the case of the normalizations with respect to the optically determined perimeter and surface, respectively, the value is 260% in the case of the normalization with respect to the Newmann surface and only 33% with respect to the Newmann perimeter. So, we can confirm by means of the polarization and impedance measurements that the cathodic reduction process takes place through the contact perimeter, that is to say, the triple phase boundary between the gas, the electrode material and the electrolyte. The same conclusions have been drawn by other authors using similar materials ($\text{La}_{0.6}\text{Ca}_{0.4}\text{MnO}_3$)⁵ or silver electrodes,⁶ in experiments performed under zero polarization.

3.3 Cathodic polarization in the 160–500 mV domain

The steady state polarization curves in the whole range studied are shown in Fig. 5 for electrodes B and C. For this section, the parameters used are those deduced from the Newmann formula. In Fig. 6 it can be seen that neither normalization by the contact perimeter nor by the contact surface area is satisfactory. This result means that the

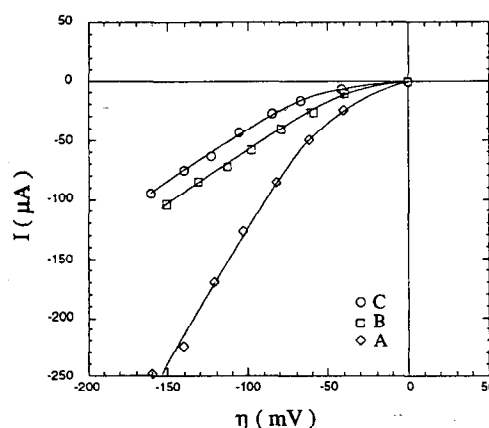


Fig. 3. Steady state polarization curves in the 0–160 mV cathodic polarization domain at 960°C on three point electrodes of $\text{La}_{0.45}\text{Sr}_{0.55}\text{MnO}_3$ (A, B and C) with different values of surface area of contact with the electrolyte.

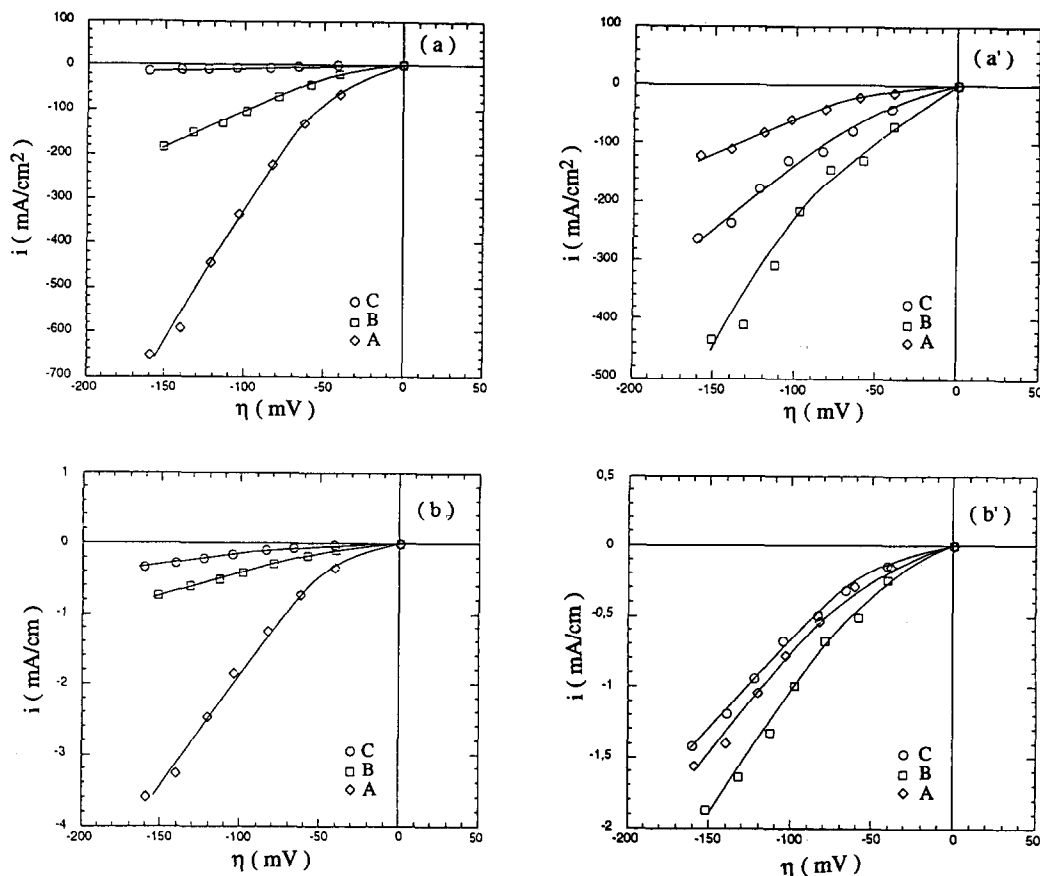


Fig. 4. Steady state polarization curves in the 0–160 mV cathodic polarization domain at 960°C on A, B and C. Currents are normalized by the geometrical parameters. (a) and (a') Optically determined length and surface area of the contact, respectively; (b) and (b') Newmann length and surface area of the contact, respectively.

reduction reaction process takes place neither at the triple phase boundary nor over the whole contact surface homogeneously. This behaviour may be explained as follows. Under high polarization (typically < -200 mV) the LSM system becomes a mixed conductor because of the formation of oxygen vacancies in the material.⁷ The electrochemical reduction of oxygen may then occur at the lateral surface of the entire electrode material. The oxygen ions produced may diffuse through the electrode material from the electrode lateral surface to the electrode/electrolyte contact where they may enter the electrolyte. Thus, to the first pathway a second one is added.

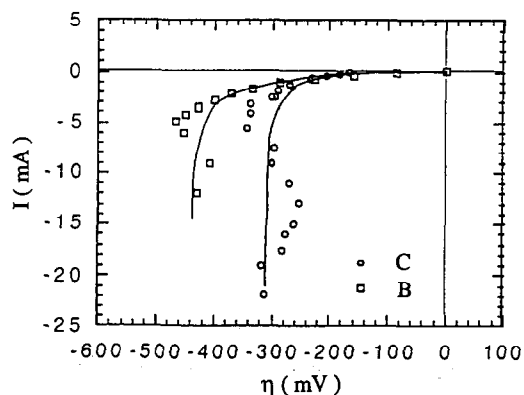


Fig. 5. Steady state polarization curves in the 0–500 mV cathodic polarization domain at 960°C on B and C.

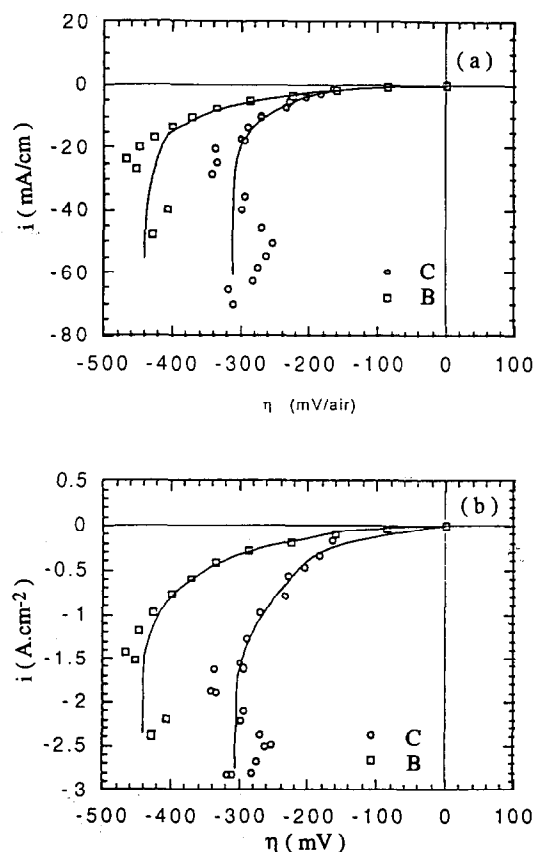


Fig. 6. Steady state polarization curves in the 0–500 mV cathodic polarization domain at 960°C on B and C. Currents are normalized by the geometrical parameters. (a) and (b) Newmann length and surface area of the contact, respectively.

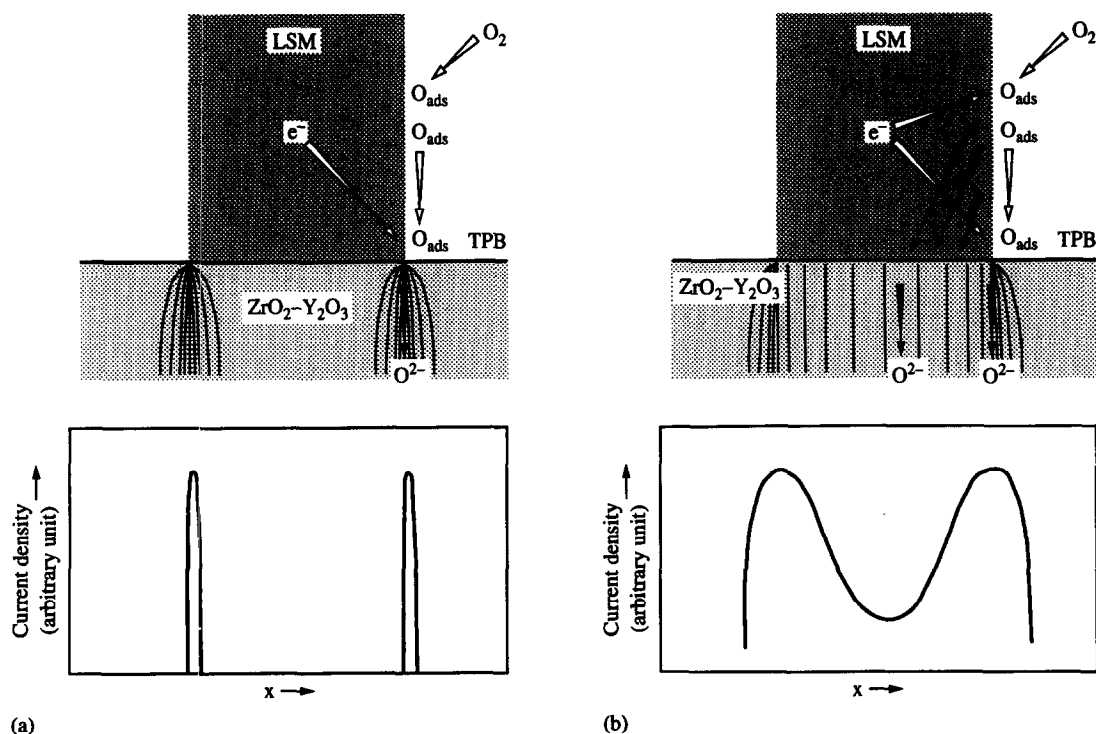


Fig. 7. Oxygen reduction pathways: (a) 0–160 mV cathodic polarization domain; (b) 160–500 mV cathodic polarization domain.

The possible outwards extension of the reaction zone from the triple phase boundary onto the free electrolyte surface by injection of electrons into the electrolyte, giving rise to another reaction pathway, cannot be neglected.⁸ In this way, the reaction zone is extended inwards and outwards from the contact perimeter, giving rise to a current density distribution as shown in Fig. 7. So, the geometrically limiting surface is neither the perimeter nor a disc, but an annular zone around the contact perimeter in which the current is not necessarily homogeneous. As the three point electrodes have the same lateral surface area this cannot be the limiting surface.

4 Conclusions

In the present work, we have demonstrated the validity of the model describing the oxygen reduction on strontium-doped lanthanum manganite electrodes. At low polarization (typically > -200 mV at 960°C), the reduction takes place along the triple contact line between the gas phase, the electrode and the electrolyte materials. At higher polarization a second process is superimposed on the first. As the material becomes a mixed conductor in this domain, the appearance of oxygen vacancies in the electrode material allows the oxygen reduction to take place at the lateral surface of the electrode. This second process leads to the extension of the reaction pathway from the triple con-

tact line to the entire contact surface between the electrode material and the electrolyte. Note that the data deduced from this second process would not be relevant to real fuel cell conditions, because of too high a cathodic overpotential. Further, it has to be emphasized that the geometrical factors used for this kind of study must be deduced from the impedance measurements by applying the Newmann formula.

References

1. Mogensen, M., *Proceedings of the 14th Symposium on Materials Science*, eds F. W. Poulsen, et al. Risø, 1993, pp. 117–35.
2. Lauret, H., Caignol, E. & Hammou, A., *Proceedings of the Second International Symposium on Solid Oxide Fuel Cells*, eds F. Grosz, P. Zegers, S. C. Singhal and H. Iwahara. Official Publications of the European Communities, Luxembourg, 1991, pp. 479–86.
3. Chen, C. C., Nasrallah, M. M. & Anderson, H. U., *Proceedings of the Third International Symposium on Solid Oxide Fuel Cells*, eds S. C. Singhal and H. Iwahara. The Electrochemical Society, Inc., Pennington, NJ, 1993, pp. 598–612.
4. Newmann, J., *J. Electrochem. Soc.*, **113** (1966) 501–2.
5. Mizusaki, J., Tagawa, T., Tsuneyoshi, K. & Sawata, A., *J. Electrochem. Soc.*, **138** (1991) 1867–73.
6. Kleitz, M., Dessemond, L., Kloidt, T. & Steil, M. C., *Proceedings of the Fourth International Symposium on Solid Oxide Fuel Cells*, eds M. Dokiya, O. Yamamoto, H. Tagawa and S. C. Singhal. The Electrochemical Society, Inc., Pennington, NJ, 1995, pp. 527–36.
7. Hammouche, A., Siebert, E., Hammou, A., Kleitz, M. & Caneiro, A., *J. Electrochem. Soc.*, **138** (1991) 1212–16.
8. Kleitz, M., PhD Thesis, Université de Grenoble, France, 1968.

Impedance Spectroscopy of Mg-Partially Stabilized Zirconia and Cubic Phase Decomposition

E. N. S. Muccillo^a & M. Kleitz^b

^aInstituto de Pesquisas Energéticas e Nucleares, Comissão Nacional de Energia Nuclear, CP 11049, Pinheiros, 05422-970, S. Paulo, SP, Brazil

^bLaboratoire d'Ionique et d'Electrochimie du Solide de Grenoble, INPG, CNRS, UJF, BP 75, 38402, St Martin d'Hères, France

(Received 3 April 1995; revised version received 30 June 1995; accepted 14 July 1995)

Abstract

Electrical conductivity measurements were carried out by impedance spectroscopy on nominally pure and magnesia-doped zirconia in the 3–13.7 mol% concentration range. In the partial-stabilization field, the impedance diagrams show the characteristic grain and grain boundary semicircles, as well as an extra arc at intermediate frequencies. This extra arc is interpreted as a characteristic of partial blocking of electrolyte conduction by the monoclinic grains. As usual, the resistances associated with the blocking processes exhibit activation energies slightly higher than the bulk resistance. All these activation energies increase with the MgO content. The cubic phase decomposition can easily and accurately be monitored by impedance spectroscopy.

1 Introduction

Recently, the electrical behaviour of a 13.7 mol% MgO-fully stabilized zirconia (Mg-FSZ) ceramic was characterized by impedance spectroscopy.¹ Electrical conduction through the grains and the blocking effect at the grain boundaries have similar characteristics to those of yttria-fully stabilized zirconia (YSZ) when the microstructures are similar.

For technological applications, MgO-partially stabilized zirconias (Mg-PSZ) are favoured because of their better mechanical properties.^{2,3} Mechanical and microstructural properties of compositions in the 8–10 mol% MgO range have been extensively described in the literature. On the other hand, relatively few investigations have dealt with their electrical properties.^{4,5} Conductivity values at 1000°C of 2.43 and 0.017 S m⁻¹ have been reported,^{4,5} respectively, for 8.2 and 9 mol% MgO.

Below 1100°C, Mg-PSZ can be a mixture of up to five crystallographic phases: cubic (c), tetrago-

nal (t), monoclinic (m), orthorhombic (o) and the δ -phase (Mg₂Zr₅O₁₂). In general, the c, t and m phases are the main components. The phase diagram shows an eutectoid point at ~13.5 mol% and 1400°C. The metastable cubic solid solutions undergo a decomposition reaction with a maximum rate at ~1200 °C.⁶ The destabilization of hyper- as well as hypo-eutectoid compositions has been studied, with emphasis on its effect on the material's mechanical properties.^{7–11}

This study is focused on the electrical conductivity of various Mg-PSZ ceramics. For comparison, results¹ recently reported on a fully-stabilized composition of 13.7 mol% MgO will be included in some of the tables and figures. To obtain more data which could support the interpretations of the blocking effects, the conductivity and permittivity of nominally pure zirconia (NPZ) have also been evaluated with the same measurement technique. A conclusion of this work is that the presence of monoclinic zirconia can be detected and characterized by impedance spectroscopy. The decomposition of cubic zirconia could therefore be monitored by this technique. Exploratory measurements were carried out to confirm this conclusion.

2 Experimental Procedures

The starting materials were powders of ZrO₂ with impurity contents lower than 1% (Merck and DK-2 type from Zirconia Sales) and analytical reagent grade MgO (Merck). Mg-PSZ and Mg-FSZ pellets of 0.92 to 0.95 cm diameters and 0.13 to 0.16 cm thicknesses were prepared by wet mixing, pressing, sintering at 1650°C for 2 h and machining. NPZ pellets were prepared from both ZrO₂ powders by uniaxial and isostatic pressing without any high temperature heat treatment.

The apparent densities of the sintered specimens

were determined by the hydrostatic method and their phase contents by X-ray diffraction analysis. In the PSZ, the monoclinic phase content was calculated from the ratio of appropriate diffraction peaks, following the procedure recommended by Porter and Heuer.¹² Specimens for the electron microprobe analyses were polished to 1 μm . For electron microscopy, they were either fractured or polished and thermally etched. Magnesium content was checked by neutron activation analysis.

For electrical measurements, platinum electrodes (Demetron A308) were painted on the pellet bases and baked at 800°C for 15 h. The impedance measurements were performed from 5 Hz to 13 MHz with an HP 4192A impedancemeter. The results were analysed in impedance mode, using software developed for the Hydro Quebec Research Center. The Mg-PSZ diagrams were measured over the 270–700°C temperature range. Data were collected during heating and cooling cycles.

The reversible monoclinic–tetragonal ($m \leftrightarrow t$) phase transformation of the NPZ samples was studied by thermal cycling between 800 and 1370°C. Heating and cooling rates were 8.3 and 2.8°C min⁻¹, respectively. The Mg-FSZ and Mg-PSZ phase destabilization experiments were carried out at 1100°C for different annealing times, up to 14 h. In this case, the impedance diagrams were measured at a lower temperature of 553°C.

3 Physical, Chemical and Microstructural Characterizations

Table 1 shows the impurity contents of the Merck ZrO₂ powder determined by spectrographic analysis. The particle size was in the 10–40 μm range. Results for the other powders have already been published.¹ The relative density of the sintered Mg-PSZ pellets was evaluated to be ~85%, with pore sizes $\leq 0.5 \mu\text{m}$. The density of the pressed NPZ samples was 60% of the theoretical value.

The MgO contents of the samples, as determined by neutron activation, are listed in Table 2. Solid mixtures may present some degree of chemical heterogeneity.¹³ Such a non-homogeneous distribution of the solute is shown in the micrograph of the Mg X-ray image of the ZM5 sample (Fig. 1). The Mg-PSZ samples are also heterogeneous in terms of grain sizes. Figure 2 is a representative micrograph (ZM2 sample) showing two distinct

Table 1. Metallic impurity content of pure zirconia powder from Merck

Element	Fe	Ti	Si	Ca	K
Content (ppm)	< 50	< 500	< 200	< 500	< 50

Table 2. MgO content and monoclinic phase volume fractions (V_m) in sintered specimens

Specimen	MgO content (mol%)	V_m (%)
ZM1	3.16	> 90
ZM2	5.14	62
ZM3	6.82	57
ZM4	8*	51
ZM5	11.89	16
ZM6	13.7	0

*Nominal concentration fixed by preparation.



Fig. 1. X-ray image showing Mg distribution for ZM5 sample.

regions of dissimilar grain sizes. Such bimodal distributions are found in biphasic ceramics when the phases have different grain growth rates. The larger grains have a higher MgO content, and the porosity is preferentially located within them and at the triple junctions. The small grains have a more homogeneous size distribution, as shown in the micrograph of the fractured surface of the ZM1 sample (Fig. 3).

The main difference among the Mg-PSZ samples is the relative fraction of the large to small

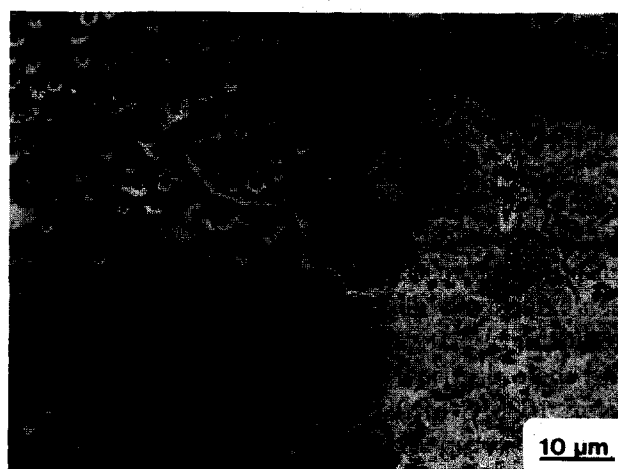


Fig. 2. Scanning electron micrograph showing zones with different grain sizes for ZM2 sample.

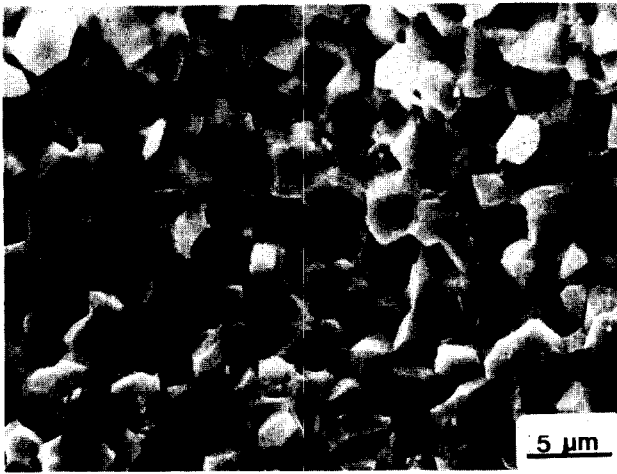


Fig. 3. Fractured surface for ZM1 sample.

grains. Increasing the magnesium content increases the fraction of large grains. The fully stabilized cubic sample has a homogeneous microstructure of rather large grains of $18 \mu\text{m}$ average size. This is consistent with a frequent observation that cubic grains have a grain growth larger than the other common phases. All the Mg-PSZ samples exhibit these chemical and microstructural heterogeneities to various extents.

The volume fractions V_m of the monoclinic phase shown in Table 2 were determined after the electrical measurements, to take into account a possible extra destabilization during the processing of the electrodes. As an example of such an alteration, Fig. 4 shows two X-ray diffractograms obtained with a sample of a composition similar to ZM4 but sintered only for 1 h at 1650°C . A

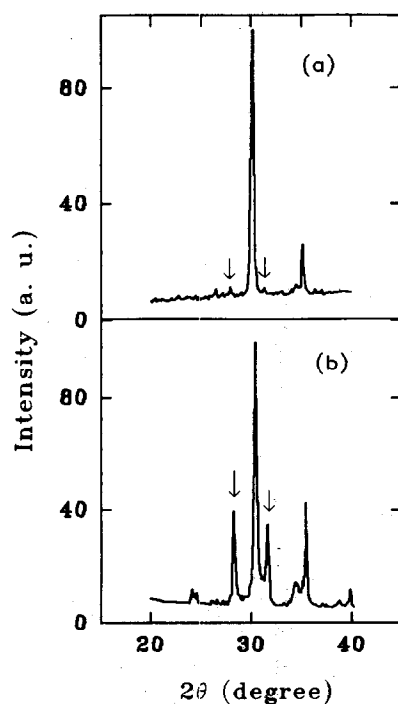


Fig. 4. X-ray diffractograms of 8 mol% MgO zirconia, sintered at 1650°C for 1 h: (a) as-sintered and (b) after measurements. The arrows point to monoclinic lines.

significant increase in the intensities of the main monoclinic phase reflections is clearly seen in the 'after measurement' profile (b) with respect to the 'as fired' profile (a). The corresponding $t \rightarrow m$ phase transformation most likely occurred during the electrode heat treatment. The absence of any hysteresis effect during the measurement temperature cycling ensures that this phenomenon did not occur during our measurements. The temperature range was lower than that of the electrode curing.

4 Electrical Conductivity and Blocking Effects of Mg-PSZ

For the sake of clarity, the electrode characteristics have been subtracted from the experimental diagrams. This could be done without ambiguity. As reported previously, the impedance diagrams of fully stabilized zirconia [ZM6, Fig. 5(a)] shows two well separated semicircles typical of the grains (g) and grain boundaries (gb), with characteristic parameters similar to those of cubic YSZ. The partially stabilized zirconias give more complex diagrams, as shown in Figs 5(b) and 5(c) (ZM5 and ZM4 samples) in which similar components can still be detected, referring to the relaxation frequencies. In the intermediary frequency domain between these conventional high and low frequency

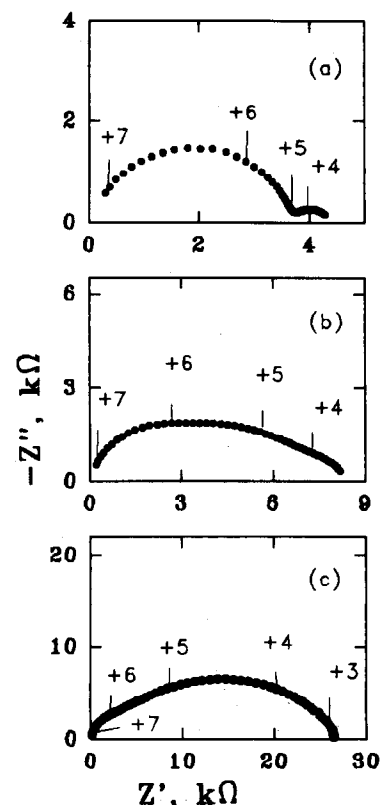


Fig. 5. Typical impedance diagrams for: (a) ZM6; (b) ZM5; and (c) ZM4 samples. $T = 507^\circ\text{C}$. (Note that the axis scales are different.) The figures indicate the decimal logarithm of the measuring frequencies.

semicircles, which can also be assigned to the grains and grain boundaries for reasons given below, a third arc hereafter referred to as the extra arc (or ex) can be separated. Its contribution to the overall (or d.c.) electrolyte resistivity markedly increases with the decrease in MgO content. It dominates in the ZM1 and ZM2 impedance spectra. Because of this strong correlation, this extra arc has been ascribed to the electrical effect of the monoclinic grains, the concentration of which also varies markedly with the MgO content (Table 2). The pores, which have a relatively high concentration in the samples, certainly induce a blocking effect as well, but the reported results unambiguously show that their contribution is not dominant. Their concentration is fairly constant and should not induce highly variable effects. A further quantitative argument in favour of this statement will be given below.

For technical applications, the overall electrolyte resistivity is a key parameter. For all the investigated compositions, it was calculated from the resistance measured at the low frequency real axis intersection of the impedance diagrams. Figure 6 shows the Arrhenius plots of the corresponding resistivities ρ . As expected, these overall resistivities decrease with the increase in MgO concentration but, surprisingly enough, there is no sharp transition and no maximum at the phase boundary between the pure cubic material (ZM6) and the biphasic partially stabilized compounds. This rather smooth evolution is illustrated in Fig. 7 which shows the variations of the overall resistivities as a function of the MgO content, at 500°C. The apparent activation energies deduced from the Arrhenius diagrams of Fig. 6 also vary in a rather continuous manner as a function of the

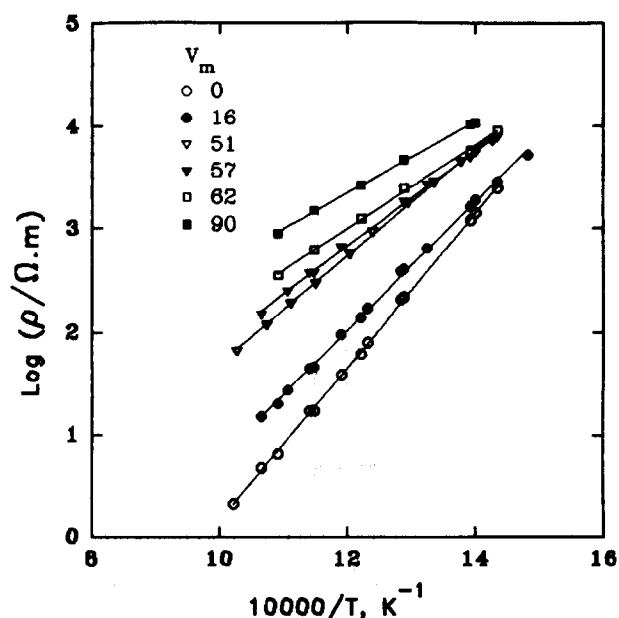


Fig. 6. Arrhenius plots of d.c. resistivities of investigated samples.

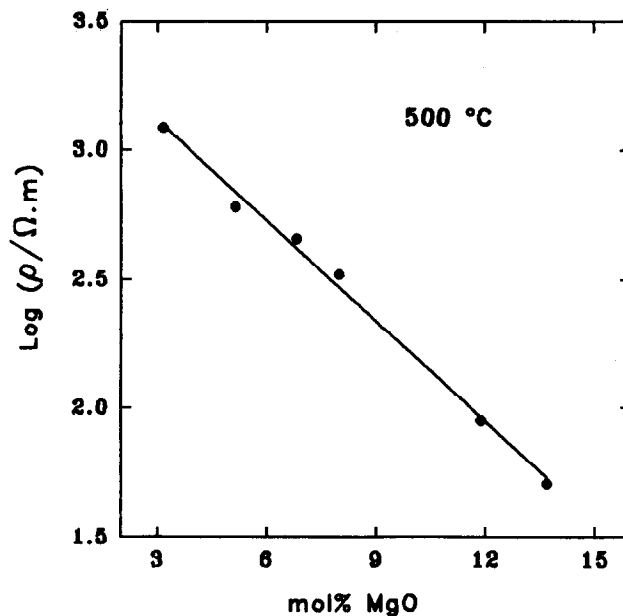


Fig. 7. Variations of resistivities at 500°C with MgO concentration.

MgO content (Fig. 8). Similar observations have already been made by Ioffe *et al.*¹⁴ and Badwal¹⁵ on the $Y_2O_3-ZrO_2$ and $Sc_2O_3-ZrO_2$ systems. For the Mg-PSZ compositions, in the temperature range of this investigation, the only available literature data (59 kJ mol⁻¹) were obtained with a 9 mol% MgO sample prepared from a high-silica content zirconia powder.⁵ Under such conditions, magnesium silicate could have formed at the grain boundaries, thereby depleting the Mg inside the grains. In addition, the measurements were carried out at a fixed 10 kHz frequency. In zirconia-based solid solutions, the frequency distribution of the electrolyte relaxation processes (and of the electrodes) shifts towards higher frequencies with

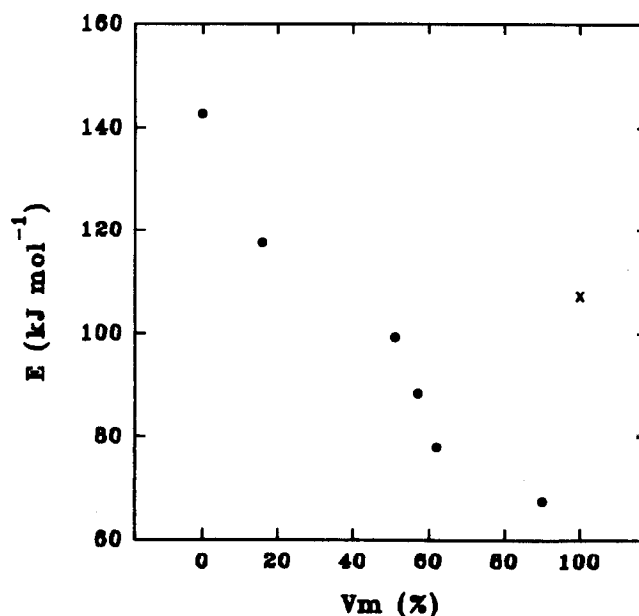


Fig. 8. Variations of d.c. resistivity apparent activation energies with monoclinic phase volume fraction V_m . The 100% point (X) is that of pure zirconia.

increasing temperature.^{16,17} Therefore, measurements at a fixed frequency may give erroneous activation energies, with too low values. In the 1200–1600°C temperature range, Janke & Fischer¹⁸ determined an activation energy of 65 kJ mol⁻¹ for the 6 mol% composition.

As evident in the examples given in Fig. 5, resolution of the diagrams of our Mg-PSZ samples was not always straightforward. Note that when the ratio of the relaxation frequencies of two adjoining semicircles is of the order of 10, the overlapping is such that any resolution is questionable. Conversely, a ratio of 1000 results in an unambiguous separation. Our diagram analysis was restricted to the 350–570°C temperature range, where the fitting accuracy was good (see below). As an example of results of our resolutions, Figs 9(a) and 9(b) present the Arrhenius diagrams of the relaxation frequencies and resistivities of the ZM4 sample. The fitted straight lines are approximately parallel and the experimental scatter is small. Similar parallelism observations were also made in Mg-FSZ¹ and YSZ¹⁹ ceramics. With this ZM4 sample, the values for the relaxation frequency ratios f_g/f_{ex} and f_{ex}/f_{gb} are ~35 and 40 (f_g , f_{ex} and f_{gb} are, respectively, the relaxation frequencies of the grain, the extra arc and the grain boundary

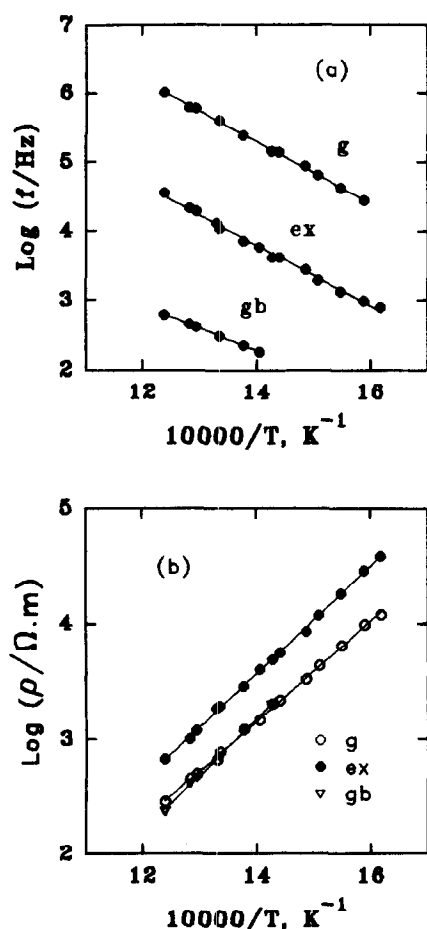


Fig. 9. Arrhenius diagrams of relaxation frequencies (a) and resistivities (b) of the three semicircles for ZM4 sample.

semicircles). The f_g/f_{ex} ratio monotonically shifts towards lower values with increasing Mg concentrations, thus increasing the overlapping.

The first feature to be ascertained in the resolution was the shape of the extra arc. For better insight concerning the possible variations in the shape of this component, the resolution was performed by successive individual fittings and subtractions. In all the resolutions we performed, the extra component did appear to be a semicircle. To test the quality of the resolution, we referred to the following criteria, as well as the coherence of the results, which will be presented below:

- the absence of any significant 'structure' in the differences between the experimental results and the fitted curves; and
- the values of the permittivity deduced from the semicircle fitting the grain response.

Figure 10 shows a typical difference diagram between the experimental results and the corresponding fitted curve (ZM4 sample, 507°C). No significant 'structure' can in fact be detected in such a diagram.

Figure 11 shows the average permittivities that were calculated for the grain semicircles of all the samples. These values are very close to the values reported in the literature¹ for the fully stabilized compositions, at temperatures similar to those of our experiments, and under conditions for which there was no ambiguity in the curve fitting. The experimental scatter of these values is also low. The values show a significant decrease as the content in the monoclinic phase increases. This is consistent with the theoretical expectation, assuming that at high temperature the permittivity of the

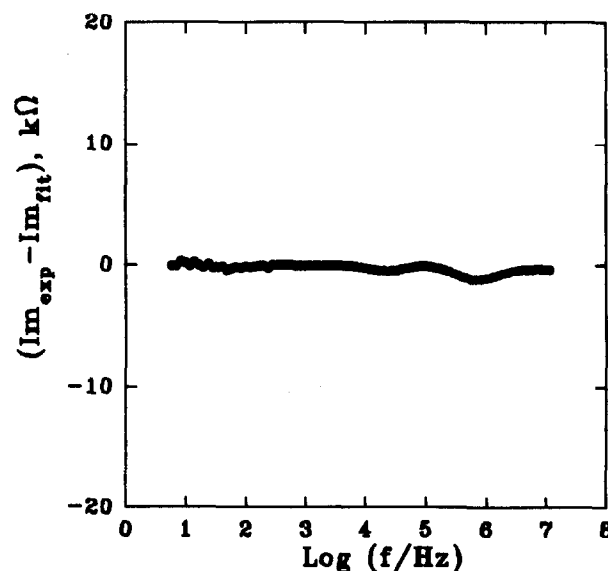


Fig. 10. Example of a difference plot between experimental (exp) and fitted (fit) values of the impedance imaginary part for ZM4 sample. $T = 507^\circ\text{C}$. (The corresponding impedance moduli are of the order of 10 k Ω .)

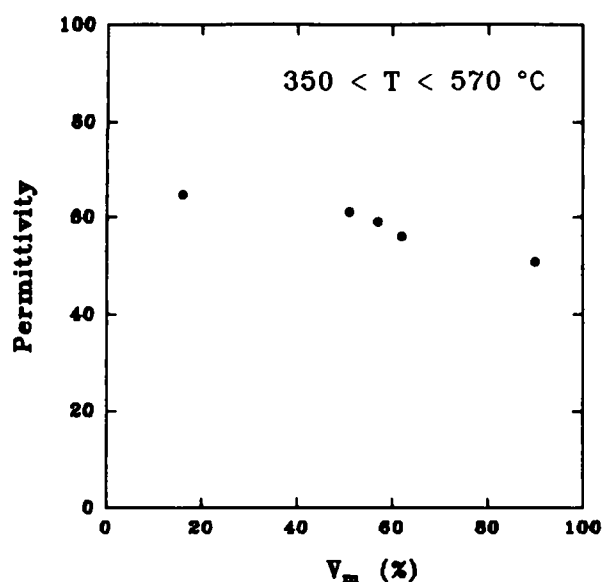


Fig. 11. Average relative permittivity deduced from the high frequency semicircle as a function of monoclinic volume fraction V_m .

monoclinic phase remains smaller than that of the other phases. At room temperature, the values are 29.3, 39.8 and 12.5, respectively, for the cubic, tetragonal and monoclinic phases.²¹ A highly similar behaviour was observed²⁰ for Al_2O_3 -YSZ composites in which the relative permittivity is 12 for the alumina grains and 55 for the YSZ grains.

The other supporting features that the resolutions revealed include:

- The Arrhenius diagrams of the relaxation frequencies of the three semicircles are almost parallel for each MgO composition, as mentioned for the ZM4 sample (see Fig. 9). This is a general observation²² which has been made with various 'blockers' in YSZ.
- The depression angles are ~ 13 and 16 – 18° , respectively, for the grain and grain boundary responses, which are usual values. For the extra arc it is around 24° . This high value indicates a rather broad distribution of the determining blocker parameters (such as the size of the monoclinic grains).
- The resistivities that can be deduced from the extra arc and the grain boundary semicircle obey Arrhenius laws. For most compositions, the corresponding activation energies are slightly higher than those of the grains (Table 3). This is also a general observation. The relatively low precision of some of the grain boundary parameters is mainly due to the small size of the corresponding semicircles. The trend reported above for the d.c. resistivities is the same here: the activation energy of each semicircle decreases with the decrease in MgO content.

Table 3. Resistivity activation energies of the grain (E_g), extra arc (E_{ex}) and grain boundary (E_{gb}) semicircles (numbers given in parentheses are the corresponding regression coefficients)

Specimen	E_g (kJ mol ⁻¹)	E_{ex} (kJ mol ⁻¹)	E_{gb} (kJ mol ⁻¹)
ZM1	43.5 (0.999)	65 (0.999)	45.3 (0.982)
ZM2	78.1 (0.999)	73.3 (0.998)	57 (0.997)
ZM3	78.1 (0.999)	86 (0.999)	78.1 (0.999)
ZM4	83 (0.999)	89 (0.999)	94.5 (0.999)
ZM5	105 (0.999)	112 (0.999)	116 (0.999)
ZM6	126 (0.999)	—	141 (0.999)

A curious result must be stressed here. The variations of the grain resistivity are relatively small despite the important variations in concentration in the conducting phases (refer to the variations in the fraction V_m of the monoclinic phase in Table 2). Figure 12(a) shows that in the intermediate range of MgO compositions the grain resistivity is even approximately independent of the MgO concentration. For the extreme concentrations (ZM1 on one side and ZM5 on the other), the activation energies vary significantly [Fig. 12(b)], but the orders of magnitude of the resistivities do not differ greatly. The relatively large variations of the d.c. resistivities reported above (Fig. 6) are in fact mostly due to the important changes in the extra arc magnitude.

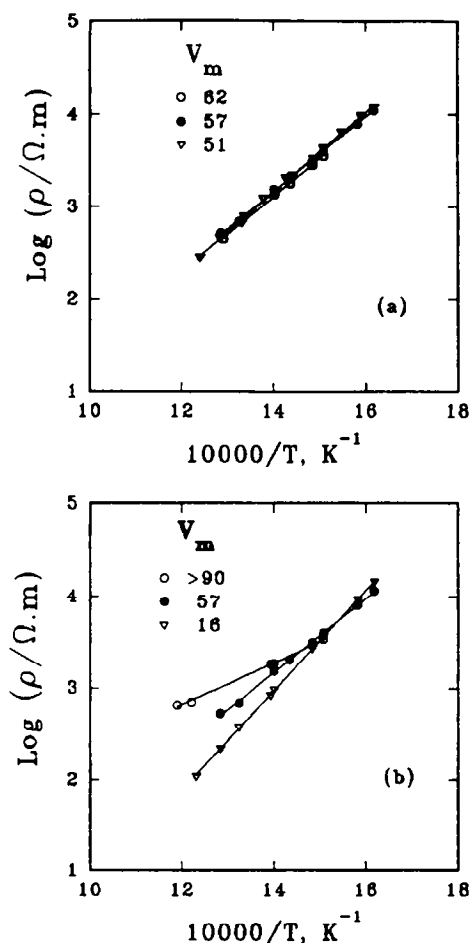


Fig. 12. Arrhenius diagrams of grain resistivities: (a) intermediate MgO contents; (b) extreme MgO contents.

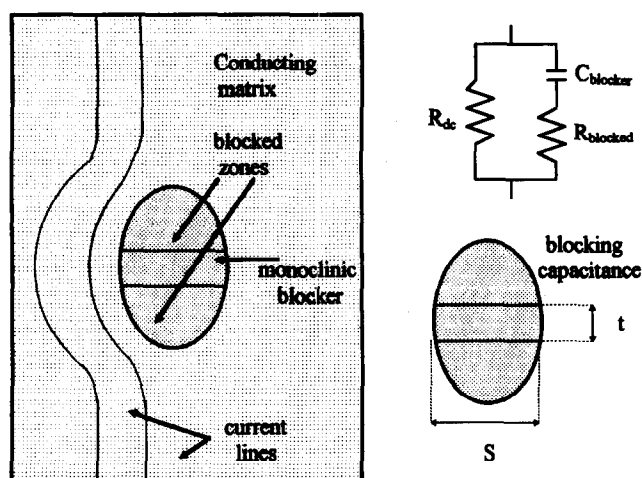


Fig. 13. Basic diagram of blocking process.

Most of our results show a strong analogy in electrical behaviour between the investigated Mg-PSZ and Al_2O_3 -YSZ composites previously investigated.²⁰ This could indicate that the monoclinic grains in the Mg-PSZ materials mostly act as insulator grains. For the blocking process in the Al_2O_3 composites, a simple model summarized in Fig. 13 has been put forward.²⁰ In accordance with this model, the extra arc will be viewed as the response of a blocked RC circuit in which the capacitance C is associated with an 'average' isolating grain of monoclinic zirconia of area S and thickness t . Accordingly,

$$C = \epsilon \epsilon^0 S t^{-1}$$

where ϵ^0 and ϵ are, respectively, the vacuum permittivity and the relative permittivity of monoclinic zirconia. The resistance R stands for the part of the conducting matrix blocked by the capacitance (in a sort of space charge). Its volume is assumed to be approximately proportional to the blocker surface area S and its thickness approximately constant at a given temperature. It can be written as:

$$R \propto \rho S^{-1}$$

where ρ is the conducting matrix resistivity. According to the above equations, the relaxation frequency of the extra arc obeys the equation:

$$f_{\text{ex}} = (2\pi R C)^{-1}$$

or

$$f_{\text{ex}} \propto (\epsilon \epsilon^0 \rho t^{-1})^{-1}$$

The fact that the resistance and relaxation frequency associated with the blocking process usually exhibit activation energies very close to that of the matrix resistivity ρ , in agreement with the above equations, strongly supports the assumptions.

For verification and application of this simple model, two specific parameters have been defined:²⁶ the blocking factor α_R which measures the fraction of electric carriers being blocked by the blockers, and the frequency factor α_F . The blocking factor should be proportional to the overall area of the blocker cross-sections perpendicular to the electric field. The frequency factor should be proportional to the average blocker thickness and to the material permittivity. These correlations have been verified²³ with pores and voids in YSZ. The equation correlating α_F to the blocker thickness has even been numerically standardized. Steil *et al.*²⁰ give the following formula:

$$\alpha_F = 7.8 \times 10^{-3} \epsilon t$$

where t is the average blocker thickness, in μm .

According to the model, the above specific parameters α_R and α_F should be calculated from the admittance diagrams of the results. Because of high overlapping in our diagrams and more difficult resolution in the admittance representation, we used impedance diagrams to determine α_R and α_F . This may have introduced some errors in the calculated values.

The first feature to be verified to ascertain the validity of this simple model is the independence of α_R and α_F with respect to the measurement conditions. Figures 14 and 15 show typical variations of these parameters with the measurement temperature for an intermediate composition (ZM4 sample). The measured parameters are not fully independent with respect to T , but the variations remain small. This corresponds to the close parallelism mentioned above between the grain and blocking processes relaxation frequency and resistivity Arrhenius diagrams.

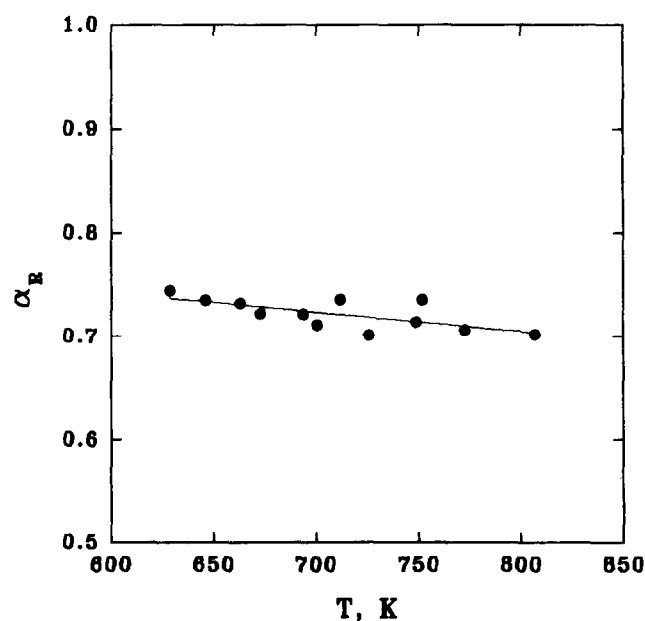


Fig. 14. Variation of blocking factor α_R with temperature for ZM4 sample.

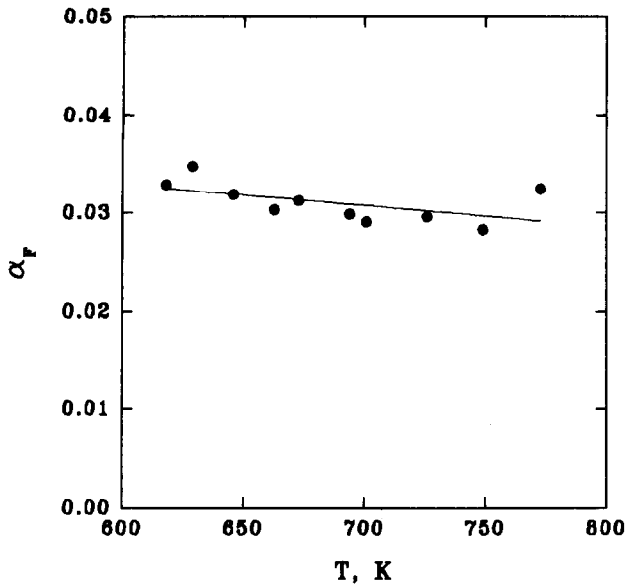


Fig. 15. Variation of frequency factor α_F with temperature for ZM4 sample.

From the average value of α_F calculated from the data in Fig. 15, and applying the previous equation, we calculated an average diameter of $4 \mu\text{m}$ for the monoclinic grains. This is in fairly good agreement with the micrographic observations. A similar calculation applied to the pores of $0.5 \mu\text{m}$ indicates that the corresponding relaxation frequency is about 100 times smaller than f_{ex} . This is a further argument supporting the assumption that the extra semicircle is mostly associated with the monoclinic grains.

Figure 16 shows the variations of the blocking factor with the monoclinic zirconia content V_m in our Mg-PSZ samples. As expected, α_R markedly increases with V_m . Despite large heterogeneities in the samples and significant uncertainties in the diagram resolutions, the scatter in the experimental results

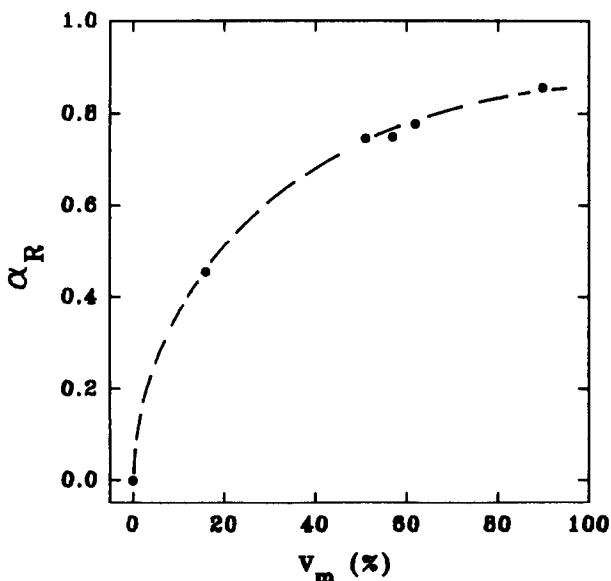


Fig. 16. Variation of blocking factor with monoclinic volume fraction V_m . $T = 500^\circ\text{C}$.

remained small and the agreement with the matrix-conduction-blocking model is reasonably good.

5 Electrical Properties of Nominally Pure Zirconia

Another straightforward interpretation can be envisaged for the extra arc. It is sketched in Fig. 17. It assumes that the complex network of the conducting and monoclinic grains are electrically equivalent to two circuits in series describing, respectively, the electrical behaviours of the conducting grains (cubic and tetragonal) and the monoclinic grains. Interpretations of this type are frequently adopted to explain the grain boundary effects.²⁴

Before entering into the details of our experimental results, let us recall an essential feature which is useful in solid state impedance spectroscopy. With a sufficiently 'simple' sample geometry and at a frequency sufficiently low for the skin effect to remain negligible, the sample resistance can be written as:

$$R = \rho k$$

where k is its geometrical factor; and its capacitance as:

$$C = \epsilon \epsilon^0 k^{-1}$$

Accordingly, the specific relaxation that we will determine by impedance measurements on the sample, is given by the equation:

$$f_{rel} = (2\pi \epsilon \epsilon^0)^{-1}$$

It is a specific property of the material, independent of the geometrical factor of the sample, and should be the same for a cubic sample and a grain

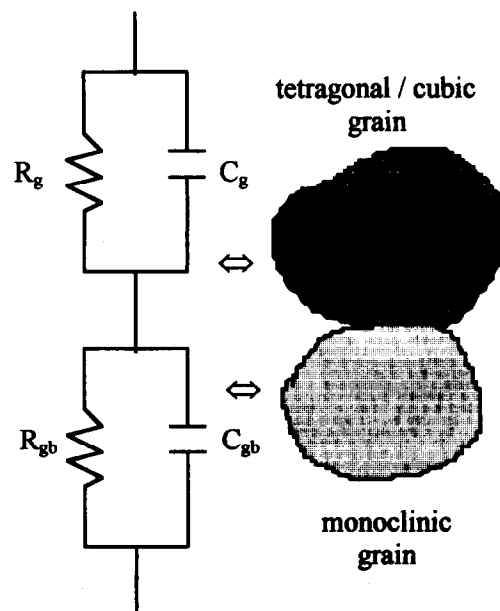


Fig. 17. Series model.

in a sintered material. It may be thought of as the signature of the material. Relaxation frequency measurements are therefore an easy test to identify a semicircle. In composite materials the electrical behaviours are slightly more complicated²⁰ because of interference between the components, especially related to the contribution of both components to the relative permittivity which determines the conducting grain relaxation.²⁰ However, this identification technique can still be used with appropriate adjustments.

To check the above assumption, impedance measurements were carried out on the NPZ samples prepared with the two pure zirconia powders (see Experimental Procedures section). They gave very similar results. All the recorded diagrams are essentially composed of a dominant bulk semicircle (Fig. 18) and a small low frequency arc which will not be examined in the following. The Arrhenius diagrams of the corresponding resistivity and relaxation frequency are shown in Figs 19(a) and 19(b), respectively. These experimental values should be regarded as approximate, because of the high porosity of the samples. For our purposes, only the orders of magnitude of these parameters are important (referring to a recent investigation of porous YSZ,²⁷ alteration factors of about 0.5 and 50 can be anticipated, respectively, for the permittivity and resistivity but with no major changes in the corresponding variations with temperature, especially in the resistivity activation energy).

The relaxation frequencies of monoclinic zirconia measured here are far lower than the values measured for the extra semicircles. For example, at 500°C, the monoclinic phase value is 51 Hz and those of the extra arc are in the 6.3–61 kHz range.

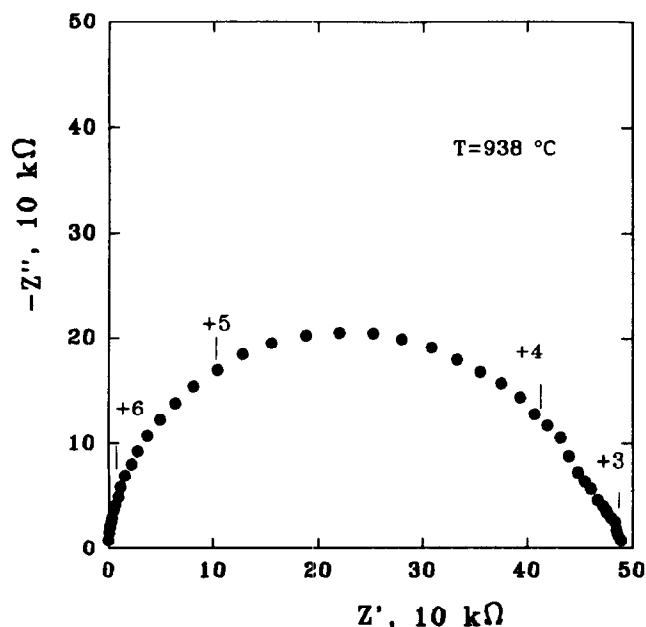


Fig. 18. Typical impedance diagram of monoclinic zirconia for NPZ sample.

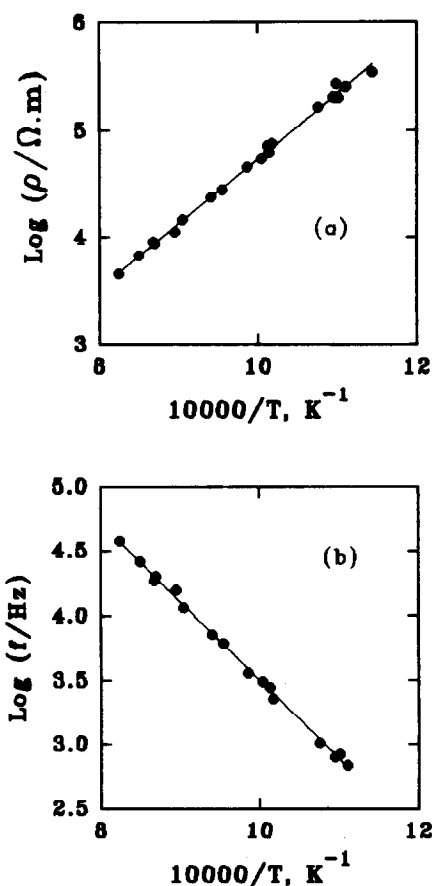


Fig. 19. Arrhenius diagram of resistivity (a) and relaxation frequency (b) of monoclinic zirconia in the 600–950°C temperature range for NPZ sample.

The resistivity activation energies also point to marked differences. The calculated value for the monoclinic phase is 118 kJ mol⁻¹ in the 600–950°C temperature range. For the extra arc, the calculated activation energies are all significantly smaller (see Table 3). Furthermore, the extra arc activation energy is variable and markedly depends on the MgO content. The assumption of the extra arc describing the specific electrical properties of the monoclinic grains can clearly be rejected.

6 Electrical Observation of the $m \leftrightarrow t$ Phase Transformation of Nominally Pure Zirconia

We took advantage of the availability of these monoclinic samples to observe the reversible $m \leftrightarrow t$ phase transformation also. Impedance measurements were carried out at various temperatures between 800 and 1370°C.

In the high-temperature range (>1000°C), the NPZ diagram looks like a regular zirconia conducting phase diagram (Fig. 20). As above, only the high-frequency semicircle, which describes the specific properties of the grains, is taken into consideration here. Figure 21 shows the corresponding resistivities measured during the cooling cycle.

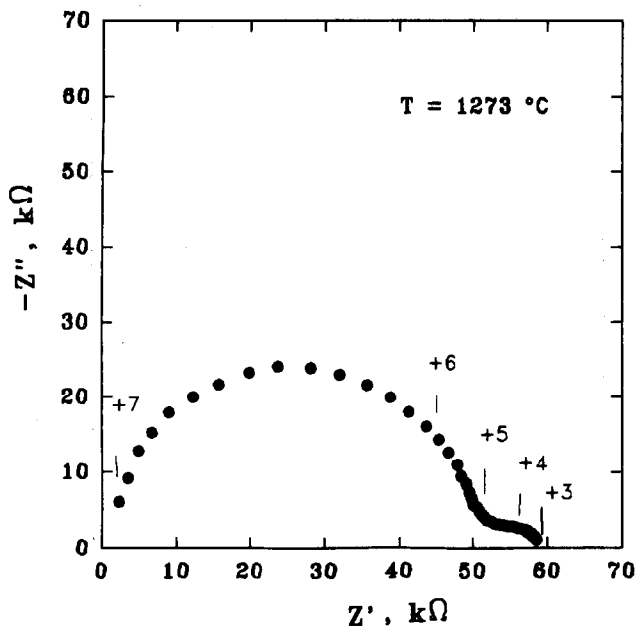


Fig. 20. Impedance diagram of tetragonal zirconia for NPZ sample.

As expected, the plot exhibits two straight lines describing the variations of the tetragonal phase conductivity, at high temperature, and those of the monoclinic phase conductivity at low temperature. The activation energies calculated from these lines are 91 and 118 kJ mol^{-1} , respectively, for the tetragonal and monoclinic phases.

The width of the temperature range over which the transition occurs is $\sim 170^\circ\text{C}$, in fair agreement with earlier d.c. measurements.²⁵ The points obtained in this temperature range of 'athermal' transition correspond to steady-state conditions. As a check, measurements were also performed after 15 h of annealing. The results marked by filled circles

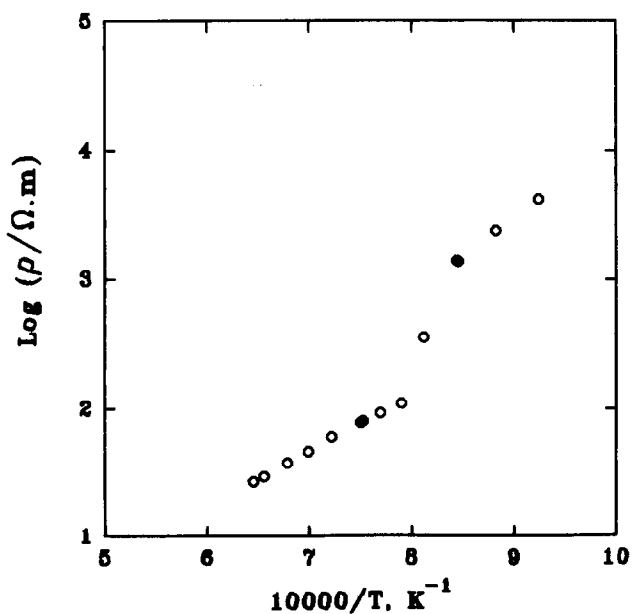


Fig. 21. Effect of $t \rightarrow m$ transformation on specific resistivity of pure zirconia for NPZ sample.

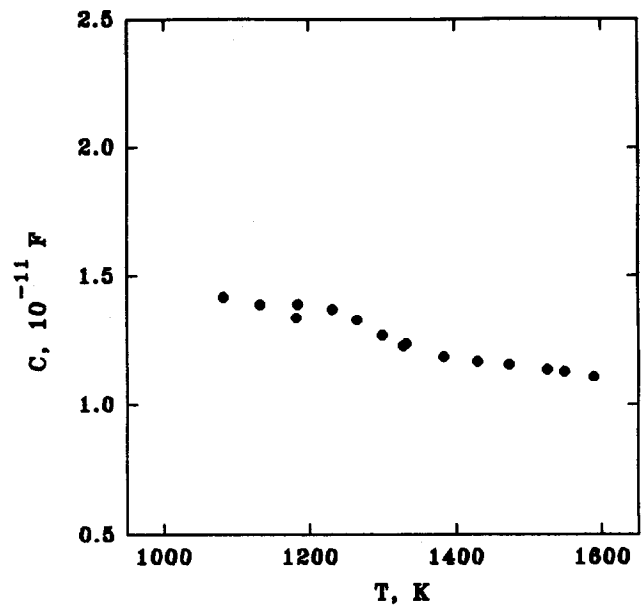


Fig. 22. Capacitance variations of pure zirconia sample (NPZ).

on the plot (Fig. 21) are perfectly aligned with the others which were more rapidly obtained.

From the impedance semicircles, the sample capacitances have also been determined. Since the effect of the sample porosity is likely to be constant and the permittivity to remain proportional to the measured capacitances, the curve shown in Fig. 22 indicates that the tetragonal \leftrightarrow monoclinic phase change does not alter much the permittivity of pure zirconia. The absence of any significant strong variation in the transition range is another interesting result.

7 Phase Decomposition of Mg-FSZ and Mg-PSZ

On the basis of the reported observations, it was concluded that impedance spectroscopy can easily measure the blocking effect due to the presence of a monoclinic phase. Therefore, it should be an appropriate technique to quantitatively follow the destabilization of a conducting zirconia matrix. Destabilization annealings of Mg-FSZ and Mg-PSZ samples were carried out to confirm this assumption.

From several previous micrographic studies^{8,9,11,12} on Mg-FSZ, it has been well established that during destabilization, the monoclinic phase is generated at grain boundaries. The cubic phase may crack because of a large difference in the thermal expansion coefficients of the c and m phases. After reaction completion, the observed microstructure usually consists of a fine-grained ($1\text{--}5\ \mu\text{m}$) monoclinic phase containing thoroughly dispersed magnesia-rich pipes.

The compositions of the samples we investigated were 13.7 mol% (ZM6) and 8 mol% MgO (ZM4). The annealing temperature was 1100 °C and the annealing times 1, 2, 3, 4, 6, 8 and 14 h. At this temperature, a rather high decomposition rate is expected. In fact, no cubic phase reflections were observed by X-ray diffraction after 14 h annealing.

The destabilization of the material results in significant changes of the impedance diagram which affect all the semicircles. The diagrams were more easily analysed for the Mg-FSZ sample for which the initial diagram is simpler [see Fig. 5(a)]. The details below are given for this sample. After 1 h annealing, the impedance spectra is similar in shape to the original diagram. However, a more careful analysis shows that the grain boundary semicircle has more markedly changed. Besides the expected increase in the corresponding resistivity, the relaxation frequency has also increased. According to the model cited above, this can be interpreted in terms of simultaneous increases in the surface areas and the thicknesses of the growing monoclinic phase which still behaves as a grain boundary blocker. The depression angle also increases, indicating an increase in the heterogeneity of this grain boundary blocking effect. After 2 h annealing, the impedance diagram no longer exhibits the original shape, as shown in Fig. 23. Most likely, the monoclinic grains are already large enough to result in an extra arc with a relatively high relaxation frequency. The very large depression angle (38°) of the blocking semicircle and the relative increase in its relaxation frequency suggest the growth of another semicircle which overlaps with the true grain boundary arc. After this 'first stage', the overlaps become so

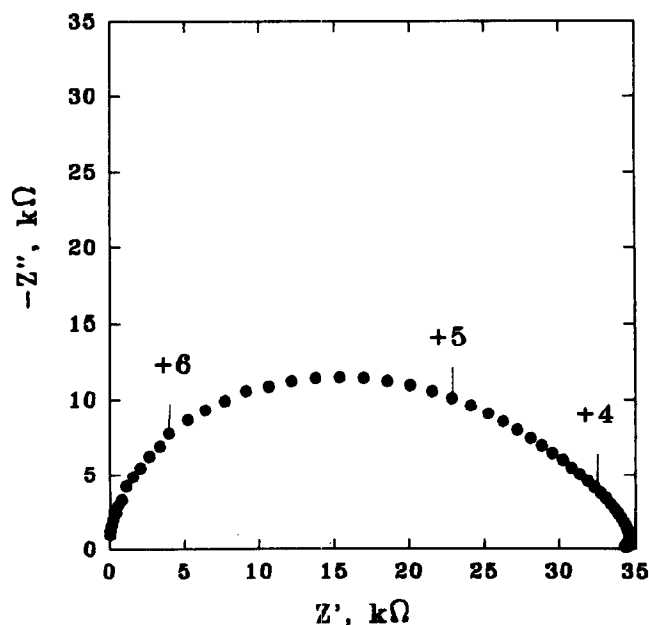


Fig. 23. Impedance diagram of ZM6 after 2 h annealing at 1100°C. Measuring temperature 553°C.

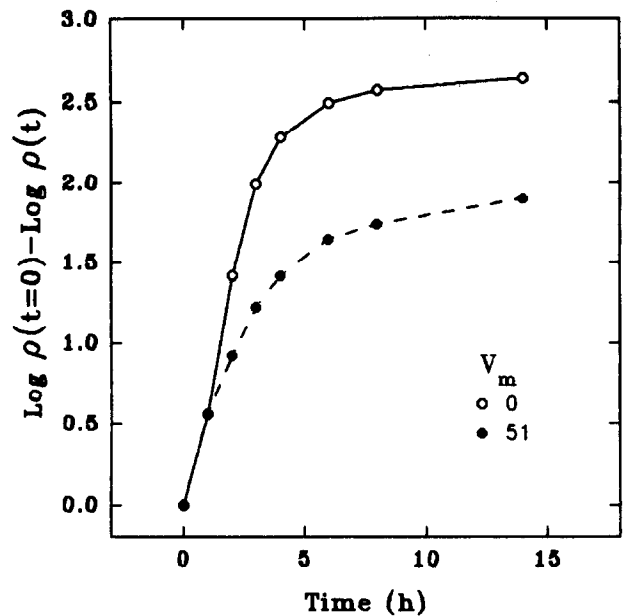


Fig. 24. Variations of ZM6 (○) and ZM4 (●) resistivities with annealing time. Annealing temperature 1100°C; measuring temperature 553°C.

strong among all the electrical responses, that it would not be realistic to envisage any semicircle separation. (The cracks that are known to be generated during the destabilization may also contribute to impedance diagram complexity.)

To quantitatively characterize the destabilization process, we simply determined the corresponding variations in the overall sample resistivity. The measurements were performed after temporarily cooling the samples to 553°C. For that, we measured the real impedance components at 10 kHz. We checked on the diagrams that this frequency approximately corresponds to the real intercept which includes the blocking effect (in other words, to the d.c. resistance). Figure 24 shows that the resistivities of the ZM6 and ZM4 samples increase very fast at a 1100°C annealing temperature. From these impedance results, it can be estimated that after 3 h at 1100°C, the d.c., resistivities have approximately increased by a factor of 100. Both samples behave similarly. After the 14 h annealing time, a steady-state situation seems to be reached which probably corresponds to a full transformation of the conducting phases into the monoclinic phase.

Table 4 compares the resistivities at 553°C

Table 4. Resistivity values at 553°C and activation energies of samples containing mostly monoclinic zirconia

Specimen	ρ (Ωm)
Annealed ZM6	2.13×10^4
Annealed ZM4	2.84×10^4
NPZ	1.62×10^6
ZM1	6.24×10^2

obtained under these conditions to that of the true monoclinic zirconia (NPZ sample) and to that of a material (ZM1 sample) which contains ~90% monoclinic zirconia. The resistivity of the monoclinic ZM6 and ZM4 materials and that of the nominally pure zirconia differ significantly and the difference is too large to be explained in terms of porosity effects. This may indicate that the MgO solubility in the monoclinic phase is not nil and that dissolved MgO induces a noticeable decrease in its resistivity or that the complex microstructure of the destabilized materials strongly influences their resistivities.

The ZM1 sample also behaves differently, with a much lower resistivity. This clearly indicates that even at its composition (with ~90% monoclinic phase), the electrical behaviour of the material is still dominated by the conducting grains present in it. A similar observation was made with Al₂O₃-YSZ composites²⁰ which show the characteristic features of YSZ up to more than 70% Al₂O₃.

8 Conclusions

In terms of electrical behaviour, the monoclinic grains in partially stabilized zirconias mostly act as an insulating second phase. There is no sharp discontinuity at the cubic phase limit. As the MgO content decreases below this limit, the main effect is a gradual increase in the blocking process due to the increasing population of monoclinic grains. As observed with other zirconia-based systems, the activation energy of the conducting phase (or the mixture of the conducting phases) markedly decreases with the MgO contents. Impedance spectroscopy is a powerful tool to study zirconia phase transformations and the destabilization processes.

Acknowledgements

The authors would like to express their appreciation to Zirconia Sales for providing the zirconia powder, to M. Hénault from the LIESG and to the research staff at IPEN for technical assistance. One of the authors (ENSM) also acknowledges CNPq/RHAE (process 260134/91.0) and FAPESP (process 92/2962-6) support.

References

1. Muccillo, E. N. S. & Kleitz, M., Ionic conductivity of fully stabilized ZrO₂: MgO and blocking effects. *J. Eur. Ceram. Soc.*, **15** (1995) 51-5.
2. Subbarao, E. C., Zirconia, an overview. In *Advances in Ceramics, Vol. 3: Science and Technology of Zirconia I*,

- eds A. H. Heuer and L. W. Hobbs. American Ceramic Society, Columbus, OH, 1981, pp. 1-24.
3. Hannink, R. H. J. & Garvie, R. C., Sub-eutectoid aged Mg-PSZ alloy with enhanced thermal up-shock resistance. *J. Mater. Sci.*, **17** (1982) 2637-43.
4. Wen, T. L., Li, N. X., Kuo, C. & Weppner, W., Conductivity of MgO-doped zirconia. *Solid State Ionics*, **18/19** (1986) 715-19.
5. Poulsen, F. W., Sorensen, J. B. B., Ahari, K. G., Knab, G. G. & Hartmanova, M., Oxygen ion conduction in ternary zirconia mixtures: effect of SrO on MgSZ. *Solid State Ionics*, **40/41** (1990) 947-51.
6. Viechnicki, D. & Stubican, V. S., Mechanism of decomposition of the cubic solid solutions in the system ZrO₂-MgO. *J. Am. Ceram. Soc.*, **48** (1965) 292-7.
7. Swain, M. V., The effect of decomposition on the thermal shock behaviour of Mg-CSZ. *J. Mater. Sci. Lett.*, **2** (1983) 279-82.
8. Hannink, R. H. J., Microstructural development of sub-eutectoid aged MgO-ZrO₂ alloys. *J. Mater. Sci.*, **18** (1983) 457-70.
9. Swain, M. V., Garvie, R. C. & Hannink, R. H. J., Influence of thermal decomposition on the mechanical properties of magnesia-stabilized cubic zirconia. *J. Am. Ceram. Soc.*, **66** (1983) 358-62.
10. Lamon, J., Thorel, A. & Broussaud, D., Influence of long-term ageing upon the mechanical properties of partially stabilized zirconia (Mg-PSZ) for heat-engine applications. *J. Mater. Sci.*, **21** (1986) 2277-82.
11. Farmer, S. C., Heuer, A. H. & Hannink, R. H. J., Eutectoid decomposition of MgO-partially stabilized ZrO₂. *J. Am. Ceram. Soc.*, **70** (1987) 431-40.
12. Porter, D. L. & Heuer, A. H., Microstructural development in MgO-partially stabilized zirconia (Mg-PSZ). *J. Am. Ceram. Soc.*, **62** (1979) 298-305.
13. Paulus, M., The influence of powder synthesis techniques on processes occurring during compact formation and its sintering. In *Materials Science Research, Vol. 17: Emergent Process Methods for High-Technology Ceramics*, eds R. F. Davis, H. Palmour III and R. L. Porter. Plenum Press, New York, 1984, pp. 177-91.
14. Ioffe, A. I., Rutman, D. S. & Karpachov, S. V., On the nature of the conductivity maximum in zirconia-based solid electrolytes. *Electrochim. Acta*, **23** (1978) 141-2.
15. Badwal, S. P. S., Effect of dopant concentration on electrical conductivity in the Sc₂O₃-ZrO₂ system. *J. Mater. Sci.*, **22** (1987) 4125-32.
16. Schouler, E., Kleitz, M. & Deportes, C., Applications selon Bauerle du tracé des diagrammes d'admittance complexe en électrochimie des solides. II - Etude de la conductivité de la zircone stabilisée à l'yttrium. *J. Chim. Phys.*, **9** (1973) 1309-16.
17. Stratton, T. G., Reed, D. & Tuller, H. L., Study of boundary effects in stabilized zirconia electrolytes. In *Advances in Ceramics, Vol. 1: Grain Boundary Phenomena in Electronic Ceramics*, eds L. M. Levinson. American Ceramic Society, Columbus, OH, 1981, pp. 114-23.
18. Janke, D. & Fischer, W. A., Elektrische eigenschaften oxidkeramischer festelektrolyte bei stahlschmelz-temperaturen. *Arch. Eisenhüttenwes.*, **48** (1977) 311-18.
19. Kleitz, M., Bernard, H., Fernandez, E. & Schouler, E., Impedance spectroscopy and electrical resistance measurements on stabilized zirconia. In *Advances in Ceramics, Vol. 3: Science and Technology of Zirconia I*, eds A. H. Heuer and L. W. Hobbs. American Ceramic Society, Columbus, OH, 1981, pp. 310-36.
20. Steil, M. C., Thévenot, F., Dessemond, L. & Kleitz, M., Impedance spectroscopy analysis of conduction percolation in zirconia-alumina composites. In *Proceedings of 3rd European Ceramic Society Conference*, eds P. Duran and J. F. Fernandez. Faenza Editrice Iberica SL, San Vicente, 1993, pp. 271-80.
21. Cormack, A. N. & Parker, S. C., Some observations on the role of dopants in phase transitions in zirconia from

- atomistic calculations. *J. Am. Ceram. Soc.*, **73** (1990) 3220–4.
22. Dessemond, L., Muccillo, R., Hénault, M. and Kleitz, M., Electric conduction–blocking effects of voids and second phases in stabilized zirconia. *Appl. Phys.*, **A57** (1993) 57–60.
 23. Kleitz, M., Pescher, C. & Dessemond, L., Impedance spectroscopy of microstructure defects and crack characterization. In *Zirconia V: Science and Technology of Zirconia*, eds S. P. S. Badwal, M. J. Bannister and R. H. J. Hannink. Technomic Publishing Co., Lancaster, 1992, pp. 593–608.
 24. Chu, S. H., Seitz, M. A., J., The a.c. electrical behavior of polycrystalline ZrO_2 : CaO. *J. Solid State Chem.*, **23** (1978) 297–314.
 25. Subbarao, E. C., Maiti, H. S. & Srivastava, K. K., Martensitic transformation in zirconia. *Phys. Stat. Sol. (a)*, **21** (1974) 9–40.
 26. Dessemond, L., Spectroscopie d'impédance des fissures dans la zircone cubique. Thesis, Grenoble, November 1992.
 27. Kleitz, M., Dessemond, L., Steil, M. C., Effects of pores, inclusions and cracks on the ionic conduction in YSZ, 22d Meeting of the Japanese Solid Oxide Fuel Cells Society, Yokohama, March 1994.

Structural and Electrical Properties of PbTiO_3 Thin Films Grown on Silicon Substrates

D. Remiens, B. Jaber, P. Tronc & B. Thierry

CRITT Céramiques Fines, Laboratoire des Matériaux Avancés Céramiques, Université de Valenciennes et du Hainaut-Cambrésis, Z.I. Champ de l'Abbesse, 59600 Maubeuge, France

(Received 18 November 1994; revised version received 30 June 1995; accepted 14 July 1995)

Abstract

Thin films of ceramic materials take an important place in microelectronics and in microtechnologies. They present many properties which can be used for the realization of new devices and sensors. We present the growth of PbTiO_3 thin films on silicon and platinized silicon substrates by RF magnetron sputtering. The electrode deposition and thicknesses were optimized to produce metallization without the defects which are frequently observed with Pt electrodes. The influence of the bottom electrodes on the film properties in terms of structure and microstructure was analysed. The PbTiO_3 crystallization was optimized for the two types of substrates: Si/SiO_2 and $\text{Si}/\text{SiO}_2/\text{Ti}/\text{Pt}$. The electrical properties of the films and in particular the ferroelectricity were evaluated.

1 Introduction

Recently, interest in ferroelectric thin films has grown rapidly with active studies directed towards exploring several ferroelectric compositions, while involving a variety of deposition techniques. The techniques usually used for fabricating ferroelectric thin films have included sol-gel processing,¹ metallo-organic chemical vapour deposition (MOCVD),² laser ablation³ and radio-frequency (RF) magnetron sputtering.⁴ Sputtering is very well adapted to grow ferroelectric thin films at low temperatures and for optical applications.⁶ The growth of ferroelectric thin films on silicon substrates offers several advantages for integrated circuit and miniaturized devices. The applications are very important: piezoelectric and pyroelectric sensors, electro-optic devices and non-volatile memories. For many applications the silicon substrate must be metallized: a Ti/Pt electrode is usually used mainly because of its superior barrier effect against chemical reactions between the film and the Si substrate.

We report on the growth of PbTiO_3 thin films, deposited at room temperature, from an oxide target by RF magnetron sputtering. The films were deposited onto different substrates: oxidized (100) silicon (Si) wafers and oxidized (100) Si coated with Ti–Pt electrodes. A subsequent annealing treatment was performed to crystallize the film. The electrodes have an important influence on the film properties and so we have optimized the metallization growth conditions and annealing treatment. We have studied the influence of the electrodes on the PbTiO_3 film qualities and, in particular, on the structures and the microstructures. Electrical properties were evaluated by measuring the ferroelectric behaviour.

2 Experimental Procedures

An RF magnetron sputtering system, described previously,⁷ was used to prepare PbTiO_3 thin films. The sputtering target was a mixture of PbO and TiO_2 powders; they were obtained by uniaxially cold pressing. The targets composition are $x\text{PbO} + y\text{TiO}_2$ where x and y represent the mole fraction of PbO and TiO_2 , respectively. The sputtering conditions used in this experiment are summarized in Table 1; depositions were performed at room temperature. For targets $0.54\text{PbO} + \text{TiO}_2$, the films are nearly stoichiometric ($\text{Pb}/\text{Ti} = 1.15$). The lead excess is evaporated during the post-annealing treatment to obtain stoichiometric films. The substrate temperature increased during sputtering (60°C), induced by the particle bombardment (electrons, ions, etc.).

We have limited the RF power to 10 W; for higher power, microcracks appear at the single composite oxide surface target and, more precisely, in the erosion area (magnetron system) after a few hours of sputtering. The target contains much porosity (the target fabrication is described previously⁸), which limits evacuation of

Table 1. Sputtering conditions for preparation of PbTiO₃ films

RF power	10 W
Target diameter	25 mm
Target composition	0.54 PbO + TiO ₂
Interelectrode distance	35 mm
Gas pressure	100 mT
Sputtering gas	Ar
Substrate temperature	Ambient–60°C

the energy loss in the target during sputtering and so induces thermal stress.

These growth conditions were selected in order to have a relatively important deposition rate (for oxides), which is of the order of 20 Å min⁻¹ on Si/SiO₂ substrates. The substrate preparation before the growth is crucial to obtain PbTiO₃ film of good crystalline quality and adherence. We have used a procedure well known in semiconductor technology⁹ for the preparation of the Si/SiO₂. The Si/SiO₂/Ti/Pt substrates were only degreased and dried. The film thicknesses were measured by profilometry. Then, after photolithography the films were chemically etched to make a step between the film and the substrate. The deposition of Ti/Pt metallization is an important parameter, directly related to the ferroelectric thin film properties. We have studied the growth and annealing conditions of the Ti/Pt layers.

Since the films were deposited on unheated substrates they were amorphous and a post-deposition annealing was necessary to crystallize the film into the perovskite structure. We have used conventional annealing and have optimized the annealing parameters, i.e. temperature and time, for both the Si/SiO₂ and Si/SiO₂/Ti/Pt structures. The presence of the metallization affects the morphology and the crystal structure formation of the PbTiO₃ film.

3 Results and Discussion

3.1 Bottom electrode deposition and post-annealing treatment

Titanium and platinum films were deposited on (100) oriented silicon substrates, passivated with a thermally grown silicon dioxide layer of 5000 Å. The same substrates without metallization were used for the growth of PbTiO₃ films in order to study the influence of the metallization on the PbTiO₃ crystallization. The electrodes were grown by a RF magnetron sputtering technique without substrate heating. Ti/Pt metallizations were fabricated by a sequential deposition process in a single pump-down cycle without breacking the vacuum. The growth conditions were fixed in order to have a very slow growth rate: RF power is 70 W (the target diameter is 150 mm) and the

gas pressure is 20 mT. With these conditions the Pt layer is very dense and the surface morphology is smooth. The titanium layer is employed to promote adhesion. The thickness of the electrodes was varied between 100 and 500 Å for Ti and 800 and 2000 Å for Pt, and we have studied the influence of the electrode thickness on the morphology after annealing. The Pt layer presents a (111) preferred orientation just after deposition. The annealing treatment of the electrode is the same as for the PbTiO₃ films: the annealing temperature is 680°C and the annealing time is fixed to 1 h. After thermal annealing the metallized substrates were systematically observed with a scanning electron microscope (SEM). The annealing treatment induced a more pronounced (111) preferred orientation with no (200) oriented grains detectable by X-ray diffraction (XRD) analysis.

Figure 1 shows the surface morphology of Ti/Pt films after annealing; the thicknesses of Ti and Pt were 200 and 1000 Å, respectively. The platinum, originally very small-grained, has coalesced into larger grains which have holes in between them. The recrystallization of the Pt layer results in the formation of Pt droplets; the surface morphology was very rough.

A PbTiO₃ film was grown on this electrode; the morphology is a replica of the Ti/Pt layers. All test capacitors measured on these exhibit electrical shorts which are attributed to the Pt hillocks and holes formation. For a thicker Pt layer, the thickness of the Ti layer was maintained constant, the morphology is different. Figure 2 shows a scanning electron micrograph of a Ti/Pt layer after annealing; the thickness of the Pt layer is 2000 Å. The Pt layer was continuous without holes or hillocks. With such an electrode, the PbTiO₃ film presents no degradation and electrical characterizations are possible; identical results were obtained for the thicker Ti layer (500 Å).

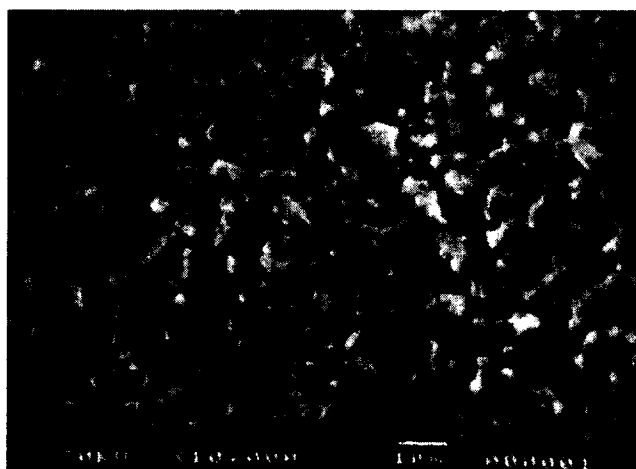


Fig. 1. SEM photograph of Ti/Pt films after annealing (Ti = 200 Å, Pt = 1000 Å).

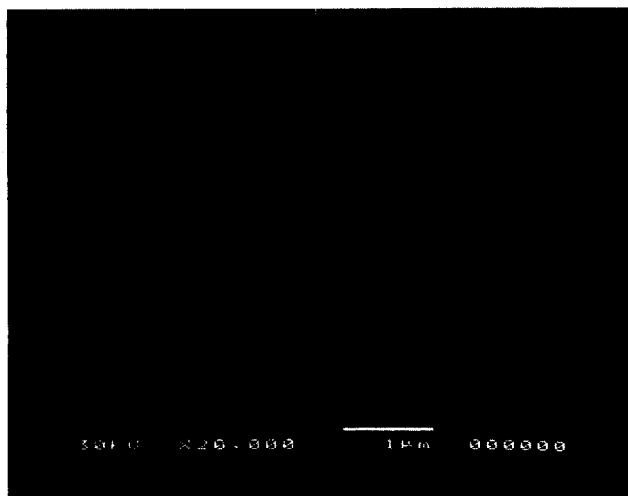


Fig. 2. SEM photography of Ti/Pt films after annealing (Ti = 200 Å, Pt = 2000 Å).

3.2 Post-annealing treatment of PbTiO_3 on silicon and platinized silicon substrates

As we have mentioned previously, deposition of PbTiO_3 was performed at room temperature and the film is amorphous. A post-annealing treatment is necessary to crystallize the film into the perovskite phase and to remove the porosity of the film. We have optimized the conventional annealing treatment for the two types of substrates: Si/SiO₂ and Si/SiO₂/Ti/Pt (annealing at 680°C for 1 h).

Figure 3 shows the XRD pattern of the PbTiO_3 film (thickness 0.6 μm) grown on Si/SiO₂ (a) and Si/SiO₂/Ti/Pt (b) substrates; the annealing temperature is 680°C and the annealing time is 30 min. The ramp down is fixed to 5°C min⁻¹; for higher values microcracks appear on films grown on Si/SiO₂ substrates but not on Si/SiO₂/Ti/Pt. The ambient gas is air. We observed an improvement in the crystallinity of the film in the case of platinized substrates, evidenced by higher and sharper XRD peaks. The platinum layer favours the crystallization of the PbTiO_3 film. The films are preferentially (101) oriented for the two types of substrates, but the preferred orientation is more pronounced on annealing platinized substrate. Without annealing the Pt layer, the XRD pattern of the PbTiO_3 film is similar to that obtained on Si/SiO₂ substrates. The degree of orientation of Pt affects the orientation of the PbTiO_3 deposited on it. No second phases were observed to occur after annealing and the (111) Pt orientation was retained.

The annealing time influences considerably the crystallinity of the film. Figure 4 shows the XRD diffraction pattern of PbTiO_3 films grown on Si/SiO₂/Ti/Pt substrates. The annealing times are 30 min (a), 1 h (b) and 2 h (c); the annealing temperature is 680°C. When the annealing time increased, the crystallinity of the film decreased.

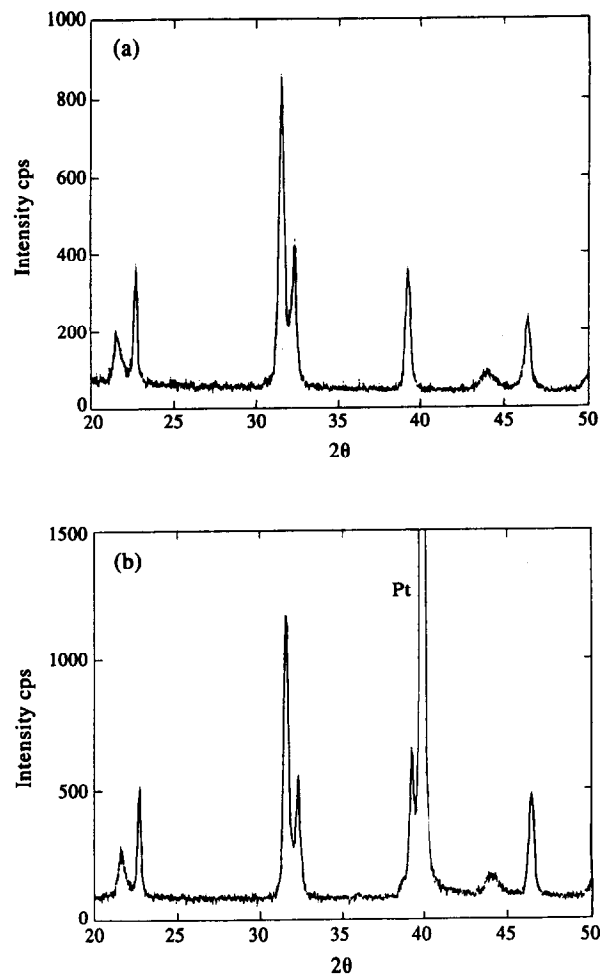


Fig. 3. (a) XRD pattern of PbTiO_3 film on Si/SiO₂ substrate (annealing temperature = 680°C, annealing time = 30 min). (b) XRD pattern of PbTiO_3 film on Si/SiO₂/Ti/Pt substrate (annealing temperature = 680°C, annealing time = 30 min).

So we can conclude that the best annealing parameters for the structure Si/SiO₂/Ti/Pt/ PbTiO_3 are 680°C for 30 min. The same study was made for Si/SiO₂ substrates; the annealing time must be fixed to 1 h to obtain a film crystallinity similar to that obtained on a platinized silicon substrate.

The annealing time controls the grain size; the grain size increased as the annealing time increased, as shown in Fig. 5 (Si/SiO₂/Ti/Pt substrates) with an annealing temperature of 680°C. For an annealing time of 30 min, the grain size is of the order of 150 nm (measured from a scanning electron micrograph) with a uniform distribution; the film has a dense morphology without porosity. A large amount of porosity appears for an annealing time of 2 h, induced by grain growth.

The same behaviour was observed for Si/SiO₂ substrates but the microstructure of the PT film appears different, having large grains with very fine grains between them. The Pt metallization seems to affect also the microstructure of the PbTiO_3 film. Further studies are in progress to confirm and to understand this behaviour.

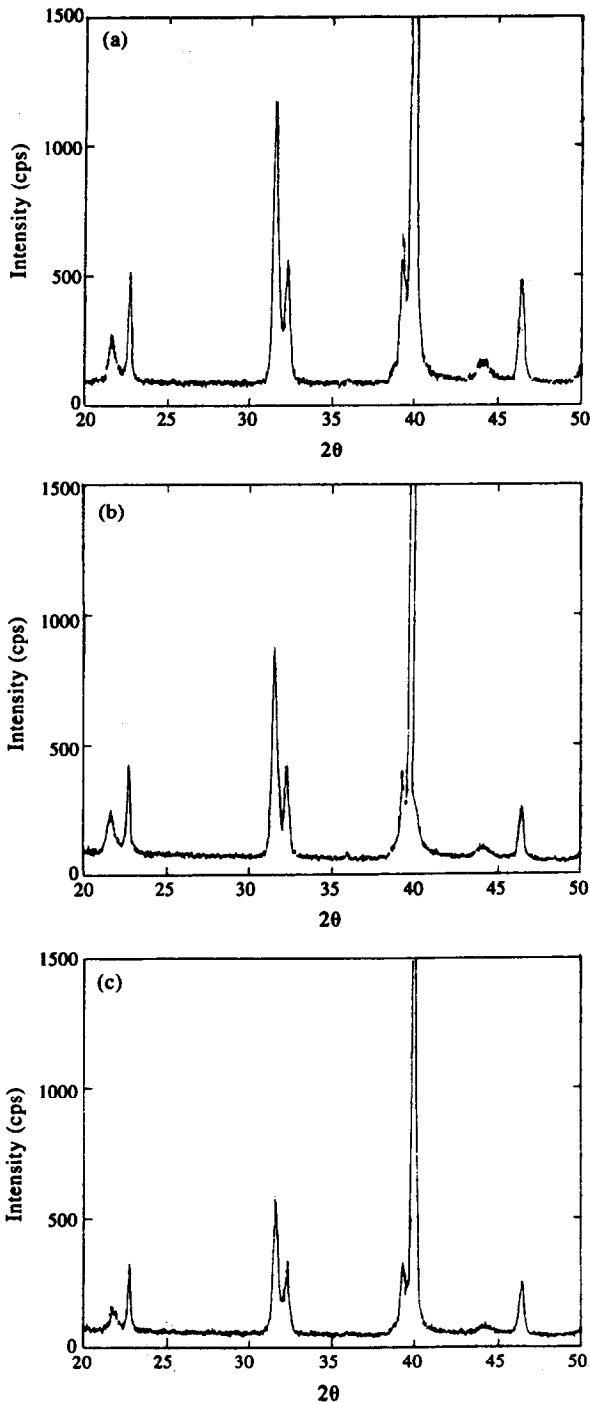


Fig. 4. XRD pattern of PbTiO_3 on $\text{Si}/\text{SiO}_2/\text{Ti}/\text{Pt}$ substrate (annealing temperature = 680°C): (a) annealing time = 30 min; (b) annealing time = 1 h; (c) annealing time = 2 h.

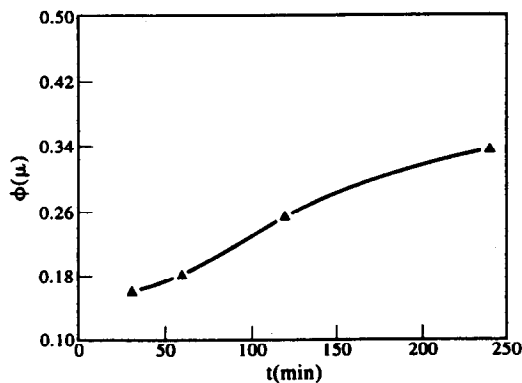


Fig. 5. Grain size as function of annealing time.

3.3 Electrical properties

Films were characterized for their electrical properties through the measurement of polarization hysteresis. Polarization reversal is generally taken as a measure of the degree of ferroelectricity. Hence, the ferroelectric nature of the films was examined by observing the hysteresis loop taken at room temperature at a frequency of 1 kHz by means of a modified Sawyer–Tower circuit.

The test capacitors were fabricated with a $\text{Si}/\text{SiO}_2/\text{Ti}/\text{Pt}/\text{PT}/\text{Pt}$ structure (Fig. 6); the bottom electrode was preannealed at 680°C for 1 h before the PbTiO_3 deposition and the ferroelectric layers were annealed at 680°C for 30 min. Pt top electrodes of $100\ \mu\text{m}$ diameter were fabricated by photolithography and sputtering (lift-off process). On some test capacitors we have performed a top electrode annealing of 450°C for 1 h. All the films discussed here have a thickness of $\sim 0.9\ \mu\text{m}$.

In order to give significant results concerning hysteresis properties, it is necessary to consider all the hysteresis loops obtained at voltages between 10 and 30 V (Fig. 7). In this example, the top electrodes were not annealed. For 10 tested samples, we find an average value of the coercive field (for an applied voltage of 30 V) of $V_c^+ = 18\ \text{V}$ and $V_c^- = -12\ \text{V}$ (see Fig. 7 for notation); the remanent

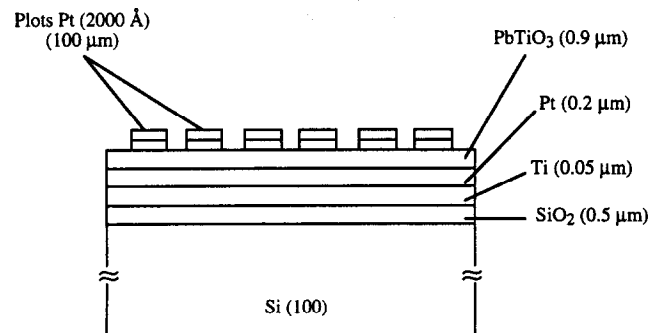


Fig. 6. Test capacitor structure.

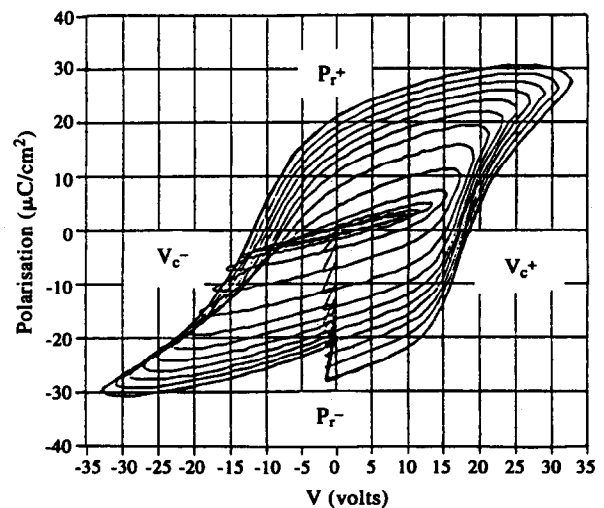


Fig. 7. Typical hysteresis loops with applied voltage between 10 and 30 V.

polarization is $P_r^+ = 18 \mu\text{C cm}^{-2}$ and $P_r^- = -22 \mu\text{C cm}^{-2}$ (at 30 V). The presence of leakage currents was observed at high voltages. It was found that at higher applied electric field strengths ($> 180 \text{ kV cm}^{-1}$) the layer became conducting. The relatively high coercive field compared to that of bulk ceramic may be associated with the fine grain microstructure of the film (150 nm). The stress stored in the film also influenced the high value of the coercive field. For an applied voltage below 15 V, the remanent polarization is equal to zero (Fig. 8); this proves the existence of a blocking layer between the ferroelectric material and the electrodes.

As we can observe on Fig. 7, the hysteresis loop showed a pronounced shift along the axis of the electric field. The asymmetry of the hysteresis loop for an unannealed top electrode sample is presented in Fig. 9 (low values of V_c^- compared to V_c^+); the saturation of the material is attained for a high applied voltage. The shift may be attributed to the existence of an internal field induced by the space charge effect (blocking layer) at the electrodes (top and bottom) and the PbTiO₃ layer interface (and may be at the grain boundaries and domain walls). The asymmetry tends to disappear when the top electrodes are annealed (450°C, 1 h). We must now optimize this annealing treatment. The possible interdiffusion at the interface of species such as Pb and Si and the for-

mation of a dielectric layer (we have observed, essentially on Si/SiO₂ substrates, the formation of lead silicate) with electrical properties different to the PbTiO₃ layer also affects the ferroelectric properties of the structure.

4 Conclusions

PbTiO₃ thin films were grown on silicon and platinumized silicon substrates by RF magnetron sputtering. The growth conditions, thicknesses and annealing of the bottom Ti/Pt electrodes were optimized. PbTiO₃ films in these electrodes yielded films without holes or hillocks, with good adhesion and no electrical shorts in the test capacitors.

The presence of platinum has an important effect on the structure and microstructure of the PbTiO₃ films. The annealing treatment of the PbTiO₃ films was optimized, as well as on Si/SiO₂ and on Si/SiO₂/Ti/Pt substrates. The ferroelectric properties of the PbTiO₃ films were tested; it appears that annealing of the top electrode (Pt) plays a key role in the film properties. Without annealing, the hysteresis loop presents an important asymmetry (presence of an internal field) which is limited when an annealing treatment is performed. We must now optimize the top contact annealing and study whether the asymmetry of the loop is only due to a contact problem. The diffusion of lead must also perturb the electrical properties of the films.

Acknowledgements

The authors would like to thank P. Gaucher from Thomson LCR for help with electrical characterizations.

References

1. Budd, K. D., Dey, S. K. & Payne, D. A., *Br. Ceram. Proc.*, **36** (1985) 107.
2. de Keijser, M., Dormans, G. J. M., Van Veldhoven, P. J. & Larsen, P. K., *Integrated Ferroelectrics*, **3** (1993) 131.
3. Auciello, O., Mantese, L., Duarte, J., Chen, X., Rou, S. H., Kingon, A. I., Schreiner, A. F. & Krauss, A. R., *J. Appl. Phys.*, **73** (1993) 5197.
4. Wasa, K. & Hayakawa, S., *Thin Solid Films*, **52** (1978) 31.
5. Li, X., Liu, J., Zng, Y. & Liang, J., *Appl. Phys. Lett.*, **67** (1993) 2345.
6. Kawaguchi, K., Adachi, H., Setsune, K., Yamazaki, D. & Wasa, K., *Appl. Opt.*, **23** (1984) 2187.
7. Rèmes, D., Jaber, B., Tirlet, J. F., Joire, H., Thierry, B. & Moriamez, Cl., *J. Eur. Ceram. Soc.*, **13** (1994) 493.
8. Rèmes, D., Jaber, B. & Jouan, P. Y., *J. de Physique IV*, **4** (1994) C2-107.
9. Azoulay, R., Rèmes, D., Ménigaux, L. & Dugrand, L., *Appl. Phys. Lett.* **54**(19) (1989) 1857.

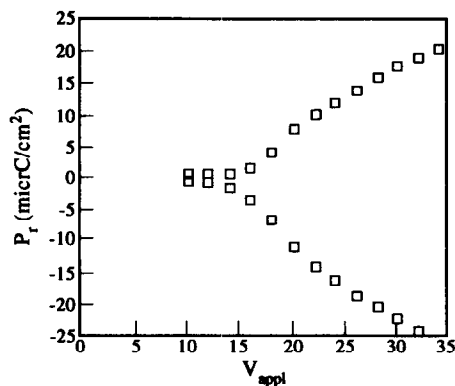


Fig. 8. Remanent polarization as function of applied voltage.

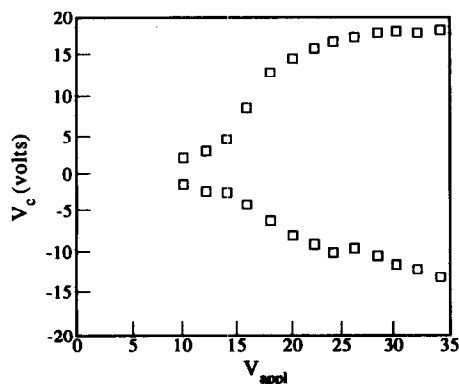


Fig. 9. Coercive voltage as function of applied voltage.

Dielectric and Microstructure Studies of Lead Magnesium Niobate Prepared by Partial Oxalate Route

Surya Mohan Gupta & Ajit R. Kulkarni

Department of Metallurgical Engineering and Materials Science, Indian Institute of Technology, Powai, Bombay 400 076, India

(Received 27 January 1995; revised version received 12 June 1995; accepted 28 June 1995)

Abstract

Lead magnesium niobate (PMN) has been prepared using the partial oxalate method without addition of excess PbO and sintering at four different temperatures, 900, 1000, 1100 and 1200°C. Increase in the sintering temperature resulted in increased dielectric constant which is attributed to an increase in the grain size. Here we report an unusually high dielectric constant (24 000 at -16°C , 1 kHz) observed in PMN sintered at 1200°C [PMN(1200)]. The room temperature dielectric constant and dissipation factor at 1 kHz is ~ 15000 and 0.0025, respectively, for PMN(1200). These values are superior to the reported values. A detailed and systematic study on phase, physical and dielectric properties and microstructure has been carried out. Grain size appears to be a dominant factor in controlling dielectric constant rather than the pyrochlore phase, as claimed earlier.

1 Introduction

Lead magnesium niobate (PMN) has been widely studied in recent years because of its attractive properties, such as: (i) high dielectric constant of 18 000 and 20 000 at T_c for poly- and single crystals,¹ respectively; (ii) low firing temperature (900°C) that allows the use of low cost Ag:Pd electrodes; and (iii) a very broad dielectric constant against temperature curve. The main hindrance in the commercial exploitation of this material arises from processing difficulties. It has been recognized and widely accepted that the reproducibility is diminished by the stable pyrochlore phase that forms at low temperature (700°C). It has been reported that a very small amount of this phase reduces the dielectric constant remarkably.

A number of methods have been suggested to eliminate or minimize the pyrochlore phase. These

involve modification of solid state or wet chemical methods, but most of them leave 3–5% pyrochlore phase in the sintered product.^{2–10} Authors have recently compiled advantages and disadvantages of these methods.^{11,12} Among all the methods reported so far, the Columbite method has proved to be one of the most successful. It gives nearly single-phase PMN because of the non-availability of free niobium oxide and lead oxide to form the pyrochlore phase. However, inhomogeneous mixing in the Columbite precursor leads to formation of pyrochlore phase and subsequent deterioration of dielectric properties. To improve the mixing and the reactivity of ceramic powders the partial oxalate route was adopted successfully for the fabrication of perovskite PMN.¹³

All methods have claimed perovskite phase formation from X-ray diffraction studies but dielectric behaviour varies considerably from method to method, and under such conditions microstructure examination of the ceramic proves useful. Shrout *et al.*¹⁴ using transmission electron microscopy (TEM) observed that each grain is covered with a very thin layer of second phase of the order of 1–2 nm. This phase is also found at triple point boundaries along with impurities derived from the raw materials or introduced during processing, and was believed to be PbO. Wang and Schulze¹⁵ examined the role of a PbO grain boundary phase on the dielectric properties of PMN. The PbO grain boundary layer for stoichiometric PMN was calculated to be 1.2 nm thick when the sample was sintered at 1200°C for 1 h.

The objective of this work was to study the effect of change in the PbO grain boundary layer on the dielectric properties of PMN. A chemical route with high purity starting reagents may lead to a product in which only unreacted or excess PbO will be present at the grain boundaries. A systematic and detailed study of phase analysis, physical properties, dielectric properties and microstructure has been carried out to reveal the

effect of the PbO grain boundary layer on the dielectric properties of PMN.

2 Experimental Procedure

Starting powders niobium oxide (Nb_2O_5) (special pure grade, Aldrich, USA), magnesium carbonate (MgCO_3) and lead nitrate ($\text{Pb}(\text{NO}_3)_2$) (reagent grade, BDH, UK) were used as-received. The lead solution was prepared by dissolving $\text{Pb}(\text{NO}_3)_2$ in double-distilled water. The flow diagram of the partial oxalate route is shown in Fig. 1. The Columbite precursor was prepared by mixing MgCO_3 and Nb_2O_5 in methanol for 1 h using an automated agate mortar and pestle (RETSCH Mortar Grinder, Type RMO, Germany) and, after drying, was fired at 1100°C for 4 h. The procedure was repeated twice to ensure complete reaction. The formation of single-phase magnesium niobate was confirmed by X-ray diffraction (XRD). The precursor was sprinkled in oxalic acid solution, stirred for 1 h and then lead nitrate solution was added dropwise. In the reaction that follows lead nitrate precipitates as lead oxalate and it was assumed to coat¹⁶ the calcined powders giving a homogeneous mixture. These precipitates were washed several times with distilled water. The powder was presintered at 800°C . Presintered powder was crushed and mixed for 1 h in methanol using automated agate mortar and pestle. The mixed powder was pressed as discs (15 mm diameter, 2–3 mm thick) and sintered at 900, 1000, 1100 and 1200°C for 2 h in a closed alumina crucible at a rate of 3°C min^{-1} . It may be mentioned here that the pellets were buried in MgO powder and fired in a closed alumina crucible to minimize the lead oxide loss from the pellets. The phase analysis of the presintered and sintered ceramic was carried out using XRD (JEOL DL 5400, Japan) using Cu $K\alpha$ radiation of wavelength 1.5406 \AA .

For dielectric measurements, the sintered discs were polished on different grades of emery paper. Electrical contacts on the parallel surfaces were made by gold sputtering (Edward 360, UK). In addition the gold layer was covered with room temperature curable silver paint (Eltech, Bangalore, India) to improve the contacts. Dielectric properties were measured with an impedance gain phase analyser (Schlumberger, SI 1260, UK) at four different frequencies (0.1, 1, 10 and 50 kHz) with $1 V_{\text{rms}}$, during cooling over a range of temperatures (-30 to $+80^\circ\text{C}$). The temperature was controlled to $\pm 1^\circ\text{C}$. Microstructure analysis was performed by scanning electron microscopy (SEM) (Jeol JSM 6400, Japan) on the fractured surface.

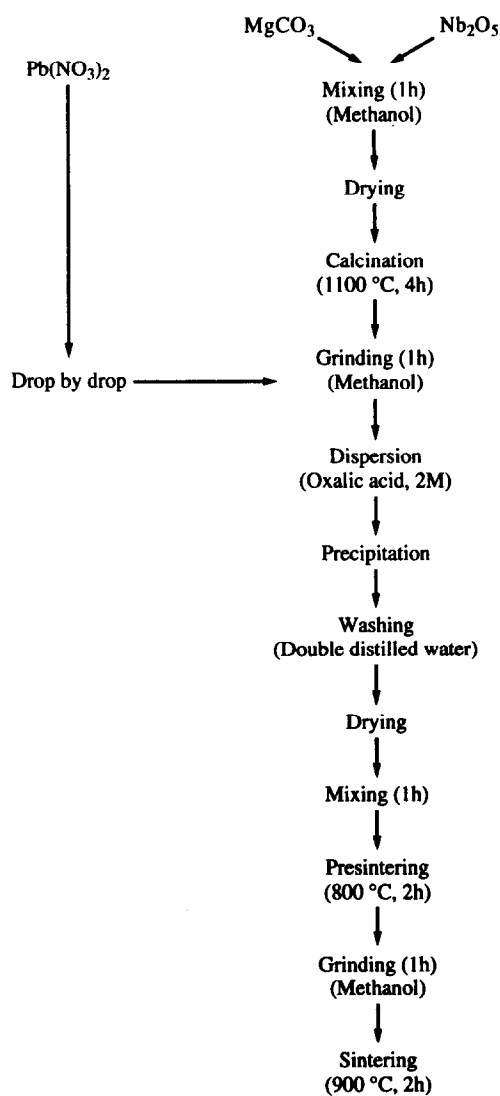
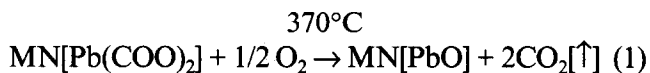


Fig. 1. Flow diagram of partial oxalate route for PMN preparation.

3 Results and Discussion

Differential thermal analysis (DTA) and thermal gravimetry analysis (TGA) of the PMN precursor, i.e. lead oxalate-coated magnesium niobate, are shown in Fig. 2. This study reveals that at 370°C , lead oxalate decomposes to lead oxide:



Here, MN stands for magnesium niobate. TGA shows a sharp weight loss at 370°C . The calculated weight loss agrees with the weight loss from reaction (1). Before proceeding to phase analysis, it may be mentioned that excess PbO was not added at any stage during fabrication, as it may increase the thickness of the PbO grain boundary layer around each grain. Most methods reported so far, however, emphasize the addition of excess PbO to minimize pyrochlore phase formation. This appears to be a major advantage over all other methods.

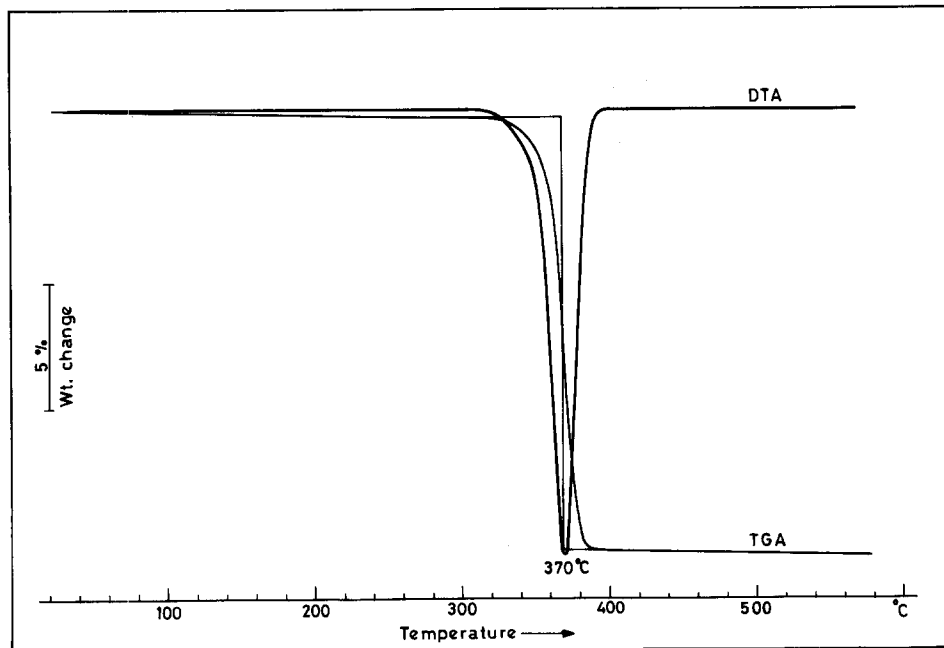
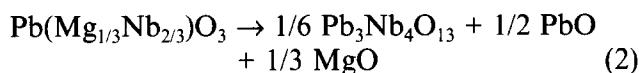


Fig. 2. Differential thermal analysis (DTA) and thermal gravimetric analysis (TGA) of uncalcined powder.

One important step in this process is to avoid lead oxide loss during firing. The processes that lead to PbO loss during firing induce an increase in the amount of pyrochlore phase, as is evident from the following reverse reaction:¹²



It may be mentioned that factors such as excess MgO and Nb₂O₅, mixing time, presinter temperature, etc., which are known to influence pyrochlore phase formation, were optimized while preparing PMN by the partial oxalate method.^{11,12}

3.1 Phase analysis

In general, the difficulty in sintering lead-containing materials is mainly attributed to the loss of lead oxide. Therefore, all the pellets were sintered in a closed crucible. The pellets were weighed before and after firing. This showed a 0.8 and 1.5% weight loss in PMN(900) and PMN(1000) samples, respectively, but nearly 6 and 9% weight loss was recorded for the PMN(1100) and PMN(1200) samples. (Numbers in bracket represent the sintering temperature of that sample.) The weight loss in the pellets is due to lead oxide loss only

because of the high volatility of lead oxide. The presintered powders and sintered pellets were analysed for the phases present XRD. The XRD pattern of the sintered samples as a function of sintering temperature is shown in Fig. 3. The recorded spectra agree well with the JCPDS values and confirm the formation of PMN. The amount of pyrochlore phase present in each sample is calculated from the relative intensities of the major X-ray reflection for the pyrochlore and the perovskite phase as reported in the literature:²

$$\text{Pyrochlore phase} = \frac{I_{\text{pyro}}}{I_{\text{pyro}} + I_{\text{PMN}}} \times 100 \quad (3)$$

where I_{pyro} refers to the (222) pyrochlore peak and I_{PMN} refers to the (110) perovskite peak. The percentage of perovskite phase and pyrochlore phase present in the sintered samples along with sample codes, physical properties and dielectric properties are given in Table 1.

It may be noticed that sintered specimens [Figs 3(b)–(e)] show nearly the same percentage of perovskite phase as compared to the presintered powders (PMN[P], Fig. 3(a)). No pyrochlore phase peak (222) was found in the PMN(900) and

Table 1. Phase analysis, physical and dielectric properties for PMN prepared by partial oxalate route at four different sintering temperatures

Sample No.	Samples	Phase analysis		Physical properties		Dielectric properties (1 kHz)		
		Perovskite (%)	Pyrochlore (%)	Density (g cm ⁻³)	Porosity	K _{max}	Tanδ	T _c (°C)
1	PMN(900)	100.0%	0.0%	4.78	41.28%	4000	0.019	-5
2	PMN(1000)	100.0%	0.0%	5.31	34.8%	8000	0.027	-7
3	PMN(1100)	98.0%	2.0%	5.42	32.78%	12000	0.037	-11
4	PMN(1200)	96.0%	4.0%	7.21	06.88%	24000	0.046	-16

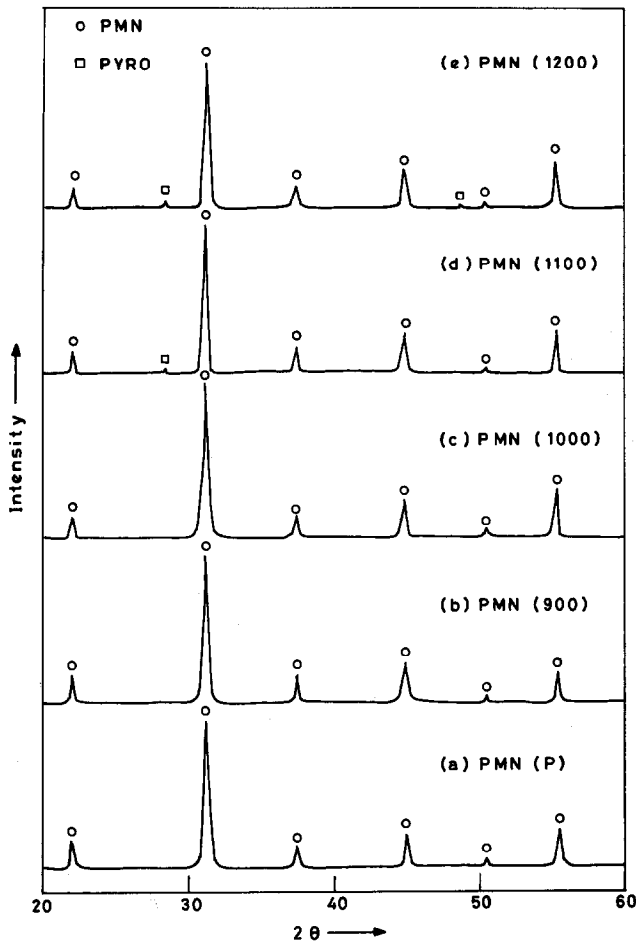


Fig. 3. X-ray diffraction pattern of PMN powder prepared by partial oxalate route: (a) presintered at 800°C, PMN(P); (b) sintered at 900°C, PMN(900); (c) sintered at 1000°C, PMN(1000); (d) sintered at 1100°C, PMN(1100); (e) sintered at 1200°C, PMN(1200). The material was soaked for 2 h at each sintering temperature.

PMN(1000) samples. However, it increases to 4% in the PMN(1200) sample, which is due to a fair amount of lead oxide loss during sintering.

3.2 Dielectric properties

The temperature dependence of the dielectric constant and dissipation factor at 1 kHz as a function of sintering temperature is shown in Figs 4(a) and (b). All the specimens show a broad maxima for the dielectric constant and negligible dissipation factor (0.0025) at room temperature. The dissipation factor increases to ~0.046 at the Curie temperature (T_c). The dielectric constant (K_{max}) and loss maxima shift towards a higher temperature (T_c) with increasing frequency, exhibiting typical relaxor behaviour. The maxima in the dielectric constant versus temperature plots increases remarkably with increase in the sintering temperature. The maximum dielectric constant of PMN at 1 kHz increases from 4000 to 24000 as the sintering temperature increases from 900 to 1200°C.

Two interesting features in this study are as follows. Firstly, the sample containing a small

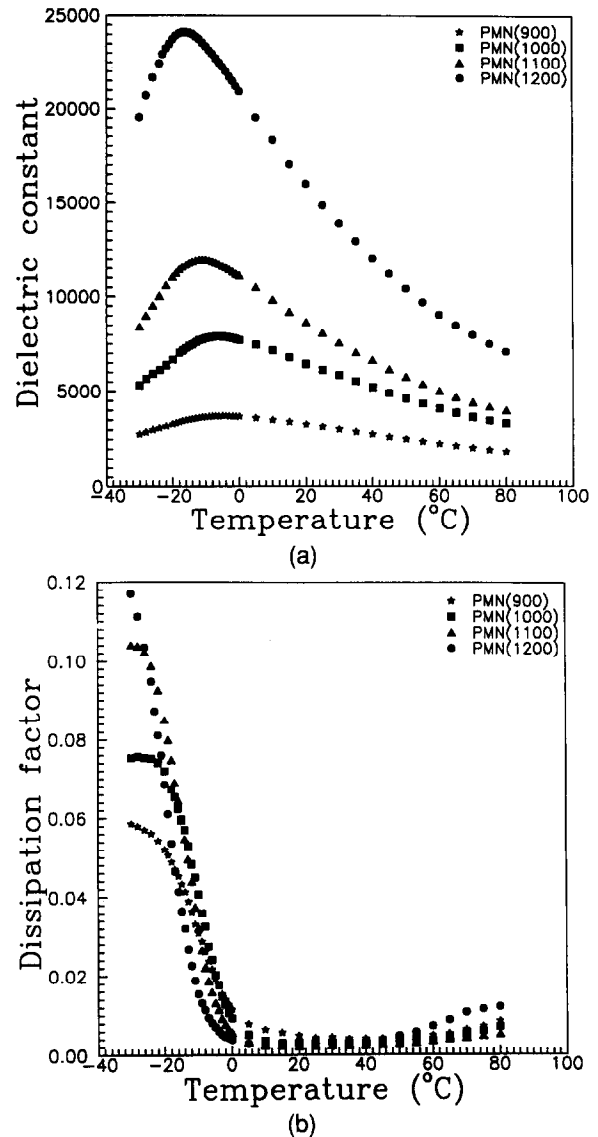


Fig. 4. Comparison of (a) dielectric constant (1 kHz) and (b) dissipation factor (1 kHz) versus temperature at different sintering temperatures.

amount of pyrochlore phase [0–2%, Figs 3(b)–(d)] shows a low dielectric constant (~4000–12000) which is contradictory to that in the work of ShROUT and Swartz¹⁷ but reinforces the work of Jie Chen *et al.*¹⁸ The latter found purity of the starting reagents more influential than the pyrochlore phase in controlling the dielectric properties of the materials.

The second feature is the dielectric constant (K_{max}) and dissipation factor behaviour of PMN(1200) shown in Figs 5(a) and (b). The sample shows all the characteristics of a relaxor material but with an exceptionally high dielectric constant of nearly 24000 at 1 kHz. This value is much higher than the highest reported values (~20000) for polycrystalline PMN.

It may be noted from Table 1 that the density of PMN(900) is very low compared to other samples but it shows all the characteristics of a relaxor material, which is generally difficult to achieve at

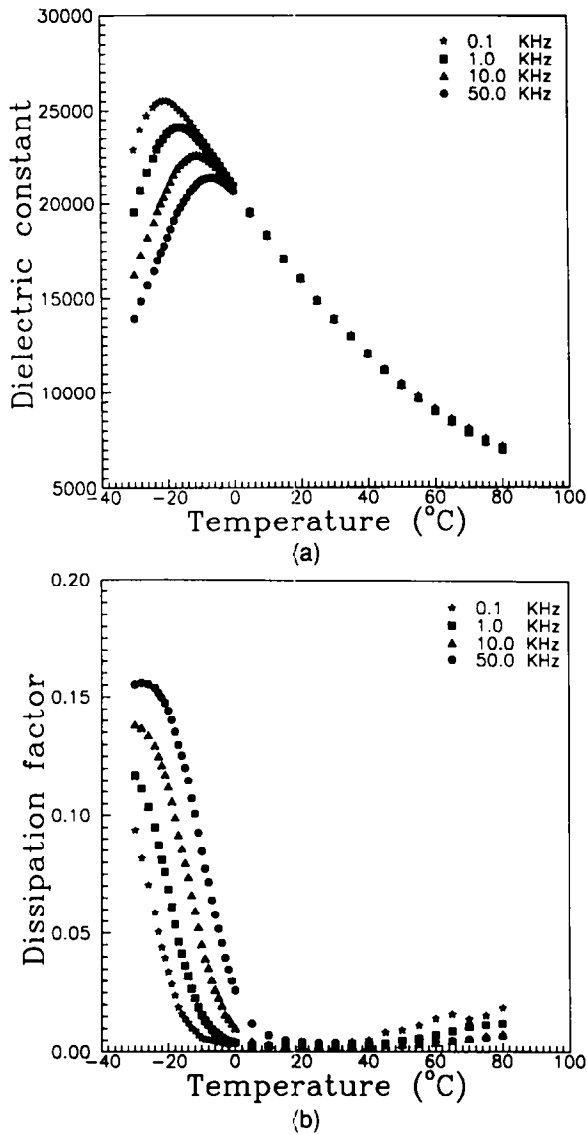


Fig. 5. Dielectric constant (a) and dissipation factor (b) versus temperature for PMN(1200) (stoichiometric composition, calcined at 800°C, sintered at 1200°C).

lower sintering temperatures. It is known that dielectric constant depends upon (i) phases present, (ii) density/porosity of the sample and (iii) grain size. To comment on the grain size effect, the dielectric constant values should first be corrected for porosity and the second phase present. The density and porosity of the compacts are determined using Archimedes' principle¹⁹ and are reported in Table 1. The dielectric constant (K_{\max}) is corrected for porosity of the samples using Rushman and Strivens' equation²⁰ which explains the effect of dispersed porosity (dielectric constant = 1) upon the dielectric constant of pure barium titanate. This equation has been widely used for correcting the porosity effect on the dielectric constant in ceramics.

$$K_{\text{corrected}} = \frac{K_{\text{observed}} \times (2 + V_2)}{2(1 - V_2)} \quad (4)$$

where V_2 is the volume fraction of porosity in the sample. The above equation was experimentally verified up to ~35% porosity ($V_2 = 0.35$). The samples containing more than this porosity has been corrected using Wiener's equation:²⁰

$$\begin{aligned} (K_{\text{PMN}} - K_S) \times (K_{\text{PORE}} + 2 K_{\text{PMN}}) \\ = (K_{\text{PMN}} - K_{\text{PORE}}) \times V_2 \end{aligned} \quad (5)$$

where K_{PMN} , K_{PORE} and K_S are the dielectric constant of the pure PMN, pore and sample, respectively. The observed and corrected dielectric constant (K_{\max}) values are reported in Table 2. The corrected value of dielectric constant (K_{\max}) shows a monotonic increase as the grain size increases. Similar dielectric grain size dependency in PMN and other lead-based relaxors has been observed.^{14,21} This dielectric dependency was explained by considering (i) microdipole-dipole co-operative interaction between superparaelectric regions²² and (ii) a low polarizable phase boundary. According to Viehland *et al.*²² the microdipole-dipole co-operative interaction accounts for the dispersive response of relaxor behaviour, and it maximizes near T_c to ~10–20 nm. Dielectric values of PMN as a function of grain are determined by following expression:

$$\ln K_{\text{PMN}} = V_{\text{Shell}} \ln K_{\text{Shell}} + V_{\text{Core}} \ln K_{\text{Core}} \quad (6)$$

where V_{Shell} and K_{Shell} and V_{Core} and K_{Core} are the volume and dielectric constants of the inactive 'shell' and core regions, respectively. The K_{Shell} value of ~300 was selected,²³ being of the order of an incipient ferroelectric and as the value found for PMN at cryogenic temperatures (~1 K) where domain effects would be frozen-out. Viehland *et al.*²² suggested a microdipole-dipole co-operative interaction between superparaelectric regions which enhances K and accounts for the dispersive response. This inactive or coherence length maximizes near T_c of the order of 10–20 nm. Inserting values of $K_{\text{Core}} = 20000$, the K_{\max} value of single crystal PMN, $K_{\text{Shell}} \sim 300$ and an inactive shell region of the order of 15 nm in eqn (6), the dielectric constant of PMN was determined as a function of size, where the core region is assumed to be the grain size. The dielectric constant of PMN as a function of grain size is presented in Table 2. It may be noted that the dielectric constant values derived from the logarithmic mixing rule [eqn (6)] show no agreement to the $K_{\text{Corrected}}$ values. It seems that the dielectric constant value of K_{Shell} and the thickness of the layer does not coincide with the second phase present around the grain in the present study.

Wang and Schulze¹⁵ also found that the dielectric constant decreases with the addition of excess

Table 2. Density correction on dielectric constant and average grain size for PMN prepared at four different sintering temperatures

Sample No.	Samples	K_{observed} (1 kHz)	$K_{\text{corrected}}^*$ (1 kHz)	Grain size (μm)	K_{PMN}^\dagger (1 kHz)	D_{gb} (nm)
1	PMN(900)	4000	8200 [‡]	~ 0.5	17697	0.72
2	PMN(1000)	8000	14300	~ 1.0	18796	0.39
3	PMN(1100)	12000	20800	~ 1.5	19185	<0.01
4	PMN(1200)	24000	26700	~ 3.0	19563	—

$$*K_{\text{corrected}} = \frac{K_{\text{observed}} \times (2 + V_2)}{2(1 - V_2)}$$

$$^\dagger \ln K_{\text{PMN}} = V_{\text{Shell}} \ln K_{\text{Shell}} + V_{\text{Core}} \ln K_{\text{Core}}$$

$$^\ddagger (K_{\text{PMN}} - K_{\text{s}}) \times (K_{\text{PORE}} + 2 K_{\text{PMN}}) = (K_{\text{PMN}} - K_{\text{PORE}}) \times V_2$$

PbO introduced during processing and explained the dependence according to a series mixing theory used for diphasic systems. This theory uses the following equation:

$$\frac{D}{K_{\text{s}}} = \frac{D_{\text{g}}}{K_{\text{g}}} + \frac{D_{\text{gb}}}{K_{\text{gb}}} \quad (7)$$

where K_{s} is the dielectric constant of the sample, K_{g} the dielectric constant of the perovskite PMN grain, K_{gb} the dielectric constant of the PbO solid solution in the grain boundary, D the thickness of the sample, D_{g} the thickness of the PMN grains and D_{gb} the thickness of the PbO grain boundary layers. Hilton²⁴ observed the presence of a very thin layer of second phase of the order of 1–2 nm located around each grain, using TEM, believed to be PbO-based regardless of process conditions. ShROUT *et al.*¹⁴ postulated that along the grain boundaries amorphous PbO phase exists, which may be the reason for the reduction of the dielectric constant when grain size is small. Thus, the dielectric constant of the grain boundary is taken as the dielectric constant of PbO in eqn (7). The grain boundary in PMN is very thin. Therefore, D is approximately equal to D_{g} and eqn (7) reduces to:

$$\frac{1}{K_{\text{s}}} = \frac{1}{K_{\text{g}}} + \frac{1}{RK_{\text{gb}}} \quad (8)$$

where $R = D_{\text{g}}/D_{\text{gb}}$, i.e. the thickness ratio of the grain to the grain boundary layer. In the present study K_{g} (dielectric constant of the grain) is very much higher than K_{gb} (dielectric constant of the PbO in the grain boundary). The K_{gb} for PbO is 20 and not temperature dependent, whereas K_{s} is taken as $K_{\text{corrected}}$ and K_{g} is 20000, and these values are at T_{c} for the sample prepared and a single crystal of PMN, respectively.

Equation (8) has been used to calculate the thickness of the grain boundary layer. The thickness of the PbO grain boundary layer for each sample is calculated and presented in Table 2. Wang and Swartz¹⁵ compared the K_{max} of 13700

at 1 kHz with 20000, using the grain size of 2.1 μm for stoichiometric PMN, and the PbO grain boundary layer was calculated to be 1.2 nm thick when the sample was sintered at 1200°C for 1 h. It may be noted that the thickness reduces (0.72 to <0.1 nm) with increase in the sintering temperature (from 900 to 1100°C) or grain size (0.5 to 1.5 μm). The thickness of the PbO grain boundary layer could not be calculated for the PMN(1200) sample because the dielectric constant value is greater than the dielectric constant value of a single crystal. The reason for this unusual value has been explained²⁵ using X-ray photoelectron spectroscopy (XPS) studies on these samples. It has been found that the Pb atom is in two oxidation states (e.g. Pb^{2+} and Pb^{4+}) instead of one Pb^{2+} oxidation state. This dual oxidation state of Pb leads to an increased dipole moment and hence the high dielectric constant.

ShROUT *et al.*¹⁴ observed drastically different values of K_{max} in PMN-PT (where PT = PbTiO_3) samples of similar grain sizes. These samples were kept underneath coarse zirconate sand and fired at different sintering temperatures. These different values have been explained on the basis of the amount of the amorphous PbO grain boundary phase present. It has been proposed that zirconate sand promotes amorphous PbO loss during sintering. Similarly, samples were kept underneath MgO powder in the present study and fired. It may be concluded that MgO powder promotes the amorphous PbO loss at low sintering temperature (up to 1100°C). This may be the reason for the very low density of the PMN(900), PMN(1000) and PMN(1100) samples.

The transition temperature shifts to the lower side with increase in the grain size. A similar transition temperature shift has also been observed in PMN and PMN-PT systems by other workers.^{14,17,21} No explanation as to why T_{c} shifts with grain size can be given at this time. The grain size variation with sintering temperature is described below with the results on microstructure.

3.3 Microstructure

The scanning electron micrographs of a fracture surface of the compact obtained on firing at 900, 1000, 1100 and 1200°C are shown in Figs 6(a)–(d). These micrographs demonstrate the effect of sintering temperature. All samples show 100% intergranular fracture. In Fig. 6(a), i.e. SEM(900), there are grains of an average grain size $\sim 0.5 \mu\text{m}$ with high porosity. It can be noticed in Figs 6(a)–(d) that porosity decreases and grain size increases with increase in the sintering temperature, which is generally observed. A gradual development of grain structure is clearly observed in other samples [PMN(1000) and PMN(1200)] which show well-developed grain morphology. It may be noticed that the magnification and voltage is kept the same while studying the microstructure of these samples. Careful observation of the microstructure reveals that grain size increases with increase in the sintering temperature. It may be noted that there is no secondary phase present in these samples. The average grain size increases from 0.5 to $3.0 \mu\text{m}$ with increase in the sintering temperature. On comparing the grain size and dielectric constant ($K_{\text{corrected}}$) in Table 2 it may be

concluded that the dielectric constant value increases remarkably with increase in grain size.

The most important result of this investigation was the apparent grain size dependence on the dielectric constant of PMN ceramics. The grain size, dependency was caused by the influence of the grain boundary volume, as suggested by Swartz *et al.*¹⁷ As the grain size increases, the number of boundaries in series with the grains decreases and the large permittivity of the PMN grains becomes less affected by the permittivity of the grain boundary. Present results suggest that the pyrochlore phase is not the only major detrimental factor to the dielectric behaviour of PMN.

4 Conclusions

Single-phase PMN with good dielectric properties has been prepared successfully by the partial oxalate method. Thermal analysis shows that lead oxalate decomposes at 370°C to form lead oxide. Phase analysis shows the formation of a single phase at low sintering temperature whereas the presence of nearly 4% pyrochlore phase in

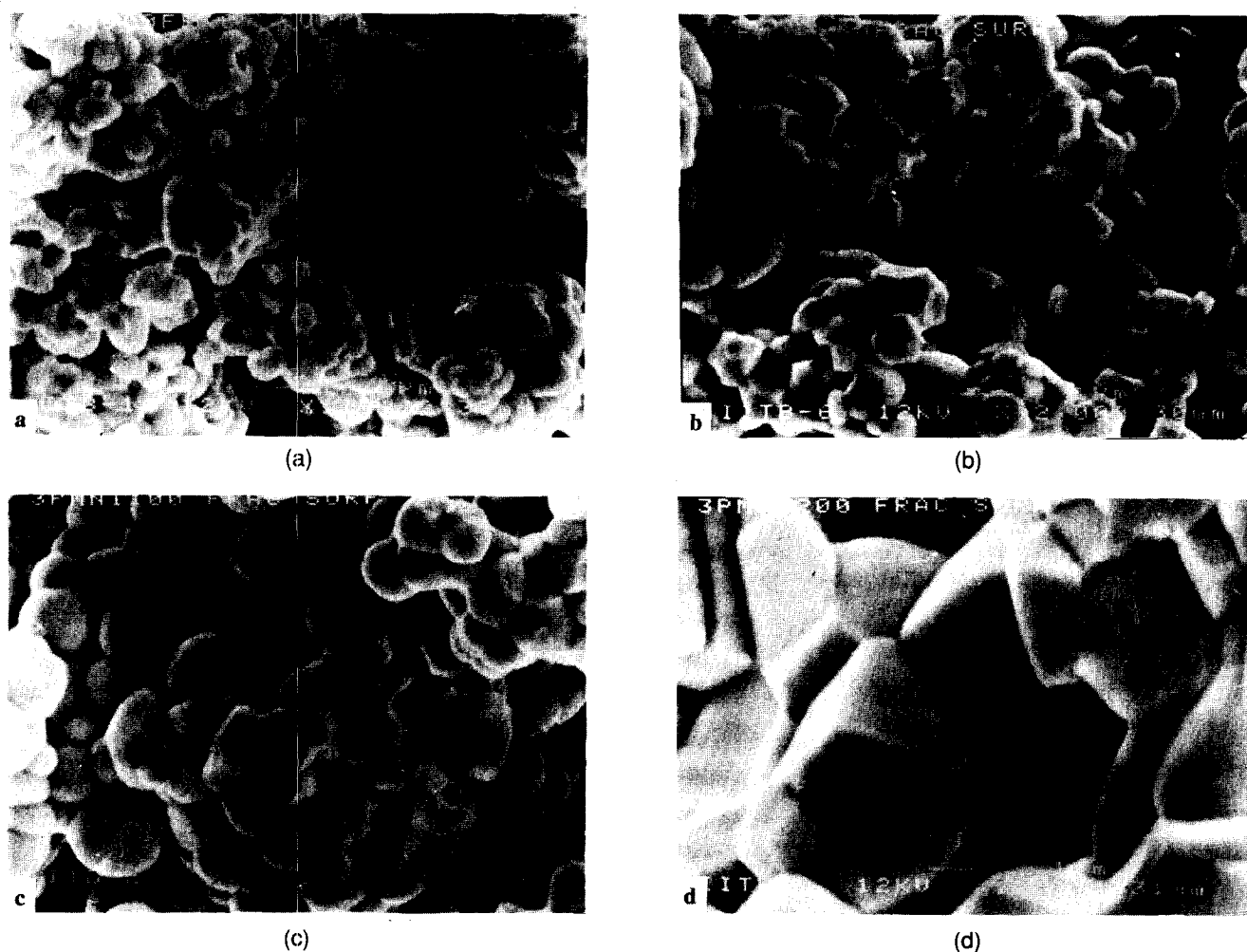


Fig. 6. Microstructure of sample: (a) sintered at 900°C, PMN(900); (b) sintered at 1000°C, PMN(1000); (c) sintered at 1100°C, PMN(1100); (d) sintered at 1200°C, PMN(1200) (calcined at 800°C for 2 h).

PMN(1200) sample is attributed to lead oxide loss. Dielectric constant values after porosity correction increase with increase in sintering temperature or grain size, which is due to the decrease in the thickness of the PbO grain boundary layer. All the sintered samples show good relaxor behaviour, including PMN(900), which shows a very low dielectric constant value because of large porosity. The dielectric properties reveal that the pyrochlore phase is not the main detrimental factor to the dielectric properties. Microstructure analysis reveals that grain size also controls the dielectric properties and in this case appears to be more dominant than the pyrochlore phase.

Acknowledgements

The authors thank their colleagues for kind support and helpful suggestions. They are particularly grateful to Dr J. Bellare of the Chemical Engineering Department for providing the SEM facility.

References

1. Bokov, V. A. & Myl'nikova, I. E., Electrical and optical properties of single crystals of ferroelectrics with a diffused phase transition. *Sov. Phys. Solid State*, **3**(3) (1961) 613–23.
2. Swartz, S. L. & Shrout, T. R., Fabrication of perovskite lead magnesium niobate. *Mater. Res. Bull.*, **17** (1982) 1245–50.
3. Lejeune, M. & Boilot, J. P., Optimisation of dielectric properties of lead magnesium niobate ceramics. *Am. Ceram. Soc. Bull.*, **64**(4) (1984) 679–82.
4. Lejeune, M. & Boilot, J. P., Low firing dielectric based on lead magnesium niobate. *Mater. Res. Bull.*, **20** (1985) 493–9.
5. Guha, J. P. & Anderson, H. U., Preparation of perovskite $\text{Pb}(\text{Mg}_{1/3}\text{Nb}_{2/3})\text{O}_3$ using $\text{Pb}_3\text{Nb}_2\text{O}_8$ and MgO. *J. Am. Ceram. Soc.*, **69**(11) (1986) C-287–8.
6. Chaput, F., Boilot, J. P., Lejeune, M., Papiernik, R. & Pfaizrag, L. G., Low temperature route to lead magnesium niobate. *J. Am. Ceram. Soc.*, **72**(8) (1989) 1355–7.
7. Katayama, K., Abe, M. & Akiba, T., Preparation of $\text{Pb}(\text{Mg}_{1/3}\text{Nb}_{2/3})\text{O}_3$ powder by molten salt method. *Ceram. Intl*, **15** (1989) 289–95.
8. Choy, J. H., Yoo, J. S., Kang, S. Gu., Hong, S.T. & Kim, D. G., Ultrafine $\text{Pb}(\text{Mg}_{1/3}\text{Nb}_{2/3})\text{O}_3$ (PMN) powder synthesised from metal citrate gel by thermal shock method. *Mater. Res. Bull.*, **25** (1990) 283–91.
9. Shrout, T. R., Papet, P., Kim, S. & Lee, Gye-Song, Conventionally prepared submicrometer lead-based perovskite powders by reactive calcination. *J. Am. Ceram. Soc.*, **73**(7) (1990) 1862–7.
10. Watanabe, A., Haneda, H., Mosiyoshi, Y., Shirasaki, S., Kuramoto, S. & Yamamura, A., Preparation of lead magnesium niobate by a coprecipitation method. *J. Mater. Sci.*, **27** (1992) 1245–9.
11. Gupta, S. M. & Kulkarni, A. R., Synthesis and dielectric properties of lead magnesium niobate – a review. *Mater. Chem. Phys. J.*, **39** (1994) 98–109.
12. Gupta, S. M. & Kulkarni, A. R., Synthesis of perovskite lead magnesium niobate using partial oxalate method. *Mater. Res. Bull.*, **28**(12) (1993) 1295–301.
13. Lejeune, M. & Boilot, J. P., Influences of ceramic processing on dielectric properties of perovskite type compound: $\text{Pb}(\text{Mg}_{1/3}\text{Nb}_{2/3})\text{O}_3$. *Ceram. Intl*, **9**(4) (1983) 119–22.
14. Shrout, T. R., Kumar, U., Megheri, M., Yang, N. & Jang, S. J., Grain size dependence and dielectric and electrostriction of $\text{Pb}(\text{Mg}_{1/3}\text{Nb}_{2/3})\text{O}_3$ -based ceramics. *Ferroelectrics*, **76** (1987) 479–87.
15. Wang, H. C. & Schulze, W. A., The role of excess MgO or PbO in determining the microstructure and properties of lead magnesium niobate. *J. Am. Ceram. Soc.*, **73** (1990) 825–32.
16. Okazaki, K., Advanced technology in electroceramics in Japan. *Am. Ceram. Soc. Bull.*, **67**(12) (1988) 1946.
17. Swartz, S. L., Shrout, T. R., Schulze, W. A. & Cross, L. E., Dielectric properties of lead magnesium niobate ceramics. *J. Am. Ceram. Soc.*, **67**(5) (1984) 311–15.
18. Chen, J., Gorton, A., Chen, H. M. & Harmer, M. P., Effect of powder purity and second phase on the dielectric properties of lead magnesium niobate ceramics. *J. Am. Ceram. Soc.*, **69**(12) (1986) C-303–5.
19. ASTM Standard: 1989 Annual Book of ASTM Standards Vol. 15.02, C373–88, P109–110. ASTM, Philadelphia, PA., pp. 19103–18.
20. Rushman, D. F. & Strivens, M. A., The effective permittivity of two-phase systems. *Proc. Phys. Soc.*, **59** (1947) 1011–16.
21. Papet, P., Dougherty, J. P. & Shrout, T. R., Particle and grain size effects on the dielectric behavior of the relaxor ferroelectric $\text{Pb}(\text{Mg}_{1/3}\text{Nb}_{2/3})\text{O}_3$. *J. Mater. Res.*, **5** (1990) 2902–9.
22. Viehland, D., Jang, S. J., Wuttig, M. & Cross, L. E., The glassy behaviour of relaxor Ferroelectrics. *Ferroelectrics*, **120** (1991) 71–7.
23. Ackerman, D. A., Moy, D., Potter, R. C., Anderson, A. C. & Lawless, W. N., Glassy behaviour of crystalline solids at low temperature. *Phys. Rev. B*, **23** (1981) 3886–93.
24. Hilton, A., TEM studies of relaxor ferroelectric materials, PhD Thesis, University of Essex, UK (1989).
25. Gupta, S. M., Kulkarni, A. R., Vedpathak, M. & Kulkarni, S. K., Surface study of lead magnesium niobate ceramic using X-ray photoelectron spectroscopy. *J. Mat. Sci. Eng. B* in press.

Erratum

POLYMER-DERIVED Si-BASED BULK CERAMICS, PART II: MICROSTRUCTURAL CHARACTERISATION BY ELECTRON SPECTROSCOPIC IMAGING

Joachim Mayer, D. Vinga Szabó, Manfred Rühle, Martin Seher & Ralf Riedel, *Journal of the European Ceramic Society*, **15** (1995) 717–727.

Figure 10, p. 725: part (a) of this figure was incorrectly printed in black and white. The Publishers would like to apologise for this error. The correct version of Figure 10 is printed below:

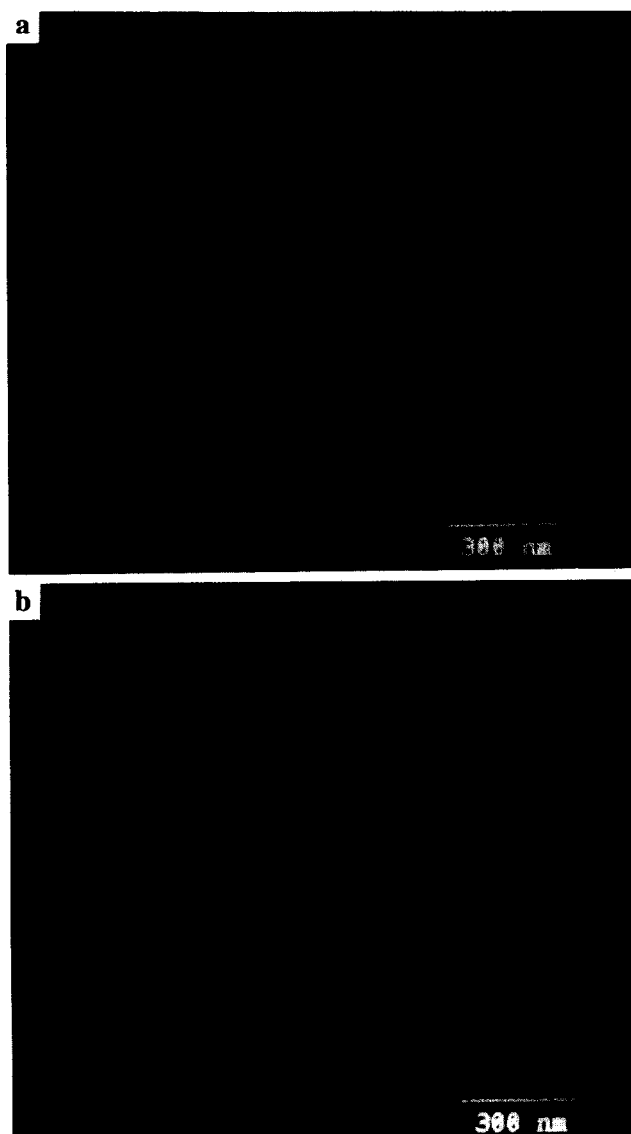


Fig. 10. The microstructure of the $\text{Si}_2\text{N}_2\text{O}$ materials sintered with 3 wt% (a) and 15 wt% (b) sintering additives. In the images the nitrogen distribution is shown in red, the oxygen distribution in green. The $\text{Si}_2\text{N}_2\text{O}$ grains are characterised by their mixed colour (red + green = yellow). At 3 wt% unfilled pores remain. In the 15 wt% samples the microstructure is dense but Si_3N_4 grains were present (red).

Wet Erosive Wear Behaviour of Fine-grain Zircon Ceramic

A. Wootton, M. Miranda-Martinez,* R. W. Davidge & F. L. Riley†

School of Materials, University of Leeds, Leeds LS2 9JT, UK

(Received 27 January 1995; revised version received 4 August 1995; accepted 27 August 1995)

Abstract

The wet erosive wear rates of a set of hot-pressed, dense, fine-grained zircon materials of grain size in the range 2 to 6 μm have been measured. There is no correlation between wear rate and hardness or fracture toughness: wear rate instead appears to be strongly linked to grain size and pore fraction. The wear rate–grain size relationship is explicable in terms of a model based on grain-boundary micro-fracture and crack linking, which allow grain detachment to occur. Wear rates for this set of zircon materials are slightly lower than those measured for a set of pure polycrystalline aluminas with a similar grain size range.

1 Introduction

Zircon (zirconium silicate, ZrSiO_4) is widely used as the constituent of many traditional ceramic materials, refractories and glazes,^{1–6} and there is interest in its use as a basis for milling media because of its hardness and low cost. At high temperature ($\sim 1675^\circ\text{C}$) zircon dissociates into zirconium dioxide and silicon dioxide,^{7,8} but by the use of liquid forming sintering additives it is possible to densify zircon powder at relatively low temperatures with retention of the zircon phase.^{9–11}

Zircon has a hardness of ~ 7.5 on the Mohs scale,⁶ and although this is significantly less than that of alumina [~ 9 , corresponding to a Vickers indentation hardness of ~ 25 GPa (Ref. 12)] zircon-based materials might be expected to be reasonably wear resistant. For the milling application considered wet erosion resistance is of primary importance, and this wear mode was assessed during the preliminary investigation reported here. Wear testing was carried out using laboratory equipment, with a set of dense zircon discs of tailored

grain size and controlled porosities, obtained by hot-pressing zircon powder in the presence of a siliceous liquid phase. The CaO-MgO-SiO_2 system was used as densification aid, because it provides a suitable liquid at $< 1300^\circ\text{C}$.⁸

Many attempts have been made to model the wear behaviour of brittle ceramics in terms of the parameters which intuitively seem likely to control wear, and which can be justified on the basis of a fracture mechanics approach. Several of these have led (see, for example, ref. 13) to the development of equations of the general form:

$$V \propto P^a H^{-b} K^{-c} \quad (1)$$

in which the volume of material removed (V) is related to the applied load (P), hardness (H) and fracture toughness (K), for which in this particular instance the exponents are given by $a = 5/4$, $b = 1/2$ and $c = 3/4$. It would be expected, and is indeed found, that in general good wear resistance is obtained in materials which have high hardness and fracture toughness, and over a broad range of materials types convincing correlations are found.

However, this type of expression has its limitations in that it takes into account only three possible wear controlling parameters, and other possibilities, such as the electrical effects noted in insulating materials during dry sliding,¹⁴ are disregarded. These limitations become particularly apparent when comparing the members of a specific class of material (such as the aluminas, and the zircons examined here) for which differences in hardness are small, and the effects of microstructure on toughness not clear. A number of arguments can be advanced to show that such a simple type of relationship is not appropriate for accounting for the differences in wear rates observed in these cases. For example, correlations between wear resistance and toughness for pure and liquid-phase sintered aluminas are poor, and variations of crack propagation resistance with crack length (R -curve behaviour) might be expected to influence wear behaviour.¹⁵ However, although coarse-grained alumina shows marked R -curve behaviour this is

* Now at ISQ, Lisbon, Portugal.

† To whom correspondence should be addressed.

not necessarily an advantage when the critical wear events occur over dimensions of a single grain. A similar problem exists with the application of hardness data obtained from the use of an indenter giving penetration over many grain dimensions, and doubts have been expressed about the appropriateness of such data. Within a specific class of material other factors must operate to provide differences in wear rate, and microstructure very clearly is an important one. For materials of normal grain size a strong influence of grain size has been found in a wide range of wear modes, with low rates associated with fine grain size. For many wear modes, ranging from sliding to grinding and cutting, wear rate is observed to vary as a function of (grain size)⁻ⁿ, where n commonly approximates to 1/2.¹⁶⁻²³ These relationships have in general been attributed either to residual grain boundary stress (native to anisotropic materials such as alumina), or to the presence of defects, the size of which scales with the grain size. It seems clear, however, that the basis for the wear process must reside at the sub-grain level, even though the observed material loss process commonly consists of the detachment of whole grains. For very fine grained materials (<1 μm) polishing seems to be the preferred wear mechanism, and it is likely that in these cases an underlying tribochemical wear mechanism becomes the dominant process, albeit at a very slow overall rate.

Recently, a tentative model has been presented for the wear of polycrystalline materials of grain sizes in the range 1 to 12 μm ,²⁴ which makes the assumption that in the mechanical component of the wear process fracture occurs predominantly along two-grain boundaries (that is, the grain faces), with cracks progressing along individual grain faces at a mean rate characteristic of the material. There is then a delay in crack propagation, for readjustment of the direction of propagation, at each three-grain junction.

The time (t) for the crack to progress a specified distance (d) is given by:

$$t = 2 (t_f + t_j).d/G \quad (2)$$

where t_f is the time (proportional to the mean grain dimension, G) to traverse a two-grain boundary face of dimension $\sim G/2$, and t_j is the time (a constant) taken to realign at a three-grain junction. The experimentally observed wear rate (W) is thus:

$$W = Ad/t \quad (3)$$

$$\text{or} \quad W = AG/2 (t_f + t_j) \quad (4)$$

where A is a constant related to the microstructural crack linking process and the experimental

conditions of the test. t_f can be eliminated by defining a characteristic grain size (G_o) for which $t_f = t_j$. Thus:

$$t_f = (G/G_o) t_j \quad (5)$$

and substitution into (4) gives

$$W = A G G_o/[2t_j(G + G_o)] \quad (6)$$

A proportionality between W and $G/(G + G_o)$ is thus predicted, with the plot passing through the origin. This prediction has been shown to be supported by a wide range of wear data for which the value of G_o ranges from 1 to 100 μm , depending on the nature of the wear process. G_o is expected to vary with the nature of the wear process and conditions, which affect in particular the scale of the damage and the way that individual cracks link to form a chip. This wear model specifically focuses on grain size effects and ignores possible contributions from other material removal processes not likely to be grain size dependent, such as tribochemical wear. It is therefore considered to be applicable to materials with grain size above a lower limit of $\sim 1 \mu\text{m}$. An upper limit cannot at present be identified, though the wear rates of a material of infinite grain size (single crystal sapphire) are generally much slower than the simple extrapolation of the essentially polycrystalline model would predict. The precise details of the mechanisms of the grain-boundary crack nucleation and propagation processes are of necessity at this stage undefined.

2 Experimental

Dense zircon materials were prepared from a premium grade Australian zircon sand (R.Z.M. Premium B). This was ball milled in water using alumina media to give a set of four powders with mean particle sizes in the range 1.7 to 8.7 μm . Particle size determinations were carried out on aqueous suspensions using a Coulter LS130 Laser Diffraction Particle Size Analyzer, with 0.2% Dispersant N40 (Allied Colloids, Bradford) dispersant. Chemical analysis of the milled powders obtained by X-ray fluorescence (Philips model 1606) on fused borate glass discs showed that appreciable levels of alumina were introduced during the milling, with the maximum quantity in the longest milled, and finest, zircon powder (Z1). In order to obtain the same overall composition for each of the four powders, varying amounts of alumina were added to powders Z2, Z3 and Z4, as the equivalent amounts of the isopropanol soluble aluminium nitrate (Aldrich Chemical Co. Ltd), to bring the total up to that of powder Z1 (4.24%).

A liquid-forming densification aid corresponding to the composition CaO-MgO-2SiO_2 , at the level of 8% by weight, was blended by wet mixing into each powder using appropriate quantities of calcium and magnesium nitrates (Aldrich Chemical Co. Ltd, or BDH Chemicals, Poole) and ultra-fine silicon dioxide powder (Aerosil 380, Degussa AG, Frankfurt). Thermogravimetric analysis established the dry oxide equivalent for each additive. Each powder blend was mixed in isopropanol for 2 h using zirconia media, and then dried at 30°C under low pressure in a rotary evaporator to avoid melting the nitrates. Dried powders were lightly crushed, sieved through a 100 μm aperture nylon sieve, calcined in alumina crucibles at 700°C for 1 h, and then crushed and re-sieved.

Powders were hot-pressed to high density in a 25 mm bore graphite die, with powder sufficient to give a final disc thickness of 5 mm. Temperature, pressure and die punch movement were continuously monitored and data processed by computer to provide a measure of extent of densification as a function of time. Trial hot-pressings on the three finer powders (Z1, Z2, and Z3) established their optimum conditions of 1375°C and 20 MPa, and times between 0.5 and 2 h. Onset of liquid formation (and of rapid densification) occurred at ~1300°C. The coarsest powder (Z4) was hot-pressed under varying conditions, to give a second set of materials of mean grain size 6.2 μm , with a range of densities and thus residual porosities.

Discs of hot-pressed materials were cleaned with SiC powder, sectioned, and polished to 1 μm diamond for examination by X-ray diffraction (XRD), and by scanning electron microscopy (SEM) (Cambridge Instruments Camscan models 3 and 4) with a Link X-ray microanalysis system attachment. Mean zircon grain sizes were measured from photographs of polished and thermally etched materials, using the standard line intercept technique, and counting a minimum of 600 grains. The composition of the material was estimated by analyses of areas using point counting and line intercept measurements and the multiplication factor 1.56.²⁵

Disc densities were measured by the standard water immersion technique (BS 7134 Section 1.2). Theoretical (true solid) density values (ρ) for the dense materials were obtained using powder crushed to pass through a 100 μm sieve and immersed in deionized water, on the basis of BS 7134. Microindentation hardness (H) and fracture toughness (K_{1c}) were measured on polished faces, by Vickers indentation with a load of 29 N, and the equation of Anstis *et al.*²⁶

Wet erosion was carried out in a modified high torque attritor mill using 0.5 to 1 mm dimension crushed fused alumina aggregate in water. A

detailed description of the wear test has been given.^{23,27} Zircon discs 25 mm diameter and ~5 mm thick were clamped between shaped discs of hard polyurethane attached to the shaft of the mill, with ~50% of the zircon disc exposed. The sample holder was immersed in a slurry consisting of 700 g of alumina grit (of stated purity 92.2% Al_2O_3 , with SiO_2 and TiO_2 as the major impurities) in 250 cm^3 of deionised water, and rotated at a speed of 8 Hz with a disc track radius of 36 mm (giving a disc perimeter linear velocity of ~1.9 m s^{-1}). Disc weights to ± 0.1 mg were measured after 2 h (t_1) and 6 h (t_2) testing (w_1 and w_2), using the standardized procedure. A wear rate (R) measured in m s^{-1} was calculated on the basis of the expression:

$$R = [(w_1 - w_2) / (t_2 - t_1)] / (A\rho)$$

where A is the area of the exposed leading quadrant of the disc (approximately 1/4 of the disc surface area). This time period was chosen in order to minimize any effects of the disc's initial surface finish, and the significant smoothing of the grit particles at longer times. Worn surfaces were examined by SEM. Each disc generally provided two wear values, and these were averaged.

3 Results

Table 1 shows the chemical compositions of the four zircon powders after milling; a 'balanced' composition Z1 was used as the basis for the zircon materials used. Analysis also showed the presence in the powders of small amounts of CaO (0.12%) and MgO (0.08%), possibly, introduced by the milling media, and these amounts were taken into account in the calculation of the weights of liquid-forming sintering additives used. Figures 1(a) to (d) show the frequency distribution curves for the four zircon starting powders. Figure 2 shows a typical scanning electron micrograph of the Z2 powder of mean size 2.7 μm . The hot-pressing conditions chosen initially (1375°C and 20 MPa) and found to be satisfactory for the three finest powders, are shown in Table 2, together with the resulting mean grain sizes and densities. The hot-pressing densification conditions for powder

Table 1. Chemical composition (weight%) of milled zircon powders: compositions used for hot-pressing were adjusted to give that of composition Z1

Powder	Median dimension (μm)	ZrO ₂	HfO ₂	SiO ₂	Al ₂ O ₃
Z1	1.4	62.1	1.3	32.4	4.3
Z2	2.0	63.8	1.3	32.5	2.4
Z3	3.8	63.7	1.3	32.3	2.7
Z4	7.3	63.4	1.3	33.3	2.0

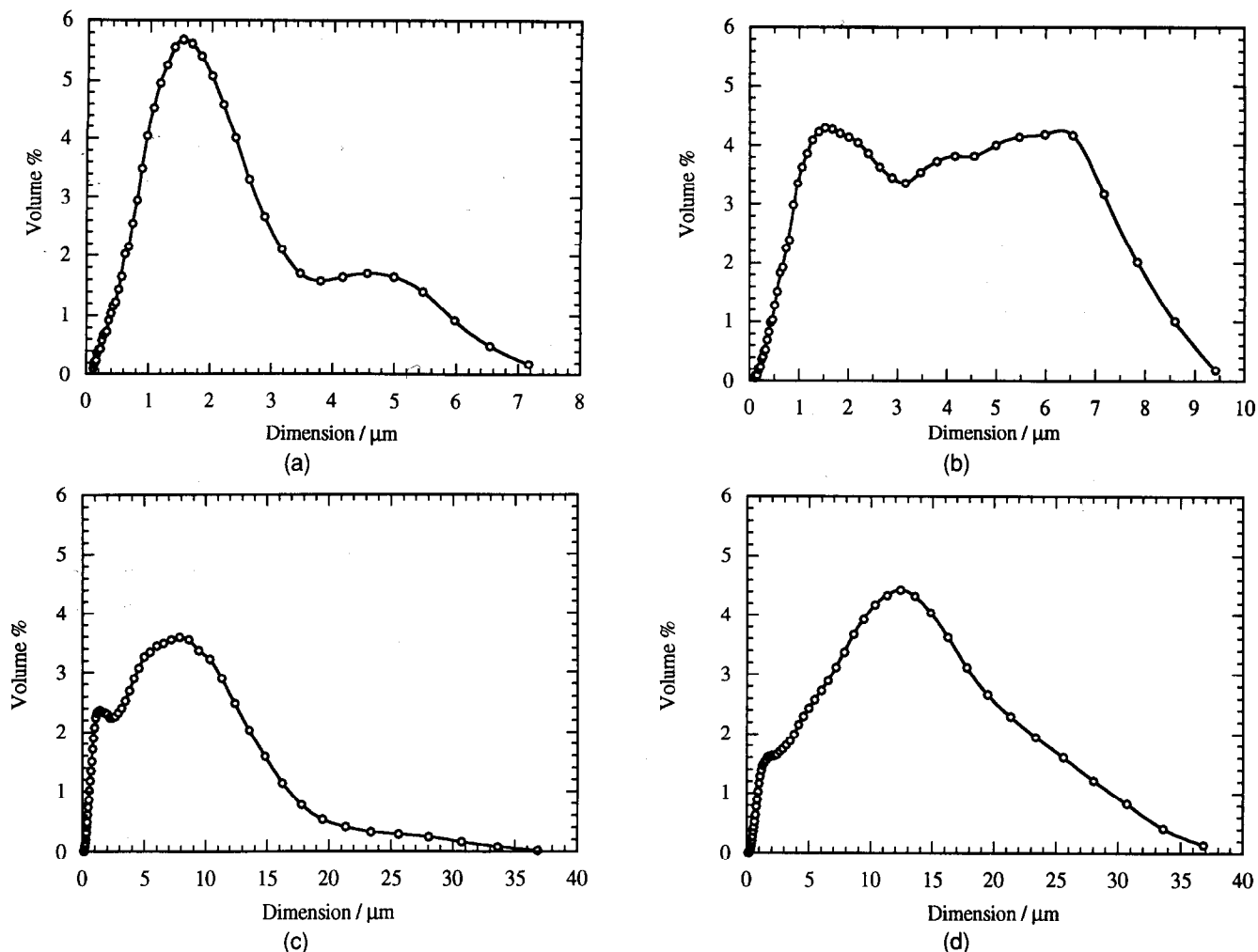


Fig. 1. Frequency distribution curves for the four milled zircon powders, of the computed median dimensions: (a) Z1, 1.4 μm ; (b) Z2, 2.0 μm ; (c) Z3, 3.8 μm ; (d) Z4, 7.3 μm .

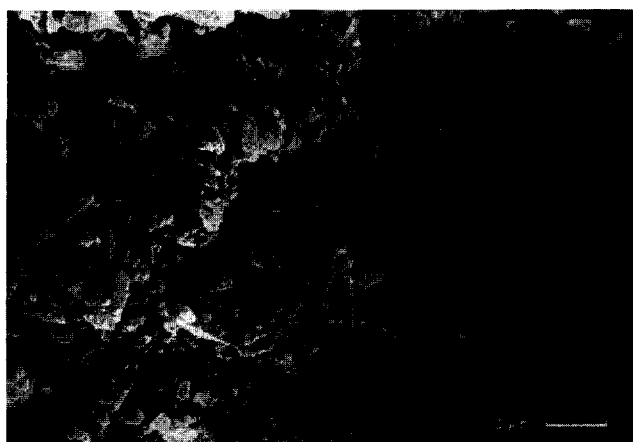


Fig. 2. A scanning electron micrograph of the 2.7 μm zircon powder.

Table 2. Hot-pressing conditions and material densities (temperature 1375°C; pressure 20 MPa)

Material	Time (h)	Mean grain size (μm)	Bulk density (Mg m^{-3})	%Theoretical
Z1	0.5	2.8 ± 0.2	4.35 ± 0.01	98.9
Z2	0.5	4.2 ± 0.3	4.32 ± 0.01	98.2
Z3	1.0	5.2 ± 0.3	4.40 ± 0.01	100.0
Z4.2	1.0	6.2 ± 0.3	4.24 ± 0.01	96.4

Z4, and material densities and grain sizes, are given in Tables 3(a) and 3(b) respectively. Table 4 shows hardness and fracture toughness data for the four most dense materials.

It was clear from the micrographs, and the relationship between initial powder mean particle size and the corresponding mean grain size of the derived materials (Fig. 3), that the hot-pressing

Table 3(a). Hot-pressing conditions for the set of 8.7 μm based zircon powder materials

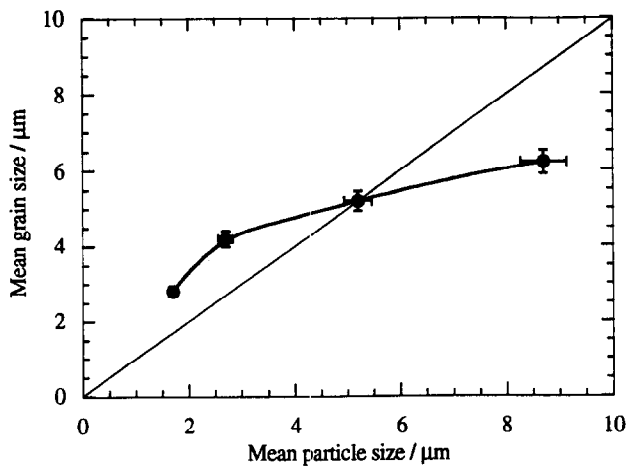
Material	Pressure (MPa)	Temperature ($^{\circ}\text{C}$)	Time (h)
Z4.1	10	1350	0.8
Z4.2	20	1375	1.0
Z4.3	10	1450	1.1

Table 3(b). Z4 densities and porosities

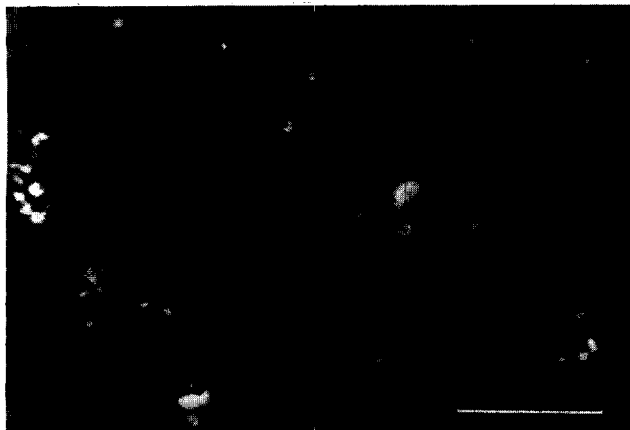
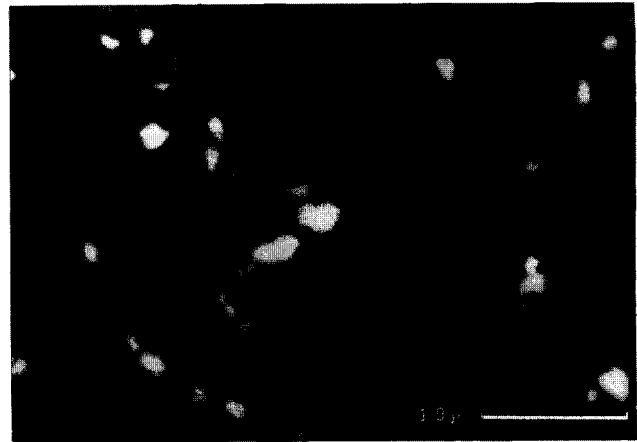
Material	Grain size (μm)	Bulk density (Mg m^{-3})	Pore fraction
Z4.1	6.2 ± 0.3	4.03 ± 0.01	0.084
Z4.2	6.2 ± 0.3	4.24 ± 0.01	0.036
Z4.3	6.2 ± 0.3	4.34 ± 0.01	0.014

Table 4. Property data for dense zircon materials

Material	Grain size (μm)	Hardness (GPa)	K_{Ic} ($\text{MPa m}^{1/2}$)
Z1	2.8 ± 0.5	10.6 ± 1.0	2.9 ± 0.3
Z2	4.2 ± 0.5	10.2 ± 1.0	2.3 ± 0.3
Z3	5.2 ± 0.5	10.9 ± 1.0	2.1 ± 0.3
Z4.3	6.2 ± 0.5	10.3 ± 1.0	2.6 ± 0.3
	mean	10.5 ± 1.0	2.5 ± 0.3

**Fig. 3.** Mean grain size of dense materials as a function of mean zircon particle size.

technique had been successful in giving high densities with no significant grain growth. Figure 4 shows a typical back-scattered electron micrograph of dense material Z1 obtained by hot-pressing at 1375°C for 0.5 h. Figure 5 shows fully dense Z4.3 ($6.2 \mu\text{m}$ grain size), after hot-pressing at 1450°C for 1.1 h. The grey areas were shown by EDS analysis to be zircon; the white regions of dimension $0.5\text{--}1 \mu\text{m}$ for Z1 and $1\text{--}3 \mu\text{m}$ for Z4.3 (determined by the line intercept method) contained predominantly Zr with small amounts of Ca, indicating that they were zirconia with solid-solution calcium oxide. Analyses of the phase areas in all dense materials by point counting and line

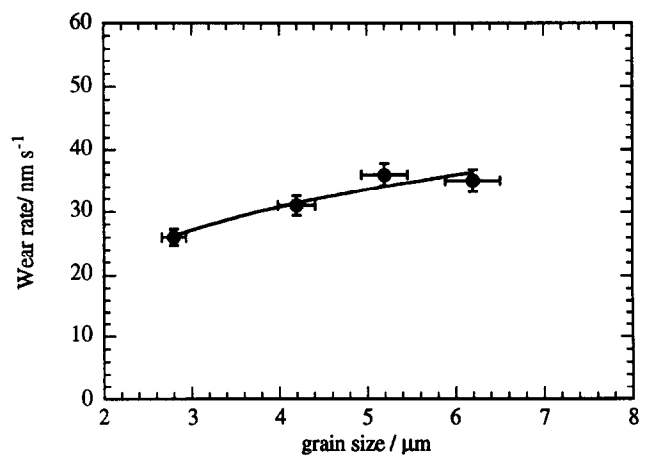
**Fig. 4.** A back-scattered electron micrograph of material of Z1 (mean grain size $2.8 \mu\text{m}$); white regions zirconia, grey regions zircon.**Fig. 5.** A back-scattered electron micrograph of material Z4.2 (mean grain size $6.2 \mu\text{m}$); white regions zirconia, grey regions zircon.**Table 5.** Wear rate data for all zircon materials

Material	Grain size (μm)	Pore fraction	Wear rate (nm s^{-1})
Z1	2.8	<0.02	26
Z2	4.2	<0.02	31
Z3	5.2	<0.02	36
Z4.1	6.2	0.082	58
Z4.2	6.2	0.036	53
Z4.3	6.2	0.014	35

intercept measurements showed that the mean zirconia content was $\sim 2.5\%$ and the mean glass content $\sim 21\%$; there was no obvious trend with powder particle size or hot-pressing conditions.

Wear tests were carried out on 25 mm discs of all materials using the standard conditions. Mean wear rate data derived from the weight losses between 2 and 6 h of wearing are given in Table 5. Repeated measurements of wear rates for the same disc using different disc quadrants showed that the R values were constant within $\pm 3\%$.

Wear rates as a function of mean grain size are shown in Fig. 6, and wear rate as function of

**Fig. 6.** Wear rate as a function of mean grain size.

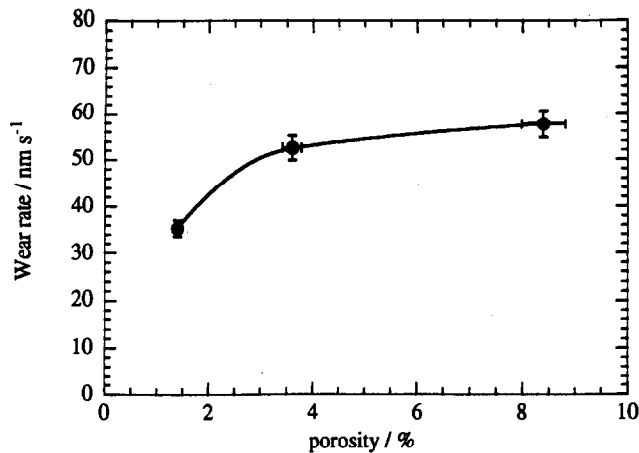


Fig. 7. Wear rate as function of porosity.

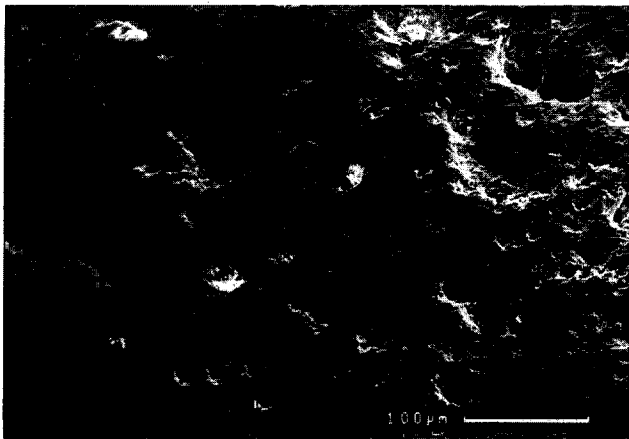


Fig. 8. A scanning electron micrograph of a disc of porous Z4.1 material after 6 h wear.



Fig. 9. A scanning electron micrograph of the edge of a disc of Z4.1 material after 6 h wear.

porosity is shown in Fig. 7. Figures 8, 9 and 10 show typical views of the surface structures of worn discs. Fig. 8, at lower magnification, shows the extensive wear taking place in the vicinity of porosity after 6 h wear. Figure 9, of the dense material, provides strong evidence for grain detachment. Figure 10, at higher magnification, shows for a smoother section of the surface the relief polishing effects, with the loss of some grains by detachment.

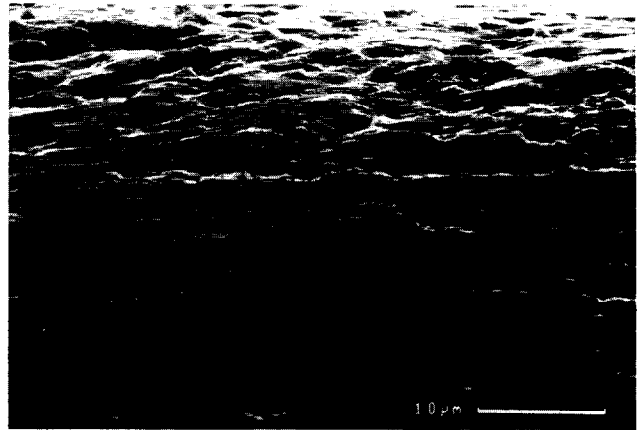


Fig. 10. A scanning electron micrograph of a disc of Z4.2 material after 6 h wear.

4 Discussion

The zircon powders had a trend towards bimodal size distribution, which was most marked for the two intermediate size powders Z2 and Z3. This results in the tendency, shown clearly in the SEM micrographs of Z2 powder in Fig. 2, for very small ($\sim 1 \mu\text{m}$) fragments to split off from large ($\sim 10 \mu\text{m}$) particles during milling. Nonetheless, the spread of the four median sizes was sufficiently wide that the powders could be regarded as having an identifiable mean dimension. Coefficients of variation, defined as standard deviation/mean particle dimension, were in the range 0.72 to 0.93.

During hot-pressing an appreciable proportion of the zircon powder (likely to be mainly the finer particle size fraction) dissolves in the aluminosilicate liquid to yield the large ($\sim 21\%$) volume of siliceous liquid, seen as a glass phase in the dense material. EDS analysis showed this glass to contain relatively small amounts of Ca and Al, and a very much larger proportion of Si and Zr, confirming the dissolution of a significant amount of zircon into the liquid. The overall system is very complex, but viewed at the simplest level the incorporation of the 'impurity' Al_2O_3 into the silicate system will generate liquids of lower forming temperature than those in the simple CaO-MgO-2SiO_2 system; certainly at temperatures well below the melting point of diopside ($\text{CaO.MgO.2Al}_2\text{O}_3$) of 1392°C and probably lower than that of the 1170°C eutectic in the $\text{Al}_2\text{O}_3\text{-CaO-SiO}_2$ system. During densification very little direct fusion by sintering of the zircon grains occurs, and even after 1 h at 1450°C there is no significant grain growth; the correlation between starting zircon median particle size and measured mean grain size in the dense materials is close (Fig. 3). Some shift of median particle size occurs because a greater proportion of fines is likely to be lost by dissolution; in addition,

the fundamentally different techniques used in the estimations of the two dimensions have to be taken into account. Figures 4 and 5 show that there is only a small amount of direct bridging of the zircon grains at the original particle contact points; the glass is therefore generally the continuous phase. An estimated 2.5% by volume of very fine ($\sim 1 \mu\text{m}$) zirconia particles develops. These zirconia particles are well distributed in the material, in a pattern which is independent of zircon particle size. It appears that they nucleate and develop at zircon surfaces during the release of an equivalent proportion of silica into the liquid phase. Some apparent bridging of zircon particles by zirconia particles can also be seen. The zirconia particles were assumed to be the cubic, fully stabilized ZrO_2 phase, but this was not firmly established.

The microindentation hardness (mean 10.5 ± 1.0 GPa) and fracture toughness (mean $2.5 \pm 0.3 \text{ MPa m}^{1/2}$) values are independent of zircon grain size. The relatively low hardness values are assumed to be the consequence of the large volume of glass present in these materials.

There is clearly no relationship between wear rate and hardness or fracture toughness within this set of materials. The wear surfaces were in general fairly smooth, with some local roughening delineated by the zircon grain edges. There was very severe, localized pitting in coarser grain size materials, and particularly in those containing higher levels of porosity. In the smooth surface regions grain outlines are just visible, and differences in wear rate between the zircon grains and intergranular glass were not marked. This general impression of a polishing effect suggests that another, quite different, process such as the tribochemical loss of material is contributing to wear, by superposition on an underlying mechanical wear process involving grain fracture. Grain facetting seen on the flatter surfaces, and the large extents of wear at pore shoulders, indicate that whole grain detachment is also occurring.

The overall wear rate is clearly related to grain size (Fig. 6) and, at this stage of the investigation of the erosive wear of polycrystalline materials of this type, emphasis has been placed on developing an understanding of the relationship between grain size and the probability of grain detachment, in the context of a wear process largely initiated by the point impact of a grit particle on a surface. For polycrystalline alumina materials with mean grain size less than $\sim 2 \mu\text{m}$, tribochemical polishing appeared to be the major wear mechanism.²³ In the case of the polycrystalline zircon materials examined here, because the finest grain size was of the order of $3 \mu\text{m}$, it would be expected that tribochemical wear might not be an impor-

tant component of the erosive wear process. The nature of the wear pattern on the discs (with the most extensive wear taking place on surfaces normal to the direction of travel of the surface through the abrasive fluid) indicates that the effects of sliding, and thus particle-surface frictional effects, are also of lesser importance than particle impact events. For this reason it would seem that the erosive wear damage process of these insulator materials is likely to be largely mechanical, rather than electrical, in origin.

An approximate dependence of wear rate on $(\text{grain size})^{-1/2}$ is suggested (shown in Fig. 11), similar to that seen for fully dense hot-pressed and sintered 100% alumina materials.²² However, treatment in accord with the supposition that wear proceeds by a 'stop-go' process, involving grain boundary microcracking and crack arrest at multiple grain boundary junctions and giving a wear rate proportional to $G/(G + G_0)$, also yields a straight line passing through the origin for $G_0 = 3 \mu\text{m}$ (shown in Fig. 12). The wear rates for the zircon materials are similar to those for pure polycrystalline alumina of comparable grain size (Fig. 13), though the zircon wear is some 30% slower at each grain size. In view of the large glass content of the zircon materials this is surprising, but

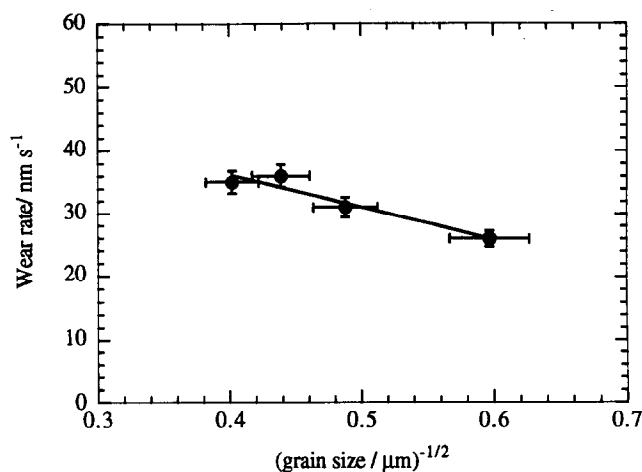


Fig. 11. Wear rate as a function of $(\text{grain size})^{-0.5}$.

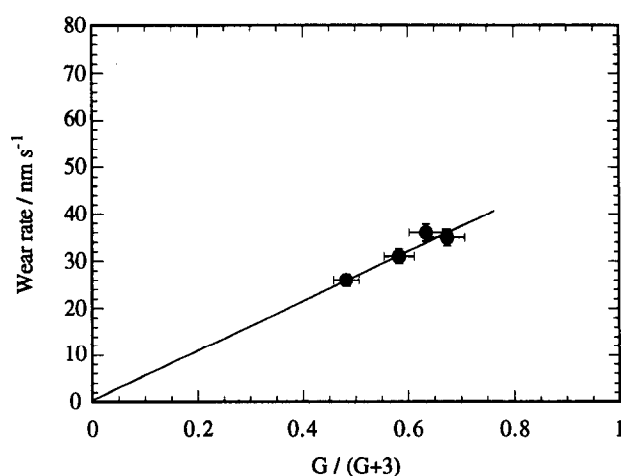


Fig. 12. Wear rate as a function of $G/(G+3)$.

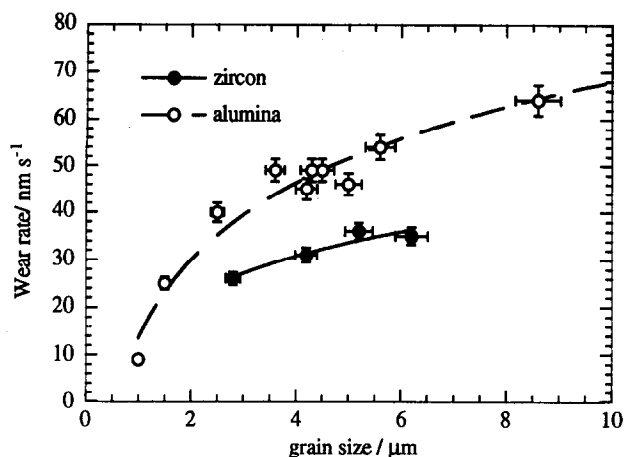


Fig. 13. Wear rate as a function of grain size for dense zircon and pure alumina materials.

preliminary wear rate data for sintered alumina materials containing 5 to 10% of a liquid-forming silicate system suggest that wear rate is insensitive to the intergranular glass content at this level.²⁸

A second clear factor controlling wear rate is porosity: the relationship between pore fraction and wear rate shown by Fig. 7 for the three 6.2 μm zircon materials. Although there are only three points there is the suggestion that wear, by grain dislodgment, occurs preferentially at the edges of the pores. This is supported by Figs 8 to 10 which show the wear damage in Z4 material of 0.036 pore fraction.

On the basis of this study, it seems that fine-grained liquid phase sintered zircon materials will have low wet erosive wear rates, comparable with those of fine-grained sintered alumina materials, provided full density can be attained. Unlike the alumina materials, grain growth in zircon does not readily occur, which provides an added intrinsic advantage for this type of material. Densification is therefore predominantly the result of the combined processes of void filling by liquid, and particle rearrangement.

5 Conclusions

Two wear mechanisms appear to be responsible for the loss of material during the wet erosive wear of liquid phase densified zircon. One is probably a non-selective tribochemical dissolution of the zircon grains and intergranular glass phase in which the zircon grains are embedded. This process leads to a polishing action, and would not be expected to be related to the zircon grain size for material with a constant volume fraction of glass phase. Another, and probably dominant, factor with this group of zirconia materials is grain-size related, and seems likely to be a grain detachment

process, occurring through localized microfracture and crack linking. The variations in wear rate seen within this set of materials are not explicable in terms of H or K_{Ic} , because these are essentially constant. Porosity is an important additional factor and leads to considerable enhancement of wear rate. Exploration is being continued of the precise basis for, and form of, the quantitative relationship between the rate wear by grain detachment, and grain size, in materials of this type.

Acknowledgements

Gramcol Zircon Ltd, Stoke-on-Trent, UK, is thanked for the provision of zircon powders, and for assistance with particle milling and particle size analyses. Financial support from the Asturian Research Foundation to M. Miranda-Martinez is gratefully acknowledged. Dr. E. Gilbert provided invaluable technical assistance with powder hot-pressing.

References

1. Speer, J. A., Orthosilicates. Zircon, *Rev. Mineral.*, **5** (1980) 67–112.
2. Beretka, J., Bowman, R. G. & Brown, T., Studies on zircon pigments for ceramic glazes, *J. Aust. Ceram. Soc.*, **17** [2] (1981) 37–43.
3. Hathaway, A. J. C., Holmes, R. & Peters, R. Effective use of zircon opacifiers. *Ceram. Eng. Sci. Proc.*, **4**[11–12] (1983) 1036–46.
4. Adams, W. T., Zircon: from curiosity to commodity. *Am. Ceram. Soc. Bull.*, **68**[5] (1989) 1024–7.
5. Garnar, T. E., Zircon. *Am. Ceram. Soc. Bull.*, **69**[5] (1990) 888–90.
6. Ryshkewitch, E. & Richerson, D. W., *Oxide Ceramics: Physical Chemistry and Technology*. Academic Press Inc., Orlando, FL, 1985, 2nd Ed.
7. Butterman, W. C. & Foster, W. R., Zircon stability and the $\text{ZrO}_2\text{-SiO}_2$ phase diagram. *Am. Mineral.*, **52** (1967) 880–5.
8. Levin, E. M., Robbins, C. R. & McMurdie, H. F. (Eds), *Phase Diagrams for Ceramists*. American Ceramic Society Inc., Columbus, OH, 1964.
9. Curtis, C. E. & Sowman, H. G., Investigation of the thermal dissociation, reassociation, and synthesis of zircon. *J. Am. Ceram. Soc.*, **36**[6] (1953) 190–9.
10. Boch, P., Kapelski, G. & Giry, J. P., Sintering properties of dissociated and reassociated zircon. *Proc. Br. Ceram. Soc.*, **38**, (1986) 149–60.
11. Anseau, M. R., Leblud, C. & Cambier, F., Reaction sintering of mixed zircon-based powders as a route for producing ceramics containing zirconia with enhanced mechanical properties. *J. Mater. Sci. Lett.*, **2**[7] (1983) 366–70.
12. Dörre, E. & Hübner, H., *Alumina — Processing Properties and Applications*. Springer Verlag, Berlin, 1984.
13. Evans, A. G. & Wilshire, T. R., Quasi static solid particle damage in brittle solids — I: Observations, analysis and implications. *Acta Metall.*, **24** (1976) 939–56.
14. Fayeulle, S., Berroug, H., Hamzaoui, B. & Tréheux, D., Role of dielectric properties in the tribological behaviour of insulators. *Wear*, **162–164** (1993) 906–12.

15. Cho, S. J., Hockley, B. J., Lawn, B. R. & Bennison, J., Grain-size and *R*-curve effects in the abrasive wear of alumina. *J. Am. Ceram. Soc.*, **72**[7] (1989) 1249–52.
16. Rice, R. W. & Sponello, B. K., Effect of microstructure on rate of machining of ceramics. *J. Am. Ceram. Soc.*, **59**[7–8] (1976) 330–3.
17. Wiederhorn, S. M. & Hockey, B. J., Effect of material parameters on the erosion resistance of brittle materials. *J. Mater. Sci.*, **18** (1983) 766–89.
18. Wu, C. C., Rice, R. W., Johnson, D. & Platt, B. A., Grain size dependence of wear in ceramics. *Ceram. Eng. Sci. Proc.*, **6**[7–8] (1985) 995–1011.
19. Rice, R. W., Micromechanics of microstructural aspects of ceramic wear. *Ceram. Eng. Sci. Proc.*, **6**[7–8] (1985) 940–58.
20. Marshall, D. B., Lawn, B. R. & Cook, R. F., Microstructural effects on grinding of alumina and glass ceramics. *J. Am. Ceram. Soc.*, **70**[6] (1987) C-139–40.
21. Gee, M. G. & Almond, E. A., The effects of surface finish on the sliding wear of alumina. *J. Mater. Sci.*, **25**(1A) (1990) 296–310.
22. Cho, S. J., Moon, H., Hockley, B. J. & Hsu, S. M., Wear transformation phenomenon in alumina during sliding. In *C-MRS Int. Symp. Meeting 1990*, ed. B. Wu., North-Holland, Amsterdam, 1991, vol. 5, pp. 387–9.
23. Miranda-Martinez, M., Davidge, R. W. & Riley, F. L., Grain size effects on the wet erosive wear of high purity polycrystalline alumina. *Wear*, **172** (1994) 41–8.
24. Davidge, R. W. & Riley, F. L., Grain size dependence of the wear of alumina. *Wear*, **186–187** (1995) 45–9.
25. Mendelson, M. I., Average grain size in polycrystalline ceramics. *J. Am. Ceram. Soc.*, **52**[8] (1969) 332–46.
26. Anstis, G. R., Chantikul, P., Lawn, B. R. & Marshall, D. B., A critical evaluation of indentation techniques for measuring fracture toughness: I. Direct crack measurements. *J. Am. Ceram. Soc.*, **64** (1981) 533–6.
27. Miranda-Martinez, M. & Riley, F. L., Wet abrasive wear of technical ceramics. *Br. Ceram. Trans. J.*, **90** (1991) 118–21.
28. Miranda-Martinez, M., Davidge, R. W. & Riley, F. L., The reduction of erosive wear rates of advanced technical ceramic materials. In *2nd International Conference Proceedings, Ceramics in Energy Applications*. The Institute of Energy, London, 1994, pp. 239–52.

Microstructure and Thermal Stability of a Glass-Coated SiC/SiC Composite

M. Li & F. Guiu*

Department of Materials, Queen Mary and Westfield College, University of London, Mile End Road, London E1 4NS, UK

(Received 6 October 1994; revised version received 22 August 1995; accepted 27 August 1995)

Abstract

Fully glass-coated samples of two-dimensionally layered SiC/SiC composite, which had a thin carbon interfacial layer between the fibre and the matrix, were heat-treated in air for 50 h at temperatures of 1000, 1150, 1300 and 1400°C. The mechanical properties of these heat-treated samples were assessed by means of wedge opening tests, and the microstructural changes due to different heat treatments were subsequently investigated. The glass coating prevented the environmental oxidation of the bulk material whose mechanical properties were retained after heating up to 1200°C. Heating above 1200°C drastically changed the mechanical properties of the composite. This property degradation is attributed to both the structural changes in the fibres and a greatly weakened fibre–matrix interphase. Heating uncoated SiC/SiC specimens at 800°C for 100 h resulted in oxidation of the composite up to a depth of 0.5 mm below the surface. This oxidized layer did not affect the mechanical properties of the bulk material when specimens for wedge opening tests were notched after the heat treatment. However, heat treatments at 860 and 1200°C degraded the properties of the specimens which had been notched before the heat treatment. It is believed that such degradation in mechanical properties arises from the oxidation of the carbon interphase in the unprotected notch tip region.

1 Introduction

Structural ceramic materials have become increasingly important in modern industrial and consumer technology. However, the intrinsic brittleness or low resistance to crack propagation, characteristic of most ceramic materials, severely restricts their use and applications. There is great interest, and

much research effort is being invested, in developing methods to improve the fracture toughness of ceramics.^{1–7} Amongst these methods the reinforcement of ceramic materials with high strength fibres is believed to offer great potential. The increase in toughness that can be achieved by means of fibre reinforcement arises from both crack deflection at the fibre–matrix interface and from bridging of the crack faces by unbroken fibres. The effectiveness of these processes depends strongly on the strength of the fibre–matrix interface.^{8,9} A strong fibre–matrix bonding can produce a large increase in stiffness and strength but it is ineffective for toughness improvement. This is because matrix cracking around the fibres in such a material is followed by failure of the fibres and hence the composite breaks like a monolithic ceramic. A relatively weaker interface, on the other hand, can provide great toughness improvement since failure of the matrix around the fibres is followed by debonding and fibre sliding, or pull-out. This relaxes the stress in the fibres which can remain unbroken, providing effective crack bridging. The extra load taken by the fibres causes reductions in both the crack-tip stresses and the magnitude of the crack extension force.

An efficient way of tailoring the strength of fibre–matrix interfaces in ceramic matrix composites is to form a thin layer of adequate shear strength around the fibres. The principal challenge is to identify a coating material that has the necessary mechanical properties and is also stable in the working environment and at elevated temperatures. The thermal stability of fibre, matrix and interface should therefore be fully investigated before ceramic matrix composites can be widely used at high temperatures. In the present investigation, a study of the effect of heat treatment on the microstructure and mechanical properties has been carried out on a silicon carbide fibre-reinforced silicon carbide matrix composite, which has a thin carbon coating as the interphase.

*To whom correspondence should be addressed.

2 Experimental Procedures

2.1 Materials

The material investigated was a silicon carbide fibre (Nicalon fibre) reinforced silicon carbide matrix composite. Bundles of Nicalon fibres woven into two-dimensional layers were coated with a thin carbon layer by the decomposition of methane, and then embedded in a chemical vapour infiltrated (CVI) SiC matrix, during which process methyl-trichlorosilane gas decomposed at high temperature to yield solid silicon carbide and HCl gas. Infiltration takes place over three stages: after the first stage the mould is removed, while machining is carried out between the subsequent stages of densification. The final material had a density of 2.55 g cm^{-3} with a volume fraction of fibre equal to 38%.

The finished samples were covered with a chemical vapour deposition (CVD) SiC layer and a proprietary glass layer to provide additional protection against oxidation when the material is exposed to high temperature in air. Information about the glass coating was not available from the supplier of the material for industrial protection reasons. However, external seal coatings based mainly on CVD SiC and high temperature glass have already been extensively studied in the case of C/C composites,¹⁰⁻¹² C/SiC composites¹³ and SiC/SiC composites.^{14,15} Oxidation of the CVD SiC of the surface forms an amorphous SiO₂ layer, which has extremely low oxygen permeability up to 1800°C and provides an effective barrier to the diffusion of the oxygen towards the carbon interphase. Scanning electron microscopy (SEM) examination of the coating in our material reveals that this is a silica-based glass containing alkali oxide. The alkali additives are most likely used to reduce the viscosity of the coating layer, which can flow at relatively low temperature (see Section 3.3) to heal any crack or surface damage which may be introduced accidentally at low temperatures, when the coating is brittle. Flux additives may compromise the apparent advantages of SiO₂ by increasing oxygen permeability.¹⁰

2.2 Experimental techniques

The SiC/SiC composite material was supplied in the form of square tablets of $10 \times 10 \times 3 \text{ mm}^3$ in size. Some of these samples were heat-treated at high temperatures in air in order to study the thermal stability of the composite.

Because of the small size of the specimens available, a wedge opening test method had to be developed to assess the mechanical properties of the material both before and after the heat treatment. A small notch, 3 mm deep and 1 mm wide, was cut on each tablet perpendicular to the fibre

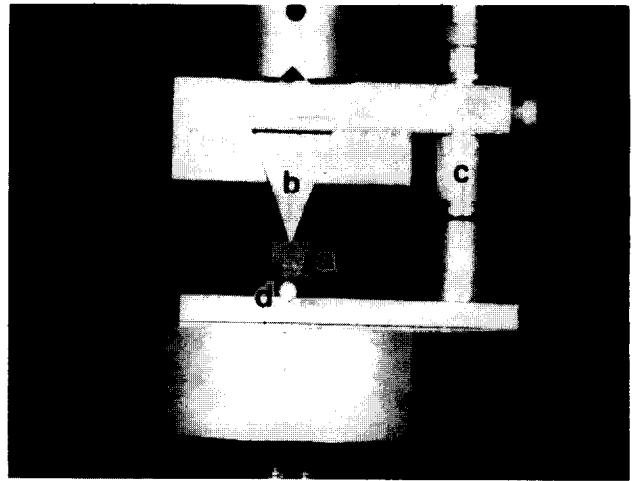


Fig. 1. Set-up for the wedge opening test showing (a) specimen, (b) wedge, (c) displacement transducer and (d) supporting roller.

cloth layers. By forcing a wedge into the notch, a crack was made to propagate across the specimen using the experimental set-up shown in Fig. 1. The loading wedge is made of a hard steel and the wedge angle is 40°. The specimen was supported by a steel roller of 3 mm in diameter. The wedge opening tests were performed under position control mode at a crosshead speed of 0.2 mm min^{-1} . The wedge displacement (vertical displacement) was measured by a capacitance transducer with a sensitivity of 1 mm V^{-1} and the applied load vs. wedge displacement curve was recorded on an X-Y plotter. During the wedge opening test, a travelling microscope was mounted close to the specimen to observe the crack propagation.

After the wedge opening tests, the crack paths and fracture surfaces were examined under a scanning electron microscope (Jeol JSM-35 CF). After the specimens were split into two pieces, thin foils were prepared from different positions and orientations as shown in Fig. 2 for structural examination under a transmission electron microscope (TEM) (Jeol 200 CX). The compositions of various areas such as interphase, Nicalon fibres and CVI SiC matrix were analysed using the energy dispersive X-ray spectrometer (EDS) attached to the SEM and TEM.

3 Experimental Results

3.1 As-received material

Four phases could be identified in the as-received composite: the Nicalon fibre, the carbon interphase, the CVI SiC matrix, and pores. The range of fibre diameters was between 10 and $18 \mu\text{m}$, while the mean value was approximately $14 \mu\text{m}$. The selected area diffraction (SAD) pattern of the Nicalon fibre exhibited three rings, corresponding

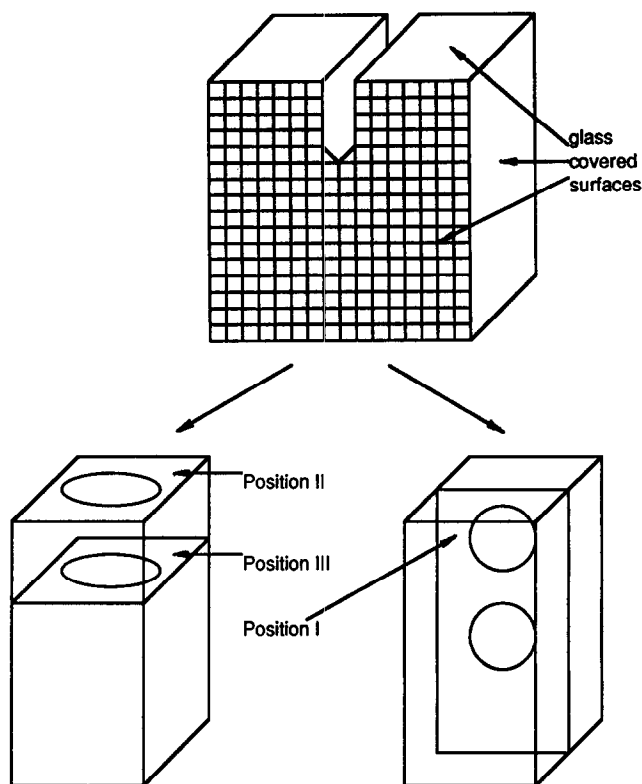


Fig. 2. Schematic diagram showing the sectioning of the SiC/SiC tablet after mechanical test for the preparation of TEM specimens.

to β -SiC₁₁₁, β -SiC₂₂₀ and β -SiC₃₁₁ scattered beams. The silicon carbide in the fibre was not fully crystalline, therefore the hkl diffraction rings were diffuse and faint. The TEM bright-field image of the composite (Fig. 3) reveals the carbon coating layer, which ranged from 0.1 to 0.2 μm in thickness. SAD patterns from the interphase and the matrix show three primary rings of β -SiC matrix plus two unique additional rings, which are associated with the carbon coating layer [(002) and (010) graphite planes]. The chemical vapour infiltrated SiC matrix of the composite had both equiaxed and columnar grains. The initially deposited SiC



Fig. 3. TEM image of the fibre, the interfacial carbon layer and the matrix. SAD pattern corresponding to the interphase and the matrix.



Fig. 4. TEM micrograph of equiaxed β -SiC grains of the CVI matrix.

crystallites which were adjacent to the fibre coating layer were equiaxed and ranged in size from 20 to 300 nm (Fig. 4). The columnar SiC grains grew radially from the equiaxed SiC zone (Fig. 5). Every columnar grain was up to 0.3 μm wide and several μm long. The transverse cross-section of the fibres and their adjacent matrix showed the fibre-interphase (carbon coating)-equiaxed SiC zone-columnar SiC grains arrangement.

To investigate the effect of heat treatment on the mechanical integrity of the material, three as-received composite tablets were tested by the wedge opening method to obtain reference curves. The results showed good repeatability of the technique. The three specimens gave almost identical load-displacement curves as shown in Fig. 6, with a variation of maximum applied load between 1.75 and 1.88 kN. The composite exhibited an initial linear elastic behaviour followed by a non-linear load-displacement relationship until the maximum load was reached (Fig. 6). The first load drop terminated the linearity and a sound was heard coincidentally with this load drop. No crack was observed on the specimen surface, but sign of



Fig. 5. TEM micrograph of columnar β -SiC grains of the CVI matrix.

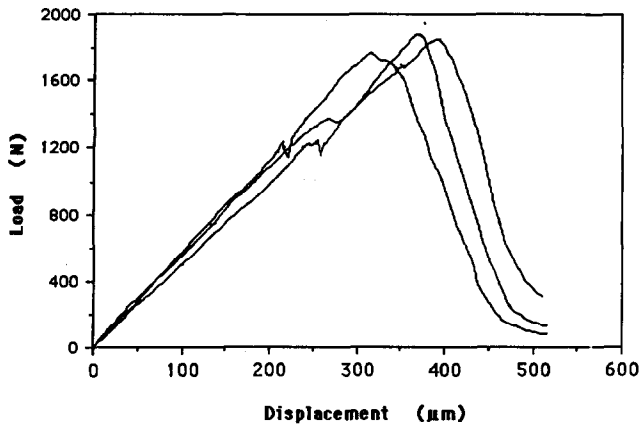


Fig. 6. Applied load vs. wedge displacement curves for as-received SiC/SiC specimens.

debris jumping from the notch tip was noted. From the first load drop to the maximum load, there was no evident main crack on the specimen surface and emission of particles from the notch front continued. The non-linearity towards maximum load is probably due to the progressive cracking of both matrix and fibres which are inside a limited damage zone just at the notch tip. It is possible that the resolution of the observation method used was not sufficient to obtain detailed image of what was happening at the notch tip before the maximum load was reached. After the maximum load, a dominant crack started to be gradually revealed, which propagated from the notch tip through the middle of the specimen to the contacting point of the supporting roller. For the SiC/SiC composite, the fracture by wedge opening test is non-catastrophic, and hence some load-bearing ability is still retained beyond the maximum load because fibres bridge the crack.

The specimen broke by the propagation of a single dominant crack (Fig. 7) and at the end of the test the two halves of the split specimen were still firmly held together by unbroken pulled-out fibres bridging the crack (Fig. 8).

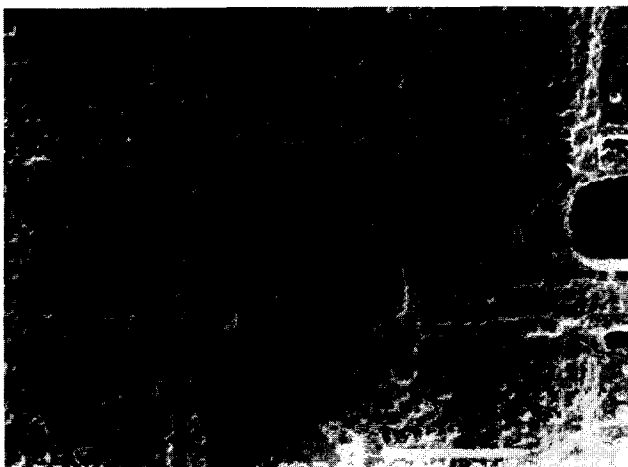


Fig. 7. Straight crack path in the as-received material after the wedge opening test.

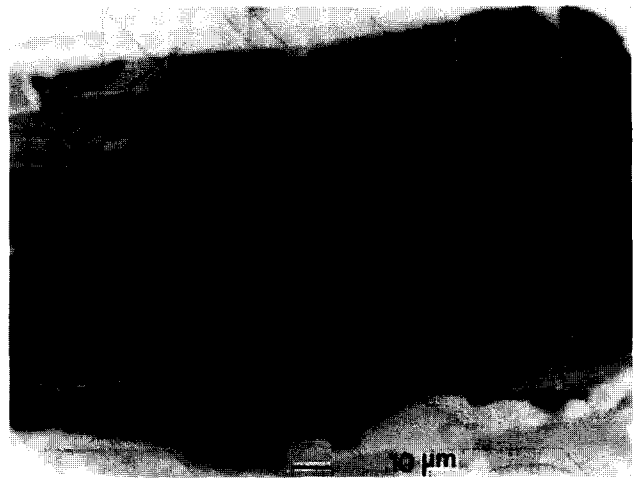


Fig. 8. Fibre bridging in the crack wake in an as-received specimen.

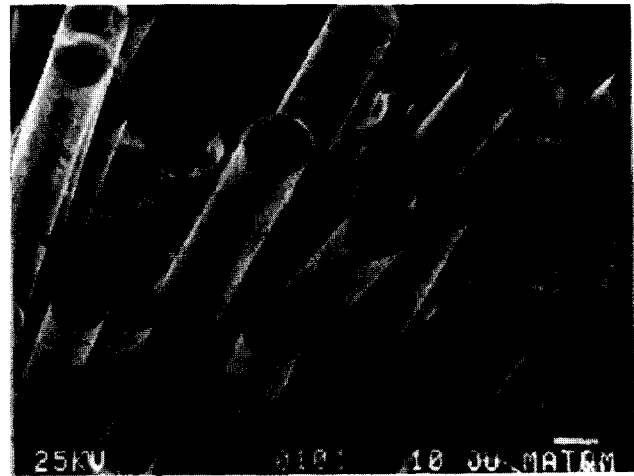


Fig. 9. Fracture surface of the as-received material showing various degree of fibre pull-out.

After crack path examination, the tested specimens were manually pulled apart so that fracture surfaces could be studied under the microscope. Fracture surfaces of as-received specimens were characterized by fibre pull-out (Fig. 9) and debonding between the fibre and the matrix.

Heat treatments and wedge opening tests were carried out on both fully and partially glass-coated SiC/SiC tablets.

3.2 Effect of heat treatment of fully glass-coated specimens

As-received SiC/SiC tablets were heat-treated in air for 50 h at 1000, 1150, 1300 and 1400°C. They were subsequently notched and tested using the wedge opening test method.

It could be seen from the recorded load-displacement curves (Fig. 10) that heat treatment up to 1150°C for 50 h did not significantly change the mechanical properties of the composite. The microstructures observed under SEM and TEM of the heat-treated specimens showed similar features to those of the as-received material.

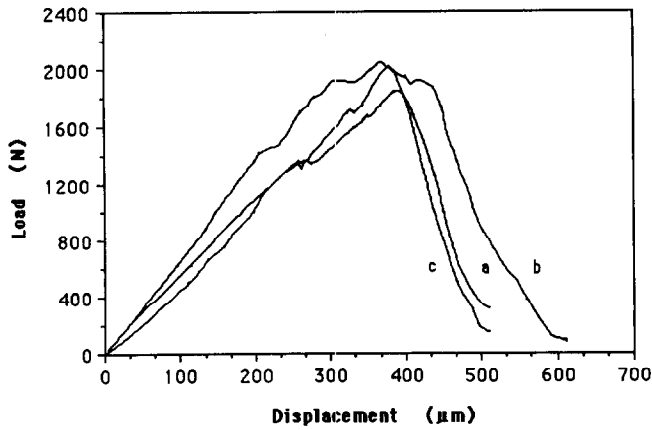


Fig. 10. Applied load vs. wedge displacement curves for SiC/SiC specimens: (a) as-received, (b) heat-treated at 1000°C for 50 h, (c) heat-treated at 1150°C for 50 h.

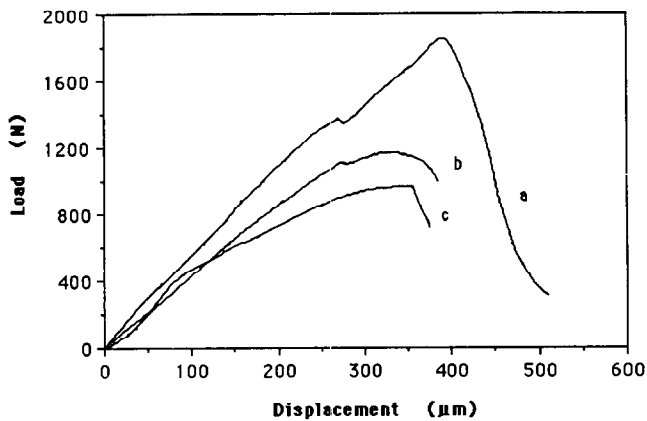


Fig. 11. Applied load vs. wedge displacement curves for SiC/SiC specimens: (a) as-received, (b) heat-treated at 1300°C for 50 h, (c) heat-treated at 1400°C for 50 h.

A heat treatment for 50 h at both 1300 and 1400°C produces a drastic degradation of the composite's mechanical properties (Fig. 11). In the wedge opening tests the specimens did not fail by the propagation of a single main crack, as observed for the material heat-treated below 1150°C, but by massive delamination of the fibre layers (Fig. 12) and severe damage at supporting points. The frac-

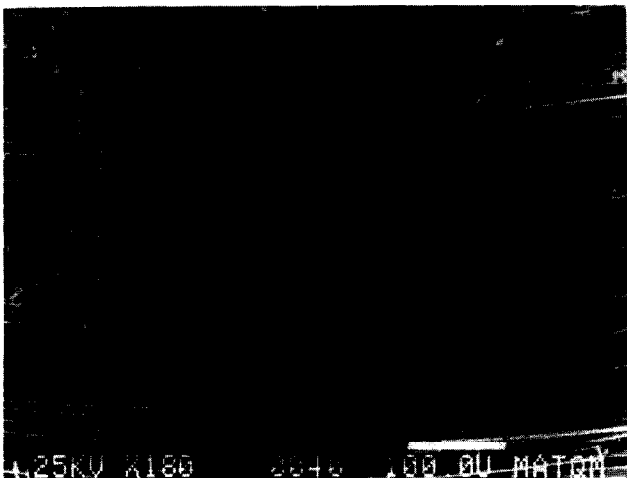


Fig. 12. Delamination surface of the specimen tested after heat treatment at 1400°C for 50 h.

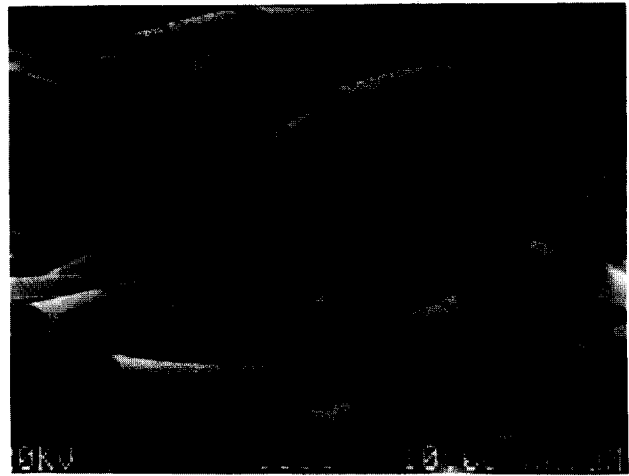


Fig. 13. Extensive fibre pull-out in the SiC/SiC specimen heat-treated at 1400°C for 50 h.

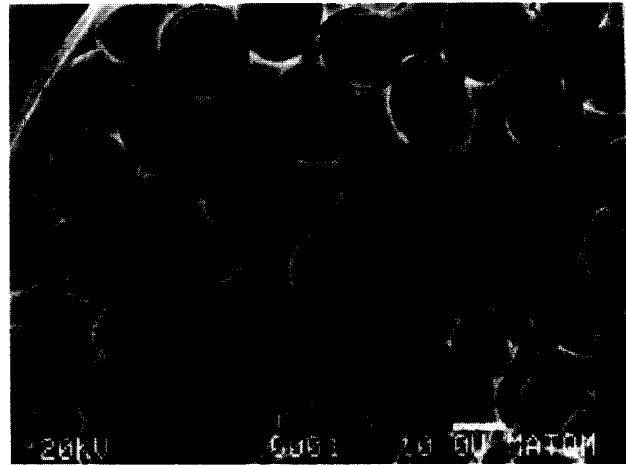


Fig. 14. Extensive debonding between the fibre and the matrix in a specimen heat-treated at 1400°C for 50 h.

ture surfaces of these specimens showed extensive fibre pull-out with segmental patches of interphase adhered to the fibre surface (Fig. 13). All these observations are clear evidence that the strength of the fibre–matrix interface has been severely degraded. It can be seen in Fig. 14 that delamination

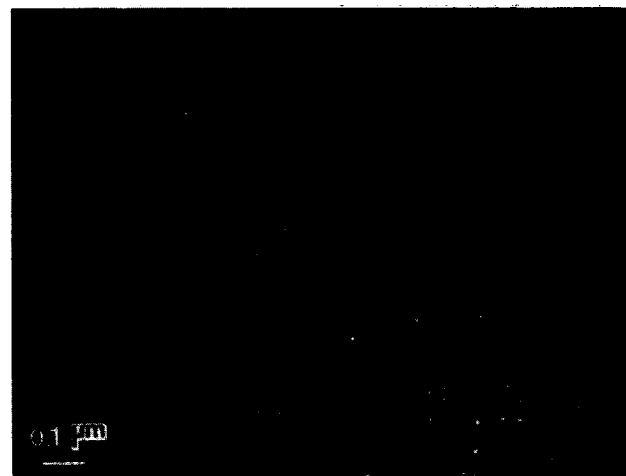


Fig. 15. TEM dark-field images of the SiC fibre after crystallization caused by high temperature heat treatment (1400°C for 50 h).

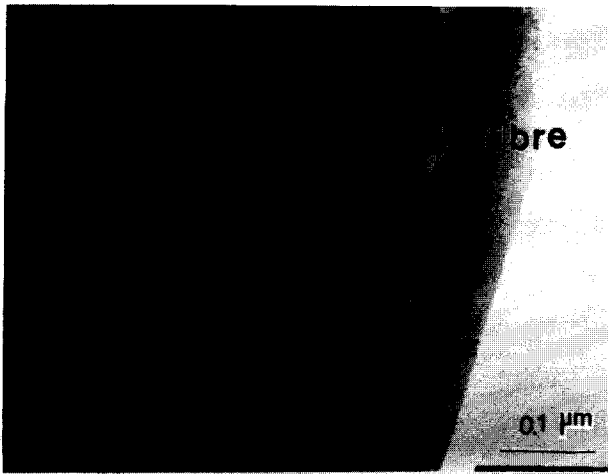


Fig. 16. Microporous carbon interfacial layer between two fibres after high temperature heat treatment.

of the material has taken place not only between the fibre layers, but also within the fibre bundles.

TEM observations made on thin foils prepared from the specimens heat-treated at 1300 and 1400°C showed that the β -SiC in the fibres had changed from an incompletely crystallized to a crystalline structure with an average grain size of 10 nm (Fig. 15). Changes also took place in the interfacial region. The carbon layer existed in the composite, but the carbon in contact with the fibres had become microporous (Fig. 16). Complete debonding of the carbon layer was also observed in some areas.

3.3 Determination of the glass flow temperature

The protection that the covering glass layer offers against oxidation of the bulk material is important for the applications of SiC/SiC composites at moderately high temperatures, and it is therefore of interest to know how efficient this glass layer can be. When local damages in the glass layer occur, the consequent oxidation of bulk SiC/SiC material should not lead to the rapid deterioration of the component.

It was noticed that on the glass layer of the as-received materials there were microcracks and small voids in this layer, and it is possible that when the composite is under load this layer can be damaged. If the glass flows moderately at the service temperature this should have a 'smoothing' or 'healing' effect on the microcracks or small voids. The 'healed' glass layer must then lead to a decreased degree of oxygen infiltration from the environment into the bulk SiC/SiC material. From this point of view it was important to determine the temperature at which the glass coating can flow easily.

Glass flow tests were conducted on as-received SiC/SiC tablets. A scratch approximately 0.3 mm wide was made on the surface of some specimens

through the glass layer and slightly into the underlying SiC/SiC material. These specimens were subsequently heat-treated in air for 5 h at 840, 860, 880 and 900°C respectively and were then examined under the SEM.

It could be seen that the glass coating started to flow at between 840 and 860°C and it flowed easily above 880°C. It can be inferred that higher temperatures above 900°C may cause sufficient glass flow to heal a damaged surface layer. A temperature of 800°C was therefore chosen for the heat treatment of partially uncoated specimens.

3.4 Effect of heat treatment of partially glass-coated specimens

Some composite tablets were polished on one surface to remove the glass layer. They were subsequently heat-treated at 800°C for 100 h. TEM specimens were prepared after the heat treatment from different positions of the tablet. Important structural changes were observed to have taken place to a depth of 0.5 mm from the uncovered surface. The original interfacial carbon layer had disappeared, having been replaced by a thin layer of amorphous structure (Fig. 17), as evidenced by a lack of contrast change during specimen tilting in the microscope and by the SAD pattern showing continuous halos. EDS analysis revealed the presence of oxygen and silicon peaks in this layer, which probably consists of silica.

It is thought that this superficial oxidation process, which occurs at the uncovered surface up to a limited depth, will not affect the mechanical properties of the composite in the wedge opening test, which measures resistance to crack growth in the bulk material that is not oxidized, provided that the specimens are notched after the heat treatments. Hence wedge opening tests were not performed on these partially glass-coated samples heat-treated at 800°C.

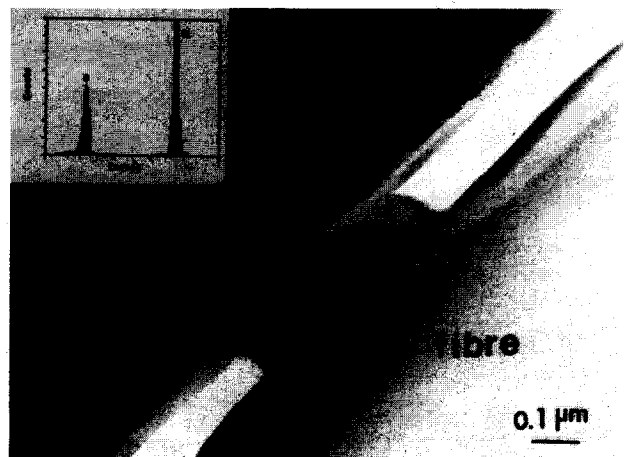


Fig. 17. TEM image and EDS spectrum of the new interphase (silica) in the oxidized specimen heat-treated at 800°C for 100 h.

However, it was considered to be of interest to investigate the effect of heat treatment on specimens which were notched before being heat-treated. During heat treatment, chemical reactions could occur in the notch-tip region and it is possible that the macrocrack initiation and its propagation may be strongly dependent on this region with respect to the first fibre bundle failure.

Notches 3 mm deep were cut into the specimens which were subsequently heat treated at 860 or 1200°C for 50 h. Wedge opening tests were then conducted on these specimens and SEM examinations were performed afterwards.

It can be seen in Fig. 18 that in the notched and heat-treated specimens both the first load drop and the maximum load were considerably lower than for the as-received specimens. However, the composite still exhibited a non-catastrophic failure behaviour as indicated by the curves.

SEM examinations revealed that a single dominant crack had propagated across the specimen for both heat treatment conditions. Fibre pull-out and debonding between the fibres and the matrix were

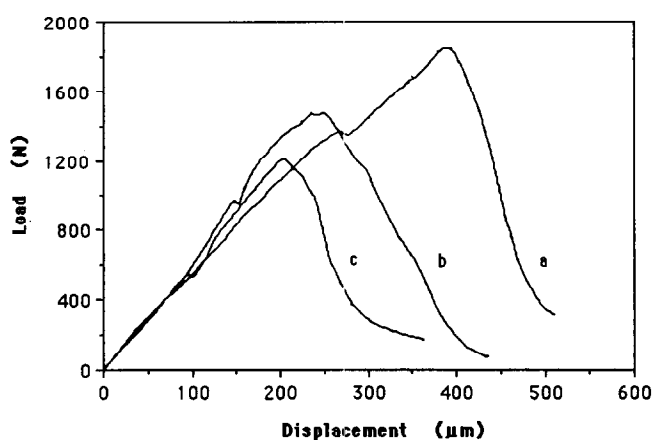


Fig. 18. Applied load vs. wedge displacement curves for SiC/SiC specimens: (a) as-received, (b) notched and heat-treated at 860°C for 50 h, (c) notched and heat-treated at 1200°C for 50 h.



Fig. 19. Oxidized region (flat area) adjacent to the notch tip in SiC/SiC specimen of heat-treated at 1200°C for 50 h, showing strong bonding between the fibre and the matrix.

observed in the bulk fractured area. However, the fracture surface adjacent to the notch tip exhibited a flat region with no fibre pull-out (Fig. 19). The lack of mirror boundary structure in the fractured fibres seems to indicate that the fibre was perfectly bonded to the matrix in this oxidized zone, where the propagating crack may pass directly from the matrix through the fibre with little or no change in direction. The width of the flat region is about 60 μm in the specimen heat-treated at 1200°C, and 40 μm in the specimen heat-treated at 860°C.

4 Discussion

The experimental results have shown that the heat-treated SiC/SiC composite which is fully covered with a glass layer retains its mechanical properties after heat treatment up to 1150°C for 50 h. This glass surface layer drastically limits the oxidation of the bulk material when the specimen is heat-treated in air.

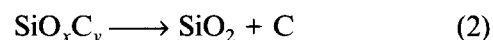
Heating above 1200°C drastically degrades the mechanical properties of the composite. This property degradation can be correlated with both chemical and structural evolutions of the fibre and a greatly weakened fibre-matrix interphase. It has been reported that in addition to silicon carbide, both silica and free carbon are also present in Nicalon fibres,^{16,17} and more recent studies have detected a non-stoichiometric silicon oxycarbide (SiO_xC_y) which accounts for most of the oxygen content,^{18,19} although the existence of a surface layer of silica is not ruled out.⁸ Due to the presence of these compounds, Nicalon fibres have a non-equilibrium composition which would result in its intrinsic degradation at high temperatures.^{20,21} It has also been suggested that at the beginning of the heat treatment above 1200°C, in a low partial pressure of carbon monoxide, decomposition of SiO_xC_y produces carbon monoxide,²¹ according to the reaction:



The evolution of carbon monoxide from the fibres creates porosity which can reduce the fibre strength.

The current TEM observations also showed that after heat treatment at 1300 and 1400°C, β -SiC in the fibres changed from an incompletely crystallized structure to grains of 10 nm in average size. Therefore, grain growth is another reason for the fibre degradation at 1300 and 1400°C.²⁰

If the material is glass-coated, carbon monoxide can accumulate beneath the glass layer building up its partial pressure. Under these conditions SiO_xC_y may decompose as.²¹



to produce silica. This silica, or that which may be present as a product of the fibre manufacturing process, can react with the interfacial carbon layer under a low partial pressure of oxygen to produce silicon monoxide and carbon monoxide. The evolution of carbon monoxide produces the micro-porosity observed in the carbon interfacial layer after the heat treatment. Debonding can easily occur between the fibre and the carbon coating, or inside the carbon layer, and this is the reason for the massive delamination experienced in the wedge opening test by the specimens heat-treated above 1200°C. Hence the loss of interlaminar strength in this case is due to the thermal degradation of the fibre strength and the carbon layer, and not to inner surface oxidation.

The microstructural examinations on glass-uncovered specimens showed that the oxidation process at 800°C only occurred to a depth of 0.5 mm (after 100 h). This limited oxidation could be explained by the fact that two chemical reactions, carbon oxidation and silica formation, occur simultaneously at high temperatures.²² When the uncovered specimens were heat-treated above 800°C, the carbon interphase firstly oxidized starting from the exposed surface, which left interstitial cavities between the fibre and the matrix. Then oxygen easily diffused into these interfacial cavities and reacted with exposed silicon carbide, leading to the formation of silica (Fig. 17). The formation of silica layer, either on the exposed surface or in the interphase, stopped the diffusion of oxygen and hence the oxidation of carbon interphase in the bulk material. Therefore, the oxidation process only occurred over a limited depth in the composite.

It should be pointed out that the mechanical properties of specimens in which the surface had been oxidized up to a limited depth, can be strongly dependent on the testing technique. It is believed that the oxidation process discussed does not affect properties of partially glass-covered samples using wedge opening test method, because for these specimens, the bulk material is not oxidized during the heat treatment and the notch cut after the heat treatment is already inside the bulk material. It has been reported for example that for an uncoated SiC/SiC composite with a thin carbon interphase the strength, measured by three-point bending tests, dropped appreciably after heat treatment at 800°C.²³ It is important to note that the strength measured from a bending test is strongly dependent on the presence of surface flaws, where cracks can easily initiate and propagate. Therefore, even if oxidation is confined to the specimen surface, it can reduce the bending strength of the composite significantly.

The wedge opening tests also showed that heat treatment affected the properties of specimens which were notched before heat treatments at 860 and 1200°C. During the heat treatment in this experimental routine, chemical reaction occurring at the unprotected notch tip may have influenced the initiation of cracks in this region. Absence of fibre pull-out and the lack of mirror boundary structure in the fractured fibres indicated that silica layer had possibly replaced the original carbon interphase in this region, leading to strong bond between the fibre and the matrix. The maximum applied load, at which a single dominant crack started to propagate, consequently dropped. However, because the carbon interphase still remained in the bulk material, the composite retained the mechanical strength and showed non-catastrophic failure.

The toughness of a material is usually characterized on the basis of linear elastic fracture mechanics, which may not be applicable straightforwardly to ceramic matrix composites. Toughness depends on the crack length at which it is measured and materials usually exhibit 'crack growth resistance,' or increase in toughness with the length of the crack. An absolute value of toughness as an intrinsic material property of ceramic matrix composites is difficult to define. However, if toughness is measured in a consistent manner, toughness values can be used for comparison purposes to provide an idea of the resistance to crack growth. The use of the wedge opening test described before to measure fracture toughness presents various problems. The most important is the indentation of the wedge when it is forced into the notch and the uncontrolled friction which results between the wedge and the specimen. This makes it difficult to know the value of the crack opening force. However, excellent repeatability of the results seems to suggest that this testing method can be used for comparative purposes for specimens with small dimensions before a more controlled testing method has been developed.

The relationship between normalized stress intensity factor and crack length for the present wedge opening test has been obtained by finite element calculations²⁴ as a function of applied load, angle of the wedge and coefficient of friction between wedge and specimen. Using this information, values of fracture toughness have been calculated for the composite in different conditions. They are given in Tables 1 and 2. Two different load values have been used: one corresponds to the first load drop, which may indicate the initiation of a crack at the notch tip; the other is the maximum load. Coefficients of friction of 0.1 and 0.5 have been assumed in the calculation of the fracture toughness. The results of these tables

Table 1. Fracture toughness of the SiC/SiC composite (results based on maximum applied load)

Conditions	Maximum applied load (KN)	K_{Ic} (MPa m ^{1/2}) [$\mu = 0.1$]	K_{Ic} (MPa m ^{1/2}) [$\mu = 0.5$]
As-received:	1.75	26.76	10.27
	1.85	28.29	10.86
	1.88	28.75	11.04
Heat-treated and notched:			
1000°C	2.02	30.89	11.86
1150°C	2.05	31.24	12.03
Notched and heat-treated:			
860°C	1.48	22.63	8.69
1200°C	1.21	18.50	7.10

Table 2. Fracture toughness of the SiC/SiC composite (results based on crack initiation load)

Conditions	First load drop (KN)	K_{Ic} (MPa m ^{1/2}) [$\mu = 0.1$]	K_{Ic} (MPa m ^{1/2}) [$\mu = 0.5$]
As-received:	1.24	18.96	7.28
	1.37	20.95	8.04
	1.23	18.81	7.22
Heat-treated and notched:			
1000°C	1.37	20.95	8.04
1150°C	1.40	21.41	8.22
Notched and heat-treated:			
860°C	0.98	14.98	5.75
1200°C	0.55	8.41	3.23

illustrate both the effectiveness of the glass coating in preventing the degradation of the material heated below 1200°C, and the damaging effect of having notched the specimens before heat treatment. No results could be obtained for the material heated above 1200°C due to its total loss of interlayer strength and massive delamination.

Acknowledgement

The authors wish to acknowledge the support received from Rolls-Royce plc, and they are grateful to Dr M. J. L. Percival for his help and discussion through this work.

References

- Wei, G. C. & Becher, P. F., *J. Am. Ceram. Soc.*, **67** (1984) 571.
- Marshall, D. B., Cox, B. N. & Evans, A. G., *Acta Metall.*, **33** (1985) 2013.
- Fitzer, E. & Gadow, R., *Am. Ceram. Soc. Bull.*, **65** (1985) 326.
- Lamicq, P. J., Bernhart, G. A., Dauchier, M. M. & Mace, J. G., *Am. Ceram. Soc. Bull.*, **65** (1986) 336.
- Evans, A. G. & McMeeking, R. M., *Acta Metall.*, **34** (1986) 2435.
- Evans, A. G. & Cannon, R. M., *Acta Metall.*, **34** (1986) 761.
- Marshall, D. B. & Swain, M. V., *J. Am. Ceram. Soc.*, **71** (1988) 399.
- Evans, A. G. & Marshall, D. B., *Acta Metall.*, **37** (1989) 2567.
- Evans, A. G., Zok, F. W. & Davis, J., *Compos. Sci. Technol.*, **42** (1991) 3.
- Strife, J. R. & Sheehan, J. E., *Am. Ceram. Soc. Bull.*, **67** (1988) 369.
- Buchanan, F. J. & Little, J. A., *J. Mater. Sci.*, **28** (1993) 2324.
- Luthra, K. L., *Carbon*, **26** (1988) 217.
- Lamouroux, F., Naslain, R. & Jouin, J. M., *J. Am. Ceram. Soc.*, **77** (1994) 2058.
- Naslain, R., *Journal of Alloys and Compounds*, **188** (1992) 42.
- Cavalier, J. C., Lacombe, A. & Rouges, J. M., in *Developments in the Science and Technology of Composite Materials. Proc. ECCM-3*, ed. A. R. Bunsell, P. Lamicq & A. Massiah. Elsevier Applied Science, London 1989, p. 99.
- Yajima, S., Silicon carbide fibres. In *Handbook of Composites, Vol 1*, ed. W. Watt & B. V. Perov. Elsevier Science Publishers, London, 1985, Ch. VI.
- Laffon, C., Flank, A., Lagarde, P., Laridjani, M., Hagege, R., Olry, P., Cotteret, J., Miquel, J., Hommel, H. & Legrand, A., *J. Mater. Sci.*, **24** (1989) 1503.
- Porte, L. & Sartre, A., *J. Mater. Sci.*, **24** (1989) 271.
- Bleay, S. M., Chapman, A. R., Love, G. & Scott, V. D., *J. Mater. Sci.*, **27** (1992) 5389.
- Man, T., Hecht, N. L., McCullum, D. E., Hoenigman, J. R., Kin, H. M., Katz, A. P. & Cipsitt, H. A., *J. Mater. Sci.*, **19** (1984) 1191.
- Bibbo, G. S., Benson, P. M. & Pantano, C. G., *J. Mater. Sci.*, **26** (1991) 5075.
- Grathwohl, G. & Thummler, F., *J. Mater. Sci.*, **13** (1978) 1177.
- Frety, N., Molins, R. & Bousuge, M., *J. Mater. Sci.*, **27** (1992) 5084.
- Zarate, F., PhD Thesis, University of London, 1995.